Thesis Title: Hydrophobic coatings and organic additives in Hellenistic-Roman mortars: the case study of Crete.

Degree: PhD Conservation (part-time), SHARE

Candidate: Vasiliki Kontogianni

Year of Presentation: January 2022

Contents

List of Figures

List of Tables

Summary

The thesis evaluated the applicability of Reflectance FTIR micro-spectroscopy for detecting and identifying organic additives in mortar matrices. The advantage of the method to provide spatially resolved data non-destructively, was balanced against reported limitations associated with reflectance spectral distortions and interference of inorganic mortar components in the spectral projection of organic additives. The identification methodology was designed according to these specifications and tested on laboratory prepared analogues of organic additives likely used in ancient mortars and their mortar mixtures of pre-defined concentrations and on ancient mortar samples suspected to contain organic additive in their composition.

The evaluation was carried out progressively, beginning from the development of a Chemical Peak Assignment Database (CPAD) that incorporated all the reflectance spectral data obtained from the analogues, exploring approaches of spectra interpretation and determining characteristic reflectance spectral features of organic mortar additives. The methodological outcomes were assessed through a series of identification experiments on laboratory analogues of which the nature of the organic material and its concentration in the mortar mixture were unknown at the time of analysis. The use of Principal Component Analysis as a complementary validation method to the CPAD identification methodology was assessed, following common practices on case studies employing Reflectance FTIR spectroscopy (Sarmiento et al., 2011; Rosi et al., 2010; 2009).

The challenges of identification posed by the physico-chemical properties of organic materials and the interference with inorganic mortar components were further studied through the analysis of archaeological mortar samples which were expected to deliver more complex reflectance spectral profiles due to their susceptibility to decay and biological attack.

The thesis structure offers a holistic approach to the evaluation of the method, incorporating the theory of Reflectance Spectroscopy and the specifications of the analysed materials into the design and execution of the identification methodology.

Acknowledgements

Writing these final lines of my thesis, I bring back the people who inspired, motivated and guided me throughout these years of hard work; The archaeologists and excavators of the three archaeological sites, Ms. Stavroula Markoulaki (Polyrrhenia), Dr Elpida Hadjidaki (Phalasarna) and Dr Vanna Niniou-Kindeli (Aptera) who provided the archaeological material and shared my excitement on the research of organic mortar additives. These three women shaped my perception of archaeology through enlightening conversations and visits on the sites, sharing their knowledge and experience in the interpretation of outcomes.

I am particularly grateful to the archaeologist Anastasia Tzigounaki, former director of the of the 25th Ephorate of Prehistoric and Classical Antiquities of Chania (until October 2014) and current director of the Ephorate of Antiquities of Rethymno, for authorizing permission of sampling and study, the provision of relevant photographic material from her systematic excavation at the coastal Middle Minoan III – Late Minoan I settlement “Kalo Chorafi” of Milopotamos, Rethymnon, for mentoring and patiently tolerating me all these years talking about mortars and reflectance spectroscopy at work.

Special thanks are due to the director Dr Eleni Papadopoulou and the staff of the Ephorate of Antiquities of Chania, archaeologists Eua Tegou, Maria Skordou, Dr Katerina Tzanakaki who granted permission to sample and study the archaeological material under their jurisdiction and showed personal interest on the implementation of this research.

I am obliged to the architect Yiannis Christodoulakos, Ephorate of Antiquities of Chania, supervisor at the project “Consolidation and Completion of Selected Towers at the Hellenistic Fortification of Pollyrhenia, Chania” where the idea of researching organic mortar additives has initiated, while working as an archaeological conservator; to my wonderful colleague, architect Sofia Lousa, who provided me with the paper by Hellner on the Crene of Megara, when I was puzzling myself with the origin of the dark residue on the cistern floor of Polyrrhenia; the archaeologist Dimitra Goula, who accompanied me on my visits to Phalasarna.

My deep gratitude is due to my former thesis supervisor Dr Yiota Manti (2014-2018), Cardiff University, who saw the potential of the research topic and initiated its research. She also saw the potential in me and guided me towards high standards of research.

I cannot thank enough my supervisor Prof. David Watkinson (2018 onwards) for his guidance and support. Working under his supervision has been a life lesson and I will always cherish his advice.

Many thanks are due to supervisor Dr Nicola Emmerson who contributed knowledge and experience on the implementation of the thesis and supervisor Dr Ruth Westgate, Cardiff University, for her insight on the archaeological aspect of the thesis outcomes; Prof. Jane Henderson who also saw the potential of this research at its initial stage and who always shared precious advice on balancing studies and work.

This task would be much harder without the unconditional support from my husband, Yiorgos Iosifidis, to whom I dedicate this work. Deep gratitude is due to my mother, Kiriaki and my father, Yiannis, my brother Kostas and my closest friends Matina and Dimitra; my friends at Cardiff, Kuldip and Fotis, who always welcomed me to their home; my friends Eleftheria from Crete and Chris from the USA who had completed their PhDs and offered me comfort in desperate times and kept me in the right track.

Hard work, commitment and discipline describe the life of a PhD candidate. Frustration, guilts and hopeless nights give way to moments of extreme happiness and sense of achievement. Thus, if there is something that I could pass on to a new candidate is that all the hard work is worth it, offering a personal journey towards knowledge and a sense of contribution to science.

Chapter 1: Introduction

1.1 Research, Challenges and Prospects of Ancient Construction Technologies

Architecture encompasses and reflects the needs of humanity, its aesthetics, the interaction of people with their surroundings, even the personal relationships among individuals, forming a discipline that is affecting and being affected (Duyan, 2012, 7). Traces of this dialogue, between humanity and stimulus, are imprinted in architectural remains, assisting archaeology to reconstruct the history of mankind (Duyan, 2012, 7; Humphrey et al., 1998, 235).

Archaeological knowledge does not merely satisfy our inherited curiosity to understand our ancestors; it essentially evidences the constant presence of the same needs in humanity for shelter, defense, socialization and improvement in the quality of life. These needs, although affected by environmental and cultural factors which change decision-making and the selection of construction materials, are met through the surviving technological knowledge and practical experience which served as the baseline for the progression of civil engineering and architecture (Babu and Neeraja, 2017; Goldsworthy and Min, 2009).

Aspects of the action of “affecting and being affected” are embodied in the choices that the ancient builders made; different compositions and characteristics of materials would serve different construction needs, influenced by the availability of materials, trade and exchange of technological knowledge (Miriello et al., 2010, 2207, Theodoridou et al., 2013, 3263). Consequently, the study of ancient construction materials requires a multidisciplinary approach which involves civil engineering, material science, archaeology and architecture (Theodoridou et al., 2013, 3263).

Understanding technological knowledge employed in the past is important both for the archaeological record and more practically for heritage preservation. Today, traditional practices and materials are integrated in the restoration and conservation of monuments, as evidenced through the numerous case studies and experiments examining the durability of ancient constructions and the physico-chemical properties of materials (Moropoulou et al., 2005; Papayianni et al., 2013, 85; Degryse et al., 2002; Maravelaki-Kalaitzaki et al., 2011). This understanding not only ensures authenticity in the preservation process but can avoid the use of unsuitable incompatible materials that can speed up the decay of ancient structures. Of particular importance in this respect is the

composition, development and use of mortars and plasters, as they have an ongoing presence within the archaeological record from the Neolithic to the present day (Ventola et al., 2011, 3313; Theodoridou et al., 2013, 3263). They are composites consisting of a binder, water and natural or artificial aggregates in suitable proportions, used for bonding different types of stones and bricks in ancient and modern masonry or for plastering the surface of walls and cisterns (Miriello et al., 2010, 2207; Moropoulou et al., 2000, 45).

As lime and hydraulic lime mortars are the most common mortars historically, they have been extensively tested for their compatibility in the conservation of monuments (Theodoridou et al., 2013, 3263; Papayianni et al., 2013). Hydraulic lime mortars set and strengthen in aqueous environments, whereas lime mortars require air to strengthen (Ch.2, sections 2.2 and 2.3), (Papayianni and Stefanidou, 2006, 152). The hydraulic property was introduced to the lime mortar by the addition of natural or artificial aluminosilicate minerals, such as volcanic ash or crushed ceramics respectively (Regev et al., 2010, 3000; Papayianni and Stefanidou, 2006, 152).

The durability of hydraulic lime mortars is evidenced by the use of "*opus caementicium"* (Roman concrete) to construct major civil engineering works, such as aqueducts and watercourses for the supply of fresh water within cities (Bull et al., 2003, 149; Viaene, 1997, 406; Regev et al., 2010, 3000; Malinowski, 1981, 342). Reflecting the high degree of sophistication in Roman engineering, through its remarkable preservation, is the gamma-shaped cistern of the Ancient city of Aptera in west Crete, Greece. The cistern was constructed during the early Roman period (1st century AD) in the *opus caementicium* form (fig.1) (Niniou-Kindeli, 2000, 323). The walls of the cistern were lined with bricks and plastered with hydraulic mortar for achieving maximum hydrophobicity (Niniou-Kindeli, 2002; 2008).

At Ancient Polyrrhenia, west Crete, Greece, the continuation of mortar and plaster use from the Hellenistic to Roman period is evident in the surviving constructions; an open cistern, dated to the Roman period (2nd century AD), was adjusted to the Hellenistic masonry as an addition to the pre-existing Hellenistic water-management system of the city, which likely date from the 2nd century BC (Markoulaki and Goula, 2013, 139-141). Both the wall and the floor of the cistern were plastered with hydraulic mortar, whereas mortar and rubble stones were used in the masonry (fig.2), (Markoulaki and Goula, 2013, 143).

Figure 1: The gamma-shaped cistern of Aptera. The walls of the cistern are built in the opus caementicium form and the brick surface is plastered with hydraulic mortar (view from the side).

Figure 2:The plastered floor of the open cistern, attached to the Hellenistic wall, Polyrrhenia (view from above).

These particular water-related constructions are not selected as random examples, as they will be an integral part of this thesis which examines a potential methodology for detecting the presence of organic additives within plasters. It is postulated that organic materials, such as egg white, blood, egg yolk, animal glue and casein, were added to mortars to improve their plasticity, impermeability, hardness and regulation of setting rates (Moropoulou et al., 2005, 295; Ventola et al., 2011, 3313).

Ancient texts report their use. Vitruvius, in the books VII and VIII from his multivolume work *De Architectura* records the use of organic additives, such as olive oil, pitch, wax and glue in flooring and stuccowork. While this provides historical support for their use, there is debate about the source of the information Vitruvius reported (Lewis, 1999, 172; Erişmiş and Gezerman, 2013, 13326). Applying scientific analysis to archaeological samples has the potential to confirm the presence of organic additives but this requires an analytical methodology that is proven to be accurate and reproducible for this purpose.

The challenge of identifying organic materials and understanding how they were utilized technologically within mortars begins from the chemistry of organic materials. These are chemically complex components that are susceptible to decay, with unpredictable and complex chemical alterations caused by the synergy of time and exposure or burial conditions, as well as biological attack (Kuckova et al., 2009, 42; Sarmiento et al., 2011, 3601; Sickels, 1981, 28). Additionally, the likely low initial quantity of organic additive in the mortar, a lack of physical evidence and the limited historic background (see Ch.3) seem to have discouraged the systematic study of organic mortar additives (Kuckova et al., 2009, 42; Sarmiento et al., 2011, 3601; Sabbioni et al., 2003; Maravelaki-Kalaitzaki, 2005; Polikreti and Maniatis, 2003; Buergo and Gonzales, 2003; Rampazzi et al., 2004, Martin-Gil et al., 2005, Fang et al., 2013, 1). Consequently, evidence derived from the use of a standardized qualitative methodology that offers accuracy, precision and reproducibility is not widely available (Fang et al., 2013, 1). This presents problems for a broader study of these additives, while an analysis method may offer sound evidence that an organic residue is present, these can only be assessed individually taking into account the methodology employed each time (Ch. 3).

This absence of a standardized methodology is reflected in the range of analytical methods which have been employed for the identification of organic mortar additives, such as chemical spot testing, Fourier Transform Infrared Spectroscopy (FTIR), Gas Chromatography-Mass Spectrometry (GC-MS) and immunological methods (Fang et al., 2013, 1; Singh and Arbad, 2014, 385; Rampazzi et al., 2004; Kuckova et al., 2009). The

common ground of the methods reported is their destructive application on samples likely to have retained organic residues, in order to overcome problems of inorganic interference during the chemical identification of the organic component (Singh and Arbad, 2014; Rampazzi et al., 2004; Buergo and Gonzalez, 2003; Buonasera, 2007; Oudemans and Erhardt, 1996, 137). Considering the preservation and quantity issues described above, sample size necessary for destructive analysis and the presence of microorganisms sharing similar chemistry with the organic additives, the outcomes of such analysis may be misleading in either direction (Kuckova et al., 2009, 42; Fremout et al., 2012, 39). Extracting organic components cannot provide spatial information on the distribution of an organic additive, limiting the exploration of technology and purpose (Ramirez-Barat and De la Vina, 2001, 282).

Taking into consideration the limitations of current methodologies for detecting organic residues in mortars the thesis aim is:

- To explore the potential of Reflectance Fourier Transform Infrared micro-Spectroscopy (micro-FTIR) as a non-destructive methodology for detecting the presence, chemistry and spatial distribution of organic additives within mortar mixtures, and assess its value for identifying past technologies and developing best practice within heritage conservation.

The following objectives were employed to address this aim:

- Use historical and analytical evidence to identify the range of organic additives likely used in building mortar in ancient contexts.
- Apply Reflectance micro-FTIR to a range of organic additives and their mixtures with mortar to produce a database for identifying small quantities of organic additives in mortar.
- Assess the effectiveness of statistics for enhancing interpretation of the spectral database.
- Employ the FTIR database to examine archaeological mortar samples and discuss the success of the database as a standardised methodology for detecting organic residues in mortars.

1.2 Thesis structure

Acknowledging that *"how"* defines the first milestone in the study of organic mortar additives of antiquity, the thesis focuses on the detection and characterisation methodology employed. Evaluating the application of Reflectance FTIR micro-spectroscopy for detecting and identifying organic additives in mortar mixtures begins with considering which organic materials may have been added to ancient mortars. A review of the available historic sources, archaeological evidence and methodologies employed introduces existing knowledge and analytical approaches. The evaluation of the available information and the reported limitations of analytical methods directs the design of the methodology. The challenges of analysis posed by the physico-chemical properties of organic materials, interference of inorganic mortar components in the data collection and the susceptibility of organic materials to decay are discussed to underpin the experimental work.

The experimental research focuses on the development of a Reflectance micro-FTIR methodology for detecting organic residues in mortar via a series of connected experiments using laboratory prepared standards and authentic ancient mortar samples. These begin with selecting organic materials that are representative of ancient mortar additives and producing a mortar analogue that reflects a typical composition used in the past as standards. Reflectance micro-FTIR spectra of these were produced and a set of spectra of organic additive/mortar mixtures in pre-defined concentrations were collected to produce a set of standard reference spectra. The Reflectance micro-FTIR spectra of these standards were used to develop a chemical peak assignment database (CPAD). This records all the characteristic spectral information of each analyzed material in the CPAD including any spectral features affected by reflectance spectral distortions and inorganic interference.

The effectiveness of the CPAD as an identification tool was tested on spectra obtained from laboratory prepared standards in which the nature of the organic material and its concentration in the mortar mixture were unknown at the time of analysis. Each unknown spectrum was interpreted based on peak-by-peak comparative chemical assignments through the CPAD, instead of merely visual interpretation and comparisons between spectra to overcome potential issues of false identification, due to chemical similarities among materials that share common absorption bands. This was followed by statistical analysis as a complementary validation method to the CPAD identification, using Principal Component Analysis (PCA), (Sarmiento et al., 2011; Rosi et al., 2010, 2009).

Using the CPAD methodology derived from the results of the experimental study, Hellenistic to Late Roman period (4th century BC – 4th century AD) mortar samples from water-related constructions located on archaeological sites in West Crete, were characterised. These constructions were thought likely to have included organic additives in their composition due to the expected requirement for waterproofing. The objective was to test the capability of the CPAD methodology for detection and identification of organic additives present in complex spectral profiles produced by prolonged exposure to environmental conditions supporting biological activity, aging and external depositions. The outcomes were used to improve the CPAD identification methodology for discriminating between peaks produced by biogenic organic depositions and intentionally incorporated organic additives. Optical and Scanning Electron microscopy were also employed in the analysis of samples as complementary methods to Reflectance FTIR micro-spectroscopy.

The thesis concludes with a discussion of the use of the CPAD to detect and identify organic additives in mortar, its confidence level and the potential for its wider adoption as an analytical methodology.

Chapter 2: The Technology of Mortars and Plasters

2.1 Early use of mortars

An important and continuous concern of early humans was the securing of shelter (Humphrey et al., 1998, 235). Natural protected spaces, such as caves, were the first to be occupied, but as the population grew and gathered in fertile areas more permanently, natural shelters were no longer sufficient and humans had to construct their own shelters. The growth and increasing complexity of societies required buildings of religious practice, fortifications and water-related public works (Humphrey et al., 1998, 235).

Construction technology developed gradually following the progress of society, the availability of materials and the limitations or advantages of the surrounding environment (Humphrey et al., 1998, 235). The discovery of mortars provided the technological means for producing constructions of increased durability against natural weathering, adequate to serve more complex demands than merely housing. The continuous use of mortars from as early as the Neolithic period to nowadays reflects their important role in construction technology (Ventola et al., 2011, 3313).

As defined in section 1.1, *"Mortar"* is the composite material prepared from a binder (mud or lime), an aggregate (e.g., sand) and the appropriate amount of water (Viaene et al., 1997, 405; Ventola et al., 2011, 3313). When mortars are applied on the surface of walls or cisterns are referred to as "*plasters*", whereas when used as the binding agent within a masonry are referred to as "*joints*" (Moropoulou et al., 2000, 45).

Early construction materials included mud and stone either rubble or worked in blocks. Mud was used as the binding medium in masonry and for the production of mud bricks, since the material was readily available and abundant (Moropoulou et al., 2005, 295). The production and use of lime as binding medium and protective surface layer on masonry was developed in the Middle East and dated as early as the Neolithic period, circa 12,000 BC (Chiotis et al., 2001, 328; Regev et al., 2010, 3000, Ventola et al., 2011, 3313). In Catal Huyuk, Turkey, lime and its admixtures with raw materials served different construction requirements from at least the 6th millennium BC (Viaene et al., 1997, 405).

In the earliest Minoan buildings, the consolidation of rubble walls was achieved by the application of subsequent layers of mud or mixture of mud with lime and straw. These layers were left to harden before a final layer of lime was applied over them and polished after drying (Chiotis et al., 2001, 328). The plastering technique, combined with archaeological evidence of lime stored in Minoan bowls rather than in large reservoirs,

suggests that lime was produced in small quantities and thus, it was treated as a precious binding material (Chiotis et al., 2001, 328).

Lumps of lime mixed with crushed bones were unearthed at the systematic excavation at the coastal Middle Minoan III – Late Minoan I settlement “Kalo Chorafi” of Milopotamos, Rethymnon, Crete (Tzigounaki, 2020, personal communication). Crushed bones used as aggregates were also identified in lime plasters from the Late Helladic III period in Thebes, Greece, supporting the influence of the Minoan craftmanship in the Greek mainland (Brysdaert, 2008).

The lime/crushed bone mortar was attested in two areas of the “Kalo Chorafi” settlement in Crete (fig.3). However, in two other areas, where the remains of wall paintings were found, the plaster did not contain any crushed bones or shells, suggesting that different lime mixtures or different size of aggregates were preferred when the surface was intended for painting (Tzigounaki, 2020, personal communication). A lump of lime in conical form that preserves the imprints of a conical cup was discovered in close proximity to pigments, indicating its use in the preparation of the wall painting (fig.4).

Figure 3: Lumps of lime and crushed bones from Area 6, associated with wall plasters, “Kalo Chorafi” MMIII-LMI settlement (courtesy of Anastasia Tzigounaki, Director of Ephorate of Antiquities of Rethymno and excavator of the site).

Figure 4: Lump of lime in the shape of conical cup "Kalo Chorafi" MMIII-LMI settlement associated with wall painting (courtesy of Anastasia Tzigounaki, Director of Ephorate of Antiquities of Rethymno and excavator of the site, photography by N. Daskalakis).

Crushed bones and shells incorporate calcium carbonate in their chemical composition thus, they would have been considered as compatible aggregates to lime which derives from the firing of calcium carbonate stones (Brysdaert, 2008, 2765). Their presence in the lime mixture as fragments suggests that bones and shells were added after the production of lime as fillers and strengthening aggregates rather than as a source of calcareous binder (Brysdaert, 2008, 2765; Regev, 2010, 3007; Chiotis et al., 2001, 328).

2.2 Production of Lime Mortar

The production of lime required the firing of limestone in kilns where temperature reached 800-900°C (Chiotis et al., 2001, 328). An example of a lime kiln, likely of the *"pit"* type, was discovered near the Bishop's Basilica in Egnatia, SE Italy and it is dated between the 4th to 6th century AD (fig.5). The limestones for firing were placed over a pile of fuel producing a cone which was then lined with mud and straw for maintaining the firing process (Stellati et al., 2012, 196).

Figure 5: Limekiln, likely of the "pit" type, Egnatia, SE Italy (Stellati et al., 2012, 195).

When limestone or other forms of calcium carbonate ($CaCO_3$) are fired in such temperatures they evolve carbon dioxide, leaving a white residue of calcium oxide (lime, quicklime) according to reaction (a):

$CaCO_3$ (in ↑T°) → $CaO + CO_2$ ↑ (Gauri and Bandyopadhyay, 1999) (a).

The freshly calcined lime will react readily with water to form "slaked lime", a mixture of oxide and hydroxide, which in the presence of excess water forms a soluble paste of calcium hydroxide ($Ca(OH)_2$) (Edwards and Farwell, 2008, 985), according to reaction (b):

$CaO + H_2O \rightarrow Ca(OH)_2$ (Gauri and Bandyopadhyay, 1999) (b).

When added as an aggregate to the mortar, sand does not react with lime but serves as a bulking agent in the mixture and controls its shrinkage during drying (Edwards and Farwell, 2008, 985; Duran et al., 2008, 353). Alternative sources of aggregate would be used when sand was not available. In Sagalassos, Turkey, mortar samples dated from the beginning of the Imperial period to the 6^{th} – 7^{th} centuries AD, obtained from different architectural structures, tombs, as well as from water-related constructions (casings of water conduits, jointing of terracotta pipes and plasters from cisterns) contained neither river nor quarry sand but local limestone, since neither rivers or quarries were available within the Sagalassos territory (Degryse et al., 2002, 1458).

Lime mortars are considered "*aerial*" because they harden in air though the reaction of calcium hydroxide ($Ca(OH)_2$) with carbon dioxide (CO_2) that results in the calcination of lime into calcium carbonate ($CaCO_3$), according to reaction (c):

$(Ca(OH)_2) + CO_2 \rightarrow CaCO_3 + H_2O$ (Papayianni and Stefanidou, 2006, 152) (c)

Water serves as the medium for reaction between carbon dioxide and calcium hydroxide. Carbon dioxide dissolves in water forming H^+, HCO_3^- and CO_3^{2-} ions, reducing the pH of the solution. The acidic solution enables the dissolution of calcium hydroxide and the release of Ca^{2+} ions which react with the CO_3^{2-} to form $CaCO_3$. The reaction continues until all the calcium hydroxide becomes calcite or until water evaporates in the capillaries due to the heat generated from the exothermic reaction (Ventola et al., 2011, 3315).

Although water is essential for the calcination process, excess amount produces the opposite outcomes, since the diffusion of carbon dioxide is prohibited (Edwards and Farwell, 2008, 985; Moropoulou et al., 2000, 53). Thus, the amount of water added to the mortar, as well as the prevailing humidity during construction, are crucial during setting.

Calcination is a slow process and may remain incomplete in environmental conditions of very high or very low humidity. Thus, lime mortars may have had reduced mechanical properties and durability against moisture (Ventola et al., 2011, 3315). However, despite the hardening flaws, lime mortars were innovative materials in antiquity and had spread from the Middle East to Greece and then Rome with continuous use until modern times (Moropoulou et al., 2005, 295; Ventola et al., 2011, 3313).

Extended use of lime mortars, usually mixed with river sand or local crushed calcite stones in various fractions, is found on irregular wall surfaces from porous stone, floors, walls and ceilings, as well as sub-layers of murals (Papayianni and Stefanidou, 2006, 151; Orlandos, 1955-60, 57; Viaene et al., 1997, 405). Such applications are archaeologically evident in

Greece from the late Archaic period until the end of the 2nd century BC / early 1st century BC, when hydraulic mortars were developed by the Romans (Chiotis et al., 2001, 328; Orlandos, 1955-60, 57).

2.3 Hydraulic Lime Mortar and Roman Concrete

The Roman concrete or "*opus caementicium"* was a hydraulic lime mortar characterized by increased mechanical strength and durability against moisture, enabling the construction of large-scale works, such as bridges and harbors (Viaene, 1997, 406; Regev et al., 2010, 3000; Malinowski, 1981, 342). The advanced properties of hydraulic mortar rely on its strengthening in aqueous environments and in the absence of carbon dioxide, overcoming the incomplete calcination issues observed in lime mortars (Papayianni and Stefanidou, 2006, 152).

Hydraulic or pozzolanic properties were achieved by the addition of aluminosilicate minerals ("*pozzolans*") in the mortar. The name derives from "*pozzolana*", a sandy volcanic ash that was firstly quarried in Puteoli (Pozzuoli), an area near the Bay of Naples and was the main component in Roman hydraulic mortars (Humphrey et al., 1998, 244). The term has been traditionally used thereafter for all the materials that enabled pozzolanic reactions, such as highly disordered aluminosilicate minerals of natural origin (volcanic ash or limestone tuffs) or fabricated ones (crushed ceramics of low firing or brick powder) (Regev et al., 2010, 3000; Papayianni and Stefanidou, 2006, 152).

Sample S6, obtained from a plastered stone related to the wall of the cistern of Ancient Polyrrhenia (see Ch.11), provides an example of hydraulic lime mortar that contains artificial aluminosilicate minerals in the form of ceramic inclusions and sand aggregates (fig.6).

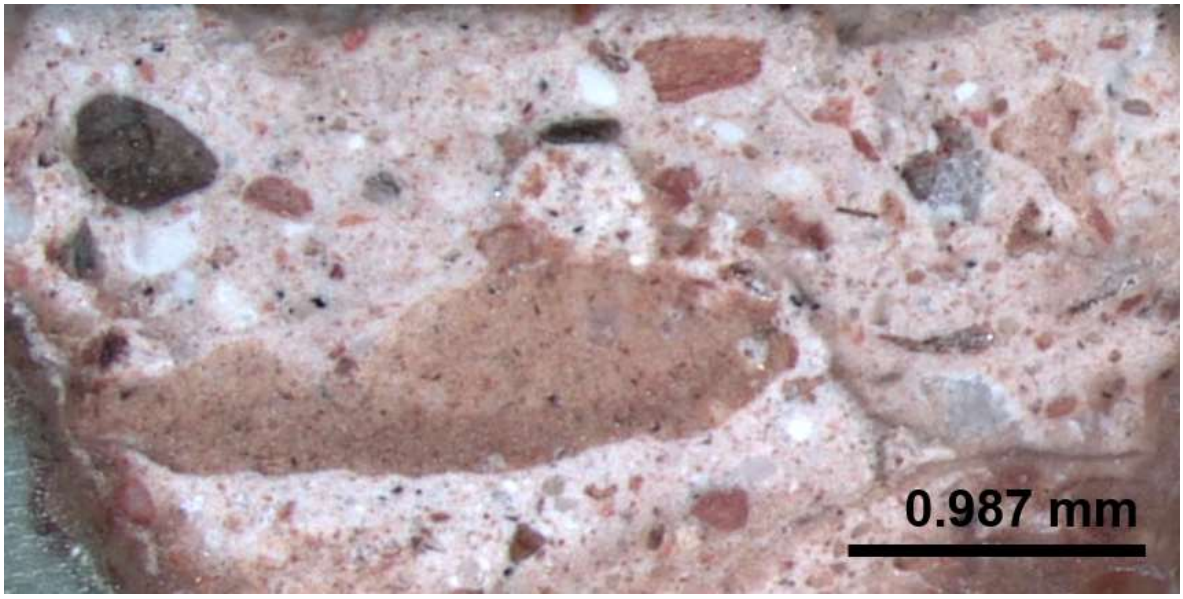

Figure 6: Cross-section of sample S6, Polyrrhenia, showing ceramic inclusions of different size (red-brown particles) and sand aggregates (black and grey particles) in the hydraulic lime mortar composition.

The ability of hydraulic mortars to harden in aqueous environments and in the absence of air and carbon dioxide, derives from the reaction of lime with the aluminosilicates which results in the formation of calcium silicate hydrates and calcium aluminum hydrates according to reaction (d):

$Ca(OH)_2$ + aluminosilicates + $H_2O \rightarrow$ C-S-H + C-A-H (d).

where C = CaO, S = SiO_2, H = H_2O and A = Al_2O_3 (Papayianni and Stefanidou, 2006, 152; Regev et al., 2010, 3008).

The aluminosilicates were added either in the mortar mixture of slaked lime and aggregate or during the lime production phase by adding clay to the calcite material. In both cases, hydrated calcium aluminosilicate minerals were formed and set in the presence of water (Regev et al., 2010, 3008). The use of impure limestone that naturally contained aluminosilicates would also have produced lime that had a degree of hydraulic properties (Moropoulou et al., 2005, 296).

2.4 Mortar Compositions and Additives

The analysis of the physico-chemical properties of aerial and hydraulic mortars enables a further understanding of construction technology and the criteria of selecting the most appropriate type of mortar in relation to its intended function. The chemical composition / source, size and quantity of the aluminosilicates present in the mixture

produced different types of hydraulic mortars, or more precisely, mortars of different degrees of hydraulic properties (Duran et al., 2008, 353, Moropoulou et al., 2000, 53).

The analytical work of Maravelaki-Kalaitzaki et al. (2003) on the physico-chemical properties of mortars from Crete, Greece, dated from the Minoan period to the present, identified four types of mortars based on the quantity of aluminosilicates and their source. The hydraulic properties were measured based on the amount of CO_2 bound to carbonates and that of water bound to hydraulic components, measured as weight loss percentage using Thermal Analysis (Maravelaki-Kalaitzaki et al., 2003, 655):

1. Typical lime mortars contain less than 1.5% of chemically bound water to hydraulic components and have a CO_2 content of 30-38%.
2. Hydraulic lime mortars contain 5% of chemically bound water to hydraulic components and have a CO_2 content of 27-34%.
3. Crushed brick – lime mortars contain 4-5% of chemically bound water to hydraulic components and have a CO_2 content of 24-26%.
4. Pozzolanic mortars contain more than 7% of chemically bound water to hydraulic components and have a CO_2 content less than 20%.

The classification above shows that a typical lime mortar may also contain some portion of hydraulic components but in negligible quantities, not capable of producing sufficient pozzolanic reactions.

Crushed brick mortar or mortars that contain ceramic inclusions exhibit hydraulic behavior because of adhesion reactions that occur at the ceramic-matrix interface. The hydraulicity depends on the ceramic size and type (raw materials, clays and firing temperature) and the calcium hydrate content of the mortar that is necessary for the formation of calcium silicate at the interface along the ceramic fragment (Moropoulou, 2000, 53; Maravelaki et al., 2003, 651). Additionally, the penetration of lime within the ceramic pores decreases their size and produces a less permeable mortar which is preferred in waterproofing applications (Moropoulou, 2000, 53). The crushed brick mortar is less frost-resistant and mechanically weaker than mortars made with pozzolanic ash, thus it was not used for joints (Degryse et al., 2002, 1459).

Although the extended use and development of systematic application techniques of hydraulic mortars is attributed to the Romans in the 1st century BC (Hamphrey et al., 1998, 243; Silva et al., 2005, 35), archaeological evidence suggests that pre-Roman masons were aware of the waterproofing effects of pozzolans in the mortars. Mycenean

constructions (1500 BC) that required increased moisture resistance, such as the floor of the Courtyard in the Tiryns Palace and the Cistern at the Argive Heraion, Greece, incorporated ceramic inclusions in the plasters (Chiotis et al., 2001, 330). Similar plastering practices have been identified at cisterns of the 6th to 5th century Classical Greece at Corinth, Olympia, Delos and Thera (Viaene et al.1997, 405; Papadimitriou and Kordatos, 1995, 277) and at the Hellenistic harbor of Zea (Orlandos, 1955-60, 5).

Hydraulic mortars were not intended to replace lime mortars in use, since each served to provide different mechanical requirements. The analysis of mortar samples from the Colosseum (80 AD) and the cistern of the Roman Legion in Albano (2nd century AD) showed that both types were in use during the Roman period: a lime mortar of low aluminosilicate content was used at the Colosseum where water resistance was not necessary, whereas a hydraulic mortar was used on the cistern (Silva et al., 2005, 40).

The coexistence of lime and hydraulic lime mortars within an extended chronological period is evident from the study of mortars from Rhodes, Greece, dating from the 2nd century BC to modern days, including Byzantine, Knight's 1st and 2nd period (14th to 16th centuries AD), Ottoman (16th-19th centuries) and modern restoration. Both types of mortars were being used throughout these periods, selected according to the intended purpose (Moropoulou et al., 2000).

At Sagalassos, the water-related constructions dating from the early Hellenistic to Byzantine period were plastered by crushed ceramic mortars for ensuring the waterproofing of surfaces. Where higher compressive strength was necessary, such as in the masonry of the Roman baths, the selected mortar included volcanic aggregates instead of ceramic inclusions (Degryse et al., 2002, 1459).

Although the waterproofing properties of hydraulic mortar were based on the chemical composition of the components, achieving a fine polished plaster surface finish would improve hydrophobic performance. Additionally, the polished surface would minimize the accumulation of calcium carbonate deposits (also referred to as "*sinter*") and ensure their easy removal during maintenance and thus minimizing interruption to the flow and supply of water (Bobee et al., 2010, 12; Hodge, 2002, 227). The fine mixture of quicklime, sand and crushed bricks applied on the U-shaped channel at the city of Forum Julii, south-eastern France (circa 20-25 AD) served such purposes (Bobee et al., 2010, 3).

A black coating composed of a mixture of asphalt and animal fat, applied over the crushed brick plaster on the fountain house in Megara, Greece (1st quarter of the 5th century BC),

indicates practices that aimed on the improvement of the hydrophobic properties of hydraulic mortars and their protection against sinter (Hellner, 2006, 177). In this instance, hydrophobicity was achieved through the use of organic materials.

The surface treatment of hydraulic plasters suggests that improvements of hydrophobic properties and durability against damaging factors were desirable if not necessary. Winter (1971) states that hydraulic Roman mortars, especially those applied on water-related constructions, would not have been entirely waterproof and regular maintenance or covering by a tiled roof would be required. Although the author does not discuss further the possible factors affecting the hydrophobic properties of these mortars, there are many potential routes that facilitate their decay during use.

The environmental factors that would trigger physical and chemical deterioration processes against the hydrophobic behaviour of mortars include the supply of moisture and salts, temperature fluctuations and/or extremes and dynamic load (e.g., wind) (Hees et al., 2004, 644). Accordingly, possible degradation processes would occur, such as: freeze/thaw cycles, crystallization of soluble salts in the pores of the mortar, chemical conversion of components and/or deposits leading to the formation of high-volume compounds, wind and water erosion, biological deterioration, increase of hygroscopic absorption due to salts which produced swelling and shrinkage leading to crack propagation (Hees et al., 2004, 645; Ashurst, 1998, 4; Degryse et al., 2002, 1458). These processes are likely to have taken place during the use of a water-related construction, causing powdering, cracking and spalling of the plaster surface, decreasing its durability and waterproofing properties (Hees et al., 2004, 647; Degryse et al., 2002, 1458).

Adding specific organic materials to mortar aimed at improving their physical properties and consequently their durability against decay. In some instances, these additives also improved working properties. Protein containing egg whites, egg yolk, blood, animal glue and casein, along with the terpene containing milk of figs, are referenced as mortar additives that improved the plasticity, impermeability, hardness and the regulation of setting rates of the mixture (Moropoulou et al., 2005, 295; Ventola et al., 2011, 3313). Fibrous organic materials were used for avoiding cracks due to the shrinkage of the mortar during setting (Moropoulou et al., 2005, 295).

The addition of blood was practiced by the Egyptian, Greek and Roman masons for modifying the physical behavior of the mortar. During wet phase, blood acted as a foaming agent that would enable air entraining that increased the workability of the mortar. Upon drying, the air bubbles would mineralize, enabling a fine distribution of the binder and the

pores in the inorganic matrix that improved its hydrophobic properties and its durability against freeze/thaw cycles (Jasiczak and Zielinski, 2006, 451).

Organic additives have also been used in ancient repair mortars and reconstructions. Andreotti et al. (2018) conducted research on repair mortars dated from 1st-3rd centuries AD and identified various organic additives used in the lime-based mixture. Combinations of lipids-proteins, beeswax and resins, plant oil and animal glue were added to the mortar depending on the type of the repair or the weight of the detached stone to be reattached in its original location (2018, 868).

These references describe the advantageous performance of organic materials as mortar additives and suggest that mortar technology may not have solely relied on the properties of the inorganic components. The use of organic mortar additives in antiquity defines the fundamental hypothesis of the thesis and is discussed through the available literature in Chapter 3.

Chapter 3: The Use of Organic Additives in Mortars

The study of ancient mortars is not merely a topic of archaeological interest in past technologies but also an applicable tool in Cultural Heritage Science for the preservation of architectural remains. Understanding the mortar formulations used in the past enables practitioners to either provide compatible modern materials or reproduce ancient recipes, which will improve the preservation of physical and historical integrity within the conservation process (Papayianni et al., 2013, 85).

The need to re-discover traditional materials and practices became more apparent when failures of Portland cement restorations were noticed (Ventola et al., 2011, 3313). Portland cement is the most widely manufactured and used construction material from its discovery in the second half of the 19th century to nowadays (Celik et al., 2014, 136; Ventola et al., 2011, 3313). Architectural conservation has followed this trend until damaging effects on stone monuments were associated with its use (Morillas et al., 2018, 43).

Portland cement is a composite material of two basic components, lime and clay, with additions of iron oxides (Fe_2O_3), alumina (Al_2O_3), silica (SiO_2) and gypsum in different chemical forms, for creating minerals that react readily with water to create bonds of pozzolanic properties (Aitkin, 2016, 27-33). The fabrication of Portland cement is complex and the end product varies in quality and properties, often carrying alkali oxide impurities (Na_2O and K_2O), sulphates (SO_3) and magnesium oxides (MgO) (Aitkin, 2016, 33). The advantages of cement are the quick setting times and its high mechanical resistance (Ventola et al., 2011, 3313). However, the incompatibility of the material with various natural stones and the leaching of soluble calcium and sodium sulphate salts with damaging effects on the stone have led to its rejection for such purposes (Ventola et al., 2011, 3313). Salt crystallization may cause efflorescence, fissures and cracks during the transition from the hydrated to the anhydrous form and vice versa (Morillas et al., 2018, 43). Effects of volume expansion have also been observed due to the delayed hydration of calcium and magnesium oxides, compared to the rest of the oxide additives in Portland cement (Chatterji, 1995). The strength of Portland cement binding agents often exceeds the materials they are binding, which can cause differential weathering issues and stresses (Maravelaki et al., 2003, 660). Another drawback is that the manufacturing of Portland cement causes the liberation of extreme amounts of green gas (CO_2) emissions into the environment which accelerates global warming (Babu and Neeraja, 2017, 43; Celik et al., 2014, 136).

Such corrosion and weathering effects should be minimized in mortars intended for application in architectural conservation. Restoration mortars must be characterized by compatibility with the ancient construction materials relative to their physico-chemical properties and should derive from environmentally sustainable processes (Papayianni et al., 2013, 84). Within this framework, natural organic materials reported in traditional practices of the past should be explored, in order to thoroughly understand the technology of mortars, their properties and quality of preservation against decay (Ventola et al., 2011, 3313).

This chapter introduces the organic materials that have either been reported in ancient texts as additives in mortars and plasters or detected and identified as additives by analysis (3.1). The critical review of available evidence assesses the degree of consistency in both analysis and reporting in order to define areas of uncertainty in the confirmation of the hypothesis (3.2). The outcome of this review and critique process shapes the study reported in this thesis, leading to a decision to evaluate reflectance FTIR micro-spectroscopy for detecting organic additive residues in mortar in a systematic manner (3.3).

3.1 Sources of Information for Detecting and Identifying Organic Additives

The evidence for additive usage starts with historic reporting by historically contemporary and later authors on the use of organic materials and their function in mortars (Table 1), followed by analytical evidence (Table 2) then evidence derived from the presence of oxalates on structures, analysis of later historic patinas and indirect detection from analysis targeting inorganic mortar components (Table 3). General scientific interest is identified via reviews of traditional mortar recipes (Table 4). This is followed by reviewing of experimental work investigating the properties of organic mortar additives and studies on the effectiveness of analysis techniques to detect them (Table 5).

3.1.1 Historic sources record instances of organic additives and their intended function in mortars and plasters.

Historic sources		
Organic Material / Purpose of Use	**Dating and Provenance**	**Reference**
Olive Oil - Waterproofing and anti-frosting coating or additive in lime mortars.	1st cent. BC	Vitruvius,Book VII, Ch.I, 6; 7
Pitch - Moisture repellent on walls.	1st cent. BC	Vitruvius, Book VII, Ch.VI, 2
Phoenician wax and oil - Protection of marble and wall plaster against light damage.	1st cent. BC	Vitruvius, Book VII, Ch.IX, 3
Maltha: slaked lime in wine mixed with pork fat and figs - Hard plaster for the walls of baths.	Uncertain	Pliny, Book XXXVI, LVIII
Milk and saffron - Plaster additive.	Uncertain Date - Elis, temple of Minerva	Pliny, Book XXXVI, LV

Table 1: Historic sources reporting the use of organic additives in mortars and plasters.

Vitruvius in his work, *De Architectura,* describes different organic mortar additives relevant to the purpose of use (Table 1): olive oil served as a waterproofing coating on mortars or in mixture with lime for anti-frosting applications in tiling (Book VII, Ch.I, 6; 7) and on the joints of terracotta tubes (Book VIII, Ch.VI, 8); pitch served as moisture repellent on walls (Book VII, Ch. VI, 2); a mixture of Phoenician wax and oil, also referred to as "*ganosis*", was applied on marble and wall plaster against light damage (Book VII, Ch. IX, 3); size (glue) served as a binder for pigments on wall paintings (Vitruvius, Book VII, Ch.X, 3).

Pliny, in his Natural History book, describes the application of a plaster worked with milk and saffron, likely dated at the classical period in Greece (Book XXXVI, LV). Another recipe of hard plaster, used especially for the walls of baths, is referred to as "*Maltha*". This plaster was prepared from freshly calcined lime, part of which was slaked in wine and then mixed with pork fat and figs that served as softening agents. The surface that received this plaster was firstly rubbed with olive oil (Book XXXVI, LVIII).

Most of the literary evidence on structural engineering derives from Roman writers, especially Vitruvius (late 1st century BC) and Pliny the Elder (1st century AD) (Humphrey et al., 1198, 235; Tavernor, 2009). Vitruvius was a military engineer and architect who produced a complete treatise on architecture, based on his practical professional experience and knowledge of Greek architecture of the previous three centuries (Tavernor,

2009; Lewis, 1999). Certain parts of his work are critically discussed in relation to his sources, questioning whether his writings are the outcome of personal experience or descriptions of past Hellenistic practices (Lewis, 1999). Similarly, Pliny's work is regarded by scholars as descriptive rather than explanatory, since the author focused on the collection of facts rather than checking for their accuracy and reliability (Paparazzo, 2001, 74).

Although Pliny acknowledges Vitruvius as a source of information in his Natural History book (Lewis, 1999), there are authors challenging the actual existence of Vitruvius as a person and writer of his books, based on the fact that many of his structural descriptions fail to work in practice (Erişmiş and Gezerman, 2013, 13327).

The validity of information from a historian's perspective is beyond the scope of this thesis. However, the description of organic mortar additives by both authors, especially that of the mixture of lime and oil for lining water pipes, suggests common or continual practices (Holland, 1962, 331). The systematic analysis of relevant structures will provide the evidence of such practices and contribute to the historian's dialogue.

3.1.2 Evidence of organic additives derived from analysis targeting organic detection.

Analytical Evidence			
Organic Material / Purpose of Use	**Dating and Provenance**	**Analysis**	**Reference**
Egg proteins, animal glue, plant oil, beeswax, resin - Ancient repair and bonding mortars.	1st - 3rd AD, Roman Imperial and Byzantine buildings of Hierapolis in Phrygia, Turkey.	Pyrolosis, GC-MS, XRD, Optical Microscopy	Andreotti et al, 2018
Sticky rice (starch), blood, juice of plants, drying oil, egg white - Mixed in lime mortars.	959 - 1636 AD - China, various buildings	FTIR - KBr pellet / peak identification, chemical analysis - reagents spot tests	Fang et al, 2013
Mixture of animal fat and asphalt - Layer on crushed ceramic lime plaster on floor, improvement of liquification of asphalt (lowering of Melting Point by fat), water repelent, no built-up of calcite sediment.	1st quarter of 5th cent. BC - Krene of Megara, Greece	Chemical analysis - no further information	Helner, 2006
Proteinaceous material - Mixed in mud mortar, encouraging clay flocculation.	6th-10th cent. AD - Ellora caves, W. India	FTIR - KBr pellet / peak identification	Singh and Arbad, 2014
Hygroscopic organic - C=O active group - Mixed in lime plaster, improvinng binding capacity.	16th cent. AD - Mughal monument, India	FTIR - KBr pellet	Singh et al, 2014
Sticky rice (starch) - Mixed in lime mortars	1368 - 1911 AD - China, Dutifulness Monument	FTIR / peak identification, chemical analysis - reagents spot tests	Zeng et al, 2008; Yang et al, 2010

Table 2: Evidence of organic mortar additives in archaeological and historic structures as derived from analysis targeting organic detection.

A number of organic additives have been positively identified on archaeological and historic structures dated from the 5th BC to the 20th century, by analytical methods targeting organic detection (Table 2).

The addition of “sticky rice” solution in lime mortars was detected in Chinese monuments dated to 900-1900 AD. Its adhering properties improved the hardening process and the durability of the lime mortar since mortars of hydraulic behavior were not developed in China (Zeng et al., 2008; Yang et al., 2010). The detection of “sticky rice” was carried out by chemical spot testing and FTIR spectroscopy on mortar samples. The same analytical methods were applied by Fang et al. (2013) in a comparative assessment of simulated

mortar samples containing starch, blood, plant juice, drying oil and egg white with traditional Chinese lime mortars (959-1911 AD). The outcomes suggested that all these organic materials have been used as mortar additives in historic Chinese buildings.

A proteinaceous material was detected in mud mortars from caves in West India (6th-10th c. AD), possibly added for encouraging clay flocculation (Singh and Arbad, 2014, 385). The analysis was carried out by FTIR spectroscopy showing the presence of protein, although further identification was not achieved. It is worth noting that the authors consider the absence of oxalates as a drawback on the detection of the protein, since they perceive oxalates as the oxidative product of protein and hence a strong indicator of the particular organic material. This is interesting because the origin of calcium oxalates on the surface of mortars is often debatable, even when additional analysis on morphology rules out their biological origin (Maravelaki-Kalaitzaki, 2005; Polikreti and Maniatis, 2003).

Carbonyl active group (C=O) of an organic additive was detected through FTIR analysis in the lime plaster of a 16th century AD Mughal monument, India (Singh et al., 2014). Thermal analysis showed appreciable quantity of the organic additive that improved the overall binding capacity of the plaster (Singh et al., 2014, 433). Further chemical identification of what the carbonyl was attached to was not provided.

The analysis of a thin, black residue from the floor and wall plasters of the Krene of Megara, Greece (5th century BC) showed that a mixture of asphalt with animal fat was applied as a coating (Hellner, 2006). The coating prevented the build-up of calcite sediments and improved the water-repelling properties of the crushed brick plasters. The author suggests that the animal fat improved the liquification of asphalt by lowering its melting point, making it applicable by brush. The application of the mixture while hot produced calcite soap from the reaction between the mortar and the animal fat, resulting in the hydrophobic behavior of the plaster (Hellner, 2006, 176). However, the lack of any information on the analytical methodology and the fact that no physical evidence survived in situ after its discovery in 1958 pose difficulties in the evaluation of the evidence (Hellner, 2006).

3.1.3 Formation of oxalates, later protective patinas and indirect detection of organic additives.

Oxalates /Later Organic Patinas/ Indirect detection			
Organic Material / Purpose of Use	**Dating and Provenance**	**Analysis**	**Reference**
Hydroxyapatite and calcium oxalates - Ancient treatments: patinas on stone.	5th cent. BC - Greece, Parthenon and Erechteum, Acropolis	XRF, XRD, FTIR, SEM	Maravelaki-Kalaitzaki, 2005
Oxalates - Protective patinas on stone or mortar / product from micro-organism metabolism.	1st cent. BC-20th cent. AD - Roman Ancient and Historic buildings	Ion chromatography	Sabbioni et al, 2003
Paraffin wax, calcium oxalate, apatite, proteins, lipids of animal origin - Later protective patinas on marble.	Romanesque, churches in Lucca (St. Frediano, St. Michele in Foro) and Pisa (St. Frediano, St. Pierino)	OM, SEM-EDX, FTIR-ATR, GC-MS	Rampazzi et al, 2004
Hydroxyapatite - collagen, recipes with egg white, milk, animal glue, linseed oil, oxalates/phosphates - artificial coating theory - Ancient treatments - patinas on stone or protective coatings for conservation purposes (later additions).	5th cent. BC - Greece, Propylaea, Acropolis	SEM-EDX, XRD	Polikreti and Maniatis, 2003
Bone and unidentified collagen binder - Empirical protective treatment on stone.	Greco-Latin - Salisbury's Cathedral	FTIR-ATR	Martin-Gil et al, 2005
Milk - Later protective patinas on limestone.	1709-1713 - Palacio de Nuevo Baztan, Madrid	FTIR - KBr pellet / peak identification, XRD, SEM, ICP-AES	Buergo and Gonzalez, 2003
Organic matter (unspecified) - Additive to promote carbonization, workability, setting time, durability of mortars.	Ancient, Byzantine, Later historic - Greece, various monuments	DTA and TG analyses (exothermic effects within specific range indicate organics)	Moropoulou et al, 1995
Stretching vibrations of the bond C-H in CH_2 - Mixed in lime mortars.	Roman (80 AD, 2nd cent. AD respectively) - Colosseum and a cistern from Albano Laziale	FTIR - KBr pellet / peak identification	Silva et al, 2005

Table 3: Detection of oxalates associated with ancient organic patinas, composition of later protective patinas and detection of organic presence through analysis targeting the identification of inorganic mortar components.

A number of case studies dealt with the origin of oxalates on the surface of monuments and their potential association with applied stone patinas, whereas others

focused on the analysis of stone patinas and their date of application (Table 3). The analysis included detection methods suitable for both organic and inorganic materials, such as FTIR and X-ray Diffraction (XRD) spectroscopies. Morphology appears to be an important indicator of intentionally applied stone patinas, thus Scanning Electron Microscopy was also employed.

The Scanning Electron Microscopy coupled with Energy-Dispersive X-ray Spectroscopy (SEM-EDX) and X-ray Diffraction (XRD) analysis on marble surfaces from the Athenian Acropolis (5th century BC) have detected a uniform and compact layer of hydroxyapatite. Its presence and morphology indicate the application of a coating, likely made by pulverized animal bones in an appropriate solvent, with the containing collagen acting as an adhesive (Polikreti and Maniatis, 2003, 118). The morphology of the coating and the state of preservation of the underlying marble suggest that the coating was not contemporary to the construction phase but applied later for surface protection.

Ancient protective coatings (patinas) have been detected on marble surfaces from the Parthenon and Erechtheum monuments of the Athenian Acropolis. The presence of hydroxyapatite combined with that of calcium oxalates in the patinas and the analysis of their stratigraphy enhances the assumption that oxalates are not biogenic but derive from the transformation of these organic coatings (Maravelaki, 2005, 196).

In both Athenian Acropolis cases, the exact dating of organic applications was not feasible, despite the clear discrimination between ancient patinas and later protective coatings. Nevertheless, the presence of such aesthetic and protective applications during the use of the monuments reflects established practices.

Calcium oxalates originated from the biological transformation of protective patinas were also detected on the stone surfaces of Italian monuments and were identified by Ion Chromatography (Sabbioni et al., 2003). The construction dating of the monuments ranges between the 1st century BC to the 20th century AD, showing that these protective patinas have been in use over long time periods.

FTIR and Gas Chromatography-Mass Spectrometry (GC-MS) on marbles from Romanesque monuments identified the presence of paraffin wax, calcium oxalate, apatite, proteins and lipids of animal origin (Rampazzi et al., 2004). Apart from the paraffin wax that was used in modern applications, the rest of the organic materials indicate protective coatings dated from at least as early as the 19th century (Rampazzi et al., 2004, 976).

Milk was detected by FTIR and Inductively Coupled Plasma Atomic Emission Spectroscopy (ICP-AES) on protective patinas on limestone from a 1700s AD monument in Spain (Buergo and Gonzalez, 2003). Bone and unidentified collagen binder have been detected by FTIR in Salisbury's Cathedral and referenced by the authors as a Greco-Latin empirical protective treatment of stone (Martin-Gil et al., 2005).

Organic additives have been indirectly detected or assumed through analysis targeting the inorganic mortar components (Table 3); Moropoulou et al.(1995) describe the analysis of mortars from ancient, Byzantine and historic Greek monuments by Differential Thermal / Thermogravimetric analysis (DTA-TG), where inorganic exothermic effects within a specific range could also reflect organic reaction. The authors do not provide further information on the form (solid or liquid) or chemical composition of the organic component, although the used term *"matter"* could indicate fibrous plants or animal hair (Moropoulou et al., 1995, 781; 2005, 297).

Indications of organic material mixed with lime and hydraulic mortars from the Colosseum and Roman cistern are described by Silva et al. (2005, 38). The FTIR analysis showed the presence of C-H stretching vibrations of methylene group. As previously, the organic presence was not studied further.

3.1.4 Reviews of historic sources and past analysis reporting organic additives.

Reviews			
Organic Material / Purpose of Use	**Dating and Provenance**	**Analysis**	**Reference**
Hide glue - Ingredient of plaster.	3rd millennium BC - Egypt	No evidence - Note on Lucas, 1934	Bleicher et al, 2015
Bitumen, vegetable oil, fat - Additive in clay or quicklime or mortar coating.	Hellenenistic and Roman - Sagalassos, Turkey	Review of historic sources	Viaene et al, 1997
Animal glue and egg yolk - Protective patinas on stone.	Roman and Veronese monuments	Review of historical sources and past analysis by SEM, FTIR, HPLC	Martin-Gil et al, 1999
Animal glue, blood, egg whites, fig juice, gum arabic, lard, casein, eggs, oil - Organic additives in mortars.	150 BC to 1850 - Egypt, Roman, Medieval and Later Europe	Review of historic sources	Sickels, 1981
Olive oil - Mixture with quicklime, lead pipe sealant, floor mosaic water-proofing paste.	Roman - Pergamon	Review of historic sources	Malinowski, 1981
Egg whites, blood, milk of figs, egg yolk, casein, animal glue, beer, vegetable juices, tannin, urine - Increase plasticity and regulate setting rates.	Ancient Greek, Hellenistic, Roman, Byzantine, post-Byzantine and later historic - Mediterranean Basin Fortifications, Monasteries, Churches, Historical Buildings and masonry.	Review of analysis work - DTA-TG, mechanical testing	Moropoulou et al, 2005

Table 4: Reviews of historic texts and past analysis reporting organic materials used as mortar and plaster additives and as protective patinas.

Relevant information is also found in reviews of historic sources and past analysis reporting detection of organic additives (Table 4): Bleicher et al. mention the addition of hide glue in 3rd m. BC Egyptian plaster (2015); Viaene et al., in the study of mortars from Sagalassos, discuss the use of bitumen, vegetable oil and fat as additives in clay and quicklime mortars or as mortar coatings (1997); Martin-Gil et al. review historic sources and past analysis on protective patinas on stone from Roman and Veronese monuments, describing recipes of animal glue and egg yolk (1999). Malinowski describes recipes of Roman pastes of quicklime and olive oil in waterproofing of mosaic floors (1981). Egg whites, blood, milk of figs, egg yolk, casein, animal glue, beer, vegetable juices, tannin and urine are some of the materials likely to have been used in the Mediterranean basin for increasing the plasticity and regulate the setting rates of mortars dating from the ancient to later historic period (Moropoulou et al., 2005).

Sickels tested natural organic mortar additives against synthetic ones of similar properties as potentially improved alternatives (1981). Her work contains an extended list of organic additives such as animal glue, blood, egg whites, fig juice, gum Arabic, lard, etc. covering a wide chronological and geographical range of use. Although the literature sources and methodologies of analysis are limited, it is still worth noting that scientific interest in the topic can be traced back to the early 1900s (Sickels 1981).

3.1.5 Experimentation on traditional mortar recipes containing organic additives.

Experimental work on Traditional Recipes			
Organic Material / Purpose of Testing	**Dating and Provenance**	**Analysis**	**Reference**
Animal glue, casein, nopal (polysaccharide), olive oil - Experimental in non-hydraulic lime mortars, improvement of mechanical resistance - porosity reduction (animal glue and olive oil), improvement of carbonization (nopal).	Traditional recipes, S.America and Mexico used up to early 20th cent. AD.	SEM, porosity test, loss of water and carbonization test.	Ventolá et al, 2011
Proteinaceous material (blood, animal fat, milk) - Experimental in mortars with added cow's and pig's blood to assess workability, waterproofing and freeze-thaw properties.	Uncertain Date - Ancient Egyptians, Greeks and Romans.	Mechanical testing	Jasiczak and Zielinski, 2006
Milk - Experimental on identification of different milk mortar additives.	Traditional historic recipes.	Immunological methods	Kuckova et al, 2009
Linseed oil - Additive in repair mortar, improvement of workability (wet phase), waterproofing (dry phase).	N/A	Mechanical and Ageing Testing	Papayianni et al, 2013

Table 5: Experimental work on the properties of organic mortar additives reported in traditional recipes.

Experimental work has been carried out on the properties of different organic additives in modern mortars (Table 5): Jasiczak and Zielinski (2006) assessed the workability, waterproofing and freeze-thaw properties of cow's and pig's blood in mortars through mechanical testing. Ventolá et al. (2011) experimented with traditional recipes of South America and Mexico on non-hydraulic mortars and the addition of animal glue and olive oil: their work showed that both organic materials improved the mechanical

resistance of mortars and reduced their porosity. Nopal additive was found to improve the carbonization process of the mortar (Ventolá et al., 2011, 3317).

Papayianni et al. (2013) worked on the production of compatible repair mortars aiming for the conservation of ancient structures. The addition of linseed oil to the proposed pozzolanic mortar improved its water-repelling behavior and its resistance to humidity. Additionally, linseed oil increased the workability of the mortar during its wet phase and its durability against weathering after setting (Papayianni et al., 2013, 91).

The experimental work of Mydin (2018) on the physico-mechanical properties of modern lime mortars mixed with egg albumen demonstrated the ongoing interest in the potential of future applications of traditional materials in cultural heritage conservation.

Immunological methods were experimentally tested on laboratory prepared mortar samples mixed with different milk products according to historic building recipes (Kuckova et al., 2009). The study targeted the methodology aspect of detection of organic mortar additives.

3.2 Discussion on Literature and Analytical Techniques

While there is a range of historical reports and a number of analytical studies on organic additives, the results are open to discussion. Classifying available evidence by its research aim (Tables 1 to 5) highlights the fragmentary knowledge produced by the unsystematic study of organic additives. Variability in approach, assumptions, archaeological context and methodology restricts objective assessment of the quality of the reported evidence for organic additive usage.

3.2.1 Critical review of available literature

Case studies focusing on the detection and identification of organic additives are limited in number compared to those dedicated to studying the inorganic components of mortars (Fang et al., 2013, 1). The analytical work on the use of “sticky rice” in Chinese mortars is the only example in which aspects of both archaeometry and methodology are investigated, through the analysis of ancient and laboratory prepared samples. The Chinese team focuses on the development of a standardized protocol for the in-situ analysis of mortars. Their proposed methodology, centered on chemical spot testing, aims to overcome issues of false or negative identification that arise from the limited quantity of organic materials in the mortar or their poor preservation (Fang et al., 2013, 1).

The excessive decay of organic materials is considered the primary reason for the inconclusive scientific evidence of the presence and chemical composition of organics in mortars (Kuckova et al., 2009, 42; Sarmiento et al., 2011, 3601). This generic statement on the decay mechanisms of ancient organic materials contrasts the observations made by Yang et al. (2008), who noted the anti-bacterial action of unaltered calcium hydroxide in lime mortars inhibited the decay of starch. Such contradiction highlights the need for standardized detection and identification methodologies and targeted degradation studies of different organic materials in mortar matrices, assessed through exposure to different environmental conditions.

An important factor that may have discouraged research into organic additives could be the lack of macroscopic evidence, since organic mortar additives may not have been visible. Biological activity may also produce outcomes that can mislead and result in incorrect conclusions, while intentional use of additives may be overlooked or considered to be biological depositions. The debate is well established through the study of the origin of calcium oxalates and concerns both ancient and historic monuments (Sabbioni et al., 2003; Maravelaki-Kalaitzaki, 2005; Polikreti and Maniatis, 2003; Buergo and Gonzales, 2003; Rampazzi et al., 2004, Martin-Gil et al., 2005). Methods for differentiating between biogenic organic depositions and intentional use should be included within the analysis design for ancient mortar samples. Similarly, organic materials that originate from the burial environments, as well as external depositions, may also interfere with the detection of organic additives. An analytical methodology should have a capacity to differentiate purposefully added organic materials from random depositions.

The interference of the inorganic mortar components with detection and chemical profiling of organic additives has been encountered in studies employing FTIR spectroscopy (Miliani et al., 2012; Rosi et al., 2010; Rosi et al., 2009). Since these components are always present in the mortar, their discrimination from the organic compounds is a fundamental requirement of any FTIR methodology.

This overwhelming accumulation of constraints should not discourage research into organic mortar additives in antiquity, rather it should inspire strategies and solutions to seek a standardized methodology for detection and identification that overcomes issues of interference (Kuckova et al., 2009, 42).

3.2.2 Critical review of analytical techniques

Case studies identify FTIR spectroscopy as a commonly employed method for the detection and identification of organic mortar additives, either individually (Singh and Arbad, 2014) or in a preliminary stage that is followed by chromatography (Rampazzi et al., 2004) or other destructive analysis such as ICP-AES (Buergo and Gonzalez, 2003). As a preliminary method, FTIR is reported to narrow down the organic group to support the subsequent sample separation phase for destructive analysis (Buonasera, 2007; Oudemans and Erhardt, 1996, 137). As a validation method, FTIR spectroscopy has been used after chemical spot testing to verify its outcomes (Fang et al., 2013, 4).

The fact that FTIR spectroscopy is employed as a preliminary, main and validation method shows the capability of the instrument is evaluated according to individual perception. Consequently, the FTIR outcomes are interpreted according to expectation of what the instrument will deliver. Thus, as a main or preliminary method, it is limited to generic organic profiling (Singh and Arbad, 2014; Singh et al., 2014). However, when it was used as a validation method in the analysis of mortars from Chinese monuments, it appears to have been adequate to provide clear identification of individual organic compounds, with the exception of differentiating between starch and milk additives (Fang et al., 2013, 6; Zeng et al., 2008; Yang et al., 2010). This paradox reflects the lack of systematic experimental study of the capabilities of IR spectroscopy for the analysis of organic additives.

The case studies reviewed often reported a preference for application of FTIR in which the sample is pulverized and pressed into a Potassium Bromide (KBr) pellet and analysed by Transmission FTIR spectroscopy (Singh and Arbad, 2014; Singh et al., 2014; Fang et al., 2013). Alternatively, solvent extraction followed by analysis using Attenuated Total Reflectance (ATR) provided analysis free from inorganic chemical interference (Rampazzi et al., 2015, 5). In the case of extraction, Rampazzi et al., acknowledge the successful detection of polysaccharides in mortar but they too, consider FTIR spectroscopy as being preliminary to the use of GC-MS to provide more conclusive evidence (2015, 14).

Although Gas Chromatography – Mass Spectrometry (GC-MS) is perceived as an analytical tool able to provide more rigid conclusions than FTIR, certain conditions may produce inconclusive outcomes. This occurs when the quantity of the organic additive available for analysis is low, either due to the original low amount added in the mortar or due to its poor preservation (Kuckova et al., 2009, 42). The analysis of proteinaceous materials by GC-MS is also problematic because of the possible loss of amino acids

during the steps of hydrolysis and derivatization, leading to false results (Kuckova et al., 2009, 42). Andreotti et al. (2018, 867) on the analysis of ancient repair mortars state that GC-MS was unable to determine whether egg yolk or egg white was used as additive since the method could not distinguish their similar amino acid composition. Microbiological contamination may also affect the discrimination of these closely related materials (Fremout et al., 2012, 39).

Cuni (2016) describes the analysis of Roman mural samples for the detection and identification of organic binders. The GC-MS analysis on the samples showed absence of organic binder, whereas subsequent FTIR analysis showed the opposite. GC-MS was reapplied using a different extraction method that confirmed the FTIR outcomes and the presence of beeswax (Cuni, 2016, 4).

The example above and the discussion so far illustrate the importance of understanding the scope and limitations of a methodology and the nature of a sample for producing data adequate for deriving conclusions.

These analytical aspects are well defined in organic residue analysis in pottery for the identification of content and use, where destructive FTIR spectroscopy and Chromatography are commonly employed and sample preparation methodologies are standardized (Röttländer, 1990; Evershed and Dudd, 1999; Buonasera, 2007; Oudemans and Erhardt, 1996). Again, FTIR is considered preliminary analysis assisting sample preparation for chromatography (Buonasera, 2007; Oudemans and Erhardt, 1996, 137). In pottery analysis, the identification of the organic material is related to the use of the container and not to its manufacturing technology.

However, in the analysis of organic mortar additives where the analytical aim is related to technology, their spatial distribution within the inorganic matrix is a fundamental requirement of the selected methodology in order to define the purpose of the additive as either a coating or an additive to the mixture before it sets. Both FTIR (KBr and ATR sample preparation) and Chromatography cannot provide this spatially resolved data since they are destructive (Ramirez-Barat and De la Vina, 2001, 282). Although staining applications that produce coloration of the organic additive can provide information on its chemical origin and distribution within a sample, the method cannot distinguish different proteins and significantly alters the visual appearance of the samples (Ramirez-Barat and De la Vina, 2001, 282). To answer the major questions regarding the presence and use of organic additives in mortar, a non-destructive analytical method is preferred to enable additive detection in-situ, within the mortar.

The considerable work of MOLAB (European Mobile Laboratory) on the analysis of organic binders on wall paintings and art works by non-destructive FTIR methods, specifically Reflectance FTIR Spectroscopy, provided valuable information on the effectiveness of the method to detect and identify organic materials within complex inorganic matrices. Their work enabled the interpretation of reflectance spectral distortions, characteristic to the specific FTIR method and produced a spectra database that facilitates detection of inorganic interference on the spectral representation of organic absorption bands (Miliani et al., 2012; Rosi et al., 2010; Rosi et al., 2009). To increase the confidence level of FTIR analysis in such circumstances the complementary use of statistics, as Principal Component Analysis (PCA), has been proposed for verifying FTIR identification outcomes without the need of further destructive analysis (Sarmiento et al., 2011; Rosi et al., 2010; 2009).

Reflectance FTIR Spectroscopy conducted through an FTIR microscope offers advantages for the analysis of organic mortar additives, facilitating collection of spectra from different areas of multi-layered, optically thick samples, without destructive layer separation procedures. This is highly beneficial when samples are small and may preserve thin organic coatings. The correlation of stratigraphy with chemical composition enables the study of technology through the mapping of the organic additive in the inorganic matrix (Chalmers et al., 1996, 315).

Unlike FTIR/ATR micro-spectroscopy, External Reflectance micro-spectroscopy requires no sample preparation such as the resin embedding, cross sectioning and polishing used to analyse paint layers of wall paintings and art works (Joseph et al., 2010; Rizzo, 2008; Fonjaudran et al., 2008). Although such embedding techniques allow chemical data to be linked to spatial distribution, the overlapping of absorption bands of the embedding resin with the organic binder and the physical removal of the organic material, led to the testing of alternative sample preparation methods (Fonjaudran et al., 2008, 79; Nevin and Fonjaudran, 2015, 113).

When using External Reflectance micro-spectroscopy, issues of contamination and loss of material are minimized. The samples are placed on the microscope stage and the area of interest is then isolated by an adjustable aperture. Analysis can be performed either on individual layers or selected areas within the same layer (Joseph et al., 2010, 899). It is also suited to rough and irregular surfaces, such as those expected on a mortar sample, whereas ATR requires good contact between the surface and the ATR cell to collect spectra (Macková et al., 2003, 512; Scuitto et al., 2012).

The literature review highlights the limited research and lack of consistency in the analysis and identification of organic mortar additives in ancient mortars. Consequently, little is proven regarding either the presence of specific organic compounds in ancient mortars or claims of their contextual use as an established technological practice. Since this absence of evidence does not mean that such ancient technology did not exist across a wide chronological and geographic range, it merits further scientific attention.

The restrictions posed by the physical properties of mortar samples and the desire to not only detect and characterize organic additives, but to understand their technological application within mortar, point to External Reflectance micro-spectroscopy as a useful methodology to examine for the non-destructive fulfilment of these goals.

3.3 Experimental Aims and Objectives

The experimental research within this thesis explores and reports the development of a potential methodology for the detection, identification and spatial distribution of organic additives in mortar, based on External Reflectance FTIR Micro-Spectroscopy, which is then utilised to analyse ancient mortar samples. Central to the study is the development of a database approach to overcome issues of chemical discrimination of organic additives and interference with other mortar components.

Experimental aim:

- Develop and reproducibly test a database methodology using External Reflectance FTIR Micro-Spectroscopy to non-destructively detect and identify organic additives contained in mortar matrices.

Experimental objectives are to:

- Use External Reflectance FTIR micro-spectroscopy to produce a Chemical Peak Assignment Database (CPAD onwards) derived from analogues comprised of organic additives and their mixtures with mortar in predefined concentrations.
- Assess changes in the spectral profiling of organic additives in the presence of inorganic mortar components and define diagnostic spectral features for identification purposes.
- Test the effectiveness of the CPAD for detecting additives using mortar analogues in which the organic additive and its concentration is unknown prior to analysis.
- Investigate the potential role of statistics for enhancing the accuracy of the database identification results.
- Collect External Reflectance micro-FTIR spectra from archaeological samples and use the CPAD in a standardized and methodological manner to interpret results.
- Discuss the level of confidence that can be assigned to the CPAD methodology for detecting organic additive residues within archaeological mortars.

Chapter 4: Theory of External Reflectance FTIR micro-spectroscopy

The absorption of light by the molecular bonds of a medium causes transition from an energetic ground state to a particular excited state (Hof, 2003, 40). A molecule absorbs radiation when a net change in dipole moment takes place in its vibrational or rotational motions, altering their amplitude (Skoog et al., 1998, 382). Molecular species that are able to absorb infrared radiation are those composed of atoms of more than one chemical element (heteronuclear) and are able to undergo a net change in their dipole moment. Homonuclear species, such as O_2 and N_2 do not experience changes in their dipole moment in their rotation and vibration motions and cannot absorb infrared radiation (Skoog et al., 1998, 382).

The IR absorbent molecular species produce absorption bands recorded on an IR spectrum. The parameters characterizing a band are the position of the band maximum in a specific wavenumber (cm^{-1}), its intensity and shape (Hof, 2003, 41). These parameters and the number of bands recorded on a spectrum are directly related to a specific compound and are used for its identification (Hof, 2003, 42). Organic molecules exhibit *skeletal vibrations* mostly within the range 1400-700 cm^{-1}, a spectral region also known as the "*fingerprint region*" (Banwell and McCash, 1994, 83). Within this region, the linear and branched parts of the molecule exhibit several skeletal modes of vibration, thus several absorption bands. The spectral profile that results from these modes within the fingerprint region is usually adequate to provide identification of the compound (Banwell and McCash, 1994, 83).

The vibrations of light terminal groups of molecules, such as $-CH_3$ and -OH, are detected on regions well above the fingerprint region and are referred to as "*group frequencies*". Heavy atoms (e.g. -C-Cl, -C-Br) vibrate in low frequencies, below 700 cm^{-1}. Group frequencies are useful in the identification of a compound and are assessed together with the absorption bands in the fingerprint region (Banwell and McCash, 1994, 84).

Recording the absorption of IR radiation from a compound is dictated by the general principle that describes the interaction of a compound with the incident light; when the incident light of intensity $\boldsymbol{I_O}$ reaches the surface of a compound will be partially scattered $\boldsymbol{I_S}$, reflected $\boldsymbol{I_R}$ and absorbed $\boldsymbol{I_A}$ in the compound, with the remaining part transmitted $\boldsymbol{I_T}$. The individual light contributions add up in order to satisfy the law of the conservation of energy, according to equation 4.1 below (Steiner, 2003, 70):

Equation 4.1: $I_O = I_S + I_R + I_A + I_T$

Although absorption intensity is the value that carries all the information, it cannot be measured directly. The measurement derives from evaluating equation 4.1, specifically the value I_O and one of the remaining intensity values. Commercial spectrometers have one single detector that measures one pair of intensity values each time. Sample preparation aims to bring the rest of the values at zero or close to it in order to minimize measurement errors (Steiner, 2003, 70). For External Reflectance FTIR micro-spectroscopy absorption derives from the measurement of intensities I_O and I_R from the equation 4.2 (Steiner, 2003, 71):

Equation 4.2: $I_A = I_O - I_R$

aiming for the values $I_S = I_T = 0$.

The selection of the appropriate intensity values to be measured depends on the form of the compound (liquid, gaseous or solid/film) and its optical properties in respect to the propagation of the incident IR radiation through its structure (Chalmers et al., 1996, 315). Additionally, parameters such as sample preparation and spatially-resolved requirements define the final selection of the FTIR method (Chalmers et al., 1996, 315; Macková et al., 2003, 512).

IR Transmission techniques are applied to all the different compound forms with the appropriate sample preparation. For solid samples, pulverizing and blending with an appropriate transparent medium, such as potassium bromide, is required (Stuart, 2004, 26).

IR Reflectance methods are employed when sample preparation is not preferable or feasible and/or spatially-resolved information is required; Attenuated Total Reflectance (ATR) is performed where good contact can be achieved between the sample and the ATR cell, such as in the case of elastomers (Macková et al., 2003, 512). Reflection-Absorption spectroscopy is used on thin films over a highly reflected mirror or mirror-like surface, such as that of metals (Stuart, 2004). Diffuse Reflectance (DRIFTS) examines the surface IR absorption of powders (Steiner, 2003, 78). External Reflectance techniques are the most non-destructive, non-contact ones and are used for assessing “optically-thick” compounds (Chalmers et al., 1996, 315).

Two types of reflection occur when the incident IR radiation strikes the surface of “optically-thick” compounds analyzed by External Reflectance spectroscopy: Specular (or Surface) R_S and Diffuse (or Volume) R_V reflection (Miliani, 2012, 296). When the incident

IR radiation strikes a smooth and polished surface, the radiation reflects back at an angle identical to the incident angle of radiation, causing Specular reflection (Skoog et al., 1998, 418). If the incident radiation strikes a coarse and bulk surface, it may penetrate, be absorbed, refracted, reflected and/or scattered prior to reaching again the surface and coming out as a reflection beam (Miliani et al., 2012, 296). This interaction promotes Diffuse reflectance.

Specular reflectance R_S is controlled by the Refractive index ***n*** of the surface that receives the incident IR radiation and its Absorption index ***k***, following Fresnel's law, according to equation 4.3 below (Miliani, 2012, 296):

Equation 4.3: $$R_S = (n-1)^2 + k^2 / (n+1)^2 + k^2$$

where 1.0 is the refractive index of air (Maddams,1998). As a surface absorbs some of the incident IR radiation, its refractive index changes and absorption information are carried within the generated reflected beam (Hendra, 1997). The equation considers reflection at normal angle of incident radiation (30º) (Chalmers et al., 1996, 315). However, at different angles of incident radiation, reflection depends on the polarization of radiation (Spragg, 1998). Polymers and minerals are dichroic (direction dependent) thus, the resulting reflectance is also dichroic and the resulting absorption spectrum will carry orientation information (Hendra, 1997).

Since change in the refractive index (RI) occurs upon absorption, the specular reflectance spectrum is essentially an overlaid pattern of both dispersion of RI and absorbance (Maddams, 1998). Consequently, the spectrum is characterized by distortions that follow the behaviour of the refractive index across the wavelength; low absorption index (*k*) bands appear as first-order derivatives whereas high absorption bands appear totally reflected and inverted on the spectrum (reststrahlen effect) (Buti et al., 2013, 2700). Most organic molecules with k<1 produce derivative-like bands. Inorganic salts such as carbonates, sulphates and phosphates show reststrahlen distortions because their k>1, due to strong oscillation during absorbance (Miliani, 2012, 296).

A characteristic specular reflectance spectrum is that of a calcium carbonate ($CaCO_3$) pressed-disk of smooth texture, obtained during the present study (fig.7). The *v3* antisymmetric stretching of the carbonate ion (CO_3^{2-}) at around 1400 cm^{-1} is highly absorbent, appearing as totally reflected, thus inverted by the reststrahlen effect. The absorption band of symmetric CO_3^{2-} stretching (*v1*) at 887 cm^{-1} is comparatively less

absorbent than the *v3* and appears as a first-order derivative band (Miliani et al., 2012, 297).

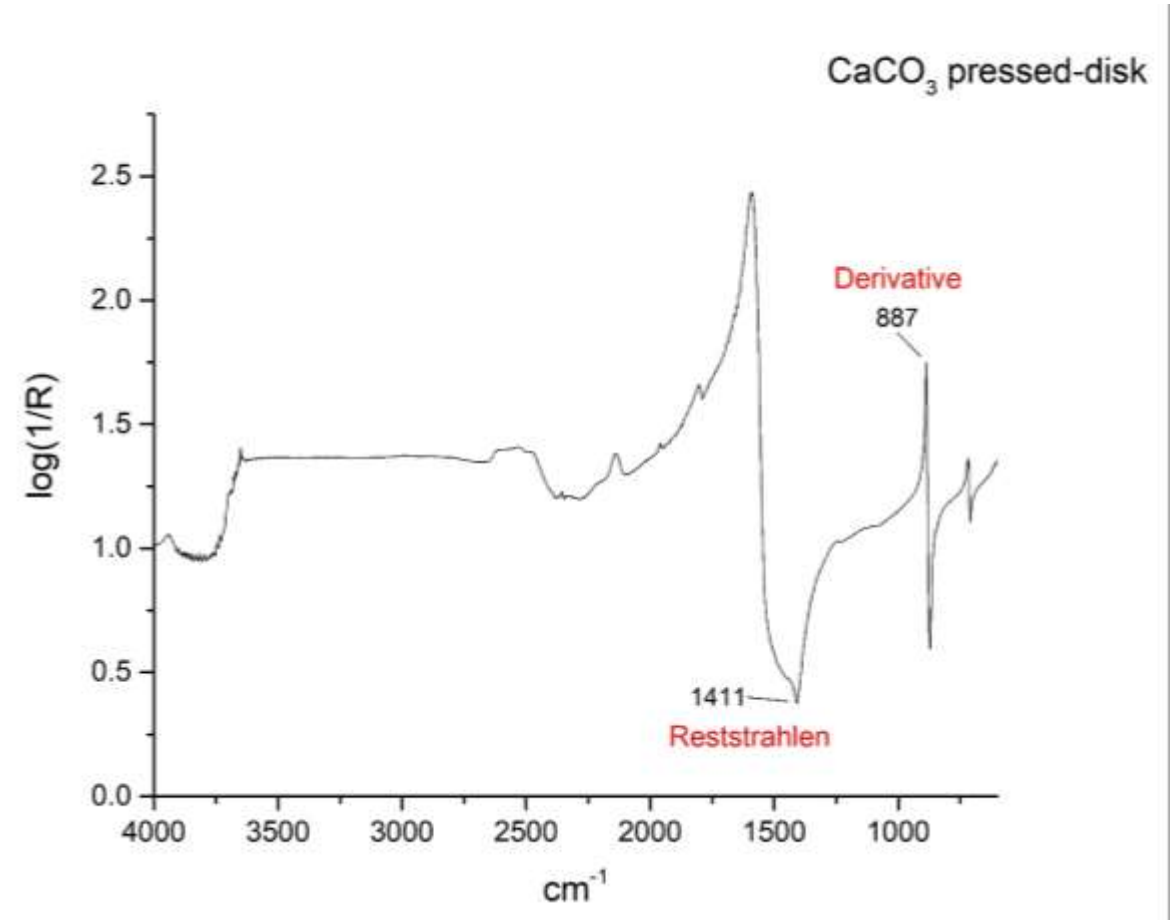

Figure 7: The specular reflectance spectrum of a $CaCO_3$ pressed-disk.

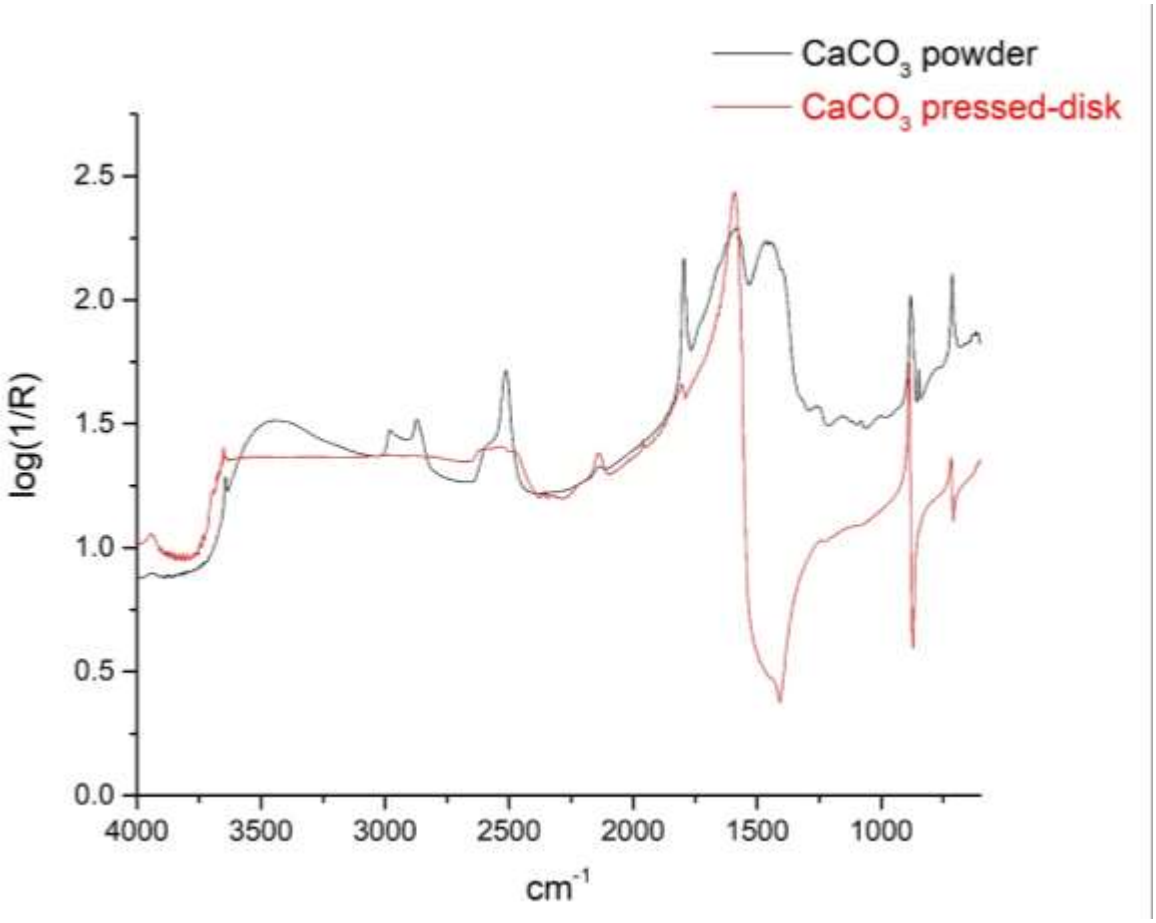

Figure 8: Overlaid comparison of diffuse (black line) and specular (red line) spectra of calcium carbonate.

Diffuse reflectance spectra appear similar to transmittance spectra because both originate solely from the absorption process (Miliani, 2012, 296). As a rule of thumb, diffuse reflectance infrared spectroscopy (DRIFTS) is usually applied on powdered samples where scattering of the incident radiation improves absorption (Raphulu et al., 2010; Hafez et al., 2014).

A characteristic of diffuse reflectance spectra is that minor absorption peaks are enhanced, although they retain the same peak location as in transmittance and hence could be comparable to those (Skoog et al., 1998, 418; Miliani et al., 2012, 296).

In contrast, specular distortions may sometimes prevent identification of the position of spectral features even those that are characteristic to specific compounds in transmittance (Rosi et al., 2010, 620). It is thus assumed that spectra of specular distortions may not be comparable to transmittance spectra, at least in the degree that reflection spectra are.

However, retention of peak location is observed between the diffuse spectrum of $CaCO_3$ powder and the specular spectrum of the pressed-disk, indicating that distortions may also assist identification of specific compounds (fig.8).

It is evident that surface texture dictates the type of generated reflectance and consequently, the amount and quality of information that is carried within the reflected beam. In the case of materials consisting of both smooth and coarse components it is expected that both types of reflection will occur and appear on the resulting spectrum (Rosi et al., 2010, 620). Reflectance spectra obtained from the in-situ analysis of wall paintings and polychrome artwork are representative of such conditions (Monico et al., 2013; Miliani et al., 2007; Milani et al., 2012).

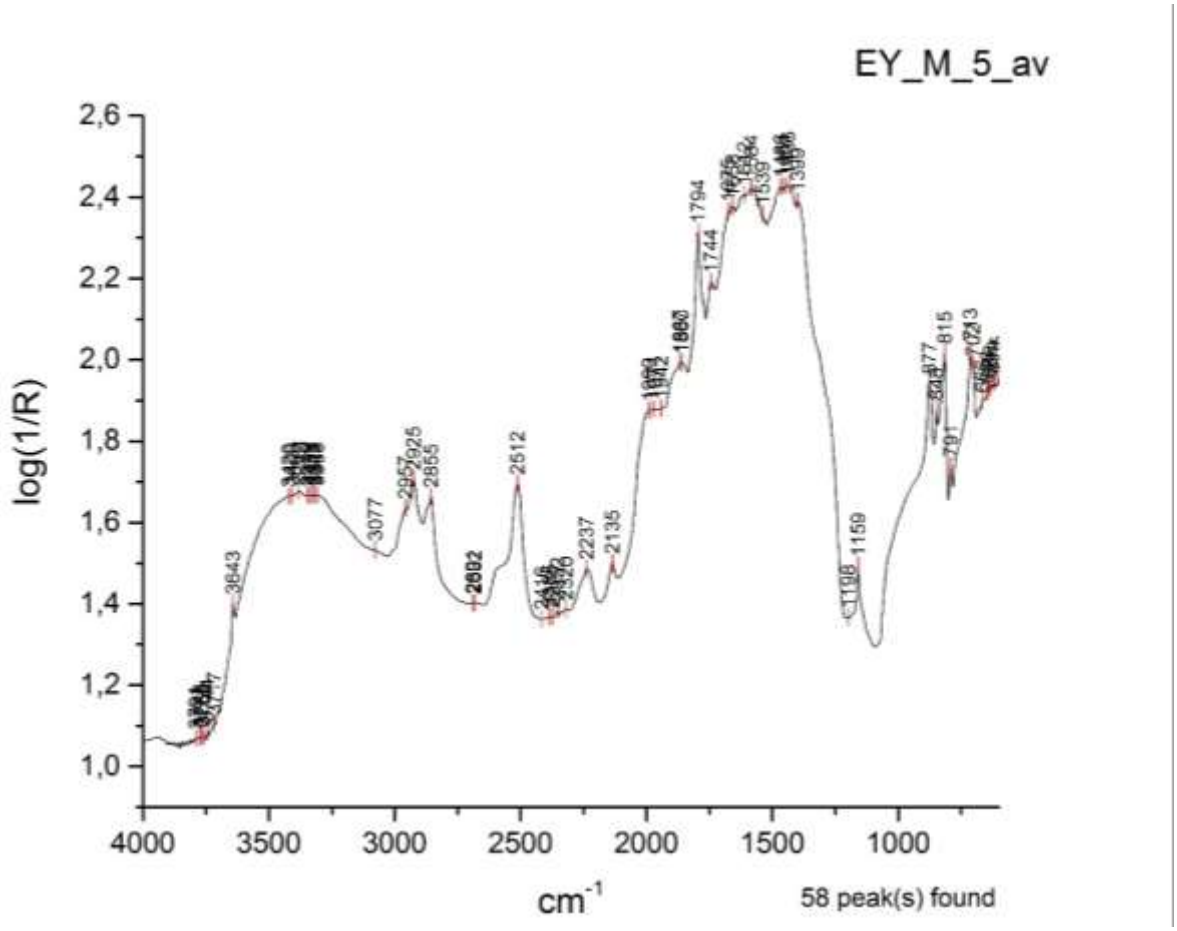

Figure 9: Reflectance spectrum of laboratory prepared standard EY_M_5 consisting of mortar (CaCO3 and quartz 1:3 ratio) and 5% w/w of egg yolk.

A similar condition to that of wall paintings is presented in figure 9 that shows the reflectance spectrum of a laboratory prepared mixture of a mortar with 5% w/w egg yolk. The spectrum is representative of the co-existence of specular and diffuse reflectance: the first order derivative at 815 cm^{-1} and the reststrahlen at 1399 cm^{-1} are characteristic of

specular distortions of Si-O antisymmetric stretching of quartz (Miliani et al., 2012, 303) and the *v3* antisymmetric stretching of the carbonate ion (CO_3^{2-}) of calcium carbonate respectively (Ricci et al., 2006, 1222). The effect of enhancement of minor peaks due to the occurrence of diffuse reflectance is evident within the 1700-1400 cm^{-1} region and the lipid C=O stretching peak at 1744 cm^{-1} that belongs to the egg yolk (Ricci et al., 2006, 1223).

The coexistence of specular and diffuse reflectance on the spectrum due to texture characteristics of the sample is only part of the overall complexity of the spectrum (fig.9). The composite chemical composition of the sample that incorporates three different materials in its structure (calcium carbonate, quartz and egg yolk) produces overlapping and masking of diagnostic peaks on the spectrum, especially within the fingerprint region and of those of the organic component (Rosi et al., 2009, 2099).

The identification of complex reflectance spectra dictates the development of a database specific to Reflectance FTIR micro-spectroscopy and tailored according to the chemical composition of the samples in question (Rosi et al., 2010, 617). Spectral features and distortions can then be assessed as diagnostic features (Ricci et al., 2006, 1223).

Chapter 5: Acquisition of Reflectance micro-FTIR spectra

5.1 Acquisition parameters: method and standardisation

The initial experimental work targeted the standardization of acquisition parameters for obtaining high quality reflectance spectra that would enable the development of a database specific to Reflectance FTIR micro-spectroscopy. Such spectra are considered those of high signal-to-noise ratio that contain the maximum number of absorbance peaks able to provide identification. Accordingly, the number of scans and the selection of the mid-infrared range length that carries the maximum chemical information were defined as the main acquisition parameters that influence spectra quality.

Experimentation on different sets of these parameters was performed through the analysis of laboratory prepared standards and the delivered spectra were assessed for meeting the quality requirements. The assignment of diagnostic peaks was carried out from reflectance spectra available in relevant case studies.

Standards of calcium carbonate precipitated (Fisher Chemical) and pure sand 40-100 mesh (ACROS Organics) were analysed as powders (in their purchased form) and pressed-disks. The disks were made from 1000 mg ground powder, prepared by using a mortar and pestle for 20 minutes (fig.10). The thickness of the pressed disks ensured safe handling during their analysis. Bone glue standard from the FTIR reference collection held at the Department of Archaeology and Conservation was analyzed in its purchased granule form (fig.11).

The selection of standards was based on the available literature: The inorganic standards represent the two main components of ancient and historic mortars (Moropoulou et al., 2000, 57; 2005, 298). Bone glue is referenced as mortar additive in traditional recipes (Ventola et al., 2011).

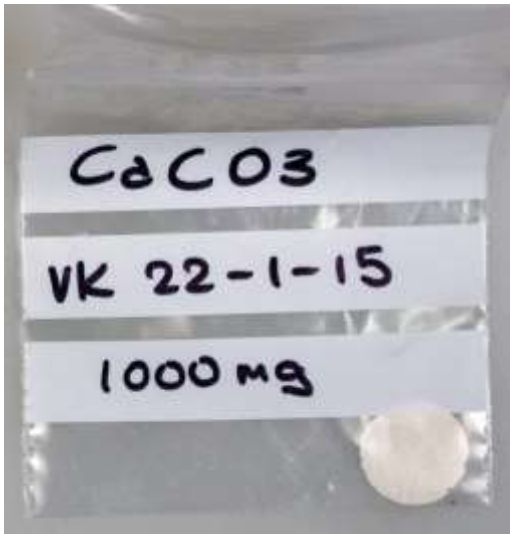

Figure 10: $CaCO_3$ pressed-disk standard.

Figure 11: Bone glue granules.

External Reflectance micro-FTIR spectra were obtained under the Perkin-Elmer Multiscope™ System Microscope connected to the Perkin Elmer™ Spectrum One FTIR Spectrometer (fig.12). The microscope is equipped with a liquid nitrogen cooled Mercury, Cadmium and Telluride (MCT) detector. Live image was obtained through WinTV software for Windows. The Perkin-Elmer Spectrum v.10.3, Speckwin32 (Menges, 2011, v.1.71.6) and OriginPro 2015 software were used for spectra graphic illustration and data handling. The OriginPro 2015 *Quick Gadget Peak Finder* tool was used for locating the *x* and *y* parameters of absorption bands in the spectra. The instrument was used according to the instructions of the Perkin-Elmer Information Manual (1999).

Figure 12: The FTIR microscope and spectrometer.

Background correction was performed by subtracting the spectrum of a golden mirror obtained prior to the analysis of each standard (fig.13). Open aperture ensured standardized spatial resolution of 500μ width X 700μ length and allowed the maximum IR signal to reach the surface of the standard, enabling the improvement of the signal-to-noise ratio (Nevin and Fonjaudran, 2015, 116; Joseph et al., 2010, 899).

Figure 13: The Polystyrene film (PE) standard and the golden mirror for the background correction.

Optimal operation conditions of the instrument at the beginning of each analytical session, require regular inspection of the IR maximum signal, measured in Transmittance mode and retained around 6000 energy gain units (Perkin-Elmer Information Manual, 1999). Energy gain measurements were also obtained in Reflectance mode from: a) the surface of the golden mirror at the beginning of each background collection and b) the surface of each standard before each spectrum collection. These measurements although not required, provided information relevant to the performance of the instrument between runs and the assessment of accuracy and precision (Ch. 6). Additionally, they provided a rough estimation of the maximum signal of reflected IR radiation returning to the detector and the comparative degree of absorptivity of the standards.

Five reflectance micro-FTIR spectra were obtained from the surface of $CaCO_3$ pressed-disk under different acquisition parameters (fig.14). The black spectrum was obtained after 40 scans, 4 cm^{-1} resolution, within the 4000-450 cm^{-1} scan range. The remaining four spectra were collected after 60, 100, 150 and 200 scans, 4 cm^{-1} resolution within the 4000-600 cm^{-1} scan range. The comparison among the spectra, demonstrates that the mid-infrared range below 600 cm^{-1} has a low signal-to-noise ratio and does not provide clear absorption peaks (Banwell and McCach, 1994, 16). The absence of diagnostic peaks below 600 cm^{-1} is further supported by the available literature (Ylmen and Jaglid, 2013, 119; Miliani et al., 2012, 297).

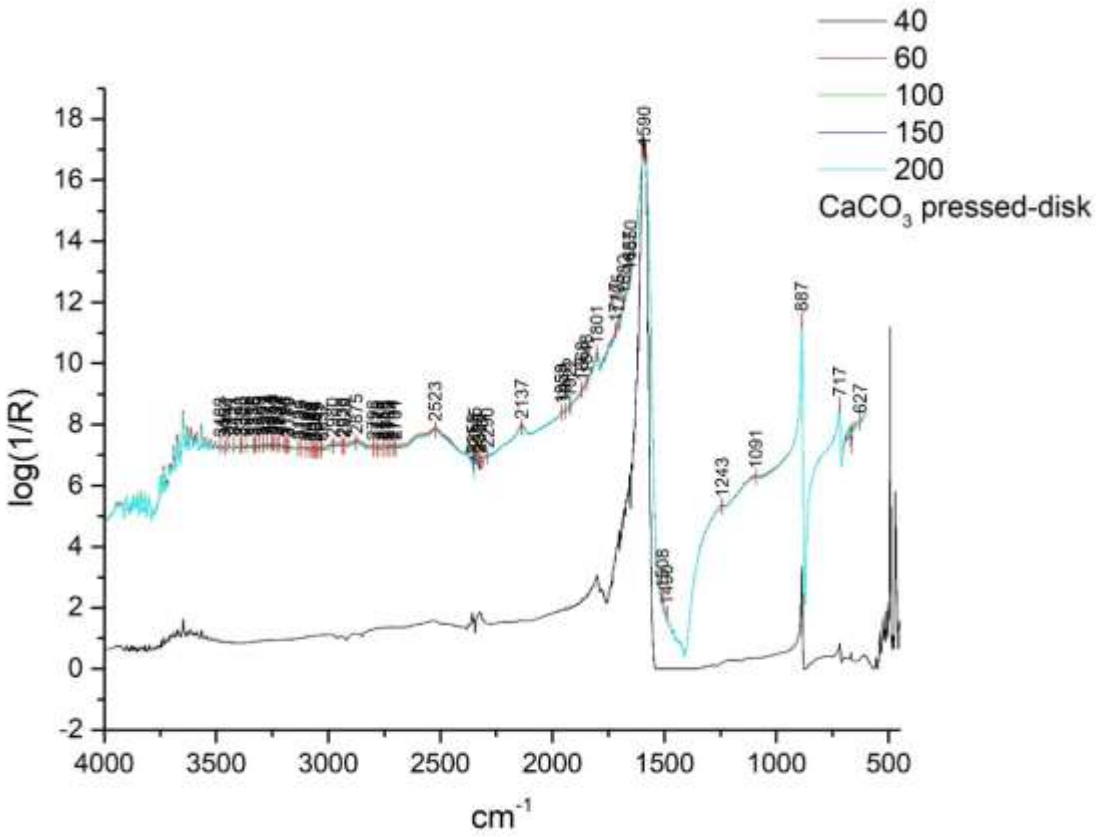

Figure 14: The spectra of $CaCO_3$ pressed-disk, obtained under different sets of acquisition parameters: black spectrum - 40 scans, 4000-450 cm^{-1}, red – 60 scans, 4000-600 cm^{-1}, green – 100 scans, blue – 150 scans and light blue – 200 scans, within 4000-600 cm^{-1}.

All the characteristic absorption peaks of calcium carbonate fall within the 4000-600 cm^{-1} spectral range. The inverted peak (reststrahlen) around 1400 cm^{-1} is typically assigned to calcite and demonstrates the occurrence of specular reflectance in the spectrum (Ricci et al., 2006, 1222). Specular reflectance is also present at the derivative-like distortion at 887 cm^{-1}, characteristic to v2 stretching vibration of carbonate ion (Ylmen and Jaglid, 2013, 119). The combination band at 2523 cm^{-1} is also attributed to calcite and derives from the simultaneous absorption of energy of the two fundamental bands v1 and v3 (Ricci et al., 2006, 1222; Stuart, 2004, 11). Combination bands are also visible as weak absorptions at 2875 and 2980 cm^{-1} due to the 2v3 absorption of carbonate ion (Ylmen and Jaglid, 2013, 119).

The number of diagnostic peaks is significantly increased on the spectra obtained after 60 scans, showing an improvement in spectra quality, compared to the spectrum of 40 scans that contains only the most intense absorption bands. Spectra quality did not improve further above 100 scans.

Surface reflectance properties and spectrum acquisition time affects the quality of the spectrum; an absorbent substance, such as calcium carbonate, allows a maximum IR signal gain of 550 units to reach the detector, which is significantly lower than the 4590 units allowed by the golden mirror during background correction. This may mean that when the detector attempts to collect weak reflectance from highly absorbent materials in short time periods the resulting spectrum will be less detailed. Scan increase seems to resolve this issue.

High signal-to-noise ratio was achieved on spectra obtained from $CaCO_3$ powder after 60 and 100 scans, with overlying revealing no significant difference between the two spectra (fig.15). As expected from a powder sample, diffuse reflectance prevails in the spectrum producing enhancement of the diagnostic bands that were less defined in the spectrum of the pressed-disk where specular reflectance prevailed.

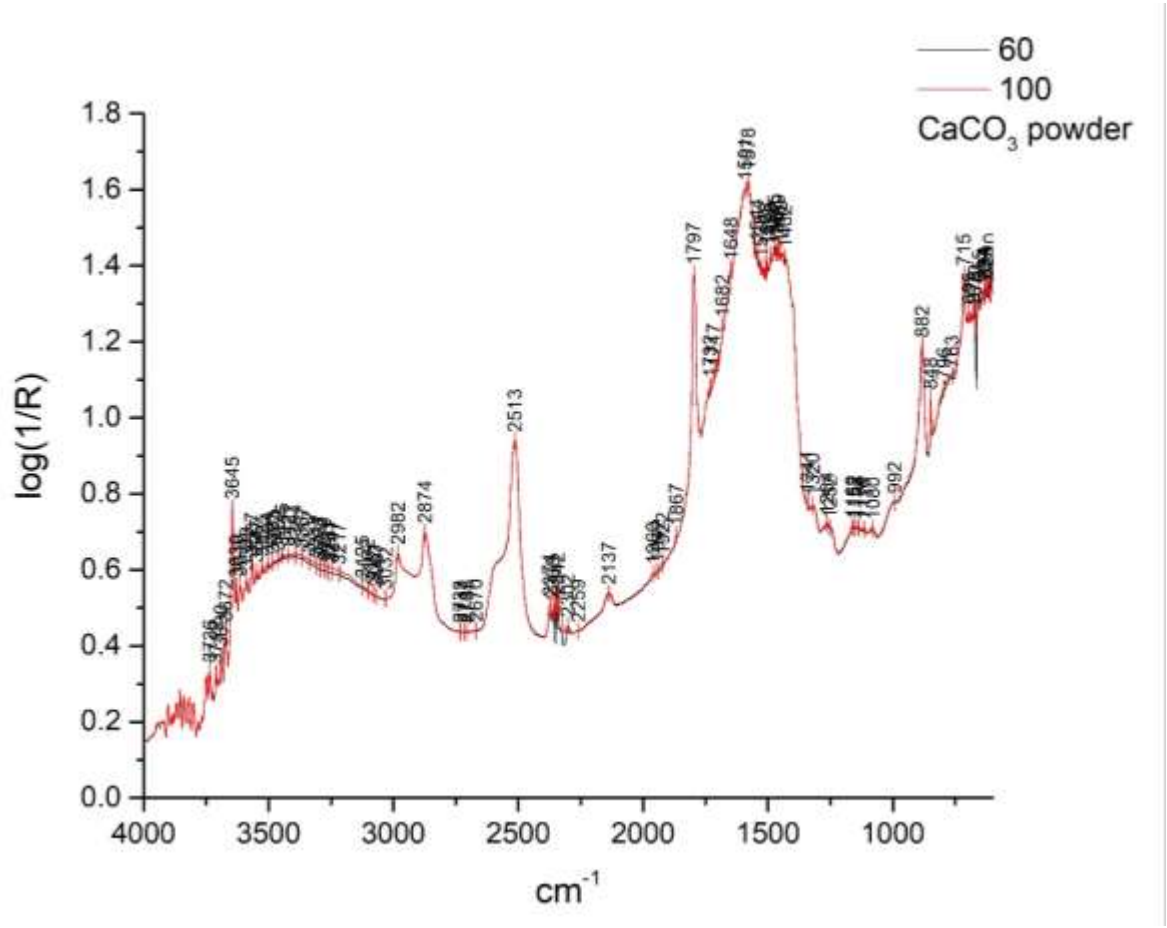

Figure 15: The spectra of $CaCO_3$ powder, obtained under different sets of acquisition parameters: black spectrum - 60 scans, red – 100 scans, 4000-600 cm^{-1}.

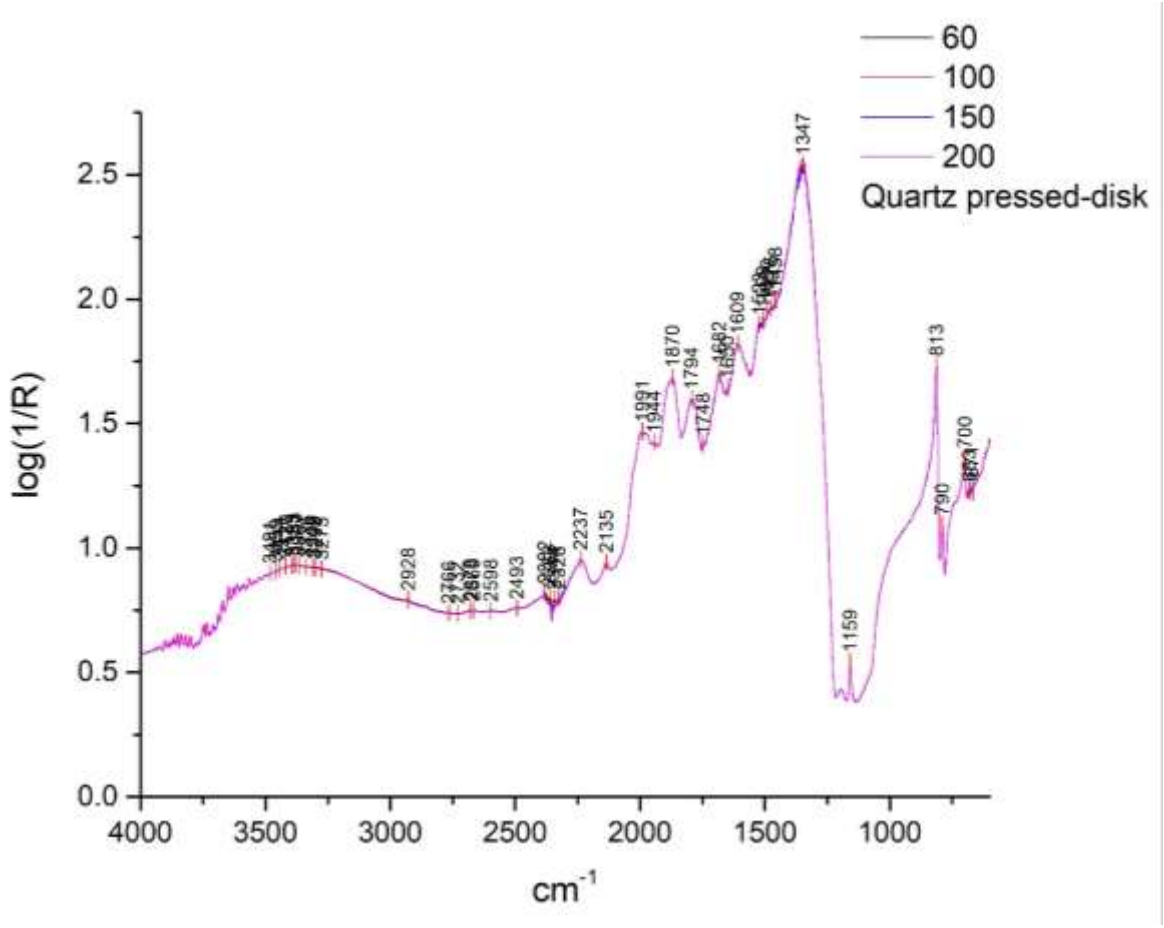

Figure 16: Overlapping comparison of spectra of quartz pressed-disk: black spectrum obtained after 60 scans, red-100 scans, blue – 150 scans and purple – 200 scans, 4000-600 cm^{-1}.

Reflectance micro-FTIR spectra were also obtained from the quartz pressed-disk within the 4000-600 cm^{-1} scan range, 4 cm^{-1} resolution after 60, 100, 150 and 200 scans (fig.16). Spectra quality did not increse significantly above 60 scans.

The 4000-600 cm^{-1} scan range contained characteristic quartz peaks: The derivative-like distortion at 813 cm^{-1} is attributed to Si-O antisymmetric modes (Miliani et al., 2012, 302). The combination bands $v+\delta$ at 1991-1682 cm^{-1} are characteristic to Si-O stretching mode (Miliani et al., 2012, 303). The distortions at 813 and 1347 cm^{-1} show the contribution of specular reflectance, whereas the shape of absorption bands within the range 2237-1609 cm^{-1} the presence of diffuse reflectance.

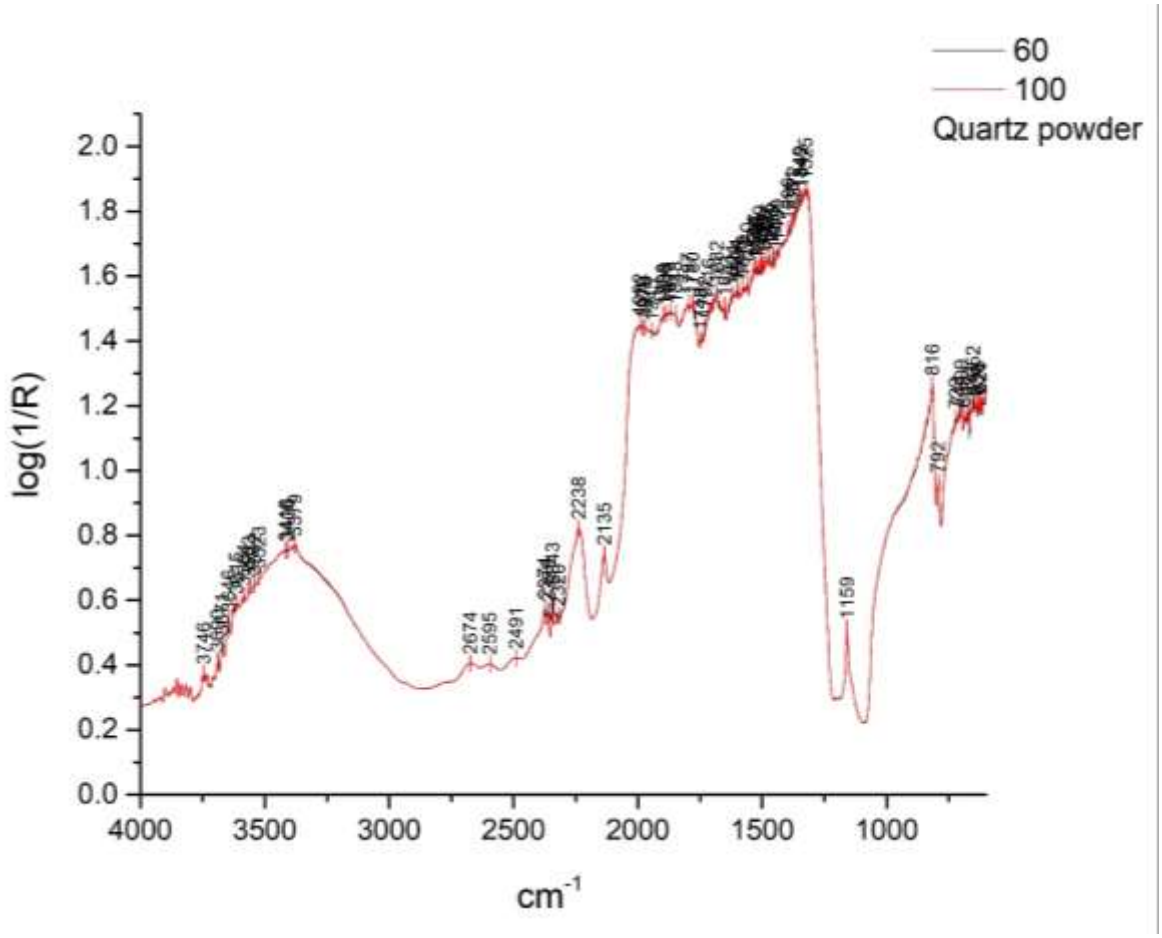

Figure 17: Overlapping comparison of spectra of quartz powder: black spectrum obtained after 60 scans, red-100 scans, 4000-600 cm^{-1}.

Spectra quality was highly similar on the spectra obtained from the quartz powder after 60 and 100 scans (fig.17). Diagnostic peaks are present similarly to those in the pressed-disk spectrum. Enhancement of weak peaks is observed in the entire spectrum showing the contribution of diffuse reflectance. The reststrahlen at 1325 cm^{-1} indicates that specular reflectance is also present.

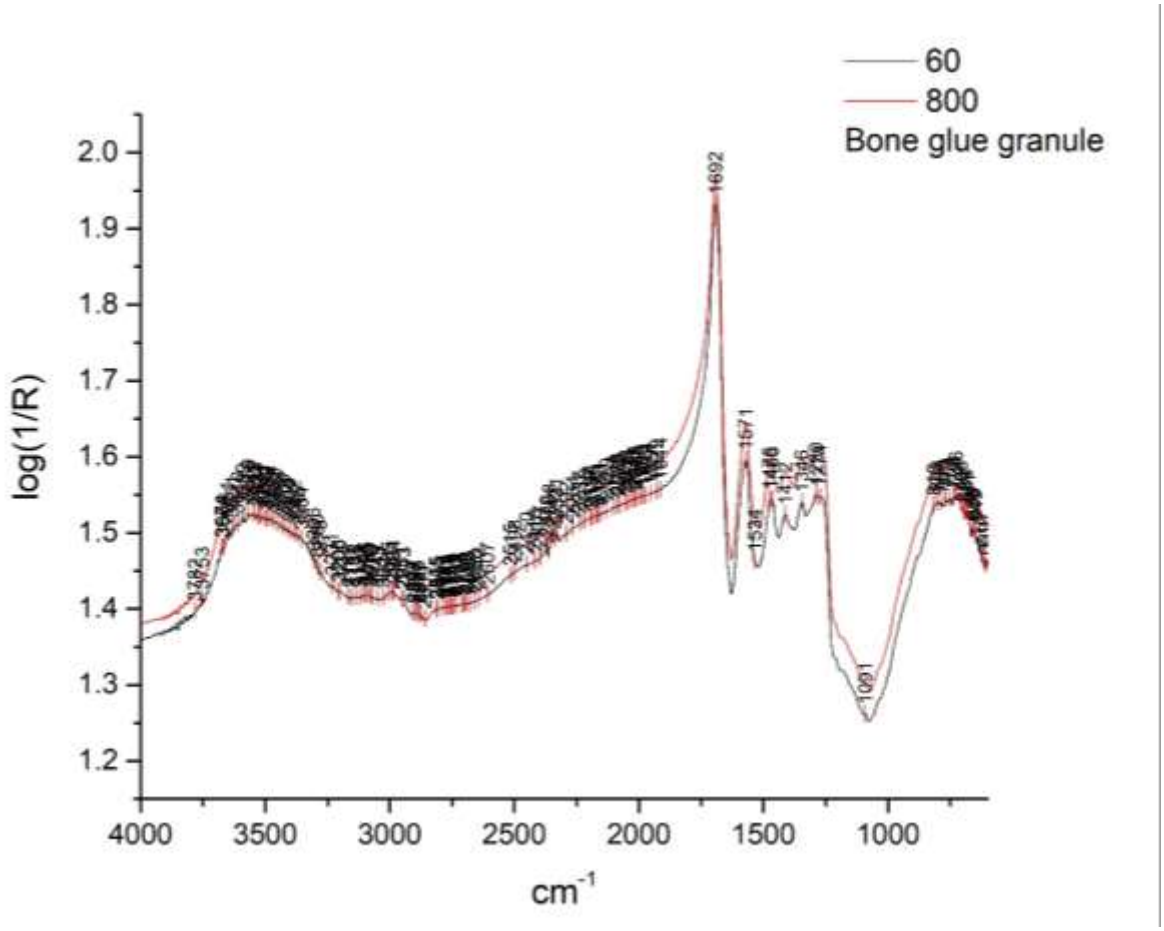

Figure 18: Overlapping comparison of spectra of bone glue: black spectrum obtained after 60 scans, red-800 scans, 4000-600 cm^{-1}.

Spectra were also obtained from the surface of a bone glue granule after 60 scans and 800 scans, 4000-600 cm^{-1} scan range, in order to assess changes in spectral quality when organic materials are under investigation (fig. 18). The quality remains high and unaltered between the two spectra, suggesting that 60 scans are adequate to deliver the necessary information for the identification of the compound.

Indeed, the characteristic stair-step type intensities of Amide III within the 1470-1260 cm^{-1} region (Rosi et al., 2009, 2099), the strong absorption of C-N-H bending amide II or N-H bond at 1571 cm-1, the dominant absorption of N-H bond at 1692 cm^{-1} (Miliani et al., 2012, 304; Rosi et al., 2009, 2104) and the weak absorption and 1st overtone of Amide I at 2885 cm^{-1} and 3103 cm^{-1} respectively are present in the spectra (Rosi et al., 2009, 2099). The shape of 1692 cm^{-1} peak and the reststrahlen at 1091 cm^{-1} indicate the influence of specular reflectance on the spectrum.

Based on the comparative assessment of spectra obtained under different acquisition parameters, it was decided to analyze all the laboratory prepared standards used in the

thesis under the following standardized operational conditions: spectra were collected in Reflectance mode after 60 scans of 4 cm^{-1} spectral resolution, for the 4000-600 cm^{-1} mid-infrared frequency range (Dirwono et al., 2010, 7).

The experiment proved in practice that the quality of the spectrum, in relation to the shape and intensity of absorption bands, is also influenced by the type of reflectance that prevails within the spectrum which is dictated by the surface texture of the sample.

5.2 Selection of IR intensity units

All spectra were collected in Reflectance mode and the IR intensity was measured in Absorbance units. Depending on the surface texture of the analyzed standard, the spectra exhibited diffuse, specular or combination of the two reflectance types.

The unit that describes IR intensity vs wavenumber on reflectance spectra is not standardized in literature: some case studies dealing with spectra of combined diffuse and specular reflectance use Pseudo-absorbance units, defined as $A' = log\ (1/R)$, where R is the total reflectivity (Rosi et al., 2010, 614; Miliani et al., 2012, 297). In case studies focusing on diffuse reflectance, intensity is measured in Absorbance units (Tewari et al., 2017). However, pseudo-absorbance units are used elsewhere as an expression of diffuse reflectance R (here R is not the total reflectivity as previously) and the logarithm $log\ (1/R)$ defines Absorbance too (Berntsson et al., 1998, 243). The logarithm is also combined with the term “Arbitrary units” (Ploeger et al., 2010) or “Absorbance arbitrary units” (Poli et al., 2009, 175; Nevin and Fonjaudran, 2015, 117).

The Perkin-Elmer Spectrum v.10.3 Software provides selection between the two units A or $log\ 1/R$. Figure 19 shows the overlapping spectra of the Perkin-Elmer polystyrene (PS) film standard (black line) viewed in A and in $log\ (1/R)$ (red line). The spectra are almost identical and any minor differences are attributed to repeatability operational variables. The same stands for the spectra of $CaCO_3$ pressed-disk standard obtained and viewed in both units (fig.20).

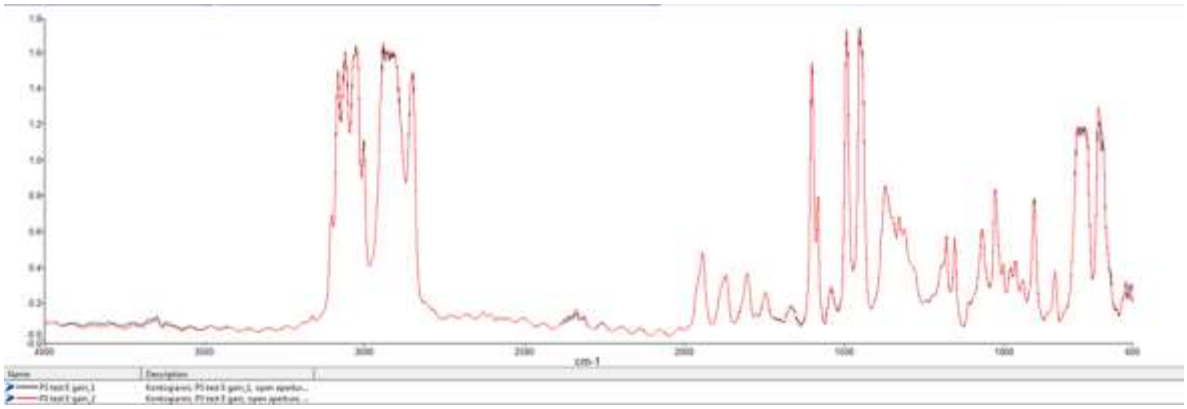

Figure 19: Comparison of PS spectra viewed in A (black line) and log (1/R) units (red line).

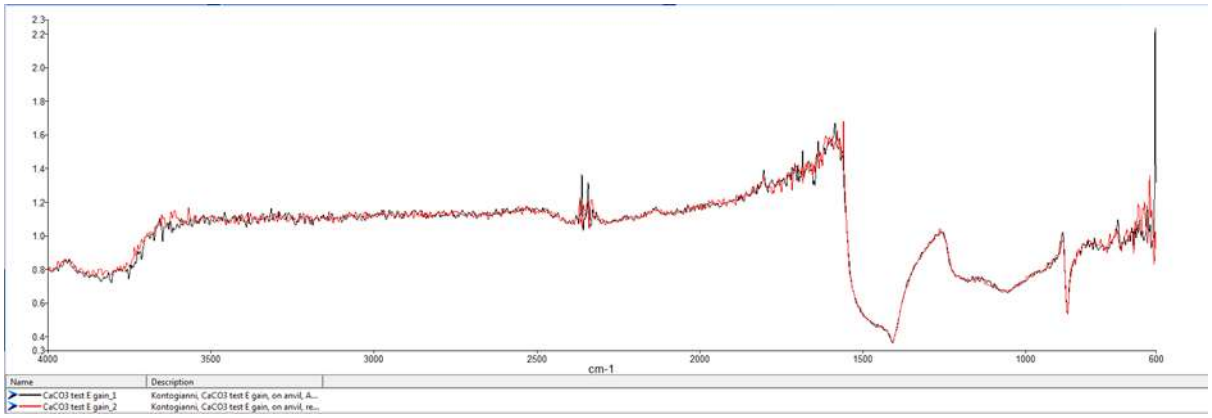

Figure 20: Comparison of $CaCO_3$ spectra viewed in A (black line) and log (1/R) units (red line).

Since Absorbance and Pseudo-absorbance units do not affect spectral features, it was decided to measure IR intensity in Absorbance units and to graphically change the spectrum legend in *log (1/R)* for consistency with the most representative literature that uses Pseudo-absorbance units to simply demonstrate the coexistence of specular and diffuse reflectance in spectra obtained from materials that exhibit differential texture (Miliani et al., 2012; Rosi et al., 2010; Rosi et al., 2009).

5.3 Manipulation of Spectral Data

When quantitative information is required from reflectance spectra or comparison to Transmittance spectra, mathematical models are applied that calculate absorbance according to the type of reflectance (Skoog et al., 1998, 419). The Kramers-Kronig (K-K) algorithm is applied on specular reflectance spectra for the separation of absorption index from the refractive index, whereas the Kubelca-Munk (K-M) algorithm provides corrections for diffuse spectra (Poli et al., 2009). However, in spectra of combined reflectance such corrections are not recommended since each algorithm will ignore the spectral data of the type of reflectance that is not dealing with (Buti et al., 2013, 2705; Miliani et al. 2012, 295).

According to the Perkin-Elmer software instructions, K-M correction of highly absorbing peaks is not performed and peaks are truncated, resulting in loss of information. This is evident in figure 21, where the K-M algorithm was applied on the spectrum of Calcium Oxalate powder standard.

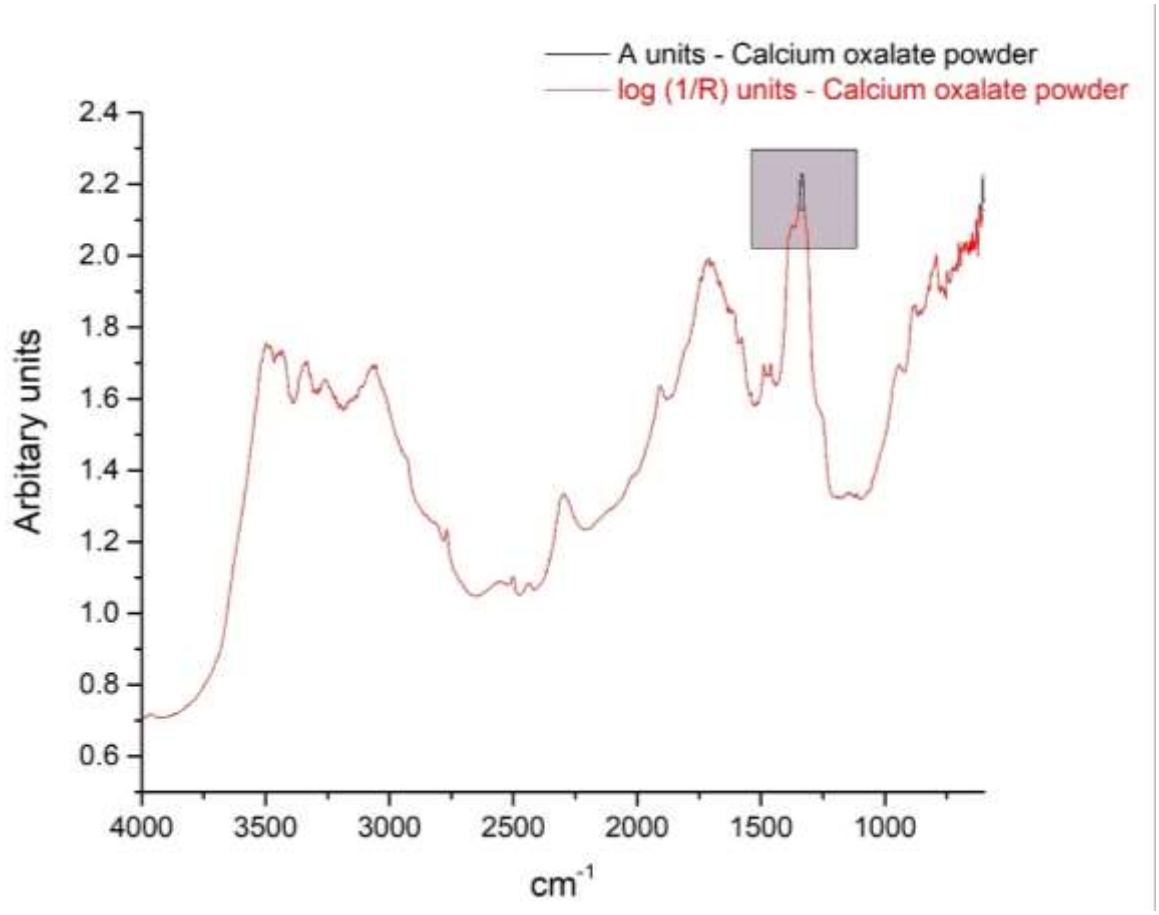

Figure 21: Comparison of calcium oxalate powder spectrum viewed in A (black line) and after K-M correction (red line). The highlighted peak at 1400 cm^{-1} is truncated.

Consequently, the application of K-K and K-M algorithms on the reflectance spectra obtained for the thesis is excluded since:

- quantitative analysis is beyond the scope of the thesis,
- the combined presence of specular and diffuse reflectance in some of the standards, such as bone glue granule, quartz and mortar/organic mixtures, rules out either correction,
- specular reflectance spectra carry diagnostic features that would be lost by the K-K correction,
- diffuse reflectance spectra may lose high absorption peaks during K-M correction,

- the characteristic enhancement of minor peaks in diffuse reflectance spectra should be retained and assessed for its contribution to the identification processes.

Most importantly, any mathematical processing on reflectance spectra that alters their characteristic features in order to resemble spectra obtained by other FTIR spectroscopy methods does not serve the thesis aims. Reflectance micro-FTIR spectroscopy should be evaluated independently as an analytical method, through the spectral data that is able to provide.

Chapter 6: Accuracy and Precision

For confidence in the quality and repeatability of data, the accuracy and precision of the spectra acquisition methodology have to be determined and any systematic and/or random errors to be detected and dealt with, in order to achieve a standardized framework for the identification of reflectance spectra through comparative assessments (Miller and Miller, 2010, 5).

Accuracy and precision were determined from the analysis of standards of known composition (Markucic, 2002, [online]). Two standards of differing texture, the Perkin-Elmer Polystyrene (PS) film and the $CaCO_3$ pressed-disk were analyzed by External Reflectance FTIR micro-spectroscopy. Two spectra were collected daily from each standard, at the beginning of each analytical session (Sect. 6.1 and 6.2) The spectra were collected randomly from the surface of each standard in order to evaluate the influence of surface texture and morphology in the degree of accuracy and precision. The daily assessment of accuracy and precision was based on the calculation of the “true value” for both standards and the deviations of the measurements from it (Miller and Miller, 2010, 5).

The influence of sample morphology and texture in the degree of accuracy and precision was also assessed by comparing the spectra obtained randomly from the surface of the standards with spectra obtained from the same surface spot (6.3).

Following the spectra acquisition methodology (sec. 5.1), energy gain was recorded in Transmittance mode at the beginning of each analytical session (instrument performance check). Energy gain measurements were also obtained in Reflectance mode from a) the surface of the golden mirror before background collection (instrument performance between runs) and b) from the surface of each standard before spectra collection (texture and morphology influence). Upon analysis, the PS film was placed over the reflective golden mirror for achieving maximum reflectance and minimizing the rest individual intensities according to equation 4.2, Chapter 4.

Accuracy is defined as the “closeness of agreement between a test result and the accepted reference value” (Miller and Miller, 2010, 5). Accordingly, the reference or “true value” for the PS film standard was the mean PS film spectrum averaged from the two individual PS spectra obtained at the day that the maximum energy gain in Reflectance mode was recorded. The same stands for the mean $CaCO_3$ pressed-disk spectrum.

Precision in terms of repeatability examines the closeness of the agreement between repeated measurements taken with the same method, standards, operator and laboratory

and within short time intervals: their dispersion around the mean provides information on the occurrence of random errors (Markucic, 2002, [online]).

Since the same standards were used in the measurement of accuracy and precision, systematic errors deriving from the sampling process were excluded (Cullum and Vo-Dinh, 2003, 18). In contrast, random errors could occur, especially due to the variation in the maximum energy gain in Transmittance (instrument variable) and Reflectance (instrument variable between runs and surface texture variable) modes (Stone and Ellis, 2008, [Online]).

Confidence intervals evaluate the presence of outliers and consequently the occurrence of random errors in the precision of the measurements (Cullum and Vo-Dinh, 2003, 18). The recommendation of the International Union of Pure and Applied Chemistry (IUPAC) for spectroscopy measurements is to use $\pm 3\sigma$ (3 times the standard deviation of the measurements from the reference value). Doing so, a confidence level of approximately 90% is ensured and all the representative samples will fall within it, enabling secure rejection of outliers (Thomsen et al., 2003, 112).

6.1 During a single analytical session

The spectra of PS film and $CaCO_3$ pressed-disk obtained during the 2017 analytical session are listed in table 6. The spectra highlighted in dark green (PS film) and light green ($CaCO_3$ pressed-disk), obtained at 17/10/17, were averaged and served as reference values. The selection criterion was that the equipment operated with the highest and most repeatable measured energy gain in Reflectance for both standards for the entire experimental session.

Spectrum ID	Energy gain - Surface	Energy gain in R	Date of Acquision
PS_1_c	4487	6200	16/10/2017
PS_2_c	4348	6200	16/10/2017
Ca_1_c	647	6483	16/10/2017
Ca_2_c	645	6483	16/10/2017
PS_1_t	4915	6500	17/10/2017
PS_2_t	4664	6500	17/10/2017
Ca_1_t	577	6500	17/10/2017
Ca_2_t	671	6500	17/10/2017
PS_1_O	4485	6319	18/10/2017
PS_2_O	4437	6319	18/10/2017
Ca_1_O	467	6319	18/10/2017
Ca_2_O	486	6319	18/10/2017
PS_1_TR	4296	6239	20/10/2017
PS_2_TR	4350	6239	20/10/2017
Ca_1_TR	675	6090	20/10/2017
Ca_2_TR	651	6090	20/10/2017
PS_1_TE	5197	6454	21/10/2017
Ca_1_TE	674	6172	21/10/2017
PS_1_TES	4729	6663	23/10/2017
Ca_1_TES	571	6427	23/10/2017
PS_1_TEST	3974	5608	24/10/2017
Ca_1_TEST	748	5528	24/10/2017

Table 6: List of Energy gain measurements for the acquisition of PS film and $CaCO_3$ pressed-disk spectra, 2017 analytical session.

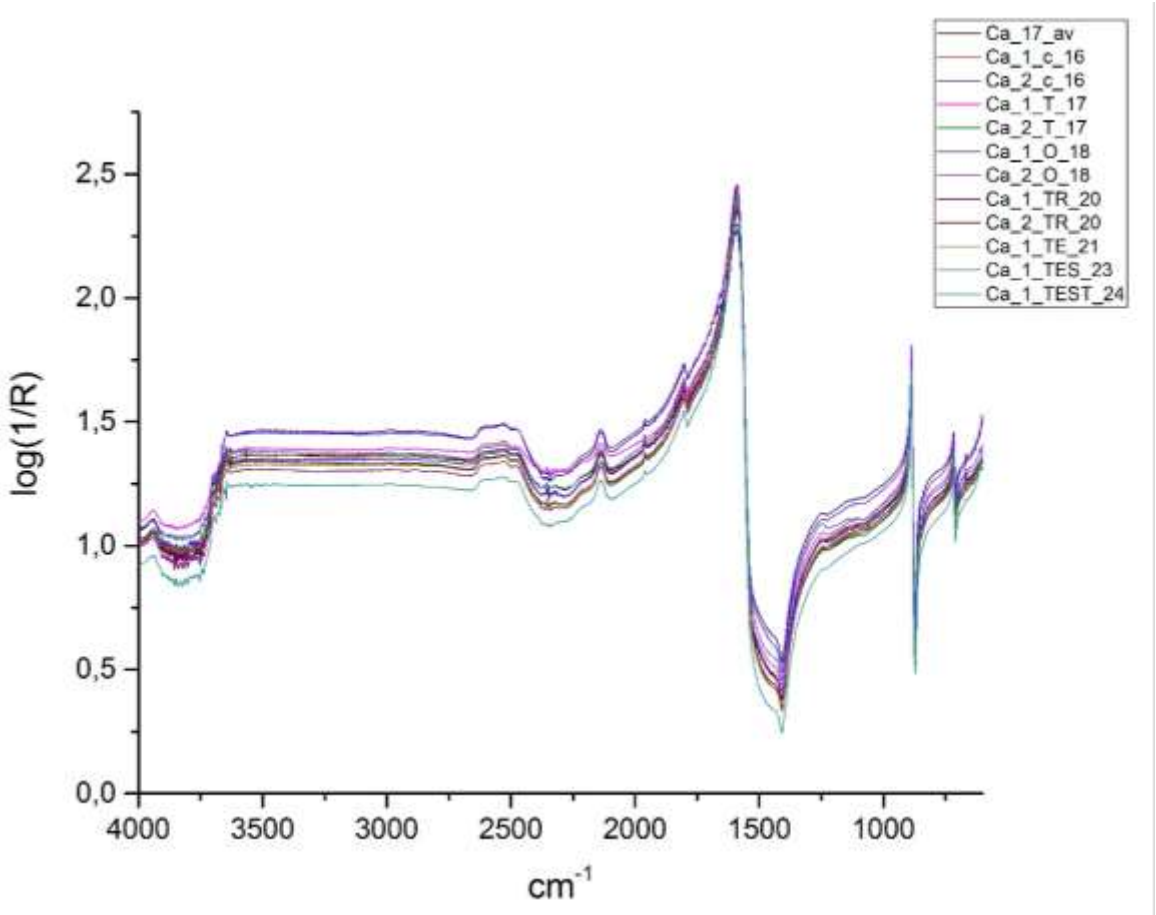

Figure 22: Accuracy of reflectance micro-FTIR spectra for the $CaCO_3$ pressed-disk standard.

High accuracy was recorded between the spectra of $CaCO_3$ pressed-disk obtained daily and the reference spectrum Ca_17_av (fig.22). High spectra quality is evident from the low detector interference around 2300 cm^{-1} (Ricci et al., 2006, 1222), the similar baseline, the presence of sharp representative peaks of $CaCO_3$ and the high signal-to-noise ratio for all spectra. Specular reflectance is pronounced as expected from the smooth and polished surface of the pellet.

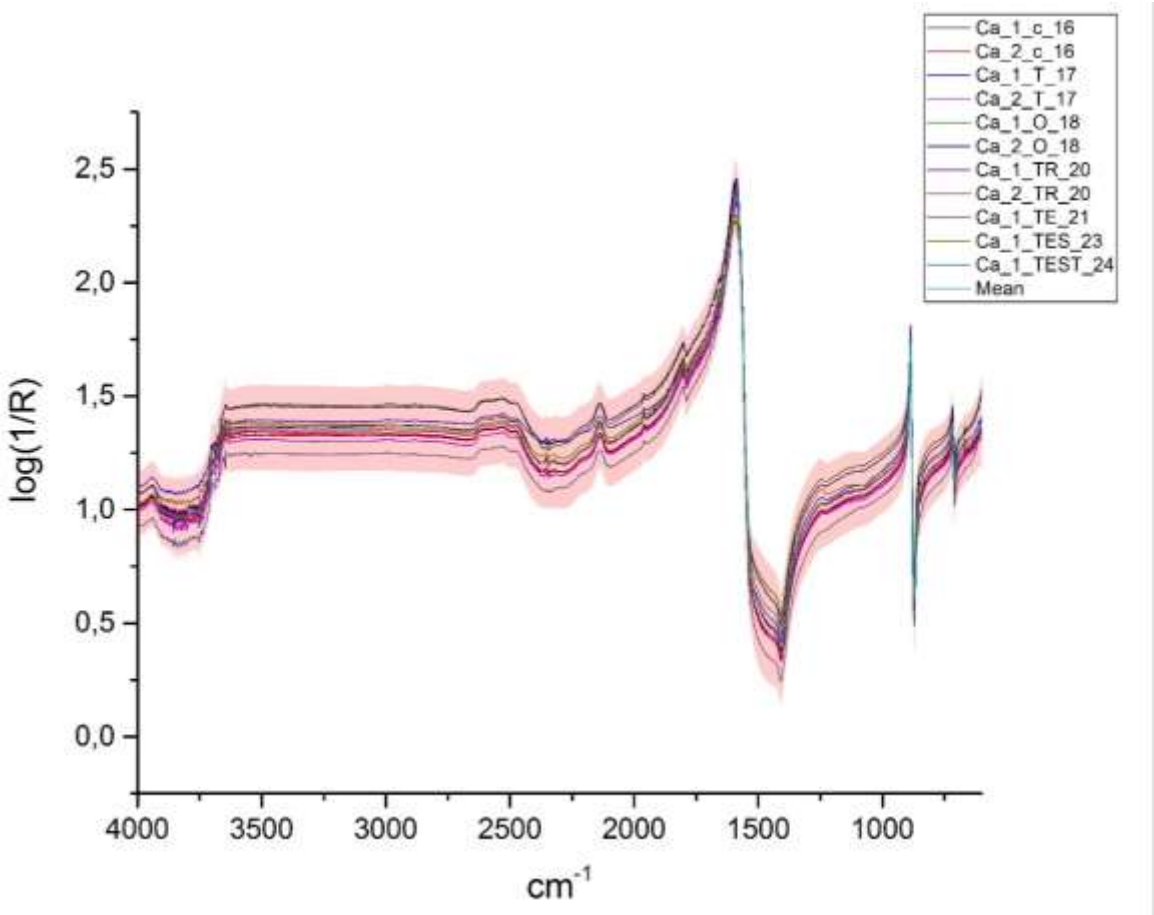

Figure 23: Precision of reflectance micro-FTIR spectra for the $CaCO_3$ pressed-disk standard.

The precision (repeatability) of measurements is also high and within confidence intervals (fig.23). Spectra Ca_1_O_18 and Ca_2_O_18, collected on the 18/10/17 and the Ca_1_TEST_24, collected on the 24/10/17, differ slightly from the bulk spectra in terms of absorption intensity and are responsible for the broadening of confidence intervals. However, the precision of the reststrahlen at 1404 cm^{-1} (Ricci et al., 2006, 1222) and first order derivatives of the *v4* carbonate ion at 887 and 718 cm^{-1} remains high (Ylmen and Jaglid, 2013, 119).

Since the spectra were collected from the same standard, random errors should have derived from the equipment performance on the day and/or the inhomogeneous surface texture of the pressed-disk: Spectra Ca_1_O_18 and Ca_2_O_18 were obtained at high energy gain in Reflectance (6319) but low energy gain on the pressed-disk surface (approx. 470, Table 6). This value is the lowest recorded from the pressed-disk surface and likely to have resulted in lower absorption intensities on the spectra. The opposite occurred for the spectrum Ca_1_TEST_24, collected on a day that the IR radiation source operated with a maximum reflectance energy gain of 5528 (lowest recorded) and produced energy gain of 748 units when the IR radiation reached the surface of the pressed-disk.

Since the detector interference remains very low for all spectra, indicating that the performance of the instrument was satisfactory, it is assumed that random errors are more likely deriving from the surface morphology of the pressed-disk and its absorption properties that may differ regionally. The potential that random errors occur on pressed-disks more than films is reinforced by the assessment of the PS outcomes below.

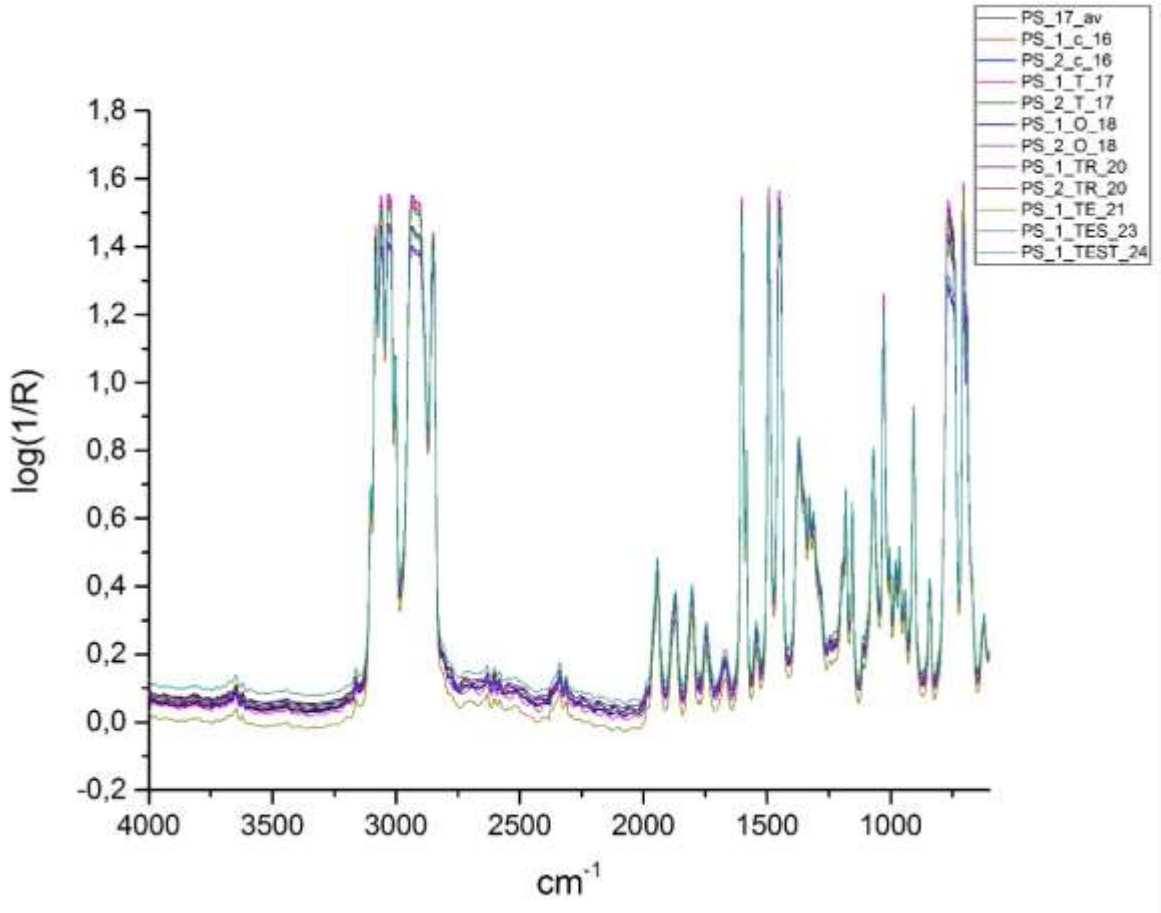

Figure 24: Accuracy of reflectance micro-FTIR spectra for the PS film standard.

High quality spectra were collected from the PS film standard showing high accuracy with the reference spectrum PS_17_av (fig.24). The minor peaks within the region 2500-2000 cm^{-1} exhibit insignificant shifting relevant to the reference spectrum, attributed to noise due to the detector interference that takes place within this region.

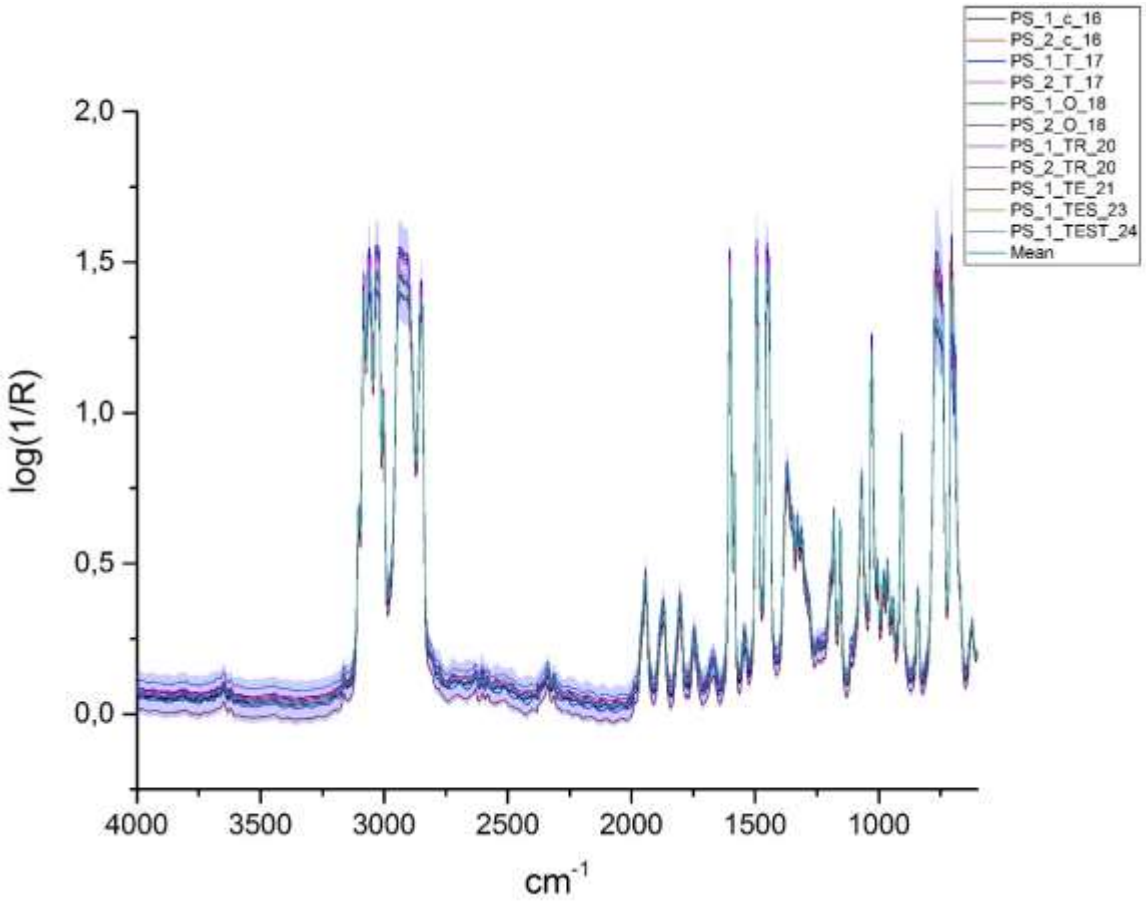

Figure 25: Precision of reflectance micro-FTIR spectra for the PS film standard.

High repeatable measurements within very narrow confidence intervals show low potential for random errors (fig.25). The spectrum PS_1_TE_21, collected on the 21/10/17 differs slightly from the bulk. According to table 6, the energy gain from the film surface was 5197 units, which is the maximum measured from the PS film surface. Again, regional difference on the film surface texture influences absorption intensities and spectra repeatability, although in a lesser extent than that observed on pressed-disks.

6.2 Between analytical sessions

The degree of accuracy and precision between analytical sessions that take place in a wider time interval than within successive days as in a single session was assessed, in order to evaluate whether the quality of spectra remains unaltered and allows their comparative assessment. Accordingly, the spectra of $CaCO_3$ pressed-disk and PS film obtained during the analytical session of 2017 were compared with those obtained a year earlier in 2016. The Energy gain measurements from the PS film and $CaCO_3$ pressed-disk standards from the 2016 analytical session are provided in Appendix I, table 1.

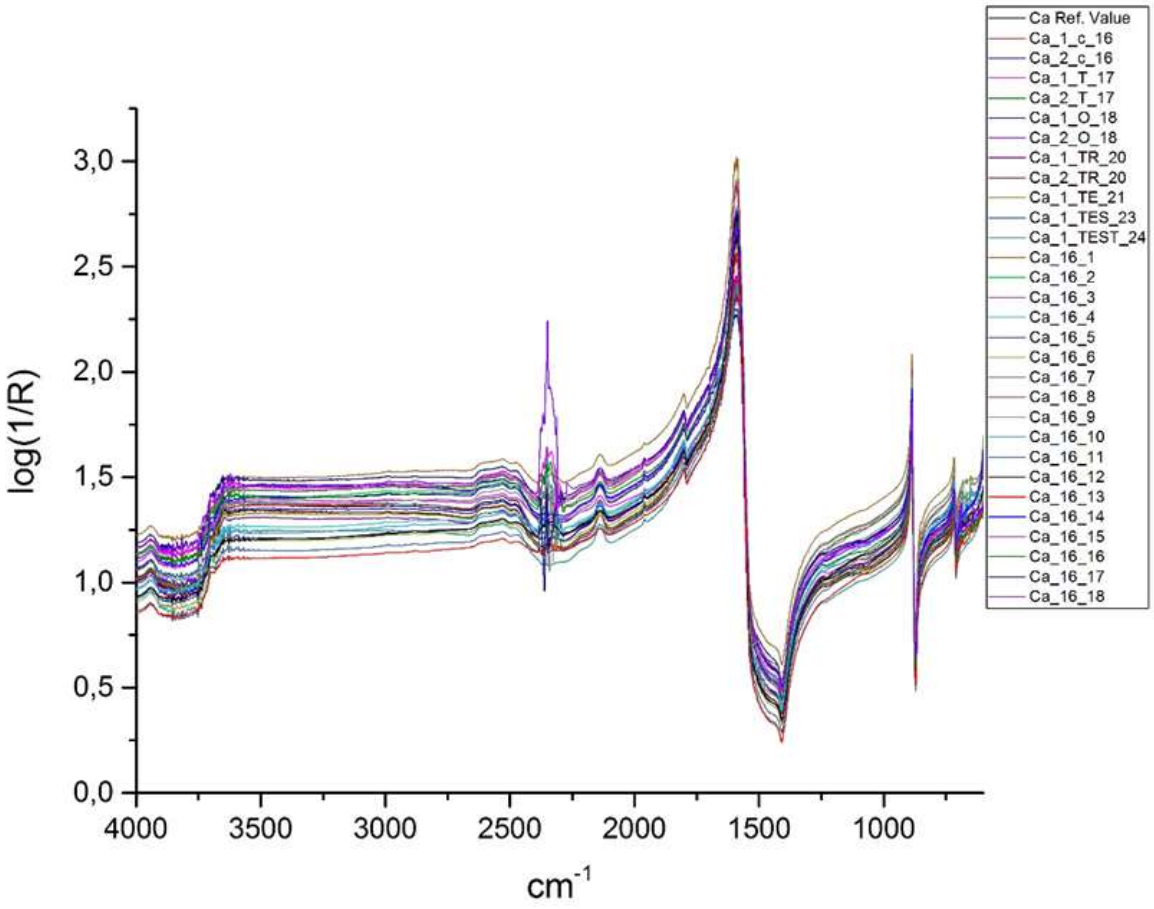

Figure 26: Accuracy of reflectance micro-FTIR spectra of $CaCO_3$ pressed-disk standard obtained during the 2016 and 2017 analytical sessions.

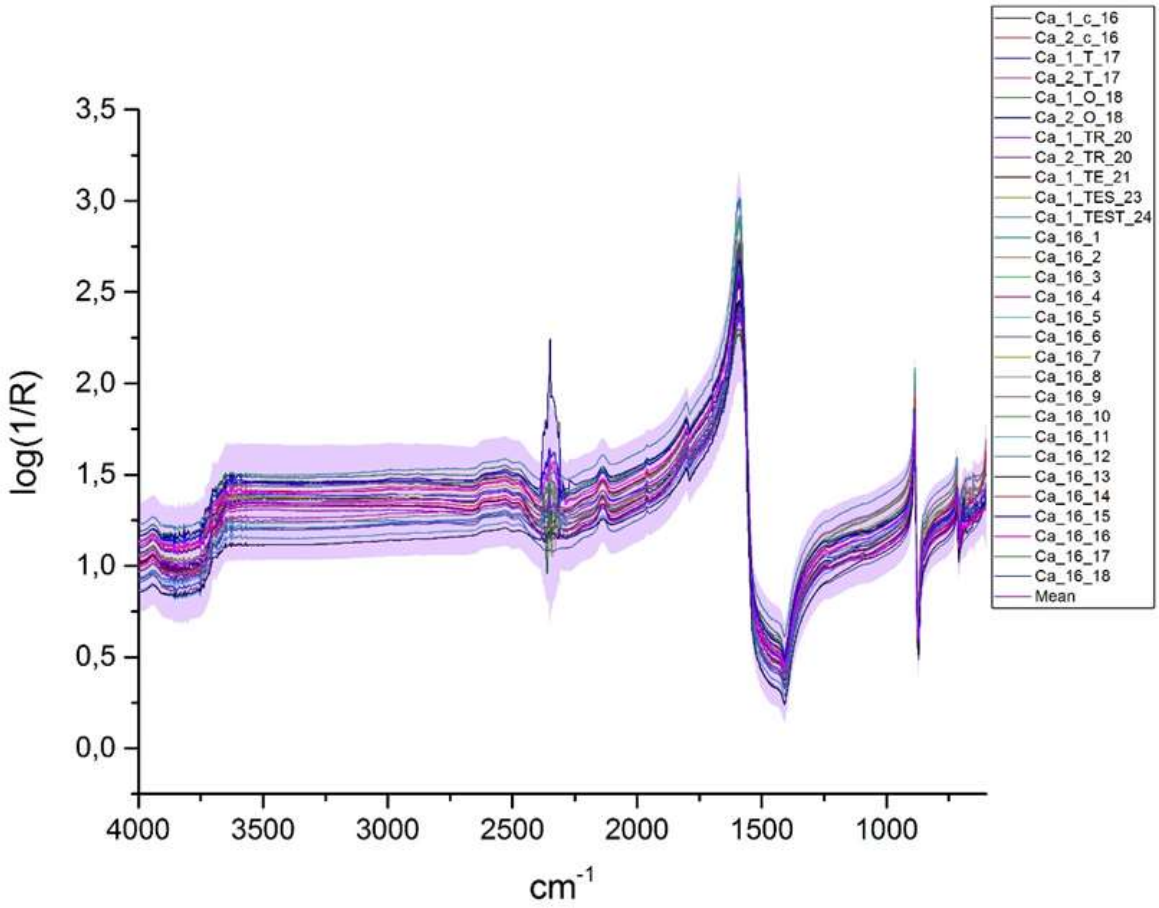

Figure 27: Precision of reflectance micro-FTIR spectra of $CaCO_3$ pressed-disk standard obtained during the 2016 and 2017 analytical sessions.

High accuracy and precision are observed among the spectra of $CaCO_3$ pressed-disk standard obtained during the 2016 and 2017 analytical sessions, despite the high detector interference at 2300 cm^{-1} and noise below 700 cm^{-1} observed at the Ca_16_18 spectrum obtained on the 23/6/16 (fig.26-27). These effects are responsible for the broadening of the confidence intervals and are attributed to random errors from the performance of the equipment on the specific day rather than surface texture, since they are detected on spectral areas sensitive to the detector.

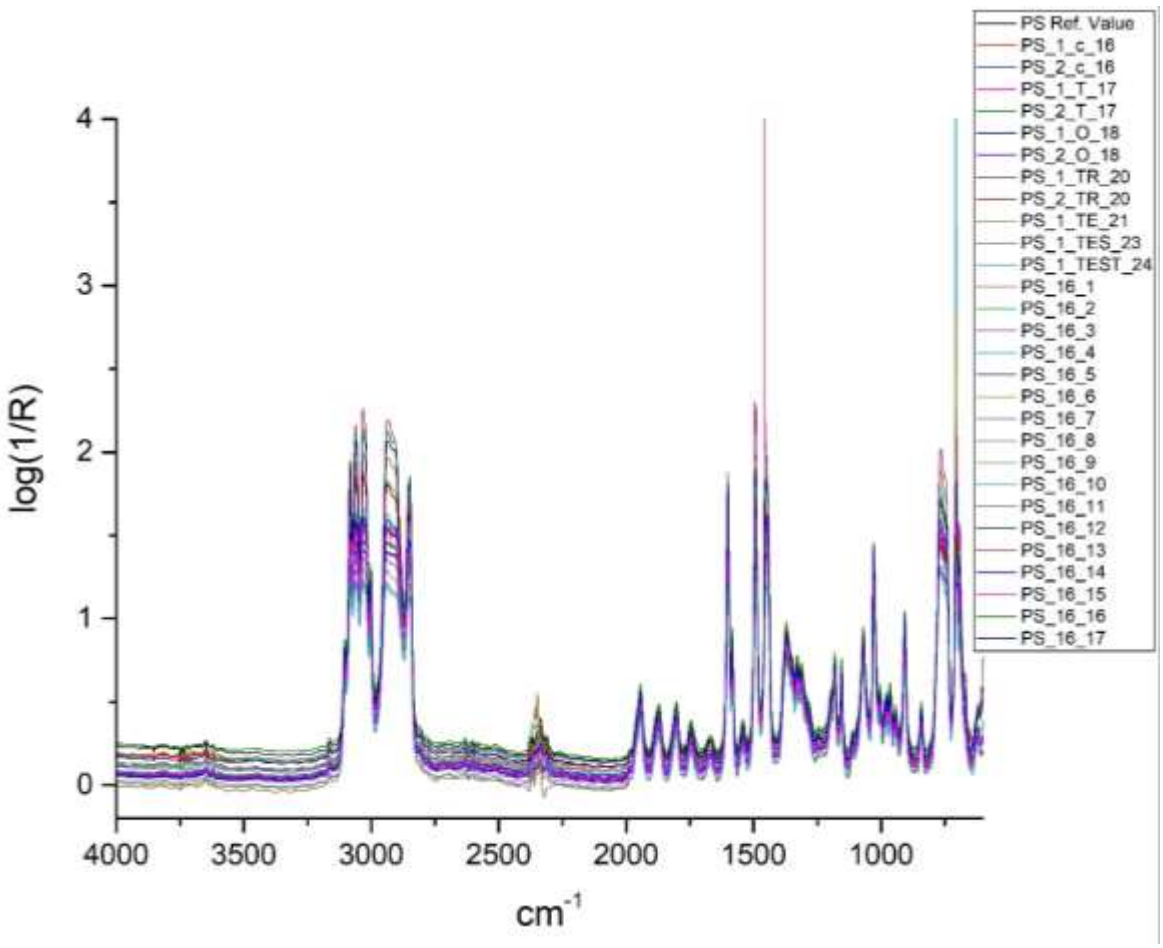

Figure 28: Accuracy of reflectance micro-FTIR spectra for the PS film standard obtained during the 2016 and 2017 analytical sessions.

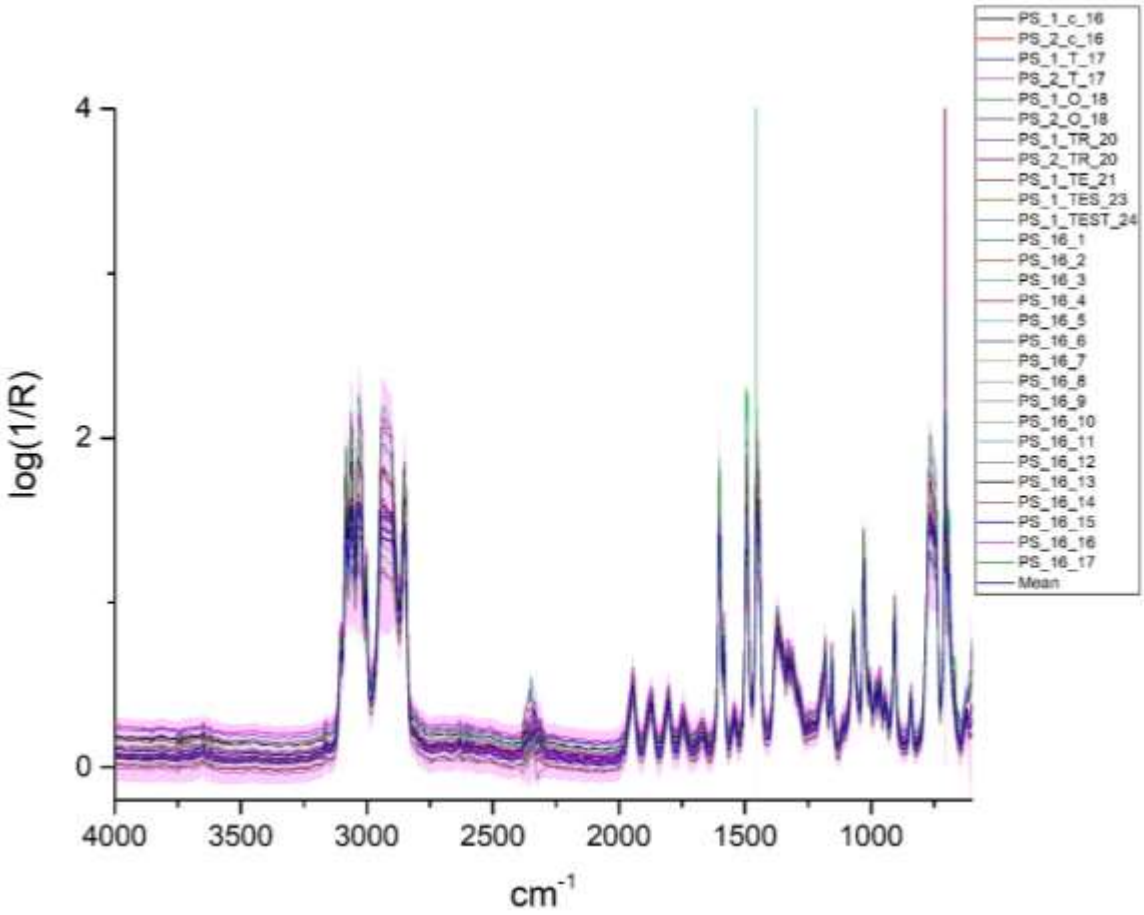

Figure 29: Precision of reflectance micro-FTIR spectra for the PS film standard obtained during the 2016 and 2017 analytical sessions.

Accuracy and precision among the spectra obtained from the PS film standard during the 2016 and 2017 analytical sessions are high (fig. 28-29). Confidence intervals are narrow, showing low potential of random errors. Small broadening of confidence intervals is observed around 3000 cm^{-1} without affecting the overall precision.

Relevant to texture, the spectra from the PS film standard show better results from those obtained from the $CaCO_3$ pressed-disk, reinforcing the assumption that surface morphology affects spectra quality, accuracy and precision. The uniform, homogenous surface texture of the PS film provides more accurate and repeatable spectra than the crystalline texture of the $CaCO_3$ pressed-disk that may incorporate crystals of different size. The crystal lattice is expected to be affected by the grinding and pressure during the production of the pressed-disk, which in turn may shift absorption bands in the spectrum (Stuart, 2004, 97).

Differing texture will exhibit different absorbing properties even within the same material, as it is observed from the spectra of both standards and the energy gain measurements

for each spectrum. This is more easily detected in the case of $CaCO_3$ pressed-disk, although minor abrasions on the surface of the PS film also resulted in differing absorbing capacity. However, the fact that the PS film was analyzed over the highly reflective golden mirror, allowed higher IR radiation to reach the detector and improved the spectra quality.

6.3 Same surface spot vs randomly selected

A final test for securely verifying the influence of differential surface texture on the degree of accuracy and precision of the spectra was carried out by visually assessing repeatable spectra obtained from the same surface spot compared to spectra obtained randomly from the surface of the standards.

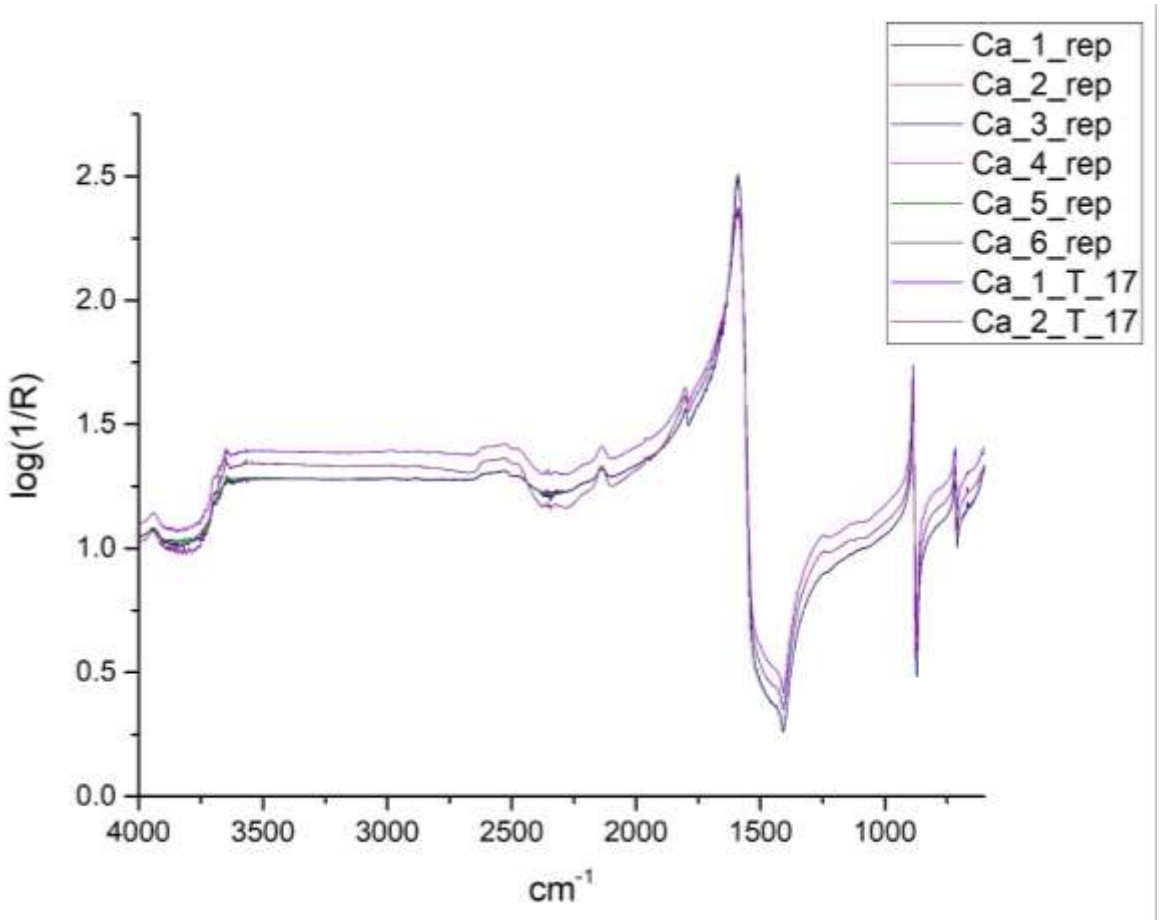

Figure 30: Repeatable spectra obtained from the same surface spot of the $CaCO_3$ pressed-disk compared to spectra obtained randomly from the surface (Ca_1_T_17 and Ca_2_T_17).

Spectrum ID	Energy gain - Surface	Energy gain in R	Date of Acquisition
Ca_1_rep	830	6910	19/10/2018
Ca_2_rep	830	6910	19/10/2018
Ca_3_rep	831	6910	19/10/2018
Ca_4_rep	831	6910	19/10/2018
Ca_5_rep	832	6910	19/10/2018
Ca_6_rep	833	6910	19/10/2018
PS_1_repr	5288	6183	19/10/2018
PS_2_repr	5291	6183	19/10/2018
PS_3_repr	5294	6183	19/10/2018
PS_4_repr	5280	6183	19/10/2018
PS_5_repr	5294	6183	19/10/2018
PS_6_repr	5299	6183	19/10/2018

Table 7: List of Energy gain measurements for the acquisition of PS film and $CaCO_3$ pressed-disk spectra from the same surface spot, 2018 analytical session.

The spectra Ca_1_rep to Ca_6_rep obtained from the same surface spot are highly repeatable because they were collected under stable energy gain of 830-833 units, showing the relationship between IR absorbing capacity and texture (fig.30 and Table 7). The remaining two spectra differ slightly because they were collected randomly from the surface, exhibiting different energy gain (577 and 671, Table 6, sect.6.1). Their lower energy gain than that observed on the highly repeatable spectra is responsible for the higher baseline and lower signal-to-noise ratio in the 4000-3600 cm^{-1} region. The accuracy of spectral data remains high regarding the position of absorption bands.

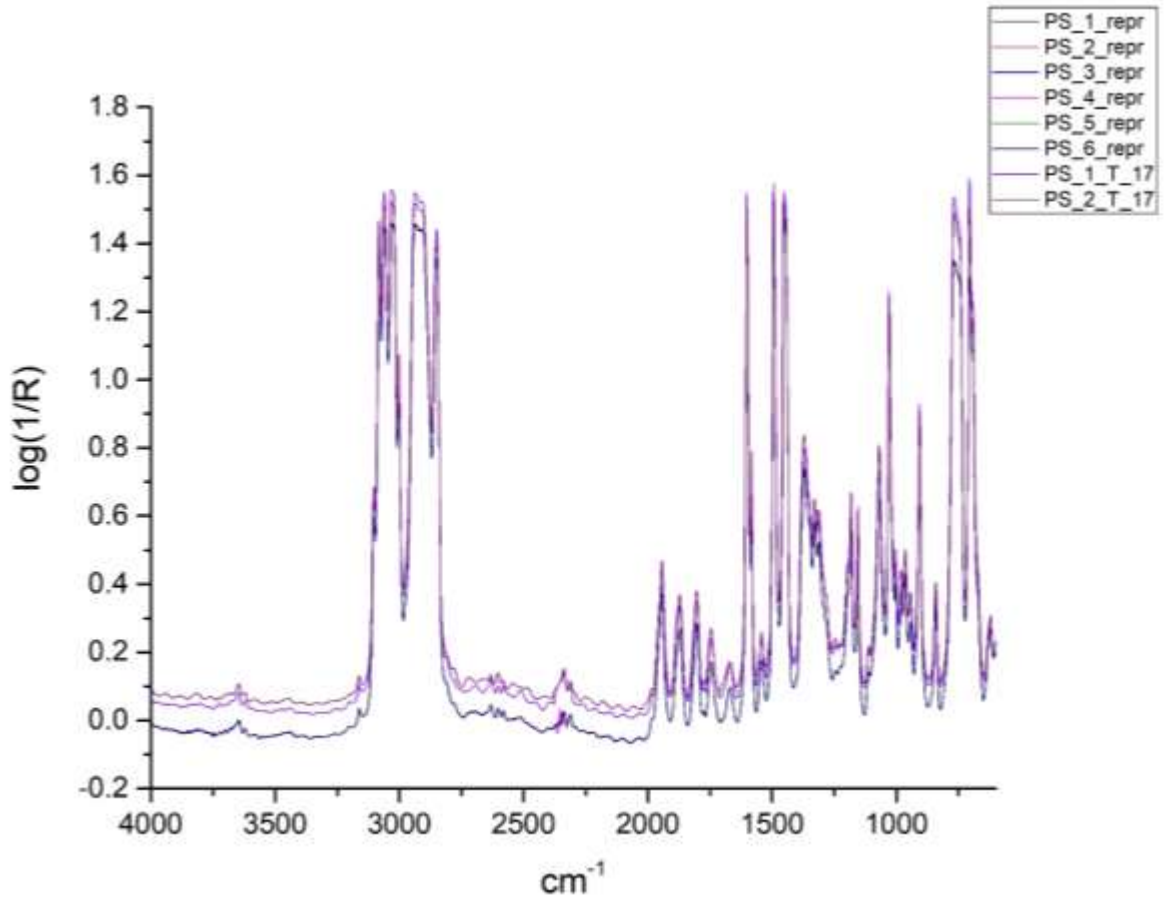

Figure 31: Repeatable spectra obtained from the same surface spot of the PS film compared to spectra obtained randomly from the surface (PS_1_T_17 and PS_2_T_17).

Similarly, the repeatability among spectra obtained from the same spot of the PS film is higher than that of spectra collected randomly from the surface (fig.31, Table 7). The accuracy of spectral data remains high relevant to the position of absorption bands with negligible fluctuations in baseline and absorbance intensity.

6.4 Outcome

The determination of accuracy and precision of reflectance micro-FTIR spectra obtained from the $CaCO_3$ pressed-disk and PS film standards, provided the quality verification of the spectra acquisition methodology. The successive assessments within a single analytical session and between sessions with wide time intervals of implementation proved that confidence in the quality and repeatability of data through the designed spectra acquisition methodology is high.

The influence of texture was verified and is considered responsible for the occurrence of random errors than mainly affect the absorption intensity and not the position of absorption bands in the spectrum. However, in homogenous standards it is expected that the effect

will be negligible, especially in the acquisition of spectra from films that are free from crystal latices.

The collection of spectra from randomly selected surface areas will be retained in the acquisition methodology since it provides a complete spectral profiling of the analyzed material.

Chapter 7: Chemical Peak Assignment Database

The effectiveness of External Reflectance FTIR Micro-Spectroscopy in the detection and identification of organic mortar additives relies on the development of a Chemical Peak Assignment Database (CPAD onwards) tailored according to the chemical composition of the materials in question, where the reflectance characteristic spectral features and distortions can be used for diagnostic purposes (Rosi et al., 2010, 617; Ricci et al., 2006, 1223).

Accordingly, the CPAD must effectively utilize all the available Reflectance FTIR spectral data for the chemical discrimination of organic additives in mortar matrices and overcome issues of interference with other components present (Miliani et al., 2012; Rosi et al., 2010; Rosi et al., 2009). This process requires comparative assessments of spectra and depends on the appropriate selection of representative standards, the design of the CPAD and its effective application.

The Chemical Peak Assignment Database is developed from:

- Spectra obtained from standards by Reflectance FTIR micro-spectroscopy
- Chemical assignments of bands from spectra obtained by different Reflectance FTIR methods in literature (DRIFT, portable FTIR spectrometer, micro-FTIR)

The standards were selected according to their reference in the available literature as organic additives and mortar components (Ch.2 and 3). The selected organic materials represent the organic groups of proteins, oils/fats, starch/sugars and hydrocarbons (Mills and White, 1987; Lombardi and Santarelli, 2009). Spectra were obtained from individual organic materials and mortar components (Table 8) and from their combined state in mortar mixtures (Sect. 7.3, Table 9).

Standard	Analysis As	Spectrum ID	Product Information
Bone glue	Film	**BG_av**	Granules - FT-IR reference collection, Department of Archaeology and Conservation
Egg whole	Film	**E_av**	Welsh egg
Egg white	Film	**EW_av**	Welsh egg
Egg yolk	Film	**EY_av**	Welsh egg
Milk	Film	**Mi_av**	M+S Welsh whole milk: fat = 40 g - saturates = 2.5 g, carbohydrate sugars = 4.7 g, protein = 3.2 g, salt = 0.15 g all per 100 g
Rice solution	Film	**R_av**	Long grain rice: Golden Sun Lidl: fat < 0.5 g, carbohydrates = 23 g, sugars < 0.5 g, fibre < 0.5 g, protein = 2.1 g all per 100 g
Olive oil	Film	**O_av**	Sainsbury's brand
Lard	Film	**L_av**	250 gr: Lidl: fat = 10 g, saturates = 4.4 g both per 10 g, pork lard, extracts of rosemary, antioxidants, Tocepherol rich extract
Asphalt	Powder	**A_av**	Asphalt of Syria, FT-IR reference collection
Calcium Carbonate	Powder	**Ca_av**	Precipitated Fisher Chemical
Quartz	Powder	**Q_av**	Pure, 40-100 mesh ACROS ORGANICS

Table 8: List of organic and inorganic materials analysed by External Reflectance FTIR micro-spectroscopy as standards.

7.1 Mortar standard

The mortar standard was prepared by mixing Calcium carbonate precipitated (Fisher Chemical) with pure sand 40-100 mesh (ACROS Organics) in 1:3 binder/aggregate ratio by volume, following the typical composition of ancient and historic mortars (Moropoulou et al., 2000, 57; 2005, 298). The measured components were then dry-mixed in a polystyrene weighing boat by stirring the mixture with a medical wooden tongue depressor, until the binder and sand were evenly mixed.

Calcium carbonate in the mortar mixture provides the spectral profiling of the binder after curing, imitating the end product of the reaction of Calcium hydroxide (lime) with Carbon dioxide, according to the reaction c (Sect.2.2) (Ventola et al., 2011, 3315). Thus, water was not involved in the process, since its function as the medium where the reaction takes place was unnecessary.

Mixing the mortar standard in this representation of its cured state with organic materials in different concentrations, will provide repeatable and comparable spectra that would allow the assessment of the inorganic interference in the spectral representation of organic bonds. If this was attempted in an active mortar mixture, where Calcium hydroxide was used instead of Calcium carbonate, it is likely that the spectra profiling would undergo frequent changes, following the calcination process and water evaporation, as well as changes in organic profiling caused by the exothermic reaction of calcination (Ventola et al., 2011, 3315).

Furthermore, the mortar standard in its cured state will be directly comparable to the ancient mortar samples studied in the thesis, which are approximately two millennia in age and the carbonation of their lime is expected to be complete.

Reflectance micro-FTIR spectra were obtained from the mortar (M_av), as well as the $CaCO_3$ (Ca_av) and sand (Q_av) standards in powder form.

7.2 Organic standards

Standard of bone glue (BG_av) was prepared by granules from the FTIR reference collection held at the Department of Archaeology and Conservation. A 5% w/v solution of bone glue was prepared by adding 5 g of granules in tap water until the mixture was made up to 100 ml. The mixture was placed in a glass beaker and then heated slowly, by stirring with a glass stirring rod, until a viscous solution was achieved. A portion was poured on a polystyrene weighing boat and left to dry. The portion was not transferred by a polyethylene pipette because of the quick drying of the solution as soon as it was removed from the hotplate. The hardened film was then analyzed on a microscopy glass slide.

Standards of egg and its individual parts, egg yolk and egg white were prepared from Welsh eggs. An egg was cracked open in a polystyrene weighing boat and a 3 ml portion of egg white was removed by a polyethylene transfer pipette to a microscopy glass slide and left to dry. The procedure was repeated for egg yolk with a new polyethylene transfer pipette. Another egg was cracked open and stirred with the tip of a pipette and a 3ml portion was transferred on a microscopy glass slide and left to dry. Reflectance micro-FTIR spectra were obtained from egg (E_av), egg yolk (EY_av) and egg white (EW_av) standards in film form (Ch.7, Table 8).

One standard of cow's milk (Mi_av) was prepared by Marks and Spencer Welsh whole milk. The purchased milk contained 40 g of fat, 2.5 g of which are saturates, 4.7 g of

carbohydrate sugars, 3.2 g of protein and 0.15 g of salt per 100 ml. A 3 ml portion was poured on a microscopy glass slide by a polyethylene transfer pipette and left to dry.

Olive oil standard (O_av), Sainsbury's brand, was prepared by pouring 3 ml of oil on a microscopy glass slide by a polyethylene transfer pipette. Since olive oil does not dry, the pouring on the microscopy glass slide took place just before the analysis of the standard (fig.32).

Figure 32: Olive oil standard (O_av).

The lard standard (L_av) was prepared using pork lard (Lidl brand-250 g) that contained 10 g of fat and 4.4 g saturates per 10 g, extracts of rosemary, antioxidants, Tocepherol rich extract. A portion of lard was spread over a microscopy glass slide with a scalpel.

The rice solution standard (R_av) was prepared by long grain rice (Golden Sun Lidl) and contained fat < 0.5 g, 23 g of carbohydrates, sugars < 0.5 g, fibre < 0.5 g, and 2.1 g of protein, per 100 g. A 5% w/v solution was prepared by adding 5 g of rice in tap water until the mixture was made up to 100 ml. The mixture was placed in a glass beaker and then heated until boiling, by occasionally stirring with a glass stirring rod, until a viscous, white solution was formed. The solution was transferred into another glass beaker by pouring, in order to separate it from the boiled rice grains. A 3 ml portion was poured on a microscopy glass slide by a polyethylene transfer pipette and left to dry.

Asphalt of Syria, from the FTIR reference collection, was used for the preparation of the standard (A_av). The standard was analysed in its purchased powder form.

The film standards of egg, egg yolk, egg white, bone glue, milk and rice solution were left to dry on the microscopy glass slides for five days prior to their analysis. The standards in powder form were analyzed in gelatine capsules which were adhered by double sided adhesive tape on microscopy glass slides, ensuring the safe transfer and easy loading on the microscope sample stage (fig. 33). The capsules were filled with powder up to the rim and the powder was leveled by gently pressing it with a scalpel. Reflectance micro-FTIR spectra were obtained from the leveled surface of the powder within an area of approximately 5 mm diameter.

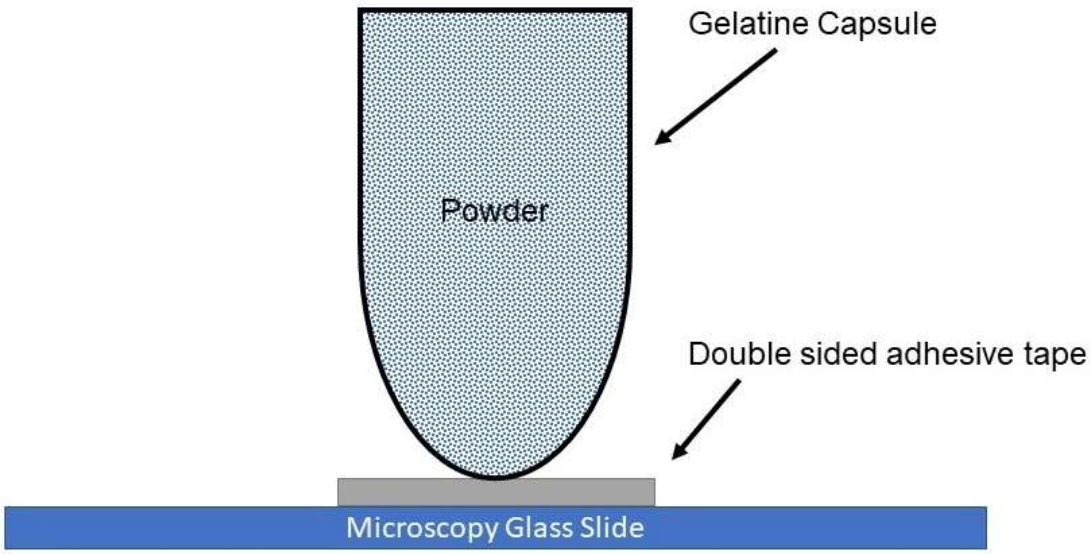

Figure 33: Graphic illustration of the capsule that contained the powder standards during their analysis by External Reflectance FTIR micro-spectroscopy.

7.3 Organic/Mortar standards

Standard	Spectrum ID	% Organic	Preparation
Mortar	**M_av**	**N/A**	1:3 binder:aggregate ratio ($CaCO_3$: quartz)
Bone glue-Mortar	**BG_M_75_av**	75% w/w	10 g mixture = 7.5 g of 5% w/v bone glue/water + 2.5 g mortar
Bone glue-Mortar	**BG_M_50_av**	50% w/w	10 g mixture = 5 g of 5% w/v bone glue/water + 5 g mortar
Bone glue-Mortar	**BG_M_25_av**	25% w/w	10 g mixture = 2.5 g of 5% w/v bone glue/water + 7.5 g mortar
Bone glue-Mortar	**BG_M_5_av**	5% w/w	10 g mixture = 0.5 g of 5% w/v bone glue/water + 9.5 g mortar
Egg-Mortar	**E_M_75_av**	75% w/w	10 g mixture = 7.5 g of egg + 2.5 g mortar
Egg-Mortar	**E_M_50_av**	50% w/w	10 g mixture = 5 g of egg + 5 g mortar
Egg-Mortar	**E_M_25_av**	25% w/w	10 g mixture = 2.5 g of egg + 7.5 g mortar
Egg-Mortar	**E_M_5_av**	5% w/w	10 g mixture = 0.5 g of egg + 9.5 g mortar
Egg white-Mortar	**EW_M_75_av**	75% w/w	10 g mixture = 7.5 g of egg white + 2.5 g mortar
Egg white-Mortar	**EW_M_50_av**	50% w/w	10 g mixture = 5 g of egg white + 5 g mortar
Egg white-Mortar	**EW_M_25_av**	25% w/w	10 g mixture = 2.5 g of egg white + 7.5 g mortar
Egg white-Mortar	**EW_M_5_av**	5% w/w	10 g mixture = 0.5 g of egg white + 9.5 g mortar
Egg yolk-Mortar	**EY_M_75_av**	75% w/w	10 g mixture = 7.5 g of egg yolk + 2.5 g mortar
Egg yolk-Mortar	**EY_M_50_av**	50% w/w	10 g mixture = 5 g of egg yolk + 5 g mortar
Egg yolk-Mortar	**EY_M_25_av**	25% w/w	10 g mixture = 2.5 g of egg yolk + 7.5 g mortar
Egg yolk-Mortar	**EY_M_5_av**	5% w/w	10 g mixture = 0.5 g of egg yolk + 9.5 g mortar
Milk-Mortar	**Mi_M_75_av**	75% w/w	10 g mixture = 7.5 g of milk + 2.5 g mortar
Milk-Mortar	**Mi_M_50_av**	50% w/w	10 g mixture = 5 g of milk + 5 g mortar
Milk-Mortar	**Mi_M_25_av**	25% w/w	10 g mixture = 2.5 g of milk + 7.5 g mortar
Milk-Mortar	**Mi_M_5_av**	5% w/w	10 g mixture = 0.5 g of milk + 9.5 g mortar
Rice-Mortar	**R_M_75_av**	75% w/w	10 g mixture = 7.5 g of 5% w/v rice/water solution + 2.5 g mortar
Rice-Mortar	**R_M_50_av**	50% w/w	10 g mixture = 5 g of 5% w/v rice/water solution + 5 g mortar
Rice-Mortar	**R_M_25_av**	25% w/w	10 g mixture = 2.5 g of 5% w/v rice/water solution + 7.5 g mortar
Rice-Mortar	**R_M_5_av**	5% w/w	10 g mixture = 0.5 g of 5% w/v rice/water solution + 9.5 g mortar
Lard-Mortar	**L_M_75_av**	75% w/w	10 g mixture = 7.5 g of lard + 2.5 g mortar
Lard-Mortar	**L_M_50_av**	50% w/w	10 g mixture = 5 g of lard + 5 g mortar
Lard-Mortar	**L_M_25_av**	25% w/w	10 g mixture = 2.5 g of lard + 7.5 g mortar
Lard-Mortar	**L_M_5_av**	5% w/w	10 g mixture = 0.5 g of lard + 9.5 g mortar
Olive oil-Mortar	**O_M_75_av**	75% w/w	10 g mixture = 7.5 g of oil + 2.5 g mortar
Olive oil-Mortar	**O_M_50_av**	50% w/w	10 g mixture = 5 g of oil + 5 g mortar
Olive oil-Mortar	**O_M_25_av**	25% w/w	10 g mixture = 2.5 g of oil + 7.5 g mortar
Olive oil-Mortar	**O_M_5_av**	5% w/w	10 g mixture = 0.5 g of oil + 9.5 g mortar
Asphalt-Mortar	**A_M_75_av**	75% w/w	10 g mixture = 7.5 g of asphalt + 2.5 g mortar
Asphalt-Mortar	**A_M_50_av**	50% w/w	10 g mixture = 5 g of asphalt + 5 g mortar
Asphalt-Mortar	**A_M_25_av**	25% w/w	10 g mixture = 2.5 g of asphalt + 7.5 g mortar
Asphalt-Mortar	**A_M_5_av**	5% w/w	10 g mixture = 0.5 g of asphalt + 9.5 g mortar

Table 9: List of mortar and organic/mortar mixtures analysed by External Reflectance FTIR micro-spectroscopy as standards.

Each organic material was mixed with mortar in 75%, 50%, 25% and 5% w/w organic concentration for preparing standards of gradually decreasing organic content (Table 9). Water was only used in the preparation of the rice solution and bone glue (sect.7.2), since the binding process among mortar components was excluded from the thesis objectives (sect.7.1). All the organic materials apart from the asphalt, were mixed with mortar in their natural liquidus state and they were left to dry for three days prior to analysis. Drying does not apply for olive oil and lard mortar mixtures.

The organic material and the mortar were weighed separately on a Mettler Toledo XS205 analytical balance, on polystyrene weighing boats. Then they were mixed in a weighing boat with a scalpel and a portion was placed within a gelatine capsule which was then adhered on the microscopy glass slide (fig.34-35).

The standards of 75% and 50% w/w bone glue/mortar mixture hardened excessively while mixing and could not be transferred into capsules. These standards were placed on microscopy glass slides upon analysis.

Figure 34: The laboratory prepared standards: films of organic materials, inorganic powders, mortar powder and organic/mortar mixtures.

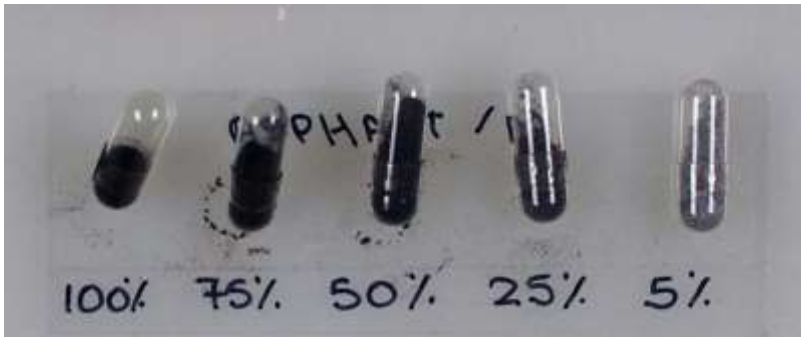

Figure 35: The standards of asphalt in gelatine capsules: 100% asphalt and asphalt/mortar mixtures in 75%, 50%, 25% and 5% organic concentration.

7.4 Spectra acquisition and data entry in the CPAD

All the laboratory prepared standards used in the thesis were analyzed by External Reflectance FTIR micro-spectroscopy under the following standardized operational conditions: spectra were collected in Reflectance mode after 60 scans of 4 cm^{-1} spectral resolution, for the 4000-600 cm^{-1} mid-infrared frequency range (Sec.5.1). Three spectra were collected randomly from the surface of each standard. The three spectra were then averaged and the resulting spectral data (peak position *x* and peak intensity *y*) were added in the CPAD.

The spectral data of standards were recorded in MS Excel Worksheet and the CPAD was developed in pivot table format. The CPAD entries aimed to include all the necessary information for identification exercises: material description, spectrum acquisition parameters, description of absorption peaks (position, shape and intensity), chemical assignments and filtering entries relevant to peak chemical origin and significance in the identification process (Table 10).

CPAD Entries	Description
Spectrum ID	Standards
Peak x (position)	cm^{-1}
Peak y (intensity)	log(1/R)
Type of band	Terminology - strong/weak absorptions, distortions
Chemical Band Assignement	Chemical bond and type of motion
Priority peak	YES or NO
ID as	ORG (organic) or INORG (inorganic)
Reference	Literature and standards spectra
Comments	Additional Info - spectra acquisition
Sample Origin	Standard or Literature
Sample Type	Organic, Inorganic, Organic/inorganic
Sample form	Film, Pellet, Powder, Mixture, Material
Component 1	Single component or major mixture component
Ratio Comp.1	Related to mixture standards
Component 2	Related to mixture standards
Ratio Comp.2	Related to mixture standards
Component 3	Related to mixture standards
Ratio Comp.3	Related to mixture standards
Averaged from	ID of individual spectra of standards
Energy gain	Of individual spectra of standards
Date of Acquision	Of individual spectra of standards

Table 10: Spectral data entries for the development of the Chemical Peak Assignment Database.

The OriginPro 2015 *Quick Gadget Peak Finder* tool was used for locating the *x* and *y* parameters of absorption bands in the spectra. Spectra pre-treatment (baseline correction and normalization) was excluded due to loss of weak absorptions. The region of interest (ROI) was set between 3800-600 cm^{-1} since peaks above 3800 cm^{-1} represent mainly noise.

The default setting in Quick Gadget Peak Finder produces a large number of detected peaks, including those that are close together and of weak absorption intensity. Several trials in different settings for extracting less peaks resulted in losing information on peaks of interest. The addition of the filtering entry ***"Priority Peak"***, enabled separation of peaks of interest from those that represent noise, detector interference and those occurring on either side of a peak of interest. Manual peak finding was excluded because it is subjected to *x* and *y* variations and bias of selection.

The filtering entry ***"ID as"*** enables differentiation of organic from inorganic peaks allowing direct comparison of organic standards with their corresponding organic/mortar mixtures

and assessment of presence, absence and position shifting of organic peaks in the mixtures as the concentration of organic component decreases. Blank entries in this field are either peaks not identified or those that may belong to either chemical group in the mixture.

The design of the CPAD in pivot format, with the individual spectral entries, aimed at overcoming practical constraints that are often encountered in visual spectral comparisons. The overlapping spectra of bone glue (BG_av), 75%, 50%, 25%, and 5% bone glue/mortar and mortar (M_av) demonstrate the complexity of interpreting the changes of the bone glue spectral representation as the mortar concentration increases in the mixture (fig.36). The crowded x and y plot cannot be practically assessed in detail and minor spectral features can be overlooked, especially within the fingerprint region, where most protein bonds vibrate. The figure would be even more confusing if all the peaks detected through the Quick Gadget Peak Finder would be placed in the plot. Avoiding this would require manual peak finding which is subjected to bias from the manual handling of the cursor over a peak. Minor position shifting or minor changes in intensity would then be inaccurate.

In cases where spectra of low organic concentration are assessed, where inorganic interference prevails, such as in the case of 5% bone glue/mortar mixture (fig.36), identification depends on such minor shifting and weak peaks. Their assessment through accurate measurements, peak by peak through the CPAD, should lead in secure outcomes.

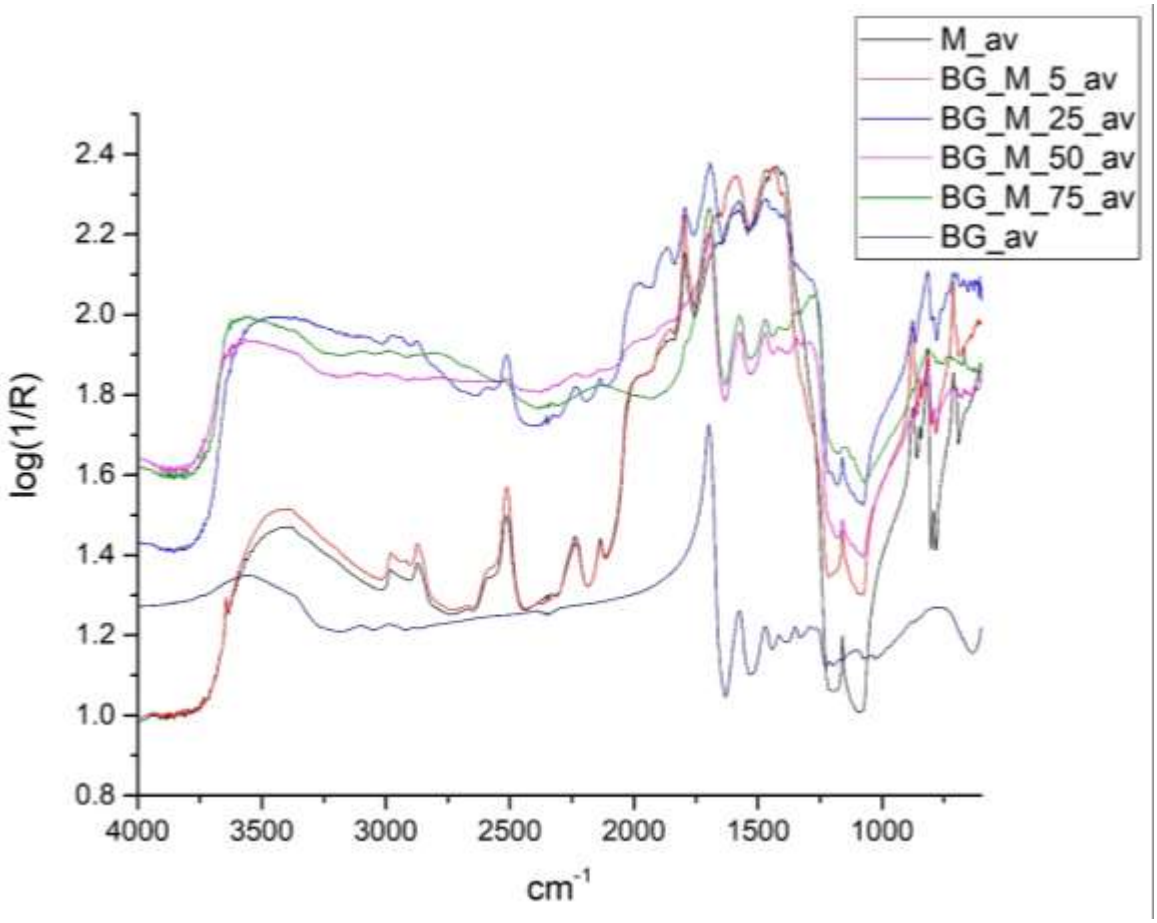

Figure 36: Overlapping spectra of bone glue (BG_av), 75%, 50%, 25%, and 5% bone glue/mortar and mortar (M_av).

7.5 Spectral Interpretation of Standards

The Chemical Peak Assignment Database aims to provide the means to utilize all the available reflectance features for the chemical characterization of materials analyzed by Reflectance FTIR micro-spectroscopy, overcoming constrains posed by the method itself, the complexity of spectra from composite materials (Ch.4) and practicalities of visual spectral comparisons (sect.7.4).

The Reflectance micro-FTIR spectra obtained from the organic and inorganic standards in their pure form are assessed peak-by-peak in order to define diagnostic features for each standard. Absorption peak position, intensity and shape/distortion are entered in the CPAD and where feasible, chemical bonds are assigned to specific peaks through the available literature.

The results are then utilized in the interpretation of spectra obtained from the organic/mortar mixtures in order to assess any spectral changes occurring to the

diagnostic features of organic bonds from their interaction with the inorganic mortar components. The impact of inorganic interference in the position of the organic absorption peaks (shifting), intensity variation and occurrence of newly formed peaks are assessed through CPAD spectral comparisons between the organic additive in its pure form and the corresponding organic/mortar standards in the predefined organic concentrations (Miliani et al., 2012; Rosi et al., 2010; Rosi et al., 2009). This exercise will reveal any newly formed diagnostic features of the selected organic additives resulting from the interaction with the defined inorganic mortar components, assisting their identification.

The coexistence of Specular and Diffuse Reflectance in spectra obtained from materials with differing smooth and coarse texture is expected to appear on the spectra of standards, especially on those from organic/mortar mixtures, in the form of distortions and enhanced minor peaks (Ch.4). These features are also assessed for their characterization as diagnostic in the identification of organic additives in mortar matrices.

7.5.1 Bone glue and mortar mixtures

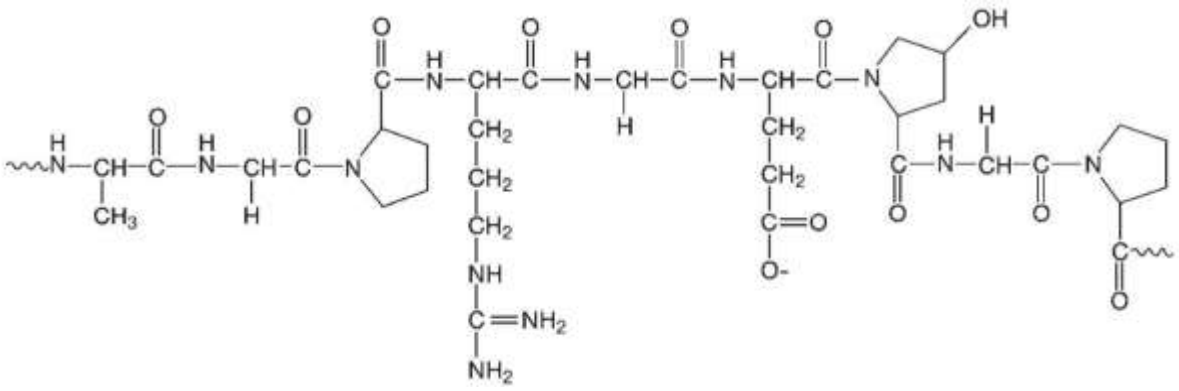

Figure 37: The basic chemical structure of gelatin (Kommaredy et al., 2007, 332).

Materials that derive from animals contain proteins in their structures. Collagen is the structural protein of animal skin, muscle tissue and bones. The partially degraded protein that derives from the extended boiling of collagen-containing materials is called gelatin and is the main protein of bone glue (fig.37) (Mills and White, 1987, 75). Proteins are composed mainly from amino acids blocks which contain nitrogen in their chemical bonds (Mills and White, 1987, 73). These bonds are present on the reflectance micro-FTIR spectrum of bone glue (fig.38-39).

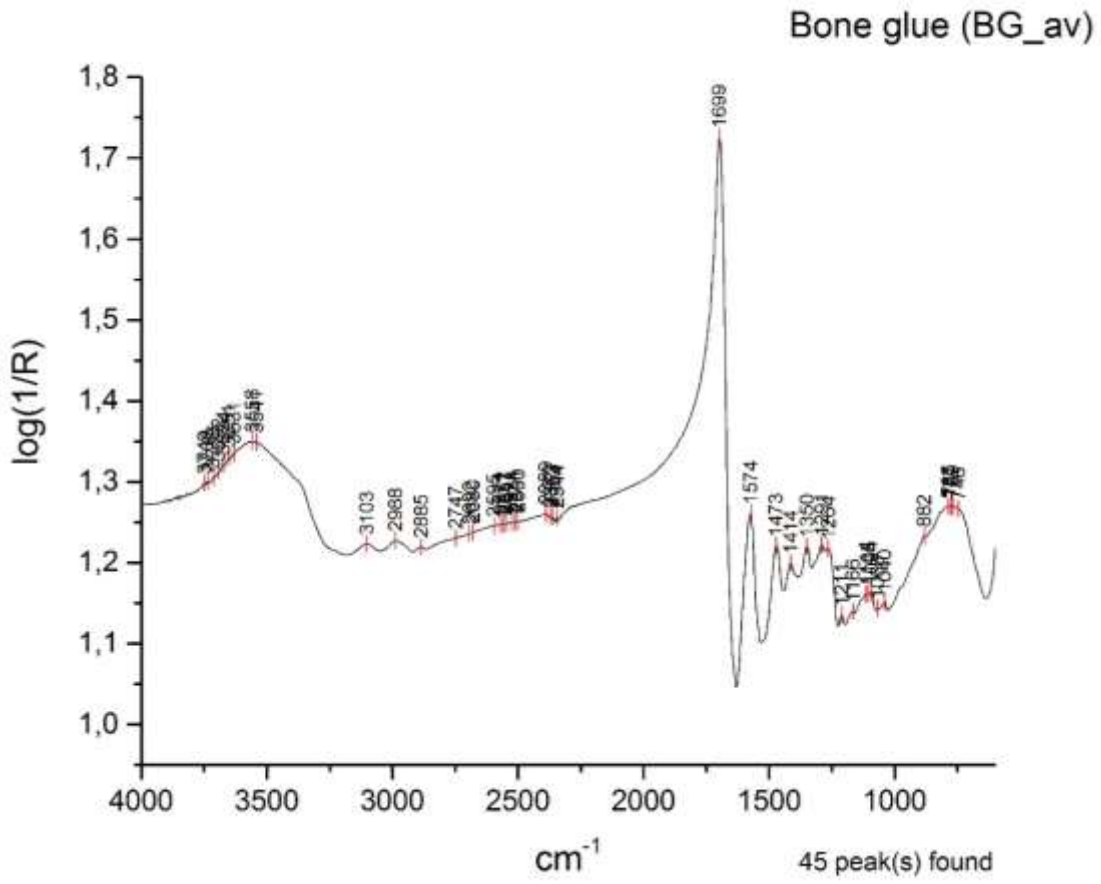

Figure 38: The spectrum of bone glue.

Peak x (position)	Spectrum ID	Type of band	Chemical Band Assignement	Reference
746	**BG_av**	weak absorption	**(blank)**	(blank)
769	**BG_av**	weak absorption	**(blank)**	(blank)
777	**BG_av**	weak absorption	**(blank)**	(blank)
785	**BG_av**	weak absorption	**(blank)**	(blank)
882	**BG_av**	weak absorption	**(blank)**	(blank)
1040	**BG_av**	weak absorption	**(blank)**	(blank)
1068	**BG_av**	weak absorption	**PO4-3anion stretching**	Ricci et al, 2006, p. 1223
1094	**BG_av**	weak absorption	**(blank)**	(blank)
1105	**BG_av**	weak absorption	**(blank)**	(blank)
1114	**BG_av**	weak absorption	**(blank)**	(blank)
1166	**BG_av**	weak absorption	**(blank)**	(blank)
1211	**BG_av**	weak absorption	**(blank)**	(blank)
1264	**BG_av**	stair-step type intensities	**(blank)**	(blank)
1291	**BG_av**	stair-step type intensities	**(blank)**	(blank)
1350	**BG_av**	stair-step type intensities	**(blank)**	(blank)
1414	**BG_av**	stair-step type intensities	**(blank)**	(blank)
1473	**BG_av**	stair-step type intensities	**Amide III**	Rosi et al, 2009, p. 2099
1574	**BG_av**	strong absorption	**C-N-H bending amide II, N-H bands**	Miliani et al, 2012, p. 304, Rosi et al, 2009, p. 2104, Ploeger et al, 2010, p. 37
1699	**BG_av**	strong absorption	**N-H bands**	Miliani et al, 2012, p. 304, Rosi et al, 2009, p. 2104
2885	**BG_av**	weak absorption	**C-H stretching**	Miliani et al, 2012, p. 304, Rosi et al, 2009, p. 2104
2988	**BG_av**	weak absorption	**(blank)**	(blank)
3103	**BG_av**	1st overtone	**amide I**	Rosi et al, 2009, p. 2099

Figure 39: Filtered CPAD entries for the bone glue spectrum.

The spectrum of bone glue (BG_av) is described through the corresponding CPAD entries of spectral data and the assignment of chemical bonds to absorption peaks (fig. 38-39). The dominant presence of protein is evident in both the region of skeletal vibrations within 1400-600 cm^{-1} and in the group frequency region above 1400 cm^{-1} (Banwell and McCash, 1994, 84). The spectrum of bone glue is characterized by the stair-step type intensities of Amide III within the 1473-1264 cm^{-1} region (Rosi et al., 2009, 2099), the strong absorption of C-N-H bending amide II or N-H bond at 1574 cm-1, the dominant absorption of N-H bond at 1699 cm^{-1} (Miliani et al., 2012, 304; Rosi et al., 2009, 2104) and the weak absorption and 1^{st} overtone of Amide I at 2885 cm^{-1} and 3103 cm^{-1} respectively (Rosi et al., 2009, 2099). The weak absorptions within the 1211-600 cm^{-1} region, mainly that at

1068 cm^{-1}, could be attributed to the presence of residual phosphates from the bones used in the production of the glue (Martin-Gil et al., 1999, 58).

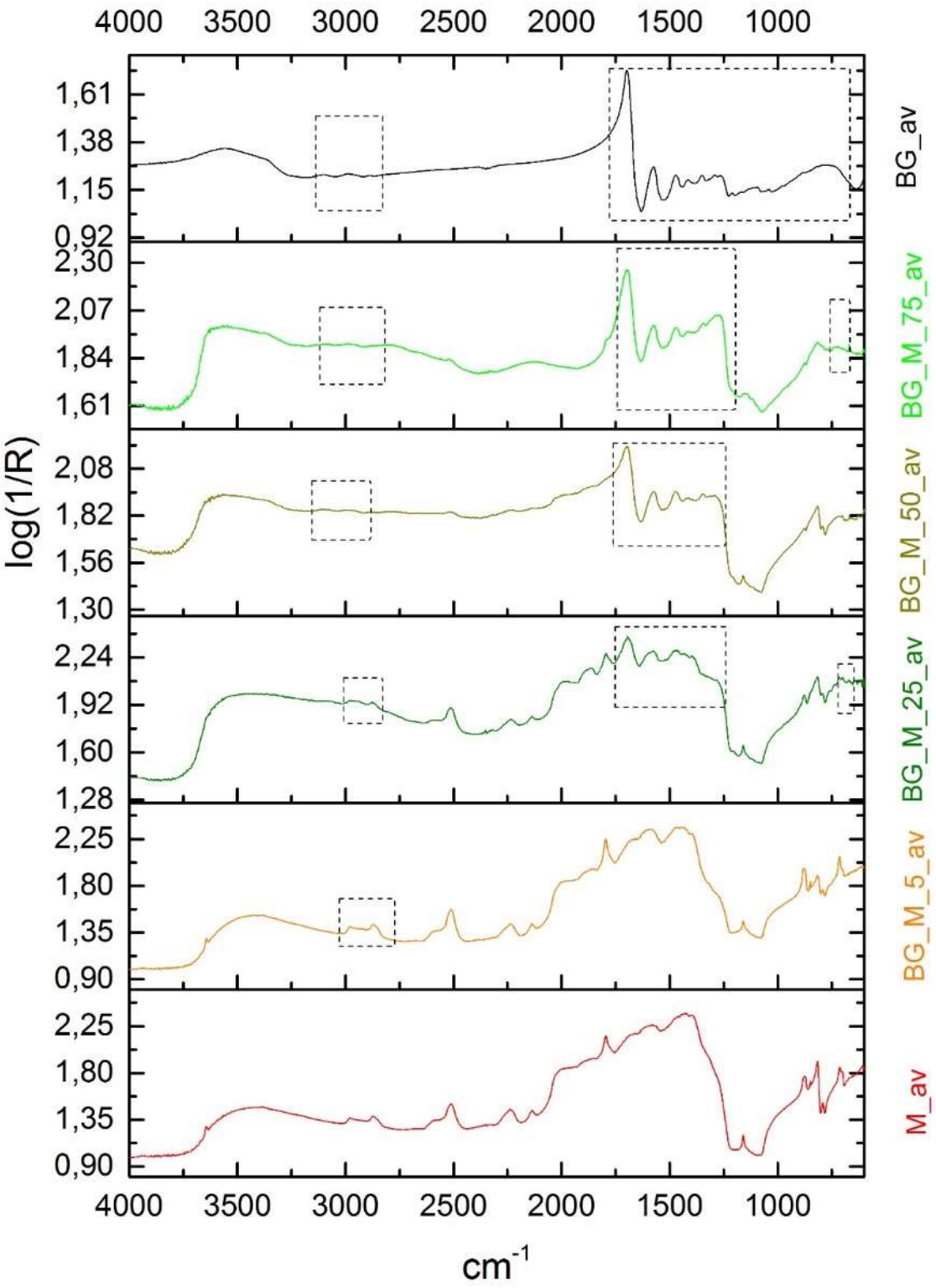

Figure 40: Spectra comparison of bone glue (BG_av) with mortar mixtures of 75, 50, 25 and 5% bone glue additive and mortar (M_av).

Figure 40 shows the decreasing presence of bone glue peaks (in dotted frame) as the inorganic concentration increases in the mixture, towards the 100% mortar. Accordingly, the $CaCO_3$ peaks at 2979 and 2872 cm^{-1}, the $CaCO_3$ combination band at 2512 cm^{-1} (Ricci et al., 2006, 1222), the quartz peaks at 2238-1863 cm^{-1}, the $CaCO_3$ combination band at 1794 cm^{-1} (Ricci et al., 2006, 1222), the quartz peak at 1159 cm^{-1} and the *v2* and *v4* carbonate ion vibrations at 873-702 cm^{-1} (Ylmen and Jaglid, 2013, 119) emerge and their intensity increases towards higher inorganic concentrations. The mortar spectrum and its CPAD entries are provided in Appendix I (fig.1-2).

Peak x (position)	Spectrum ID	Type of band	Chemical Band Assignement	Reference
668	**BG_M_75_av**	sharp and weak absorption	**CaCO3**	spectrum Ca_av
738	**BG_M_75_av**	weak absorption	**bone glue**	Spectrum BG_av
746	**BG_av**	weak absorption	**(blank)**	(blank)
761	**BG_M_75_av**	weak absorption	**bone glue**	Spectrum BG_av
769	**BG_av**	weak absorption	**(blank)**	(blank)
770	**BG_M_75_av**	weak absorption	**bone glue**	Spectrum BG_av
777	**BG_av**	weak absorption	**(blank)**	(blank)
785	**BG_av**	weak absorption	**(blank)**	(blank)
790	**BG_M_75_av**	weak absorption	**bone glue**	Spectrum BG_av
817	**BG_M_75_av**	sharp absorption	**Si-O antisymmetric stretching**	Spectrum Q_av, spectrum M_av, Miliani et al, 2012, p. 303
875	**BG_M_75_av**	weak absorption	**v2 carbonate ion**	Spectrum Ca_av, spectrum M_av, Ylmen and Jaglid, 2013, p. 119
882	**BG_av**	weak absorption	**(blank)**	(blank)
1040	**BG_av**	weak absorption	**(blank)**	(blank)
1068	**BG_av**	weak absorption	**PO4-3anion stretching**	Ricci et al, 2006, p. 1223
1094	**BG_av**	weak absorption	**(blank)**	(blank)
1105	**BG_av**	weak absorption	**(blank)**	(blank)
1114	**BG_av**	weak absorption	**(blank)**	(blank)
1116	**BG_M_75_av**	weak absorption	**CaCO3**	spectrum Ca_av
1146	**BG_M_75_av**	weak absorption	**CaCO3 and quartz**	Spectrum Ca_av, spectrum Q_av, spectrum M_av
1153	**BG_M_75_av**	weak absorption	**CaCO3 and quartz**	Spectrum Ca_av, spectrum Q_av, spectrum M_av
1166	**BG_av**	weak absorption	**(blank)**	(blank)
1211	**BG_av**	weak absorption	**(blank)**	(blank)
1264	**BG_av**	stair-step type intensities	**(blank)**	(blank)
1268	**BG_M_75_av**	stair-step type intensities	**bone glue**	Spectrum BG_av
1287	**BG_M_75_av**	stair-step type intensities	**bone glue**	Spectrum BG_av
1291	**BG_av**	stair-step type intensities	**(blank)**	(blank)

Figure 41: Filtered CPAD entries of bone glue (BG_av) and 75% bone glue/mortar mixture (BG_M_75_av).

1341	**BG_M_75_av**	stair-step type intensities	**bone glue**	Spectrum BG_av
1350	**BG_av**	stair-step type intensities	**(blank)**	(blank)
1414	**BG_av**	stair-step type intensities	**(blank)**	(blank)
1415	**BG_M_75_av**	stair-step type intensities	**bone glue**	Spectrum BG_av
1471	**BG_M_75_av**	stair-step type intensities	**Amide III**	Spectrum BG_av, Rosi et al, 2009, p. 2099
1473	**BG_av**	stair-step type intensities	**Amide III**	Rosi et al, 2009, p. 2099
1572	**BG_M_75_av**	strong absorption	**C-N-H bending amide II, N-H bands**	Spectrum BG_av, Rosi et al, 2009, p. 2099, Miliani et al, 2012, p. 304
1574	**BG_av**	strong absorption	**C-N-H bending amide II, N-H bands**	Miliani et al, 2012, p. 304, Rosi et al, 2009, p. 2104, Ploeger et al, 2010, p. 37
1697	**BG_M_75_av**	strong absorption	**N-H bands**	Spectrum BG_av, Rosi et al, 2009, p. 2104, Miliani et al, 2012, p. 304
1699	**BG_av**	strong absorption	**N-H bands**	Miliani et al, 2012, p. 304, Rosi et al, 2009, p. 2104
1790	**BG_M_75_av**	weak absorption	**v1+v4 carbonate ion**	Spectrum Ca_av, spectrum M_av, Ricci et al, 2006, p. 1222
2131	**BG_M_75_av**	weak absorption	**CaCO3 and quartz**	Spectrum Q_av, spectrum M_av, spectrum Ca_av
2238	**BG_M_75_av**	weak absorption	**quartz**	Spectrum Q_av, spectrum M_av
2523	**BG_M_75_av**	combination band	**v1+v3 carbonate ion**	Spectrum Ca_av, spectrum M_av, Ricci et al, 2006, p. 1222
2660	**BG_M_75_av**	weak absorption	**CaCO3**	Spectrum Ca_av, spectrum M_av
2677	**BG_M_75_av**	weak absorption	**CaCO3**	Spectrum Ca_av, spectrum M_av
2802	**BG_M_75_av**	weak absorption	**C-H stretching**	Rosi et al, 2009, p. 2099
2881	**BG_M_75_av**	weak absorption	**C-H stretching**	Spectrum BG_av, Miliani et al, 2012, p. 304; Rosi et al, 2009, p. 2104
2885	**BG_av**	weak absorption	**C-H stretching**	Miliani et al, 2012, p. 304, Rosi et al, 2009, p. 2104
2889	**BG_M_75_av**	weak absorption	**C-H stretching**	Spectrum BG_av, Miliani et al, 2012, p. 304; Rosi et al, 2009, p. 2104
2985	**BG_M_75_av**	weak absorption	**bone glue**	Spectrum BG_av
2988	**BG_av**	weak absorption	**(blank)**	(blank)
3103	**BG_av**	1st overtone	**amide I**	Rosi et al, 2009, p. 2099
	BG_M_75_av	weak absorption	**amide I**	Spectrum BG_av, Rosi et al, 2009, p. 2099

Figure 41: continued

Peak comparison through the CPAD assessing the presence of bone glue peaks (BG_av) in the 75% bone glue/mortar mixture (BG_M_75_av) shows that bone glue peaks within the 1211-882 cm^{-1} range are absent in the mixture due to the presence of quartz at 1153 cm^{-1} (fig.41). The rest of the amide peaks above 1268 cm^{-1} are present and show negligible position shifting, below 10 cm^{-1} on either side of the spectrum. The peaks preserve their shape and intensity. Similar outcomes derive from the peak comparison between the bone glue CPAD entries and those of the 50% bone glue/mortar mixture (Appendix I, fig.3).

In the 25% bone glue/mortar mixture the weak absorptions of bone glue around 761 cm^{-1} and 735 cm^{-1} reappear (Appendix I, fig.4). However, the specific peaks cannot be safely used as diagnostic to bone glue since the area below 800 cm^{-1} is dominated by $CaCO_3$ peaks. The stair-step type intensities at 1286, 1461-69 cm^{-1} are still present although their shape and intensity is less distinct. The main diagnostic N-H peak at 1694 cm^{-1} and the C-H stretching at 2897-2949 cm^{-1} are also present within the mortar absorption at 2979 and 2872 cm^{-1}.

The diagnostic bone glue peaks are absent from the 5% bone glue/mortar mixture apart from the 1473 cm^{-1} peak (Appendix I, fig.5). The peaks at 2918, 2927 and 2935 cm^{-1}, indicating the C-H stretching could belong to more than one organic group and cannot be considered diagnostic to bone glue. However, the combined presence of a 1473 cm^{-1} peak with these group frequencies would lead to the conclusion that protein was present. The absence of bone glue peaks however, cannot be securely linked to concentration dependencies since the physical properties of bone glue in terms of mixing capacity with the mortar may have influenced the outcome.

7.5.2 Egg white and mortar mixtures

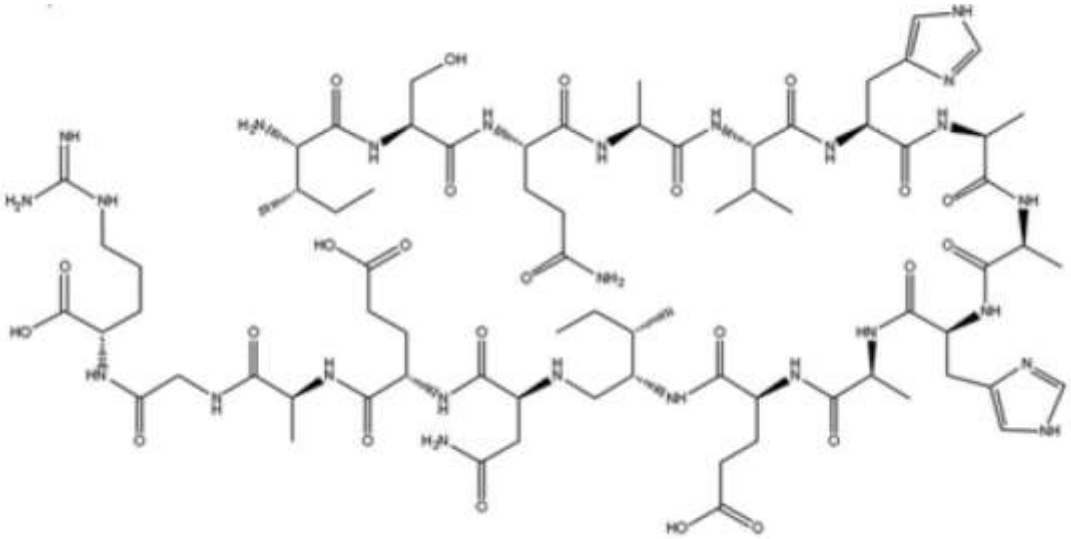

Figure 42: The chemical structure albumen (Zahedi and Fallah-Darrehchi, 2015, 2185).

The main protein of egg is albumin (fig.42). The highest percentage of this protein is found in egg white. An egg, based on its size, consists of 56-60% egg white (albumen), which consists of 12% dry matter (protein) and 88% water (Mydin, 2018, 378).

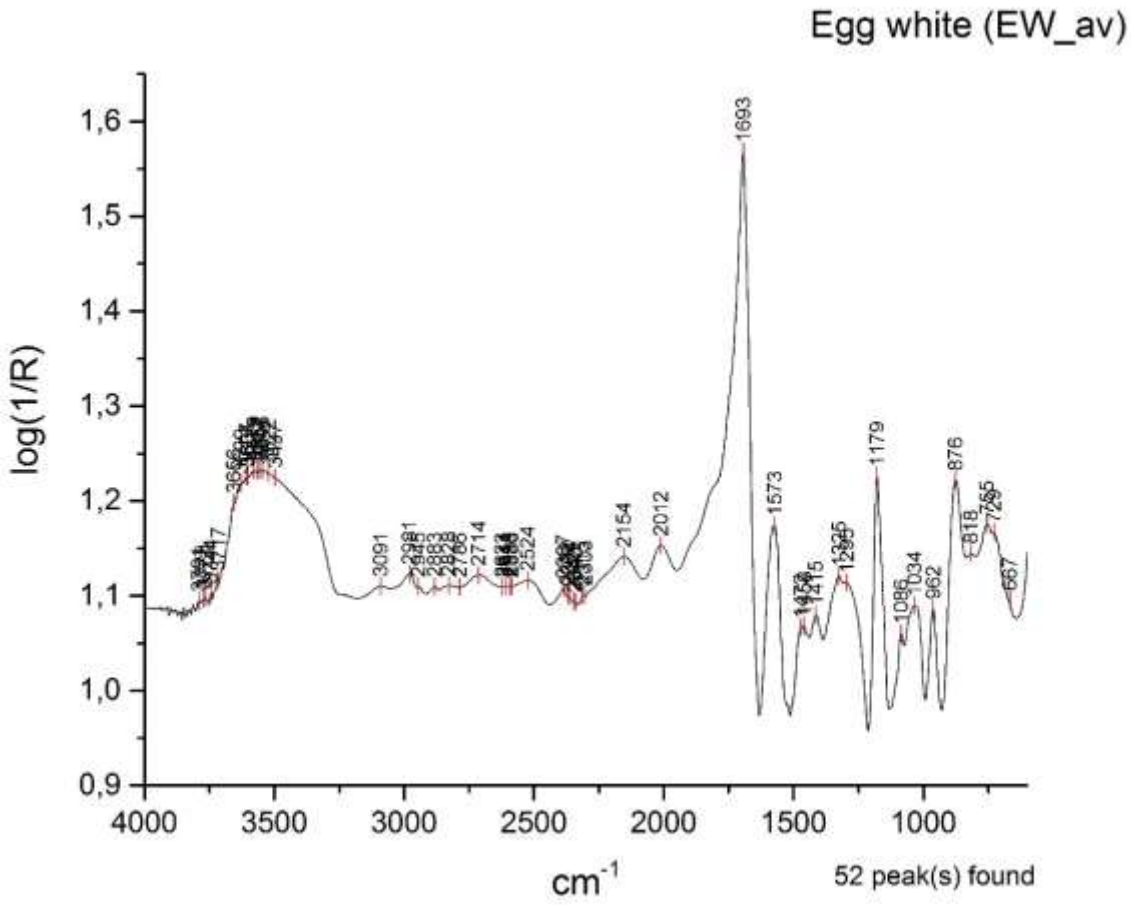

Figure 43: The spectrum of egg white.

Egg white and bone glue are both proteinaceous materials: Albumin is the main protein of egg, whereas gelatin is the structural protein of bone glue (Mills and White, 1987, 76). Consequently, differences should be reflected in their spectra, following the differences in their chemical formulas (fig.42-43).

Egg white spectrum (EW_av) is characterized by a number of strong absorptions within the 1693-729 cm^{-1} region (fig.43). The peaks at 1693, 1573 cm^{-1} and the stair-step type intensities within the 1472-1295 cm^{-1}, similar to bone glue, define the proteinaceous origin of egg white. However, the shape and intensities of the peaks below 1573 cm^{-1} and that of the C-H stretching at 2981-2883 cm^{-1} are considered diagnostic to egg white. The weak absorptions at 2714-2524 cm^{-1} should also be taken into account in identification experiments.

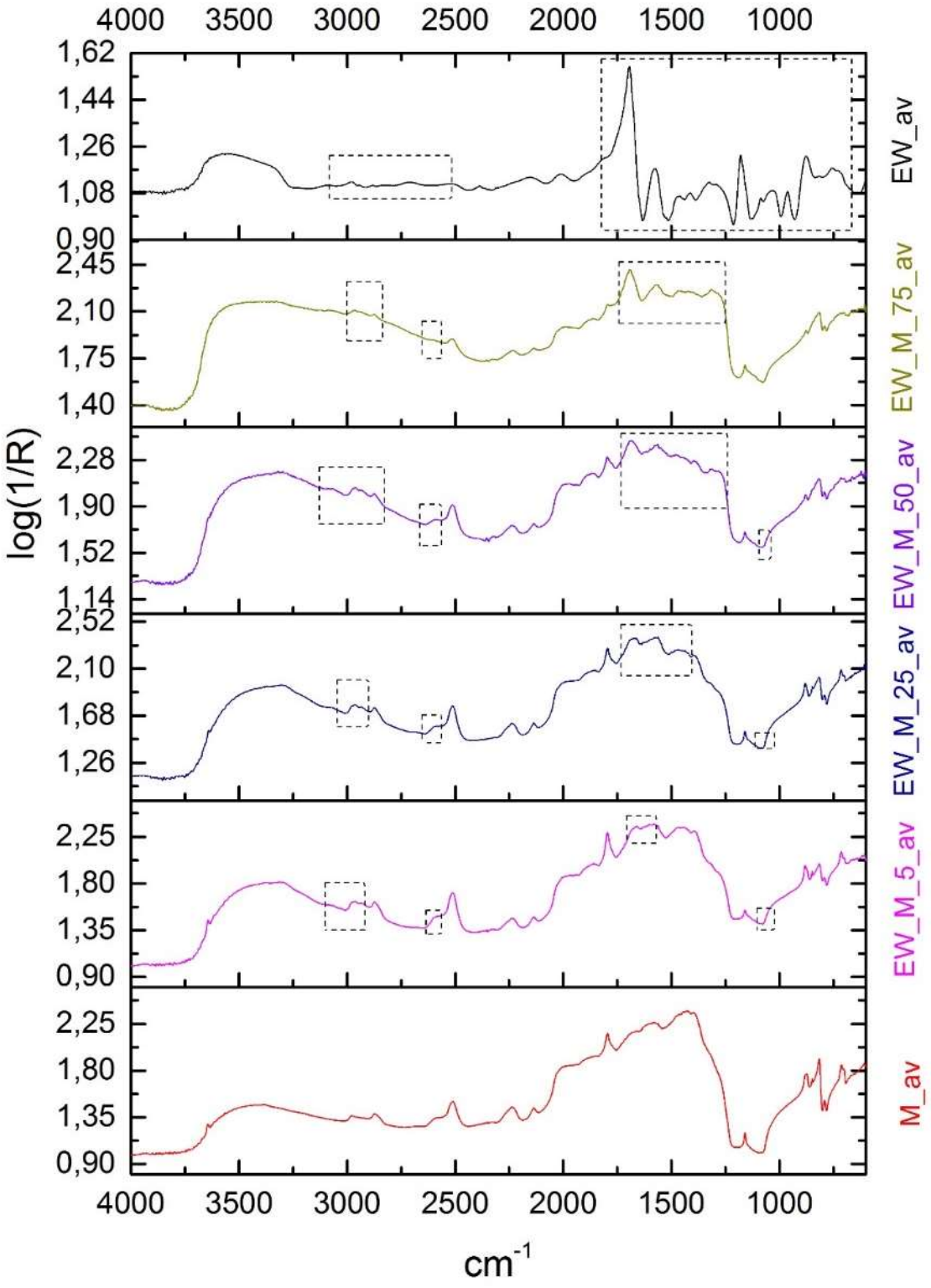

Figure 44: Spectra comparison of egg white (EW_av) with mortar mixtures of 75, 50, 25 and 5% egg white additive and mortar (M_av).

Spectra comparison of egg white with its mortar mixtures shows distinct presence of inorganic components at 2515, 2235-1794 cm^{-1} and below 1159 cm^{-1} on the mortar

mixtures that gradually intensifies as the concentration of egg white in the mixture decreases (fig.44).

The peak comparison through the CPAD between the 75% egg white/mortar mixture (EW_M_75_av) and the egg white (EW_av) shows that the presence of peaks at the region 3091-2940 cm^{-1} and 1692-1285 cm^{-1} and their shape and intensity indicate egg white (Appendix I, fig.6). Shifting is negligible especially for the main protein peaks at 1692, 1575 and 1461 cm^{-1}. Their shape resembles that of the egg white peaks, that is why the 1575 cm^{-1} peak is assigned to egg white rather than $CaCO_3$ that also shows strong absorption in that frequency. It is already apparent that the assignment of peaks to specific bonds requires assessment of both location and shape of the peaks.

Despite the fact that inorganic presence becomes more pronounced in the spectrum of 50% egg white (EW_M_50_av), the egg white peaks are retained at 3094-2934 cm^{-1} and within the 1685-1283 cm^{-1} region where the shape and spreading of peaks resembles that of egg white (Appendix I, fig.7).

The fact that the main protein peaks remain visible in the spectra of low concentrations of organic (EW_M_25_av and EW_M_5_av) should also be attributed to the mixing capacity of egg white with the mortar as opposed to that of bone glue. Although shifting of the N-H band at 1693 cm^{-1} (egg white value) is wider in both spectra of egg white/mortar mixtures and the inorganic presence is pronounced, the combined presence and characteristic shape of peaks at 1641-1630, 1579-1577 cm^{-1} and the C-H stretching in 3314-2936 cm^{-1} are diagnostic to egg white protein. Also, very weak peaks at 1086 cm^{-1}, and 2703 cm^{-1} are also encountered as diagnostic in combination with the above peaks (Appendix I, fig.8-9).

7.5.3 Egg yolk and mortar mixtures

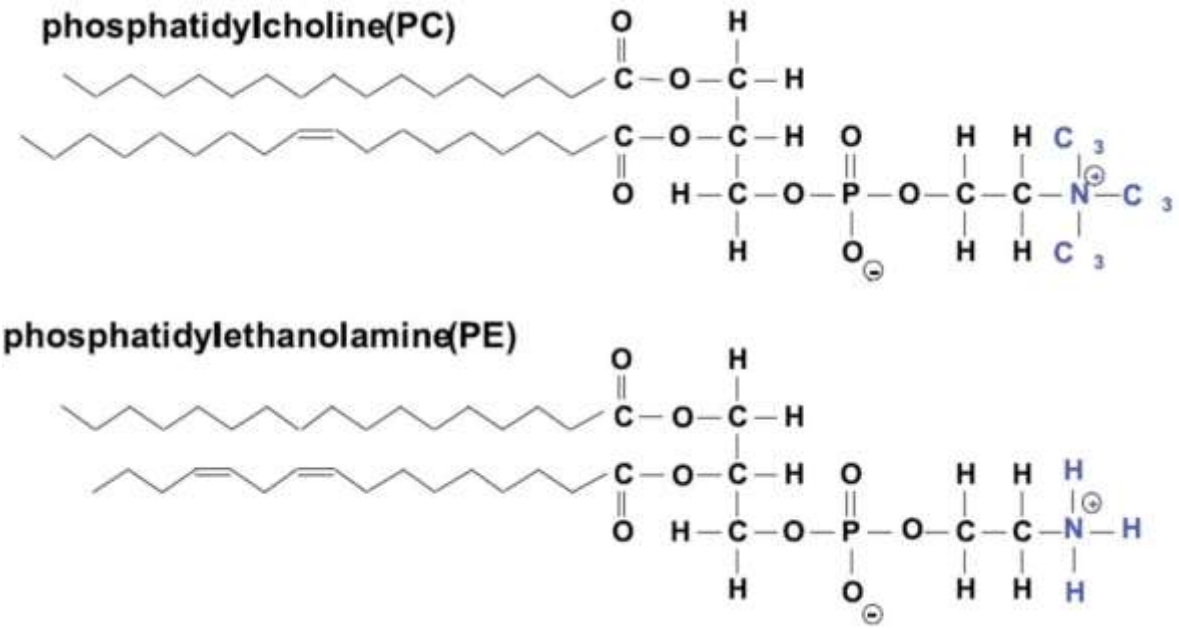

Figure 45: Chemical structure of most important phospholipids in egg yolk (Guerrand, 2017, 4).

Egg yolk is also rich in proteins which differ from those in egg white in their association with phosphorous-containing lipids (fig.45) (Mills and White, 1987, 76). These lipids should be identifiable in the reflectance micro-FTIR spectrum of egg yolk (46).

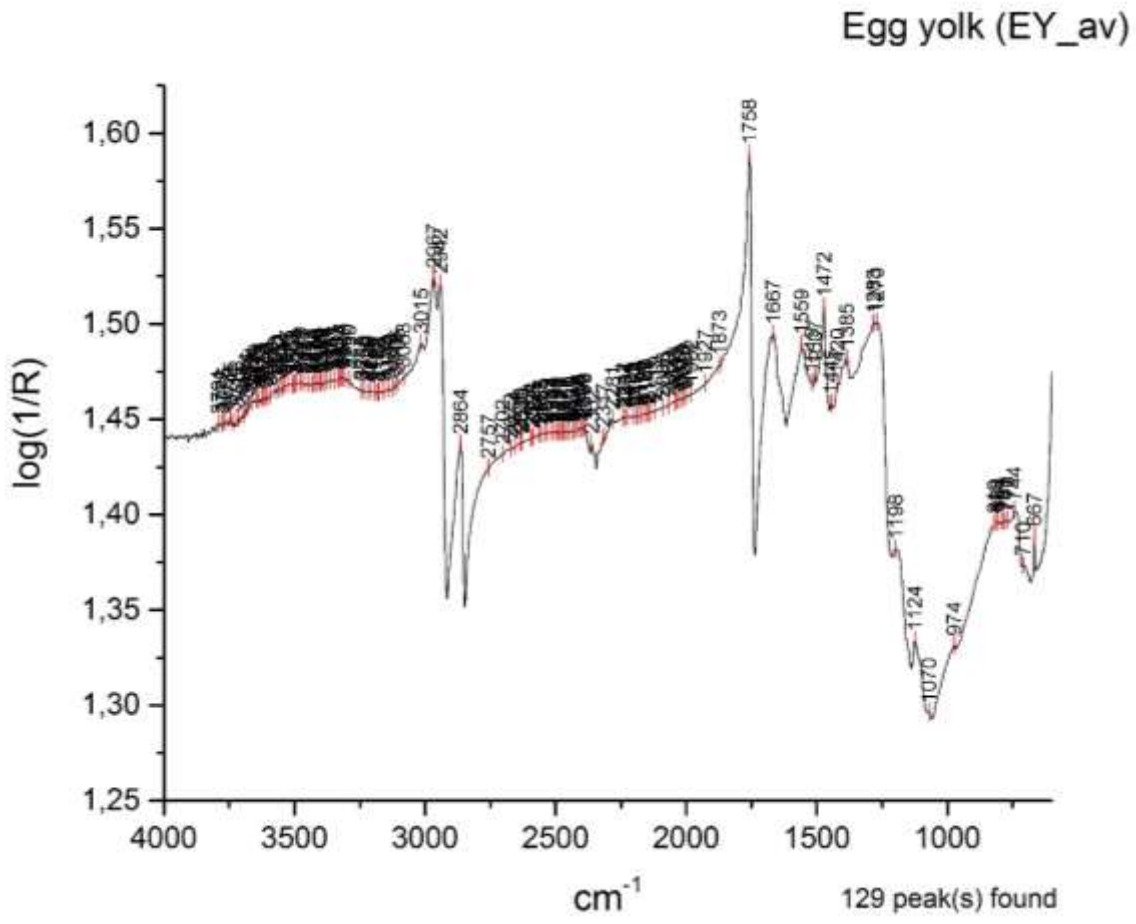

Figure 46: The spectrum of egg yolk.

The peaks in the spectrum of egg yolk (EY_av) above 3015 cm^{-1} and within the 2757-1873 cm^{-1} region are not taken into account since they are very weak (fig.46). The characteristic shape of C-H stretching absorptions at 3015-2864 cm^{-1} is diagnostic to esters (Rosi et al., 2009, 2099). Their derivative-like shape indicates the prevalence of specular reflectance, an expected effect given the smooth texture of the film. Ester diagnostic peaks are present within the 1758-1158 cm^{-1} region, with the most characteristic ones being the 1st order derivative at 1758 cm^{-1}, the C=O vibrations at 1667 and 1559 cm^{-1} (Rosi et al., 2009, 2099) and the C-O bending at 1472 cm^{-1} (Ricci et al., 2006, 1223).

The peaks within the 1124-974 cm^{-1} indicate the presence of phospholipids (Ricci et al., 2006, 1223). The phosphorous-containing lipids in egg yolk should be taken into consideration in the identification of different esteric materials (Mills and White, 1987, 76). Few weak peaks within 819-667 cm^{-1} are also included in the CPAD as indicative to egg yolk.

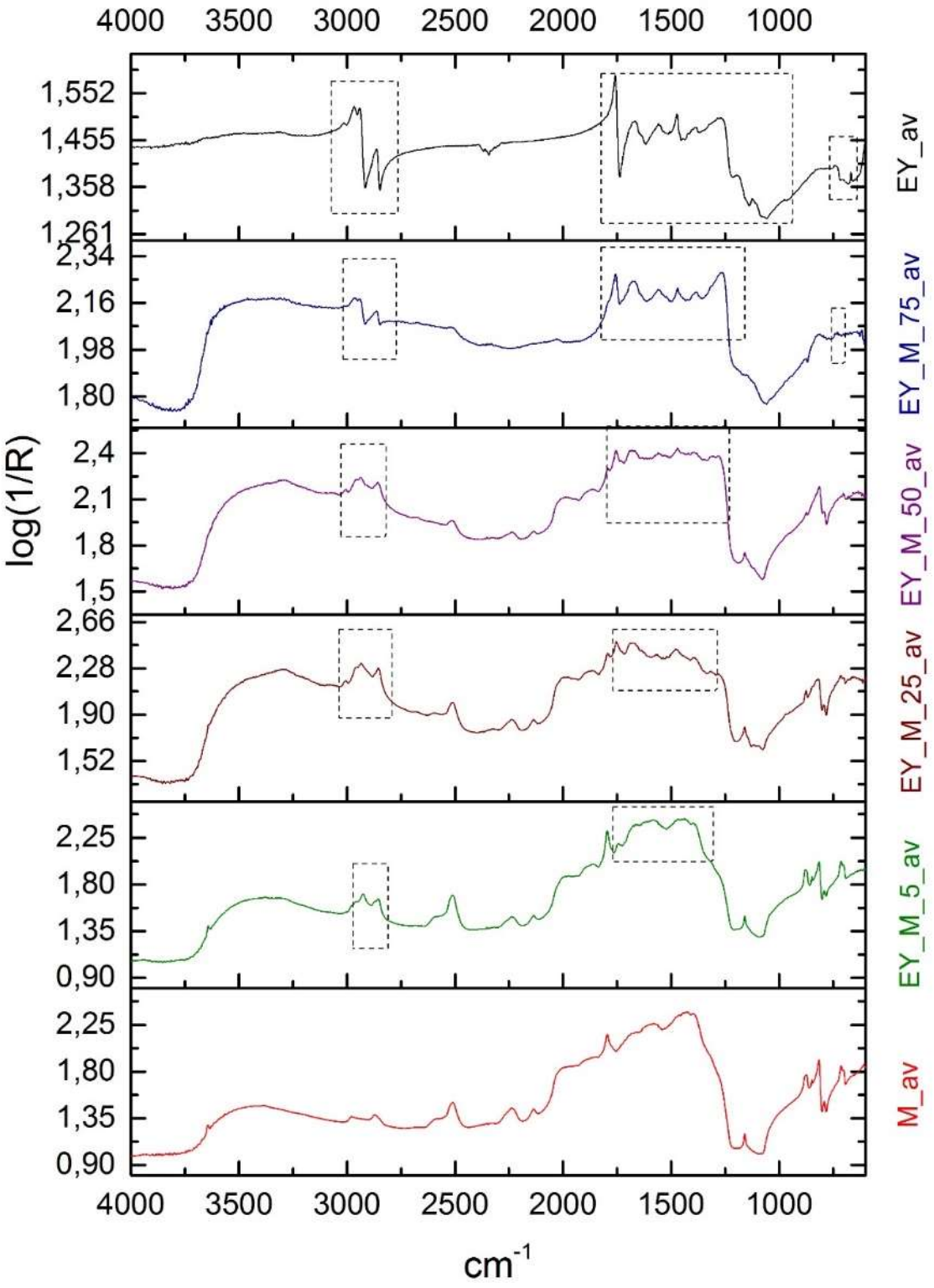

Figure 47: Spectra comparison of egg yolk (EY_av) with mortar mixtures of 75, 50, 25 and 5% egg yolk additive and mortar (M_av).

Spectra comparison shows that egg yolk peaks are present and distinct even in the mortar mixtures of the lowest organic concentration (fig.47). The spectrum of the 75% egg

yolk/mortar mixture (EY_M_75_av) shows all the characteristic major ester peaks, as well as the weak peaks at 1522, 1500, 1424 and 1382 cm^{-1} also observed in the egg yolk spectrum. Shifting is negligible and the shape and intensity of peaks resembles these of egg yolk. Inorganic presence is low and assumed by the absence of the phospholipids in the quartz area around 1159 cm^{-1} and below 875 cm^{-1}. The shape and intensity of the C-H stretching peaks at the region 3011-2864 cm^{-1} clearly places the spectrum in ester groups (Appendix I, fig.10).

The number of weak peaks within the 1755-1281 cm^{-1} region of major ester peaks increases in the spectrum of 50% egg yolk/mortar mixture (EY_M_50_av). This is due to the inorganic interference from both quartz and calcium carbonate components. However, the area retains the diagnostic egg yolk peaks as it appears through the CPAD comparison between EY_M_50_av and EY_av (Appendix I, fig.11). The combined presence of 1755, 1682, 1560, 1470 and 1381 cm^{-1}, as well as the weak peaks in between, can only indicate esters. Amide peaks observed in bone glue and egg white spectra at 1690 cm^{-1} differ considerably in shape and intensity and should not be confused with the ester C=O bond (Rosi et al., 2009, 2099). Similar outcomes are drawn by the observation of the peaks in the 25% egg yolk/mortar mixture (EY_M_25_av) although inorganic presence is more pronounced (Appendix I, fig. 12).

In the spectrum of 5% egg yolk/mortar mixture (EY_M_5_av), where organic peaks are reduced in number and intensity, weak peaks are significant in the identification of the organic component. The shape and intensity of the peaks 3015-2855 cm^{-1} and 1744 cm^{-1} define the presence of esters and the weak peaks at 1675, 1539 and 1198 cm^{-1} indicate egg yolk (Appendix I, fig.13).

7.5.4 Egg and mortar mixtures

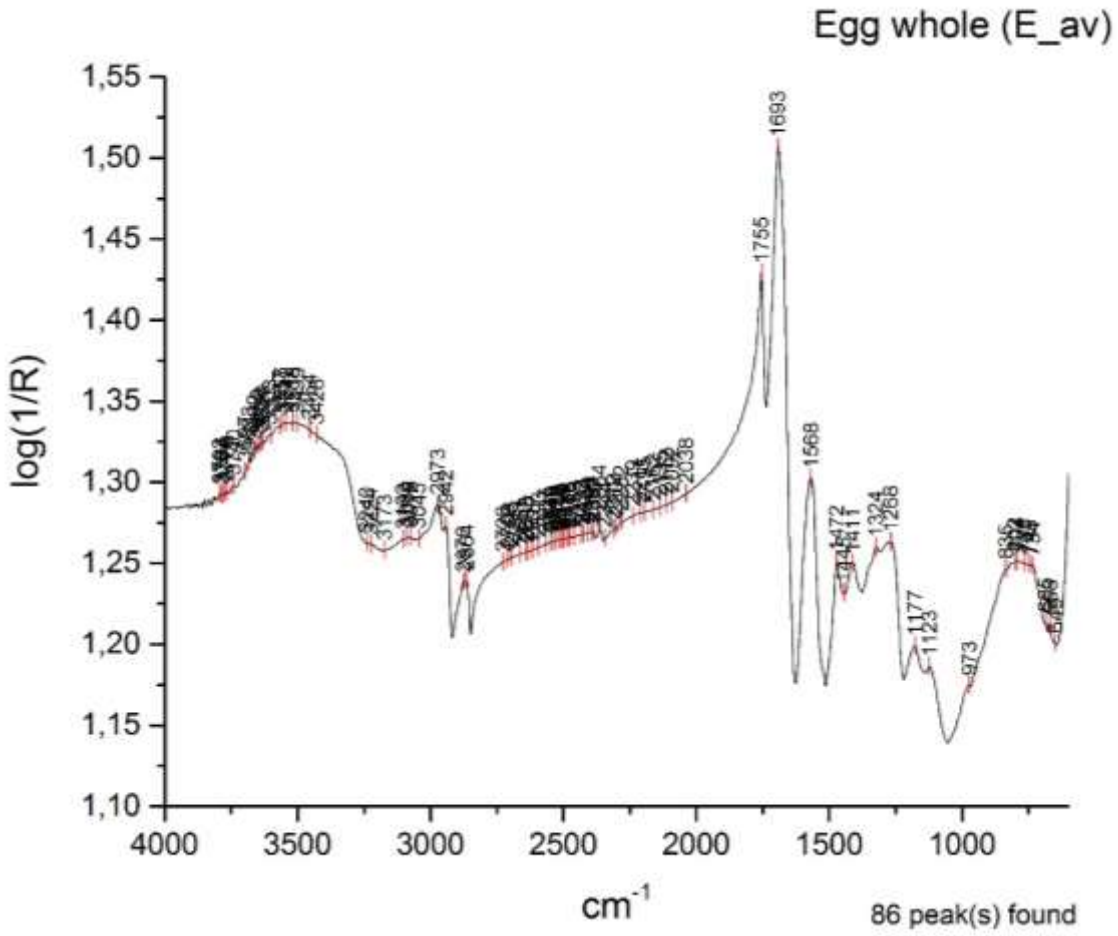

Figure 48: The spectrum of egg (whole).

As expected, the spectrum of egg (E_av) combines the spectra of egg white and egg yolk, showing esters, amides and phospholipids (fig.48). Characteristic amide peaks are detected at 1693, 1568 and 1445 cm^{-1}, ester bands at 2973-2864 and 1755 cm^{-1} and phospholipids at 1123 and 973 cm^{-1}. The shape and intensity of peaks within the 1472-1268 cm^{-1} resemble those of egg white and should be assigned to amides.

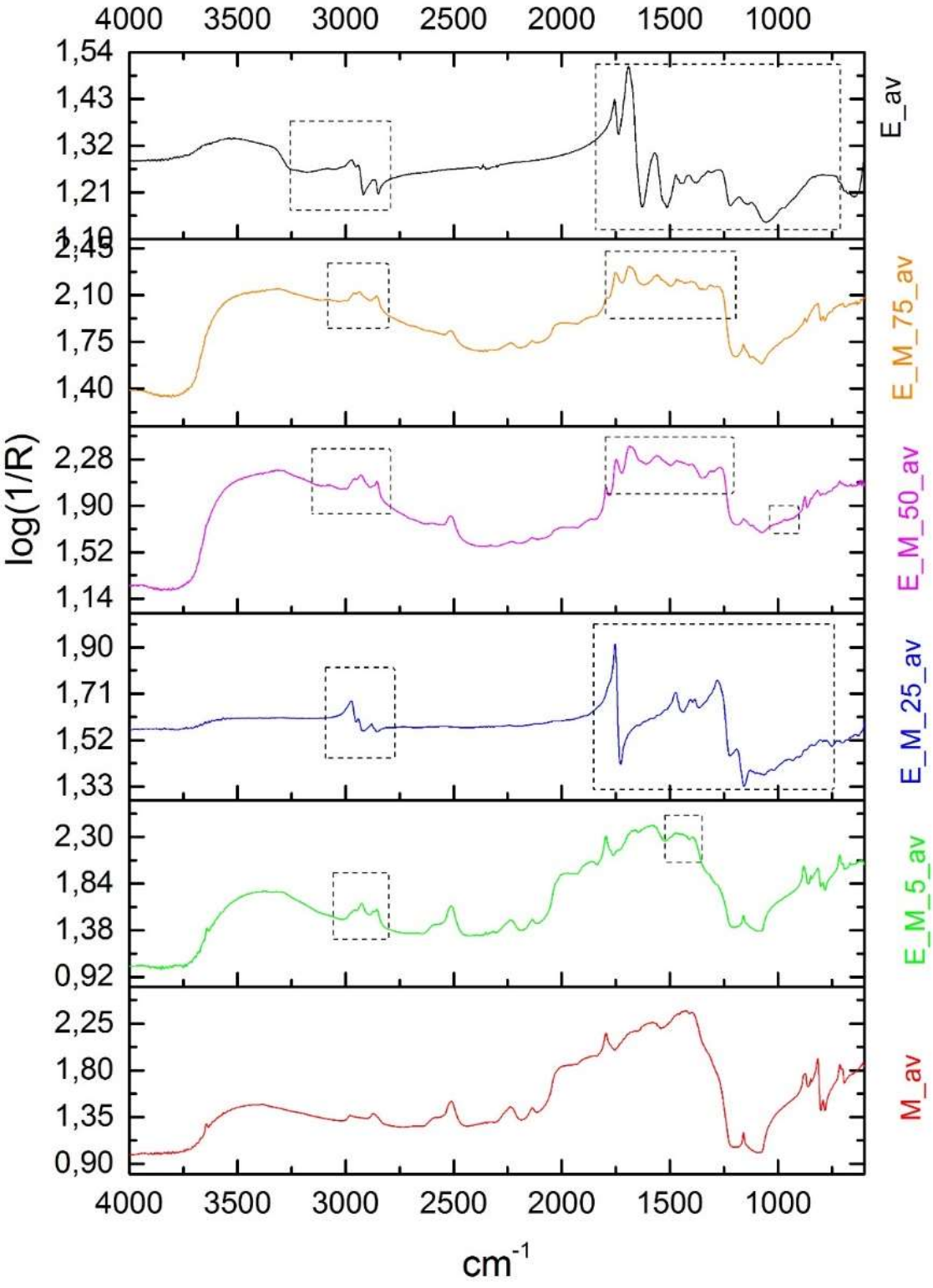

Figure 49: Spectra comparison of egg whole (E_av) with mortar mixtures of 75, 50, 25 and 5% egg additive and mortar (M_av).

Inorganic interference occurs already at the 75% egg/mortar mixture (E_M_75_av), although the combined presence of amides and esters, their shape and development in

the region 1686-1274 cm^{-1} are considered diagnostic to egg (fig.49). Similar outcomes are seen on the spectrum of 50% egg/mortar mixture (E_50_M_av), although the intensity of inorganic peaks is more pronounced. Phospholipids appear at 970 cm^{-1} (Appendix I, fig.14-15).

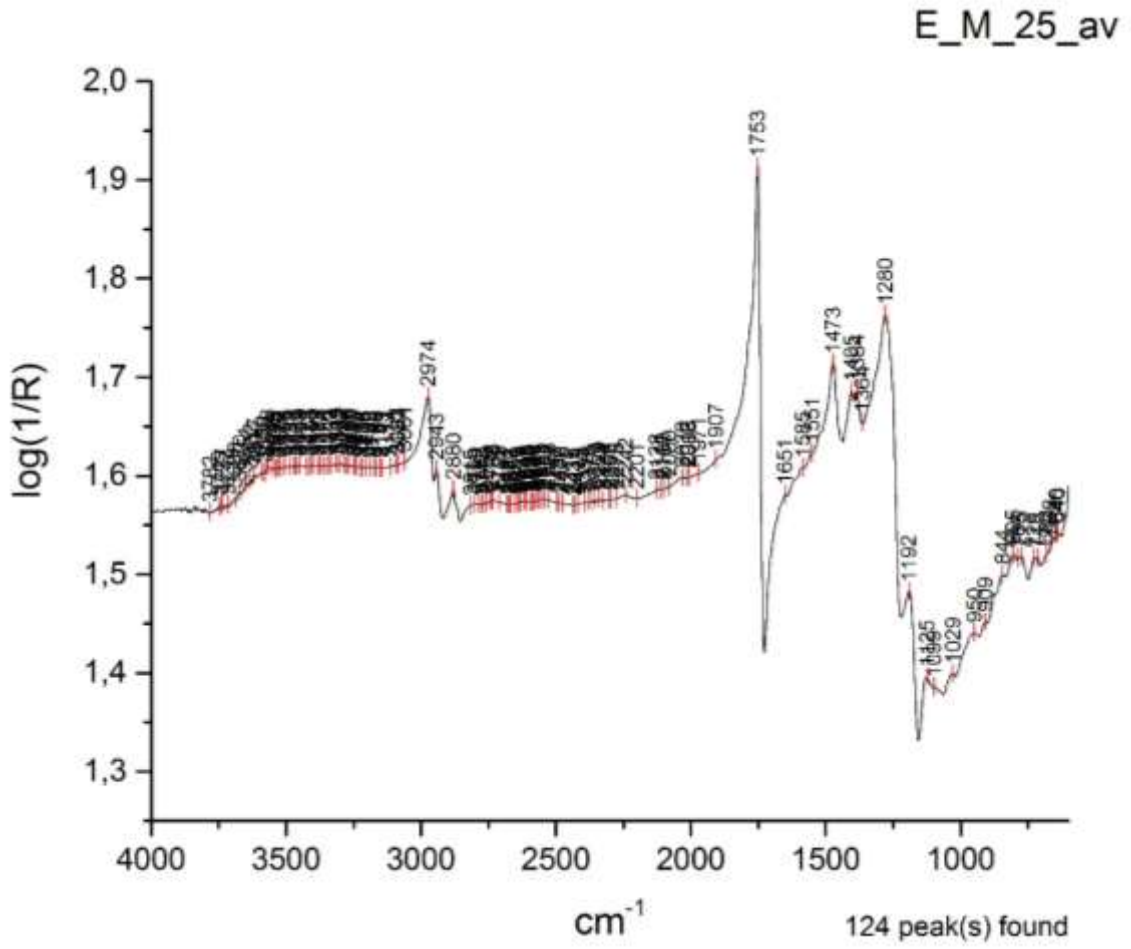

Figure 50: The spectrum of 25% egg additive in mortar mixture (E_M_25_av).

The spectrum of 25% egg/mortar mixture was expected to be similar to the spectra of 50% and 75% egg/mortar mixtures, relative to the presence of the inorganic components and differ only in the intensity of their peaks. However, almost all the inorganic peaks are absent from the spectrum and the same stands for peaks representing amides (fig.50). $CaCO_3$ and quartz are indicated at 1651-1551 cm^{-1}. The remaining peaks in the region show esters and lipids. Identification of egg would be based on the peaks below 1280 cm^{-1} and on the shape and intensity of the 2974-2880 cm^{-1} that resembles that of egg (Appendix I, fig.16). This dominance of esters in the spectrum, as well as the prevailing of specular reflectance, shows that the analyzed surface was covered by a relatively higher amount of

egg yolk rather than of whole egg. The effect should be attributed to the mixing procedure during the preparation of the standard.

Identification of 5% egg in the mortar mixture is based on the few peaks present, mainly showing ester bonds at 2957-2855 cm^{-1} and a combination of weak peaks indicating both esters and amides at 1472-1394 cm^{-1} (Appendix I, fig.17). The intensity and shape of peaks are the diagnostic properties in this spectrum.

7.5.5 Lard and mortar mixtures

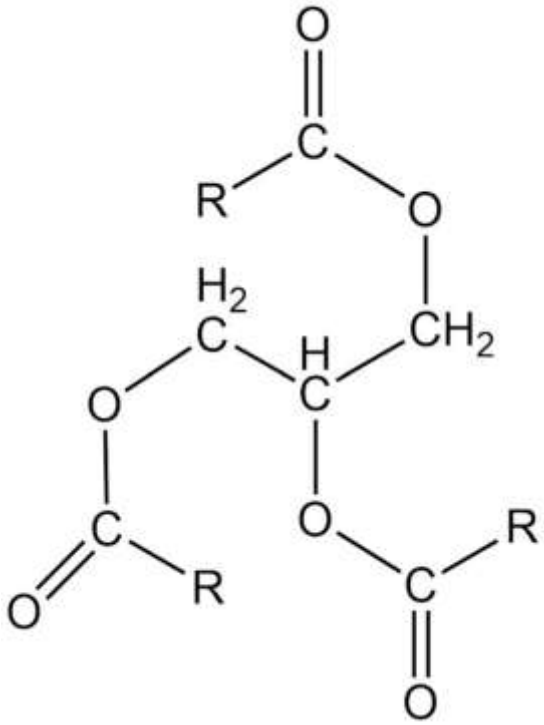

Figure 51: The chemical structure of triglyceride fatty acids (Xing et al., 2020, 4).

Lard and Olive oil represent fats/oils. Oils and fats are both composed by mixtures of mixed triglycerides (esters of the trihydric alcohol glycerol with a range of possible long fatty acid chains) (fig.51). Although the chemistry of oils and fats is similar; oils are liquids at room temperature due to the higher number of unsaturated triglycerides in their structure, whereas fats are solids (Mills and White, 1987, 26).

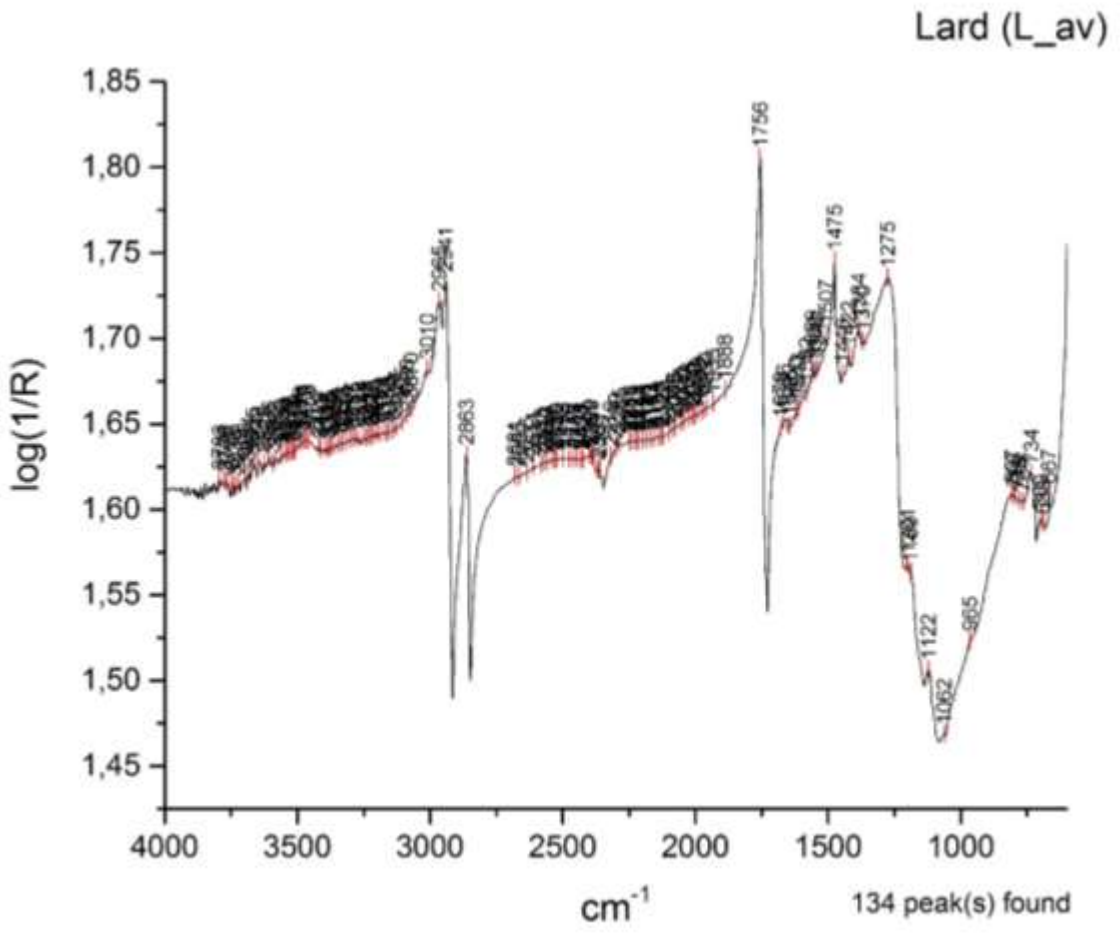

Figure 52: The reflectance micro-FTIR spectrum of lard.

The pronounced derivative-like CH_2 stretching peaks at 3010-2863 cm^{-1} (Ploeger et al., 2010, 37), the 1st order derivative C=O stretching peak at 1756 cm^{-1} (Mazzeo et al., 2008, 69) and the C-O bending vibration at 1475 cm^{-1} (Ricci et al., 2006, 1223), as well as the weak peaks below 1475 cm^{-1} define the lard spectrum, L_av (fig.52). The smooth surface of the lard standard produces specular reflectance effects.

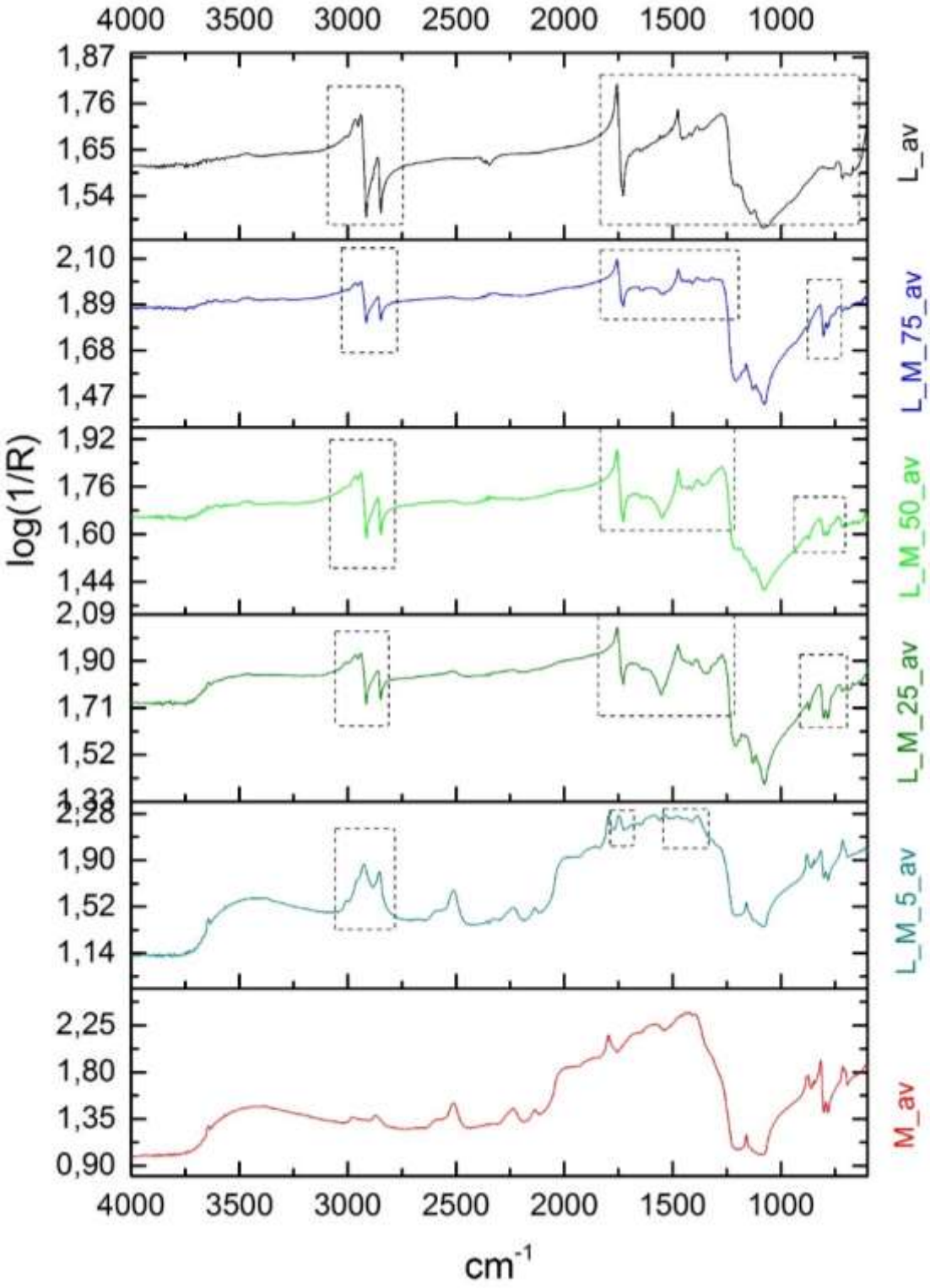

Figure 53: Spectra comparison of lard (L_av) with mortar mixtures of 75, 50, 25 and 5% lard additive and mortar (M_av).

Spectra comparison in figure 53 shows the dominance of the CH_2 stretching vibrations of lard at 3010-2863 cm^{-1}, even in the 5% lard mixture (L_M_5_av). The same stands for the

ester peaks at 1755 and 1475 cm^{-1}. Inorganic peaks in the spectrum of 75% lard/mortar mixture (L_M_75_av) are limited within the 1679-1579 cm^{-1} and below 1159 cm^{-1}, interfering with weak lard peaks. Similar outcomes are seen on the spectra of 50 and 25% lard/mortar mixtures. The unique patterns that the inorganic peaks produce at the area 1691-1616 cm^{-1} and below 889 cm^{-1} are also useful in identification studies of lard/mortar mixtures (Appendix I, fig. 18-21). It is likely that inorganic components are masked by the lard film due to its thickness and rheology properties in the mixing. The high lipid content in the spectrum of 5% lard/mortar mixture is evident in the region of CH_2 stretching at 3005-2854 cm^{-1}, the peak at 1747, and the weak peaks within the 1473-1384 cm^{-1} region.

7.5.6 Olive oil and mortar mixtures

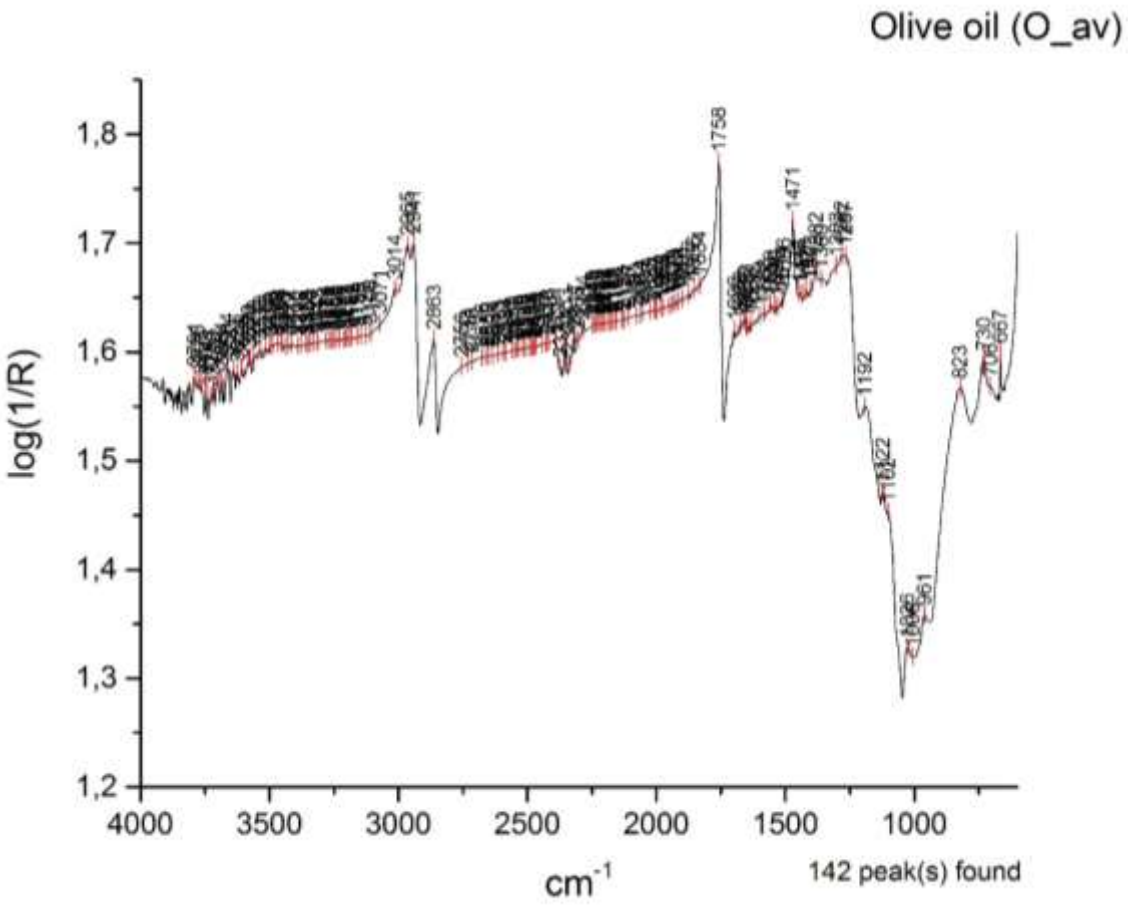

Figure 54: The spectrum of olive oil.

Olive oil (O_av) and lard spectra show similarities as expected from materials sharing the same basic chemical structure (Mills and White, 1987, 26) (fig.54). However, small differences in peak position, shape and intensity of peaks at 3014-2863 cm^{-1}, 1758 cm^{-1}, 1382 cm^{-1} and 1267-1102 cm^{-1} distinguish the two similar materials.

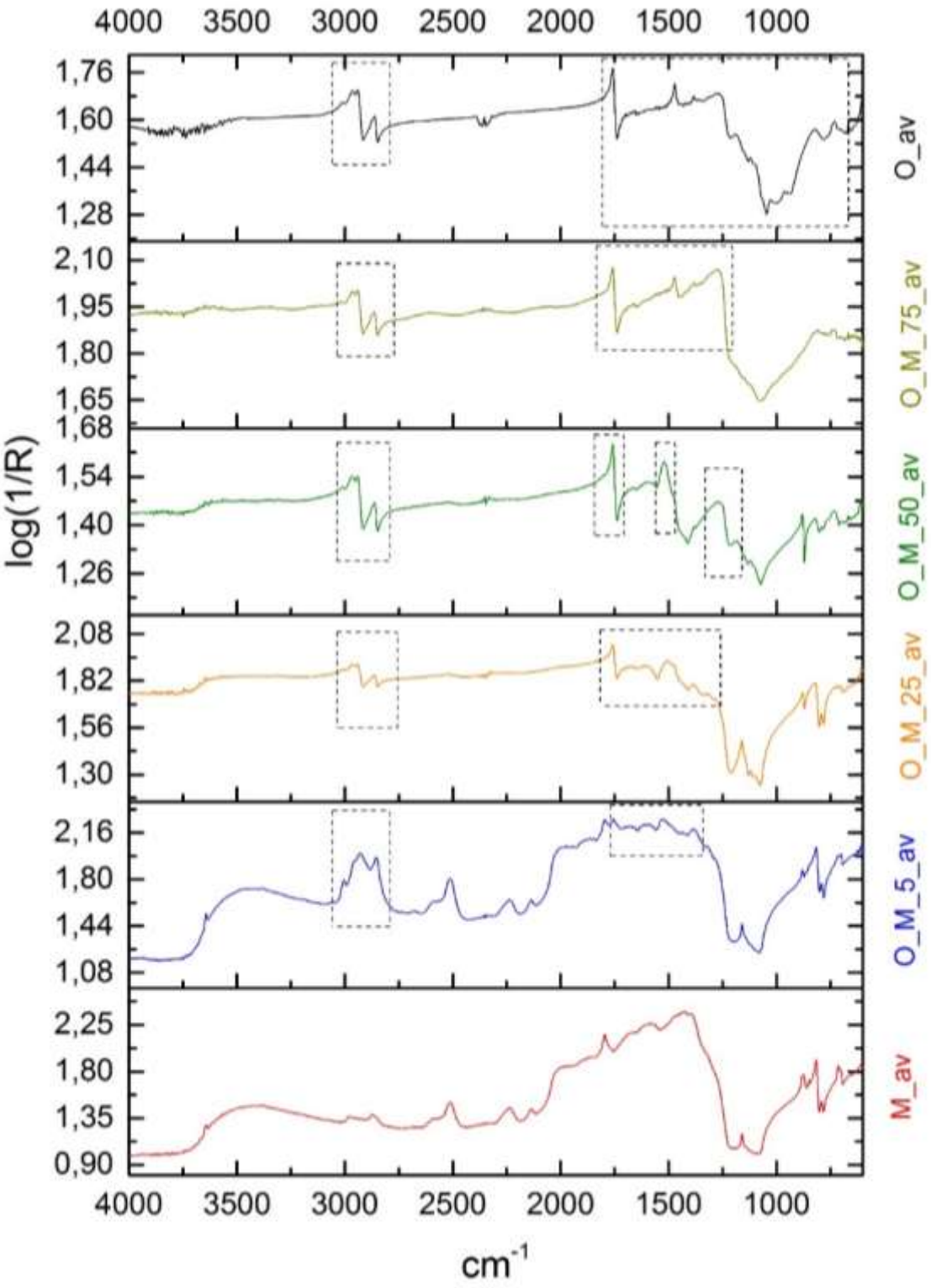

Figure 55: Spectra comparison of olive oil (O_av) with mortar mixtures of 75, 50, 25 and 5% olive oil additive and mortar (M_av).

Organic presence is evident in all the different concentrations spectra, on the CH_2 stretching of esters in 3019-2864 cm^{-1} and the peak at 1755 (fig.55). The spectrum of 75%

olive oil (O_M_75_av) is almost identical to that of olive oil, showing limited inorganic interference below 1271 cm^{-1}. The spectrum of 50% olive oil in mortar shows a different pattern from the rest spectra at the broad peaks at 1518 and 1268 cm^{-1} indicating C-O bending (Ricci et al., 2006, 1223) and stretching respectively (Buti et al., 2013, 2705). In the spectrum of 25% olive oil/mortar mixture the influence of quartz at 1160 cm^{-1} and $CaCO_3$ below this point is evident, although the sharp and weak peak at 727 cm^{-1} is present and similar to the one observed in the olive oil spectrum. Olive oil diagnostic peaks at 1758, 1660, 1507, 1381 and 1282 cm^{-1} are present and show negligible position shifting from the peaks at the olive oil spectrum. The 5% olive oil/mortar spectrum, although showing high inorganic presence, is indicative to oil from the peaks at 3005-2855 cm^{-1} and shape and intensities of 1755, 1680, 1530 and 1384 cm^{-1} (Appendix I, fig.22-25).

7.5.7 Milk and mortar mixtures

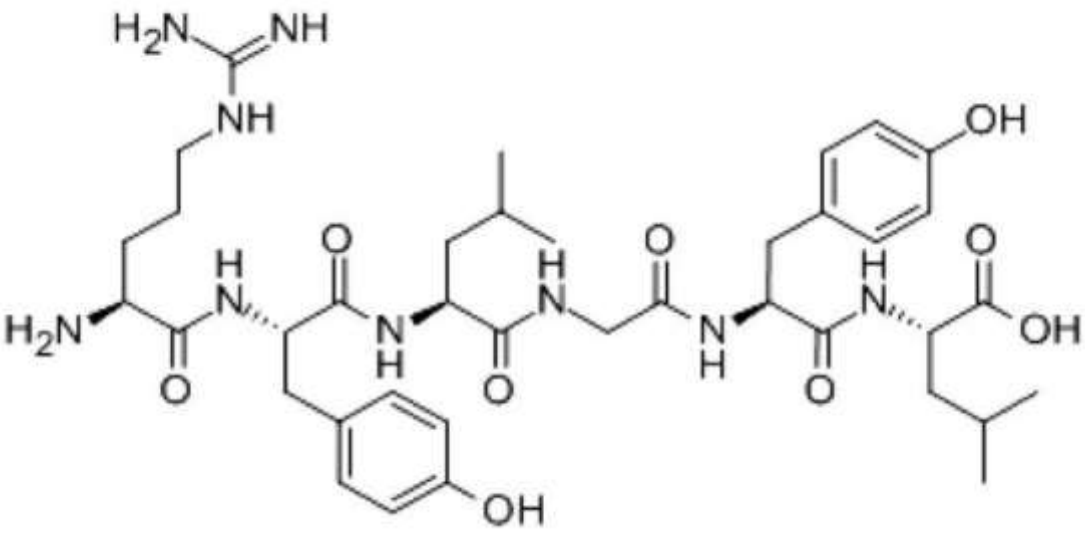

Figure 56: The chemical structure of casein (Garbosa et al., reproduced in Patni et al., 2015).

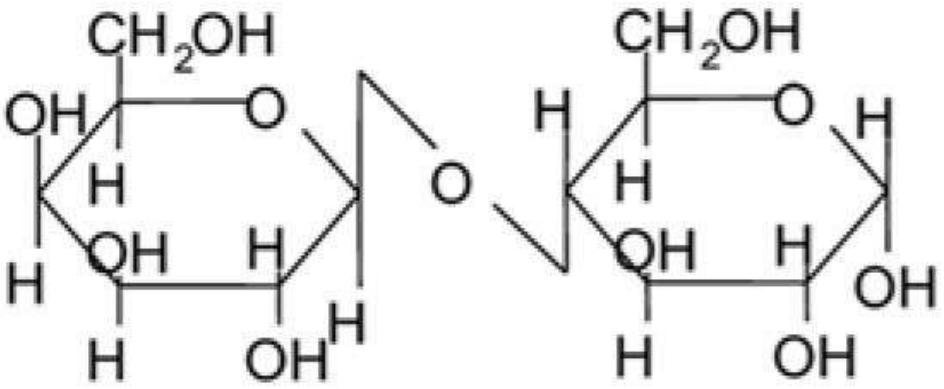

Figure 57: Structural formula of lactose (Mahlin, 2004, 21).

The main protein of milk is casein, a phosphoprotein complex (fig.56). Fats and lactose are also parts of the composition of milk (fig.57) (Mills and White, 1987, 76).

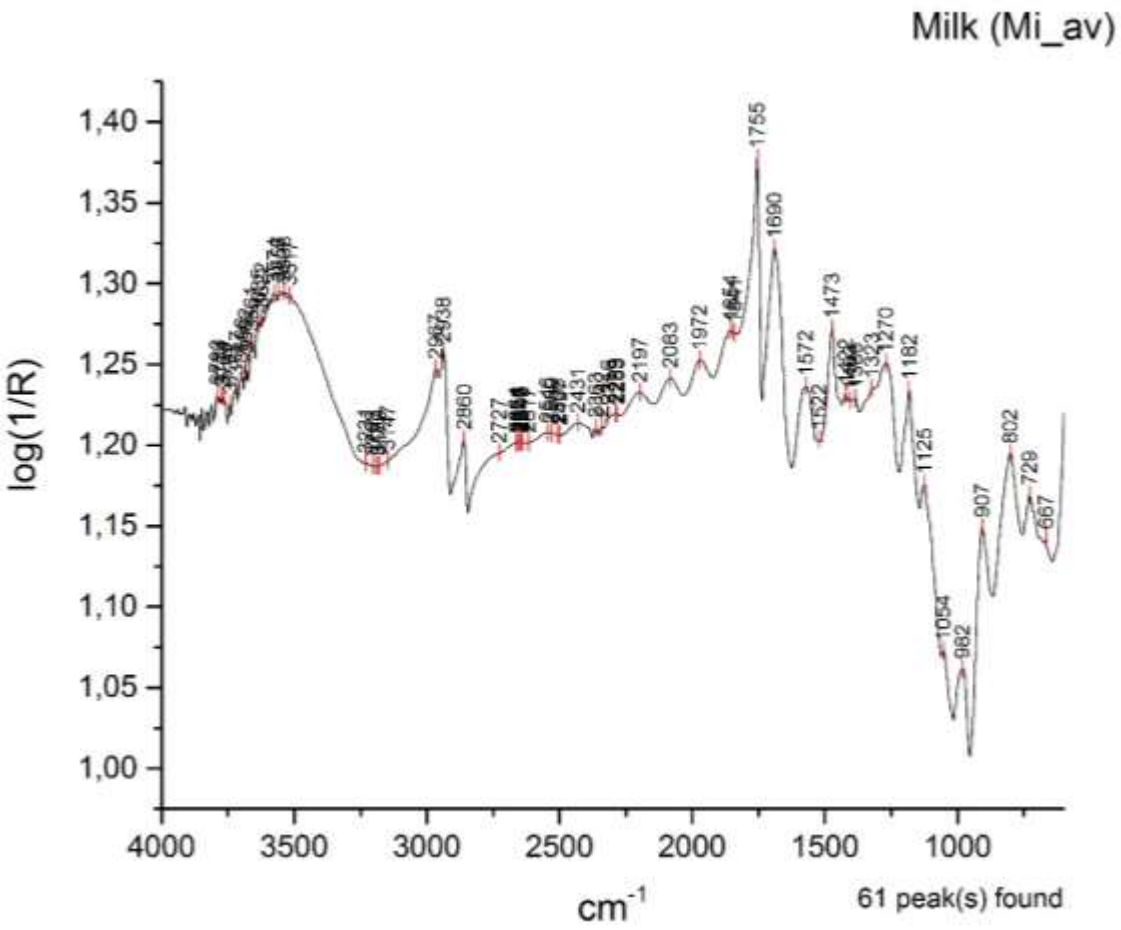

Figure 58: The milk spectrum.

The chemical complexity of milk (Mi_av) is evident in its spectrum, where proteins, fats and sugars (lactose) co-exist (fig.58) (Mills and White, 1987, 26). The shape of C-H stretching bands at 2967-2860 cm^{-1} is attributed to esters (Daher et al., 2017, 8). The absorptions at 1755 and 1690 cm^{-1} show the coexistence of esters and protein (casein) together with the amide peaks at 1572 and 1473 cm^{-1} (Rosi et al., 2009, 2104). The area below 1182 cm^{-1} shows the presence of sugars (Synytsya and Novak, 2014, 6).

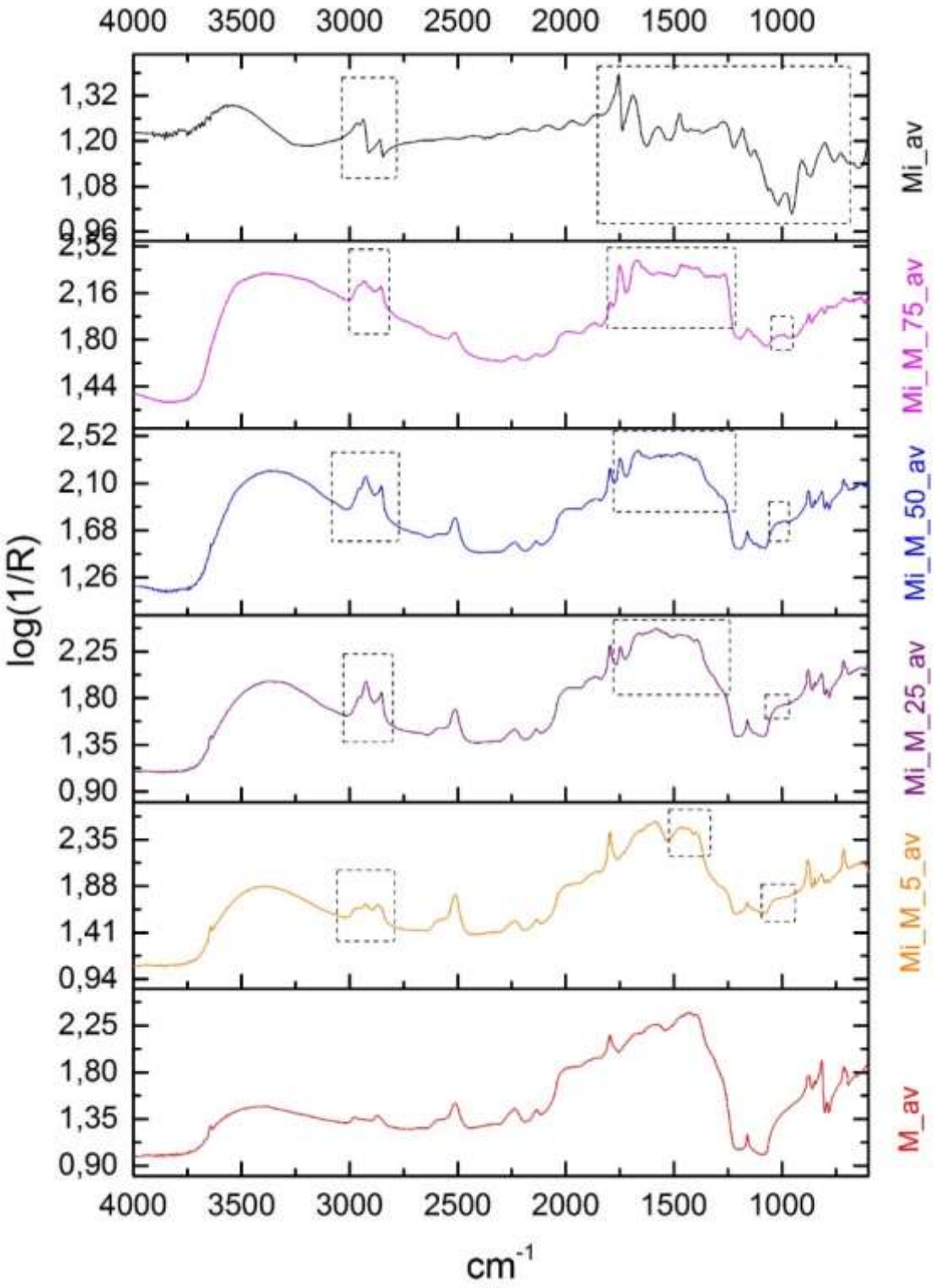

Figure 59: Spectra comparison of milk (Mi_av) with mortar mixtures of 75, 50, 25 and 5% milk additive and mortar (M_av).

Inorganic peaks appear already at the spectrum of 75% milk/mortar mixture and increase gradually as the concentration of organic decreases (fig.59). The low viscosity of milk

should have contributed to that effect. However, organic presence is evident in all spectra especially in the 3007-2857 cm^{-1} group frequency region.

In the 75% milk/mortar spectrum, amide and ester peaks are visible as well as the sugar content in the peak at 989 cm^{-1}. Similar outcomes are observed in the 50% and 25% milk mixtures. Inorganic peaks are pronounced between the 2511-1794 cm^{-1} and below 1159 cm^{-1} without however masking the sugars at 1200 and 988 cm^{-1}. The presence of sugars distinguishes milk/mortar mixtures from those containing egg, in which esters and amides coexist.

The 5% milk/mortar mixture retains the sugar peak at 990 cm^{-1}. Amide peaks are highly masked by inorganic ones, although the peaks at 1652 and 1476 cm^{-1} should indicate Amide III. The presence of esters in 2958 and 2926 cm^{-1} is retained, although masked from the doublet of mortar (Appendix I, fig.26-29).

7.5.8 Rice and mortar mixtures

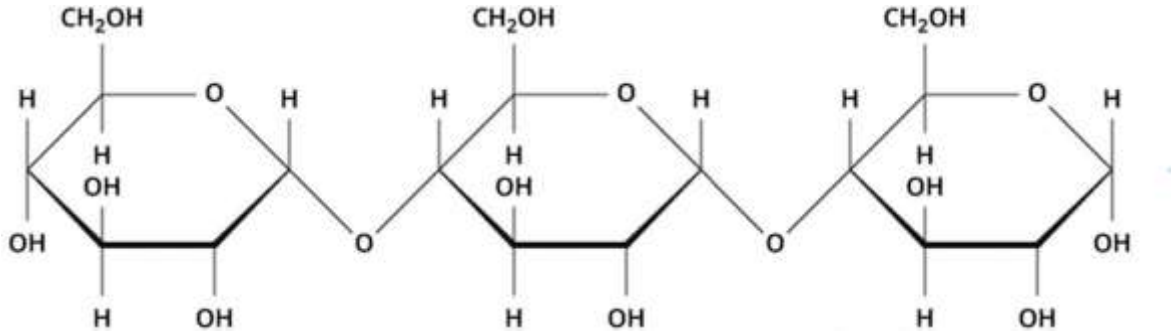

Figure 60: Basic chemical structure of polymeric starch (Othman et al., 2018, 194).

The rice solution standard (R_av) represents starch, a carbohydrate consisting of the two polymers amylose and amylopectin (fig.60) (Mills and White, 1987, 66).

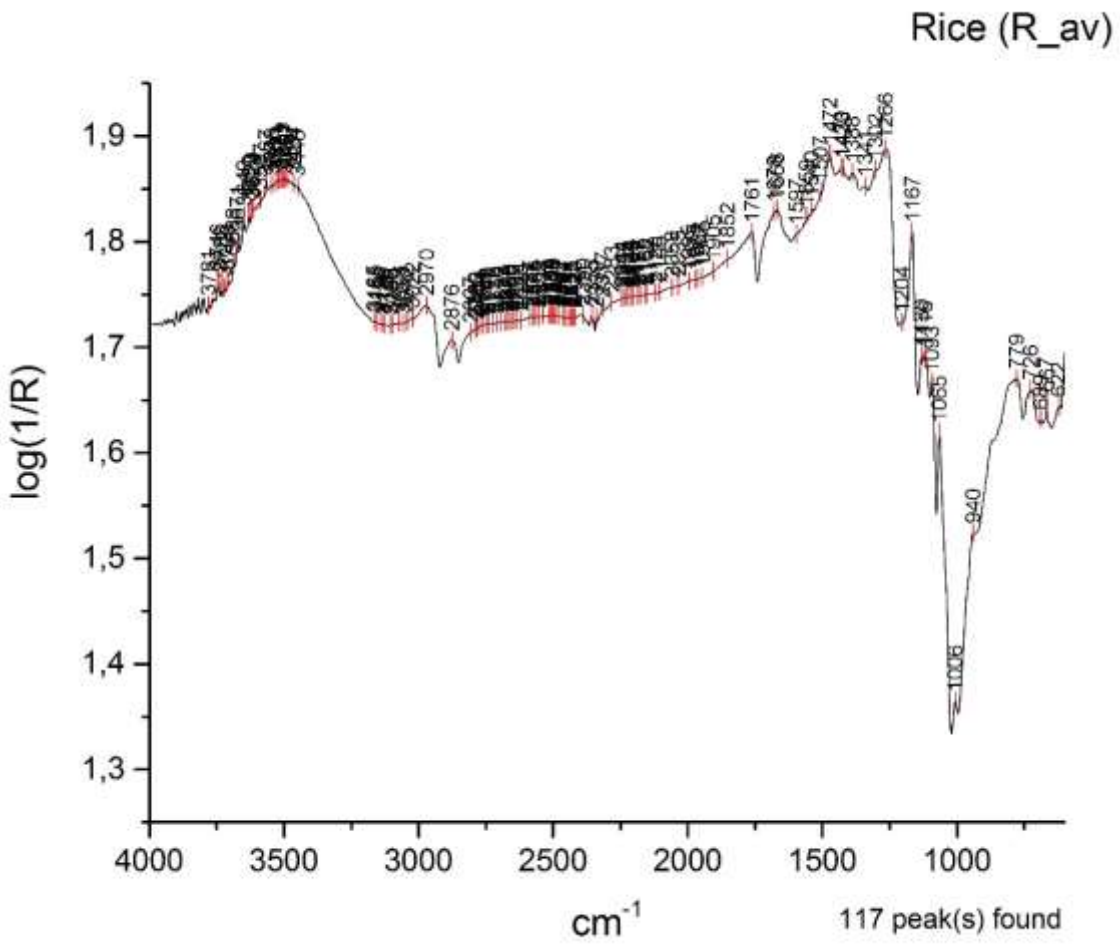

Figure 61: The rice spectrum.

Weaker C-H vibrations than the ones observed in the previous ester-containing standards are visible in rice starch at 2970-2876 cm^{-1} (fig.61). The peaks at 1678-1668 cm^{-1} indicate water molecules (Ylmen and Jaglid, 2013, 119). The peak at 1761 cm^{-1} is weak and should not be confused with that observed in esters. Peaks of interest appear from 1472 cm^{-1} C-H bending and below, in the region of sugars (Synytsya and Novak, 2014, 6).

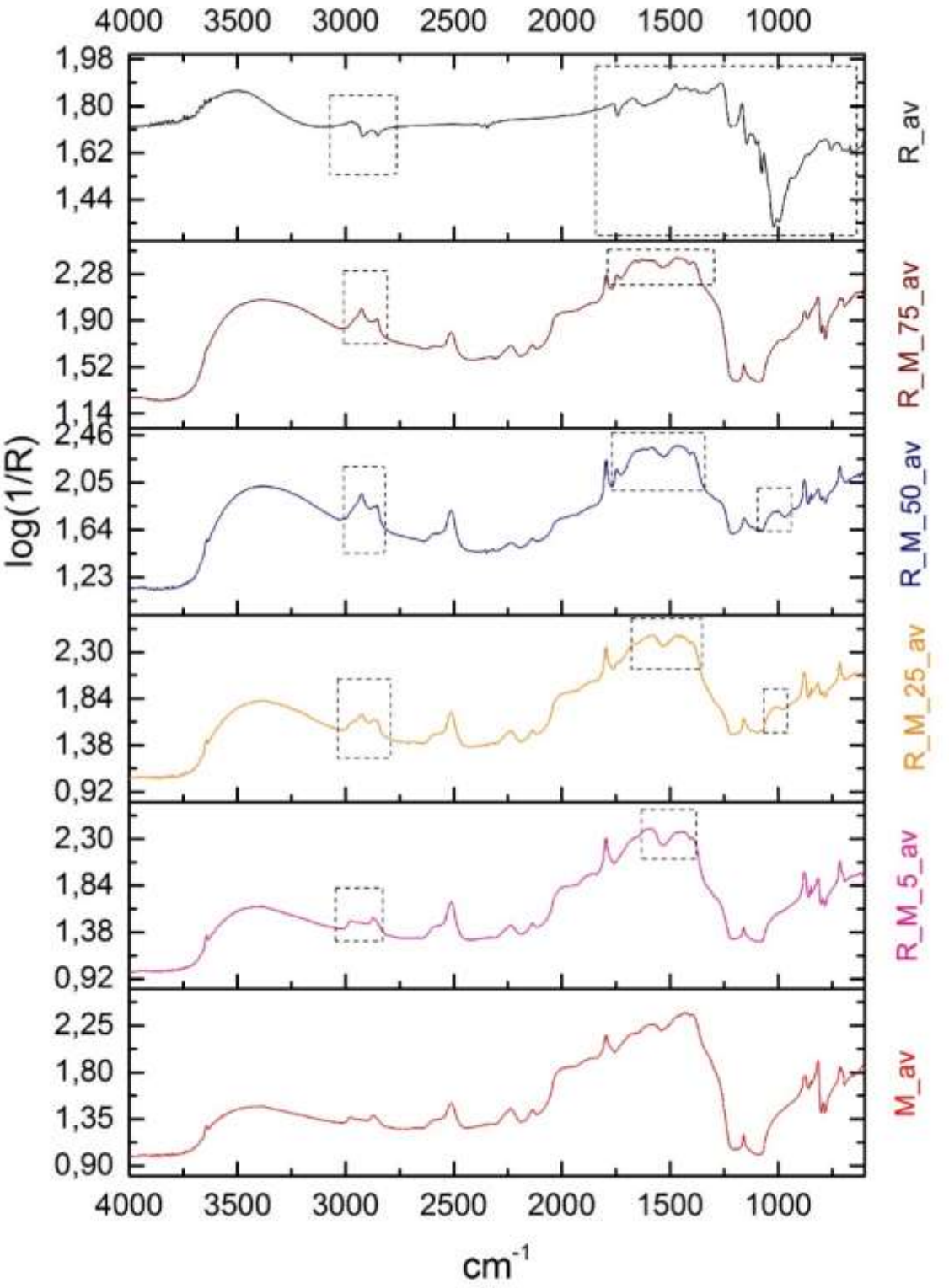

Figure 62: Spectra comparison of rice (R_av) with mortar mixtures of 75, 50, 25 and 5% rice additive and mortar (M_av).

Similar to milk mixtures, inorganic interference is evident even in the 75% rice/mortar mixture and should be attributed to the low viscosity of the rice solution during mixing with

the mortar (fig.62). Organic peaks are visible above 1474 cm^{-1} but highly masked by inorganic peaks (Appendix I, fig.30).

It is interesting to note that the spectrum of 50% rice/mortar mixture shows sugars in the region below 1001 cm^{-1} but none of the C-H vibrations within the 1678-1001 cm^{-1}. This is due to the inorganic interference and the fact that the shape and intensity of the peaks within this area resembles inorganics peaks best. Thus, it is not safe to assign organic bonds to these peaks. The peaks at 3008-2857 cm^{-1} indicate C-H stretching. The fact that C-H stretching and sugars are present without any presence of esters in between, shows that the overall spectrum belong to hydrocarbons, such as starch, rather than lipids (Appendix I, fig.31).

The assignment of diagnostic peaks in the 25% rice/mortar mixture spectrum is even more difficult since fewer C-H vibrations peaks can be safely detected. Area of interest could be defined above 1475 cm^{-1} and at 1019 cm^{-1} (sugars). The spectrum of 5% rice/mortar mixture is almost identical to the mortar spectrum with the exception of the C-H stretching at 2933 cm^{-1} and the weak peaks at 2670-2719 cm^{-1}. The peaks within 1596-1398 cm^{-1} should be carefully studied since they overlap with the main inorganic peaks (Appendix I, fig.32-33).

The complexity of the spectra of rice/mortar mixtures relevant to the high inorganic interference even in mixtures of high rice concentration should be attributed to the low viscosity of the rice solution. The interpretation of such spectra and the detection of rice in the mortar mixtures through solely visual comparisons would be limited, as it is evident in figure 63 below, since differences mainly rely on minor peaks that can only be assessed through CPAD comparisons.

Similar effects were observed on the spectra of milk/mortar mixtures (sect. 7.5.7). Both organic materials exhibit low viscosity compared to that of the rest organic standards that their spectral representation in mortar mixtures followed a gradual decrease as the inorganic portion increased.

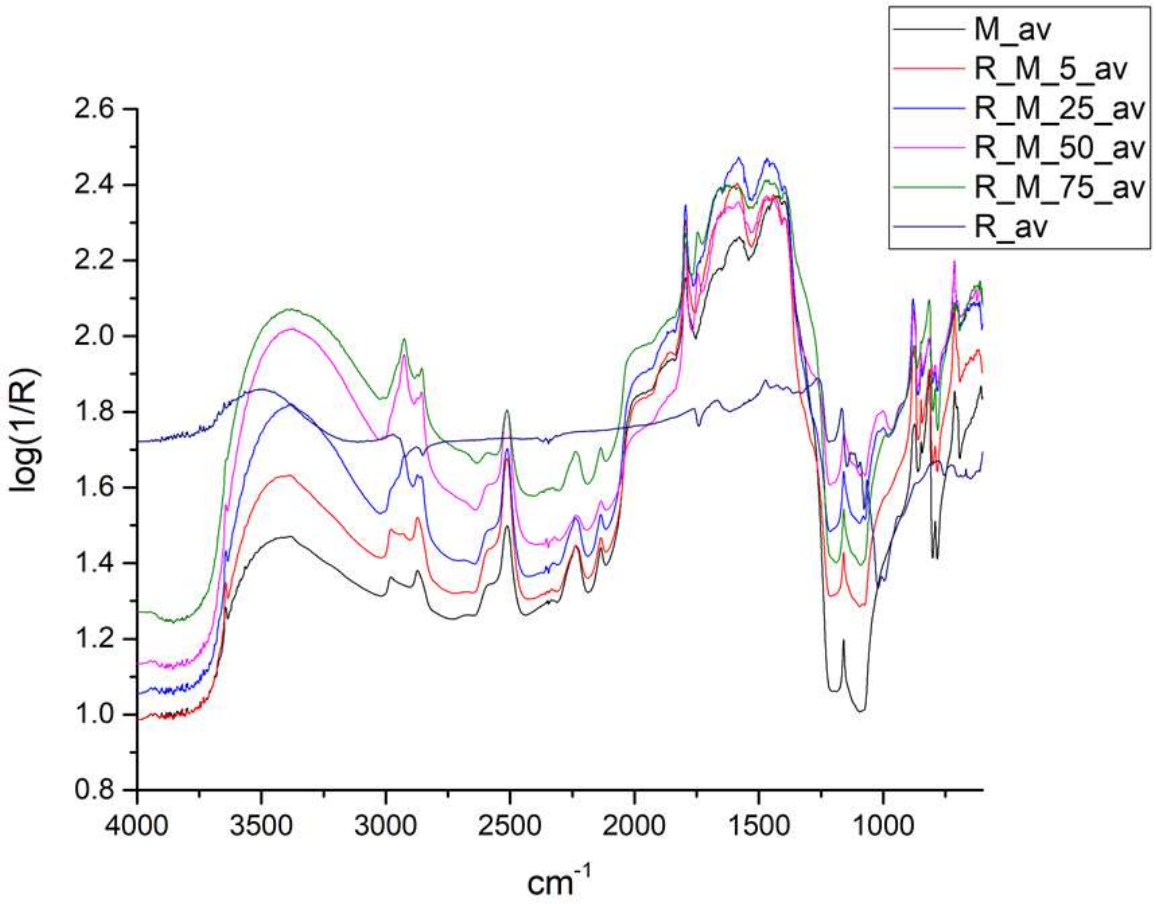

Figure 63: Overlapping spectra of rice (R_av), 75%, 50%, 25%, and 5% rice/mortar and mortar (M_av).

7.5.9 Asphalt and mortar mixtures

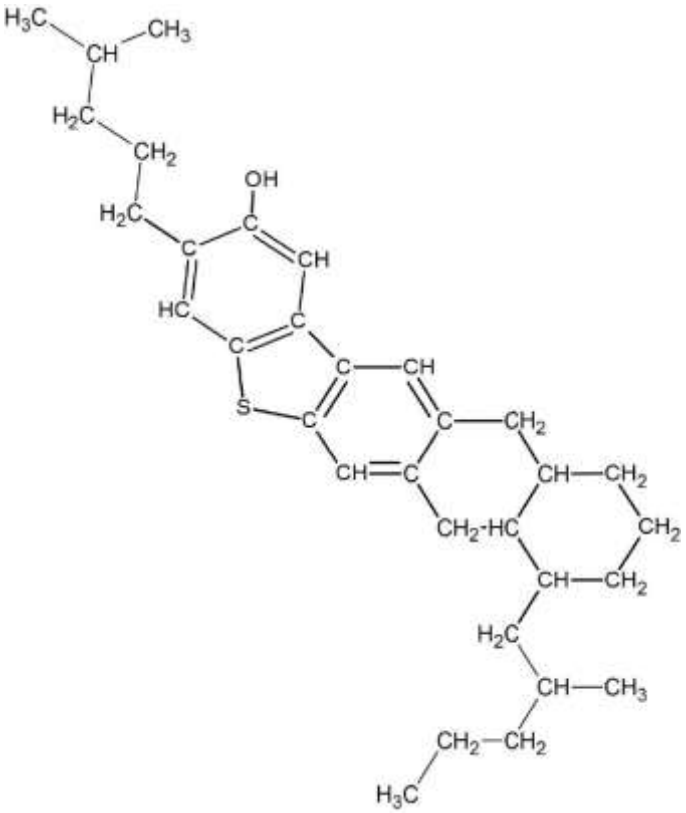

Figure 64: Bitumen molecule (Redelius et al., reproduced in Nahar, 2016, 10).

Asphalt (A_av) represents a natural occurring organic (bitumen) / inorganic material. Bitumen is a substance that derives from the decomposition of organic matter and is composed of a mixture of hydrocarbons of different molecular mass (fig.64), (Lombardi and Santarelli, 2009, 541).

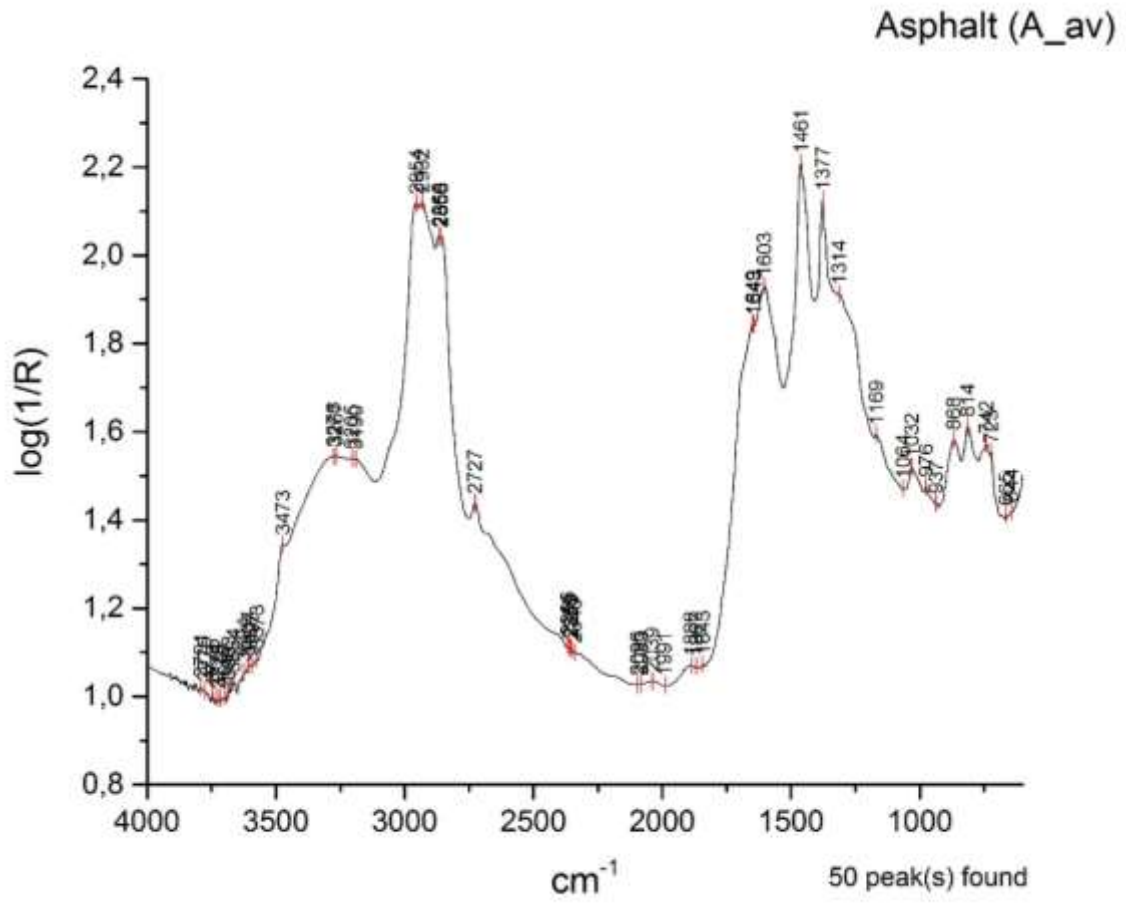

Figure 65: The spectrum of asphalt.

Asphalt (A_av) has a very unique spectrum that cannot be confused with the rest of the organic materials in the CPAD (fig.65). The shape and intensity of the CH_2 / CH_3 stretching at 2954-2858 cm^{-1}, the sharp peak at 2727 cm^{-1}, the benzene ring vibration at 1603 cm^{-1}, the strong peaks at 1461 and 1377 cm^{-1} and the triplet at 868-723 cm^{-1} are characteristic to asphalt (Lombardi and Santarelli, 2009, 542).

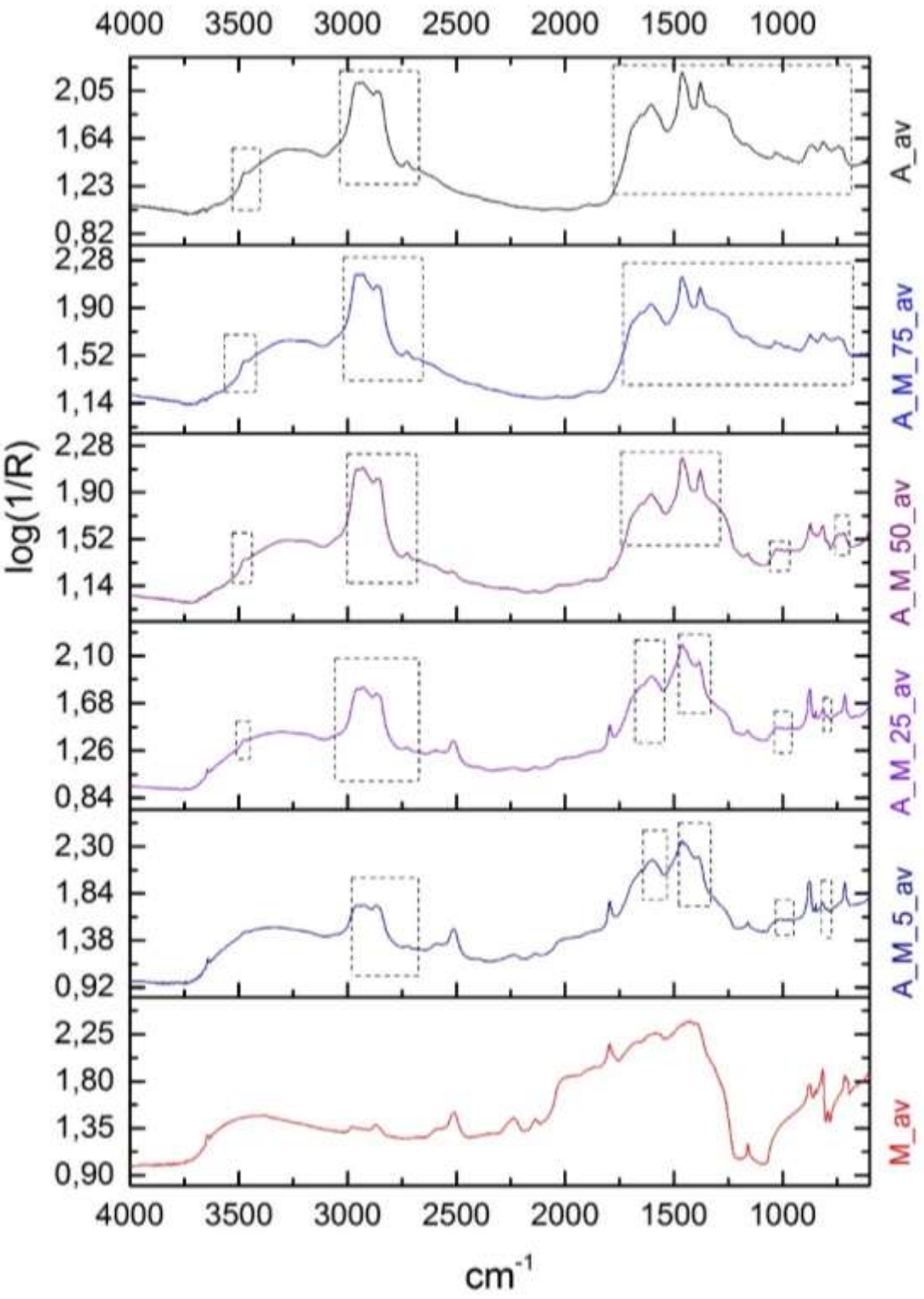

Figure 66: Spectra comparison of asphalt (A_av) with mortar mixtures of 75, 50, 25 and 5% asphalt additive and mortar (M_av).

The characteristic asphalt peaks above 1377 cm^{-1} are retained to all spectra regardless the organic concentration, ensuring the direct identification of the specific component

(fig.66). The 75% asphalt/mortar mixture spectrum is almost identical to the spectrum of asphalt. The same stands for the 50% spectrum with the only difference being the masking of the triplet at 872-732 cm^{-1} due to the emerging $CaCO_3$ and quartz peaks. Inorganic presence intensifies in lower organic concentrations but does not affect the diagnostic asphalt peaks (Appendix I, fig.34-37).

7.6 Outcomes

The peak-by-peak assessment of the reflectance micro-FTIR spectra of organic additives revealed spectral features specific to each organic material analyzed by the specific method. Their comparative assessment through the CPAD with spectra from mortar mixtures of differing concentration of organic additive produced further diagnostic outputs to be used in the identification of organic additives in mortars. These are listed below:

- *Diagnostic peaks* are considered those unique to a specific compound and/or those forming a unique spectral pattern.
- Identification of organic additives, in both pure form and in mortar mixtures, requires assessment of the spectral pattern relevant to the presence, absence and combination of diagnostic peaks in both the group frequency and fingerprint regions (Banwell and McCash, 1994, 84).
- The C-H stretching within the 3000-2850 cm^{-1} group frequency region is the least affected by inorganic interference and visible even in the lowest concentrations for all the tested organic additives/mortar mixtures. This region provides evidence of organic presence in a reflectance spectrum.
- Peak location, shape and intensity within the 3000-2850 cm^{-1} region reflect whether the organic material is proteinaceous, esteric or other.
- The assessment of peaks within the 3000-2850 cm^{-1} region is the starting point in identification studies.
- Weak peaks within the group frequency and fingerprint regions are encountered as diagnostic, especially in the identification of mortar mixtures of low organic concentration, where main organic peaks are masked by inorganic components.
- Position shifting of diagnostic peaks and changes in shape and intensity due to inorganic interference may also provide information relevant to the organic additive and its concentration in the mortar mixture.
- Not all peaks are referenced in the available literature: weak peaks are often overlooked or mentioned within a spectral range. Thus, identification studies

cannot solely depend on literature. The development of a database tailored according to the identification objectives and under standardized analysis protocol is crucial.

- Viscosity and mixing capacity of organic additives influence their projection in the mortar mixture spectrum.
- Specular distortions in a spectrum are indicative of materials of smooth texture and could provide indications of an organic compound within a mortar mixture.

The development of an easy-to-use chemical peak assignment database (CPAD) that includes both physical and chemical description of all the detected absorption peaks, was shown to successfully differentiate between differing organic additives over a range of concentrations within the mortar.

The filters introduced into the design of the CPAD enabled direct peak comparisons that could be used to assess the smallest position shifting of diagnostic peaks or the emergence of new ones (Appendix I, fig.3-37). The CPAD format essentially “describes” a spectrum, peak by peak, rather than providing solely graphic spectra.

Spectra comparisons through the CPAD can include more than two spectra without any obscuring visual effects as those observed in overlapping graphic spectra comparisons or on stacked spectra. CPAD comparisons allow the identification of a spectrum based on what should be expected and what is actually present in terms of peaks and their individual characteristics.

Chapter 8: CPAD applicability in identification of reflectance micro-FTIR spectra.

8.1 Experimental: Identification of unknown samples using the CPAD

The effectiveness of the CPAD for interpreting External Reflectance micro-FTIR spectra was tested by its use for identifying unknown organic additives in mortar mixtures and in pure form.

A range of spectra from the non-averaged spectra obtained from the standards, excluding the standards of $CaCO_3$ powder and quartz, was selected and re-labelled as unknown spectra by a third party to mask their identity (Ch.7, Tables 8 and 9, sect. 7.4). Since three spectra were obtained randomly from the surface of each standard, 138 spectra were available for identification. The unknown spectra would carry different x and y values from the averaged spectra entered in the CPAD, ensuring their differentiation from the averaged ones and eliminating the possibility of direct identification. The CPAD was then used to interpret these unknown spectra to identify the organic additive. The results were then cross-referenced to the identification list held by the third party.

The experiment was conducted four times (I-IV): each time a different set of 10 spectra of unknown chemical composition was subjected to identification. Each of the experimental sets I, II and III contained 9 spectra of organic additive/mortar mixtures and 1 spectrum of an organic in its pure form. All the 9 organic standards were represented in each experimental set either as a mixture or pure material.

Additional difficulty was added in the experimental set IV, by selecting spectra without the restriction above: the selected spectra could be duplicated, derived from the mortar standard or from the same organic additive or from mortar mixtures that contained the same additive but in different concentrations. This set reduced the bias of what was expected to be identified if each of the unknowns had contained a different additive and could not rely on the process of elimination.

The identification of the unknown spectra was carried out through the following steps:

1. The OriginPro 2015 *Quick Gadget Peak Finder* tool was used for locating the *x* and *y* parameters of absorption bands in the unknown spectra.
2. Inorganic presence was assessed by detecting diagnostic peaks assigned to $CaCO_3$ and quartz in order to conclude whether the unknown spectrum belonged to an organic material or an organic/mortar mixture.

3. Peaks of interest, likely diagnostic to an organic component, were inserted in the CPAD as "*ORG"* in the *"ID As"* entry.
4. Following the interpretation of standards (Ch.7), possible identifications were narrowed down to potential matching spectra of standards, by assessing organic presence within the 3000-2850 cm^{-1} group frequency region and determining the organic type (proteinaceous, esteric or other).
5. The presence, absence and combination of diagnostic peaks were examined through the CPAD by comparing the unknown spectrum with the potential matching spectra of standards.
6. Similarities in shape and intensity of the diagnostic peaks were taken into consideration, through the relevant CPAD entries and from the graphic spectrum.

The unknown spectra were compared through the CPAD with all the possible matching spectra of standards. For example, an unknown spectrum, narrowed down to an organic additive/mortar mixture and to a specific organic group, such as protein, would be compared to all mortar mixtures of 75, 50, 25 and 5% protein additive (bone glue and egg white).

8.1.1 Experimental set I – Results and discussion

Using the Chemical Peak Assignment Database (CPAD) and the identification methodology, the organic additive was correctly identified in all 10 unknown spectra (Table 11). The percentage composition of additive was correctly identified for 7 out of the 10 spectra. The identification process for the 3 misidentified spectra, UN_1, UN_6 and UN_9 is described below. For ease, the final comparisons are provided here, dealing mainly with the identification of the organic additive concentration.

The identification process of two more unknown spectra, UN_3 and UN_5 is also described in detail, because the similarities between them demonstrate the detailed assessment that is required to produce secure outcomes. The rest of the correctly identified spectra and their peaks of interest, compared to possible matching spectra of standards through the CPAD, are given in Appendix I (Experimental set I, Table 2 and fig.38-47).

Experimental Set I				
UN_Label	Spectrum ID	Positive Organic ID	Positive Concentration ID	Comments
UN_1	**A_M_25_3**	**YES**	**NO**	**Identified as 5% asphalt/mortar mixture**
UN_2	BG_M_50_1	YES	YES	
UN_3	R_M_5_1	YES	YES	
UN_4	O_M_25_2	YES	YES	
UN_5	Mi_M_5_2	YES	YES	
UN_6	**L_M_75_1**	**YES**	**NO**	**Identified as 50% lard/mortar mixture**
UN_7	EY_M_25_3	YES	YES	
UN_8	EW_M_50_1	YES	YES	
UN_9	**E_M_75_3**	**YES**	**NO**	**Identified as 50% egg/mortar mixture**
UN_10	E_2	YES	YES	

Table 11: Summary of Experimental set I identification outcomes.

The figures provided here, are CPAD filtered entries of “ORG” and “INORG” peaks of the unknown spectrum and the spectra of standards that appear as possible identification candidates. The peaks that are considered diagnostic to the unknown spectrum are compared to those of the standards. The comparisons are colour-coded as best matching and second-best matching according to table 12.

Blue	**Peaks of unknown spectrum**
Yellow	**Peaks of best matching standard spectrum**
Green	**Peaks of second-best matching standard spectrum**

Table 12: Colour-coding of peaks for the comparative assessment of the unknown spectrum (blue) with the best matching spectrum of standard (yellow) and the second-best matching (green).

Sample UN_I_1

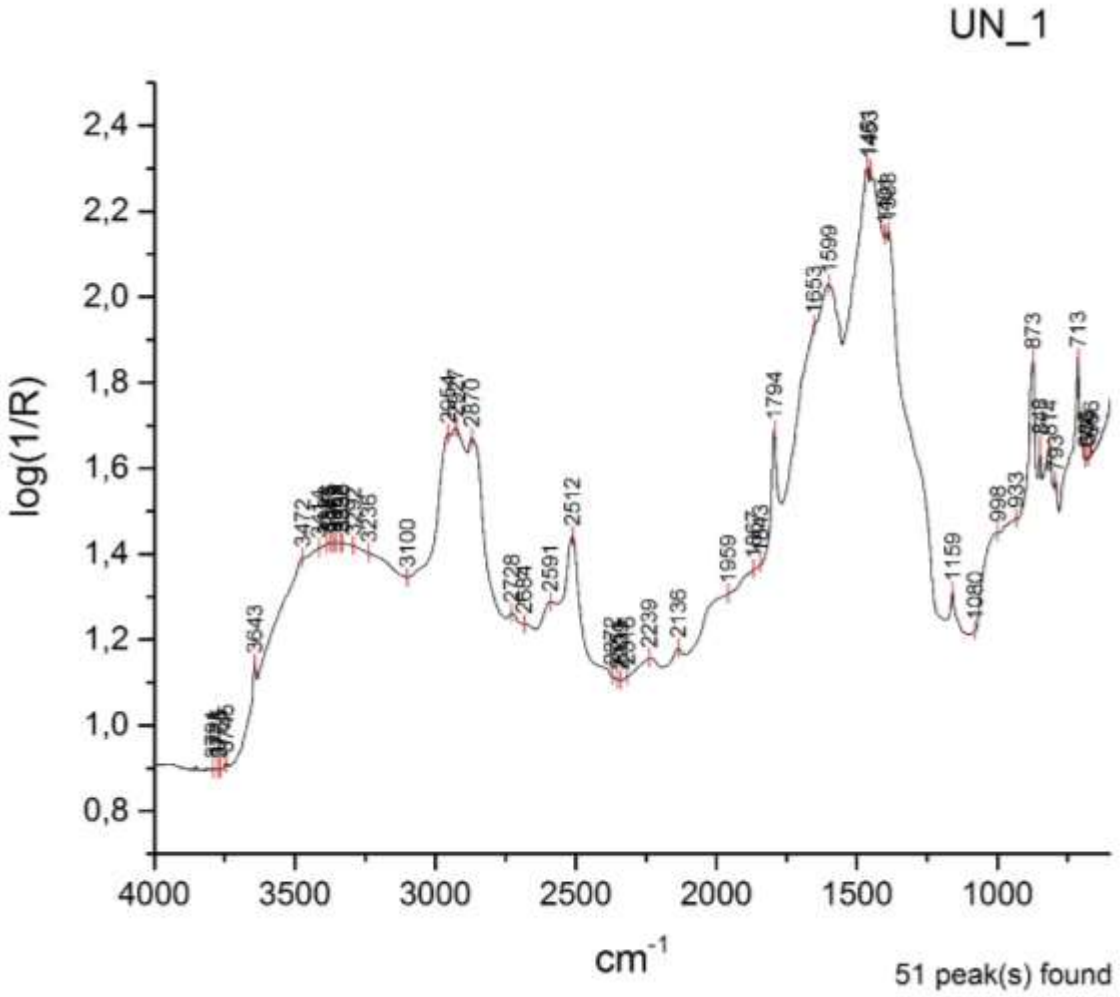

Figure 67: The unknown spectrum UN_I_1.

Spectrum UN_1_1 was correctly identified as being an asphalt/mortar mixture but incorrectly determined to be 5% concentration of asphalt. The true concentration of spectrum UN_I_1 is 25% asphalt additive in the mortar (fig.67). Mortar components are directly assigned to 1159, 1794, 2512 cm^{-1} peaks according to the spectral interpretation of standards (sect. 7.5). The characteristic shape of the CH_2 / CH_3 stretching at 2954-2870 cm^{-1} and the sharp peak at 2728 cm^{-1} show asphalt (Lombardi and Santarelli, 2009, 542).

Peak x (position)	Spectrum ID	Type of band	Chemical Band Assignement	Reference
814	A_M_25_av	triplet	asphalt	Spectrum A_av, Lombardi and Santarelli, 2009, 542
	A_M_5_av	triplet	asphalt	Spectrum A_av, Lombardi and Santarelli, 2009, 542
933	UN_1	(blank)	(blank)	(blank)
934	A_M_25_av	weak absorption	asphalt	Spectrum A_av
952	A_M_25_av	weak absorption	(blank)	(blank)
974	A_M_5_av	weak absorption	asphalt	Spectrum A_av
975	A_M_25_av	weak absorption	asphalt	Spectrum A_av
1017	A_M_25_av	weak absorption	(blank)	(blank)
1385	A_M_25_av	strong absorption	CH2, CH3 stretching	Spectrum A_av, Lombardi and Santarelli, 2009, 542
1386	A_M_5_av	strong absorption	CH2, CH3 stretching	Spectrum A_av, Lombardi and Santarelli, 2009, 542
1453	UN_1	(blank)	(blank)	(blank)
1461	A_M_25_av	strong absorption	asphalt	Spectrum A_av
	UN_1	(blank)	(blank)	(blank)
1462	A_M_5_av	strong absorption	asphalt	Spectrum A_av
1599	A_M_5_av	strong absorption	C6H6 (benzene rings)	Spectrum A_av, Lombardi and Santarelli, 2009, 542
	UN_1	(blank)	(blank)	(blank)
1600	A_M_25_av	strong absorption	C6H6 (benzene rings)	Spectrum A_av, Lombardi and Santarelli, 2009, 542
1642	A_M_25_av	shoulder	asphalt	Spectrum A_av
1652	A_M_5_av	shoulder	asphalt	Spectrum A_av
1653	UN_1	(blank)	(blank)	(blank)
2727	A_M_5_av	weak absorption	asphalt	Spectrum A_av
2728	A_M_25_av	weak absorption	asphalt	Spectrum A_av
	UN_1	(blank)	(blank)	(blank)
2868	A_M_25_av	strong absorption	CH2, CH3 stretching	Spectrum A_av, Lombardi and Santarelli, 2009, 542
2870	A_M_5_av	strong absorption	CH2, CH3 stretching	Spectrum A_av, Lombardi and Santarelli, 2009, 542
	UN_1	(blank)	(blank)	(blank)
2927	UN_1	(blank)	(blank)	(blank)
2928	A_M_5_av	strong absorption	CH2, CH3 stretching	Spectrum A_av, Lombardi and Santarelli, 2009, 542
2929	A_M_25_av	strong absorption	CH2, CH3 stretching	Spectrum A_av, Lombardi and Santarelli, 2009, 542
2953	A_M_25_av	strong absorption	CH2, CH3 stretching	Spectrum A_av, Lombardi and Santarelli, 2009, 542
2954	A_M_5_av	strong absorption	CH2, CH3 stretching	Spectrum A_av, Lombardi and Santarelli, 2009, 542
	UN_1	(blank)	(blank)	(blank)
3451	A_M_5_av	weak absorption	(blank)	(blank)
3467	A_M_5_av	weak absorption	asphalt	Spectrum A_av
3472	A_M_25_av	weak absorption	asphalt	Spectrum A_av
	UN_1	(blank)	(blank)	(blank)
3572	A_M_5_av	weak absorption	(blank)	(blank)

Figure 68: Filtered CPAD of peaks of interest for UN_I_1 spectrum and possible matches.

The peaks of interest for asphalt, as they were defined from the spectral interpretation of standards, are highlighted in blue (fig.68). Five peaks of the 25% asphalt/mortar mixture (A_M_25, yellow) match the unknown spectrum and the same stands for the 5% asphalt/mortar mixture (A_M_5, green), making the selection of the best matching spectrum of standard difficult. However, a second assessment of figure 68 shows that the false identification could have been avoided if the weak peak at 933 cm^{-1} was encountered as diagnostic, since this peak is observed only in the unknown spectrum and the 25% asphalt/mortar mixture.

Sample UN_I_3

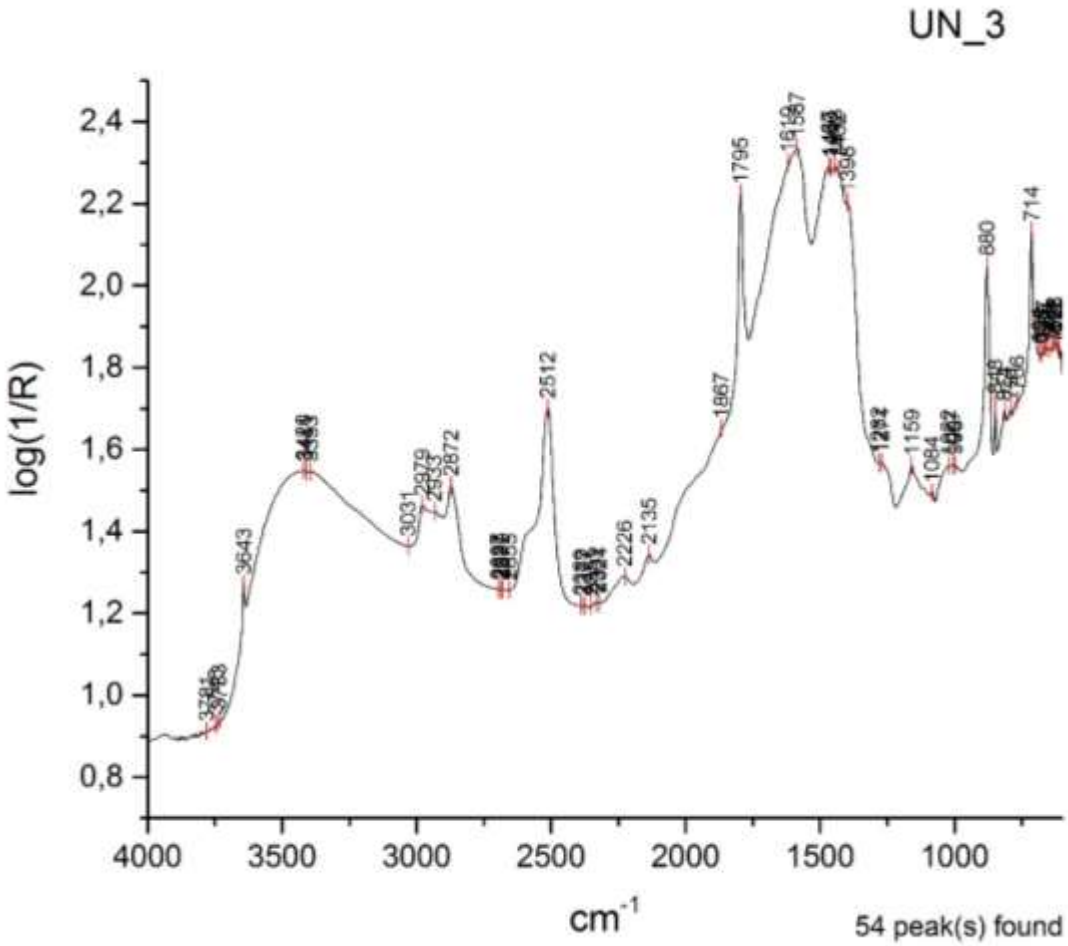

Figure 69: The unknown spectrum UN_I_3.

The true identity of spectrum UN_I_3 is 5% of rice additive in mortar and it was correctly identified (fig.69). However, the spectrum appears highly similar to the spectrum UN_I_5 identified as 5% milk additive in mortar due to the interference from high level of inorganic presence in both spectra (fig.71). The comparison of possible matches through

the CPAD shows the difficulty of discriminating between different organic additives in mortar matrices when these are present in low concentrations (fig.70).

The parameters that lead to the correct identification of UN_I_3 (blue) as 5% rice/mortar mixture (R_M_5_av, yellow) are:

1. The identical presence of 1587 and 2933 cm^{-1} between the two spectra.
2. The absence of amide and ester peaks within the 1750-1398 cm^{-1} region that should be detected on the unknown spectrum if milk was present.
3. The presence of weak peaks within 2697-2655 cm^{-1} diagnostic to rice/mortar mixtures.

The presence of sugars below 1022 cm^{-1} were not helpful since they could belong to either rice or milk additives (Fang et al., 2013, 6). Inorganic peaks were important in the identification process since they carried information of interference with the specific organic additive.

Peak x (position)	Spectrum ID	Type of band	Chemical Band Assignement	Reference
611	Mi_M_5_av	weak absorption	CaCO3	Spectrum M_av, spectrum Ca_av
622	Mi_M_5_av	weak absorption	CaCO3	Spectrum M_av, spectrum Ca_av
624	R_M_5_av	weak absorption	rice	Spectrum R_av
632	Mi_M_5_av	weak absorption	CaCO3	Spectrum M_av, spectrum Ca_av
642	R_M_5_av	weak absorption	rice	Spectrum R_av
648	Mi_M_5_av	weak absorption	CaCO3	Spectrum M_av, spectrum Ca_av
649	R_M_5_av	weak absorption	rice	Spectrum R_av
668	R_M_5_av	weak absorption	rice	Spectrum R_av
714	R_M_5_av	sharp absorption	v4 carbonate ion	Spectrum M_av, spectrum Ca_av, Ylmen and Jaglid, 2013, p. 119
	Mi_M_5_av	sharp absorption	v4 carbonate ion	Spectrum M_av, spectrum Ca_av, Ylmen and Jaglid, 2013, p. 119
791	Mi_M_5_av	sharp absorption	quartz	Spectrum M_av, spectrum Q_av
792	R_M_5_av	sharp absorption	quartz	Spectrum M_av, spectrum Q_av
815	R_M_5_av	sharp absorption	quartz	Spectrum M_av, spectrum Q_av
816	Mi_M_5_av	sharp absorption	quartz	Spectrum M_av, spectrum Q_av
848	R_M_5_av	sharp and weak absorption	v2 carbonate ion	Spectrum M_av, spectrum Ca_av, Ylmen and Jaglid, 2013, p. 119
	Mi_M_5_av	weak absorption	v2 carbonate ion	Spectrum M_av, spectrum Ca_av, Ylmen and Jaglid, 2013, p. 119
880	R_M_5_av	sharp absorption	v2 carbonate ion	Spectrum M_av, spectrum Ca_av, Ylmen and Jaglid, 2013, p. 119
881	Mi_M_5_av	sharp absorption	v2 carbonate ion	Spectrum M_av, spectrum Ca_av, Ylmen and Jaglid, 2013, p. 119
990	Mi_M_5_av	weak absorption	sugar region	Spectrum Mi_av, Synytsya and Novak, 2014, p. 6
1007	UN_3	(blank)	(blank)	(blank)
1016	Mi_M_5_av	weak absorption	CaCO3	spectrum Ca_av
1080	R_M_5_av	sharp and weak absorption	v1 carbonate ion	Spectrum M_av, spectrum Ca_av, Ylmen and Jaglid, 2013, p. 119
1082	Mi_M_5_av	weak absorption	v1 carbonate ion	Spectrum Ca_av, Ylmen and Jaglid, 2013, p. 119
1084	UN_3	(blank)	(blank)	(blank)
1091	Mi_M_5_av	weak absorption	v1 carbonate ion	Spectrum Ca_av, Ylmen and Jaglid, 2013, p. 119
1159	R_M_5_av	sharp absorption	quartz	Spectrum M_av, spectrum Q_av
	Mi_M_5_av	sharp absorption	quartz	Spectrum M_av, spectrum Q_av
1282	UN_3	(blank)	(blank)	(blank)
1396	Mi_M_5_av	strong absorption	CaCO3	Spectrum M_av, spectrum Ca_av
1398	R_M_5_av	strong absorption	CaCO3	Spectrum M_av, spectrum Ca_av
1432	R_M_5_av	strong absorption	v3 antisymmetric stretching CO3-2	Spectrum M_av, spectrum Ca_av, Ylmen and Jaglid, 2013, p. 119
	Mi_M_5_av	strong absorption	v3 antisymmetric stretching CO3-2	Spectrum Ca_av, Ylmen and Jaglid, 2013, p. 119
	UN_3	(blank)	(blank)	(blank)
1440	Mi_M_5_av	strong absorption	v3 antisymmetric stretching CO3-2	Spectrum Ca_av, Ylmen and Jaglid, 2013, p. 119
1443	R_M_5_av	strong absorption	v3 antisymmetric stretching CO3-2	Spectrum M_av, spectrum Ca_av, Ylmen and Jaglid, 2013, p. 119
1449	Mi_M_5_av	strong absorption	v3 antisymmetric stretching CO3-2	Spectrum Ca_av, Ylmen and Jaglid, 2013, p. 119
1460	R_M_5_av	strong absorption	v3 antisymmetric stretching CO3-2	Spectrum M_av, spectrum Ca_av, Ylmen and Jaglid, 2013, p. 119
1467	Mi_M_5_av	strong absorption	v3 antisymmetric stretching CO3-2	Spectrum Ca_av, Ylmen and Jaglid, 2013, p. 119

Figure 70: Filtered CPAD of peaks of interest for UN_I_3 spectrum and possible matches.

1476	**Mi_M_5_av**	strong absorption	**Amide III**	Spectrum Mi_av, Rosi et al, 2009, p. 2099
1584	**Mi_M_5_av**	strong absorption	**v3 antisymmetric stretching CO3-2**	Spectrum Ca_av, Ylmen and Jaglid, 2013, p. 119
1587	**R_M_5_av**	strong absorption	**v3 antisymmetric stretching CO3-2**	Spectrum Ca_av, Ylmen and Jaglid, 2013, p. 119
	UN_3	(blank)	**(blank)**	(blank)
1596	**R_M_5_av**	strong absorption	**quartz**	Spectrum M_av, spectrum Q_av
1602	**Mi_M_5_av**	strong absorption	**quartz**	Spectrum M_av, spectrum Q_av
1612	**Mi_M_5_av**	strong absorption	**quartz**	Spectrum M_av, spectrum Q_av
1619	**UN_3**	(blank)	**(blank)**	(blank)
1652	**Mi_M_5_av**	strong absorption	**quartz**	Spectrum M_av, spectrum Q_av
1795	**R_M_5_av**	combination band	**v1+v4**	Spectrum M_av, spectrum Ca_av, Ricci et al, 2006, p. 1222
	Mi_M_5_av	combination band	**v1+v4**	Spectrum M_av, spectrum Ca_av, Ricci et al, 2006, p. 1222
1844	**Mi_M_5_av**	weak absorption	**quartz**	Spectrum M_av, spectrum Q_av
1855	**Mi_M_5_av**	weak absorption	**quartz**	Spectrum M_av, spectrum Q_av
1856	**R_M_5_av**	weak absorption	**quartz**	Spectrum M_av, spectrum Q_av
1868	**R_M_5_av**	weak absorption	**quartz**	Spectrum M_av, spectrum Q_av
1942	**Mi_M_5_av**	weak absorption	**quartz**	Spectrum M_av, spectrum Q_av
1961	**R_M_5_av**	weak absorption	**quartz**	Spectrum M_av, spectrum Q_av
1966	**Mi_M_5_av**	weak absorption	**quartz**	Spectrum M_av, spectrum Q_av
2135	**R_M_5_av**	weak absorption	**calcium carbonate and quartz**	Spectrum Ca_av, spectrum M_av, spectrum Q_av
	Mi_M_5_av	weak absorption	**calcium carbonate and quartz**	Spectrum Ca_av, spectrum M_av, spectrum Q_av
2237	**R_M_5_av**	weak absorption	**quartz**	spectrum Q_av
	Mi_M_5_av	weak absorption	**quartz**	spectrum Q_av
2511	**Mi_M_5_av**	combination band	**v1+v3**	Spectrum M_av, spectrum Ca_av, Ricci et al, 2006, p. 1222
2512	**R_M_5_av**	combination band	**v1+v3**	Spectrum M_av, spectrum Ca_av, Ricci et al, 2006, p. 1222
2670	**R_M_5_av**	weak absorption	**(blank)**	(blank)
2680	**R_M_5_av**	weak absorption	**(blank)**	(blank)
2688	**Mi_M_5_av**	weak absorption	**(blank)**	(blank)
2692	**R_M_5_av**	weak absorption	**(blank)**	(blank)
2697	**UN_3**	(blank)	**(blank)**	(blank)
2699	**Mi_M_5_av**	weak absorption	**(blank)**	(blank)
2719	**R_M_5_av**	weak absorption	**rice**	Spectrum R_av
2872	**Mi_M_5_av**	sharp and weak absorption	**CaCO3**	Spectrum Ca_av, spectrum M_av
2873	**R_M_5_av**	sharp and weak absorption	**CaCO3**	Spectrum Ca_av, spectrum M_av
2926	**Mi_M_5_av**	strong absorption	**CH stretching**	Spectrum Mi_av, Daher et al, 2017, p.8
2933	**R_M_5_av**	strong absorption	**CH stretching**	Daher et al, 2017, p.8
	UN_3	(blank)	**(blank)**	(blank)
2958	**Mi_M_5_av**	sharp absorption	**CH2 stretching**	Ploeger et al, 2010, p. 37
2979	**R_M_5_av**	strong absorption	**CaCO3**	Spectrum Ca_av, spectrum M_av
3031	**UN_3**	(blank)	**(blank)**	(blank)
3643	**R_M_5_av**	doublet	**OH stretching**	Spectrum M_av, spectrum Ca_av, Rosi et al, 2009, p. 2100
	Mi_M_5_av	doublet	**OH stretching**	Spectrum M_av, spectrum Ca_av, Rosi et al, 2009, p. 2100

Figure 70: continued.

Sample UN_I_5

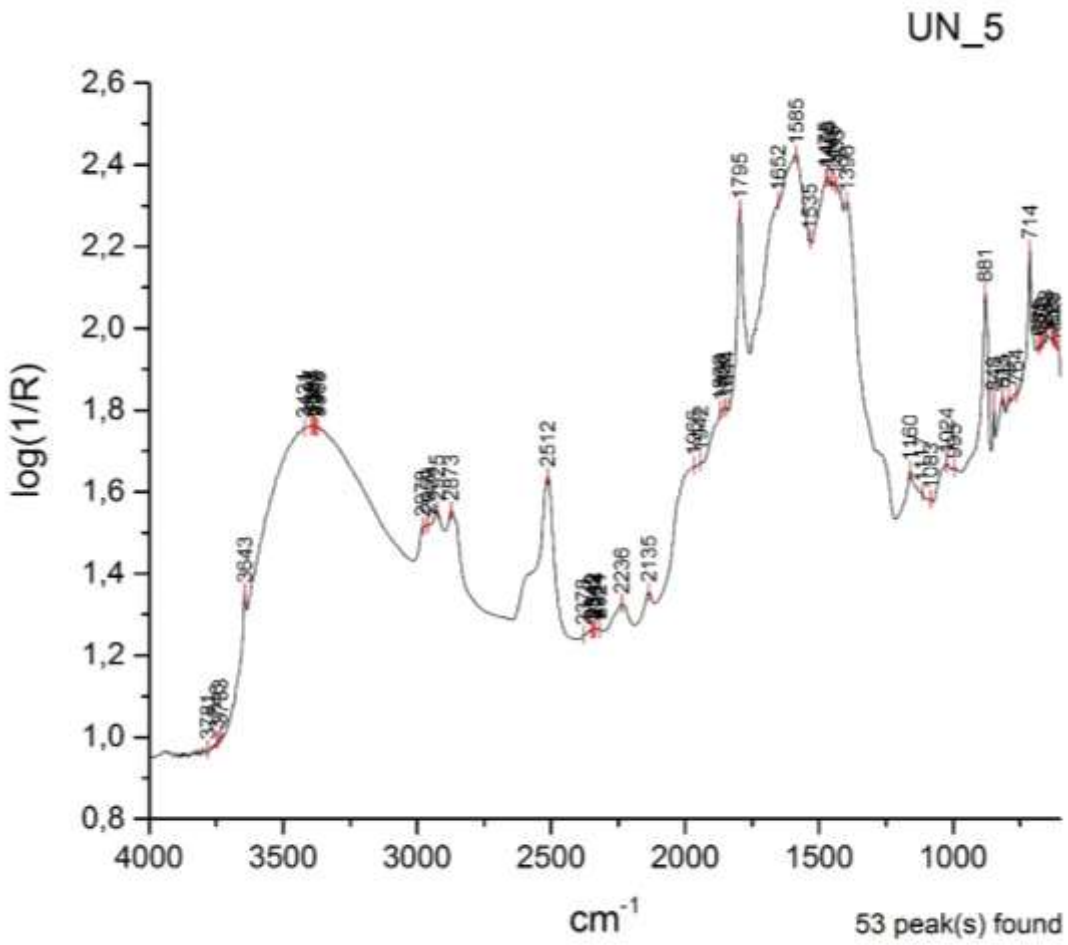

Figure 71: The unknown spectrum UN_I_5.

Since the UN_I_5 spectrum is visually similar to UN_I_3, the risk of false identification would be high if the only criterion for identification was spectra similarity with closely matching standards through visual comparisons (fig.71). The risk was eliminated through the use of CPAD, which correctly identified it as 5% milk additive in mortar (fig.72). The presence of the two weak ester CH peaks at 2959 and 2925 cm^{-1} (Daher et al., 2017, 8), the amide peaks at 1652 cm^{-1} and 1475 cm^{-1} and the sugar matching at 995 cm^{-1} show coexistence of amides, esters and sugars that could only be assigned to milk.

Peak x (position)	Spectrum ID	Type of band	Chemical Band Assignement	Reference
611	Mi_M_5_av	weak absorption	CaCO3	Spectrum M_av, spectrum Ca_av
622	Mi_M_5_av	weak absorption	CaCO3	Spectrum M_av, spectrum Ca_av
624	R_M_5_av	weak absorption	rice	Spectrum R_av
632	Mi_M_5_av	weak absorption	CaCO3	Spectrum M_av, spectrum Ca_av
642	R_M_5_av	weak absorption	rice	Spectrum R_av
648	Mi_M_5_av	weak absorption	CaCO3	Spectrum M_av, spectrum Ca_av
649	R_M_5_av	weak absorption	rice	Spectrum R_av
668	R_M_5_av	weak absorption	rice	Spectrum R_av
714	R_M_5_av	sharp absorption	v4 carbonate ion	Spectrum M_av, spectrum Ca_av, Ylmen and Jaglid, 2013, p. 119
	Mi_M_5_av	sharp absorption	v4 carbonate ion	Spectrum M_av, spectrum Ca_av, Ylmen and Jaglid, 2013, p. 119
791	Mi_M_5_av	sharp absorption	quartz	Spectrum M_av, spectrum Q_av
792	R_M_5_av	sharp absorption	quartz	Spectrum M_av, spectrum Q_av
815	R_M_5_av	sharp absorption	quartz	Spectrum M_av, spectrum Q_av
816	Mi_M_5_av	sharp absorption	quartz	Spectrum M_av, spectrum Q_av
848	R_M_5_av	sharp and weak absorption	v2 carbonate ion	Spectrum M_av, spectrum Ca_av, Ylmen and Jaglid, 2013, p. 119
	Mi_M_5_av	weak absorption	v2 carbonate ion	Spectrum M_av, spectrum Ca_av, Ylmen and Jaglid, 2013, p. 119
880	R_M_5_av	sharp absorption	v2 carbonate ion	Spectrum M_av, spectrum Ca_av, Ylmen and Jaglid, 2013, p. 119
881	Mi_M_5_av	sharp absorption	v2 carbonate ion	Spectrum M_av, spectrum Ca_av, Ylmen and Jaglid, 2013, p. 119
990	Mi_M_5_av	weak absorption	sugar region	Spectrum Mi_av, Synytsya and Novak, 2014, p. 6
995	UN_5	(blank)	(blank)	(blank)
1016	Mi_M_5_av	weak absorption	CaCO3	spectrum Ca_av
1024	UN_5	(blank)	(blank)	(blank)
1080	R_M_5_av	sharp and weak absorption	v1 carbonate ion	Spectrum M_av, spectrum Ca_av, Ylmen and Jaglid, 2013, p. 119
1082	Mi_M_5_av	weak absorption	v1 carbonate ion	Spectrum Ca_av, Ylmen and Jaglid, 2013, p. 119
1083	UN_5	(blank)	(blank)	(blank)
1091	Mi_M_5_av	weak absorption	v1 carbonate ion	Spectrum Ca_av, Ylmen and Jaglid, 2013, p. 119
1159	R_M_5_av	sharp absorption	quartz	Spectrum M_av, spectrum Q_av
	Mi_M_5_av	sharp absorption	quartz	Spectrum M_av, spectrum Q_av
1396	Mi_M_5_av	strong absorption	CaCO3	Spectrum M_av, spectrum Ca_av
	UN_5	(blank)	(blank)	(blank)
1398	R_M_5_av	strong absorption	CaCO3	Spectrum M_av, spectrum Ca_av
1432	R_M_5_av	strong absorption	v3 antisymmetric stretching CO3-2	Spectrum M_av, spectrum Ca_av, Ylmen and Jaglid, 2013, p. 119
	Mi_M_5_av	strong absorption	v3 antisymmetric stretching CO3-2	Spectrum Ca_av, Ylmen and Jaglid, 2013, p. 119
1440	Mi_M_5_av	strong absorption	v3 antisymmetric stretching CO3-2	Spectrum Ca_av, Ylmen and Jaglid, 2013, p. 119
1443	R_M_5_av	strong absorption	v3 antisymmetric stretching CO3-2	Spectrum M_av, spectrum Ca_av, Ylmen and Jaglid, 2013, p. 119
1449	Mi_M_5_av	strong absorption	v3 antisymmetric stretching CO3-2	Spectrum Ca_av, Ylmen and Jaglid, 2013, p. 119
1460	R_M_5_av	strong absorption	v3 antisymmetric stretching CO3-2	Spectrum M_av, spectrum Ca_av, Ylmen and Jaglid, 2013, p. 119
1467	Mi_M_5_av	strong absorption	v3 antisymmetric stretching CO3-2	Spectrum Ca_av, Ylmen and Jaglid, 2013, p. 119

Figure 72: Filtered CPAD of peaks of interest for UN_I_5 spectrum (blue) and possible matches (yellow=best matching spectrum, green=second-best match).

1475	**UN_5**	(blank)	**(blank)**	(blank)
1476	**Mi_M_5_av**	strong absorption	**Amide III**	Spectrum Mi_av, Rosi et al, 2009, p. 2099
1535	**UN_5**	(blank)	**(blank)**	(blank)
1584	**Mi_M_5_av**	strong absorption	**v3 antisymmetric stretching CO3-2**	Spectrum Ca_av, Ylmen and Jaglid, 2013, p. 119
1585	**UN_5**	(blank)	**(blank)**	(blank)
1587	**R_M_5_av**	strong absorption	**v3 antisymmetric stretching CO3-2**	Spectrum Ca_av, Ylmen and Jaglid, 2013, p. 119
1596	**R_M_5_av**	strong absorption	**quartz**	Spectrum M_av, spectrum Q_av
1602	**Mi_M_5_av**	strong absorption	**quartz**	Spectrum M_av, spectrum Q_av
1612	**Mi_M_5_av**	strong absorption	**quartz**	Spectrum M_av, spectrum Q_av
1652	**Mi_M_5_av**	strong absorption	**quartz**	Spectrum M_av, spectrum Q_av
	UN_5	(blank)	**(blank)**	(blank)
1795	**R_M_5_av**	combination band	**v1+v4**	Spectrum M_av, spectrum Ca_av, Ricci et al, 2006, p. 1222
	Mi_M_5_av	combination band	**v1+v4**	Spectrum M_av, spectrum Ca_av, Ricci et al, 2006, p. 1222
1844	**Mi_M_5_av**	weak absorption	**quartz**	Spectrum M_av, spectrum Q_av
1855	**Mi_M_5_av**	weak absorption	**quartz**	Spectrum M_av, spectrum Q_av
1856	**R_M_5_av**	weak absorption	**quartz**	Spectrum M_av, spectrum Q_av
1868	**R_M_5_av**	weak absorption	**quartz**	Spectrum M_av, spectrum Q_av
1942	**Mi_M_5_av**	weak absorption	**quartz**	Spectrum M_av, spectrum Q_av
1961	**R_M_5_av**	weak absorption	**quartz**	Spectrum M_av, spectrum Q_av
1966	**Mi_M_5_av**	weak absorption	**quartz**	Spectrum M_av, spectrum Q_av
2135	**R_M_5_av**	weak absorption	**calcium carbonate and quartz**	Spectrum Ca_av, spectrum M_av, spectrum Q_av
	Mi_M_5_av	weak absorption	**calcium carbonate and quartz**	Spectrum Ca_av, spectrum M_av, spectrum Q_av
2237	**R_M_5_av**	weak absorption	**quartz**	spectrum Q_av
	Mi_M_5_av	weak absorption	**quartz**	spectrum Q_av
2511	**Mi_M_5_av**	combination band	**v1+v3**	Spectrum M_av, spectrum Ca_av, Ricci et al, 2006, p. 1222
2512	**R_M_5_av**	combination band	**v1+v3**	Spectrum M_av, spectrum Ca_av, Ricci et al, 2006, p. 1222
2670	**R_M_5_av**	weak absorption	**(blank)**	(blank)
2680	**R_M_5_av**	weak absorption	**(blank)**	(blank)
2688	**Mi_M_5_av**	weak absorption	**(blank)**	(blank)
2692	**R_M_5_av**	weak absorption	**(blank)**	(blank)
2699	**Mi_M_5_av**	weak absorption	**(blank)**	(blank)
2719	**R_M_5_av**	weak absorption	**rice**	Spectrum R_av
2872	**Mi_M_5_av**	sharp and weak absorption	**CaCO3**	Spectrum Ca_av, spectrum M_av
2873	**R_M_5_av**	sharp and weak absorption	**CaCO3**	Spectrum Ca_av, spectrum M_av
2925	**UN_5**	(blank)	**(blank)**	(blank)
2926	**Mi_M_5_av**	strong absorption	**CH stretching**	Spectrum Mi_av, Daher et al, 2017, p.8
2933	**R_M_5_av**	strong absorption	**CH stretching**	Daher et al, 2017, p.8
2958	**Mi_M_5_av**	sharp absorption	**CH2 stretching**	Ploeger et al, 2010, p. 37
2959	**UN_5**	(blank)	**(blank)**	(blank)
2979	**R_M_5_av**	strong absorption	**CaCO3**	Spectrum Ca_av, spectrum M_av
3643	**R_M_5_av**	doublet	**OH stretching**	Spectrum M_av, spectrum Ca_av, Rosi et al, 2009, p. 2100
	Mi_M_5_av	doublet	**OH stretching**	Spectrum M_av, spectrum Ca_av, Rosi et al, 2009, p. 2100

Figure 72: continued.

Sample UN_I_6

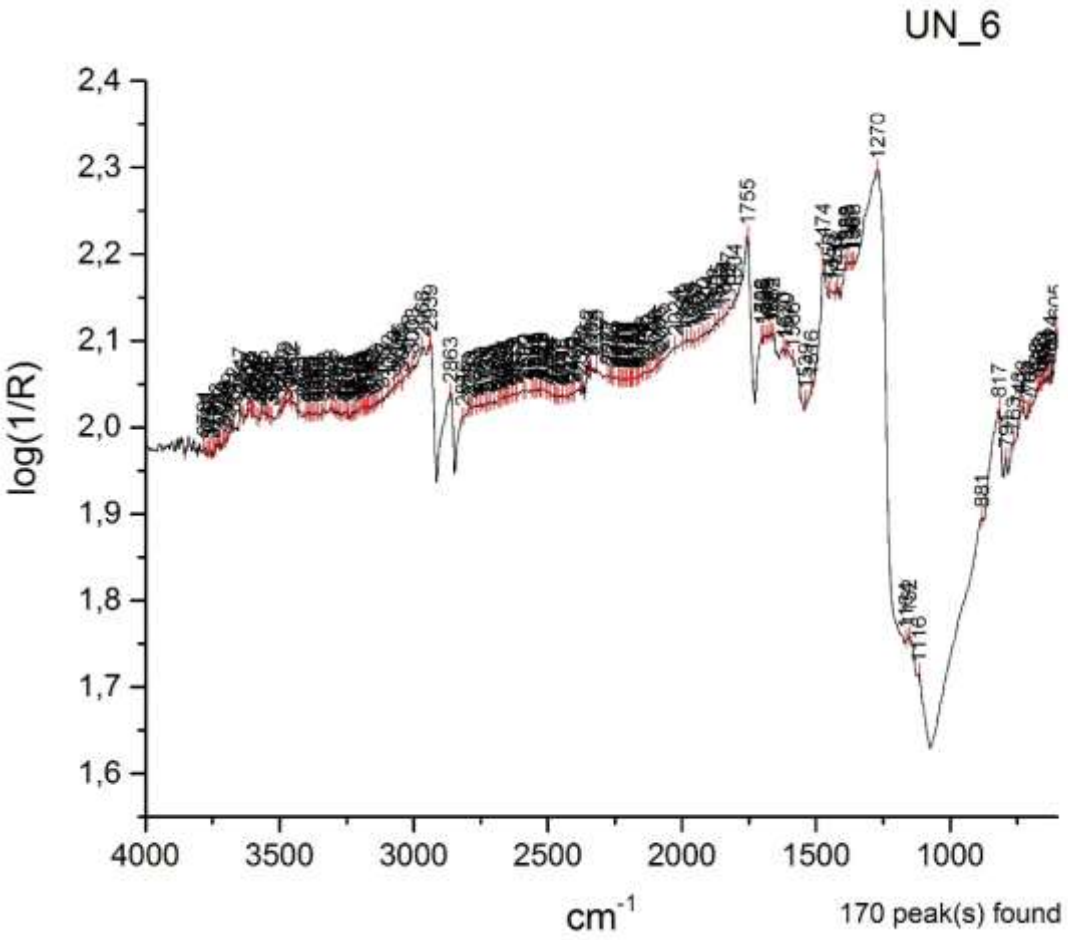

Figure 73: The unknown spectrum UN_I_6.

The spectrum UN_I_6 was correctly identified as having lard as the organic additive in the mortar mixture but this was incorrectly identified as being 50% concentration (fig.73). Its true concentration is 75% lard additive in mortar. The presence of diagnostic lipid peaks, as defined in section 7.5.5, and the absence of proteins and/or sugars narrowed down the potential matches to lard/mortar mixtures. Inorganic presence is indicated at 1152 and 817 cm^{-1}, showing that the mixture contains high amount of organic additive. This illustrates the problem of determining proportion of additive, although such high concentrations of lard are not expected to occur archaeologically or historically.

The diagnostic peaks of the spectrum of 75% of lard additive in mortar (L_M_75_av, yellow) and 50% of lard additive in mortar (L_M_50_av, green) share similar wavenumbers (fig.74). The false identification could have been avoided if the peaks in group frequency region 3018-2968 cm^{-1} were better considered since they provide absolute match to the unknown spectrum (blue).

Peak x (position)	Spectrum ID	Type of band	Chemical Band Assignement	Reference
700	L_M_75_av	weak absorption	lard	Spectrum Q_av, spectrum M_av, spectrum L_av
725	L_M_75_av	sharp absorption	lard	Spectrum L_av
734	L_M_50_av	sharp absorption	lard	Spectrum L_av
1115	L_M_75_av	sharp absorption	lard	Spectrum L_av
1117	L_M_50_av	sharp and weak absorption	lard	Spectrum L_av
1184	L_M_50_av	weak absorption	v(C-O) stretching	Spectrum L_av, Ricci et al, 2006, p. 1224
1197	L_M_75_av	weak absorption	v(C-O) stretching	Spectrum L_av, Ricci et al, 2006, p. 1224
1199	L_M_50_av	weak absorption	lard	(blank)
1270	UN_6	(blank)	(blank)	(blank)
1273	L_M_50_av	strong absorption	C-O	Spectrum L_av, Ploeger et al, 2010, p. 37
1279	L_M_75_av	strong absorption	C-O	Spectrum L_av, Ploeger et al, 2010, p. 37
1289	L_M_75_av	strong absorption	C-O	Spectrum L_av, Ploeger et al, 2010, p. 37
1381	L_M_75_av	sharp and weak absorption	C-H bending	Spectrum L_av, Buti et al, 2013, p. 2705
1384	L_M_50_av	sharp and weak absorption	C-H bending	Spectrum L_av, Buti et al, 2013, p. 2705
1388	UN_6	(blank)	(blank)	(blank)
1389	L_M_75_av	sharp and weak absorption	C-H bending	Spectrum L_av, Buti et al, 2013, p. 2705
1418	UN_6	(blank)	(blank)	(blank)
1421	L_M_75_av	weak absorption	(blank)	Spectrum L_av
	L_M_50_av	weak absorption	lard	Spectrum L_av
1446	L_M_75_av	weak absorption	(blank)	Spectrum L_av
1447	L_M_50_av	weak absorption	lard	Spectrum L_av
1450	UN_6	(blank)	(blank)	(blank)
1474	L_M_75_av	strong absorption	C-O bending	Spectrum L_av, Ricci et al, 2006, p. 1224
	L_M_50_av	sharp absorption	C-O bending	Spectrum L_av, Ricci et al, 2006, p. 1224
	UN_6	(blank)	(blank)	(blank)
1610	UN_6	(blank)	(blank)	(blank)
1662	L_M_75_av	weak absorption	(blank)	Spectrum L_av, spectrum M_av, Spectrum Q_av
	UN_6	(blank)	(blank)	(blank)
1669	L_M_75_av	weak absorption	(blank)	Spectrum L_av, spectrum M_av, Spectrum Q_av
1679	L_M_75_av	weak absorption	(blank)	Spectrum L_av, spectrum M_av, Spectrum Q_av
1683	UN_6	(blank)	(blank)	(blank)
1696	UN_6	(blank)	(blank)	(blank)
1755	UN_6	(blank)	(blank)	(blank)
1756	L_M_75_av	1st order derivative	C=O stretching band	Spectrum L_av, Mazzeo et al, 2008, p. 69
	L_M_50_av	1st order derivative	C=O stretching band	Spectrum L_av, Mazzeo et al, 2008, p. 69
2862	L_M_75_av	strong absorption	CH2 stretching	Spectrum L_av, Ploeger et al, 2010, p. 37
	L_M_50_av	strong absorption	CH2 stretching	Spectrum L_av, Ploeger et al, 2010, p. 37
2863	UN_6	(blank)	(blank)	(blank)
2939	L_M_50_av	strong absorption	CH2 stretching	Spectrum L_av, Ploeger et al, 2010, p. 37
	UN_6	(blank)	(blank)	(blank)
2940	L_M_75_av	sharp absorption	CH2 stretching	Spectrum L_av, Ploeger et al, 2010, p. 37
2965	L_M_50_av	strong absorption	CH2 stretching	Spectrum L_av, Ploeger et al, 2010, p. 37
2968	L_M_75_av	sharp absorption	CH2 stretching	Spectrum L_av, Ploeger et al, 2010, p. 37
	UN_6	(blank)	(blank)	(blank)
3003	L_M_75_av	weak absorption	CH stretching	Spectrum L_av, Miliani et al, 2012, p. 302
	UN_6	(blank)	(blank)	(blank)
3014	L_M_50_av	weak absorption	lard	Spectrum L_av
3018	L_M_75_av	weak absorption	CH stretching	Spectrum L_av, Miliani et al, 2012, p. 302
	UN_6	(blank)	(blank)	(blank)
3448	L_M_50_av	weak absorption	lard	Spectrum L_av
3452	L_M_75_av	weak absorption	lard	Spectrum L_av
3461	L_M_75_av	weak absorption	lard	Spectrum L_av
3468	L_M_50_av	weak absorption	lard	Spectrum L_av
3480	L_M_75_av	weak absorption	lard	Spectrum L_av
3483	L_M_50_av	weak absorption	lard	Spectrum L_av

Figure 74: Filtered CPAD of peaks of interest for UN_I_6 spectrum and possible matches.

Sample UN_I_9

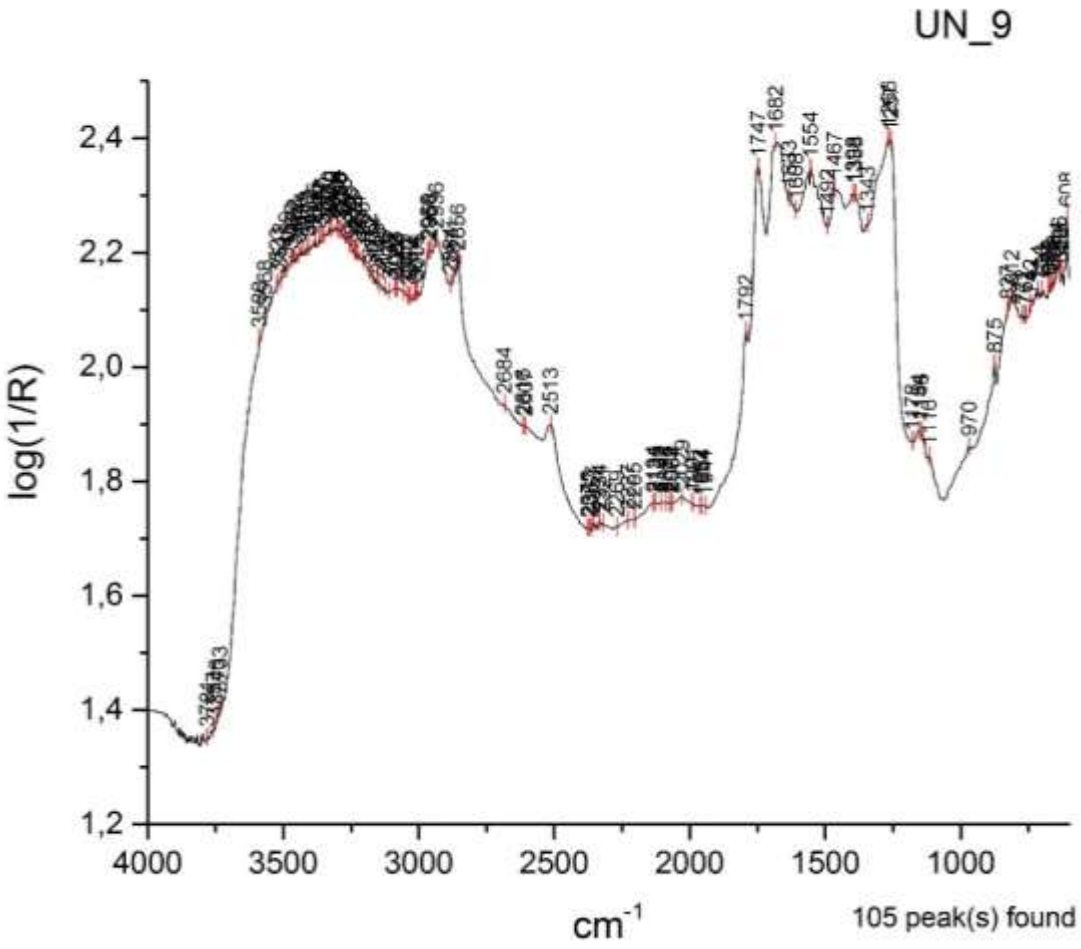

Figure 75: The unknown spectrum UN_I_9.

The combined presence of proteins and phospholipids correctly indicated the presence of egg in the mortar mixture (fig.75). The weak inorganic peaks suggest that the concentration of the organic additive in the mixture was high and this was 75% of egg additive in the mortar mixture rather than the 50% identified using the CPAD methodology. The filtered CPAD illustrates the difficulty identifying concentration, since both the 75% and 50% egg/mortar mixtures spectra share peaks equally with the unknown spectrum (fig.76). The fact that phospholipids are visible in the 50% egg/mortar spectrum made it the best candidate and misidentification could not have been avoided. However, the CPAD clearly identifies the egg additive.

Peak x (position)	Spectrum ID	Type of band	Chemical Band Assignement	Reference
660	E_M_50_av	weak absorption	(blank)	Spectrum E_av, Spectrum EW_av, spectrum EY_av
666	E_M_5_av	weak absorption	whole egg	Spectrum E_av
668	E_M_75_av	weak absorption	(blank)	Spectrum E_av, Spectrum EW_av, spectrum EY_av
715	E_M_25_av	doublet	in-plane rotation of linear long C chains δ(CH2)n	Spectrun E_av, Iwanicka et al, 2017, p. 18
729	E_M_25_av	doublet	in-plane rotation of linear long C chains δ(CH2)n	Spectrun E_av, Iwanicka et al, 2017, p. 18
743	E_M_50_av	weak absorption	whole egg	Spectrum E_av
775	E_M_25_av	weak absorption	whole egg	Spectrun E_av
786	E_M_25_av	weak absorption	whole egg	Spectrun E_av
805	E_M_25_av	weak absorption	whole egg	Spectrun E_av
844	E_M_25_av	weak absorption	whole egg	Spectrun E_av
950	E_M_25_av	weak absorption	PO4-3 anion stretching	Spectrum E_av, Ricci et al. 2006, p. 1223
970	E_M_50_av	weak absorption	PO4-3 anion stretching	Spectrum E_av, Ricci et al. 2006, p. 1223
	UN_9	(blank)	(blank)	(blank)
1125	E_M_25_av	sharp absorption	PO4-3 anion stretching	Spectrum E_av, Ricci et al. 2006, p. 1223
1192	E_M_25_av	sharp absorption	v(C-O) stretching	Spectrum E_av, Ricci et al. 2006, p. 1224
1265	E_M_50_av	strong absorption	C-O	Spectrum E_av, Ploeger et al, 2010, p. 17
1266	UN_9	(blank)	(blank)	(blank)
1274	E_M_75_av	strong absorption	C-O	Spectrum E_av, Spectrum Ca_av, Ploeger et al, 2010, p. 17
1280	E_M_25_av	strong absorption	C-O	Spectrum E_av, Ploeger et al, 2010, p. 17
1282	E_M_75_av	strong absorption	C-O	Spectrum E_av, Spectrum Ca_av, Ploeger et al, 2010, p. 17
1303	E_M_50_av	weak absorption	whole egg	Spectrum E_av
1313	E_M_50_av	weak absorption	whole egg	Spectrum E_av
1315	E_M_75_av	weak absorption	whole egg	Spectrum E_av
1398	UN_9	(blank)	(blank)	(blank)
1433	E_M_50_av	strong absorption	C-O bending	Spectrum E_av, Spectrum Ca_av, Ricci et al, 2006, p. 1223
1438	E_M_5_av	weak absorption	whole egg	Spectrum E_av
1467	UN_9	(blank)	(blank)	(blank)
1468	E_M_50_av	strong absorption	C-O bending	Spectrum E_av, Spectrum Ca_av, Ricci et al, 2006, p. 1223
	E_M_75_av	strong absorption	C-O bending	Spectrum E_av, Spectrum Ca_av, Ricci et al, 2006, p. 1223
1472	E_M_5_av	strong absorption	C-O bending	Spectrum E_av, Ricci et al, 2006, p. 1223
1473	E_M_25_av	strong absorption	C-O bending	Spectrum E_av, Ricci et al, 2006, p. 1223
1554	UN_9	(blank)	(blank)	(blank)
1555	E_M_75_av	strong absorption	N-H bands, amide I, II	Spectrum E_av, Miliani et al, 2012, p. 304
1561	E_M_50_av	strong absorption	N-H bands, amide I, II	Spectrum E_av, Miliani et al, 2012, p. 304
1680	E_M_50_av	strong absorption	N-H bands, amide I, II	Spectrum E_av, Miliani et al, 2012, p. 304
1682	UN_9	(blank)	(blank)	(blank)
1686	E_M_50_av	strong absorption	N-H bands, amide I, II	Spectrum E_av, Miliani et al, 2012, p. 304
	E_M_75_av	strong absorption	N-H bands, amide I, II	Spectrum E_av, Miliani et al, 2012, p. 304
1747	E_M_50_av	strong absorption	C-H stretching bands, esters	Spectrum E_av, Mazzeo et al, 2008, p. 69
	UN_9	(blank)	(blank)	(blank)
1751	E_M_75_av	strong absorption	C-H stretching bands, esters	Spectrum E_av, Mazzeo et al, 2008, p. 69
1753	E_M_25_av	strong absorption	C-H stretching bands, esters	Spectrum E_av, Mazzeo et al, 2008, p. 69

Figure 76: Filtered CPAD of peaks of interest for UN_I_9 spectrum and possible matches.

1907	E_M_25_av	weak absorption	(blank)	(blank)
2030	E_M_25_av	weak absorption	(blank)	(blank)
2607	UN_9	(blank)	(blank)	(blank)
2855	E_M_5_av	strong absorption	CH stretching	Spectrum E_av, Daher et al, 2017, p.8
2856	E_M_50_av	strong absorption	CH stretching	Spectrum E_av, Daher et al, 2017, p.8
	UN_9	(blank)	(blank)	(blank)
2857	E_M_75_av	strong absorption	CH stretching	Spectrum E_av, Daher et al, 2017, p.8
2871	E_M_5_av	strong absorption	CH stretching	Spectrum E_av, Daher et al, 2017, p.8
	UN_9	(blank)	(blank)	(blank)
2880	E_M_25_av	strong absorption	CH stretching	Spectrum E_av, Daher et al, 2017, p.8
2884	UN_9	(blank)	(blank)	(blank)
2926	E_M_5_av	weak absorption	CH2 stretching	Spectrum E_av, Ploeger et al, 2010, p. 37
2930	E_M_50_av	strong absorption	CH stretching	Spectrum E_av, Daher et al, 2017, p.8
2936	UN_9	(blank)	(blank)	(blank)
2937	E_M_75_av	strong absorption	CH stretching	Spectrum E_av, Daher et al, 2017, p.8
2943	E_M_25_av	strong absorption	CH stretching	Spectrum E_av, Daher et al, 2017, p.8
2957	E_M_5_av	weak absorption	CH2 stretching	Spectrum E_av, Ploeger et al, 2010, p. 37
2958	UN_9	(blank)	(blank)	(blank)
2959	E_M_50_av	weak absorption	CH2 stretching	Spectrum E_av, Ploeger et al, 2010, p. 37
	E_M_75_av	weak absorption	CH2 stretching	Spectrum E_av, Ploeger et al, 2010, p. 37
2966	UN_9	(blank)	(blank)	(blank)
2974	E_M_25_av	weak absorption	CH2 stretching	Spectrum E_av, Ploeger et al, 2010, p. 37
3005	E_M_50_av	weak absorption	(blank)	(blank)
3006	E_M_75_av	weak absorption	(blank)	(blank)
	UN_9	(blank)	(blank)	(blank)
3014	UN_9	(blank)	(blank)	(blank)
3071	E_M_50_av	weak absorption	2δNH	Spectrum E_av, Rosi et al, 2010, p. 621
3080	E_M_75_av	weak absorption	2δNH	Spectrum E_av, Rosi et al, 2010, p. 621
3084	E_M_50_av	weak absorption	2δNH	Spectrum E_av, Rosi et al, 2010, p. 621
3098	E_M_75_av	weak absorption	2δNH	Spectrum E_av, Rosi et al, 2010, p. 621
3106	E_M_50_av	weak absorption	2δNH	Spectrum E_av, Rosi et al, 2010, p. 621
3108	E_M_75_av	weak absorption	2δNH	Spectrum E_av, Rosi et al, 2010, p. 621

Figure 76: continued.

8.1.2 Experimental set II – Results and discussion

Using the CPAD, all organic additives in the 10 unknown spectra comprising Experimental set II were successfully identified. The concentration of the organic additive in two of the unknown spectra (UN_II_1 and UN_II_6) was falsely identified.

The identification process through the CPAD and the results for each unknown spectrum of the experimental set II are summarised in table 13, (the unknown spectra and their filtered CPAD comparisons with possible matching spectra from standards are provided in Appendix I - Experimental set II, fig.48-63.)

UN_ sp	Inorganic Presence	Peaks of Interest	CPAD matching	Interpretation	ID As	True ID	Comment on ID
UN_II_1	Low: 1792	722, 741, 813, 872, 1378, 1461, 1605, 1643, 2728, 2870, 2930, 2960	Match diagnostic peaks of asphalt.	11 peaks match 75% asphalt additive, 12 peaks match 50% asphalt additive.	A_M_75	A_M_50	Mistake could have been avoided since more peaks match 50% asphalt. 1792 inorganic peak should be taken into acount in ID.
UN_II_2	Medium: 2510, 2235, 1992, 1793, 1159, 877, 813	1316, 1327, 1599, 1606, 1682, 1694	Possible matches: Bone glue or egg white additive. Absolute match to 1694 bone glue peak.	Protein due to 1694, absence of lipid or other.	BG_M_25	YES	1206 and absence of OH above 3000 are diagnostic and discriminate the two matching candidates.
UN_II_3	Medium: 2512, 2237, 1794, 1159, 880, 815	1473, 1586, 1655, 1674, 2855, 2871, 2925, 2956	Closest match to egg (8 peaks) followed by egg yolk (5 peaks).	Protein (low) and lipid coexistence shows egg.	E_M_5	YES	
UN_II_4	YES	3014-2898, 1684-1281	Compared to 50, 25 and 5% egg white additive. Clear matching to 50%.	Protein at 1694, absence of esters or sugars, high OH above 3000 shows egg white.	EW_M_50	YES	
UN_II_5	NO	3012-2862, 1759-1271	Compared to egg yolk and egg, 18 peaks match egg yolk vs 11 for egg. Absence of protein peak 1693 of egg.	Mainly lipid, phosphates indicating egg component, low protein in 1683.	EY	YES	1069, 1126, 1204 phosphates also used in ID.
UN_II_6	Medium: 1791, 2512, 1159, 813, 792	3004-2858, 1758-1471, including 1691 protein.	Close match to both 50% and 25% egg yolk additive but best the 50%.	Lipid and protein.	EY_M_25	EY_M_50	Mistake should be avoided - wrong counting of the number of common peaks.
UN_II_7	Low: 2517, 821, 972	3004-2858, 1755-1271, 894	Compared to 25% olive oil additive and 25% lard additive. 14 peaks matching to lard additive. Olive oil diagnostic peaks are missing.	Lipid indicates olive oil or lard mortar additive.	L_M_25	YES	Characteristic spectral pattern at 1669-1613 assessed visually in final step.
UN_II_8	Low: 2516, 1793, 713	2957-2856, 1751-1261, 1038-914, 781	50% egg yolk additive is the second closest match. Checked in the sugar region for presence of phosphates. Protein and sugar region absolute match to 75% milk additive.	High OH above 3000, lipids, protein and sugars coexist.	Mi_M_75	YES	
UN_II_9	High: 2512, 2237, 2135, 1159, 880, 825, 791	1383, 1443, 1533, 1576, 1593, 1602, 1672, 1683, 1695, 1756, 2855, 2930, 3005	Peaks match 5% olive oil additive, absence of 1473 peak of 5% lard rules it out.	Dominant presence of esters.	O_M_5	YES	
UN_II_10	High: 2512, 2237, 2135, 1158, 880	1004, 1024, 1400, 1442, 1449, 1467, 1534, 1579, 1619, 1635, 1654, 2858, 2926, 2956	Very few organic peaks, sugar region influenced by inorganic but 1024 present. 1534 weak peak is important.	Group frequency region provides evidence of organic presence.	R_M_25	YES	Absence of lipids and proteins could be due to inorganic interference (also observed in milk/mortar standatds of low concentration).

Table 13: Summary of Experimental set II identification outcomes.

The final stage of the identification process is provided in Table 13, where comparisons are narrowed down between the unknown spectrum and the most closely matching candidates. The misidentifications of **UN_II_1** and **UN_II_6** could have been avoided by more careful examination of the CPAD relevant to the number of common peaks between the unknown spectrum and its best match (Table 13, blue highlight). It is human error on the part of the CPAD user that produces the outcome, not a design error in the CPAD.

In the case of UN_II_1, one more mistake was made, apart from the erroneous counting of the number of common peaks (Appendix I, fig.48-49). This was the disregarding of the weak peak at 1792 cm^{-1} which was initially noticed and assigned to $CaCO_3$. This peak showed that the concentration of the asphalt additive in the mortar mixture was lower than the suspected 75% asphalt/mortar mixture that does not have the 1792 cm^{-1} peak in its spectrum. The error occurred because the inorganic peaks of the unknown spectrum, although assessed and included in table 13 and in the identification process to determine the presence of mortar, were not inserted in the CPAD. The inserted peaks were only those of interest as diagnostic for organics, so during the comparison process in the CPAD the inorganic peak was forgotten because it did not appear on the filtered entries.

Conclusions were also drawn from the correct identifications of the unknown spectra, relative to the diagnostic peaks and their occurrence or their absence within a spectrum, as well as the selection of diagnostic peaks for inserting in the CPAD. The CPAD comparison between the UN_II_2 and the two closest matching spectra showed that the 25% bone glue/mortar mixture spectrum had two additional features that were not taken into consideration when the spectrum was selected as the best match to the unknown spectrum (fig.77-78). These were the weak peak at 1206 cm^{-1} and the absence of OH above 3000 cm^{-1} (Rosi et al., 2009, 2100) that was considered diagnostic and discriminated the unknown spectrum from the next possible protein candidate, egg white that showed broad and strong absorption in that region (sect. 7.5.2). These features are visible on the unknown spectrum and should be included in the CPAD as diagnostic.

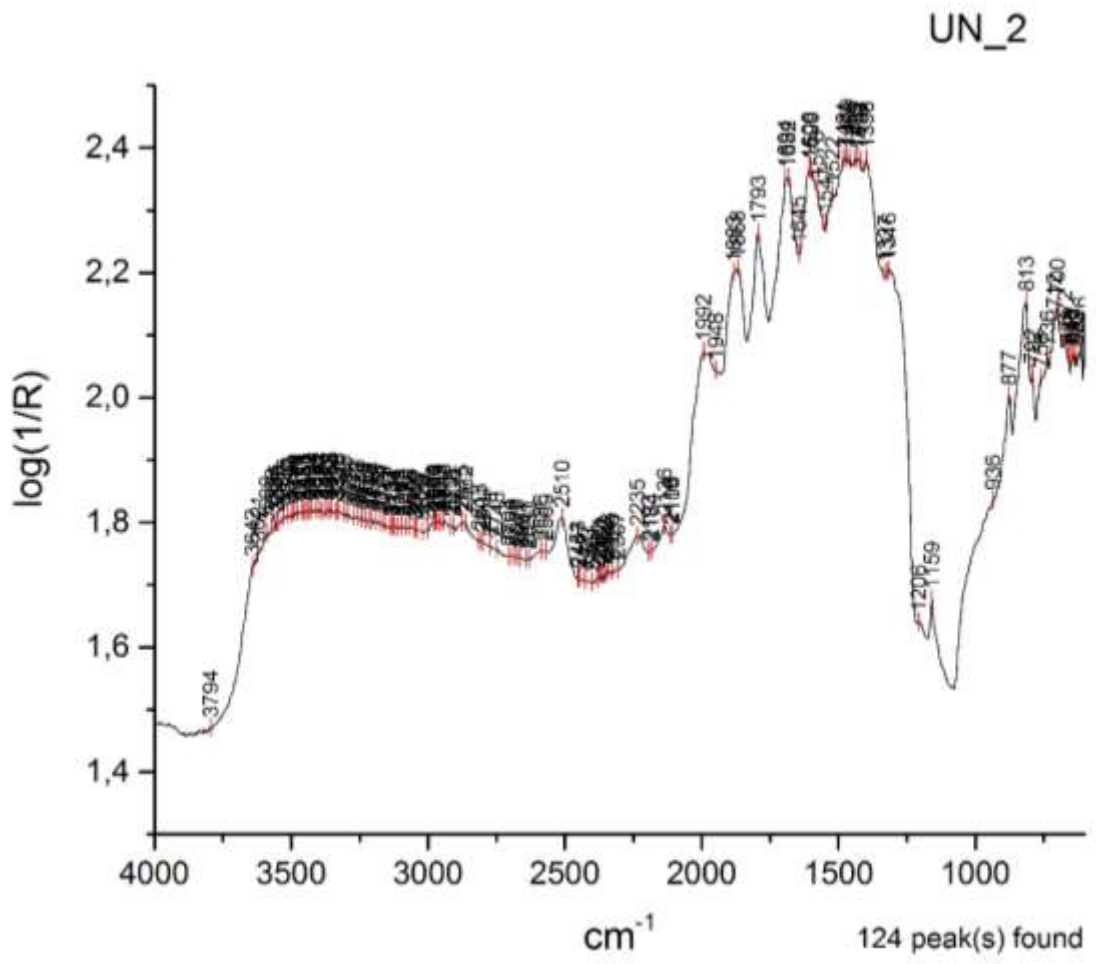

Figure 77: UN_II_2 correctly identified as 25% bone glue additive in mortar (BG_M_25).

Peak x (position)	Spectrum ID	Type of band	Chemical Band Assignement	Reference
623	EW_M_50_av	weak absorption	CaCO3	spectrum Ca_av
647	BG_M_25_av	(blank)	CaCO3	spectrum Ca_av
664	EW_M_50_av	weak absorption	CaCO3	spectrum Ca_av
672	BG_M_25_av	(blank)	CaCO3	spectrum Ca_av
699	BG_M_25_av	weak absorption	quartz	Spectrum Q_av, spectrum M_av
	EW_M_50_av	weak absorption	quartz	spectrum Q_av
714	BG_M_25_av	weak absorption	v4 carbonate ion	Spectrum Ca_av, spectrum M_av, Ylmen and Jaglid, 2013, p. 119
715	EW_M_50_av	weak absorption	v4 carbonate ion	Spectrum Ca_av, spectrum M_av, Ylmen and Jaglid, 2013, p. 119
735	BG_M_25_av	weak absorption	(blank)	(blank)
761	BG_M_25_av	weak absorption	(blank)	(blank)
792	EW_M_50_av	sharp and weak absorption	quartz	Spectrum Q_av, spectrum M_av
793	BG_M_25_av	sharp and weak absorption	quartz	Spectrum Q_av, spectrum M_av
815	BG_M_25_av	sharp absorption	Si-O antisymmetric stretching	Spectrum Q_av, spectrum M_av, Miliani et al, 2012, p. 303
816	EW_M_50_av	sharp absorption	quartz	Spectrum Q_av, spectrum M_av
877	BG_M_25_av	weak absorption	v2 carbonate ion	Spectrum Ca_av, spectrum M_av, Ylmen and Jaglid, 2013, p. 119
879	EW_M_50_av	sharp and weak absorption	v2 carbonate ion	Spectrum Ca_av, spectrum M_av, Ylmen and Jaglid, 2013, p. 119
1082	EW_M_50_av	weak absorption	egg white	spectrum EW_av
1086	BG_M_25_av	weak absorption	v1 carbonate ion	Spectrum Ca_av, spectrum M_av, Ylmen and Jaglid, 2013, p. 119
1116	EW_M_50_av	weak absorption	C-O stretching	Buti et al, 2013, p. 2705
1117	BG_M_25_av	weak absorption	CaCO3	spectrum Ca_av
1159	BG_M_25_av	sharp absorption	quartz	Spectrum Q_av, spectrum M_av
	EW_M_50_av	sharp absorption	quartz	Spectrum Q_av, spectrum M_av
1205	BG_M_25_av	weak bands	bone glue	Spectrum BG_av
1283	EW_M_50_av	weak absorption	egg white	spectrum EW_av
1286	BG_M_25_av	stair-step type intensities	bone glue	Spectrum BG_av
1313	EW_M_50_av	weak absorption	egg white	spectrum EW_av
1316	UN_2	(blank)	(blank)	(blank)
1327	UN_2	(blank)	(blank)	(blank)
1341	BG_M_25_av	weak absorption	quartz	spectrum Q_av
1397	EW_M_50_av	weak absorption	CaCO3	Spectrum Ca_av, spectrum M_av
1399	BG_M_25_av	weak absorption	CaCO3	Spectrum Ca_av, spectrum M_av
1431	BG_M_25_av	weak absorption	CaCO3 and quartz	Spectrum M_av
1437	BG_M_25_av	weak absorption	CaCO3 and quartz	Spectrum M_av
1446	EW_M_50_av	weak absorption	egg white	spectrum EW_av
1461	BG_M_25_av	stair-step type intensities	Amide III	Spectrum BG_av, Rosi et al, 2009, p. 2099
1469	BG_M_25_av	stair-step type intensities	Amide III	Spectrum BG_av, Rosi et al, 2009, p. 2099
1480	EW_M_50_av	weak absorption	egg white	spectrum EW_av
1561	EW_M_50_av	weak absorption	quartz	spectrum Q_av
1575	BG_M_25_av	strong absorption	v3 antisymmetric stretching CO3-2 or amide III	Spectrum BG_av, spectrum M_av, Ylmen and Jaglid, 2013, 119; Miliani et al, 2012, p. 304
1576	EW_M_50_av	strong absorption	C-N-H bending amide II, N-H bands	Spectrum EW_av, Rosi et al, 2009, p. 2104
1597	BG_M_25_av	strong absorption	quartz	Spectrum Q_av, spectrum M_av
1599	UN_2	(blank)	(blank)	(blank)
1606	UN_2	(blank)	(blank)	(blank)
1616	EW_M_50_av	weak absorption	quartz	spectrum Q_av
1682	UN_2	(blank)	(blank)	(blank)
1685	EW_M_50_av	strong absorption	N-H bands	Spectrum EW_av, Ploeger et al, 2010, p.37, Miliani et al, 2012, p. 305
1694	BG_M_25_av	strong absorption	N-H bands	Spectrum BG_av, Rosi et al, 2009, p. 2104, Miliani et al, 2012, p. 304
	UN_2	(blank)	(blank)	(blank)

Figure 78: Filtered CPAD of peaks of interest for UN_II_2 spectrum and possible matches.

1793	**BG_M_25_av**	strong absorption	**v1+v4**	Spectrum Ca_av, spectrum M_av, Ricci et al, 2006, p. 1222
1797	**EW_M_50_av**	combination band	**v1+v4**	Spectrum Ca_av, spectrum M_av, Ricci et al, 2006, p. 1222
1854	**EW_M_50_av**	weak absorption	**quartz**	spectrum Q_av
1866	**EW_M_50_av**	weak absorption	**quartz**	spectrum Q_av
1867	**BG_M_25_av**	weak absorption	**quartz**	Spectrum Q_av, spectrum M_av
1941	**EW_M_50_av**	weak absorption	**quartz**	spectrum Q_av
1944	**BG_M_25_av**	weak absorption	**quartz**	Spectrum Q_av, spectrum M_av
1950	**EW_M_50_av**	weak absorption	**quartz**	spectrum Q_av
1972	**EW_M_50_av**	weak absorption	**quartz**	spectrum Q_av
1973	**BG_M_25_av**	weak absorption	**quartz**	Spectrum Q_av, spectrum M_av
1988	**BG_M_25_av**	weak absorption	**quartz**	Spectrum Q_av, spectrum M_av
	EW_M_50_av	weak absorption	**quartz**	spectrum Q_av
2135	**EW_M_50_av**	weak absorption	**calcium carbonate and quartz**	Spectrum Ca_av, spectrum M_av, spectrum Q_av
2136	**BG_M_25_av**	weak absorption	**CaCO3 and quartz**	Spectrum Q_av, spectrum M_av, spectrum Ca_av
2236	**BG_M_25_av**	weak absorption	**quartz**	Spectrum Q_av, spectrum M_av
2237	**EW_M_50_av**	weak absorption	**quartz**	spectrum Q_av
2512	**EW_M_50_av**	combination band	**v1+v3**	Spectrum Ca_av, spectrum M_av, Ricci et al, 2006, p. 1222
2513	**BG_M_25_av**	combination band	**v1+v3 carbonate ion**	Spectrum Ca_av, spectrum M_av, Ricci et al, 2006, p. 1222
2564	**EW_M_50_av**	weak absorption	**egg white**	spectrum EW_av
2589	**EW_M_50_av**	weak absorption	**egg white**	spectrum EW_av
2595	**EW_M_50_av**	weak absorption	**egg white**	spectrum EW_av
2694	**EW_M_50_av**	weak absorption	**egg white**	spectrum EW_av
2875	**BG_M_25_av**	strong absorption	**CaCO3**	Spectrum Ca_av, spectrum M_av
	EW_M_50_av	sharp and weak absorption	**CaCO3**	Spectrum Ca_av, spectrum M_av
2897	**BG_M_25_av**	weak bands	**C-H stretching**	Spectrum BG_av, Miliani et al, 2012, p. 304; Rosi et al, 2009, p. 2104
2905	**BG_M_25_av**	weak absorption	**bone glue**	Spectrum BG
2934	**EW_M_50_av**	weak absorption	**CH stretching**	Spectrum EW_av, Daher et al, 2017, p. 8
2940	**BG_M_25_av**	weak absorption	**(blank)**	(blank)
2943	**EW_M_50_av**	weak absorption	**CH3 stretching**	Spectrum EW_av, Iwanicka et al, 2017, p. 18
2949	**BG_M_25_av**	weak absorption	**(blank)**	(blank)
2961	**EW_M_50_av**	sharp and weak absorption	**CaCO3**	Spectrum Ca_av, spectrum M_av
2979	**BG_M_25_av**	strong absorption	**CaCO3**	Spectrum Ca_av, spectrum M_av
3084	**EW_M_50_av**	1st overtone	**amide I**	Spectrum EW_av, Rosi et al, 2009, p. 2099
3094	**EW_M_50_av**	1st overtone	**amide I**	Spectrum EW_av, Rosi et al, 2009, p. 2099

Figure 78: continued.

The identification of UN_II_10 as 25% rice additive in mortar, although correct, offers challenges if accepting this as being a definitive identification. The inorganic interference is high and masks most of the organic peaks (fig.79). The only indication of organic presence occurs at the group frequency region and is not adequate to further identify the organic component. The absence of lipids and proteins cannot be taken as indication of starch, since inorganic presence could have masked their peaks. The 1024 and 1534 cm^{-1} weak peaks were diagnostic to the unknown spectrum, matching those present in the 25%

rice/mortar spectrum (fig.80).

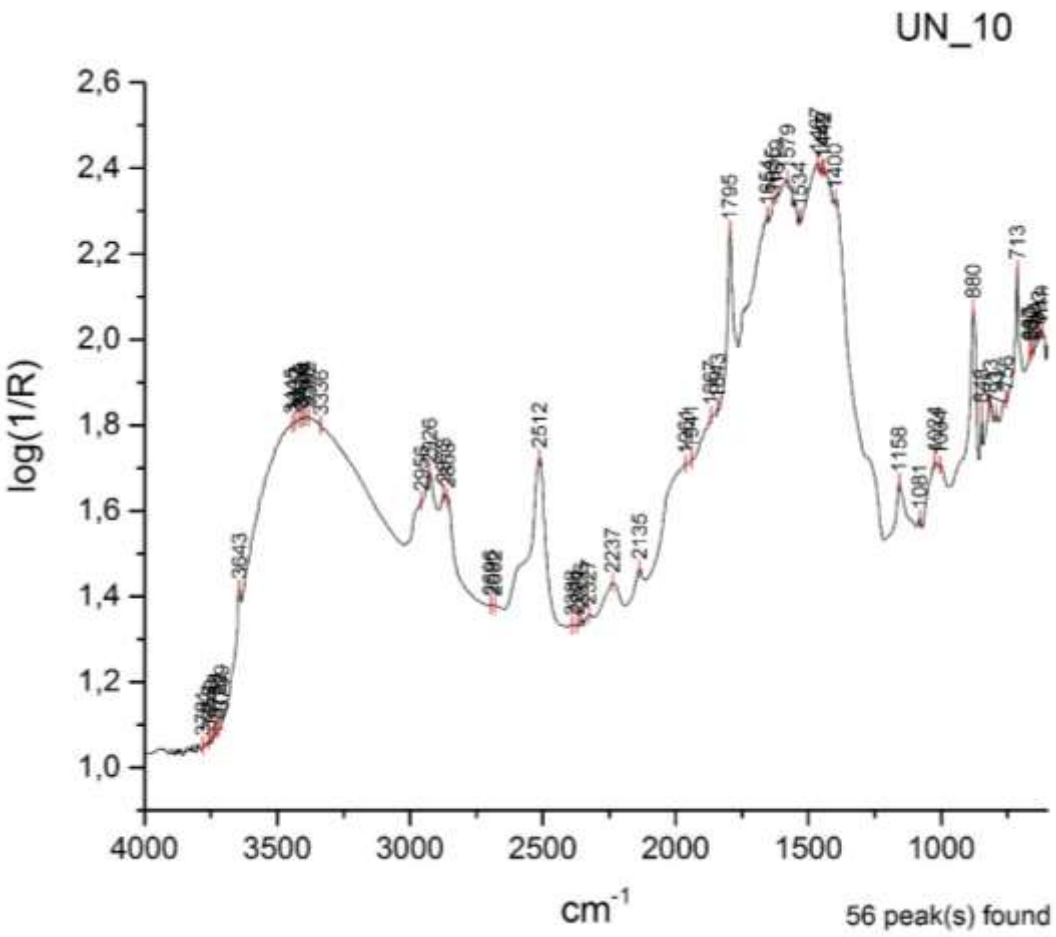

Figure 79: UN_II_10 correctly identified as 25% rice additive in mortar (R_M_25).

Peak x (position)	Spectrum ID	Type of band	Chemical Band Assignement	Reference
621	R_M_25_av	weak absorption	rice	Spectrum R_av
648	R_M_25_av	weak absorption	rice	Spectrum R_av
659	R_M_25_av	weak absorption	rice	Spectrum R_av
688	R_M_25_av	weak absorption	rice	Spectrum R_av
990	Mi_M_5_av	weak absorption	sugar region	Spectrum Mi_av, Synytsya and Novak, 2014, p. 6
1004	UN_10	(blank)	(blank)	(blank)
1019	R_M_25_av	strong absorption	rice	Spectrum R_av
1024	UN_10	(blank)	(blank)	(blank)
1400	UN_10	(blank)	(blank)	(blank)
1442	UN_10	(blank)	(blank)	(blank)
1449	UN_10	(blank)	(blank)	(blank)
1467	UN_10	(blank)	(blank)	(blank)
1475	R_M_25_av	weak absorption	C-H bending	Spectrum R_av, Buti et al, 2013, p. 2705
1476	Mi_M_5_av	strong absorption	Amide III	Spectrum Mi_av, Rosi et al, 2009, p. 2099
1518	R_M_25_av	weak absorption	rice	Spectrum R_av
1534	UN_10	(blank)	(blank)	(blank)
1535	R_M_25_av	weak absorption	rice	Spectrum R_av
1579	UN_10	(blank)	(blank)	(blank)
1619	UN_10	(blank)	(blank)	(blank)
1635	UN_10	(blank)	(blank)	(blank)
1654	UN_10	(blank)	(blank)	(blank)
2688	R_M_25_av	weak absorption	(blank)	(blank)
	Mi_M_5_av	weak absorption	(blank)	(blank)
2697	R_M_25_av	weak absorption	(blank)	(blank)
2699	Mi_M_5_av	weak absorption	(blank)	(blank)
2709	R_M_25_av	weak absorption	rice	Spectrum R_av
2857	R_M_25_av	strong absorption	CH stretching	Spectrum E_av, Daher et al, 2017, p.8
2858	UN_10	(blank)	(blank)	(blank)
2926	R_M_25_av	strong absorption	CH stretching	Spectrum E_av, Daher et al, 2017, p.8
	Mi_M_5_av	strong absorption	CH stretching	Spectrum Mi_av, Daher et al, 2017, p.8
	UN_10	(blank)	(blank)	(blank)
2956	UN_10	(blank)	(blank)	(blank)
2958	Mi_M_5_av	sharp absorption	CH2 stretching	Ploeger et al, 2010, p. 37
3009	R_M_25_av	weak absorption	CH stretching	Miliani et al, 2012, p. 302

Figure 80: Filtered CPAD of peaks of interest for UN_II_10 spectrum and possible matches.

8.1.3 Experimental set III – Results and discussion

The unknown spectra comprising Experimental set III were successfully identified regarding both the organic additive and its concentration in the mortar mixture. The identification process through the CPAD is summarized in Table 14. The 10 unknown spectra and the CPAD comparative analysis data are included in Appendix I (Experimental set III, fig.64-83).

UN_sp	Inorganic Presence	Peaks of Interest	CPAD matching	Interpretation	ID As	True ID	Comment on ID
UN_III_1	Medium: 2510, 2237, 2136, 1794, 1159, 872, 815	3011-2577, 1746-1387	1539, 1597, 1746 and 3011-2577 absolute match to 75% mortar mixture.	C=O at 1746 and CH at 3011-2577 only indications of glucose.	R_M_75	YES	Inorganic intereference is high even in high rice content in the mortar mixture.
UN_III_2	Low: 2511, 878	1283, 1317, 1382, 1423, 1472, 1516, 1679, 1758, 2863, 2941, 2966, 3012	Up to 1472 matches both L_M_75 and O_M_75. 1516 diagnostic to O_M_50. Group frequency region best match too.	Peaks of interest indicate strong presence of lipids.	O_M_50	YES	
UN_III_3	Medium: 2512, 2237, 2136, 1794, 1159, 879, 816	1096, 1116, 1397, 1477, 1575, 1660, 1746, 2854, 2924, 2955	Absolute match in the 2955-2854 and 1746 to Mi_M_25.	Protein and phosphates are masked by inorganic but indicative at 1575 and 1660.	Mi_M_25	YES	Shape of OH and CH above 2854 ruled out rice additive.
UN_III_4	Low: 1160	2971-2861, 1756-1318	Inorganic peaks best match to 75% rather than the suspected 25%. Same for 1756-1318.	Strong lipid content.	L_M_75	YES	Shape of 1686-1540 diagnostic.
UN_III_5	NO	1270, 1395, 1475, 1550, 1559, 1620, 1654, 1700, 1756, 2864, 2941, 2967, 3009	1475 and 1756 absolute match to lard.	Egg yolk ruled out because strong 1559 and 1667 are missing from the unknown.	L	YES	Compared to lard, olive oil and egg yolk. Shape and intensity of peaks are important here.
UN_III_6	Medium: 2514, 2237, 2135, 1792, 1159, 876, 815, 792	3004-2855, 1753-1389, 968, 911	Peaks shared with 25% rather than with 50% and showed less peak shifting.	Lipid content, indication of phosphates.	EY_M_25	YES	
UN_III_7	Medium: 2511, 2237, 2135, 1795, 1159, 880, 818, 792	3028-2933, 1667-1321	Match protein peaks at 1601, 1633, 1660.	Protein content	EW_M_5	YES	Inorganic intereference important in ID.
UN_III_8	Low: 798, 714	2973-2881, 1753-1032, 940, 908	Close match to 25% egg/mortar.	Phosphates and lipids present, 2973 indicates egg.	E_M_25	YES	Inorganic content masked by organic distortions.
UN_III_9	Medium: 2513, 2237, 2135, 1794, 1160, 878, 815, 792	2959-2904, 1703-1286	1694 diagnostic to bone glue (1665 at egg white), 2959-2904 absolute match.	Stair-step type intensities in 1399-1703, absence of CH above 2878.	BG_M_25	YES	
UN_III_10	Medium: 2514, 1793, 1160	1383, 1461, 1602, 1642, 2727, 2869, 2928, 2951	Most peaks match 25% asphalt/mortar.	Diagnostic shape of asphalt peaks.	A_M_25	YES	

Table 14: Summary of Experimental set III identification outcomes.

The spectrum of UN_III_1 was correctly identified as 75% rice/mortar mixture (Appendix I, Experimental set III, fig.64-65). The inorganic interference was high despite the high organic concentration in the mixture. This effect was observed during the spectral interpretation of standards for the rice and its mortar mixtures (sec.7.5.8). It is assumed that the low viscosity of the rice solution is responsible for the prevailing of the inorganic spectral features in the spectrum of high organic concentration.

8.1.4 Experimental set IV – Results and discussion

As described in the experiment layout (Ch.8), the selection of the unknown spectra in the Experimental set IV differed from that followed on experimental sets I-III. Instead of selecting 9 spectra of organic additive/mortar mixtures and 1 spectrum of an organic standard in order for all the 9 different organic standards to be represented in the set either in a mortar mixture or in its pure form, in experimental set IV the selection had no restrictions: the selected spectra could be duplicated, derived from the mortar standard or from the same organic additive or from mortar mixtures that contained the same additive but in different concentrations.

The identification process and outcomes for each unknown spectrum are summarized in Table 15. The unknown spectra and their CPAD comparisons with possible matching spectra are provided in Appendix I (Experimental set IV, fig.84-101). Three spectra were falsely identified in experimental set IV (Table 15, blue highlight).

UN_sp	Inorganic Presence	Peaks of Interest	CPAD matching	Interpretation	ID As	True ID	Comment on ID
UN_IV_1	No diagnostic mortar peaks.	724, 742, 759, 872, 918, 937, 976, 1033, 1089, 1169, 1308, 1377, 1460, 1603, 1643, 1843, 1866, 1888, 2039, 2726, 2858, 2868, 2930, 2954, 2961	12 peaks absolute match to A_av. 16 peaks to A_M_75.	Shape and intensity of peaks diagnostic to asphalt.	A	A_M_75	1089, 786, 759, 617 on the unknown should have been assigned to calcium carbonate and mistake would have been avoided.
UN_IV_2	Medium: 2512, 2237, 2135, 1796, 1159, 879	967, 1286-1695, 2930, 2940, 2961, 3086	8 peaks match 50% vs 7 peaks that match 25% egg white/mortar. 2 peaks absolute match to 50%.	Absence of 1750 rules out protein-lipid. High OH above 3000 indicates egg white protein.	EW_M_50	YES	967 also present in egg white spectrum.
UN_IV_3	High: 2512, 2237, 2135, 1796, 1159, 879, 714 strong peaks	924, 1009, 1026, 1263, 1446, 1472, 1539, 1551, 1578, 1611, 1619, 1652, 1746, 2857, 2927, 3007	Close matching to R_M_50.	1746 C=O stretching and 1026-931 sugar region suggests rice.	R_M_50	YES	Absence of protein and lipid peaks rule out milk.
UN_IV_4	Low: 2516, 1793, 1160, 874, 791	954, 963, 1274, 1449, 1470, 1518, 1535, 1557, 1631, 1665, 1681, 1691, 1755, 2685, 2768, 2869, 2906, 2950, 3003	963 match 50% egg mixture and it is absent in 50% egg yolk. Best match to weak peaks 1557-1470 and 1691, 1755 to 50% egg yolk.	1755 lipid, 963 phosphates and 1961 protein co-exist.	EY_M_50	YES	Comparison to egg and egg yolk mixtures.
UN_IV_5	NO	979, 1124, 1178, 1274, 1324, 1419, 1472, 1574, 1690, 1756, 2876, 2945, 2974, 3025, 3089	Absence of milk peaks 2860-1840. Peaks match egg best, also above 3000.	Lipid-protein, stair-step type intensities of protein, phosphates.	E	YES	Comparisons to egg, egg yolk and milk standards.

Table 15: Summary of Experimental set IV identification outcomes.

UN_sp	Inorganic Presence	Peaks of Interest	CPAD matching	Interpretation	ID As	True ID	Comment on ID
UN_IV_6	High: 2512, 2236, 2135, 1795, 1160, 881, 714 strong peaks	995, 1475, 1535, 2925, 2959	Equal matching of organic peaks to both candidates. 19 peaks vs 16 including inorganic peaks match milk best.	1024-995 sugars match both candidates. 2959 CH_2 stretching of lipid.	R_M_25	Mi_M_5	Narrowed down to Mi_M_5 and R_M_25. Milk rejected due to lack of expected strong peaks at 1602-1612. Mistake could be avoided by including inorganic peaks in ID.
UN_IV_7	High	1281, 1432, 1448, 1466, 1475, 1505, 1561, 1585, 1599	Best match to mortar, absence of 2936-2963 egg white peaks.	Mostly inorganic, 1281 and 1500 weak peaks suspected organic.	EW_M_5	M	Narrowed down to mortar spectrum and EW_M_5. Inorganic peaks should be considered in ID. EW_M_5 matching due to inorganic similarities.
UN_IV_8	High	986, 1117, 1255, 1320, 1384, 1442, 1483, 1542, 1618, 1705, 2679, 2731, 2856, 2930, 3004	Equal matching of organic peaks to both candidates. Absence of 2954 peak of oil rules it out.	Lipid content at 2930 and 1751.	L_M_5	YES	Narrowed down to olive oil and lard mixtures.
UN_IV_9	Low: 2522, 1791	1267, 1285, 1313, 1340, 1471, 1572, 1692	BG_M_75 match shape and intensity of both the organic and inorganic peaks.	1692 protein, absence of lipids.	BG_M_75	YES	1791 and 2522 inorganic shape and intensity.
UN_IV_10	Low: 1797, below 800 weak peaks	1281, 1472, 1518, 1545, 1561, 1576, 1615, 1669, 1702, 2864, 2940, 2964, 3014	Close match to oil, followed by lard. 1702 diagnostic to oil.	Lipids 2940-2964, 1760	O_M_75	YES	Also considering the presence and absence of inorganic peaks.

Table 15: continued.

The organic component of UN_IV_1 was correctly identified as being asphalt but the process failed to detect the mortar component. Taking into consideration the peaks below 1089 cm^{-1} on the unknown spectrum, clearly assigned to $CaCO_3$, would have produced correct identification in this instance (Appendix I, fig.84-85).

UN_IV_6 was falsely identified as 25% rice/mortar mixture instead of the correct 5% milk/mortar mixture (fig.81). The similarities between rice and milk mortar mixtures of low organic concentration, noted in experimental set I, persist here due to the prevailing of mortar peaks on the spectra. The CPAD comparison between the unknown spectrum and

the two closest matching spectra candidates, showed that all spectra shared equal number of peaks of interest (fig.82). However, the weak peak at 2959 cm^{-1} on the UN_IV_6 indicates CH_2 stretching of lipids that only matches the Mi_M_5 spectrum.

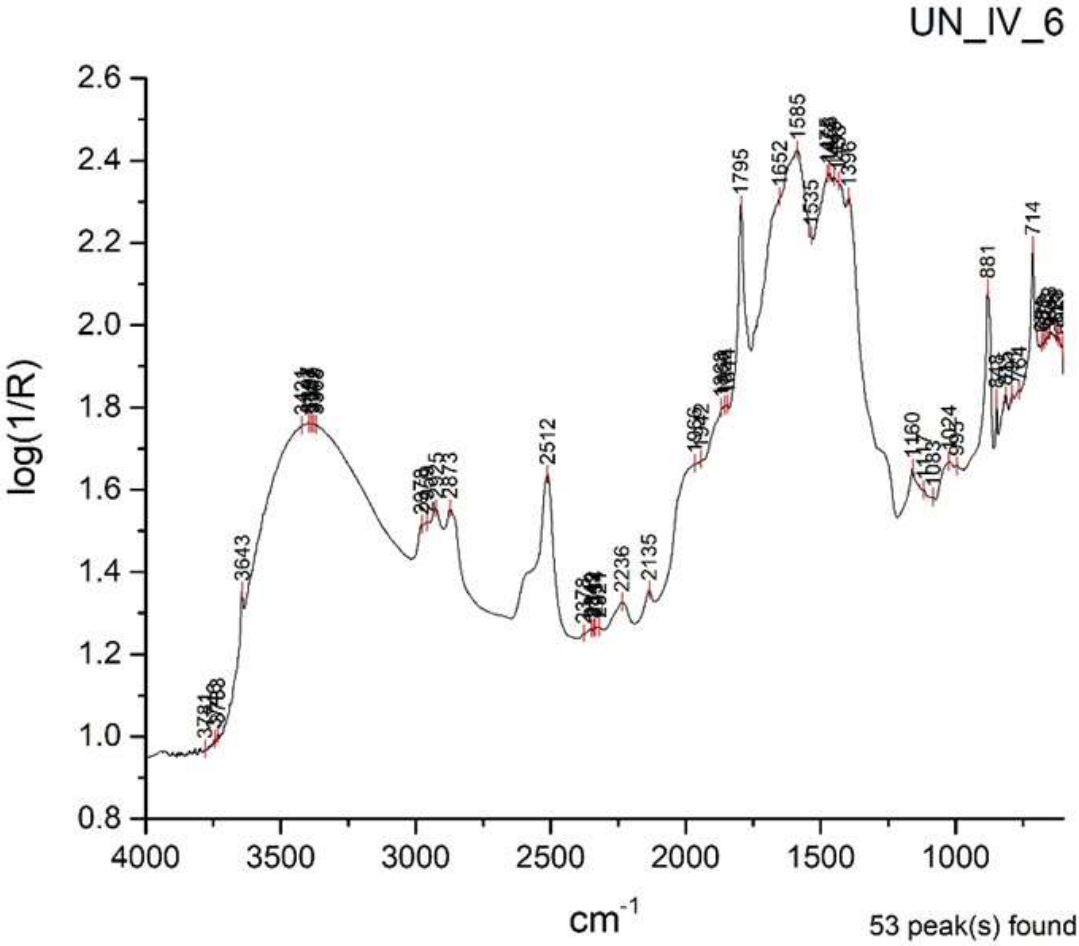

Figure 81: UN_IV_6 falsely identified as 25% rice additive in mortar (R_M_25) instead of the correct 5% milk additive in mortar (Mi_M_5).

Peak x (position)	Spectrum ID	Type of band	Chemical Band Assignement	Reference
621	R_M_25_av	weak absorption	rice	Spectrum R_av
648	R_M_25_av	weak absorption	rice	Spectrum R_av
659	R_M_25_av	weak absorption	rice	Spectrum R_av
688	R_M_25_av	weak absorption	rice	Spectrum R_av
990	Mi_M_5_av	weak absorption	sugar region	Spectrum Mi_av, Synytsya and Novak, 2014, p. 6
995	UN_IV_6	(blank)	(blank)	(blank)
1019	R_M_25_av	strong absorption	rice	Spectrum R_av
1024	UN_IV_6	(blank)	(blank)	(blank)
1083	UN_IV_6	(blank)	(blank)	(blank)
1117	UN_IV_6	(blank)	(blank)	(blank)
1160	UN_IV_6	(blank)	(blank)	(blank)
1396	UN_IV_6	(blank)	(blank)	(blank)
1433	UN_IV_6	(blank)	(blank)	(blank)
1449	UN_IV_6	(blank)	(blank)	(blank)
1466	UN_IV_6	(blank)	(blank)	(blank)
1475	R_M_25_av	weak absorption	C-H bending	Spectrum R_av, Buti et al, 2013, p. 2705
	UN_IV_6	(blank)	(blank)	(blank)
1476	Mi_M_5_av	strong absorption	Amide III	Spectrum Mi_av, Rosi et al, 2009, p. 2099
1518	R_M_25_av	weak absorption	rice	Spectrum R_av
1535	R_M_25_av	weak absorption	rice	Spectrum R_av
	UN_IV_6	(blank)	(blank)	(blank)
1585	UN_IV_6	(blank)	(blank)	(blank)
1652	UN_IV_6	(blank)	(blank)	(blank)
2688	R_M_25_av	weak absorption	(blank)	(blank)
	Mi_M_5_av	weak absorption	(blank)	(blank)
2697	R_M_25_av	weak absorption	(blank)	(blank)
2699	Mi_M_5_av	weak absorption	(blank)	(blank)
2709	R_M_25_av	weak absorption	rice	Spectrum R_av
2857	R_M_25_av	strong absorption	CH stretching	Spectrum E_av, Daher et al, 2017, p.8
2925	UN_IV_6	(blank)	(blank)	(blank)
2926	R_M_25_av	strong absorption	CH stretching	Spectrum E_av, Daher et al, 2017, p.8
	Mi_M_5_av	strong absorption	CH stretching	Spectrum Mi_av, Daher et al, 2017, p.8
2958	Mi_M_5_av	sharp absorption	CH2 stretching	Ploeger et al, 2010, p. 37
2959	UN_IV_6	(blank)	(blank)	(blank)
3009	R_M_25_av	weak absorption	CH stretching	Miliani et al, 2012, p. 302

Figure 82: the unknown spectrum (UN_IV_6) shares the same number of organic peaks with both spectra of standards.

The indication of lipid, combined with the expanded CPAD comparison that includes the inorganic peaks, would have produced the correct identification (fig.83). It is clear that inorganic peaks are equally important to identification since they are influenced by the organic presence. Therefore, inorganic peaks should be included in the CPAD comparisons, especially when spectra of organic/mortar mixtures of low organic concentration are under investigation.

Peak x (position)	Spectrum ID	Type of band	Chemical Band Assignement	Reference
605	UN_IV_6	(blank)	(blank)	(blank)
611	Mi_M_5_av	weak absorption	CaCO3	Spectrum M_av, spectrum Ca_av
619	UN_IV_6	(blank)	(blank)	(blank)
621	R_M_25_av	weak absorption	rice	Spectrum R_av
622	Mi_M_5_av	weak absorption	CaCO3	Spectrum M_av, spectrum Ca_av
628	UN_IV_6	(blank)	(blank)	(blank)
632	Mi_M_5_av	weak absorption	CaCO3	Spectrum M_av, spectrum Ca_av
648	R_M_25_av	weak absorption	rice	Spectrum R_av
	Mi_M_5_av	weak absorption	CaCO3	Spectrum M_av, spectrum Ca_av
653	UN_IV_6	(blank)	(blank)	(blank)
659	R_M_25_av	weak absorption	rice	Spectrum R_av
663	UN_IV_6	(blank)	(blank)	(blank)
672	UN_IV_6	(blank)	(blank)	(blank)
681	UN_IV_6	(blank)	(blank)	(blank)
688	R_M_25_av	weak absorption	rice	Spectrum R_av
714	R_M_25_av	sharp absorption	v4 carbonate ion	Spectrum M_av, spectrum Ca_av, Ylmen and Jaglid, 2013, p. 119
	Mi_M_5_av	sharp absorption	v4 carbonate ion	Spectrum M_av, spectrum Ca_av, Ylmen and Jaglid, 2013, p. 119
	UN_IV_6	(blank)	(blank)	(blank)
764	UN_IV_6	(blank)	(blank)	(blank)
791	Mi_M_5_av	sharp absorption	quartz	Spectrum M_av, spectrum Q_av
	UN_IV_6	(blank)	(blank)	(blank)
793	R_M_25_av	sharp absorption	quartz	Spectrum M_av, spectrum Q_av
815	UN_IV_6	(blank)	(blank)	(blank)
816	R_M_25_av	sharp absorption	quartz	Spectrum M_av, spectrum Q_av
	Mi_M_5_av	sharp absorption	quartz	Spectrum M_av, spectrum Q_av
848	R_M_25_av	sharp and weak absorption	v2 carbonate ion	Spectrum M_av, spectrum Ca_av, Ylmen and Jaglid, 2013, p. 119
	Mi_M_5_av	weak absorption	v2 carbonate ion	Spectrum M_av, spectrum Ca_av, Ylmen and Jaglid, 2013, p. 119
	UN_IV_6	(blank)	(blank)	(blank)
880	R_M_25_av	sharp absorption	v2 carbonate ion	Spectrum M_av, spectrum Ca_av, Ylmen and Jaglid, 2013, p. 119
881	Mi_M_5_av	sharp absorption	v2 carbonate ion	Spectrum M_av, spectrum Ca_av, Ylmen and Jaglid, 2013, p. 119
	UN_IV_6	(blank)	(blank)	(blank)
990	Mi_M_5_av	weak absorption	sugar region	Spectrum Mi_av, Synytsya and Novak, 2014, p. 6
995	UN_IV_6	(blank)	(blank)	(blank)
999	R_M_25_av	weak absorption	CaCO3	spectrum Ca_av
1016	Mi_M_5_av	weak absorption	CaCO3	spectrum Ca_av
1019	R_M_25_av	strong absorption	rice	Spectrum R_av
1024	UN_IV_6	(blank)	(blank)	(blank)
1080	R_M_25_av	sharp and weak absorption	v1 carbonate ion	Spectrum M_av, spectrum Ca_av, Ylmen and Jaglid, 2013, p. 119
1082	Mi_M_5_av	weak absorption	v1 carbonate ion	Spectrum Ca_av, Ylmen and Jaglid, 2013, p. 119
1083	UN_IV_6	(blank)	(blank)	(blank)
1091	Mi_M_5_av	weak absorption	v1 carbonate ion	Spectrum Ca_av, Ylmen and Jaglid, 2013, p. 119
1117	UN_IV_6	(blank)	(blank)	(blank)
1159	R_M_25_av	sharp absorption	quartz	Spectrum M_av, spectrum Q_av
	Mi_M_5_av	sharp absorption	quartz	Spectrum M_av, spectrum Q_av
1160	UN_IV_6	(blank)	(blank)	(blank)

Figure 83: Retrospective CPAD comparison between the UN_IV_6 and the two possible matching spectra of standards. Inorganic peaks are included in the comparison.

1396	Mi_M_5_av	strong absorption	CaCO3	Spectrum M_av, spectrum Ca_av
	UN_IV_6	(blank)	(blank)	(blank)
1397	R_M_25_av	strong absorption	CaCO3	Spectrum M_av, spectrum Ca_av
1432	Mi_M_5_av	strong absorption	v3 antisymmetric stretching CO3-2	Spectrum Ca_av, Ylmen and Jaglid, 2013, p. 119
1433	UN_IV_6	(blank)	(blank)	(blank)
1439	R_M_25_av	strong absorption	v3 antisymmetric stretching CO3-2	Spectrum M_av, spectrum Ca_av, Ylmen and Jaglid, 2013, p. 119
1440	Mi_M_5_av	strong absorption	v3 antisymmetric stretching CO3-2	Spectrum Ca_av, Ylmen and Jaglid, 2013, p. 119
1448	R_M_25_av	strong absorption	v3 antisymmetric stretching CO3-2	Spectrum M_av, spectrum Ca_av, Ylmen and Jaglid, 2013, p. 119
1449	Mi_M_5_av	strong absorption	v3 antisymmetric stretching CO3-2	Spectrum Ca_av, Ylmen and Jaglid, 2013, p. 119
	UN_IV_6	(blank)	(blank)	(blank)
1466	UN_IV_6	(blank)	(blank)	(blank)
1467	R_M_25_av	strong absorption	v3 antisymmetric stretching CO3-2	Spectrum M_av, spectrum Ca_av, Ylmen and Jaglid, 2013, p. 119
	Mi_M_5_av	strong absorption	v3 antisymmetric stretching CO3-2	Spectrum Ca_av, Ylmen and Jaglid, 2013, p. 119
1475	R_M_25_av	weak absorption	C-H bending	Spectrum R_av, Buti et al, 2013, p. 2705
	UN_IV_6	(blank)	(blank)	(blank)
1476	Mi_M_5_av	strong absorption	Amide III	Spectrum Mi_av, Rosi et al, 2009, p. 2099
1518	R_M_25_av	weak absorption	rice	Spectrum R_av
1535	R_M_25_av	weak absorption	rice	Spectrum R_av
	UN_IV_6	(blank)	(blank)	(blank)
1582	R_M_25_av	strong absorption	v3 antisymmetric stretching CO3-2	Spectrum Ca_av, Ylmen and Jaglid, 2013, p. 119
1584	Mi_M_5_av	strong absorption	v3 antisymmetric stretching CO3-2	Spectrum Ca_av, Ylmen and Jaglid, 2013, p. 119
1585	UN_IV_6	(blank)	(blank)	(blank)
1602	Mi_M_5_av	strong absorption	quartz	Spectrum M_av, spectrum Q_av
1612	Mi_M_5_av	strong absorption	quartz	Spectrum M_av, spectrum Q_av
1652	R_M_25_av	strong absorption	quartz	Spectrum M_av, spectrum Q_av
	Mi_M_5_av	strong absorption	quartz	Spectrum M_av, spectrum Q_av
	UN_IV_6	(blank)	(blank)	(blank)
1794	R_M_25_av	combination band	v1+v4	Spectrum M_av, spectrum Ca_av, Ricci et al, 2006, p. 1222
1795	Mi_M_5_av	combination band	v1+v4	Spectrum M_av, spectrum Ca_av, Ricci et al, 2006, p. 1222
	UN_IV_6	(blank)	(blank)	(blank)
1844	R_M_25_av	weak absorption	quartz	Spectrum M_av, spectrum Q_av
	Mi_M_5_av	weak absorption	quartz	Spectrum M_av, spectrum Q_av
	UN_IV_6	(blank)	(blank)	(blank)
1855	Mi_M_5_av	weak absorption	quartz	Spectrum M_av, spectrum Q_av
1856	UN_IV_6	(blank)	(blank)	(blank)
1867	R_M_25_av	weak absorption	quartz	Spectrum M_av, spectrum Q_av
1868	UN_IV_6	(blank)	(blank)	(blank)
1941	R_M_25_av	weak absorption	quartz	Spectrum M_av, spectrum Q_av
1942	Mi_M_5_av	weak absorption	quartz	Spectrum M_av, spectrum Q_av
	UN_IV_6	(blank)	(blank)	(blank)
1961	R_M_25_av	weak absorption	quartz	Spectrum M_av, spectrum Q_av
1966	Mi_M_5_av	weak absorption	quartz	Spectrum M_av, spectrum Q_av
	UN_IV_6	(blank)	(blank)	(blank)

Figure 83: continued.

2135	**R_M_25_av**	weak absorption	**calcium carbonate and quartz**	Spectrum Ca_av, spectrum M_av, spectrum Q_av
	Mi_M_5_av	weak absorption	**calcium carbonate and quartz**	Spectrum Ca_av, spectrum M_av, spectrum Q_av
	UN_IV_6	(blank)	**(blank)**	(blank)
2236	**UN_IV_6**	(blank)	**(blank)**	(blank)
2237	**Mi_M_5_av**	weak absorption	**quartz**	spectrum Q_av
2238	**R_M_25_av**	weak absorption	**quartz**	spectrum Q_av
2511	**Mi_M_5_av**	combination band	**v1+v3**	Spectrum M_av, spectrum Ca_av, Ricci et al, 2006, p. 1222
2512	**R_M_25_av**	combination band	**v1+v3**	Spectrum M_av, spectrum Ca_av, Ricci et al, 2006, p. 1222
	UN_IV_6	(blank)	**(blank)**	(blank)
2688	**R_M_25_av**	weak absorption	**(blank)**	(blank)
	Mi_M_5_av	weak absorption	**(blank)**	(blank)
2697	**R_M_25_av**	weak absorption	**(blank)**	(blank)
2699	**Mi_M_5_av**	weak absorption	**(blank)**	(blank)
2709	**R_M_25_av**	weak absorption	**rice**	Spectrum R_av
2857	**R_M_25_av**	strong absorption	**CH stretching**	Spectrum E_av, Daher et al, 2017, p.8
2872	**Mi_M_5_av**	sharp and weak absorption	**CaCO3**	Spectrum Ca_av, spectrum M_av
2873	**R_M_25_av**	sharp and weak absorption	**CaCO3**	Spectrum Ca_av, spectrum M_av
	UN_IV_6	(blank)	**(blank)**	(blank)
2925	**UN_IV_6**	(blank)	**(blank)**	(blank)
2926	**R_M_25_av**	strong absorption	**CH stretching**	Spectrum E_av, Daher et al, 2017, p.8
	Mi_M_5_av	strong absorption	**CH stretching**	Spectrum Mi_av, Daher et al, 2017, p.8
2958	**Mi_M_5_av**	sharp absorption	**CH2 stretching**	Ploeger et al, 2010, p. 37
2959	**UN_IV_6**	(blank)	**(blank)**	(blank)
2978	**UN_IV_6**	(blank)	**(blank)**	(blank)
3009	**R_M_25_av**	weak absorption	**CH stretching**	Miliani et al, 2012, p. 302
3565	**R_M_25_av**	weak absorption	**quartz**	Spectrum M_av, spectrum Q_av
3643	**R_M_25_av**	doublet	**OH stretching**	Spectrum M_av, spectrum Ca_av, Rosi et al, 2009, p. 2100
	Mi_M_5_av	doublet	**OH stretching**	Spectrum M_av, spectrum Ca_av, Rosi et al, 2009, p. 2100

Figure 83: continued.

The false identification of UN_IV_7 as 5% egg white/mortar mixture instead of the correct plain mortar (M_av) is a matter of bias in the identification protocol, rather than evidence of organic presence. The CPAD clearly showed the absolute match to mortar and the absence of any organic presence in the group frequency region of the unknown spectrum (Appendix I, fig.94-95).

8.2 Summary and discussion

The experiment tested the proposed identification methodology and through that, the ability of External Reflectance FTIR micro-spectroscopy to detect and identify organic additives in mortar matrices.

The identification of unknown spectra using the Chemical Peak Assignment Database developed from the analysis of standards and literature, is twofold in its operation:

1. Chemical characterization of an unknown spectrum according to the Spectral Interpretation Outcomes (Sect. 7.5 and 7.6).
2. Comparative assessment of an unknown spectrum with possible matching spectra.

Number of Trials	Success	Test Performance %	Comment
40	32	80%	Including 2 false identifications and 6 false identification of concentration
40	38	95%	Excluding 6 false identifications of concentration

Table 16: Overall performance of the identification methodology tested through the Experimental sets I-IV.

A 95% successful identification of the organic additive indicates that the CPAD methodology has a high level of reliability (Table 16), especially when considering that the available alternative method of identification relies on visually comparing spectra that poses practical constraints, as described in sections 7.4 to 7.6. This level of successful identification is encouraging, for the primary goal of successfully identifying the presence of a deliberately added organic component. Calculated as a function of the total number of false identifications the CPAD was 80% successful (table 16), as detecting concentration may be of limited value in the study of archaeological samples that likely have undergone degradation leading to reduction or total loss of additives during burial. The overall performance could have been even higher as the CPAD user's experience increases with its use, since 5 out of 6 misidentified concentrations could have been avoided by better interpretation of the CPAD information. This is potentially evidenced by Experimental set I having three organic additive concentration misidentifications, Experimental set II two and Experimental set III none.

Experimental set IV produced many successful outcomes, despite the increased difficulty of identification supplied by the more complex set of unknown spectra. In this set too, it

was identified that mistakes could have been avoided by better interpretation of the CPAD spectral information. In the case of spectrum UN_IV_ 7, falsely identified as 5% egg white additive in mortar instead of plain mortar, could have been avoided if the identification relied solely on the CPAD spectral information, without the personal bias of what was expected to be found. This aspect of human nature and bias is something to consider in relation to all such detection regimes; the desire to find a product is present.

8.2.1 Advantages of the CPAD methodology

The analysis of organic additive/mortar mixtures of decreasing organic concentration assessed qualitatively the influence of inorganic presence in the absorption intensities of the organic additive (sec. 7.5). Shifting of wavenumber due to the differing concentrations, newly formed spectral patterns that included absence/presence of diagnostic peaks and weak peaks, were accessible through the CPAD and available for comparative assessment. The advantage of the CPAD relies on the ability to assess and compare even the smallest change in spectral characteristics deriving from changes in concentration.

The correct identification of concentrations in the majority of unknown spectra and the fact that misidentified concentrations were close to the true concentration, either just above or below it, shows the effectiveness of the CPAD to identify the best matching spectrum. Concentration serves the qualitative assessment of the methodology to support accuracy of identification, rather than providing data for quantitative studies.

The CPAD cannot be used for quantitative approximations outside the experimental/laboratory framework, since the spectral projection of an organic additive in a mortar mixture can be affected by its viscosity. This was evident in the identification of UN_III_1 correctly identified as 75% rice/mortar mixture, where the projection of the organic additive on the spectrum resembled that of high inorganic content mixture.

A fundamental advantage of the CPAD methodology is the minimum requirement for visual spectral comparisons between an unknown spectrum and possible matching spectra of standards, where weak peaks and minor peak shifting are easily and understandably often overlooked. The CPAD experiment demonstrated the importance of these weak peaks and shifts in peak position for accurate identification using reflectance micro-FTIR spectra. These features could only be assessed through the CPAD and assigned as diagnostic, as within visual comparisons of spectra overcrowded with peaks, their assessment is practically impossible and this is evident in the plethora of assigned peaks in the spectra included in this thesis. The similarities between the spectra of low concentrations of milk

and rice mortar mixtures demonstrated further the potential for error in visual spectral comparisons. The influence of viscosity in the spectral representation of the particular organic components and excessive inorganic interference with diagnostic peaks identified the necessity to examine weak peaks and position shifting through the CPAD.

Reflectance FTIR micro-spectroscopy has not been extensively used in the detection and identification of organic/mortar mixtures, databases and chemical assignments from literature are either not widely available or are limited to chemical characterization of pronounced peaks (Ch.3). By offering a great deal of detailed information, the CPAD makes a strong contribution to filling this gap.

8.2.2 Complementary diagnostic data

This use of the CPAD in practice on unknown mixtures, was a testing procedure and yielded data to compliment and improve the information on diagnostic peaks defined in sections 7.5 and 7.6, increasing understanding of how to use the CPAD. The experiment also identified lessons to be learnt. Collectively these enhancements are:

- The presence of OH stretching above 3000 cm^{-1} and its shape/intensity is diagnostic to organic materials such as rice solution, egg white, egg yolk, egg and milk, indicating water molecules. Absence of this feature is diagnostic to bone glue, asphalt, oil and lard.
- The group frequency region of lipids is the least affected by inorganic components compared to that of amides.
- The best identification candidate of an unknown spectrum is the one that exhibits either complete matches between wavenumbers or peak shifting no greater than 4 cm^{-1} in either side of the peak.
- Organic additives such as olive oil and lard are chemically similar and this is also visible in their mortar mixtures. Weak peaks and their characteristics are used to discriminate the one material from the other. The peak at 1702 cm^{-1} for oil additive is absent in spectra of lard and its mixtures. The shape and intensity of peaks within 1686-1613/1540 cm^{-1} form a pattern characteristic to lard/mortar mixtures that is absent in oil/mortar mixtures.
- Inorganic peaks are also diagnostic, especially to organic/mortar mixtures of low organic concentration, since they are too influenced by organic presence.
- Stair-step type intensities for proteins in the fingerprint region (1400-700 cm^{-1}) and derivative-like peaks for lipids in the group frequency region (above 1700 cm^{-1}) should be taken into account during identification.

- Mistakes can be made, even in characteristic spectra such as asphalt when solely relying on the appearance of the spectrum and disregarding weak peaks that define the inorganic presence and concentration in the mortar mixture. The specific mistake highlights the misleading potential of visual comparative assessment of spectra against the effectiveness of the CPAD methodology.

The term “diagnostic peaks” defined in section 7.6 was clarified further after the experiment: in order for a specific compound to be identified in a spectrum, certain peaks need to be present. This is straightforward for spectra of pure organic materials. However, in the case of organic additive/mortar mixtures, diagnostic peaks change to diagnostic/inorganic combination peaks which are influenced by the concentration of the inorganic component. In certain cases, major diagnostic peaks are highly masked by the inorganic component, leaving the weak peaks, which seem to be less affected, to determine the chemical composition of the organic. The assignment of such peaks as diagnostic is feasible through the CPAD, providing an in depth understanding of the behavior of an organic additive in the mortar matrix.

Accordingly, improvements can be made in the use of the CPAD and the identification methodology:

- The selection of peaks of interest (diagnostic) for an unknown spectrum for entering the CPAD should also include inorganic peaks.
- The presence of diagnostic peaks of the unknown spectrum should match those of possible identification candidates either in absolute matching or low peak shifting.
- The possible identification candidates should then be assessed for diagnostic peaks that should also appear in the unknown spectrum for a match to be defined.
- The inorganic peaks and their characteristics relative to their co-existence with the organic component should be assessed, especially when their presence indicates high inorganic concentration.

The experiment validated the effectiveness of the identification methodology defined in Chapter 7, provided additional information that improved the identification steps and revealed that the degree of bias present in visual comparisons is reduced by using the CPAD. Inorganic interference and reflectance distortions are overcome and are diagnostically employed in the CPAD. Within the limits of this experimental structure, the Chemical Peak Assignment Database can be used to detect and identify organic additives in mortar mixtures.

The effectiveness of the CPAD was tested on carefully prepared analogues in controlled conditions within the laboratory. Standards were prepared from fresh organic materials that provided spectra containing all the diagnostic chemical features necessary for their identification, there had been no change in bonding or loss of components due to decay of the organic. Two inorganic components used in the preparation of the mortar, calcium carbonate and quartz, influenced changes of the diagnostic peaks of the differing concentrations of organic additives. While this analogue approach based on knowledge of additives used in the past and mortar composition proved that the principle of the method was effective, the reality of analyzing ancient mortar samples involves more complex spectra whose chemical composition has likely been subjected to decay and/or contamination with external depositions from their surrounding environment.

These issues are assessed in Chapter 11, where the identification tool is used to examine ancient mortars, with the remit of detecting and identifying organic additives. To do this, the CPAD is updated and extended with spectra of new standards derived from external depositions and additives likely to be present according to the dating and sampling location of the ancient mortar samples. Prior to this testing, the potential role of statistics for improving the effectiveness of the CPAD is explored.

Chapter 9: Principal Component Analysis

Chapter 9 is devoted to testing the applicability of Principal Component Analysis (PCA) in this thesis, as it is frequently used as a complementary method to spectroscopy in studies dealing with large numbers of spectra (Sect. 9.2, Table 17). Cultural Heritage studies employing FTIR spectroscopy and PCA are reviewed and compared to spectroscopy studies in other scientific disciplines with a focus on examining the purpose behind using PCA, the methodology used to apply it and how the results are interpreted.

The outcomes of the review are incorporated in a series of PCA tests conducted on spectra used in the thesis, with the aim of evaluating the effectiveness of PCA as a complimentary identification tool to the CPAD methodology (Ch.10).

9.1 Theory and Application in Spectroscopy

Multivariate data, such as those collected in spectroscopy, consist of a vast number of variables (wavenumbers) and their corresponding values (absorption intensities). Identification of materials by visual inspection and spectral comparisons underutilizes the amount of available data since only the most pronounced absorption peaks can be used. Thus, patterns and relationships among variables of different materials may remain hidden (Miller and Miller, 2010, 224).

Such issues were encountered during the identification experiment (Ch.8) and successfully dealt with by the appropriate use of the Chemical Peak Assignment Database. However, PCA has the potential to provide further validation of the CPAD methodology.

Most multivariate statistical methods aim to reduce data while retaining the systematic variation of the data matrix. In doing so, data that are considered redundant are separated from the ones carrying most of the information (Miller and Miller, 2010, 224). Such methods are divided into; a) unsupervised pattern recognition methods and b) supervised pattern recognition methods. Principal Component Analysis is an unsupervised pattern recognition method, being considered the basis of multivariate data analysis (Christer, 2005, 39).

PCA is used in the classification of objects of similar properties (samples/materials in question), especially when there is no prior knowledge of the number of groups to be expected or the influence of variables in the classification patterns (Miller and Miller, 2010, 231). Accordingly, it is expected that the classification of an unknown object (spectrum) to

a group of standards of similar chemical composition would result in its identification. This aspect is assessed through the PCA tests conducted in this chapter (sect.9.4 and 10).

PCA enables the reduction of multivariate data matrices ***X*** formed by ***N*** rows (objects = samples) and ***K*** columns (variables) (Christer, 2005, 39). Data reduction can only be performed on correlated values, such as those obtained in spectroscopy (Miller and Miller, 2016, 224).

In algebra terms, PCA finds principal components Z_1, Z_2…...Z_n (or PC1, PC2…PC_n) which are linear combinations of the original variables describing each object, according to equation 9.1 below:

Equation 9.1: $\mathbf{Z_1 = a_{11}X_1 + a_{12}X_2 + \ldots a_{1n}X_n}$,

where $x_1 \ldots x_n$ are the IR intensities of each object at a given variable (wavenumber) and a_{11}, a_{12} etc. are coefficients (or eigenumbers) that produce new non-correlated variables. The process is repeated for $Z_2 \ldots Z_n$ with computed coefficients for each PC and for each object. The coefficients derive from the *eigenanalysis* of the covariance matrix of variables and the calculation of variance among them. The degree of variance is expressed by the eigenvalue of each PC and reflects the variation among the data set for the given PC (Smith, 2002, 14; Miller and Miller, 2016, 225).

The new dataset has the same number of objects and variables but different values due to the different coefficients used in each PC, so reduction is not yet achieved. However, the calculations allow the first few PCs for each object to account for the highest variation in the dataset in decreasing order (Miller and Miller, 2016, 224).

The objects are then projected on a new two-dimensional orthogonal plane formed by the selected PCs (e.g., PC1vsPC2). The horizontal axis shows the projection of objects in the plane according to the highest variance (PC1) and the vertical axis according to the next highest one (PC2). The object co-ordinates on the new plane are called *scores* resulting from equation 9.1 (Miller and Miller, 2010, 226). This is where data reduction is achieved. The objects are now visible by observing their position according to the selected PCs instead of plotting their original variables on an orthogonal system, a non-feasible action due to the vast quantity of variables which would require an N dimensional plane.

In the PCs plane it is possible to observe relationships among objects of similar properties. The *loadings* represent the projection of the variables into the two-dimensional plane and are used to understand their contribution to the projection of scores (objects) and also the

relationship between variables on the specific two-dimensional PC plane (Christer, 2005, 48).

The biplot below shows the positioning of 8 organic standards in the PC1vsPC2 plane resulted from the calculation of variance among the variables 3000-2800, 1760-1680 and 1500-1300 cm^{-1} (fig.84). The resulting PC1 explains the 60.18% of the total variance of the data set and PC2 the 23.41%. Within this condition, it is possible to examine the relationship among objects (organic standards) relevant to similarities in their chemical composition as they are expressed by the systematic variation of the data matrix. The spreading of loadings in the plot shows the contribution of variables in the positioning of the standards.

Certain groups and sub-groups are formed in the plot (fig.84): PC1 separates olive oil from the rest of the organic standards which are positioned within one large group. The strong shifting of PC1 towards olive oil demonstrates the differentiation of the particular standard from the rest, based on the selected variables. PC2 is the principal component that sub-divides the large group of the remaining 7 organic standards into smaller groups based on chemical similarities. Egg white and bone glue are placed in the same quadrant due to their similarity in the protein content and their low variance in the regions 3000-2800 and 1760-1680 cm^{-1}. Whole egg and milk are placed in close proximity to proteins because of the similar chemical composition but differ due to the additional presence of lipids. A third distinct group is formed by lard and egg yolk due to the dominance of lipids in their chemical composition. Rice is isolated from the rest, although some relationship with milk is assumed due to the low variance of their absorption intensities in the region 1500-1300 cm^{-1} deriving from the sugar content.

The example shows that the selection of variables was adequate in achieving chemical classification of the organic standards and verified the observations made in Chapters 7 and 8 relevant to their spectral similarities and differences.

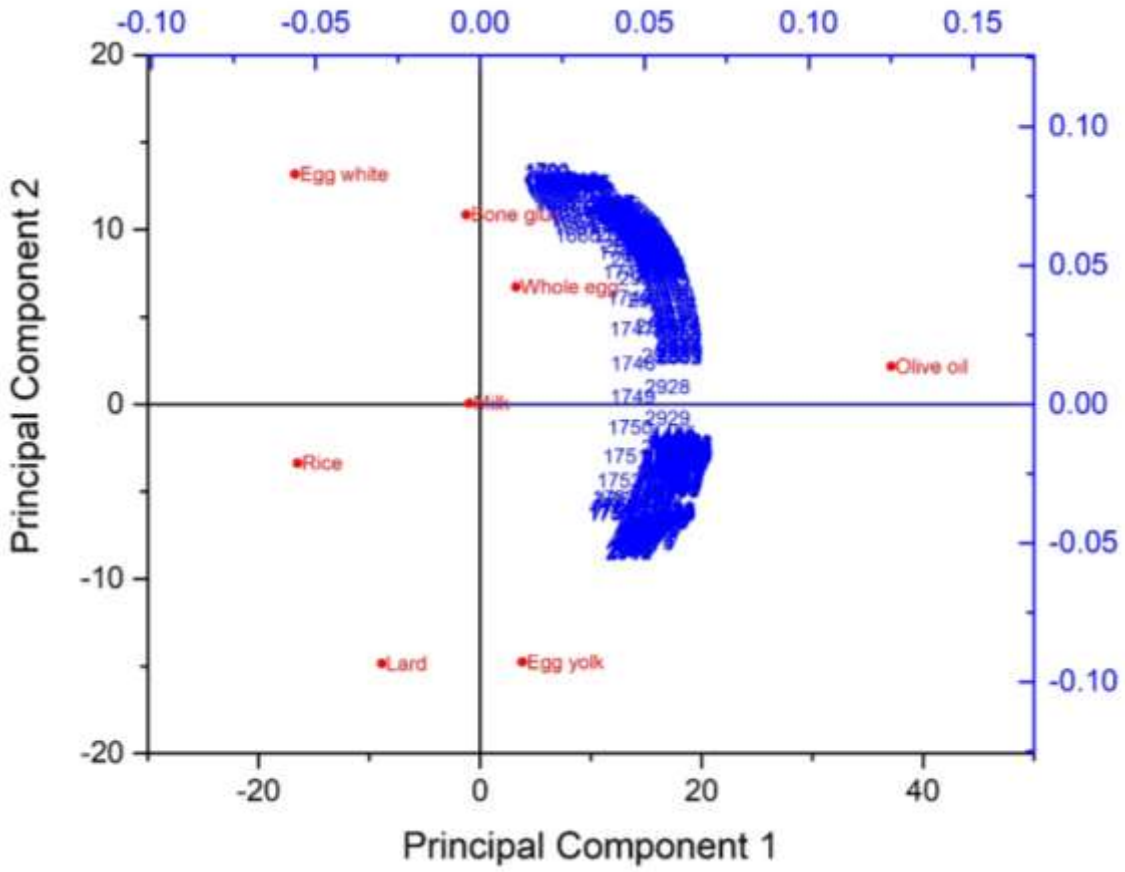

Figure 84: The classification of organic standards in the PC1VsPC2 biplot.

9.2 Review of available literature

Table 17 summarizes case studies that combine spectroscopy with statistical analysis, focusing on PCA applications. Most of the reviewed case studies derive from Cultural Heritage (CH) due to their relevance to the thesis. Case studies from other scientific disciplines such as organic chemistry (OC), biology (BI), forensics (F) and food industry (FI), as well as tutorials in statistics (T), are reviewed and compared to those of Cultural Heritage in order to understand the rationale behind PCA selection and purpose of use, the employed PCA methodologies and the interpretation of PCA results. The outcomes were utilized in the design of PCA models to be tested on the spectral data of the thesis.

Author(s)	Topic	Analysis / Statistics	Variables	Objects	Pretreatment and Matrix	Interpretation Process	Comments
Andersen et al, 2017, CH	Protein identification	FTIR-ATR, µFTIR / PCA	6 protein peaks from both analytical methods.	121 protein standards and 2 unknowns.	Not stated.	No discussion on process and outcomes.	Variables less than objects.
Arizio et al, 2013, CH	Inorganic mortar content	FTIR, TG/DTA, IC, Calcimetry / Cluster analysis, PCA	8 variables from different analytical methods.	16 samples	Auto-scaling and hierarchical agglomerate methods.	Ward's and Single Linkage clustering of variables and objects seperately, Euclidean or 1-r Pearson distances, PCA Loading plot and score plot seperately.	Separate representation of variables and objects and then comparison and cross-reference, variables less than objects, autoscaling because variables are in differen counts.
Bacci et al, 1997, CH	Calcite stone degradation	NIR Diffuse Reflectance / PCA	1001	30	1200-2200 cm^{-1}, subtracted reflectance value from 1st cm^{-1} from each spectrum, then matrix centered with respect to the mean spectrum, 2nd normalization when spectra of both mixtures and tablets were used by dividing each row elements by the sum of all row elements.		
Daveri et al, 2008, CH	Identification of organic binders in wall paintings	Reflectance Mid FT-IR / PCA	Entire spectrum.	174	Baseline corrected in the last 100 variables and divided by the average value calculated on the entire spectrum.		

Table 17: Summary of selected spectroscopy/statistical analysis studies and statistic tutorials.

Author(s)	Topic	Analysis / Statistics	Variables	Objects	Pretreatment and Matrix	Interpretation Process	Comments
Gonzalez and Wess, 2008, CH	Collagen degradation in parchment	ATR-FTIR, XRD	5	20	Average spectrum from 19 samples was subtracted from each spectrum, the 5 differences on the remaining spectrum are expressed as basic functions.	Each function describes a spectral component that changes, they are numbered according to their weighing (biggest change) and each sample is given an eigenvalue that is graphically represented.	
Medeghini et al, 2016, CH	Archaeological ceramics - pottery production classification	pFTIR / PCA	Initial spectral range (1089 variables), gradually reduced (799 variables).	59	Normalized between 0 and 1, second derivative in the region 1500-400 cm^{-1}.	First elaboration -0.3 and +0.3 removed, then gradually removing loading values -0.4 and +0.4 up to -0.7 and +0.7.	Series of elaboration, i.e.gradually reducing variables by excluding the lowest loading values going to the second lowest.
Moropoulou and Polikreti, 2009, CH	Building materials - classification and origin	NAA / Hotelling's T2 (propability of a sample to belong to each group), PCA	PCA: 7 variables from different analytical methods.	Seems that they use more objects than variables.	No pre-treatment info.	Standard probability ellipses for 90% confidence limits.	
Nielsen and Kristiansen, 2014, CH	Identification of ancient manuring in soil	ICP-MS / Shapiro-Wilk test for normality, Mann-Whitney non parametric test, PCA	42	58 (5 of which are reference).	Standardized / normalized (subtracting mean values of each element from the value of the element and then taking 1/STD from the element multiplied with √(N-1)), correlation matrix.		
Noake et al, 2017, CH	Identification of synthetic polymers	pFTIR-ATR / PCA	2000-700 cm^{-1} spectral range.	121	No pre-treatment since past pre-treatment showed bad results.		Not good separation, use of 2nd derivative is not recommented since broad bands are removed.

Table 17: continued.

Author(s)	Topic	Analysis / Statistics	Variables	Objects	Pretreatment and Matrix	Interpretation Process	Comments
Pina-Torres et al, 2017, CH	Classification of resins	FTIR-KBr / PCA, LDA	11 variables, band selection, max of absorbances.	42	Covariance matrix.	PCA 2D and 3D plots, LDA leave-one-out method, confusion matrix and cross validation matrix.	States problems when using entire spectra.
Romero-Pastor et al, 2013, CH	Heat-induced alterations in paintings (organic and bone)	ATR-FTIR, Raman / PCA	Raman PCA: 1730-650, 833-912 $cm^{-1.}$ FTIR PCA: 1700-760, 1730-950 cm^{-1}.	40	No pre-treatment, coveriance and correlation matrices (better outcomes).	Selection of variables depending on the question.	
Rosi et al, 2009, CH	Identification of organic binders in wall paintings	Reflectance pFTIR, FTIR transmittance, micro-FTIR / PCA	4000-1000 cm^{-1}.	48 (4 from each standard), 2nd attempt = 150, 3rd attempt = 120, depending on the question.	Baseline and overall intensity corrections, normalization (100 variable method), correlation matrix.	Loading profiles due to the high number of variables, second reduction of variables (no info).	Looking at higher PCs because of inorganic interference on the first PCs.
Rosi et al, 2010, CH	Identification of organic binders in paintings	midFT-IR / PCA	Spectral regions.	650	Baseline correction / normalization (100 variable method): removing baseline and overall intensity of each element of the matrix by subtracting the average value of the last 100 variables and then normalize by dividing the average value calculated on the entire spectral range.		
Sarmiento et al, 2011, CH	Classification and identification of binding media	FTIR-KBr / PCA	3000-2500 and 1730-1750, 2000-1000 cm^{-1}.	Less than variables.	Baseline correction, removal of 2300 cm^{-1} band, variables scaled and centered, correlation matrix (likely).	Checking up to PC3 depending on the explained variance.	They tried different regions depending on what they examined (e.g. 2000-1000 cm^{-1} for glues).

Table 17: continued.

Author(s)	Topic	Analysis and Statistics	Variables	Objects	Pre-treatment and Matrix	Interpretation Process	Comments
Sciutto et al, 2012, CH	Painting cross sections identification	μFTIR-ATR mapping and imaging / PCA	685,780, and 2800–3600 cm^{-1}.	More than 200 for each sample.	Savitsky-Golay derivative, baseline correction, correlation matrix.		Describes the use of loading profiles.
Sciutto et al, 2017, CH	Painting cross sections, multivarite chemical mapping	μFTIR-ATR mapping / PCA	Spectral regions.	192	Different for each row sample, linear detreding, SNV (or row auto-scaling), column auto-scaling, column centering different for each sample, PCA by using NIPALS algorithm.	Loading values and profiles description of their use.	
Bro and Smilde, 2014, T		PCA	14	44	No need when variables are measured in the same scale.	Use both the PCA scores and the residuals, take note on the plot distances and scales.	Very important tutorial.
Christer, 2005, T				Less than variables.	Description of Scaling, Mean centering for data measured in different scales.	Score plot interpretation, distance of objects from plot center.	
Cordela, 2012, T		1N-NMR / PCA	1001	189			Examples of use of PCA on spectra.
Johnstone and Yu Lu, 2009, T	PCA				Transformation of data in orthogonal basis (e.g. wavelet).		Focuses on mathematic description but some info on data reduction.
Miller and Miller, 2010, T	Statistics		Suggest to reduce number of variables.				
Shlens, 2014, T		PCA				Non-parametric method.	Describes limitations of PCA relevant to applications.
Smith, 2002, T		PCA			Unit variance scaling not necessary for spectra.		

Table 17: continued.

Author(s)	Topic	Analysis and Statistics	Variables	Objects	Pre-treatment and Matrix	Interpretation Process	Comments
Hori and Sugiyama, 2003, OC	Chemical variations between softwood species.	Transmittanse FTIR / PCA	1200-800 cm^{-1} (109 variables).	209	Normalized, smoothed, 2nd derivative, all within ROI.	Use of loading spectra.	
Riba et al, 2018, OC	Classification	ATR-FTIR / PCA, CVA, kNN	PCA: entire spectrum, reduced variables derived from PCA to CVA and kNN.	Less than variables.	Raw data, then 1st (Savitzky-Golay, 5 points either side, best) and 2nd derivative.		CVA reguires objects more than variables, PCA is used for the reduction of variables.
Rohman et al, 2011, OC	Product analysis.	FTIR / PLS, PCR				Leave-one-out cross validation, RMSEC (root mean error of calibration), coefficient of determination R2 and RMSEP (prediction).	Quantitative analysis of prediction.
Saute et al, 2012, OC	Identification of pesticides.	Raman / Barcode PCA			Normalized, converted to barcode i.e. a series of zeros and ones based on the sign of the 2nd derivative. Minumum value aprox. 10% of the maximim. 2nd derivative - threshold for zero (one).		Similarities with the approach of Joanstone and Yu Lu (waveletes).
Chauhan et al, 2018, F	Trace evidence in soil.	ATR-FTIR / LDA, PCA			Normalized to 0 or 100 (better), for LDA used selected PCs whose eigevalues are >1. PCA = 1800-426 normalized, KMO, Bartlett's test of sphericity, checking adequacy of sample Kaiser-Meyer-Olekin KMO before and after PCA, Varimax rotation.	LDA: Wilk's λ statistics for checking effectiveness of the model, parsial Wilk's λ, post hoc classification of training dataset.	Normalization on table of peaks seems that intensity is not taken into account.

Table 17: continued.

Author(s)	Topic	Analysis and Statistics	Variables	Objects	Pre-treatment and Matrix	Interpretation Process	Comments
Kher et al, 2006, F	Classification of inks.	HPLC, DRIFTS / SIMCA-PCA, LDA	4 wavelenghts, 103 variables (SIMCA-PCA, LDA), PCA-LDA: 2000-650 cm^{-1} (PCA reduction), residuals and discrete spectral features.	96	No data reduction before LDA, mean centered, covariance PCA using cross validation for data reduction before LDA, block normalized, unit scaled.	PCA scores and residuals were then used in LDA, also discrete spectral features.	Additional methods to detect outliers, explains the steps of PCA-decomposed data matrix.
Santos-Silva et al, 2013, F	Classification of inks.	ATR-FTIR / PCA, LDA-SPA, LDA-GA	3 algorithms for variable selection: succesive projection algorithm (SPA), SW and leave-one-out cross validation, GA, apparently entire spectrum.		Several different methods, all tested by PCA. Best: SNV, 1st Savitzy-Golay derivative.		
Bonnier and Byrne, 2012, BI	Discrimination of different samples from their chemical composition and identification.	Raman / K-means, PCA mapping.	Entire spectrum.	Depends on the balanced and inbalanced dataset some spectra are duplicated.	Savitsky-Golay filter smooting (5th order and 7 points), subtraction of background signal spectrum, baseline correction / vector normalization.	K-means - number of clusters known a priori, PCA loading spectra are compared to subtracted spectra from the original ones, balanced and inbalanced matrices.	Describes the use of loading profiles.
Mobili et al, 2010, BI	Discrimination of microorganisms.	Raman / PCA, PLS-DA, leave-one-out.	Entire spectrum and 2 regions, 1700-1500 cm^{-1} best.		Polynomial function, best fitting, hand made and subtracted for PLS-DA, Raw data in PCA.		Good explanation, use of spectra regions where most differences are located.

Table 17: continued.

Author(s)	Topic	Analysis and Statistics	Variables	Objects	Pre-treatment and Matrix	Interpretation Process	Comments
Bardin et al, 2014, FI	Coffee quality and chemical discriminatio n of varieties.	FTIR / Review of different statistics (PCA, LDA, PLS).	Mostly spectral ranges.				
Bureau et al, 2009, FI	Determinatio n of components in fruit juice.	FT-MIR / PCA, PLS	Entire spectrum.	757	Standard normal variate (SNV).	Validation by RMSEC (root mean error of calibration), coefficient of determination R2 and RMSEP (prediction).	
Christou et al, 2018, FI	Carob origin.	FTIR-ATR, KBr / PCA, CA, PLS, OPLS-DA	Entire spectrum and specific ranges (4000-2500 cm^{-1}).		Baseline correction, normalization transcuted to 250 points. PCA mean centered, UV scaling, log transformation. The same for 1st derivatives.		
De Luca et al, 2011, FI	Classificatio n.	ATR-FTIR / CA (hierarhical), PCA, PLS, PLS-DA	CA: entire spectrum, PLS-DA: regions after Marten's Uncertainty Test.	29 (21 calibration, 8 validation).	MSC, SNV, Derivative (best) - Savitsky-Golay, 2nd order, nember of smoothing points 5, polynomial order 2.	RMSEP and R2 for validation of PLS-DA.	

Table 17: continued.

9.2.1 PCA selection and purpose of use

Principal Component Analysis is the primary and most popular statistical method among the case studies reviewed, followed by Cluster Analysis and Linear Discriminant Analysis (LDA) in two cases (Table 17).

PCA in Cultural Heritage (CH) has been employed for:

- **Classification** of materials in respect to concentration (Arizio et al., 2013), origin (Medeghini et al., 2016; Moropoulou and Polikreti, 2009) and chemical composition of resins (Pina-Torres et al., 2017).

- **Identification** of proteins (Andersen et al., 2017), organic binders in wall painting (Daveri et al., 2008; Rosi et al., 2009; 2010; Sarmiento et al., 2011; Sciutto et al., 2012; 2017), manuring in soil (Nielsen and Kristiansen, 2014) and synthetic polymers (Noake et al., 2017).
- **Degradation alterations** of stone (Bacci et al., 1997), collagen (Gonzales and Wess, 2008) and paintings (Romero-Pastor et al., 2013).

The three PCA applications above are essentially different types of classification. In all cases the goal is to group materials of similar properties together.

PCA is highly popular in Food Industry (FI) as a preliminary method of classification of edible products. However, supervised pattern recognition methods such as Partial Least Squares (PLS) and Linear Discriminant Analysis (LDA) are preferred, as well as other statistical methods based on these two (Bureau et al., 2009; Yang et al., 2005; Christou et al., 2018). Such methods work with large training sets of objects of known composition that are used for finding a rule of classifying new objects of similar chemical composition (Miller and Miller, 2016, 237). Biology (BI) and Forensics (F) follow the same combination of unsupervised and supervised pattern recognition methods, since both sectors deal with materials of similar chemical composition and large reference datasets. Less standardization in respect to method selection is encountered in Organic Chemistry (OC) studies, although PCA is the most frequently used.

Multivariate statistical analysis is not routinely employed in Cultural Heritage, as is evident from the relatively small number of such case studies in Table 17. The issue has been acknowledged by authors dealing with the identification of paint cross-sections by FTIR spectroscopy (Sciutto et al., 2012). However, when statistical analysis is employed, PCA seems to be the preferable method, likely due to the minimum requirement of theoretical background in statistics and data pre-treatment.

Supervised pattern recognition methods are not popular in Cultural Heritage. This is especially true in non-destructive FTIR spectroscopy studies in which the materials to be analyzed are often composite or show similarities from the presence of inorganic components rather than original chemical composition (Rosi et al., 2009). Consequently, training datasets such as those used in Forensics and Food Industry for classifying new objects in already known groups of relatively singular types of materials (e.g., inks and coffee varieties) are not available.

Issues of misleading chemical similarities induced by inorganic interference in the study of organic mortar additives may too, pose constraints on the use of an unsupervised pattern recognition method such as PCA, since the outcomes may not reflect the organic similarities. This issue forms an important objective of the PCA testing in the thesis and is discussed in section 9.4 and chapter10.

9.2.2 PCA methodology

As described earlier, PCA produces classification of objects of similar properties, or in statistical terms, groups of low variation. Accordingly, it is expected that matrix construction (selection of objects and variables) and data pre-treatment for the removal of variables that do not carry information and/or increase correlation among variables, are the parameters to be considered in PCA for obtaining strong principal components that reflect the true variance in the dataset (Daveri et al., 2008; Christer, 2005).

Theoretically, PCA being an unsupervised pattern recognition method, should be applicable in matrices consisting of as many objects in question and their entire spectra as variables, where all the wavenumbers and their corresponding IR absorption intensity values are used in the calculation of the total variance.

However, in practice this is not the case: according to Table 17, the selection and ratio of variables vs objects differ considerably in each case study, although a preference is shown in the use of specific spectral ranges (e.g., 2000-700 cm^{-1} (Noake et al., 2017)) or selected variables instead of the entire spectrum. In most case studies variables are more than objects.

Tutorials use variables less than objects, likely for simplicity in order to explain the construction of the matrix and the calculation of covariance (Miller and Miller, 2010, 223; Smith, 2002). Cordela follows this simplified manner but also provides spectroscopy examples where variables are more than objects (2012). Bro and Smilde use variables less than objects, focusing on the interpretation of PCA scores and residuals (2014). Johnstone and Yu Lu discuss data reduction prior to PCA (2009). The Cardiff Mathematics centre suggests performing PCA on variables less that objects, following a rule of thumb of variables counting for the 2/3 of objects (personal communication, drop-in statistics sessions in the School of Mathematics, October 2017).

It seems that most case studies are aiming for data reduction prior to PCA. Based on PCA theory, the systematic variation in a dataset should derive from representative variables expressed by the resulting PCs and would expose the redundant ones. It is assumed that

variables from spectral regions of low-signal-to-noise ratio or detector interference can be disregarded from the start as redundant since they could lead to low variation among objects, thus false classification. Such regions do not carry chemical information and would interfere with the interpretation of the PCA outcomes and the positioning of the objects within the PC plot.

Accordingly, case studies that use spectral ranges (regions of the spectrum) or selected variables (wavenumbers) are focusing on those carrying chemical information relevant to the objects in question (Romero-Pastor et al., 2013). Medeghini et al., perform PCA on spectral ranges and gradually reduce variables based on the PCA loadings (2016).

The way in which these statistical methods work projects the highest variance within a data matrix, hence the outcomes will be influenced by the data selection performed by the analyst. Thus, initial data selection should be carefully considered and guided by a clear rationale for rejecting spectral regions.

Accordingly, it is expected that in the identification of organic mortar additives from spectra of organic/mortar mixtures, spectral regions of inorganic presence would increase correlation among the spectra and should be removed from the PCA matrix.

The paper that explores the influence of data selection and its pre-treatment is provided by Bonnier and Byrne (2012). The amount of data used in PCA, the type of data and manipulation of the datasets produce different outcomes that reflect the choices of the analyst. Bonnier and Byrne also employ K-means Clustering for color-mapping the areas of spectra origin on biological cell samples. The method requires pre-determination of the number of clusters to be formed and this may lead to biased outcomes (Miller and Miller, 2016, 228; Bonier and Byrne, 2012, 324). However, the method was successfully used since spectra origin was known.

It is assumed that in spectra of complex chemical composition, such as in those from organic/mortar mixtures, different PCA models need to be applied in order to study the resulting classifications.

In case studies where PCA is followed by supervised pattern recognition methods, such as Partial Least Squares (PLS) and Linear Discriminant Analysis (LDA), the matrices include entire spectra since PCA is used for data reduction. Such studies derive mainly from Forensic, Biology and Food Industry where LDA is the main classification method.

9.2.3 Pre-treatment of data

Another important issue that arises from reading the selected literature is the lack of standardized pre-treatment of data and there is a question as to whether it is required. Data pre-treatment aims to remove variables that do not carry information and is performed by baseline correction, normalization by different methods and smoothing, either individually or in combination (Daveri et al., 2008; Medeghini et al., 2016; Sciutto et al., 2012). Scaling and mean centering are also performed for increasing correlation among variables. Doing so, any new high variance on the resulting PCs should reflect the most pronounced patterns and trends in the dataset (Christer, 2005). This may be necessary in data measured in different scales but is not highly recommended for spectra variables (Bro and Smilde, 2014; Smith, 2002; Miller and Miller, 2016). Miller and Miller express concerns for spectra that their original variables have very different variances, which would be minimized if pre-treated and not reflected in the resulting PCs (2016, 227). Some analysists assess the variance of their data by normality tests before performing PCA (Nielsen and Kristiansen, 2014).

Noake et al., choose not to perform any pre-treatment on their pFTIR-ATR data after assessing methods of removing redundant variables (2017). It their case study, broad nitrate bands of C-N, necessary for the identification of different synthetic organic polymers were hidden by the data pre-treatment of second derivative transformation (smoothing process) that enhances sharp peaks and masks the broader ones (2017, 6). Although other authors perform PCA on raw data, in most cases in table 17, a range of different pre-treatments, such as baseline correction (Daveri et al., 2008), normalization and second derivative (Medeghini et al., 2016), is used without following a standardized methodology.

The issues discussed by Noake et al. concern this thesis too. The interpretation of reflectance micro-FTIR spectra from standards (Ch.7) and the identification experiment (Ch.8) demonstrated the importance of weak peaks and reflectance distortions in the chemical characterization of organic mortar additives, especially those in low concentration in the mortar mixture. The application of any data pre-treatment in spectra obtained by External Reflectance FTIR micro-spectroscopy would affect their characteristic spectral features which were those that produced successful identifications through the CPAD. Thus, weak and distorted spectral features should be retained, ruling out any data pre-treatment.

Another form of increasing correlation among variables is to apply scaling on the matrix itself instead of pre-treating the raw data before the application of PCA. This is done by

analysing a correlation matrix instead of the covariance one. In correlation matrices, each variable is standardized to zero mean and unit variance. Correlation matrices are preferable when variables are measured in different scales or when a variable within the dataset has already a larger variance among variables and would dominate the first PCs (Miller and Miller, 2016, 227).

Most case studies do not state which matrix analysis was carried out, although correlation matrices are preferred in pre-treated data (Table 17). One Cultural Heritage study analysed raw data in covariance matrix (Pina-Torres et al., 2017) and one used both matrices to extract PCs from raw data, concluding that the correlation matrix produced better outcomes (Romero-Pastor et al., 2013).

9.2.4 PCA interpretation

The lack of a standardized methodology is reflected in the interpretation of PCA results. Some authors examine score and loading plots separately and then cross-reference them, in order to assess the influence of variables in classification (Arizio et al., 2013). Others focus on the loading values of variables in order to assess their significance in classification (Medeghini et al., 2016). The number of PCs and their representation in 2D or 3D plots and the representation of loadings as spectra profiles instead of values within PCA plots are also used for extracting information (Pina-Torres et al., 2017; Rosi et al., 2009). Residuals and distances among objects are also encountered as informative (Bro and Smilde, 2014; Kher et al., 2006).

All these different approaches in the application of PCA and the interpretation of results create uncertainty in its utilization. It seems that every step of application, from the purpose of use to the selection of data and the interpretation of results requires constant decision-making. In this respect, the identification of reflectance micro-FTIR spectra through the CPAD methodology is straightforward, based on true correlations of variables among a spectrum in question and those of standards. In CPAD identifications, correlations derive from the peak-by-peak assessment and chemical assignment, allowing the exclusion of false similarities from inorganic presence. The degree of certainty appears to be higher than that offered by PCA.

A basic question is formed, concerning the validity of PCA results. All Cultural Heritage case studies report successful PCA outcomes relevant to their research questions. In these studies, the PC score plots that provide the best classification among objects and likely the ones that agree with the main analysis results are demonstrated. This agreement could be encountered as criterion of PCA effectiveness. However, since all score plots

provide different variance information relative to the selected variables, it would be highly informative for this to be included in the papers and rejected, where possible, by rigid criteria. This action would reflect the rationale behind interpretation and consequently, the validity of classification.

9.3 Outcomes of literature review

The review of the selected literature shows that PCA applications in spectroscopy are not standardized relative to methodology and interpretation of results. This outcome, supported by the limited number of case studies in Cultural Heritage, could potentially reflect a limited background knowledge in statistical analysis in the specific scientific discipline. Alternatively, the variety of applications could be attributed to the search to discover the best methodology for using PCA to address specific analytical questions.

This lack of standardization and the application of multiple different PCA models for answering a single analytical question points out the difficulty in evaluating its failure or success. PCA is a non-parametric method; it is a method that will evaluate any numerical dataset it is being given and an answer will always come out, regardless of any parameters relevant to the source of data (Shlens, 2014, 9).

The evaluation of results becomes more complicated from the fact that PCA is used as a supervised pattern recognition method due to the preliminary data selection, as it is reflected in the literature review. PCA outcomes are effectively the linear representation of variance of selected variables, hence they potentially reflect the analyst's perspective of classification or significance of variables. The degree of bias requires estimation at least in qualitative terms relevant to the PCA outcomes.

Having provided a context for the approaches to using PCA, there now follows a description of experiments carried out for the evaluation of data selection, pre-treatment and interpretation rationale to explore the applicability of PCA as a complimentary method of identification in this thesis.

9.4 Preliminary Evaluation of Principal Component Analysis

Preliminary PCA testing was performed prior to the development and use of the CPAD methodology and its experimental evaluation (Ch.7 and 8). The aim of this preliminary work was to evaluate the parameters that influence PCA. In the review these were identified as being:

- Purpose of use

- Methodology (selection of variables, matrix construction, data pre-treatment)
- Interpretation of PCA results

9.4.1 Method: Preliminary PCA Testing

PCA was performed on spectral data obtained from:

- 8 organic standards
- 8 cross-sections of mortar replicas coated with each organic standard,
- 8 cross-sections of mortar replicas coated with each organic standard and marked as UNKOWN.

The 8 organic standards were prepared from egg, egg yolk, egg white, bone glue, milk, lard, olive oil and rice, following the standards preparation procedure (sect.7.2). The 8 mortar replicas were prepared by wet mixing of lime (CaO) and quarry sand (<0.5mm) in 1:3 ratio according to ancient mortar recipes (Moropoulou et al., 2000, 57) and left to dry for 30 days. The amount of water in the mixture was empirical, gradually incorporated in the mixture until a coherent mortar was prepared. After drying, the mortar replicas were coated by each of the organic standard by brush (fig.85).

Figure 85: Mortar replica coated with egg yolk.

Eight cross-sections were cut from the coated replicas and adhered on microscopy glass slides using 5-minute epoxy. The same procedure was followed for eight more cross-sections whose coating composition was revealed after their spectra had been identified.

All spectra were obtained by External Reflectance FTIR micro-spectroscopy, using the standardised acquisition parameters (sect.7.4).

Table 18 summarizes the preliminary PCA tests, including the purpose for each test, its methodology and the interpretation of results. The process was incremental in that each test was developed gradually guided by the outcomes of the previous test.

Tests, **T_1 to T_9**, were performed on spectral data of organic standards and mortar replicas coated with organic standards (cross-sections). The test objective was to assess the accuracy of PCA classifications of standards to groups according to their chemical composition, which is known *a priori*.

The results from **T_1 to T_9** shaped the PCA parameters that were applied in Tests **T_10 to T_13** that targeted the identification of replicas coated with unknown organic standard (cross-sections). The PCA Tests, **T_10** and **T_11**, were performed as a complimentary method after identification by visual inspection and comparisons to the spectra of standards. The PCA Tests, **T_12** and **T_13**, were employed as the main identification method.

Test No.	PCA Aim - Objectives	Spectra (Objects)	Data Pre-treatment	ROI (Variables)	Outcomes	Notes
T_1	Classification: Testing PCA matrix parameters and outcomes when origin of materials is known.	8 organic standards - 8 mortar replicas coated with organic standards.	Baseline correction, normalization, correlation matrix (centered and scaled to unit variance).	3000-2800, 1760-1680 and 1500-1300 cm^{-1}. Objects less than variables.	PC1vsPC2: Replicas are grouped separately from organic standards. Achieved discrimination and sub-grouping of organic standards according to chemical composition. Replicas intra-correlated due to mortar. Higher PCs not usefull.	Suspected problem: data pre-treatment incresed correlation. Use of organic standards and replicas in one matrix formed two groups.
T_2	Classification: Removal of variables of inorganic interference in order to reduce correlation among mortar replicas.	8 organic standards - 8 mortar replicas coated with organic standards.	Baseline correction, normalization, correlation matrix (centered and scaled to unit variance).	Removal of $CaCO_3$ 1461 cm^{-1} (PC3 vs PC4) and 2875 cm^{-1} (PC1 vs PC2). Objects less than variables.	As above	Regected since outcomes were the same as in T_1.
T_3	Classification: Further removal of variables of inorganic interference, reduce correlation due to inorganic similarities.	8 organic standards - 8 mortar replicas coated with organic standards.	Baseline correction, normalization, correlation matrix (centered and scaled to unit variance).	ROI 3000-2800 (removal of 2984, 2876, 2875 cm^{-1}) and 1760-1680 cm^{-1}. Removal of 1500-1300 cm^{-1}. Objects less than variables.	As above	Regected since outcomes were the same as in T_1.
T_4	Classification: Further removal of variables of inorganic interference, reduce correlation due to inorganic similarities.	8 organic standards - 8 mortar replicas coated with organic standards.	Baseline correction, normalization, correlation matrix (centered and scaled to unit variance).	Use of 3000-2800 (removal of 2984, 2876, 2875 cm^{-1}). Likely the less affected range relevant to inorganic interference. Objects less than variables.	As above	Regected since outcomes were the same as in T_1.

Table 18: Summary of preliminary PCA tests.

Test No.	PCA Aim - Objectives	Spectra (Objects)	Data Pre-treatment	ROI (Variables)	Outcomes	Notes
T_5	Classification: Discrimination of organic standards in the absence of mortar replicas coated with organic standards. Assessment of intra-correlation when each group of standards is plotted individually. Evaluation of the effectiveness of selected spectra ranges to discrimination.	8 organic standards.	Baseline correction, normalization, correlation matrix (centered and scaled to unit variance).	3000-2800, 1760-1680 and 1500-1300 cm^{-1}. Objects less than variables.	Achieved discrimination according to chemical composition. Strong shift of PC1 towards olive oil due to its highest variance compared to the rest objects in the matrix.	The one problem of intra-correlation is solved since one group is introduced. Data pre-treatment may not be significant. Variable selection successful.
T_6	Classification: Discrimination of mortar replicas coated with organic standards in the absence of organic standards. Assessment of intra-correlation when each group of standards is plotted individually. Evaluation of the effectiveness of selected spectra ranges to discrimination.	8 mortar replicas coated with organic standards.	Baseline correction, normalization, correlation matrix (centered and scaled to unit variance).	3000-2800, 1760-1680 and 1500-1300 cm^{-1}. Objects less than variables.	Achieved discrimination according to chemical composition, insignificant inorganic interference.	The one problem of intra-correlation is solved since one group is introduced. Data pre-treatment may not be significant. Variable selection succesful.

Table 18: continued.

Test No.	PCA Aim - Objectives	Spectra (Objects)	Data Pre-treatment	ROI (Variables)	Outcomes	Notes
T_7	Classification: Use of imbalanced PCA matrix for minimizing replica variance. Imbalanced matrix increases correlation by increasing the number of less strong variances.	24 spectra of organic standards (3x8) and 1 mortar replica spectrum coated with organic standard.	Baseline correction, normalization, correlation matrix (centered and scaled to unit variance).	3000-2800, 1760-1680 and 1500-1300 cm^{-1}. Objects less than variables.	Succesful classifications but biased since composition of replica is known a priori. Not possible to standardize rationale of interpreting score plots and securely reject invalid ones. The use of many spectra in the matrix does not assist visualization of the PCA outcomes. Highest variance of olive oil and replica rules PC1 out.	Higher PCs than PC1 were used. Necessary to observe loadings for selecting best grouping of replica to the correct organic standard. PCA reflects observations on spectra similarities of organic materials.
T_8	Classification: Assessment of effectiveness of imbalanced PCA matrix for minimizing replica domination. Imbalanced matrix increases correlation by increasing the number of less strong variances.	23 organic standards and 8 mortar replicas coated with organic standards.	Baseline correction, normalization, correlation matrix (centered and scaled to unit variance).	3000-2800, 1760-1680 and 1500-1300 cm^{-1}. Objects less than variables.	Intra-correlation of replicas.	Regected since outcomes were the same as in T_1 to T_4.
T_9	Classification: Assessment of effectiveness of imbalanced PCA matrix for minimizing replica domination. Imbalanced matrix increases correlation by increasing the number of less strong variances. Smaller matrix - same concept.	8 organic standards and 1 mortar replica coated with organic standard.	Baseline correction, normalization, correlation matrix. One replica is pre-treated with the 8 organic standards in one single matrix (increase of correlation between spectra by data pre-treatment).	3000-2800, 1760-1680 and 1500-1300 cm^{-1}. Objects less than variables.	Same outcomes as T_7.	Data pre-treatment seems to achieve the goal without the need of large number of spectra in the matrix. However, successful classification remains biased since identity of replicas is known.

Table 18: continued.

Test No.	PCA Aim - Objectives	Spectra (Objects)	Data Pre-treatment	ROI (Variables)	Outcomes	Notes
T_10	Identification: replica (cross-section) coated with unknown organic standard.	8 organic standards and 1 replica coated with unknown organic standard.	Baseline correction, normalization, correlation matrix. One replica is pre-treated with the 8 organic standards in one single matrix (increase of correlation between spectra by data pre-treatment).	3000-2800, 1760-1680 and 1500-1300 cm^{-1}. Objects less than variables.	Agreeable outcomes between visual identification and PCA. 4 unknowns were falsely identified due to bias from visual spectral comparisons.PC1 not useful and not taken into consideration (olive oil shift of variance on PC1 positive side).	Use of highest variance in score interpretation, distance and position in orthogonal axis. Loading profiles important as well as higher PCs (lowest variance). Retrospective outcome after failures: matrices need objects chemically similar.
T_11	Identification: replica (cross-section) coated with unknown organic standard.	8 replicas coated with organic standards and 1 replica coated with unknown organic standard.	Baseline correction, normalization, correlation matrix. One unknown replica is pre-treated with the 8 replicas coated with organic standards in one single matrix (increase of correlation between spectra by data pre-treatment).	3000-2800, 1760-1680 and 1500-1300 cm^{-1}. Objects less than variables.	The outcomes were biased by the visual spectral identification and T_10 results. Same mistakes were made.	Objects have highly correlated values (all replicas). Thus, first PCs can be used.

Table 18: continued.

Test No.	PCA Aim - Objectives	Spectra (Objects)	Data Pre-treatment	ROI (Variables)	Outcomes	Notes
T_12	Identification: replica (cross-section) coated with unknown organic standard.	8 replicas coated with organic standards and 1 unknown (T_10 matrix). 8 organic standards and 1 unknown (T_11 matrix).	Baseline correction, normalization, correlation matrix. One unknown is pre-treated with the 8 replicas or organic standards in one single matrix (increase of correlation between spectra by data pre-treatment).	3000-2800, 1760-1680 and 1500-1300 cm^{-1}. Objects less than variables.	Not biased because PCA was used as the main ID method, spectra assessed visually only for narrowing down the chemical group (i.e. protein). Improved number of correct identifications but not successful due to presence of objects not chemically related to the unknown that produce correlations.	Reinforces the idea of matrix construction from only chemical similar objects for avoiding false correlations.
T_13	Identification: improvement of T_12.	1 unknown and only chemically related spectra selected after visual inspection.	Baseline correction, normalization, correlation matrix. One unknown is pre-treated with the selected spectra of either organic standards or replicas in one single matrix (increase of correlation between spectra by data pre-treatment).	3000-2800, 1760-1680 and 1500-1300 cm^{-1}. Objects less than variables.	Biased because the unknown spectra of T_12 were used here and their id was revealed. Both matrices with replicas and organic standards are necessary for reaching outcome. Olive oil interference persists when this is included in matrices.	

Table 18: continued.

9.4.2 Results of Preliminary PCA testing

The most representative PCA tests of Table 18 are discussed in detail, demonstrating:

- the interpretation process of PCA plots
- the evaluation of the selected parameters for matrix construction
- the evaluation of the selected PCA method relevant to the purpose of use.

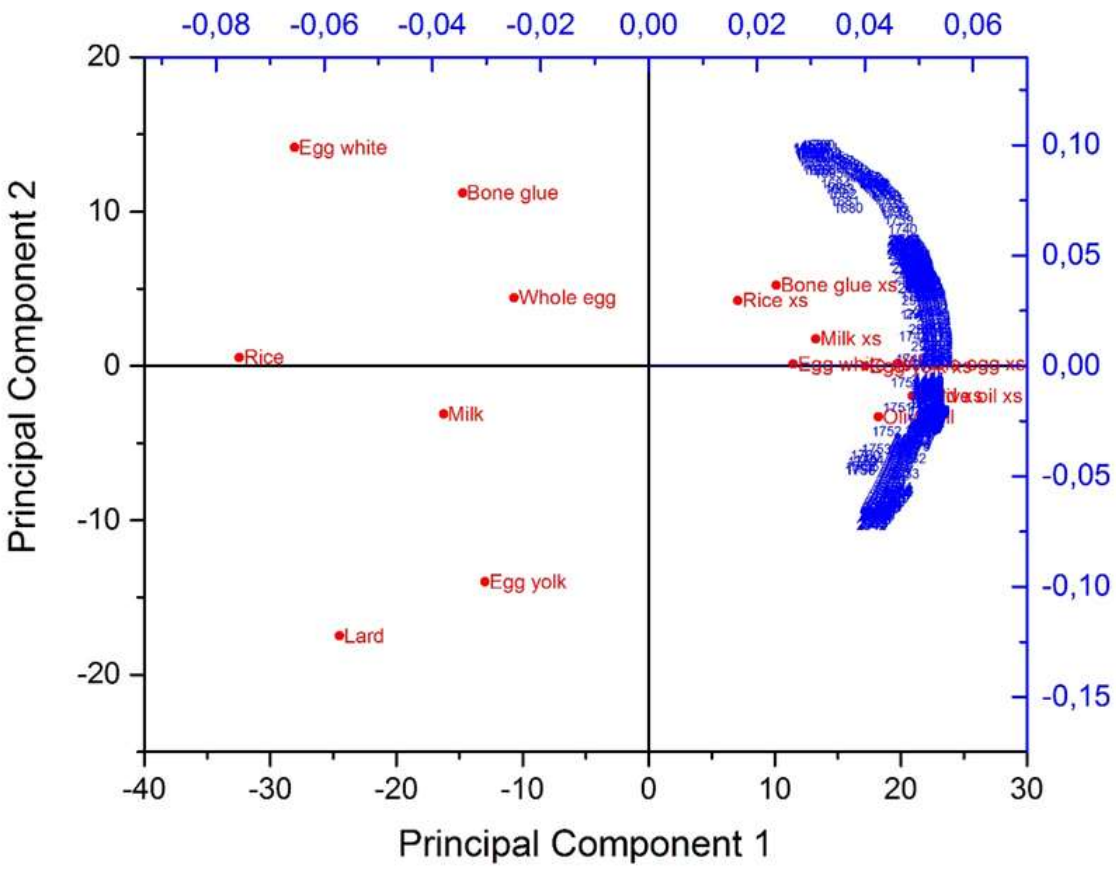

Figure 86: Test T_1: Organic standards are classified separately from the mortar/organic coated standard replicas (_xs) in the PC1vs.PC2 subspace.

Test T_1 (fig.86) aimed in the classification of objects according to their chemical composition. The 8 organic standards and the 8 mortar replicas coated with organic standards were introduced in the PCA matrix as objects for classification. The spectral Regions of Interest (ROIs) 3000-2800, 1760-1680 and 1500-1300 cm^{-1} were selected as variables. The criterion for their selection was that most of the organic peaks occur within these ROIs. The calculation of PCs was carried out on a correlation matrix which increases correlation among variables by centering and scaling them to unit variance (Romero-Pastor et al., 2013).

The first two PCs, explained the 91.16% of the total variance in the PCA matrix. PC1 is the principal component that carries the maximum information of variance among objects (78.58%), followed by PC2 (12.58%). In plot terms, PC1 explains the differences among objects and PC2 the similarities among them. Accordingly, two distinct groups of objects are formed in the PC1vsPC2 biplot (scores and loadings in one plot) based on the highest explained variance (fig.86).

The 7 organic standards are grouped in the negative side of PC1 and spread relevant to the explained variance among them in both sides of PC2. PC2 is the component that discriminates the organic standards based on their chemical composition. Sub-grouping is observed here: the proteinaceous standards, egg white and bone glue, are positioned closely to each other, followed by egg and milk. The second organic sub-grouping is that of standards of lipid origin, lard and egg yolk. Rice stands alone. The results of the sub-grouping of these 7 organic standards showed that the selected variables reflected the similarities and differences in their chemical composition.

An interesting feature derived from the positioning of olive oil in the group of mortar replicas coated with organic standards (_xs), in the positive side of PC1, closely placed with the mortar replica coated with olive oil. Based on the chemical composition of olive oil and the classification of the rest of the organics, it was expected that olive oil would be positioned close to lard. Thus, the differentiation of olive oil from the rest of the organic standards did not reflect differences in chemical composition, but the contribution of the selected variables in the degree of variance in the matrix.

Regarding the positioning of the replicas in the plot, this is characterized by high intra-correlation of the objects in the positive side of PC1. Sub-grouping based on chemical composition of the organic coatings was not achieved, as it is visible on the close positioning of the two mortar replicas coated with bone glue and rice. Three parameters are suspected to have produced this high inter-correlation:

- Data pre-treatment.
- The shared presence of the same inorganic components in all the replicas, expressed by the selected variables.
- Use of both organic standards and replicas in one matrix that strongly affected the degree of variance in the matrix.

The subsequent removal of specific inorganic peaks from the selected variables in Tests T_2 to T_4, did not alter the PCA results (Table 18).

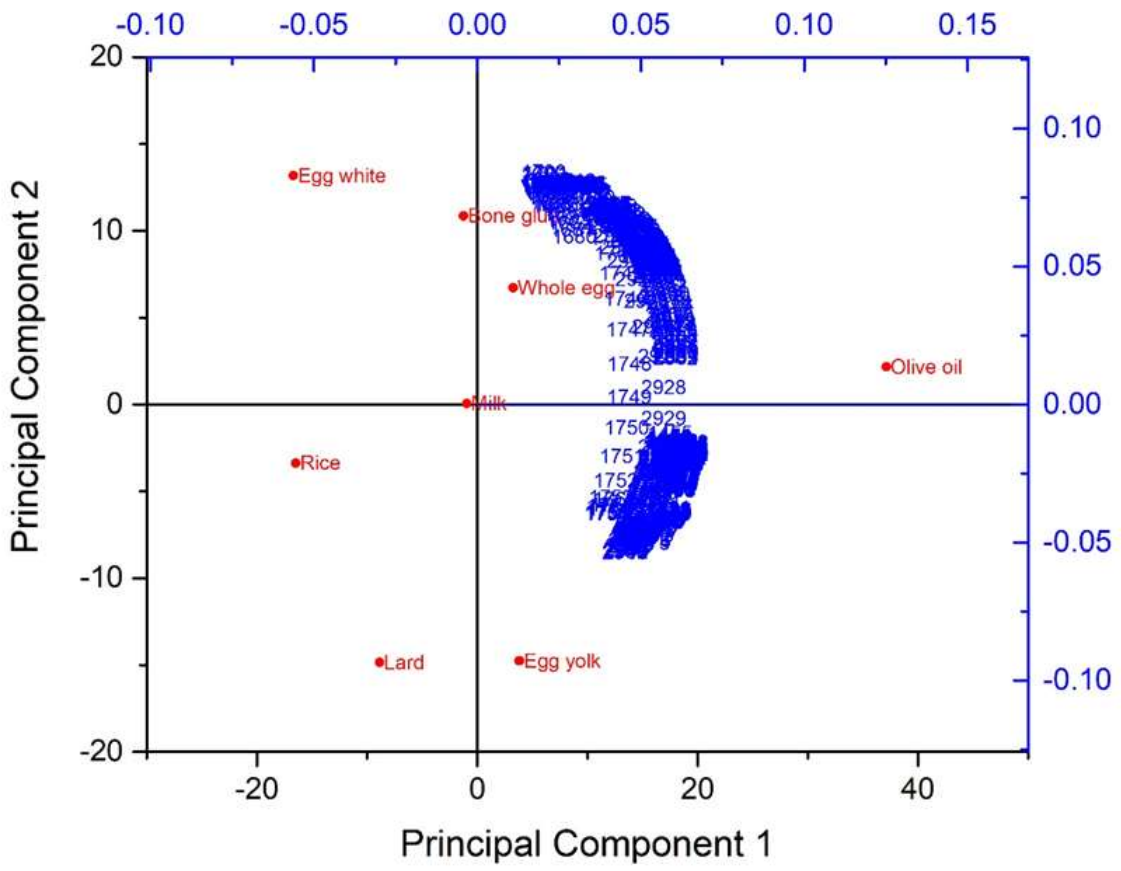

Figure 87: Test T_5: Organic standards are classified according to the selected ROIs in the PC1vsPC2 plot.

Test T_5 (fig.87) assessed the classification of organic standards in the absence of mortar replicas coated with organic standards in order to understand the parameter of object selection and intra-correlation, observed in Test T_1.

The first two principal components explained the 83.56% of the total variance in the matrix (data not shown). The objects were positioned according to their chemical composition in the PC1vsPC2 plot. The sub-grouping of objects is the same as the one produced in Test T_1. Olive oil remains the object with the highest variance from the rest of the organic standards. The reason is that the values of the selected variables for the specific organic differ considerably from those of the rest organic standards, shifting the highest explained variance (PC1) towards olive oil.

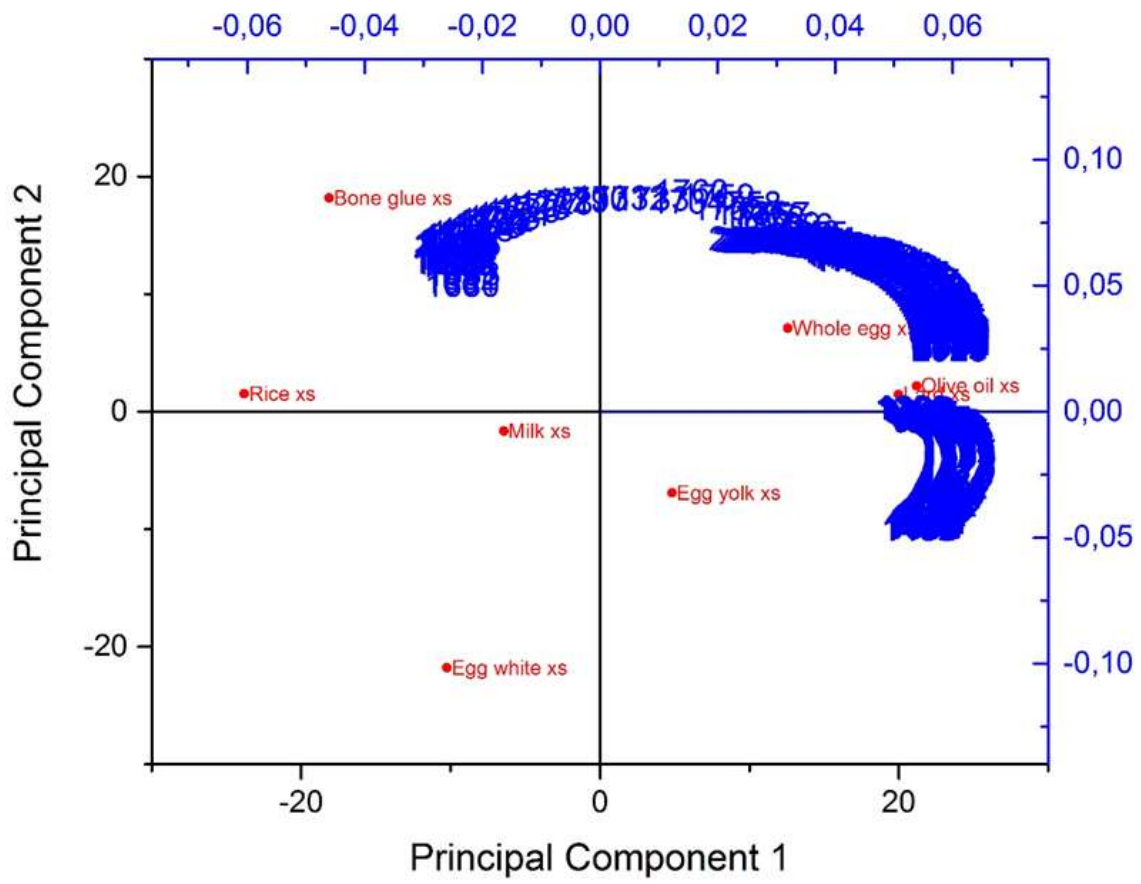

Figure 88: Test T_6: Mortar replicas coated with organic materials (_xs) are classified according to the selected ROIs in the PC1vsPC2 plot.

Test T_6 (fig.88) assessed the classification of mortar replicas coated with organic standards in the absence of organic standards. The first two PCs explain the 88.36% of the total variance in the matrix. This variance is expressed in the PC1vsPC2 biplot where the objects are positioned according to their chemical composition. The close positioning of lard and olive oil replicas, followed by egg yolk and egg replicas and the spread of the variables within this group, shows that the selected variables mainly explain the degree of variance of the lipid coated replicas. PC1 is the principal component that reflects chemical composition, whereas PC2 is the one that expresses similarities among the objects. Thus, proteinaceous coated replicas are placed on the negative side of PC1 and the rice coated replica stands alone.

Test T_6 showed that the similarities among the replicas due to their shared inorganic components did not contribute to the positioning of the objects. Nor did they produce high

correlation and intra-grouping that would obscure the classification of the replicas according to their organic coating.

Tests T_5 and T_6 demonstrated that the selection of objects in the PCA matrices is equally as important as variables in the calculation of the total variance. When all objects in the matrix differ due to chemical composition or when all objects share something common in their chemical composition, true variance can be achieved. In the first case, similarities among objects will emerge and groups will be formed. In the second case, the differences among objects will emerge, resulting too, in the formation of groups. When both types of objects are introduced in the same matrix the variance cannot override the strong intra-correlations of the two groups.

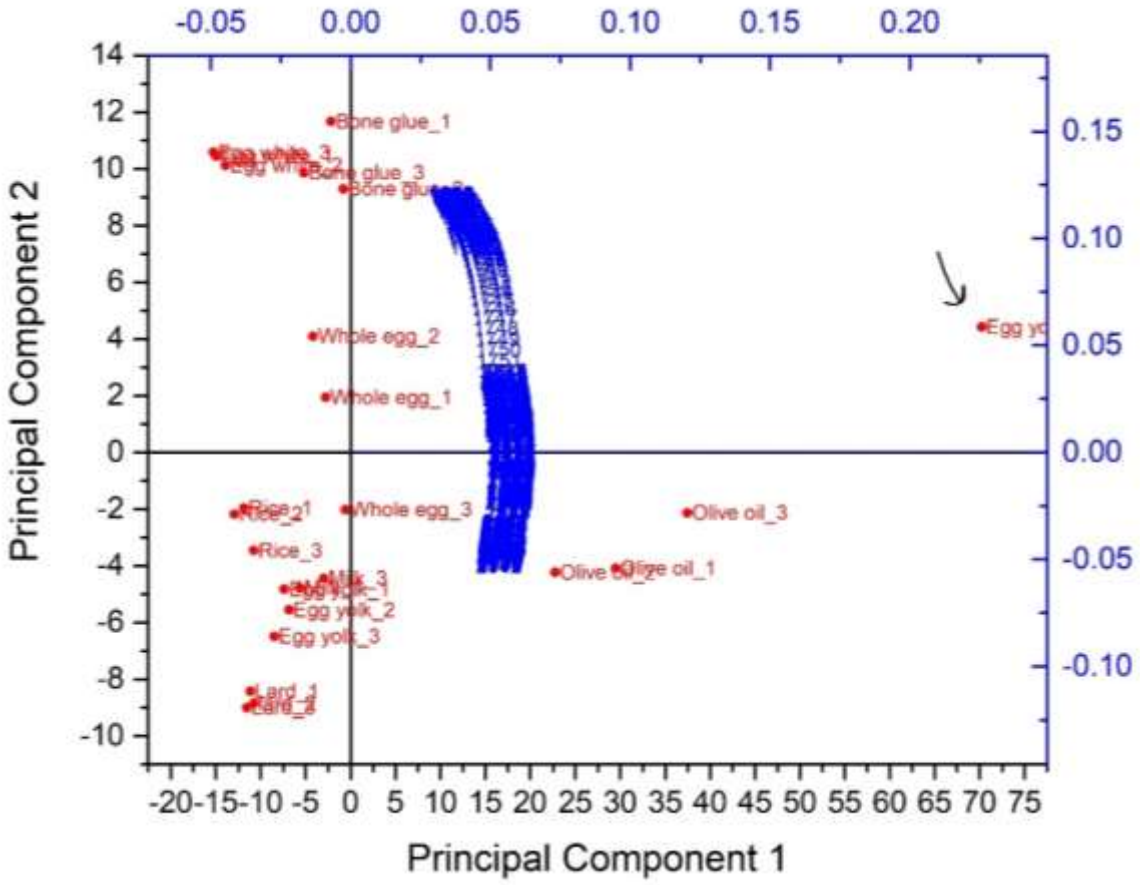

Figure 89: Test T_7: PC1vsPC2 biplot of the imbalanced matrix containing 24 organic standards and the mortar replica coated with egg yolk (egg yolk_xs).

Test T_7 (fig.89), aimed to classify a replica coated with organic standard in the correct group of organic standards (Table 18). Based on the outcomes of the previous tests, it was expected that the replica would shift the total variance towards itself and all the organics would be grouped separately in one large group. In order to avoid this result, the matrix in

test T_7 was “imbalanced”: an imbalanced matrix increases correlation among objects of less strong variances by increasing their number in the matrix (Bonnier and Byrne, 2012, 327). Accordingly, the matrix comprised of 24 spectra of organic standards (3 replicated spectra from each standard) and 1 mortar replica spectrum coated with organic standard.

The PC1vsPC2 biplot (fig.89) shows the positioning of the replica coated with egg yolk (egg yolk_xs) in the far positive side of PC1, isolated from the large group of organic standards (pointed by the arrow, fig.89). The sub-grouping of organic standards reflects their chemical composition although the distances are closer due to the strong shifting of variance from the presence of the replica. Although the first two PCs account for the 95.07% of the total variance in the matrix, classification of the mortar/organic replica to the correct organic standard was not achieved, because total variance is dictated by the high variance of the replica against the rest of the objects in the matrix.

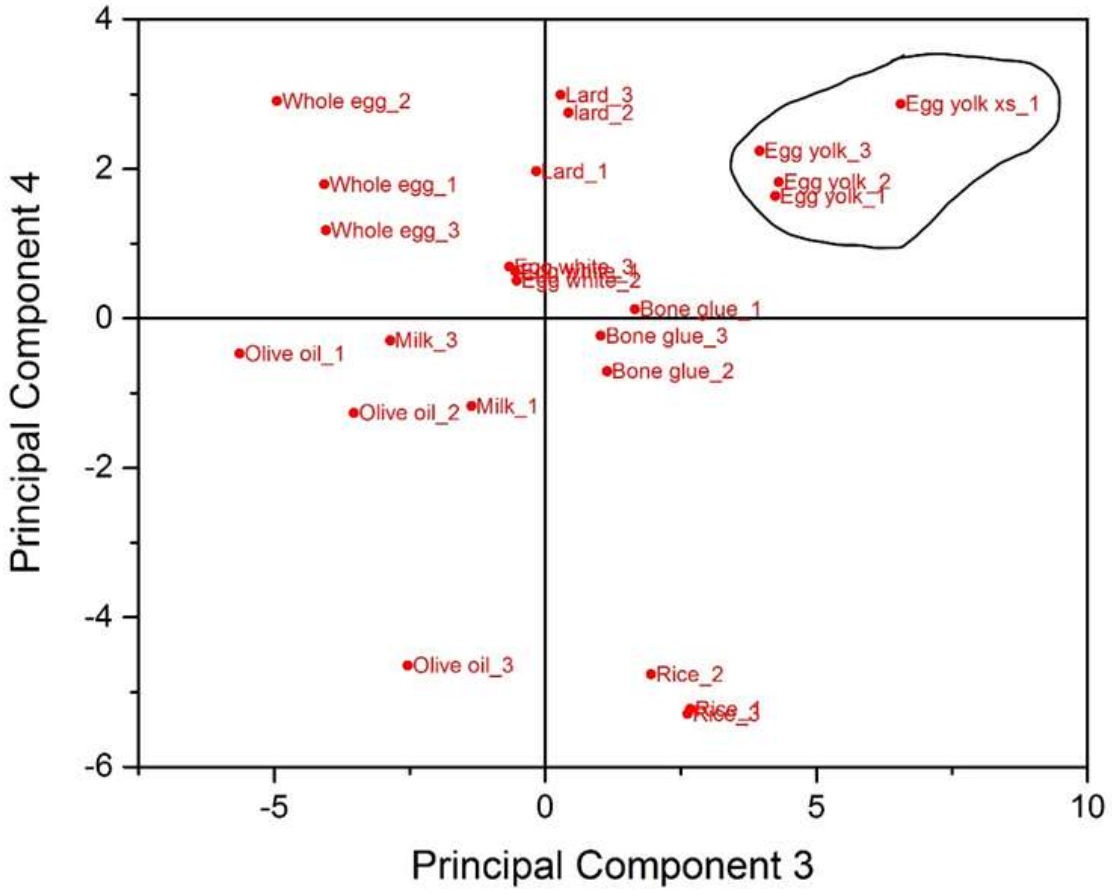

Figure 90: Test T_7 PC3vsPC4: Successful classification of mortar replica coated with egg yolk (Egg yolk_xs) to the corresponding organic standard.

Successful classification of the replica was achieved through PC3vsPC4 which explains the 2.14% and 1.41% of the total variance respectively (fig.90). Higher PCs show lower degree of variance among the differing objects and reveal correlations.

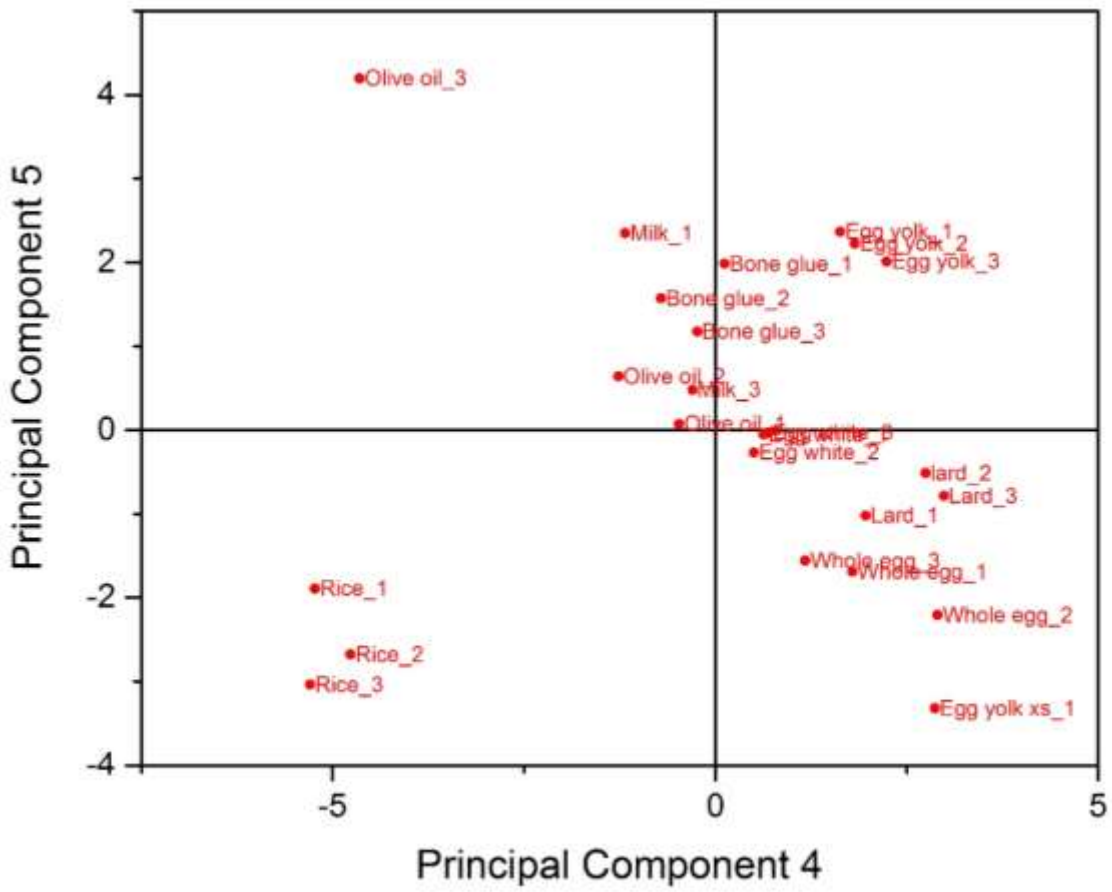

Figure 91: Test T_7 PC4vsPC5: Misleading classification of the replica coated with egg yolk (egg yolk_xs) with whole egg standard.

However, higher PCs might produce misleading correlations among objects, as it is evident from the PC4vsPC5 plot (fig.91). Here, the outcome is that the mortar/organic replica is positioned in close proximity to the whole egg standard, whereas the correct egg yolk standard is placed in the positive side of PC5, away from the mortar/organic replica.

Decision-making for selecting the most valid PCA plot cannot solely rely on the positioning of the objects in each plot or the contribution of the loadings. The non-parametric behavior of PCA, where results are always produced from the given numerical dataset without consideration of other parameters, in this case chemical composition, is evident (Shlens, 2014, 9).

The selection of the most valid PCA plot in Test T_7 and the rejection of the invalid ones was possible because the identity of the replica was known *a priori*. It was thus necessary to examine decision-making when classification concerns objects of unknown chemical composition.

The use of replicated objects for producing an “imbalanced matrix” that would increase correlation among objects of less strong variances, produced overcrowded PCA plots that were difficult to assess visually. The issue was resolved in Test T_9 which was performed on a matrix of 8 organic standards and 1 mortar replica coated with organic standard. The results were the same as in test T_7 without the need to triplicate objects (Table 18).

Test T_10 incorporated the outcomes of the previous tests on matrix construction and assessed the interpretation of PCA plots when classification concerns objects of unknown chemical composition (Table 18). The objective was the identification of cross-sections of mortar replicas coated with unknown organic standards through their classification to the appropriate group of organic standards.

Eight cross-sections were cut from the standards of mortar replicas coated with the 8 organic materials (sect.9.4.1). The labelling of these cross-sections as Un_1 to UN_8 was prepared by a third party (Table.19). The identity of the organic coating on these cross-sections was revealed after testing.

The spectra of the 8 cross-sections coated with organic standard of unknown chemical composition were identified prior to the use of PCA by visual comparisons with spectra of standards (both organic materials and coated replicas). PCA was performed on each unknown spectrum. The true identity of the unknown spectra was revealed after PCA (Table 19).

Unknown Spectrum	ID from Organic Standards (Visual)	ID from Replica Standards (Visual)	PCA Results	True Identity
Un_1	Bone glue_xs	Bone glue_xs	Agreeable	Bone glue_xs
Un_2	Whole egg_xs	Whole egg_xs	Agreeable	Whole egg_xs
Un_3	Olive Oil_xs	Olive Oil_xs	False - Agreeable	Lard_xs
Un_4	Milk_xs	Milk_xs	False - Agreeable	Rice_xs
Un_5	Lard_xs	Lard_xs	False - Agreeable	Olive Oil_xs
Un_6	Rice_xs	Rice_xs	False - Agreeable	Milk_xs
Un_7	Egg yolk_xs	Egg yolk_xs	Agreeable	Egg yolk_xs
Un_8	Egg white_xs	Egg white_xs	Agreeable	Egg white_xs

Table 19: Test T_10: The results from the visual identification of Unknown spectra and from PCA identification.

According to table 19, the results between the visual identification and PCA were agreeable. However, 4 unknown spectra (highlighted in blue) were falsely identified by

visual spectra comparisons with the standards. PCA supported this false identification because the plots were interpreted according to the visual identification outcomes.

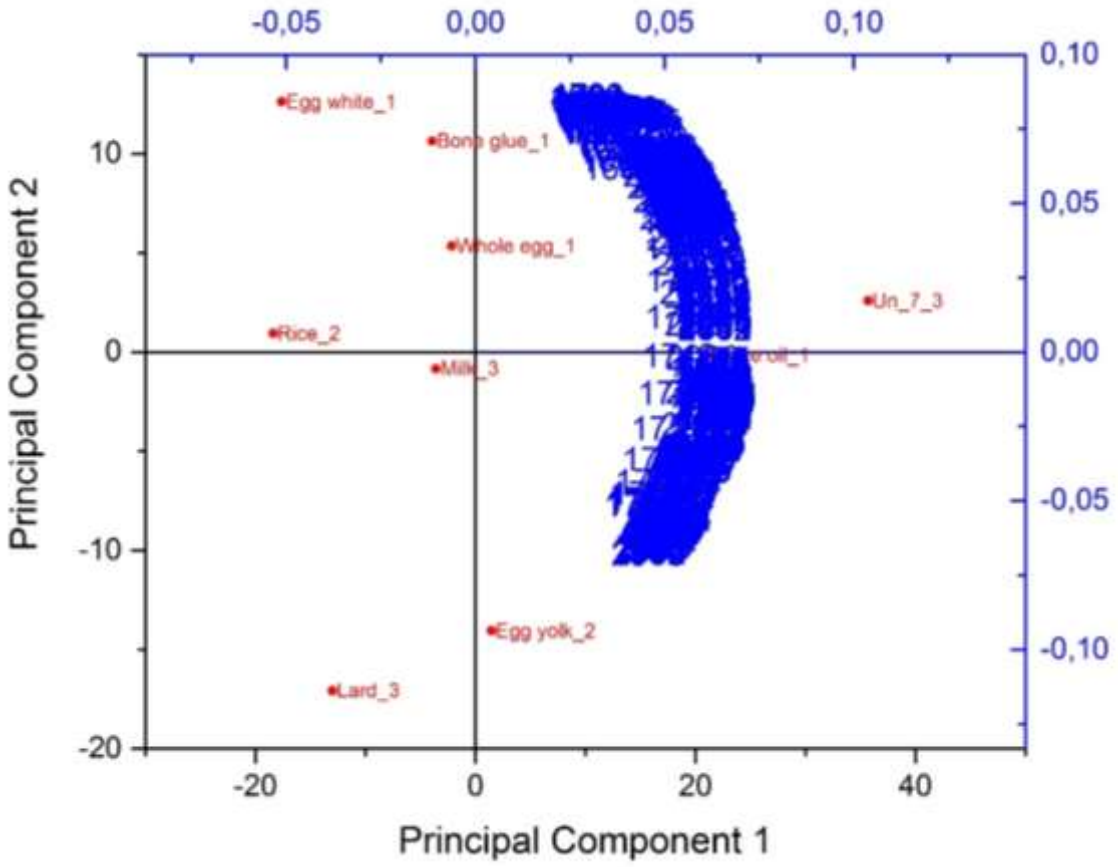

Figure 92: Test T_10 on Un_7: PC1vsPC2 plot positioning Un_7 on the positive side of PC1 with olive oil and egg yolk standards.

The difficulty of interpreting PCA plots, when these are used for identification purposes, is illustrated in the example of **UN_7** correctly identified as mortar replica coated with egg yolk (egg yolk_xs). PC1vsPC2 plot positioned UN_7 in the positive side of PC1 together with olive oil and egg yolk standards (fig.92). As in the previous tests, the total variance in the matrix is dictated by the individual strong variances of the olive oil and the replica (always relevant to the selected variables) and cannot be encountered as representative of chemical composition grouping. Nevertheless, the arrangement of the remaining organic standards provided intra-grouping that reflects correlation due to chemical composition.

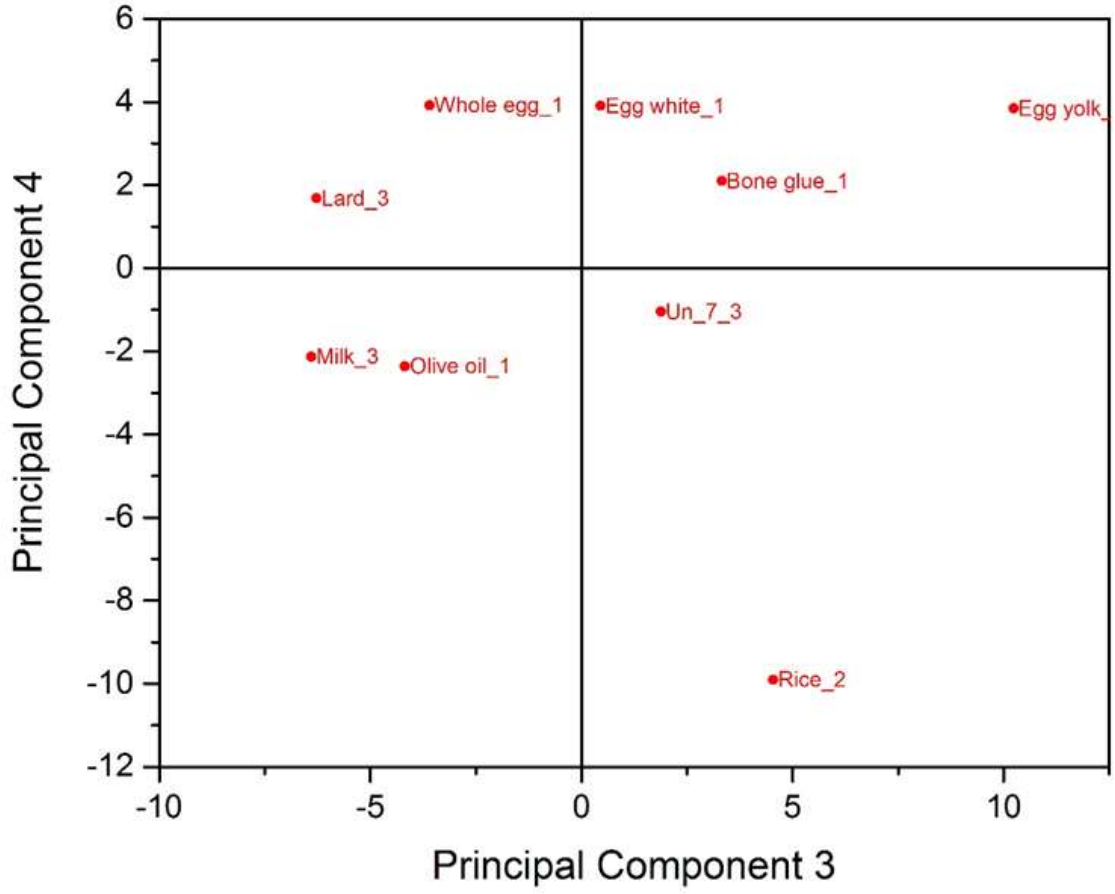

Figure 93: Test T_10 PC3vsPC4: UN_7 is classified with bone glue, egg white and egg yolk (true identity), although absolute matching cannot be achieved.

Higher PCs demonstrated different correlations between the unknown object and the organic standards. The PC3vsPC4 plot showed the positioning of UN_7 close to bone glue and egg white standards, followed by egg yolk which was the true organic component present on the replica (fig.93). However, the distances among objects suggested that bone glue should be the closest correlated standard to UN_7.

The issue of uncertainty was assessed through the examination of the PC3 and PC4 loading profiles (Bonnier and Byrne, 2012, 325). Each variable used in the matrix is arranged in the x axis. The variance of each variable, expressed as absorption intensity, is presented in the y axis (fig.94). The PC3 and PC4 loading profiles are compared to those of the objects that are grouped closely to UN_7 (bone glue, egg white and egg yolk standards). These profiles differ from original spectra because they contain only the variables (wavenumbers) used in the PCA matrix.

The loading profile of PC4 is almost identical to that of egg yolk, showing that PC4 mainly explains the variance of egg yolk (fig.94). The loading profile of PC3, particularly the

variables below 1700 cm^{-1} are those grouping bone glue, egg white and UN_7 together and create strong correlation among these objects. However, UN_7 is the only object that shares similar peaks with egg yolk in the region above 2800 cm^{-1}. This relationship between UN_7 and egg yolk, that provides the true identification of the unknown object is not visible in the PCA plot, but accessible only through the loading profiles.

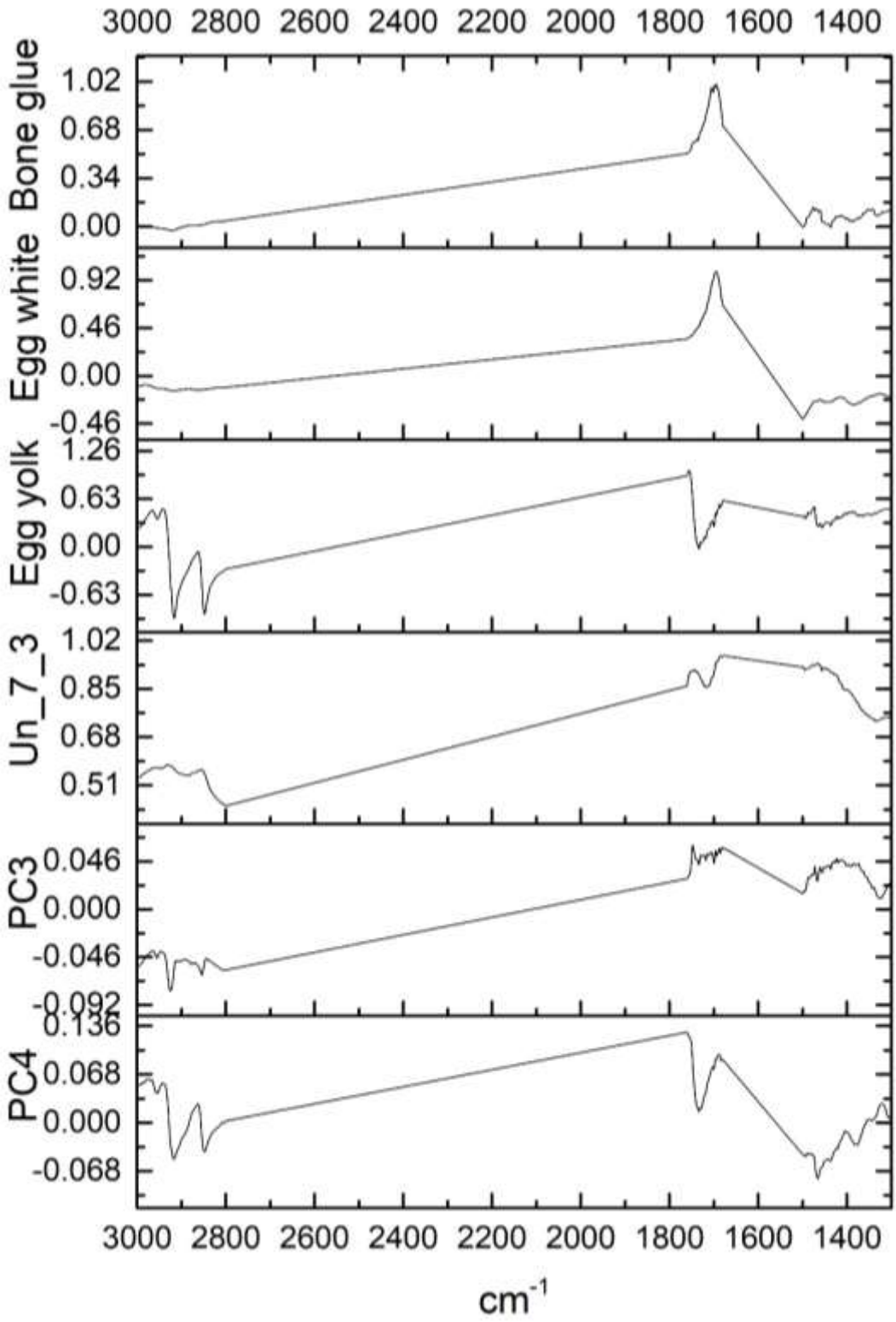

Figure 94: Loading profiles of organic standards, UN_7, PC3 and PC4.

Following the parameters of T_10, Test T_11 was conducted by using 8 replicas coated with organic standards and 1 replica coated with unknown organic standard. The outcomes were similar to those of T_10. However, since the matrix was constructed from objects of low variance (all replicas) the first PCs could be used (Table 18).

Test T_12 was carried out on newly labelled unknown spectra, following the parameters of Tests T_10 and T_11 (Table 18). In Test T_12, PCA was used as the main ID method. Prior visual assessment of the unknown spectra was carried out only for narrowing down the chemical group (i.e., protein) in the ROI 3000-2900 cm^{-1} and did not include identification by visual comparison with spectra from standards. This action reduced the bias of prior identification during the interpretation of PCA plots.

The test produced improved number of correct identifications compared to Tests T_10 and T_11 (data not shown). However, misleading correlations between the unknown object and standards not chemically similar did occur, reinforcing the idea that PCA matrices should contain objects of low variance in order to produce realistic correlations.

The final preliminary Test T_13 was designed according to the outcomes of Tests T_10 to T_12 and used only those objects chemically similar to the unknown (Table 18). Its success however could not be safely assessed since the true identity of the unknown objects was revealed in T_12. Nevertheless, Test T_13 provided the basis for the design of a PCA methodology and its experimental evaluation (section 10).

9.4.3 Summary of preliminary PCA testing

The preliminary PCA testing demonstrated that the selection of objects in the PCA matrices is equally important with that of variables in the calculation of the total variance. According to the results, true variance can be achieved in matrices where all the objects differ from each other, as in the case of organic standards, or when all objects share something in common relevant to their chemical composition (replicas).

Consequently, these tests led to the conclusions that PCA could not work for this specific data set as an “unsupervised pattern recognition method”. True variance was highly influenced by the selection of objects.

In relation to selecting the most valid PCA plot, the uncertainty induced by the non-parametric behavior of PCA, was not eliminated.

The fallibility of PCA for producing secure identification outcomes is also attributed to the false results of visual identification of spectra which influenced the interpretation of PCA plots. PCA seems to be as strong as the main identification method.

Chapter 10: Design and testing the PCA methodology

The outcomes of the preliminary PCA testing were utilized in the design of a PCA model to be applied on the spectral data from **Experimental sets I** and **IV** (Ch. 8). The aim was to evaluate the effectiveness of PCA as a complementary identification tool. Thus, PCA was performed after the identification of the reflectance micro-FTIR spectra through the CPAD, for both sets of spectral data.

The decision to use PCA as a complementary identification tool after the use of the CPAD, is derived from the fundamental outcome of the preliminary PCA testing (sect. 9.4.3). This indicated that realistic grouping of objects is based on chemical similarities derived from PCA matrices that contained objects of low variance or equally shared variance (Christer, 2005).

The successful use of the CPAD identification methodology was established in Chapter 8. The identification process itself worked by narrowing down possible matches between the spectra from standards and the spectrum in question. This information could be used for producing PCA matrices of objects of low variance and selecting variables adequate to achieve realistic results.

The hypothesis shapes the objective of the current tests which are divided into two parts:

1. Sections 10.1 to 10.4: Design of the PCA methodology: Experimental Set I spectral data – identity of spectra established though the CPAD and revealed **prior** to PCA.
2. Sections 10.5 to 10.6: Application of PCA methodology: Experimental Set IV spectral data – identity of spectra established though the CPAD and revealed **after** PCA.

10.1 Design of the PCA methodology: parameters

The basic PCA parameters, as derived from the preliminary testing (sect.9.4), are defined as follows:

10.1.1 Matrix construction – Selection of objects

The use of objects of similar properties will allow any true high variance in the dataset to be revealed on the PC scores. Objects that differ greatly from the spectrum in question will be avoided, if possible, since they will shift the PC variance towards themselves on PC1 and produce false classifications (T_1-T_7 results, Table 18, sect.9.4). For example, when the unknown object is identified through the CPAD as an organic/mortar mixture, the matrix will consist of the unknown object and organic/mortar

mixture standards, excluding the organic standards. The action is expected to produce representative highest variance in the dataset from the first 2 or 3 PCs, adequate to produce classification, enabling the safe rejection of higher PCs (T_11 results, Table 18, sect.9.4).

10.1.2 Matrix construction – Selection of variables

Entire spectra are ruled out because:

- They contain spectral data of detector interference and noise that do not carry information relevant to the organic additive and increase correlation of objects (spectra). This correlation will reduce the true variance and result in broad classifications.
- The calculation of correlation or covariance matrices of entire spectra produces PCs equal to the number of variables. However, above the first 10 PCs their values equal to zero since they do not express any remaining variance (Miller and Miller, 2016, 224).
- Calculation of such large matrices is time-consuming (more than 24 hours).

Variables will be selected according to those contributing most in the identification of the unknown spectrum as they were determined through the CPAD. These are ranges of interest (ROIs) and specific diagnostic peaks (Ch.8).

10.1.3 Data pre-treatment of variables

The spectral data was used raw without any pre-treatment, based on the PCA tutorials (Table 17, sect.9.2) and the preliminary PCA outcomes. It was considered essential to preserve and utilize the values of weak peaks, characteristic to Reflectance micro-FTIR spectra, which proved crucial for the identification of unknown organic additives though the CPAD.

For comparative reasons, the PCA plots from both correlation and covariance matrices will be assessed. A correlation matrix incorporates scaling treatment performed automatically through the OriginPro 2015 software.

10.1.4 Interpretation of scores and loadings

The information gathered from the literature review and the preliminary tests will be combined in order to fully understand the scores and loadings before rejecting the redundant ones.

10.1.5 Purpose of Use

This parameter is discussed last because it highlights the main testing objective. As described earlier, the non-parametric PCA cannot access information that is not provided to it: the absence of diagnostic peaks on the unknown spectrum relevant to a possible match cannot be accessed as it can when using the CPAD, so it cannot reject incompatible matches. Since PCA will always produce some kind of classification among objects relative to the selected variables, its use cannot be other than complimentary to the main identification method (Shlens, 2014, 9). Following the successful use of the CPAD where all spectra information can be utilized to provide identification, PCA can only be used as a complimentary method and probably as a validation method of the CPAD outcomes.

In these tests PCA is not used as an unsupervised pattern recognition method since variable and object selection is performed. Accordingly, the aim is not to examine relationships among unknown objects relevant to the contributions of variables but to classify an unknown object to the correct chemical group. The influence of matrix selection on the PCA outcomes is expected to clarify the use of PCA as a complementary identification tool or as a mathematical representation of the CPAD outcomes.

Principal Component Analysis was performed through the OriginPro 2015 software. The absorption peaks within the regions 4000-3800 $cm^{-1}$and 2400-2300 cm^{-1} (detector interference) are excluded from the PCA matrices. **Regions of Interest (ROIs)** and **Diagnostic Peaks** that are included in the matrix are those that contributed to the identification of the spectrum in question through the CPAD.

The resulting PCA model was tested on the identified spectra from the Experimental set I (Ch.8, sect.8.1, 8.1.1). The objective is to classify the identified spectra to the correct groups of standards and if possible, to their individual chemical matching.

10.2 Results: PCA on Regions of Interest (ROIs)

Table 20 summarizes the PCA parameters and classification results for each spectrum in question (UN_I_1 to UN_I_10). PCA is performed on matrices that contain both Regions of Interest (ROIs) and Diagnostic Peaks as variables, as determined through the CPAD identification process for each unknown spectrum (Ch.8, sect.8.1, 8.1.1). The objects involved in the matrix are either organic/inorganic mixtures, when the spectrum in

question is a mixture, or organic standards when the unknown spectrum is identified as organic material.

PCA Matrix Label	Revealed ID	Objects	Variables (cm^{-1})	Variables vs. Objects	Results	Comments
ROI_1_covariance	UN_I_1 is **A_M_25** (25% asphalt additive in mortar).	Total 37: UN_I_1 + 36 mixtures. Selection according to CPAD outcomes.	1000-933, 1653-1453, 2954-2728 and the peak 3472 that cannot be ignored (total 497).	Variables more than objects.	Correct classification.	Distances among objects reflect original variance, showing the correct concentration of organic additive.
ROI_1_correlation	UN_I_1 is **A_M_25** (25% asphalt additive in mortar).	Total 37: UN_I_1 + 36 mixtures. Selection according to CPAD outcomes.	1000-933, 1653-1453, 2954-2728 and the peak 3472 that cannot be ignored (total 497).	Variables more than objects.	Correct classification - similar to covariance.	Pre-treatment in correlation matrix reduces original variance and distances among objects appear smaller.
ROI_2_covariance	UN_I_2 is **BG_M_50** (50% bone glue additive in mortar).	Total 37: UN_I_2 + 36 mixtures. Selection according to CPAD outcomes.	1707-1344 (364).	Variables more than objects.	Correct classification of organic additive, uncertain concentration.	All 3 PCs necessary. Plots can be interpreted in different ways posing uncertainty to results.
ROI_2_correlation	UN_I_2 is **BG_M_50** (50% bone glue additive in mortar).	Total 37: UN_I_2 + 36 mixtures. Selection according to CPAD outcomes.	1707-1344 (364).	Variables more than objects.	Similar to covariance but smaller distances among objects, hence can be misleading.	Misleading intra-classifications within broad group. Asphalt mixtures suspected of shifting variance.
ROI_3_covariance	UN_I_3 is **R_M_5** (5% rice additive in mortar).	Total 37: UN_I_3 + 36 mixtures. Selection according to CPAD outcomes.	1022-998, 1282-1271, 1619-1432, 2697, 2933, 3031 (last three peaks are diagnostic and are included) (228).	Variables more than objects.	Correct classification through higher PCs.	2697 cm^{-1} diagnostic peak is the classification variable.
ROI_3_correlation	UN_I_3 is **R_M_5** (5% rice additive in mortar).	Total 37: UN_I_3 + 36 mixtures. Selection according to CPAD outcomes.	1022-998, 1282-1271, 1619-1432, 2697, 2933, 3031 (last three peaks are diagnostic and are included) (228).	Variables more than objects.	Correct classification, better than covariance.	

Table 20: Summary of PCA parameters for matrix construction combining Regions of Interest and Diagnostic peaks and PCA classification results for each spectrum in question.

PCA Matrix Label	Revealed ID	Objects	Variables (cm^{-1})	Variables vs. Objects	Results	Comments
ROI_4_covariance	UN_I_4 is **O_M_25** (25% olive oil additive in mortar).	Total 37: UN_I_4 + 36 mixtures. Selection according to CPAD outcomes.	1759-1282, 2863-3011 (627).	Variables more than objects.	Places UN_I_4 in correct class, but uncertainty on best matching.	Higher PCs assist correct classification.
ROI_4_correlation	UN_I_4 is **O_M_25** (25% olive oil additive in mortar).	Total 37: UN_I_4 + 36 mixtures. Selection according to CPAD outcomes.	1759-1282, 2863-3011 (627).	Variables more than objects.	Same as 4.	
ROI_4.1_covariance	UN_I_4 is **O_M_25** (25% olive oil additive in mortar).	Total 37: UN_I_4 + 36 mixtures. Selection according to CPAD outcomes.	3011-2941, 2863, 1759, 1702-1660, 1617-1605, 1506-1472, 1380-1282 (including single diagnostic peaks) (263).	Variables more than objects.	Improved matching to true identity.	Selection of narrowed down variables (less than ROI_4).
ROI_4.2_correlation	UN_I_4 is **O_M_25** (25% olive oil additive in mortar).	Total 37: UN_I_4 + 36 mixtures. Selection according to CPAD outcomes.	3011-2941, 2863, 1759, 1702-1660, 1617-1605, 1506-1472, 1380-1282 (including single diagnostic peaks) (263).	Variables more than objects.	Smaller distances among groups.	
ROI_5_covariance	UN_I_5 is **Mi_M_5** (5% milk additive in mortar).	Total 37: UN_I_5 + 36 mixtures. Selection according to CPAD outcomes.	2959, 2925, 1652-1535, 1475-1433, 1024-995 (including single diagnostic peaks) (193).	Variables more than objects.	Classification according to inorganic similarities, visible from the loadings 1652-1535, 1475-1433, not absolute match, best match with egg white.	ROIs affected by inorganic presence should be removed.
ROI_5_correlation	UN_I_5 is **Mi_M_5** (5% milk additive in mortar).	Total 37: UN_I_5 + 36 mixtures. Selection according to CPAD outcomes.	2959, 2925, 1652-1535, 1475-1433, 1024-995 (including single diagnostic peaks) (193).	Variables more than objects.	Smaller distances among groups, not better results than covariance.	

Table 20: continued.

PCA Matrix Label	Revealed ID	Objects	Variables (cm^{-1})	Variables vs. Objects	Results	Comments
ROI_6_covariance	UN_I_6 is **L_M_75** (75% lard additive in mortar).	Total 38: UN_I_6 + 36 mixtures + mortar standard. Selection according to CPAD outcomes.	3018-2939, 2863, 1755, 1702-1683, 1474, 1450-1418, 1388-1360,1270 (166).	Variables more than objects.	Broad classification, PC1 explains high organic concentration. PC2 explains chemical similarity.	UN_I_6 is placed within the correct class but identification is uncertain.
ROI_6_correlation	UN_I_6 is **L_M_75** (75% lard additive in mortar).	Total 38: UN_I_6 + 36 mixtures + mortar standard. Selection according to CPAD outcomes.	3018-2939, 2863, 1755, 1702-1683, 1474, 1450-1418, 1388-1360,1270 (166).	Variables more than objects.	Similar as in covariance but distances are smaller among objects.	
ROI_7_covariance	UN_I_7 is **EY_M_25** (25% egg yolk additive in mortar).	Total 38: UN_I_7 + 36 mixtures + mortar standard. Selection according to CPAD outcomes.	3006-2858, 1754, 1695-1677, 1561, 1481, 1319-1281 (210).	Variables more than objects.	Classification based on lipid 3006-2858 variables. Not absolute match to true identity.	Could be misleading if true identity was not known.
ROI_7_correlation	UN_I_7 is **EY_M_25** (25% egg yolk additive in mortar).	Total 38: UN_I_7 + 36 mixtures + mortar standard. Selection according to CPAD outcomes.	3006-2858, 1754, 1695-1677, 1561, 1481, 1319-1281 (210).	Variables more than objects.	Similar to covariance but smaller distances among objects.	
ROI_8_covariance	UN_I_8 is **EW_M_50** (50% egg white additive in mortar).	Total 38: UN_I_8 + 36 mixtures + mortar standard. Selection according to CPAD outcomes.	3084-3071 (added although not used in CPAD), 3012-2975, 2944-2900, 1691-1578, 1318-1283 (247).	Variables more than objects.	Correct classification according to protein content in higher PCs.	Reflects similarities observed during CPAD identification.
ROI_8_correlation	UN_I_8 is **EW_M_50** (50% egg white additive in mortar).	Total 38: UN_I_8 + 36 mixtures + mortar standard. Selection according to CPAD outcomes.	ROI: 3084-3071 (added although not used in CPAD), 3012-2975, 2944-2900, 1691-1578, 1318-1283 (247).	Variables more than objects.	Smaller distances between objects, introduces more matching candidates.	

Table 20: continued.

PCA Matrix Label	Revealed ID	Objects	Variables (cm^{-1})	Variables vs. Objects	Results	Comments
ROI_9_covariance	UN_I_9 is **E_M_75** (75% egg additive in mortar)	Total 38: UN_I_9 + 36 mixtures + mortar standard. Selection according to CPAD outcomes.	970, 1257-1266, 1467, 1554, 1682, 1747, 2607-2616, 2936-2966, 3006-3014 (65).	Variables more than objects.	False classification, although UN_I_9 is grouped with lipids due to 2900 ROIs.	ROIs 3000-2900 strong correlation of variables that weakens the fingerprint ROI.
ROI_9_correlation	UN_I_9 is **E_M_75** (75% egg additive in mortar).	Total 38: UN_I_9 + 36 mixtures + mortar standard. Selection according to CPAD outcomes.	970, 1257-1266, 1467, 1554, 1682, 1747, 2607-2616, 2936-2966, 3006-3014 (65).	Variables more than objects.	Similar to covariance.	
ROI_10_covariance	UN_I_10 is **E_av** (egg standard).	Total 13: UN_I_10 + 12 organic standards. Selection according to CPAD outcomes. Rosin (RO), Casein (Cas) and Beeswax (BW) standards were also added.	978, 1122, 1177, 1266-1471, 1568, 1692, 1755, 2865-2875, 2941-2972 (255).	Variables more than objects.	Classification within protein-lipid group. Not absolute match to true identity.	Proteins can be ruled out since CPAD identification showed combined presence of protein-lipids.
ROI_10_correlation	UN_I_10 is **E_av** (egg standard).	Total 13: UN_I_10 + 12 organic standards. Selection according to CPAD outcomes. Rosin (RO), Casein (Cas) and Beeswax (BW) standards were also added.	978, 1122, 1177, 1266-1471, 1568, 1692, 1755, 2865-2875, 2941-2972 (255).	Variables more than objects.	Similar to covariance.	

Table 20: continued.

ROI_1_covariance

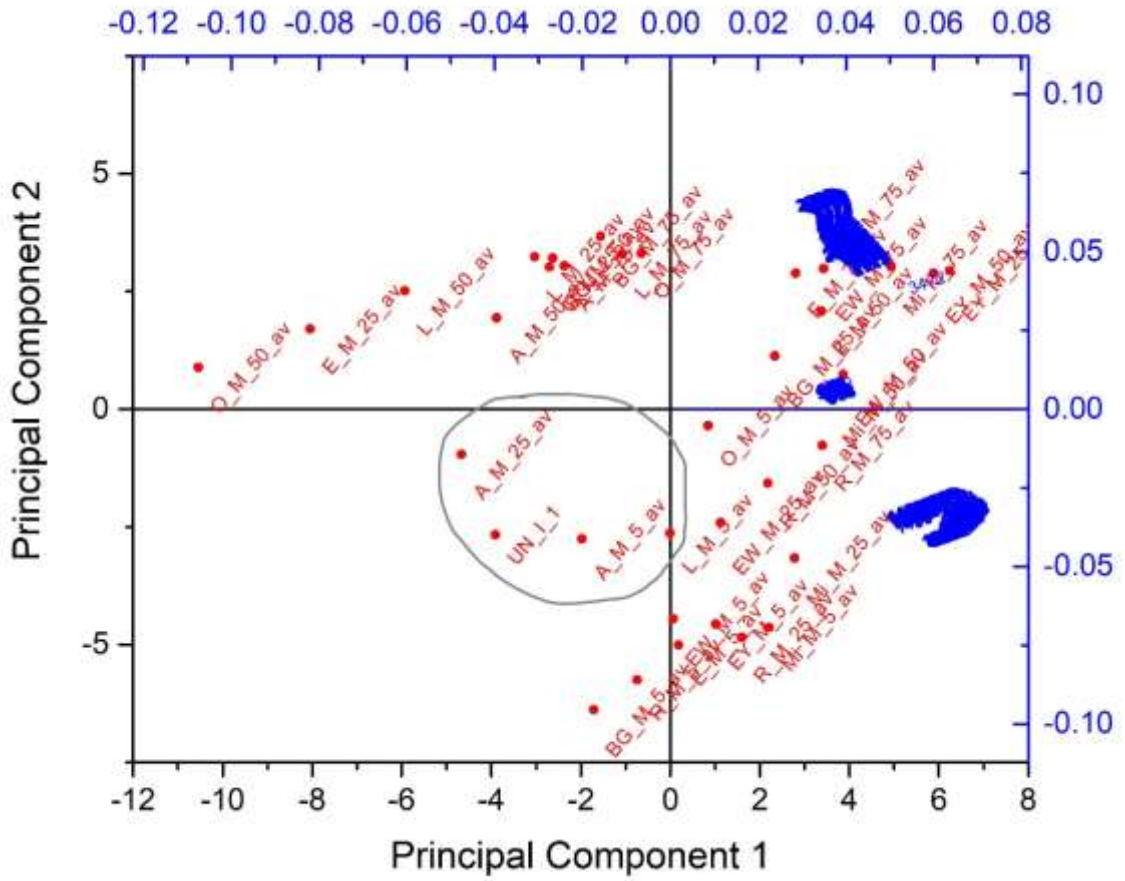

Figure 95: ROI_ covariance PC1vsPC2 for UN_I_1 (25% asphalt in mortar).

PC1 explains the 53.59% of the total variance and PC2 the 39.96% (fig.95). UN_I_1 is correctly classified by the selected variables among asphalt/mortar mixtures. The fact that UN_I_1 is between A_M_25 and A_M_5 expresses the same dilemma faced during the CPAD identification when identifying the concentration of the organic additive. The distance between UN_I_1 and A_M_25 in PC1 is smaller than that of A_M_5 and thus it is the best match. PCA could assist the CPAD identification in that aspect. The correlation matrix produced similar classification, although distances among objects appear smaller due to the scaling involved in the process (Appendix II, fig.1).

ROI_2_covariance

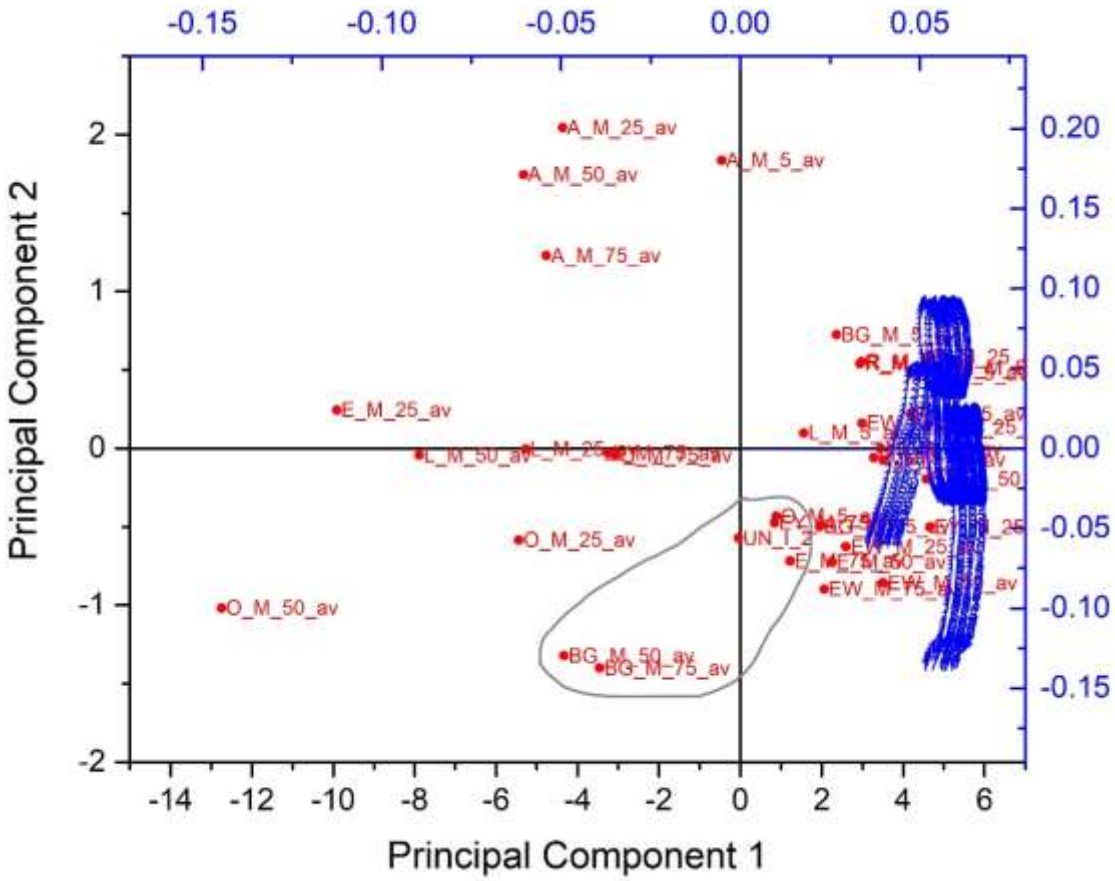

Figure 96: ROI_ covariance PC1vsPC2 for UN_I_2 (50% bone glue in mortar).

PC1 explains the 94.41% of the total variance thus taken as the baseline for classification, followed by PC2 2.96% and PC3 1.59% explained variance. All 3 PCs are plotted in order to understand relationships among objects.

UN_I_2 is positioned at the negative side of PC1 and PC2, closer to BG_M_50 (true identity) and BG_M_75 (fig.96). However, classification is uncertain due to the closeness with the broad class on the positive side of PC1, containing most of the organic/mortar mixtures. It appears that the variables in the specific ROI explain mostly the inorganic similarities in the mixtures. Asphalt/mortar mixtures, differing considerably in chemical composition from the rest of the standards, form a distinct class. Better classification is achieved in PC1vsPC3, although UN_I_2 appears closer to BG_M_75 instead of the correct BG_M_50 (data not shown).

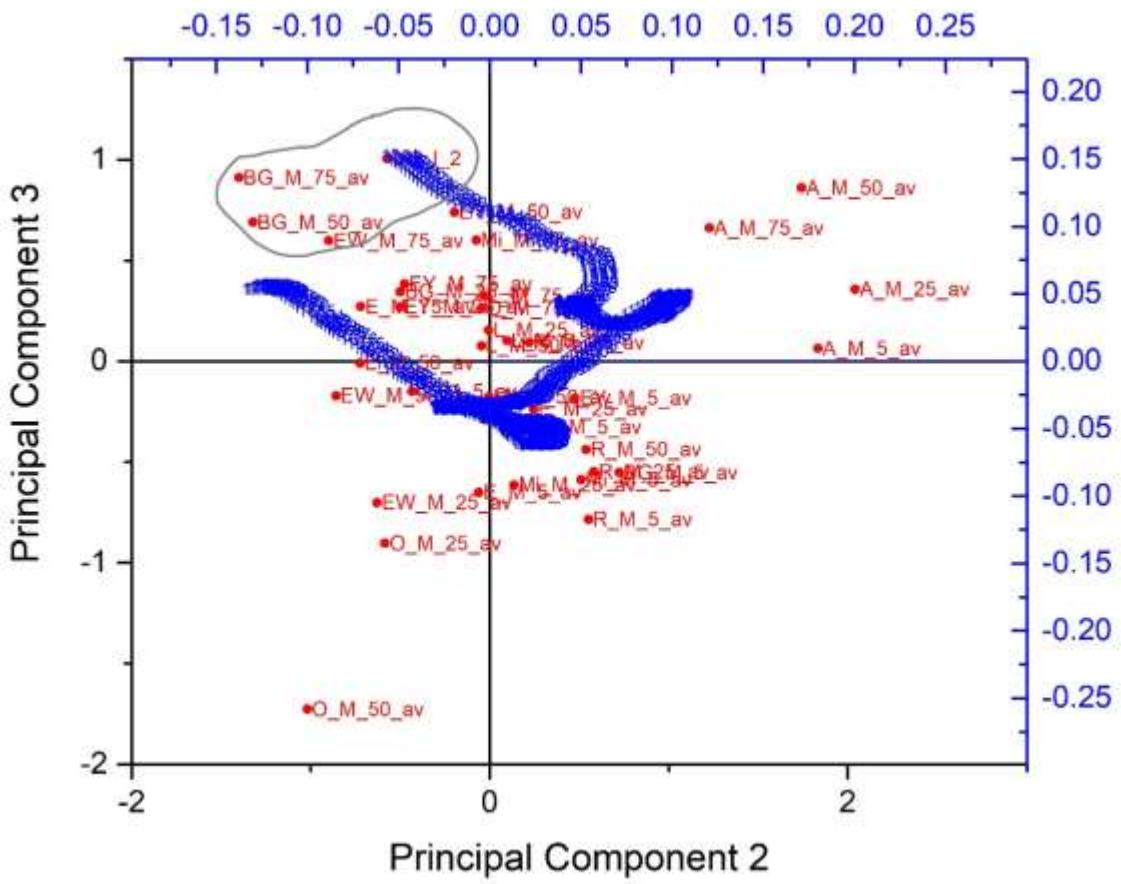

Figure 97: ROI_ covariance PC2vsPC3 for UN_I_2 (50% bone glue in mortar).

PC2vsPC3 correctly classifies UN_I_2 to bone glue/mortar mixtures but it fails to identify the correct concentration (fig.97). It is likely that asphalt/mortar mixtures shift highest variance towards themselves and produce intra-classification of the rest of the objects. However, if the distances among objects in PC2 are taken into consideration and the fact that objects close to the centre have average variance (Christer, 2005, 42), then the best match is BG_M_50 which is the correct identity. The uncertainty in the interpretation of plots is evident.

ROI_2_correlation

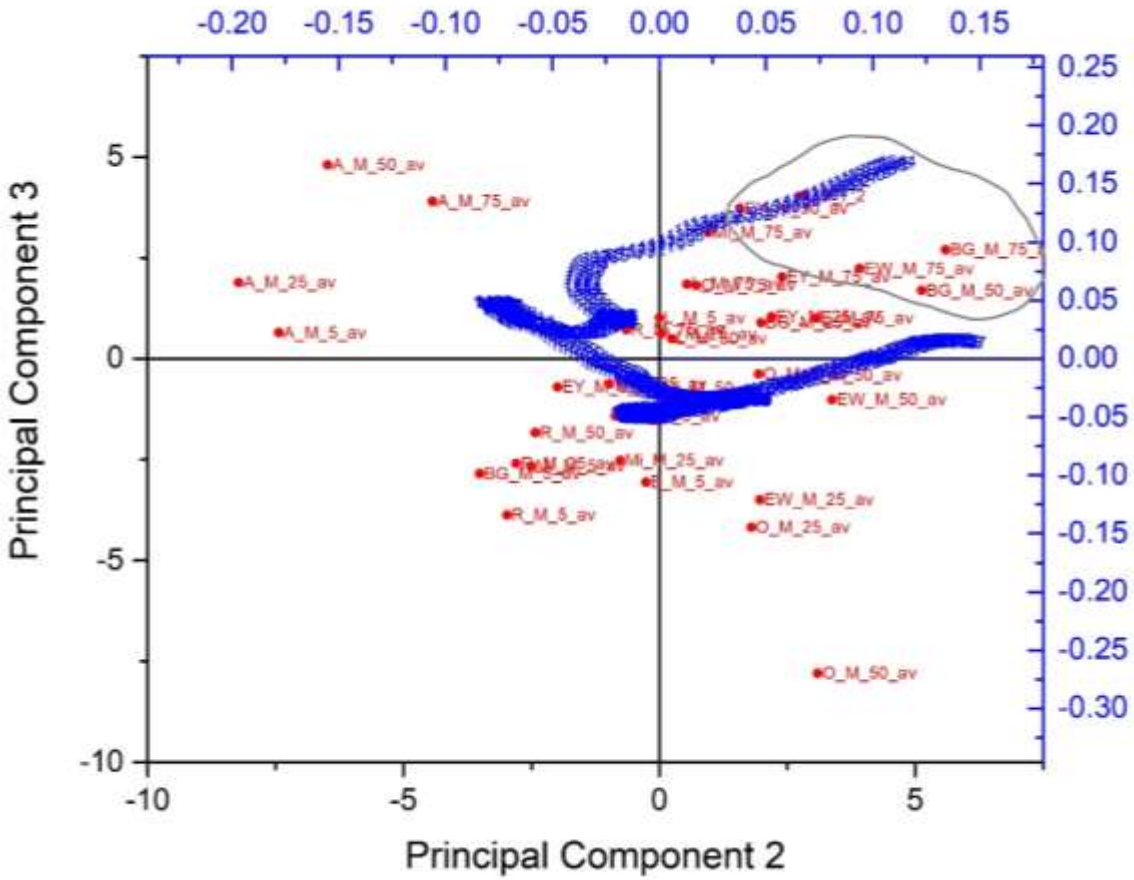

Figure 98: ROI_ correlation PCA matrix shows UN_I_2 misleading classification. PC1 explained variance is 94.00%, PC2 is 2.91% and PC3 is 2.02%.

Correlation matrices produced closer distances among objects making interpretation of plots less direct (data not shown). The PC2vsPC3 correlation plot produced misleading classification among broad group of standards (fig.98).

ROI_3_covariance

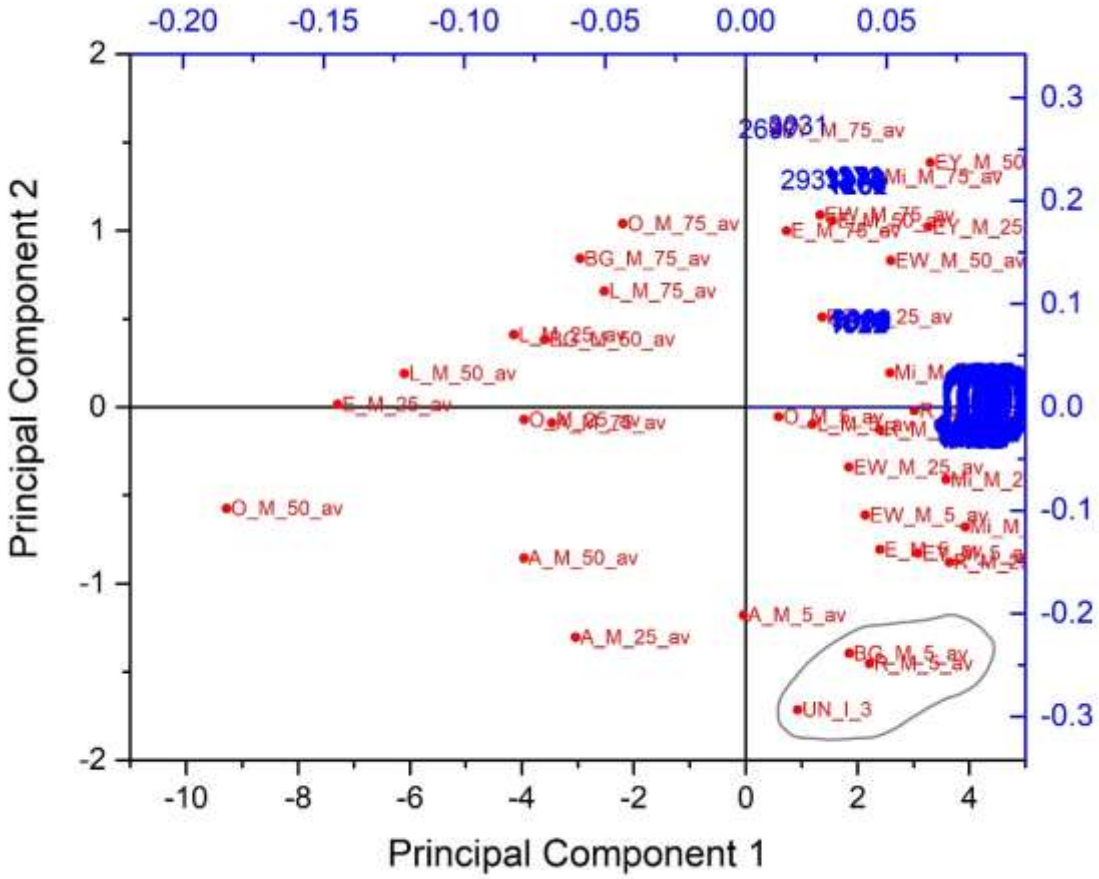

Figure 99: ROI_ covariance PC1vsPC2 for UN_I_3 (5% rice in mortar).

PC1 explains the 90.61% of total variance, PC2 the 6.16% and PC3 the 2.10%. Variables seem to classify objects according to their inorganic concentration (fig.99). The correct identity R_M_5 (5% rice additive in mortar) is within this group but positive matching is uncertain.

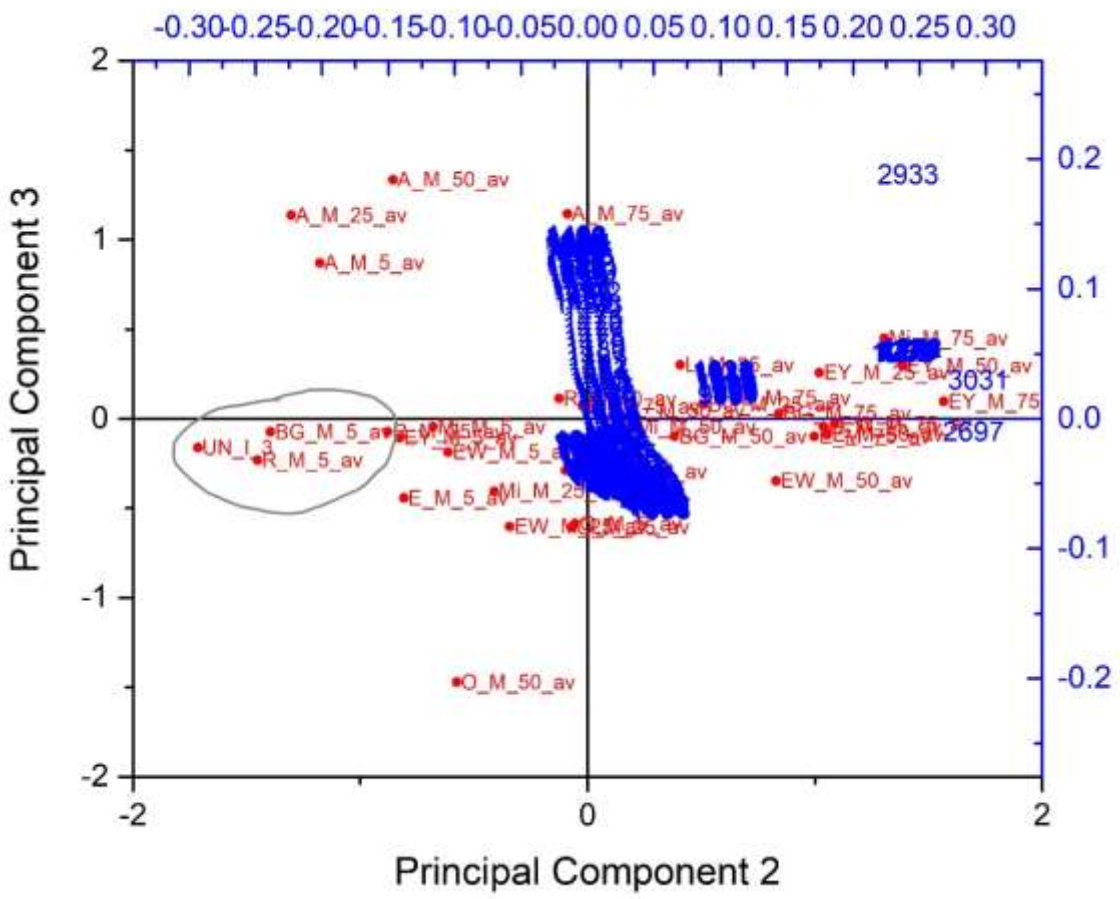

Figure 100:ROI_ covariance PC2vsPC3 for UN_I_3 (5% rice in mortar).

In the PC2vsPC3, PC2 is the principal component that provides correct classification, whereas PC3 groups everything together (fig.100). The variables further away from the zero centre are the ones contributing more to the positioning of the objects (Christer, 2005, 42). This is in fact true for the 2697 cm^{-1} variable that it was found to be diagnostic to rice additive through the CPAD identification. This variable-peak rules out chemical similarities with bone glue/mortar mixture which is the next closest matching candidate in the PCA plot.

ROI_3_correlation

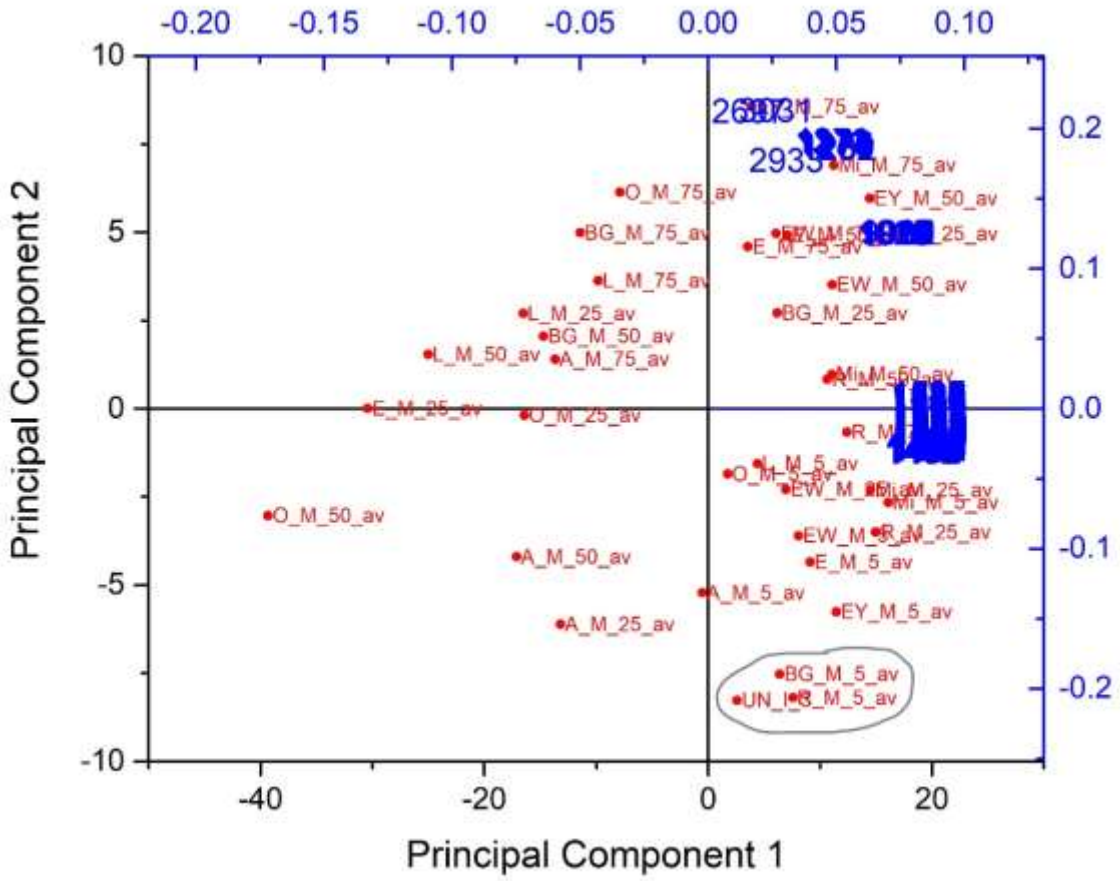

Figure 101: PC1vsPC2 correlation matrix for UN_I_3.

In the correlation matrix, PC1 explains the 87.25% of the total variance and PC2 the 9.12%. Better classification of UN_I_3 is produced from the correlation matrix than that calculated from the covariance one, showing the necessity to evaluate PCA from both matrices (fig.101).

ROI_4_covariance

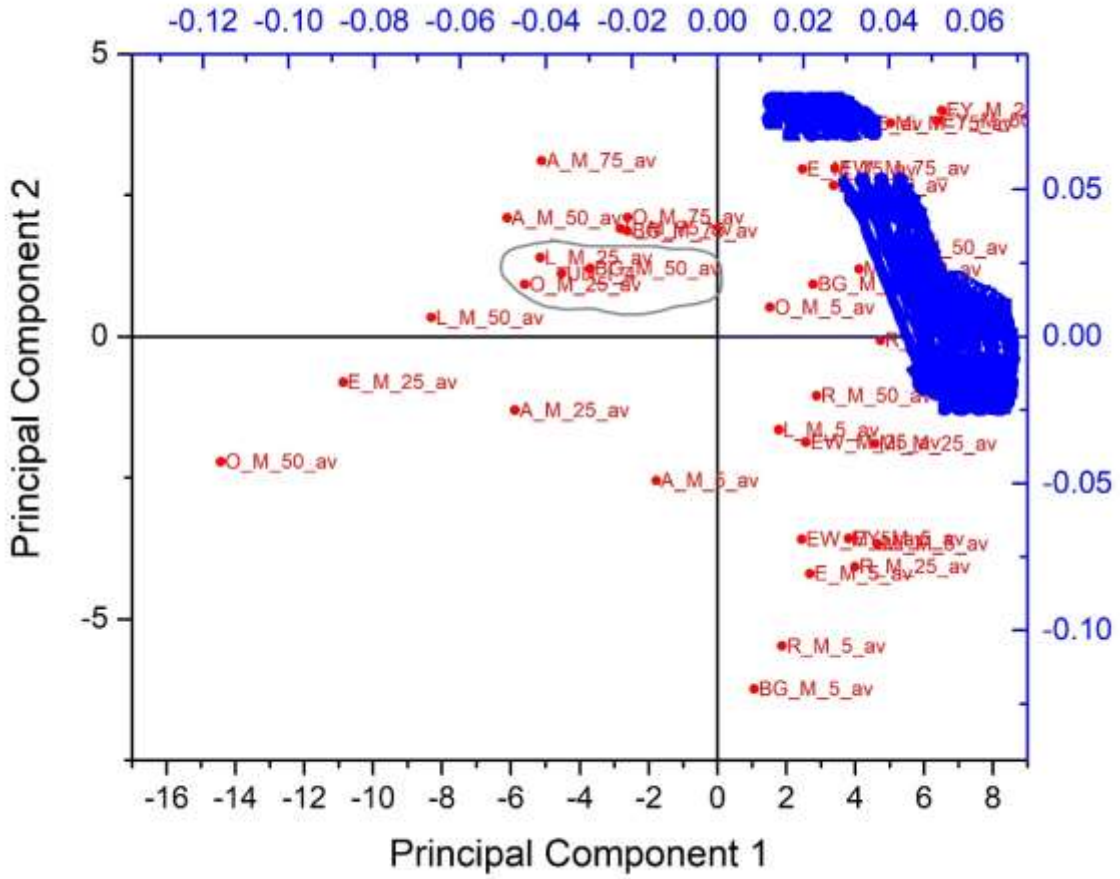

Figure 102: ROI_ covariance PC1vsPC2 for UN_I_4 (25% olive oil in mortar).

PC1 explains the 71.25% of the total variance, PC2 the 21.95% and PC3 the 4.35%. UN_I_4 is successfully classified between the two closest matches of L_M_25 (25% lard additive in mortar) and O_M_25 (25% olive oil additive in mortar), although bone glue mortar is also within the group (fig. 102). The latter can be safely ruled out since the CPAD identification showed that only lipids are present in the UN_I_4 spectrum.

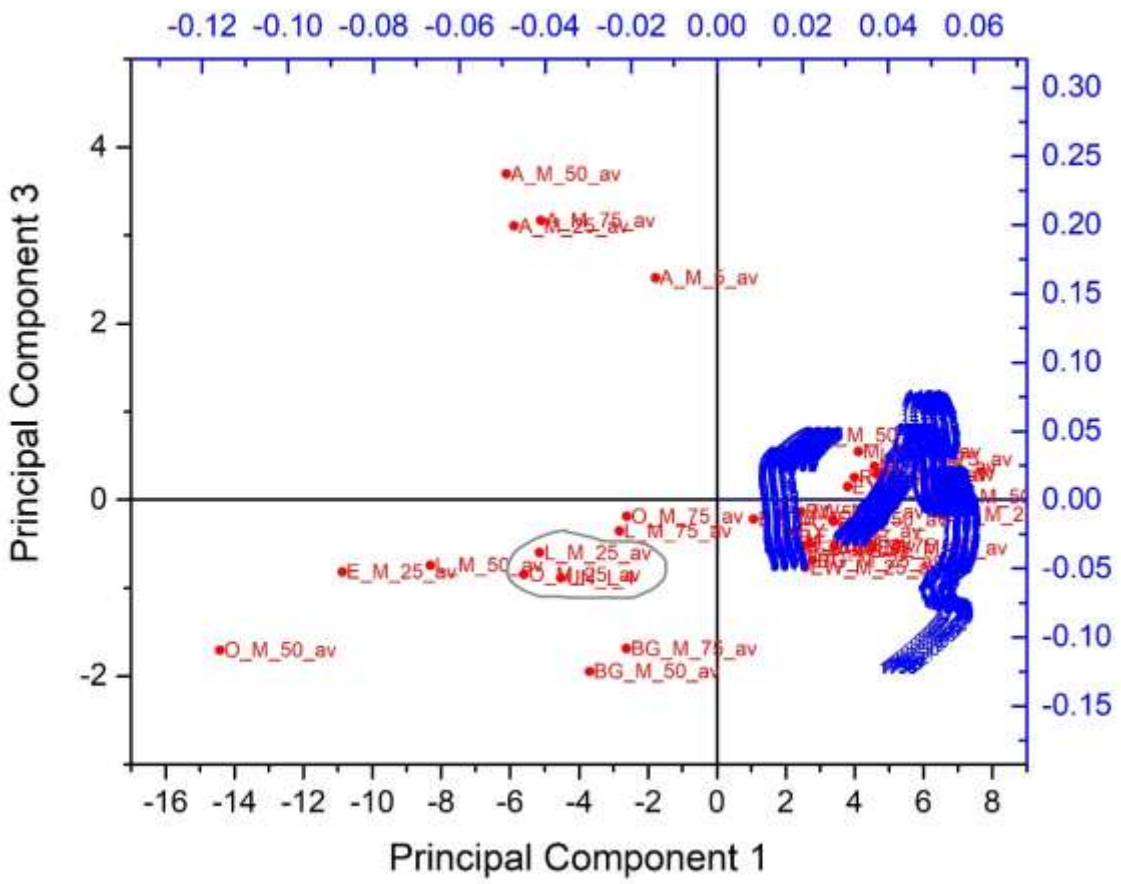

Figure 103: ROI_ covariance PC1vsPC3 for UN_I_4 (25% olive oil in mortar).

PC1vsPC3 reinforces the matching of UN_I_4 to the true identity O_M_25 although the relationship with L_M_25 persists (fig.103).

ROI_4.1_covariance

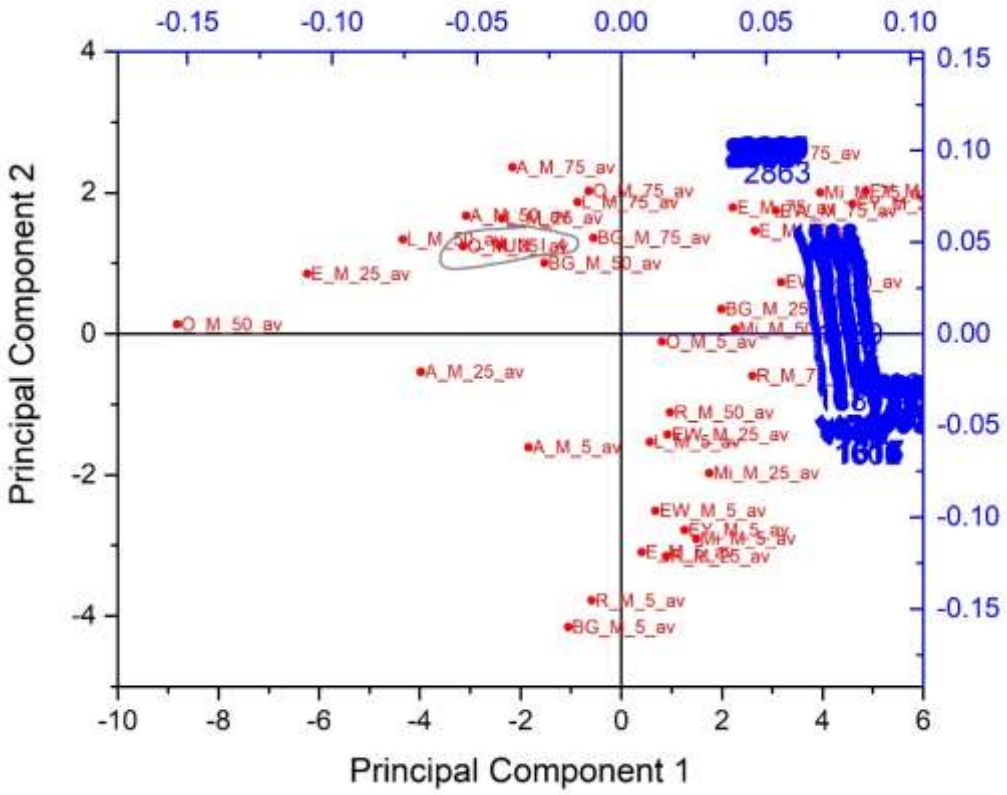

Figure 104: PC1vsPC2 for UN_I_4 after narrowed selection of ROI_ covariance.

PCA was repeated for UN_I_4 after narrowing down the ROI and including also diagnostic peaks (Table 20). PC1 explains the 65.97% of the total variance, PC2 the 28.92% and PC3 the 2.69%. Closeness to the best match was improved (fig.104). A better matrix was achieved when ROI contained fewer variables specific to the object in question.

ROI_5_covariance

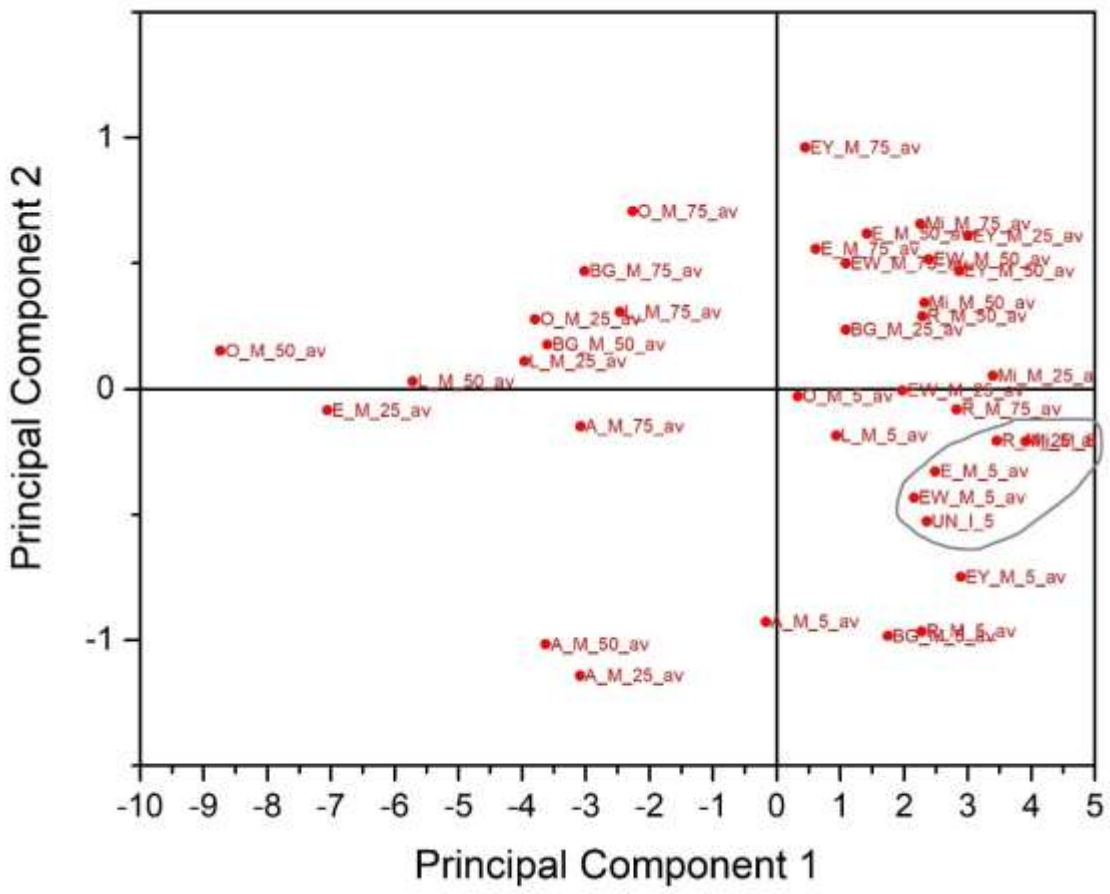

Figure 105: ROI_ covariance PC1vsPC2 for UN_I_5 (5% milk in mortar).

PC1 explains the 94.31% of the total variance in the dataset, PC2 the 2.65% and PC3 the 2.21%. The objects are classified mainly according to similarities in their inorganic concentration in the range 1433-1475 cm^{-1} (fig.105). This effect is visible to all 3 PCs and their plots (data not shown).

UN_I_5 is classified in the same group with Mi_M_5 (true identity) in PC1vsPC2. However, if this was an identification exercise, the outcomes would be misleading, since the closest match appears to be the EW_M_5 standard (fig.105).

ROI_6_Covariance

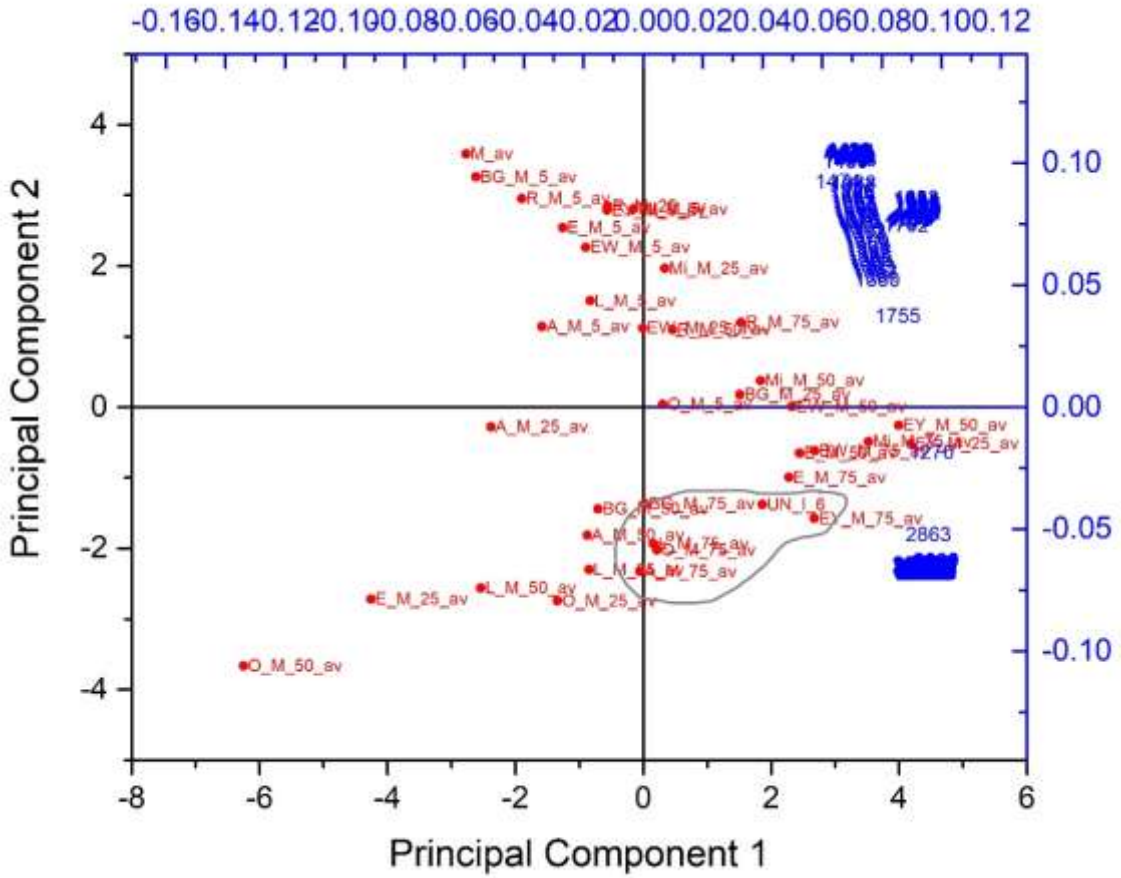

Figure 106: ROI_ covariance PC1vsPC2 for UN_I_6 (75% lard in mortar).

From here onwards, the spectrum of mortar standard (M_av) was included in all PCA matrices. PC1 explains the 52.97% of the total variance, PC2 the 41.69% and PC3 the 4.14%. UN_I_6 is classified in PC1 according to the concentration of organic additive based on the contribution of variables above 2863 cm^{-1} (fig.106). Although it is placed within the same correct group with its true identity (L_M_75, 75% lard additive in mortar) absolute match cannot be achieved.

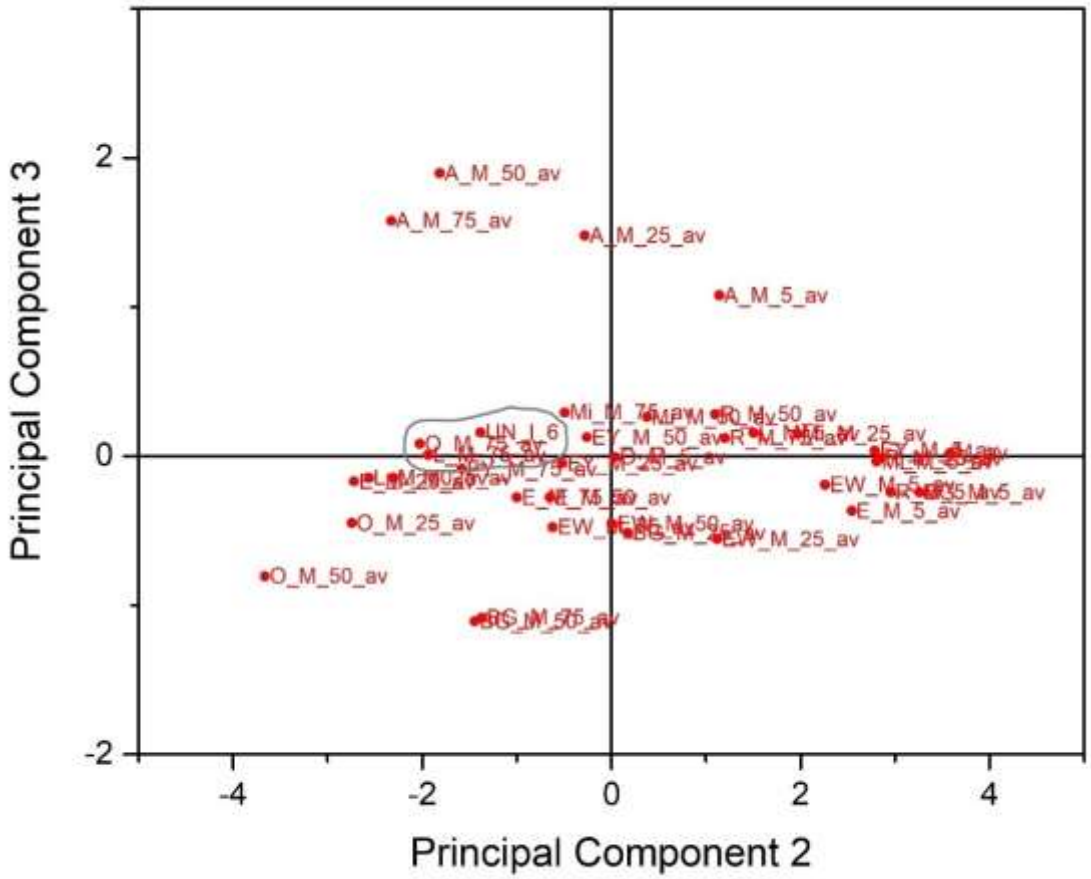

Figure 107: ROI_ covariance PC2vsPC3 for UN_I_6 (75% lard in mortar).

In PC2vsPC3 plot, UN_I_6 is closely linked to L_M_75 because PC2 is the one that describes the chemical similarities (fig.107). However, PC3 that explains a small variance in the dataset, forms a broad class of objects.

ROI_7_Covariance

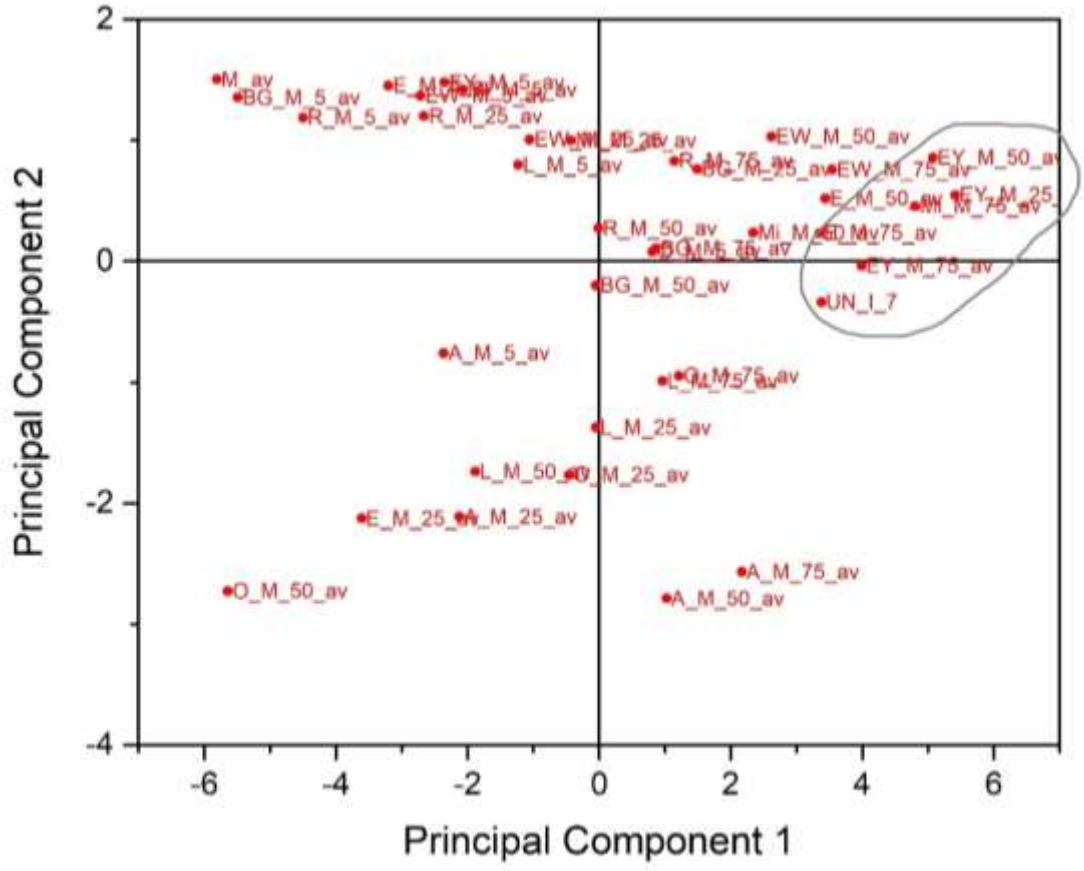

Figure 108: ROI_ covariance PC1vsPC2 for UN_I_7 (25% egg yolk in mortar).

PC1 explains the 80.95%, PC2 the 14.92% and PC3 the 2.62% of the total variance. PC1vsPC2 classifies UN_I_7 with egg and egg yolk mortar mixtures into a broad class of lipid materials according to 3006-2858 cm^{-1} variables (fig.108). Since the true identity of UN_I_7 is EY_M_25 (25% egg yolk additive in mortar), the plot could be misleading if used for identification.

ROI_8_Covariance

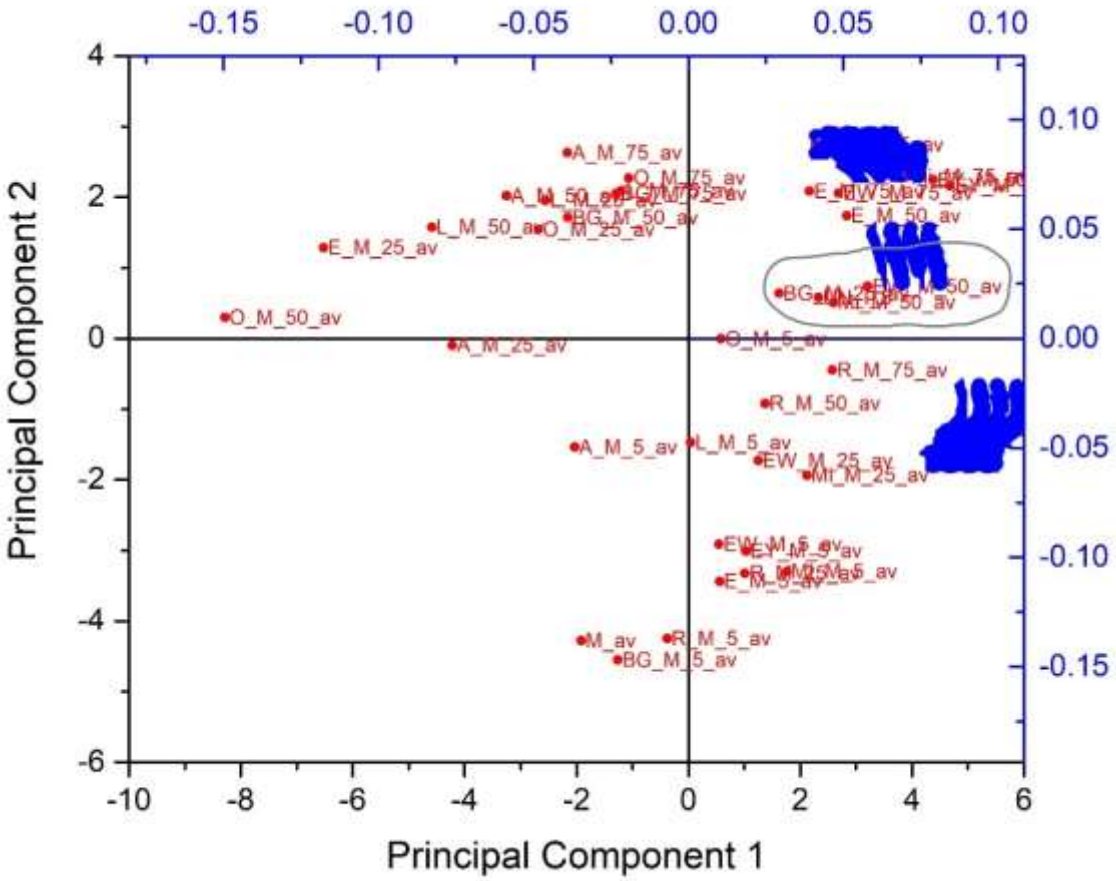

Figure 109: ROI_ covariance PC1vsPC2 for UN_I_8 (50% egg white in mortar).

PC1 explains the 59.40%, PC2 the 35.59% and PC3 the 3.25% of the total variance in the dataset. In PC1vsPC2, UN_I_8 is placed within the correct group with EW_M_50 (true identity), formed by the 1318-1283 cm^{-1} variables (fig.109). However, absolute matching between the unknown object and the true identity standard is not possible. The ROIs above 2900 cm^{-1} group lipids together in both PCs.

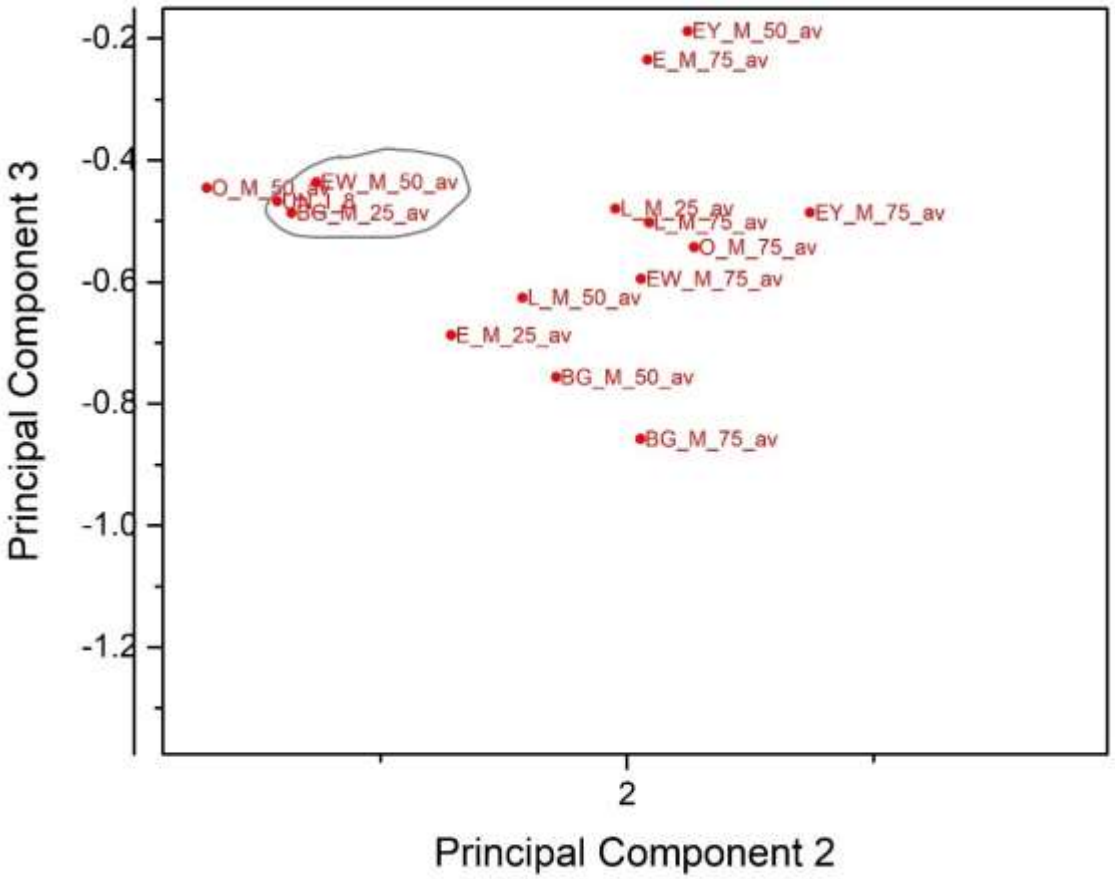

Figure 110: Enlarged PC2vsPC3 for UN_I_8 (50% egg white in mortar).

PC2vsPC3 provides better classification to the true identity (EW_M_50) although similarities to BG_M_25 (25% bone glue additive in mortar) are also present due to the protein content (fig.110). The correlation matrix produced smaller distances among objects and introduced more matching candidates, thus identification would not be certain (Appendix II, fig.2).

ROI_9_Covariance

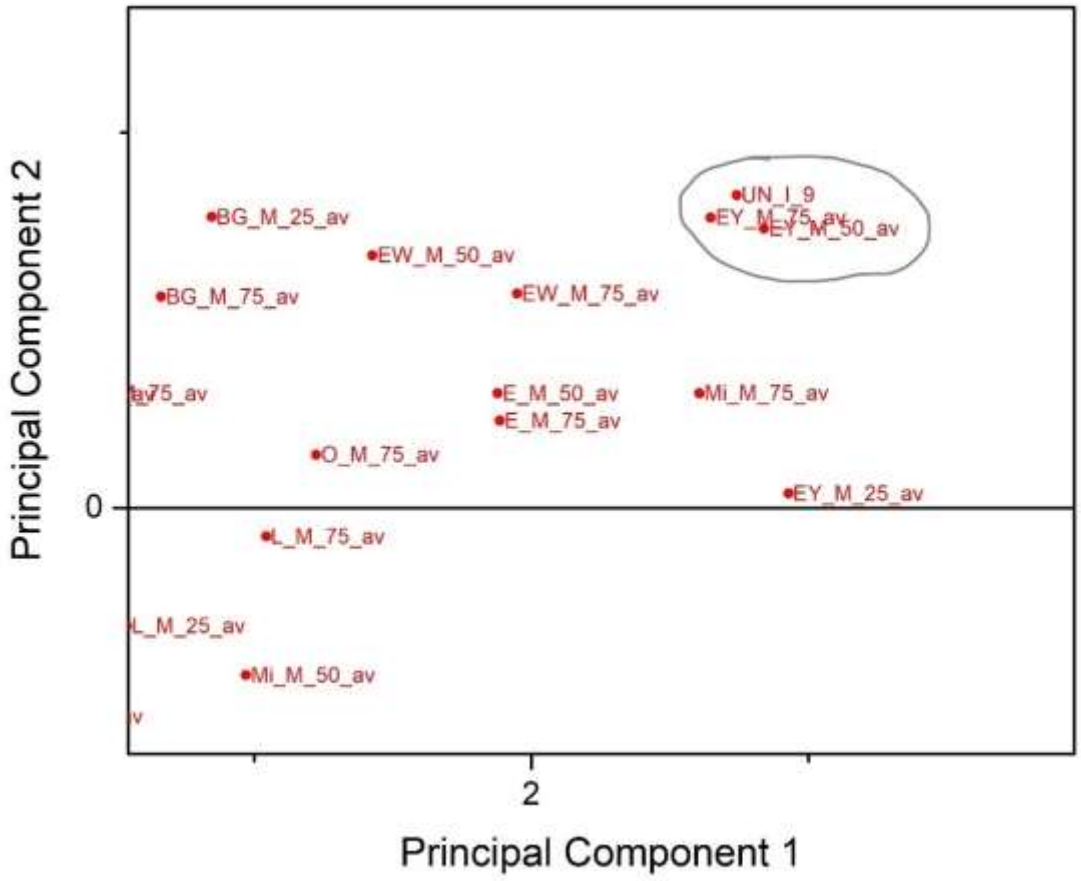

Figure 111: Enlarged ROI_ covariance PC1vsPC2 for UN_I_9 (75% egg in mortar).

PC1 explained variance is 82.94%, PC2 is 8.90% and PC3 is 6.52%. Although UN_I_9 is placed with lipids due to the contribution of 2900 cm^{-1} ROIs, the identification is false (fig.111). The true identity of UN_I_9 is E_M_75 (75% egg additive in mortar) which appears further away in PC1vsPC2. Classification would be misleading if used for identification.

No further information is drawn from the plots of PC2 and PC3 and correlation matrix (data not shown).

ROI_10_Covariance

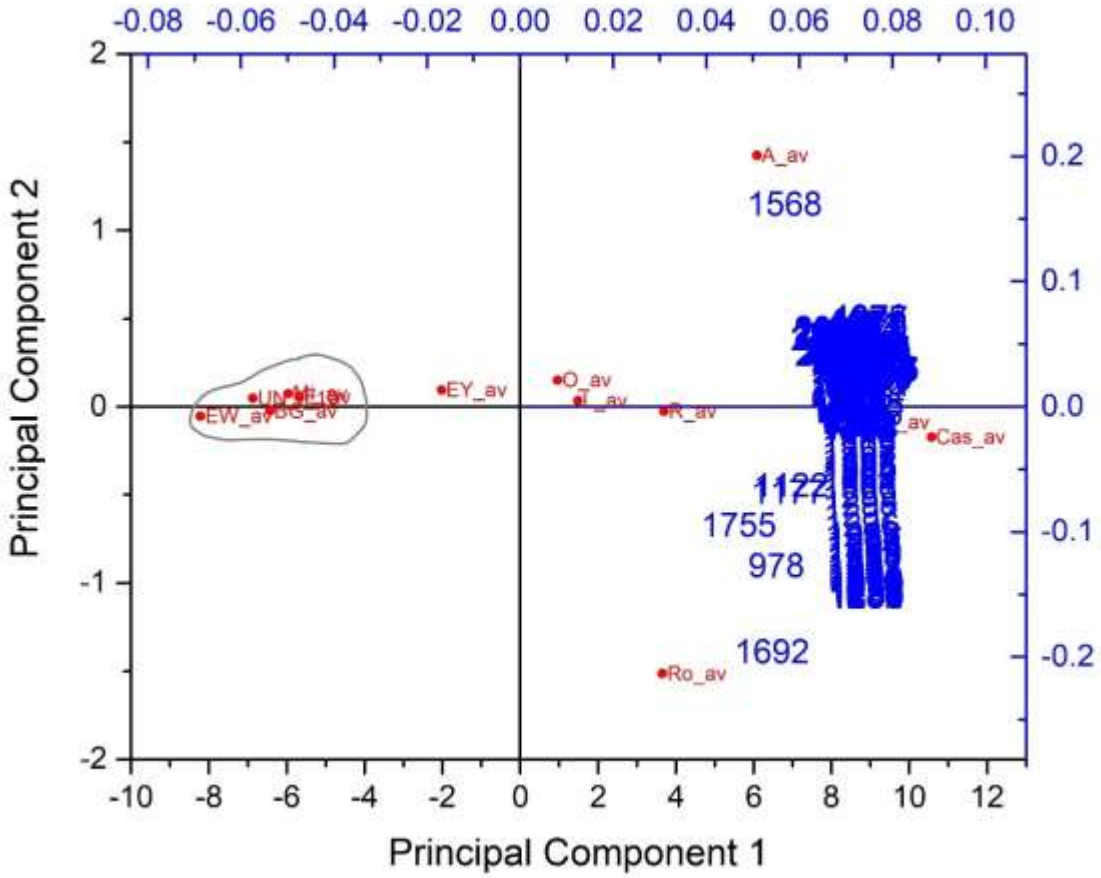

Figure 112: ROI_ covariance PC1vsPC2 for UN_I_10 (egg, E_av).

PC1 explains the 98.12% and PC2 the 0.90% of the total variance. Based on the selected variables, PC1, which explains almost entirely the total variance in the dataset, classifies UN_I_10 with the correct group of protein-lipids, whereas PC2 separated pure proteins (EW_av and BG_av) on the negative side, from protein-lipid materials on the positive side of PC2 (fig.112). The classification of the rest of the organic materials makes sense.

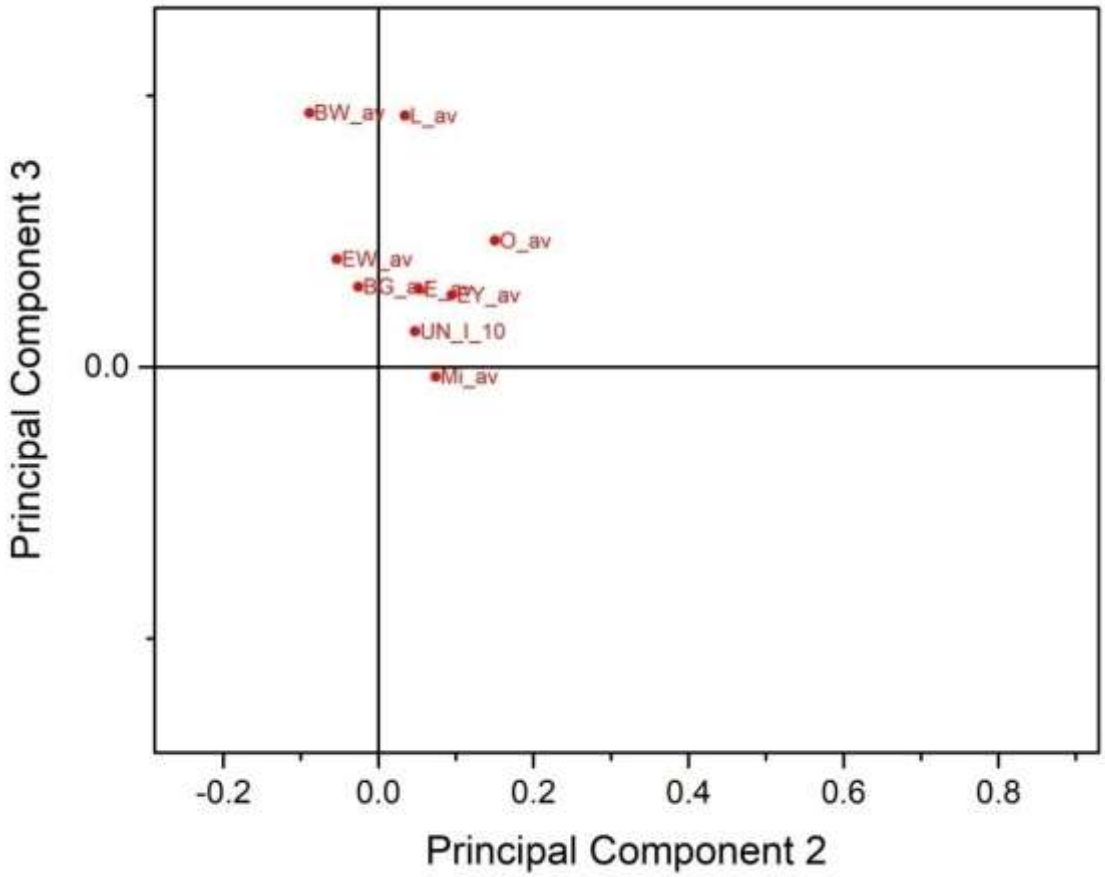

Figure 113: Enlarged PC2vsPC3 for UN_I_10 (egg, E_av).

Better matching of UN_I_10 to the true identity (Egg – E_av) is produced in PC2vsPC3 plot based on the distances among objects in PC2, although not absolute (fig.113).

10.3 Results: PCA on Diagnostic Peaks

Table 21 summarizes the PCA parameters and classification results from matrices that contain only diagnostic peaks as variables for each spectrum in question (UN_I_1 to UN_I_10). The selection of diagnostic peaks was determined through the CPAD identification process for each unknown spectrum (Ch.8). The selection of objects is the same as in the PCA on ROIs. The PC plots are provided in Appendix II, *10.3 Results: PCA on Diagnostic peaks (fig.3-13)*.

PCA Matrix Label	Revealed ID	Objects	Variables (cm^{-1})	Variables vs. Objects	Results	Comments
D_1_covariance (Appendix II, fig.3)	UN_I_1 is **A_M_25** (25% asphalt additive in mortar).	Total 38: UN_I_1 + 36 mixtures + mortar standard. Selection according to CPAD outcomes.	3472, 2954, 2927, 2870, 2728, 1653, 1599, 1461, 933 (9 variables).	Variables less than objects.	Correct classification relevant to additive. Closeness to both A_M_25 and A_M_5 reflects same dillema as in ROIs and CPAD.	ROIs PCA produced better classification (all objects in the same quadrant).
D_1_correlation	UN_I_1 is **A_M_25** (25% asphalt additive in mortar).	Total 38: UN_I_1 + 36 mixtures + mortar standard. Selection according to CPAD outcomes.	3472, 2954, 2927, 2870, 2728, 1653, 1599, 1461, 933 (9 variables).	Variables less than objects.	Almost identical biplot to that of covariance.PC1 is 57.22%, PC2 is 32.96% and PC3 is 8.15% of the total variance.	
D_2_covariance (Appendix II, fig.4)	UN_I_2 is **BG_M_50** (50% bone glue additive in mortar).	Total 38: UN_I_2 + 36 mixtures + mortar standard. Selection according to CPAD outcomes.	1707, 1693, 1576, 1471, 1411, 1344 (6 variables).	Variables less than objects.	Correct clssification to proteins, misleading individual matching.	ROIs PCA produced better intra-classification.
D_2_correlation	UN_I_2 is **BG_M_50** (50% bone glue additive in mortar).	Total 38: UN_I_2 + 36 mixtures + mortar standard. Selection according to CPAD outcomes.	1707, 1693, 1576, 1471, 1411, 1344 (6 variables).	Variables less than objects.	Similar to covariance. PC1 is 88.42%, PC2 is 7.26% and PC3 is 3.69% of the total variance.	
D_3_covariance (Appendix II, fig.5)	UN_I_3 is **R_M_5** (5% rice additive in mortar).	Total 38: UN_I_3 + 36 mixtures + mortar standard. Selection according to CPAD outcomes.	3031, 2933, 2697, 1619, 1587, 1467, 1460, 1443, 1432, 1282, 1271, 1022, 1007, 998 (14).	Variables less than objects.	Classification according to low organic concentration. True identity within the group.	ROIs PCA produced better intra-classification.
D_3_correlation (Appendix II, fig.6)	UN_I_3 is **R_M_5** (5% rice additive in mortar).	Total 38: UN_I_3 + 36 mixtures + mortar standard. Selection according to CPAD outcomes.	3031, 2933, 2697, 1619, 1587, 1467, 1460, 1443, 1432, 1282, 1271, 1022, 1007, 998 (14).	Variables less than objects.	Better outcomes, more close to the true identity.	Same results in ROIs PCA.

Table 21: Summary of PCA parameters for matrix construction using solely Diagnostic peaks and PCA classification results for each spectrum in question.

PCA Matrix Label	Revealed ID	Objects	Variables (cm^{-1})	Variables vs. Objects	Results	Comments
D_4_covariance (Appendix II, fig.7)	UN_I_4 is **O_M_25** (25% olive oil additive in mortar).	Total 38: UN_I_4 + 36 mixtures + mortar standard. Selection according to CPAD outcomes.	3011, 2992, 2966, 2941, 2863, 1759, 1702, 1681, 1668, 1660, 1617, 1605, 1506, 1380, 1318, 1282 (16).	Variables less than objects.	Successful classification reflects organic concentration.PC 1 is 61.86%, PC2 is 30.87% and PC3 is 4.62%.	Same results in ROIs PCA.
D_4_correlation	UN_I_4 is **O_M_25** (25% olive oil additive in mortar).	Total 38: UN_I_4 + 36 mixtures + mortar standard. Selection according to CPAD outcomes.	3011, 2992, 2966, 2941, 2863, 1759, 1702, 1681, 1668, 1660, 1617, 1605, 1506, 1380, 1318, 1282 (16).	Variables less than objects.	Almost identical outcomes to covariance.PC1 is 60.42%, PC2 is 32.18% and PC3 is 4.50%.	
D_5_covariance (Appendix II, fig.8)	UN_I_5 is **Mi_M_5** (5% milk additive in mortar).	Total 38: UN_I_5 + 36 mixtures + mortar standard. Selection according to CPAD outcomes.	2959, 2925, 1652, 1585, 1535, 1475, 995 (7).	Variables less than objects.	Classification according to low organic concentration. True identity within the group. Misleading intra-classification. PC1 is 65.93%, PC2 is 31.51% and PC3 is 1.26%.	Same results in ROIs PCA.
D_5_correlation	UN_I_5 is **Mi_M_5** (5% milk additive in mortar).	Total 38: UN_I_5 + 36 mixtures + mortar standard. Selection according to CPAD outcomes.	2959, 2925, 1652, 1585, 1535, 1475, 995 (7).	Variables less than objects.	Identical to covariance. PC1 is 66.05%, PC2 is 30.01% and PC3 is 2.47%.	
D_6_covariance (Appendix II, fig.9)	UN_I_6 is **L_M_75** (75% lard additive in mortar).	Total 38: UN_I_6 + 36 mixtures + mortar standard. Selection according to CPAD outcomes.	3018, 3003, 2968, 2939, 2863, 1755, 1696, 1683, 1662, 1474, 1450, 1418, 1388, 1270 (14).	Variables less than objects.	Classification of lipids, true identity within the group. PC1 is 56.82%, PC2 is 34.33% and PC3 is 6.27%.	Same results in ROIs PCA.
D_6_correlation	UN_I_6 is **L_M_75** (75% lard additive in mortar).	Total 38: UN_I_6 + 36 mixtures + mortar standard. Selection according to CPAD outcomes.	3018, 3003, 2968, 2939, 2863, 1755, 1696, 1683, 1662, 1474, 1450, 1418, 1388, 1270 (14).	Variables less than objects.	Same outcomes with that of covariance. PC1 is 55.93%, PC2 is 35.45% and PC3 is 6.04%.	

Table 21: continued

PCA Matrix Label	Revealed ID	Objects	Variables (cm^{-1})	Variables vs. Objects	Results	Comments
D_6.1_covariance	UN_I_6 is **L_M_75** (75% lard additive in mortar).	Total 38: UN_I_6 + 36 mixtures + mortar standard. Selection according to CPAD outcomes.	Only Fingerprint variables: 1755, 1696, 1683, 1662, 1474, 1450, 1418, 1388, 1270 (9).	Variables less than objects.	Insignificant improvement when variables above 2900 are excluded. PC1 is 81.51%, PC2 is 12.71% and PC3 is 3.61%.	
D_6.2_correlation	UN_I_6 is **L_M_75** (75% lard additive in mortar).	Total 38: UN_I_6 + 36 mixtures + mortar standard. Selection according to CPAD outcomes.	Only Fingerprint variables: 1755, 1696, 1683, 1662, 1474, 1450, 1418, 1388, 1270 (9).	Variables less than objects.	Objects appear more spread but the information is the same as in covariance. PC1 is 80.42%, PC2 is 13.57% and PC3 is 4.02%.	
D_7_covariance (Appendix II, fig.10)	UN_I_7 is **EY_M_25** (25% egg yolk additive in mortar).	Total 38: UN_I_7 + 36 mixtures + mortar standard. Selection according to CPAD outcomes.	3006, 2957, 2936, 2858, 1754, 1695, 1561, 1481, 1319, 1281 (10).	Variables less than objects.	Correct classification to lipids, close to true identity but not absolute matching. PC1 is 59.91%, PC2 is 31.34% and PC3 is 5.56%.	Same results in ROIs PCA.Could be misleading if true identity was not known.
D_7_correlation	UN_I_7 is **EY_M_25** (25% egg yolk additive in mortar).	Total 38: UN_I_7 + 36 mixtures + mortar standard. Selection according to CPAD outcomes.	3006, 2957, 2936, 2858, 1754, 1695, 1561, 1481, 1319, 1281 (10).	Variables less than objects.	Similar to covariance. PC1 is 62.16%, PC2 is 29.22% and PC3 is 5.17%.	
D_8_covariance (Appendix II, fig.11)	UN_I_8 is **EW_M_50** (50% egg white additive in mortar).	Total 38: UN_I_8 + 36 mixtures + mortar standard. Selection according to CPAD outcomes.	1283, 1318, 1578, 1681, 1691, 2900, 2913, 2933, 2944, 2967, 2975, 3001, 3012, 3071, 3084 (15).	Variables less than objects.	Classification close to true identity.	Better results in ROIs PCA.
D_8_correlation	UN_I_8 is **EW_M_50** (50% egg white additive in mortar).	Total 38: UN_I_8 + 36 mixtures + mortar standard. Selection according to CPAD outcomes.	1283, 1318, 1578, 1681, 1691, 2900, 2913, 2933, 2944, 2967, 2975, 3001, 3012, 3071, 3084 (15).	Variables less than objects.	Similar to covariance.PC1 is 72.99%, PC2 is 20.74% and PC3 is 4.42%.	

Table 21: continued

PCA Matrix Label	Revealed ID	Objects	Variables (cm^{-1})	Variables vs. Objects	Results	Comments
D_9_covariance (Appendix II, fig.12)	UN_I_9 is **E_M_75** (75% egg additive in mortar).	Total 38: UN_I_9 + 36 mixtures + mortar standard. Selection according to CPAD outcomes.	970, 1266, 1467, 1554, 1682, 1747, 2607, 2856, 2936, 2958, 2966, 3006, 3014 (13).	Variables less than objects.	Closer classification to true identity at PC2vsPC3. First PCs group unknown to false Mi_M_75. PC1 is 62.36%, PC2 is 28.53% and PC3 is 6.65%.	Similar dilemmas with ROIs PCA (PC1vsPC2 false matching to EY_M_75).
D_9_correlation	UN_I_9 is **E_M_75** (75% egg additive in mortar).	Total 38: UN_I_9 + 36 mixtures + mortar standard. Selection according to CPAD outcomes.	970, 1266, 1467, 1554, 1682, 1747, 2607, 2856, 2936, 2958, 2966, 3006, 3014 (13).	Variables less than objects	Highly similar to covariance. PC1 is 64.12%, PC2 is 26.51% and PC3 is 6.67%.	
D_10_covariance (Appendix II, fig.13)	UN_I_10 is **E_av** (egg standard).	Total 13: UN_I_10 + 12 organic standards. Selection according to CPAD outcomes. Rosin (RO), Casein (Cas) and Beeswax (BW) standards were also added.	3019, 2972, 2941, 2875, 2865, 1755, 1692, 1568, 1471, 1445, 1409, 1382, 1324, 1283, 1266, 1177, 1122, 978 (18).	Variables more than objects.	Successful classification.	Similar but better results than ROIs PCA.
D_10_correlation	UN_I_10 is **E_av** (egg standard).	Total 13: UN_I_10 + 12 organic standards. Selection according to CPAD outcomes. Rosin (RO), Casein (Cas) and Beeswax (BW) standards were also added.	3019, 2972, 2941, 2875, 2865, 1755, 1692, 1568, 1471, 1445, 1409, 1382, 1324, 1283, 1266, 1177, 1122, 978 (18).	Variables more than objects.	Same as in covariance. PC1 is 92.28%, PC2 is 3.82% and PC3 is 2.37%.	

Table 21: continued.

PCA on Diagnostic Peaks (Table 21) provided similar outcomes to that on Regions of Interest (Sect. 10.2, Table 20). In four cases, (D_1, D_2, D_3 and D_8), PCA on ROIs produced better outcomes than that on Diagnostic Peaks relative to the distances among objects and positioning on the score plots. However, the overall classification was not improved. The issues of absolute matching of the spectrum in question to the true identity standard remained the same as in the PCA on ROIs.

The main advantage of using selected Diagnostic Peaks instead of ROIs in PCA is the fast calculation of variance and the clearer depiction of scores and loadings on the PCA plots.

10.4 Discussion of PCA methodology tests

The PCA methodology, designed according to the outcomes of sections 9.2 (literature review) and 9.4 (preliminary testing), was assessed through a series of tests on spectra of known identity. The objective was to classify these spectra to the correct groups of standards and if possible, to their individual chemical matching.

The central outcome of this exercise is that PCA plots could not provide conclusive results regarding the classification of the object in question (spectrum). The uncertainty, associated with PCA analysis previously observed in section 9.4, persists. This originates from two factors: first is the dependency of PCA on the selection of objects and variables; second is the non-standardized reading of PCA plots which allows different interpretations of results that may carry equal weight for justifying identity. Decision-making for acceptance or rejection of PCA results proved difficult, *despite* the fact that the identity of the objects was known.

The dependency of PCA on the selection of objects and variables was demonstrated by object groups formed due to their similar variance, being products of the specific selection of objects and variables included in the matrix.

When objects that differed greatly from the rest were included in the matrix, they shifted the total variance towards themselves and influenced the entire classification. Consequently, true variance could not be reflected in the first PC that describes the highest variance in the dataset. Within this condition, the remaining objects were classified closely together and distances among them were smaller, usually forming one large group. Therefore, it was concluded that PCA matrices should include objects that do not differ greatly from the object in question. This is possible when the selection takes place after the identification of a spectrum through the CPAD and the narrowing down of possible

chemical matching spectra from standards. The action would at least minimize the problem of shifting the true variance in the first PCs.

Another observation was that groups of organic/mortar mixtures (objects) would be formed from similarities in concentration of organic components rather than chemical composition, due to the influence of the peaks (variables) of inorganic materials present in the mixtures. Thus, groups should be examined in relation to the variables that contributed the most to their formation by observing the PCA loadings.

Because of these observations, it appears that Principal Component Analysis heavily depends on the CPAD identification outcomes and cannot be used as an unsupervised pattern recognition method when the objective is the identification of a spectrum.

Additionally, since PCA plots could be read in more than one manner, the CPAD data are also necessary during interpretation in order to dismiss similarities between objects from correlations other than chemical composition. The definition of PCA as a non-parametric method by Shlens (2014, 9) must be kept in mind during interpretation; the CPAD information relevant to which peaks should be present in the object in question in order to have a positive match with a standard must be incorporated in the assessment (Ch.8, sect.8.2, Summary and Discussion).

Although interpretation of PCA results is problematic, this can be reduced by plotting and assessing all the resulting PCs before reaching a conclusion. Object classification in a group or intra-classification between the object in question and its possible match, should be assessed relative to the distances between the objects on each PC in the plot and according to the percentage of variance that each PC represents (Bro and Smilde, 2014).

The exercise showed that the distances among objects in a PC plot which are calculated from covariance matrices reflect the original variance of the data without pre-treatment hence they are considered to be more realistic. However, in certain cases, correlation matrices (data scaling) produced closer distances among similar objects in the PC plot and provided better individual matching. Both matrices should be assessed before reaching conclusions.

Regarding the number of variables introduced in the matrix, the exercise showed no significant difference in classification results between PCA matrices incorporating ROIs/diagnostic peaks and solely Diagnostic Peaks. Practical aspects, such as fast PC calculation and easy-to-read scores and loadings, are favored when solely Diagnostic Peaks are used.

The outcomes define a framework of supervised use of PCA which is opposite to its original definition and purpose (Christer, 2005, 39). If the CPAD methodology is necessary for the selection of objects and variables then the PCA outcomes will reflect the analyst's decisions. Classification will occur reflecting chemical similarities but deciding which PC plot should be accepted as representative of true variance still lacks in levels of confidence in the decision.

Despite these shortcomings, it was decided to carry out the final evaluation of PCA based on testing samples whose composition is only revealed once an identification has been reached using PCA. This is expected to confirm the range of shortcomings identified form the experimental study of PCA thus far.

10.5 Evaluation of PCA methodology

Using the PCA methodology established from the experimental study, a final evaluation involved the ten unknown spectra used in the Experimental set IV (Ch.8, sect. 8.1.4), which had been identified using the standardized the CPAD (Ch.8). PCA was then performed with reference to the CPAD outcomes. The identity of the spectra was revealed after PCA had been used to suggest their identity. The experimental aim was to decide on whether PCA can act as a complimentary identification tool for the CPAD methodology.

The following objectives were assessed:

- The degree of successful classification of the unknown object (spectrum) to a group of standards of similar chemical composition.
- The degree of certainty of classification (interpretation).
- The quality and quantity of the objects and variables necessary to produce representative variance in the dataset (methodology).

The PCA methodology employed was developed from the outcomes defined in section 10.4:

- Principal Components were calculated from both covariance and correlation matrices.
- PCA matrices were prepared from solely Diagnostic peaks as variables, selected according to the CPAD identification outcomes as those that contributed most to the identification of the unknown spectrum. Regions of Interest (ROIs) were not included for clarity in the interpretation of score plots.

- The number of objects was further reduced to include only comparative spectra that exhibit chemical similarities with the unknown spectrum, as defined through the CPAD identification process. This action improves the calculation of true variance in the dataset and avoids false classifications caused by the prevalence of objects that differ significantly from the remainder. It also produces a more balanced matrix, where the number of objects is close to the number of variables, allowing the calculation of true variance to resemble that of matrices with ROIs.

10.5.1 Results of Principal Component Analysis

Table 22 summarizes the PCA parameters and outcomes for each unknown spectrum (**UN_IV_1 to UN_IV_10**). The parameters (objects and variables) were selected based on the CPAD identification process (Ch.8, sect.8.1.4, Table 15). The last column in Table 22 includes the retrospective assessment of the identification results from both the CPAD and PCA applications, after revealing the true identity of the spectra.

Label	CPAD ID	Objects	Variables (cm^{-1})	Variables vs. Objects	PCA Outcome	Retrospective - After Revealing True ID
UN_IV_1_ Covariance	A_av (Asphalt)	UN_IV_1, A_av, M_av, A_M_75_av, A_M_50_av, A_M_25_av, A_M_5_av (7).	724, 742, 759, 872, 918, 937, 976, 033, 1089, 1169, 1308, 1377, 1460, 1603, 1643, 1843, 1866, 1888, 2039, 2726, 2858, 2868, 2930, 2954, 2961 (25).	Variables more than objects.	Intra-classification to A_M_75, supported by most PCs.	**ID is A_M_75** supported by PCA. Better utilization of CPAD would produce agreeable outcomes (Ch.8, sect.8.1.4, Table 15).
UN_IV_1_ Correlation	A_av (Asphalt)	UN_IV_1, A_av, M_av, A_M_75_av, A_M_50_av, A_M_25_av, A_M_5_av (7).	724, 742, 759, 872, 918, 937, 976, 033, 1089, 1169, 1308, 1377, 1460, 1603, 1643, 1843, 1866, 1888, 2039, 2726, 2858, 2868, 2930, 2954, 2961 (25).	Variables more than objects.	Same results as in covariance. PC1 is 62.67%, PC2 is 25.41% and PC3 is 9.12%.	
UN_IV_2_ Covariance	EW_M_50 (50% egg white additive in mortar).	UN_IV_2 plus egg white and bone glue mortar mixtures (9 spectra).	967, 1286, 1313, 1480, 1575, 1616, 1624, 1673, 1686, 1695, 2930, 2940, 2961, 3086 (14).	Variables more than objects.	Absolute match to EW_M_50, according to inorganic presence and organic material.	**Correct ID**. CPAD and PCA agreeable.
UN_IV_2_ Correlation	EW_M_50 (50% egg white additive in mortar).	UN_IV_2 plus egg white and bone glue mortar mixtures (9 spectra).	967, 1286, 1313, 1480, 1575, 1616, 1624, 1673, 1686, 1695, 2930, 2940, 2961, 3086 (14).	Variables more than objects.	Same results as in covariance. PC1 is 60.81% and PC2 is 37.77%.	

Table 22: Summary of PCA parameters for matrix construction and PCA classification results for each UN_IV spectrum in question.

Label	CPAD ID	Objects	Variables (cm^{-1})	Variables vs. Objects	PCA Outcome	Retrospective - After Revealing True ID
UN_IV_3_ Covariance	R_M_50 (50% rice additive in mortar).	UN_IV_3 plus egg yolk, egg, milk, lard, oil and rice mortar mixtures (25).	924, 1009, 1026, 1263, 1446, 1472, 1539, 1551, 1578, 1611, 1619, 1652, 1746, 2857, 2927, 3007 (16).	Variables less than objects.	Match to R_M_50 by PC2vsPC3, clear interpretation of loadings in the classification of the organic material. Informative PCs.	**Correct ID**. CPAD and PCA agreeable.
UN_IV_3_ Correlation	R_M_50 (50% rice additive in mortar).	UN_IV_3 plus egg yolk, egg, milk, lard, oil and rice mortar mixtures (25).	924, 1009, 1026, 1263, 1446, 1472, 1539, 1551, 1578, 1611, 1619, 1652, 1746, 2857, 2927, 3007 (16).	Variables less than objects.	Smaller distances among objects lead to intra-classification with Mi_M_50. Higher PCs same results as in covariance.	
UN_IV_4_ Covariance	EY_M_50 (50% egg yolk additive in mortar).	UN_IV_4 plus egg yolk, egg, milk mortar mixtures (13).	954, 963, 1274, 1449, 1470, 1518, 1535, 1557, 1631, 1665, 1681, 1691, 1755, 2685, 2768, 2869, 2906, 2950, 3003 (19).	Variables more than objects.	Absolute match to EY_M_50 by PC1vsPC2, and PC1vsPC3, clear interpretation of loadings in the classification of the organic material. Informative PCs.	**Correct ID**. CPAD and PCA agreeable.
UN_IV_4_ Correlation	EY_M_50 (50% egg yolk additive in mortar).	UN_IV_4 plus egg yolk, egg, milk mortar mixtures (13).	954, 963, 1274, 1449, 1470, 1518, 1535, 1557, 1631, 1665, 1681, 1691, 1755, 2685, 2768, 2869, 2906, 2950, 3003 (19).	Variables more than objects.	Same results as in covariance, smaller distances among objects. PC1 is 67.99%, PC2 is 29.57% and PC3 is 0.96%.	
UN_IV_5_ Covariance	E_av (Egg).	UN_IV_5 plus 12 organic standards (13). Rosin (RO), Casein (Cas) and Beeswax (BW) standards were also added (New standards for Ch.9 CPAD).	979, 1124, 1178, 1274, 1324, 1419, 1472, 1574, 1690, 1756, 2876, 2945, 2974, 3025, 3089 (15).	Variables more than objects.	Absolute match to E_av by PC1vsPC3, clear interpretation of loadings and their contribution in each plot.	**Correct ID**. CPAD and PCA agreeable.
UN_IV_5_ Correlation	E_av (Egg).	UN_IV_5 plus 12 organic standards (13). Rosin (RO), Casein (Cas) and Beeswax (BW) standards were also added (New standards for Ch.9 CPAD).	979, 1124, 1178, 1274, 1324, 1419, 1472, 1574, 1690, 1756, 2876, 2945, 2974, 3025, 3089 (15).	Variables more than objects.	Same results as in covariance. PC1 is 91.30%, PC2 is 4.17% and PC3 is 2.73%	

Table 22: continued.

Label	CPAD ID	Objects	Variables (cm^{-1})	Variables vs. Objects	PCA Outcome	Retrospective - After Revealing True ID
UN_IV_6_ Covariance	R_M_25 (25% rice additive In mortar).	UN_IV_6 plus milk and rice mortar mixtures (9).	995, 1475, 1535, 2925, 2959 (5).	Variables less than objects.	PC1vsPC2 show matching to R_M_5. PC1vsPC3 indicates R_M_25. Mi_M_75 matching in PC2vsPC3.	**ID is Mi_M_5**. PCA same dilemmas as in CPAD on similarities between milk and rice mortar mixtures. PCA conclusion biased by CPAD identification. Both methods false results. CPAD mistake could have been avoided (Ch.8, sect.8.1.4, Table 15).
UN_IV_6_ Correlation	R_M_25 (25% rice additive In mortar).	UN_IV_6 plus milk and rice mortar mixtures (9).	995, 1475, 1535, 2925, 2959 (5).	Variables less than objects.	Same results as in covariance, but smaller distances among objects. PC1 is 59.51%, PC2 is 31.87% and PC3 is 7.44%.	
UN_IV_7_ Covariance	EW_M_5 (5% egg white in mortar).	UN_IV_7 plus egg white and bone glue mortar mixtures and mortar spectrum (10).	1081, 1281, 1432, 1448, 1466, 1475, 1505, 1561, 1585, 1599, 2872, 2979, 3064 (13).	Variables more than objects.	Closest match to EW_M_5 in PC1VsPC2 within the same quadrant. Same classification in PC2vsPC3.	**ID is M_av.** Uncertainty in plot interpretation and absolute match since BG_M_5 is also present. CPAD mistake could have been avoided (Ch.8, sect.8.1.4, Table 15).
UN_IV_7_ Correlation	EW_M_5 (5% egg white in mortar).	UN_IV_7 plus egg white and bone glue mortar mixtures and mortar spectrum (10).	1081, 1281, 1432, 1448, 1466, 1475, 1505, 1561, 1585, 1599, 2872, 2979, 3064 (13).	Variables more than objects.	Same results as in covariance. PC1 is 68.08%, PC2 is 28.35% and PC3 is 2.45%.	
UN_IV_8 (before CPAD)_ Covariance	CPAD ID was performed after PCA.	Selection based on the presence of lipids in 1751 and 2856-3004 region on UN_IV_8. Egg, egg yolk, oil, lard, rice, milk mortar mixtures (21).	986, 1255, 1320, 1384, 1442, 1483, 1501, 1542, 1587, 1618, 1652, 1705, 1751, 2679, 2731, 2856, 2930, 3004, 3067 (19).	Variables less than objects.	Average variance, UN_IV_8 is placed close to zero centers but linked to O_M_75 and L_M_75 in PC1vsPC2. Appears as an outlier in PC1vsPC3 with closeness to O_M_5 and L_M_5.	PCA indicates classification with olive oil/mortar mixtures.

Table 22: continued.

Label	CPAD ID	Objects	Variables (cm^{-1})	Variables vs. Objects	PCA Outcome	Retrospective - After Revealing True ID
UN_IV_8_ Covariance	L_M_5 (5% lard additive in mortar).	UN_IV_8 plus egg, egg yolk, oil, lard, rice, milk mortar mixtures (21).	986, 1117, 1255, 1320, 1384, 1442, 1483, 1542, 1618, 1705, 2679, 2731, 2856, 2930, 3004 (15).	Variables less than objects.	No impovement when variables reduced after CPAD ID. PC1 is 61.41%, PC2 is 33.15% and PC3 is 2.21%.	CPAD outcomes differ from PCA.
UN_IV_8_ Correlation	L_M_5 (5% lard additive in mortar).	UN_IV_8 plus egg, egg yolk, oil, lard, rice, milk mortar mixtures (21).	986, 1117, 1255, 1320, 1384, 1442, 1483, 1542, 1618, 1705, 2679, 2731, 2856, 2930, 3004 (15).	Variables less than objects.	Same results as in covariance. PC1 is 60.91%, PC2 is 32.18% and PC3 is 3.10%.	
UN_IV_8_ (reduced objects)_ Covariance	L_M_5 (5% lard additive in mortar).	Reduced objects to the closest candidates: oil and lard mortar mixtures plus UN_IV_8 (9).	986, 1117, 1255, 1320, 1384, 1442, 1483, 1542, 1618, 1705, 2679, 2731, 2856, 2930, 3004 (15).	Variables more than objects.	Closeness to O_M_5 is retained. PC1 is 71.55%, PC2 is 20.56% and PC3 is 3.99%.	Correct ID through the CPAD. PCA misleading.
UN_IV_9_ Covariance	BG_M_75 (75% bone glue additive in mortar).	UN_IV_9 plus egg white and bone glue mortar mixtures (9).	1267, 1285, 1313, 1340, 1471, 1572, 1692 (7).	Variables less than objects.	Absolute match to BG_M_75.	**Correct ID**. CPAD and PCA agreeable.
UN_IV_9_ Correlation	BG_M_75 (75% bone glue additive in mortar).	UN_IV_9 plus egg white and bone glue mortar mixtures (9).	1267, 1285, 1313, 1340, 1471, 1572, 1692 (7).	Variables less than objects.	Same results as in covariance. PC1 is 65.83%, PC2 is 32.44% and PC3 is 1.35%.	
UN_IV_10_ Covariance	O_M_75 (75% olive oil additive in mortar).	UN_IV_10 plus olive oil and lard mortar mixtures (9).	1281, 1472, 1518, 1545, 1561, 1576, 1615, 1669, 1702, 2864, 2940, 2964, 3014 (13).	Variables more than objects.	Absolute match to O_M_75.	**Correct ID**. CPAD and PCA agreeable.
UN_IV_10_ Correlation	O_M_75 (75% olive oil additive in mortar).	UN_IV_10 plus olive oil and lard mortar mixtures (9).	1281, 1472, 1518, 1545, 1561, 1576, 1615, 1669, 1702, 2864, 2940, 2964, 3014 (13).	Variables more than objects.	Same results as in covariance. PC1 is 77.86%, PC2 is 19.97%, PC3 is 1.56%.	

Table 22: continued.

UN_IV_1_Covariance

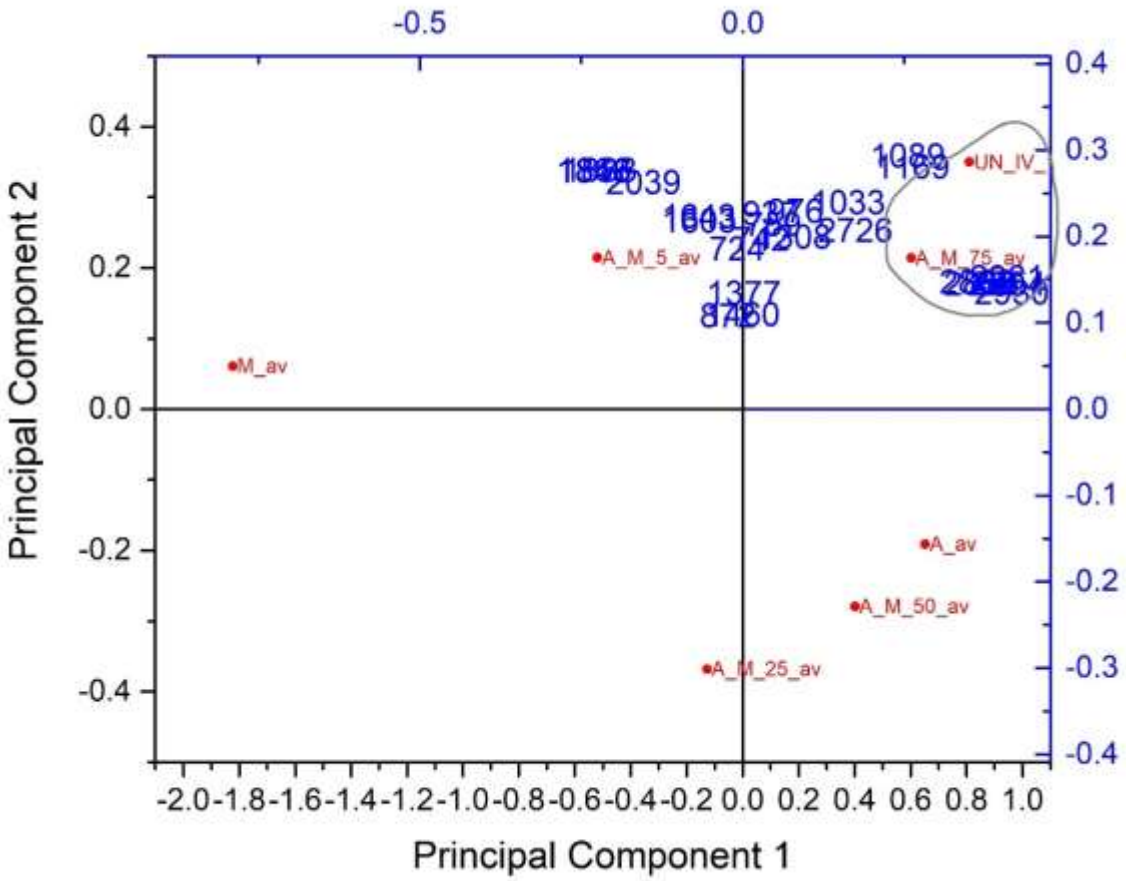

Figure 114: Covariance_PC1vsPC2 for UN_IV_1 (75% Asphalt in mortar).

PC1 explained the 86.85% of the total variance, PC2 the 7.78% and PC3 the 4.13%. The PC1vsPC2 plot showed close matching of UN_IV_1 to A_M_75 (fig.114). The loadings of the variables in PC1 positioned the objects according to their asphalt content in the mortar mixture.

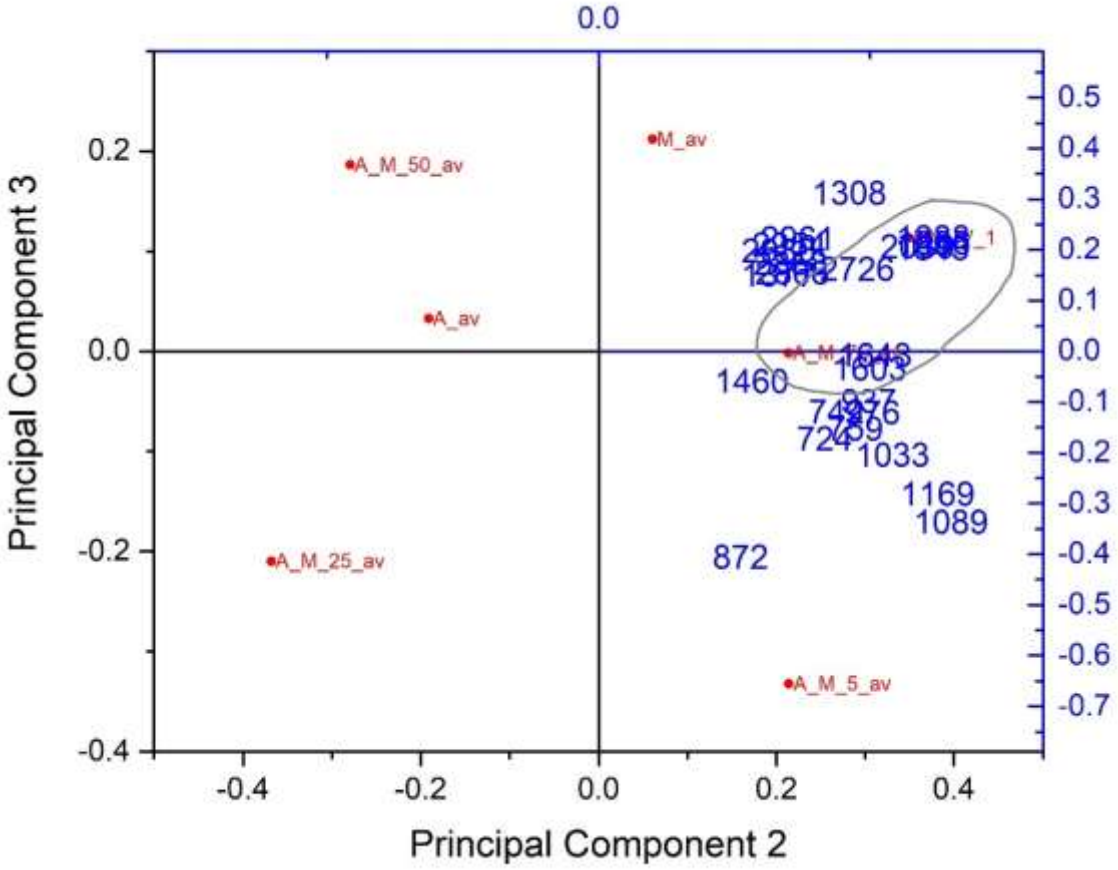

Figure 115: Covariance_PC2vsPC3 for UN_IV_1.

The PC2vsPC3 plot supported the intra-classification of UN_IV_1 to A_M_75 and showed that the selected variables described these two objects more than the rest in the matrix (fig.115).

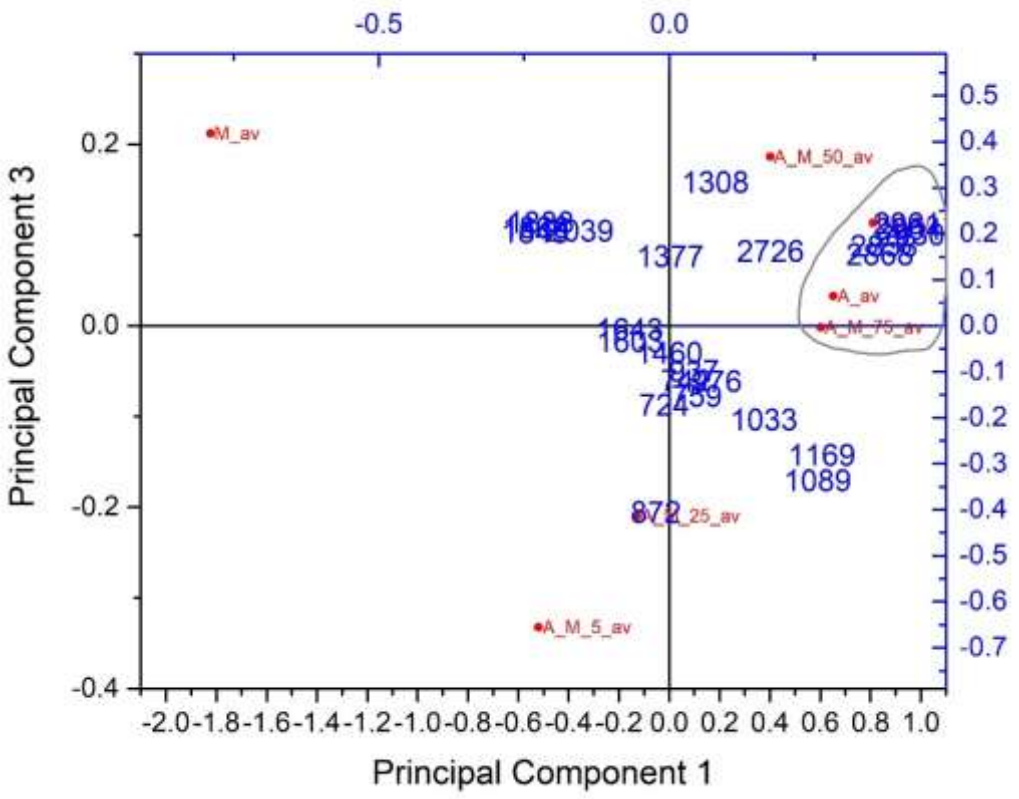

Figure 116: Covariance_PC1vsPC3 for UN_IV_1.

The PC1vsPC3 plot groups objects that share the highest asphalt content together (fig.116). The peaks that contribute most in the classification are the ones above 2800 cm^{-1}. Similar outcomes were produced from the correlation matrix (data not shown).

PCA produced different identification results (A_M_75) from those derived from the CPAD methodology (A_av).

UN_IV_2_Covariance

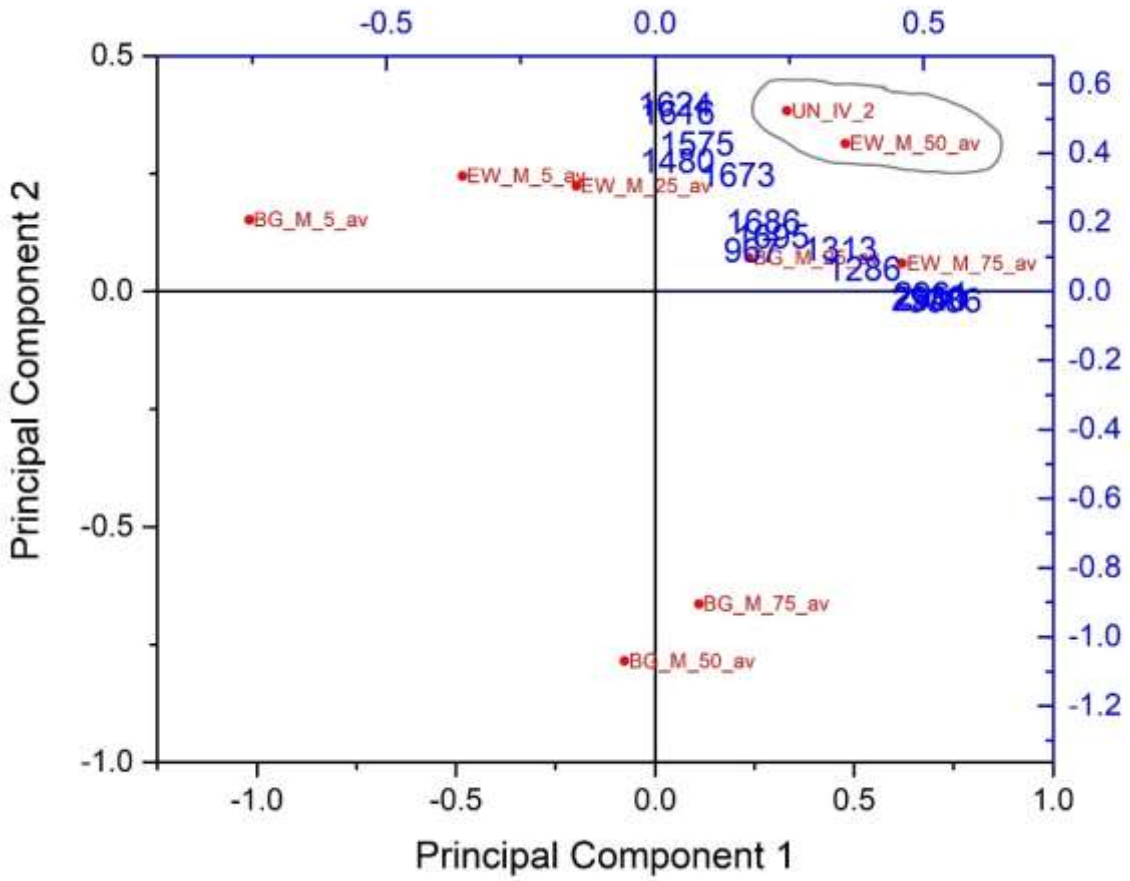

Figure 117: Covariance_PC1vsPC2 for UN_IV_2 (50% egg white in mortar).

Two PCs were produced from the selected objects and variables in the covariance matrix (Table 22): PC1 explained the 58.83% and PC2 the 40.29% of the total variance. PCA and CPAD produced the same identification outcome (fig.117).

UN_IV_3_Covariance

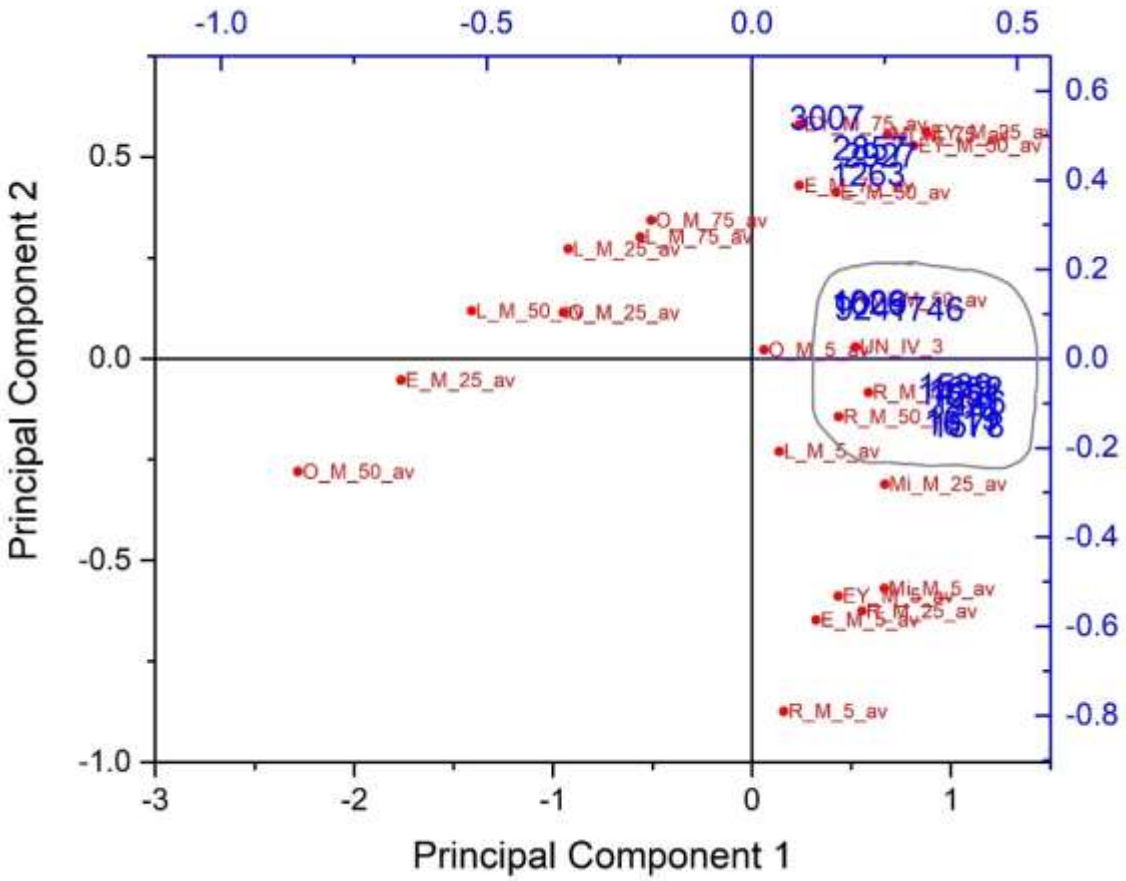

Figure 118: Covariance_PC1vsPC2 for UN_IV_3 (50% rice in mortar).

PC1 explained the 77.54% of the total variance, PC2 the 19.63% and PC3 the 1.16%. Following the highest variance in PC1, the distances among objects along the x axis show that R_M_50 is the closest match to UN_IV_3 (fig.118). The grouping reflected the possible candidates considered during the CPAD identification (Ch.8, 8.1.4 Experimental Set IV–Results and Discussion). Higher PCs were necessary for reaching a conclusion, since milk/mortar mixtures were also placed within the classification.

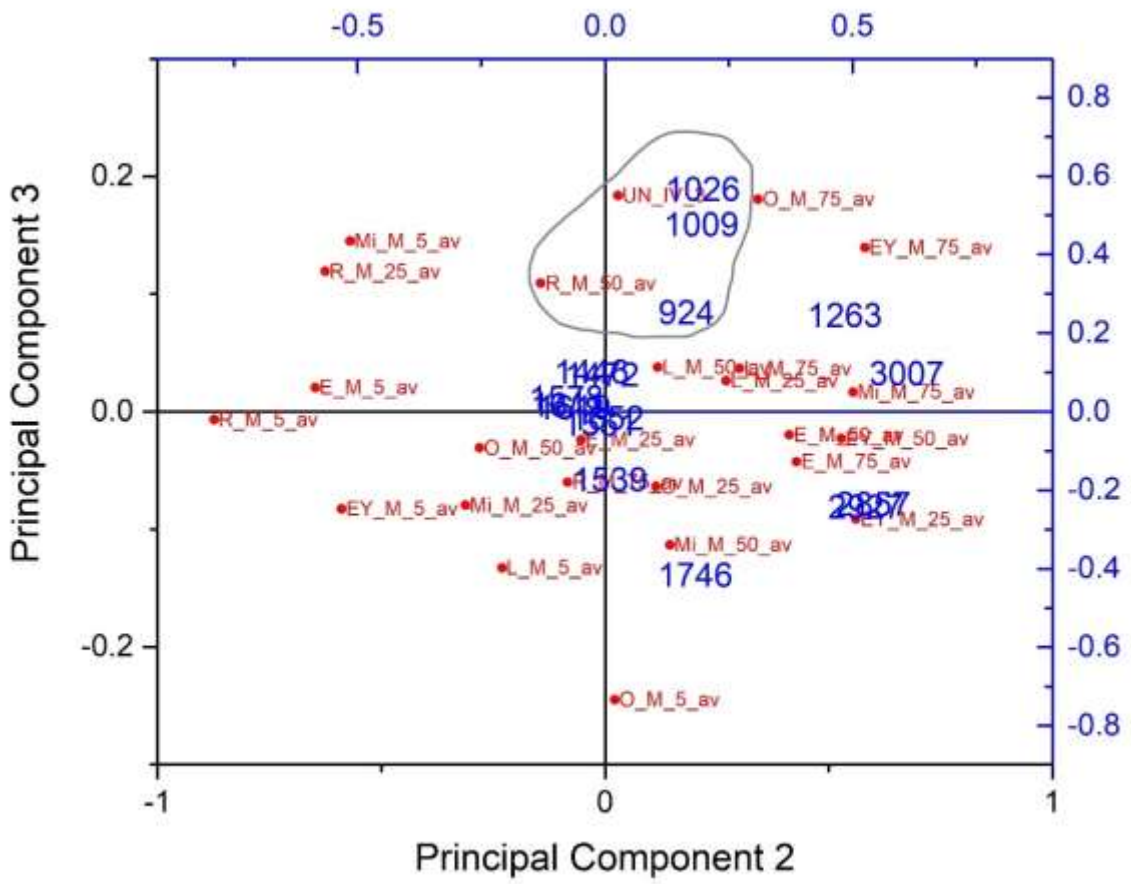

Figure 119: Covariance_PC2vsPC3 for UN_IV_3 (50% rice in mortar).

PC2vsPC3 showed the relationship between the UN_IV_3 and R_M_50 formed by the starch peaks (fig.119). Identification by PCA and CPAD were in agreement.

The correlation matrix produced similar outcomes on higher PCs but closer matching to milk/mortar mixture in PC1vsPC2 (Appendix II, fig.14).

UN_IV_4_Covariance

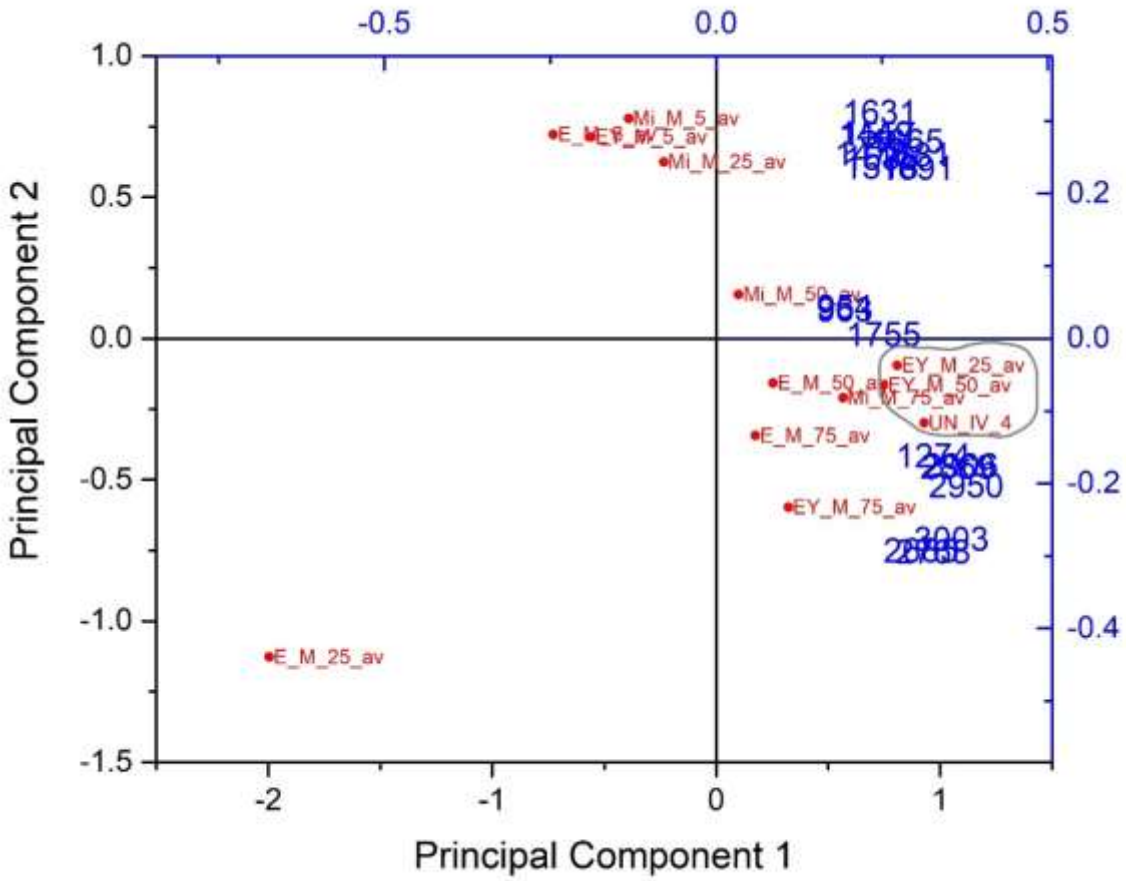

Figure 120: Covariance_PC1vsPC2 for UN_IV_4 (50% egg yolk in mortar).

PC1 explained the 64.36% of the total variance, PC2 the 33.63% and PC3 the 1.00%. The PC1vsPC2 plot showed classification of UN_IV_4 with egg yolk/mortar mixtures. The intra-classification with EY_M_50 is supported by the distances among the objects in both PCs (fig.120).

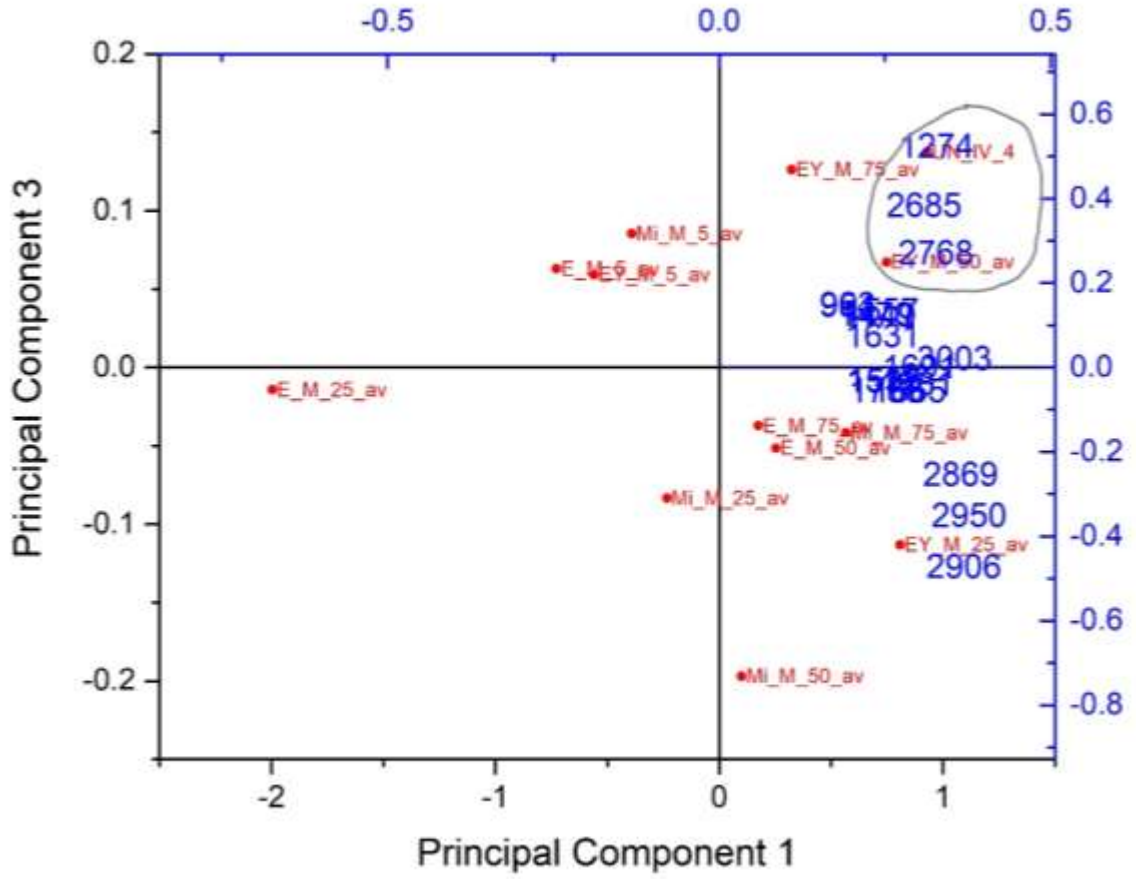

Figure 121: Covariance_PC1vsPC3 for UN_IV_4.

PC1vsPC3 produces clear intra-classification of the UN_IV_4 with the EY_M_50 (fig.121). PCA and CPAD identification produced agreeable outcomes.

The PCA calculated from correlation matrix showed similar percentages of variance as those produced from the covariance matrix and returned similar classification outcomes (Table 22).

UN_IV_5_Covariance

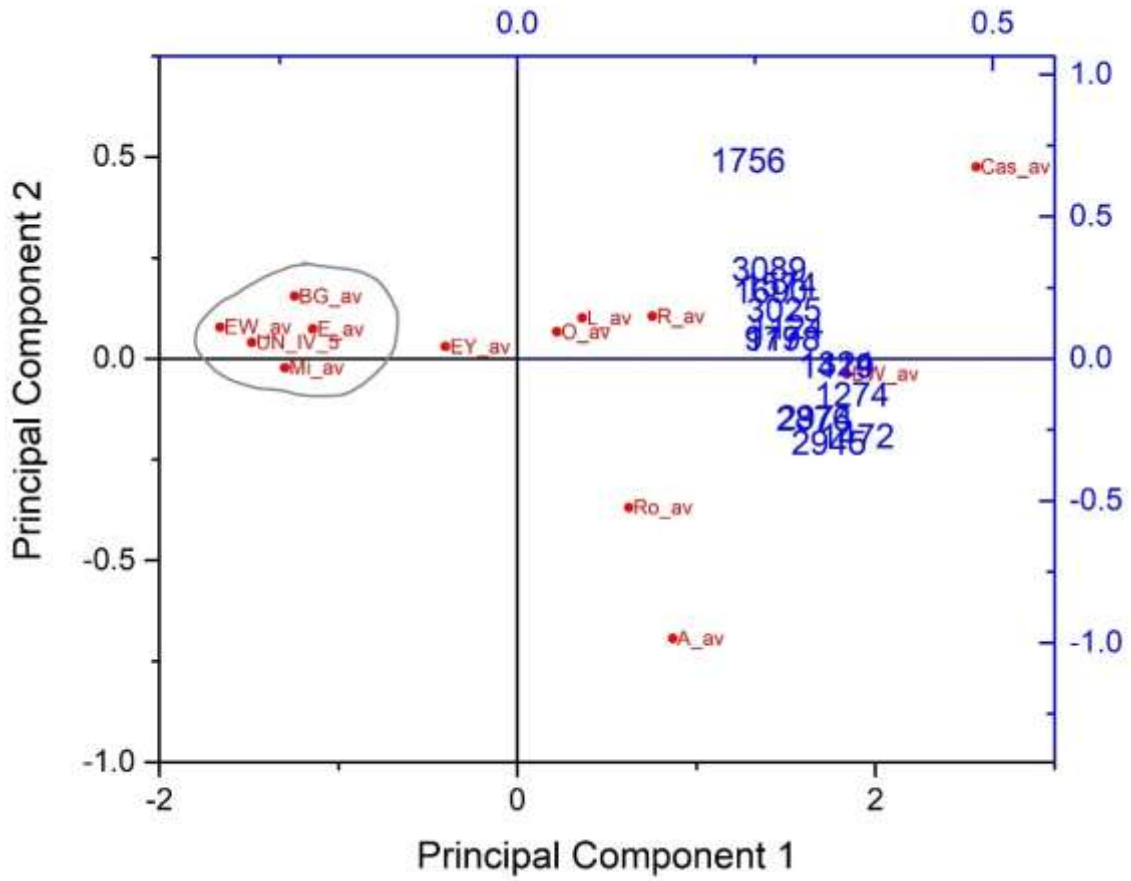

Figure 122: Covariance_PC1vsPC2 for UN_IV_5 (Egg, E_av).

The covariance matrix consisted of the UN_IV_5, all the 12 organic standards, increased by the addition of Rosin (RO), Casein (Cas) and Beeswax (BW) standards in the CPAD, and the selected 15 variables (Table 22). The inclusion of more organic standards in the matrix rather than only the suspected matching standards to the UN_IV_5, which were the egg, egg yolk and milk standards according to the CPAD outcomes, was expected to assist the calculation of covariance through a more symmetric matrix (Bonnier and Byrne, 2012, 327). The addition of the 3 new standards in the CPAD is discussed in Chapter 11.

PC1 explained the 91.92% of the total variance, PC2 the 3.88% and PC3 the 2.56%. UN_IV_5 is positioned between egg white and egg in PC1vsPC2, within a class formed by objects high in protein (fig.122). Following the distances between objects in PC1, egg white should be the closest match to UN_IV_5. However, the assessment of higher PCs

was necessary for reaching conclusion since the CPAD identification showed the co-existence of protein and lipid.

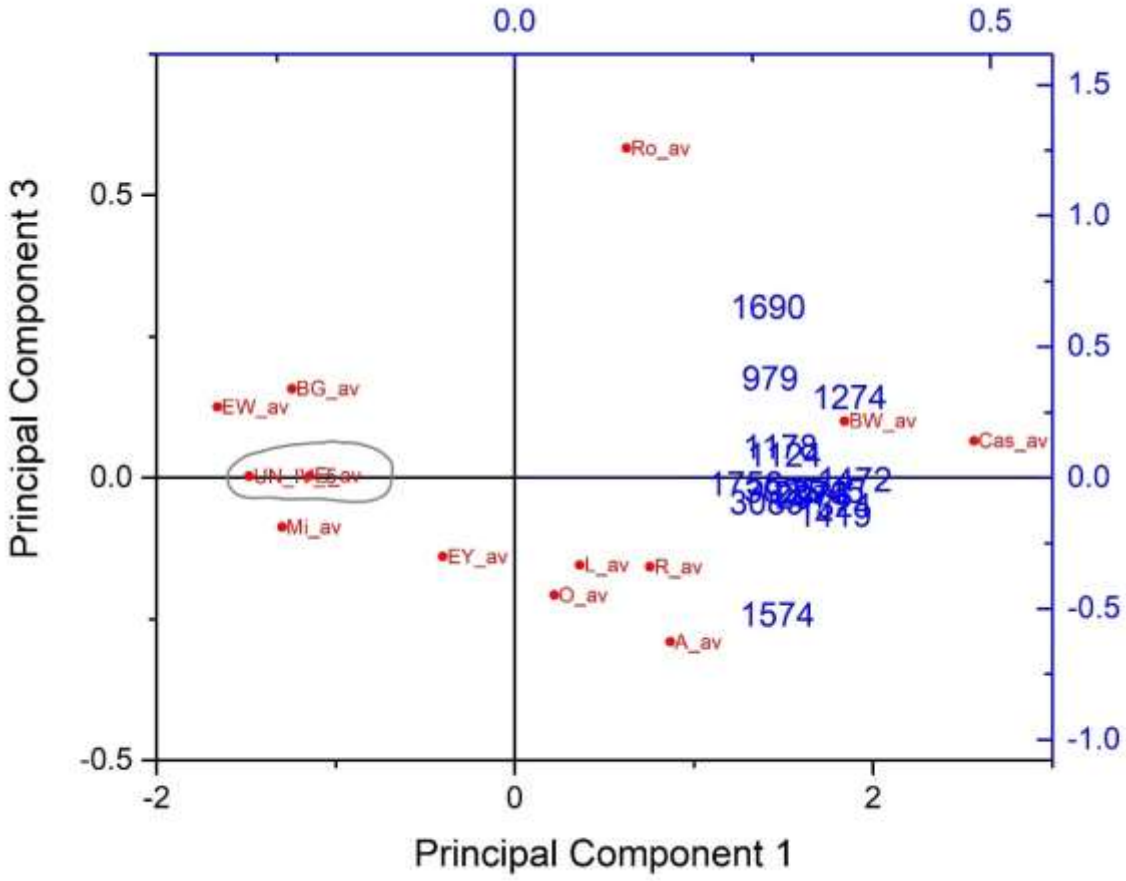

Figure 123: Covariance_PC1vsPC3 for UN_IV_5 (Egg, E_av).

PC1vsPC3 showed the presence of lipid through the contribution of most of the selected peaks, the absolute match to egg standard and the discrimination of the proteins by the 1690 cm^{-1} peak (fig.123). PCA and CPAD identification outcomes were in agreement.

UN_IV_6_Covariance

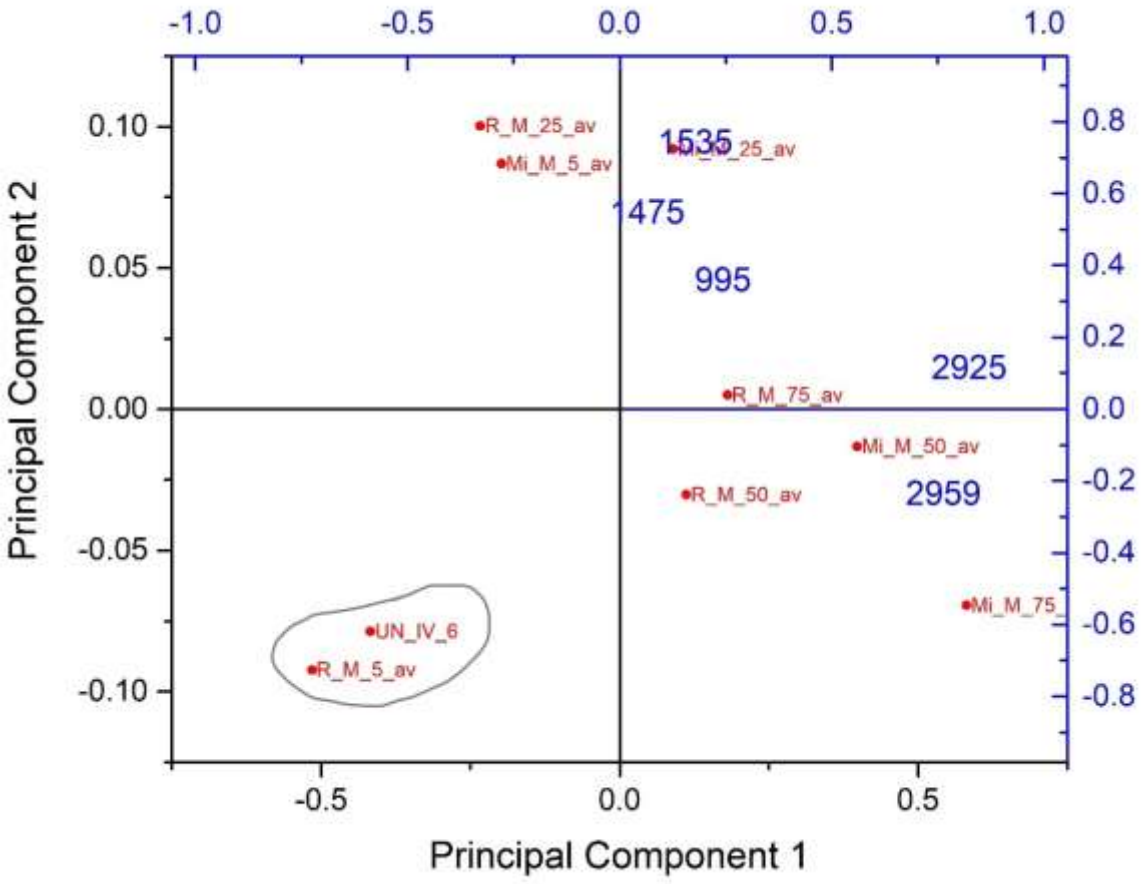

Figure 124: Covariance_PC1vsPC2 for UN_IV_6 (5% milk in mortar).

PC1 explained the 93.88% of the total variance, PC2 the 4.05% and PC3 the 1.53%. UN_IV_6 is positioned at the negative side of PC1 with those standards defined as possible matching candidates through the CPAD identification (Ch.8, Sect.8.1.4 Experimental Set IV-Results and Discussion, table 15) (fig.124).

UN_IV_6 was intra-classified with R_M_5 in PC1vsPC2, likely because the selected variables contributed more on the classification of the rest of the objects rather than these two (fig.124). However, the intra-classification required further validation because according to the CPAD outcomes, the peak at 2959 cm^{-1} showing lipid, was present in the UN_IV_6 and absent in the rice/mortar mixtures. This relationship should have been reflected in PCA data, demonstrating its limitations here.

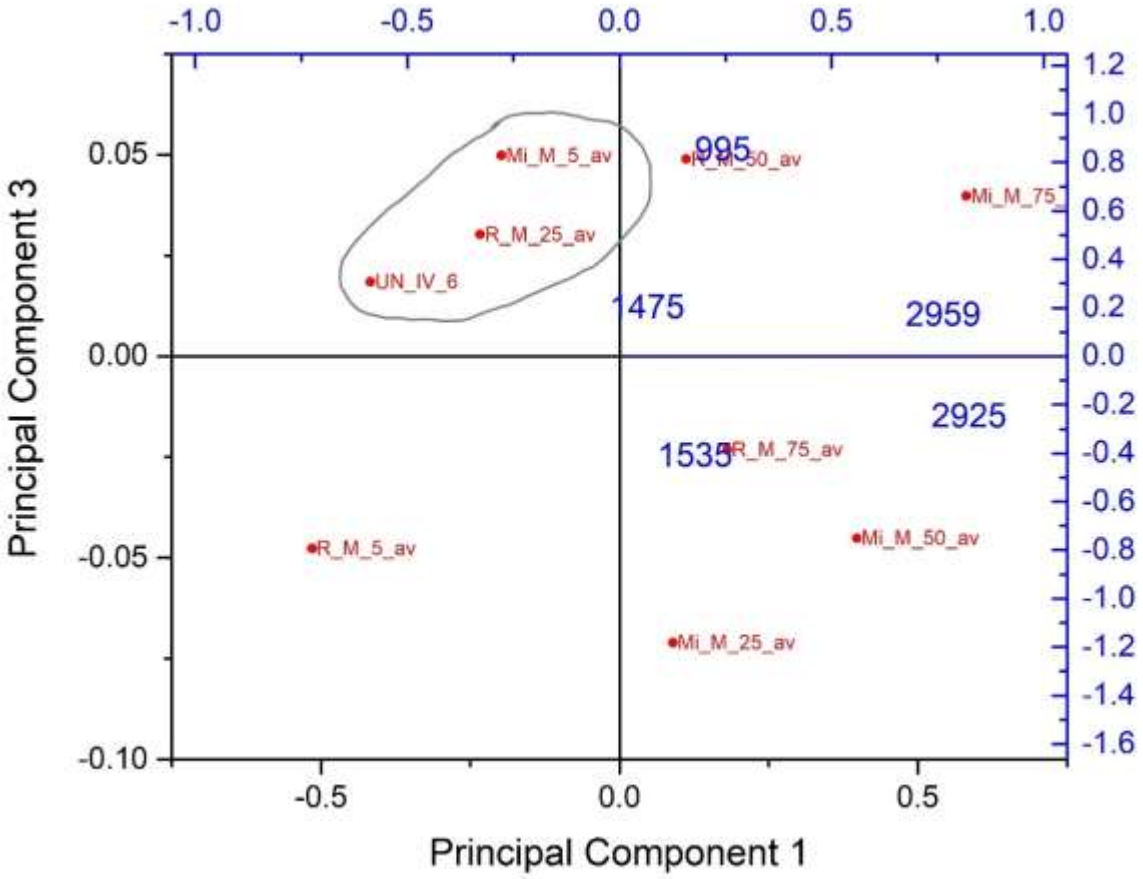

Figure 125: Covariance_PC1vsPC3 for UN_IV_6 (5% milk in mortar).

PC1vsPC3 projected the same dilemma with that faced during the CPAD identification, where R_M_25 (25% rice additive in mortar) followed by Mi_M_5 (5% milk additive in mortar) appeared as the closest matching candidates to UN_IV_6 (fig.125). It appears that the variables in the plot separate the high organic content mortar mixtures from those of low organic content. The lipid peak at 2959 cm^{-1} did not contribute to the classification of UN_IV_6.

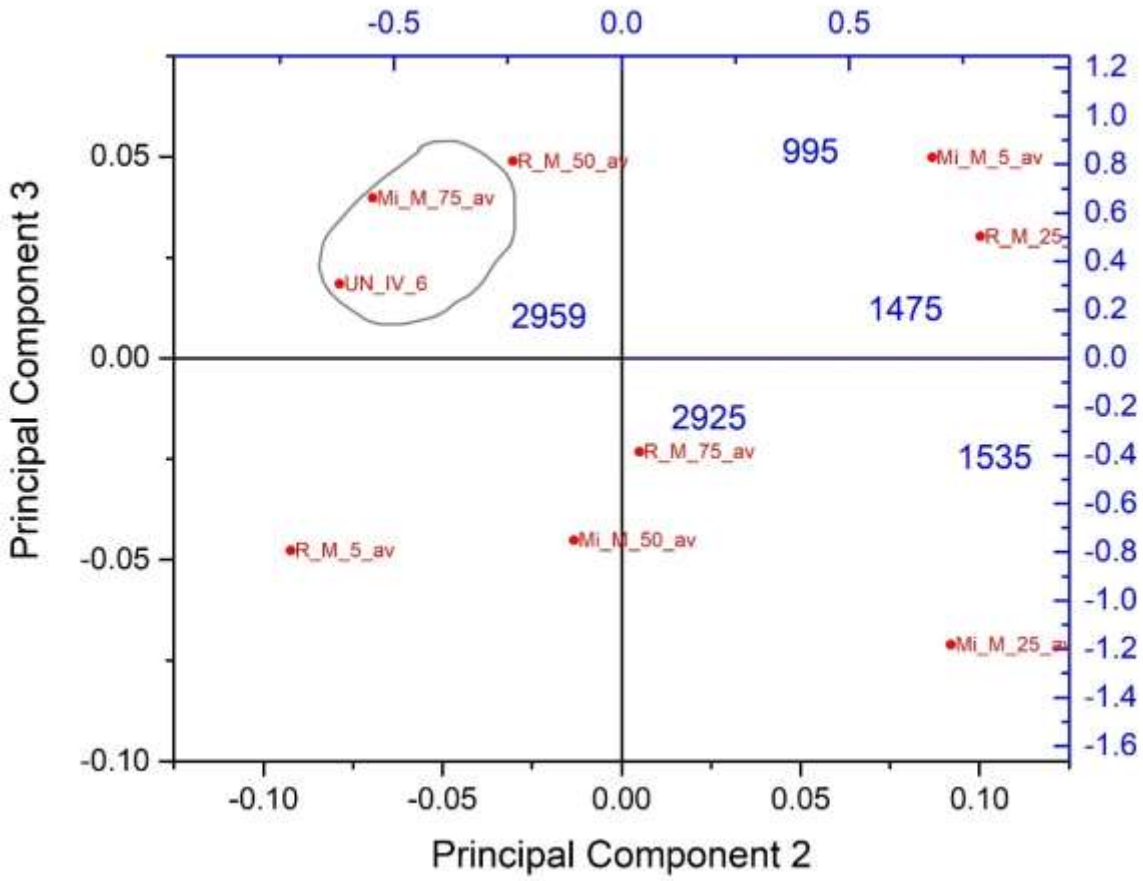

Figure 126: Covariance_PC2vsPC3 for UN_IV_6.

The contribution of the 2959 cm^{-1} appears in the PC2vsPC3 plot, where UN_IV_6 is closely positioned with Mi_M_75 (75% milk additive in mortar) (fig.126). The relationship was rejected since the previous plots agreed with the classifying of UN_IV_6 as a rice/mortar mixture. In this instance, the PCA results were biased by the CPAD identification outcomes.

UN_IV_7_Covariance

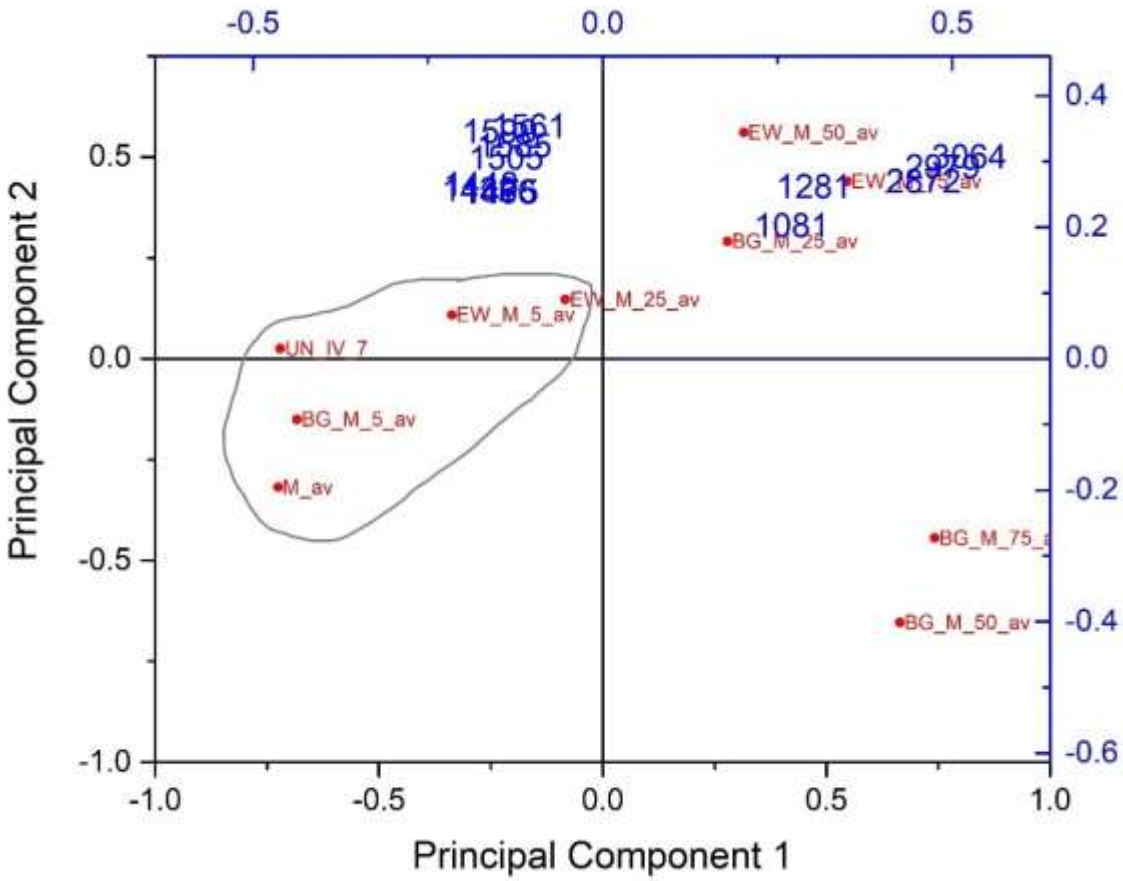

Figure 127: Covariance_PC1vsPC2 for UN_IV_7 (Mortar, M_av).

PC1 explains the 67.28%, PC2 the 29.82% and PC3 the 2.02% of the total variance. The selected variables classified the objects with low organic content at the negative side of PC1 and the ones with high organic content at its positive side (fig.127). Considering that PC2 explained almost 30% of the total variance, then the position of UN_IV_7 in the same quadrant with EW_M_5 should indicate intra-classification, verifying the CPAD identification results.

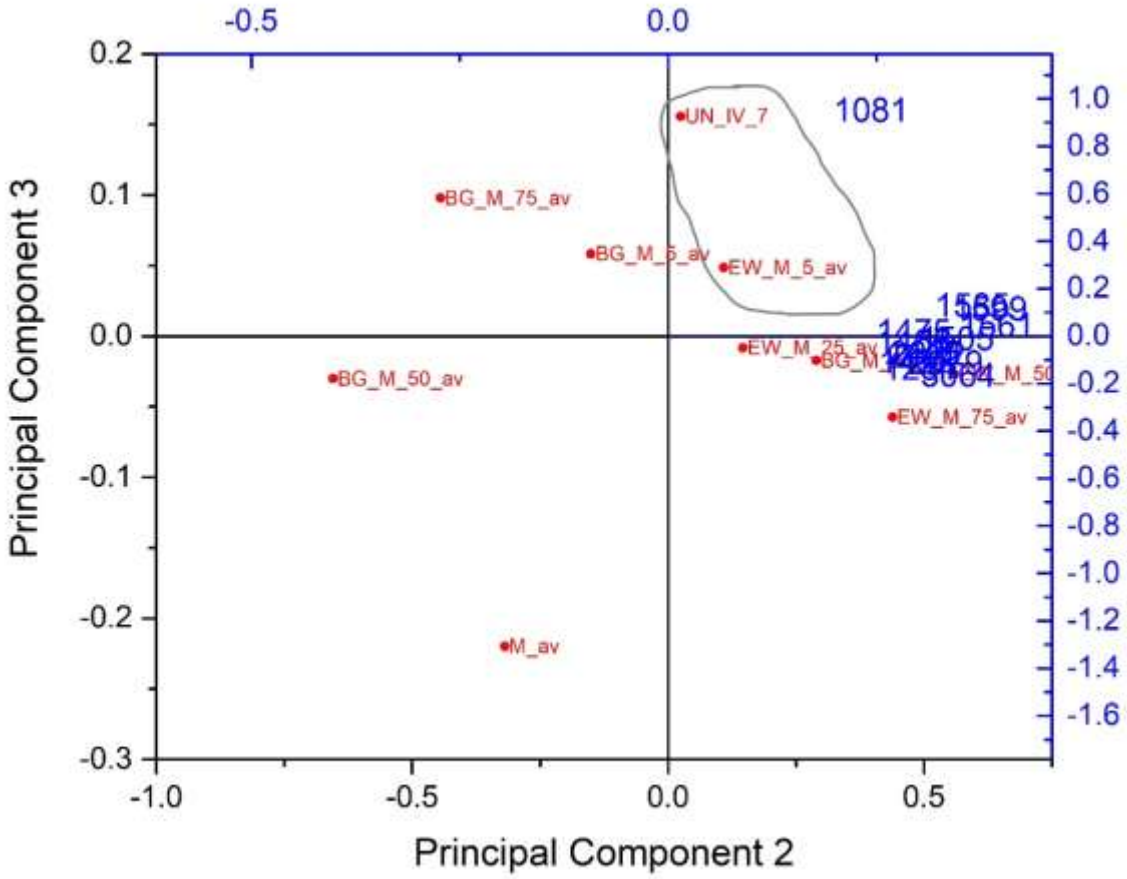

Figure 128: Covariance_PC2vsPC3 for UN_IV_7 (Mortar, M_av).

A similar intra-classification is observed in PC2vsPC3 (fig.128).

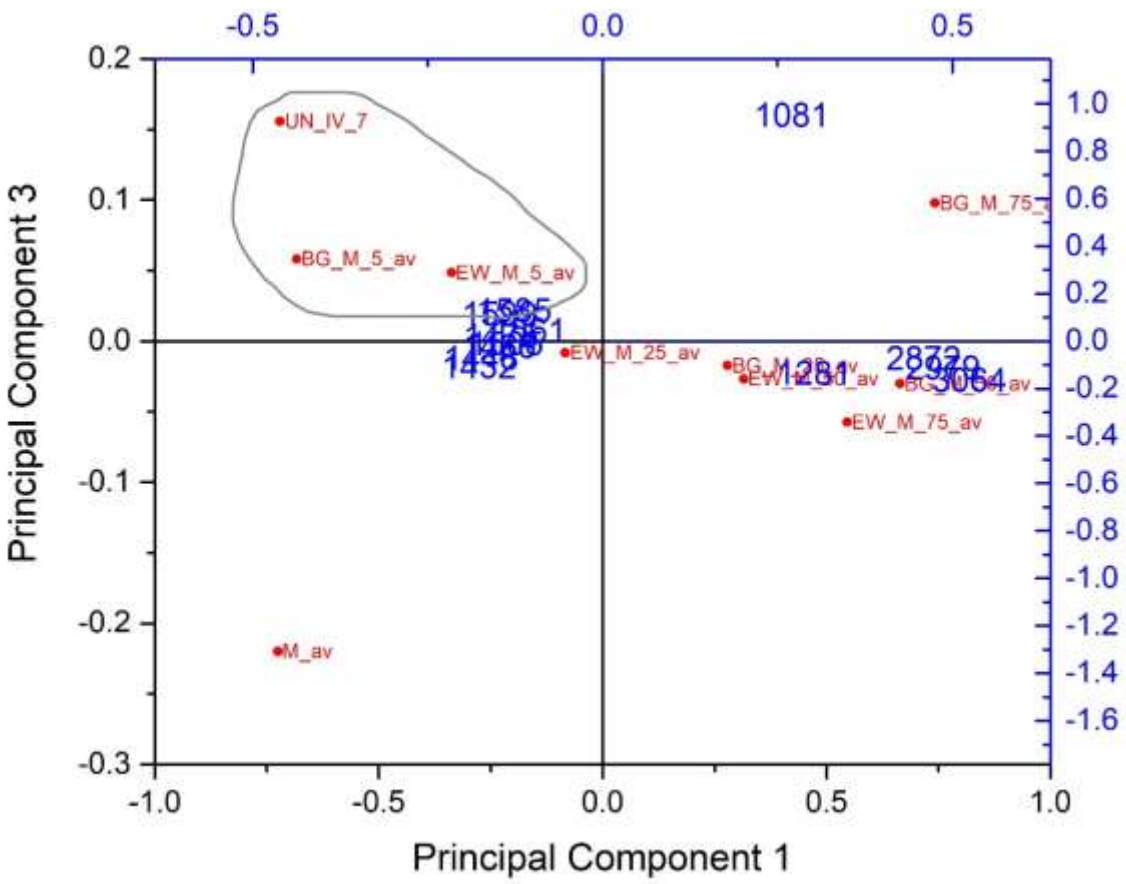

Figure 129: Covariance_PC1vsPC3 for UN_IV_7.

A new intra-classification appears in PC1vsPC3, where UN_IV_7 is positioned closely to BG_M_5 (fig.129). However, the position of loadings closer to the centre and on the positive side of PC1 indicate that the selected variables do not contribute significantly in the positioning of UN_IV_7 in the plot, thus it appears as an outlier (Christer, 2005, 42). While the PCA results agreed with the CPAD outcomes, they were also biased by it.

UN_IV_8 (before CPAD) _Covariance

So far, PCA was used after the CPAD identification as a complimentary tool and it was designed using the CPAD outcomes. In the case of UN_IV_8, PCA was performed before reaching identification through the CPAD. The matrix was constructed based on the presence of 1751 and 2856-3004 cm^{-1} region in the spectrum of UN_IV_8 that indicated the presence of lipids. Thus, all lipid/mortar mixtures were included as objects in the PCA matrix. The aim was to evaluate the ability of PCA to assist the CPAD identification by narrowing down the possible matching standards.

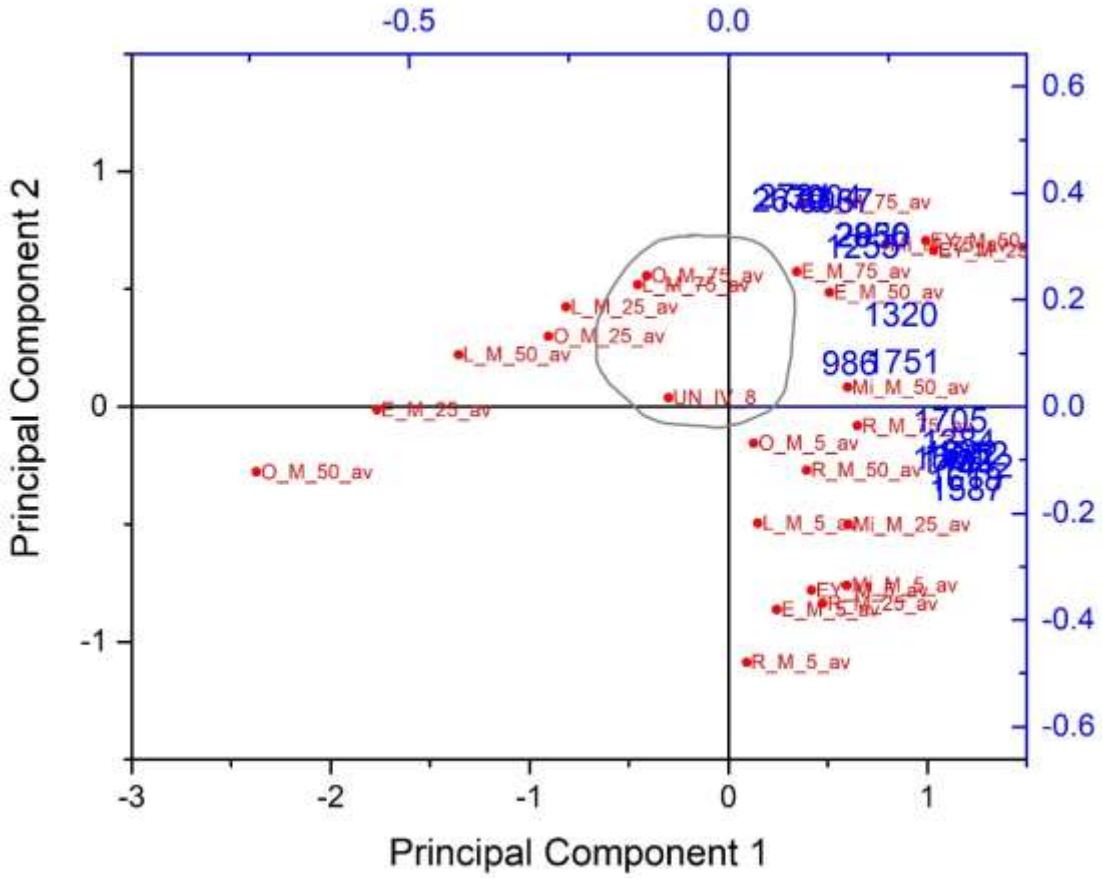

Figure 130: Covariance_PC1vsPC2 for UN_IV_8 (5% lard in mortar) before CPAD identification.

PC1 explained the 66.03%, PC2 the 30.02% and PC3 the 1.96% of the total variance. In the PC1vsPC2 plot, the mortar/mixtures of low organic concentration were placed in the positive side of PC1 and the negative side of PC2 (fig.130). Lipid-protein/mortar mixtures of higher organic concentration were placed on the positive side of PC1 and PC2. Oil and lard/mortar mixtures of high organic concentration formed a separate group in which UN_IV_8 could be classified, likely closer to O_M_75. However, the positioning of UN_IV_8 close to zero centres could indicate an average variance, not sufficient to show similarities with other objects in the plot (Christer, 2005, 42).

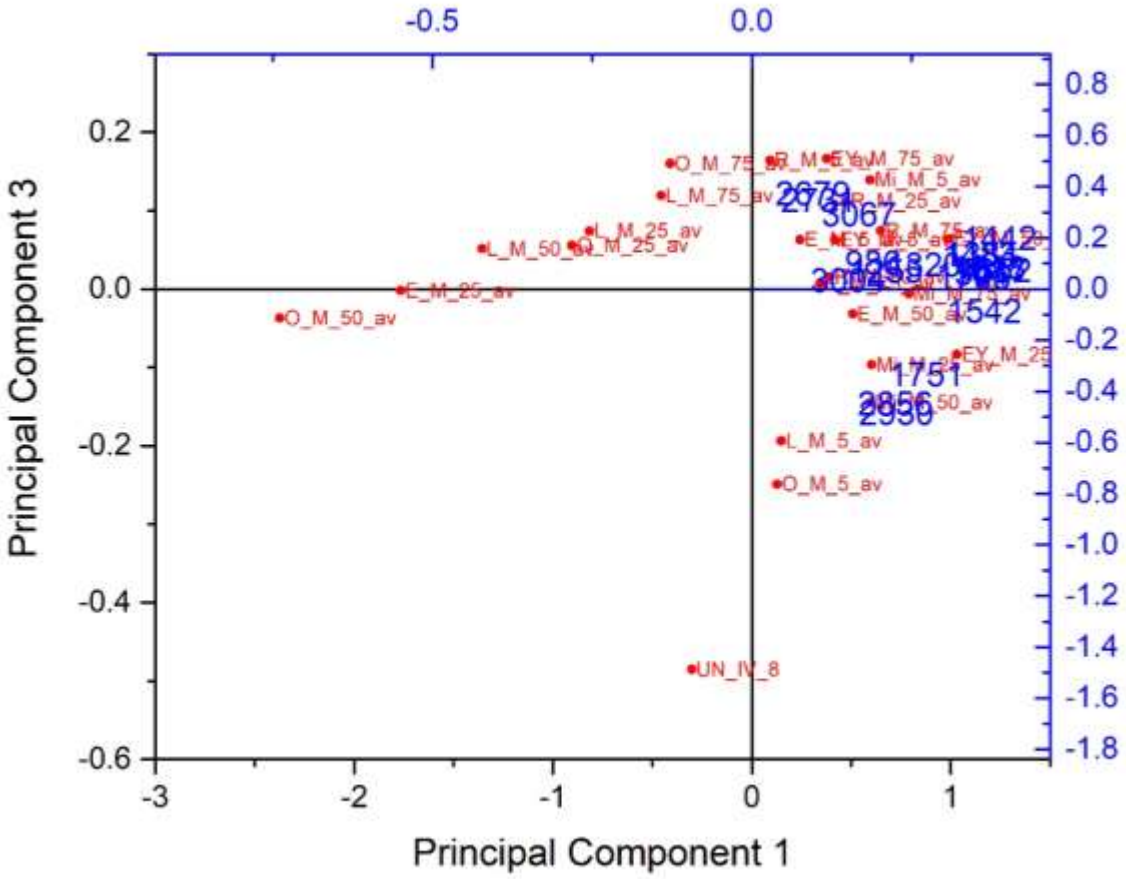

Figure 131: Covariance_PC1vsPC3 for UN_IV_8 (5% lard in mortar).

PC1vsPC3 positioned UN_IV_8 as an outlier following a grouping tendency towards O_M_5 followed by L_M_5 (fig.131). Similar classifications were observed in PC2vsPC3 (Appendix II, fig.15).

The CPAD identification, performed after PCA, has ruled out the olive oil/mortar mixtures due to the absence of the strong oil peak at 2059 cm^{-1} on the of UN_IV_8 spectrum (Table 15, Ch.8, 8.1.4 Experimental Set IV). Additionally, the high inorganic content in the UN_IV_8 spectrum and the strong $CaCO_3$ combination band at 1795 cm^{-1} (Ricci et al., 2006, 1222) lead to its identification as L_M_5 (5% lard additive in mortar). PCA did not produce strong evidence of such matching.

Similar PCA results were obtained from the covariance and correlation matrices that included reduced variables, selected according to the CPAD identification of UN_IV_8 as L_M_5, and the same number of objects (Table 22).

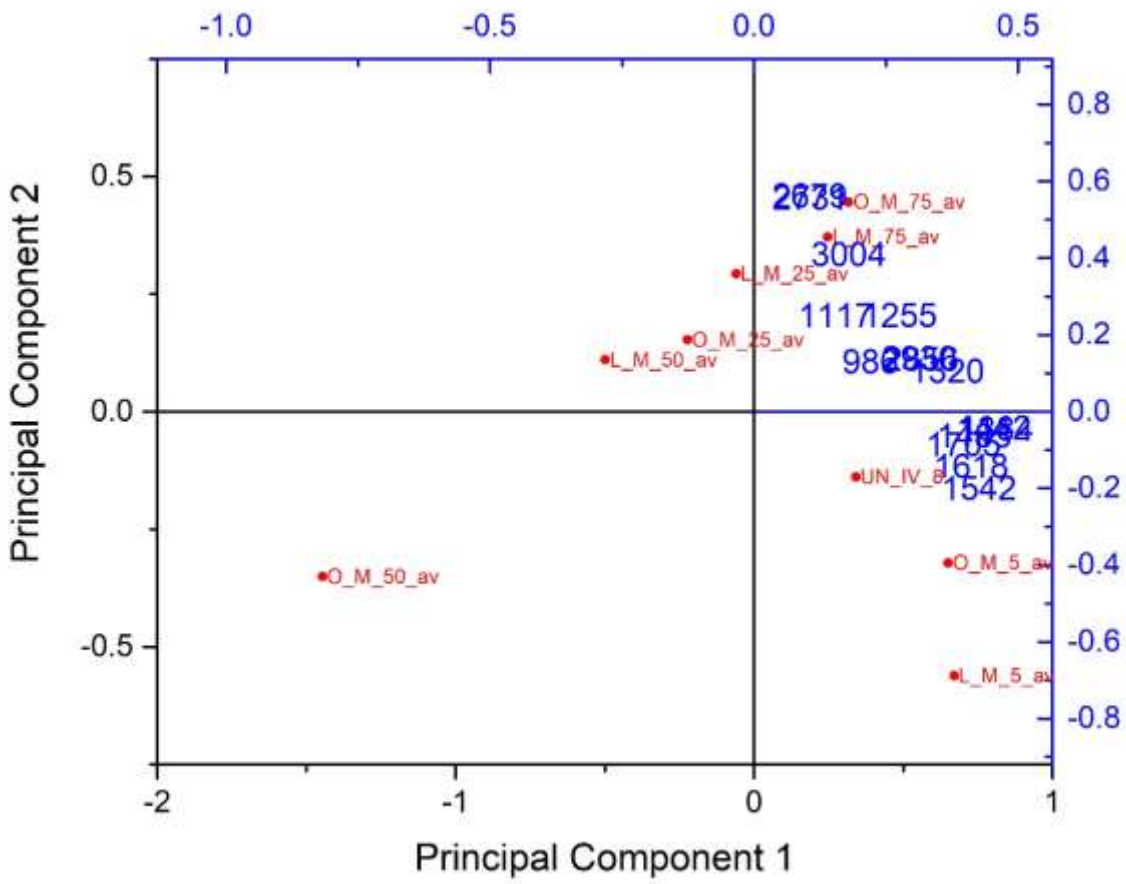

Figure 132: PC1vsPC2 for UN_IV_8, from matrix containing reduced number of objects.

The reduction of objects in the covariance matrix, narrowed down to olive oil and lard/mortar mixtures according to the CPAD identification outcomes, retained the closeness of UN_IV_8 to O_M_5 (fig.132). The results differ from that of the CPAD identification that indicated L_M_5 as the true identity of UN_IV_8.

UN_IV_9_Covariance

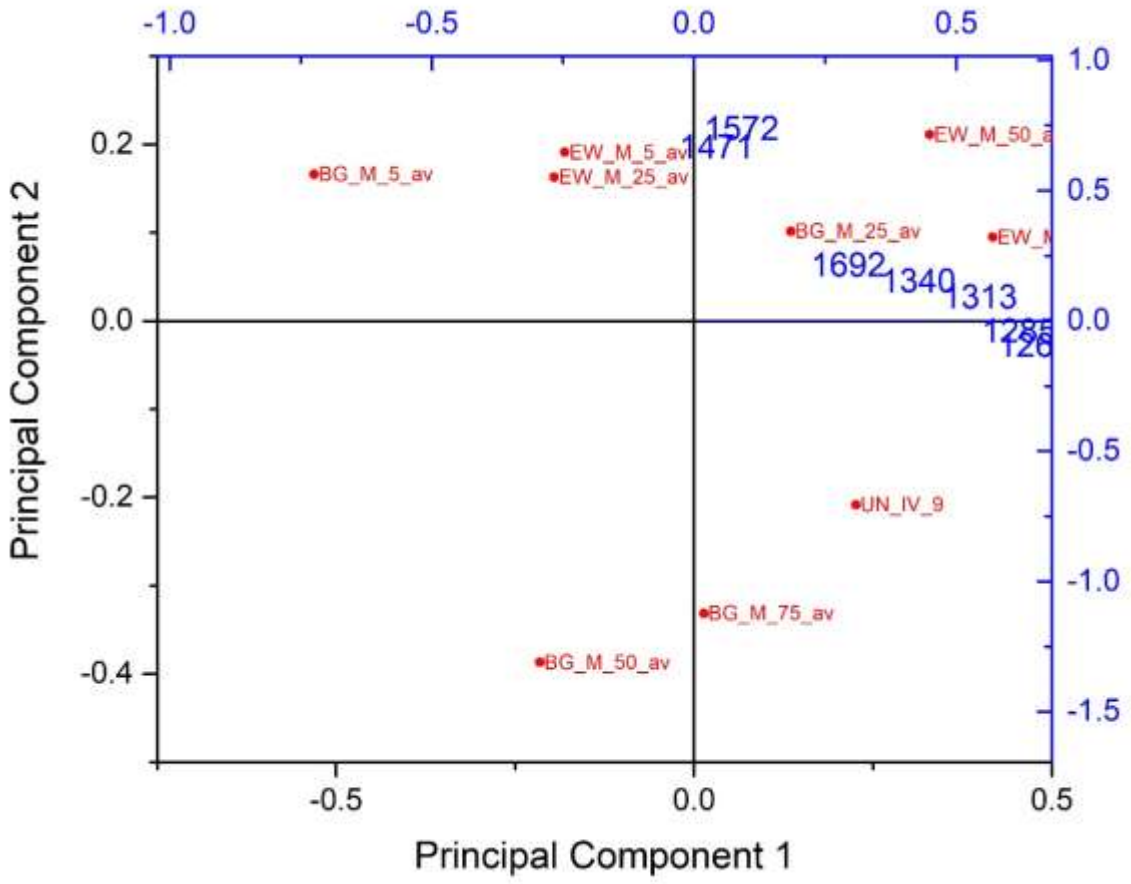

Figure 133: Covariance_PC1vsPC2 for UN_IV_9 (75% bone glue in mortar).

PC1 explained the 61.48% and PC2 the 37.40% of the total variance. UN_IV_9 is grouped together with BG_M_75, within the same quadrant (fig.133). PCA and CPAD identifications were in agreement.

UN_IV_10_Covariance

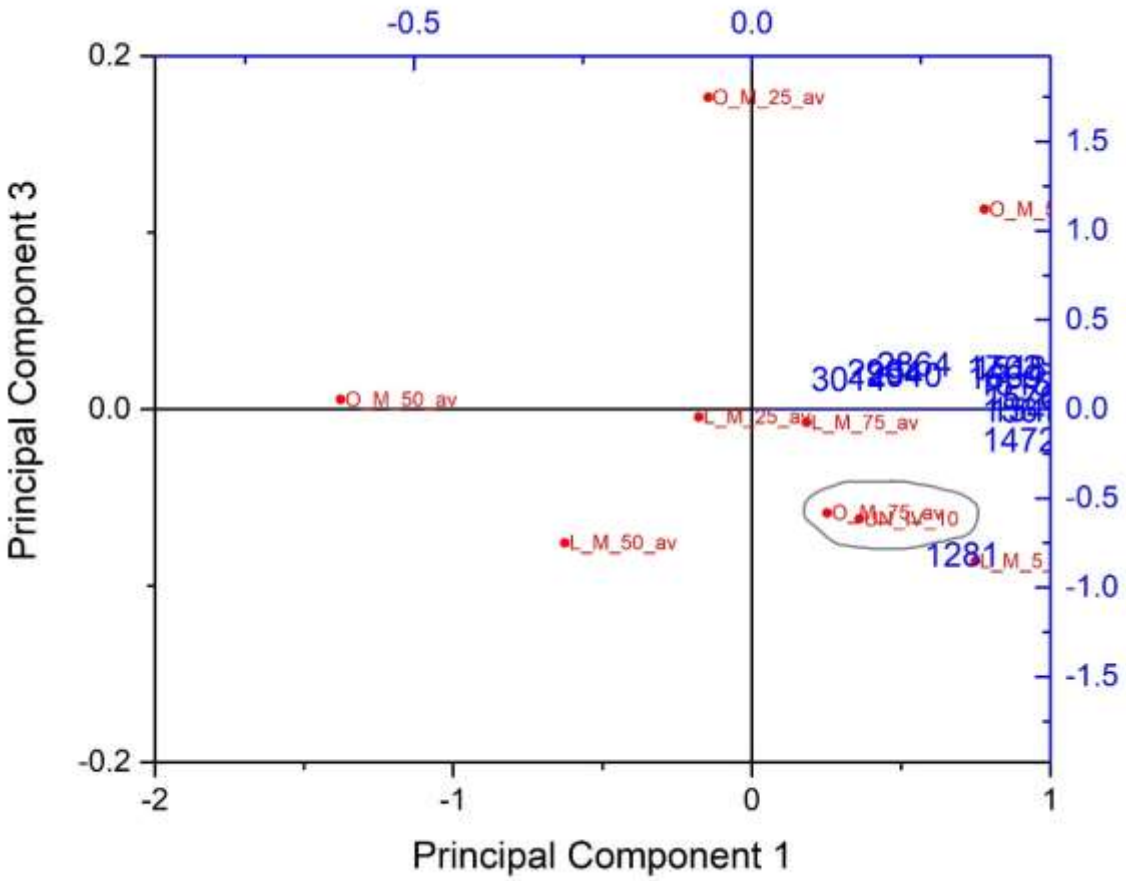

Figure 134: Covariance_PC1vsPC3 for UN_IV_10 (75% olive oil in mortar).

PC1 explained the 83.46%, PC2 the 14.41% and PC3 the 1.44% of the total variance. Close intra-classification is observed in PC1vsPC3 between the UN_IV_10 and O_M_75 (fig.134). The same results were observed in all PC plots (Appendix II, fig.16-17). The same stands for the correlation matrix (data not shown). PCA and CPAD produced agreeable results.

10.6 Discussion of PCA results

The PCA results were evaluated after revealing the true identity of the unknown spectra **UN_IV_1** to **UN_IV_10** and compared to the CPAD identification results (Sect.10.5, Table 22).

Six unknown spectra (**UN_IV_2, 3, 4, 5, 9** and **10**) were correctly identified by both the CPAD and PCA, showing agreement between the two methods and reflecting the correct

choice of objects and variables from the CPAD to construct the covariance matrix for the PCA.

However, the PCA results for the remaining four unknown spectra of the UN_IV set (**UN_IV_1, 6, 7** and **8**) differed from those derived from the CPAD identification. Regarding UN_IV_1, PCA clearly showed the correct intra-classification to A_M_75 (75% asphalt additive in mortar). This chemical relationship was dismissed during the CPAD identification, where UN_IV_1 was identified as pure asphalt (A_av). Although both methods indicated the correct organic additive, the CPAD failed to identify its concentration in the mortar mixture. The mistake would have been avoided by taking into consideration the peaks below 1089 cm^{-1} on UN_IV_1, clearly assigned to $CaCO_3$ (Ch. 8, 8.1.4 Experimental set IV, Results and Discussion). The high asphalt content in UN_IV_1 and its chemical correlation to both A_M_75 and A_av spectra was projected in PC1vsPC3 (fig.116). However, since the first two PCs explained the highest variance in the dataset, the matching of UN_IV_1 to A_av by PC3 was rejected, revealing the correct identity of the spectrum (A_M_75).

UN_IV_6 was misidentified through the CPAD as R_M_25 (25% rice additive in mortar), instead of Mi_M_5 (5% milk additive in mortar). The true identity was considered during the CPAD process but rejected due to the lack of strong milk peaks at 1602-1612 cm^{-1} in the UN_IV_6 spectrum. The mistake would have been avoided by including the inorganic peaks in the comparison and the weak peak at 2959 cm^{-1} in the UN_IV_6 spectrum which indicated lipids that only matched the Mi_M_5 spectrum (Ch. 8, 8.1.4 Experimental set IV, Results and Discussion). PCA confirmed the difficulty of separating the identify of these two organic additive/mortar mixtures where similarities lie not in their organic chemistry but in the prevailing of inorganic components in both due to the low viscosity of milk and rice additives. PCA results reflected the same dilemma as in the CPAD identification because the selection of objects and variables was made according to the CPAD outcomes.

For UN_IV_7, a first inspection of the CPAD data identified the spectrum as M_av (mortar) or EW_M_5 (5% egg white additive in mortar). The true identity was M_av (mortar) but rejected due to bias in the identification protocol, rather than evidence of organic presence (Ch. 8, 8.1.4 Experimental set IV, Results and Discussion). PCA showed classification of UN_IV_7 with objects (spectra) of low organic concentration but failed to produce strong intra-classification with M_av spectrum. The PCA results were interpreted according to the false CPAD identification.

CPAD correctly identified UN_IV_8 as L_M_5 (5% lard additive in mortar), whereas PCA showed matching to O_M_5 (5% oil additive in mortar). CPAD detected the absence of olive oil diagnostic peaks on UN_IV_8 spectrum to immediately rule out any matching to oil/mortar mixtures (Table 15, Ch.8, 8.1.4 Experimental Set IV). The non-parametric behaviour of PCA was highlighted since it could not access this information.

10.7 PCA Conclusions

Principal Component Analysis behaved as the mathematical projection of the CPAD identification outcomes, often producing the same dilemmas as the ones faced during spectra identification through the CPAD. This occurs because objects and variables are selected using the CPAD identification procedure, therefore making PCA perform as a supervised pattern recognition method instead of an unsupervised one.

If strong PCs are necessary to reach conclusions, variable and object reduction is necessary and the safest way to go about this is through the CPAD, by selecting variables (diagnostic peaks) specific to the unknown spectrum and objects (standards) based on the closest possible matches.

PCA could not be used for identification without the CPAD outcomes since relationships among objects would be interpreted without knowledge of other spectral parameters, such as absence or presence of peaks and their intensity on the possible matching spectra of standards. Additionally, generic object and variable selection would mask intra-classification between the unknown spectrum and its possible match.

The reduction of objects and variables through the CPAD is a reasonable and justified action that derived through experiment reported in sections 9.4 and 10.1 to 10.4. The action improved the interpretation of the PC score plots by reducing the number of projected data and excluding redundant ones, which decreased their complexity. However, the interpretation of the PCA results remained problematic: the relationship among objects could be read in more than one way, producing uncertainty in reaching conclusion without any doubt.

It is concluded that PCA cannot contribute secure **classification** outcomes of unknown objects to classes of known standards (either organic or organic/mortar mixtures) and consequently it cannot be utilized either as an **identification** method or a **validation** method for the CPAD identification methodology. Its application in the thesis, where the CPAD methodology has provided secure identification outcomes, is not considered necessary.

Chapter 11: Case study

This chapter reports the analysis of ancient mortar samples by External Reflectance FTIR micro-spectroscopy, using the methodology developed in Chapters 7 and 8. The methodology is applied on heterogenous mortar samples that have undergone chemical decay and physical weathering during their long exposure to different environmental conditions. The effects on chemical composition and texture are expected to influence the reflectance micro-FTIR spectra collected. Their interpretation effectively examines the applicability of the methodology for its intended purpose, analysis of archaeological materials.

The ancient mortar samples derived from three archaeological sites in West Crete, Greece; Polyrrhenia, Phalasarna and Aptera. The samples were collected from water-related structures, such as cisterns and bathtubs (basins), where waterproofing organic materials may have been used during their construction and working life. Their chronology ranged between the 4th century BC and the 4th century AD. Sites and constructions for sampling were chosen based on dating and purpose, as Hellenistic and Roman mortar technologies were likely to have incorporated organic additives to improve physical properties, such as the need for hydrophobicity (Tables 1-4, Chapter 3). The example from the Krene of Megara, although earlier, offers realistic grounds for research of such applications in Greece (Helner, 2006).

11.1 Archaeological sites and Sample collection

11.1.1 Polyrrhenia

Ancient Polyrrhenia is located in West Crete, 17 kilometers south of the Kissamos coast, which served as the city's harbor. Polyrrhenia is a fortified *polis*, built on the summit and slopes of a steep hill in NW Crete. The earliest estimated settlement is dated at the second quarter of the 5th century BC. The city flourished from the 4th century BC onwards especially during the Hellenistic period up to the 2nd century BC when the leading role passed to Kydonia (Markoulaki and Christodoulakos, 2018, 78-79). Its territorial dominance during the Hellenistic period was vast, sharing borders with Kydonia to the east and Phalasarna to the west.

The name of the city, *Πολυρρήν*, is of Mycenaean origin and means "location with many sheep". The city minted its own coins as early as the 4th century BC with the head of a bull at the reverse. The head of Zeus, Athena, Apollo and other deities often decorated the obverse of the coin (Markoulaki, 2005, 24). Polyrrhenia was an aristocracy, thus it aligned

with the Roman dominance in the Greek territory and it was rewarded for this; It continued to circulate its own currency and took over the great sanctuary of Diktynna.

The city lacked natural water springs, which led to the development of a complex public water-supply system that consisted of rock-cut aqueducts and subterranean channels, with private cisterns scattered around the city (Markoulaki and Christodoulakos, 2018, 140). The natural conglomerate rock was easily carved and served for the collection of water through its pores. The Hellenistic aqueduct at the entrance of the modern village and the semicircular fortification tower that guarded it, create a landmark for the site (fig.135-137). Improvements and repairs on the public water-supply system and the construction of the tower had taken place during Hadrian's period (117-138 AD) (Markoulaki, 2005, 30). The construction of an open cistern between the Hellenistic rock-cut aqueduct and the tower is also dated to the Roman period (Markoulaki and Goula, 2013, 143).

Figure 135: Polyrrhenia: the entrance of the rock-cut aqueduct (left) and the floor of the open cistern covered with red pebbles for protection.

Figure 136: Polyrrhenia: the interior of the rock-cut aqueduct.

Figure 137: Polyrrhenia: the semi-circular fortification tower adjacent to the water-supply complex.

Nine mortar samples were collected from a) the surface of the floor of the Roman open cistern, b) the plastered stone, related to the walls of the cistern, found in close proximity (Markoulaki and Goula, 2013, 140) and c) the surface of the low wall that separates the rock-cut aqueduct from the open cistern, which was revealed after the demolition of the latest addition of masonry (Appendix III, fig.1-6). All the sampled surfaces were covered with a dark brown-black substance.

11.1.2 Phalasarna

The harbor city of Phalasarna is located at the northeast border of Polyrrhenia on the neck of Cape Grambousa, overlooking the western gateway to the Aegean (Hadjidaki, 1988, 463). Pottery sherds found in the surrounding cliffs suggest that the area was inhabited from as early as the Middle Minoan period. An organized settlement is dated at least from the 6th century BC (Hadjidaki,2003, 106).

Phalasarna became an independent maritime power by the end of the 4th century BC, minting its own coins. The establishment of Phalasarna as a naval power at the beginning of the 3rd cent. BC is further enforced by the discovery of the late 4th – early 3rd cent. BC stone inscription that describes the peace treaty between Phalasarna and Polyrrhenia (Hadjidaki, 1988, 467).

The main channel, leading into the military harbour, was artificial. The harbour was surrounded by fortification walls and defensive towers that were in fact extensions of the city's own defences (Frost and Hadjidaki, 1990, 527). The round circular tower on the south of the fortification wall and its adjustment cistern are dated to the end of the 4th century BC (Hadjidaki, 2003, 125). The cistern was used for supplying the garrison of the tower with water or for resupplying the ships (Frost and Hadjidaki, 1990, 516-517). The floor of the cistern was paved with colored pebbles set in mortar, whereas the walls were plastered with mortar and painted with black substance, likely a sealant (fig.138). The same black substance is macroscopically observed on the surface of the lead lining on the lowest part of the west wall, over a circular depression on the floor that served as a silt trap (fig.139) (Frost and Hadjidaki, 1990, 516-517). The cistern was likely to have been modified in the Late Hellenistic period, as it appears from the reconstruction of the upper parts of the west and north walls (fig.140) (Frost and Hadjidaki, 1990, 516-517).

Figure 138: Phalasarna: the interior of the cistern, where traces of the black substance are visible on the plastered walls.

Figure 139: Phalasarna: the circular depression on the floor of the cistern, lined with Lead. The black substance is observed on the lead surface adjusted to the wall.

Figure 140: Phalasarna: the north wall of the cistern, likely reconstructed during the Late Hellenistic period.

Five stone basins plastered with mortar were found within a rectangular room at the industrial area of the city dated to the 4th- 3rd century BC (fig.141). Their original use was for bathing, used from the temple visitors of the acropolis. Secondary use is related to pottery production, since they were found filled with unbaked clay (Hadjidaki, 2001, 157). It seems that the basins (bathtubs) were entirely covered by thin plaster in both their interior and exterior surface. Dark brown-black substance is observed locally on the plastered surfaces. Lead lining survives in the circular depression in one of them (fig.141).

Figure 141: Phalasarna: the five plastered stone bathtubs (basins). Lead lining survives in one of them (pointed by the arrow). Basins 1 and 3 were sampled.

The remains of a cistern floor and walls are visible on the East, SE of the Three Hierarchs Church (fig.142). Based on the pottery sherds and architectural remains on the surrounding area, as well as the crushed-brick mortar of the cistern, its dating could be placed between the 2nd to the 4th cent. AD (in situ survey with the excavator of the site, Dr Elpida Hadjidaki, October 2020).

Figure 142: Phalasarna: the remains of a cistern, area of the Three Hierarchs Church (in red frame).

Seven mortar samples were collected from a) the walls of the cistern, b) two basins (1 and 3, fig.141) and c) the cistern in the area of the Three Hierarchs Church (Appendix III, fig.7-9).

11.1.3 Aptera

The ancient city of Aptera is situated on a wide hill plateau at the southeast of the Souda Bay, west Crete. Its strategic geography over the surrounding territory enabled the development of the city as a powerful trade and cultural center (Niniou-Kindeli, 2000, 313).

The earliest excavation finds suggest occupation during the 8th century BC. The city flourished during the early Hellenistic period, when it minted its own coins. During the Roman period, Aptera was under the control of Rome and although lost its political status, it remained a flourishing city as evidenced from the excavated public buildings. Aptera was deserted in the 7th century AD likely as a result of the two great earthquakes, especially the one in 670 AD (Niniou-Kindeli, 2000, 313-314).

The excavation of a private residence revealed foundation layers from the Geometric period until the Hellenistic, whereas the overlying layers produced mixed finds of the 1st -

3rd century AD (Niniou-Kindeli, 2000, 319). The residence (Roman Villa) is dated on the 1st century BC - 1st century AD and had several adjacent rooms serving the house needs and two yards surrounded by tiled-roof stoa. A bottle-shaped cistern of 6 meters depth was found on the smallest yard of the Roman Villa (fig. 143) Niniou-Kindeli, 2000, 319; Niniou-Kindeli, Ministry of Culture 25th Ephorate of Prehistoric and Classical Antiquities, 2008, 43).

The public baths were constructed during the early Roman period (1st century AD) and they were closely linked to the two large public cisterns that supplied them with water (fig. 144) (Niniou-Kindeli, 2000, 323). The Three-aisled cistern (17x25m) is likely to have incorporated an earlier Hellenistic form in its structure (fig.145-146). The gamma-shaped cistern (large side: 55.80m, small: 34,20m., width: 25m) was also vaulted, although the roof is not preserved (fig.147) (Niniou-Kindeli, Ministry of Culture 25th Ephorate of Prehistoric and Classical Antiquities, 2008). The walls of the cisterns were constructed in the *opus caementicium* form and plastered with hydraulic mortar (Niniou-Kindeli, 2002; 2008).

Figure 143: Aptera: the opening of the bottle-shaped cistern at the Roman Villa.

Figure 144: Aptera: view of the public baths.

Figure 145: Aptera: the three-aisled cistern (exterior view).

Figure 146: Aptera: the three-aisled cistern (interior view).

Figure 147: Aptera: the gamma-shaped cistern.

Thirteen mortar samples were collected from the cisterns, both private and public and from one bathtub of the Roman baths (Appendix III, fig.10-16).

11.2 Reflectance micro-FTIR Analysis Methodology

Sample	Origin	Sampling
POL_S1	Cistern floor (2nd AD - Roman)	Buried in rural soil.
POL_S2	Cistern floor (2nd AD - Roman)	Buried in rural soil - surface cleaned with spring water.
POL_S3	Cistern floor (2nd AD - Roman)	Buried in rural soil - same area with S2.
POL_S4	Mortar on stone related to the cistern wall (2nd AD - Roman)	Exposed to rural environment.
POL_S5	Mortar on stone related to the cistern wall (2nd AD - Roman)	Exposed to rural environment - surface cleaned with spring water.
POL_S6	Mortar on stone related to the cistern wall (2nd AD - Roman)	Exposed to rural environment - same area with S5.
POL_S14	Low wall between cistern and aqueduct (2nd AD - Roman)	Inner Part towards aqueduct - Horizontal surface - buried beneath masonry - surface cleaned with spring water.
POL_S15a	Low wall between cistern and aqueduct (2nd AD - Roman)	Outer Part towards cistern - Horizontal surface - buried beneath masonry - surface cleaned with spring water.
POL_S15b	Low wall between cistern and aqueduct (2nd AD - Roman)	Outer Part towards cistern - Horizontal surface - buried beneath masonry - surface cleaned with spring water - different texture from S15a.
FAL_S7	Cistern wall (4th BC - Hellenistic)	From the S wall - exposed to marine environment since the 80s excavation.
FAL_S13	Cistern wall (4th BC - Hellenistic)	Loose piece from the N wall - exposed to marine environment since the 80s excavation.
FAL_S8	Bathtub 1 (4th -3rd BC -Hellenistic)	Seat - exposed to marine environment.
FAL_S9	Bathtub 1 (4th -3rd BC -Hellenistic)	Bottom - exposed to marine environment.
FAL_S10	Bathtub 3 (4th -3rd BC -Hellenistic)	Side wall - exposed to marine environment.
FAL_S11	Bathtub 3 (4th -3rd BC -Hellenistic)	Front wall - exposed to marine environment.
FAL_S12	Cistern - 3 Hierarchs Church area - (2nd - 4th AD)	Exposed to marine environment.
APT_S16	Bottle-shaped cistern (Roman Villa - 1st - 3rd AD)	North inner side surface of the opening - 0.5m depth - exposure to high humidity.
APT_S17	Bottle-shaped cistern (Roman Villa - 1st - 3rd AD)	Loose piece from the bottom - exposure to high humidity.
APT_S18	Bathtub (Roman Baths - 1st AD)	From the wall - exposed to rural environment.
APT_S19	3-aisled cistern (Roman - 1st AD)	1st aisle - from the wall opposite the entrance - Biological growth on the wall - high humidity content - Pigeon nests.
APT_S20	3-aisled cistern (Roman - 1st AD)	1st aisle - from the floor - highly contaminated by pigeon droppings and other deposits from frequent flooding (rain water).
APT_S21	3-aisled cistern (Roman - 1st AD)	2nd aisle - connection of floor to wall towards the entrance.
APT_S22	3-aisled cistern (Roman - 1st AD)	2nd aisle - from wall opposite the entrance.
APT_S23	3-aisled cistern (Roman - 1st AD)	3rd aisle - from low part of the side wall - water staining - biological activity.
APT_S24	Gamma-shaped cistern (Roman - 1st AD)	NW section - from the right wall (towards the south section) - exposed to external, dry, rural and marine environment.
APT_S25	Gamma-shaped cistern (Roman - 1st AD)	NW section - from the left wall towards the south - exposed to external, rural and marine environment.
APT_S26	Gamma-shaped cistern (Roman - 1st AD)	NW section - connection of the right wall to the floor - exposed to external, rural and marine environment.
APT_S27	Gamma-shaped cistern (Roman - 1st AD)	NW section, from floor - exposed to rural and marine environment - occasional rain water accumulation.
APT_S28	Gamma-shaped cistern (Roman - 1st AD)	S. section - from wall - exposed to rural and marine environment.

Table 23: List of mortar samples collected from water-related constructions from Polyrrhenia (POL), Phalasarna (FAL) and Aptera (APT).

Twenty-nine mortar samples were collected from the water-related constructions of Polyrrhenia (POL), Phalasarna (FAL) and Aptera (APT). The precise sampling location and the description of environmental conditions that the samples were exposed to, are summarized in Table 23.

Reflectance micro-FTIR spectra were obtained under the standardized acquisition parameters (section 5.1); spectra were collected in Reflectance mode after 60 scans of 4 cm^{-1} spectral resolution, for the 4000-600 cm^{-1} mid-infrared frequency range. Multiple spectra were obtained from each sample along each distinct layer, according to the layer description and graphic representation (fig. 148). In certain occasions, where the surface layer was free from underlying mortar, spectra were collected from the inverted flat surface (fig.148).

The mortar samples were analysed in their original form without any preparation (embedding in resin / polishing). *"Cross-section"* refers to the position of the sample under the microscope, not to a preparation treatment. The example of the embedded and polished sample in figure 148 is merely used for picturing the distinct layers. Polished samples were only used in Optical (OM) and Electron Scanning Microscopy (SEM) after the completion of the Reflectance micro-FTIR analysis.

Abbreviation	Spectrum Layer	Description
F	Flat surface	Sample positioned flat under the microscope
S	Surface	Sample positioned in cross-section under the microscope
B	Below surface	Sample positioned in cross-section under the microscope
M	Mortar	Sample positioned in cross-section under the microscope
I	Inverted surface	Sample positioned flat and inverted under the microscope

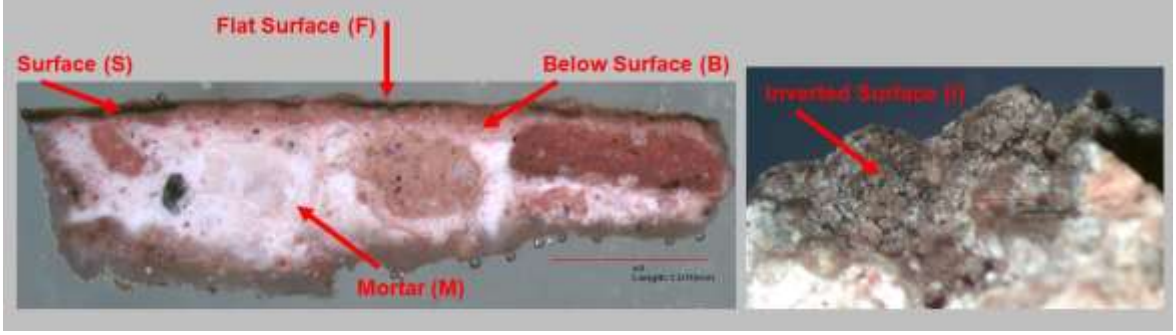

Figure 148: Graphic representation of the distinct layers of mortar samples.

Thus, in reporting analysis (sect. 11.3 and Appendix III, sect. 11.3) the abbreviation for a spectrum is ***Origin*** _ ***Sample number*** _ ***Spectra averaged*** _ ***Spectrum layer***. For example, the spectrum POL_S1_16-20_S refers to the Polyrrhenia sample S1 that was

averaged from 6 individual spectra (spectrum 16 to spectrum 20), obtained from the Surface of the sample positioned in cross-section under the microscope.

The results are divided into three sub-sections (11.3.1 to 11.3.3) according to the archaeological area that the samples derive from. Thus, the abbreviations POL (Polyrrhenia), FAL (Phalasarna) and APT (Aptera) are eliminated from the stacked spectra in the individual sections dealing with each archaeological site.

The reflectance spectra obtained from each layer of the sample were averaged. Following the methodology developed in Chapter 7, the OriginPro 2015 *Quick Gadget Peak Finder* tool was used for locating the peak position *x* and peak intensity *y* parameters of absorption bands within the ROI 3800-600 cm^{-1} in each averaged spectrum. These data were added in the CPAD.

Accordingly, the filtering entry ***"Priority Peak"***, was used for separation of peaks of interest from those that represent noise and detector interference. The filtering was performed on the averaged spectra obtained from the sample layers **F**, **S** and **I** (fig.148, above). The filtering entries related to the chemical characterization of each absorption band, ***"Type of Band", 'Chemical Band Assignment"*** and ***"ID As"*** were left blank. Data related to sample description and spectrum acquisition parameters were included in the CPAD.

The CPAD was updated with the addition of new standards to represent potential contaminants or other organic additives that may be present (Table 24). Reflectance micro-FTIR spectra were obtained from Gypsum / sulphates, calcium oxalate, clay, soil, pigeon droppings and sea salt. These standards represented possible contaminants and/or depositions that could occur in an external, rural and marine environment such as that of Ancient Polyrrhenia, Phalasarna and Aptera (Monico et al., 2013, 271; Maravelaki, 2005, 191; Rampazi et al., 2004, 967; Miliani et al., 2012, 299). Powder mixtures of Calcium carbonate, Calcium oxalate and Calcium sulphate in predefined concentrations, represented heterogenous accumulations of surface deposits and allowed the assessment of any possible spectral alteration on the diagnostic absorption bands of the individual components in the mixture (Table 24).

Calcium hydroxide, bones, casein, beeswax, rosin, dolomite and egg shell were added to the CPAD as materials likely to be present in ancient and historic man-made stone patinas and mortars (Edwards and Farwell, 2008, 986; Martin-Gil et al., 2005, 285; 1999, 59; Polikreti and Maniatis, 2003, 111; Ventola et al., 2011; Singh and Arbad, 2014). The new

standards were analyzed in their purchased form (Table 24: *material*) and as powders or pellets, following the sample preparation methodology in Chapter 7 and section 5.1 (pressed-disks).

Standard	Analysis As	Spectrum ID	Product Information
Calcium hydroxide ($Ca(OH)_2$)	Powder	**Li_av**	Analar
Calcium oxalate monohydrate ($C_2CaO_4.H_2O$)	Powder	**Ox_av**	Sigma-Aldrich and ACROS organics
Calcium oxalate monohydrate ($C_2CaO_4.H_2O$)	Pellet	**Ox_p_av**	Sigma-Aldrich and ACROS organics
Calcium sulphate ($CaSO_4.H_2O$)	Powder	**Gy_av**	BDH chemicals LTD
$CaCO_3$-Ca Oxalate	Powder mixture	**Ca_Ox_av**	50% w/w
$CaCO_3$-$CaSO_4$	Powder mixture	**Ca_Gy_av**	50% w/w
$CaCO_3$-Ca Oxalate-$CaSO_4$	Powder mixture	**Ca_Ox_Gy_av**	50%, 25%, 25% w/w
Ca Oxalate-$CaSO_4$	Powder mixture	**Ox_Gy_av**	50% w/w
Dolomite crystal ($CaMg(CO_3)_2$)	Material	**Dol_av**	Frizington, Cumbria, Richard Tayeler minerals, Conservation Reference collection.
Clay mineral	Material	**Cl_av**	London Clay Downside Cobham Surrey, Richard Tayler Minerals, Conservation Reference collection.
Gypsum mineral	Material	**GyM_av**	Morocco, Richard Tayler Minerals, Conservation Reference collection.
Casein	Powder	**Cas_av**	Aldrich
Rosin	Powder	**Ro_av**	Conservation Lab, SHARE
Beeswax	Material	**BW_av**	Conservation Lab, unbleached Frank W. Joel LTD.
Pig bone	Material	**PB_av**	1.5 yrs old Welsh pig, buried for 6 years, breed close to ancient breeds. Specimen provided by Dr. Jacqui Mulville, Dept. of Archaeology, SHARE.
Sheep bone	Material	**SB_av**	Bronze Age Scotland (1200-1000 BC).Burial and/or processing unknown. Specimen provided by Dr. Jacqui Mulville, Dept. of Archaeology, SHARE.
Sea salt	Pellet	**Sa_av**	Naturally collected, Crete, Greece
Pigeon Droppings	Material	**DR1_av**	3-aisled cistern floor, Aptera, W. Crete, Greece.
Pigeon Droppings	Material	**DR2_av**	3-aisled cistern floor, Aptera, W. Crete, Greece.
Egg Shell	Material	**ES_av**	Welsh egg, exterior surface
Grey Soil	Material	**GS_av**	W. Crete, Greece
Grey Soil	Powder	**GS_P_av**	W. Crete, Greece
Red Soil	Material	**RS_av**	W. Crete, Greece
Red Soil	Powder	**RS_P_av**	W. Crete, Greece
Ammonium Sulphate ($(NH_4)_2SO_4$)	Powder	**Am.Su_av**	GPR BDH
Ammonium Sulphate ($(NH_4)_2SO_4$)	Grinded powder	**AmSu_av**	GPR BDH
Sodium Sulphate hydrated (Na_2SO_4)	Powder	**NaSO4_hy_av**	Fisher Scientific
Sodium Sulphate anhydrous (Na_2SO_4)	Powder	**NaSO4_an_av**	VWR chemicals

Table 24: New CPAD additions of standards.

The interpretation of the reflectance micro-FTIR spectra obtained from the ancient mortar samples solely relied on the assignment of chemical bonds to absorption peaks through the CPAD and was carried out prior to visual examination of samples by Optical (OM) and Scanning Electron microscopy (SEM). This avoided the occurrence of identification bias related to the visual appearance of the samples.

Following this, spectra interpretations were related to the appearance of samples using OM and SEM and with consideration of archaeological and environmental contexts. The OM and SEM examination of the samples focused on detecting biological activity and external depositions. The visual information was compared to the FTIR spectra to attempt to identify any biological activity and to distinguish it from intentional use of an identifiable organic substance.

The NIKON™ SMZ1000 Zoom Microscope in reflected light equipped with 0.5X WD123 Nikon Plan APO objective and the GXCapture software were used for the examination of the samples. The Cam Scan Maxim – Oxford Instruments Scanning Electron Microscope and the Caesium 7 software were used for obtaining Secondary Electron Images (SEI). The samples were carbon coated and the images were obtained at accelerating voltage 20 keV, emission current 107 ± 1μÅ and filament current 2.61 Å ± 0.20 Å. Micro-photographs and SE images were obtained from the flat surface of samples and from embedded in resin/polished cross-sections. SE images were also obtained from selected standards.

11.3 Results: analysis of archaeological samples

The spectrum **S** is the averaged spectrum obtained from the surface of each sample in cross-section positioning under the FTIR microscope. This spectrum is expected to provide the most accurate chemical profile of the surface layer, since it is less contaminated by external depositions than the flat surface (**F** spectrum). Furthermore, organic preservation is more likely to occur in the inner part of the sample, from areas of alkalinity that prevent biological growth (Fang et al., 2013, 6). For clarity, the spectra of each layer of the sample are presented in stacked layout with marked Regions of Interest (ROIs). Single averaged spectra are included in *Appendix III, 11.3 Results,* where necessary.

11.3.1 Polyrrhenia Samples

Sample S1 - Cistern floor

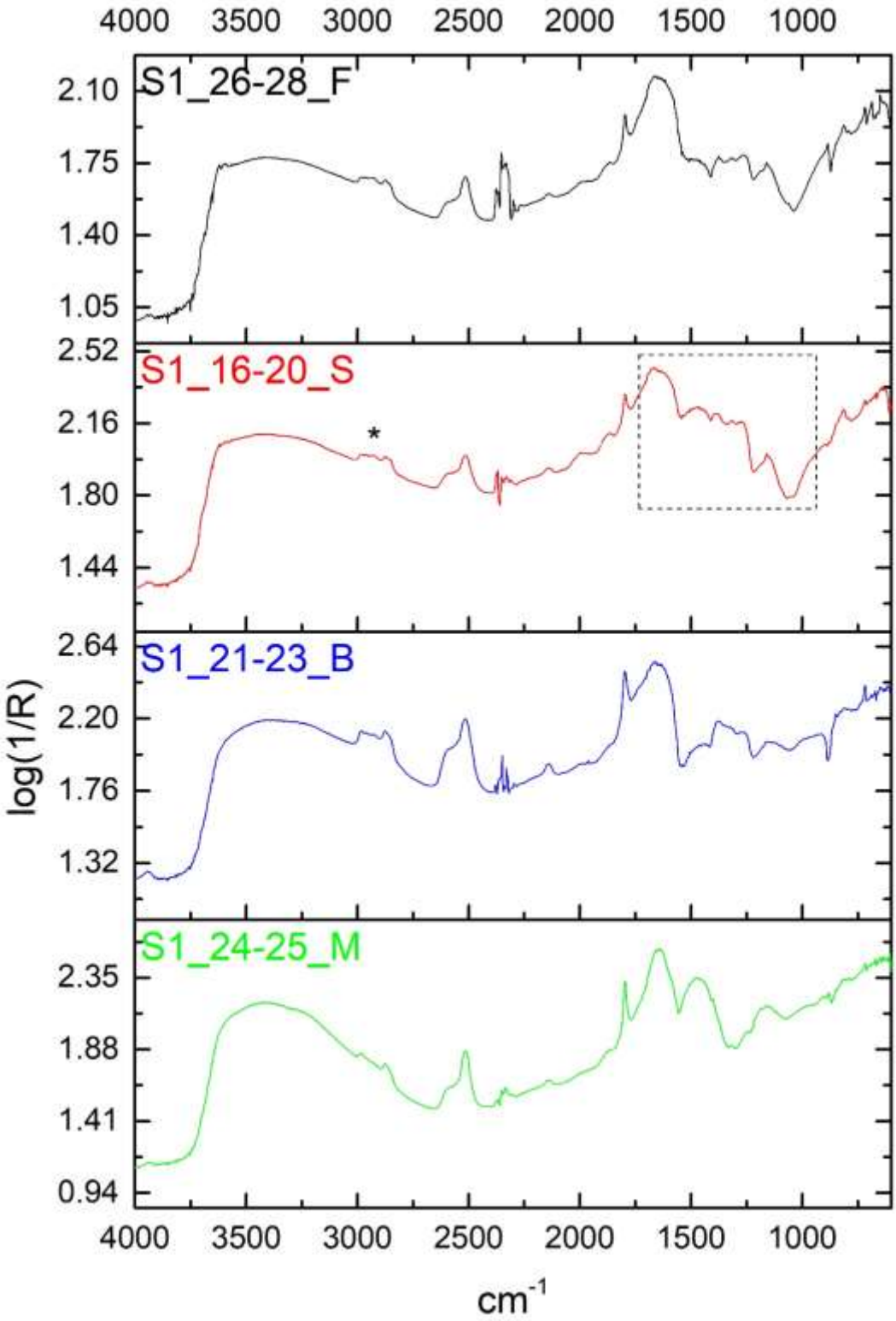

Figure 149: Sample S1: stacked spectra of individual layers. Marked area and asterisk indicate organic presence on the surface spectrum.

The surface spectrum (S1_16-20_S) shows both organic and inorganic components (red, fig.149; Appendix III, fig. 17). The comparative assessment of the spectrum through the CPAD identified mortar components in the peaks 897 cm^{-1} *v2* and *v4* carbonate ion vibrations (Ylmen and Jaglid, 2013, 119), 1795 cm^{-1} $CaCO_3$ combination band (Ricci et al., 2006, 1222), 1867-1994 cm^{-1} quartz peaks (Q_av standard spectrum), 2515-2584 cm^{-1} $CaCO_3$ combination band (Ricci et al., 2006, 1222) and 2875 and 2979 cm^{-1} (M_av, mortar standard spectrum).

Protein is evident from the stair-step type intensities in the region 1271-1539 cm^{-1} (Rosi et al., 2009, 2099), the presence of phosphates at 1044 and 1058 cm^{-1} (Ricci et al., 2006, 1223), also present in egg white and bone glue standards, the shape of 1159 cm^{-1} that resembles that of phosphates instead of quartz, the dominant absorption of N-H bond at 1630-1678 cm^{-1} (Miliani et al., 2012, 304; Rosi et al., 2009, 2104) and the weak absorption and 1^{st} overtone of amide I at 2931-2981 cm^{-1} (Rosi et al., 2009, 2099). The shape of peaks at 1630-1678 cm^{-1} resembles that of the strong amide peak at 1690 cm^{-1} on the protein standards (section 7.5) and given the fact that inorganic components are not pronounced, the peak is assigned to protein rather than $CaCO_3$ absorbing in the same region.

The peaks 1044, 1058 cm^{-1} are also detected in the standard of pigeon droppings likely because of the phosphate or Sulphur content (Miliani et al., 2012, 300) (Appendix III, fig.18). However, the sample is not contaminated by such depositions since it was buried in rural soil. The presence of phosphoproteins, similar to those detected in bone glue and egg standards, is further enforced.

The peaks at 1271-1281 cm^{-1} and 1318-1341 cm^{-1} are not unique to proteins since they belong to C-O vibrations (Ploeger et al., 2010, 37; Monico et al., 2013, 273). However, their shape and intensity resemble those in protein and egg white/ mortar standards (section 7.5). The peaks 1449-1539 cm^{-1} closely match those detected in EW_M_50_av (50% egg white additive in mortar).

The peaks at 2931-2965 cm^{-1} show CH stretching vibrations found in both proteins and lipids. However, the shape of the peaks resembles those of protein and protein/mortar standards and not the sharp reststrahlen peaks that are usually visible in lipids and lipid/mortar standards even those of low organic concentration.

Organic presence is also detected on the flat surface spectrum (F) although masked by calcareous soil (fig.149). Organic peaks (asterisk and framed ROI) decrease gradually

moving from the surface (S) towards the layers below the surface (B) and the mortar (M). Inorganic content increases accordingly. The B layer retains organic peaks in the regions of interest, whereas the M layer shows only few in the regions 1271-1388, 1472-1539, 1630-1678 cm^{-1} and none in the 1044, 1058 and 2931-2965 cm^{-1} regions. That shows that protein is preserved mainly on the surface layer and it is not mixed with the mortar.

The CPAD comparison of S1 surface spectrum with that of the Grey Soil standard showed no peak matching (GS_P_av, Appendix III, fig.19). Grey soil was assessed because similar soil particles were detected on the sample through SEM. Grey soil is highly calcareous and shares many peaks with $CaCO_3$. Its organic components such as proteins, lignin and humid acid in the 1630-1655 cm^{-1} region did not match the protein-assigned peaks in the corresponding region of the S1 surface spectrum (Chauhan et al., 2018, 79). These protein peaks are about 20 cm^{-1} shifted towards higher wavenumbers in S1 spectrum.

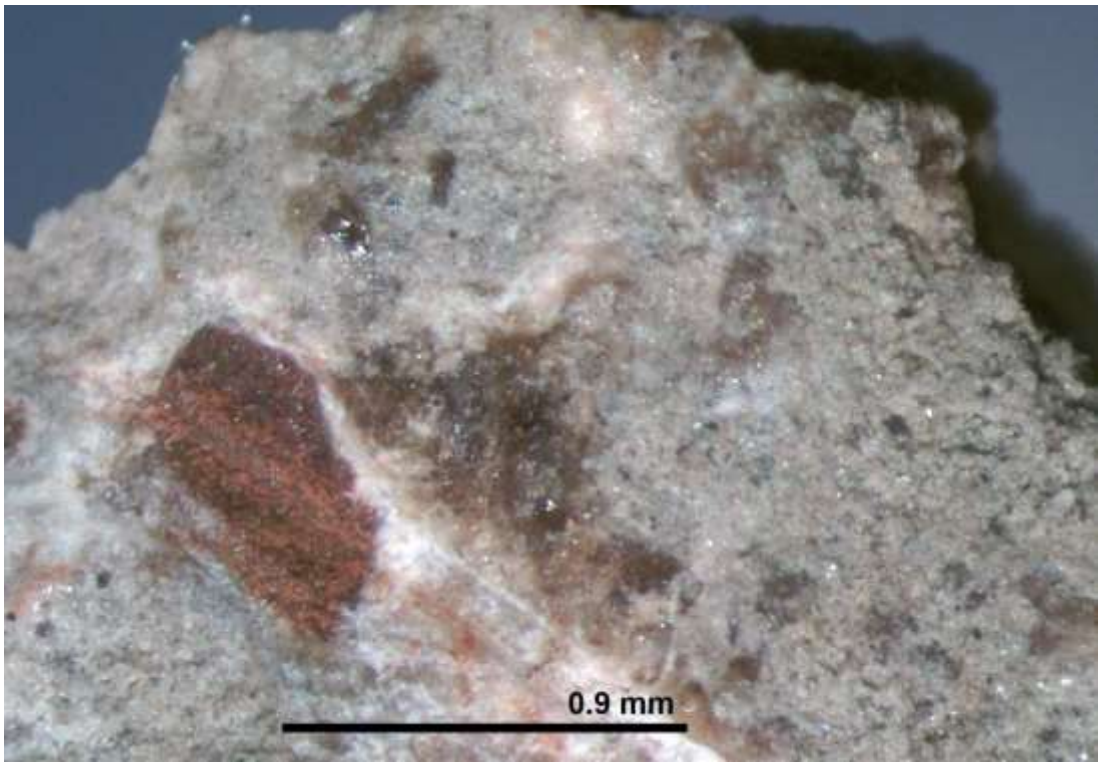

Figure 150: The flat surface of sample S1; brown, resinous substance is observed on the surface area not covered by soil.

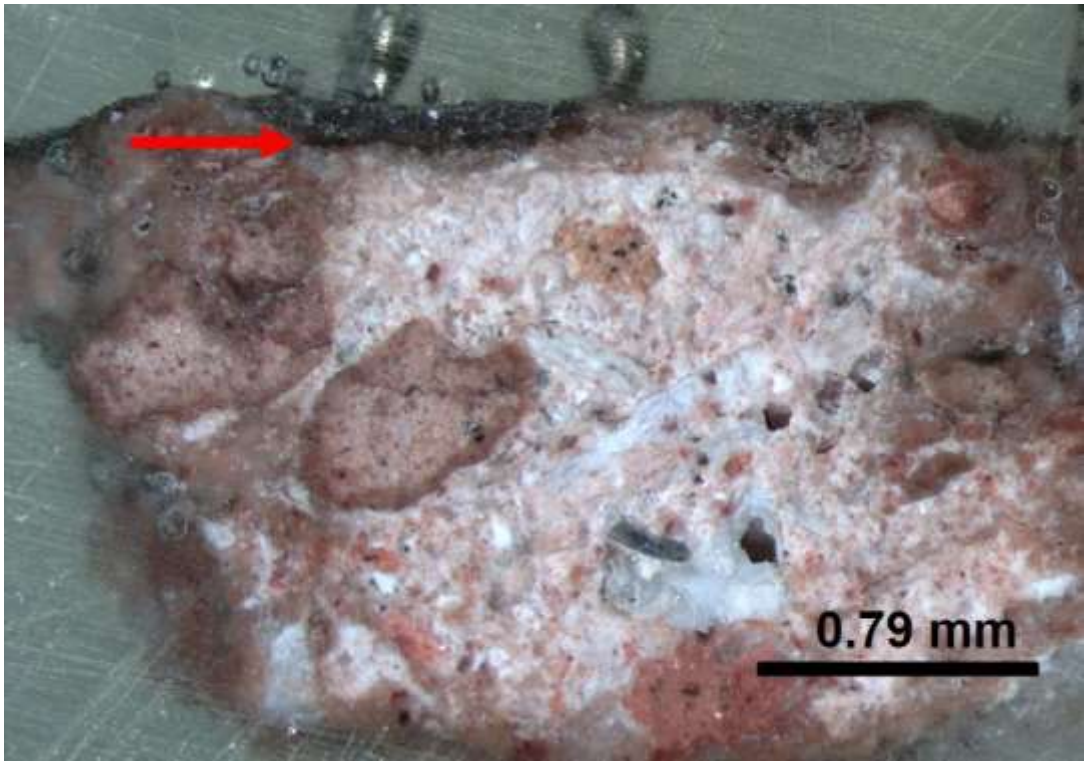

Figure 151: Polished cross-section of S1. Red arrow indicates the thin resinous brown layer.

Optical Microscopy showed that the flat surface of S1 is covered by soil. The exposed area underneath the soil contains calcite and ceramic inclusions. A resinous brown layer is visible on the flat surface of S1 (fig.150). Part of the ceramic inclusion seems to retain the resinous substance in its pores. The resinous layer is preserved over the mortar and below the soil. This stratigraphy is evident in the cross section; the resinous brown layer is thin and appears below a dark grey layer of soil (pointed by the arrow, fig.151).

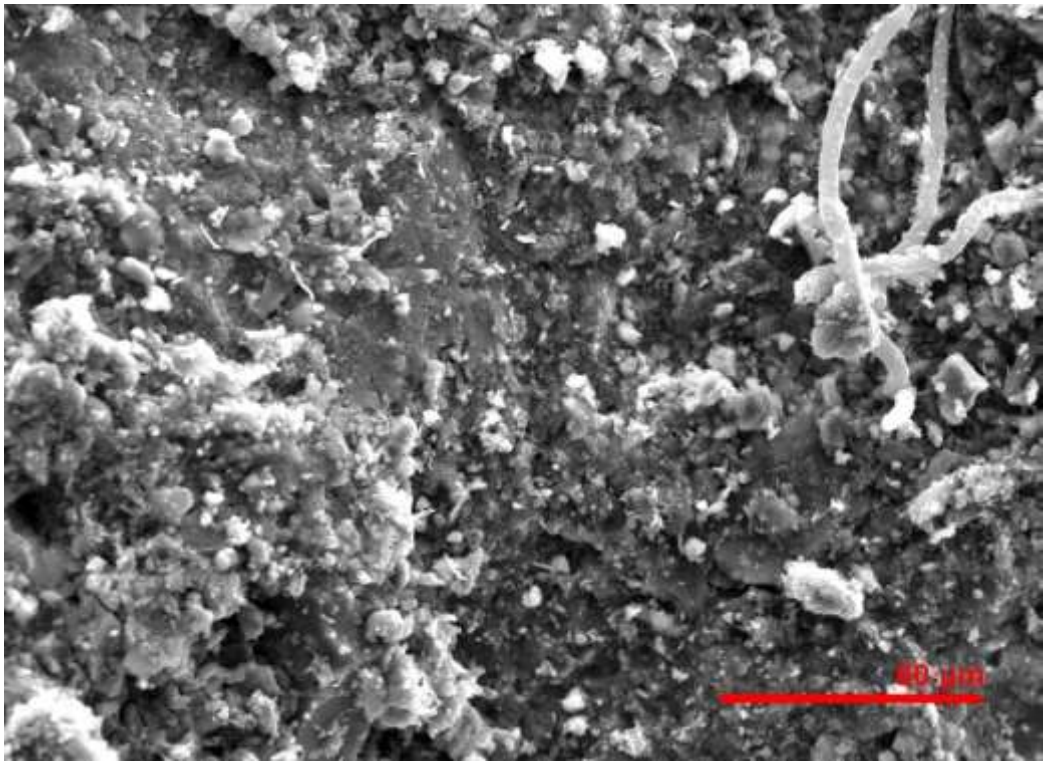

Figure 152: SE image of the S1 flat surface showing adherent soil particles.

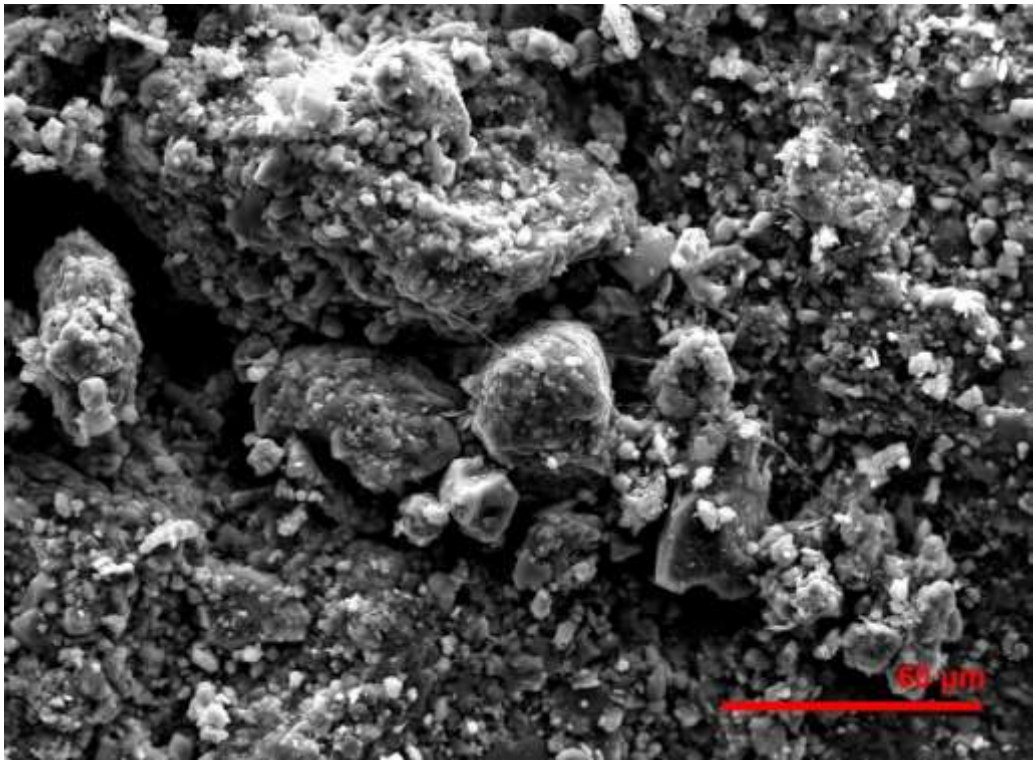

Figure 153: SE image of Grey Soil standard.

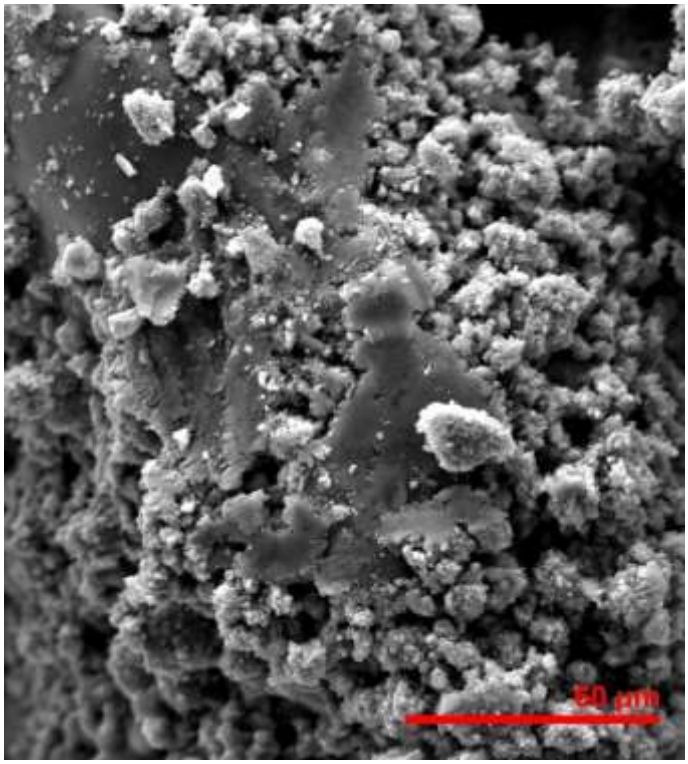

Figure 154: SE image of BG_M_25 standard.

The SE images of sample S1 (fig.152) showed that its surface is covered by soil particles similar to those of the Grey Soil standard (fig.153). Loose fibres, likely of biological origin, appear on the upper right side of the sample surface (Rosado et al., 2013). The surface layer below the soil appears dense and homogenous. The soil standard does not have such homogenous texture. The texture of the BG_M_25 (25% bone glue additive in mortar) standard resembles that of S1 (fig.154).

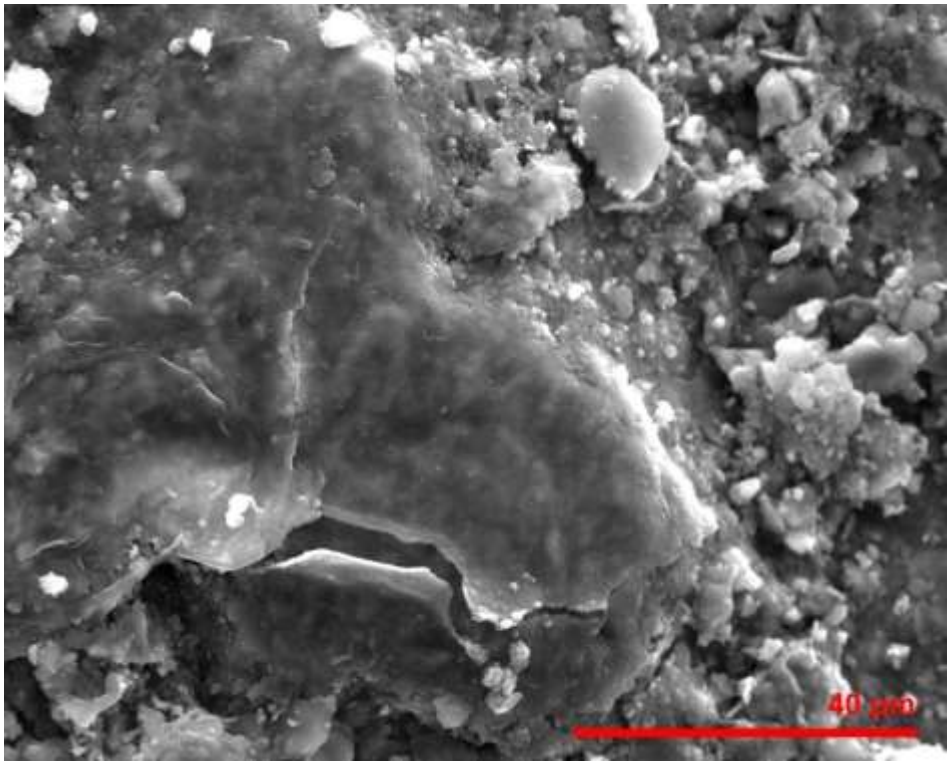

Figure 155: S1 flat surface preserving resinous substance.

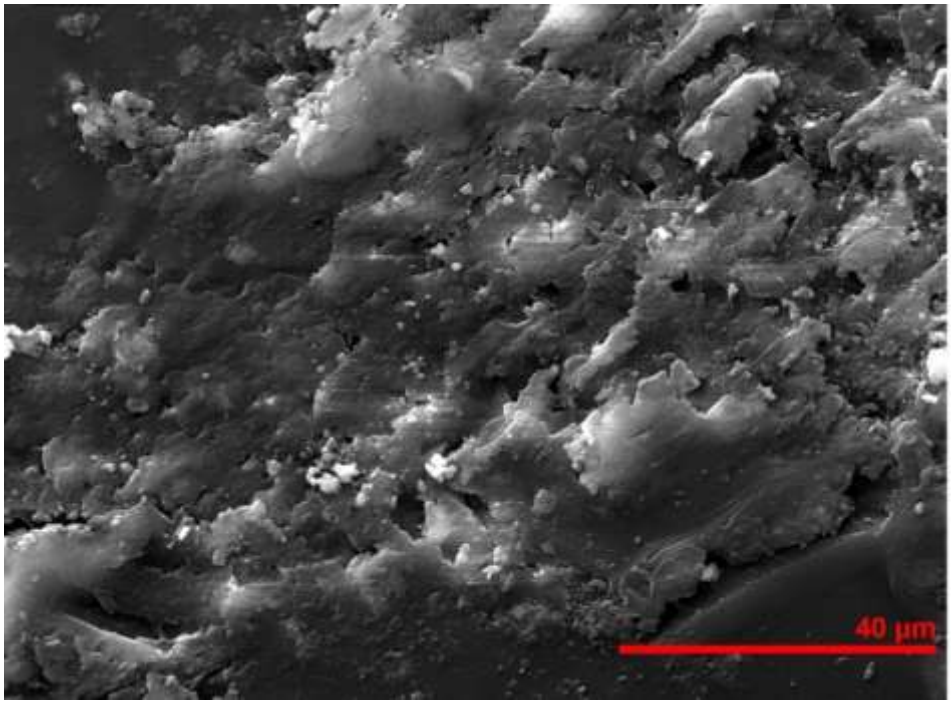

Figure 156: Mortar replica coated with Bone glue.

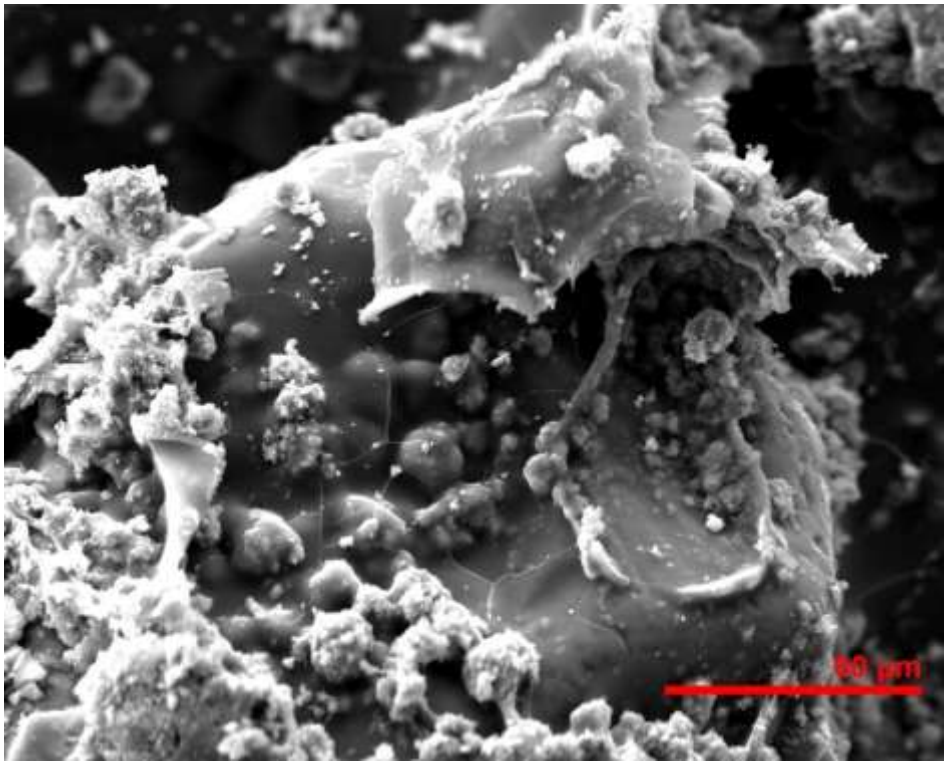

Figure 157: BG_M_25 (25% bone glue in mortar) standard.

The resinous, smooth substance covers the entire surface of S1 and does not belong to the soil layer (fig.155). The substance shows high resemblance to standards of bone glue/mortar (fig. 156-157). The cross-section SE image shows that the surface layer is less dense than the mortar. A fine calcite layer exists between the surface and the mortar (Appendix III, fig.20).

Sample S2 – Cistern floor

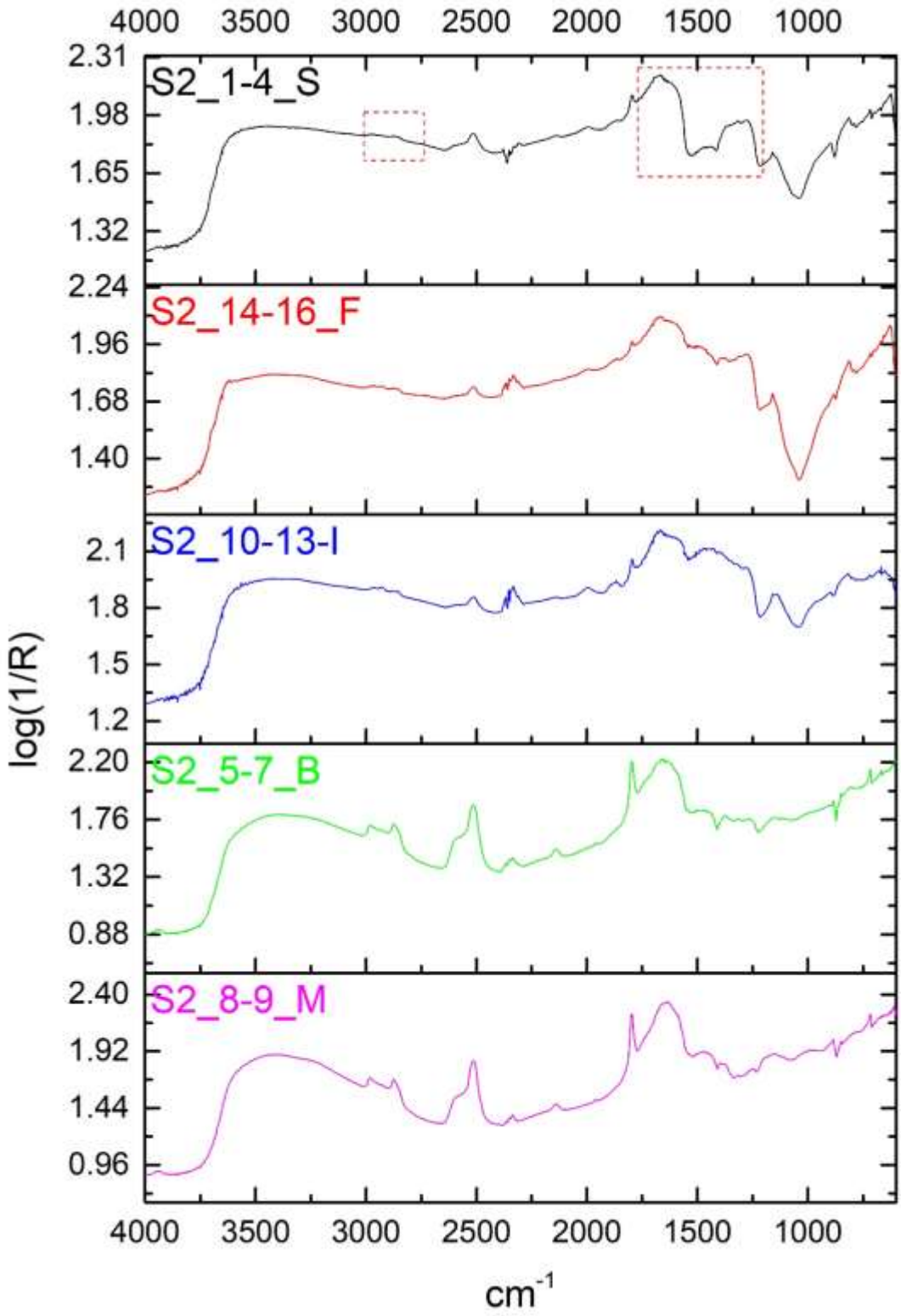

Figure 158: stacked spectra of individual layers of sample S2. Marked areas indicate organic presence on the surface spectrum.

The sample S2 was obtained from an area of the cistern floor cleaned with spring water. The removal of soil particles during its cleaning is reflected in the surface spectrum (S2_1-4_S, fig.158), where the inorganic content appears low. The absorption peaks indicating organic are: 1285, 1315, 1438-1517, 1635-1679, 1739, 2770 and the ROI 2862-3035 cm^{-1} (fig.158; Appendix III, fig.21). Similar organic peaks were detected in the S1 Surface spectrum despite the presence of soil in its surface.

The strange shape of the strong absorption at 1285-1315 cm^{-1} (fig.158, dotted frame) resembles that of egg white standard (sec. 7.5.2, fig.43). The shape of the quartz peak at 1159 cm^{-1} shows overlapping with phosphates indicating presence of phospholipids. This is further supported by the weak C=O peak of esters at 1739 cm^{-1} (Iwanicka et al., 2017, 13). The 1679 cm^{-1} peak shows protein. The weak peak at 2770 cm^{-1} appears on both BG_M_50 (50% bone glue additive in mortar) and E_M_25 (25% egg additive in mortar). An egg-related protein might be present on the surface of sample S2 due to the combined presence of proteins and lipids.

The inorganic presence is very low on the spectrum of the inverted surface S2_10-13_I (fig.158; Appendix III, fig.21). The region 1282-1679, the peaks 1771 and 2858 and 2928-3029 cm^{-1} show protein. Lipids cannot be ruled out and the fact that the N-H peak at 1570 cm^{-1} is missing may show that pure protein is not present (Miliani et al., 2012, 304; Rosi et al., 2009, 2104). The peak at 1771 cm^{-1} coincides with the one seen in EW_M_75 but should indicate esters C=O instead of protein (Lombardi and Santarelli, 2009, 542). The 2080 cm^{-1} is also visible in lipids, such as in milk standard and absent in mortar components. Egg white that retained lipid during separation from the egg, is a possible match. Visually, dried egg shows a crystallinity that could resemble the one seen on the sample (sect.7.3, fig.34).

The spectra comparison of the different layers through the CPAD shows that the organic content reduces towards the mortar. Protein is evident, although gradually reduced, on the B layer and mortar layer M at the region 1265-1535 cm^{-1}. The reduction of the organic content is visible on the stacked spectra too (fig.158).

Figure 159: The cross-section of sample S2. Arrow points on the brown resinous substance on the flat surface.

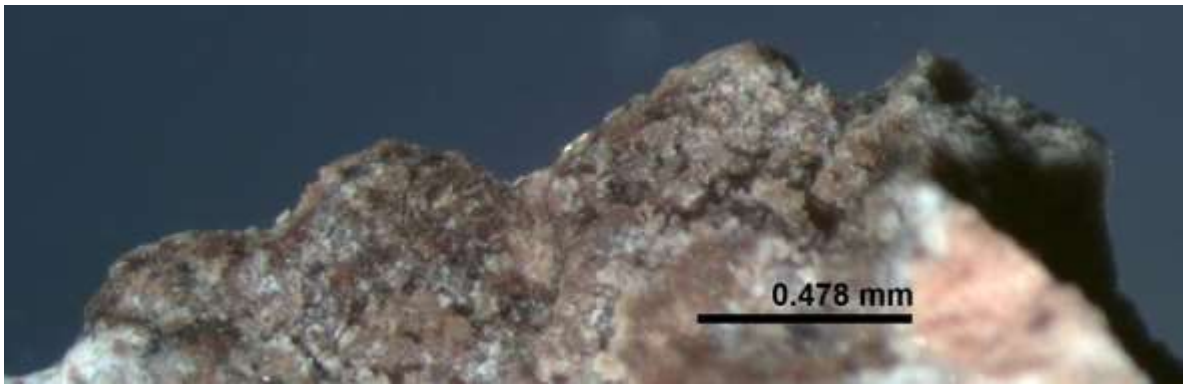

Figure 160: The inverted surface of sample S2, exposing the resinous substance of the surface.

Because the surface of sample S2 was partially cleaned, the brown resinous substance on its surface is more visible than on sample S1 (fig.159). The locally retained soil is grey and matches the coloration of the Grey Soil standard. Ceramic inclusions and calcite appear in the mortar. The inverted surface reveals a thick layer of resinous substance that clearly differs from the mortar layer underneath (fig.160).

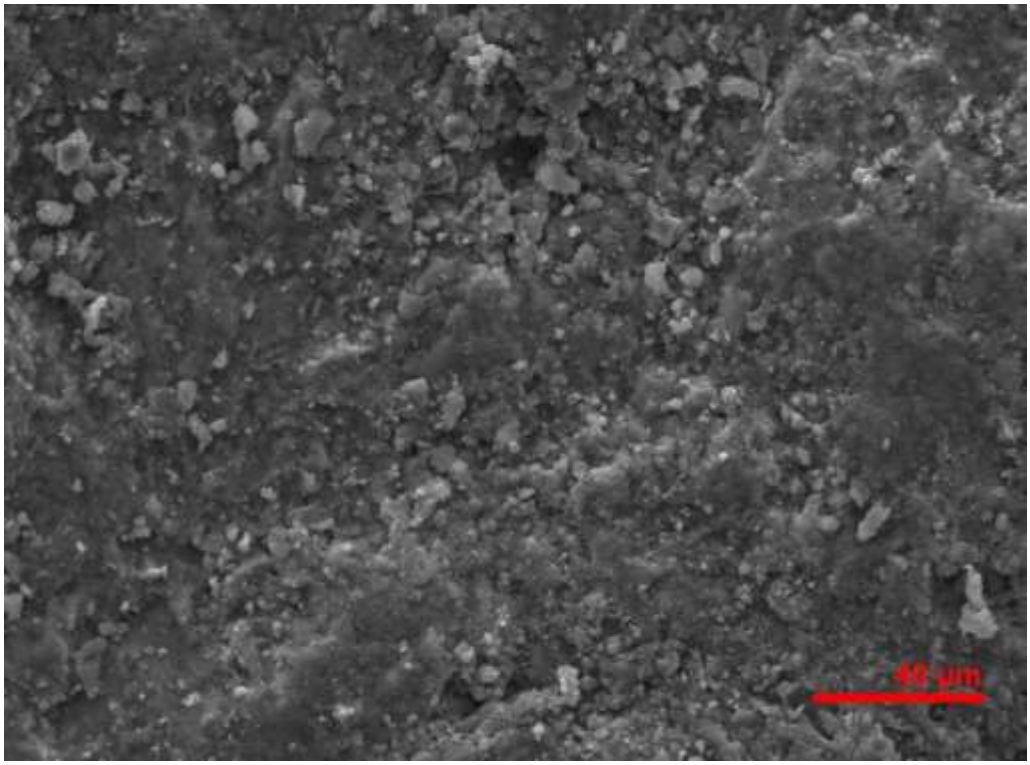

Figure 161: SE image of S2 flat surface. Few soil particles are adhered on the dense and smooth surface.

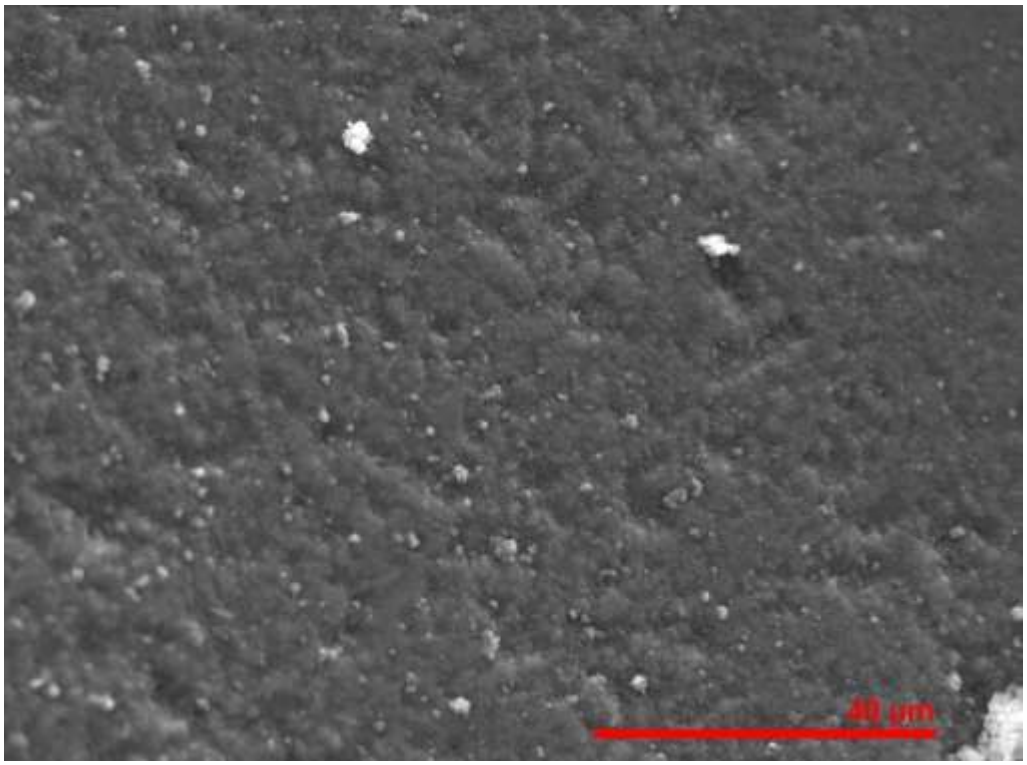

Figure 162: SE image of mortar replica standard.

The dense surface layer of sample S2 is similar to that of sample S1 (fig.161). Soil particles are fewer and there are no signs of biological activity. Similar texture is observed

on the surface of mortar replica (fig.162). However, the surface of S2 shows smoother regions, indicating a substance other than just mortar.

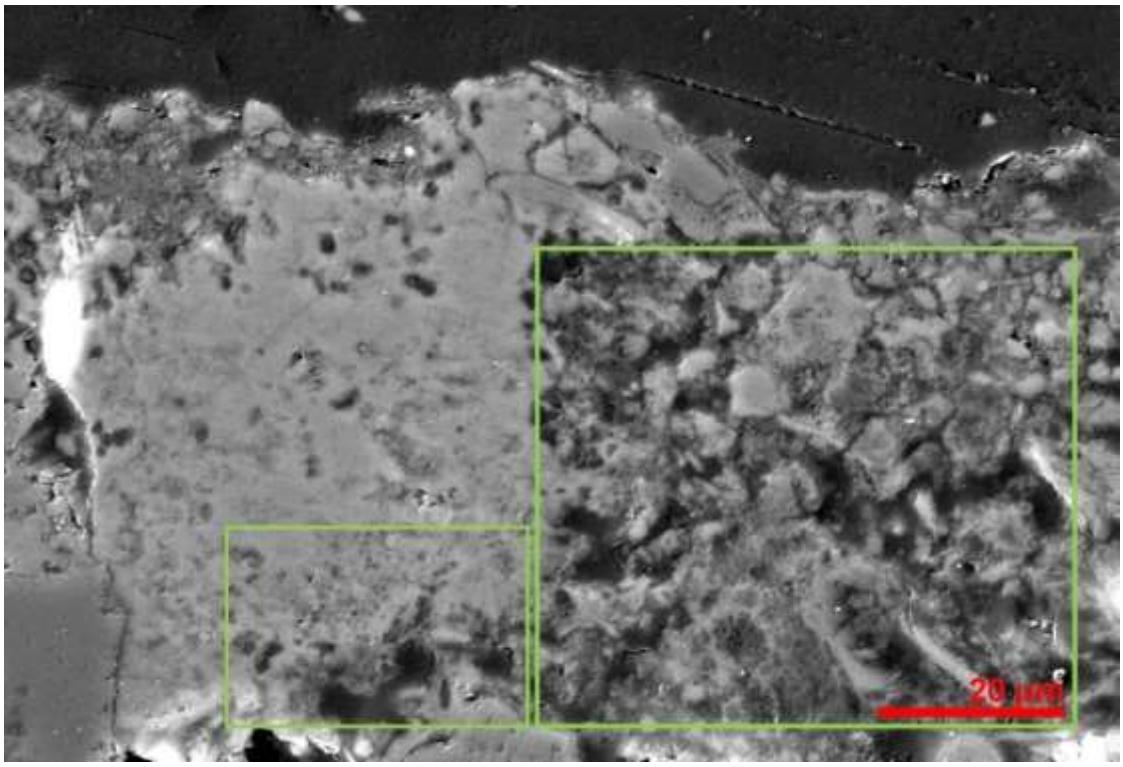

Figure 163: SE image of S2 cross-section. The green frames indicate areas of honeycomb features resembling collagen.

The cross-section of sample S2 shows a surface of loose and compact areas (fig.163). Honeycomb features (green frames) that appear in the surface layer and the layer below do not seem to be crystalline and of biological origin, but resemble collagen (Vranceanu et al., 2012, 7). The honeycomb layer differs from the mortar dense layer of calcite.

Sample S3 – Cistern floor

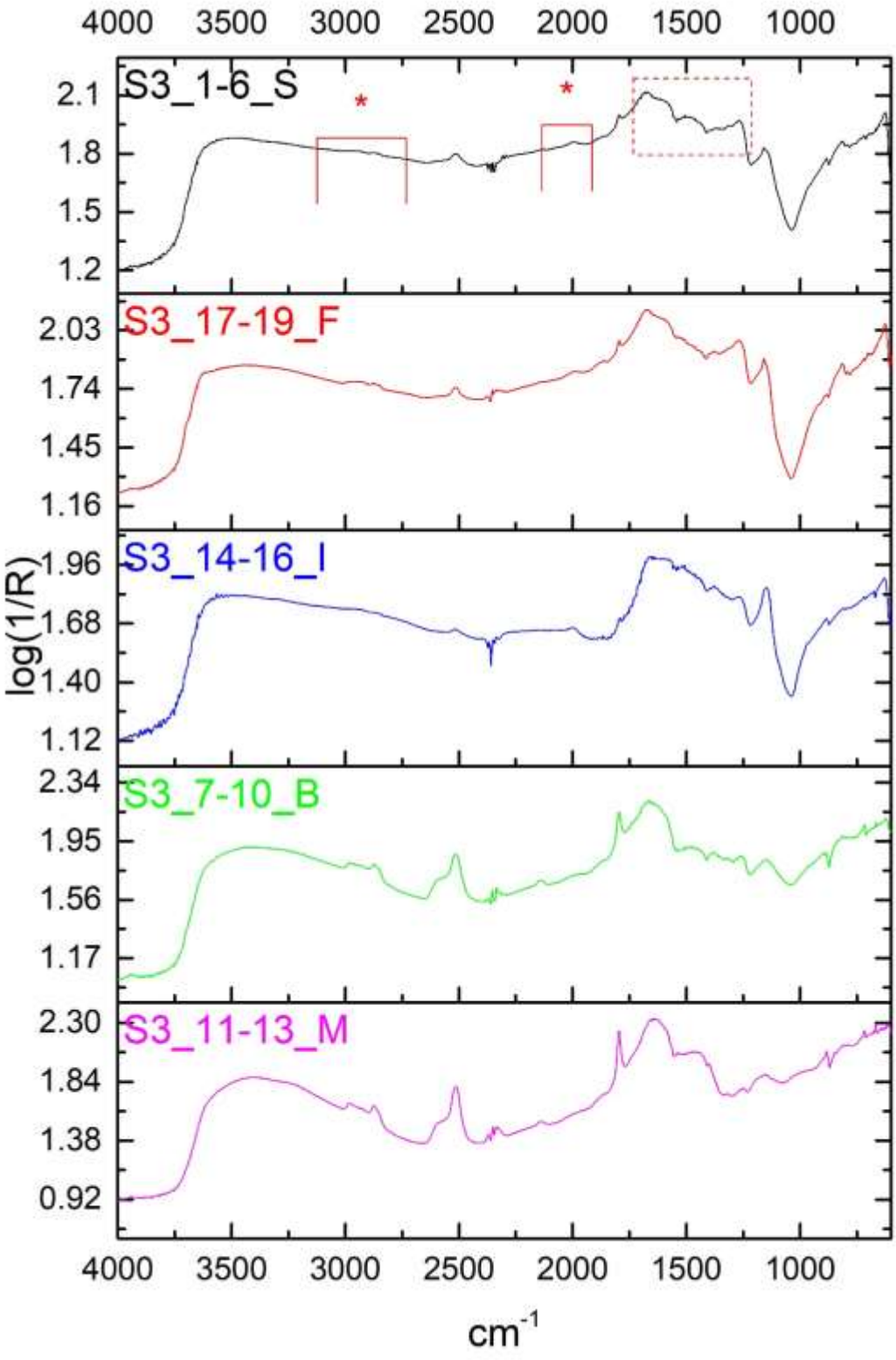

Figure 164: stacked spectra of individual layers of sample S3. Marked areas indicate organic presence on the surface spectrum.

The S3 surface spectrum (S3_1-6_S) is a straight comparison to S2 surface spectra, probably because they derive from the same sampling area (fig.164; Appendix III, fig.23). Inorganic presence is very low. Regions of interest in respect to organic content are the 1267-1704, 2077, 2732-2801 and 2885-3021 cm^{-1}.

This is the first spectrum that shows a clear C=O peak at 1704 cm^{-1} of amide I (Ploeger et al., 2010, 37). The presence of phosphates is evident at 1559 due to the characteristic shape (apart from the expected quartz). C-O at 1267 cm^{-1} is present in bone glue and bone glue/mortar standards and also in calcium oxalates (Monico et al., 2013, 273). Since there are not any other chemical evidence of oxalates, the peak is attributed to protein. The peak at 2077 and 2801 cm^{-1} is related to CH_2 and CH_3 stretching of lipids or proteins (Rosi et al., 2009, 2099).

The inverted surface spectrum (S3_14-16_I) is almost free from $CaCO_3$ peaks (fig.164; Appendix III, fig.24). The 1146 cm^{-1} reststrahlen resembles that of phosphates and cannot belong to quartz (Ricci et al., 2006, 1223). Similar peak was found on the S2 inverted surface spectrum. Although the spectrum is noisy, the overall fingerprint pattern shows amide stair-step type intensities. Amide peaks are detected in 1577 and 1668 cm^{-1} (Miliani et al., 2012, 304; Rosi et al., 2009, 2104). CO bond at 1270 cm^{-1} represents mainly protein with close similarity to that of egg standards. 1376 cm^{-1} shows C-H bending of lipids (Buti et al., 2013, 2705). The C=O bands at 1770-1779 cm^{-1} are also seen in EW_M_75 (Lombardi and Santarelli, 2009, 542). The sample shows protein content. The spectrum pattern is closely related to that of the sheep bone standard (Appendix III, fig.25).

The egg related protein is reduced towards the mortar (fig.164). Organic presence is still evident in the layer below the surface (B) mainly at 1339-1395, 1660-1679 and 2936 cm^{-1}. The mortar layer shares some peaks with the surface layer in the 1400-1535 cm^{-1} which should be mainly attributed to inorganic mortar components.

Figure 165: S3 surface layer. Resinous layer visible beneath grey soil.

S3 is the best sample to describe the surface morphology of the cistern floor mortar. Although a grey thick layer of soil is present, the brown resinous substance is visible and seems to cover the entire surface of the mortar layer (fig.165).

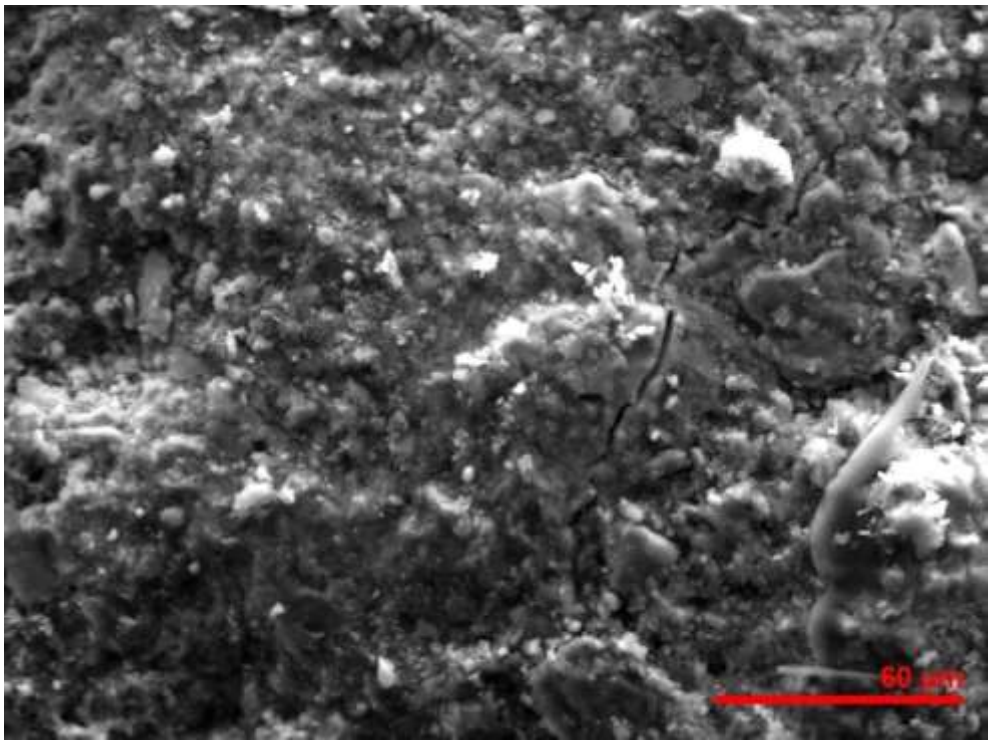

Figure 166: SE image of S3 surface with dense, smooth but cracked texture.

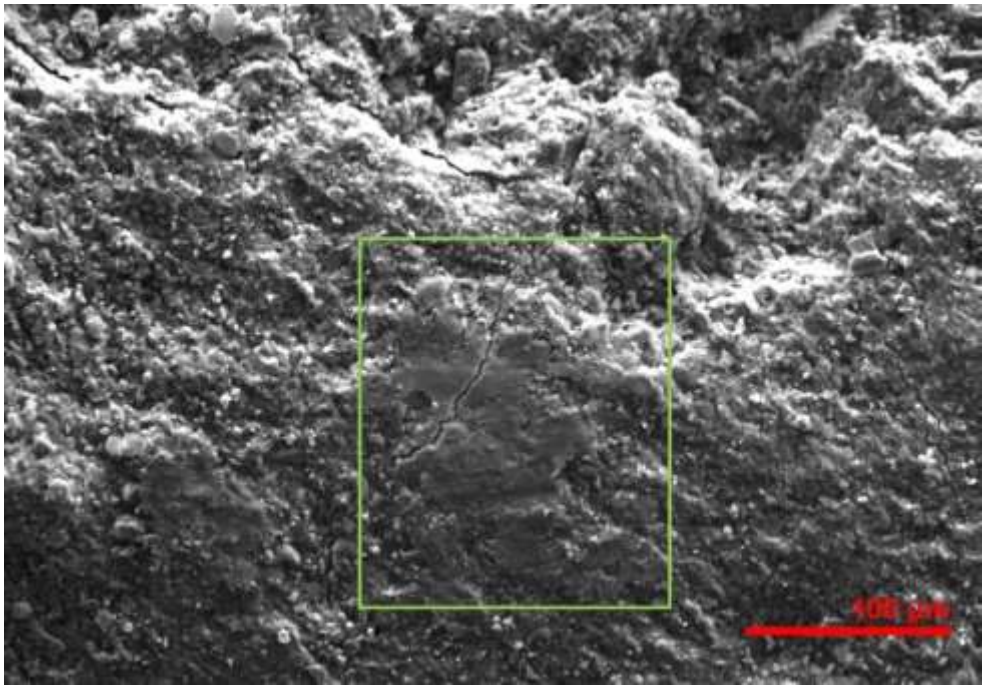

Figure 167: SE image of S3 surface with brush-stroke marks (green frame).

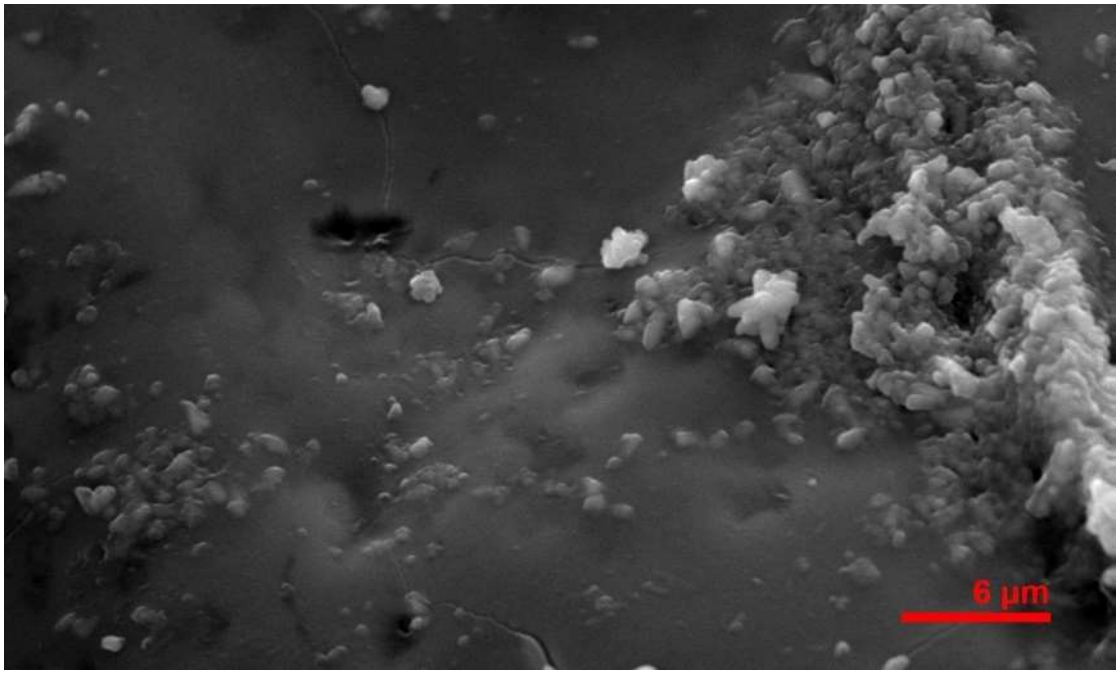

Figure 168: SE image of E_M_25 (25% egg in mortar) standard.

The surface appears smooth and dense showing cracks locally (fig.166). An interesting feature is the marks resembling brush-strokes on what it appears to be the remains of a substance above the mortar (fig.167). Similar texture is observed on E_M_25 standard (fig.168). The surface of sample S3 is free from biological activity.

Cistern Floor – Results Summary

Samples S1, S2 and S3 derived from the cistern floor and were obtained shortly after its excavation. All three samples contain organic substance not related to biological activity. The fibres observed on the surface of S1 are considered as random depositions and not biological infestation since no further evidence supports that.

All samples preserve a homogenous and resinous surface layer that differs from the mortar layer or the deposited soil particles. Protein-lipid-phosphate content similar to that of egg white/mortar standards is visible on the surface spectra. Similarities with bone glue, bone glue/mortar and sheep bone standards support the presence of protein and phosphates but do not explain the lipid content. The organic presence reduces gradually towards the inorganic mortar layer. This shows that the organic substance derives from the surface layer. Although egg white should only contain protein, the presence of lipids cannot be excluded since they could have been retained during its separation from the egg yolk.

Sample S4 - Mortar on Stone related to the cistern wall

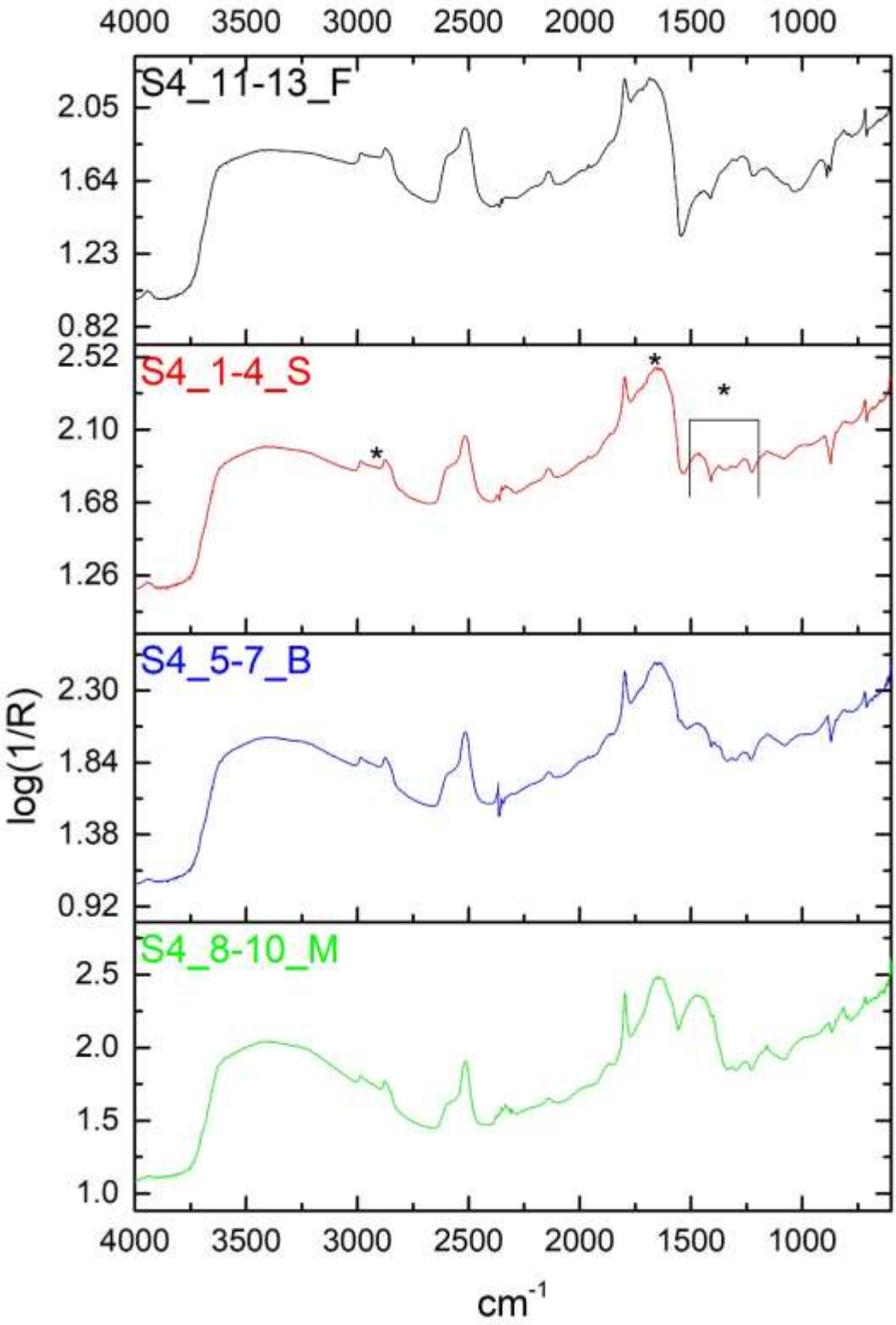

Figure 169: Sample S4: stacked spectra of individual layers. Marked area and asterisks indicate organic presence on the surface spectrum.

Mortar peaks are pronounced on the surface spectrum (fig.169; Appendix III, fig.26). The combined presence of peaks and their shape at 1006-977, 900, 848, 812 and 794 cm^{-1} show the presence of dolomite (CPAD comparison with dolomite standard, Appendix III, fig.27; Miliani et al., 2012).

It seems that if any organic is present, its concentration is low and the absence of strong indicators of amides is evident from the lack of 1539 and 1680 cm^{-1} peaks. The intensities 1466-1264 cm^{-1} should indicate amides. The 1634 amide peak is also visible in egg yolk/ mortar standard. The 1652 cm^{-1} is similar to bone glue and milk/mortar standards. The peak at 1723 cm^{-1} is C=O of protein or lipid. Lipid C-H stretching is also visible in 2924 cm^{-1} (Miliani et al., 2007, 853). The peak at 1961 cm^{-1} belongs to dolomite, not quartz, based on the CPAD comparison to dolomite standard.

Although mortar content is high in the flat surface spectrum (S4_11-13_F), amide (and some lipid) cannot be ruled out (fig.169; Appendix III, fig.28). This is because the peaks 914, 1070, 1161-1177 cm^{-1} (phosphates) in combinations with the strangely shaped peaks at 1265-1459, 1667-1683-1727 cm^{-1} and 2930-2941 cm^{-1} show organic presence. The small peak at 788 cm^{-1} is organic, found also in bone glue standard. The 788-812 cm^{-1} are also visible in egg yolk and E_M_25 standards. The 914 cm^{-1} shows Dolomite although the shape differs. 1070 cm^{-1} indicates phosphates (Ricci et al., 2006,1223). Egg and egg white standards show peaks at 1161-1177 cm^{-1}.

The surface layer (S) is the one that incorporates amide-lipid material in its composition. The spectrum below the surface (B) retains some organic and phosphate peaks at 2924, 1659-1506 and 969-1007 cm^{-1} (fig.169). The region 1264-1477 cm^{-1} is highly masked by mortar components.

Sample S4 was not covered by soil. Thus, it was expected that whatever substance is on the surface it was adhered as a layer. This layer may have derived from external depositions or it could be the residue of an original coating. The spectral similarities at the fingerprint region with those at the S1-S3 spectra, which derive from freshly excavated samples, show that the surface layer of S4 derives from the composition of the sample not from external depositions. The weakness of the organic content on the exposed mortar sample demonstrates this as the presence of any organic on the surface is reduced due to exposure and likely altered by it.

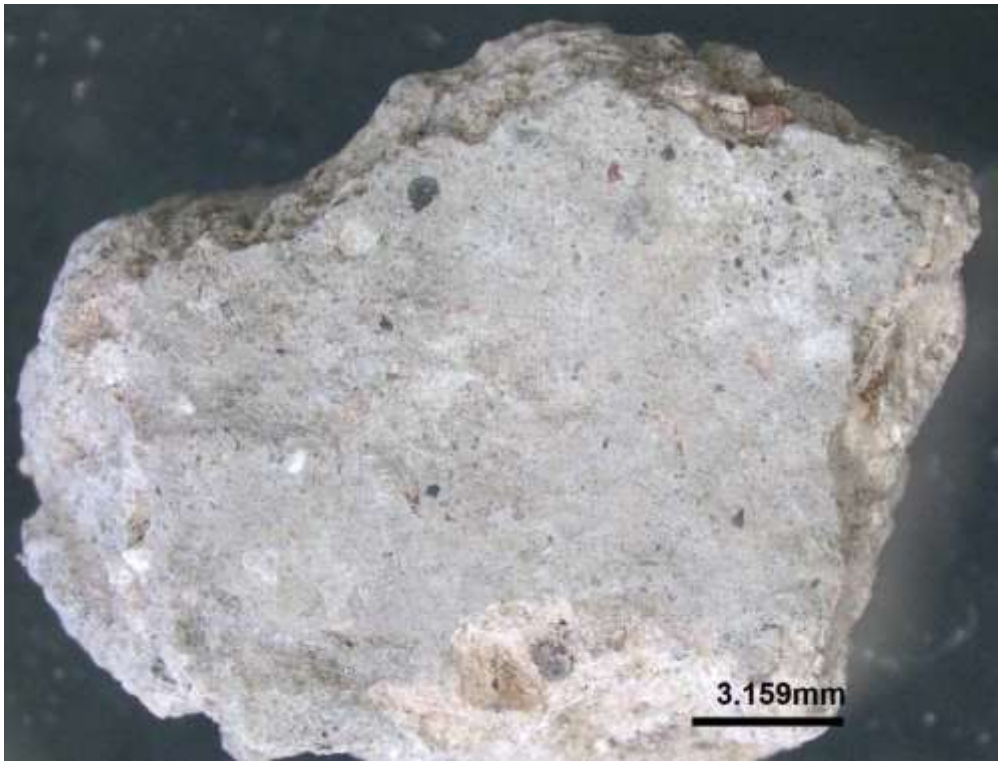

Figure 170: The surface of S4 appears grey and dense.

Figure 171: Cross-section of S4 showing a thick light brown to grey surface layer.

The surface appears grey but this layer cannot be confused with soil (fig.170) as, if it was soil, then it should also cover the exposed mortar layer. The cross-section shows that the surface layer is thick and light brown to grey (fig.171). The colour is lighter than that observed on sample S3, probably due to exposure.

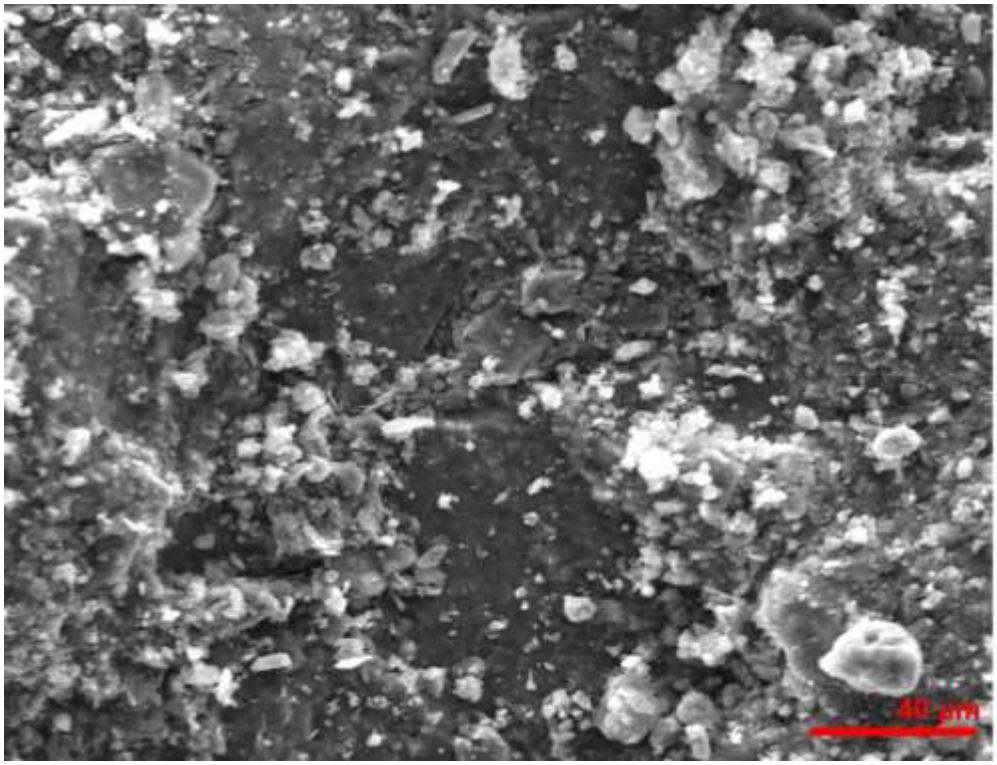

Figure 172: SE image of S4 showing a smooth flat surface under loose particles.

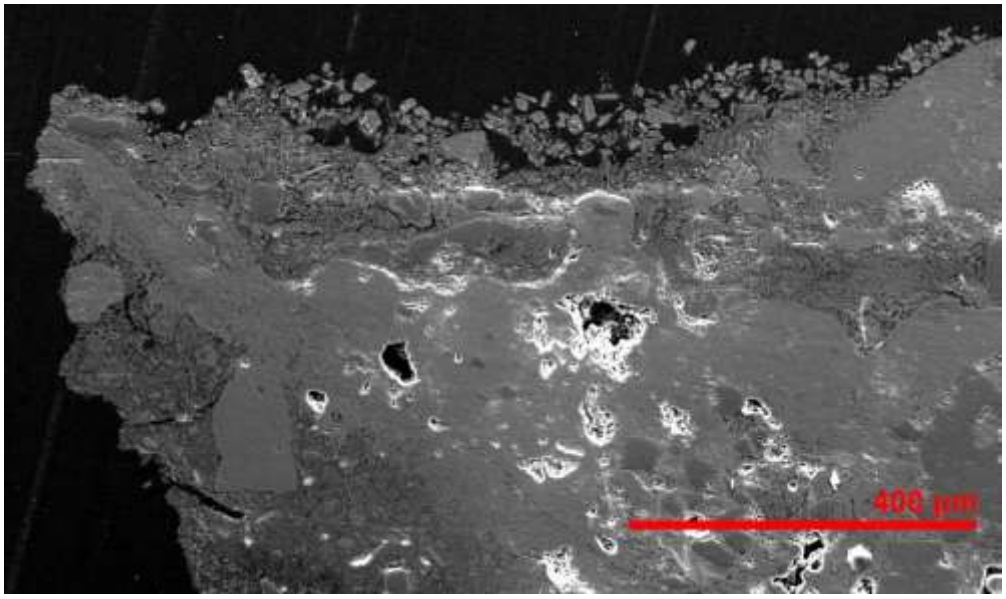

Figure 173: SE image of S4 cross-section. The surface layer appears less coherent than the mortar layer below.

A smooth surface layer appears below loose particles, some of them cubic (fig.172). There is no indication of biological activity. The SE image of the cross-section shows that the surface layer differs from that of the inner calcite and it is not compact (fig.173). The surface aggregates appear similar to those in the mortar (fig.173 - lower left side).

Sample S5 – Mortar on Stone related to the cistern wall

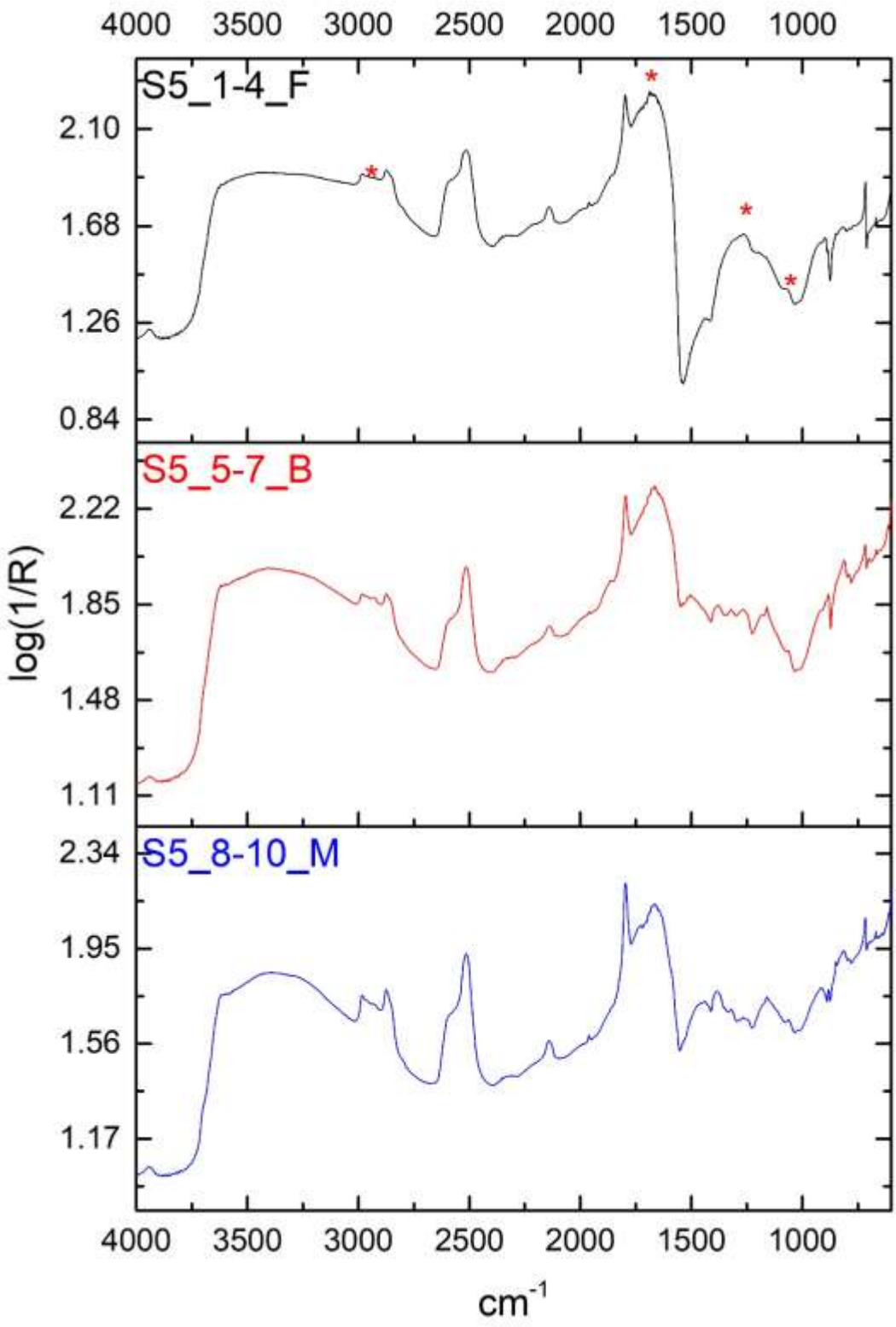

Figure 174: Sample S5: stacked spectra of individual layers. Asterisks indicate organic presence on the flat surface spectrum.

The S5 flat surface spectrum (S5_1-4_F) is almost identical to that of S4, relative to the high inorganic content and Dolomite dominance within the region 1727-1265 cm^{-1} and at the shape of *v1+v2* CO_3^{-2} combination band at 2514 cm^{-1} (Miliani et al., 2012, 300) (fig.174; Appendix III, fig.29).

However, more organic peaks are detected in S5 than in sample S4, likely because the surface of S5 was cleaned with spring water that removed surface deposits. The region 1679-1738 cm^{-1} shows N-H and C=O stretching of lipids (Ricci et al., 2006,1223). The 1280 cm^{-1} peak belongs to CO organic-related material (Monico et al., 2013, 273). Lipids are also visible at 2901-3011 cm^{-1} (Miliani et al., 2007, 853). Phosphoprotein at 1077 cm^{-1} weak absorption with some lipid content could be present. The organic presence is retained in all subsequent layers but reduces gradually towards the mortar (fig.174).

Figure 175: The surface of S5 appears grey and coherent.

Figure 176: The cross-section of S5 showing a thin grey surface layer.

A thin coherent grey layer is observed on the surface of S5 (fig.175). This layer is also visible in the cross-section, similar to that of S4 but thinner (fig.176). The thickness of the layer is reduced likely because of the removal of surface deposits during cleaning.

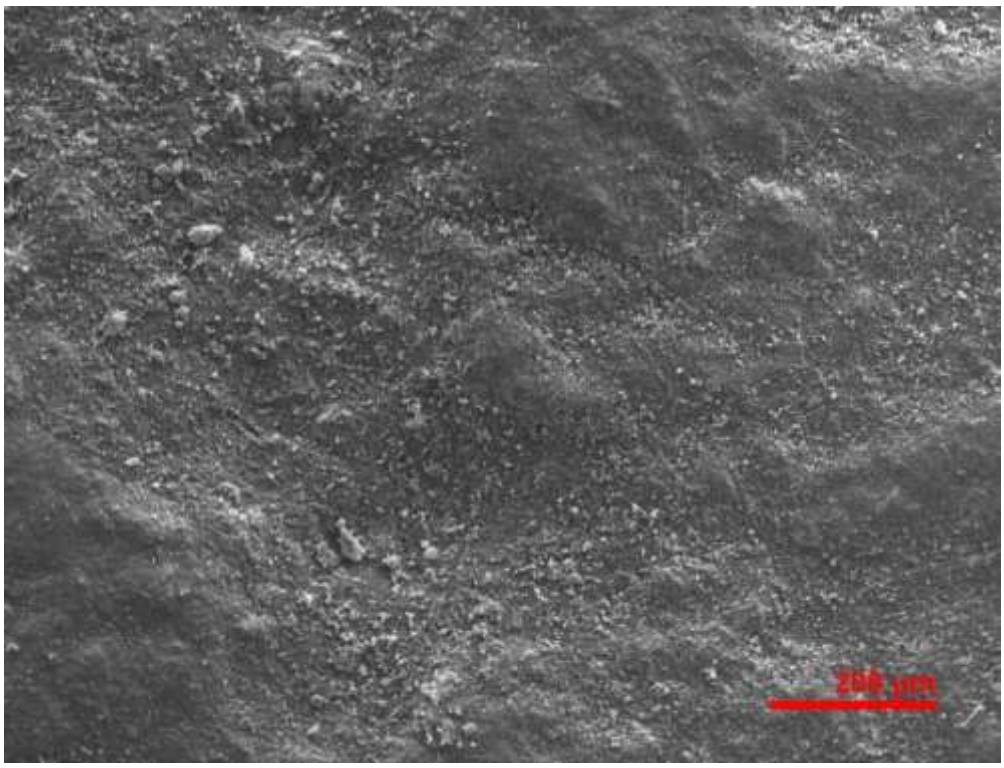

Figure 177: SE image of the surface of S5 showing similarities with the surface of mortar standard and absence of biological activity or organic additive presence.

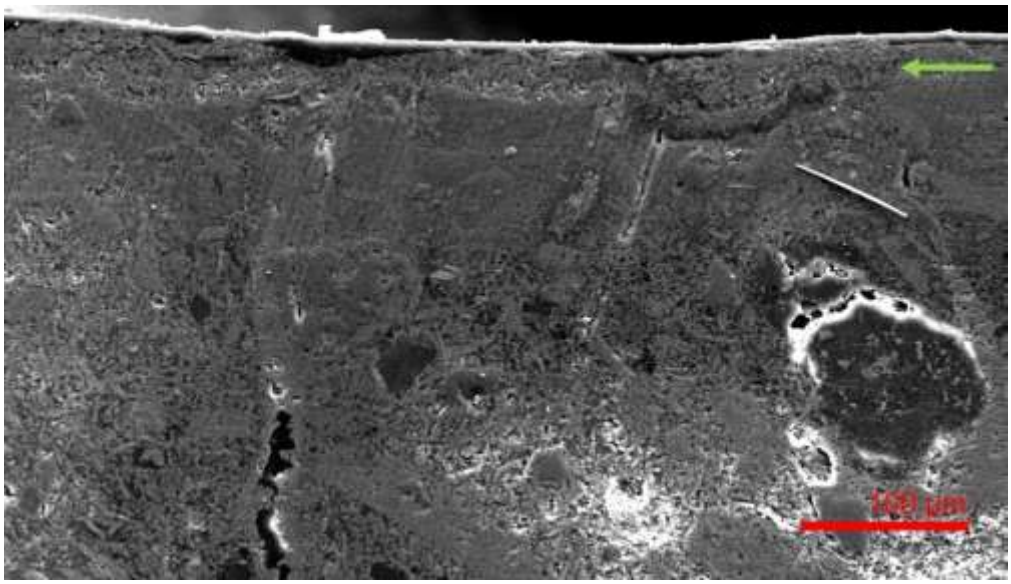

Figure 178: SE image of the cross-section of S5 showing the thin and compact surface layer (green arrow).

The surface resembles that of the mortar standard (fig.177). There is no indication of biological activity or organic presence similar to that observed on the S1 to S4 samples. The thin and compact surface layer is also visible in the cross section (fig.178, green arrow).

Sample S6 – Mortar on Stone related to the cistern wall

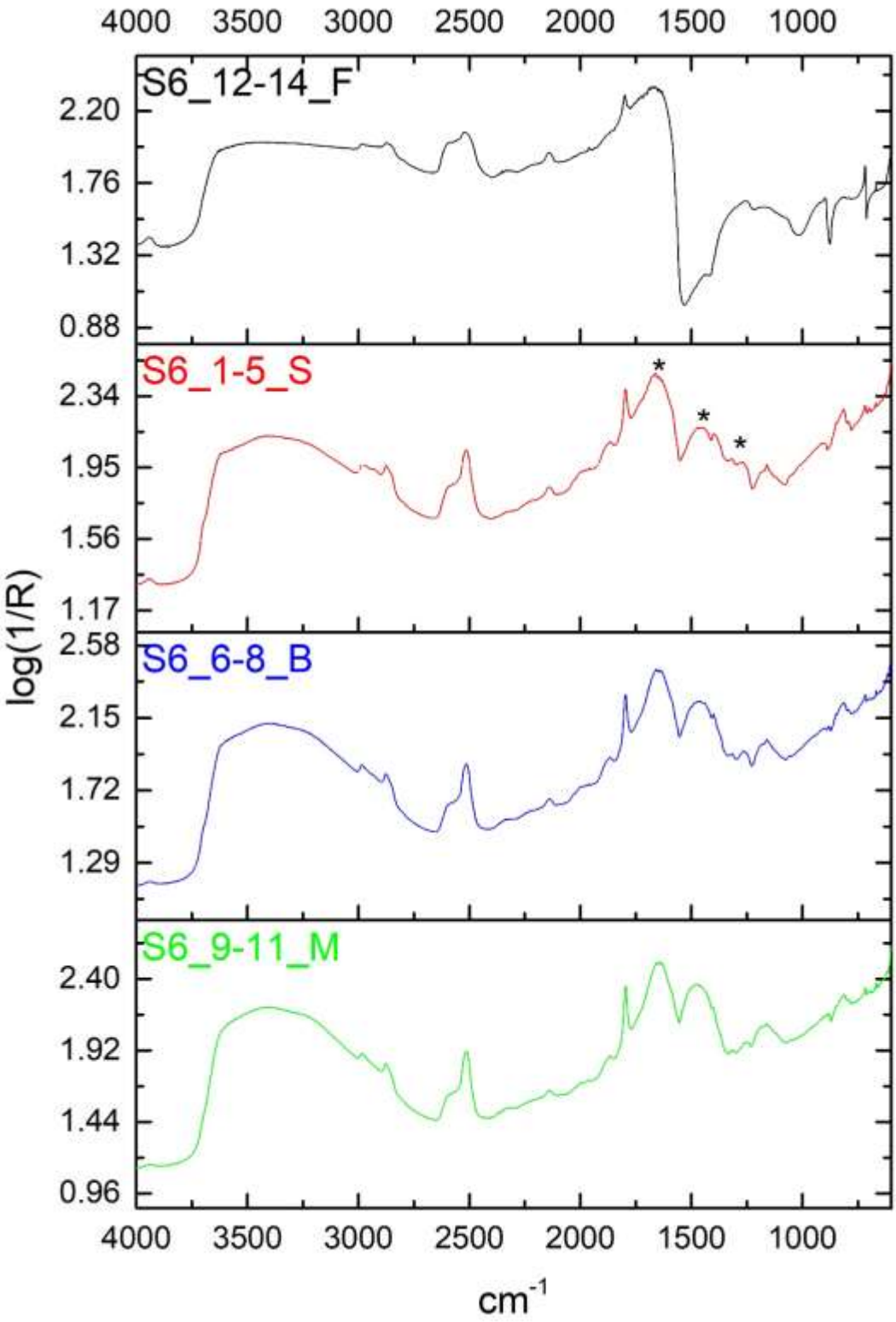

Figure 179: Sample S6: stacked spectra of individual layers. Asterisks indicate organic presence on the surface spectrum.

The presence and shape of the peaks at 901 and 2513 cm^{-1} indicate that calcite is more pronounced in the surface spectrum of sample S6 (S6_1-5_S) than dolomite (fig.179, Appendix III, fig.30). The presence of protein-lipids, similar to egg white standard are detected at 1268-1281, 1317, 1449-1465, 1632-1660 cm^{-1}.

The flat surface spectrum of S6 is highly similar to that of S5, despite the fact that sample S6 was not cleaned with water as S5 (fig.179, F spectrum). This similarity shows that water cleaning did not affect surface composition. Dolomite is present as well as phosphoproteins (and less phospholipids) at 1643-1755 and 2912-3026 cm^{-1}.

The regions 1473-1315 and 1660-1632 cm^{-1} in S, B and M spectra show protein-lipid content that gradually reduces towards the mortar (fig.179). Dolomite and protein peak at 1280 cm^{-1} are visible only at the flat surface (F). The fact that the organic content gradually decreases reinforces the idea that an organic coating is preserved on the surface.

The thin, grey surface layer is identical to that of S5 as expected, since both samples derive from the same sampling area (OM data not shown). The mortar components, calcite, ceramic inclusions and quartz aggregates appear in all samples so far (S1 to S6), likely because they derive from the same water-related construction.

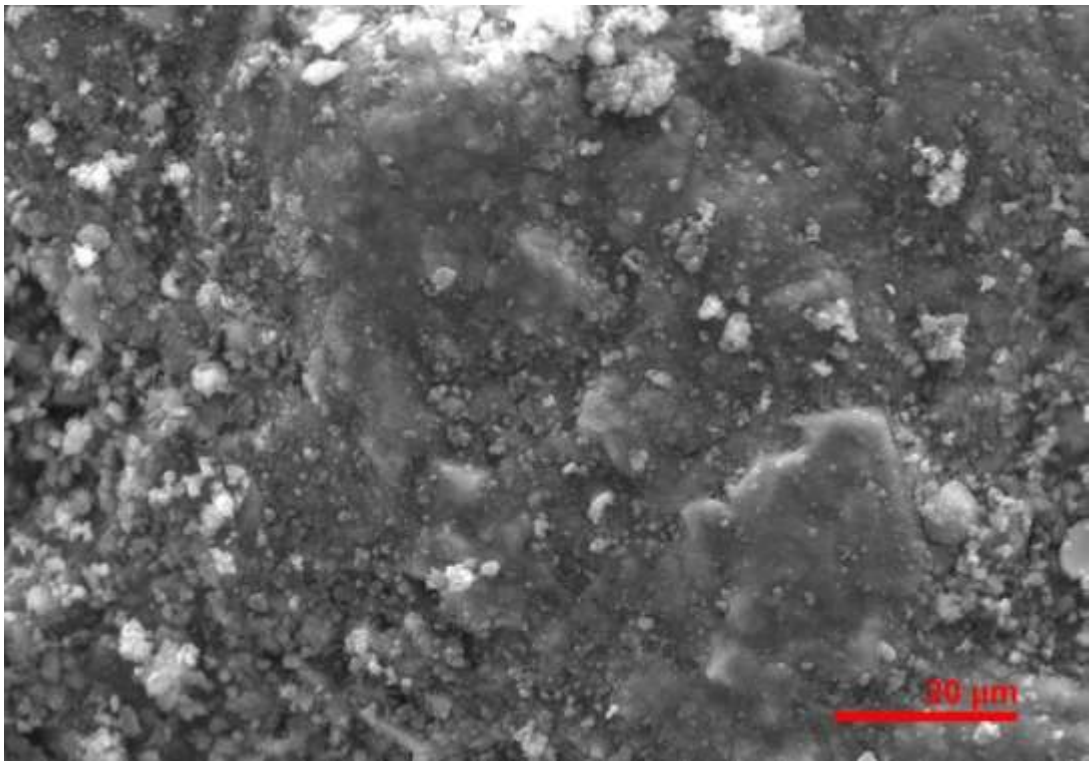

Figure 180: SE image of the surface of S6 showing compact surface layer under loose particles.

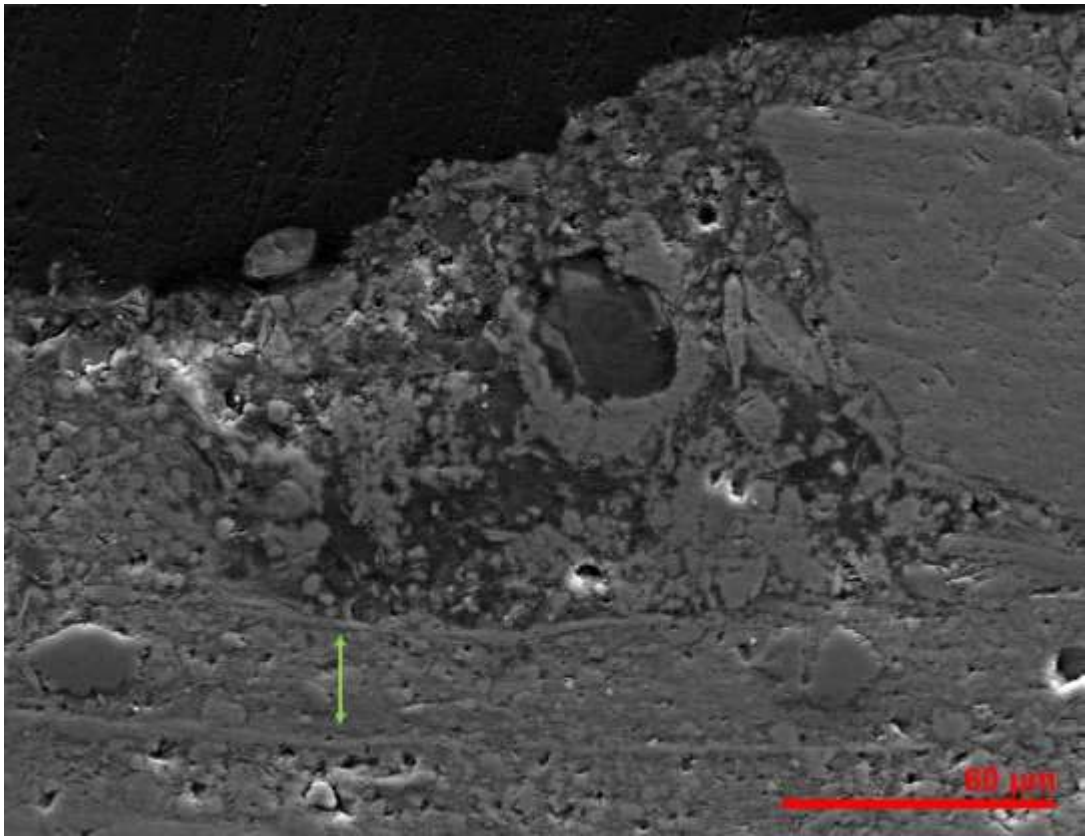

Figure 181: SE image of the cross-section surface layer of S6 showing layering of materials underneath loose surface layers (green arrow).

A compact surface layer is preserved locally under loose particles (fig.180). There is no detectable biological activity. The SE image of the cross-section shows an upper surface layer that is either a deposition or degraded (fig.181). Coherence increases towards the mortar and parallel, horizontal lines could suggest layering of materials (fig.181, green arrow).

Mortar on Stone – Results Summary

Samples S4, S5 and S6 derive from a stone related to the cistern masonry, plastered with mortar. Although the stone was exposed to rural environmental conditions, biological activity was not detected in the reflectance micro-FTIR spectra and OM and SEM images.

The samples are covered by a thin, dense, grey surface layer with amorphous texture, distinct from the mortar. Dolomite is present on the surface layer of the samples, indicating either a dolomitic source of limestone used in the mortar or the use of dolomitic aggregates (Edwards and Farwell, 2008, 986; Blaeuer and Jaegers, 1997, 226).

Protein-lipid-phosphate content is detected and similar to that on the cistern floor samples, although reduced due to exposure. Peak intensities are similar to the ones observed in

egg white/mortar (main) and egg standards. Mortar components are pronounced in all layers. The organic content reduces towards the mortar.

The mortar layer consists of calcite, ceramic inclusions and quartz. The same mortar is observed on the cistern floor, justifying the archaeological evidence that all samples derive from the same construction and used at the same time. However, the presence of dolomite on the surface layer may indicate a differentiation in technology.

Sample S14 - Low Wall between cistern and aqueduct

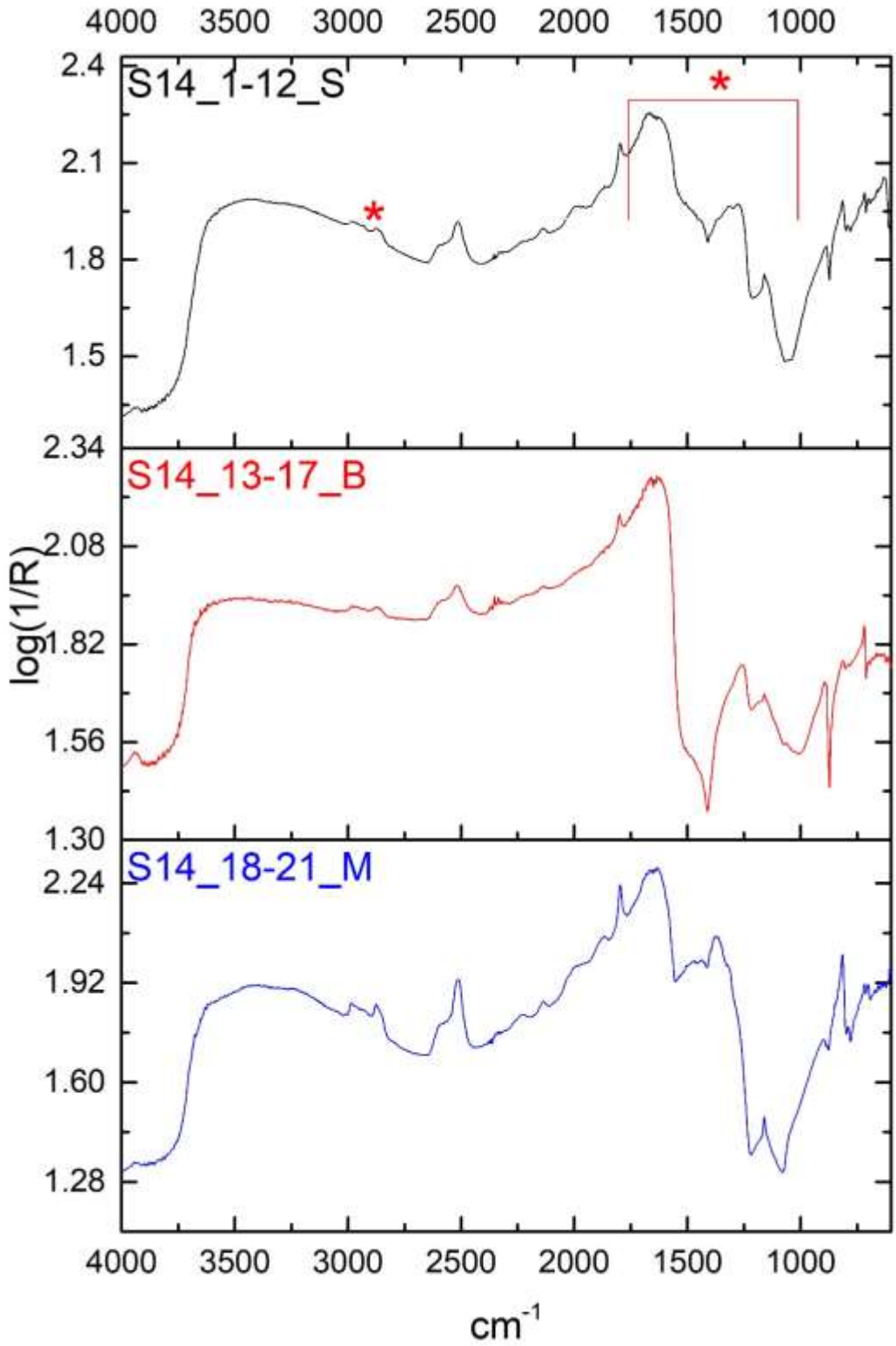

Figure 182: Sample S14: stacked spectra of individual layers. Asterisks indicate organic presence on the surface spectrum.

Twelve spectra were obtained from the surface layer and averaged (S14_1-12_S, fig.182; Appendix III, fig.31). The first two spectra obtained along the surface derive from darker areas than that of the rest 10 spectra. ROIs indicating organic are: 1060-1159 (shape), 1317-1273 (shape and chemistry), 1634-1674, 1774, and 2802, 2900-3005 cm^{-1} (fig.182). Phosphates or sulphates such as those in egg can be seen in 1060 and 1159 cm^{-1} (Mills and White, 1987, 76). Egg and egg yolk standards as well as the S2 surface spectrum share similar shaped peaks at 1273-1317 cm^{-1}, indicating CO of esters or proteins (Synytsya and Novak, 2014, 6). The peaks at 1506-1774 cm^{-1} show C=O that is present in both lipids and proteins (Rosi et al., 2009, 2099). CH stretching and CH_2, CH_3 are visible above 2802 cm^{-1} and should be mainly linked to amide similar to both egg white and bone glue standards. The absence of 1400 cm^{-1} peak differentiates the S14 surface spectrum from those of S4-S6.

Biological activity was not evident since diagnostic peaks of fungal activity, such as the 1064 cm^{-1} strong absorption, are absent (Ortiz-Miranda et al., 2017,7). In the absence of biological activity, the presence of egg is reinforced, despite the fact that both organic types absorb IR in the same regions.

The layer below the surface is highly similar to that of the surface, differing only in the intensity of the reststrahlen at 1694 cm^{-1}. Mortar peaks are weak. All layers show CH_2 and CH_3 around 2930 cm^{-1}. Main mortar peaks at 1578 cm^{-1} are missing. ROIs 1178-1374, 1442-1549, 1622-1645 and 1667-1779 cm^{-1} in all spectra show organic presence. Organic decreases inwards but it is still detected in the mortar (fig.182).

Figure 183: The dark grey flat surface of S14.

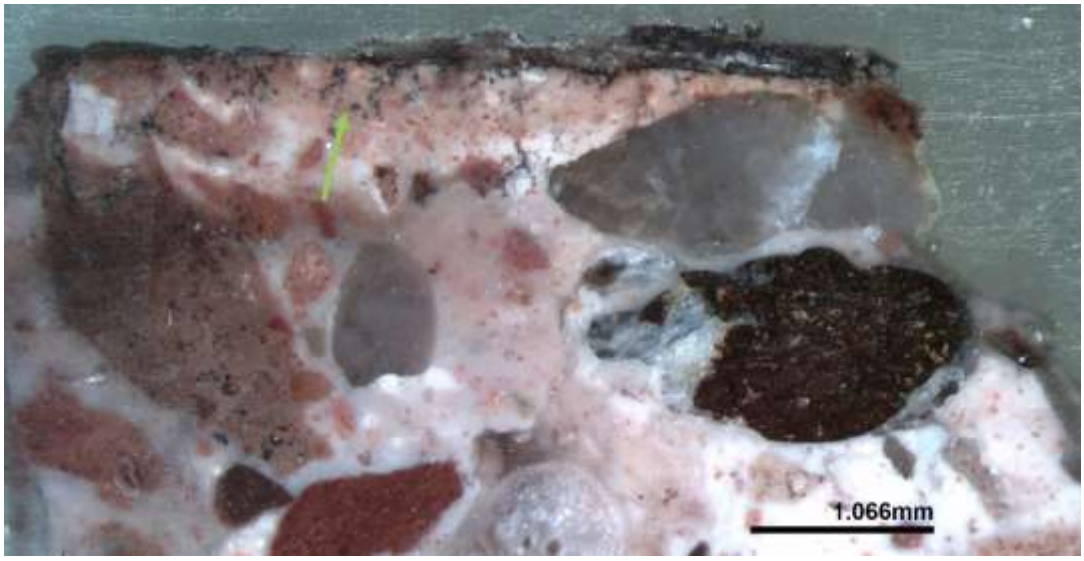

Figure 184: The cross-section of S14, showing black spots on the surface layer moving inwards (green arrow).

This dark grey surface layer resembles that on the mortar on stone samples and not the brown, thick and resinous layer detected on the cistern floor (fig.184). Black spots from the thin surface layer seem to grow or move inwards through fissures (identified by the arrow, fig.184). Large aggregate particles, mainly quartz, are visible in the mortar layer.

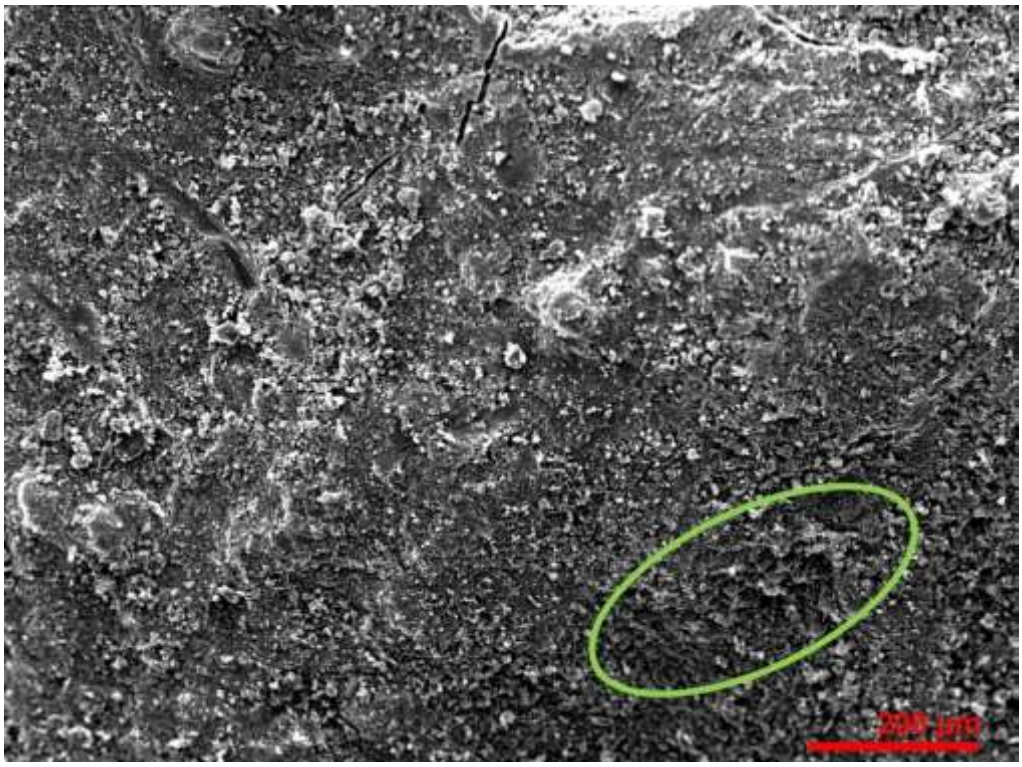

Figure 185: SE image of the surface of S14 showing crystalline patterns likely from accumulation of deposits (circled in green).

Although some amorphous areas are visible under loose particles, there is no visual indication of organic presence or biological activity. The wavy crystalline pattern likely derives from the accumulation of deposits (circled in green, fig.185).

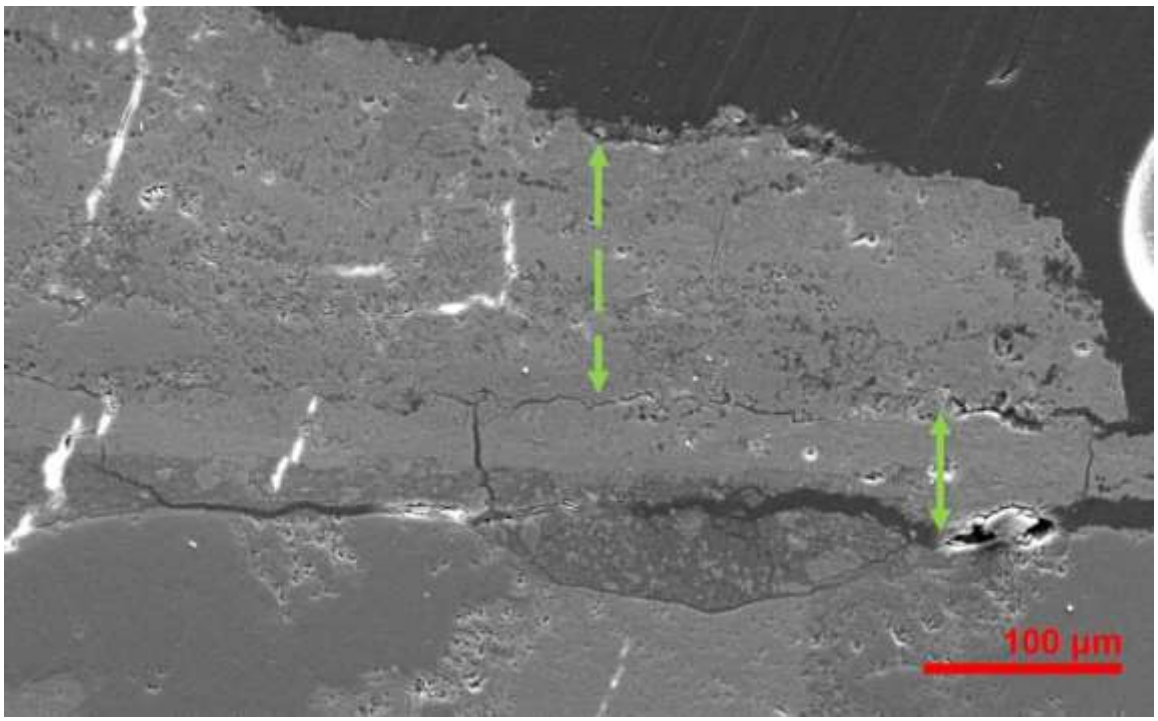

Figure 186: SE image of S14 cross-section surface, green arrows point to the two separate surface layers.

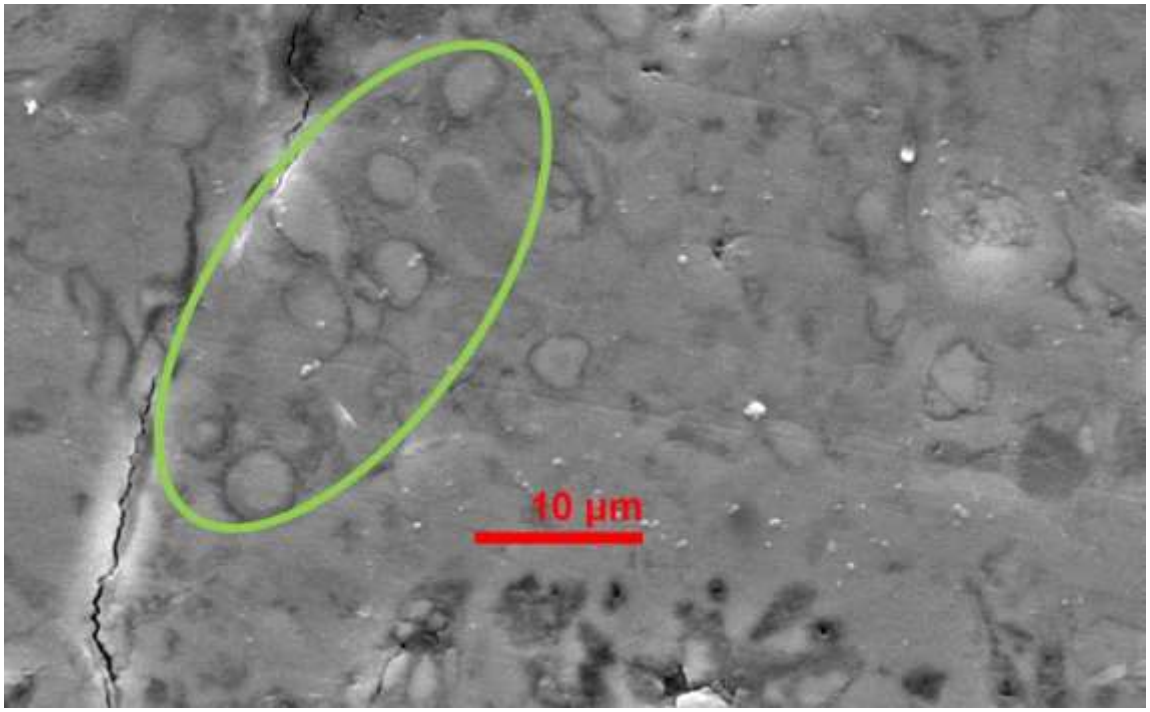

Figure 187: SE image of the black spots, circled in green, on the cross-section surface of S14.

Two surface layers are visible in the cross-section, one thin, just above the mortar and a thick, less dense, above that (fig.186). The round particles in the upper surface layer are unique to this sample (fig.187). It is likely that these particles are responsible for the dark coloration of the surface.

Sample S15a - Low Wall between cistern and aqueduct

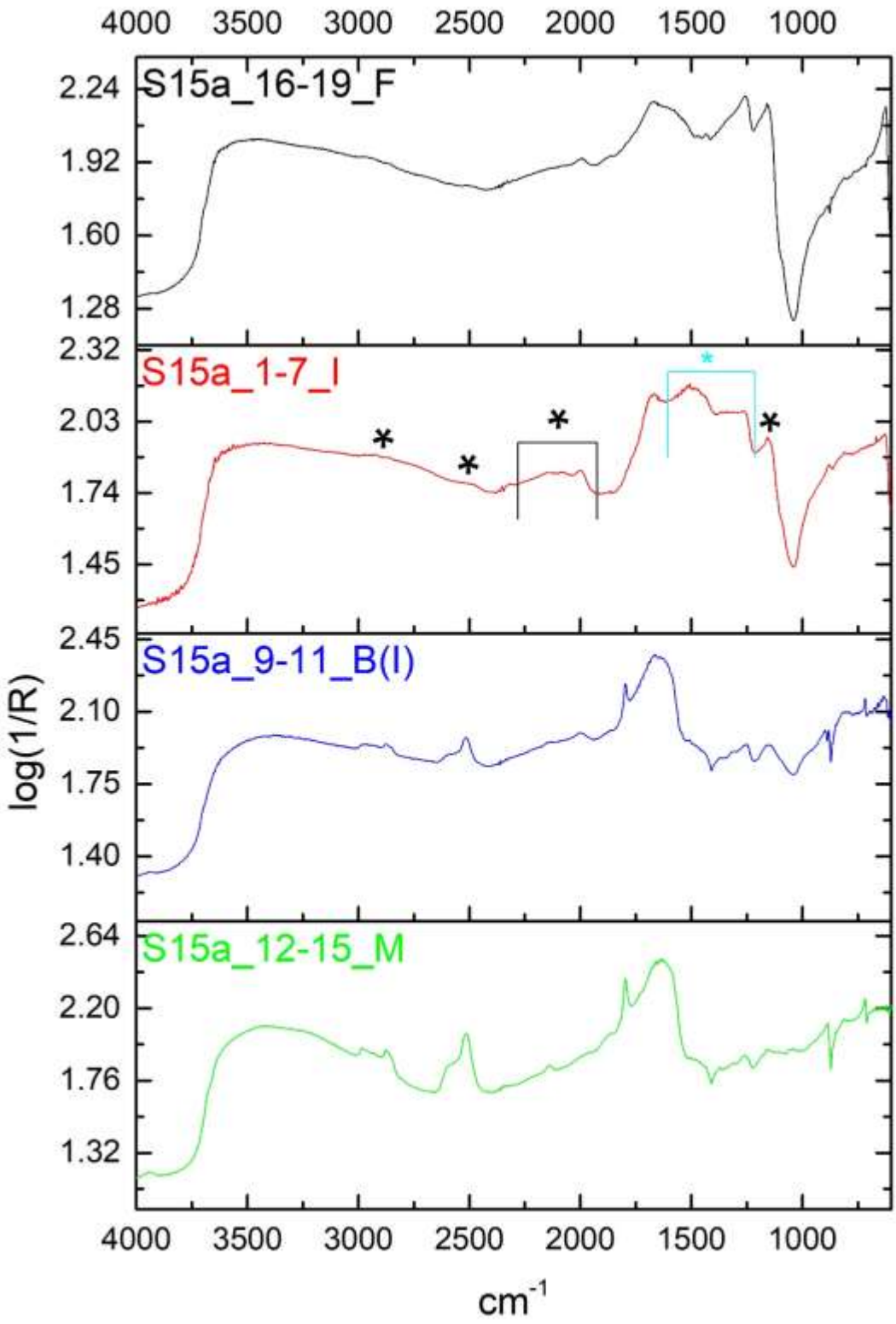

Figure 188: Sample S15a: stacked spectra of individual layers. Black asterisks indicate resemblance to sheep bone standard, cyan asterisk shows the presence of Amide on the inverted surface spectrum.

The inverted surface spectrum (S15a_1-7_I) is highly similar to that of the sheep bone standard in the shape of 1158 (phosphates) and the peaks within the ROIs 1999-2148, 2483-2532 and 2788-2924 cm^{-1} (fig.188, Appendix III, fig.32 and 25). Calcium carbonate is absent, especially at the areas above 2500 cm^{-1}. Amide is present in the ROI 1264-1680 cm^{-1}.

The spectrum is also similar to the S3 inverted surface spectrum (Appendix III, fig.6). The standards of egg white and bone glue and their mortar mixtures have similar peaks at 1264-1295 cm^{-1}. The peak at 1338 cm^{-1} is shared with that on the sheep bone spectrum. Amides are present in 1471-1680 (resemblance mainly to bone glue/mortar mixtures). Lipids are excluded, mainly due to the shape of the peaks and the resemblance to sheep bone. Bone black has a characteristic peak at 2010 which is very close to the detected peak at 1999 cm^{-1} (Miliani et al., 2007, 854).

Peaks showing bone presence are also detected in the spectrum of the flat surface (S15a_16-19_F, fig.188). However, the chemical similarities with pig bone standard prevail those with the standard of sheep bone (Appendix III, fig.33). The spectral resemblance to bone decreases moving towards the mortar, indicating that any bone-related substance derives from the surface. Protein exists in all layers, especially at the layer below the surface at the regions 1262-1521, 1689, 2001-2143 and 2933 cm^{-1}. Mortar layer shows higher presence of calcite but retains protein at the same ROIs (fig.188).

Figure 189: The flat surface of sample S15a showing accumulation of calcium carbonate deposits.

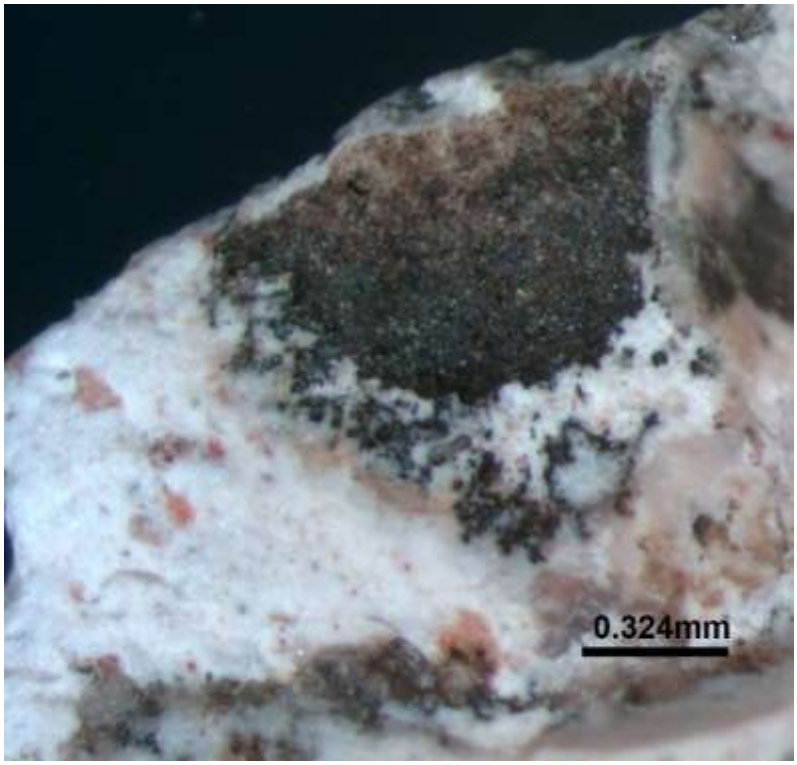

Figure 190: The inverted surface of S15a showing a dense black surface layer.

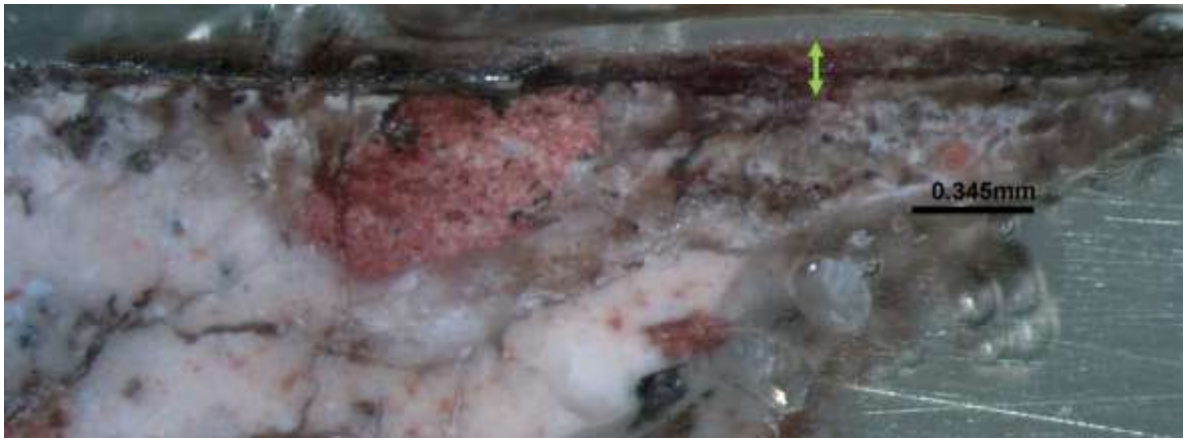

Figure 191: Cross-section of sample S15a showing a dense and thin surface layer (green arrow).

The surface is covered by subsequent layers, probably calcium carbonate deposits such as those visible on the walls of the aqueduct due to the action of water (Bobee et al., 2010) (fig.189). The inverted surface reveals the dense texture of the black layer which is similar to S1- S3 cistern floor samples (fig.190). The surface layer is dense and thin (fig.191, green arrow).

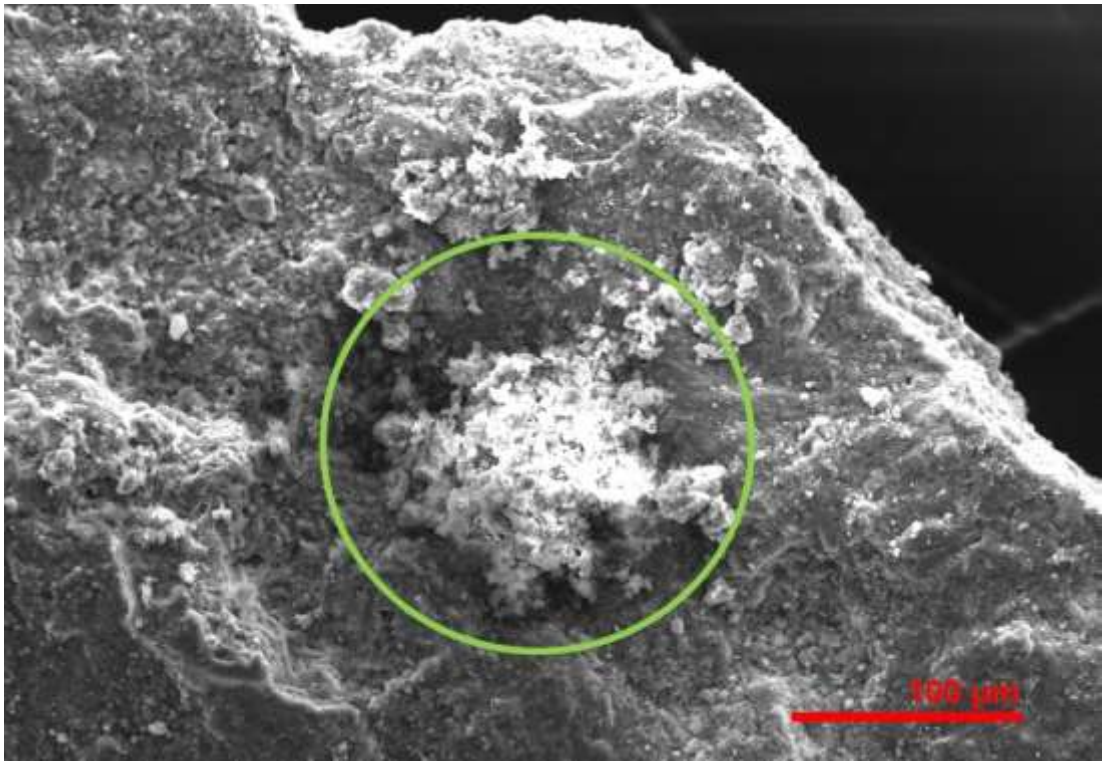

Figure 192: SE image of the flat surface of S15a showing smooth areas and localized crystalline growth (circled in green).

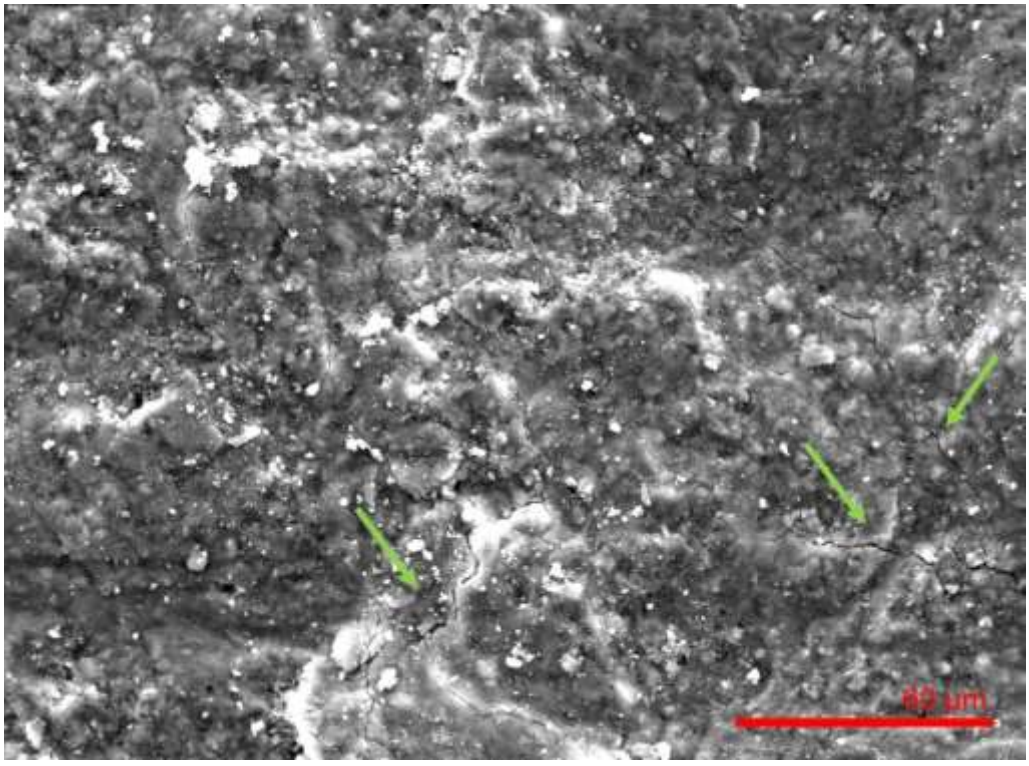

Figure 193: SE image of the homogenous surface of S15a. Arrows point to surface cracks.

A smooth upper layer is locally preserved together with areas of exposed mortar of coarse texture. The crystalline growth in the weathered mortar area could be re-deposition of

calcite due to the action of water (green circled, fig.192). The smooth, homogenous surface layer appears cracked, likely indicating loss of elasticity, incorporating or covering evenly some round particles (green arrows, fig.193). These particles, also present on sample S14, could be responsible for the black coloration of the surface layer.

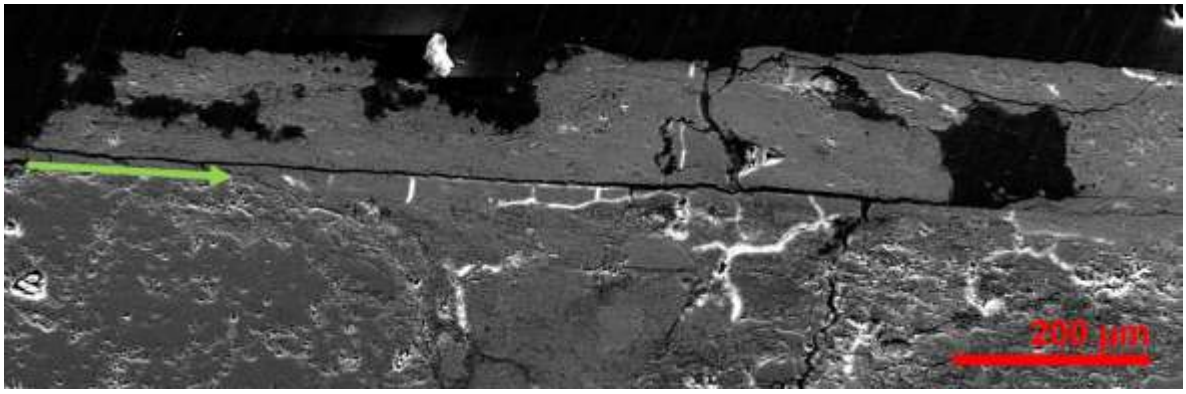

Figure 194: SE image of the cross-section of S15a.A fine smooth surface (green arrow) appears underneath detached layers.

The upper surface layer seems weathered and detached from the mortar (fig.194). Below this upper layer, a fine smooth surface is visible (green arrow). It is likely that both S14 and S15a samples preserve this fine layer underneath deposits or residues of the original layer.

Sample S15b - Low Wall between cistern and aqueduct

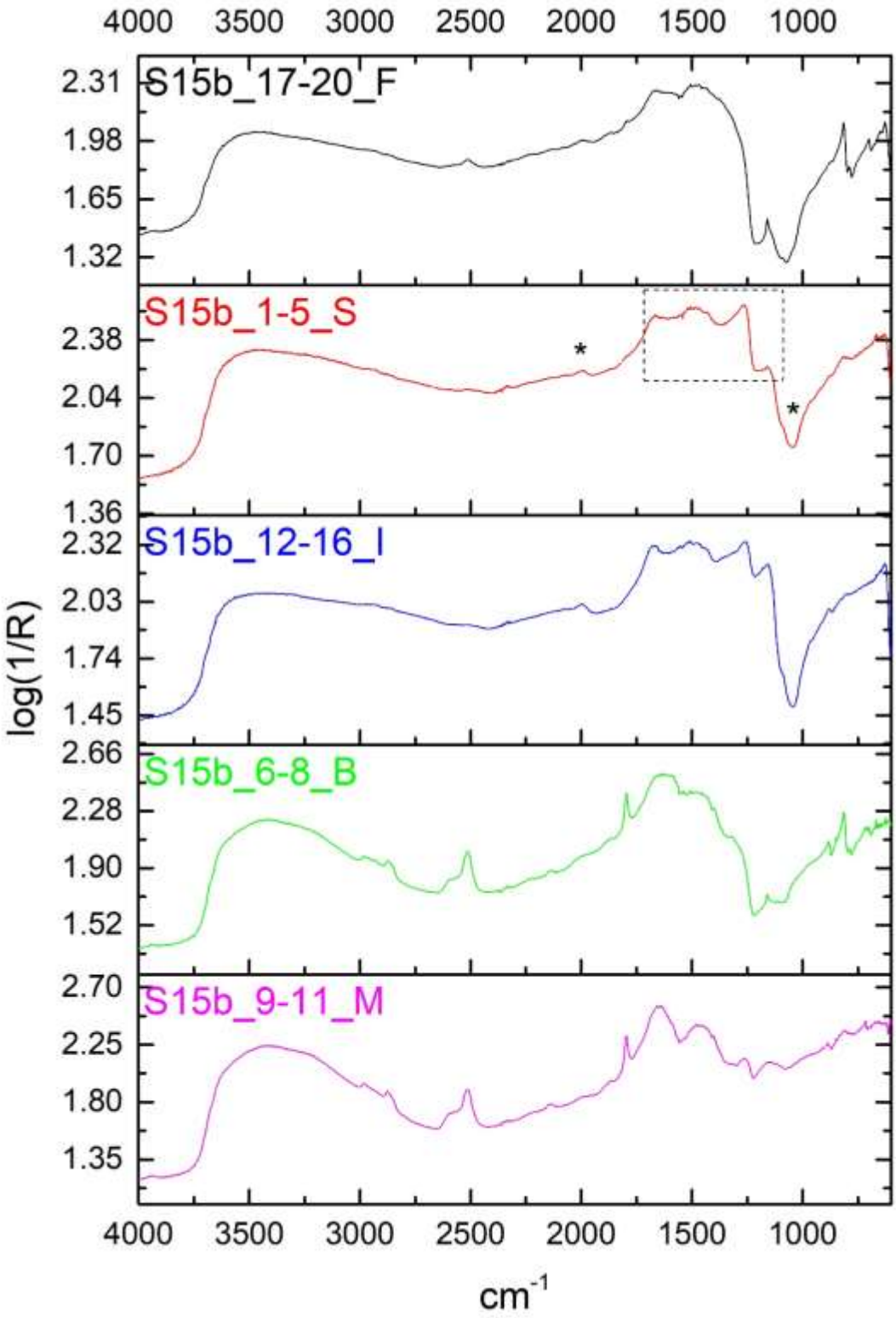

Figure 195: Sample S15b: stacked spectra of individual layers. Black asterisks and dotted frame indicate resemblance to pig bone standard and presence of phosphoproteins in the surface spectrum.

The spectra of S15b appear similar to those of sample S15a (fig.195). A weak peak at 1045 and the peaks at 1178-1665 cm^{-1} in the surface spectrum (S15b_1-5_S) show phosphoproteins. The $CaCO_3$ peaks at 1791 and 2512 cm^{-1} are weak. The peak at 1264 is very strong and is related to C=O of amides. The same stands for the ROI 1349-1665 cm^{-1} which resembles pig bone and, to some degree, bone glue and egg white standards and their mortar mixtures. The peak 1999 cm^{-1} must be the characteristic one of bone black, similarly to S15a, reinforcing the presence of bone in the surface layer (fig.195; Appendix III, fig.34).

Similar observations were made for the inverted surface spectrum (S15b_12-16_I, fig.195): very high resemblance to pig bone standard and high content of protein. Mortar peaks are almost absent. The CPAD comparison with the B and M spectra shows that the bone-related substance exists only on the surface. However, there is evidence of protein in 1320-1678 cm^{-1} (shape and intensity) in both underlying layers. The protein reduces going inwards as the mortar content increases.

Figure 196: The weathered flat surface of S15b.

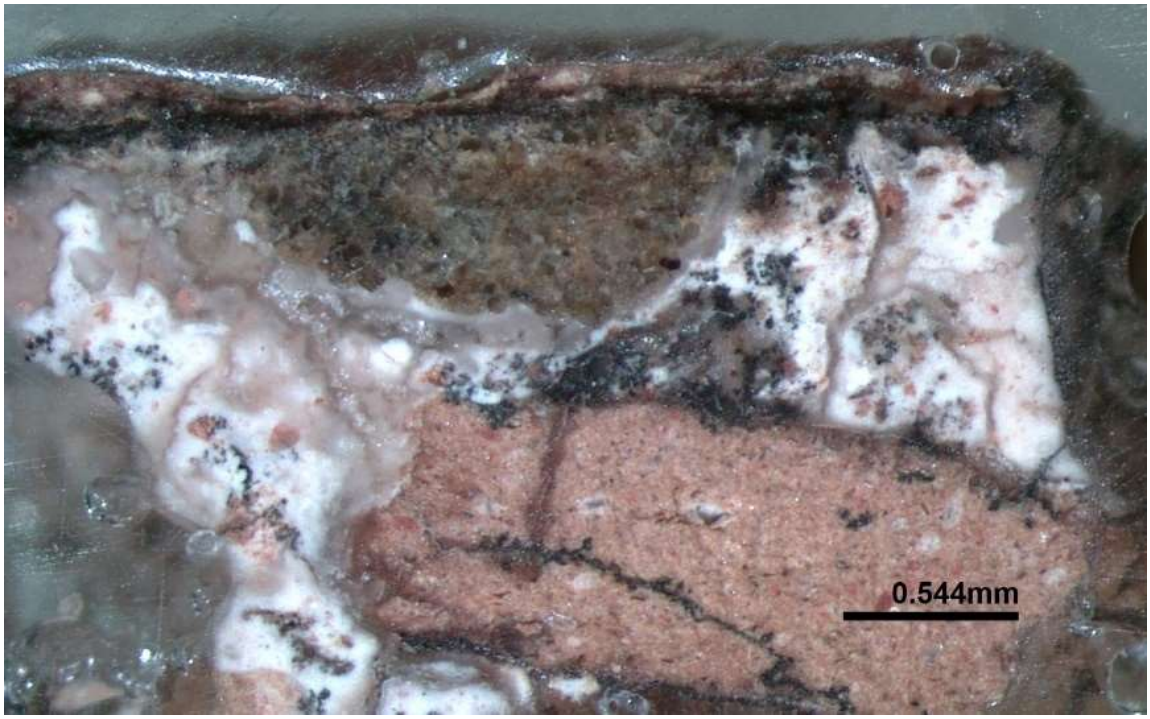

Figure 197: The cross-section of S15b showing black spots within the mortar layer and in the ceramic inclusions.

The surface shows either accumulation of calcite or differential decay of a surface layer (fig.196-197). The black substance is visible locally. The mortar contains large silica aggregates and crushed ceramic. Black spots are also visible within the mortar layer and even in the pores of the ceramic inclusions (fig.197).

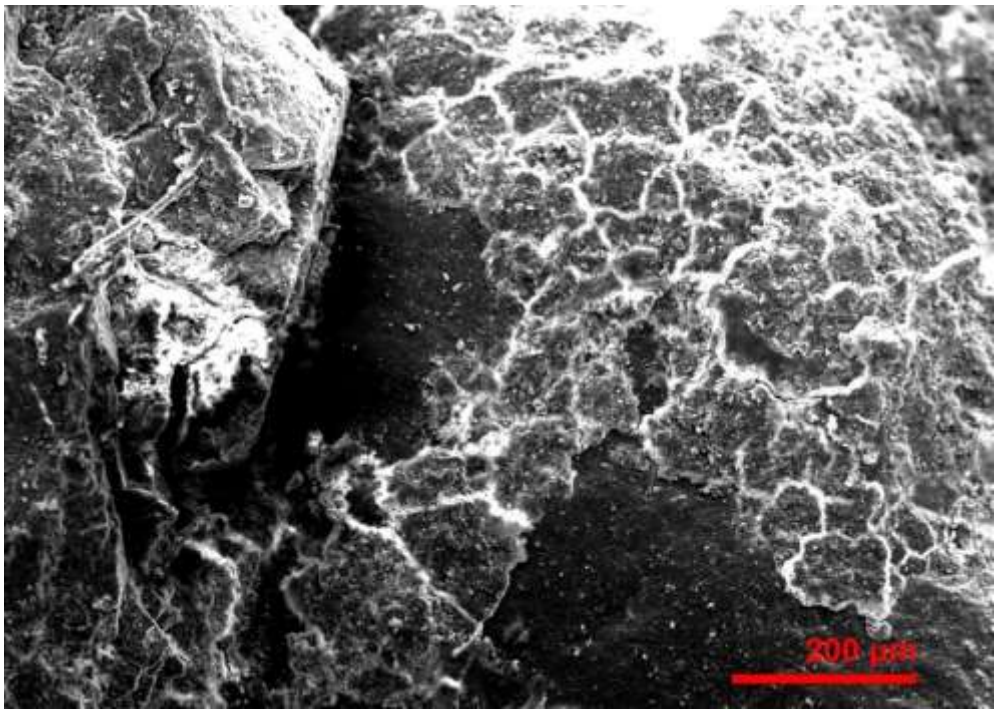

Figure 198: SE image of the surface of S15b showing weathered surface layers.

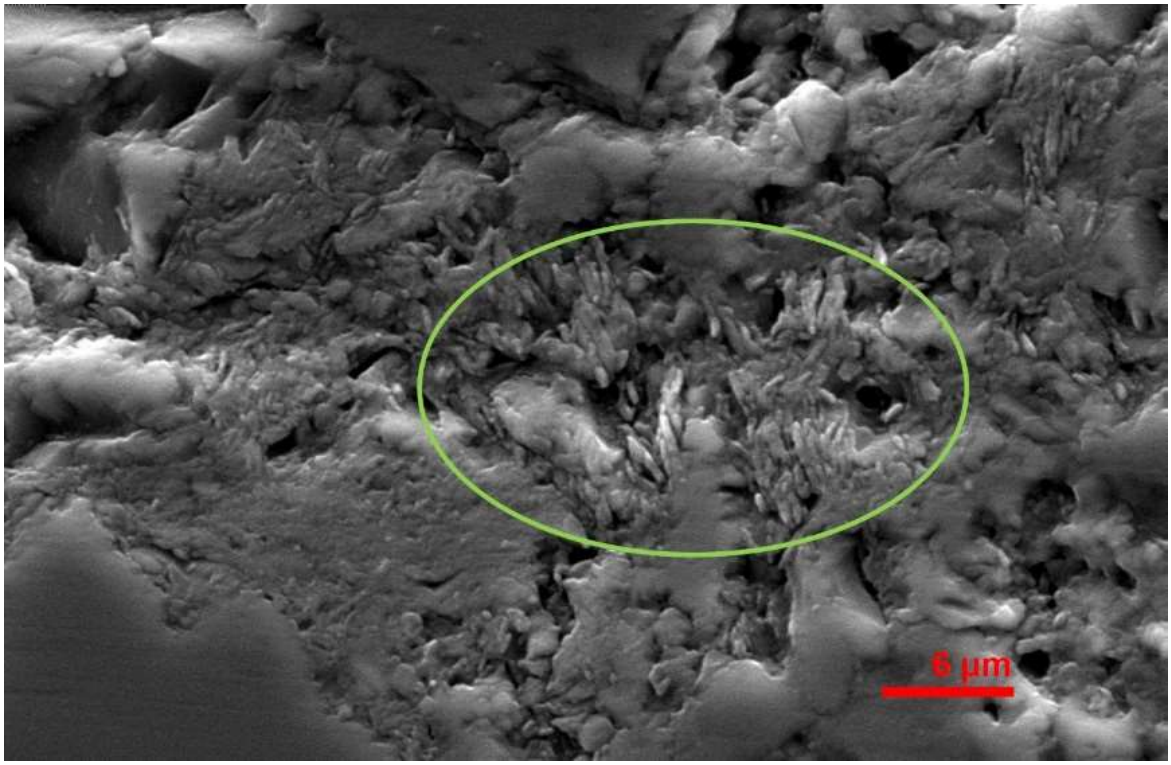

Figure 199: Cross-section of the surface layer containing particles that resemble the texture of big bone standard (green circle).

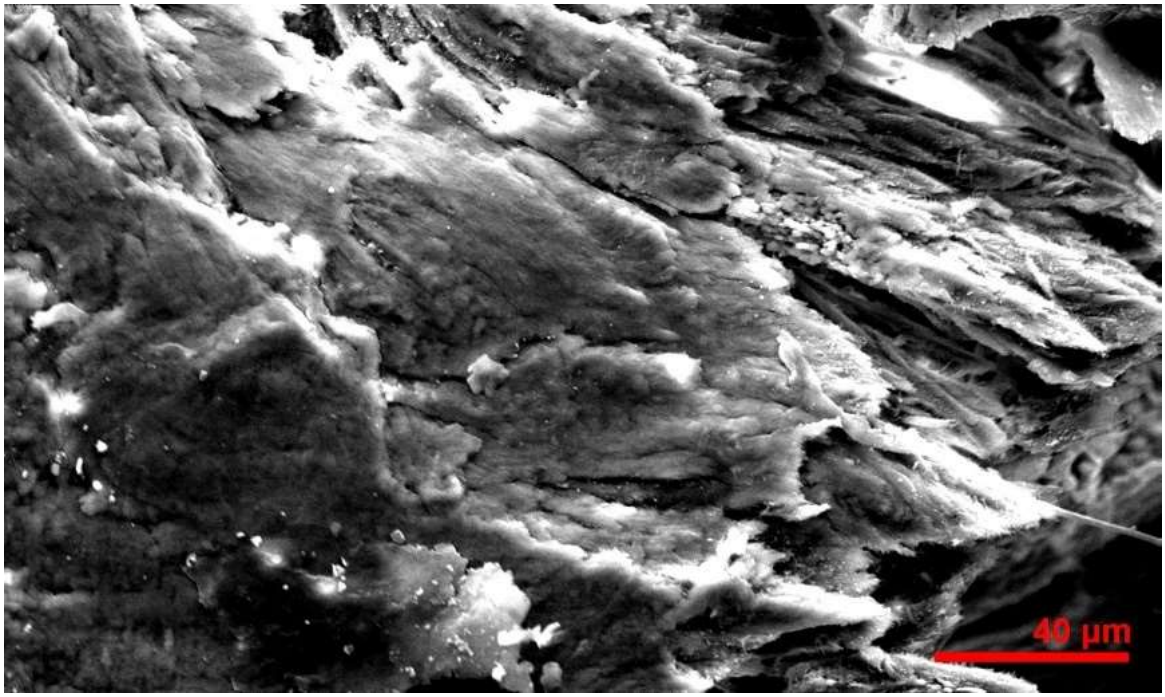

Figure 200: SE image of the pig bone standard.

The weathered surface layer under accumulated layers of deposits is also visible of the SE images (fig.198). The cross-section surface looks dense and coherent, containing particles that resemble the texture of pig bone standard (fig.199-200).

Low Cistern wall – Results Summary

The samples derive from the horizontal surface of the low wall that separated the aqueduct from the cistern and was revealed after the demolition of the overlying modern masonry.

The surface of the samples varies from dark grey to brown / black with black spots that move inwards. Peak indication of bone black pigment could explain the black spots and the color of the surface. Similarities are found with both the exposed mortar on stone samples S4 to S6 (grey and thin layer) and the cistern floor S1 to S3 (brown-black and resinous layer). There is no detectable biological activity. Differential decay and calcite accumulation are visible on their surface.

The spectra resemble those obtained from sheep and pig bone standards with high amide content similar to that found in egg white and bone glue mortar standards. Mortar content is almost absent on the surface layer of the samples. The organic material is located on the surface and reduces gradually towards the mortar layer.

Differences in the mortar components relative to the size of aggregates (quartz and ceramic inclusions) may indicate a different construction phase than that of the cistern (personal communication with the archaeologist S. Markoulaki, excavator of the site). The presence of bone, strongly suggested by FTIR and OM/SEM analysis, could reinforce this hypothesis since it is unique to these samples.

Polyrrhenia - Summary

All the Polyrrhenia samples show organic presence of the surface layer that is not attributable to biological activity or soil deposition. The cistern floor samples retain an amide, protein-based material, maybe with some lipid content that appears to be egg-related. The exposed samples of the stone plastered with mortar show the presence of dolomite on the surface but retain their protein composition, similar to that of the cistern floor. The samples from the low cistern wall retain protein related to bone and likely bone inclusions. Their phosphate content is attributed to the bone related protein and not to any external depositions or bird droppings, since the low cistern wall was preserved under modern masonry.

11.3.2 Phalasarna Samples

Sample S7 - Cistern wall (South)

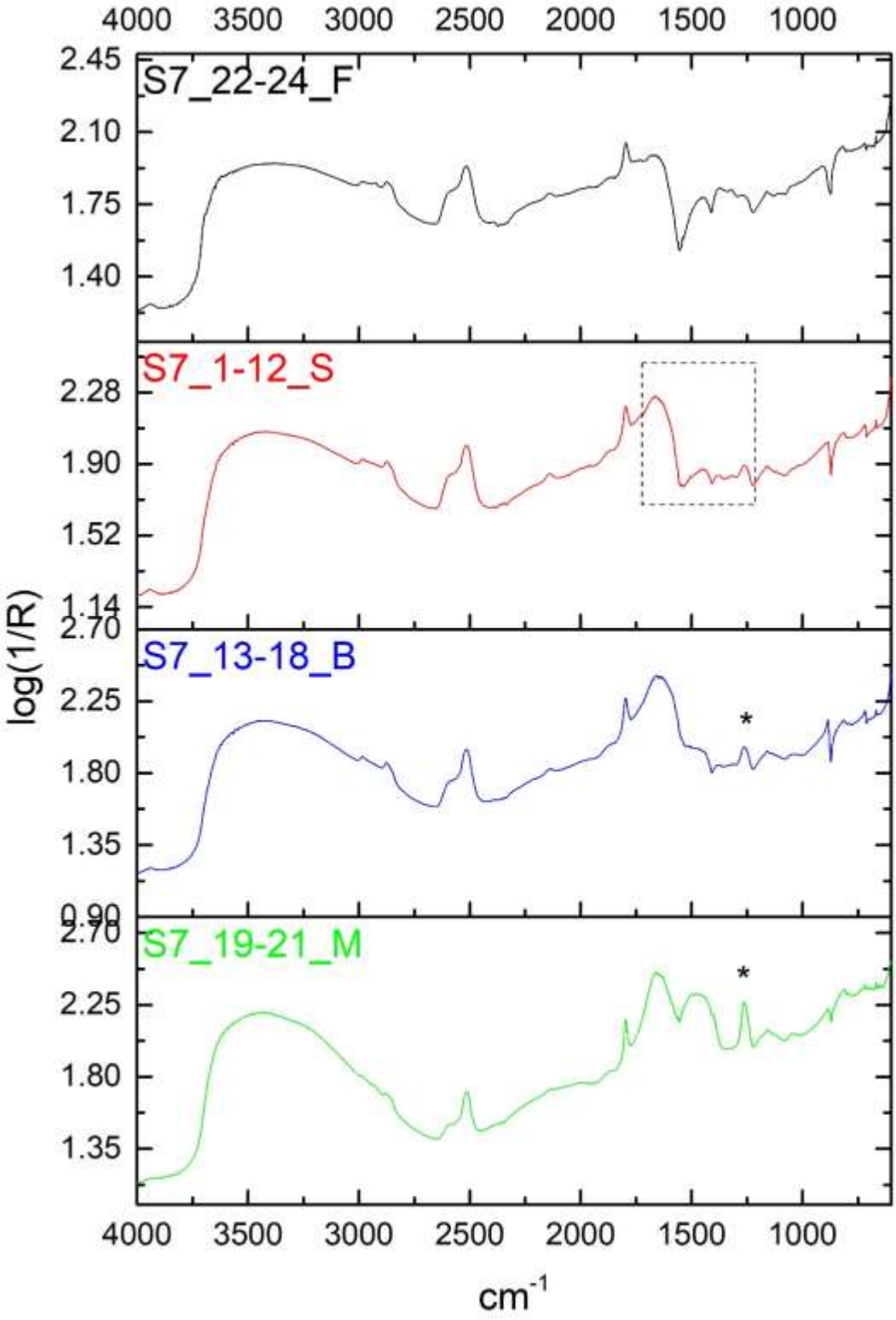

Figure 201: Sample S7: stacked spectra of individual layers. Black asterisks and dotted frame indicate organic presence, evident within the surface profile and extending into the mortar.

The S7 surface spectrum (S7_1-12_S) contains mainly mortar peaks and appears similar to sample S4 from Polyrrhenia (fig.201; Appendix III, fig.35). This similarity may derive either from the similar composition of the samples or the fact that both were exposed to external environment. However, environmental conditions differ between the two sites, especially relative to the close proximity of Phalasarna to the sea.

The peaks 1961 and 884-813 cm^{-1} are assigned to dolomite. The ROI 1722-1262 indicates organic presence, with 1262 cm^{-1} related to C-O of proteins found also in eggs and bone glue standards. The broadening of 1159 cm^{-1} should indicate the presence of phosphates. C-H bending at 1385 cm^{-1} is similar to that observed in egg yolk/ mortar standards. Amides are also detected in 1722-1444 cm^{-1} related to egg white and egg yolk/mortar standards. It appears that as the concentration of the protein decreases relative to the mortar content, the amide peaks at 1690 and 1570 cm^{-1} merge into one broad peak at 1640-1670 cm^{-1}. The O-H stretching of water above 3000 cm^{-1} looks excessive, suggesting the presence of marine salts (Ylmen and Jaglid, 2013, 119).

Dolomite is detected at the Flat Surface spectrum (S7_22-24_F), at the 909-819 reststrahlen and 1961 cm^{-1} (fig.201). The peaks at 1755-66 cm^{-1} are assigned to C=O of esters and these at 1659-1738 cm^{-1} to amides. Phosphates are present in 1085-1160 cm^{-1}. The S7_13-18_B (below) is similar to the surface spectrum since both retain organic component in the region 1262-1658 cm^{-1} and maybe dolomite at 1000 cm^{-1}. The Mortar spectrum (S7_19-21_M) contains a very strong peak at 1263 cm^{-1} that cannot be related to an inorganic component. The area 1450-1560 cm^{-1} also preserves protein content although the inorganic presence is pronounced in the mortar spectrum.

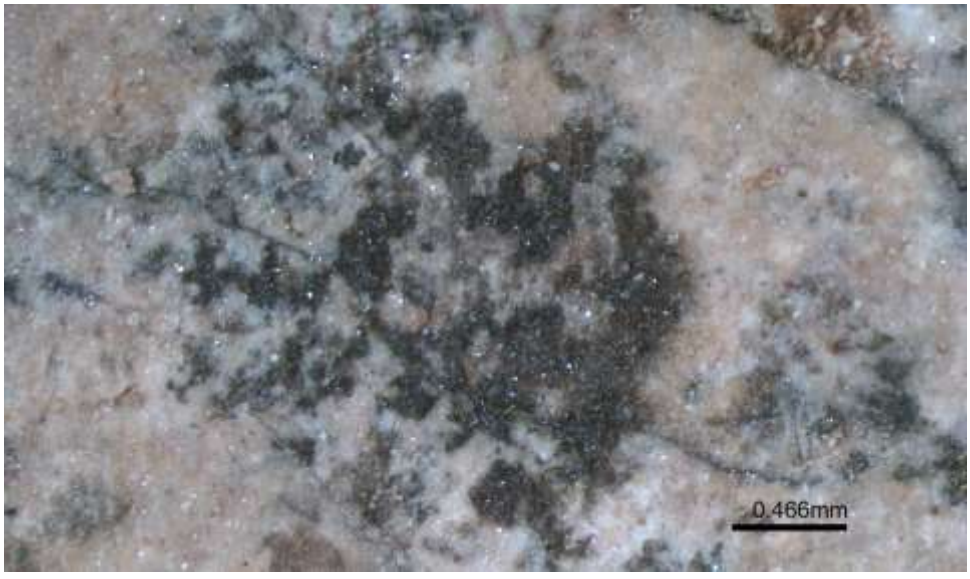

Figure 202: The surface of S7. A black surface layer is preserved under thick white crust.

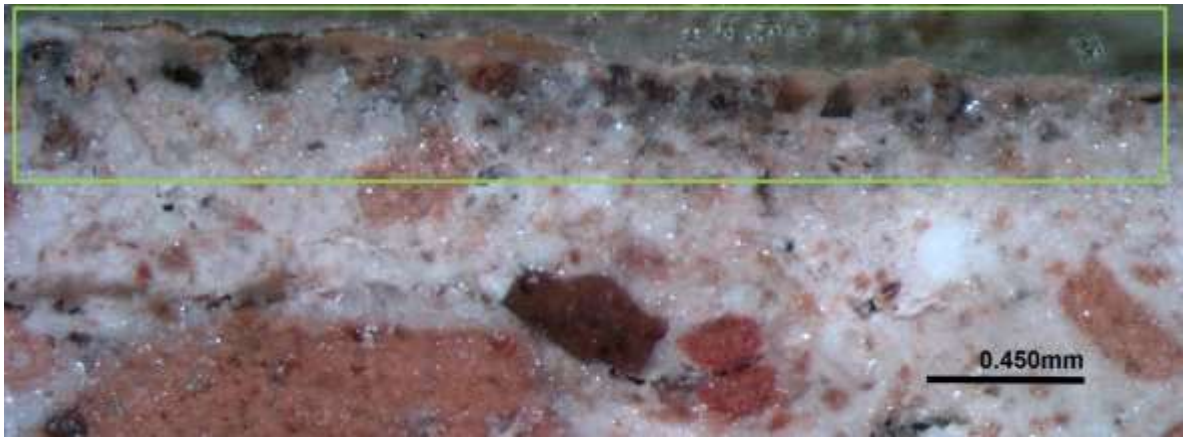

Figure 203: The cross-section surface of S7. The black layer fades out as it moves inwards (green frame).

A black surface layer is preserved under a thick white crust, appearing dense but locally cracked (fig.202). The black layer fades out as it moves towards the mortar (green frame, fig.203). The surface layer is not similar to the brown layers of S1 to S3 from the Polyrrhenia cistern, although the mortar technology appears the same (calcite, crushed ceramics and quartz).

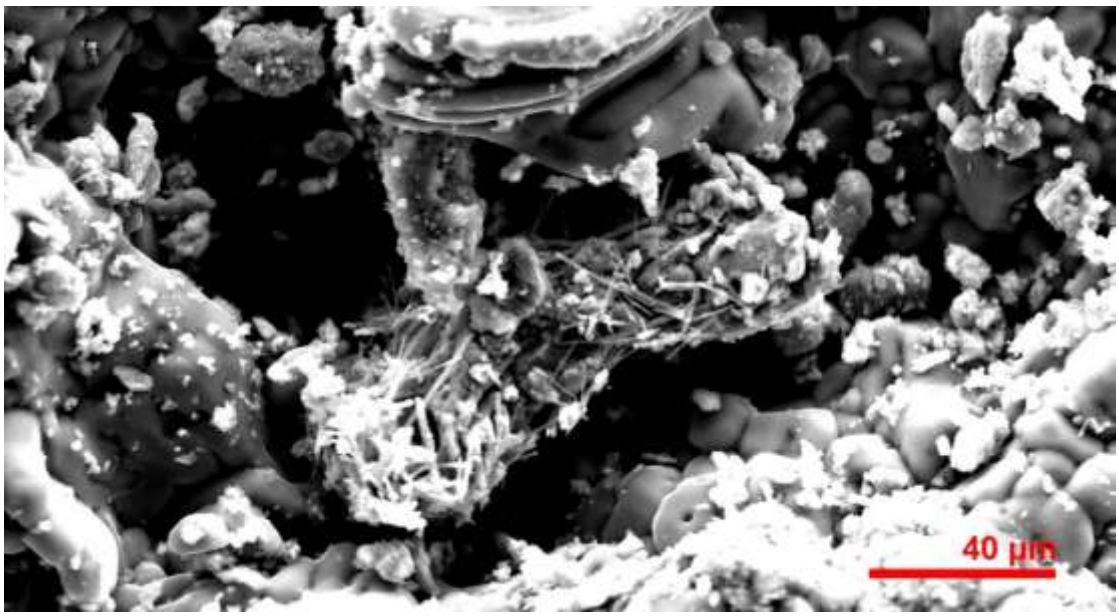

Figure 204: The surface of S7 covered with cubic crystals of sea salt and gypsum spikes.

The white crust on the surface of sample S7 is composed of cubic crystals of sea salt and spike crystals of gypsum based on the visual comparison with SE images of sea salt and mineral gypsum standards (fig.204, Appendix III, fig.36-37). Both deposits were not detected on the reflectance FTIR spectra because these were taken from areas free of crust. The water content detected could indicate the presence of sea salts.

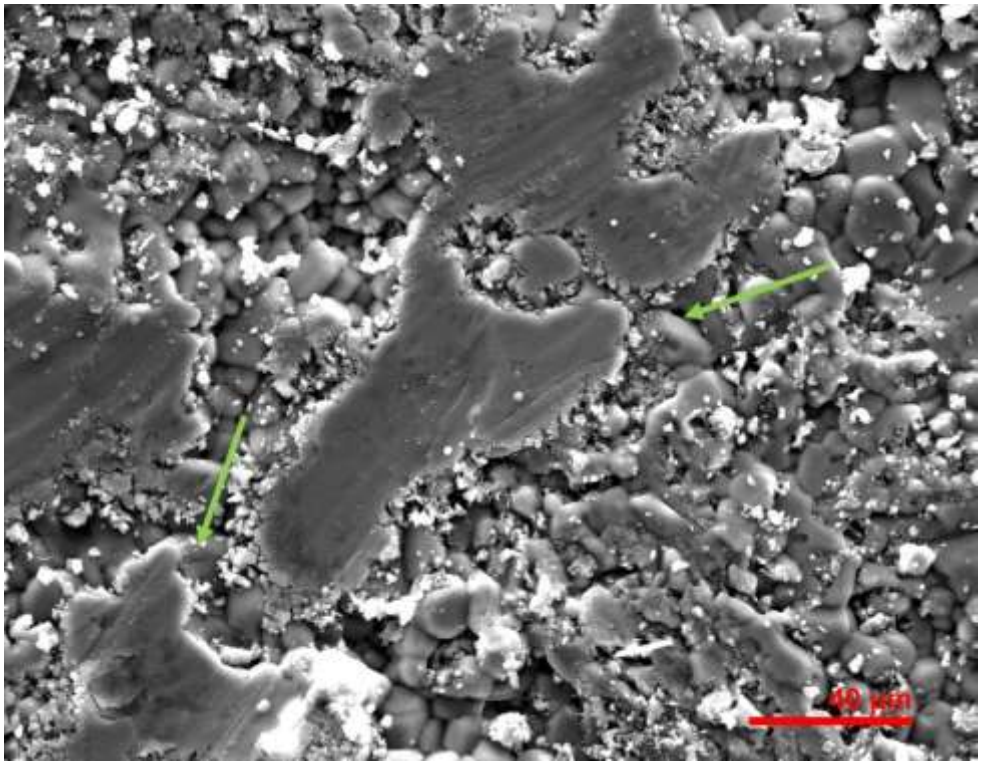

Figure 205: Surface of S7 showing original layer (green arrows) pushed outwards due to underlying salts, with potential indication of brush strokes.

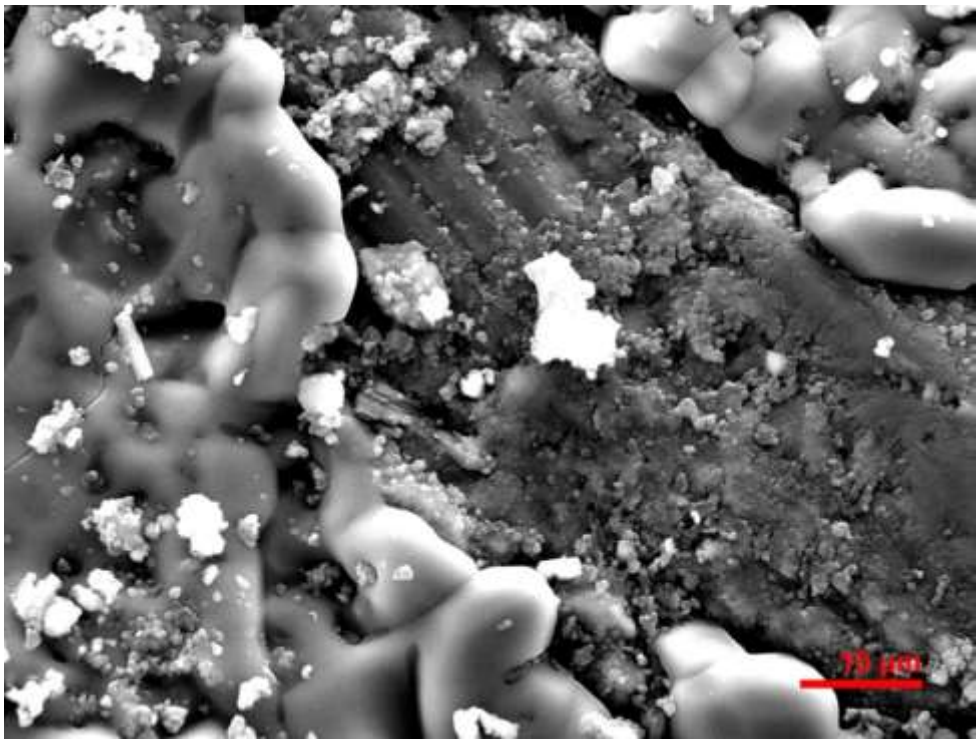

Figure 206: S7 surface layer covered partially by salt crystals.

A smooth, homogenous fragment of surface layer, that resembles a brushstroke, is pushed outwards due to underlying salt growth (fig.205). Biological activity is absent. In

another area, the surface layer is preserved below the salts and resembles the surface of organic/mortar standards (fig.206 and fig.154, Sample S1 section).

Sample S13 – Cistern wall (North)

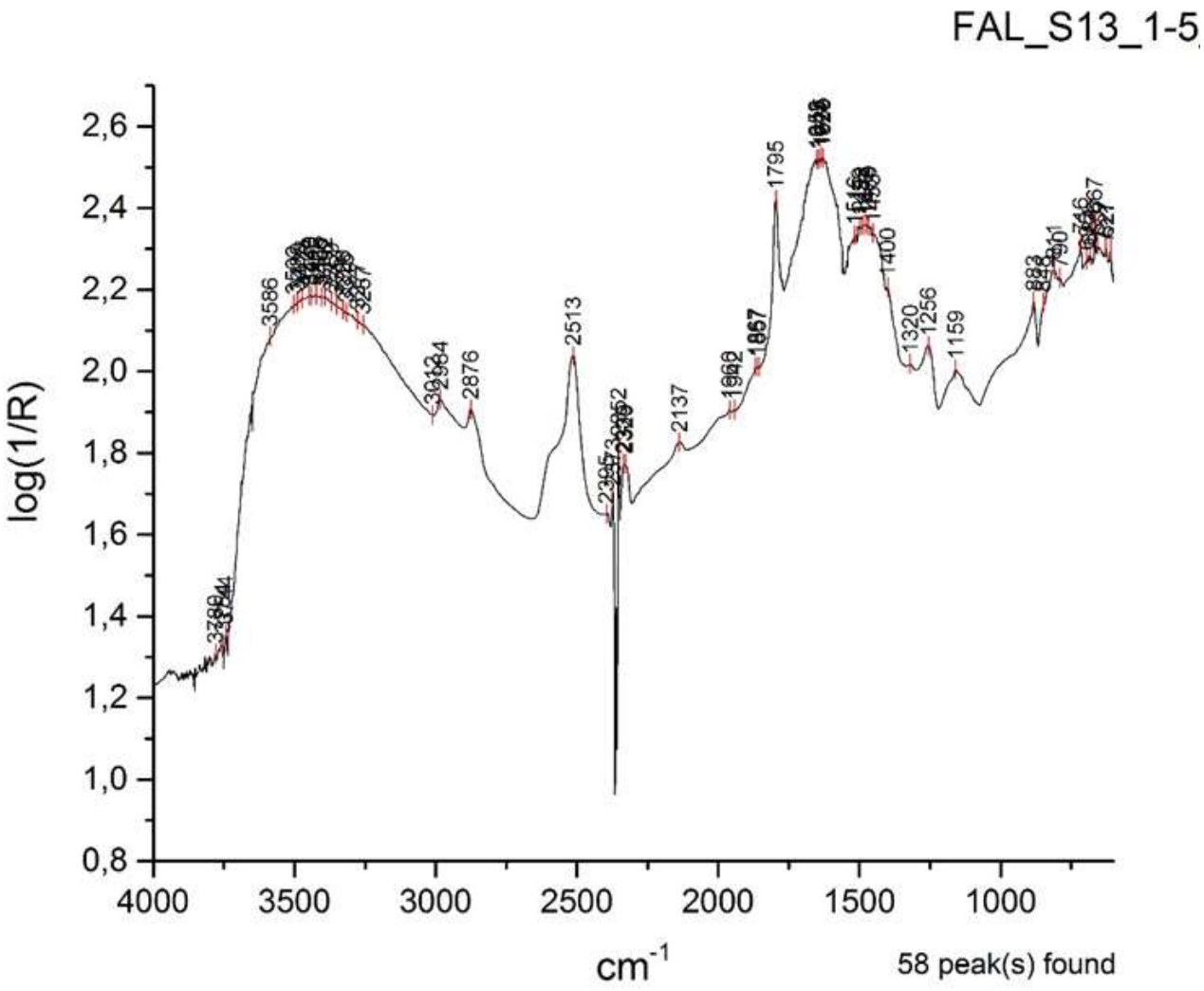

Figure 207: The spectrum of S13.

The spectrum shows high inorganic content, mainly calcite (fig.207). The reststrahlen at 1256 cm^{-1} cannot belong to lime since there are no other peaks related to it. The coexistence of amides and lipids cannot be ruled out due to the C-O of lipid at 1256 and its shape (Ploeger et al., 2010, 37) and the weak peaks at the ROI 1320-1516 cm^{-1} (Iwanicka et al., 2017, 18). The ROI 1628-1652 cm^{-1} is assigned to protein (Miliani et al., 2012, 304; Rosi et al., 2009, 2104). Standards of egg, milk and their mortar mixtures of low organic concentration are similar (sect. 7.5).

Figure 208: S13 mortar sample of the lime-quartz-crushed ceramic type.

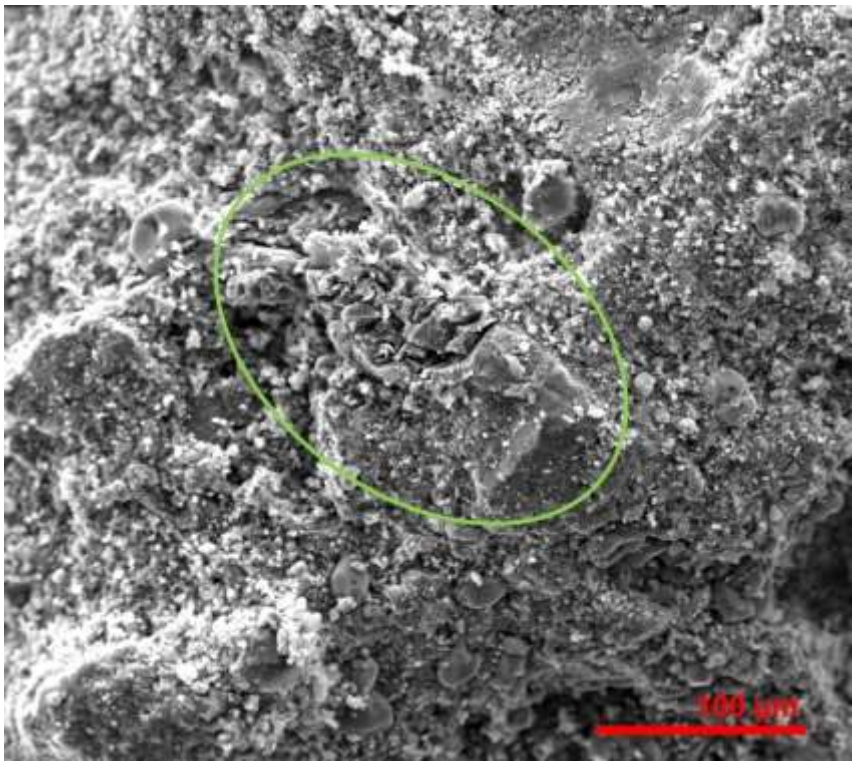

Figure 209: SE image of S13 mortar sample, showing sea salt accumulation and aluminosilicates from the ceramic aggregates (green circle).

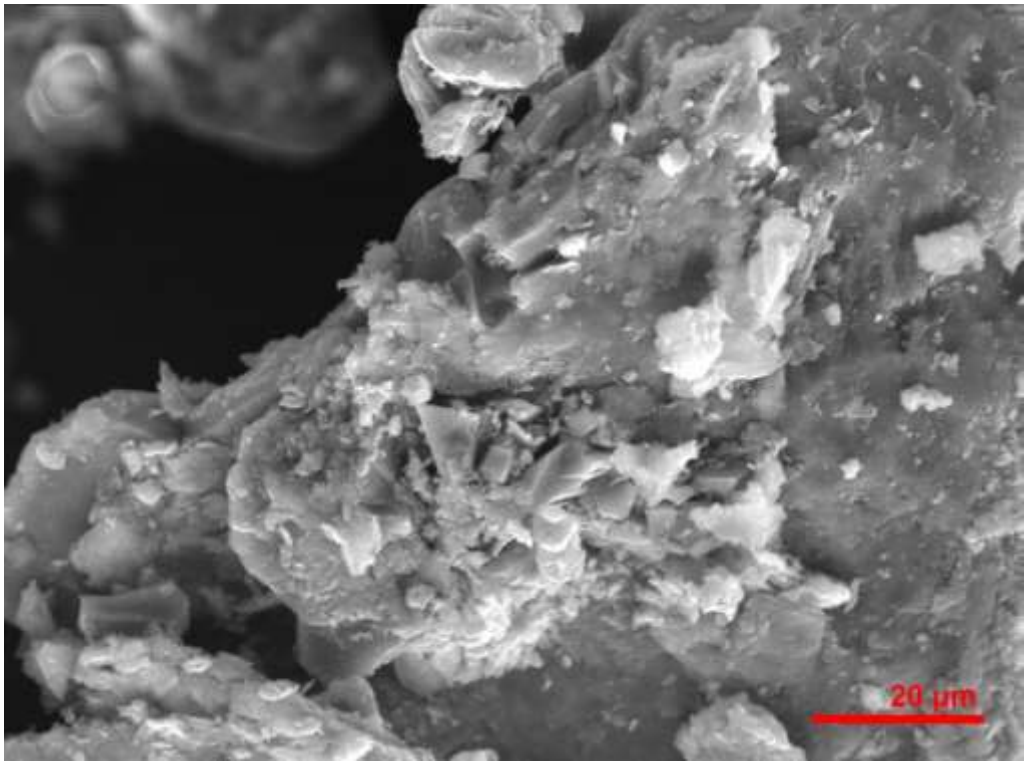

Figure 210: The SE image of Clay Standard.

The mortar sample belongs to the lime-quartz-crushed ceramic type and is identical to that used in the Polyrrhenia cistern (Moropoulou et al., 2000, 57; 2005, 298), (fig.208). Sea salt accumulation and aluminosilicates from the crushed ceramic aggregates are visible in SE image of its surface (green circle, fig.209). The aluminosilicates resemble those on the surface of Clay standard (fig.210). There is no visual evidence of organic presence and biological activity.

Cistern – Results Summary

Spectra interpretation strongly suggests the presence of protein-lipid-phosphate material, similar to egg white and/or egg yolk proteins, on the surface of sample S7. The organic peaks are preserved in all layers, although reduced in number and intensity towards the mortar. Dolomite is evident and should belong to mortar aggregates or dolomitic source of limestone. The black, uniform surface layer is not the product of biological activity. Sample S13 is mortar with low indication of protein, such as that observed in egg standards.

Sample S8 – Bathtub 1

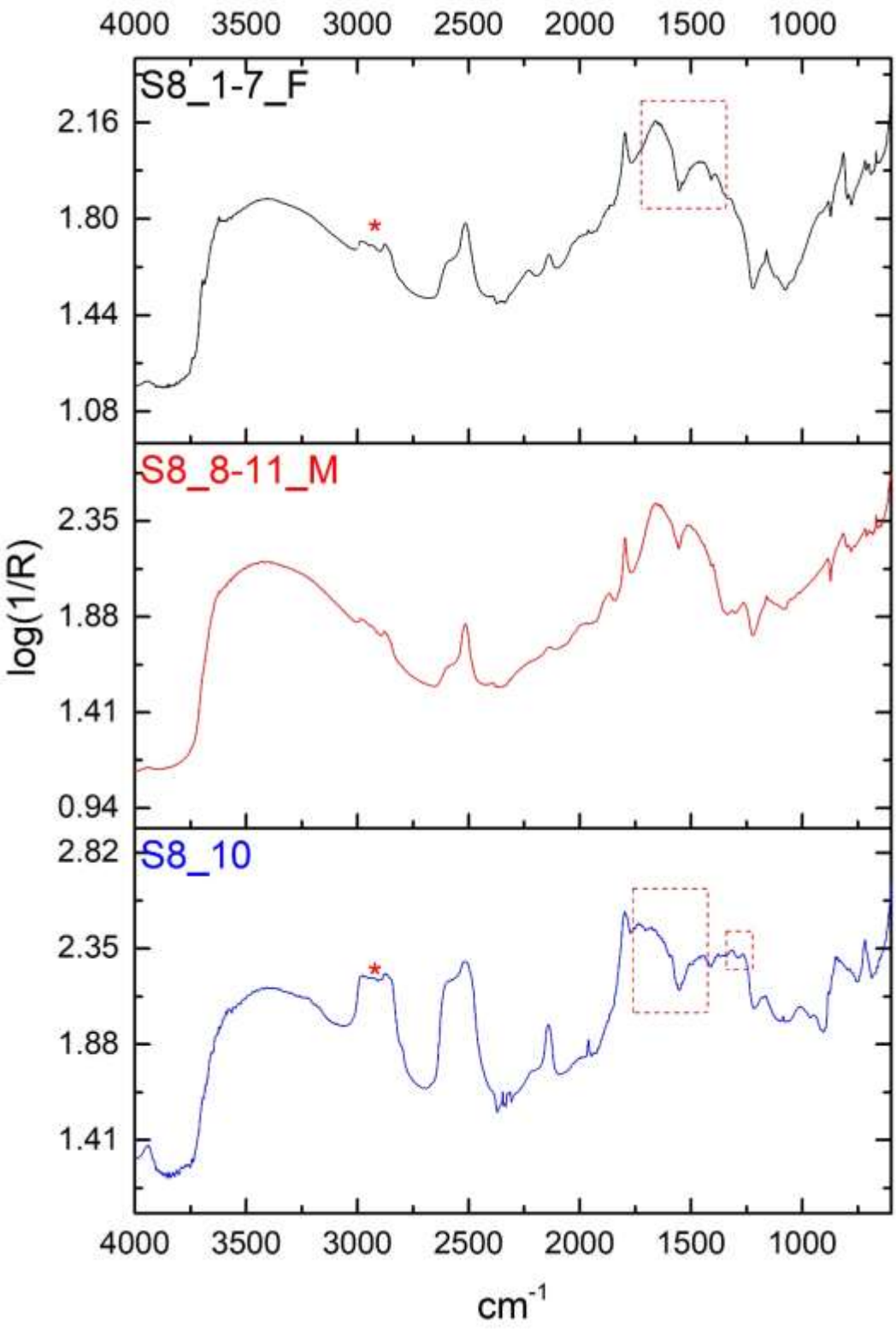

Figure 211: Sample S8: stacked spectra of individual layers. Asterisks and dotted frame indicate organic presence on the surface (F) and black area on the surface (S8_10).

Sample S8 was obtained from the surface mortar of the bathtub 1 seat. Mortar peaks are present on the flat surface spectrum (S8_1-7_F, fig.211). The peaks at 1390-1540 and 2937 cm^{-1} belong to organic bonds. The C-H bending peak at 1390 cm^{-1} is visible in proteins and lipids/mortar standards of low organic concentration. Amides dominate the region 1659-1444 cm^{-1} similar to EW_M_5 (5% egg white additive in mortar). Dolomite is indicated at 1960 and 917 cm^{-1}.

The spectrum obtained from a black area on the surface clearly shows dolomite (S8_10, fig.211). The ROIs 1755-1444,1376-1265 and 2943-2925 cm^{-1} contain peaks of ester and protein. Dolomite should be part of the original surface, probably as an aggregate (Blaeuer and Jaegers, 1997, 226), and not of the white crust that covers the sample. The spectrum of the black surface area is that of the highest organic presence, possibly because it is not masked by the white crust. The mortar layer is dominated by inorganic peaks, although protein and C=O are visible at 1633-1643 and1507 cm^{-1} respectively (S8_8-11_M, fig.211).

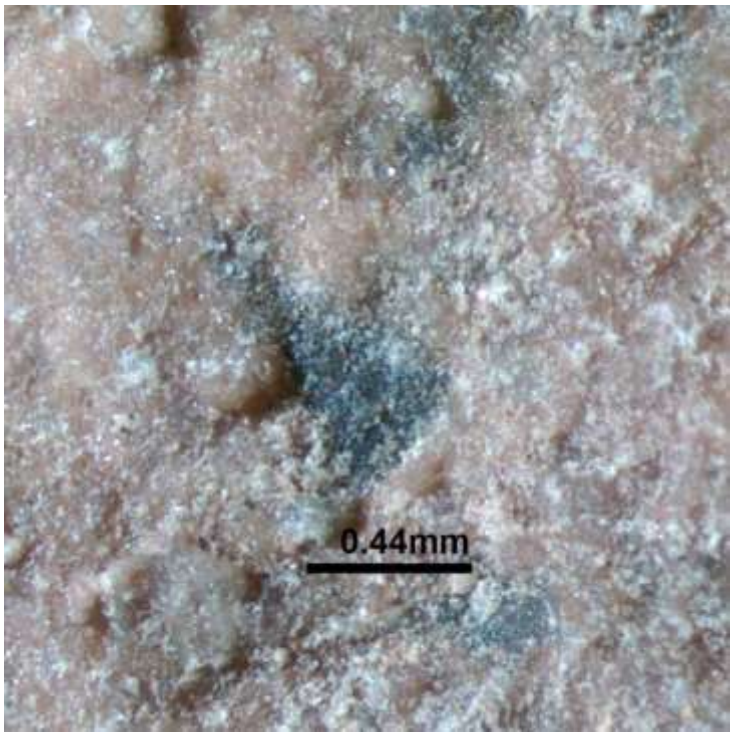

Figure 212: The surface of S8, showing the exposed black area underneath the white crust.

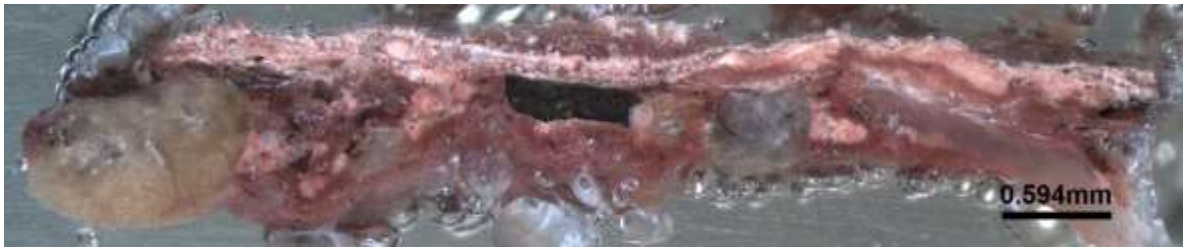

Figure 213: Cross-section of S8. The thick white crust covers the entire surface.

A very thick whitish crust covers almost the entire surface of sample S8, resembling that observed in sample S7 from the cistern wall (fig.212-213). A dark layer is observed underneath this crust, where dolomite is detected. The cross-section reveals how thin the sample is (fig.213). The low and uniform thickness of the sample seems intentional. This was evident already from the in-situ observation of the bathtubs. The lower part of the sample consists of quartz aggregates mixed with lime.

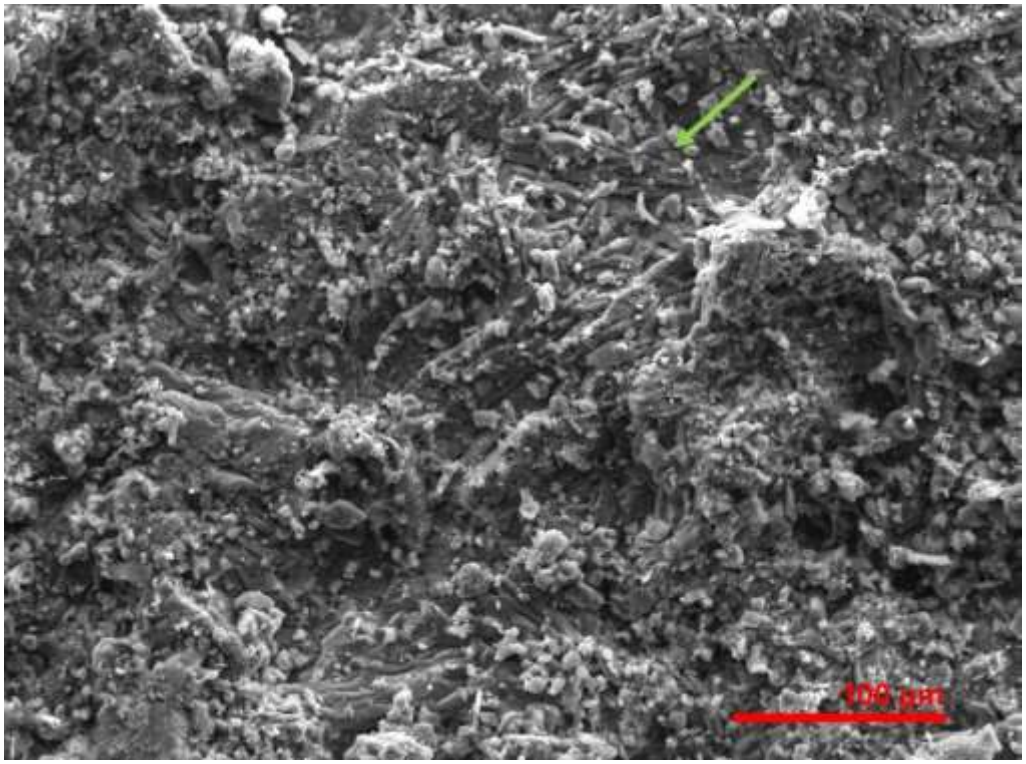

Figure 214: The surface of S8 showing deposition of sea salt crystals and long spike crystals of gypsum (green arrow).

The long spike crystals are gypsum, whereas the large loose particles resemble sea salt (fig.214). It is interesting to note that gypsum was not detected on the spectra but visual evidence suggests it is present.

Sample S9 – Bathtub 1

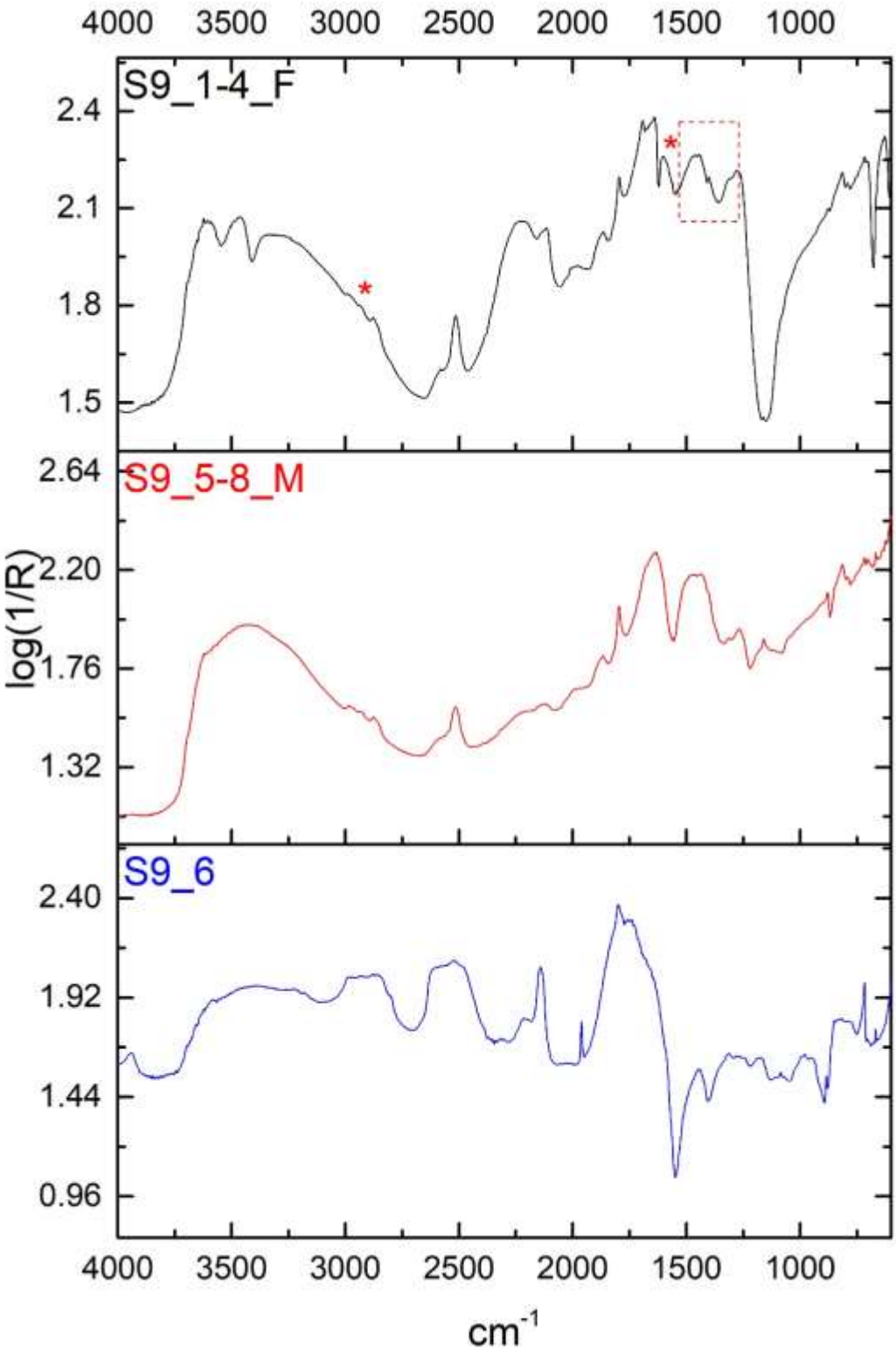

Figure 215: Sample S9: stacked spectra of individual layers. Asterisks and dotted frame indicate organic presence on the flat surface.

The sample derives from the bottom of bathtub 1. CPAD comparison of the flat surface spectrum (S9_1-4_F, fig.215) with the absorption intensities of gypsum mineral standard (GyM_av) shows that gypsum prevails, although some calcite is visible in 1401, 2514 and 2877 cm^{-1}. The peaks 3623-3463, 2227-2114, 2007, 1692-1640 double sharp peak, 1279 and the reststrahlen at 628-715 cm^{-1} are diagnostic to mineral gypsum (Appendix III, fig.38). The peaks at 1692 and 1272 cm^{-1} cannot be linked to protein in this case, since their shape and intensity resembles that of gypsum.

The CH_2 /CH_3 peak at 2991 cm^{-1} and the C-O and C-H bonds in the ROI 1310-1540 cm^{-1} indicate organic material. Protein is likely present due to spectral similarities with bone glue and egg mortar mixtures (sect.7.5).

The strong peak at 1600 could belong to amides (Miliani et al., 2012, 304; Rosi et al., 2009, 2104), oxalates (Ricci et al., 2006, 1224) or benzene rings of asphalt (Lombardi and Santarelli, 2009, 542). The shape is closer to that of the asphalt peak but there are no other diagnostic peaks supporting its presence. The next possible match should be amides.

Benzene rings are found in structures of amino acids such as tryptophan, phenylalanine and tyrosine obtained from the hydrolysis of proteins (Mills and White, 1987, 74). Tryptophan, amino groups and aldehydes may form humins of dark brown coloration (Mills and White, 1987, 74). This process may have occurred here, although environmental conditions for the duration of exposure of the bathtub after its excavation cannot be securely defined.

Phenylalanine and tyrosine are found in egg white, egg yolk, casein and gelatin (phenylalanine) (Mills and White, 1987, 75). The major proteins of eggs, the albumins, are insoluble in water after treatment with heat or reaction with certain materials (Mills and White, 1987, 76). Mills and White do not specify these materials, however experiments with lime and egg white in mortars (Mydin 2018), indicated there was increased hydrophobicity of the mortar.

The spectrum of a black surface area (S9_6, fig.203), similar to that found in sample S8, indicated the presence of dolomite. The ROIs and peaks at 2802-2931, 2712, 1800-1755, 1466, 1313 and 1281 cm^{-1} show C-H stretching and C=O of lipids (Daher et al., 2017, 8). Any evidence for protein is absent.

The S9 layers differ considerably from each other (fig.215). The flat surface spectrum (F) is dominated by gypsum, although protein is also visible. The black surface area spectrum

(S9_6) shows mainly dolomite and lipid. The mortar layer (S9_5-8_M) is mainly inorganic although 1313, 1471 and 2939 cm^{-1} show C-H stretching, whereas the strong peak at 1632 and the weak peak at 1559 cm^{-1} are assigned to N-H bands of amides.

The texture of sample S9 is identical to that of S8. The surface darkening, below the whitish gypsum crust, derives from the high amount of quartz in the mortar (image not shown). The SE images verify the presence of Gypsum and sea salt. There is no biological activity present. Areas not covered by crust are highly similar to the mortar standard. Organic presence is not visually evident on the surface, although weak resemblance to bone and organic/mortar texture is visible on the cross-section surface (images not shown).

Sample S10 – Bathtub 3

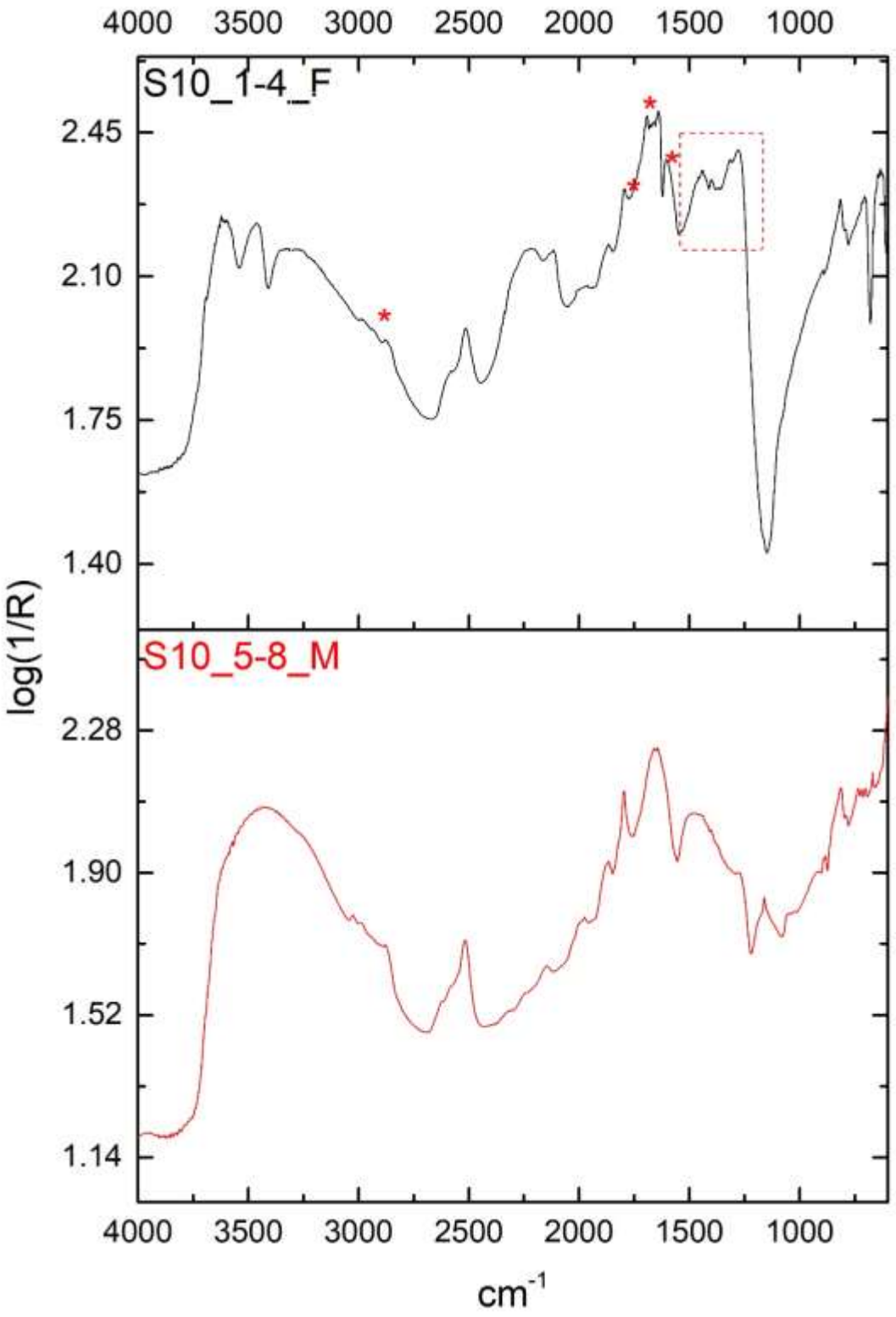

Figure 216: Sample S10: stacked spectra of individual layers. Asterisks and dotted frame indicate organic presence on the flat surface.

Sample S10 derives from the sidewall of bathtub 3. The flat surface spectrum (S10_1-4_F) is similar to the S9 one and contains mainly gypsum and mortar (fig.216). Lipids are present at 2939 and 2992 cm^{-1}. This spectrum has a stronger presence of protein indicated by the weak peaks at 1770 and the ROI 1692-1640 cm^{-1}. The 1692 and 1640 cm^{-1} are assigned to the double peaks of gypsum, whereas the in-between peaks are assigned to protein similar to egg white/mortar and bone glue standards. However, the combination with the aromatic amino acid at 1606 cm^{-1} indicates egg source rather that bone glue. The C-O and C-H bonds at 1540-1280 cm^{-1} suggest mainly the presence of protein (Miliani et al., 2012, 304).

It was assumed that Sample S10 obtained from the sidewall of the bathtub would retain more organic residue than the bottom, since it would be less exposed to leaching and precipitation of deposits. Maybe that is why the protein-lipid content is more evident here than in sample S9.

Gypsum is not present in the mortar layer although some sulphates are present in 1022 and 1046 cm^{-1} (Ylmen and Jaglid, 2013, 120). Inorganic peaks of calcite are dominant. Protein is indicated at 1275, 1643, 1659, and 2881-2988 cm^{-1} (S10_5-8_M, fig.216).

Figure 217: The cross-section of S10 showing a fine surface layer of calcite covered by thin white crust.

A fine layer of calcite, followed by calcite and quartz mortar, is preserved below a thin whitish crust (fig.217). The SE images show sea salt crystals below an extensive layer of gypsum similar to samples S8 and S9. There is no visual indication of organic presence either biological or intentional (images not shown).

Sample S11 – Bathtub 3

Sample S11 derives from the front wall of bathtub 3. The FTIR analysis is consistent with that of S10 (data not shown). Gypsum, dolomite and low lipid (main component) - protein content is detected on the surface of the sample. The spectrum of the black surface area retains the highest lipid-amide content. The mortar layer is mainly

calcite but retains low amount of protein. The microphotographs are identical to those obtained from the S8 to S10 bathtub samples (images not shown).

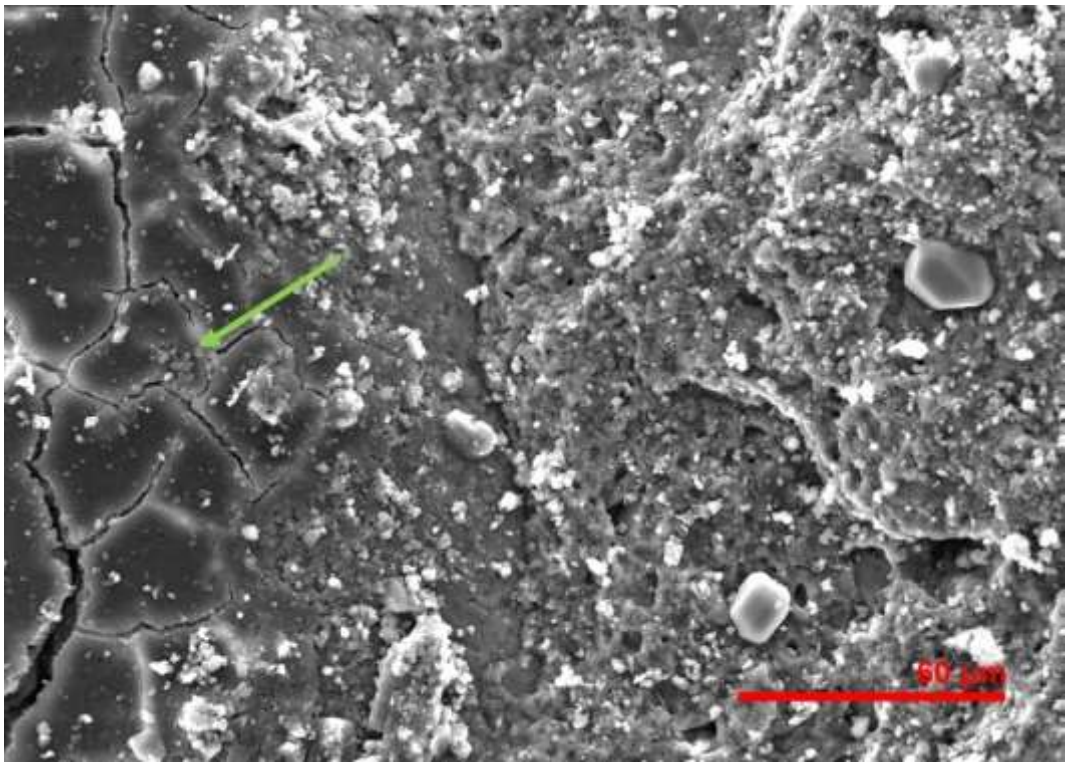

Figure 218: The surface of S11 detailing cracks (green arrow).

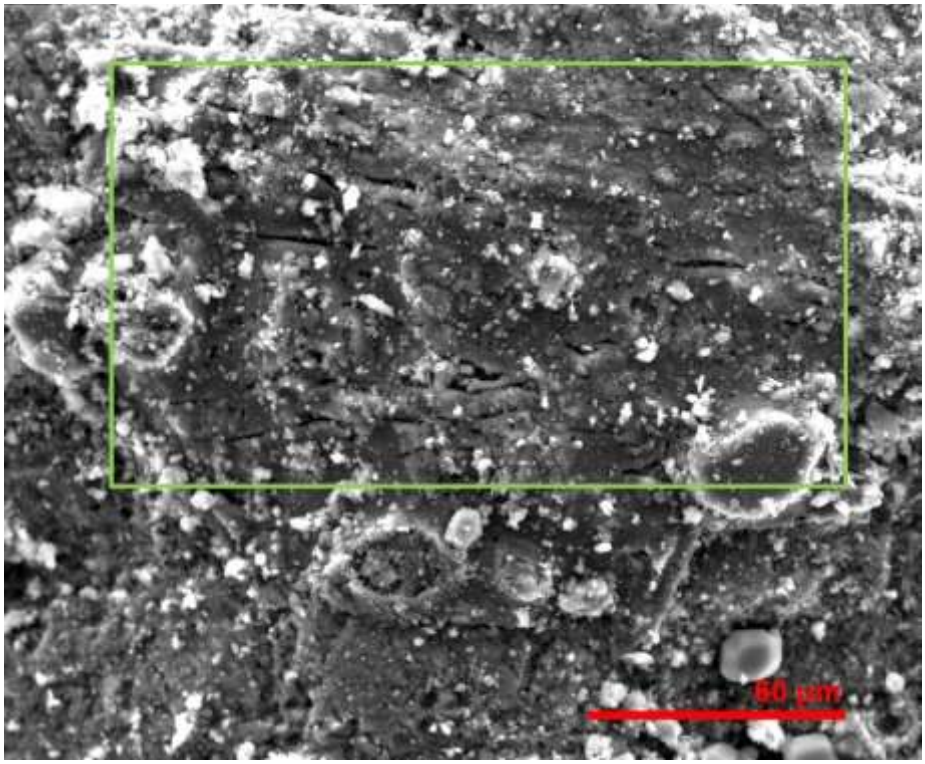

Figure 219: Ruptured surface layer of S11 (green frame).

A surface layer that appears cracked covers the mortar and is pushed upwards likely from the gypsum growth (fig.218). In other surface areas it seems that the original layer is ruptured, probably because of the induced pressure of the underlying salt growth and gypsum (green frame, fig.219). The ruptures visible indicate elasticity that could not derive from the mortar. Visual similarities were observed with bone glue/ mortar standards. The layer seems organic and biological activity is absent.

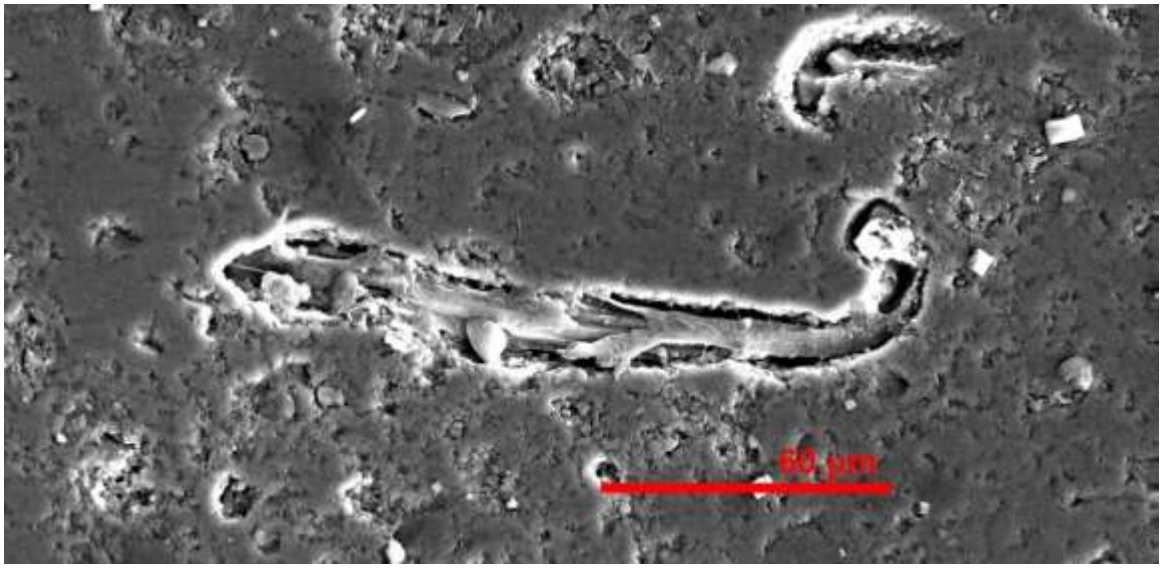

Figure 220: A fibre within the layer below the surface of S11.

A fibrous item trapped in the layer below the surface does not indicate biological activity (fig.220).

Bathtubs – Results Summary

Samples S8 to S11 obtained from the bathtubs are thin and consist mainly of calcite and quartz under a whitish crust of sea salts and gypsum, likely to derive from the marine environment where sodium sulphate and ammonium sulphate frequently occur (Maravelaki et al., 2003, 656). There is no evidence of biological activity being present. Dolomite particles were used as aggregates in pozzolanic mortars (Maravelaki et al., 2003, 656). The black surface areas analysed show the highest lipid-protein content since these were free from over-deposited white crust. Egg white/mortar standards have similar diagnostic peaks. Benzene rings related to amino acids show egg origin of protein. Physical evidence of organic surface was found in the SE images on surface raptures and cracks indicating elasticity.

Sample S12 – Cistern -Three Hierarchs Church Area

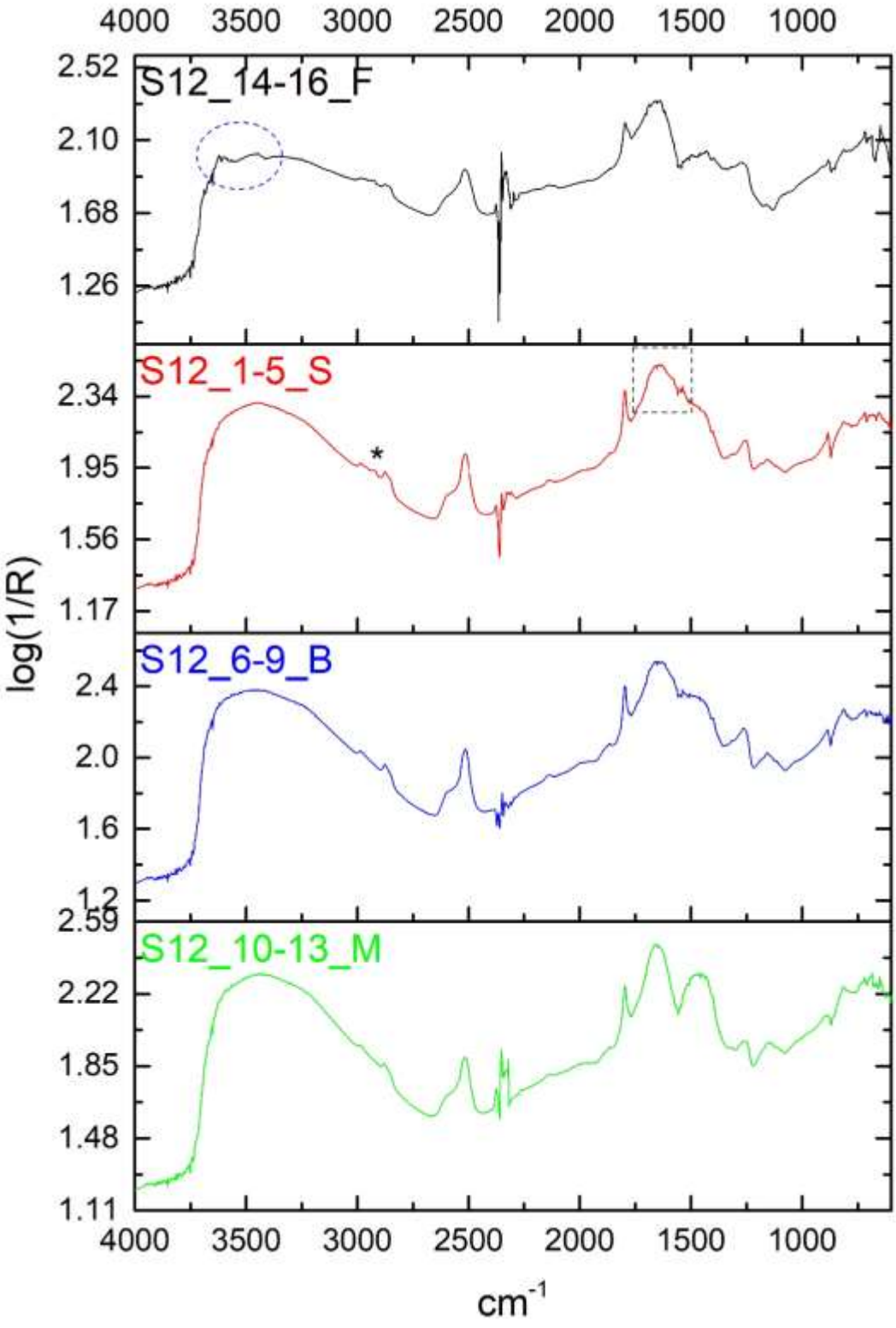

Figure 221: Sample S12: stacked spectra of individual layers. Asterisks and dotted frame indicate organic presence on the surface spectrum S12_1-5_S; dotted circle indicates gypsum on the flat surface spectrum S12_14-16_F.

Amides and lipids (less prominent) are present in the surface spectrum (S12_1-5_S) in 1773-1460 and 2926 cm^{-1} similar to EW_M_75 (75% egg white additive in mortar) (fig.221; Appendix III, fig.39). The shape of 1253-1318-1340 cm^{-1} resembles that of sheep bone rather than that of calcite. Thus, the C-O bond (or CH_2, CH_3) in this ROI is linked to protein or calcite in combination with protein.

Higher protein (dominant) – lipid content as that found in egg white/mortar standard is observed in the flat surface spectrum (S12_14-16_F). Gypsum is present on the weak peaks at 3621-3448 cm^{-1}. The layer below the surface is identical to the surface one (S12_6-9_B). The mortar layer retains low protein (S12_10-13_M, fig.221).

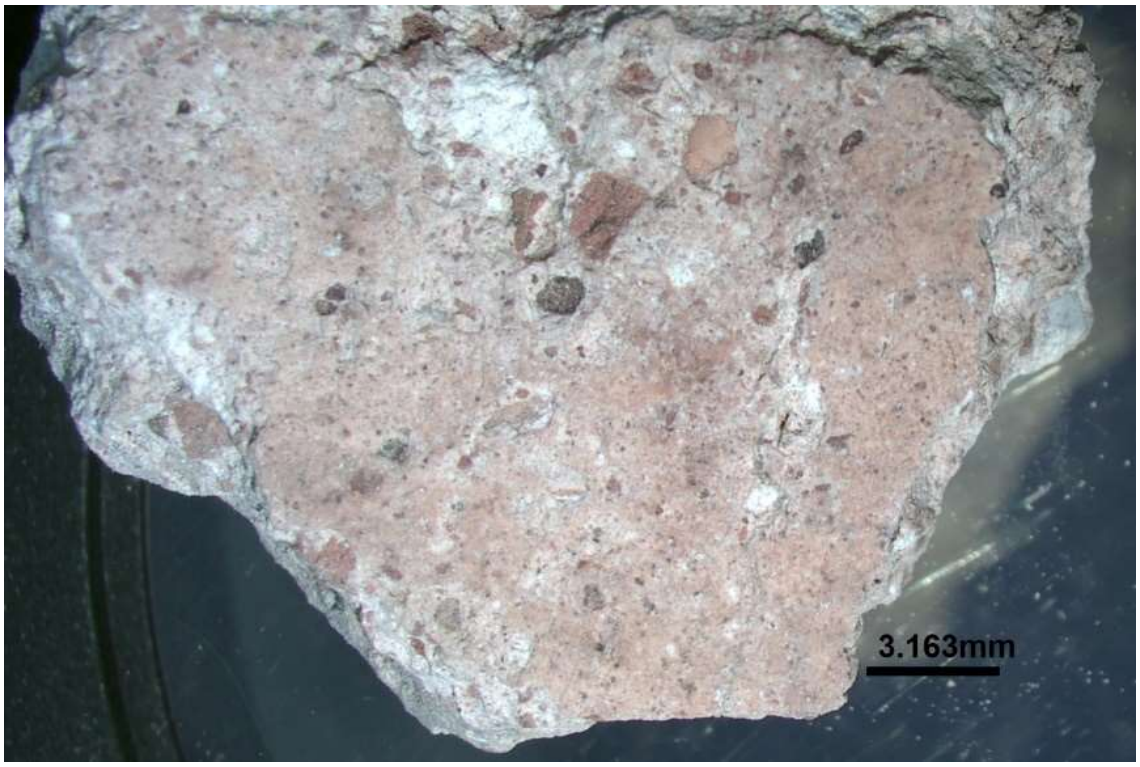

Figure 222: The flat surface of S12 appears light red to pink.

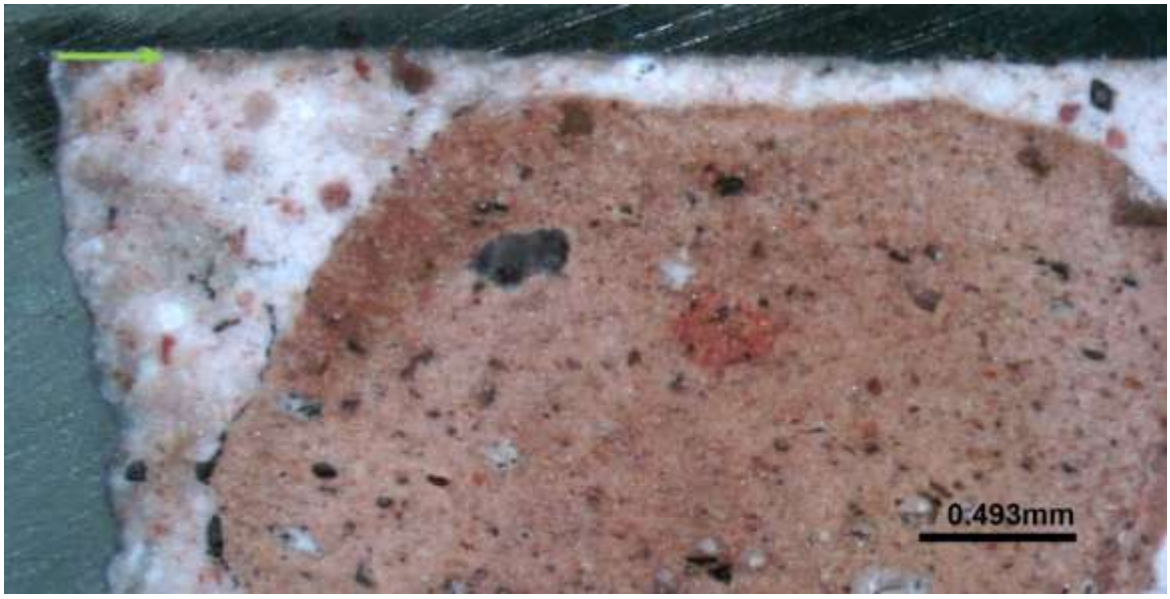

Figure 223: The cross-section of S12. The surface layer appears fine and polished (green arrow).

The color of the S12 sample differs from the rest of Phalasarna and Polyrrhenia samples as it appears light red to pink, with no visual evidence of resinous substance (fig.222). It also appears fine and polished, over a fine calcite mortar that incorporates fine quartz aggregates and large ceramic inclusions (fig.223).

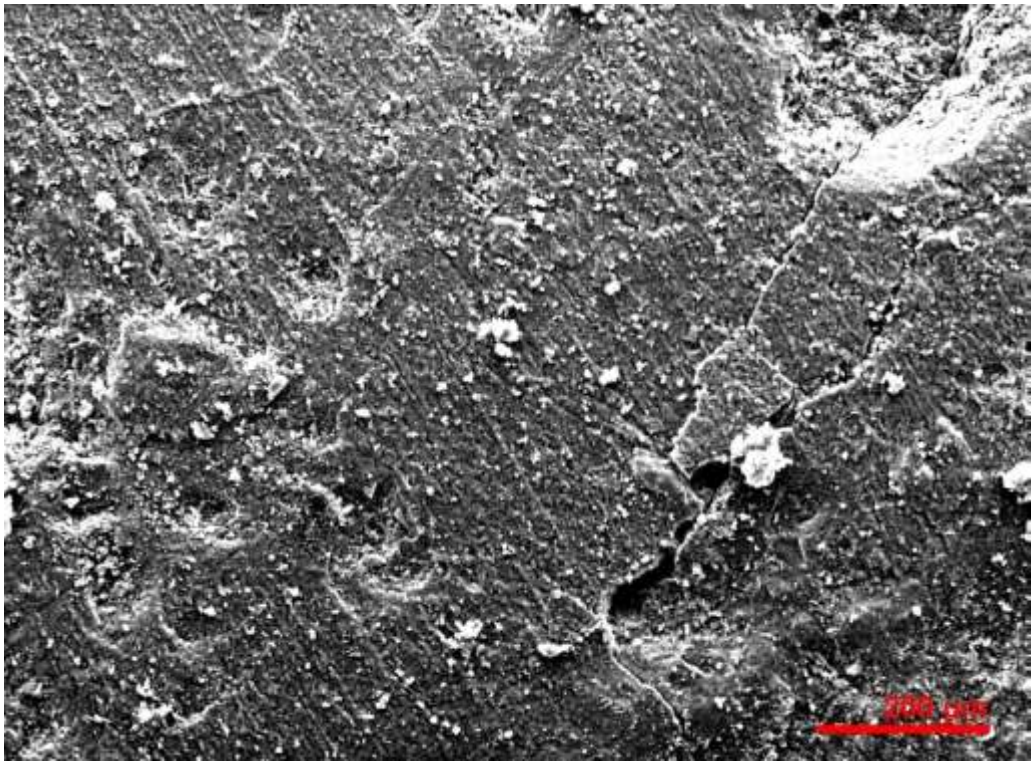

Figure 224: SE image of the surface of S12 showing parallel lines.

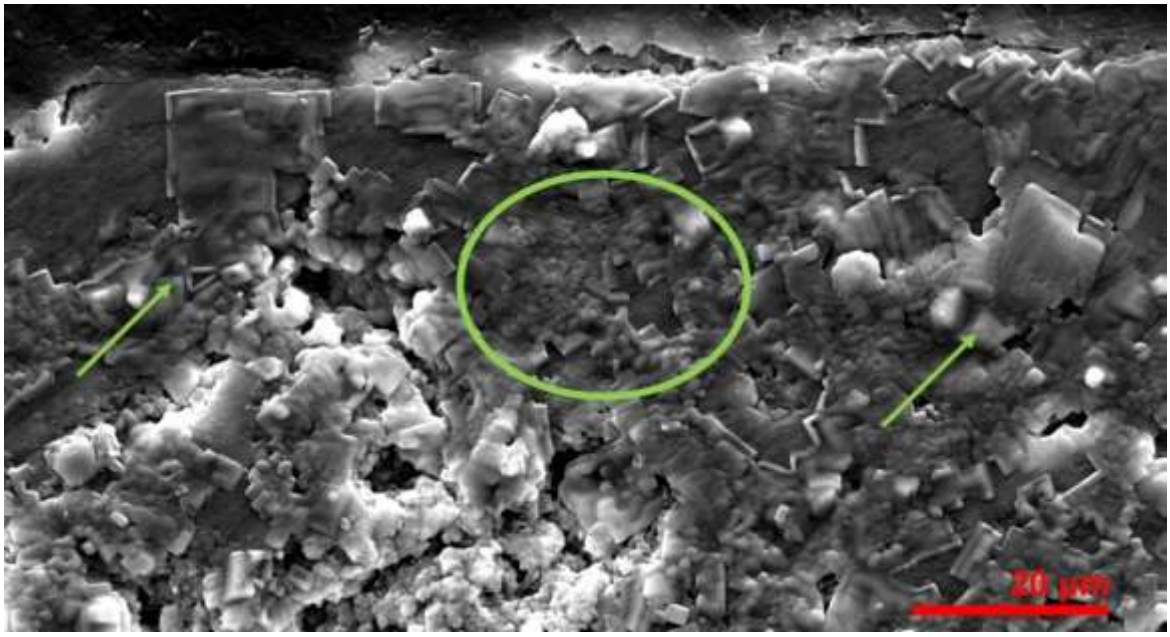

Figure 225: SE image of the cross-section surface of S12. Colloidal mass (green circle) and hopper-like crystals coexist within the surface layer.

The surface is free of deposited particles. The parallel lines could indicate polishing of the homogenous mortar surface (fig.224). The cross section shows a fine calcite surface layer, and growth of cubic crystals (fig.225). The hopper-like crystals (green arrows) are most likely chlorides (Gomez-Heras et al., 2004). Colloidal mass (green circle) could indicate an amorphous material on the surface layer.

Three Hierarchs Cistern – Results Summary

The mortar sample is likely to derive from the floor of the cistern. The area is exposed to marine conditions. The surface of the sample is light pink, fine and polished. Gypsum grows from within the mortar and this is evident from its low concentration on the flat surface spectrum (F) as opposed to the cross-section surface spectrum (S). A protein-based material resembling the egg white/mortar standard is suggested as a potential additive.

Phalasarna - Summary

Samples S7 to S13 obtained from the cisterns and bathtubs of Phalasarna show protein-based product on their surface, similar to egg/mortar standards. Biological activity is absent. Gypsum is evident in all samples, growing from within the mortar. Sea salt is visible on the SEM but undetectable on the Reflectance micro-FTIR spectra.

11.3.3 Aptera Samples

Sample S16 – Bottle-shaped Cistern

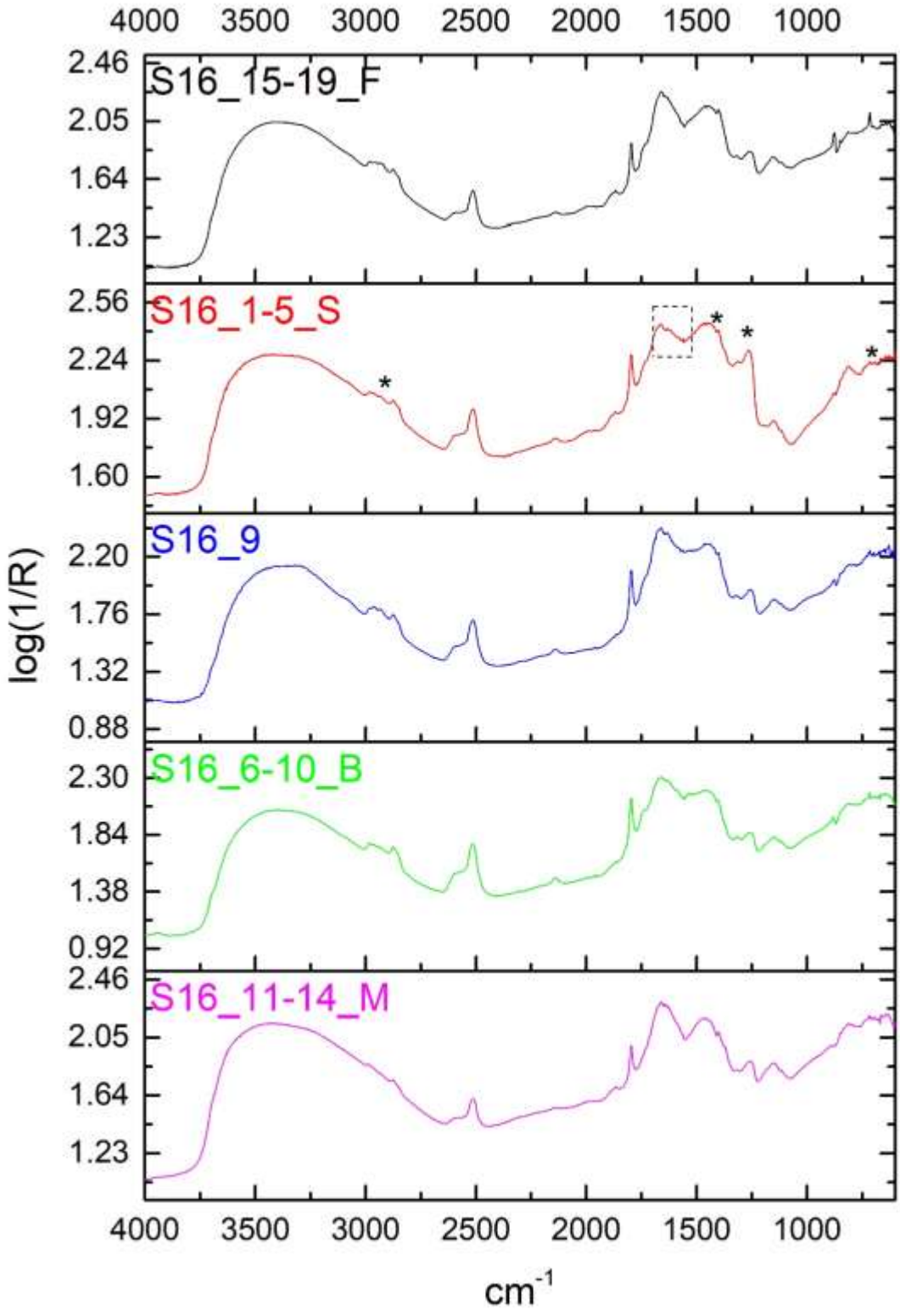

Figure 226: Sample S16: stacked spectra of individual layers. Black asterisks and dotted frame indicate organic presence on the surface layer.

The surface spectrum (S16_1-5_S) shows high mortar content above 1795 cm^{-1} and below 1151 cm^{-1} and high O-H water content above 3000 cm^{-1} (fig.226). CPAD comparisons with standards show that the very weak and sharp peaks at 666 cm^{-1} and below this are indicators of organic components. However, similar peaks occur in almost all the spectra of organic standards, including pigeon droppings. Peak 673 cm^{-1} is also present in egg white, egg and bone glue mortar mixtures and pigeon droppings standard (DR_2) indicating protein. The C-O stretching at 1265 cm^{-1} and CH_3 / CH_2 at 1313 cm^{-1} show organic content similar to egg components and bone glue mortar standards.

Mold peaks could be present in 1400 cm^{-1}, a peak also related to calcite, 1447 and 1631 (Appendix III, fig.40). However, 1445 cm^{-1} is also present in egg and egg yolk spectra indicating amide III (Buti et al., 2013, 2705). Lipid C=O of egg yolk is also visible in 1519 and 1560 cm^{-1}. Proteins are present in 1618-1667 cm^{-1} and 2938-2982 cm^{-1} similar to egg white/mortar standards. However, the amide peak at 1618 cm^{-1} is also present in pigeon droppings standard, suggesting the presence of biological contamination.

The flat surface spectrum (S16_15-19_F, fig.226) shows less organic content than the surface spectrum (cross-section position under the microscope), indicating better preservation of the organic material in the less exposed layers of the sample. The layers below the surface (S16_6-10_B) and mortar (S16_11-14_M) preserve egg related protein-lipid content that reduces gradually towards the mortar.

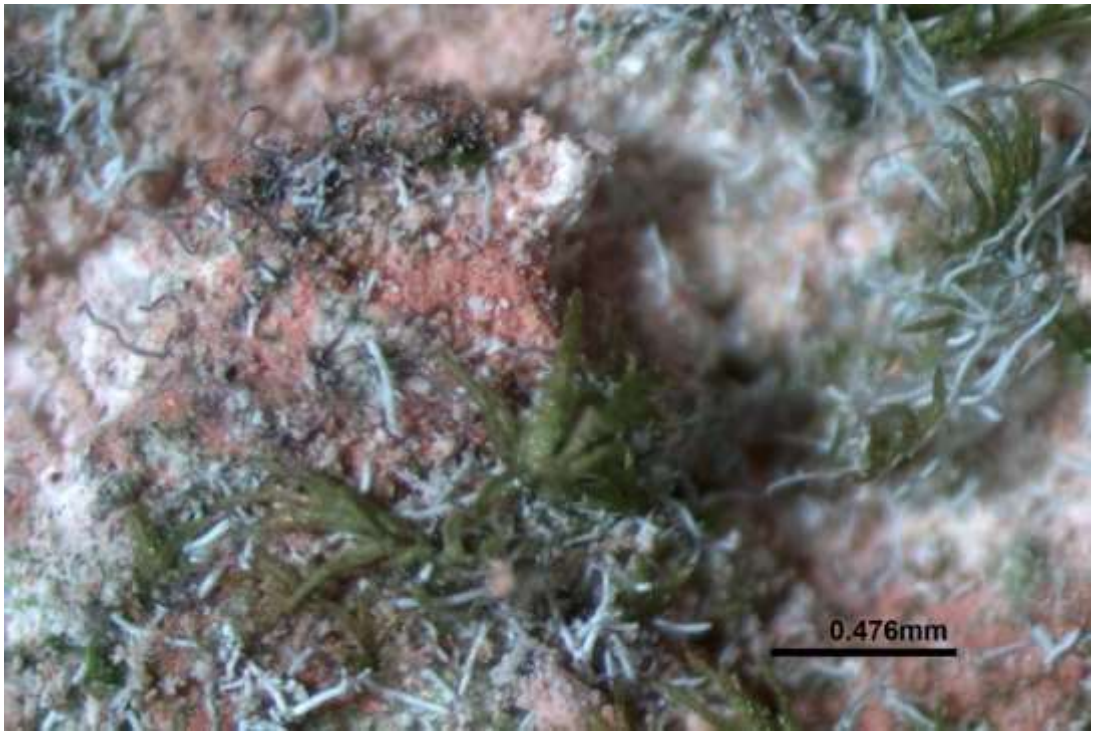

Figure 227: The surface of S16 showing biological activity.

The surface of S16 is not polished and is covered by biological activity, probably in three life stages indicated by green, white and black colorations (fig.227). The mortar consists of crushed ceramic, calcite and sand aggregates.

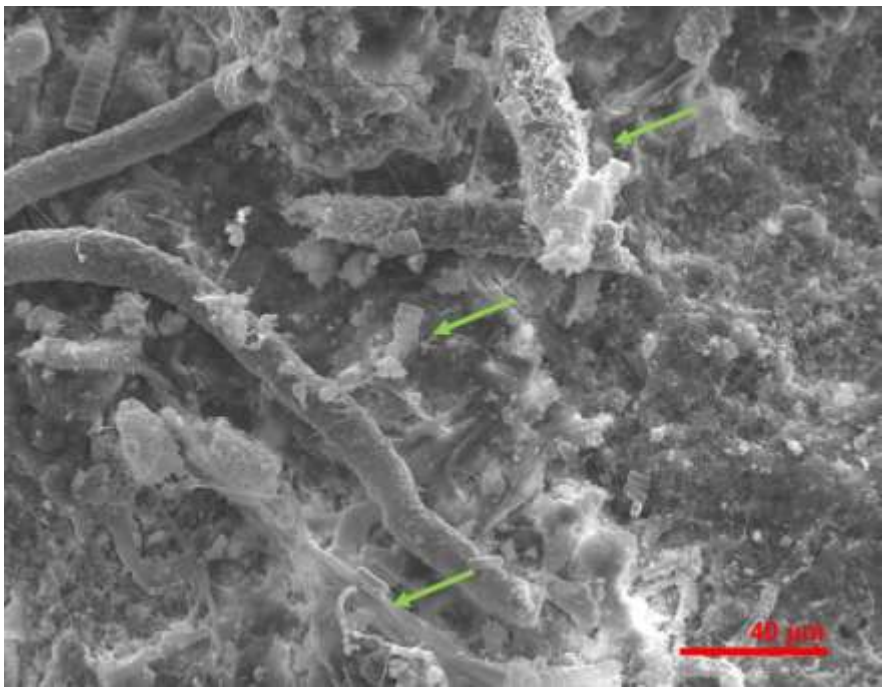

Figure 228: The surface of S16 showing variety of biological activity (green arrows).

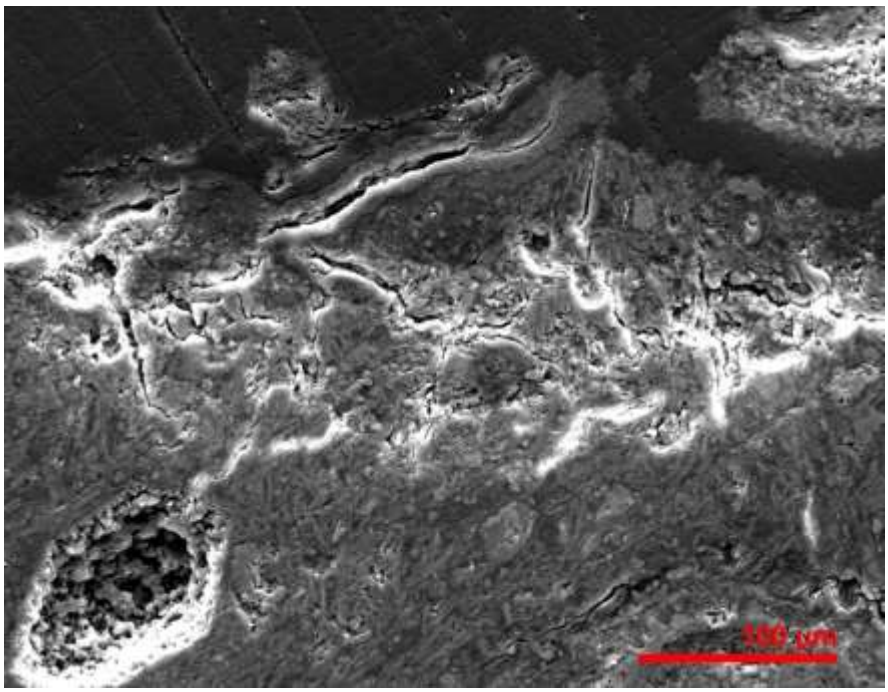

Figure 229: Cross-section showing the weathered surface of sample S16.

Variety of biological activity is observed on the surface, with filamentous fungi, hyphae and biomineralized formations (Rosado et al., 2013,4; Unkovic et al., 2017, 7) (fig.228). The

cross-section shows that the original surface is severely decayed from the increase of the biomass that causes local pressure and detachment of the surface layers as it moves inwards (Polikreti and Maniatis, 2003, 118) (fig.229).

Sample S17 – Bottle-shaped Cistern

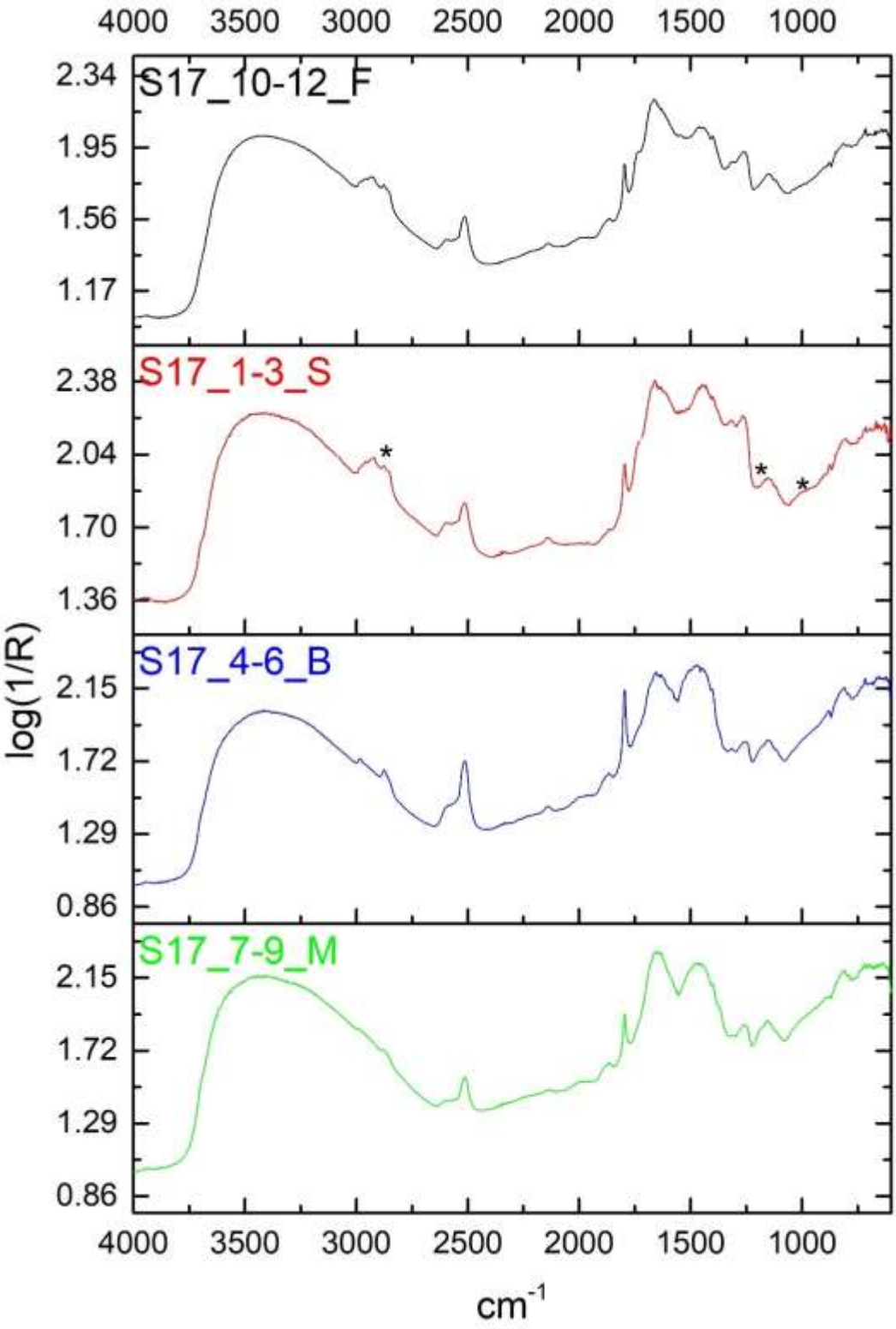

Figure 230: Sample S17: stacked spectra of individual layers. Black asterisks indicate sugars and biological activity on the surface layer.

Sample S17 is loose material collected from the bottom of the cistern, of unknown original location. Water content above 3000 cm^{-1} is high on the surface spectrum (S17_1-3_S, fig.230). Sugars or phosphates are detected at 987-1005 cm^{-1} according to CPAD comparisons to egg (whole, white and yolk) and milk standards that contain such bonds. The weak peak at 1202 cm^{-1} is assigned to sugars (Synytsya and Novak, 2014, 6) appearing also in milk/mortar standards. However, no other diagnostic milk peaks such as the 1750 cm^{-1} ester bond, were identified on the spectrum, thus milk additive is not supported. Pigeon droppings show similar peaks because of the presence of sugars and/or phosphates in their composition (Miliani et al., 2012, 300).

The peak at 1265 cm^{-1} (shape and intensity) is similar to milk, pigeon droppings but also rice (starch) standards. Egg-related CH_2 appears in 1314 cm^{-1} although milk/mortar similarities cannot be ruled out. Calcite should be indicated also due to shape at the peaks 1401-1442 cm^{-1}. The peaks at 1519-1560 indicate amides close to milk although shape similarities are detected in egg yolk and olive oil mortar standards. Amides are also present at 1631-1660 cm^{-1} (egg white/mortar). Egg, milk and rice mortar mixtures have similar shaped peaks at 2921 cm^{-1}, as does the mold standard (Appendix III, fig.40). The presence of milk-related sugar is first seen in sample S17 and likely characterises biological activity, rather than mortar additives.

The flat surface layer (S17_10-12-F) is similar to the cross section of the surface, with the presence of mold but less amide content. The B and M spectra are almost identical. The main difference is the calcite content that seems higher on the B spectrum (S17_4-6_B). Given the fact that the mortar has a high ceramic content this is expected and proven by the presence of 1771 cm^{-1} peak diagnostic to the clay standard. Amide is detected at 1317 and at the 1450 and 1650 cm^{-1} regions for both spectra. The organic content is lower than that in the surface spectrum.

Identical biological activity with S16 is observed on the surface of sample S17 on the microphotographs and SE images (images not shown).

Bottle-shaped cistern - Results Summary

The samples derive from the interior wall of the cistern and from the floor (random collection). Both are highly contaminated by biological activity in different life stages. The samples do not have polished surfaces and are basically mortar of high ceramic inclusions. Peaks related to sugars, similarities to milk/mortar and mold on bone glue standards should be interpreted as diagnostic of biological activity.

The spectra show mainly protein such as that detected in egg white and bone glue mortar standards. However, the shape of peaks shows similarities with that of pigeon droppings and may mean biological activity is responsible. Organic presence is mainly preserved on the surface (cross-section).

Sample S18 - Bathtub

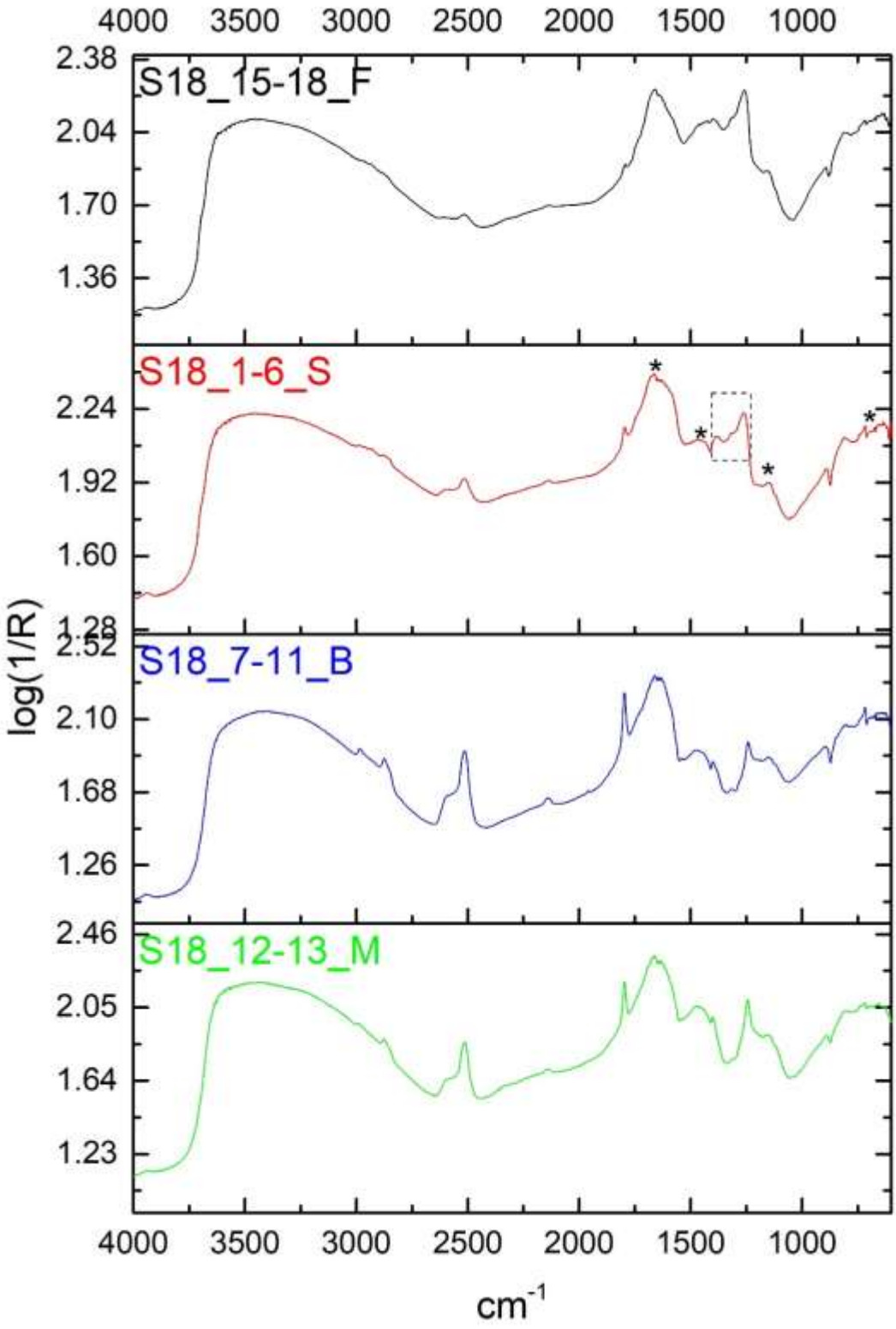

Figure 231: stacked spectra of individual layers of sample S18. Marked areas indicate organic presence on the surface spectrum.

Mortar components are low and water content is high at the surface spectrum (S18_1-6_S, fig.231). Lipids prevail in 1261, 1317 and 1375-1386 cm^{-1}. Such peaks are present in lard, egg yolk and milk mortar standards (section 7.5). Proteins related to egg yolk and milk are present in 1450-1517 cm^{-1} although their shapes differ. The same stands for the proteins in 1631-1666 cm^{-1}.

The peaks at 807 in combination with 743-717 cm^{-1} are also present in lard followed by egg yolk and milk. The reststrahlen in 888 cm^{-1} is related to calcium carbonate ion, thus it is present in both $CaCO_3$ and casein standards (Ylmen and Jaglid, 2013, 119). The 1194 falls within the sugar region although sulphates may be present. Lard and egg yolk mortar mixtures, as well as milk have similar peaks in that region.

The flat surface spectrum (S18_15-18_F) is similar to S spectrum, although less peaks are observed (fig.231). The mortar content is very low and it is debatable whether to assign the peaks 1400-1426-1437 cm^{-1} to calcite instead of lipids. Phosphates are present in 1154-1164 (bone glue and egg yolk mortar standards). The peak 1259 is very strong and there is an indication of the 1313 peak, closer to egg yolk lipid C-O peak.

The peaks 1400-1437 show C-H bonds linked to egg products and their mortars and some relationship to bone glue/mortar (although this could be the calcite in bone glue mortar mixture), as do peaks at 1641-1659 cm^{-1}. While egg, white and egg yolk mixtures are possible matches, similarities are also found in droppings standards and this could indicate biological origin.

The spectra interpretation of protein-lipid containing materials so far suggests that when the C-O absorption at 1260 cm^{-1} is higher than the rest of the organic peaks in the region, shifting towards higher wavenumbers (up to 1280) indicates higher lipid content than protein. When the opposite occurs and the shape moves to stair-step type intensities, then proteins prevail and C-O is linked to proteins. This could be useful for identifying differences among egg parts in inorganic matrices.

The spectrum below the surface contains the highest amount of calcite (S18_7-11_B). All the layers contain the same pronounced lipid-with-some-protein content. However, the surface layer contains peaks at 1375-1386 cm^{-1} which are not visible in the rest of the spectra and are attributed to a higher lipid content.

The fact that high lipid content was detected in all the layers of the sample could be attributed to a) contamination of all layers with the organic substance since the sample

was semi-detached from the bathtub wall or b) intentional use of organic substance as an additive in the mortar mixture rather than a coating.

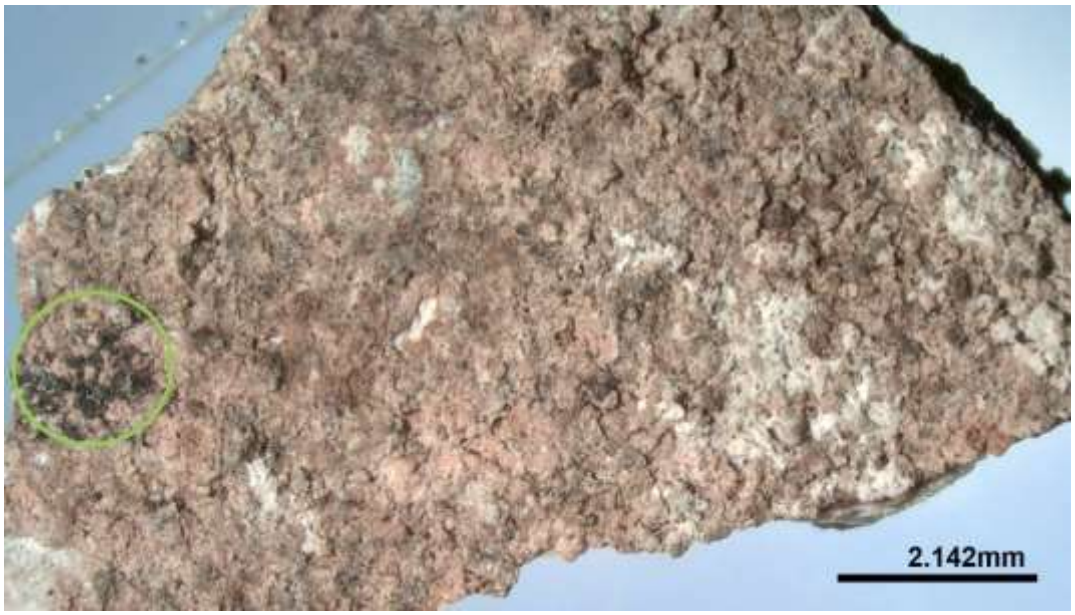

Figure 232: The surface of S18 showing built-up of deposits and localized black spots (green circle).

Figure 233: The cross-section of S18. Green arrow points to a fine white surface layer under brown patina.

The surface under the microscope reveals a built-up of deposits and black spots locally, likely of biological origin (green circle, fig.232). A fine white surface layer is visible under the brown patina (green arrow, fig.233). The mortar consists mainly of crushed ceramics and calcite. The black spots visible within the mortar are from the prior SEM carbon coating and should be ignored.

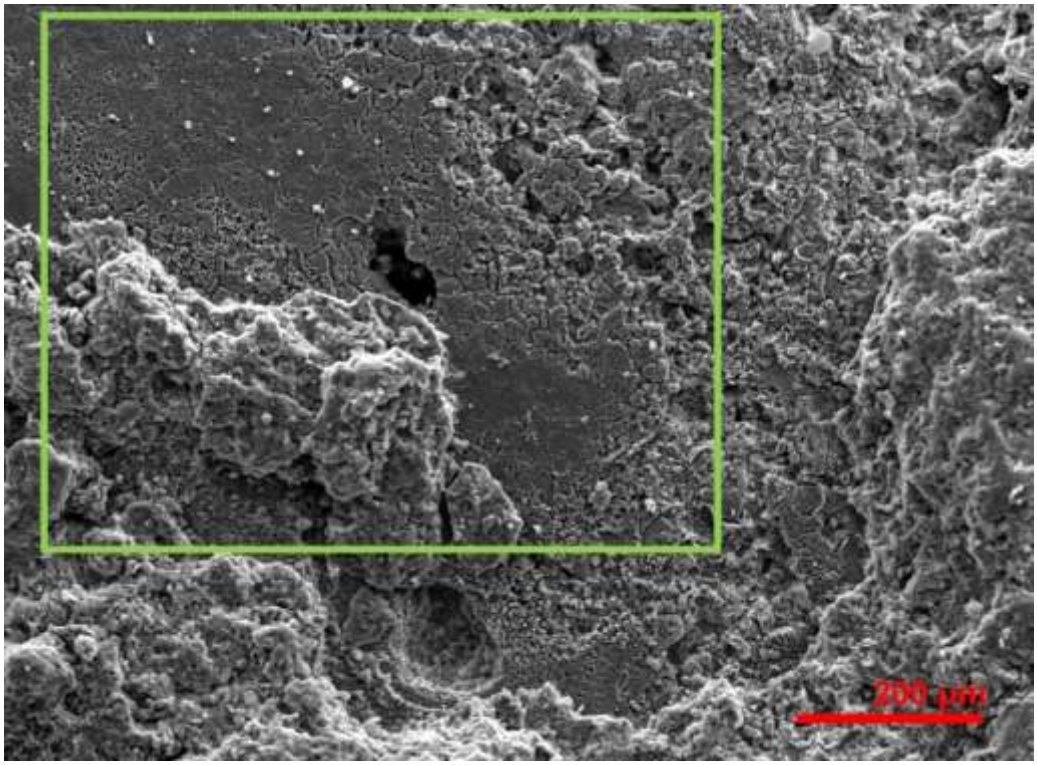

Figure 234: SE image of the surface of S18. Polished surface (green frame) underneath deposits or re-crystallized calcite.

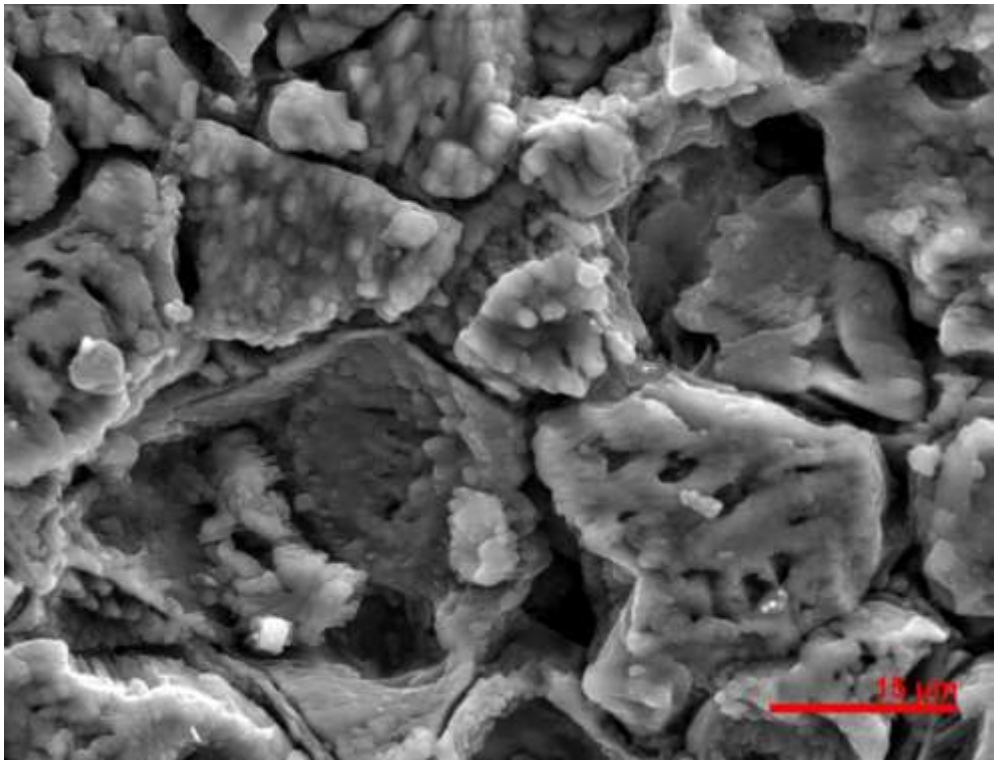

Figure 235: The polygonal crystals on the decayed original surface.

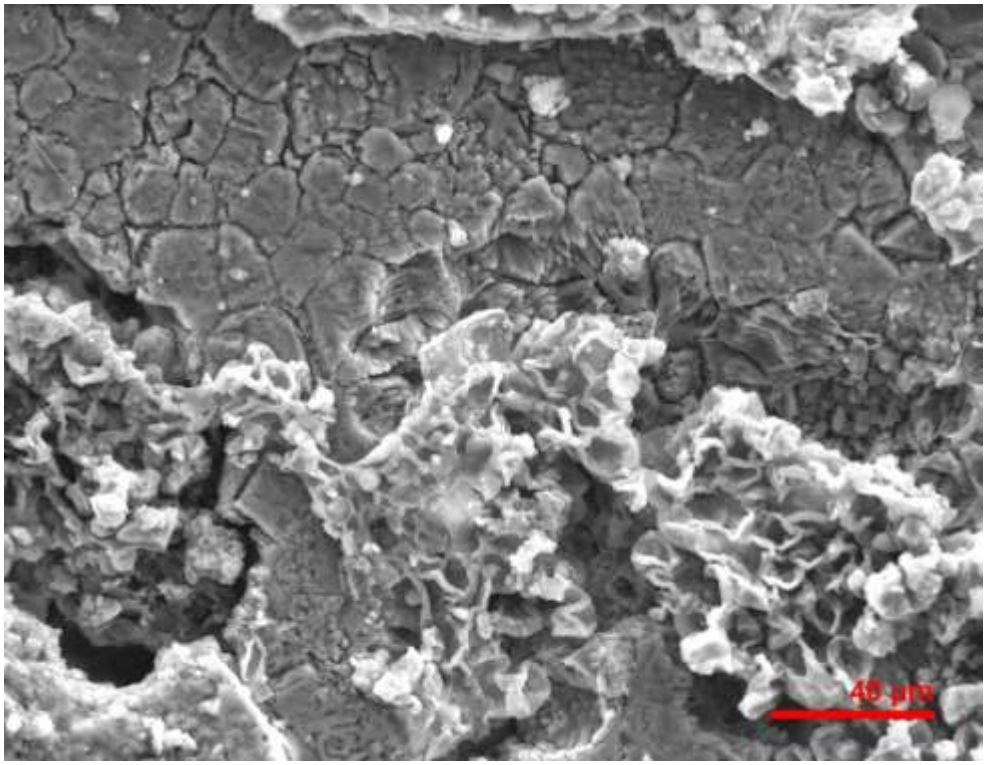

Figure 236: Algal cell growth from within the original surface.

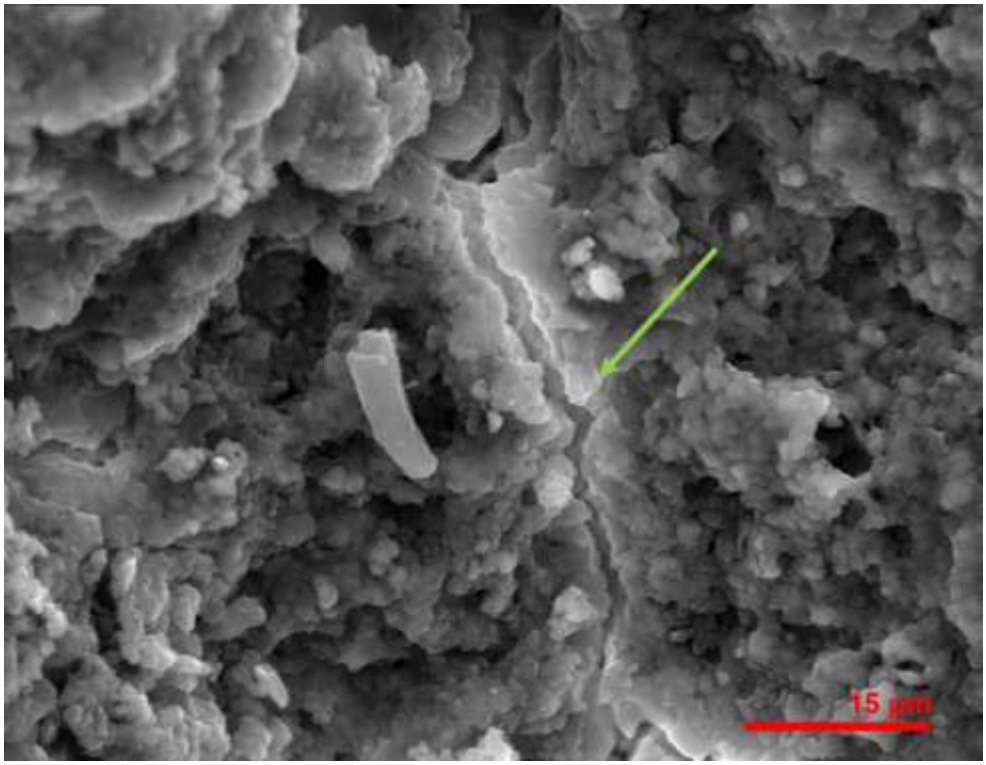

Figure 237: Suspected resinous substance on the surface of S18 (green arrow).

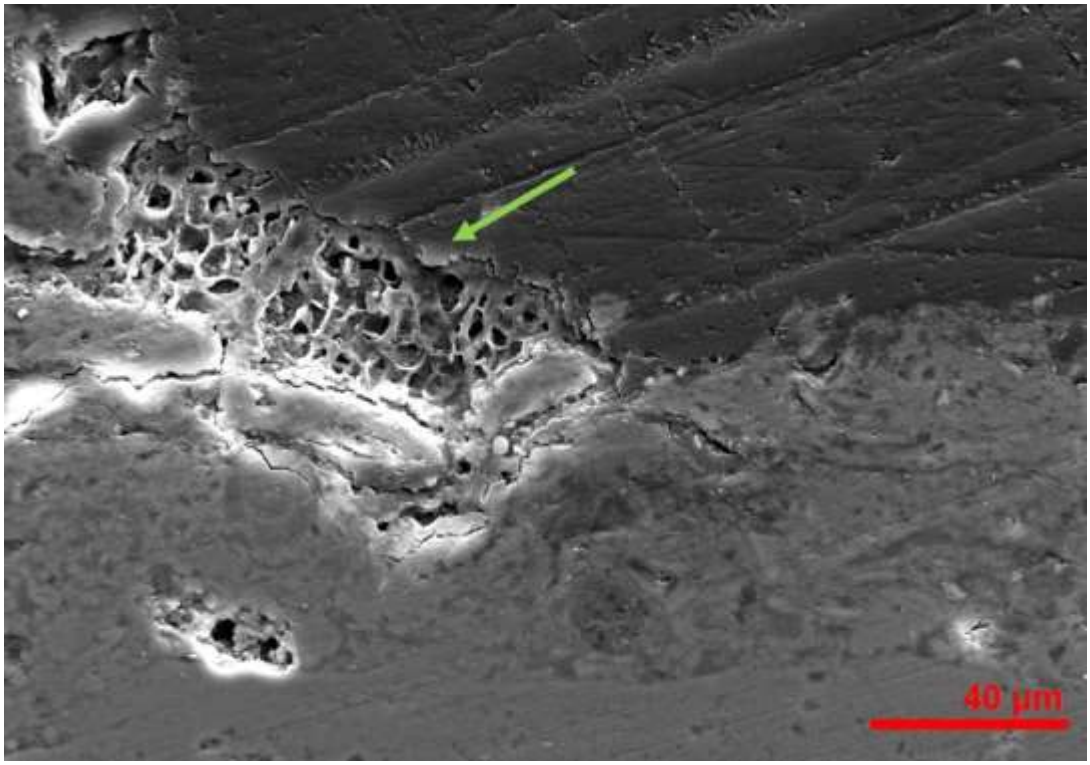

Figure 238: The suspected biological growth on the surface (cross-section).

The surface appears polished and is preserved under deposits or some form of re-crystallized calcite (marked area, fig.234). Closer look on the decayed original layer shows polygonal crystals with amorphous colloidal phase that resemble deterioration from lichen (Sanz et al., 2017, 766) (fig.235). Algal cells emerge from within the original layer showing a consumption process of calcite and/or the organic component (Sanz et al., 2017, 766) (fig.236). The resinous texture on the surface resembles that of the egg/mortar standard, although the presence of biofilm cannot be ruled out (pointed by the arrow, fig.237 and fig.168, Sample 3 sec.10.3.1). Localized algal cells appear on the upper brown surface layer affecting the coherence of the fine calcite layer (pointed by the arrow, fig.238).

Bathtub – Results Summary

Lipids prevail in the spectra, with egg yolk being the most closely related standard, followed by milk and casein. However, biological origin of lipids cannot be ruled out. The similar concentration of organic material in all layers suggests either an organic additive in the mortar mixture or biological contamination of all layers since the sample was semi-detached from the masonry.

A whitish-pink patina covers the entire sample surface with a light brown under layer. The amorphous colloidal phase within deteriorated polygonal crystals of original surface may indicate an organic that is not of biological origin. The algal cells emerging from within the

original surface show biological activity, likely lichens, but calcium oxalates that result from the action of lichens is not supported by the FTIR results (Sanz et al., 2017, 767).

Sample S19 - Three-aisled cistern

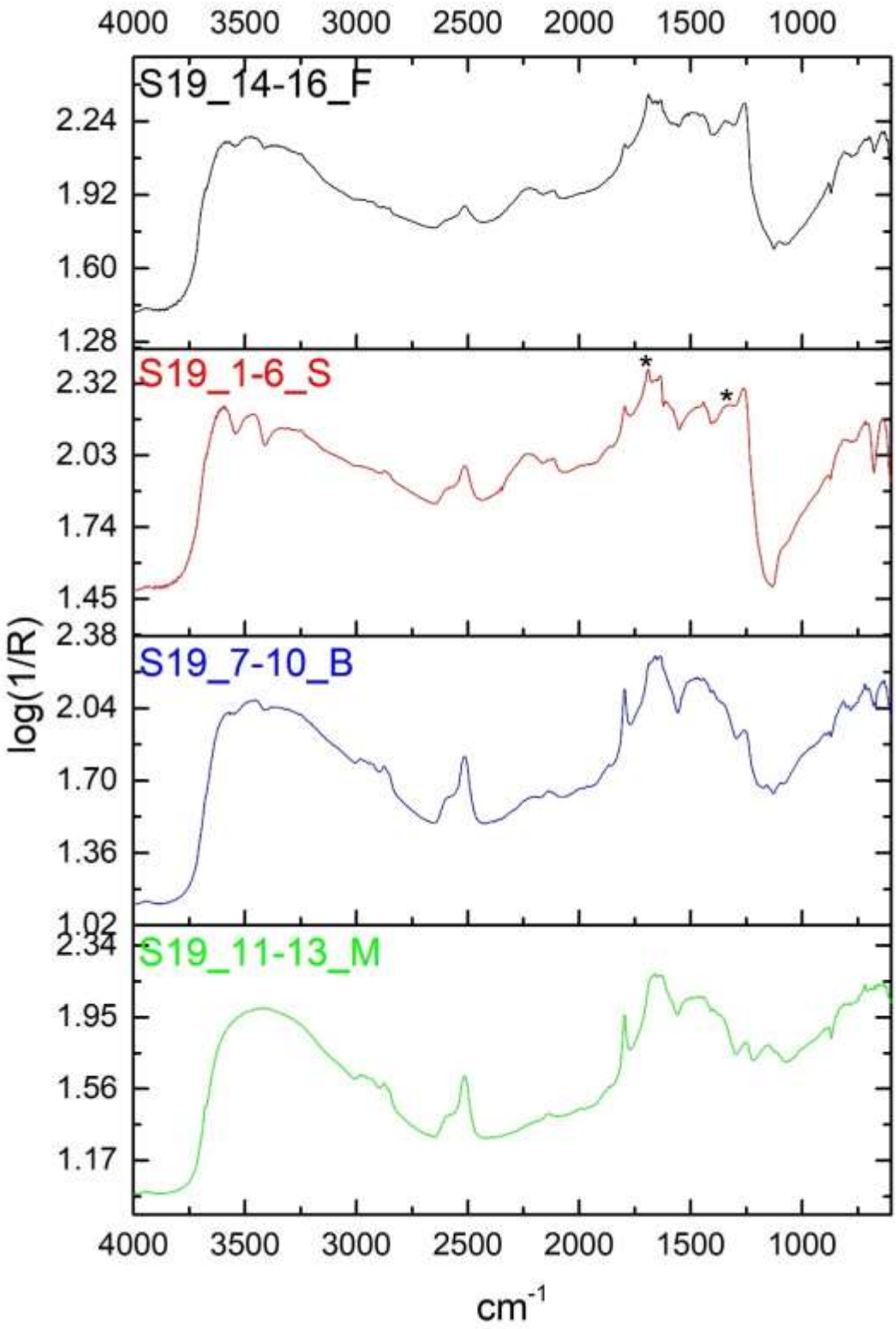

Figure 239: stacked spectra of individual layers of sample S19. Marked areas indicate organic presence on the surface spectrum.

S19 derives from the wall of the 1st aisle, opposite the entrance, where biological activity is macroscopically visible and thus is expected on the sample surface. The surface spectrum (S19_1-6_S) is dominated by gypsum and calcite (fig.239, Appendix III, fig.41). The absence of 1159 cm^{-1} quartz peak shows that $CaCO_3$ is the main detected mortar component. The peak at 1261 cm^{-1} is assigned to gypsum instead of an organic component due to its shape and intensity and the co-existence with other diagnostic gypsum peaks. The 1319 cm^{-1} should be attributed to C-O ester. The weak peak at 1398 cm^{-1} is related to C-H, possibly indicating proteins. The peaks 1443-1466 cm^{-1} should be also assigned to protein since similar peaks are detected in milk, bone glue and egg white mortar standards. However, these are mixtures of 25 and 5% organic additive therefore, these peaks may also be related to calcium carbonate ions. N-H bands are present in 1659 and 1691 cm^{-1}.

The flat surface spectrum (S19_14-16_F) exhibits lower mortar and gypsum content than the surface spectrum which may be due to gypsum growth starting within the underlying layers. Protein, similar to egg white and bone glue mortar standards, is detected (fig.239).

Peaks indicating protein and gypsum become less pronounced towards the mortar, although protein is retained in all layers. The protein in the mortar layer is observed at 1444, 1642 and 1658 cm^{-1}. The highest gypsum and protein content is preserved in the cross-section surface spectrum, underneath the white calcite crust.

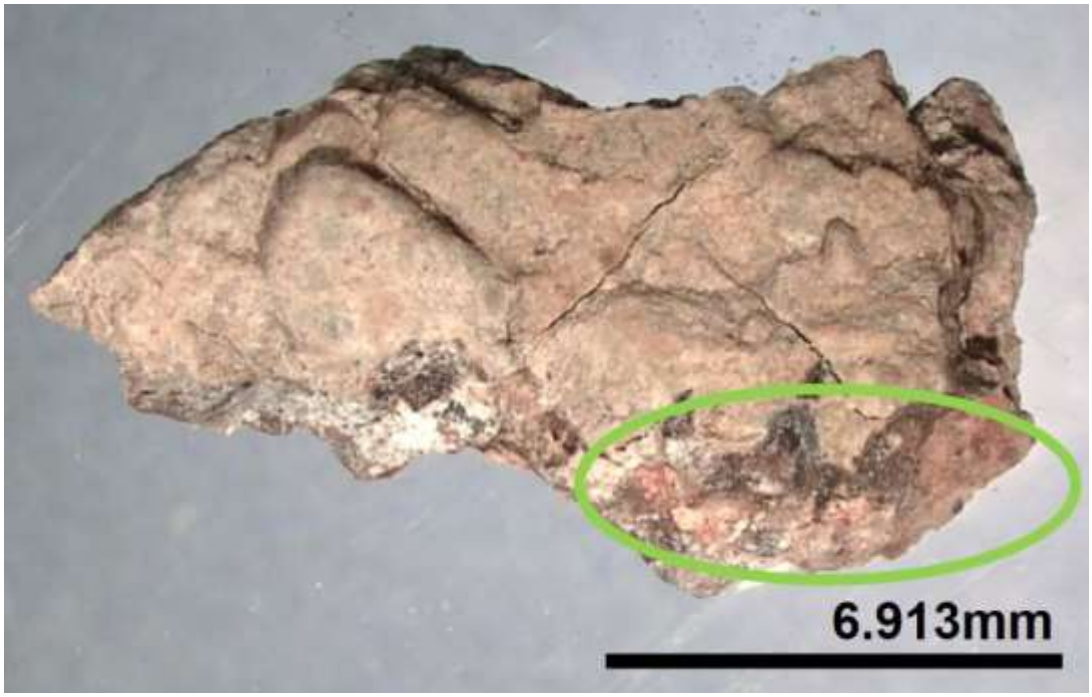

Figure 240: The thick, white crust that covers the surface of S19; part of the original surface is preserved underneath the crust (circled).

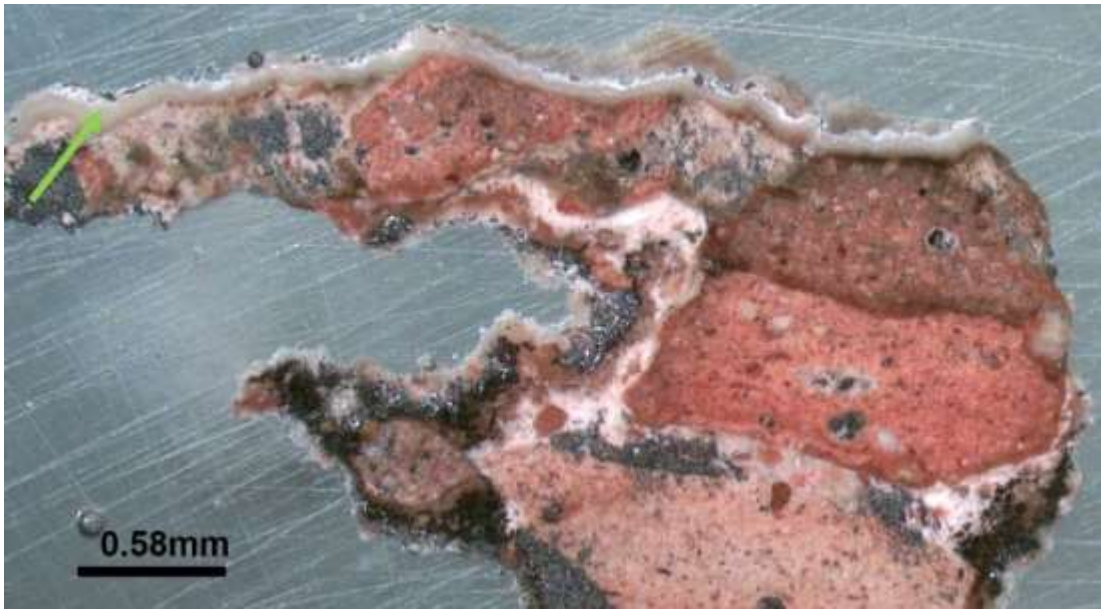

Figure 241: The cross-section of S19 showing the high amount of crushed ceramic inclusions.

A thick, white crust covers most of the surface, although the original brown surface is exposed locally (circled, fig.240). The mortar consists of high amount of crushed ceramic inclusions and calcite (fig.241). The surface layer is not easily defined, likely due to weathering and/or incorporation to the white crust (pointed by the arrow, fig.241).

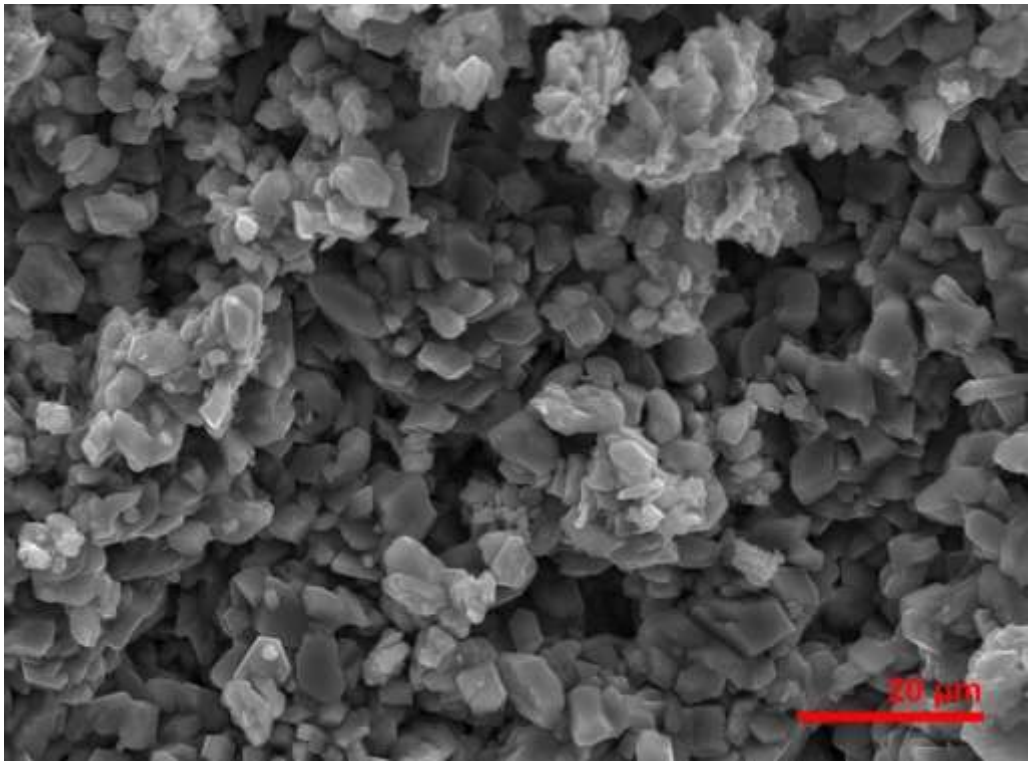

Figure 242: SE image of the white crust on the surface of S19.

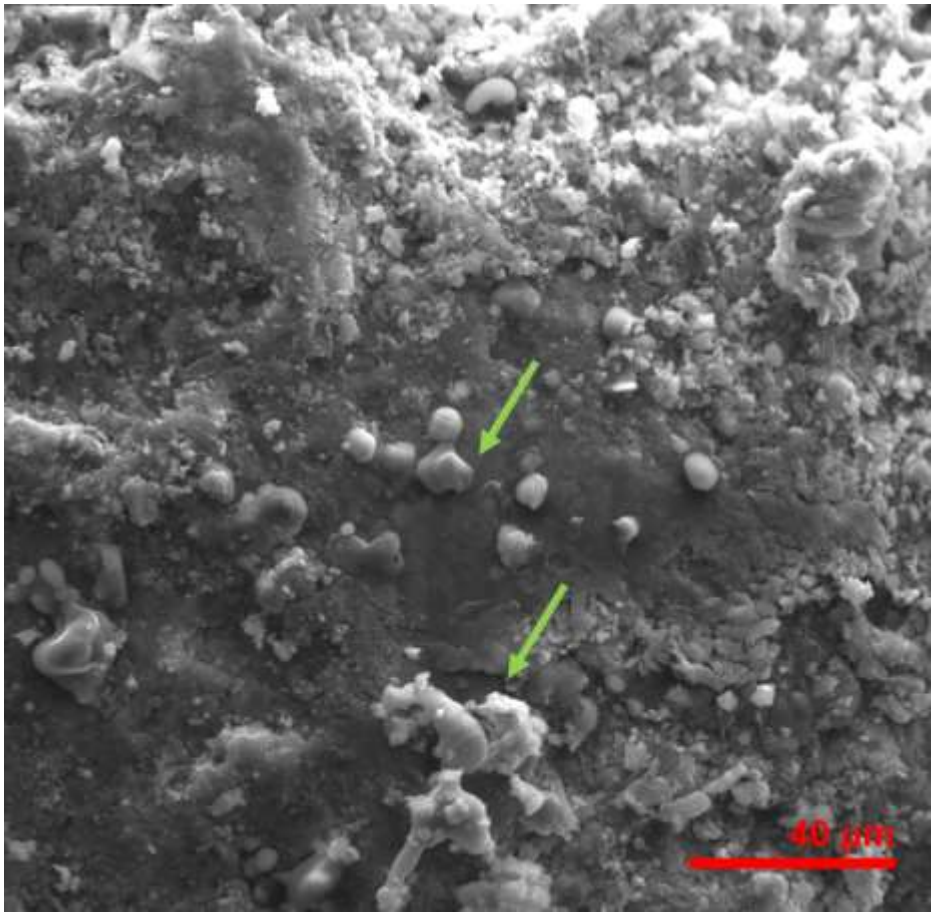

Figure 243: SE image of part of the surface that is free of white crust showing localized biological activity (green arrows).

The surface is covered by a thick layer of deposited calcite (Unkovic et al., 2017, 7), supporting the FTIR outcomes relative to the absence of gypsum on the flat surface and the presence of calcite (fig.242). The worm-like features on the original smooth surface indicate localized biological activity (Gomez-Alarcon et al., 1995, 237) (pointed by the arrow, fig.243). The texture of the original surface resembles that of S2 and S3 samples from Polyrrhenia (sect.11.3.1).

Sample S20 - Three-aisled cistern

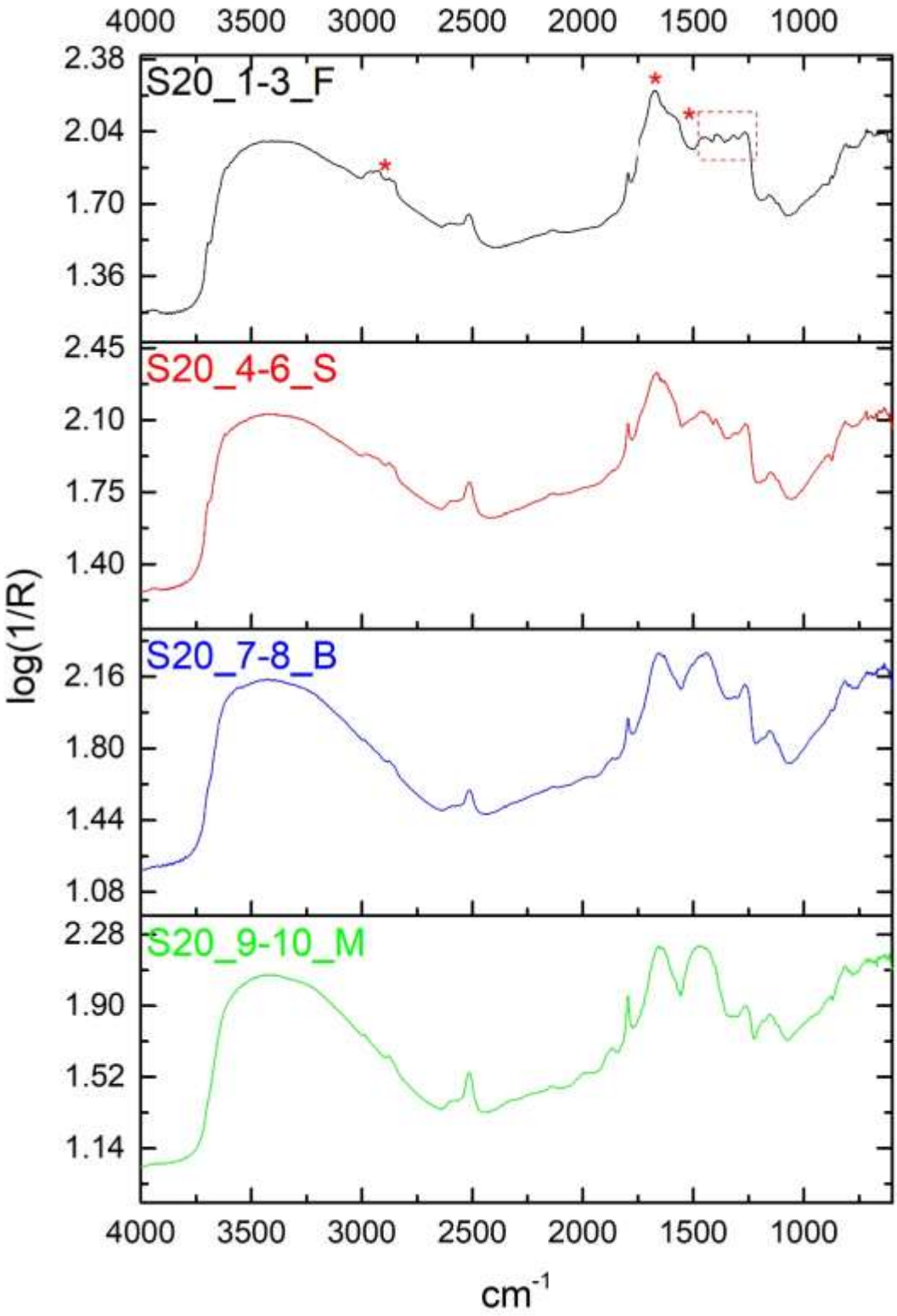

Figure 244: stacked spectra of individual layers of sample S20. Marked areas indicate organic presence on the flat surface spectrum.

The sample was taken from the floor of the 1st aisle that is highly contaminated by pigeon droppings and other deposits from the regular rainwater flooding of the cistern. The flat surface spectrum (S20_1-3_F) exhibits very low presence of mortar and high protein content, detected at the stair-step type intensities of amides in 1265-1459 cm^{-1} (fig.244). These peaks match those of bone glue although proteins of pigeon droppings are also detected in the same ROI (Fujita and Koike, 2007, 648). Egg parts and their mortar mixtures also present similarities. Phosphates at 1041-1061 cm^{-1} appear also in all these possible matches, including the pigeon droppings. Low lipid content is indicated at 1390, 1507 and 2926-2959 cm^{-1}. The amide peak at 1672 cm^{-1} is highly similar to that on the pigeon droppings spectra. This complex mixture of identifications and possible wide range of interpretations illustrates the challenges of definitive outcomes when seeking to determine both origins of organics detected and then specific organic itself.

The surface spectrum (S20_4-6_S) is highly similar to the flat surface spectrum. A sharp peak at 1400 cm^{-1}, that does not match the broad band of $CaCO_3$, should belong to CH_2 bands of esters such as those of milk and egg standards. Mold and dropping standards show the 1400 cm^{-1} peak and it is likely that this is a diagnostic peak to biological activity. The spectra of all layers show protein that decreases gradually towards the mortar (fig.244).

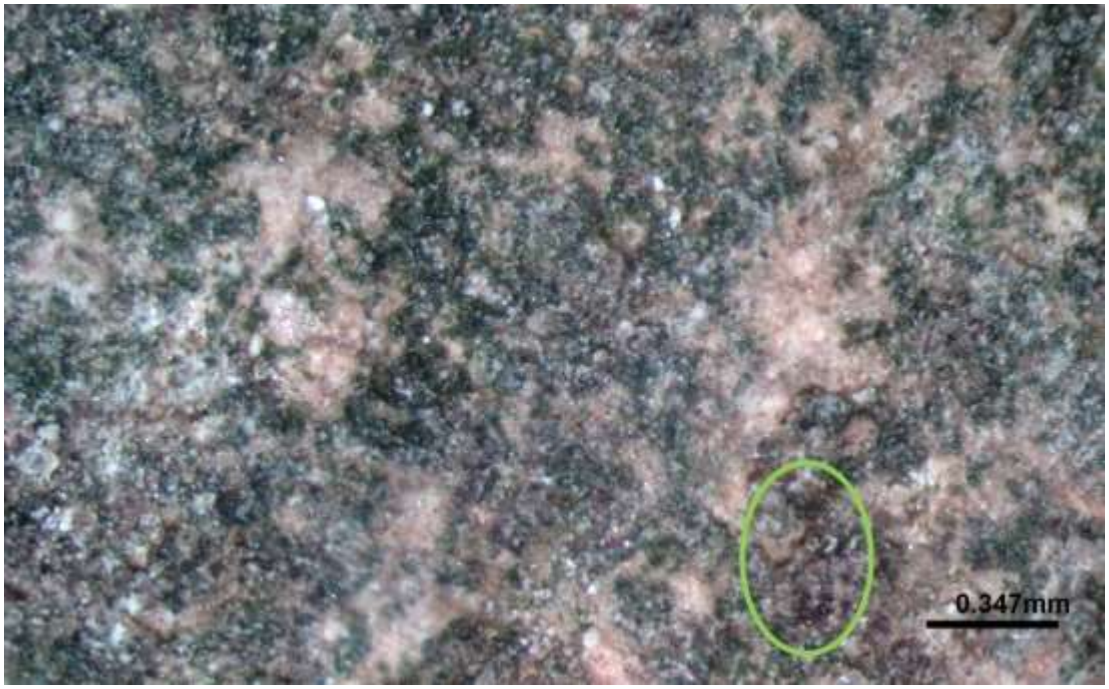

Figure 245: The surface of S20. Resinous deposits (circled) exist within a variety of other loose deposits.

Surface deposits vary in colour and texture: some are black/dark green, some are white and loose on the surface and some are resinous (green circle, fig.245). The mortar consists of high amount of crushed ceramic, calcite and low amount of quartz (image not shown).

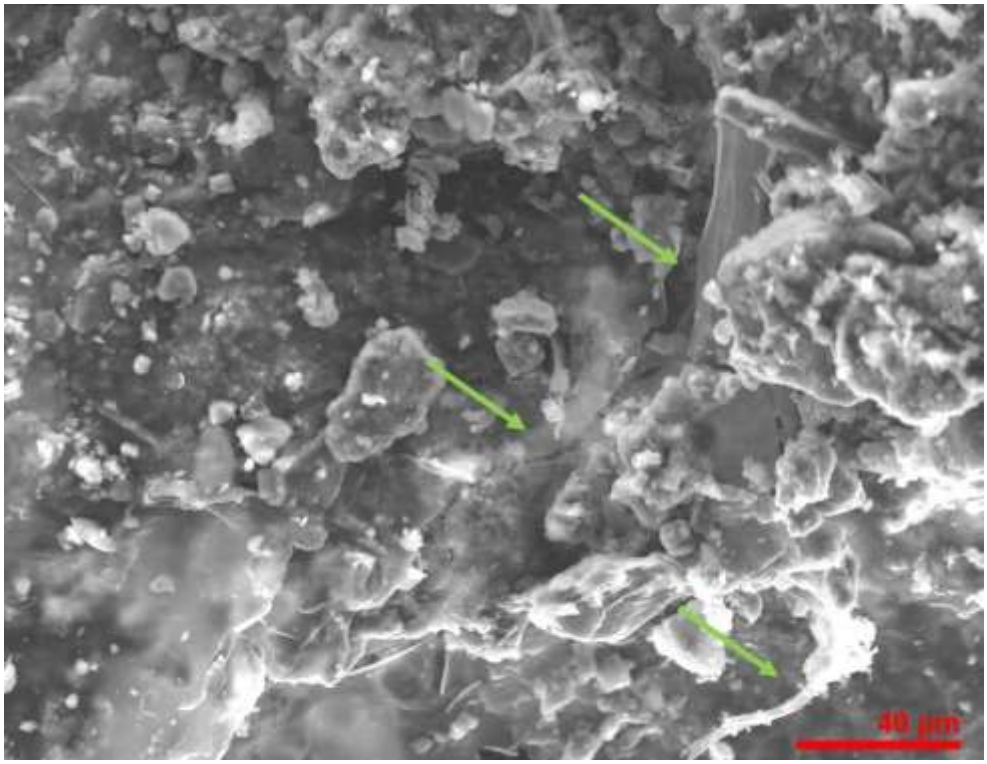

Figure 246: Resinous substance and filamentous biological activity on the surface of S20 (pointed by the arrows).

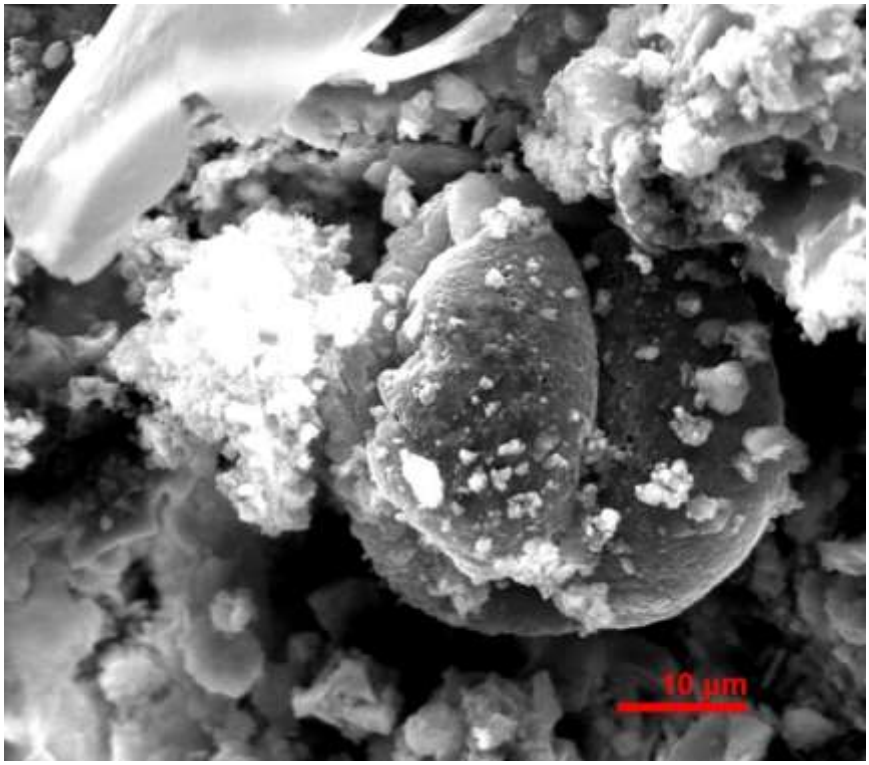

Figure 247: Deposition of spores on the surface of S20.

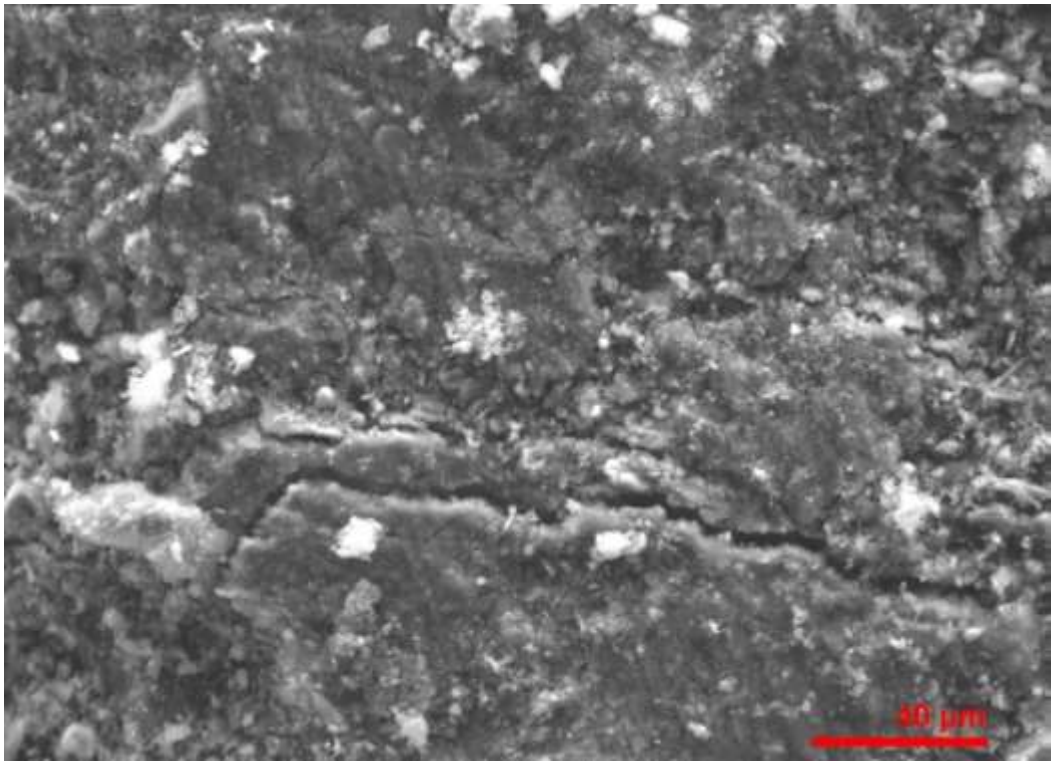

Figure 248: Original surface layer of S20. Parallel lines indicate polishing.

The surface shows filamentous biological activity, spores and flaking substance, likely a biofilm (Priester et al., 2007, 583) (fig.246-247). However, the original surface that is free

of such microorganisms appears as mortar, probably polished as indicated by the presence of parallel lines (fig.248).

Sample S21 - Three-aisled cistern

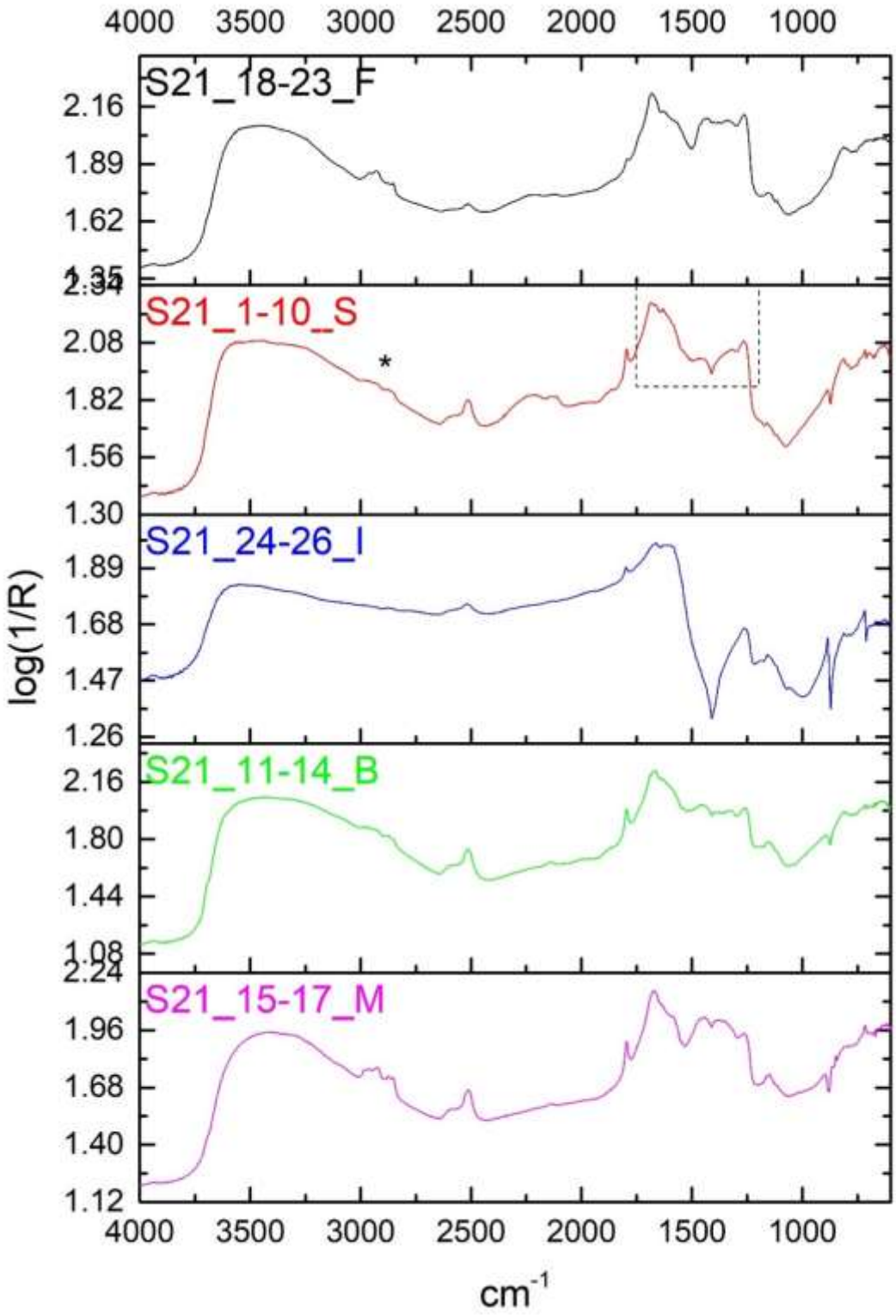

Figure 249: stacked spectra of individual layers of sample S21. Marked areas indicate organic presence on the surface spectrum.

The sample was collected from the connection of the floor to the wall, 2nd aisle. The surface spectrum (S21_1-10_S) contains gypsum and amides-esters similar to those in egg parts and their mortar mixtures and in pigeon droppings standards (fig.249).

The flat surface spectrum (S21_18-23_F) shows high amount of ester and water content and low gypsum and mortar components. Organic presence is more pronounced here than in the surface spectrum. Phosphorus or Sulphur content similar to that in the pigeon droppings standard is detected at 1045-1065 cm^{-1}. The peak 1265 cm^{-1} is not assigned to gypsum, as in the case of sample S19, because gypsum presence is low, as observed by the shape and intensity of its diagnostic peaks. Instead, the 1265-1507 cm^{-1} peaks are assigned to protein since they resemble the stair-step type intensities of egg and bone glue standards. The peaks 1377, 1401 1432 and 1507 cm^{-1} could also be assigned to pigeon droppings. The shape of 2853 and 2927 cm^{-1} resembles that of egg esters although mold is also a possible candidate.

The spectrum of the inverted black surface (S21_24-26_I) is similar to the S14_13-17_B spectrum of Polyrrhenia (fig.182, Sample S14 section 11.3.1), indicating dolomite and very low protein-lipid detection. The below and mortar spectra collected show mainly protein and ester, with an absence of gypsum (S21_11-14_B and S21_15-17_M, fig.249).

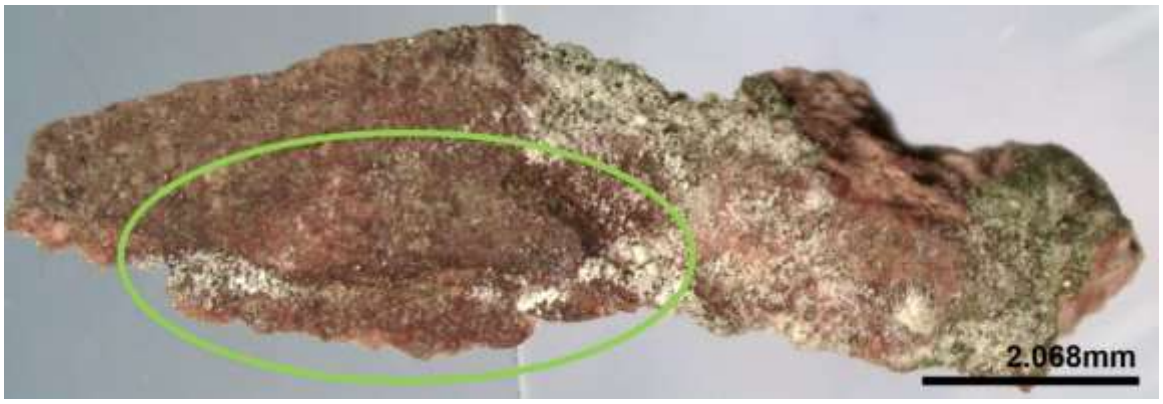

Figure 250: The surface of S21.Brown resinous substance is visible underneath deposits (circled).

The surface is locally covered by green biological activity and white loose crystals. A brown resinous substance is visible underneath these deposits (circled area, fig. 250).

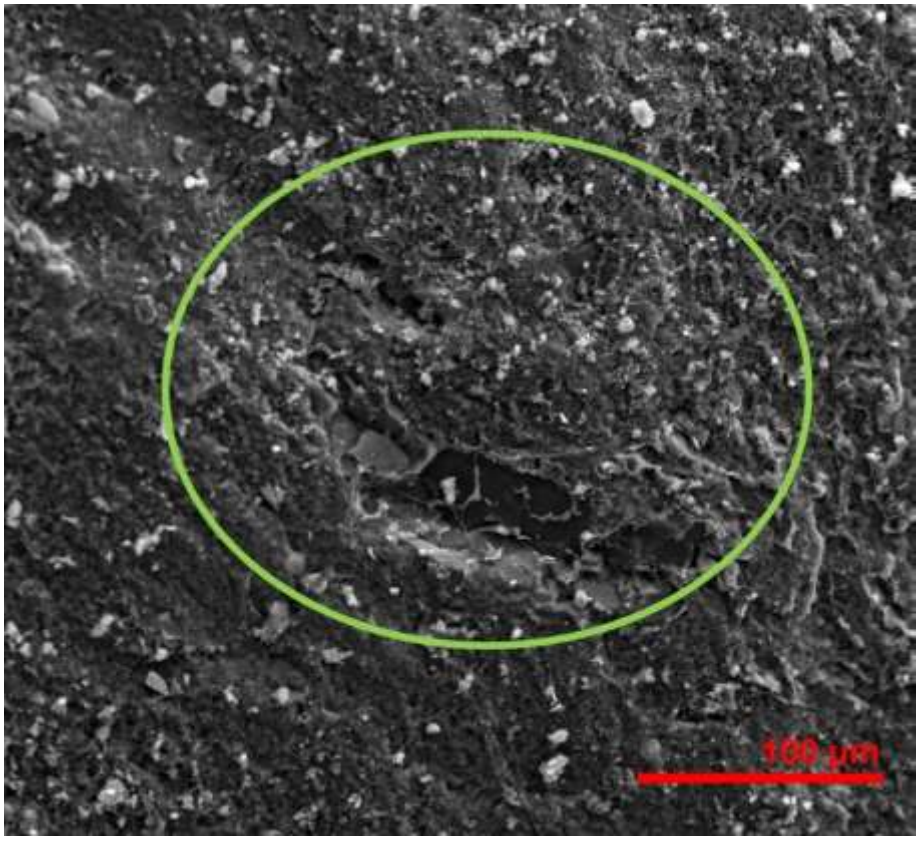

Figure 251: SE image of the surface of S21. Fibrous growth of either early biological colonization or gypsum formation (circled).

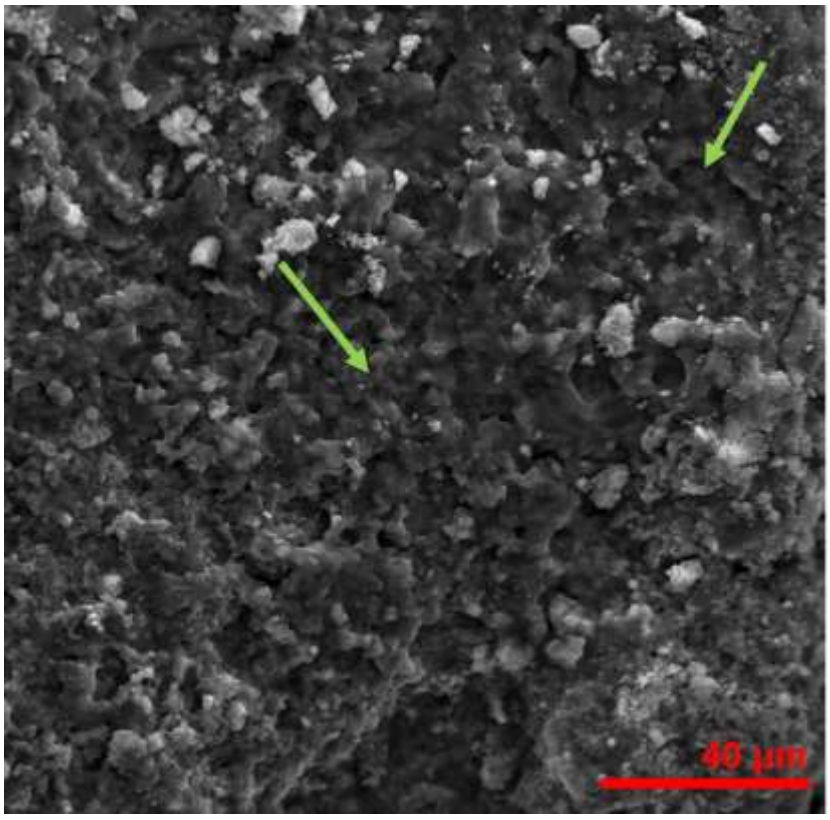

Figure 252: Amorphous regions on the surface of S21 (pointed by arrows).

Fibrous growth on the surface may indicate early biological colonization or gypsum formation (circled area, fig.251). Amorphous regions are also present, probably corresponding to the resinous substance observed on the micro-photographs (pointed by the arrows, fig.252).

Sample S22 - Three-aisled cistern

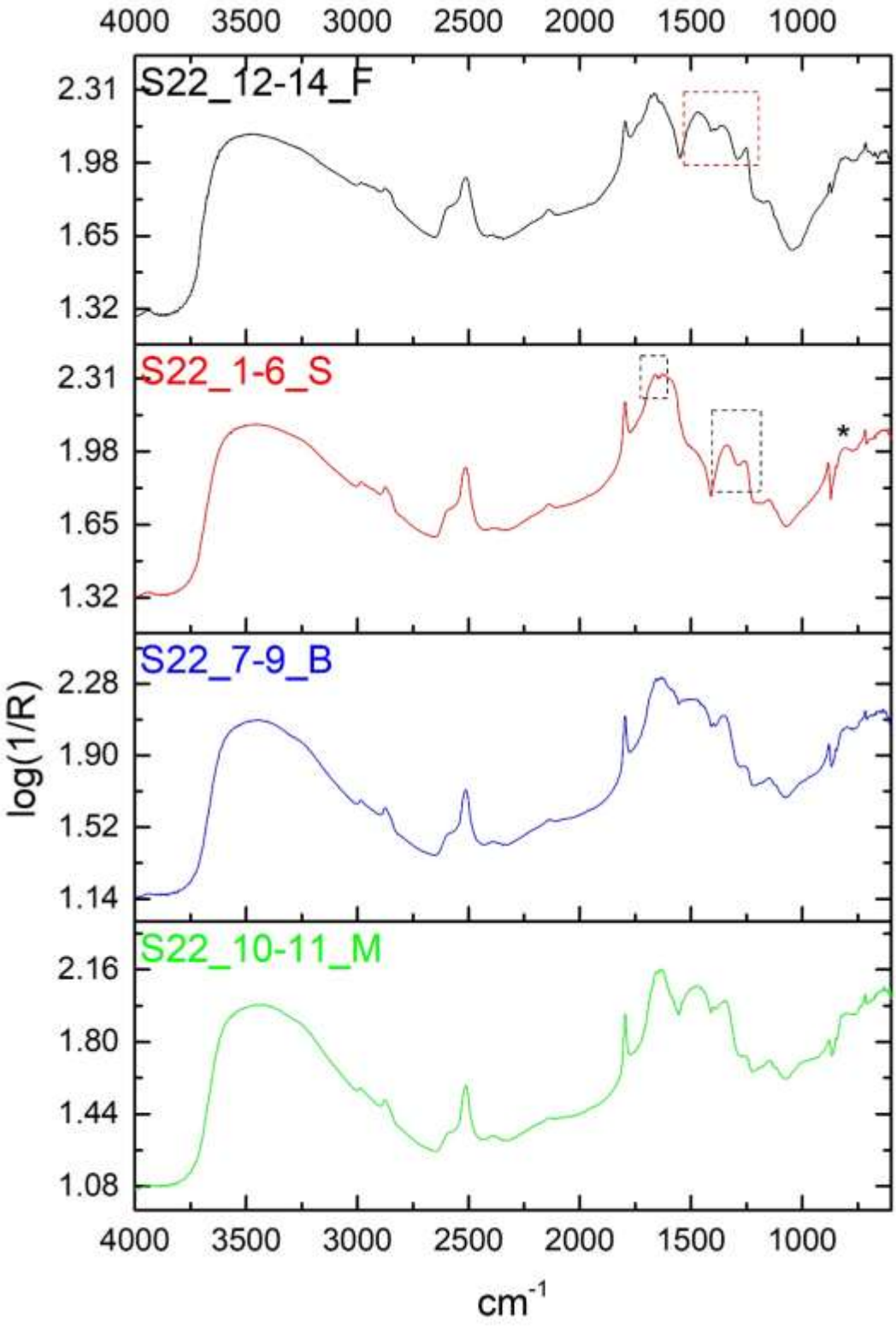

Figure 253: S22 stacked spectra of individual layers. Marked areas indicate organic presence on the surface spectrum (S) and the flat surface spectrum (F).

The sample was taken from the surface of the wall at the 2nd aisle (Appendix III, fig.13). Pronounced mortar peaks are visible on the surface spectrum (S22_1-6_S, fig.253). The broad and weak peak in 801-808 cm^{-1} could indicate CO bond, related to lipids similar to these of egg yolk, egg and milk standards. The region of interest is within 1147-1659 cm^{-1}, especially the ROI 1261-1341 cm^{-1} also seen in POL_S14 surface spectrum (S). Esters, as in egg standard, are assigned to 1261-1341 and amides to 1619-1659 cm^{-1}. The peak at 1201 cm^{-1} could indicate sugars. High egg-resembling content is detected on the flat surface spectrum (S22_12-14_F). The organic material reduces gradually towards the mortar.

Figure 254: The surface of S22 appears pink to light cream under loose white particles.

Figure 255: The cross-section of S22. The mortar consists mainly of lime and quartz.

Sample S22 and S19 have similar pink to light cream surface coloration, although S22 is not covered by white crust (fig.254). Loose white particles are visible on the surface together with black/green spots that could indicate biological activity. The mortar layer consists mainly of lime and quartz with limited inclusions of crushed ceramic, differing considerably from the S19 mortar layer that consisted mainly of ceramic inclusions (fig.255). Ignore black areas within the mortar as they are carbon coating residue.

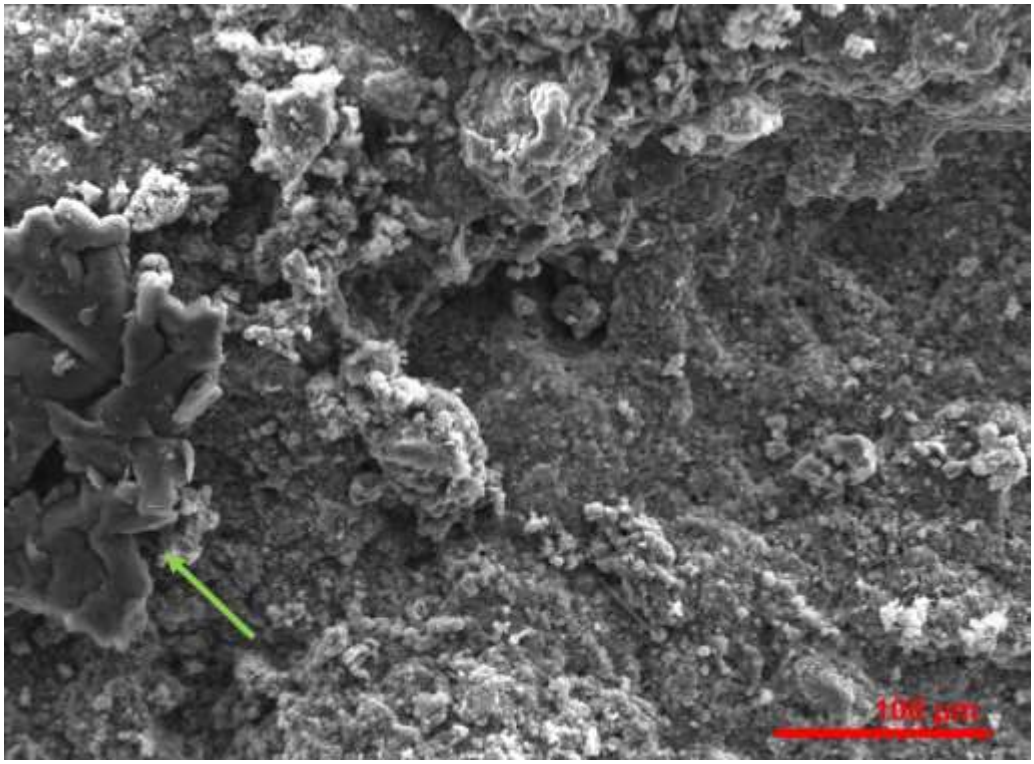

Figure 256: SE image of the surface of S22 showing built-up of crystals (pointed by the arrow).

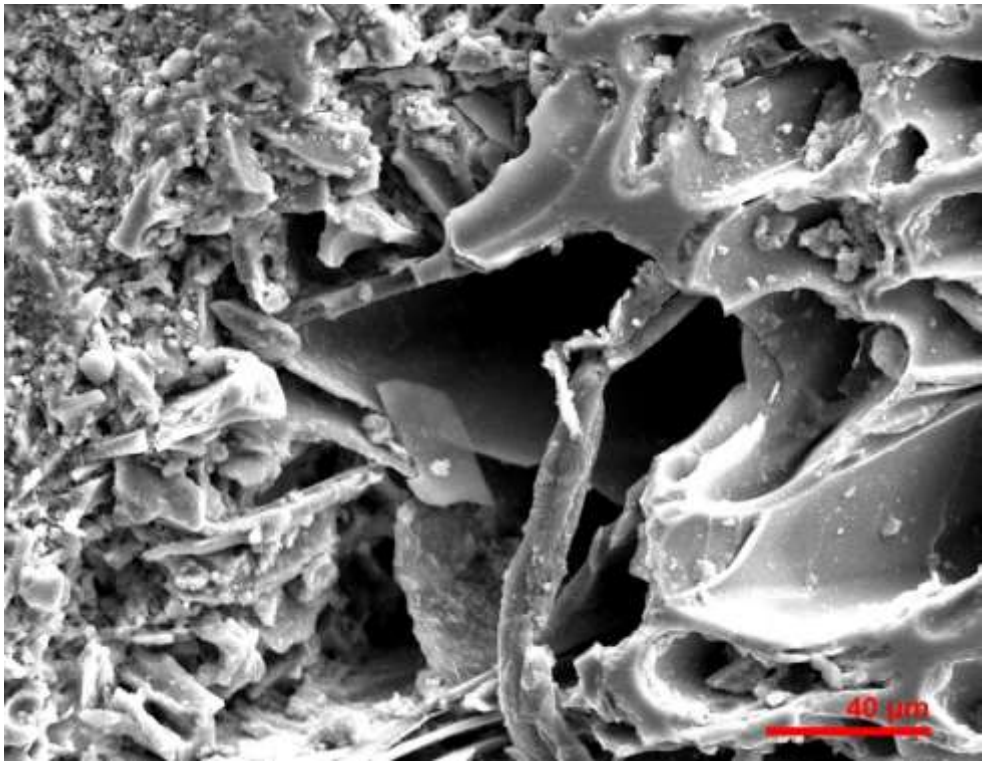

Figure 257: SE image of pumice in the mortar layer of S22.

The surface does not show evidence of organic presence either intentional or biological (fig.256). The complex built-up of crystals could be the loose white particle observed in the OM images (pointed by the arrow, fig.256). The mortar layer incorporates a high amount of pumice (Liu et al., 2019, 371). Fibres within the pumice are not considered related to biological activity (fig.257).

Sample S23 - Three-aisled cistern

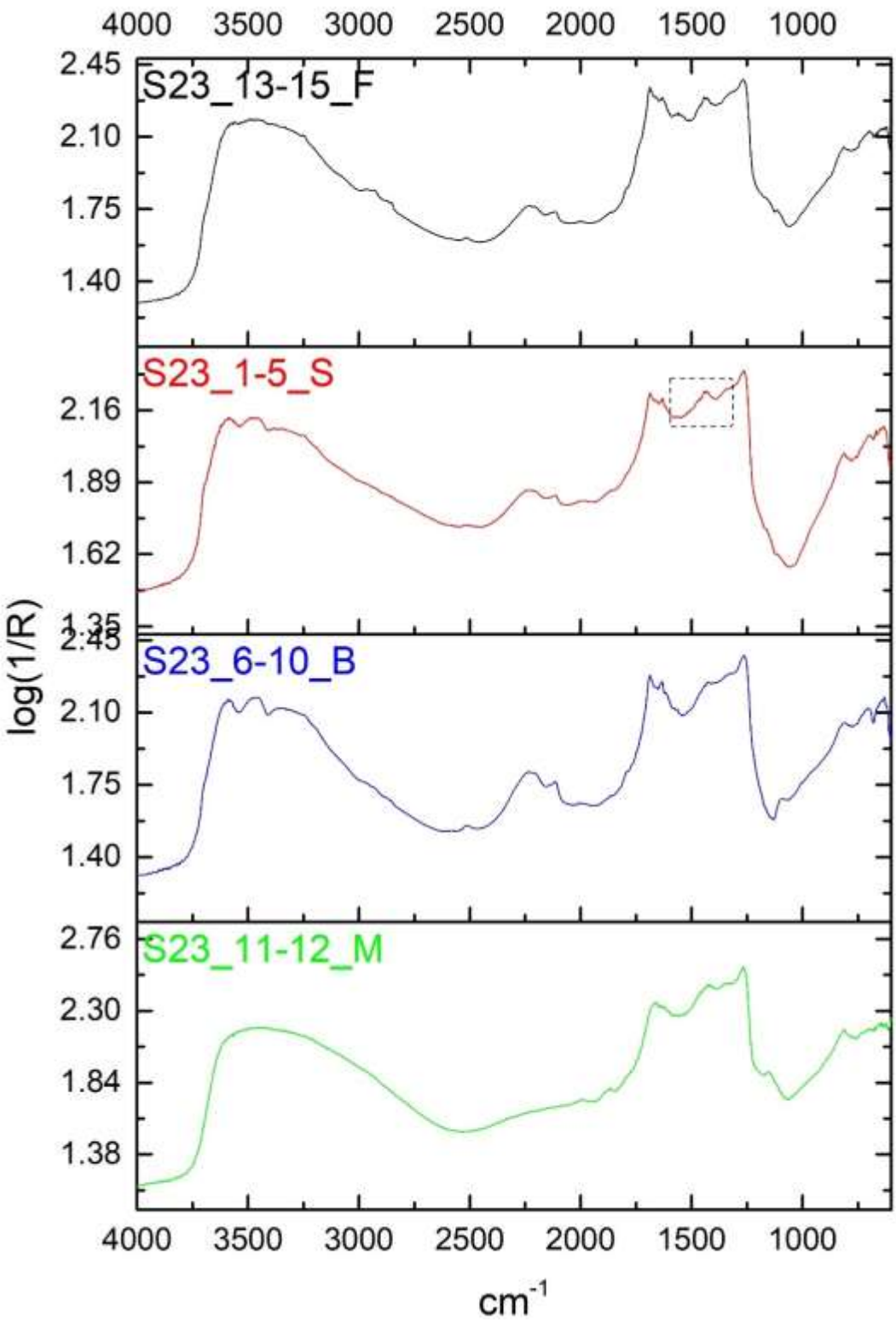

Figure 258: S23 stacked spectra of individual layers. Marked area indicates organic presence on the surface spectrum (S).

The sample was taken from the wall of the 3rd aisle (Appendix III, fig.14). The wall was stained from water running over its surface, thus biological activity was expected. Gypsum prevails on the surface spectrum whereas mortar components are almost absent (S23_1-5_S, fig. 258). A protein – lipid material related to bone glue, egg white, milk and egg mortar standards is indicated. The spectrum resembles that of droppings DR1 in the ROI 1339-1578 cm^{-1}.

Less gypsum is observed on the flat surface spectrum (S23_13-15_F). The spectrum below the surface (S23_6-10_B) has high gypsum content and resembles that of the surface spectrum (low calcite and organic presence). The mortar layer (S23_11-12_M) exhibits low calcite and quartz content, mainly below 1152 cm^{-1} and above 1800 cm^{-1}. The peaks around 1350 cm^{-1} are assigned to esters and 1771 cm^{-1} to amide. The organic content reduces gradually towards the mortar.

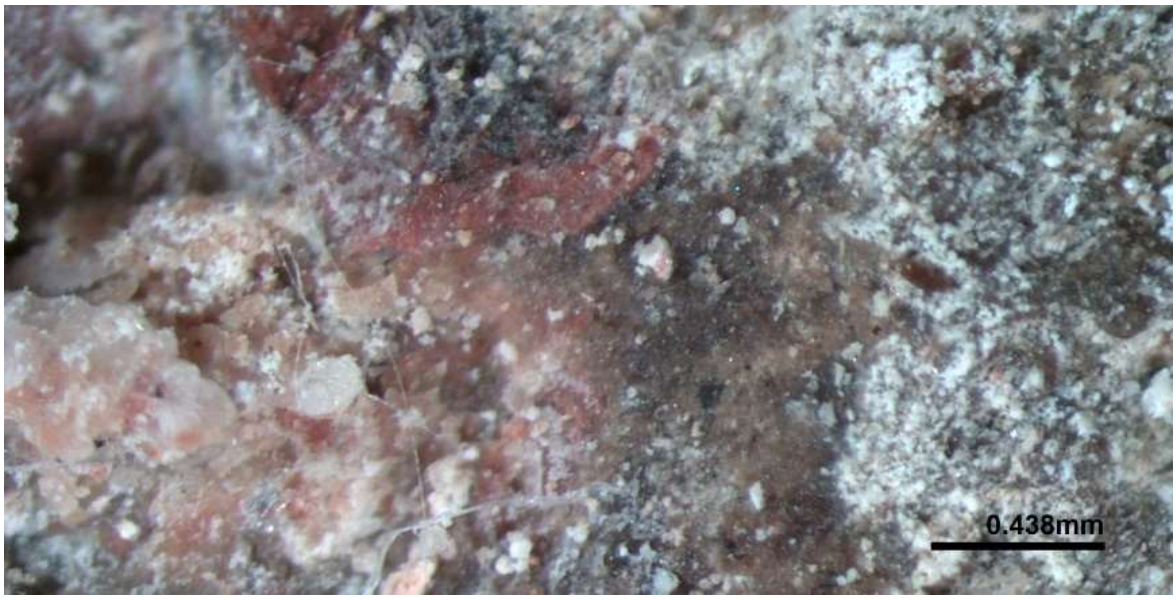

Figure 259: The surface of S23 showing resinous substance underneath loose white particles.

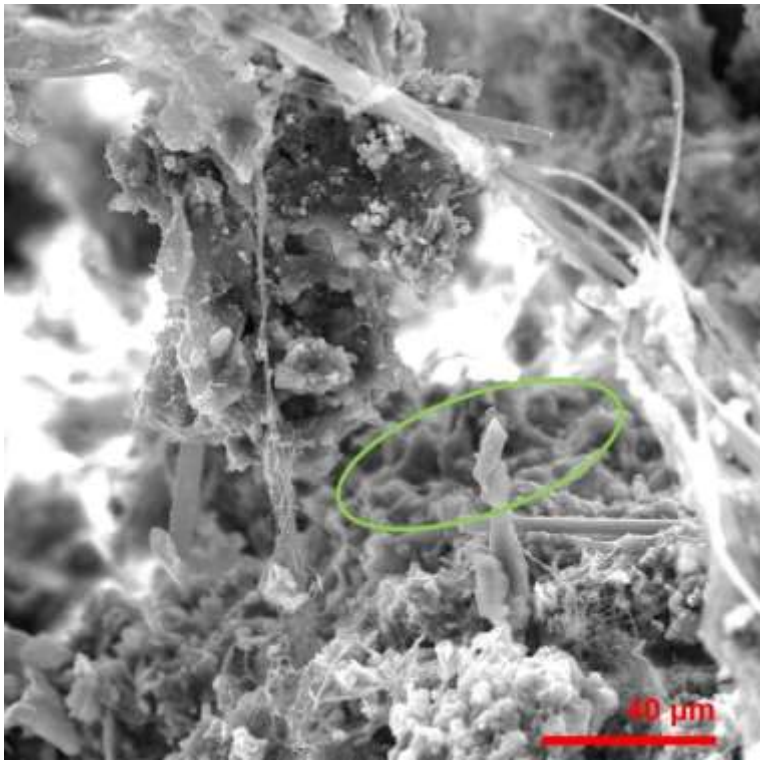

Figure 260: SE image of biological activity and gypsum (circled) on the surface of S23.

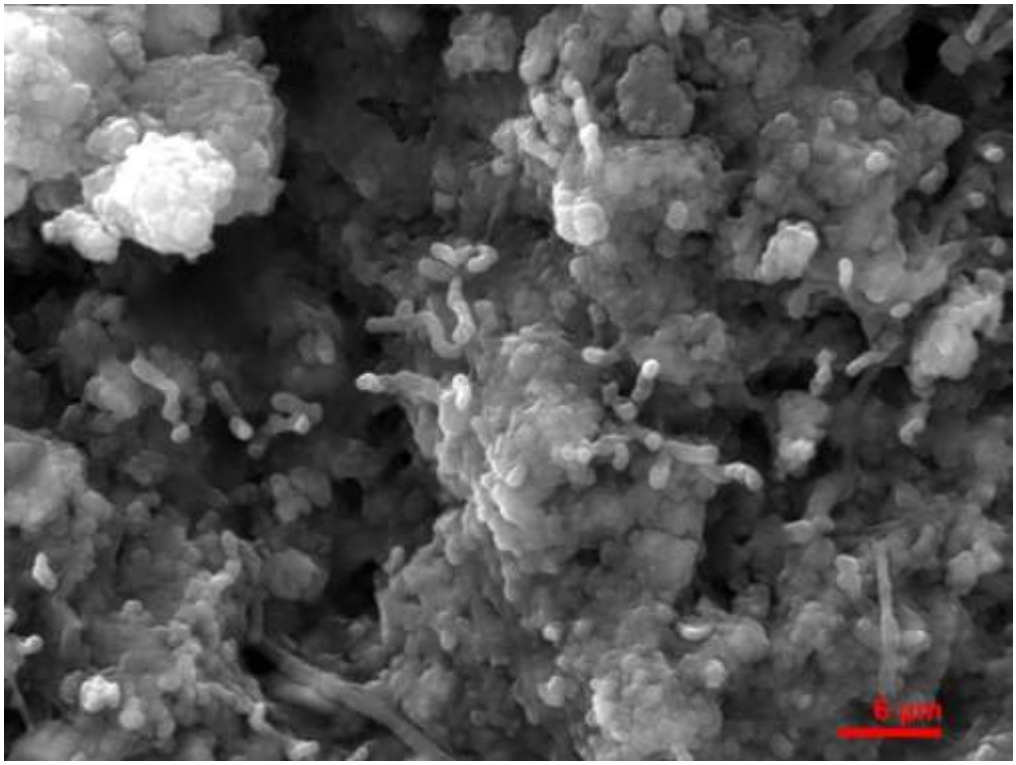

Figure 261: worm-like growth on the surface of S23.

Sample S23 is similar to S21 (connection of floor to the wall, 2nd aisle) with loose white particles over a darkened resinous surface that covers the mortar (fig.259). Fibres and hyaline mycelium growth, appearing as a network of hyphae (Savkovic et al., 2016, 215) is

visible on the surface, together with spike gypsum crystals emerging from within the mortar (circled, fig.260). In x500 magnification there is some growth of worm-like crystals possibly indicating early gypsum formation, similar to that observed in Phalasarna bathtub samples S8 to S11 (fig. 261).

Three-aisled cistern – Results Summary

The wall samples S19, S22 and S23 are covered by thick white calcite crust. S19 preserves a distinct black layer underneath this crust, similar to that observed on Polyrrhenia samples S1 to S3. Interpretation of the spectra suggests gypsum, protein-lipid content similar to that of egg mortar standards, milk and bone glue (similar protein content), while similarities with egg yolk mortar standards are observed on sample S22. The mortar composition of sample S22 differs from the rest due to the high amount of pumice inclusions and the low presence of crushed ceramics.

The spectra from the floor and from the connection of the floor to the wall (S20 and S21) show resinous substance on the surface, biological and other deposits. The floor sample S20 shows high protein content, most likely from the pigeon droppings that are abundant on the floor. Sample S21 shows gypsum and protein-lipid content, similar to egg mortar standards and filamentous biological activity. The organic content is well evidenced within spectra from all layers indicating a mixture of mortar with organic material. Dolomite is detected on the inverted surface spectrum.

Sample S24 - Gamma-shaped cistern

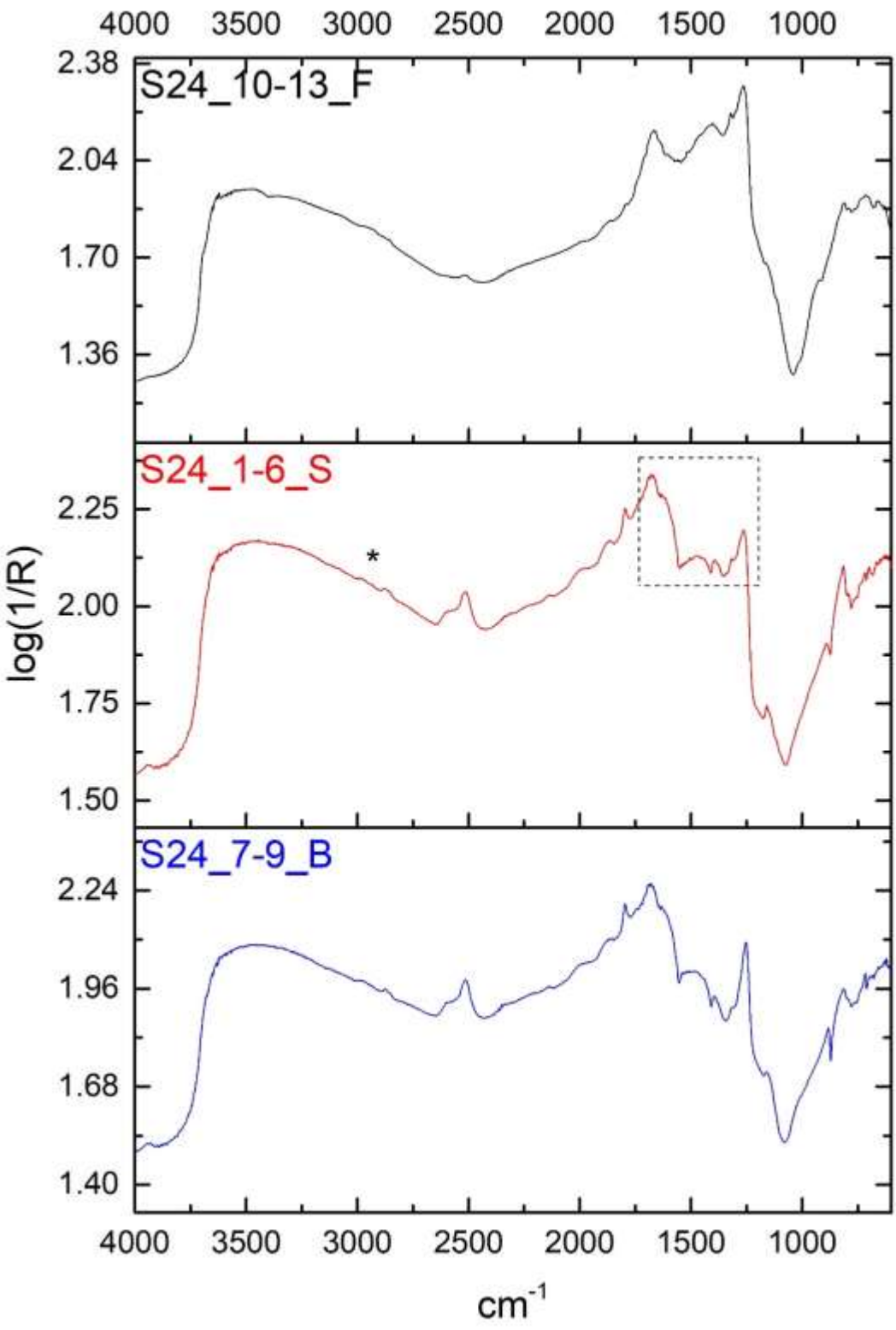

Figure 262: S24 stacked spectra of individual layers. Marked area indicates organic presence on the surface spectrum (S).

Sample S24 derives from the black surface of the wall at the NW section of the cistern. Organic presence is high on the surface spectrum (S24_1-6_S, fig.262). The C-O strong band at 1263 cm^{-1} could not be attributed to gypsum since there are no other gypsum peaks to support its presence. C-O, CH_2 and CH_3, similar to peaks in protein-lipid materials are visible at 1315-1340-1353 cm^{-1} and egg standards are possible matches. Lard and egg yolk mortar standards show the sharp peak in 1390 cm^{-1} supporting C-H bending of lipid content. Egg white similarities are detected in the shape of peaks 1441-1497 cm^{-1} showing amide and C=O respectively (Rosi et al., 2009, 2099). Amides should be assigned to the peaks 1506-1539 cm^{-1}. Strong amides are also present in 1632-1691 cm^{-1}, such as those in egg white and bone glue, although some relationship can be found in egg yolk and egg standards. The presence of amide, such as in egg white and bone glue standards, is further supported by the presence of peaks at 2988-3003-3013 cm^{-1}. The S24_7-9_B spectrum is highly similar to the surface spectrum. It preserves organic content and the peak at 1739 cm^{-1} should be attributed to esters. The 1253 cm^{-1} strong peak should be assigned to sulphates (Ylmen and Jaglid, 2013, 120).

The flat surface is almost entirely organic, showing egg yolk related protein-lipid content (S24_10-13_F, fig.262). The sugar peak at 920 cm^{-1} may derive from external deposition of soil organic matter or biological activity (Chauhan et al., 2018, 76). The closest match in terms of standards comparison is the rice/mortar due to the presence of starch (sugar content). The sugar content in the flat surface spectrum is not present on the surface profile spectra and below the surface layers, indicating external depositions, probably of biological origin and should not be attributed to rice mortar additive (Mills and White, 1987, 64). Rice cultivation was not popular in Greece before the Arabs in the 7th century AD, although the crop was known as an imported in limited scale product already from the Hellenistic period (Kokoszko et al., 2013, 49-50).

The spectra profiling of sample S24 highlights the necessity to interpret analytical outcomes within the archaeological and historical context, taking into account the geographical and regional specifications, the availability of materials and the practiced technologies in order to reach realistic conclusions.

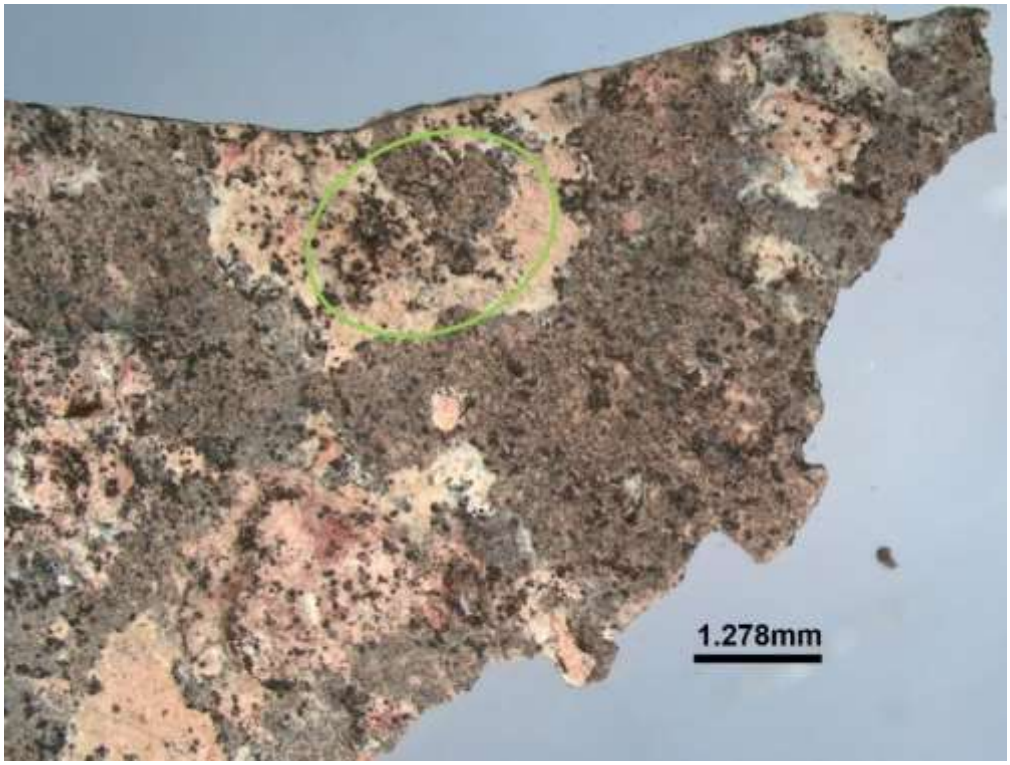

Figure 263: The surface of S24 appears light pink, covered locally with a dark patina.

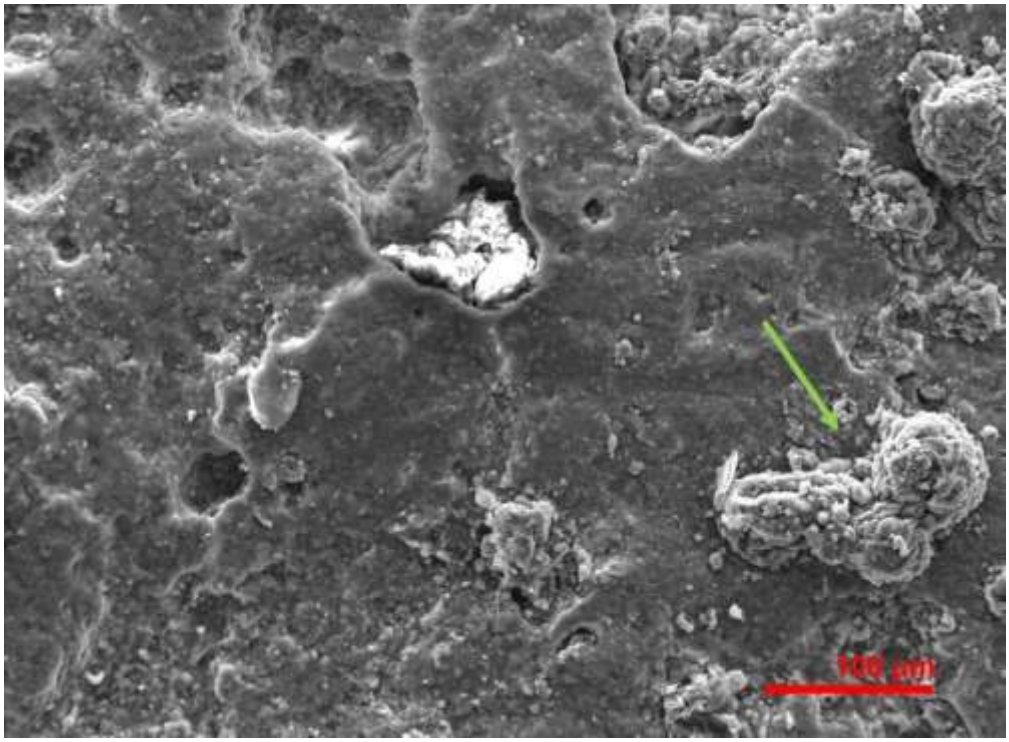

Figure 264: SE image of protein-lipid spheres on the S24 surface.

The light-pink surface is locally covered by a dark patina with black spots (fig.263). These black spots must be the spheres observed on the SE images over the amorphous flat surface layer (pointed by the arrow, fig.264). Spheres of egg protein-lipid attacked by

bacteria appear highly similar to the ones observed on the surface of S24 (Ortiz-Miranda et al., 2017, 6).

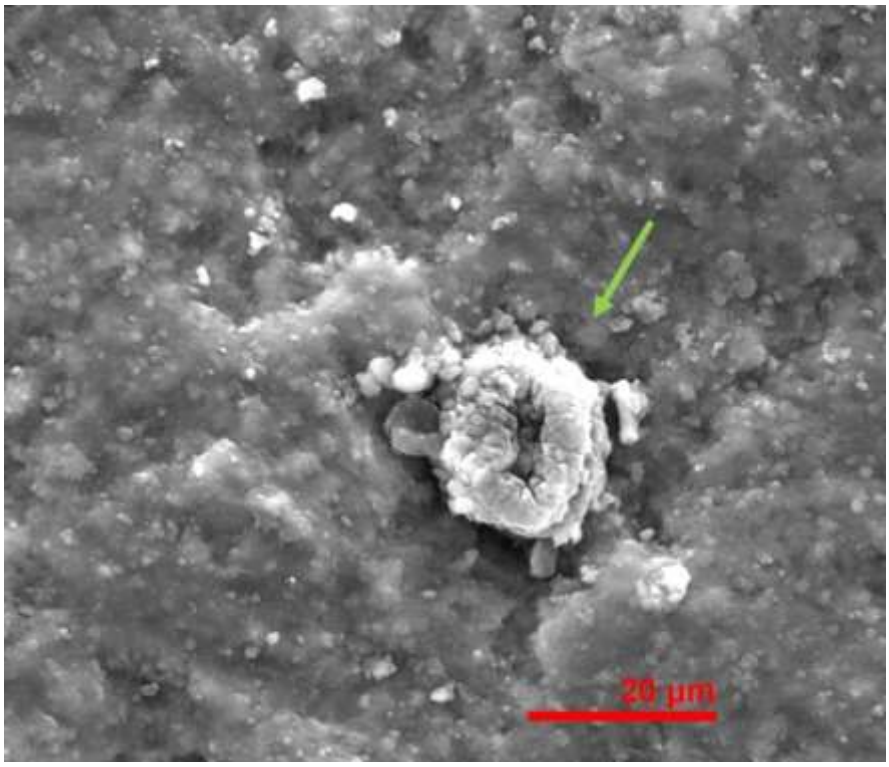

Figure 265: SE image of localized biological activity on S24.

Mycogenic minerals show similarities with round particles on the surface (pointed by the arrow, fig.265), although further research is necessary to fully identify the biological origin and transformation process (Savkovic et al., 2016, 22; Riquelme, 2013). The black meristematic fungi *Aureobasidium* which is a common inhabitant of marble in the Mediterranean appears highly similar (Burford et al., 2003, 102).

Sample S25 - Gamma-shaped cistern

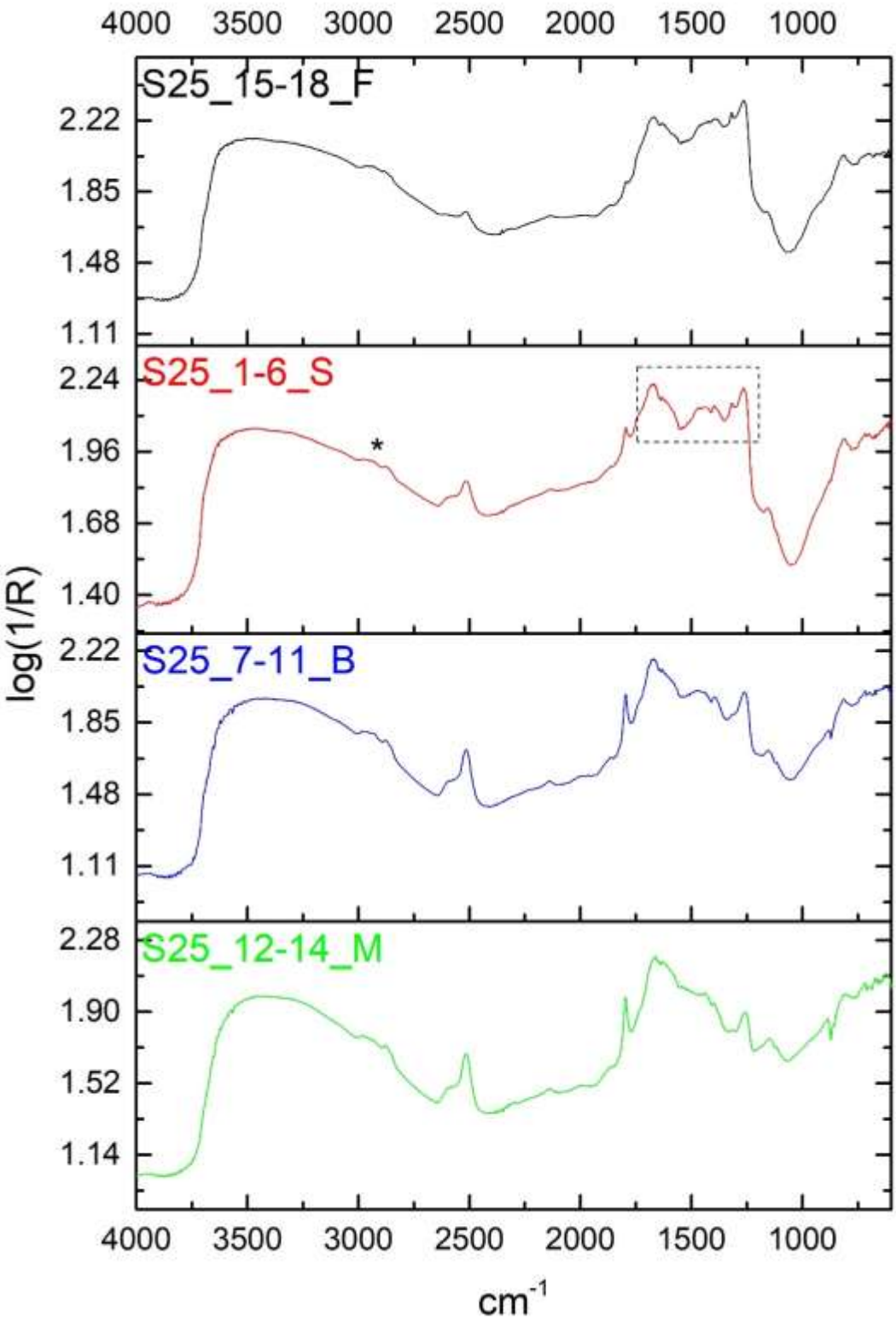

Figure 266: S25 stacked spectra of individual layers. Marked area indicates organic presence on the surface spectrum (S).

Sample S25 derives from the wall at the NW section of the cistern. Both mortar and organic peaks are present on the surface spectrum (S25_1-6_S, fig.266), similar to S24. Protein-lipid content is present and related to egg/mortar standards (mostly egg yolk). The inorganic portion increases towards the mortar, although the organic peaks are present in all layers at differing intensity. The peaks diagnostic of lipids become the weakest of the organic peaks as the centre of the sample is approached.

Figure 267: The weathered surface of S25.

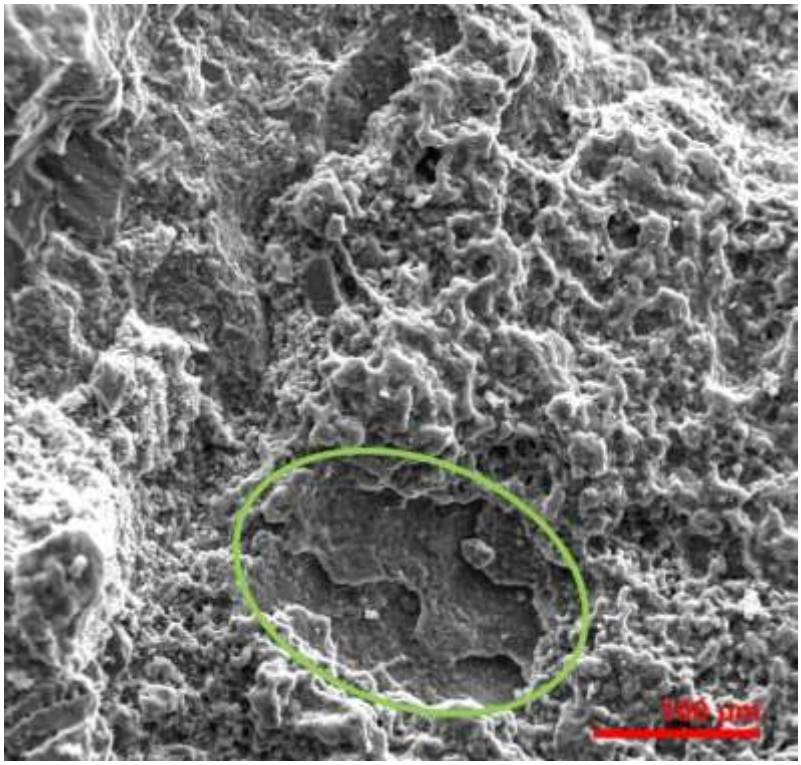

Figure 268: SE image of the S25 surface underneath the white crust (circled).

The surface is weathered, exposing the mortar layer that contains high number of ceramic inclusions (fig.267). White crust, as the one observed on S19 sample from the 3-aisled cistern, is visible locally. The SE image revealed a flat smooth surface underneath this white crust, resembling egg-pigment experimental films (Fang et al., 2013, 5; Ortiz-Miranda et al., 2017, 6). There is no indication of biological activity (fig.268).

Sample S26 - Gamma-shaped cistern

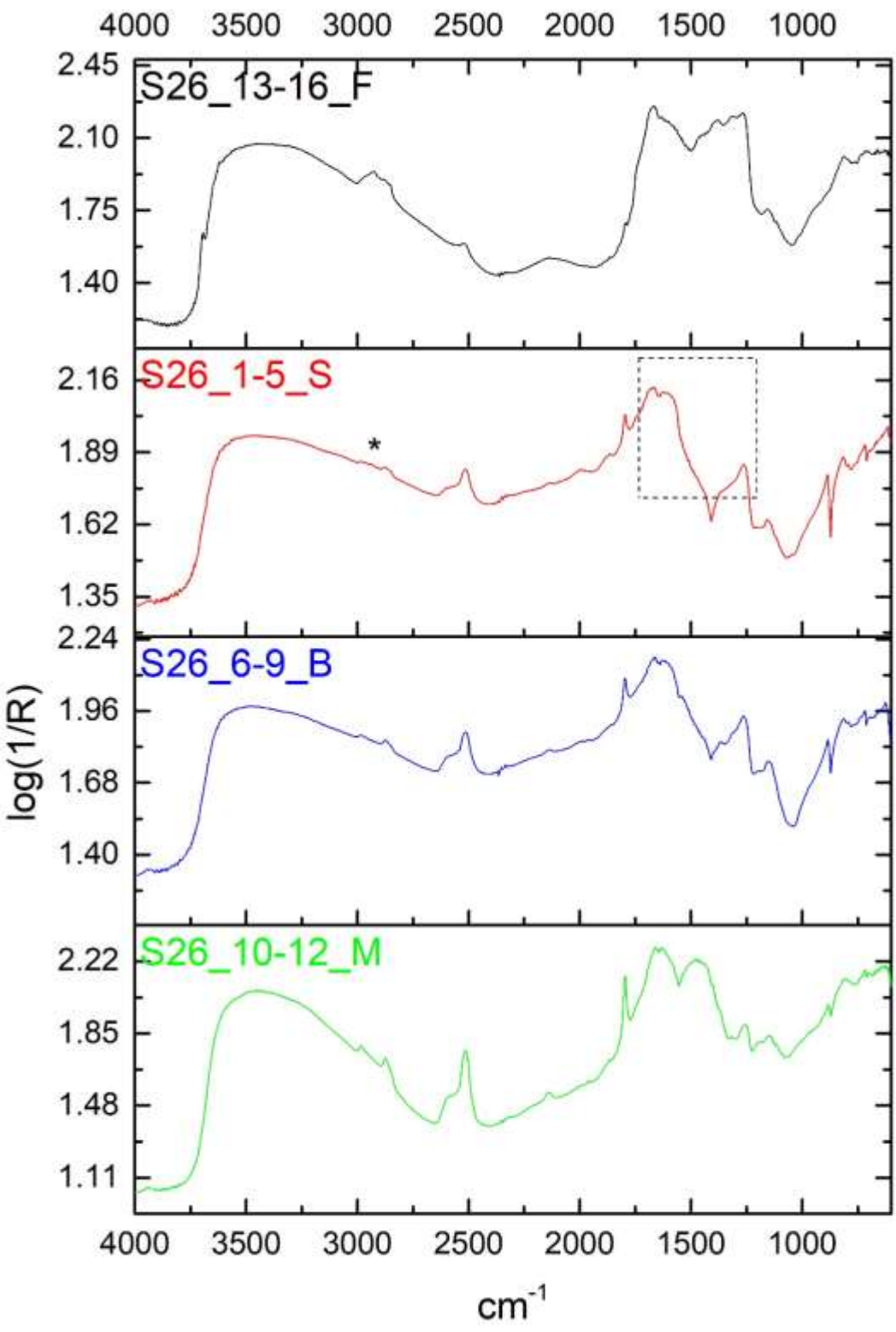

Figure 269: S26 stacked spectra of individual layers. Marked area indicates organic presence on the surface spectrum (S).

The sample was taken from the connection of the wall to the floor at NW section. The black surface crust must derive from the accumulation of water. Plant debris was adhered on the surface.

The surface spectrum exhibits similar peak at 1263 cm^{-1} with that of the S22 (Aptera-wall) and S14 samples (Polyrrhenia-wall) (S26_1-5_S, fig.269). Peaks, indicative of egg phosphates at 1046 cm^{-1}, sulphates at 1194 cm^{-1} and lipid at 1263-1338-1362 cm^{-1} resemble egg yolk standards, but are also present in pigeon droppings. However, C-O bending peaks around 1470 cm^{-1}, characteristic to egg yolk standard, are absent on the spectrum of S26, thus the presence of this mortar additive cannot be fully supported (Spectrum EY_av, Ricci et al., 2006, 1224). Amide presence is suggested in the 1489-1507-1668 cm^{-1} region and the peak at 2900 cm^{-1} is assigned to protein.

The flat surface spectrum (S26_13-16_F) shows peaks related to biological activity such as the 2928 cm^{-1} (mold on bone glue standard) and 1630 cm^{-1}. Lipid-protein content is visible at 1431 cm^{-1}, 1376 cm^{-1} and 1267 cm^{-1} (lipids), 1507-1519 cm^{-1} and 1600 cm^{-1} (amides). The S26_6-9_B spectrum is highly similar to the surface one (fig.269). The mortar layer is mainly inorganic with low lipid and protein content (S26_10-12_M).

Figure 270: The surface of S26. A thick black crust is deposited on the surface (arrow).

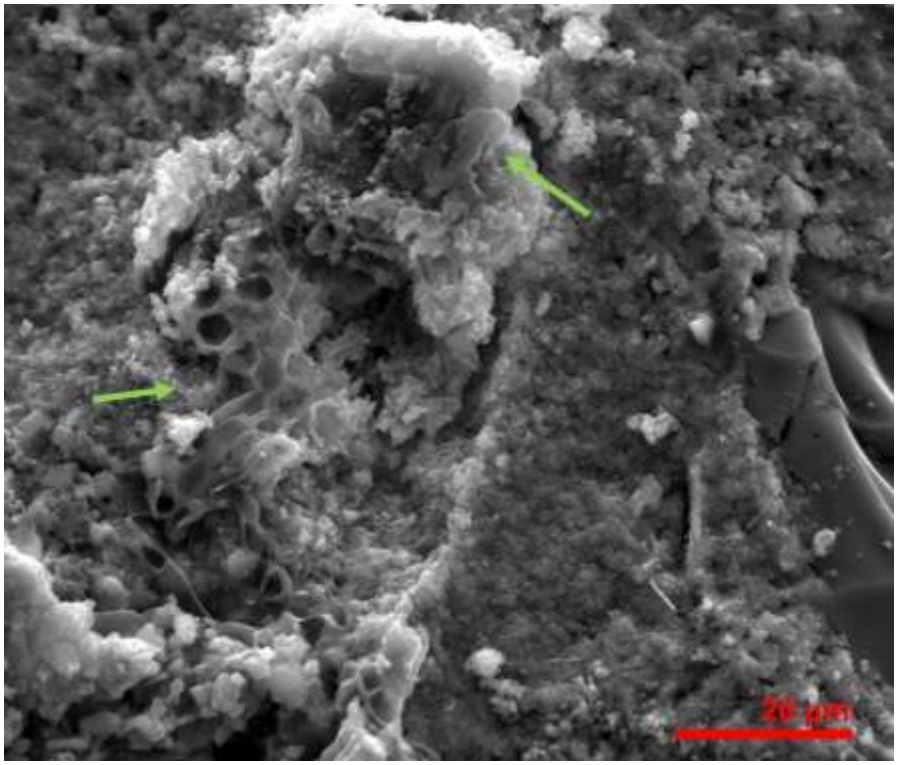

Figure 271: SE image of biological growth on the surface of S26 (arrows).

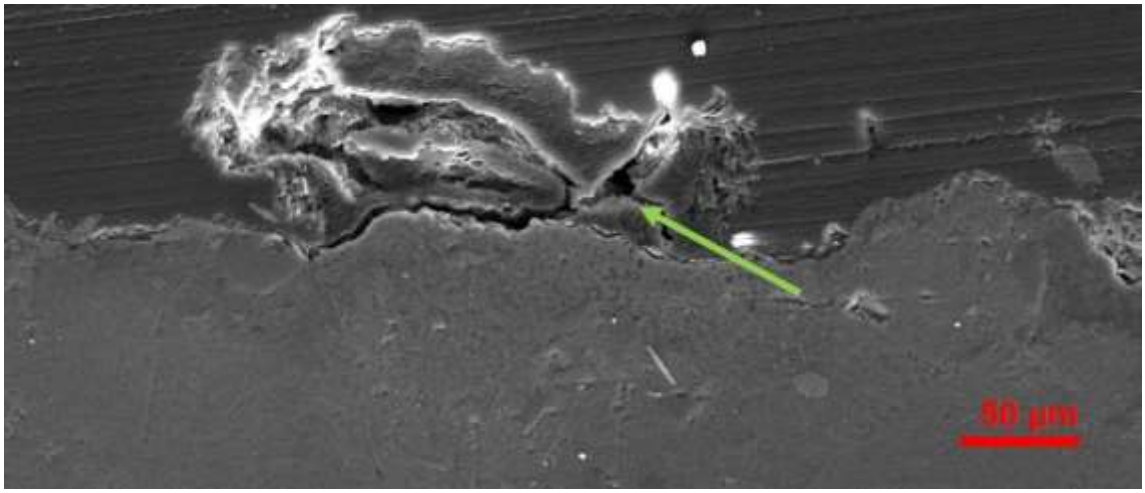

Figure 272: SE image of the cross-section of S26 showing detachment of the surface induced by microorganisms.

The thick, black crust seems deposited over a smooth lime plaster with ceramic inclusions similar to that of S24 (pointed by the arrow, fig.270). Similar biomineralization to that on S24 is observed on the surface of sample S26, mixed with honeycomb polygonal growth previously detected on S18 (pointed by the arrows, fig.271). A smooth layer of mortar is preserved underneath. The SE image of the cross-section surface shows that the honeycomb growth moves underneath the weathered surface causing its detachment

(fig.272). It is likely that algal cells associated with lichens are present on the sample (Sanz et al., 2017, 766).

Sample S27 - Gamma-shaped cistern

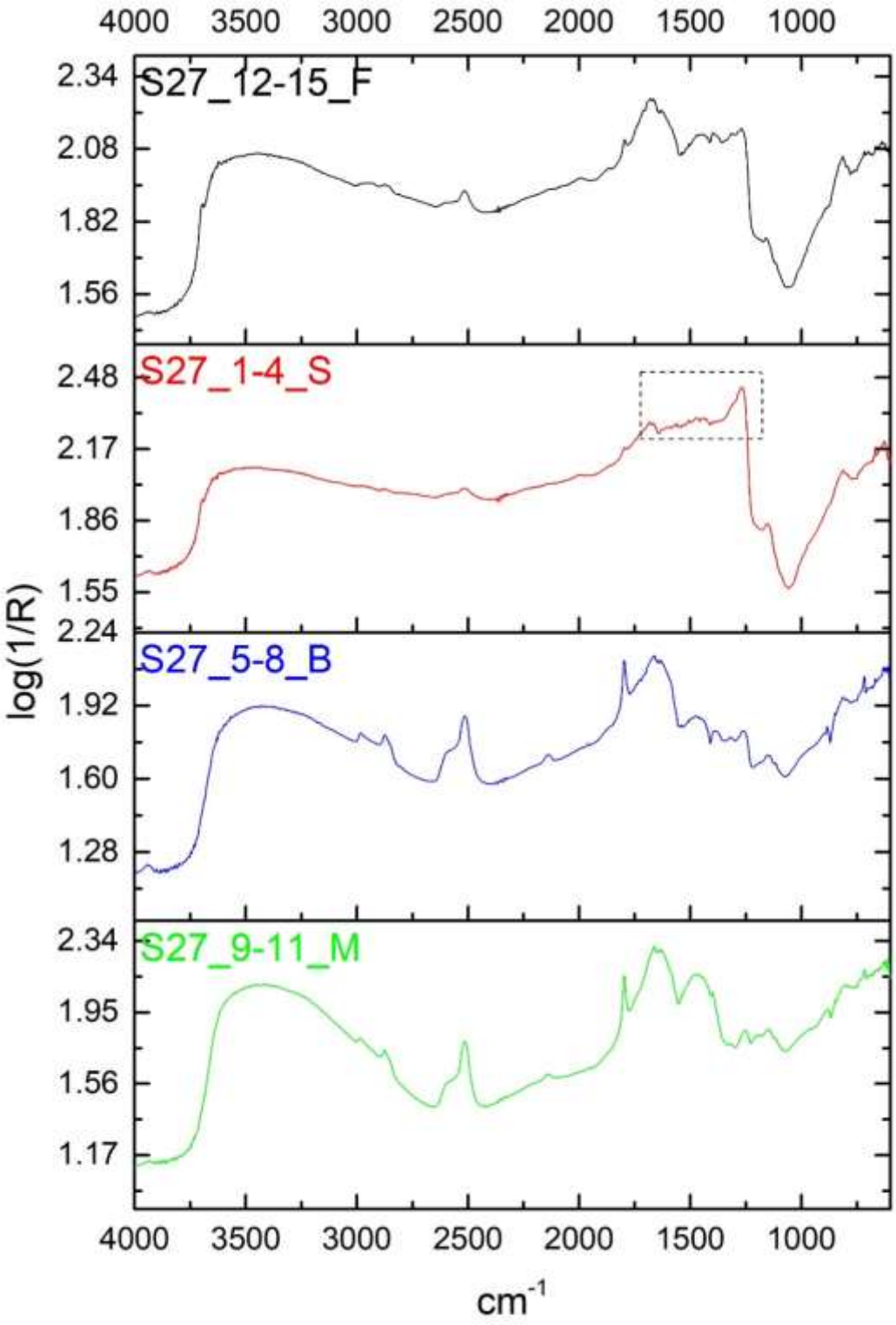

Figure 273: S27 stacked spectra of individual layers. Marked area indicates organic presence on the surface spectrum (S).

The sample derives from the black substance on the floor at the NW section of the cistern (Appendix III, fig.16). High organic and low mortar content is observed on the surface spectrum (S27_1-4_S, fig. 273). The shape of the organic area is similar to that of pigeon droppings standard (DR2). The peaks 1400-1432-1442 cm^{-1} are assigned to C-O bending that is present in almost all organic standards as well as the mortar one. The 1472 cm^{-1} should indicate egg parts although amide cannot be excluded. Amides are also present and linked to egg (yolk and white) but also to droppings (DR2 standard) in 1506-1528-1539 cm^{-1}. Amide C=O at 1547-1560-1578 cm^{-1} is linked to egg yolk and egg white mortar mixtures and amides occur in 1668-1684 cm^{-1}. The shape of 1263 cm^{-1} peak is close to that of egg yolk/mortars and C-H is characterised at 1369-1389 cm^{-1}.

The S27_12-15_F spectrum is similar to the surface spectrum with higher organic content, as expected (fig.273). The similarities to pigeon droppings suggest biological origin for the organic material rather than the presence of droppings that are not observed in situ. Amides, such as those in bone glue, are strong, although egg white is a closer match. The peak at 1706 cm^{-1} could be assigned to free fatty acids or yolk amides. The coexistence of lipids and amides is indicated in the area 2859-3007 cm^{-1}. The fact that the diagnostic lipid peak at 1740 cm^{-1} is absent suggests either total absence of a strong lipid or that this esteric bond decomposes fast or that traces of lipid are preserved in egg white additive. The S27_5-8_B spectrum retains organic closer to that of the flat surface spectrum. The mortar spectrum is predominantly inorganic.

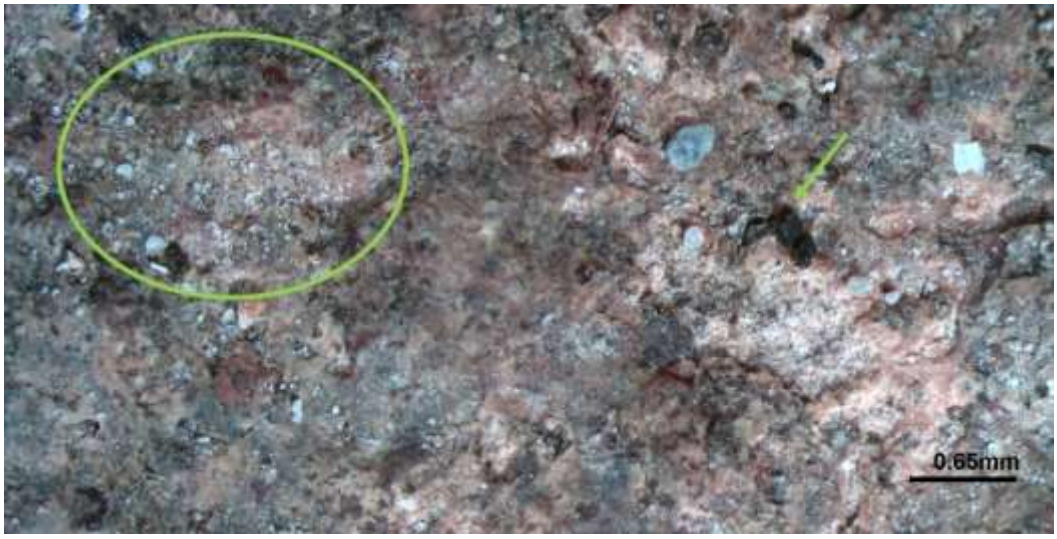

Figure 274: The surface of S27 showing black deposits and salt crystals (circled).

Figure 275: The cross-section of S27. The surface layer is fine and preserved under external depositions (arrow).

The surface is highly similar to the black deposits seen on S26, with some accumulation of salt crystals (marked areas, fig.274). The upper calcite layer is flat and fine and is preserved under the black layer that could be an external deposition (green arrow, fig.275).

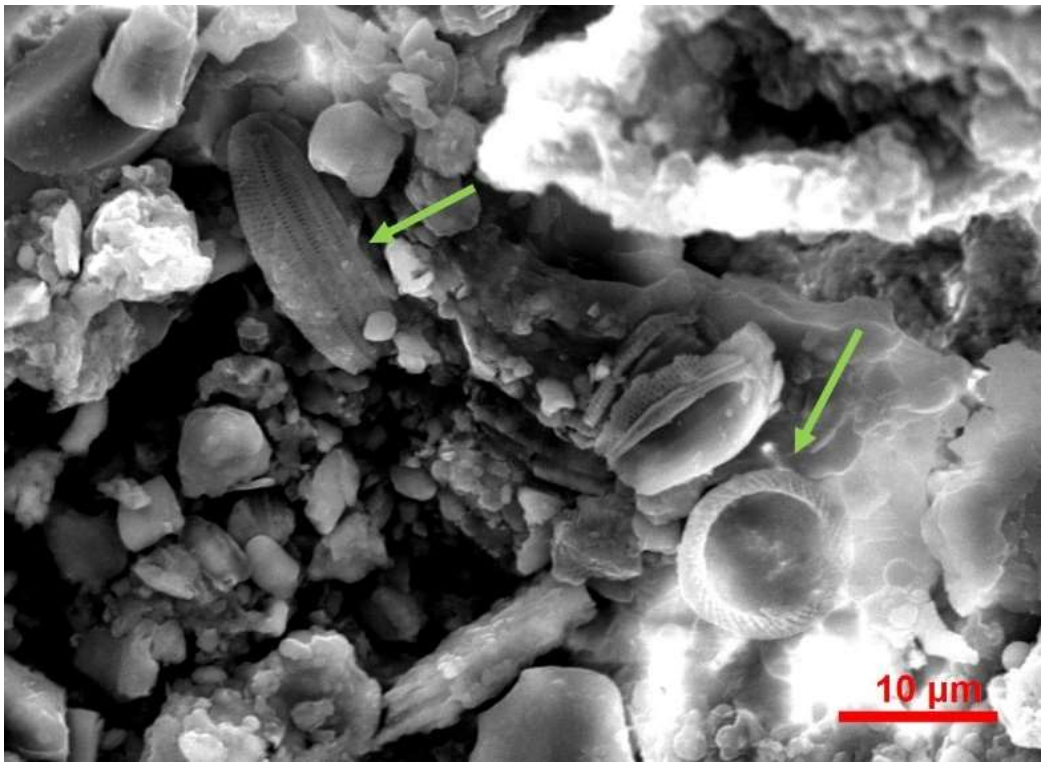

Figure 276: SE image of biological activity on the surface of S27 (green arrows).

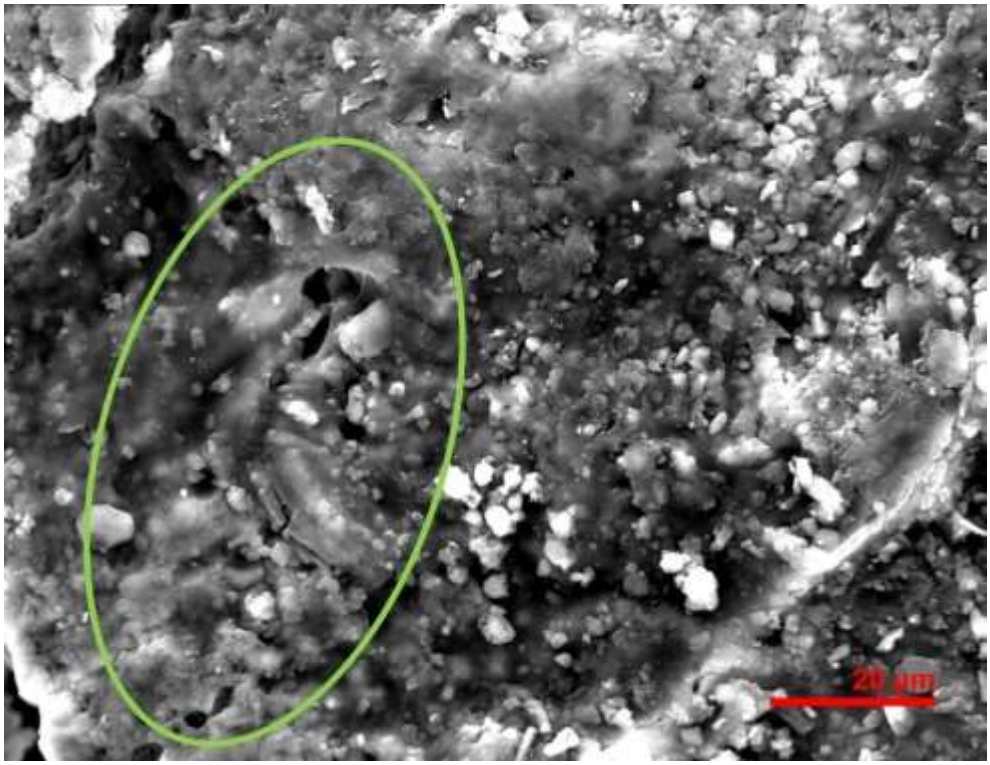

Figure 277: SE image of the resinous layer preserved on the S27 (circled).

Micro-organisms are visible on the surface within the calcite, as well as spheroidal biogenic particles (Burford et al., 2003, 103) (green arrows, fig.276). The smooth, resinous layer is partially preserved on the surface (circled, fig.277). The fine layer appears locally cracked and biological activity moves inwards (cross-section SEI not shown).

Sample S28 - Gamma-shaped cistern

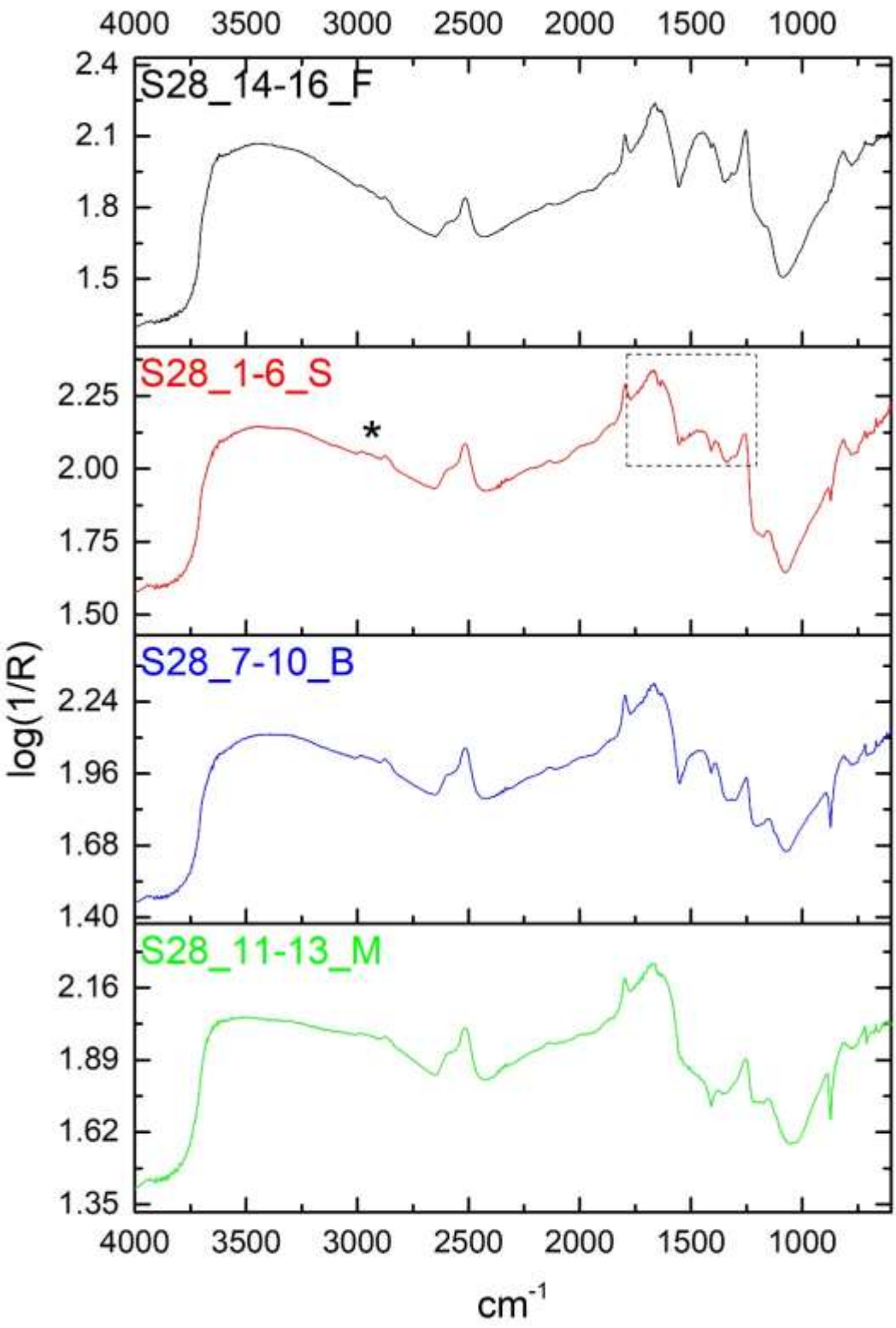

Figure 278: S28 stacked spectra of individual layers. Marked areas indicate organic presence on the surface spectrum (S).

Sample S28 derives from the wall at the S. section of the cistern. Organic and inorganic components coexist in the surface spectrum (S28_1-6_S, fig.278). The peak at 1256 cm^{-1} is assigned to C-O. Some similarities with bone, bone glue, yolk and milk mortar standards are detected at 1308-1341-1389 cm^{-1} and the peaks between 1448 - 1540 cm^{-1} for egg parts. The peak at 1632 cm^{-1} is assigned to amide. Amide related to egg yolk is detected at 1667-1668 cm^{-1} and 1704 cm^{-1} (C=O of amide). Egg yolk ester is visible in 1741 cm^{-1}. Amide is also present in 2875-2984 cm^{-1}. All layers preserve lipids and proteins.

Figure 279: The weathered surface of S28; hyaline mycelium growth is indicated by the arrow.

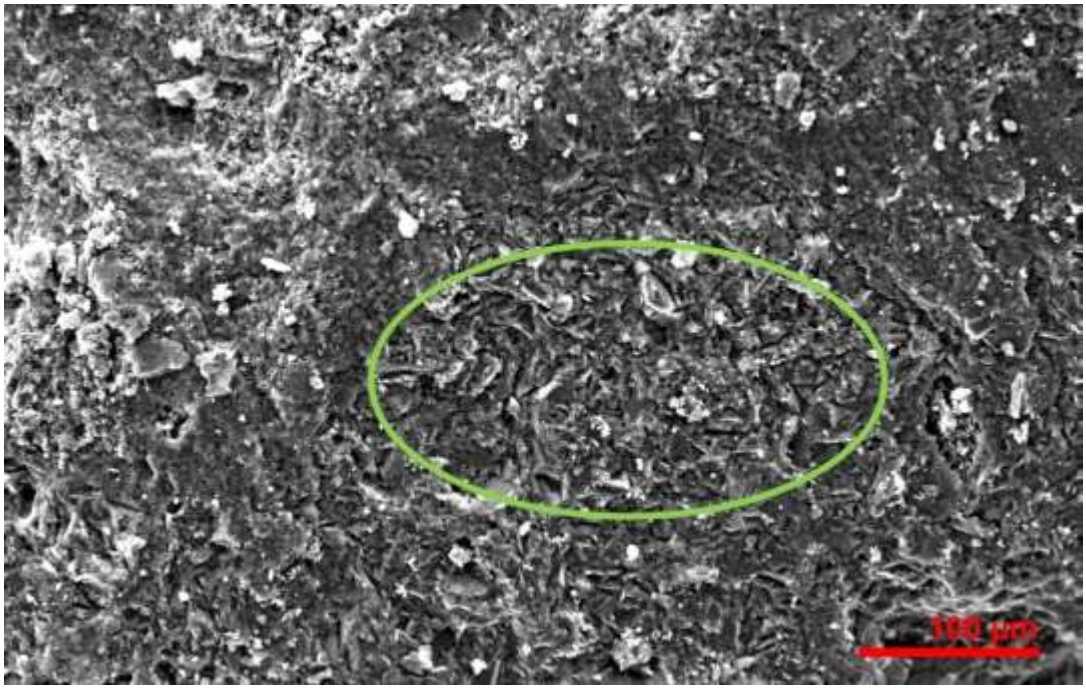

Figure 280: SE image of the surface of S28; platy particles (circled) must belong to ceramic inclusions.

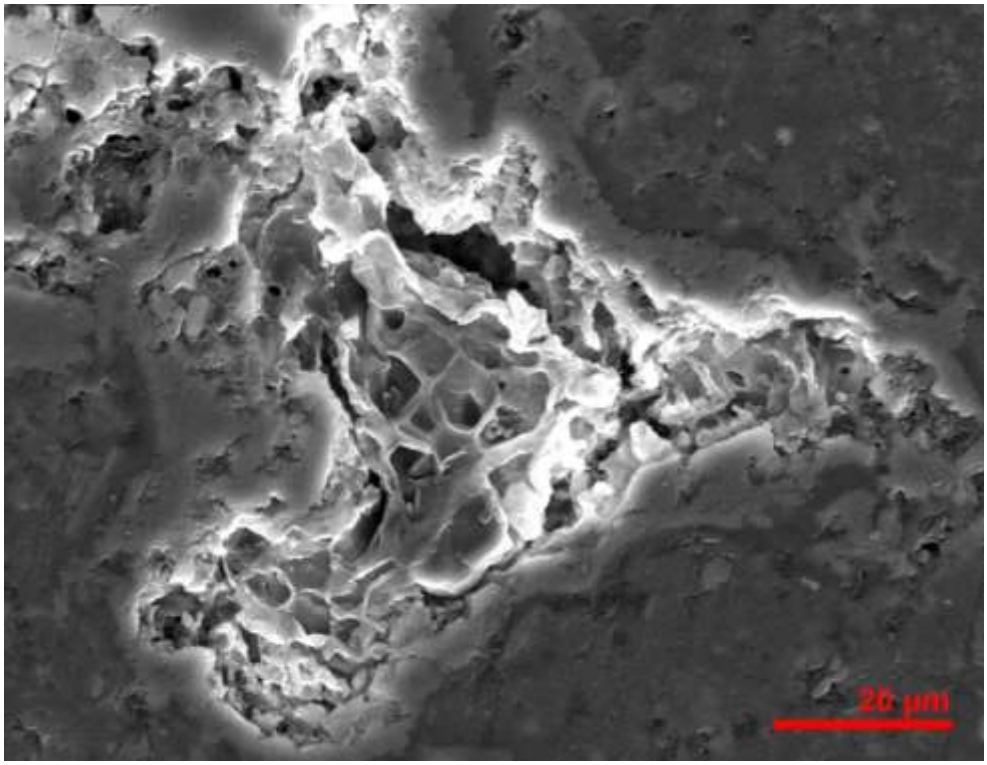

Figure 281: SE image of the honeycomb growth within the mortar layer (cross-section).

Sample S28 is highly weathered, with a local presence of white crust, hyaline mycelium growth appearing as a network of hyphae (Savkovic et al., 2016, 215) and areas of exposed mortar layer and ceramic inclusions (pointed by the arrow, fig.279). The SE image of the weathered surface is free from biological activity (fig.280). The plate like particles derive from the ceramic inclusions (fig.210 - clay standard). Honeycomb biological activity, as in samples S18 and S26, appears within the mortar layer some depth from the surface (fig.281).

Gamma-shaped cistern - Results Summary

Samples S24 and S25 from the NW cistern walls show a smooth, amorphous substance in different preservation stages on their surfaces. Biomineralization appears in one sample (S24) whereas the other is free from any biological activity (S25). Lipid-protein content and sulphates, similar to egg yolk, are mostly visible on the surface spectra. The organic component reduces towards the mortar layer. Sample S28 from the South wall also shows evidence of lipid-protein content.

The floor samples S26 and S27 show thick black crust on their surface. Biological activity and micro-organisms are visible. Lipid – protein content resembling that of egg yolk and mold is present. However, differences in the organic peaks between the cross-section

surface and flat surface spectra suggest that biological activity is mainly located on the flat surface.

Aptera - Summary

Almost all the Aptera samples show biological activity in different scale and form as well as protein-lipid content in their composition. The effect of biological activity on the sample components, both organic and inorganic, is not certain. In some samples biological activity appears deposited on the surface, whereas in other, such as in S24, biological activity seems to attack organic material already present on the surface of the sample.

11.4 Discussion

11.4.1 Overview and comparisons of data

Table 25 summarizes the Reflectance micro-FTIR results on the detection, identification and spatial distribution of the organic and inorganic (other than mortar) substances on the ancient mortar samples. The standards in brackets, in the ***"Organic/Related Inorganic"*** column, are those that exhibit similarities with the ancient samples, as derived from the comparative assessment through the CPAD. The column entries colour-coded in pink are those verified (or strongly suggested) by SEM and OM analysis. A detailed version of spectral, OM and SEM results is provided in Appendix III (Table 2, Reflectance micro-FTIR, OM and SEM results).

Sample - Origin - Dating	Sampling Location	Organic / Related Inorganic	Inorganic (other than mortar)	Detection Layer	Biological Activity
S1 - Polyrrhenia Cistern floor (2nd AD - Roman)	Buried in rural soil.	**Protein** - Phosphates (EW_M, BG_M)		**Surface**	
S2 - Polyrrhenia Cistern floor (2nd AD - Roman)	Buried in rural soil - surface cleaned with spring water.	Protein - Lipid (EW_M_75, **BG_M_50,** EW, E_M_25)		**Surface**	
S3 - Polyrrhenia Cistern floor (2nd AD - Roman)	Buried in rural soil - same sampling location as for S2.	**Protein - Lipid** - Phosphates (EW_M_75, BG_M, BG, SB)		**Surface**	
S4 - Polyrrhenia Mortar on stone related to the cistern wall (2nd AD - Roman)	Exposed to rural environment.	Protein - Lipid - Phosphates (EW, E, BG_M, EY_M)	Dolomite	**Surface**	
S5 - Polyrrhenia Mortar on stone related to the cistern wall (2nd AD - Roman)	Exposed to rural environment - surface cleaned with spring water.	Protein - Lipid - Phosphates	Dolomite	**Surface**	
S6 - Polyrrhenia Mortar on stone related to the cistern wall (2nd AD - Roman)	Exposed to rural environment - same sampling location as for S5.	Protein - Lipid - Phosphates (EW)	Dolomite	**Surface**	
S14 - Polyrrhenia Low wall between cistern and aqueduct (2nd AD - Roman)	Inner Part towards aqueduct - Horizontal surface - buried beneath masonry - surface cleaned with spring water.	Protein - Lipid - Phosphates or Sulphates (E, EY)		**Surface**	
S15a - Polyrrhenia Low wall between cistern and aqueduct (2nd AD - Roman)	Outer Part towards cistern - Horizontal surface - buried beneath masonry - surface cleaned with spring water.	Protein - Phosphates (PB, SB, EW_M, BG_M)		**Surface**	
S15b - Polyrrhenia Low wall between cistern and aqueduct (2nd AD - Roman)	Outer Part towards cistern - Horizontal surface - buried beneath masonry - surface cleaned with spring water - different texture from S15a.	Protein - Phosphates (**PB**, BG, EW, EW_M, BG_M)		**Surface**	

Table 25: Summary of Reflectance micro-FTIR results relevant to the detection and identification of organic and inorganic (other than mortar) substances; entries colour-coded in pink were those verified by SEM and OM analysis.

Sample - Origin - Dating	Sampling Location	Organic / Related Inorganic	Inorganic (other than mortar)	Detection Layer	Biological Activity
S7 - Phalasarna Cistern wall (4th BC - Hellenistic)	From the S wall - exposed to marine environment since the 80s excavation.	**Protein - Lipid** - Phosphates (EW, EY, E)	Dolomite, Water	**Surface**	
S13 - Phalasarna Cistern wall (4th BC - Hellenistic)	Loose piece from the N wall - exposed to marine environment since the 80s excavation.	Protein - Lipid (Mi_M, E_M of low organic concentration)		Mortar	
S8 - Phalasarna Bathtub 1 (4th -3rd BC - Hellenistic)	Seat - exposed to marine environment.	Protein - Lipid (EW_M_5)	Dolomite	Surface	
S9 - Phalasarna Bathtub 1 (4th -3rd BC - Hellenistic)	Bottom - exposed to marine environment.	**Protein** (BG, E, EW, EY and their mortar mixtures)	Dolomite, **Gypsum**	Surface and Mortar	
S10 - Phalasarna Bathtub 3 (4th -3rd BC - Hellenistic)	Side wall - exposed to marine environment.	Protein - **Sulphates**	Dolomite, **Gypsum**	**Surface**	
S11 - Phalasarna Bathtub 3 (4th -3rd BC - Hellenistic)	Front wall - exposed to marine environment.	Lipid - **Protein**	Dolomite, **Gypsum**	**Surface**	
S12 - Phalasarna Cistern - 3 Hierarchs Church area - (2nd - 4th AD)	Exposed to marine environment.	Protein - Lipid (EW_M_75)	Gypsum	**Surface**	
S16 - Aptera Bottle-shaped cistern (Roman Villa - 1st - 3rd AD)	North inner side surface of the opening - 0.5m depth - exposure to high humidity.	Protein - Lipid (EW, EY, E and BG_M, **Mould, DR1 and DR2**)	Water	Uncertain	√
S17 - Aptera Bottle-shaped cistern (Roman Villa - 1st - 3rd AD)	Loose piece from the bottom - exposure to high humidity.	Protein - Sugars (**Mould,** Mi, EW)	Water	Uncertain	√
S18 - Aptera Bathtub (Roman Baths - 1st AD)	Interior wall - exposed to rural environment.	Lipid - **Protein** - Sugars (L, EY, Mi)	Water	**Surface and Mortar**	√
S19 - Aptera 3-aisled cistern (Roman - 1st AD)	1st aisle - from the wall opposite the entrance - Biological growth on the wall - high humidity content -Pigeon nests.	**Protein - Lipid** (EW_M, BG_M, Mi_M)	Gypsum	**Surface**	√
S20 - Aptera 3-aisled cistern (Roman - 1st AD)	1st aisle - from the floor - highly contaminated by pigeon droppings and other deposits from frequent flooding (rain water).	Protein - Lipid (low) (EW, E, EY, BG, Mi, **DR**)		**Surface**	√

Table 25: continued.

Sample - Origin - Dating	Sampling Location	Organic / Related Inorganic	Inorganic (other than mortar)	Detection Layer	Biological Activity
S21 - Aptera 3-aisled cistern (Roman - 1st AD)	2nd aisle - connection of floor to the wall towards the entrance.	Protein - Lipid (E, BG, E_M, **Mould, DR**)	Dolomite, **Gypsum**	**Mortar**	√
S22 - Aptera 3-aisled cistern (Roman - 1st AD)	2nd aisle - wall opposite the entrance.	Protein - Lipid - Sugars (EY_M_75, E, EY, BG, Mi)	Pumice (SEM)	**Surface**	
S23 - Aptera 3-aisled cistern (Roman - 1st AD)	3rd aisle - low part of the side wall - water staining - biological activity.	Protein (main) - Lipid (EW, BG and their mortar mixtures, **Mi**, E)	**Gypsum**	**Surface**	√
S24 - Aptera Gamma-shaped cistern (Roman - 1st AD)	NW section - right wall towards the south section - exposed to external, dry, rural and marine environment.	**Protein - Lipid** - Sulphates (EW_M, EY_M, E_M)		**Surface**	√
S25 - Aptera Gamma-shaped cistern (Roman - 1st AD)	NW section - left wall towards the south section - exposed to external, rural and marine environment.	Protein - Lipid (EY)		**Surface**	
S26 - Aptera Gamma-shaped cistern (Roman - 1st AD)	NW section - connection of the right wall to the floor - exposed to external, rural and marine environment.	Protein - Lipid - Phosphates - Sulphates (EY, **Mould, DR**)		**Surface**	√
S27 - Aptera Gamma-shaped cistern (Roman - 1st AD)	NW section floor - exposed to rural and marine environment - occasional rainwater accumulation.	Protein - Lipid (EY, EW, **DR2**)		**Surface**	√
S28 - Aptera Gamma-shaped cistern (Roman - 1st AD)	S. section wall - exposed to rural and marine environment.	Lipid - Protein (BG, **Mi**, EY, EW, Bones)		**Mortar**	√

Table 25: continued.

The interpretation of the reflectance micro-FTIR spectra of the 29 mortar samples from Ancient Polyrrhenia, Phalasarna and Aptera indicate the presence of organic substance and its composition (Table 25). The organic substance is identified as a protein-lipid-phosphate material which shares spectral similarities with egg protein. The equal distribution of the organic substance within the calcite surface layer and its gradual reduction towards the inner mortar reinforces the hypothesis that egg protein was used either as an additive in the final plaster or as a surface coating.

The 9 samples from Polyrrhenia provided the most representative spectra of intentional organic presence, free from biological contamination. The samples contain a protein-lipid-phosphate material, closely matching egg white/mortar standards (table 25; Appendix III, Table 2). Spectra similarities of samples S14 to S15b with bone glue and bone standards may show that crushed bones were added as compatible calcite aggregates, or as a source of collagen that would act as an adhesive in the mortar (Polikreti and Maniatis, 2008, 118; Brysdaert, 2008, 2765; Regev, 2010, 3007; Chiotis et al., 2001, 328). The use of bone glue could be justified as an additive that would improve the workability of the mortar, increasing the plasticity and regulating the setting rates (Moropoulou et al., 2005). Bone glue as well as egg white (albumen) were experimentally tested for improving the waterproofing properties of mortars by reducing porosity (Ventola et al., 2011, Mydin, 2018). In the Polyrrhenia spectra, the resemblance of the protein peak shapes to those of egg white protein and the co-existence with lipid leads to the identification of the additive as an egg-sourced protein rather than bone glue.

The organic substance in the samples from Phalasarna is similar to that from Polyrrhenia, although exposure to an aggressive marine environment, reflected by the presence of gypsum and sea salts on the Phalasarna samples, possibly affected the number and intensity of organic peaks in the spectra. The filtered CPAD below, shows the difference in the number of organic peaks between the Polyrrhenia sample S3 (31 peaks - yellow highlight) and the environmentally exposed sample S7 from Phalasarna (14 peaks - blue) (fig.282). According to the filtered CPAD, both samples retain protein-lipid-phosphates in their composition, closely related to egg proteins. The amide peaks above 1690 cm^{-1} on the spectrum of S7 are significantly reduced in number as opposed to the retained peaks on the S3 spectrum (fig.282).

The CPAD methodology offers this information via direct comparisons between samples, effectively allowing the comparative study of preservation of additives in different exposure conditions.

Peak x (position)	Spectrum ID	Chemical Band Assignement	Reference	Type of band
1262	FAL_S7_1-12_av			
1264	BG_av			stair-step type intensities
1267	POL_S3_1-6_av			
1312	POL_S3_1-6_av			
1313	BG_M_50_av	bone glue	Spectrum BG_av	stair-step type intensities
1314	EW_M_75_av	egg white	spectrum EW_av	weak absorption
1316	FAL_S7_1-12_av			
1338	POL_S3_1-6_av			
1341	BG_M_75_av	bone glue	Spectrum BG_av	stair-step type intensities
1363	POL_S3_1-6_av			
1374	POL_S3_1-6_av			
1377	FAL_S7_1-12_av			
1385	EY_av	C-H bending	Buti et al, 2013, p. 2705	sharp absorption
	FAL_S7_1-12_av			
1444	FAL_S7_1-12_av			
1445	E_av	Amide III	Buti et al, 2013, p. 2705, spectrum EW_av	weak absorption
1453	EW_M_75_av	egg white	spectrum EW_av	weak absorption
1457	FAL_S7_1-12_av			
1458	EW_av	Amide III	Rosi et al, 2009, p. 2099	stair-step type intensities
1473	BG_av	Amide III	Rosi et al, 2009, p. 2099	stair-step type intensities
1488	POL_S3_1-6_av			
1506	POL_S3_1-6_av			
1507	EY_av	C=O	Rosi et al, 2009, p. 2099	weak absorption
	FAL_S7_1-12_av			
1516	POL_S3_1-6_av			
1519	EY_av	C=O	Rosi et al, 2009, p. 2099	weak absorption
1539	POL_S3_1-6_av			
1541	FAL_S7_1-12_av			
1616	POL_S3_1-6_av			
1635	POL_S3_1-6_av			

Figure 282: Filtered CPAD showing the organic peaks of S7 (blue highlight) and S3 (yellow highlight) and their potential matching to standards.

Peak x (position)	Spectrum ID	Chemical Band Assignement	Reference	Type of band
1643	FAL_S7_1-12_av			
1659	FAL_S7_1-12_av			
1661	BG_M_5_av	quartz	Spectrum Q_av, spectrum M_av	weak bands
1666	FAL_S7_1-12_av			
1667	EY_av	C=O		strong absorption
1669	POL_S3_1-6_av			
1679	POL_S3_1-6_av			
1687	POL_S3_1-6_av			
1692	EW_M_75_av	N-H bands	Spectrum EW_av, Ploeger et al, 2010, p.37, Miliani et al, 2012, p. 305	strong absorption
1702	BG_M_50_av	bone glue	Spectrum BG_av	
1704	POL_S3_1-6_av			
1722	FAL_S7_1-12_av			
2575	POL_S3_1-6_av			
2596	POL_S3_1-6_av			
2603	EW_M_75_av	egg white	spectrum EW_av	weak absorption
2732	POL_S3_1-6_av			
2763	POL_S3_1-6_av			
2801	POL_S3_1-6_av			
2802	BG_M_75_av	C-H stretching	Rosi et al, 2009, p. 2099	weak absorption
2876	E_av	C-H stretching	Rosi et al, 2009, p. 2099, spectrum EY_av	strong absorption
	FAL_S7_1-12_av			
	POL_S3_1-6_av			
2885	BG_av	C-H stretching	Miliani et al, 2012, p. 304, Rosi et al, 2009, p. 2104	weak absorption
	POL_S3_1-6_av			
2895	POL_S3_1-6_av			
2897	BG_M_25_av	C-H stretching	Spectrum BG_av, Miliani et al, 2012, p. 304; Rosi et al, 2009, p. 2104	weak bands
2905	BG_M_25_av	bone glue	Spectrum BG	weak absorption
	POL_S3_1-6_av			
2935	BG_M_5_av	bone glue	Spectrum BG_av	weak bands
2936	POL_S3_1-6_av			
2966	POL_S3_1-6_av			
2967	EY_av	C-H stretching	Rosi et al, 2009, p. 2099	sharp absorption
2973	E_av	C-H stretching bands, esters	Spectrum EY_av, Rosi et al, 2009, p. 2099	strong absorption
2976	POL_S3_1-6_av			
2981	EW_av			weak absorption
2984	FAL_S7_1-12_av			
2985	BG_M_75_av	bone glue	Spectrum BG_av	weak absorption
2990	BG_M_50_av	bone glue	Spectrum BG_av	weak absorption
2991	POL_S3_1-6_av			
3009	POL_S3_1-6_av			
3015	EY_av	CH stretching	Miliani et al, 2012, p. 302	weak absorption
3021	POL_S3_1-6_av			

Figure 282: continued.

The Aptera samples follow the same organic pattern as Polyrrhenia and Phalasarna samples that cannot be ignored despite the presence of biological activity in almost all of them. Protein-lipid substance that exhibits similarities with egg standards is detected within the surface of the samples. The complexity of the spectra due to the presence of biologically-derived spectral features cannot allow further specification of the egg part, as in the case of the Polyrrhenia samples.

However, the spectral interpretation of the Aptera samples enabled the assignment of diagnostic peaks to biological activity. Their detection solely on the flat surface of the Aptera samples, that is the outmost exposed surface layer and the chemical differences between the flat surface and the surface spectra (cross-section positioning under the FTIR microscope) showed that the organic substance within the surface layer did not derive from biological activity or other external depositions, rather it belonged to an intentionally added organic material in the mortar.

11.4.2 Diagnostic peaks

Table 26 lists the diagnostic reflectance peaks and ROIs of biological activity and protein-lipid-phosphate substance that occurred most often in sample composition. It is obvious that both types of organic substances (biological and intentionally added organics) share peaks in the same regions, since both contain proteins and lipids, as well as phosphates and sulphates (Gomez-Heras et al., 2004, 508). However, the shape and intensity of peaks, and the comparative behavioural change in intensity and wavenumber location differentiate one from the other.

Biological Activity - Diagnostic Peaks and ROIs	Chemical Assignment - Absorption Shape / Intensity / Behaviour
911, 1011	Sugars
1066, 1116	CH, Phosphates and Carbonates
1202, 1005, 987	Sugars
1265-1267	Blue-shifted, lower than 10 cm^{-1}
1309, 1339	Sharp and distinct peaks
1400	Sharp and weak peak
1453, 1466	Sharp and distinct peaks
1632, 1666	Sharp and distinct peaks
2921, 2928	Characteristic shape to mould
3500	High water content, broad and strong peak
Protein - Lipid - Phosphates (egg-related) - Diagnostic Peaks and ROIs	**Chemical Assignment - Absorption Shape / Intensity / Behaviour**
1044, 1058	Phosphates
1159	High intensity, strong peak, resemblance to bone standards
1267-1295	Blue-shifted, over 10 cm^{-1}
1300-1370	Broad and weak peaks
1488-1560	Broad and weak peaks
1600-1704 (1668-1704)	Broad and weak peaks
2900-3000	Shape dictates which organic in present (amides or lipids)
3500	Low water content

Table 26: List of diagnostic peaks and ROIs for the detected biological activity and protein-lipid-phosphate organic additive.

The presence of strong and broad intensity of OH above 3500 cm^{-1} and the characteristic shape of mold peak at 2921-2928 cm^{-1} in combination with sugars provide the chemical evidence of organic substances related to the action of micro-organisms (Ortiz-Miranda et al., 2017). Sugars are released from the hydrolysis of cellulose by fungal enzymes; thus, they are considered diagnostic to the action of micro-organisms (Mills and White, 1987, 64). Sugar peaks are also present in the spectra of milk/mortar mixtures and pigeon droppings (Synytsya and Novak, 2014, 6). What differentiates bio-induced sugars from those indicating milk presence is the lack of any other milk diagnostic peaks in the spectra. Once more, the outcome of Chapter 8 is highlighted, where identification requires the assessment of the peaks present as well as of those that should be present in order to have a match between the spectrum in question and the standards.

The identification of the organic substance through the CPAD revealed further information on the influence of inorganic components to the projection of proteins. It appears that the strong amide peaks at 1690 cm^{-1} and 1570 cm^{-1} expected to be detected in spectra that show protein, merge into one broad peak at 1670 -1640 cm^{-1} when the concentration of calcite is increased in the region.

Similarly, the diagnostic peak of lipids at 1740 cm^{-1} and that of protein at 1570 cm^{-1} are the most affected when inorganic content increases, thus identification of organic materials cannot rely on their presence. The fact that the diagnostic lipid peak at 1740 cm^{-1} was usually absent in spectra where protein-lipid content was detected, suggests either total absence of a strong lipid, fast decomposition of the esteric bond or preservation of traces of lipid in egg white during its separation from egg.

Ageing produces broadening of the esteric stretching band at 1735 cm^{-1} due to the hydrolysis of triglycerides and the formation of free fatty acids and other degradation products, which is detected by the appearance of an absorption band at 1711 cm^{-1} (Mazzeo et al., 2008, 69). This band was identified in the ancient mortar samples, reinforcing the assumption of the presence of an intentionally used organic additive of egg origin, possibly preserved in degraded condition.

These spectral features that derive from the inorganic interference and degradation can be used as diagnostic to egg-related materials in combination with the comparative assessment of the intensity of the C-O bond at 1260 cm^{-1} in respect to the intensity of the 1700-1300 cm^{-1} in a spectrum: higher intensity of 1260 cm^{-1}, blue-shifted up to 1280 cm^{-1} indicates higher lipid content than protein; when the intensity of the peaks at 1260-1280 cm^{-1} is lower than the ROI 1700-1300 cm^{-1} and the overall shape has stair-step type intensities the protein content exceeds the lipid content.

11.4.3 Archaeological context

Assumptions can be made by linking the spectral data to the archaeological context in order to understand the use of the additive in the water-related constructions sampled in the thesis. The presence of an organic coating rather an additive in the surface of the cistern walls of Phalasarna (S7) can be strongly supported by the in situ archaeological evidence of the black substance preserved over the lead lining at the lower part of the cistern wall (Sec.10.1.2, fig.139). The toxicity of lead to microorganisms would prohibit any infestations that would produce black films on the metal (Salvadori and

Charola, 2011, 42). Therefore, the occurrence of the organic substance on the lead could have only been intentional, pointing towards the coating application.

The Phalasarna bathtubs were made by porous stone, thus the plastering of the surface with a waterproof mortar would have been necessary for facilitating their use. This fine plastered surface showed presence of protein and lipid, similar to standards of egg parts and their mortar mixtures. The addition of protein in mortar has experimentally resulted in the beneficial reduction of porosity by air entraining of well distributed air bubbles of small size that improve the hydrophobic properties (Jasiczak and Zielinski, 2006, 451; (Mydin, 2018, 383). In this instance, it is suggested that a mixture of fine plaster with organic material was applied over the porous stone.

Different use of the organic additive is observed in the Polyrrhenia samples S14 to S15b from the surface of the low wall between the cistern and the aqueduct. The evidence of bone-related organic material on the surface layer combined with the increased size and quantity of the quartz aggregate, differentiates the mortar technology from that of the rest of the samples, probably indicating a different construction phase (personal communication with the archaeologist S. Markoulaki, excavator of the site). Different purpose of use or maintenance should also be considered, as the low wall was built from rubble masonry supporting a ceramic pipe in its upper part for controlling the water from the aqueduct towards the open cistern (Appendix III, fig.5).

The unique presence of pumice in sample S22 from the 3-aisled cistern of Aptera suggests use of a different type of hydraulic mortar in the particular area of the cistern, where natural pozzolans of volcanic provenance were used instead of artificial (crushed ceramic) (Regev et al., 2010, 3008; Moropoulou et al., 2000, 50; Maravelaki et al., 2). The consistency in the chemistry of the organic substance in its surface layer with the rest of the samples from the cistern may suggest periodical maintenance of the cistern with the same egg protein coating.

The spectral evidence is consistent with literature that describes the use of egg-related materials as mortar additives that increase hydrophobicity and reduce mortar porosity, preventing decay (Mydin, 2018, Fang et al., 2013, 4). The fact that all samples derive from constructions related to water supply and usage reinforces the idea that improvement of hydrophobicity was desirable if not necessary. In Greece, the egg white mortar additive is mentioned in the construction of the 18th and 19th century AD arched stone bridges built for connecting the river banks (Center of Environmental Training of Makrinitsa, 2007, 18). The continuation of an ancient technology to later traditional practices cannot be disregarded.

The presence of dolomite, mainly on the Phalasarna bathtubs and Polyrrhenia samples from the worked stone, should not be considered as external deposition but rather as mortar component rich in magnesium (Maravelaki et al., 2003, 653). If the available source of calcareous binder contained dolomite and thus a high amount of magnesium, then the mortar would have been susceptible to damage when wet and surface protection would have been necessary, probably facilitated with the addition of the egg protein (Singh et al., 2014, 431). Although the physical properties of magnesium-rich lime mortars are not yet clearly established, dedolomitization and formation of magnesium sulphate soluble salts may lead to weathering of the mortar (Chever et al., 2010, 285).

The polishing marks in samples S6, S12 and S20, one sample from each archaeological site, could be interpreted as attempts to improve surface durability or maintenance against the accumulation of calcium carbonate deposits ("*sinter*") (Bobee et al., 2010, 12; Hodge, 2002, 227). The use of an organic additive on the surface layer could have added to the desired effect, although experimentation is necessary to provide concrete evidence.

The presence of the organic additive in the surface layer of plaster was visually supported by OM and SEM examination in 24 out of the total 29 samples (in pink, table 26, sec.10.4.1). The organic layer is sometimes preserved underneath inorganic and biological depositions. The smooth texture of the surface layer and its differentiation from loose random depositions and build-up of biomineralization, reinforced the hypothesis of presence of an organic substance, intentionally used. The remaining 5 samples derived either from mortar within the masonry (S13), from very thin mortar layers (S8 and S9) and uncertain locations and excessive weathering (S16, S17). Organic substance on these 5 samples was indicated from the spectra interpretation but OM and SEM did not provide visual evidence.

All samples apart from S16 and S17 (Aptera – Roman Villa) derive from public water-related constructions that cover a chronological span from as early as the 4th century BC (Phalasarna cistern and bathtubs) to 4th century AD (Phalasarna, Three Hierarchs Church area-cistern floor). The mortar composition appears to be similar in all samples, suggesting that mortar technology did not change within the Hellenistic to Late Roman period in this particular geographic region, supporting the theory of use of the typical lime-quartz-crushed ceramic mortar even before the Roman period (Moropoulou, 2005, 296). It is possible that a similar preference was shown throughout this period for the use of egg protein where waterproofing was desirable.

The consistency of spectral results for the majority of the samples relevant to the identity of the organic material and its distribution, rules out any misinterpretation of random coexistence of different organic materials in a spectrum interpreted as a single organic substance. This could have occurred to some samples but not to all, especially not to those that derive from burial environment and provided less complex spectral profiles.

The dark colouration of this organic-containing layer, observed in almost all the samples, should indicate decay processes and accumulation of deposits probably interacting with the organic material. The decay mechanisms affecting the mortar additive are beyond the scope of this thesis, but require equal attention in the future.

11.4.4 Decay and biological activity

Decay and weathering effects were revealed through the differential preservation of the organic substance between the outer surface and within the cross section of the surface, especially on samples exposed to external environment. This is illustrated in the CPAD comparative assessment of the two layers of sample S24 (fig.283). The peaks within the surface layer assigned to an organic additive, closely related to egg yolk, are 24 (yellow - S24_1-6), as opposed to the 13 peaks on the flat surface spectrum (green – S24_10-13). The number of peaks related to the organic material should be indicative of the degree of its preservation in each layer.

The main peak that indicates biological contamination on the flat surface is that of sugars at 920 cm^{-1} (fig.283). This peak is missing from the spectrum within the surface, suggesting that the layer is free from any external contamination.

Certain factors have been identified in similar case studies as preventing of biological attack to an organic additive within the mortar matrix: the slow conversion of lime to $CaCO_3$ during the setting of mortar that creates alkaline environments that inhibit bacterial action (Fang et al., 2013, 6); the quick lime digestion process during the preparation of the mortar which releases heat and active oxygen which kills any bacteria present (Fang et al., 2013, 4); and lastly, the presence of the organic additive itself that reduces the porosity of the mortar restricting the access to bacteria (Fang et al., 2013, 4; Mydin, 2018, 383).

The fact that inorganic presence is more pronounced within the surface of sample S24 than on the flat surface may account for the better organic preservation in this layer according to the factors described above and the positive effect of alkalinity. In the particular sample, inorganic presence not only does not mask the organic component, but it may play a preventive role on the action of microorganisms (sec.11.3.3, S24).

The higher degree of preservation of the organic additive within the surface layer is further reinforced by the retention of the ROIs 3013-2988, 1691-1679, 1506-1441 cm^{-1} (amides) and 1390-1340 cm^{-1} (lipids), as opposed to their absence on the flat surface (fig.283). This difference in peak presence should not be encountered as occurrence of two individual organic materials, rather as a weathering effect on the outer surface. The assumption is based on the occurrence of common peaks in both spectra that shows that the same organic substance is present in both layers but reduced due to exposure on the outer surface.

The final identification of the organic substance derives from the CPAD comparison of sample S24 with standards of egg parts and their mortar mixtures, as well as pigeon droppings and soil, showing that the organic additive is closely related to egg yolk due to the occurrence of common peaks between the sample and the particular standard (fig. 270; sec.10.3.3, S24). This approach then excludes external organics such as pigeon droppings. The OM and SEM assessment verified the reflectance micro-FTIR results on the presence of biological activity in limited scale on the surface and the presence of an organic additive.

Peak x (position)	Spectrum ID	Chemical Band Assignement	Reference	Type of band
920	APT_S24_10-13_av			
921	RS_P_av	polysaccharides =CH or C=C	Chauhan et al, 2018, 79	weak absorption
1263	APT_S24_1-6_av			
	EY_M_75_av	egg yolk	spectrum EY_av	strong absorption
1264	APT_S24_10-13_av			
1266	DR1_av			strong absorption
	DR2_av	v3 asymmetric stretching SO4-2	Miliani et al, 2012, p. 300	strong absorption
1315	APT_S24_1-6_av			
	EY_M_25_av	CH2, CH3	Lombardi and Santarelli, 2009, p. 542	strong absorption
1320	APT_S24_10-13_av			
1340	APT_S24_1-6_av			
1342	EY_M_50_av	quartz	spectrum Q_av	weak absorption
1353	APT_S24_1-6_av			
1358	DR1_av			strong absorption
1390	APT_S24_1-6_av			
	EY_M_25_av	C-H bending	Spectrum EY_av, Buti et al, 2013, p. 2705	strong absorption
1393	RS_P_av	CH2 and CH3 aliphatic bending	Chauhan et al, 2018, 79	strong absorption
1401	DR2_av			weak absorption
1402	APT_S24_10-13_av			
1441	APT_S24_1-6_av			
1445	EY_av			weak absorption
1453	APT_S24_1-6_av			
	DR1_av			strong absorption
1456	RS_P_av			weak absorption
1472	APT_S24_1-6_av			
	EY_av	C-O bending	Ricci et al, 2006, p. 1223	sharp absorption
	RS_P_av			weak absorption
1495	RS_P_av			weak absorption
1497	APT_S24_1-6_av			
1500	EY_M_75_av	C=O	Spectrum EY_av, Rosi et al, 2009, p. 2099	weak absorption
1506	APT_S24_1-6_av			
1507	EY_av	C=O	Rosi et al, 2009, p. 2099	weak absorption
1516	APT_S24_10-13_av			
1518	EY_M_50_av	C=O	Spectrum EY_av, Rosi et al, 2009, p. 2096	weak absorption
1528	APT_S24_1-6_av			
1529	EY_M_50_av	C=O	Spectrum EY_av, Rosi et al, 2009, p. 2097	weak absorption
1539	APT_S24_1-6_av			
	EY_M_5_av	C=O	Spectrum EY_av, Rosi et al, 2009, p. 2098	weak absorption
1551	APT_S24_10-13_av			
1559	EY_av	C=O	Rosi et al, 2009, p. 2099	strong absorption
1560	APT_S24_10-13_av			
	EY_M_50_av	C=O	Spectrum EY_av, Rosi et al, 2009, p. 2099	weak absorption

Figure 283: Filtered CPAD for S24 surface (yellow - S24_1-6) and flat surface (green-S24_10-13) spectra compared to egg yolk (EY), egg yolk/mortar standards, pigeon droppings (DR1 and DR2), Red soil (RS) and Grey soil (GS). For clarity, the comparisons with other egg parts and their mortar mixtures are excluded.

Peak x (position)	Spectrum ID	Chemical Band Assignement	Reference	Type of band
1604	EY_M_50_av	quartz	spectrum Q_av	weak absorption
1605	APT_S24_10-13_av			
	RS_P_av	metal carboxylate, lignin, proteins, humic acids	Chauhan et al, 2018, 79	strong absorption
1632	APT_S24_1-6_av			
1666	APT_S24_10-13_av			
1667	APT_S24_1-6_av			
	EY_av	C=O		strong absorption
1679	APT_S24_1-6_av			
	EY_M_75_av	C=O	Spectrum EY_av, Rosi et al, 2009, p. 2099	weak absorption
1690	EY_M_50_av	C=O	Spectrum EY_av, Rosi et al, 2009, p. 2099	strong absorption
1691	APT_S24_1-6_av			
2546	DR1_av			weak absorption
2547	APT_S24_10-13_av			
2562	EY_M_50_av			weak absorption
2564	APT_S24_10-13_av			
2573	APT_S24_1-6_av			
2584	APT_S24_1-6_av			
2593	EY_M_25_av			weak absorption
2594	APT_S24_1-6_av			
2646	APT_S24_1-6_av			
	DR1_av			weak absorption
2805	APT_S24_1-6_av			
2965	APT_S24_10-13_av			
	EY_M_75_av	C-H stretching bands, esters	Spectrum EY_av, Rosi et al, 2009, p. 2099	strong absorption
2988	APT_S24_1-6_av			
3003	APT_S24_1-6_av			
3004	EY_M_50_av	CH stretching	Miliani et al, 2012, p. 302	weak absorption
3005	DR2_av			weak absorption
3013	APT_S24_1-6_av			
3015	EY_av	CH stretching	Miliani et al, 2012, p. 302	weak absorption
3622	APT_S24_10-13_av			
	GS_P_av			

Figure 283: continued.

Biological activity was not chemically evidenced on the samples from Polyrrhenia and Phalasarna. This was supported by the OM and SEM visual assessment. The presence of phosphates on the surface layer of the Polyrrhenia samples may have created a hostile environment for bacteria (Table 25) (Polikreti and Maniatis, 2003, 188). The fact that phosphates were detected on all the Polyrrhenia samples regardless their burial (S1 to S3 and S14 to S15b) or exposure (S4 to S6), enhances the hypothesis that phosphates are part of the composition of the samples.

11.4.5 Overview of spectra interpretation

The identification of organic substances was understandably characterized by increased difficulty compared to identification of laboratory prepared standards. A number of spectra of ancient samples exhibited significant additional complexity due to the presence of organic and inorganic substances associated with biological activity and gypsum depositions. In these samples, identification had to overcome newly introduced overlapping of peaks and spectral patterns that could be assigned to more than one organic materials. Additionally, decay and physical weathering of the samples could lead to false conclusions relevant to the presence or absence of an identified organic substance. Considering that the initial quantity of the organic additive in the mortar would have been low, since high quantity would act as a retarder of carbonization (Yang et al., 2010, 941), it was expected that the available spectral evidence to begin with would have been limited.

Spectral complexity was encountered on the spectra of Ancient Aptera samples due to the presence of biological activity, in almost all of them (Table 26). The difficulty was dealt with by comparing the Aptera samples through the CPAD with standards representing biological contaminants, soil and other external depositions as well as standards of possible organic mortar additives. This enabled the discrimination of the organic substance, likely of intentional use, from biological depositions.

The identification methodology developed through the experimental work in Chapter 7 and 8 provided the means to obtain technological information relevant to both organic and inorganic components on the ancient mortar samples. The spectral evidence of the presence of an organic additive assessed through the archaeological context suggests that improvements in the hydrophobic properties of the water-related constructions could have been practiced. This outcome offers strong grounds for further study on the topic of organic mortar additives.

The interpretation outcomes were deduced from the contextualization of the CPAD methodology results in the archaeological and historical framework, offering realistic conclusions. This process is fundamental in the utilization of analytical outcomes when studying ancient technologies.

Chapter 12: Thesis Conclusion

The thesis demonstrated that External Reflectance FTIR micro-spectroscopy offers a valid analytical approach for the non-destructive detection and identification of organic additives in mortar matrices. The degree of confidence in the identification outcomes relies on the appropriate development and use of the Chemical Peak Assignment Database (CPAD).

The diagnostic outputs from the analysis of laboratory analogues and archaeological samples introduced reflectance spectral features able to distinguish chemically similar organic additives and biological depositions from intentionally added organic materials in mortars. Spatial correlation of chemical data clarified further the origin of organic components and offered insight on the purpose of use. The identification protocol is completed by the recording of newly formed peaks, peak position shifting and intensity alterations induced by the interaction of organic additives with the inorganic mortar components and by aging processes. The study of reflectance spectra expressed as a numerical system rather than a graphic spectral pattern minimizes the risk of overlooking the spectral behavior of weak peaks that proved to be fundamentally useful in reflectance spectroscopy.

The peak-by-peak comparative assessment of a reflectance spectrum with possible matching spectra of standards allows the CPAD user to assess what bonds are present in the spectrum but also which bonds should be present in order to have a match. The results are supported by rigid criteria establishing the advantage of the CPAD identification methodology over Principal Component Analysis that fails by default to justify its outcomes.

This acquired knowledge offers strong grounds for the systematic application of External Reflectance FTIR micro-spectroscopy in identification studies of organic mortar additives and contradicts the perception of the limited capability of the method to provide secure outcomes compared to destructive methods of analysis.

Improving the confidence of identification requires that the CPAD be updated with reflectance spectra of organic additives and their mortar mixtures in different decay stages, induced by different decay mechanisms. This future work will explore the chemical transformations of organic bonds due to aging and their projection in reflectance spectra, offering accurate diagnostic reflectance features of decayed organic mortar additives,

improving the spectral profiling of archaeological samples which are subjected to prolonged decay.

The results of this study indicate the use of organic mortar additives in water-related constructions from three specific archaeological sites on West Crete. The dissemination of the thesis outcomes will lead to informed decisions on conservation implementations and the in-situ preservation of evidence.

Future comparative assessment with samples from similar archaeological context through the CPAD identification methodology will reinforce the archaeological evidence of the systematic use of organic mortar additives in antiquity. This should initiate an in-depth study of the physico-chemical properties of these additives and link them to specific applications. The outcomes can then be utilized in conservation practice, offering environmentally sustainable repair mortars that carry the knowledge of traditional practices, harmonized with the historical integrity of the monuments.

Accordingly, objectives for the next phase of this research should explore experimentally and analytically:

- How decay processes impact the chemical characterization of organic mortar additives.
- Quantitative determination of the optimum amounts of organic additives in mortars.
- Physico-chemical properties of organic mortar additives and organic coatings on mortars.
- Species-specific approaches to characterizing organic mortar additives.
- Development of non-invasive/invasive workflows to extract the maximum information from mortars containing organic additives.
- How improved understanding of organic mortar additives can support implementation and evaluation protocols for heritage conservation practices involving the use of traditional materials.

References

Aïtcin, P.-C., 2016. Chapter 3 - Portland cement. In: Aïtcin, P.-C. and Flatt,R., J. Editor(s), *Science and Technology of Concrete Admixtures.* Woodhead Publishing, 27-51

Andersen, C.K., Bonaduce, I., Andreotti, A., van Lanschot, J., Vila, A., 2017. Characterization of preparation layers in nine Danish Golden Age canvas paintings by SEM-EDX, FTIR and GC-MS. *Heritage Science*, 5, 34, 1-12

Andreotti, A., Baroni, S., Bonaduce, I., Bozza, S., Cantisani, E., Ismaelli, T., Vettori, S., 2018. Ancient restorations at Hierapolis of Phrygia (Denizli, Turkey): Interdisciplinary research on materials and technologies. *Journal of Archaeological Science: Reports 21*, 862–871

Arizio, E., Piazza, R., Cairns, W., Appolonia, L., Botteon, A., 2013. Statistical Analysis on ancient mortars: A case study of the Balivi Tower in Aosta (Italy). *Construction and Building Materials*, 47, 1309-1316

Arrizabalaga, I., Gomez-Laserna, O., Carrero, J., A., Bustamante, J., Rodrıguez, A., Arana, G., Madariaga, J., M., 2015. Diffuse reflectance FTIR database for the interpretation of the spectra obtained with a handheld device on built heritage materials. *Anal. Methods,* 7, 1061

Ashurst, J., 1998. Methods of repairing and consolidating stone buildings. In: Ashurst, J. and Dimes, F., G., *Conservation of Building and Decorative Stone*: 2nd (Second) edition, Vol. 2, Ch. 1, 1-54

Babu, T.S. R., and Neeraja, D., 2017. An experimental study of natural admixture effect on conventional concrete and high-volume class F flyash blended concrete. *Case Studies in Construction Materials,* 6, 43-62

Bacci, M., Chiari, R., Porcinai, S., Radicati, B., 1997. Principal component analysis of near-infrared spectra of alteration products in calcareous samples: An application to works of art. *Chemometrics and Intelligent Laboratory Systems,* 39, 115-121

Banwell, C., and McCash, E., M., 1994. *Fundamentals of Molecular Spectroscopy*. 4th ed. London: McGraw – Hill Publishing Company

Bardin, D., F., de Souza Madureira Felicio, A., L., Sun, D., Nixdorf, S., L., Hirooka, E., Y., 2014. Application of infrared spectral techniques on quality and compositional attributes of coffee: an overview. *Food Research International*, 61, 23-32

Berntsson, O., Danielsson, L-G., Folestad, S., 1998. Estimation of effective sample size when analyzing powders with diffuse reflectance near-infrared spectrometry. *Analytica Chimica Acta*, 364, 243-251

Blauer-Bohn, C., and Jagers, E., 1997. Analysis and Recognition of Dolomitic Lime Mortars. In: *Roman Wall Painting Materials, Techniques, Analysis and Conservation, Proceedings of the International Workshop*, Ed: Béarat, H., Fuchs, M., Maggetti, M., Paunier, D., Institute of Mineralogy and Petrography, Fribourg7-9 March 1996

Bleicher, N. and Schubert, C., 2015. Why they are still there? A model of accumulation and decay of organic prehistoric deposits. *Journal of Archaeological Science*, 61, 277-286

Bobee, C., Huon, S., Guendon, J., L., Salomon, J., Gebara, C., Michel, J., M., Regert, M., 2010. High-Resolution (PIXE) analyses of carbonate deposits in a Roman Aqueduct (Frejus, Se France): Implications for the study of Palaeohydrological variability and water resources management in Southern Gaul during the Roman Period. *Archaeometry*, 53, (2), 241-260

Bonnier, F., and Byrne, H., J., 2012. Understanding the Molecular Information contained in Principal Component Analysis of vibrational spectra of biological systems. *Analyst*, 137, 322-332

Bro, R. and Smilde, K., 2014. Principal Component Analysis. *Analytical Methods*, 6, 2812-2831

Brysbaert, A., 2008. Painted plaster from Bronze Age Thebes, Boeotia (Greece): a technological study. *Journal of Archaeological Science*, 35, 2761–2769

Buergo, M., A. and González R., F., 2003. Protective patinas applied on stony façades of historical buildings in the past. *Construction and Building Materials*, 17, (2), 83–89

Bull, I. D., Elhmmali, M. M., Roberts, D. J., Evershed, R. P., 2003. The application of steroidal biomarkers to track the abandonment of a Roman wastewater course at the Agora (Athens, Greece). *Archaeometry* 45, 1, 149–161

Buonasera, T., 2007. Investigating the presence of ancient absorbed organic residues in groundstone using GC-MS and other analytical techniques: a residue study of several prehistoric milling tools from central California. *Journal of Archaeological Science,* 34, 1379-1390

Bureau, S., Ruiz, D., Reich, M., Gouble, B., Bertrand, D., Audergon, J., Renard, C., 2009. Application of ATR-FTIR for a rapid and simultaneous determination of sugars and organic acids in apricot fruit. *Food Chemistry,* 115, 1133–1140

Burford, E., P., Kierans, M., Gadd, G., M., 2003. Geomycology: fungi in mineral substrata. *Mycologist,* 17, (3). UK: Cambridge University Press

Buti, D., Rosi, F., Brunetti, B., G., Miliani C., 2013. In-situ identification of copper-based green pigments on paintings and manuscripts by reflection FTIR. *Analytical and Bioanalytical Chemistry*, 405, (8), 2699-2711

Celik, K., Jackson, M.,D., Mancio, M., Meral, C., Emwas, A.-H., Mehta, P.,K., Monteiro, P.,J.,M., 2014. High-volume natural volcanic pozzolan and limestone powder as partial replacements for Portland cement in self-compacting and sustainable concrete. *Cement & Concrete Composites*, 45, 136-147

Chalmers, J.M., Everall, N.J., Ellison S., 1996. Specular reflectance: A convenient tool for polymer characterization by FTIR-microscopy? *Micron*, 27, (5), 315–328.

Chatterji, S., 1995. Mechanism of expansion of concrete due to the presence of dead-burnt CaO and MgO. *Cement and Concrete Research*, 25, (1), 51-56

Chauhan, R., Kumar, R., and Sharma, V., 2018. Soil forensics: A spectroscopic examination of trace evidence. *Microchemical Journal*, 139, 74-84

Chever, L., Pavıa, S., Howard, R., 2010. Physical properties of magnesian lime mortars. *Materials and Structures*, 43, 283–296

Chiotis, E., Dimou, E., Papadimitriou, G., Tzoutzopoulos, S., 2001. A study of some ancient and prehistoric plasters and watertight coatings from Greece. Edit. Basiakos, I., Aloupi, E., Fakorellis, G. *Archaeometry Issues in Greek Prehistory and Antiquity*. Athens: Hellenic Society of Archaeometry, Society of Messenian Archaeological Studies

Christer, A., 2005. PCA. In Eriksson, L., Byrne, T., Johansson, E., Trygg, J. and Wikström C., ed. *Multi- and Megavariate Data Analysis*.

Christou, C., Agapiou, A., Kokkinofta, R., 2018. Use of FTIR spectroscopy and chemometrics for the classification of carobs origin. *Journal of Advanced Research*, 10, 1-8

Cordela, C., B., Y., 2012. *PCA: The Basic Building Block of Chemometrics*. INTECH. Available at: http://www.intechopen.com/books/analytical-chemistry/pca-the-basic-building-block-of-chemometrics

Cullum, B., M., and Vo-Dinh, T., 2003. Sample Collection and Preparation of Liquid and Solids. In *Handbook of Spectroscopy*, Volume 1. Edit. Gauglitz, G. and Vo-Dinh, T. Weinheim: WILEY-VCH Verlag GmbH & Co. KGaA, Ch.2

Cuní, J., 2016. What do we know of Roman wall painting technique? Potential confounding factors in ancient paint media analysis. *Heritage Science*, 4, 44, 1-13

Daveri, A., Verri, G., Rosi, F., Miliani, C., Benedetti, P., Piqué, F., 2008. Principal Component Analysis of Reflectance Medium Infrared Spectra for the Non-Invasive Identification of Organic Materials in Wall Paintings. *Multivariate Analysis and Chemometry Applied to Environment and Cultural Heritage,* 2nd ed., CMA4CH 2008, Mediterraneum Meeting, Ventotene Island, Italy, Europe, 1-4 June 2008

Daher, C., Sutherland, K., Stratis, H., Casadio, F., 2017. Paul Gauguin's Noa Noa prints: multi-analytical characterization of the printmaking techniques and materials. *Microchemical Journal*, Accepted Manuscript

Degryse P., Elsen J., Waelkens M., 2002. Study of ancient mortars from Sagalassos (Turkey) in view of their conservation. *Cement and Concrete Research,* 32, 1457–1463

De Luca, M., Terouzi, W., Ioele, G., Kzaiber, F., Oussama, A., Oliverio, F., Tauler, R., Ragno, G., 2011. Derivative FTIR spectroscopy for cluster analysis and classification of morocco olive oils. *Food Chemistry*, 124, 1113-1118

Dirwono, W., Park, J., S., Agustin-Camacho, M.R., Kim, J., Park, H., Lee, Y., Lee, K., 2010. Application of micro-attenuated total reflectance FTIR spectroscopy in the forensic study of questioned documents involving red seal inks. *Forensic Science International*, 199, 6–8

Drop-in statistics sessions in the School of Mathematics, Cardiff University (personal attendance, October 2017)

Duran, A., Robador, M. D., Jimenez de Haro M. C., Ramirez-Valle, V., 2008. Study by Thermal Analysis of mortars belonging to wall paintings corresponding to some historical buildings of Sevillian Art. *Journal of Thermal Analysis and Calorimetry*, 92, (1), 353–359

Duyan, E., 2012. Architecture History Art. In *Interactions in the history of architecture*. ARCHHIST'12, Conference Proceedings, 23-25 May. Duyan, E., and Ozturcan, C., edit. Minar Sinan Fine Arts University, DAKAM Publishing

Edwards, G., M., H., Farwell W., D., 2008. The conservational heritage of wall paintings and buildings: an FT-Raman spectroscopic study of prehistoric, Roman, mediaeval and Renaissance lime substrates and mortars. *Journal of Raman Spectroscopy*, 39, 985–992

Erişmiş, M., C., and Gezerman, A., O., 2013. A critical look at Vitruvius, *Historic preservation*, 55A, 13324-13328

Evershed, R., P., and Dudd, S., N., 1999. Lipid Biomarkers preserved in Archaeological Pottery: Current Status and Future Prospects. In: Editors: Pike, S., and Gitin, S., *The Practical Impact of Science on Near Eastern and Aegean Archaeology.* Wiener Laboratory: Monograph 3: London Archetype

Fang, S. Q., Zhang, H., Jian, B., Zheng, Y., & Zhang, B. J., 2013. The identification of organic additives in traditional lime mortar. *Journal of Cultural Heritage*, 15, (2), 144–150

Fonjaudran, C., Nevin, A., Piqué, F., Cather, S., 2008. Stratigraphic analysis of organic materials in wall painting samples using micro-FTIR attenuated total reflectance and a novel sample preparation technique. *Analytical and Bioanalytical Chemistry*, 392, (1-2), 77-86

Fremout, W., Dhaenens, M., Saverwyns, S., Sanyova, J., Vandenabeele, P., Deforce, D., Moens, L., 2012. Development of a dedicated peptide tandem mass spectral library for conservation science. *Analytica Chimica Acta* 728, 39– 48

Frost, F., J., and Hadjidaki, E., 1990. Excavation at the harbor of Phalasarna in Crete: the 1988 season. *Hesperia – Journal of American School of Classical Studies at Athens,* 59, (3)

Fujita, M. and Koike, F., 2007. Birds transport nutrients to fragmented forests in an urban landscape. *Ecological Applications*, 17, (3), 648–654

Gauri, K., L., and Bandyopadhyay, J., K., 1999. *Carbonate Stone – Chemical Behavior, Durability and Conservation.* US: Wiley – Interscience Publication

Goldsworthy, H. and Min, Z., 2009. Mortar studies towards the replication of Roman concrete. *Archaeometry* 51, 6, 932–946

Gomez-Alarcon, G., Cilleros, B., Flores, M., Lorenzo, J., 1995. Microbial communities and alteration processes in monuments at Alcala de Henares, Spain. *The Science of the Total Environment*, 167, 231-239

Gomez-Heras, M., Benavente, D., Alvarez de Buergo, M., Fort, R., 2004. Soluble salt minerals from pigeon droppings as potential contributors to the decay of stone based Cultural Heritage. *European Journal of Mineralogy*, 16, 505-509

Gonzalez, L. and Wess, T., 2008. Use of Attenuated Total Reflection Fourier Transform Infrared to Measure Collagen Degradation in Historical Parchments. *Applied Spectroscopy*, 62, 10

Guerrand D. 2017. Lipases industrial applications: focus on food and agroindustries. *OCL*, DOI: 10.1051/ocl/2017031

Hadjidaki, E., 2001. The Roman Destruction of Phalasarna. *Archaeology of the Roman Empire. A tribute to the life and works of Professor Barri Jones.* Ed. Highan, N.,J. BAR International Series 940, 155-166

Hadjidaki, E., (Χατζηδάκη Ε..), 2003. Μυστικά της Φαλάσαρνας. *Κρητικό Πανόραμα,* 101-127

Hadjidaki, E., 1988. Preliminary Report of Excavations at the Harbor of Phalasarna in West Crete. *American Journal of Archaeology*, 92, 4, 463-479

Hafez, M., Yahia, I., S., Taha, S., 2014. Study of the optically diffused reflectance and thermal microstructure for the phase transformation of $AgNO_3$. *Applied Physics. A,* 116, 1445–1453

van Hees, R., P., J., Binda, L., Papayianni, I., and Toumbakari, E., 2004. Characterisation and damage analysis of old mortars. *Materials and Structures / Matériaux et Constructions*, 37, 644-648

Hellner, N., 2006. The Krene in Megara. The analysis of a thin black layer on the floor plaster. *Preprints in Ancient Greek Technology*. 2nd International Conference, Technical Chamber of Greece (TEE). Athens

Hendra, P., 1997. *Internet Journal of Vibrational Spectroscopy*, 1, 4, 14-25. Available at: www.ijvs.com. [Accessed 10 February 2015]

Hodge, A., T., 2002. *Roman Aqueducts and Water Supply*. 2nd Edition. Bristol Classical Press

Hof, M., 2003. Basics of Optical Spectroscopy Handbook of Spectroscopy, Volume 1. In: Gauglitz, G. and Tuan Vo-Dinh, T., ed. 2003. *Handbook of Spectroscopy, Volume 1.* Weinheim: WILEY-VCH Verlag GmbH & Co. KGaA, Ch.3

Hori, R. and Sugiyama, J., 2003. A combined FT-IR microscopy and principal component analysis on softwood cell walls. *Carbohydrate Polymers*, 52, 449–453

Humphrey, J., W., Oleson, J., P., Sherwood, A., N., 1998. *Greek and Roman Technology: a sourcebook. Annotated translations of Greek and Latin texts and documents.* London and New York: Routledge

Iwanicka, M., Moretti, P., van Oudheusden, S., Sylwestrzak, M., Cartechini, L., Berg, K., J., Targowski, P., Miliani, C., 2017. Complementary use of Optical Coherence Tomography

(OCT) and Reflection FTIR spectroscopy for in-situ non-invasive monitoring of varnish removal from easel paintings. *Microc*, accepted manuscript

Jasiczak, J. and Zielinski, K., 2006. Effect of protein additive on properties of mortar. *Cement and Concrete Composites*, 28, 451-557

Johnstone, I., M., and Yu Lu, A., 2009. On Consistency and Sparsity for Principal Component Analysis in High Dimensions. *Journal of the American Statistical Association*, 104:486, 682-693

Joseph, E., Prati, S., Sciutto, G., Ioele, M., Santopadre, P., Mazzeo, R., 2010. Performance evaluation of mapping and linear imaging FTIR microspectroscopy for the characterization of paint cross sections. *Analytical and Bioanalytical Chemistry*, 396, (2), 899-910

Κέντρο Περιβαλλοντικής Εκπαίδευσης Μακρινίτσας, (Center of Environmental Training of Makrinitsa) 2007. *Τα πέτρινα τοξωτά γεφύρια της Ελλάδας*. Available at: http://repository.edulll.gr/edulll/retrieve/4047/1228.pdf

Kher, A., Mulholland, M., Green, E., Reedy, B., 2006. Forensic classification of ballpoint pen inks using high performance liquid chromatography and infrared spectroscopy with principal component analysis and linear discriminant analysis. *Vibrational Spectroscopy*, 40, 270-277

Kokoszko, M., Jagusiak, K., Rzeźnicka, Z., 2013. Rice as a Foodstuff in Ancient and Byzantine Materia Medica. *Studia Ceranea,* 3, 47–68

Kommareddy, S., Shenoy, D., B., Amiji M., M., 2007. Gelatin Nanoparticles and Their Biofunctionalization. Nanotechnologies for the Life Sciences Vol. 1. In: Kumar, C. S. S. R., Ed., *Biofunctionalization of Nanomaterials*. WILEY-VCH Verlag GmbH & Co. KGaA, Weinheim, Ch.11

Kuckova, S., Crhova, M., Hnizda, A., Hynek, R., Kodicek, M., 2009. Towards proteomic analysis of milk proteins in historic building materials. *International Journal of Mass Spectrometry*, 284, 42-46

Lewis, M., 1999. Vitruvius and Greek Aqueducts. *Papers of the British School at Rome*, 67, 145-172

Liu, K., Yu, R., Shui, Z., Li, X., Guo, C., Yu, B., Wu, S., 2019. Optimization of autogenous shrinkage and microstructure for Ultra-High Performance Concrete (UHPC) based on appropriate application of porous pumice. *Construction and Building Materials*, 214, 369–381

Lombardi, G. and Santarelli, M., L., 2009. Multi-instrumental analysis of asphalts of archaeological interest. *Journal of Thermal Analysis and Calorimetry*, 96, 2, 541–546

Macková, A., Morton, S. A., Walker, C. G. H. and Volka, K.. Surface Analysis Techniques. In: Gauglitz, G. and Tuan Vo-Dinh, T., ed. 2003. *Handbook of Spectroscopy, Volume 1.* Weinheim: WILEY-VCH Verlag GmbH & Co. KGaA, Ch.13.

Maddams, W., 1998. Background to the Use of Specular Reflection and Reflection/Absorption Methods. Available at: *Int.J. Vib. Spect.,* [www.irdg.org/ijvs] **1**, 5, 31-38

Mahlin, D., 2004. Phase Transformations in Solid Pharmaceutical Materials Studied by AFM, ESCA, DSC and SAXS. *Comprehensive Summaries of Uppsala Dissertations from the Faculty of Pharmacy 314.*

Malinowski, R.,1981. Ancient mortars and concretes; durability aspects. Preprints in: *Mortars, Cements and Grouts used in the Conservation of Historic Buildings ICCROM Symposium*, 3- 6.11.1981, Rome, 25-52

Maravelaki-Kalaitzaki, P., Bakolas, A., Moropoulou A., 2003. Physico-chemical study of Cretan ancient mortars. *Cement and Concrete Research*, 33, 651–661

Maravelaki-Kalaitzaki, P., 2005. Black crusts and patinas on Pentelic marble from the Parthenon and Erechtheum (Acropolis, Athens): characterization and origin. *Analytica Chimica Acta*, 532, 187-198

Maravelaki-Kalaitzaki, P., Galanos, A., Doganis, I., Kallithrakas-Kontos, N., 2011. Physico-chemical characterization of mortars as a tool in studying specific hydraulic components: application to the study of ancient Naxos aqueduct. *Applied Physics A* (104), 335–348

Markoulaki, S., (Μαρκουλάκη, Σ.,) 2005. Αινιγματική Πολυρρήνια. *Κρητικό Πανόραμα*, 12, 22-42

Markoulaki S. and Christodoulakos, I., 2018. Ancient Polyrrhenia and its water supply system. *Κρητική Εστία*, Περίοδος Δ’ – Τόμος 15 (2014-2018), Χανιά: Ιστορική, Λαογραφική και Αρχαιολογική Εταιρεία Κρήτης, 75-140

Markoulaki, S., and Goula, D., 2013. Archaeological research conducted during the recovery of the two selected towers and Hellenistic fortification walls of the city of Polyrrhenia in Western Crete. In *Proceedings of the 3rd Meeting for the Archaeological Work in Crete*, Rethymno, 5-8 December 2013. Vol. B. Ed.: Karanastasi, P., Tzigounaki,

A., Tsigonaki, C. Rethymno, 2015: Faculty of Letters Publications, University of Crete, Ministry of Culture and Sports – Ephorate of Antiquities of Rethymno, 135-145

Markucic, D., 2002. Tutorial 2: How to determine Repeatability and Reproducibility. *3rd European-American Workshop on NDE Reliability*. University of Zagreb, Department of Quality, Faculty of Mechanical Engineering & Naval Architecture, Croatia, [Online]. Available at: http://www.9095.net/Damir_Markucic.pdf

Martin-Gil, J., Ramos-Sanchez, M., C., Martin-Gil, F.J., 1999. Ancient pastes for stone protection against environmental agents. *Studies in Conservation*, 44, pp 58-62

Martín-Gil, J., Martín-Gil, F., J., Ramos-Sánchez, M., and Martín-Ramos, P., 2005. The Orange-Brown Patina of Salisbury Cathedral (West Porch) Surfaces: Evidence of its Man-Made Origin. *ESPR – Environ Sci & Pollut Res*, 12, (5), 285 – 289

Mazzeo, R., Prati, S., Quaranta, M., Joseph, E., Kendix, E., Galeotti, M., 2008. Attenuated total reflection micro FTIR characterization of pigment–binder interaction in reconstructed paint films. *Analytical and Bioanalytical Chemistry,* 392, (1-2), 65-76

Medeghini, L., Mignardi, S., De Vito, C., Conte, A., M., 2016. Evaluation of a FTIR data pretreatment method for Principal Component Analysis applied to archaeological ceramics. *Microchemical Journal*, 125, 224-229

Menges, F., 2011. Spekwin 32 software, version 1.71.6. Available at: http://www.effemm2.de/spekwin/

Miliani, C., Rosi, F., Daveri, A. and Brunetti, B., G., 2012. Reflection infrared spectroscopy for the non-invasive in situ study of artists' pigments. *Applied Physics A*, 106, (2), 295-307

Miliani, C., Rosi, F., Burnstock, A., Brunetti, B., G., Sgamellotti, A., 2007. Non-invasive in-situ investigations versus micro-sampling: a comparative study on a Renoirs painting. *Appl. Phys. A*, 89, 849–856

Miller, J., N. and Miller, J., C., 2010. *Statistics and Chemometrics for Analytical Chemistry*. 6th. Ed. England: Pearson Education Limited

Mills, J., S., and White, R., 1987. *The Organic Chemistry of Museum Objects*. London: Butterworths

Miriello, D., Barca, D., Bloise, A.,Ciarallo, A., Crisci, G. M., De Rose, T., Gattuso, C., Gazineo, F., La Russa, M. F., 2010. Characterisation of archaeological mortars from Pompeii (Campania, Italy) and identification of construction phases by compositional data analysis. *Journal of Archaeological Science*, 37, 2207-2223

Mobili, P., Londer, A., De Antoni, G., Gomez-Zavaglia, A., Araujo-Andrade, C., Avila-Donoso, H., Ivanov-Tzonchev, R., Moreno, I., Frausto-Reyes C., 2010. Multivariate analysis of Raman spectra applied to microbiology: Discrimination of microorganisms at the species level. *Revista Mexicana de Fisica*, 56:5, 378-385

Monico, L., Rosi, F., Miliani, C., Daveri, A., Brunetti, B., G., 2013. Non-invasive identification of metal-oxalate complexes on polychrome artwork surfaces by reflection mid-infrared spectroscopy. *Spectrochimica Acta Part A: Molecular and Biomolecular Spectroscopy,* 116, 270–280

Morillas, H., Maguregui, M., Huallparimachi, G., Marcaida, I., García-Florentino, C., Lumbreras, L., Astete, F., Madariaga, J., M., 2018. Multianalytical approach to evaluate deterioration products on cement used as consolidant on lithic material: The case of Tello Obelisk, Lima (Peru). *Microchemical Journal*, 139, 42-49

Moropoulou, A. and Polikreti, K., 2009. PCA in monument conservation: three application examples. *Journal of Cultural Heritage*, 10, 73-81

Moropoulou, A., Bakolas, A., Bisbikou, K., 1995. Characterization of ancient, byzantine and late historic mortars by thermal and X-ray diffraction techniques. *Thermochimica Acta*, 269/270, 779-795

Moropoulou, A., Bakolas, A., Bisbikou, K., 2000. Investigation of the technology of historic mortars. *Journal of Cultural Heritage*, 1, 45-48

Moropoulou, A., Bakolas, A., Moundoulas, P., Aggelakopoulou, E., Anagnostopoulou, S., 2005. Strength development and lime reaction in mortars for repairing historic masonries. *Cement & Concrete Composites*, 27, 289–294

Mydin, A., O., 2018. Physico-Mechanical Properties of Lime Mortar by Adding Exerted Egg Albumen for Plastering Work in Conservation Work. *Journal of Materials and Environmental Sciences,* 9, (2), 376-384

Nahar, S.N., 2016. *Phase-Separation Characteristics of Bitumen and their relation to Damage-Healing*, Ph. D. Delft University of Technology

Nevin, A. and Fonjaudran, C., 2015. FTIR in Reflectance and Attenuated Total Reflectance for the Analysis of Stratigraphic Cross Sections of Wall Painting Samples. In: Piqué, F. and Verri, G. *Organic Materials in Wall Paintings: Project Report*. Getty Conservation Institute

Nielsen, N., H. and Kristiansen, S., M., 2014. Identifying ancient manuring: traditional phosphate vs multi-element analysis of archaeological soil. *Journal of Archaeological Science*, 42, 390-398

Niniou, V. and Christodoulakos, Y., (Νινιού, Β. και Χριστοδουλάκος, Γ.,) 2000. Ρωμαϊκή Απτέρα. Μια πρώτη προσέγγιση. *Creta Romanae Protobizantina atti del Congresso Internazionale.* Vol.II, Iraklion, 23-30 Sept. Bottega D'Erasmo, Aldo Ausilio Editore in Padova

Niniou-Kindeli, V.,(Νινιού – Κινδελή, Β.,) 2002. Απτέρα. *Κρητική Εστία*, Περίοδος Δ' – Τόμος 9, Χανιά: Ιστορική, Λαογραφική και Αρχαιολογική Εταιρεία Κρήτης, 252-258

Niniou-Kindeli, V., 2008. *Aptera*. Ministry of Culture 25th Ephorate of Prehistoric and Classical Antiquities. Available at: https://www.chania.gr/archive/souda/www.souda.gr/files/1/28/aptera_ok_low.pdf

Noake, E., Lau, D., Nel, P., 2017. Identification of cellulose nitrate based adhesive repairs in archaeological pottery of the University of Melbourne's Middle Eastern archaeological pottery collection using portable FTIR-ATR spectroscopy and PCA. *Heritage Science*, 5:3, 1-15

Orlandos, K., A., (Ορλάνδος, Κ., Α.,) 1955-60. *Τα υλικά δομής των αρχαίων Ελλήνων και οι τρόποι εφαρμογής αυτών, κατά τους συγγραφάς, τας επιγραφάς και τα μνημεία.* Αριθμός 37. Αθήνα: Η εν Αθήναις Αρχαιολογική Εταιρεία.

Ortiz-Miranda, A., S., Domenech-Carbo, A., Domenech-Carbo, M., T., Osete-Cortina, L., Bolivar-Galiano, F., Martin-Sanchez, I., 2017. Analyzing chemical changes in verdigris pictorial specimens upon bacteria and fungi biodeterioration using voltammetry of microparticles. *Heritage Science*, 5, (8), 1-17

Othman, N., K., Salleh, E., M., Dasuki, Z., Lazim, A., M., 2018. Dimethyl Sulfoxide-Treated Starch of Dioescorea hispida as a Green Corrosion Inhibitor for Low Carbon Steel in Sodium Chloride Medium. In: Aliofkhazraei, M., ed. *Corrosion Inhibitors, Principles and Recent Applications,* Ch. 9, IntechOpen

Oudemans, T. and Erhardt, D., 1996. Organic Residue Analysis in ceramic studies: Implications for Conservation Treatment and Collections Management. *Archaeological Conservation and its consequences*. Copenhagen, IIC, 137

Papadimitriou, G. and Kordatos, J., 1995. The brown waterproofing plaster of the ancient cisterns in Laurion and its weathering and degradation. In: *The study of marble and other*

stones used in antiquity. Edit. Maniatis, Y., Henz, N., and Basiakos, Y. London: Archetype, 277-284

Paparazzo, E., 2001. Pliny the Elder on Science and Technology by John F. Healy, Review Article. *Hermathena* , 170, 65-76

Papayianni, I., and Stefanidou, M., (Παπαγιάννη, Ι. και Στεφανίδου, Μ.,) 2006. Μελέτη δομής υδραυλικών κονιαμάτων αρχαίας τεχνολογίας. *Preprints in Ancient Greek Technology*. 2nd International Conference, Technical Chamber of Greece (TEE). Athens

Papayianni, I., Pachta, V., Stefanidou, M., 2013. Analysis of ancient mortars and design of compatible repair mortars: The case study of Odeion of the archaeological site of Dion. *Construction and Building Materials*, 40, 84–92

Patni, N., Tripathi, N., Bosmia, S.,2015. Casein Extraction from various milk samples and its role as a viable substitute for conventional plastics. *International Journal of Applied Engineering Research (IJAER)*

Perkin-Elmer Multiscope™ System Microscope Manual, 1999. UK: Perkin-Elmer Corporation

Pina-Torres, C., Lucero-Gomez, P., Nieto, S., Vazquez, A., Bucio, L., Belio, I., Vega, R., Mathe, C., Vieillescazes, C., 2017. An analytical Strategy based on Fourier transfor infrared spectroscopy, principal component analysis and linear discriminant analysis to suggest the botanical origin of resins from Bursera. Application to archaeological Aztec samples. *Journal of Cultural Heritage*, 1-12

Pliny. *Natural History*, Volume X: Books 36-37. Translated by Eichholz. D., E., 1962. Harvard University Press

Pliny. *Selections from The History of the World, commonly called The Natural History of C Plinius Secundus.* Translated by Holland, P., 1962, Centaur Press, London,

Ploeger, R., Scalarone, D., Chiantore, O., 2010. Non-invasive characterization of binding media on painted glass magic lantern plates using mid-infrared fibre-optic reflectance spectroscopy. *Journal of Cultural Heritage,* 11, 35–41

Poli, T., Elia, A., and Chiantore, O., 2009. Surface finishes and materials: Fiber-optic reflectance spectroscopy (FORS) problems in cultural heritage diagnostics, *e-PS*, 6, 174-179 [e-journal].

Polikreti, K. and Maniatis, Y., 2003. Micromorphology, composition and origin of the orange patina on the marble surfaces of Propylaea (Acropolis, Athens). *The Science of the Total Environment*, 308, 111-119

Priester, H., J., Horst A.,M., Van De Werfhorst, C., L., Saleta, J., L., Mertes, L., A., K., Holden, P., A., 2007. Enhanced visualization of microbial biofilms by staining and environmental scanning electron microscopy. *Journal of Microbiological Methods,* 68, 577–587

Ramírez-Barat, B. and de la Viña, S., 2001. Characterization of Proteins in Paint Media by Immunofluorescence. A Note on Methodological Aspects. *Studies in Conservation*, 46, 4, 282-288

Rampazzi, L., Andreotti, A., Bonaduce, I., Colombini, M.,P., Colombo, C., Toniolo, L., 2004. Analytical investigation of calcium oxalate films on marble monuments. *Talanta*, 63, (4), 967–977.

Raphulu, M.C., McPherson, J., van der Lingen, E., Anderson J.A., and Scurrell, M.S., 2010 Investigation of the active site and the mode of Au/TiO2 catalyst deactivation using Diffuse Reflectance Infrared Fourier Transform Spectroscopy (DRIFTS). *Gold Bulletin*, 43, (4), 334-344

Regev L., Zukerman A., Hitchcock L., Maeir A., M., Weiner S., Boaretto E., 2010. Iron Age hydraulic plaster from Tell es-Safi/Gath, Israel. *Journal of Archaeological Science,* 37, 3000-3009

Riba, J., R., Cailloux, J., Cantero, R., Canals, T., Maspoch, M., Ll., 2018. Multivariate methods applied to FTIR: A powerful technique to highlight architectural changes in poly(lactic acid). *Polymer Testing*, 65, 264-269

Ricci, C., Miliani, C., Brunetti, B., G., Sgamellotti, A., 2006. Non-invasive identification of surface materials on marble artifacts with fiber optic mid-FTIR reflectance spectroscopy. *Talanta*, 69, (5), 1221-1226

Riquelme, F., Alvarado-Ortega, J., Ruvalcaba, J.-L., Aguilar-Franco, M., Porras-Múzquiz, M., 2013. Chemical fingerprints and microbial biomineralization of fish muscle tissues from the Late Cretaceous Múzquiz Lagerstätte, Mexico. *Revista Mexicana de Ciencias Geológicas*, 30, (2), 417-435

Rizzo, A., 2008. Progress in the application of ATR-FTIR microscopy to the study of multi-layered cross-sections from works of art. *Analytical and Bioanalytical Chemistry*, 392, (1-2), 47-55.

Rohman, A., Che Man, Y. B., Ismail, A. and Puziah, H., 2011. FTIR spectroscopy combined with multivariate calibration for analysis of cod liver oil in binary mixture with corn oil. *International Food Research Journal,* 18, 757-761

Romero-Pastor, J., Cardell, C., Yebra-Rodríguez, A., Rodríguez-Navarro, A., 2013. Validating chemical and structural changes in painting materials by principal component analysis of spectroscopic data using internal mineral standards. *Journal of Cultural Heritage*, 14, 509–514

Rosado, T., Gil, M., Mirao, J., Candeias, A., Cldeira, A., T., 2013. Oxalate biofilm formation in mural paintings due to microorganisms – A comprehensive study. *International Biodeterioration and Biodegradation*, 85, 1-7

Rosi, F., Daveri, A., Miliani, C., Verri, G., Benedetti, P., Piqué, F., Brunetti, B., G., Sgamellotti A., 2009. Non-invasive identification of organic materials in wall paintings by fiber optic reflectance infrared spectroscopy: a statistical multivariate approach. *Analytical and Bioanalytical Chemistry*, 395, (7), 2097-2106

Rosi, F., Miliani, C., Clementi, C., Kahrim, K., Presciutti, F., Vagnini, M., Manuali, V., Daveri, A., Cartechini, L., Brunetti, B., G., and Sgamellotti A. 2010. An integrated spectroscopic approach for the non-invasive study of modern art materials and techniques. *Applied Physics A*., 100, (3), 613-624

Rottlander, R., C., A., 1990. Lipid Analysis in the Identification of Vessel Contents. In: *Organic Contents of Ancient Vessels: Materials Analysis and Archaeological Investigation*. Biers, W., R. and Mcgovern, P., E., editors. MASCA Research Papers in Science and Archaeology, Vol. 7

Steiner, G., 2003. Measurement techniques. In: Gauglitz, G. and Vo-Dinh, T. ed. *Handbook of Spectroscopy, Volume 1.* Weinheim: WILEY-VCH Verlag GmbH & Co. KGaA, Ch. 5

Sabbioni, C., Ghedini, N., Bonazza, A., 2003. Organic anions in damage layers on monuments and buildings. *Atmospheric Environment*, 37, 1261–1269

Salvadori, O. and Charola, A., E., 2011. Methods to Prevent Biocolonization and Recolonization: An Overview of Current Research for Architectural and Archaeological Heritage. *Biocolonization of Stone: Control and Preventive Methods, Proceedings from the MCI Workshop Series*, *Smithsonian Contributions to Museum Conservation, 2.* Ed: Charola, A., E., McNamara, C., Koestler, R., J. Smithsonian Institution Scholarly Press, Washington D.C, 37-50

Santos Silva, C., de Souza Lins Borba, F., Pimentel, M., F., Pontes, M., J., C., Honorato, R., S., Pasquini, C., 2013. Classification of blue pen ink using infrared spectroscopy and linear discriminant analysis. *Microchemical Journal*, 109, 122-127

Sanz, M., Oujja, M., Ascaso, C., Pérez-Ortega, S., Souza-Egipsy, V., Fort, R., de los Rios, A., Wierzchos, J., Canamares, M.,V., Castillejo, M., 2017. Influence of wavelength on the laser removal of lichens colonizing heritage stone. *Applied Surface Science*, 399, 758–768

Sarmiento, A., Pérez-Alonso, M., Olivares, M., Castro, K., Martizez-Arkarazo, I., Fernández, L. A. and Madariaga, J. M. 2011. Classification and Identification of Organic Binding Media in Artworks by means of Fourier transform infrared spectroscopy and principal components analysis. *Anal. Bioanal. Chem*., 399, 3601-3611

Saute, B., Premasiri, R., Ziegler, L., Narayanan, R., 2012. Gold nanorobs as surface enhanced Raman spectroscopy substrates for sensitive and selective detection of ultra-low levels of dithiocarbamate pesticides. *Analyst,* 137, 5082-5087

Savkovic, Z., Unkovic, N., Stupar, M., Frankovic, M., Jovanovic, M., Eric, S., Saric, K., Stankovic, S., Dimkic, I., Vukojevic, J.,Grbic, M., L., 2016. Diversity and biodeteriorative potential of fungal dwellers on ancient stone stela. *International Biodeterioration & Biodegradation,* 115, 212-223

Sciutto, G., Oliveri, P., Prati, S., Quaranta, M., Lanteri, S., Mazzeo, R., 2012. Analysis of paint cross-sections: A combined multivariate approach for the interpretation of μaTR-FTIR hyperspectral data arrays. *Analytical and Bioanalytical Chemistry*

Sciutto, G., Oliveri, P., Prati,S., Catelli, E., Bonacini,I., and Mazzeo, R., 2017. A Multivariate Methodological Workflow for the Analysis of FTIR Chemical Mapping Applied on Historic Paint Stratigraphies. *International Journal of Analytical Chemistry*, 1-12

Shlens, J., 2014. *A tutorial on Principal Component Analysis*. Available at: https://arxiv.org/abs/1404.1100

Sickels, L., B., 1981. Organics vs. synthetics: their use as additives in mortars. In: *Mortars, Cements and Grouts used in the Conservation of Historic Buildings ICCROM Symposium*, 3- 6.11.1981, Rome, 25-52

Silva, D.A., Wenk, H., R, Monteiro, P., J., M., 2005. Comparative investigation of mortars from Roman Colosseum and cistern. *Thermochimica Acta*, 438, 35-40

Singh, M., and Arbad, B., R., 2014. Characterization of traditional mud mortar of the decorated wall surfaces of Ellora caves. *Construction and Building Materials*, 65, 384-395

Singh, M., Waghmare, S., Kumar, S., V., 2014. Characterization of lime plasters used in 16th century Mughal monument. *Journal of Archaeological Science,* 42, 430-434

Skoog, D., A., Holler, J., F., and Nieman, T., A., 1998. *Principles of Instrumental Analysis*. 5th ed. USA: Saunders College Publishing

Smith, L., I., 2002. *A tutorial on Principal Components Analysis.* [pdf], Available at: http://www.cs.otago.ac.nz/cosc453/student_tutorials/principal_components.pdf

Spragg, R., 1998. Reflectance Spectra. *Internet Journal of Vibrational Spectroscopy*, 1, 5, 17-30. [Online]. Available at: http://www.irdg.org/ijvs/ijvs-volume-1-edition-5/reflection-spectra/

Stellati, A., Fiorentino, G., Cassano, R., Fioriello, C., S., 2012. The last firewood of a late ancient limekiln in Egnatia (SE Italy). *Wood and charcoal. Evidence for human and natural History*, SAGVNTVM Extra-13. Ed. Badal, E., Carrión, Y., Macías, M., Ntinou, M. UNIVERSITAT DE VALÈNCIA Departament de Prehistòria i Arqueologia de la Facultad de Geografía i Història.

Stone, D., C and Ellis, J., 2008. *Stats Tutorial - Instrumental Analysis and Calibration*. [Online]. Available at: http://www.chem.utoronto.ca/coursenotes/analsci/stats/ErrorResid.html

Stuart, B., 2004. *Infrared Spectroscopy: Fundamentals and Applications, Analytical Techniques in the Sciences*. Willey

Synytsya, A. and Novak, M., 2014. Structural analysis of glucans. *Annals of Translational Medicine*, 2, (2), 17

Tewari, J., Strong, R., Boulas, P., 2017. At-line determination of pharmaceuticals small molecule's blending end point using chemometric modeling combined with Fourier transform near infrared spectroscopy. *Spectrochimica Acta Part A: Molecular and Biomolecular Spectroscopy*, 173, 886-891

Theodoridou, M., Ioannou, I., Philokyprou, M., 2013. New evidence of early use of artificial pozzolanic material in mortars. Journal of Archaeological Science, 40, 3263-3269

Thomsen, V., Schatzlein, D. and Mercuro, D., 2003. Limits of Detection in Spectroscopy. *Spectroscopy*, 18, (12)

Unkovic, N., Eric, S., Saric, K., Stupar, M., Savkovic, Z., Stankovic, S., Stanojevic, O., Dimkic, I., Vukojevic, J., Grbic, M., L., 2017. Biogenesis of secondary mycogenic minerals related to wall paintings deterioration process. *Micron*, 100, 1-9

Ventolà, L., Vendrell,M., Giraldez, P., Merino, L., 2011. Traditional organic additives improve lime mortars: New old materials for restoration and building natural stone fabrics. *Construction and Building Materials*, 25, 3313–3318

Viaene, W., Waelkens, M., Otterburgs, R., Callebaut, K., 1997. An Archaeometric Study of Mortars used at Sagalassos. In Waelkens, K. and Poblome, J., edit. Sagalassos IV, Report on the Survey and Excavation Campaigns of 1994 and 1995. *Acta Archaeologica Lovaniensia Monagraphiae 9*. Leuren University Press, 405-423

Vitruvius, 1st BC. *On Architecture*. Introduction by Tavernor, R., Translated by Schofield, R, 2009. Penguin Books, England.

Vranceanu, M. D., Şaban, R., Antoniac, I.V., Albu, M., Miculescu, F., 2012. Development and characterization of novel porous collagen based biocomposite for bone tissue regeneration. *Scientific Bulletin, Series B: Chemistry and Materials Science*, 74, (3), 145-156

Winter, F., E., 1971. *Greek Fortifications*. Toronto: University of Toronto Press

Xing, D., Li, J., Wang, S., 2020. Comparison of the chemical and micromechanical properties of Larix spp. after eco-friendly heat treatments measured by in situ nanoindentation. Available at: <https://www.nature.com/articles/s41598-020-61314-6.pdf>, [Accessed 24 October 2021]

Yang, F., Zhang, B., and Ma, Q., 2010. Study of Sticky Rice-Lime Mortar Technology for the restoration of historical masonry construction. *Accounts of Chemical Research*, 43, (6), 936-944

Yang, H., Irudayaraj, J., Paradkar, M., 2005. Discriminant analysis of edible oils and fats by FTIR, FT-NIR and FT-Raman spectroscopy. *Food Chemistry*, 93, 25-32

Ylmén, R. and Jäglid, U., 2013. Carbonation of Portland cement studied by Diffuse Reflection Fourier Transform Infrared Spectroscopy. *International Journal of Concrete Structures and Materials*, 7 (2), 119-125.

Zahedi, P. and Fallah-Darrehchi, M., 2015. Electrospun Egg Albumin-PVA Nanofibers Containing Tetracycline Hydrochloride: Morphological, Drug Release, Antibacterial, Thermal and Mechanical Properties. *Fibers and Polymers*, 16, (10), 2184-2192

Zeng, Y., Zhang, B., & Liang, X., 2008. A case study and mechanism investigation of typical mortars used on ancient architecture in China. *Thermochimica Acta,* 473 (1-2), 1–6

Appendix I

Chapter 6: Accuracy and Precision

Spectrum ID	Energy gain - Surface	Energy gain in R	Date of Acquisition
Ca_16_1	369	5936	10/06/2016
Ca_16_2	473	5936	10/06/2016
Ca_16_3	451	5936	10/06/2016
Ca_16_4	612	5859	15/06/2016
Ca_16_5	682	5859	15/06/2016
Ca_16_6	707	5859	15/06/2016
PS_16_1	3198	5861	15/06/2016
PS_16_2	3213	5861	15/06/2016
PS_16_3	3636	5861	15/06/2016
PS_16_4	3906	5990	16/06/2016
PS_16_5	3538	5990	16/06/2016
PS_16_6	3821	5990	16/06/2016
Ca_16_7	443	5981	16/06/2016
Ca_16_8	453	5981	16/06/2016
Ca_16_9	522	5981	16/06/2016
PS_16_7	3579	5901	17/06/2016
PS_16_8	4652	5901	17/06/2016
Ca_16_10	637	5849	17/06/2016
Ca_16_11	781	5849	17/06/2016
PS_16_9	3652	5976	20/06/2016
PS_16_10	4531	5976	20/06/2016
Ca_16_12	675	5812	20/06/2016
Ca_16_13	832	5812	20/06/2016
Ca_16_14	483	5739	21/06/2016
PS_16_11	3256	5988	21/06/2016
Ca_16_15	463	5869	22/06/2016
Ca_16_16	503	5869	22/06/2016
PS_16_12	3091	5873	22/06/2016
PS_16_13	3349	5873	22/06/2016
Ca_16_17	430	5922	23/06/2016
Ca_16_18	445	5922	23/06/2016
PS_16_14	2243	3380	23/06/2016
PS_16_15	2307	3380	23/06/2016
PS_16_16	2889	5729	24/06/2016
PS_16_17	3287	5729	24/06/2016

Table 1: List of Energy gain measurements for the acquisition of PS film and $CaCO_3$ pressed-disk spectra, 2016 analytical session.

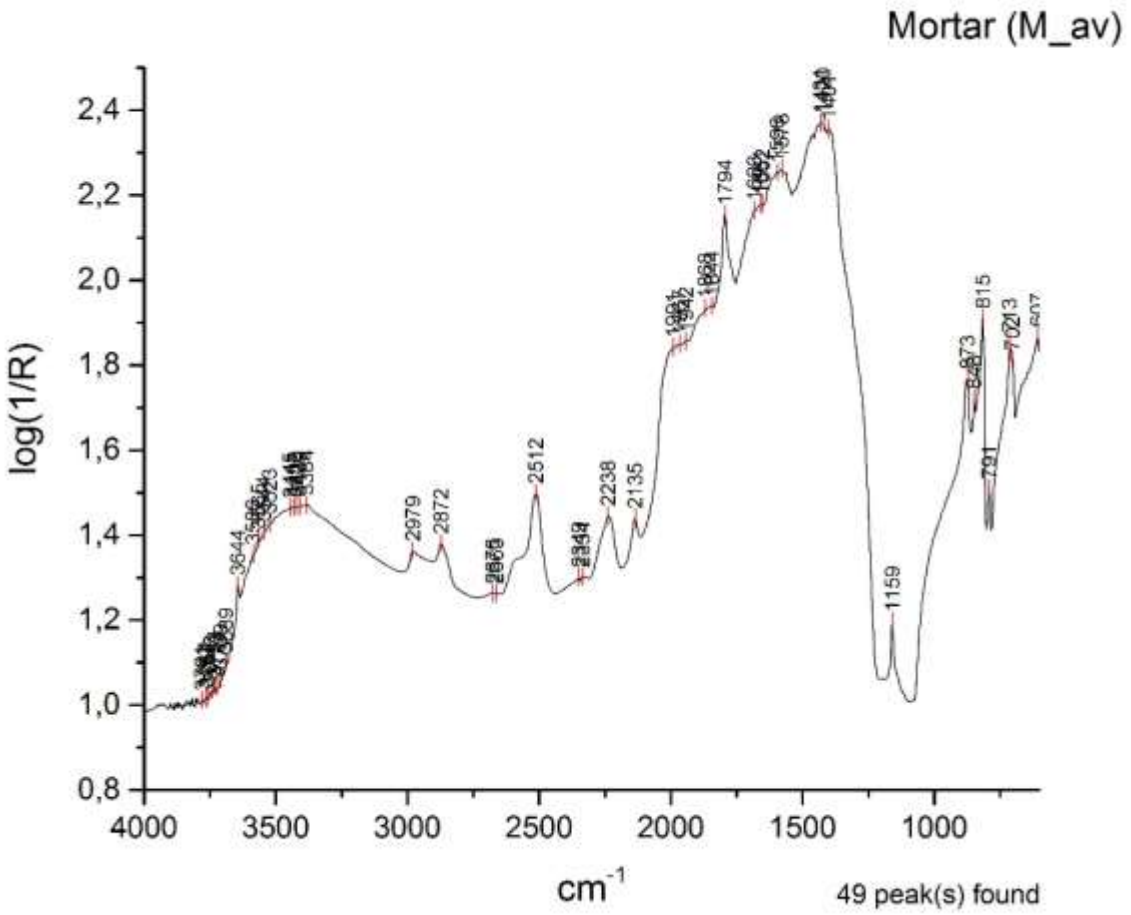

Figure 1: The spectrum of mortar standard ($CaCO_3$ and quartz in 1:3 ratio).

Peak x (position)	Spectrum ID	Type of band	Chemical Band Assignement	Reference
702	**M_av**	sharp and strong absorption	**quartz**	spectrum Q_av
713	**M_av**	sharp and strong absorption	**v4 carbonate ion**	Ylmen and Jaglid, 2013, p. 119, spectrum Ca_av
791	**M_av**	sharp absorption	**quartz**	spectrum Q_av
815	**M_av**	sharp and strong absorption	**quartz**	spectrum Q_av
848	**M_av**	weak absorption	**v2 carbonate ion**	Ylmen and Jaglid, 2013, p. 119, spectrum Ca_av
873	**M_av**	sharp absorption	**v2 carbonate ion**	Ylmen and Jaglid, 2013, p. 119, spectrum Ca_av
1159	**M_av**	sharp absorption	**quartz**	spectrum Q_av
1401	**M_av**	strong absorption	**calcium carbonate**	spectrum Ca_av
1420	**M_av**	strong absorption	**v3 antisymmetric stretching CO3-2**	Ylmen and Jaglid, 2013, p. 119, spectrum Ca_av
1431	**M_av**	strong absorption	**v3 antisymmetric stretching CO3-2**	Ylmen and Jaglid, 2013, p. 119, spectrum Ca_av
1578	**M_av**	strong absorption	**v3 antisymmetric stretching CO3-2**	Ylmen and Jaglid, 2013, p. 119, spectrum Ca_av
1596	**M_av**	strong absorption	**quartz**	spectrum Q_av
1652	**M_av**	weak absorption	**quartz**	spectrum Q_av
1661	**M_av**	weak absorption	**quartz**	spectrum Q_av
1683	**M_av**	weak absorption	**quartz**	spectrum Q_av
1794	**M_av**	combination band	**v1+v4**	Ricci et al, 2006, p. 1222, spectrum Ca_av
1844	**M_av**	weak absorption	**quartz**	spectrum Q_av
1868	**M_av**	weak absorption	**quartz**	spectrum Q_av
1942	**M_av**	weak absorption	**quartz**	spectrum Q_av
1967	**M_av**	weak absorption	**quartz**	spectrum Q_av
1991	**M_av**	weak absorption	**v+δ Si-O**	Miliani et al, 2012, p. 303, spectrum Q_av
2135	**M_av**	sharp absorption	**calcium carbonate and quartz**	spectrum Q_av and spectrum Ca_av
2238	**M_av**	sharp absorption	**quartz**	spectrum Q_av
2512	**M_av**	combination band	**v1+v3**	Ricci et al, 2006, p. 1222, spectrum Ca_av
2663	**M_av**	weak absorption	**(blank)**	spectrum Ca_av
2676	**M_av**	weak absorption	**(blank)**	spectrum Ca_av
2872	**M_av**	(blank)	**calcium carbonate**	spectrum Ca_av
2979	**M_av**	(blank)	**calcium carbonate**	spectrum Ca_av
3384	**M_av**	weak absorption	**(blank)**	spectrum Q_av
3644	**M_av**	doublet	**OH stretching**	Rosi et al, 2009, p. 2100, spectrum Ca_av

Figure 2: Filtered CPAD entries of the mortar spectrum (M_av).

7.5.1 Bone glue and mortar mixtures CPAD

Peak x (position)	Spectrum ID	Type of band	Chemical Band Assignement	Reference
668	BG_M_50_av	sharp and weak absorption	CaCO3	spectrum Ca_av
715	BG_M_50_av	weak absorption	v4 carbonate ion	Spectrum Ca_av, spectrum M_av, Ylmen and Jaglid, 2013, p. 119
746	BG_av	weak absorption	(blank)	(blank)
769	BG_av	weak absorption	(blank)	(blank)
777	BG_av	weak absorption	(blank)	(blank)
785	BG_av	weak absorption	(blank)	(blank)
792	BG_M_50_av	sharp and weak absorption	quartz	Spectrum Q_av, spectrum M_av
814	BG_M_50_av	sharp absorption	Si-O antisymmetric stretching	Spectrum Q_av, spectrum M_av, Miliani et al, 2012, p. 303
876	BG_M_50_av	weak absorption	v2 carbonate ion	Spectrum Ca_av, spectrum M_av, Ylmen and Jaglid, 2013, p. 119
882	BG_av	weak absorption	(blank)	(blank)
1040	BG_av	weak absorption	(blank)	(blank)
1068	BG_av	weak absorption	PO4-3anion stretching	Ricci et al, 2006, p. 1223
1094	BG_av	weak absorption	(blank)	(blank)
1105	BG_av	weak absorption	(blank)	(blank)
1114	BG_av	weak absorption	(blank)	(blank)
1117	BG_M_50_av	weak absorption	CaCO3	spectrum Ca_av
1159	BG_M_50_av	sharp absorption	quartz	Spectrum Q_av, spectrum M_av
1166	BG_av	weak absorption	(blank)	(blank)
1211	BG_av	weak absorption	(blank)	(blank)
1264	BG_av	stair-step type intensities	(blank)	(blank)
1291	BG_av	stair-step type intensities	(blank)	(blank)
1292	BG_M_50_av	stair-step type intensities	bone glue	Spectrum BG_av
1313	BG_M_50_av	stair-step type intensities	bone glue	Spectrum BG_av
1347	BG_M_50_av	stair-step type intensities	bone glue	Spectrum BG_av
1350	BG_av	stair-step type intensities	(blank)	(blank)
1414	BG_av	stair-step type intensities	(blank)	(blank)
1418	BG_M_50_av	stair-step type intensities	bone glue	(blank)
1471	BG_M_50_av	stair-step type intensities	Amide III	Spectrum BG_av, Rosi et al, 2009, p. 2099
1473	BG_av	stair-step type intensities	Amide III	Rosi et al, 2009, p. 2099

Figure 3: Filtered CPAD entries of bone glue (BG_av) and 50% bone glue/mortar mixture (BG_M_50_av).

1574	**BG_av**	strong absorption	**C-N-H bending amide II, N-H bands**	Miliani et al, 2012, p. 304, Rosi et al, 2009, p. 2104, Ploeger et al, 2010, p. 37
	BG_M_50_av	strong absorption	**C-N-H bending amide II, N-H bands**	Spectrum BG_av, Rosi et al, 2009, p. 2099, Miliani et al, 2012, p. 304
1693	**BG_M_50_av**	strong absorption	**N-H bands**	Spectrum BG_av, Rosi et al, 2009, p. 2104, Miliani et al, 2012, p. 304
1699	**BG_av**	strong absorption	**N-H bands**	Miliani et al, 2012, p. 304, Rosi et al, 2009, p. 2104
1702	**BG_M_50_av**	(blank)	**bone glue**	Spectrum BG_av
1846	**BG_M_50_av**	weak absorption	**quartz**	Spectrum Q_av, spectrum M_av
1875	**BG_M_50_av**	weak absorption	**quartz**	Spectrum Q_av, spectrum M_av
1940	**BG_M_50_av**	weak absorption	**quartz**	Spectrum Q_av, spectrum M_av
1954	**BG_M_50_av**	weak absorption	**quartz**	Spectrum Q_av, spectrum M_av
1964	**BG_M_50_av**	weak absorption	**quartz**	Spectrum Q_av, spectrum M_av
1986	**BG_M_50_av**	weak absorption	**quartz**	Spectrum Q_av, spectrum M_av
2133	**BG_M_50_av**	weak absorption	**CaCO3 and quartz**	Spectrum Q_av, spectrum M_av, spectrum Ca_av
2239	**BG_M_50_av**	weak absorption	**quartz**	Spectrum Q_av, spectrum M_av
2513	**BG_M_50_av**	combination band	**v1+v3 carbonate ion**	Spectrum Ca_av, spectrum M_av, Ricci et al, 2006, p. 1222
2519	**BG_M_50_av**	combination band	**v1+v3 carbonate ion**	Spectrum Ca_av, spectrum M_av, Ricci et al, 2006, p. 1222
2885	**BG_av**	weak absorption	**C-H stretching**	Miliani et al, 2012, p. 304, Rosi et al, 2009, p. 2104
2988	**BG_av**	weak absorption	**(blank)**	(blank)
2990	**BG_M_50_av**	weak absorption	**bone glue**	Spectrum BG_av
3099	**BG_M_50_av**	weak absorption	**amide I**	Spectrum BG_av, Rosi et al, 2009, p. 2099
3103	**BG_av**	1st overtone	**amide I**	Rosi et al, 2009, p. 2099
3651	**BG_M_50_av**	doublet	**OH stretching**	Spectrum Ca_av, spectrum M_av, Rosi et al, 2009, p. 2100

Figure 3: continued.

Peak x (position)	Spectrum ID	Type of band	Chemical Band Assignement	Reference
647	BG_M_25_av	(blank)	CaCO3	spectrum Ca_av
672	BG_M_25_av	(blank)	CaCO3	spectrum Ca_av
699	BG_M_25_av	weak absorption	quartz	Spectrum Q_av, spectrum M_av
714	BG_M_25_av	weak absorption	v4 carbonate ion	Spectrum Ca_av, spectrum M_av, Ylmen and Jaglid, 2013, p. 119
735	BG_M_25_av	weak absorption	(blank)	(blank)
746	BG_av	weak absorption	(blank)	(blank)
761	BG_M_25_av	weak absorption	(blank)	(blank)
769	BG_av	weak absorption	(blank)	(blank)
777	BG_av	weak absorption	(blank)	(blank)
785	BG_av	weak absorption	(blank)	(blank)
793	BG_M_25_av	sharp and weak absorption	quartz	Spectrum Q_av, spectrum M_av
815	BG_M_25_av	sharp absorption	Si-O antisymmetric stretching	Spectrum Q_av, spectrum M_av, Miliani et al, 2012, p. 303
877	BG_M_25_av	weak absorption	v2 carbonate ion	Spectrum Ca_av, spectrum M_av, Ylmen and Jaglid, 2013, p. 119
882	BG_av	weak absorption	(blank)	(blank)
1040	BG_av	weak absorption	(blank)	(blank)
1068	BG_av	weak absorption	PO4-3anion stretching	Ricci et al, 2006, p. 1223
1086	BG_M_25_av	weak absorption	v1 carbonate ion	Spectrum Ca_av, spectrum M_av, Ylmen and Jaglid, 2013, p. 119
1094	BG_av	weak absorption	(blank)	(blank)
1105	BG_av	weak absorption	(blank)	(blank)
1114	BG_av	weak absorption	(blank)	(blank)
1117	BG_M_25_av	weak absorption	CaCO3	spectrum Ca_av
1159	BG_M_25_av	sharp absorption	quartz	Spectrum Q_av, spectrum M_av
1166	BG_av	weak absorption	(blank)	(blank)
1205	BG_M_25_av	weak bands	bone glue	Spectrum BG_av
1211	BG_av	weak absorption	(blank)	(blank)
1264	BG_av	stair-step type intensities	(blank)	(blank)
1286	BG_M_25_av	stair-step type intensities	bone glue	Spectrum BG_av
1291	BG_av	stair-step type intensities	(blank)	(blank)
1341	BG_M_25_av	weak absorption	quartz	spectrum Q_av
1350	BG_av	stair-step type intensities	(blank)	(blank)
1399	BG_M_25_av	weak absorption	CaCO3	Spectrum Ca_av, spectrum M_av

Figure 4: Filtered CPAD entries of bone glue (BG_av) and 25% bone glue/mortar mixture (BG_M_25_av).

1414	**BG_av**	stair-step type intensities	**(blank)**	(blank)
1431	**BG_M_25_av**	weak absorption	**CaCO3 and quartz**	Spectrum M_av
1437	**BG_M_25_av**	weak absorption	**CaCO3 and quartz**	Spectrum M_av
1461	**BG_M_25_av**	stair-step type intensities	**Amide III**	Spectrum BG_av, Rosi et al, 2009, p. 2099
1469	**BG_M_25_av**	stair-step type intensities	**Amide III**	Spectrum BG_av, Rosi et al, 2009, p. 2099
1473	**BG_av**	stair-step type intensities	**Amide III**	Rosi et al, 2009, p. 2099
1574	**BG_av**	strong absorption	**C-N-H bending amide II, N-H bands**	Miliani et al, 2012, p. 304, Rosi et al, 2009, p. 2104, Ploeger et al, 2010, p. 37
1575	**BG_M_25_av**	strong absorption	**v3 antisymmetric stretching CO3-2 or amide III**	Spectrum BG_av, spectrum M_av, Ylmen and Jaglid, 2013, 119; Miliani et al, 2012, p. 304
1597	**BG_M_25_av**	strong absorption	**quartz**	Spectrum Q_av, spectrum M_av
1694	**BG_M_25_av**	strong absorption	**N-H bands**	Spectrum BG_av, Rosi et al, 2009, p. 2104, Miliani et al, 2012, p. 304
1699	**BG_av**	strong absorption	**N-H bands**	Miliani et al, 2012, p. 304, Rosi et al, 2009, p. 2104
1793	**BG_M_25_av**	strong absorption	**v1+v4**	Spectrum Ca_av, spectrum M_av, Ricci et al, 2006, p. 1222
1867	**BG_M_25_av**	weak absorption	**quartz**	Spectrum Q_av, spectrum M_av
1944	**BG_M_25_av**	weak absorption	**quartz**	Spectrum Q_av, spectrum M_av
1973	**BG_M_25_av**	weak absorption	**quartz**	Spectrum Q_av, spectrum M_av
1988	**BG_M_25_av**	weak absorption	**quartz**	Spectrum Q_av, spectrum M_av
2136	**BG_M_25_av**	weak absorption	**CaCO3 and quartz**	Spectrum Q_av, spectrum M_av, spectrum Ca_av
2236	**BG_M_25_av**	weak absorption	**quartz**	Spectrum Q_av, spectrum M_av
2513	**BG_M_25_av**	combination band	**v1+v3 carbonate ion**	Spectrum Ca_av, spectrum M_av, Ricci et al, 2006, p. 1222
2875	**BG_M_25_av**	strong absorption	**CaCO3**	Spectrum Ca_av, spectrum M_av
2885	**BG_av**	weak absorption	**C-H stretching**	Miliani et al, 2012, p. 304, Rosi et al, 2009, p. 2104
2897	**BG_M_25_av**	weak bands	**C-H stretching**	Spectrum BG_av, Miliani et al, 2012, p. 304; Rosi et al, 2009, p. 2104
2905	**BG_M_25_av**	weak absorption	**bone glue**	Spectrum BG
2940	**BG_M_25_av**	weak absorption	**(blank)**	(blank)
2949	**BG_M_25_av**	weak absorption	**(blank)**	(blank)
2979	**BG_M_25_av**	strong absorption	**CaCO3**	Spectrum Ca_av, spectrum M_av
2988	**BG_av**	weak absorption	**(blank)**	(blank)
3103	**BG_av**	1st overtone	**amide I**	Rosi et al, 2009, p. 2099

Figure 4: continued.

Peak x (position)	Spectrum ID	Type of band	Chemical Band Assignement	Reference
714	BG_M_5_av	weak bands	v4 carbonate ion	Spectrum Ca_av, spectrum M_av, Ylmen and Jaglid, 2013, p. 119
746	BG_av	weak absorption	(blank)	(blank)
769	BG_av	weak absorption	(blank)	(blank)
777	BG_av	weak absorption	(blank)	(blank)
785	BG_av	weak absorption	(blank)	(blank)
792	BG_M_5_av	sharp and weak absorption	quartz	Spectrum Q_av, spectrum M_av
815	BG_M_5_av	sharp absorption	Si-O antisymmetric stretching	Spectrum Q_av, spectrum M_av, Miliani et al, 2012, p. 303
848	BG_M_5_av	sharp and weak absorption	v2 carbonate ion	Spectrum Ca_av, spectrum M_av, Ylmen and Jaglid, 2013, p. 119
879	BG_M_5_av	strong absorption	v2 carbonate ion	Spectrum Ca_av, spectrum M_av, Ylmen and Jaglid, 2013, p. 119
882	BG_av	weak absorption	(blank)	(blank)
1040	BG_av	weak absorption	(blank)	(blank)
1068	BG_av	weak absorption	PO4-3anion stretching	Ricci et al, 2006, p. 1223
1094	BG_av	weak absorption	(blank)	(blank)
1105	BG_av	weak absorption	(blank)	(blank)
1114	BG_av	weak absorption	(blank)	(blank)
1159	BG_M_5_av	sharp absorption	quartz	Spectrum Q_av, spectrum M_av
1166	BG_av	weak absorption	(blank)	(blank)
1211	BG_av	weak absorption	(blank)	(blank)
1264	BG_av	stair-step type intensities	(blank)	(blank)
1291	BG_av	stair-step type intensities	(blank)	(blank)
1350	BG_av	stair-step type intensities	(blank)	(blank)
1401	BG_M_5_av	weak bands	CaCO3	Spectrum Ca_av, spectrum M_av
1414	BG_av	stair-step type intensities	(blank)	(blank)
1443	BG_M_5_av	weak bands	CaCO3 and quartz	Spectrum M_av, spectrum Ca_av
1460	BG_M_5_av	weak bands	CaCO3 and quartz	Spectrum M_av, spectrum Ca_av
1467	BG_M_5_av	weak bands	CaCO3 and quartz	Spectrum M_av, spectrum Ca_av
1473	BG_av	stair-step type intensities	Amide III	Rosi et al, 2009, p. 2099
1574	BG_av	strong absorption	C-N-H bending amide II, N-H bands	Miliani et al, 2012, p. 304, Rosi et al, 2009, p. 2104, Ploeger et al, 2010, p. 37
1582	BG_M_5_av	strong absorption	v3 antisymmetric stretching CO3-2	Spectrum Ca_av, spectrum M_av, Ylmen and Jaglid, 2013, p. 119
1652	BG_M_5_av	weak bands	quartz	Spectrum Q_av, spectrum M_av
1661	BG_M_5_av	weak bands	quartz	Spectrum Q_av, spectrum M_av
1668	BG_M_5_av	weak bands	quartz	Spectrum Q_av, spectrum M_av
1699	BG_av	strong absorption	N-H bands	Miliani et al, 2012, p. 304, Rosi et al, 2009, p. 2104

Figure 5: Filtered CPAD entries of bone glue (BG_av) and 5% bone glue/mortar mixture (BG_M_5_av).

1795	**BG_M_5_av**	strong absorption	**v1+v4**	Spectrum Ca_av, spectrum M_av, Ricci et al, 2006, p. 1222
1845	**BG_M_5_av**	weak bands	**quartz**	Spectrum Q_av, spectrum M_av
1853	**BG_M_5_av**	weak bands	**quartz**	Spectrum Q_av, spectrum M_av
1967	**BG_M_5_av**	weak bands	**quartz**	Spectrum Q_av, spectrum M_av
2135	**BG_M_5_av**	weak bands	**CaCO3 and quartz**	Spectrum Q_av, spectrum M_av, spectrum Ca_av
2237	**BG_M_5_av**	weak bands	**quartz**	Spectrum Q_av, spectrum M_av
2512	**BG_M_5_av**	combination band	**v1+v3 carbonate ion**	Spectrum Ca_av, spectrum M_av, Ricci et al, 2006, p. 1222
2677	**BG_M_5_av**	weak bands	**CaCO3**	Spectrum Ca_av, spectrum M_av
2715	**BG_M_5_av**	weak bands	**CaCO3**	Spectrum Ca_av, spectrum M_av
2873	**BG_M_5_av**	strong absorption	**CaCO3**	Spectrum Ca_av, spectrum M_av
2885	**BG_av**	weak absorption	**C-H stretching**	Miliani et al, 2012, p. 304, Rosi et al, 2009, p. 2104
2918	**BG_M_5_av**	weak bands	**C-H stretching**	Spectrum BG_av, Miliani et al, 2012, p. 304; Rosi et al, 2009, p. 2104
2927	**BG_M_5_av**	weak bands	**bone glue**	Spectrum BG_av
2935	**BG_M_5_av**	weak bands	**bone glue**	Spectrum BG_av
2979	**BG_M_5_av**	strong absorption	**CaCO3**	Spectrum Ca_av, spectrum M_av
2988	**BG_av**	weak absorption	**(blank)**	(blank)
3030	**BG_M_5_av**	strong absorption	**CaCO3**	spectrum Ca_av
3103	**BG_av**	1st overtone	**amide I**	Rosi et al, 2009, p. 2099
3643	**BG_M_5_av**	doublet	**OH stretching**	Spectrum Ca_av, spectrum M_av, Rosi et al, 2009, p. 2100

Figure 5: continued.

7.5.2 Egg white and mortar mixtures CPAD

Peak x (position)	Spectrum ID	Type of band	Chemical Band Assignement	Reference
606	EW_M_75_av	weak absorption	CaCO3	spectrum Ca_av
618	EW_M_75_av	weak absorption	CaCO3	spectrum Ca_av
659	EW_M_75_av	weak absorption	CaCO3	spectrum Ca_av
699	EW_M_75_av	weak absorption	quartz	spectrum Q_av
715	EW_M_75_av	weak absorption	v4 carbonate ion	Spectrum Ca_av, spectrum M_av, Ylmen and Jaglid, 2013, p. 119
729	EW_av	weak absorption	(blank)	(blank)
755	EW_av	weak absorption	(blank)	(blank)
791	EW_M_75_av	sharp and weak absorption	quartz	Spectrum Q_av, spectrum M_av
817	EW_M_75_av	sharp absorption	quartz	Spectrum Q_av, spectrum M_av
818	EW_av	weak absorption	(blank)	(blank)
875	EW_M_75_av	weak absorption	egg white, CaCO3 v2 carbonate ion	Spectrum EW_av, spectrum Ca_av, spectrum M_av, Ylmen and Jaglid, 2013, p. 119
876	EW_av	strong absorption	(blank)	(blank)
962	EW_av	sharp absorption	(blank)	(blank)
1034	EW_av	sharp absorption	(blank)	(blank)
1086	EW_av	sharp and weak absorption	(blank)	(blank)
1159	EW_M_75_av	sharp absorption	quartz	Spectrum Q_av, spectrum M_av
1179	EW_av	strong absorption	(blank)	(blank)
1285	EW_M_75_av	weak absorption	egg white	spectrum EW_av
1295	EW_av	strong absorption	(blank)	(blank)
1314	EW_M_75_av	weak absorption	egg white	spectrum EW_av
1325	EW_av	strong absorption	(blank)	(blank)
1412	EW_M_75_av	weak absorption	egg white	spectrum EW_av
1415	EW_av	sharp and weak absorption	(blank)	(blank)
1424	EW_M_75_av	weak absorption	v3 antisymmetric stretching CO3-2	Spectrum M_av, Ylmen and Jaglid, 2013, p. 119
1432	EW_M_75_av	weak absorption	v3 antisymmetric stretching CO3-2	Spectrum M_av, Ylmen and Jaglid, 2013, p. 119
1453	EW_M_75_av	weak absorption	egg white	spectrum EW_av
1458	EW_av	stair-step type intensities	Amide III	Rosi et al, 2009, p. 2099
1461	EW_M_75_av	weak absorption	egg white	spectrum EW_av
1472	EW_av	weak absorption	(blank)	(blank)
1561	EW_M_75_av	weak absorption	quartz	spectrum Q_av
1573	EW_av	strong absorption	C-N-H bending amide II, N-H bands	Ploeger et al, 2010, p. 37, Miliani et al, 2012, p. 304
1575	EW_M_75_av	strong absorption	C-N-H bending amide II, N-H bands	Spectrum EW_av, Rosi et al, 2009, p. 2104

Figure 6: Filtered CPAD entries of egg white (EW_av) and 75% egg white/mortar mixture (EW_M_75_av).

1692	**EW_M_75_av**	strong absorption	**N-H bands**	Spectrum EW_av, Ploeger et al, 2010, p.37, Miliani et al, 2012, p. 305
1693	**EW_av**	strong absorption	**N-H bands**	Rosi et al, 2009, p. 2104
1794	**EW_M_75_av**	combination band	**v1+v4**	Spectrum Ca_av, spectrum M_av, Ricci et al, 2006, p. 1222
1860	**EW_M_75_av**	weak absorption	**quartz**	spectrum Q_av
1867	**EW_M_75_av**	weak absorption	**quartz**	spectrum Q_av
1930	**EW_M_75_av**	weak absorption	**quartz**	spectrum Q_av
1947	**EW_M_75_av**	weak absorption	**quartz**	spectrum Q_av
1968	**EW_M_75_av**	weak absorption	**quartz**	spectrum Q_av
1976	**EW_M_75_av**	weak absorption	**quartz**	spectrum Q_av
1992	**EW_M_75_av**	weak absorption	**quartz**	spectrum Q_av
2012	**EW_av**	weak absorption	**(blank)**	(blank)
2135	**EW_M_75_av**	weak absorption	**calcium carbonate and quartz**	Spectrum Ca_av, spectrum M_av, spectrum Q_av
2154	**EW_av**	weak absorption	**(blank)**	(blank)
2235	**EW_M_75_av**	weak absorption	**quartz**	spectrum Q_av
2515	**EW_M_75_av**	combination band	**v1+v3**	Spectrum Ca_av, spectrum M_av, Ricci et al, 2006, p. 1222
2524	**EW_av**	weak absorption	**(blank)**	(blank)
2544	**EW_M_75_av**	weak absorption	**egg white**	spectrum EW_av
2603	**EW_M_75_av**	weak absorption	**egg white**	spectrum EW_av
2616	**EW_M_75_av**	weak absorption	**egg white**	spectrum EW_av
2714	**EW_av**	weak absorption	**(blank)**	(blank)
2828	**EW_av**	weak absorption	**C-H stretching**	Rosi et al, 2009, p. 2099
2873	**EW_M_75_av**	sharp and weak absorption	**CaCO3**	Spectrum Ca_av, spectrum M_av
2883	**EW_av**	weak absorption	**C-H stretching**	Rosi et al, 2009, p. 2099
2940	**EW_M_75_av**	weak absorption	**CH stretching**	Spectrum EW_av, Daher et al, 2017, p. 8
2945	**EW_av**	weak absorption	**(blank)**	(blank)
2948	**EW_M_75_av**	weak absorption	**CH3 stretching**	Spectrum EW_av, Iwanicka et al, 2017, p. 18
2965	**EW_M_75_av**	sharp and weak absorption	**CaCO3**	Spectrum Ca_av, spectrum M_av
2981	**EW_av**	weak absorption	**(blank)**	(blank)
3086	**EW_M_75_av**	1st overtone	**amide I**	Spectrum EW_av, Rosi et al, 2009, p. 2099
3091	**EW_av**	1st overtone	**amide I**	Rosi et al, 2009, p. 2099

Figure 6: continued.

Peak x (position)	Spectrum ID	Type of band	Chemical Band Assignement	Reference
623	EW_M_50_av	weak absorption	CaCO3	spectrum Ca_av
664	EW_M_50_av	weak absorption	CaCO3	spectrum Ca_av
699	EW_M_50_av	weak absorption	quartz	spectrum Q_av
715	EW_M_50_av	weak absorption	v4 carbonate ion	Spectrum Ca_av, spectrum M_av, Ylmen and Jaglid, 2013, p. 119
729	EW_av	weak absorption	(blank)	(blank)
755	EW_av	weak absorption	(blank)	(blank)
792	EW_M_50_av	sharp and weak absorption	quartz	Spectrum Q_av, spectrum M_av
816	EW_M_50_av	sharp absorption	quartz	Spectrum Q_av, spectrum M_av
818	EW_av	weak absorption	(blank)	(blank)
876	EW_av	strong absorption	(blank)	(blank)
879	EW_M_50_av	sharp and weak absorption	v2 carbonate ion	Spectrum Ca_av, spectrum M_av, Ylmen and Jaglid, 2013, p. 119
962	EW_av	sharp absorption	(blank)	(blank)
1034	EW_av	sharp absorption	(blank)	(blank)
1082	EW_M_50_av	weak absorption	egg white	spectrum EW_av
1086	EW_av	sharp and weak absorption	(blank)	(blank)
1116	EW_M_50_av	weak absorption	C-O stretching	Buti et al, 2013, p. 2705
1159	EW_M_50_av	sharp absorption	quartz	Spectrum Q_av, spectrum M_av
1179	EW_av	strong absorption	(blank)	(blank)
1283	EW_M_50_av	weak absorption	egg white	spectrum EW_av
1295	EW_av	strong absorption	(blank)	(blank)
1313	EW_M_50_av	weak absorption	egg white	spectrum EW_av
1325	EW_av	strong absorption	(blank)	(blank)
1397	EW_M_50_av	weak absorption	CaCO3	Spectrum Ca_av, spectrum M_av
1415	EW_av	sharp and weak absorption	(blank)	(blank)
1446	EW_M_50_av	weak absorption	egg white	spectrum EW_av
1458	EW_av	stair-step type intensities	Amide III	Rosi et al, 2009, p. 2099
1472	EW_av	weak absorption	(blank)	(blank)
1480	EW_M_50_av	weak absorption	egg white	spectrum EW_av
1561	EW_M_50_av	weak absorption	quartz	spectrum Q_av

Figure 7: Filtered CPAD entries of egg white (EW_av) and 50% egg white/mortar mixture (EW_M_50_av).

1573	**EW_av**	strong absorption	**C-N-H bending amide II, N-H bands**	Ploeger et al, 2010, p. 37, Miliani et al, 2012, p. 304
1576	**EW_M_50_av**	strong absorption	**C-N-H bending amide II, N-H bands**	Spectrum EW_av, Rosi et al, 2009, p. 2104
1616	**EW_M_50_av**	weak absorption	**quartz**	spectrum Q_av
1685	**EW_M_50_av**	strong absorption	**N-H bands**	Spectrum EW_av, Ploeger et al, 2010, p.37, Miliani et al, 2012, p. 305
1693	**EW_av**	strong absorption	**N-H bands**	Rosi et al, 2009, p. 2104
1797	**EW_M_50_av**	combination band	**v1+v4**	Spectrum Ca_av, spectrum M_av, Ricci et al, 2006, p. 1222
1854	**EW_M_50_av**	weak absorption	**quartz**	spectrum Q_av
1866	**EW_M_50_av**	weak absorption	**quartz**	spectrum Q_av
1941	**EW_M_50_av**	weak absorption	**quartz**	spectrum Q_av
1950	**EW_M_50_av**	weak absorption	**quartz**	spectrum Q_av
1972	**EW_M_50_av**	weak absorption	**quartz**	spectrum Q_av
1988	**EW_M_50_av**	weak absorption	**quartz**	spectrum Q_av
2012	**EW_av**	weak absorption	**(blank)**	(blank)
2135	**EW_M_50_av**	weak absorption	**calcium carbonate and quartz**	Spectrum Ca_av, spectrum M_av, spectrum Q_av
2154	**EW_av**	weak absorption	**(blank)**	(blank)
2237	**EW_M_50_av**	weak absorption	**quartz**	spectrum Q_av
2512	**EW_M_50_av**	combination band	**v1+v3**	Spectrum Ca_av, spectrum M_av, Ricci et al, 2006, p. 1222
2524	**EW_av**	weak absorption	**(blank)**	(blank)
2564	**EW_M_50_av**	weak absorption	**egg white**	spectrum EW_av
2589	**EW_M_50_av**	weak absorption	**egg white**	spectrum EW_av
2595	**EW_M_50_av**	weak absorption	**egg white**	spectrum EW_av
2694	**EW_M_50_av**	weak absorption	**egg white**	spectrum EW_av
2714	**EW_av**	weak absorption	**(blank)**	(blank)
2828	**EW_av**	weak absorption	**C-H stretching**	Rosi et al, 2009, p. 2099
2875	**EW_M_50_av**	sharp and weak absorption	**CaCO3**	Spectrum Ca_av, spectrum M_av
2883	**EW_av**	weak absorption	**C-H stretching**	Rosi et al, 2009, p. 2099
2934	**EW_M_50_av**	weak absorption	**CH stretching**	Spectrum EW_av, Daher et al, 2017, p. 8
2943	**EW_M_50_av**	weak absorption	**CH3 stretching**	Spectrum EW_av, Iwanicka et al, 2017, p. 18
2945	**EW_av**	weak absorption	**(blank)**	(blank)
2961	**EW_M_50_av**	sharp and weak absorption	**CaCO3**	Spectrum Ca_av, spectrum M_av
2981	**EW_av**	weak absorption	**(blank)**	(blank)
3084	**EW_M_50_av**	1st overtone	**amide I**	Spectrum EW_av, Rosi et al, 2009, p. 2099
3091	**EW_av**	1st overtone	**amide I**	Rosi et al, 2009, p. 2099
3094	**EW_M_50_av**	1st overtone	**amide I**	Spectrum EW_av, Rosi et al, 2009, p. 2099

Figure 7: continued.

Peak x (position)	Spectrum ID	Type of band	Chemical Band Assignement	Reference
607	**EW_M_25_av**	weak absorption	**CaCO3**	spectrum Ca_av
616	**EW_M_25_av**	weak absorption	**CaCO3**	spectrum Ca_av
715	**EW_M_25_av**	sharp absorption	**v4 carbonate ion**	Spectrum Ca_av, spectrum M_av, Ylmen and Jaglid, 2013, p. 119
729	**EW_av**	weak absorption	**(blank)**	(blank)
755	**EW_av**	weak absorption	**(blank)**	(blank)
791	**EW_M_25_av**	sharp and weak absorption	**quartz**	Spectrum Q_av, spectrum M_av
816	**EW_M_25_av**	sharp absorption	**quartz**	Spectrum Q_av, spectrum M_av
818	**EW_av**	weak absorption	**(blank)**	(blank)
848	**EW_M_25_av**	weak absorption	**v2 carbonate ion**	Spectrum Ca_av, spectrum M_av, Ylmen and Jaglid, 2013, p. 119
876	**EW_av**	strong absorption	**(blank)**	(blank)
880	**EW_M_25_av**	sharp absorption	**v2 carbonate ion**	Spectrum Ca_av, spectrum M_av, Ylmen and Jaglid, 2013, p. 119
962	**EW_av**	sharp absorption	**(blank)**	(blank)
1034	**EW_av**	sharp absorption	**(blank)**	(blank)
1085	**EW_M_25_av**	weak absorption	**egg white**	spectrum EW_av
1086	**EW_av**	sharp and weak absorption	**(blank)**	(blank)
1159	**EW_M_25_av**	sharp absorption	**quartz**	Spectrum Q_av, spectrum M_av
1179	**EW_av**	strong absorption	**(blank)**	(blank)
1295	**EW_av**	strong absorption	**(blank)**	(blank)
1325	**EW_av**	strong absorption	**(blank)**	(blank)
1400	**EW_M_25_av**	weak absorption	**CaCO3**	Spectrum Ca_av, spectrum M_av
1415	**EW_av**	sharp and weak absorption	**(blank)**	(blank)
1438	**EW_M_25_av**	weak absorption	**v3 antisymmetric stretching CO3-2**	Spectrum M_av, Ylmen and Jaglid, 2013, p. 119
1446	**EW_M_25_av**	weak absorption	**v3 antisymmetric stretching CO3-2**	Spectrum Ca_av, Ylmen and Jaglid, 2013, p. 119
1458	**EW_av**	stair-step type intensities	**Amide III**	Rosi et al, 2009, p. 2099
1467	**EW_M_25_av**	weak absorption	**v3 antisymmetric stretching CO3-2**	Spectrum Ca_av, Ylmen and Jaglid, 2013, p. 119
1472	**EW_av**	weak absorption	**(blank)**	(blank)
1476	**EW_M_25_av**	weak absorption	**egg white**	spectrum EW_av
1498	**EW_M_25_av**	weak absorption	**C=O**	Rosi et al, 2002, p. 2099
1561	**EW_M_25_av**	weak absorption	**quartz**	spectrum Q_av

Figure 8: Filtered CPAD entries of egg white (EW_av) and 25% egg white/mortar mixture (EW_M_25_av).

1571	**EW_M_25_av**	strong absorption	**C-N-H bending amide II, N-H bands**	Spectrum EW_av, Rosi et al, 2009, p. 2104
1573	**EW_av**	strong absorption	**C-N-H bending amide II, N-H bands**	Ploeger et al, 2010, p. 37, Miliani et al, 2012, p. 304
1577	**EW_M_25_av**	strong absorption	**C-N-H bending amide II, N-H bands**	Spectrum EW_av, Rosi et al, 2009, p. 2104
1621	**EW_M_25_av**	weak absorption	**N-H bands**	Miliani et al, 2012, p. 304; Rosi et al, 2009, p. 2104
1629	**EW_M_25_av**	weak absorption	**N-H bands**	Miliani et al, 2012, p. 304; Rosi et al, 2009, p. 2104
1641	**EW_M_25_av**	weak absorption	**N-H bands**	Miliani et al, 2012, p. 304; Rosi et al, 2009, p. 2104
1665	**EW_M_25_av**	strong absorption	**quartz**	Spectrum M_av
1693	**EW_av**	strong absorption	**N-H bands**	Rosi et al, 2009, p. 2104
1794	**EW_M_25_av**	combination band	**v1+v4**	Spectrum Ca_av, spectrum M_av, Ricci et al, 2006, p. 1222
1851	**EW_M_25_av**	weak absorption	**quartz**	spectrum Q_av
1965	**EW_M_25_av**	weak absorption	**quartz**	spectrum Q_av
2012	**EW_av**	weak absorption	**(blank)**	(blank)
2135	**EW_M_25_av**	weak absorption	**calcium carbonate and quartz**	Spectrum Ca_av, spectrum M_av, spectrum Q_av
2154	**EW_av**	weak absorption	**(blank)**	(blank)
2238	**EW_M_25_av**	weak absorption	**quartz**	spectrum Q_av
2512	**EW_M_25_av**	combination band	**v1+v3**	Spectrum Ca_av, spectrum M_av, Ricci et al, 2006, p. 1222
2524	**EW_av**	weak absorption	**(blank)**	(blank)
2571	**EW_M_25_av**	weak absorption	**egg white**	spectrum EW_av
2585	**EW_M_25_av**	weak absorption	**egg white**	spectrum EW_av
2690	**EW_M_25_av**	weak absorption	**egg white**	spectrum EW_av
2714	**EW_av**	weak absorption	**(blank)**	(blank)
2828	**EW_av**	weak absorption	**C-H stretching**	Rosi et al, 2009, p. 2099
2874	**EW_M_25_av**	sharp and weak absorption	**CaCO3**	Spectrum Ca_av, spectrum M_av
2883	**EW_av**	weak absorption	**C-H stretching**	Rosi et al, 2009, p. 2099
2934	**EW_M_25_av**	weak absorption	**CH stretching**	Spectrum EW_av, Daher et al, 2017, p. 8
2945	**EW_av**	weak absorption	**(blank)**	(blank)
2964	**EW_M_25_av**	sharp and weak absorption	**CaCO3**	Spectrum Ca_av, spectrum M_av
2981	**EW_av**	weak absorption	**(blank)**	(blank)
3083	**EW_M_25_av**	1st overtone	**amide I**	Spectrum EW_av, Rosi et al, 2009, p. 2099
3091	**EW_av**	1st overtone	**amide I**	Rosi et al, 2009, p. 2099
3095	**EW_M_25_av**	1st overtone	**amide I**	Spectrum EW_av, Rosi et al, 2009, p. 2099
3304	**EW_M_25_av**	weak absorption	**N-H stretching**	Rosi et al, 2002, p. 2099
3642	**EW_M_25_av**	doublet	**OH stretching of H2O**	Spectrum M_av, spectrum Ca_av, Rosi et al, 2009, p. 2100

Figure 8: continued.

Peak x (position)	Spectrum ID	Type of band	Chemical Band Assignement	Reference
607	**EW_M_5_av**	weak absorption	**CaCO3**	spectrum Ca_av
701	**EW_M_5_av**	weak absorption	**quartz**	spectrum Q_av
714	**EW_M_5_av**	sharp absorption	**v4 carbonate ion**	Spectrum Ca_av, spectrum M_av, Ylmen and Jaglid, 2013, p. 119
729	**EW_av**	weak absorption	**(blank)**	(blank)
755	**EW_av**	weak absorption	**(blank)**	(blank)
792	**EW_M_5_av**	sharp and weak absorption	**quartz**	Spectrum Q_av, spectrum M_av
816	**EW_M_5_av**	sharp absorption	**quartz**	Spectrum Q_av, spectrum M_av
818	**EW_av**	weak absorption	**(blank)**	(blank)
848	**EW_M_5_av**	weak absorption	**v2 carbonate ion**	Spectrum Ca_av, spectrum M_av, Ylmen and Jaglid, 2013, p. 119
876	**EW_av**	strong absorption	**(blank)**	(blank)
881	**EW_M_5_av**	sharp absorption	**v2 carbonate ion**	Spectrum Ca_av, spectrum M_av, Ylmen and Jaglid, 2013, p. 119
962	**EW_av**	sharp absorption	**(blank)**	(blank)
1034	**EW_av**	sharp absorption	**(blank)**	(blank)
1086	**EW_av**	sharp and weak absorption	**(blank)**	(blank)
	EW_M_5_av	weak absorption	**egg white**	spectrum EW_av
1159	**EW_M_5_av**	sharp absorption	**quartz**	Spectrum Q_av, spectrum M_av
1179	**EW_av**	strong absorption	**(blank)**	(blank)
1295	**EW_av**	strong absorption	**(blank)**	(blank)
1325	**EW_av**	strong absorption	**(blank)**	(blank)
1395	**EW_M_5_av**	weak absorption	**CaCO3**	Spectrum Ca_av, spectrum M_av
1415	**EW_av**	sharp and weak absorption	**(blank)**	(blank)
1443	**EW_M_5_av**	weak absorption	**v3 antisymmetric stretching CO3-2**	Spectrum M_av, Ylmen and Jaglid, 2013, p. 119
1452	**EW_M_5_av**	weak absorption	**v3 antisymmetric stretching CO3-2**	Spectrum M_av, Ylmen and Jaglid, 2013, p. 119
1458	**EW_av**	stair-step type intensities	**Amide III**	Rosi et al, 2009, p. 2099
1467	**EW_M_5_av**	weak absorption	**v3 antisymmetric stretching CO3-2**	Spectrum M_av, Ylmen and Jaglid, 2013, p. 119
1472	**EW_av**	weak absorption	**(blank)**	(blank)
1561	**EW_M_5_av**	weak absorption	**quartz**	spectrum Q_av

Figure 9: Filtered CPAD entries of egg white (EW_av) and 5% egg white mortar mixture (EW_M_5_av).

1573	**EW_av**	strong absorption	**C-N-H bending amide II, N-H bands**	Ploeger et al, 2010, p. 37, Miliani et al, 2012, p. 304
1579	**EW_M_5_av**	strong absorption	**C-N-H bending amide II, N-H bands**	Spectrum EW_av, Rosi et al, 2009, p. 2104
1601	**EW_M_5_av**	weak absorption	**N-H bands**	Miliani et al, 2012, p. 304; Rosi et al, 2009, p. 2104
1630	**EW_M_5_av**	weak absorption	**N-H bands**	Miliani et al, 2012, p. 304; Rosi et al, 2009, p. 2104
1660	**EW_M_5_av**	strong absorption	**quartz**	Spectrum M_av
1693	**EW_av**	strong absorption	**N-H bands**	Rosi et al, 2009, p. 2104
1795	**EW_M_5_av**	combination band	**v1+v4**	Spectrum Ca_av, spectrum M_av, Ricci et al, 2006, p. 1222
1859	**EW_M_5_av**	weak absorption	**quartz**	spectrum Q_av
1867	**EW_M_5_av**	weak absorption	**quartz**	spectrum Q_av
1941	**EW_M_5_av**	weak absorption	**quartz**	spectrum Q_av
1967	**EW_M_5_av**	weak absorption	**quartz**	spectrum Q_av
2012	**EW_av**	weak absorption	**(blank)**	(blank)
2135	**EW_M_5_av**	weak absorption	**calcium carbonate and quartz**	Spectrum Ca_av, spectrum M_av, spectrum Q_av
2154	**EW_av**	weak absorption	**(blank)**	(blank)
2238	**EW_M_5_av**	weak absorption	**quartz**	spectrum Q_av
2512	**EW_M_5_av**	combination band	**v1+v3**	Spectrum Ca_av, spectrum M_av, Ricci et al, 2006, p. 1222
2524	**EW_av**	weak absorption	**(blank)**	(blank)
2703	**EW_M_5_av**	weak absorption	**egg white**	spectrum EW_av
2714	**EW_av**	weak absorption	**(blank)**	(blank)
2828	**EW_av**	weak absorption	**C-H stretching**	Rosi et al, 2009, p. 2099
2874	**EW_M_5_av**	sharp and weak absorption	**CaCO3**	Spectrum Ca_av, spectrum M_av
2883	**EW_av**	weak absorption	**C-H stretching**	Rosi et al, 2009, p. 2099
2936	**EW_M_5_av**	weak absorption	**CH stretching**	Spectrum EW_av, Daher et al, 2017, p. 8
2945	**EW_av**	weak absorption	**(blank)**	(blank)
2963	**EW_M_5_av**	sharp and weak absorption	**CaCO3**	Spectrum Ca_av, spectrum M_av
2981	**EW_av**	weak absorption	**(blank)**	(blank)
3030	**EW_M_5_av**	weak absorption	**CaCO3**	spectrum Ca_av
3066	**EW_M_5_av**	1st overtone	**amide I**	Spectrum EW_av, Rosi et al, 2009, p. 2099
3085	**EW_M_5_av**	1st overtone	**amide I**	Spectrum EW_av, Rosi et al, 2009, p. 2099
3091	**EW_av**	1st overtone	**amide I**	Rosi et al, 2009, p. 2099
3314	**EW_M_5_av**	weak absorption	**N-H stretching**	Rosi et al, 2002, p. 2099
3643	**EW_M_5_av**	doublet	**OH stretching of H2O**	Spectrum M_av, spectrum Ca_av, Rosi et al, 2009, p. 2100

Figure 9: continued.

7.5.3 Egg yolk and mortar mixtures CPAD

Peak x (position)	Spectrum ID	Type of band	Chemical Band Assignement	Reference
667	**EY_av**	sharp and weak absorption	**(blank)**	(blank)
669	**EY_M_75_av**	weak absorption	**egg yolk**	spectrum EY_av
685	**EY_M_75_av**	weak absorption	**v4 carbonate ion**	Spectrum Ca_av, Ylmen and Jaglid, 2013, p. 119
702	**EY_M_75_av**	sharp absorption	**quartz**	Spectrum M_av, spectrum Q_av
710	**EY_av**	weak absorption	**(blank)**	(blank)
720	**EY_M_75_av**	sharp and weak absorption	**in-plane rotation of linear long C chains δ(CH2)n**	Spectrum EY_av, Iwanicka et al, 2017, p. 18
730	**EY_M_75_av**	sharp and weak absorption	**in-plane rotation of linear long C chains δ(CH2)n**	Iwanicka et al, 2017, p. 19
741	**EY_M_75_av**	sharp and weak absorption	**in-plane rotation of linear long C chains δ(CH2)n**	Spectrum EY_av, Iwanicka et al, 2017, p. 18
744	**EY_av**	weak absorption	**(blank)**	(blank)
769	**EY_M_75_av**	weak absorption	**egg yolk**	spectrum EY_av
770	**EY_av**	(blank)	**(blank)**	(blank)
781	**EY_av**	(blank)	**(blank)**	(blank)
785	**EY_M_75_av**	weak absorption	**egg yolk**	spectrum EY_av
789	**EY_av**	(blank)	**(blank)**	(blank)
795	**EY_M_75_av**	sharp absorption	**quartz**	Spectrum M_av, spectrum Q_av
808	**EY_av**	(blank)	**(blank)**	(blank)
811	**EY_M_75_av**	sharp absorption	**quartz**	Spectrum M_av, spectrum Q_av
819	**EY_av**	(blank)	**(blank)**	(blank)
875	**EY_M_75_av**	sharp absorption	**v2 carbonate ion**	Spectrum M_av, spectrum Ca_av, Ylmen and Jaglid, 2013, p. 119
974	**EY_av**	sharp and weak absorption	**PO4-3anion stretching**	Ricci et al, 2006, p. 1223
1070	**EY_av**	reststrahlen	**PO4-3anion stretching**	Ricci et al, 2006, p. 1223
1124	**EY_av**	sharp and weak absorption	**PO4-3anion stretching**	Ricci et al, 2006, p. 1223
1152	**EY_M_75_av**	sharp absorption	**quartz**	Spectrum M_av, spectrum Q_av
1162	**EY_M_75_av**	sharp absorption	**quartz**	Spectrum M_av, spectrum Q_av
1198	**EY_av**	weak absorption	**(blank)**	(blank)
1263	**EY_M_75_av**	strong absorption	**egg yolk**	spectrum EY_av
1270	**EY_av**	strong absorption	**(blank)**	(blank)
1271	**EY_M_75_av**	strong absorption	**egg yolk**	spectrum EY_av
1283	**EY_av**	sharp absorption	**(blank)**	(blank)
1382	**EY_M_75_av**	strong absorption	**C-H bending**	Spectrum EY_av, Buti et al, 2013, p. 2705
1385	**EY_av**	sharp absorption	**C-H bending**	Buti et al, 2013, p. 2705

Figure 10: Filtered CPAD entries of egg yolk (EY_av) and 75% egg yolk/mortar mixture (EY_M_75_av).

1420	**EY_av**	weak absorption	**(blank)**	(blank)
1424	**EY_M_75_av**	strong absorption	**egg yolk**	spectrum EY_av
1445	**EY_av**	weak absorption	**(blank)**	(blank)
1470	**EY_M_75_av**	strong absorption	**C-O bending**	Spectrum EY_av, Ricci et al, 2006, p. 1224
1472	**EY_av**	sharp absorption	**C-O bending**	Ricci et al, 2006, p. 1223
1500	**EY_M_75_av**	weak absorption	**C=O**	Spectrum EY_av, Rosi et al, 2009, p. 2099
1507	**EY_av**	weak absorption	**C=O**	Rosi et al, 2009, p. 2099
1519	**EY_av**	weak absorption	**C=O**	Rosi et al, 2009, p. 2099
1522	**EY_M_75_av**	weak absorption	**C=O**	Spectrum EY_av, Rosi et al, 2009, p. 2099
1559	**EY_av**	strong absorption	**C=O**	Rosi et al, 2009, p. 2099
1560	**EY_M_75_av**	weak absorption	**C=O**	Spectrum EY_av, Rosi et al, 2009, p. 2099
1596	**EY_M_75_av**	weak absorption	**quartz**	spectrum Q_av
1667	**EY_av**	strong absorption	**C=O**	(blank)
	EY_M_75_av	weak absorption	**C=O**	Spectrum EY_av, Rosi et al, 2009, p. 2099
1679	**EY_M_75_av**	weak absorption	**C=O**	Spectrum EY_av, Rosi et al, 2009, p. 2099
1757	**EY_M_75_av**	1st order derivative	**C=O stretching band**	Spectrum EY_av, Ploeger et al, 2010, p, 37
1758	**EY_av**	stretching band	**esters**	Mazzeo et al, 2008, p. 69
2033	**EY_M_75_av**	weak absorption	**(blank)**	(blank)
2520	**EY_M_75_av**	combination band	**v1+v3**	Spectrum M_av, spectrum Ca_av, Ricci et al, 2006, p. 1222
2673	**EY_M_75_av**	weak absorption	**(blank)**	(blank)
2681	**EY_M_75_av**	weak absorption	**(blank)**	(blank)
2864	**EY_av**	strong absorption	**C-H stretching**	Rosi et al, 2009, p. 2099
	EY_M_75_av	strong absorption	**C-H stretching bands, esters**	Spectrum EY_av, Rosi et al, 2009, p. 2099
2942	**EY_av**	sharp absorption	**C-H stretching**	Rosi et al, 2009, p. 2099
	EY_M_75_av	strong absorption	**C-H stretching bands, esters**	Spectrum EY_av, Rosi et al, 2009, p. 2099
2965	**EY_M_75_av**	strong absorption	**C-H stretching bands, esters**	Spectrum EY_av, Rosi et al, 2009, p. 2099
2967	**EY_av**	sharp absorption	**C-H stretching**	Rosi et al, 2009, p. 2099
3011	**EY_M_75_av**	weak absorption	**CH stretching**	Miliani et al, 2012, p. 302
3015	**EY_av**	weak absorption	**CH stretching**	Miliani et al, 2012, p. 302

Figure 10: continued.

Peak x (position)	Spectrum ID	Type of band	Chemical Band Assignement	Reference
614	EY_M_50_av	weak absorption	CaCO3	Spectrum M_av, spectrum Ca_av
635	EY_M_50_av	weak absorption	CaCO3	Spectrum M_av, spectrum Ca_av
657	EY_M_50_av	weak absorption	CaCO3	Spectrum M_av, spectrum Ca_av
667	EY_av	sharp and weak absorption	(blank)	(blank)
702	EY_M_50_av	sharp and weak absorption	quartz	Spectrum M_av, spectrum Q_av
710	EY_av	weak absorption	(blank)	(blank)
714	EY_M_50_av	sharp and weak absorption	v4 carbonate ion	Spectrum M_av, spectrum Ca_av, Ylmen and Jaglid, 2013, p. 119
744	EY_av	weak absorption	(blank)	(blank)
770	EY_av	(blank)	(blank)	(blank)
781	EY_av	(blank)	(blank)	(blank)
789	EY_av	(blank)	(blank)	(blank)
791	EY_M_50_av	sharp and weak absorption	quartz	Spectrum M_av, spectrum Q_av
808	EY_av	(blank)	(blank)	(blank)
813	EY_M_50_av	strong absorption	quartz	Spectrum M_av, spectrum Q_av
819	EY_av	(blank)	(blank)	(blank)
874	EY_M_50_av	weak absorption	v2 carbonate ion	Spectrum M_av, spectrum Ca_av, Ylmen and Jaglid, 2013, p. 119
974	EY_av	sharp and weak absorption	PO4-3anion stretching	Ricci et al, 2006, p. 1223
1070	EY_av	reststrahlen	PO4-3anion stretching	Ricci et al, 2006, p. 1223
1124	EY_av	sharp and weak absorption	PO4-3anion stretching	Ricci et al, 2006, p. 1223
1159	EY_M_50_av	sharp absorption	quartz	Spectrum M_av, spectrum Q_av
1198	EY_av	weak absorption	(blank)	(blank)
1270	EY_av	strong absorption	(blank)	(blank)
1281	EY_M_50_av	strong absorption	egg yolk	spectrum EY_av
1283	EY_av	sharp absorption	(blank)	(blank)
1301	EY_M_50_av	strong absorption	CH2, CH3	Lombardi and Santarelli, 2009, p. 542
1310	EY_M_50_av	strong absorption	CH2, CH3	Lombardi and Santarelli, 2009, p. 542
1342	EY_M_50_av	weak absorption	quartz	spectrum Q_av
1381	EY_M_50_av	strong absorption	C-H bending	Spectrum EY_av, Buti et al, 2013, p. 2705
1385	EY_av	sharp absorption	C-H bending	Buti et al, 2013, p. 2705
1395	EY_M_50_av	strong absorption	CaCO3	Spectrum M_av, spectrum Ca_av
1420	EY_av	weak absorption	(blank)	(blank)
	EY_M_50_av	weak absorption	egg yolk	spectrum EY_av
1430	EY_M_50_av	weak absorption	CaCO3	Spectrum M_av
1445	EY_av	weak absorption	(blank)	(blank)
1448	EY_M_50_av	weak absorption	egg yolk	spectrum EY_av
1470	EY_M_50_av	strong absorption	C-O bending	Spectrum EY_av, Ricci et al, 2006, p. 1224
1472	EY_av	sharp absorption	C-O bending	Ricci et al, 2006, p. 1223
1507	EY_av	weak absorption	C=O	Rosi et al, 2009, p. 2099
1508	EY_M_50_av	weak absorption	C=O	Spectrum EY_av, Rosi et al, 2009, p. 2095
1518	EY_M_50_av	weak absorption	C=O	Spectrum EY_av, Rosi et al, 2009, p. 2096
1519	EY_av	weak absorption	C=O	Rosi et al, 2009, p. 2099

Figure 11: Filtered CPAD entries of egg yolk (EY_av) and 50% egg yolk/mortar mixture (EY_M_50_av).

1529	**EY_M_50_av**	weak absorption	**C=O**	Spectrum EY_av, Rosi et al, 2009, p. 2097
1538	**EY_M_50_av**	weak absorption	**C=O**	Spectrum EY_av, Rosi et al, 2009, p. 2098
1559	**EY_av**	strong absorption	**C=O**	Rosi et al, 2009, p. 2099
1560	**EY_M_50_av**	weak absorption	**C=O**	Spectrum EY_av, Rosi et al, 2009, p. 2099
1596	**EY_M_50_av**	weak absorption	**quartz**	spectrum Q_av
1604	**EY_M_50_av**	weak absorption	**quartz**	spectrum Q_av
1617	**EY_M_50_av**	weak absorption	**quartz**	spectrum Q_av
1634	**EY_M_50_av**	weak absorption	**quartz**	spectrum Q_av
1667	**EY_av**	strong absorption	**C=O**	(blank)
1682	**EY_M_50_av**	strong absorption	**C=O**	Spectrum EY_av, Rosi et al, 2009, p. 2099
1690	**EY_M_50_av**	strong absorption	**C=O**	Spectrum EY_av, Rosi et al, 2009, p. 2099
1732	**EY_M_50_av**	weak absorption	**C=O stretching band**	Spectrum EY_av, Ploeger et al, 2010, p, 37
1755	**EY_M_50_av**	1st order derivative	**C=O stretching band**	Spectrum EY_av, Ploeger et al, 2010, p, 37
1758	**EY_av**	stretching band	**esters**	Mazzeo et al, 2008, p. 69
1792	**EY_M_50_av**	combination band	**v1+v4**	Spectrum M_av, spectrum Ca_av, Ricci et al, 2006, p. 1222
1859	**EY_M_50_av**	weak absorption	**quartz**	Spectrum M_av, spectrum Q_av
1867	**EY_M_50_av**	weak absorption	**quartz**	Spectrum M_av, spectrum Q_av
1941	**EY_M_50_av**	weak absorption	**quartz**	Spectrum M_av, spectrum Q_av
1984	**EY_M_50_av**	weak absorption	**quartz**	Spectrum M_av, spectrum Q_av
2135	**EY_M_50_av**	weak absorption	**calcium carbonate and quartz**	Spectrum Ca_av, spectrum M_av, spectrum Q_av
2189	**EY_M_50_av**	weak absorption	**egg yolk**	spectrum EY_av
2238	**EY_M_50_av**	weak absorption	**quartz**	spectrum Q_av
2512	**EY_M_50_av**	combination band	**v1+v3**	Spectrum M_av, spectrum Ca_av, Ricci et al, 2006, p. 1222
2562	**EY_M_50_av**	weak absorption	**(blank)**	(blank)
2602	**EY_M_50_av**	weak absorption	**(blank)**	(blank)
2682	**EY_M_50_av**	weak absorption	**(blank)**	(blank)
2692	**EY_M_50_av**	weak absorption	**(blank)**	(blank)
2731	**EY_M_50_av**	weak absorption	**(blank)**	(blank)
2858	**EY_M_50_av**	strong absorption	**C-H stretching bands, esters**	Spectrum EY_av, Rosi et al, 2009, p. 2099
2864	**EY_av**	strong absorption	**C-H stretching**	Rosi et al, 2009, p. 2099
2908	**EY_M_50_av**	strong absorption	**C-H stretching bands, esters**	Spectrum EY_av, Rosi et al, 2009, p. 2099
2936	**EY_M_50_av**	strong absorption	**CH stretching**	Spectrum EY_av, Daher et al, 2017, p.8
2942	**EY_av**	sharp absorption	**C-H stretching**	Rosi et al, 2009, p. 2099
2959	**EY_M_50_av**	strong absorption	**C-H stretching bands, esters**	Spectrum EY_av, Rosi et al, 2009, p. 2099
2967	**EY_av**	sharp absorption	**C-H stretching**	Rosi et al, 2009, p. 2099
3004	**EY_M_50_av**	weak absorption	**CH stretching**	Miliani et al, 2012, p. 302
3015	**EY_av**	weak absorption	**CH stretching**	Miliani et al, 2012, p. 302

Figure 11: continued.

Peak x (position)	Spectrum ID	Type of band	Chemical Band Assignement	Reference
615	EY_M_25_av	weak absorption	CaCO3	Spectrum M_av, spectrum Ca_av
637	EY_M_25_av	weak absorption	CaCO3	Spectrum M_av, spectrum Ca_av
659	EY_M_25_av	weak absorption	CaCO3	Spectrum M_av, spectrum Ca_av
667	EY_av	sharp and weak absorption	(blank)	(blank)
701	EY_M_25_av	sharp and weak absorption	quartz	Spectrum M_av, spectrum Q_av
710	EY_av	weak absorption	(blank)	(blank)
714	EY_M_25_av	sharp and weak absorption	v4 carbonate ion	Spectrum M_av, spectrum Ca_av, Ylmen and Jaglid, 2013, p. 119
744	EY_av	weak absorption	(blank)	(blank)
770	EY_av	(blank)	(blank)	(blank)
781	EY_av	(blank)	(blank)	(blank)
789	EY_av	(blank)	(blank)	(blank)
792	EY_M_25_av	sharp and weak absorption	quartz	Spectrum M_av, spectrum Q_av
808	EY_av	(blank)	(blank)	(blank)
819	EY_av	(blank)	(blank)	(blank)
	EY_M_25_av	strong absorption	quartz	Spectrum M_av, spectrum Q_av
875	EY_M_25_av	weak absorption	v2 carbonate ion	Spectrum M_av, spectrum Ca_av, Ylmen and Jaglid, 2013, p. 119
974	EY_av	sharp and weak absorption	PO4-3anion stretching	Ricci et al, 2006, p. 1223
1070	EY_av	reststrahlen	PO4-3anion stretching	Ricci et al, 2006, p. 1223
1096	EY_M_25_av	weak absorption	v1 carbonate ion	Spectrum Ca_av, Ylmen and Jaglid, 2013, p. 119
1103	EY_M_25_av	weak absorption	v1 carbonate ion	Spectrum Ca_av, Ylmen and Jaglid, 2013, p. 119
1117	EY_M_25_av	weak absorption	v1 carbonate ion	Spectrum Ca_av, Ylmen and Jaglid, 2013, p. 119
1124	EY_av	sharp and weak absorption	PO4-3anion stretching	Ricci et al, 2006, p. 1223
1159	EY_M_25_av	sharp absorption	quartz	Spectrum M_av, spectrum Q_av
1198	EY_av	weak absorption	(blank)	(blank)
1270	EY_av	strong absorption	(blank)	(blank)
1279	EY_M_25_av	strong absorption	egg yolk	spectrum EY_av
1283	EY_av	sharp absorption	(blank)	(blank)
1315	EY_M_25_av	strong absorption	CH2, CH3	Lombardi and Santarelli, 2009, p. 542
1385	EY_av	sharp absorption	C-H bending	Buti et al, 2013, p. 2705
1390	EY_M_25_av	strong absorption	C-H bending	Spectrum EY_av, Buti et al, 2013, p. 2705
1399	EY_M_25_av	strong absorption	C-H bending	Spectrum EY_av, Buti et al, 2013, p. 2705
1420	EY_av	weak absorption	(blank)	(blank)
1445	EY_av	weak absorption	(blank)	(blank)
1472	EY_av	sharp absorption	C-O bending	Ricci et al, 2006, p. 1223
1476	EY_M_25_av	strong absorption	C-O bending	Spectrum EY_av, Ricci et al, 2006, p. 1224
1507	EY_av	weak absorption	C=O	Rosi et al, 2009, p. 2099

Figure 12: Filtered CPAD entries of egg yolk (EY_av) and 25% egg yolk/mortar mixture (EY_M_25_av).

1519	**EY_av**	weak absorption	**C=O**	Rosi et al, 2009, p. 2099
1520	**EY_M_25_av**	weak absorption	**C=O**	Spectrum EY_av, Rosi et al, 2009, p. 2097
1536	**EY_M_25_av**	weak absorption	**C=O**	Spectrum EY_av, Rosi et al, 2009, p. 2098
1559	**EY_av**	strong absorption	**C=O**	Rosi et al, 2009, p. 2099
1569	**EY_M_25_av**	strong absorption	**C=O**	Spectrum EY_av, Rosi et al, 2009, p. 2098
1635	**EY_M_25_av**	weak absorption	**quartz**	spectrum Q_av
1667	**EY_av**	strong absorption	**C=O**	(blank)
1677	**EY_M_25_av**	strong absorption	**C=O**	Spectrum EY_av, Rosi et al, 2009, p. 2099
1687	**EY_M_25_av**	strong absorption	**C=O**	Spectrum EY_av, Rosi et al, 2009, p. 2099
1753	**EY_M_25_av**	1st order derivative	**C=O stretching band**	Spectrum EY_av, Ploeger et al, 2010, p, 37
1758	**EY_av**	stretching band	**esters**	Mazzeo et al, 2008, p. 69
1792	**EY_M_25_av**	combination band	**v1+v4**	Spectrum M_av, spectrum Ca_av, Ricci et al, 2006, p. 1222
1867	**EY_M_25_av**	weak absorption	**quartz**	Spectrum M_av, spectrum Q_av
1876	**EY_M_25_av**	weak absorption	**quartz**	Spectrum M_av, spectrum Q_av
1942	**EY_M_25_av**	weak absorption	**quartz**	Spectrum M_av, spectrum Q_av
1977	**EY_M_25_av**	weak absorption	**quartz**	Spectrum M_av, spectrum Q_av
1993	**EY_M_25_av**	weak absorption	**quartz**	Spectrum M_av, spectrum Q_av
2135	**EY_M_25_av**	weak absorption	**calcium carbonate and quartz**	Spectrum Ca_av, spectrum M_av, spectrum Q_av
2237	**EY_M_25_av**	weak absorption	**quartz**	spectrum Q_av
2510	**EY_M_25_av**	combination band	**v1+v3**	Spectrum M_av, spectrum Ca_av, Ricci et al, 2006, p. 1222
2593	**EY_M_25_av**	weak absorption	**(blank)**	(blank)
2642	**EY_M_25_av**	weak absorption	**(blank)**	(blank)
2683	**EY_M_25_av**	weak absorption	**(blank)**	(blank)
2700	**EY_M_25_av**	weak absorption	**(blank)**	(blank)
2857	**EY_M_25_av**	strong absorption	**C-H stretching bands, esters**	Spectrum EY_av, Rosi et al, 2009, p. 2099
2864	**EY_av**	strong absorption	**C-H stretching**	Rosi et al, 2009, p. 2099
2935	**EY_M_25_av**	strong absorption	**CH stretching**	Spectrum EY_av, Daher et al, 2017, p.8
2942	**EY_av**	sharp absorption	**C-H stretching**	Rosi et al, 2009, p. 2099
2959	**EY_M_25_av**	strong absorption	**C-H stretching bands, esters**	Spectrum EY_av, Rosi et al, 2009, p. 2099
2967	**EY_av**	sharp absorption	**C-H stretching**	Rosi et al, 2009, p. 2099
3007	**EY_M_25_av**	weak absorption	**CH stretching**	Miliani et al, 2012, p. 302
3015	**EY_av**	weak absorption	**CH stretching**	Miliani et al, 2012, p. 302
3641	**EY_M_25_av**	doublet	**OH stretching**	Spectrum M_av, spectrum Ca_av, Rosi et al, 2009, p. 2100

Figure 12: continued.

Peak x (position)	Spectrum ID	Type of band	Chemical Band Assignement	Reference
619	EY_M_5_av	weak absorption	CaCO3	Spectrum M_av, spectrum Ca_av
636	EY_M_5_av	weak absorption	CaCO3	Spectrum M_av, spectrum Ca_av
667	EY_av	sharp and weak absorption	(blank)	(blank)
702	EY_M_5_av	strong absorption	quartz	Spectrum M_av, spectrum Q_av
710	EY_av	weak absorption	(blank)	(blank)
713	EY_M_5_av	strong absorption	v4 carbonate ion	Spectrum M_av, spectrum Ca_av, Ylmen and Jaglid, 2013, p. 119
744	EY_av	weak absorption	(blank)	(blank)
770	EY_av	(blank)	(blank)	(blank)
781	EY_av	(blank)	(blank)	(blank)
789	EY_av	(blank)	(blank)	(blank)
791	EY_M_5_av	sharp absorption	quartz	Spectrum M_av, spectrum Q_av
808	EY_av	(blank)	(blank)	(blank)
815	EY_M_5_av	strong absorption	quartz	Spectrum M_av, spectrum Q_av
819	EY_av	(blank)	(blank)	(blank)
848	EY_M_5_av	sharp absorption	v2 carbonate ion	Spectrum M_av, spectrum Ca_av, Ylmen and Jaglid, 2013, p. 119
877	EY_M_5_av	strong absorption	v2 carbonate ion	Spectrum M_av, spectrum Ca_av, Ylmen and Jaglid, 2013, p. 119
974	EY_av	sharp and weak absorption	PO4-3anion stretching	Ricci et al, 2006, p. 1223
1070	EY_av	reststrahlen	PO4-3anion stretching	Ricci et al, 2006, p. 1223
1124	EY_av	sharp and weak absorption	PO4-3anion stretching	Ricci et al, 2006, p. 1223
1159	EY_M_5_av	sharp absorption	quartz	Spectrum M_av, spectrum Q_av
1198	EY_av	weak absorption	(blank)	(blank)
	EY_M_5_av	weak absorption	egg yolk	spectrum EY_av
1270	EY_av	strong absorption	(blank)	(blank)
1283	EY_av	sharp absorption	(blank)	(blank)
1385	EY_av	sharp absorption	C-H bending	Buti et al, 2013, p. 2705
1399	EY_M_5_av	strong absorption	CaCO3	Spectrum M_av, spectrum Ca_av
1420	EY_av	weak absorption	(blank)	(blank)
1436	EY_M_5_av	strong absorption	v3 antisymmetric stretching CO3-2	Spectrum Ca_av, Ylmen and Jaglid, 2013, p. 119
1445	EY_av	weak absorption	(blank)	(blank)
1451	EY_M_5_av	strong absorption	v3 antisymmetric stretching CO3-2	Spectrum Ca_av, Ylmen and Jaglid, 2013, p. 119
1466	EY_M_5_av	strong absorption	v3 antisymmetric stretching CO3-2	Spectrum Ca_av, Ylmen and Jaglid, 2013, p. 119
1472	EY_av	sharp absorption	C-O bending	Ricci et al, 2006, p. 1223

Figure 13: Filtered CPAD entries of egg yolk (EY_av) and 5% egg yolk/mortar mixture (EY_M_5_av).

1507	**EY_av**	weak absorption	**C=O**	Rosi et al, 2009, p. 2099
1519	**EY_av**	weak absorption	**C=O**	Rosi et al, 2009, p. 2099
1539	**EY_M_5_av**	weak absorption	**C=O**	Spectrum EY_av, Rosi et al, 2009, p. 2098
1559	**EY_av**	strong absorption	**C=O**	Rosi et al, 2009, p. 2099
1584	**EY_M_5_av**	strong absorption	**v3 antisymmetric stretching CO3-2**	Spectrum Ca_av, Ylmen and Jaglid, 2013, p. 119
1612	**EY_M_5_av**	weak absorption	**quartz**	spectrum Q_av
1658	**EY_M_5_av**	weak absorption	**quartz**	Spectrum M_av, spectrum Q_av
1667	**EY_av**	strong absorption	**C=O**	(blank)
1675	**EY_M_5_av**	strong absorption	**C=O**	Spectrum EY_av, Rosi et al, 2009, p. 2099
1744	**EY_M_5_av**	1st order derivative	**C=O stretching band**	Spectrum EY_av, Ploeger et al, 2010, p, 37
1758	**EY_av**	stretching band	**esters**	Mazzeo et al, 2008, p. 69
1794	**EY_M_5_av**	combination band	**v1+v4**	Spectrum M_av, spectrum Ca_av, Ricci et al, 2006, p. 1222
1860	**EY_M_5_av**	weak absorption	**quartz**	Spectrum M_av, spectrum Q_av
1867	**EY_M_5_av**	weak absorption	**quartz**	Spectrum M_av, spectrum Q_av
1942	**EY_M_5_av**	weak absorption	**quartz**	Spectrum M_av, spectrum Q_av
1971	**EY_M_5_av**	weak absorption	**quartz**	Spectrum M_av, spectrum Q_av
1990	**EY_M_5_av**	weak absorption	**quartz**	Spectrum M_av, spectrum Q_av
2135	**EY_M_5_av**	weak absorption	**calcium carbonate and quartz**	Spectrum Ca_av, spectrum M_av, spectrum Q_av
2237	**EY_M_5_av**	weak absorption	**quartz**	spectrum Q_av
2512	**EY_M_5_av**	combination band	**v1+v3**	Spectrum M_av, spectrum Ca_av, Ricci et al, 2006, p. 1222
2682	**EY_M_5_av**	weak absorption	**(blank)**	(blank)
2691	**EY_M_5_av**	weak absorption	**(blank)**	(blank)
2855	**EY_M_5_av**	strong absorption	**C-H stretching bands, esters**	Spectrum EY_av, Rosi et al, 2009, p. 2099
2864	**EY_av**	strong absorption	**C-H stretching**	Rosi et al, 2009, p. 2099
2925	**EY_M_5_av**	strong absorption	**CH stretching**	Spectrum EY_av, Daher et al, 2017, p.8
2942	**EY_av**	sharp absorption	**C-H stretching**	Rosi et al, 2009, p. 2099
2957	**EY_M_5_av**	strong absorption	**C-H stretching bands, esters**	Spectrum EY_av, Rosi et al, 2009, p. 2099
2967	**EY_av**	sharp absorption	**C-H stretching**	Rosi et al, 2009, p. 2099
3015	**EY_av**	weak absorption	**CH stretching**	Miliani et al, 2012, p. 302
3077	**EY_M_5_av**	weak absorption	**2δNH**	Rosi et al, 2010, p. 621
3643	**EY_M_5_av**	doublet	**OH stretching**	Spectrum M_av, spectrum Ca_av, Rosi et al, 2009, p. 2100

Figure 13: continued.

7.5.4 Egg (whole) and mortar mixtures CPAD

Peak x (position)	Spectrum ID	Type of band	Chemical Band Assignement	Reference
668	E_av	sharp and weak absorption	(blank)	spectrum EY_av, spectrum EW_av
	E_M_75_av	weak absorption	(blank)	Spectrum E_av, Spectrum EW_av, spectrum EY_av
700	E_M_75_av	weak absorption	quartz	Spectrun M_av, Spectrum Q_av
715	E_M_75_av	weak absorption	v4 carbonate ion	Spectrun M_av, Spectrum Ca_av, Ylmen and Jaglid, 2013, p. 119
734	E_av	weak absorption	(blank)	(blank)
745	E_av	weak absorption	(blank)	spectrum EY_av
765	E_av	weak absorption	(blank)	spectrum EY_av
791	E_M_75_av	sharp and weak absorption	quartz	Spectrun M_av, Spectrum Q_av
794	E_av	weak absorption	(blank)	spectrum EY_av
802	E_av	weak absorption	(blank)	spectrum EY_av
816	E_M_75_av	strong absorption	quartz	Spectrun M_av, Spectrum Q_av
835	E_av	weak absorption	(blank)	(blank)
875	E_M_75_av	weak absorption	v2 carbonate ion	Spectrun M_av, Spectrum Ca_av, Ylmen and Jaglid, 2013, p. 119
973	E_av	weak absorption	PO4-3anion stretching	Ricci et al, 2006, p. 1223, spectrum EY_av
1116	E_M_75_av	weak absorption	CaCO3	spectrum Ca_av
1123	E_av	weak absorption	PO4-3anion stretching	Ricci et al, 2006, p. 1223, spectrum EY_av
1159	E_M_75_av	strong absorption	quartz	Spectrun M_av, Spectrum Q_av
1177	E_av	weak absorption	v(C-O) stretching	Ricci et al, 2006, p. 1224, spectrum EW_av
1268	E_av	strong absorption	C-O	Ploeger et al, 2010, p. 37, spectrum EY_av
1274	E_M_75_av	strong absorption	C-O	Spectrum E_av, Spectrum Ca_av, Ploeger et al, 2010, p. 17
1282	E_M_75_av	strong absorption	C-O	Spectrum E_av, Spectrum Ca_av, Ploeger et al, 2010, p. 17
1315	E_M_75_av	weak absorption	whole egg	Spectrum E_av
1324	E_av	(blank)	(blank)	spectrum EW_av
1343	E_M_75_av	weak absorption	quartz	spectrum Q_av
1352	E_M_75_av	weak absorption	quartz	spectrum Q_av
1389	E_M_75_av	strong absorption	CaCO3	Spectrun M_av, Spectrum Ca_av
1402	E_M_75_av	strong absorption	CaCO3	Spectrun M_av, Spectrum Ca_av
1411	E_av	(blank)	(blank)	spectrum EW_av
1445	E_av	weak absorption	Amide III	Buti et al, 2013, p. 2705, spectrum EW_av
1468	E_M_75_av	strong absorption	C-O bending	Spectrum E_av, Spectrum Ca_av, Ricci et al, 2006, p. 1223
1472	E_av	sharp absorption	C-O bending	Ricci et al, 2006, p. 1223, spectrum EW_av and EY_av
1555	E_M_75_av	strong absorption	N-H bands, amide I, II	Spectrum E_av, Miliani et al, 2012, p. 304
1568	E_av	strong absorption	N-H bands, amide I, II	Miliani et al, 2012, p. 304, spectrum EW_av

Figure 14: Filtered CPAD entries of egg (E_av) and 75% egg/mortar mixture (E_M_75_av).

1686	**E_M_75_av**	strong absorption	**N-H bands, amide I, II**	Spectrum E_av, Miliani et al, 2012, p. 304
1693	**E_av**	strong absorption	**N-H bands, amide I, II**	Miliani et al, 2012, p. 304, spectrum EW_av
1751	**E_M_75_av**	strong absorption	**C-H stretching bands, esters**	Spectrum E_av, Mazzeo et al, 2008, p. 69
1755	**E_av**	strong absorption	**C=O stretching band, esters**	Mazzeo et al, 2008, p. 69, spectrum EY_av
1791	**E_M_75_av**	combination band	**v1+v4**	Spectrum M_av, spectrum Ca_av, Ricci et al, 2006, p. 1222
1843	**E_M_75_av**	weak absorption	**quartz**	Spectrum M_av, Spectrum Q_av
1854	**E_M_75_av**	weak absorption	**quartz**	Spectrum M_av, Spectrum Q_av
1867	**E_M_75_av**	weak absorption	**quartz**	Spectrum M_av, Spectrum Q_av
1941	**E_M_75_av**	weak absorption	**quartz**	Spectrum M_av, Spectrum Q_av
1949	**E_M_75_av**	weak absorption	**quartz**	Spectrum M_av, Spectrum Q_av
1966	**E_M_75_av**	weak absorption	**quartz**	Spectrum M_av, Spectrum Q_av
1977	**E_M_75_av**	weak absorption	**quartz**	Spectrum M_av, Spectrum Q_av
1991	**E_M_75_av**	weak absorption	**v+δ Si-O**	Spectrum M_av, Spectrum Q_av, Miliani et al, 2012, p. 303
2135	**E_M_75_av**	sharp absorption	**CaCO3 and quartz**	Spectrum M_av, Spectrum Q_av, spectrum Ca_av
2237	**E_M_75_av**	sharp absorption	**quartz**	Spectrum M_av, Spectrum Q_av
2516	**E_M_75_av**	combination band	**v1+v3**	Spectrum M_av, spectrum Ca_av, Ricci et al, 2006, p. 1222
2685	**E_M_75_av**	weak absorption	**quartz**	Spectrum M_av, Spectrum Q_av
2857	**E_M_75_av**	strong absorption	**CH stretching**	Spectrum E_av, Daher et al, 2017, p.8
2864	**E_av**	strong absorption	**C-H stretching**	Rosi et al, 2009, p. 2099, spectrum EY_av
2876	**E_av**	strong absorption	**C-H stretching**	Rosi et al, 2009, p. 2099, spectrum EY_av
2937	**E_M_75_av**	strong absorption	**CH stretching**	Spectrum E_av, Daher et al, 2017, p.8
2942	**E_av**	strong absorption	**C-H stretching bands, esters**	Spectrum EY_av, Rosi et al, 2009, p. 2099
2959	**E_M_75_av**	weak absorption	**CH2 stretching**	Spectrum E_av, Ploeger et al, 2010, p. 37
2973	**E_av**	strong absorption	**C-H stretching bands, esters**	Spectrum EY_av, Rosi et al, 2009, p. 2099
3006	**E_M_75_av**	weak absorption	**(blank)**	(blank)
3045	**E_av**	weak absorption	**2δNH**	Rosi et al, 2010, p. 621
3075	**E_av**	weak absorption	**2δNH**	Rosi et al, 2010, p. 621
3080	**E_M_75_av**	weak absorption	**2δNH**	Spectrum E_av, Rosi et al, 2010, p. 621
3089	**E_av**	weak absorption	**2δNH**	Rosi et al, 2010, p. 621
3098	**E_M_75_av**	weak absorption	**2δNH**	Spectrum E_av, Rosi et al, 2010, p. 621
3102	**E_av**	weak absorption	**2δNH**	Rosi et al, 2010, p. 621
3108	**E_M_75_av**	weak absorption	**2δNH**	Spectrum E_av, Rosi et al, 2010, p. 621
3224	**E_av**	(blank)	**(blank)**	(blank)
3240	**E_av**	(blank)	**(blank)**	(blank)

Figure 14: continued.

Peak x (position)	Spectrum ID	Type of band	Chemical Band Assignement	Reference
618	E_M_50_av	weak absorption	CaCO3	spectrum Ca_av
660	E_M_50_av	weak absorption	(blank)	Spectrum E_av, Spectrum EW_av, spectrum EY_av
668	E_av	sharp and weak absorption	(blank)	spectrum EY_av, spectrum EW_av
701	E_M_50_av	weak absorption	quartz	Spectrun M_av, Spectrum Q_av
714	E_M_50_av	weak absorption	v4 carbonate ion	Spectrun M_av, Spectrum Ca_av, Ylmen and Jaglid, 2013, p. 119
734	E_av	weak absorption	(blank)	(blank)
743	E_M_50_av	weak absorption	whole egg	Spectrum E_av
745	E_av	weak absorption	(blank)	spectrum EY_av
765	E_av	weak absorption	(blank)	spectrum EY_av
793	E_M_50_av	weak absorption	quartz	Spectrun M_av, Spectrum Q_av
794	E_av	weak absorption	(blank)	spectrum EY_av
802	E_av	weak absorption	(blank)	spectrum EY_av
816	E_M_50_av	sharp absorption	quartz	Spectrun M_av, Spectrum Q_av
835	E_av	weak absorption	(blank)	(blank)
847	E_M_50_av	weak absorption	v2 carbonate ion	Spectrun M_av, Spectrum Ca_av, Ylmen and Jaglid, 2013, p. 119
875	E_M_50_av	sharp absorption	v2 carbonate ion	Spectrun M_av, Spectrum Ca_av, Ylmen and Jaglid, 2013, p. 119
970	E_M_50_av	weak absorption	PO4-3 anion stretching	Spectrum E_av, Ricci et al. 2006, p. 1223
973	E_av	weak absorption	PO4-3anion stretching	Ricci et al, 2006, p. 1223, spectrum EY_av
1116	E_M_50_av	weak absorption	CaCO3	spectrum Ca_av
1123	E_av	weak absorption	PO4-3anion stretching	Ricci et al, 2006, p. 1223, spectrum EY_av
1158	E_M_50_av	strong absorption	quartz	Spectrun M_av, Spectrum Q_av
1177	E_av	weak absorption	v(C-O) stretching	Ricci et al, 2006, p. 1224, spectrum EW_av
1265	E_M_50_av	strong absorption	C-O	Spectrum E_av, Ploeger et al, 2010, p. 17
1268	E_av	strong absorption	C-O	Ploeger et al, 2010, p. 37, spectrum EY_av
1303	E_M_50_av	weak absorption	whole egg	Spectrum E_av
1313	E_M_50_av	weak absorption	whole egg	Spectrum E_av
1324	E_av	(blank)	(blank)	spectrum EW_av
1340	E_M_50_av	weak absorption	quartz	spectrum Q_av
1396	E_M_50_av	strong absorption	CaCO3	Spectrun M_av, Spectrum Ca_av
1411	E_av	(blank)	(blank)	spectrum EW_av
1433	E_M_50_av	strong absorption	C-O bending	Spectrum E_av, Spectrum Ca_av, Ricci et al, 2006, p. 1223
1445	E_av	weak absorption	Amide III	Buti et al, 2013, p. 2705, spectrum EW_av
1468	E_M_50_av	strong absorption	C-O bending	Spectrum E_av, Spectrum Ca_av, Ricci et al, 2006, p. 1223
1472	E_av	sharp absorption	C-O bending	Ricci et al, 2006, p. 1223, spectrum EW_av and EY_av
1561	E_M_50_av	strong absorption	N-H bands, amide I, II	Spectrum E_av, Miliani et al, 2012, p. 304
1568	E_av	strong absorption	N-H bands, amide I, II	Miliani et al, 2012, p. 304, spectrum EW_av

Figure 15: Filtered CPAD entries of egg (E_av) and 50% egg/mortar mixture (E_M_50_av).

1680	**E_M_50_av**	strong absorption	**N-H bands, amide I, II**	Spectrum E_av, Miliani et al, 2012, p. 304
1686	**E_M_50_av**	strong absorption	**N-H bands, amide I, II**	Spectrum E_av, Miliani et al, 2012, p. 304
1693	**E_av**	strong absorption	**N-H bands, amide I, II**	Miliani et al, 2012, p. 304, spectrum EW_av
1747	**E_M_50_av**	strong absorption	**C-H stretching bands, esters**	Spectrum E_av, Mazzeo et al, 2008, p. 69
1755	**E_av**	strong absorption	**C=O stretching band, esters**	Mazzeo et al, 2008, p. 69, spectrum EY_av
1793	**E_M_50_av**	combination band	**v1+v4**	Spectrum M_av, spectrum Ca_av, Ricci et al, 2006, p. 1222
1868	**E_M_50_av**	weak absorption	**quartz**	Spectrum M_av, Spectrum Q_av
1942	**E_M_50_av**	weak absorption	**quartz**	Spectrum M_av, Spectrum Q_av
1967	**E_M_50_av**	weak absorption	**quartz**	Spectrum M_av, Spectrum Q_av
1992	**E_M_50_av**	weak absorption	**v+δ Si-O**	Spectrum M_av, Spectrum Q_av, Miliani et al, 2012, p. 303
2000	**E_M_50_av**	weak absorption	**v+δ Si-O**	Spectrum M_av, Spectrum Q_av, Miliani et al, 2012, p. 303
2135	**E_M_50_av**	sharp absorption	**CaCO3 and quartz**	Spectrum M_av, Spectrum Q_av, spectrum Ca_av
2227	**E_M_50_av**	sharp absorption	**quartz**	Spectrum M_av, Spectrum Q_av
2235	**E_M_50_av**	sharp absorption	**quartz**	Spectrum M_av, Spectrum Q_av
2514	**E_M_50_av**	combination band	**v1+v3**	Spectrum M_av, spectrum Ca_av, Ricci et al, 2006, p. 1222
2603	**E_M_50_av**	weak absorption	**quartz**	Spectrum M_av, Spectrum Q_av
2856	**E_M_50_av**	strong absorption	**CH stretching**	Spectrum E_av, Daher et al, 2017, p.8
2864	**E_av**	strong absorption	**C-H stretching**	Rosi et al, 2009, p. 2099, spectrum EY_av
2876	**E_av**	strong absorption	**C-H stretching**	Rosi et al, 2009, p. 2099, spectrum EY_av
2930	**E_M_50_av**	strong absorption	**CH stretching**	Spectrum E_av, Daher et al, 2017, p.8
2942	**E_av**	strong absorption	**C-H stretching bands, esters**	Spectrum EY_av, Rosi et al, 2009, p. 2099
2959	**E_M_50_av**	weak absorption	**CH2 stretching**	Spectrum E_av, Ploeger et al, 2010, p. 37
2973	**E_av**	strong absorption	**C-H stretching bands, esters**	Spectrum EY_av, Rosi et al, 2009, p. 2099
3005	**E_M_50_av**	weak absorption	**(blank)**	(blank)
3045	**E_av**	weak absorption	**2δNH**	Rosi et al, 2010, p. 621
3071	**E_M_50_av**	weak absorption	**2δNH**	Spectrum E_av, Rosi et al, 2010, p. 621
3075	**E_av**	weak absorption	**2δNH**	Rosi et al, 2010, p. 621
3084	**E_M_50_av**	weak absorption	**2δNH**	Spectrum E_av, Rosi et al, 2010, p. 621
3089	**E_av**	weak absorption	**2δNH**	Rosi et al, 2010, p. 621
3102	**E_av**	weak absorption	**2δNH**	Rosi et al, 2010, p. 621
3106	**E_M_50_av**	weak absorption	**2δNH**	Spectrum E_av, Rosi et al, 2010, p. 621
3224	**E_av**	(blank)	**(blank)**	(blank)
3240	**E_av**	(blank)	**(blank)**	(blank)

Figure 15: continued.

Peak x (position)	Spectrum ID	Type of band	Chemical Band Assignement	Reference
668	E_av	sharp and weak absorption	(blank)	spectrum EY_av, spectrum EW_av
715	E_M_25_av	doublet	in-plane rotation of linear long C chains δ(CH2)n	Spectrun E_av, Iwanicka et al, 2017, p. 18
729	E_M_25_av	doublet	in-plane rotation of linear long C chains δ(CH2)n	Spectrun E_av, Iwanicka et al, 2017, p. 18
734	E_av	weak absorption	(blank)	(blank)
745	E_av	weak absorption	(blank)	spectrum EY_av
765	E_av	weak absorption	(blank)	spectrum EY_av
775	E_M_25_av	weak absorption	whole egg	Spectrun E_av
786	E_M_25_av	weak absorption	whole egg	Spectrun E_av
794	E_av	weak absorption	(blank)	spectrum EY_av
802	E_av	weak absorption	(blank)	spectrum EY_av
805	E_M_25_av	weak absorption	whole egg	Spectrun E_av
835	E_av	weak absorption	(blank)	(blank)
844	E_M_25_av	weak absorption	whole egg	Spectrun E_av
909	E_M_25_av	weak absorption	v2 carbonate ion	Ylmen and Jaglid, 2013, p. 119
950	E_M_25_av	weak absorption	PO4-3 anion stretching	Spectrum E_av, Ricci et al. 2006, p. 1223
973	E_av	weak absorption	PO4-3anion stretching	Ricci et al, 2006, p. 1223, spectrum EY_av
1029	E_M_25_av	weak absorption	vSiO	Buti et al, 2013, p. 2705
1099	E_M_25_av	weak absorption	v1 carbonate ion	Spectrum Ca_av, Ylmen and Jaglid, 2013, p. 119
1123	E_av	weak absorption	PO4-3anion stretching	Ricci et al, 2006, p. 1223, spectrum EY_av
1125	E_M_25_av	sharp absorption	PO4-3 anion stretching	Spectrum E_av, Ricci et al. 2006, p. 1223
1177	E_av	weak absorption	v(C-O) stretching	Ricci et al, 2006, p. 1224, spectrum EW_av
1192	E_M_25_av	sharp absorption	v(C-O) stretching	Spectrum E_av, Ricci et al. 2006, p. 1224
1268	E_av	strong absorption	C-O	Ploeger et al, 2010, p. 37, spectrum EY_av
1280	E_M_25_av	strong absorption	C-O	Spectrum E_av, Ploeger et al, 2010, p. 17
1324	E_av	(blank)	(blank)	spectrum EW_av
1384	E_M_25_av	strong absorption	CaCO3	Spectrun M_av, Spectrum Ca_av
1405	E_M_25_av	strong absorption	CaCO3	Spectrun M_av, Spectrum Ca_av
1411	E_av	(blank)	(blank)	spectrum EW_av

Figure 16: Filtered CPAD entries of egg (E_av) and 25% egg/mortar mixture (E_M_25_av).

1445	**E_av**	weak absorption	**Amide III**	Buti et al, 2013, p. 2705, spectrum EW_av
1472	**E_av**	sharp absorption	**C-O bending**	Ricci et al, 2006, p. 1223, spectrum EW_av and EY_av
1473	**E_M_25_av**	strong absorption	**C-O bending**	Spectrum E_av, Ricci et al, 2006, p. 1223
1551	**E_M_25_av**	weak absorption	**quartz**	spectrum Q_av
1568	**E_av**	strong absorption	**N-H bands, amide I, II**	Miliani et al, 2012, p. 304, spectrum EW_av
1585	**E_M_25_av**	weak absorption	**v3 antisymmetric stretching CO3-2**	Spectrum M_av, spectrum Ca_av, Ylmen and Jaglid, 2013, p. 119
1651	**E_M_25_av**	weak absorption	**quartz**	Spectrum Q_av, spectrum M_av
1693	**E_av**	strong absorption	**N-H bands, amide I, II**	Miliani et al, 2012, p. 304, spectrum EW_av
1753	**E_M_25_av**	strong absorption	**C-H stretching bands, esters**	Spectrum E_av, Mazzeo et al, 2008, p. 69
1755	**E_av**	strong absorption	**C=O stretching band, esters**	Mazzeo et al, 2008, p. 69, spectrum EY_av
1907	**E_M_25_av**	weak absorption	**(blank)**	(blank)
2030	**E_M_25_av**	weak absorption	**(blank)**	(blank)
2242	**E_M_25_av**	sharp absorption	**quartz**	Spectrun M_av, Spectrum Q_av
2864	**E_av**	strong absorption	**C-H stretching**	Rosi et al, 2009, p. 2099, spectrum EY_av
2876	**E_av**	strong absorption	**C-H stretching**	Rosi et al, 2009, p. 2099, spectrum EY_av
2880	**E_M_25_av**	strong absorption	**CH stretching**	Spectrum E_av, Daher et al, 2017, p.8
2942	**E_av**	strong absorption	**C-H stretching bands, esters**	Spectrum EY_av, Rosi et al, 2009, p. 2099
2943	**E_M_25_av**	strong absorption	**CH stretching**	Spectrum E_av, Daher et al, 2017, p.8
2973	**E_av**	strong absorption	**C-H stretching bands, esters**	Spectrum EY_av, Rosi et al, 2009, p. 2099
2974	**E_M_25_av**	weak absorption	**CH2 stretching**	Spectrum E_av, Ploeger et al, 2010, p. 37
3045	**E_av**	weak absorption	**2δNH**	Rosi et al, 2010, p. 621
3075	**E_av**	weak absorption	**2δNH**	Rosi et al, 2010, p. 621
3089	**E_av**	weak absorption	**2δNH**	Rosi et al, 2010, p. 621
3102	**E_av**	weak absorption	**2δNH**	Rosi et al, 2010, p. 621
3224	**E_av**	(blank)	**(blank)**	(blank)
3240	**E_av**	(blank)	**(blank)**	(blank)

Figure 16: continued.

Peak x (position)	Spectrum ID	Type of band	Chemical Band Assignement	Reference
666	E_M_5_av	weak absorption	whole egg	Spectrum E_av
668	E_av	sharp and weak absorption	(blank)	spectrum EY_av, spectrum EW_av
714	E_M_5_av	weak absorption	v4 carbonate ion	Spectrum M_av, Spectrum Ca_av, Ylmen and Jaglid, 2013, p. 119
734	E_av	weak absorption	(blank)	(blank)
745	E_av	weak absorption	(blank)	spectrum EY_av
765	E_av	weak absorption	(blank)	spectrum EY_av
792	E_M_5_av	sharp absorption	quartz	Spectrun M_av, Spectrum Q_av
794	E_av	weak absorption	(blank)	spectrum EY_av
802	E_av	weak absorption	(blank)	spectrum EY_av
815	E_M_5_av	strong absorption	quartz	Spectrun M_av, Spectrum Q_av
835	E_av	weak absorption	(blank)	(blank)
848	E_M_5_av	weak absorption	v2 carbonate ion	Spectrun M_av, Spectrum Ca_av, Ylmen and Jaglid, 2013, p. 119
880	E_M_5_av	weak absorption	v2 carbonate ion	Spectrun M_av, Spectrum Ca_av, Ylmen and Jaglid, 2013, p. 119
973	E_av	weak absorption	PO4-3anion stretching	Ricci et al, 2006, p. 1223, spectrum EY_av
1081	E_M_5_av	weak absorption	v1 carbonate ion	Spectrum Ca_av, Ylmen and Jaglid, 2013, p. 119
1123	E_av	weak absorption	PO4-3anion stretching	Ricci et al, 2006, p. 1223, spectrum EY_av
1159	E_M_5_av	strong absorption	quartz	Spectrun M_av, Spectrum Q_av
1177	E_av	weak absorption	v(C-O) stretching	Ricci et al, 2006, p. 1224, spectrum EW_av
1268	E_av	strong absorption	C-O	Ploeger et al, 2010, p. 37, spectrum EY_av
1324	E_av	(blank)	(blank)	spectrum EW_av
1394	E_M_5_av	strong absorption	CaCO3	Spectrun M_av, Spectrum Ca_av
1411	E_av	(blank)	(blank)	spectrum EW_av
1438	E_M_5_av	weak absorption	whole egg	Spectrum E_av
1445	E_av	weak absorption	Amide III	Buti et al, 2013, p. 2705, spectrum EW_av
1460	E_M_5_av	weak absorption	v3 antisymmetric stretching CO3-2	Spectrum M_av, spectrum Ca_av, Ylmen and Jaglid, 2013, p. 119
1472	E_av	sharp absorption	C-O bending	Ricci et al, 2006, p. 1223, spectrum EW_av and EY_av
	E_M_5_av	strong absorption	C-O bending	Spectrum E_av, Ricci et al, 2006, p. 1223
1568	E_av	strong absorption	N-H bands, amide I, II	Miliani et al, 2012, p. 304, spectrum EW_av
1573	E_M_5_av	weak absorption	v3 antisymmetric stretching CO3-2	Spectrum M_av, spectrum Ca_av, Ylmen and Jaglid, 2013, p. 119
1581	E_M_5_av	weak absorption	v3 antisymmetric stretching CO3-2	Spectrum M_av, spectrum Ca_av, Ylmen and Jaglid, 2013, p. 119
1599	E_M_5_av	weak absorption	quartz	Spectrun M_av, Spectrum Q_av

Figure 17: Filtered CPAD entries of egg (E_av) and 5% egg/mortar mixture (E_M_5_av).

1659	**E_M_5_av**	strong absorption	**quartz**	Spectrun M_av, Spectrum Q_av
1676	**E_M_5_av**	strong absorption	**quartz**	Spectrun M_av, Spectrum Q_av
1693	**E_av**	strong absorption	**N-H bands, amide I, II**	Miliani et al, 2012, p. 304, spectrum EW_av
1755	**E_av**	strong absorption	**C=O stretching band, esters**	Mazzeo et al, 2008, p. 69, spectrum EY_av
1794	**E_M_5_av**	combination band	**v1+v4**	Spectrum M_av, spectrum Ca_av, Ricci et al, 2006, p. 1222
1858	**E_M_5_av**	weak absorption	**quartz**	Spectrun M_av, Spectrum Q_av
1943	**E_M_5_av**	weak absorption	**quartz**	Spectrun M_av, Spectrum Q_av
1974	**E_M_5_av**	weak absorption	**quartz**	Spectrun M_av, Spectrum Q_av
2135	**E_M_5_av**	sharp absorption	**CaCO3 and quartz**	Spectrun M_av, Spectrum Q_av, spectrum Ca_av
2237	**E_M_5_av**	sharp absorption	**quartz**	Spectrun M_av, Spectrum Q_av
2512	**E_M_5_av**	combination band	**v1+v3**	Spectrum M_av, spectrum Ca_av, Ricci et al, 2006, p. 1222
2673	**E_M_5_av**	weak absorption	**CaCO3**	Spectrum M_av, spectrum Ca_av
2682	**E_M_5_av**	weak absorption	**CaCO3**	Spectrum M_av, spectrum Ca_av
2855	**E_M_5_av**	strong absorption	**CH stretching**	Spectrum E_av, Daher et al, 2017, p.8
2864	**E_av**	strong absorption	**C-H stretching**	Rosi et al, 2009, p. 2099, spectrum EY_av
2871	**E_M_5_av**	strong absorption	**CH stretching**	Spectrum E_av, Daher et al, 2017, p.8
2876	**E_av**	strong absorption	**C-H stretching**	Rosi et al, 2009, p. 2099, spectrum EY_av
2926	**E_M_5_av**	weak absorption	**CH2 stretching**	Spectrum E_av, Ploeger et al, 2010, p. 37
2942	**E_av**	strong absorption	**C-H stretching bands, esters**	Spectrum EY_av, Rosi et al, 2009, p. 2099
2957	**E_M_5_av**	weak absorption	**CH2 stretching**	Spectrum E_av, Ploeger et al, 2010, p. 37
2973	**E_av**	strong absorption	**C-H stretching bands, esters**	Spectrum EY_av, Rosi et al, 2009, p. 2099
3045	**E_av**	weak absorption	**2δNH**	Rosi et al, 2010, p. 621
3075	**E_av**	weak absorption	**2δNH**	Rosi et al, 2010, p. 621
3089	**E_av**	weak absorption	**2δNH**	Rosi et al, 2010, p. 621
3102	**E_av**	weak absorption	**2δNH**	Rosi et al, 2010, p. 621
3224	**E_av**	(blank)	**(blank)**	(blank)
3240	**E_av**	(blank)	**(blank)**	(blank)
3642	**E_M_5_av**	doublet	**OH stretching of H2O**	Spectrum M_av, spectrum Ca_av, Rosi et al, 2009, p. 2100

Figure 17: continued.

7.5.5 Lard and mortar mixtures CPAD

Peak x (position)	Spectrum ID	Type of band	Chemical Band Assignement	Reference
667	**L_av**	weak absorption	**(blank)**	(blank)
689	**L_av**	weak absorption	**(blank)**	(blank)
700	**L_av**	weak absorption	**(blank)**	(blank)
	L_M_75_av	weak absorption	**lard**	Spectrum Q_av, spectrum M_av, spectrum L_av
725	**L_M_75_av**	sharp absorption	**lard**	Spectrum L_av
734	**L_av**	weak absorption	**(blank)**	(blank)
764	**L_av**	weak absorption	**(blank)**	(blank)
779	**L_av**	weak absorption	**(blank)**	(blank)
791	**L_M_75_av**	sharp absorption	**quartz**	Spectrum Q_av, spectrum M_av
796	**L_av**	weak absorption	**(blank)**	(blank)
807	**L_av**	weak absorption	**(blank)**	(blank)
818	**L_M_75_av**	sharp absorption	**Si-O antisymmetric stretching**	Spectrum Q_av, spectrum M_av, Miliani et al, 2013, p. 303
965	**L_av**	weak absorption	**(blank)**	(blank)
1062	**L_av**	weak absorption	**(blank)**	(blank)
1115	**L_M_75_av**	sharp absorption	**lard**	Spectrum L_av
1122	**L_av**	weak absorption	**(blank)**	(blank)
1160	**L_M_75_av**	sharp absorption	**quartz**	Spectrum Q_av, spectrum M_av
1189	**L_av**	weak absorption	**v(C-O) stretching**	Ricci et al, 2006, p. 1224
1197	**L_M_75_av**	weak absorption	**v(C-O) stretching**	Spectrum L_av, Ricci et al, 2006, p. 1224
1201	**L_av**	weak absorption	**(blank)**	(blank)
1275	**L_av**	strong absorption	**C-O**	Ploeger et al, 2010, p. 37
1279	**L_M_75_av**	strong absorption	**C-O**	Spectrum L_av, Ploeger et al, 2010, p. 37
1289	**L_M_75_av**	strong absorption	**C-O**	Spectrum L_av, Ploeger et al, 2010, p. 37
1349	**L_M_75_av**	sharp and weak absorption	**quartz**	spectrum Q_av
1370	**L_av**	weak absorption	**C-H bending**	Buti et al, 2013, p. 2705
1381	**L_M_75_av**	sharp and weak absorption	**C-H bending**	Spectrum L_av, Buti et al, 2013, p. 2705
1384	**L_av**	sharp and weak absorption	**(blank)**	(blank)
1389	**L_M_75_av**	sharp and weak absorption	**C-H bending**	Spectrum L_av, Buti et al, 2013, p. 2705
1421	**L_M_75_av**	weak absorption	**(blank)**	Spectrum L_av
1422	**L_av**	weak absorption	**(blank)**	(blank)

Figure 18: Filtered CPAD entries of lard (L_av) and 75% lard/mortar mixture (L_M_75_av).

1446	**L_av**	weak absorption	**(blank)**	(blank)
	L_M_75_av	weak absorption	**(blank)**	Spectrum L_av
1474	**L_M_75_av**	strong absorption	**C-O bending**	Spectrum L_av, Ricci et al, 2006, p. 1224
1475	**L_av**	strong absorption	**C-O bending**	Ricci et al, 2006, p. 1223
1579	**L_M_75_av**	weak absorption	**quartz**	Spectrum Q_av, spectrum M_av
1606	**L_M_75_av**	weak absorption	**quartz**	Spectrum Q_av, spectrum M_av
1662	**L_M_75_av**	weak absorption	**(blank)**	Spectrum L_av, spectrum M_av, Spectrum Q_av
1666	**L_av**	weak absorption	**(blank)**	(blank)
1669	**L_M_75_av**	weak absorption	**(blank)**	Spectrum L_av, spectrum M_av, Spectrum Q_av
1678	**L_av**	weak absorption	**(blank)**	(blank)
1679	**L_M_75_av**	weak absorption	**(blank)**	Spectrum L_av, spectrum M_av, Spectrum Q_av
1756	**L_av**	1st order derivative	**C=O stretching band**	Mazzeo et al, 2008, p. 69
	L_M_75_av	1st order derivative	**C=O stretching band**	Spectrum L_av, Mazzeo et al, 2008, p. 69
2862	**L_M_75_av**	strong absorption	**CH2 stretching**	Spectrum L_av, Ploeger et al, 2010, p. 37
2863	**L_av**	strong absorption	**CH2 stretching**	Ploeger et al, 2010, p. 37
2940	**L_M_75_av**	sharp absorption	**CH2 stretching**	Spectrum L_av, Ploeger et al, 2010, p. 37
2941	**L_av**	sharp absorption	**CH2 stretching**	Ploeger et al, 2010, p. 37
2965	**L_av**	sharp absorption	**CH2 stretching**	Ploeger et al, 2010, p. 37
2968	**L_M_75_av**	sharp absorption	**CH2 stretching**	Spectrum L_av, Ploeger et al, 2010, p. 37
3003	**L_M_75_av**	weak absorption	**CH stretching**	Spectrum L_av, Miliani et al, 2012, p. 302
3010	**L_av**	sharp absorption	**CH2 stretching**	Ploeger et al, 2010, p. 37
3018	**L_M_75_av**	weak absorption	**CH stretching**	Spectrum L_av, Miliani et al, 2012, p. 302
3452	**L_M_75_av**	weak absorption	**lard**	Spectrum L_av
3458	**L_av**	(blank)	**(blank)**	(blank)
3461	**L_M_75_av**	weak absorption	**lard**	Spectrum L_av
3470	**L_av**	(blank)	**(blank)**	(blank)
3477	**L_av**	(blank)	**(blank)**	(blank)
3480	**L_M_75_av**	weak absorption	**lard**	Spectrum L_av
3488	**L_av**	(blank)	**(blank)**	(blank)

Figure 18: continued.

Peak x (position)	Spectrum ID	Type of band	Chemical Band Assignement	Reference
667	**L_av**	weak absorption	**(blank)**	(blank)
689	**L_av**	weak absorption	**(blank)**	(blank)
700	**L_av**	weak absorption	**(blank)**	(blank)
734	**L_av**	weak absorption	**(blank)**	(blank)
	L_M_50_av	sharp absorption	**lard**	Spectrum L_av
764	**L_av**	weak absorption	**(blank)**	(blank)
779	**L_av**	weak absorption	**(blank)**	(blank)
792	**L_M_50_av**	sharp and weak absorption	**quartz**	Spectrum Q_av and spectrum M_av
796	**L_av**	weak absorption	**(blank)**	(blank)
807	**L_av**	weak absorption	**(blank)**	(blank)
819	**L_M_50_av**	strong absorption	**Si-O antisymmetric stretching**	Spectrum Q_av, spectrum M_av, Miliani et al, 2013, p. 303
876	**L_M_50_av**	weak absorption	**v2 carbonate ion**	Spectrum Ca_av and spectrum M_av, Ylmen and Jaglid, 2013, p. 119
889	**L_M_50_av**	weak absorption	**v2 carbonate ion**	Spectrum Ca_av and spectrum M_av, Ylmen and Jaglid, 2013, p. 119
965	**L_av**	weak absorption	**(blank)**	(blank)
1062	**L_av**	weak absorption	**(blank)**	(blank)
1117	**L_M_50_av**	sharp and weak absorption	**lard**	Spectrum L_av
1122	**L_av**	weak absorption	**(blank)**	(blank)
1184	**L_M_50_av**	weak absorption	**v(C-O) stretching**	Spectrum L_av, Ricci et al, 2006, p. 1224
1189	**L_av**	weak absorption	**v(C-O) stretching**	Ricci et al, 2006, p. 1224
1199	**L_M_50_av**	weak absorption	**lard**	(blank)
1201	**L_av**	weak absorption	**(blank)**	(blank)
1273	**L_M_50_av**	strong absorption	**C-O**	Spectrum L_av, Ploeger et al, 2010, p. 37
1275	**L_av**	strong absorption	**C-O**	Ploeger et al, 2010, p. 37
1370	**L_av**	weak absorption	**C-H bending**	Buti et al, 2013, p. 2705
1384	**L_av**	sharp and weak absorption	**(blank)**	(blank)
	L_M_50_av	sharp and weak absorption	**C-H bending**	Spectrum L_av, Buti et al, 2013, p. 2705
1421	**L_M_50_av**	weak absorption	**lard**	Spectrum L_av
1422	**L_av**	weak absorption	**(blank)**	(blank)

Figure 19: Filtered CPAD entries of lard (L_av) and 50% lard/mortar mixture (L_M_50_av).

1446	**L_av**	weak absorption	**(blank)**	(blank)
1447	**L_M_50_av**	weak absorption	**lard**	Spectrum L_av
1474	**L_M_50_av**	sharp absorption	**C-O bending**	Spectrum L_av, Ricci et al, 2006, p. 1224
1475	**L_av**	strong absorption	**C-O bending**	Ricci et al, 2006, p. 1223
1616	**L_M_50_av**	strong absorption	**(blank)**	Spectrum L_av, spectrum M_av, Spectrum Q_av
1626	**L_M_50_av**	strong absorption	**(blank)**	Spectrum L_av, spectrum M_av, Spectrum Q_av
1659	**L_M_50_av**	strong absorption	**(blank)**	Spectrum L_av, spectrum M_av, Spectrum Q_av
1666	**L_av**	weak absorption	**(blank)**	(blank)
1669	**L_M_50_av**	strong absorption	**(blank)**	Spectrum L_av, spectrum M_av, Spectrum Q_av
1678	**L_av**	weak absorption	**(blank)**	(blank)
1680	**L_M_50_av**	strong absorption	**(blank)**	Spectrum L_av, spectrum M_av, Spectrum Q_av
1691	**L_M_50_av**	strong absorption	**(blank)**	Spectrum L_av, spectrum M_av, Spectrum Q_av
1756	**L_av**	1st order derivative	**C=O stretching band**	Mazzeo et al, 2008, p. 69
	L_M_50_av	1st order derivative	**C=O stretching band**	Spectrum L_av, Mazzeo et al, 2008, p. 69
2862	**L_M_50_av**	strong absorption	**CH2 stretching**	Spectrum L_av, Ploeger et al, 2010, p. 37
2863	**L_av**	strong absorption	**CH2 stretching**	Ploeger et al, 2010, p. 37
2939	**L_M_50_av**	strong absorption	**CH2 stretching**	Spectrum L_av, Ploeger et al, 2010, p. 37
2941	**L_av**	sharp absorption	**CH2 stretching**	Ploeger et al, 2010, p. 37
2965	**L_av**	sharp absorption	**CH2 stretching**	Ploeger et al, 2010, p. 37
	L_M_50_av	strong absorption	**CH2 stretching**	Spectrum L_av, Ploeger et al, 2010, p. 37
3010	**L_av**	sharp absorption	**CH2 stretching**	Ploeger et al, 2010, p. 37
3014	**L_M_50_av**	weak absorption	**lard**	Spectrum L_av
3448	**L_M_50_av**	weak absorption	**lard**	Spectrum L_av
3458	**L_av**	(blank)	**(blank)**	(blank)
3468	**L_M_50_av**	weak absorption	**lard**	Spectrum L_av
3470	**L_av**	(blank)	**(blank)**	(blank)
3477	**L_av**	(blank)	**(blank)**	(blank)
3483	**L_M_50_av**	weak absorption	**lard**	Spectrum L_av
3488	**L_av**	(blank)	**(blank)**	(blank)

Figure 19: continued.

Peak x (position)	Spectrum ID	Type of band	Chemical Band Assignement	Reference
667	**L_av**	weak absorption	**(blank)**	(blank)
689	**L_av**	weak absorption	**(blank)**	(blank)
700	**L_av**	weak absorption	**(blank)**	(blank)
701	**L_M_25_av**	weak absorption	**lard**	Spectrum L_av, spectrum M_av, Spectrum Q_av
732	**L_M_25_av**	sharp and weak absorption	**lard**	Spectrum L_av
734	**L_av**	weak absorption	**(blank)**	(blank)
764	**L_av**	weak absorption	**(blank)**	(blank)
779	**L_av**	weak absorption	**(blank)**	(blank)
792	**L_M_25_av**	sharp and weak absorption	**quartz**	Spectrum Q_av, spectrum M_av
796	**L_av**	weak absorption	**(blank)**	(blank)
807	**L_av**	weak absorption	**(blank)**	(blank)
821	**L_M_25_av**	strong absorption	**Si-O antisymmetric stretching**	Spectrum Q_av, spectrum M_av, Miliani et al, 2013, p. 303
876	**L_M_25_av**	weak absorption	**v2 carbonate ion**	Spectrum Ca_av and spectrum M_av, Ylmen and Jaglid, 2013, p. 119
889	**L_M_25_av**	weak absorption	**v2 carbonate ion**	Spectrum Ca_av and spectrum M_av, Ylmen and Jaglid, 2013, p. 119
965	**L_av**	weak absorption	**(blank)**	(blank)
1062	**L_av**	weak absorption	**(blank)**	(blank)
1115	**L_M_25_av**	sharp and weak absorption	**lard**	Spectrum L_av
1122	**L_av**	weak absorption	**(blank)**	(blank)
1161	**L_M_25_av**	sharp and weak absorption	**quartz**	spectrum Q_av
1180	**L_M_25_av**	sharp absorption	**v(C-O) stretching**	Spectrum L_av, Ricci et al, 2006, p. 1224
1189	**L_av**	weak absorption	**v(C-O) stretching**	Ricci et al, 2006, p. 1224
1197	**L_M_25_av**	sharp absorption	**v(C-O) stretching**	Spectrum L_av, Ricci et al, 2006, p. 1224
1201	**L_av**	weak absorption	**(blank)**	(blank)
1271	**L_M_25_av**	strong absorption	**C-O**	Spectrum L_av, Ploeger et al, 2010, p. 37
1275	**L_av**	strong absorption	**C-O**	Ploeger et al, 2010, p. 37
1288	**L_M_25_av**	strong absorption	**C-O**	Spectrum L_av, Ploeger et al, 2010, p. 37

Figure 20: Filtered CPAD entries of lard (L_av) and 25% lard/mortar mixture (L_M_25_av).

1311	**L_M_25_av**	weak absorption	**lard**	Spectrum L_av
1370	**L_av**	weak absorption	**C-H bending**	Buti et al, 2013, p. 2705
1384	**L_av**	sharp and weak absorption	**(blank)**	(blank)
1390	**L_M_25_av**	sharp absorption	**C-H bending**	Spectrum L_av, Buti et al, 2013, p. 2705
1422	**L_av**	weak absorption	**(blank)**	(blank)
1424	**L_M_25_av**	weak absorption	**lard**	Spectrum L_av
1446	**L_av**	weak absorption	**(blank)**	(blank)
1475	**L_av**	strong absorption	**C-O bending**	Ricci et al, 2006, p. 1223
	L_M_25_av	sharp absorption	**C-O bending**	Spectrum L_av, Ricci et al, 2006, p. 1224
1628	**L_M_25_av**	strong absorption	**(blank)**	Spectrum L_av, spectrum M_av, Spectrum Q_av
1666	**L_av**	weak absorption	**(blank)**	(blank)
1669	**L_M_25_av**	strong absorption	**(blank)**	Spectrum L_av, spectrum M_av, Spectrum Q_av
1678	**L_av**	weak absorption	**(blank)**	(blank)
1683	**L_M_25_av**	strong absorption	**(blank)**	Spectrum L_av, spectrum M_av, Spectrum Q_av
1692	**L_M_25_av**	strong absorption	**(blank)**	Spectrum L_av, spectrum M_av, Spectrum Q_av
1755	**L_M_25_av**	1st order derivative	**C=O stretching band**	Spectrum L_av, Mazzeo et al, 2008, p. 69
1756	**L_av**	1st order derivative	**C=O stretching band**	Mazzeo et al, 2008, p. 69
2511	**L_M_25_av**	combination band	**v1+v3**	Spectrum Ca_av and spectrum M_av, Ricci et al, 2006, p. 1222
2518	**L_M_25_av**	combination band	**v1+v3**	Spectrum Ca_av and spectrum M_av, Ricci et al, 2006, p. 1222
2862	**L_M_25_av**	strong absorption	**CH2 stretching**	Spectrum L_av, Ploeger et al, 2010, p. 37
2863	**L_av**	strong absorption	**CH2 stretching**	Ploeger et al, 2010, p. 37
2939	**L_M_25_av**	strong absorption	**CH2 stretching**	Spectrum L_av, Ploeger et al, 2010, p. 37
2941	**L_av**	sharp absorption	**CH2 stretching**	Ploeger et al, 2010, p. 37
2965	**L_av**	sharp absorption	**CH2 stretching**	Ploeger et al, 2010, p. 37
2966	**L_M_25_av**	strong absorption	**CH2 stretching**	Spectrum L_av, Ploeger et al, 2010, p. 37
3005	**L_M_25_av**	weak absorption	**lard**	Spectrum L_av
3010	**L_av**	sharp absorption	**CH2 stretching**	Ploeger et al, 2010, p. 37
3458	**L_av**	(blank)	**(blank)**	(blank)
3470	**L_av**	(blank)	**(blank)**	(blank)
3477	**L_av**	(blank)	**(blank)**	(blank)
3488	**L_av**	(blank)	**(blank)**	(blank)

Figure 20: continued.

Peak x (position)	Spectrum ID	Type of band	Chemical Band Assignement	Reference
667	**L_av**	weak absorption	**(blank)**	(blank)
	L_M_5_av	weak absorption	**(blank)**	Spectrum L_av
682	**L_M_5_av**	weak absorption	**(blank)**	Spectrum L_av
689	**L_av**	weak absorption	**(blank)**	(blank)
700	**L_av**	weak absorption	**(blank)**	(blank)
714	**L_M_5_av**	sharp absorption	**v4 carbonate ion**	Spectrum Ca_av, spectrum M_av, Ylmen and Jaglid, 2013, p. 119
734	**L_av**	weak absorption	**(blank)**	(blank)
764	**L_av**	weak absorption	**(blank)**	(blank)
779	**L_av**	weak absorption	**(blank)**	(blank)
792	**L_M_5_av**	sharp absorption	**quartz**	Spectrum Q_av, spectrum M_av
796	**L_av**	weak absorption	**(blank)**	(blank)
807	**L_av**	weak absorption	**(blank)**	(blank)
815	**L_M_5_av**	sharp absorption	**Si-O antisymmetric stretching**	Spectrum Q_av, spectrum M_av, Miliani et al, 2013, p. 303
848	**L_M_5_av**	sharp absorption	**v2 carbonate ion**	Spectrum Ca_av, spectrum M_av, Ylmen and Jaglid, 2013, p. 119
879	**L_M_5_av**	sharp absorption	**v2 carbonate ion**	Spectrum Ca_av, spectrum M_av, Ylmen and Jaglid, 2013, p. 119
965	**L_av**	weak absorption	**(blank)**	(blank)
1062	**L_av**	weak absorption	**(blank)**	(blank)
1118	**L_M_5_av**	weak absorption	**CaCO3**	spectrum Ca_av
1122	**L_av**	weak absorption	**(blank)**	(blank)
1159	**L_M_5_av**	sharp absorption	**quartz**	Spectrum Q_av, spectrum M_av
1189	**L_av**	weak absorption	**v(C-O) stretching**	Ricci et al, 2006, p. 1224
1201	**L_av**	weak absorption	**(blank)**	(blank)
1275	**L_av**	strong absorption	**C-O**	Ploeger et al, 2010, p. 37
1370	**L_av**	weak absorption	**C-H bending**	Buti et al, 2013, p. 2705
1384	**L_av**	sharp and weak absorption	**(blank)**	(blank)
	L_M_5_av	sharp absorption	**lard**	Spectrum L_av
1422	**L_av**	weak absorption	**(blank)**	(blank)
1433	**L_M_5_av**	weak absorption	**lard**	Spectrum L_av
1446	**L_av**	weak absorption	**(blank)**	(blank)
	L_M_5_av	weak absorption	**lard**	Spectrum L_av
1473	**L_M_5_av**	weak absorption	**C-O bending**	Spectrum L_av, Ricci et al, 2006, p. 1224
1475	**L_av**	strong absorption	**C-O bending**	Ricci et al, 2006, p. 1223

Figure 21: Filtered CPAD entries of lard (L_av) and 5% lard/mortar mixture (L_M_5_av).

1499	**L_M_5_av**	weak absorption	**v3 antisymmetric stretching CO3-2**	Spectrum Ca_av, spectrum M_av, Ylmen and Jaglid, 2013, p. 119
1517	**L_M_5_av**	weak absorption	**v3 antisymmetric stretching CO3-2**	Spectrum Ca_av, spectrum M_av, Ylmen and Jaglid, 2013, p. 119
1538	**L_M_5_av**	weak absorption	**v3 antisymmetric stretching CO3-2**	Spectrum Ca_av, spectrum M_av, Ylmen and Jaglid, 2013, p. 119
1581	**L_M_5_av**	weak absorption	**v3 antisymmetric stretching CO3-2**	Spectrum Ca_av, spectrum M_av, Ylmen and Jaglid, 2013, p. 119
1652	**L_M_5_av**	weak absorption	**quartz**	Spectrum Q_av , spectrum M_av
1661	**L_M_5_av**	weak absorption	**quartz**	Spectrum Q_av , spectrum M_av
1666	**L_av**	weak absorption	**(blank)**	(blank)
1668	**L_M_5_av**	weak absorption	**quartz**	Spectrum Q_av , spectrum M_av
1678	**L_av**	weak absorption	**(blank)**	(blank)
1685	**L_M_5_av**	weak absorption	**quartz**	Spectrum Q_av , spectrum M_av
1747	**L_M_5_av**	1st order derivative	**C=O stretching band**	Spectrum L_av, Mazzeo et al, 2008, p. 69
1756	**L_av**	1st order derivative	**C=O stretching band**	Mazzeo et al, 2008, p. 69
1795	**L_M_5_av**	combination band	**v1+v4**	Spectrum Ca_av, spectrum M_av, Ricci et al, 2006, p. 1222
1857	**L_M_5_av**	weak absorption	**quartz**	Spectrum Q_av, spectrum M_av
1867	**L_M_5_av**	weak absorption	**quartz**	Spectrum Q_av, spectrum M_av
1942	**L_M_5_av**	weak absorption	**quartz**	Spectrum Q_av, spectrum M_av
1966	**L_M_5_av**	weak absorption	**quartz**	Spectrum Q_av, spectrum M_av
1990	**L_M_5_av**	weak absorption	**v+δ Si-O**	Spectrum Q_av, spectrum M_av, Miliani et al, 2012, p. 303
2135	**L_M_5_av**	sharp absorption	**CaCO3 and quartz**	Spectrum Q_av, spectrum M_av, spectrum Ca_av
2237	**L_M_5_av**	sharp absorption	**quartz**	Spectrum Q_av, spectrum M_av
2511	**L_M_5_av**	combination band	**v1+v3**	Spectrum Ca_av, spectrum M_av
2679	**L_M_5_av**	weak absorption	**CaCO3**	Spectrum Ca_av, spectrum M_av
2731	**L_M_5_av**	weak absorption	**CaCO3**	Spectrum Ca_av, spectrum M_av
2854	**L_M_5_av**	strong absorption	**CH2 stretching**	Spectrum L_av, Ploeger et al, 2010, p. 37
2863	**L_av**	strong absorption	**CH2 stretching**	Ploeger et al, 2010, p. 37
2926	**L_M_5_av**	strong absorption	**CH2 stretching**	Spectrum L_av, Ploeger et al, 2010, p. 37
2941	**L_av**	sharp absorption	**CH2 stretching**	Ploeger et al, 2010, p. 37
2965	**L_av**	sharp absorption	**CH2 stretching**	Ploeger et al, 2010, p. 37
3005	**L_M_5_av**	weak absorption	**lard**	Spectrum L_av
3010	**L_av**	sharp absorption	**CH2 stretching**	Ploeger et al, 2010, p. 37
3381	**L_M_5_av**	weak absorption	**quartz**	Spectrum Q_av, spectrum M_av
3458	**L_av**	(blank)	**(blank)**	(blank)
3470	**L_av**	(blank)	**(blank)**	(blank)
3477	**L_av**	(blank)	**(blank)**	(blank)
3488	**L_av**	(blank)	**(blank)**	(blank)
3644	**L_M_5_av**	doublet	**CaCO3**	Spectrum Ca_av, spectrum M_av, Rosi et al, 2009, p. 2100

Figure 21: continued.

7.5.6 Olive oil and mortar mixtures CPAD

Peak x (position)	Spectrum ID	Type of band	Chemical Band Assignement	Reference
667	**O_av**	(blank)	**(blank)**	(blank)
668	**O_M_75_av**	sharp and weak absorption	**olive oil**	Spectrum O_av
706	**O_av**	(blank)	**(blank)**	(blank)
	O_M_75_av	sharp and weak absorption	**olive oil**	Spectrum O_av
729	**O_M_75_av**	sharp and weak absorption	**olive oil**	Spectrum O_av
730	**O_av**	(blank)	**(blank)**	(blank)
813	**O_M_75_av**	sharp and weak absorption	**olive oil**	Spectrum O_av
823	**O_av**	(blank)	**(blank)**	(blank)
961	**O_av**	(blank)	**(blank)**	(blank)
1006	**O_av**	(blank)	**(blank)**	(blank)
1026	**O_av**	(blank)	**(blank)**	(blank)
1102	**O_av**	weak absorption	**C-O stretching**	Buti et al, 2013, p. 2705
1122	**O_av**	weak absorption	**C-O stretching**	Buti et al, 2013, p. 2705
1192	**O_av**	weak absorption	**C-O stretching**	Buti et al, 2013, p. 2705
1267	**O_av**	weak absorption	**C-O stretching**	Buti et al, 2013, p. 2705
1271	**O_M_75_av**	strong absorption	**C-O stretching**	Spectrum O_av, Buti et al, 2013, p. 2705
1281	**O_M_75_av**	strong absorption	**olive oil**	Spectrum O_av
1282	**O_av**	weak absorption	**(blank)**	(blank)
1303	**O_av**	weak absorption	**(blank)**	(blank)
1354	**O_M_75_av**	sharp and weak absorption	**olive oil**	Spectrum O_av
1360	**O_av**	weak absorption	**(blank)**	(blank)
1364	**O_M_75_av**	sharp and weak absorption	**olive oil**	Spectrum O_av
1381	**O_M_75_av**	sharp and weak absorption	**C-H bending**	Spectrum O_av, Buti et al, 2013, p. 2705
1382	**O_av**	sharp and weak absorption	**C-H bending**	Buti et al, 2013, p. 2705
1403	**O_av**	(blank)	**(blank)**	(blank)
1420	**O_M_75_av**	weak absorption	**olive oil**	Spectrum O_av
1421	**O_av**	(blank)	**(blank)**	(blank)
1437	**O_av**	(blank)	**(blank)**	(blank)

Figure 22: Filtered CPAD entries of olive oil (O_av) and 75% olive oil/mortar mixture (O_M_75_av).

1442	**O_M_75_av**	weak absorption	**olive oil**	Spectrum O_av
1446	**O_av**	(blank)	**(blank)**	(blank)
1471	**O_av**	sharp absorption	**C-O bending**	Ricci et al, 2006, p. 1223
	O_M_75_av	sharp absorption	**C-H bending**	Spectrum O_av, Ricci et al, 2006, p. 1223
1559	**O_av**	weak absorption	**(blank)**	(blank)
1560	**O_M_75_av**	weak absorption	**olive oil**	Spectrum O_av
1595	**O_M_75_av**	weak absorption	**quartz**	Spectrum M_av, spectrum Q_av
1653	**O_av**	weak absorption	**(blank)**	(blank)
1657	**O_M_75_av**	weak absorption	**olive oil**	Spectrum O_av
1660	**O_av**	weak absorption	**(blank)**	(blank)
1676	**O_av**	weak absorption	**(blank)**	(blank)
1683	**O_M_75_av**	weak absorption	**olive oil**	Spectrum O_av, Mazzeo et al, 2008, p. 69
1696	**O_av**	weak absorption	**Free fatty acids**	Mazzeo et al, 2008, p. 69
1705	**O_M_75_av**	weak absorption	**free fatty acids**	Spectrum O_av, Ploeger et al, 2010, p. 37
1758	**O_av**	1st order derivative	**C=O stretching**	Ploeger et al, 2010, p. 37, Miliani et al, 2012, p. 304
1759	**O_M_75_av**	1st order derivative	**C=O stretching band**	Spectrum O_av
2135	**O_M_75_av**	weak absorption	**calcium carbonate and quartz**	Spectrum Ca_av, spectrum M_av, spectrum Q_av
2284	**O_av**	weak absorption	**(blank)**	(blank)
2584	**O_M_75_av**	weak absorption	**quartz**	spectrum Q_av
2601	**O_M_75_av**	weak absorption	**quartz**	spectrum Q_av
2863	**O_av**	sharp absorption	**CH2 stretching**	Ploeger et al, 2010, p. 37
2864	**O_M_75_av**	strong absorption	**CH2 stretching**	Spectrum O_av, Ploeger et al, 2010, p. 37
2941	**O_av**	sharp absorption	**CH2 stretching**	Ploeger et al, 2010, p. 37
	O_M_75_av	strong absorption	**CH2 stretching**	Spectrum O_av, Ploeger et al, 2010, p. 37
2964	**O_M_75_av**	strong absorption	**v(CH) stretching**	Spectrum O_av, Miliani et al, 2007, p. 853
2965	**O_av**	sharp absorption	**v(CH) stretching**	Miliani et al, 2007, p. 853
3014	**O_av**	sharp absorption	**v(CH) stretching**	Miliani et al, 2007, p. 853
3019	**O_M_75_av**	weak absorption	**v(CH) stretching**	Spectrum O_av, Miliani et al, 2007, p. 853
3071	**O_av**	(blank)	**(blank)**	(blank)
3108	**O_av**	(blank)	**(blank)**	(blank)

Figure 22: continued.

Peak x (position)	Spectrum ID	Type of band	Chemical Band Assignement	Reference
608	**O_M_50_av**	weak absorption	**CaCO3**	Spectrum Ca_av, spectrum M_av
667	**O_av**	(blank)	**(blank)**	(blank)
668	**O_M_50_av**	sharp and weak absorption	**olive oil**	Spectrum O_av
699	**O_M_50_av**	weak absorption	**quartz**	spectrum Q_av
706	**O_av**	(blank)	**(blank)**	(blank)
730	**O_av**	(blank)	**(blank)**	(blank)
733	**O_M_50_av**	sharp and weak absorption	**olive oil**	Spectrum O_av
792	**O_M_50_av**	sharp and weak absorption	**quartz**	Spectrum Q_av, spectrum M_av
819	**O_M_50_av**	sharp absorption	**olive oil**	Spectrum O_av
823	**O_av**	(blank)	**(blank)**	(blank)
880	**O_M_50_av**	sharp absorption	**v2 carbonate ion**	Spectrum Ca_av, spectrum M_av, Ylmen and Jaglid, 2013, p. 119
961	**O_av**	(blank)	**(blank)**	(blank)
1006	**O_av**	(blank)	**(blank)**	(blank)
1026	**O_av**	(blank)	**(blank)**	(blank)
1102	**O_av**	weak absorption	**C-O stretching**	Buti et al, 2013, p. 2705
1122	**O_av**	weak absorption	**C-O stretching**	Buti et al, 2013, p. 2705
	O_M_50_av	sharp and weak absorption	**C-O stretching**	Spectrum O_av, Buti et al, 2013, p. 2705
1184	**O_M_50_av**	sharp and weak absorption	**C-O stretching**	Spectrum O_av, Buti et al, 2013, p. 2705
1192	**O_av**	weak absorption	**C-O stretching**	Buti et al, 2013, p. 2705
1267	**O_av**	weak absorption	**C-O stretching**	Buti et al, 2013, p. 2705
1268	**O_M_50_av**	strong absorption	**C-O stretching**	Spectrum O_av, Buti et al, 2013, p. 2705
1278	**O_M_50_av**	strong absorption	**C-O stretching**	Spectrum O_av, Buti et al, 2013, p. 2705
1282	**O_av**	weak absorption	**(blank)**	(blank)
1303	**O_av**	weak absorption	**(blank)**	(blank)
1360	**O_av**	weak absorption	**(blank)**	(blank)
1380	**O_M_50_av**	sharp and weak absorption	**C-O bending**	Spectrum O_av, Buti et al, 2013, p. 2705
1382	**O_av**	sharp and weak absorption	**C-H bending**	Buti et al, 2013, p. 2705

Figure 23: Filtered CPAD entries of olive oil (O_av) and 50% olive oil/mortar mixture (O_M_50_av).

1403	**O_av**	(blank)	**(blank)**	(blank)
1421	**O_av**	(blank)	**(blank)**	(blank)
1437	**O_av**	(blank)	**(blank)**	(blank)
1446	**O_av**	(blank)	**(blank)**	(blank)
1471	**O_av**	sharp absorption	**C-O bending**	Ricci et al, 2006, p. 1223
1518	**O_M_50_av**	strong absorption	**C-O bending**	Spectrum O_av, Ricci et al, 2006, p. 1223
1559	**O_av**	weak absorption	**(blank)**	(blank)
1583	**O_M_50_av**	weak absorption	**v3 antisymmetric stretching CO3-2**	Spectrum Ca_av, spectrum M_av, Ylmen and Jaglid, 2013, p. 119
1590	**O_M_50_av**	weak absorption	**quartz**	Spectrum Ca_av, spectrum M_av
1600	**O_M_50_av**	weak absorption	**quartz**	Spectrum Ca_av, spectrum M_av
1653	**O_av**	weak absorption	**(blank)**	(blank)
1660	**O_av**	weak absorption	**(blank)**	(blank)
	O_M_50_av	weak absorption	**quartz**	Spectrum Ca_av, spectrum M_av
1668	**O_M_50_av**	weak absorption	**quartz**	Spectrum Ca_av, spectrum M_av
1676	**O_av**	weak absorption	**(blank)**	(blank)
1696	**O_av**	weak absorption	**Free fatty acids**	Mazzeo et al, 2008, p. 69
1758	**O_av**	1st order derivative	**C=O stretching**	Ploeger et al, 2010, p. 37, Miliani et al, 2012, p. 304
	O_M_50_av	1st order derivative	**C=O stretching band**	Spectrum O_av, Ploeger et al, 2010, p, 37
2284	**O_av**	weak absorption	**(blank)**	(blank)
2517	**O_M_50_av**	combination band	**v1+v3**	Spectrum Ca_av, spectrum M_av, Ricci et al, 2006, p. 1222
2525	**O_M_50_av**	weak absorption	**v1+v2 CO3-2**	Miliani et al, 2012, p. 302
2863	**O_av**	sharp absorption	**CH2 stretching**	Ploeger et al, 2010, p. 37
	O_M_50_av	strong absorption	**CH2 stretching**	Spectrum O_av, Ploeger et al, 2010, p. 37
2941	**O_av**	sharp absorption	**CH2 stretching**	Ploeger et al, 2010, p. 37
	O_M_50_av	strong absorption	**CH2 stretching**	Spectrum O_av, Ploeger et al, 2010, p. 37
2965	**O_av**	sharp absorption	**v(CH) stretching**	Miliani et al, 2007, p. 853
2966	**O_M_50_av**	strong absorption	**v(CH) stretching**	Spectrum O_av, Miliani et al, 2007, p. 853
3012	**O_M_50_av**	weak absorption	**v(CH) stretching**	Spectrum O_av, Miliani et al, 2007, p. 853
3014	**O_av**	sharp absorption	**v(CH) stretching**	Miliani et al, 2007, p. 853
3071	**O_av**	(blank)	**(blank)**	(blank)
3108	**O_av**	(blank)	**(blank)**	(blank)
3647	**O_M_50_av**	doublet	**OH stretching**	Spectrum M_av, spectrum Ca_av, Rosi et al, 2009, p. 2100

Figure 23: continued.

Peak x (position)	Spectrum ID	Type of band	Chemical Band Assignement	Reference
608	**O_M_25_av**	weak absorption	**CaCO3**	Spectrum Ca_av, spectrum M_av
641	**O_M_25_av**	weak absorption	**CaCO3**	spectrum Ca_av
667	**O_av**	(blank)	**(blank)**	(blank)
	O_M_25_av	sharp and weak absorption	**olive oil**	Spectrum O_av
701	**O_M_25_av**	weak absorption	**quartz**	Spectrum Q_av, spectrum M_av
706	**O_av**	(blank)	**(blank)**	(blank)
715	**O_M_25_av**	weak absorption	**v4 carbonate ion**	Spectrum Ca_av, spectrum M_av, Ylmen and Jaglid, 2013, p. 119
727	**O_M_25_av**	sharp and weak absorption	**olive oil**	Spectrum O_av
730	**O_av**	(blank)	**(blank)**	(blank)
792	**O_M_25_av**	sharp and weak absorption	**quartz**	Spectrum Q_av, spectrum M_av
821	**O_M_25_av**	sharp absorption	**olive oil**	Spectrum O_av
823	**O_av**	(blank)	**(blank)**	(blank)
878	**O_M_25_av**	sharp absorption	**v2 carbonate ion**	Spectrum Ca_av, Ylmen and Jaglid, 2013, p. 119
961	**O_av**	(blank)	**(blank)**	(blank)
1006	**O_av**	(blank)	**(blank)**	(blank)
1026	**O_av**	(blank)	**(blank)**	(blank)
1098	**O_M_25_av**	sharp and weak absorption	**v1 carbonate ion**	Spectrum Ca_av, spectrum M_av, Ylmen and Jaglid, 2013, p. 119
1102	**O_av**	weak absorption	**C-O stretching**	Buti et al, 2013, p. 2705
1119	**O_M_25_av**	sharp and weak absorption	**C-O stretching**	Spectrum O_av, Buti et al, 2013, p. 2705
1122	**O_av**	weak absorption	**C-O stretching**	Buti et al, 2013, p. 2705
1160	**O_M_25_av**	sharp absorption	**quartz**	Spectrum Q_av, spectrum M_av
1192	**O_av**	weak absorption	**C-O stretching**	Buti et al, 2013, p. 2705
1267	**O_av**	weak absorption	**C-O stretching**	Buti et al, 2013, p. 2705
1282	**O_av**	weak absorption	**(blank)**	(blank)
	O_M_25_av	weak absorption	**C-O stretching**	Spectrum O_av, Buti et al, 2013, p. 2705
1303	**O_av**	weak absorption	**(blank)**	(blank)
1318	**O_M_25_av**	weak absorption	**C-O stretching**	Spectrum O_av, Buti et al, 2013, p. 2705
1360	**O_av**	weak absorption	**(blank)**	(blank)
1381	**O_M_25_av**	sharp absorption	**C-O bending**	Spectrum O_av, Buti et al, 2013, p. 2705
1382	**O_av**	sharp and weak absorption	**C-H bending**	Buti et al, 2013, p. 2705

Figure 24: Filtered CPAD entries of olive oil (O_av) and 25% olive oil/mortar mixture (O_M_25_av).

1403	**O_av**	(blank)	**(blank)**	(blank)
1421	**O_av**	(blank)	**(blank)**	(blank)
1437	**O_av**	(blank)	**(blank)**	(blank)
1446	**O_av**	(blank)	**(blank)**	(blank)
1471	**O_av**	sharp absorption	**C-O bending**	Ricci et al, 2006, p. 1223
1507	**O_M_25_av**	strong absorption	**C-O bending**	Spectrum O_av, Ricci et al, 2006, p. 1223
1559	**O_av**	weak absorption	**(blank)**	(blank)
1600	**O_M_25_av**	weak absorption	**v3 antisymmetric stretching CO3-2**	Spectrum Ca_av, spectrum M_av, Ylmen and Jaglid, 2013, p. 119
1606	**O_M_25_av**	weak absorption	**quartz**	Spectrum Ca_av, spectrum M_av
1616	**O_M_25_av**	weak absorption	**quartz**	Spectrum Ca_av, spectrum M_av
1653	**O_av**	weak absorption	**(blank)**	(blank)
1660	**O_av**	weak absorption	**(blank)**	(blank)
	O_M_25_av	weak absorption	**quartz or olive oil**	Spectrum Q_av, spectum M_av, spectrum O_av
1669	**O_M_25_av**	weak absorption	**olive oil**	Spectrun O_av
1676	**O_av**	weak absorption	**(blank)**	(blank)
1678	**O_M_25_av**	weak absorption	**olive oil**	Spectrun O_av
1696	**O_av**	weak absorption	**Free fatty acids**	Mazzeo et al, 2008, p. 69
1703	**O_M_25_av**	weak absorption	**olive oil**	Spectrun O_av
1758	**O_av**	1st order derivative	**C=O stretching**	Ploeger et al, 2010, p. 37, Miliani et al, 2012, p. 304
	O_M_25_av	1st order derivative	**C=O stretching band**	Spectrum O_av, Ploeger et al, 2010, p, 37
2284	**O_av**	weak absorption	**(blank)**	(blank)
2527	**O_M_25_av**	weak absorption	**v1+v2 CO3-2**	Miliani et al, 2012, p. 302
2863	**O_av**	sharp absorption	**CH2 stretching**	Ploeger et al, 2010, p. 37
	O_M_25_av	strong absorption	**CH2 stretching**	Spectrum O_av, Ploeger et al, 2010, p. 37
2941	**O_av**	sharp absorption	**CH2 stretching**	Ploeger et al, 2010, p. 37
	O_M_25_av	strong absorption	**CH2 stretching**	Spectrum O_av, Ploeger et al, 2010, p. 37
2965	**O_av**	sharp absorption	**v(CH) stretching**	Miliani et al, 2007, p. 853
2966	**O_M_25_av**	strong absorption	**v(CH) stretching**	Spectrum O_av, Miliani et al, 2007, p. 853
3009	**O_M_25_av**	weak absorption	**v(CH) stretching**	Spectrum O_av, Miliani et al, 2007, p. 853
3014	**O_av**	sharp absorption	**v(CH) stretching**	Miliani et al, 2007, p. 853
3071	**O_av**	(blank)	**(blank)**	(blank)
3108	**O_av**	(blank)	**(blank)**	(blank)
3647	**O_M_25_av**	doublet	**OH stretching**	Spectrum M_av, spectrum Ca_av, Rosi et al, 2009, p. 2100

Figure 24: continued.

Peak x (position)	Spectrum ID	Type of band	Chemical Band Assignement	Reference
623	**O_M_5_av**	weak absorption	**CaCO3**	spectrum Ca_av
645	**O_M_5_av**	weak absorption	**CaCO3**	spectrum Ca_av
667	**O_av**	(blank)	**(blank)**	(blank)
701	**O_M_5_av**	weak absorption	**quartz**	Spectrum Q_av, spectrum M_av
706	**O_av**	(blank)	**(blank)**	(blank)
715	**O_M_5_av**	weak absorption	**v4 carbonate ion**	Spectrum Ca_av, spectrum M_av, Ylmen and Jaglid, 2013, p. 119
730	**O_av**	(blank)	**(blank)**	(blank)
791	**O_M_5_av**	sharp and weak absorption	**quartz**	Spectrum Q_av, spectrum M_av
816	**O_M_5_av**	sharp absorption	**quartz**	Spectrum Q_av, spectrum M_av
823	**O_av**	(blank)	**(blank)**	(blank)
879	**O_M_5_av**	sharp and weak absorption	**v2 carbonate ion**	Spectrum Ca_av, spectrum M_av, Ylmen and Jaglid, 2013, p. 119
961	**O_av**	(blank)	**(blank)**	(blank)
1006	**O_av**	(blank)	**(blank)**	(blank)
1026	**O_av**	(blank)	**(blank)**	(blank)
1102	**O_av**	weak absorption	**C-O stretching**	Buti et al, 2013, p. 2705
1122	**O_av**	weak absorption	**C-O stretching**	Buti et al, 2013, p. 2705
1159	**O_M_5_av**	sharp absorption	**quartz**	Spectrum Q_av, spectrum M_av
1192	**O_av**	weak absorption	**C-O stretching**	Buti et al, 2013, p. 2705
1267	**O_av**	weak absorption	**C-O stretching**	Buti et al, 2013, p. 2705
1282	**O_av**	weak absorption	**(blank)**	(blank)
1303	**O_av**	weak absorption	**(blank)**	(blank)
1360	**O_av**	weak absorption	**(blank)**	(blank)
1382	**O_av**	sharp and weak absorption	**C-H bending**	Buti et al, 2013, p. 2705
1384	**O_M_5_av**	sharp absorption	**C-O bending**	Spectrum O_av
1403	**O_av**	(blank)	**(blank)**	(blank)
1421	**O_av**	(blank)	**(blank)**	(blank)
1437	**O_av**	(blank)	**(blank)**	(blank)
1442	**O_M_5_av**	weak absorption	**olive oil**	Spectrum O_av, Buti et al, 2013, p. 2706
1446	**O_av**	(blank)	**(blank)**	(blank)
1471	**O_av**	sharp absorption	**C-O bending**	Ricci et al, 2006, p. 1223
1530	**O_M_5_av**	strong absorption	**C-O bending**	Spectrum O_av, Ricci et al, 2006, p. 1223
1559	**O_av**	weak absorption	**(blank)**	(blank)
1585	**O_M_5_av**	weak absorption	**v3 antisymmetric stretching CO3-2**	Spectrum Ca_av, spectrum M_av, Ylmen and Jaglid, 2013, p. 119
1593	**O_M_5_av**	weak absorption	**v3 antisymmetric stretching CO3-2**	Spectrum Ca_av, spectrum M_av, Ylmen and Jaglid, 2013, p. 119

Figure 25: Filtered CPAD entries of olive oil (O_av) and 5% olive oil/mortar mixture (O_M_5_av).

1604	**O_M_5_av**	weak absorption	**quartz**	Spectrum Ca_av, spectrum M_av
1653	**O_av**	weak absorption	**(blank)**	(blank)
1660	**O_av**	weak absorption	**(blank)**	(blank)
1674	**O_M_5_av**	weak absorption	**olive oil**	Spectrun O_av
1676	**O_av**	weak absorption	**(blank)**	(blank)
1680	**O_M_5_av**	weak absorption	**olive oil**	Spectrun O_av
1695	**O_M_5_av**	weak absorption	**olive oil**	Spectrun O_av
1696	**O_av**	weak absorption	**Free fatty acids**	Mazzeo et al, 2008, p. 69
1755	**O_M_5_av**	1st order derivative	**C=O stretching band**	Spectrum O_av, Ploeger et al, 2010, p, 37
1758	**O_av**	1st order derivative	**C=O stretching**	Ploeger et al, 2010, p. 37, Miliani et al, 2012, p. 304
1794	**O_M_5_av**	combination band	**v1+v4**	Spectrum Ca_av, spectrum M_av, Ricci et al, 2006, p. 1222
1857	**O_M_5_av**	weak absorption	**quartz**	spectrum Q_av
1942	**O_M_5_av**	weak absorption	**quartz**	spectrum Q_av
1948	**O_M_5_av**	weak absorption	**quartz**	spectrum Q_av
1964	**O_M_5_av**	weak absorption	**quartz**	spectrum Q_av
1975	**O_M_5_av**	weak absorption	**quartz**	spectrum Q_av
1987	**O_M_5_av**	weak absorption	**quartz**	spectrum Q_av
2135	**O_M_5_av**	weak absorption	**calcium carbonate and quartz**	Spectrum Ca_av, spectrum M_av, spectrum Q_av
2237	**O_M_5_av**	weak absorption	**quartz**	spectrum Q_av
2284	**O_av**	weak absorption	**(blank)**	(blank)
2512	**O_M_5_av**	combination band	**v1+v3**	Spectrum Ca_av, spectrum M_av, Ricci et al, 2006, p. 1222
2582	**O_M_5_av**	weak absorption	**quartz**	spectrum Q_av
2677	**O_M_5_av**	weak absorption	**quartz**	spectrum Q_av
2735	**O_M_5_av**	weak absorption	**quartz**	spectrum Q_av
2855	**O_M_5_av**	strong absorption	**CH2 stretching**	Spectrum O_av, Ploeger et al, 2010, p. 37
2863	**O_av**	sharp absorption	**CH2 stretching**	Ploeger et al, 2010, p. 37
2929	**O_M_5_av**	strong absorption	**CH2 stretching**	Spectrum O_av, Ploeger et al, 2010, p. 37
2941	**O_av**	sharp absorption	**CH2 stretching**	Ploeger et al, 2010, p. 37
2954	**O_M_5_av**	strong absorption	**v(CH) stretching**	Spectrum O_av, Miliani et al, 2007, p. 853
2965	**O_av**	sharp absorption	**v(CH) stretching**	Miliani et al, 2007, p. 853
3005	**O_M_5_av**	weak absorption	**v(CH) stretching**	Spectrum O_av, Miliani et al, 2007, p. 853
3014	**O_av**	sharp absorption	**v(CH) stretching**	Miliani et al, 2007, p. 853
3062	**O_M_5_av**	weak absorption	**olive oil**	Spectrum O_av
3071	**O_av**	(blank)	**(blank)**	(blank)
3108	**O_av**	(blank)	**(blank)**	(blank)
3382	**O_M_5_av**	weak absorption	**quartz**	Spectrum M_av, spectrum Ca_av
3643	**O_M_5_av**	doublet	**OH stretching**	Spectrum M_av, spectrum Ca_av, Rosi et al, 2009, p. 2100

Figure 25: continued.

7.5.7 Milk and mortar mixtures CPAD

Peak x (position)	Spectrum ID	Type of band	Chemical Band Assignement	Reference
609	Mi_M_75_av	weak absorption	CaCO3	Spectrum M_av, spectrum Ca_av
634	Mi_M_75_av	weak absorption	CaCO3	spectrum Ca_av
657	Mi_M_75_av	weak absorption	CaCO3	spectrum Ca_av
667	Mi_av	weak absorption	(blank)	(blank)
671	Mi_M_75_av	weak absorption	milk	Spectrum Mi_av
702	Mi_M_75_av	sharp and weak absorption	quartz	Spectrum M_av, spectrum Q_av
713	Mi_M_75_av	sharp and weak absorption	v4 carbonate ion	Spectrum M_av, spectrum Ca_av, Ylmen and Jaglid, 2013, p. 119
729	Mi_av	weak absorption	(blank)	(blank)
789	Mi_M_75_av	weak absorption	quartz	Spectrum M_av, spectrum Q_av
802	Mi_av	strong absorption	(blank)	(blank)
814	Mi_M_75_av	sharp absorption	quartz	Spectrum M_av, spectrum Q_av
847	Mi_M_75_av	weak absorption	v2 carbonate ion	Spectrum M_av, spectrum Ca_av, Ylmen and Jaglid, 2013, p. 119
874	Mi_M_75_av	sharp absorption	v2 carbonate ion	Spectrum M_av, spectrum Ca_av, Ylmen and Jaglid, 2013, p. 119
907	Mi_av	strong absorption	PO4-3anion stretching	Ricci et al, 2006, p. 1223
982	Mi_av	sharp absorption	sugar region	Synytsya and Novak, 2014, p.6
989	Mi_M_75_av	sharp absorption	sugar region	Spectrum Mi_av, Synytsya and Novak, 2014, p. 6
1019	Mi_M_75_av	weak absorption	CaCO3	spectrum Ca_av
1054	Mi_av	sharp absorption	sugar region	Synytsya and Novak, 2014, p.6
1125	Mi_av	sharp and weak absorption	sugar region	Synytsya and Novak, 2014, p.6
1159	Mi_M_75_av	sharp absorption	quartz	Spectrum M_av, spectrum Q_av
1182	Mi_av	strong absorption	sugar region	Synytsya and Novak, 2014, p.6
1203	Mi_M_75_av	weak absorption	sugar region	Spectrum Mi_av, Synytsya and Novak, 2014, p. 6
1263	Mi_M_75_av	strong absorption	milk	Spectrum Mi_av
1270	Mi_av	strong absorption	(blank)	(blank)
1322	Mi_M_75_av	weak absorption	milk	Spectrum Mi_av
1323	Mi_av	weak absorption	(blank)	(blank)
1341	Mi_M_75_av	weak absorption	quartz	spectrum Q_av
1383	Mi_M_75_av	strong absorption	C-H bending	Spectrum Mi_av, Buti et al, 2013, p. 2705
1385	Mi_av	weak absorption	C-H bending	Buti et al, 2013, p. 2705
1396	Mi_M_75_av	strong absorption	CaCO3	Spectrum M_av, spectrum Ca_av
1403	Mi_av	weak absorption	(blank)	(blank)
1422	Mi_av	weak absorption	(blank)	(blank)
1424	Mi_M_75_av	strong absorption	CaCO3 or milk	Spectrum M_av, spectrum Ca_av, spectrum Mi_av
1438	Mi_M_75_av	strong absorption	v3 antisymmetric stretching CO3-2	Spectrum M_av, spectrum Ca_av, Ylmen and Jaglid, 2013, p. 119
1451	Mi_M_75_av	strong absorption	v3 antisymmetric stretching CO3-2	Spectrum Ca_av, Ylmen and Jaglid, 2013, p. 119
1459	Mi_M_75_av	strong absorption	v3 antisymmetric stretching CO3-2	Spectrum Ca_av, Ylmen and Jaglid, 2013, p. 119
1468	Mi_M_75_av	strong absorption	v3 antisymmetric stretching CO3-2	Spectrum Ca_av, Ylmen and Jaglid, 2013, p. 119
1473	Mi_av	sharp absorption	Amide III	Rosi et al, 2009, p. 2099

Figure 26: Filtered CPAD entries of milk (Mi_av) and 75% milk/mortar mixture (Mi_M_75_av).

1509	**Mi_M_75_av**	strong absorption	**Carbonyl absorption**	Rosi et al, 2002, p. 2099
1522	**Mi_av**	weak absorption	**(blank)**	(blank)
1524	**Mi_M_75_av**	strong absorption	**milk**	Spectrum Mi_av
1539	**Mi_M_75_av**	strong absorption	**N-H bands**	Spectrum Mi_av, Miliani et al, 2012, p. 304
1571	**Mi_M_75_av**	strong absorption	**N-H bands**	Spectrum Mi_av, Miliani et al, 2012, p. 304
1572	**Mi_av**	strong absorption	**N-H bands**	Miliani et al, 2012, p.304, Rosi et al, 2009, p. 2104
1665	**Mi_M_75_av**	strong absorption	**N-H bands**	Spectrum Mi_av, Miliani et al, 2012, p. 304
1673	**Mi_M_75_av**	strong absorption	**N-H bands**	Spectrum Mi_av, Miliani et al, 2012, p. 304
1690	**Mi_av**	strong absorption	**N-H bands**	Rosi et al, 2009, p. 2104
1750	**Mi_M_75_av**	1st order derivative	**C=O stretching band**	Spectrum Mi_av, Ploeger et al, 2010, p, 37
1755	**Mi_av**	strong absorption	**C=O stretching band, esters**	Ricci et al, 2006, p. 1223
1793	**Mi_M_75_av**	combination band	**v1+v4**	Spectrum M_av, spectrum Ca_av, Ricci et al, 2006, p. 1222
1841	**Mi_av**	weak absorption	**(blank)**	(blank)
1854	**Mi_av**	weak absorption	**C-O**	Ploeger et al, 2010, p. 37
1868	**Mi_M_75_av**	weak absorption	**quartz**	Spectrum M_av, spectrum Q_av
1942	**Mi_M_75_av**	weak absorption	**quartz**	Spectrum M_av, spectrum Q_av
1950	**Mi_M_75_av**	weak absorption	**quartz**	Spectrum M_av, spectrum Q_av
1972	**Mi_av**	weak absorption	**(blank)**	(blank)
1977	**Mi_M_75_av**	weak absorption	**quartz**	Spectrum M_av, spectrum Q_av
1992	**Mi_M_75_av**	weak absorption	**quartz**	Spectrum M_av, spectrum Q_av
2083	**Mi_av**	weak absorption	**(blank)**	(blank)
2136	**Mi_M_75_av**	weak absorption	**calcium carbonate and quartz**	Spectrum Ca_av, spectrum M_av, spectrum Q_av
2197	**Mi_av**	weak absorption	**(blank)**	(blank)
2237	**Mi_M_75_av**	weak absorption	**quartz**	spectrum Q_av
2431	**Mi_av**	weak absorption	**(blank)**	(blank)
2514	**Mi_M_75_av**	combination band	**v1+v3**	Spectrum M_av, spectrum Ca_av, Ricci et al, 2006, p. 1222
2530	**Mi_av**	weak absorption	**(blank)**	(blank)
2546	**Mi_av**	weak absorption	**(blank)**	(blank)
2640	**Mi_av**	(blank)	**(blank)**	(blank)
2647	**Mi_av**	(blank)	**(blank)**	(blank)
2655	**Mi_av**	(blank)	**(blank)**	(blank)
2664	**Mi_av**	(blank)	**(blank)**	(blank)
2857	**Mi_M_75_av**	sharp absorption	**C=O stretching band**	Spectrum Mi_av, Rosi et al, 2009, p. 2099
2860	**Mi_av**	sharp absorption	**C=O stretching band**	Rosi et al, 2009, p. 2099
2905	**Mi_M_75_av**	weak absorption	**CH stretching**	Miliani et al, 2012, p. 302
2933	**Mi_M_75_av**	strong absorption	**CH stretching**	Spectrum Mi_av, Daher et al, 2017, p.8
2938	**Mi_av**	strong absorption	**CH stretching**	Daher et al, 2017, p.8
2958	**Mi_M_75_av**	sharp absorption	**CH2 stretching**	Ploeger et al, 2010, p. 37
2967	**Mi_av**	sharp absorption	**CH2 stretching**	Ploeger et al, 2010, p. 37
3007	**Mi_M_75_av**	weak absorption	**CH stretching**	Miliani et al, 2012, p. 302

Figure 26: continued.

Peak x (position)	Spectrum ID	Type of band	Chemical Band Assignement	Reference
612	Mi_M_50_av	weak absorption	CaCO3	Spectrum M_av, spectrum Ca_av
619	Mi_M_50_av	weak absorption	CaCO3	Spectrum M_av, spectrum Ca_av
633	Mi_M_50_av	weak absorption	CaCO3	Spectrum M_av, spectrum Ca_av
657	Mi_M_50_av	weak absorption	CaCO3	Spectrum M_av, spectrum Ca_av
667	Mi_av	weak absorption	(blank)	(blank)
672	Mi_M_50_av	weak absorption	milk	Spectrum Mi_av
700	Mi_M_50_av	sharp absorption	quartz	Spectrum M_av, spectrum Q_av
714	Mi_M_50_av	sharp absorption	v4 carbonate ion	Spectrum M_av, spectrum Ca_av, Ylmen and Jaglid, 2013, p. 119
729	Mi_av	weak absorption	(blank)	(blank)
791	Mi_M_50_av	weak absorption	quartz	Spectrum M_av, spectrum Q_av
802	Mi_av	strong absorption	(blank)	(blank)
814	Mi_M_50_av	sharp absorption	quartz	Spectrum M_av, spectrum Q_av
848	Mi_M_50_av	weak absorption	v2 carbonate ion	Spectrum M_av, spectrum Ca_av, Ylmen and Jaglid, 2013, p. 119
877	Mi_M_50_av	sharp absorption	v2 carbonate ion	Spectrum M_av, spectrum Ca_av, Ylmen and Jaglid, 2013, p. 119
907	Mi_av	strong absorption	PO4-3anion stretching	Ricci et al, 2006, p. 1223
982	Mi_av	sharp absorption	sugar region	Synytsya and Novak, 2014, p.6
988	Mi_M_50_av	sharp absorption	sugar region	Spectrum Mi_av, Synytsya and Novak, 2014, p. 6
1017	Mi_M_50_av	weak absorption	CaCO3	spectrum Ca_av
1054	Mi_av	sharp absorption	sugar region	Synytsya and Novak, 2014, p.6
1099	Mi_M_50_av	sharp absorption	v1 carbonate ion	Spectrum Ca_av, Ylmen and Jaglid, 2013, p. 119
1118	Mi_M_50_av	weak absorption	CaCO3	spectrum Ca_av
1125	Mi_av	sharp and weak absorption	sugar region	Synytsya and Novak, 2014, p.6
1159	Mi_M_50_av	sharp absorption	quartz	Spectrum M_av, spectrum Q_av
1182	Mi_av	strong absorption	sugar region	Synytsya and Novak, 2014, p.6
1200	Mi_M_50_av	weak absorption	sugar region	Spectrum Mi_av, Synytsya and Novak, 2014, p. 6
1270	Mi_av	strong absorption	(blank)	(blank)
1323	Mi_av	weak absorption	(blank)	(blank)
1385	Mi_av	weak absorption	C-H bending	Buti et al, 2013, p. 2705
1396	Mi_M_50_av	strong absorption	CaCO3	Spectrum M_av, spectrum Ca_av
1403	Mi_av	weak absorption	(blank)	(blank)
1422	Mi_av	weak absorption	(blank)	(blank)
1439	Mi_M_50_av	strong absorption	v3 antisymmetric stretching CO3-2	Spectrum Ca_av, Ylmen and Jaglid, 2013, p. 119
1466	Mi_M_50_av	strong absorption	v3 antisymmetric stretching CO3-2	Spectrum Ca_av, Ylmen and Jaglid, 2013, p. 119
1473	Mi_av	sharp absorption	Amide III	Rosi et al, 2009, p. 2099
1475	Mi_M_50_av	strong absorption	Amide III	Spectrum Mi_av, Rosi et al, 2009, p. 2099
1483	Mi_M_50_av	strong absorption	CH2 bending	Iwanicka et al, 2017, p. 18
1500	Mi_M_50_av	strong absorption	Carbonyl absorption	Rosi et al, 2002, p. 2099
1520	Mi_M_50_av	strong absorption	milk	Spectrum Mi_av
1522	Mi_av	weak absorption	(blank)	(blank)
1535	Mi_M_50_av	strong absorption	N-H bands	Spectrum Mi_av, Miliani et al, 2012, p. 304

Figure 27: Filtered CPAD entries of milk (Mi_av) and 50% milk/mortar mixture (Mi_M_50_av).

1546	**Mi_M_50_av**	strong absorption	**N-H bands or quartz**	Spectrum Q_av, Miliani et al, 2012, p. 304
1561	**Mi_M_50_av**	strong absorption	**N-H bands or quartz**	Spectrum Q_av, Miliani et al, 2012, p. 305
1571	**Mi_M_50_av**	strong absorption	**N-H bands**	Spectrum Mi_av, Miliani et al, 2012, p. 304
1572	**Mi_av**	strong absorption	**N-H bands**	Miliani et al, 2012, p.304, Rosi et al, 2009, p. 2104
1635	**Mi_M_50_av**	strong absorption	**N-H bands**	Spectrum Mi_av, Miliani et al, 2012, p. 304
1666	**Mi_M_50_av**	strong absorption	**N-H bands**	Spectrum Mi_av, Miliani et al, 2012, p. 304
1690	**Mi_av**	strong absorption	**N-H bands**	Rosi et al, 2009, p. 2104
1747	**Mi_M_50_av**	1st order derivative	**C=O stretching band**	Spectrum Mi_av, Ploeger et al, 2010, p, 37
1755	**Mi_av**	strong absorption	**C=O stretching band, esters**	Ricci et al, 2006, p. 1223
1794	**Mi_M_50_av**	combination band	**v1+v4**	Spectrum M_av, spectrum Ca_av, Ricci et al, 2006, p. 1222
1841	**Mi_av**	weak absorption	**(blank)**	(blank)
1854	**Mi_av**	weak absorption	**C-O**	Ploeger et al, 2010, p. 37
1855	**Mi_M_50_av**	weak absorption	**quartz**	Spectrum M_av, spectrum Q_av
1867	**Mi_M_50_av**	weak absorption	**quartz**	Spectrum M_av, spectrum Q_av
1942	**Mi_M_50_av**	weak absorption	**quartz**	Spectrum M_av, spectrum Q_av
1971	**Mi_M_50_av**	weak absorption	**quartz**	Spectrum M_av, spectrum Q_av
1972	**Mi_av**	weak absorption	**(blank)**	(blank)
2083	**Mi_av**	weak absorption	**(blank)**	(blank)
2135	**Mi_M_50_av**	weak absorption	**calcium carbonate and quartz**	Spectrum Ca_av, spectrum M_av, spectrum Q_av
2197	**Mi_av**	weak absorption	**(blank)**	(blank)
2237	**Mi_M_50_av**	weak absorption	**quartz**	spectrum Q_av
2431	**Mi_av**	weak absorption	**(blank)**	(blank)
2511	**Mi_M_50_av**	combination band	**v1+v3**	Spectrum M_av, spectrum Ca_av, Ricci et al, 2006, p. 1222
2530	**Mi_av**	weak absorption	**(blank)**	(blank)
2546	**Mi_av**	weak absorption	**(blank)**	(blank)
2589	**Mi_M_50_av**	weak absorption	**CaCO3**	Spectrum M_av, spectrum Ca_av
2640	**Mi_av**	(blank)	**(blank)**	(blank)
2647	**Mi_av**	(blank)	**(blank)**	(blank)
2655	**Mi_av**	(blank)	**(blank)**	(blank)
2664	**Mi_av**	(blank)	**(blank)**	(blank)
2855	**Mi_M_50_av**	sharp absorption	**C=O stretching band**	Spectrum Mi_av, Rosi et al, 2009, p. 2099
2860	**Mi_av**	sharp absorption	**C=O stretching band**	Rosi et al, 2009, p. 2099
2926	**Mi_M_50_av**	strong absorption	**CH stretching**	Spectrum Mi_av, Daher et al, 2017, p.8
2938	**Mi_av**	strong absorption	**CH stretching**	Daher et al, 2017, p.8
2957	**Mi_M_50_av**	sharp absorption	**CH2 stretching**	Ploeger et al, 2010, p. 37
2967	**Mi_av**	sharp absorption	**CH2 stretching**	Ploeger et al, 2010, p. 37
3642	**Mi_M_50_av**	doublet	**OH stretching**	Spectrum M_av, spectrum Ca_av, Rosi et al, 2009, p. 2100

Figure 27: continued.

Peak x (position)	Spectrum ID	Type of band	Chemical Band Assignement	Reference
606	**Mi_M_25_av**	weak absorption	**CaCO3**	Spectrum M_av, spectrum Ca_av
616	**Mi_M_25_av**	weak absorption	**CaCO3**	Spectrum M_av, spectrum Ca_av
629	**Mi_M_25_av**	weak absorption	**CaCO3**	Spectrum M_av, spectrum Ca_av
642	**Mi_M_25_av**	weak absorption	**CaCO3**	Spectrum M_av, spectrum Ca_av
667	**Mi_av**	weak absorption	**(blank)**	(blank)
701	**Mi_M_25_av**	sharp absorption	**quartz**	Spectrum M_av, spectrum Q_av
714	**Mi_M_25_av**	sharp absorption	**v4 carbonate ion**	Spectrum M_av, spectrum Ca_av, Ylmen and Jaglid, 2013, p. 119
729	**Mi_av**	weak absorption	**(blank)**	(blank)
791	**Mi_M_25_av**	sharp absorption	**quartz**	Spectrum M_av, spectrum Q_av
802	**Mi_av**	strong absorption	**(blank)**	(blank)
815	**Mi_M_25_av**	sharp absorption	**quartz**	Spectrum M_av, spectrum Q_av
848	**Mi_M_25_av**	weak absorption	**v2 carbonate ion**	Spectrum M_av, spectrum Ca_av, Ylmen and Jaglid, 2013, p. 119
879	**Mi_M_25_av**	sharp absorption	**v2 carbonate ion**	Spectrum M_av, spectrum Ca_av, Ylmen and Jaglid, 2013, p. 119
907	**Mi_av**	strong absorption	**PO4-3anion stretching**	Ricci et al, 2006, p. 1223
982	**Mi_av**	sharp absorption	**sugar region**	Synytsya and Novak, 2014, p.6
988	**Mi_M_25_av**	sharp absorption	**sugar region**	Spectrum Mi_av, Synytsya and Novak, 2014, p. 6
1054	**Mi_av**	sharp absorption	**sugar region**	Synytsya and Novak, 2014, p.6
1125	**Mi_av**	sharp and weak absorption	**sugar region**	Synytsya and Novak, 2014, p.6
1159	**Mi_M_25_av**	sharp absorption	**quartz**	Spectrum M_av, spectrum Q_av
1182	**Mi_av**	strong absorption	**sugar region**	Synytsya and Novak, 2014, p.6
1270	**Mi_av**	strong absorption	**(blank)**	(blank)
1323	**Mi_av**	weak absorption	**(blank)**	(blank)
1385	**Mi_av**	weak absorption	**C-H bending**	Buti et al, 2013, p. 2705
1394	**Mi_M_25_av**	strong absorption	**CaCO3**	Spectrum M_av, spectrum Ca_av
1403	**Mi_av**	weak absorption	**(blank)**	(blank)
1422	**Mi_av**	weak absorption	**(blank)**	(blank)
1443	**Mi_M_25_av**	strong absorption	**v3 antisymmetric stretching CO3-2**	Spectrum Ca_av, Ylmen and Jaglid, 2013, p. 119
1459	**Mi_M_25_av**	strong absorption	**v3 antisymmetric stretching CO3-2**	Spectrum Ca_av, Ylmen and Jaglid, 2013, p. 119
1467	**Mi_M_25_av**	strong absorption	**v3 antisymmetric stretching CO3-2**	Spectrum Ca_av, Ylmen and Jaglid, 2013, p. 119
1473	**Mi_av**	sharp absorption	**Amide III**	Rosi et al, 2009, p. 2099
1476	**Mi_M_25_av**	strong absorption	**Amide III**	Spectrum Mi_av, Rosi et al, 2009, p. 2099
1497	**Mi_M_25_av**	strong absorption	**Carbonyl absorption**	Rosi et al, 2002, p. 2099

Figure 28: Filtered CPAD entries of milk (Mi_av) and 25% milk/mortar mixture (Mi_M_25_av).

1522	**Mi_av**	weak absorption	**(blank)**	(blank)
1538	**Mi_M_25_av**	strong absorption	**N-H bands**	Spectrum Mi_av, Miliani et al, 2012, p. 304
1572	**Mi_av**	strong absorption	**N-H bands**	Miliani et al, 2012, p.304, Rosi et al, 2009, p. 2104
1582	**Mi_M_25_av**	strong absorption	**v3 antisymmetric stretching CO3-2**	Spectrum Ca_av, Ylmen and Jaglid, 2013, p. 119
1624	**Mi_M_25_av**	strong absorption	**N-H bands**	Spectrum Mi_av, Miliani et al, 2012, p. 304
1661	**Mi_M_25_av**	strong absorption	**N-H bands**	Spectrum Mi_av, Miliani et al, 2012, p. 304
1690	**Mi_av**	strong absorption	**N-H bands**	Rosi et al, 2009, p. 2104
1746	**Mi_M_25_av**	1st order derivative	**C=O stretching band**	Spectrum Mi_av, Ploeger et al, 2010, p, 37
1755	**Mi_av**	strong absorption	**C=O stretching band, esters**	Ricci et al, 2006, p. 1223
1794	**Mi_M_25_av**	combination band	**v1+v4**	Spectrum M_av, spectrum Ca_av, Ricci et al, 2006, p. 1222
1841	**Mi_av**	weak absorption	**(blank)**	(blank)
1854	**Mi_av**	weak absorption	**C-O**	Ploeger et al, 2010, p. 37
1859	**Mi_M_25_av**	weak absorption	**quartz**	Spectrum M_av, spectrum Q_av
1868	**Mi_M_25_av**	weak absorption	**quartz**	Spectrum M_av, spectrum Q_av
1934	**Mi_M_25_av**	weak absorption	**quartz**	Spectrum M_av, spectrum Q_av
1942	**Mi_M_25_av**	weak absorption	**quartz**	Spectrum M_av, spectrum Q_av
1967	**Mi_M_25_av**	weak absorption	**quartz**	Spectrum M_av, spectrum Q_av
1972	**Mi_av**	weak absorption	**(blank)**	(blank)
1974	**Mi_M_25_av**	weak absorption	**quartz**	Spectrum M_av, spectrum Q_av
2083	**Mi_av**	weak absorption	**(blank)**	(blank)
2136	**Mi_M_25_av**	weak absorption	**calcium carbonate and quartz**	Spectrum Ca_av, spectrum M_av, spectrum Q_av
2197	**Mi_av**	weak absorption	**(blank)**	(blank)
2237	**Mi_M_25_av**	weak absorption	**quartz**	spectrum Q_av
2431	**Mi_av**	weak absorption	**(blank)**	(blank)
2512	**Mi_M_25_av**	combination band	**v1+v3**	Spectrum M_av, spectrum Ca_av, Ricci et al, 2006, p. 1222
2530	**Mi_av**	weak absorption	**(blank)**	(blank)
2546	**Mi_av**	weak absorption	**(blank)**	(blank)
2587	**Mi_M_25_av**	weak absorption	**CaCO3**	Spectrum M_av, spectrum Ca_av
2640	**Mi_av**	(blank)	**(blank)**	(blank)
2647	**Mi_av**	(blank)	**(blank)**	(blank)
2655	**Mi_av**	(blank)	**(blank)**	(blank)
2664	**Mi_av**	(blank)	**(blank)**	(blank)
2854	**Mi_M_25_av**	sharp absorption	**C=O stretching band**	Spectrum Mi_av, Rosi et al, 2009, p. 2099
2860	**Mi_av**	sharp absorption	**C=O stretching band**	Rosi et al, 2009, p. 2099
2924	**Mi_M_25_av**	strong absorption	**CH stretching**	Spectrum Mi_av, Daher et al, 2017, p.8
2938	**Mi_av**	strong absorption	**CH stretching**	Daher et al, 2017, p.8
2954	**Mi_M_25_av**	sharp absorption	**CH2 stretching**	Ploeger et al, 2010, p. 37
2967	**Mi_av**	sharp absorption	**CH2 stretching**	Ploeger et al, 2010, p. 37
3643	**Mi_M_25_av**	doublet	**OH stretching**	Spectrum M_av, spectrum Ca_av, Rosi et al, 2009, p. 2100

Figure 28: continued.

Peak x (position)	Spectrum ID	Type of band	Chemical Band Assignement	Reference
611	Mi_M_5_av	weak absorption	CaCO3	Spectrum M_av, spectrum Ca_av
622	Mi_M_5_av	weak absorption	CaCO3	Spectrum M_av, spectrum Ca_av
632	Mi_M_5_av	weak absorption	CaCO3	Spectrum M_av, spectrum Ca_av
648	Mi_M_5_av	weak absorption	CaCO3	Spectrum M_av, spectrum Ca_av
667	Mi_av	weak absorption	(blank)	(blank)
714	Mi_M_5_av	sharp absorption	v4 carbonate ion	Spectrum M_av, spectrum Ca_av, Ylmen and Jaglid, 2013, p. 119
729	Mi_av	weak absorption	(blank)	(blank)
791	Mi_M_5_av	sharp absorption	quartz	Spectrum M_av, spectrum Q_av
802	Mi_av	strong absorption	(blank)	(blank)
816	Mi_M_5_av	sharp absorption	quartz	Spectrum M_av, spectrum Q_av
848	Mi_M_5_av	weak absorption	v2 carbonate ion	Spectrum M_av, spectrum Ca_av, Ylmen and Jaglid, 2013, p. 119
881	Mi_M_5_av	sharp absorption	v2 carbonate ion	Spectrum M_av, spectrum Ca_av, Ylmen and Jaglid, 2013, p. 119
907	Mi_av	strong absorption	PO4-3anion stretching	Ricci et al, 2006, p. 1223
982	Mi_av	sharp absorption	sugar region	Synytsya and Novak, 2014, p.6
990	Mi_M_5_av	weak absorption	sugar region	Spectrum Mi_av, Synytsya and Novak, 2014, p. 6
1016	Mi_M_5_av	weak absorption	CaCO3	spectrum Ca_av
1054	Mi_av	sharp absorption	sugar region	Synytsya and Novak, 2014, p.6
1082	Mi_M_5_av	weak absorption	v1 carbonate ion	Spectrum Ca_av, Ylmen and Jaglid, 2013, p. 119
1091	Mi_M_5_av	weak absorption	v1 carbonate ion	Spectrum Ca_av, Ylmen and Jaglid, 2013, p. 119
1125	Mi_av	sharp and weak absorption	sugar region	Synytsya and Novak, 2014, p.6
1159	Mi_M_5_av	sharp absorption	quartz	Spectrum M_av, spectrum Q_av
1182	Mi_av	strong absorption	sugar region	Synytsya and Novak, 2014, p.6
1270	Mi_av	strong absorption	(blank)	(blank)
1323	Mi_av	weak absorption	(blank)	(blank)
1385	Mi_av	weak absorption	C-H bending	Buti et al, 2013, p. 2705
1396	Mi_M_5_av	strong absorption	CaCO3	Spectrum M_av, spectrum Ca_av
1403	Mi_av	weak absorption	(blank)	(blank)
1422	Mi_av	weak absorption	(blank)	(blank)
1432	Mi_M_5_av	strong absorption	v3 antisymmetric stretching CO3-2	Spectrum Ca_av, Ylmen and Jaglid, 2013, p. 119
1440	Mi_M_5_av	strong absorption	v3 antisymmetric stretching CO3-2	Spectrum Ca_av, Ylmen and Jaglid, 2013, p. 119
1449	Mi_M_5_av	strong absorption	v3 antisymmetric stretching CO3-2	Spectrum Ca_av, Ylmen and Jaglid, 2013, p. 119

Figure 29: Filtered CPAD entries of milk (Mi_av) and 5% milk/mortar mixture (Mi_M_5_av).

1467	**Mi_M_5_av**	strong absorption	**v3 antisymmetric stretching CO3-2**	Spectrum Ca_av, Ylmen and Jaglid, 2013, p. 119
1473	**Mi_av**	sharp absorption	**Amide III**	Rosi et al, 2009, p. 2099
1476	**Mi_M_5_av**	strong absorption	**Amide III**	Spectrum Mi_av, Rosi et al, 2009, p. 2099
1522	**Mi_av**	weak absorption	**(blank)**	(blank)
1572	**Mi_av**	strong absorption	**N-H bands**	Miliani et al, 2012, p.304, Rosi et al, 2009, p. 2104
1584	**Mi_M_5_av**	strong absorption	**v3 antisymmetric stretching CO3-2**	Spectrum Ca_av, Ylmen and Jaglid, 2013, p. 119
1602	**Mi_M_5_av**	strong absorption	**quartz**	Spectrum M_av, spectrum Q_av
1612	**Mi_M_5_av**	strong absorption	**quartz**	Spectrum M_av, spectrum Q_av
1652	**Mi_M_5_av**	strong absorption	**quartz**	Spectrum M_av, spectrum Q_av
1690	**Mi_av**	strong absorption	**N-H bands**	Rosi et al, 2009, p. 2104
1755	**Mi_av**	strong absorption	**C=O stretching band, esters**	Ricci et al, 2006, p. 1223
1795	**Mi_M_5_av**	combination band	**v1+v4**	Spectrum M_av, spectrum Ca_av, Ricci et al, 2006, p. 1222
1841	**Mi_av**	weak absorption	**(blank)**	(blank)
1844	**Mi_M_5_av**	weak absorption	**quartz**	Spectrum M_av, spectrum Q_av
1854	**Mi_av**	weak absorption	**C-O**	Ploeger et al, 2010, p. 37
1855	**Mi_M_5_av**	weak absorption	**quartz**	Spectrum M_av, spectrum Q_av
1942	**Mi_M_5_av**	weak absorption	**quartz**	Spectrum M_av, spectrum Q_av
1966	**Mi_M_5_av**	weak absorption	**quartz**	Spectrum M_av, spectrum Q_av
1972	**Mi_av**	weak absorption	**(blank)**	(blank)
2083	**Mi_av**	weak absorption	**(blank)**	(blank)
2135	**Mi_M_5_av**	weak absorption	**calcium carbonate and quartz**	Spectrum Ca_av, spectrum M_av, spectrum Q_av
2197	**Mi_av**	weak absorption	**(blank)**	(blank)
2237	**Mi_M_5_av**	weak absorption	**quartz**	spectrum Q_av
2431	**Mi_av**	weak absorption	**(blank)**	(blank)
2511	**Mi_M_5_av**	combination band	**v1+v3**	Spectrum M_av, spectrum Ca_av, Ricci et al, 2006, p. 1222
2530	**Mi_av**	weak absorption	**(blank)**	(blank)
2546	**Mi_av**	weak absorption	**(blank)**	(blank)
2640	**Mi_av**	(blank)	**(blank)**	(blank)
2647	**Mi_av**	(blank)	**(blank)**	(blank)
2655	**Mi_av**	(blank)	**(blank)**	(blank)
2664	**Mi_av**	(blank)	**(blank)**	(blank)
2688	**Mi_M_5_av**	weak absorption	**(blank)**	(blank)
2699	**Mi_M_5_av**	weak absorption	**(blank)**	(blank)
2860	**Mi_av**	sharp absorption	**C=O stretching band**	Rosi et al, 2009, p. 2099
2872	**Mi_M_5_av**	sharp and weak absorption	**CaCO3**	Spectrum Ca_av, spectrum M_av
2926	**Mi_M_5_av**	strong absorption	**CH stretching**	Spectrum Mi_av, Daher et al, 2017, p.8
2938	**Mi_av**	strong absorption	**CH stretching**	Daher et al, 2017, p.8
2958	**Mi_M_5_av**	sharp absorption	**CH2 stretching**	Ploeger et al, 2010, p. 37
2967	**Mi_av**	sharp absorption	**CH2 stretching**	Ploeger et al, 2010, p. 37
3643	**Mi_M_5_av**	doublet	**OH stretching**	Spectrum M_av, spectrum Ca_av, Rosi et al, 2009, p. 2100

Figure 29: continued.

7.5.8 Rice and mortar mixtures CPAD

Peak x (position)	Spectrum ID	Type of band	Chemical Band Assignement	Reference
622	**R_av**	(blank)	**(blank)**	(blank)
	R_M_75_av	weak absorption	**rice**	Spectrum R_av
667	**R_av**	(blank)	**(blank)**	(blank)
689	**R_av**	(blank)	**(blank)**	(blank)
701	**R_M_75_av**	sharp absorption	**quartz**	Spectrum M_av, spectrum Q_av
714	**R_M_75_av**	sharp absorption	**v4 carbonate ion**	Spectrum M_av, spectrum Ca_av, Ylmen and Jaglid, 2013, p. 119
726	**R_av**	(blank)	**(blank)**	(blank)
779	**R_av**	overlapping	**CO, CC stretching, COH bending**	Synytsya and Novak, 2014, p.6
792	**R_M_75_av**	sharp absorption	**quartz**	Spectrum M_av, spectrum Q_av
815	**R_M_75_av**	sharp absorption	**quartz**	Spectrum M_av, spectrum Q_av
877	**R_M_75_av**	sharp absorption	**v2 carbonate ion**	Spectrum M_av, spectrum Ca_av, Ylmen and Jaglid, 2013, p. 119
940	**R_av**	overlapping	**sugar region**	Synytsya and Novak, 2014, p.6
1006	**R_av**	(blank)	**(blank)**	(blank)
1065	**R_av**	(blank)	**(blank)**	(blank)
1093	**R_av**	(blank)	**(blank)**	(blank)
1116	**R_av**	(blank)	**(blank)**	(blank)
1130	**R_av**	(blank)	**(blank)**	(blank)
1159	**R_M_75_av**	sharp absorption	**quartz**	Spectrum M_av, spectrum Q_av
1167	**R_av**	(blank)	**(blank)**	(blank)
1204	**R_av**	overlapping	**sugar region**	Synytsya and Novak, 2014, p.6
1266	**R_av**	(blank)	**(blank)**	(blank)
1302	**R_av**	overlapping	**CO, CC stretching, COH bending**	Synytsya and Novak, 2014, p.6
1341	**R_av**	(blank)	**(blank)**	(blank)
1388	**R_av**	weak absorption	**C-H stretching**	Buti et al, 2013, p. 2705
1399	**R_M_75_av**	strong absorption	**CaCO3**	Spectrum M_av, spectrum Ca_av
1423	**R_av**	(blank)	**CH2, CH, OH bending**	Synytsya and Novak, 2014, p.6
1430	**R_av**	(blank)	**(blank)**	(blank)
1439	**R_M_75_av**	strong absorption	**v3 antisymmetric stretching CO3-2**	Spectrum M_av, spectrum Ca_av, Ylmen and Jaglid, 2013, p. 119
1448	**R_M_75_av**	strong absorption	**v3 antisymmetric stretching CO3-2**	Spectrum M_av, spectrum Ca_av, Ylmen and Jaglid, 2013, p. 119
1459	**R_M_75_av**	strong absorption	**v3 antisymmetric stretching CO3-2**	Spectrum Ca_av, Ylmen and Jaglid, 2013, p. 119

Figure 30: Filtered CPAD entries of rice (R_av) and 75% rice/mortar mixture (R_M_75_av).

1466	**R_M_75_av**	strong absorption	**v3 antisymmetric stretching CO3-2**	Spectrum Ca_av, Ylmen and Jaglid, 2013, p. 119
1472	**R_av**	(blank)	**C-H bending**	Buti et al, 2013, p. 2705
1474	**R_M_75_av**	strong absorption	**C-H bending**	Spectrum R_av, Buti et al, 2013, p. 2705
1507	**R_av**	(blank)	**(blank)**	(blank)
1528	**R_M_75_av**	weak absorption	**rice**	Spectrum R_av
1539	**R_M_75_av**	weak absorption	**rice**	Spectrum R_av
1540	**R_av**	(blank)	**(blank)**	(blank)
1559	**R_av**	(blank)	**(blank)**	(blank)
1578	**R_M_75_av**	strong absorption	**v3 antisymmetric stretching CO3-2**	Spectrum Ca_av, Ylmen and Jaglid, 2013, p. 119
1585	**R_M_75_av**	strong absorption	**quartz**	Spectrum M_av, spectrum Q_av
1597	**R_av**	(blank)	**(blank)**	(blank)
	R_M_75_av	strong absorption	**rice**	Spectrum R_av
1616	**R_M_75_av**	strong absorption	**quartz**	Spectrum M_av, spectrum Q_av
1625	**R_M_75_av**	strong absorption	**quartz**	Spectrum M_av, spectrum Q_av
1634	**R_M_75_av**	strong absorption	**quartz**	Spectrum M_av, spectrum Q_av
1644	**R_M_75_av**	strong absorption	**quartz**	Spectrum M_av, spectrum Q_av
1659	**R_M_75_av**	strong absorption	**quartz**	Spectrum M_av, spectrum Q_av
1668	**R_av**	strong absorption	**v2 bending H2O**	Ylmen and Jaglid, 2013, p. 119
1678	**R_av**	strong absorption	**v2 bending H2O**	Ylmen and Jaglid, 2013, p. 119
1746	**R_M_75_av**	sharp absorption	**rice**	Spectrum R_av
1761	**R_av**	(blank)	**(blank)**	(blank)
1794	**R_M_75_av**	combination band	**v1+v4**	Spectrum M_av, spectrum Ca_av, Ricci et al, 2006, p. 1222
1845	**R_M_75_av**	weak absorption	**quartz**	Spectrum M_av, spectrum Q_av
1868	**R_M_75_av**	weak absorption	**quartz**	Spectrum M_av, spectrum Q_av
1943	**R_M_75_av**	weak absorption	**quartz**	Spectrum M_av, spectrum Q_av
1955	**R_M_75_av**	weak absorption	**quartz**	Spectrum M_av, spectrum Q_av
1967	**R_M_75_av**	weak absorption	**quartz**	Spectrum M_av, spectrum Q_av
1992	**R_M_75_av**	weak absorption	**v+δ Si-O**	Spectrum M_av, spectrum Q_av, Miliani et al, 2012, p. 303
2136	**R_M_75_av**	weak absorption	**calcium carbonate and quartz**	Spectrum Ca_av, spectrum M_av, spectrum Q_av
2236	**R_M_75_av**	weak absorption	**quartz**	spectrum Q_av
2511	**R_M_75_av**	combination band	**v1+v3**	Spectrum M_av, spectrum Ca_av, Ricci et al, 2006, p. 1222
2576	**R_M_75_av**	weak absorption	**CaCO3**	(blank)
2588	**R_M_75_av**	weak absorption	**CaCO3**	(blank)
2686	**R_M_75_av**	weak absorption	**(blank)**	(blank)
2855	**R_M_75_av**	strong absorption	**CH stretching**	Spectrum E_av, Daher et al, 2017, p.8
2872	**R_M_75_av**	sharp and weak absorption	**CaCO3**	Spectrum Ca_av, spectrum M_av
2876	**R_av**	strong absorption	**C-H stretching**	Rosi et al, 2009, p. 2099
2926	**R_M_75_av**	strong absorption	**CH stretching**	Spectrum E_av, Daher et al, 2017, p.8
2970	**R_av**	strong absorption	**C-H stretching**	Rosi et al, 2009, p. 2099
3010	**R_M_75_av**	weak absorption	**CH stretching**	Miliani et al, 2012, p. 302

Figure 30: continued.

Peak x (position)	Spectrum ID	Type of band	Chemical Band Assignement	Reference
622	R_av	(blank)	(blank)	(blank)
627	R_M_50_av	weak absorption	rice	Spectrum R_av
646	R_M_50_av	weak absorption	rice	Spectrum R_av
667	R_av	(blank)	(blank)	(blank)
685	R_M_50_av	weak absorption	rice	Spectrum R_av
689	R_av	(blank)	(blank)	(blank)
714	R_M_50_av	sharp absorption	v4 carbonate ion	Spectrum M_av, spectrum Ca_av, Ylmen and Jaglid, 2013, p. 119
726	R_av	(blank)	(blank)	(blank)
779	R_av	overlapping	CO, CC stretching, COH bending	Synytsya and Novak, 2014, p.6
792	R_M_50_av	sharp absorption	quartz	Spectrum M_av, spectrum Q_av
814	R_M_50_av	sharp absorption	quartz	Spectrum M_av, spectrum Q_av
848	R_M_50_av	sharp and weak absorption	v2 carbonate ion	Spectrum M_av, spectrum Ca_av, Ylmen and Jaglid, 2013, p. 119
880	R_M_50_av	sharp absorption	v2 carbonate ion	Spectrum M_av, spectrum Ca_av, Ylmen and Jaglid, 2013, p. 119
924	R_M_50_av	overlapping	sugar region	Spectrum R_av, Synytsya and Novak, 2014, p. 6
940	R_av	overlapping	sugar region	Synytsya and Novak, 2014, p.6
1001	R_M_50_av	strong absorption	rice	Spectrum R_av
1006	R_av	(blank)	(blank)	(blank)
1065	R_av	(blank)	(blank)	(blank)
1083	R_M_50_av	sharp and weak absorption	v1 carbonate ion	Spectrum M_av, spectrum Ca_av, Ylmen and Jaglid, 2013, p. 119
1093	R_av	(blank)	(blank)	(blank)
1116	R_av	(blank)	(blank)	(blank)
1130	R_av	(blank)	(blank)	(blank)
1158	R_M_50_av	sharp absorption	quartz	Spectrum M_av, spectrum Q_av
1167	R_av	(blank)	(blank)	(blank)
1204	R_av	overlapping	sugar region	Synytsya and Novak, 2014, p.6
1266	R_av	(blank)	(blank)	(blank)
1302	R_av	overlapping	CO, CC stretching, COH bending	Synytsya and Novak, 2014, p.6
1341	R_av	(blank)	(blank)	(blank)
1388	R_av	weak absorption	C-H stretching	Buti et al, 2013, p. 2705
1396	R_M_50_av	strong absorption	CaCO3	Spectrum M_av, spectrum Ca_av
1423	R_av	(blank)	CH2, CH, OH bending	Synytsya and Novak, 2014, p.6
1430	R_av	(blank)	(blank)	(blank)
1439	R_M_50_av	strong absorption	v3 antisymmetric stretching CO3-2	Spectrum M_av, spectrum Ca_av, Ylmen and Jaglid, 2013, p. 119
1449	R_M_50_av	strong absorption	v3 antisymmetric stretching CO3-2	Spectrum Ca_av, Ylmen and Jaglid, 2013, p. 119
1467	R_M_50_av	strong absorption	v3 antisymmetric stretching CO3-2	Spectrum Ca_av, Ylmen and Jaglid, 2013, p. 119
1472	R_av	(blank)	C-H bending	Buti et al, 2013, p. 2705
1507	R_av	(blank)	(blank)	(blank)

Figure 31: Filtered CPAD entries of rice (R_av) and 50% rice/mortar mixture (R_M_50_av).

1540	**R_av**	(blank)	**(blank)**	(blank)
1559	**R_av**	(blank)	**(blank)**	(blank)
1582	**R_M_50_av**	strong absorption	**v3 antisymmetric stretching CO3-2**	Spectrum Ca_av, Ylmen and Jaglid, 2013, p. 119
1597	**R_av**	(blank)	**(blank)**	(blank)
1612	**R_M_50_av**	strong absorption	**quartz**	Spectrum M_av, spectrum Q_av
1620	**R_M_50_av**	strong absorption	**quartz**	Spectrum M_av, spectrum Q_av
1652	**R_M_50_av**	strong absorption	**quartz**	Spectrum M_av, spectrum Q_av
1668	**R_av**	strong absorption	**v2 bending H2O**	Ylmen and Jaglid, 2013, p. 119
1678	**R_av**	strong absorption	**v2 bending H2O**	Ylmen and Jaglid, 2013, p. 119
1746	**R_M_50_av**	sharp absorption	**rice**	Spectrum R_av
1761	**R_av**	(blank)	**(blank)**	(blank)
1794	**R_M_50_av**	combination band	**v1+v4**	Spectrum M_av, spectrum Ca_av, Ricci et al, 2006, p. 1222
1843	**R_M_50_av**	weak absorption	**quartz**	Spectrum M_av, spectrum Q_av
1867	**R_M_50_av**	weak absorption	**quartz**	Spectrum M_av, spectrum Q_av
1941	**R_M_50_av**	weak absorption	**quartz**	Spectrum M_av, spectrum Q_av
2135	**R_M_50_av**	weak absorption	**calcium carbonate and quartz**	Spectrum Ca_av, spectrum M_av, spectrum Q_av
2237	**R_M_50_av**	weak absorption	**quartz**	spectrum Q_av
2512	**R_M_50_av**	combination band	**v1+v3**	Spectrum M_av, spectrum Ca_av, Ricci et al, 2006, p. 1222
2586	**R_M_50_av**	weak absorption	**CaCO3**	(blank)
2857	**R_M_50_av**	strong absorption	**CH stretching**	Spectrum E_av, Daher et al, 2017, p.8
2872	**R_M_50_av**	sharp and weak absorption	**CaCO3**	Spectrum Ca_av, spectrum M_av
2876	**R_av**	strong absorption	**C-H stretching**	Rosi et al, 2009, p. 2099
2927	**R_M_50_av**	strong absorption	**CH stretching**	Spectrum E_av, Daher et al, 2017, p.8
2970	**R_av**	strong absorption	**C-H stretching**	Rosi et al, 2009, p. 2099
3008	**R_M_50_av**	weak absorption	**CH stretching**	Miliani et al, 2012, p. 302
3643	**R_M_50_av**	doublet	**OH stretching**	Spectrum M_av, spectrum Ca_av, Rosi et al, 2009, p. 2100

Figure 31: continued.

Peak x (position)	Spectrum ID	Type of band	Chemical Band Assignement	Reference
621	R_M_25_av	weak absorption	rice	Spectrum R_av
622	R_av	(blank)	(blank)	(blank)
648	R_M_25_av	weak absorption	rice	Spectrum R_av
659	R_M_25_av	weak absorption	rice	Spectrum R_av
667	R_av	(blank)	(blank)	(blank)
688	R_M_25_av	weak absorption	rice	Spectrum R_av
689	R_av	(blank)	(blank)	(blank)
714	R_M_25_av	sharp absorption	v4 carbonate ion	Spectrum M_av, spectrum Ca_av, Ylmen and Jaglid, 2013, p. 119
726	R_av	(blank)	(blank)	(blank)
779	R_av	overlapping	CO, CC stretching, COH bending	Synytsya and Novak, 2014, p.6
793	R_M_25_av	sharp absorption	quartz	Spectrum M_av, spectrum Q_av
816	R_M_25_av	sharp absorption	quartz	Spectrum M_av, spectrum Q_av
848	R_M_25_av	sharp and weak absorption	v2 carbonate ion	Spectrum M_av, spectrum Ca_av, Ylmen and Jaglid, 2013, p. 119
880	R_M_25_av	sharp absorption	v2 carbonate ion	Spectrum M_av, spectrum Ca_av, Ylmen and Jaglid, 2013, p. 119
940	R_av	overlapping	sugar region	Synytsya and Novak, 2014, p.6
999	R_M_25_av	weak absorption	CaCO3	spectrum Ca_av
1006	R_av	(blank)	(blank)	(blank)
1019	R_M_25_av	strong absorption	rice	Spectrum R_av
1065	R_av	(blank)	(blank)	(blank)
1080	R_M_25_av	sharp and weak absorption	v1 carbonate ion	Spectrum M_av, spectrum Ca_av, Ylmen and Jaglid, 2013, p. 119
1093	R_av	(blank)	(blank)	(blank)
1116	R_av	(blank)	(blank)	(blank)
1130	R_av	(blank)	(blank)	(blank)
1159	R_M_25_av	sharp absorption	quartz	Spectrum M_av, spectrum Q_av
1167	R_av	(blank)	(blank)	(blank)
1204	R_av	overlapping	sugar region	Synytsya and Novak, 2014, p.6
1266	R_av	(blank)	(blank)	(blank)
1302	R_av	overlapping	CO, CC stretching, COH bending	Synytsya and Novak, 2014, p.6
1341	R_av	(blank)	(blank)	(blank)
1388	R_av	weak absorption	C-H stretching	Buti et al, 2013, p. 2705
1397	R_M_25_av	strong absorption	CaCO3	Spectrum M_av, spectrum Ca_av

Figure 32: Filtered CPAD entries of rice (R_av) and 25% rice mortar mixture (R_M_25_av).

1423	**R_av**	(blank)	**CH2, CH, OH bending**	Synytsya and Novak, 2014, p.6
1430	**R_av**	(blank)	**(blank)**	(blank)
1439	**R_M_25_av**	strong absorption	**v3 antisymmetric stretching CO3-2**	Spectrum M_av, spectrum Ca_av, Ylmen and Jaglid, 2013, p. 119
1448	**R_M_25_av**	strong absorption	**v3 antisymmetric stretching CO3-2**	Spectrum M_av, spectrum Ca_av, Ylmen and Jaglid, 2013, p. 119
1467	**R_M_25_av**	strong absorption	**v3 antisymmetric stretching CO3-2**	Spectrum M_av, spectrum Ca_av, Ylmen and Jaglid, 2013, p. 119
1472	**R_av**	(blank)	**C-H bending**	Buti et al, 2013, p. 2705
1475	**R_M_25_av**	weak absorption	**C-H bending**	Spectrum R_av, Buti et al, 2013, p. 2705
1507	**R_av**	(blank)	**(blank)**	(blank)
1518	**R_M_25_av**	weak absorption	**rice**	Spectrum R_av
1535	**R_M_25_av**	weak absorption	**rice**	Spectrum R_av
1540	**R_av**	(blank)	**(blank)**	(blank)
1559	**R_av**	(blank)	**(blank)**	(blank)
1582	**R_M_25_av**	strong absorption	**v3 antisymmetric stretching CO3-2**	Spectrum Ca_av, Ylmen and Jaglid, 2013, p. 119
1597	**R_av**	(blank)	**(blank)**	(blank)
1652	**R_M_25_av**	strong absorption	**quartz**	Spectrum M_av, spectrum Q_av
1668	**R_av**	strong absorption	**v2 bending H2O**	Ylmen and Jaglid, 2013, p. 119
1678	**R_av**	strong absorption	**v2 bending H2O**	Ylmen and Jaglid, 2013, p. 119
1761	**R_av**	(blank)	**(blank)**	(blank)
1794	**R_M_25_av**	combination band	**v1+v4**	Spectrum M_av, spectrum Ca_av, Ricci et al, 2006, p. 1222
1844	**R_M_25_av**	weak absorption	**quartz**	Spectrum M_av, spectrum Q_av
1867	**R_M_25_av**	weak absorption	**quartz**	Spectrum M_av, spectrum Q_av
1941	**R_M_25_av**	weak absorption	**quartz**	Spectrum M_av, spectrum Q_av
1961	**R_M_25_av**	weak absorption	**quartz**	Spectrum M_av, spectrum Q_av
2135	**R_M_25_av**	weak absorption	**calcium carbonate and quartz**	Spectrum Ca_av, spectrum M_av, spectrum Q_av
2238	**R_M_25_av**	weak absorption	**quartz**	spectrum Q_av
2512	**R_M_25_av**	combination band	**v1+v3**	Spectrum M_av, spectrum Ca_av, Ricci et al, 2006, p. 1222
2688	**R_M_25_av**	weak absorption	**(blank)**	(blank)
2697	**R_M_25_av**	weak absorption	**(blank)**	(blank)
2709	**R_M_25_av**	weak absorption	**rice**	Spectrum R_av
2857	**R_M_25_av**	strong absorption	**CH stretching**	Spectrum E_av, Daher et al, 2017, p.8
2873	**R_M_25_av**	sharp and weak absorption	**CaCO3**	Spectrum Ca_av, spectrum M_av
2876	**R_av**	strong absorption	**C-H stretching**	Rosi et al, 2009, p. 2099
2926	**R_M_25_av**	strong absorption	**CH stretching**	Spectrum E_av, Daher et al, 2017, p.8
2970	**R_av**	strong absorption	**C-H stretching**	Rosi et al, 2009, p. 2099
3009	**R_M_25_av**	weak absorption	**CH stretching**	Miliani et al, 2012, p. 302
3565	**R_M_25_av**	weak absorption	**quartz**	Spectrum M_av, spectrum Q_av
3643	**R_M_25_av**	doublet	**OH stretching**	Spectrum M_av, spectrum Ca_av, Rosi et al, 2009, p. 2100

Figure 32: continued.

Peak x (position)	Spectrum ID	Type of band	Chemical Band Assignement	Reference
622	**R_av**	(blank)	**(blank)**	(blank)
624	**R_M_5_av**	weak absorption	**rice**	Spectrum R_av
642	**R_M_5_av**	weak absorption	**rice**	Spectrum R_av
649	**R_M_5_av**	weak absorption	**rice**	Spectrum R_av
667	**R_av**	(blank)	**(blank)**	(blank)
668	**R_M_5_av**	weak absorption	**rice**	Spectrum R_av
689	**R_av**	(blank)	**(blank)**	(blank)
714	**R_M_5_av**	sharp absorption	**v4 carbonate ion**	Spectrum M_av, spectrum Ca_av, Ylmen and Jaglid, 2013, p. 119
726	**R_av**	(blank)	**(blank)**	(blank)
779	**R_av**	overlapping	**CO, CC stretching, COH bending**	Synytsya and Novak, 2014, p.6
792	**R_M_5_av**	sharp absorption	**quartz**	Spectrum M_av, spectrum Q_av
815	**R_M_5_av**	sharp absorption	**quartz**	Spectrum M_av, spectrum Q_av
848	**R_M_5_av**	sharp and weak absorption	**v2 carbonate ion**	Spectrum M_av, spectrum Ca_av, Ylmen and Jaglid, 2013, p. 119
880	**R_M_5_av**	sharp absorption	**v2 carbonate ion**	Spectrum M_av, spectrum Ca_av, Ylmen and Jaglid, 2013, p. 119
940	**R_av**	overlapping	**sugar region**	Synytsya and Novak, 2014, p.6
1006	**R_av**	(blank)	**(blank)**	(blank)
1065	**R_av**	(blank)	**(blank)**	(blank)
1080	**R_M_5_av**	sharp and weak absorption	**v1 carbonate ion**	Spectrum M_av, spectrum Ca_av, Ylmen and Jaglid, 2013, p. 119
1093	**R_av**	(blank)	**(blank)**	(blank)
1116	**R_av**	(blank)	**(blank)**	(blank)
1130	**R_av**	(blank)	**(blank)**	(blank)
1159	**R_M_5_av**	sharp absorption	**quartz**	Spectrum M_av, spectrum Q_av
1167	**R_av**	(blank)	**(blank)**	(blank)
1204	**R_av**	overlapping	**sugar region**	Synytsya and Novak, 2014, p.6
1266	**R_av**	(blank)	**(blank)**	(blank)
1302	**R_av**	overlapping	**CO, CC stretching, COH bending**	Synytsya and Novak, 2014, p.6
1341	**R_av**	(blank)	**(blank)**	(blank)
1388	**R_av**	weak absorption	**C-H stretching**	Buti et al, 2013, p. 2705
1398	**R_M_5_av**	strong absorption	**CaCO3**	Spectrum M_av, spectrum Ca_av

Figure 33: Filtered CPAD entries of rice (R_av) and 5% rice/mortar mixture (R_M_5_av).

1423	**R_av**	(blank)	**CH2, CH, OH bending**	Synytsya and Novak, 2014, p.6
1430	**R_av**	(blank)	**(blank)**	(blank)
1432	**R_M_5_av**	strong absorption	**v3 antisymmetric stretching CO3-2**	Spectrum M_av, spectrum Ca_av, Ylmen and Jaglid, 2013, p. 119
1443	**R_M_5_av**	strong absorption	**v3 antisymmetric stretching CO3-2**	Spectrum M_av, spectrum Ca_av, Ylmen and Jaglid, 2013, p. 119
1460	**R_M_5_av**	strong absorption	**v3 antisymmetric stretching CO3-2**	Spectrum M_av, spectrum Ca_av, Ylmen and Jaglid, 2013, p. 119
1472	**R_av**	(blank)	**C-H bending**	Buti et al, 2013, p. 2705
1507	**R_av**	(blank)	**(blank)**	(blank)
1540	**R_av**	(blank)	**(blank)**	(blank)
1559	**R_av**	(blank)	**(blank)**	(blank)
1587	**R_M_5_av**	strong absorption	**v3 antisymmetric stretching CO3-2**	Spectrum Ca_av, Ylmen and Jaglid, 2013, p. 119
1596	**R_M_5_av**	strong absorption	**quartz**	Spectrum M_av, spectrum Q_av
1597	**R_av**	(blank)	**(blank)**	(blank)
1668	**R_av**	strong absorption	**v2 bending H2O**	Ylmen and Jaglid, 2013, p. 119
1678	**R_av**	strong absorption	**v2 bending H2O**	Ylmen and Jaglid, 2013, p. 119
1761	**R_av**	(blank)	**(blank)**	(blank)
1795	**R_M_5_av**	combination band	**v1+v4**	Spectrum M_av, spectrum Ca_av, Ricci et al, 2006, p. 1222
1856	**R_M_5_av**	weak absorption	**quartz**	Spectrum M_av, spectrum Q_av
1868	**R_M_5_av**	weak absorption	**quartz**	Spectrum M_av, spectrum Q_av
1961	**R_M_5_av**	weak absorption	**quartz**	Spectrum M_av, spectrum Q_av
2135	**R_M_5_av**	weak absorption	**calcium carbonate and quartz**	Spectrum Ca_av, spectrum M_av, spectrum Q_av
2237	**R_M_5_av**	weak absorption	**quartz**	spectrum Q_av
2512	**R_M_5_av**	combination band	**v1+v3**	Spectrum M_av, spectrum Ca_av, Ricci et al, 2006, p. 1222
2670	**R_M_5_av**	weak absorption	**(blank)**	(blank)
2680	**R_M_5_av**	weak absorption	**(blank)**	(blank)
2692	**R_M_5_av**	weak absorption	**(blank)**	(blank)
2719	**R_M_5_av**	weak absorption	**rice**	Spectrum R_av
2873	**R_M_5_av**	sharp and weak absorption	**CaCO3**	Spectrum Ca_av, spectrum M_av
2876	**R_av**	strong absorption	**C-H stretching**	Rosi et al, 2009, p. 2099
2933	**R_M_5_av**	strong absorption	**CH stretching**	Daher et al, 2017, p.8
2970	**R_av**	strong absorption	**C-H stretching**	Rosi et al, 2009, p. 2099
2979	**R_M_5_av**	strong absorption	**CaCO3**	Spectrum Ca_av, spectrum M_av
3643	**R_M_5_av**	doublet	**OH stretching**	Spectrum M_av, spectrum Ca_av, Rosi et al, 2009, p. 2100

Figure 33: continued.

7.5.9 Asphalt and mortar mixtures CPAD

Peak x (position)	Spectrum ID	Type of band	Chemical Band Assignement	Reference
723	**A_av**	triplet	**(blank)**	Lombardi and Santarelli, 2009, 542
724	**A_M_75_av**	triplet	**asphalt**	Spectrum A_av, Lombardi and Santarelli, 2009, 542
742	**A_av**	triplet	**(blank)**	Lombardi and Santarelli, 2009, 542
	A_M_75_av	triplet	**asphalt**	Spectrum A_av, Lombardi and Santarelli, 2009, 542
759	**A_M_75_av**	(blank)	**(blank)**	(blank)
814	**A_av**	triplet	**(blank)**	Lombardi and Santarelli, 2009, 542
	A_M_75_av	triplet	**asphalt**	Spectrum A_av, Lombardi and Santarelli, 2009, 542
868	**A_av**	triplet	**(blank)**	Lombardi and Santarelli, 2009, 542
872	**A_M_75_av**	triplet	**asphalt**	Spectrum A_av, Lombardi and Santarelli, 2009, 542
937	**A_av**	(blank)	**(blank)**	(blank)
	A_M_75_av	(blank)	**asphalt**	Spectrum A_av
976	**A_av**	(blank)	**(blank)**	(blank)
	A_M_75_av	(blank)	**asphalt**	Spectrum A_av
1032	**A_av**	sharp absorption	**quartz**	Lombardi and Santarelli, 2009, 542
1033	**A_M_75_av**	sharp absorption	**quartz**	Spectrum A_av, Lombardi and Santarelli, 2009, 542
1064	**A_av**	(blank)	**(blank)**	(blank)
1169	**A_av**	weak absorption	**(blank)**	(blank)
	A_M_75_av	weak absorption	**asphalt**	Spectrum A_av
1314	**A_av**	weak absorption	**CH2, CH3**	Lombardi and Santarelli, 2009, 542
1377	**A_av**	strong absorption	**CH2, CH3**	Lombardi and Santarelli, 2009, 542
1378	**A_M_75_av**	strong absorption	**CH2, CH3**	Spectrum A_av, Lombardi and Santarelli, 2009, 542
1461	**A_av**	strong absorption	**(blank)**	(blank)
	A_M_75_av	strong absorption	**asphalt**	Spectrum A_av
1603	**A_av**	strong absorption	**C6H6 (benzene rings)**	Lombardi and Santarelli, 2009, 542
	A_M_75_av	strong absorption	**C6H6 (benzene rings)**	Spectrum A_av, Lombardi and Santarelli, 2009, 542
1643	**A_av**	(blank)	**(blank)**	(blank)
	A_M_75_av	weak absorption	**(blank)**	Spectrum A_av
1649	**A_av**	(blank)	**(blank)**	(blank)

Figure 34: Filtered CPAD entries of asphalt (A_av) and 75% asphalt/mortar mixture (A_M_75_av).

1843	**A_av**	weak absorption	**quartz**	Spectrum Q_av, spectrum M_av, spectrum A_av
	A_M_75_av	weak absorption	**quartz**	Spectrum Q_av, spectrum M_av, spectrum A_av
1866	**A_M_75_av**	weak absorption	**quartz**	Spectrum Q_av, spectrum M_av, spectrum A_av
1867	**A_av**	weak absorption	**quartz**	Spectrum Q_av, spectrum M_av, spectrum A_av
1888	**A_av**	weak absorption	**quartz**	spectrum A_av, spectrum Q_av
	A_M_75_av	weak absorption	**quartz**	spectrum A_av, spectrum Q_av
2032	**A_M_75_av**	weak absorption	**(blank)**	Spectrum A_av
2039	**A_av**	(blank)	**(blank)**	(blank)
2727	**A_av**	(blank)	**(blank)**	(blank)
	A_M_75_av	weak absorption	**(blank)**	Spectrum A_av
2858	**A_av**	strong absorption	**CH2, CH3 stretching**	Lombardi and Santarelli, 2009, 542
	A_M_75_av	strong absorption	**CH2, CH3 stretching**	Spectrum A_av, Lombardi and Santarelli, 2009, 542
2866	**A_av**	strong absorption	**CH2, CH3 stretching**	Lombardi and Santarelli, 2009, 542
2867	**A_M_75_av**	strong absorption	**CH2, CH3 stretching**	Spectrum A_av, Lombardi and Santarelli, 2009, 542
2931	**A_M_75_av**	strong absorption	**CH2, CH3 stretching**	Spectrum A_av, Lombardi and Santarelli, 2009, 542
2932	**A_av**	strong absorption	**CH2, CH3 stretching**	Lombardi and Santarelli, 2009, 542
2954	**A_av**	strong absorption	**CH2, CH3 stretching**	Lombardi and Santarelli, 2009, 542
	A_M_75_av	strong absorption	**CH2, CH3 stretching**	Spectrum A_av, Lombardi and Santarelli, 2009, 542
2961	**A_M_75_av**	strong absorption	**CH2, CH3 stretching**	Spectrum A_av, Lombardi and Santarelli, 2009, 542
3190	**A_av**	(blank)	**(blank)**	(blank)
3200	**A_M_75_av**	weak absorption	**asphalt**	Spectrum A_av
3205	**A_av**	(blank)	**(blank)**	(blank)
3215	**A_M_75_av**	weak absorption	**asphalt**	Spectrum A_av
3267	**A_av**	(blank)	**(blank)**	(blank)
	A_M_75_av	weak absorption	**asphalt**	Spectrum A_av
3276	**A_av**	(blank)	**(blank)**	(blank)
3288	**A_M_75_av**	weak absorption	**asphalt**	Spectrum A_av
3473	**A_av**	(blank)	**(blank)**	(blank)
	A_M_75_av	weak absorption	**asphalt**	Spectrum A_av
3664	**A_av**	(blank)	**(blank)**	(blank)
	A_M_75_av	weak absorption	**asphalt**	Spectrum A_av

Figure 34: continued.

Peak x (position)	Spectrum ID	Type of band	Chemical Band Assignement	Reference
722	A_M_50_av	triplet	asphalt	Spectrum A_av, Lombardi and Santarelli, 2009, 542
723	A_av	triplet	(blank)	Lombardi and Santarelli, 2009, 542
740	A_M_50_av	triplet	asphalt	Spectrum A_av, Lombardi and Santarelli, 2009, 542
742	A_av	triplet	(blank)	Lombardi and Santarelli, 2009, 542
793	A_M_50_av	weak absorption	quartz	Spectrum Q_av, spectrum M_av
814	A_av	triplet	(blank)	Lombardi and Santarelli, 2009, 542
815	A_M_50_av	sharp absorption	Si-O antisymmetric stretching	Spectrum Q_av, spectrum M_av, Miliani et al, 2013, p. 303
849	A_M_50_av	weak absorption	v2 carbonate ion	Spectrum Ca_av, spectrum M_av, Ylmen and Jaglid, 2013, p. 119
868	A_av	triplet	(blank)	Lombardi and Santarelli, 2009, 542
872	A_M_50_av	triplet	asphalt	Spectrum A_av, Lombardi and Santarelli, 2009, 542
934	A_M_50_av	weak absorption	asphalt	Spectrum A_av
937	A_av	(blank)	(blank)	(blank)
953	A_M_50_av	weak absorption	(blank)	(blank)
976	A_av	(blank)	(blank)	(blank)
	A_M_50_av	weak absorption	asphalt	Spectrum A_av
1016	A_M_50_av	(blank)	(blank)	(blank)
1030	A_M_50_av	(blank)	quartz	Spectrum A_av, Lombardi and Santarelli, 2009, 542
1032	A_av	sharp absorption	quartz	Lombardi and Santarelli, 2009, 542
1064	A_av	(blank)	(blank)	(blank)
1160	A_M_50_av	sharp absorption	quartz	Spectrum A_av, spectrum Q_av, spectrum M_av
1169	A_av	weak absorption	(blank)	(blank)
1314	A_av	weak absorption	CH2, CH3	Lombardi and Santarelli, 2009, 542
1377	A_av	strong absorption	CH2, CH3	Lombardi and Santarelli, 2009, 542
1378	A_M_50_av	strong absorption	CH2, CH3	Spectrum A_av, Lombardi and Santarelli, 2009, 542
1461	A_av	strong absorption	(blank)	(blank)
	A_M_50_av	strong absorption	asphalt	Spectrum A_av
1603	A_av	strong absorption	C6H6 (benzene rings)	Lombardi and Santarelli, 2009, 542
	A_M_50_av	strong absorption	C6H6 (benzene rings)	Spectrum A_av, Lombardi and Santarelli, 2009, 542
1643	A_av	(blank)	(blank)	(blank)
	A_M_50_av	shoulder	(blank)	Spectrum A_av
1649	A_av	(blank)	(blank)	(blank)

Figure 35: Filtered CPAD entries of asphalt (A_av) and 50% asphalt/mortar mixture (A_M_50_av).

1792	**A_M_50_av**	combination band	**v1+v4**	Spectrum Ca_av, spectrum M_av, Ricci et al, 2006, p. 1222
1843	**A_av**	weak absorption	**quartz**	Spectrum Q_av, spectrum M_av, spectrum A_av
	A_M_50_av	weak absorption	**quartz**	Spectrum Q_av, spectrum M_av, spectrum A_av
1867	**A_av**	weak absorption	**quartz**	Spectrum Q_av, spectrum M_av, spectrum A_av
	A_M_50_av	weak absorption	**quartz**	Spectrum Q_av, spectrum M_av, spectrum A_av
1888	**A_av**	weak absorption	**quartz**	spectrum A_av, spectrum Q_av
	A_M_50_av	weak absorption	**quartz**	Spectrum Q_av, spectrum A_av
2016	**A_M_50_av**	weak absorption	**asphalt**	Spectrum A_av
2023	**A_M_50_av**	weak absorption	**asphalt**	Spectrum A_av
2039	**A_av**	(blank)	**(blank)**	(blank)
2138	**A_M_50_av**	weak absorption	**(blank)**	Spectrum Q_av, spectrum M_av, spectrum Ca_av
2519	**A_M_50_av**	combination band	**v1+v3**	Spectrum M_av, spectrum Ca_av, Ricci et al, 2006, p. 1222
2727	**A_av**	(blank)	**(blank)**	(blank)
	A_M_50_av	sharp and weak absorption	**asphalt**	Spectrum A_av
2856	**A_M_50_av**	strong absorption	**CH2, CH3 stretching**	Spectrum A_av, Lombardi and Santarelli, 2009, 542
2858	**A_av**	strong absorption	**CH2, CH3 stretching**	Lombardi and Santarelli, 2009, 542
2866	**A_av**	strong absorption	**CH2, CH3 stretching**	Lombardi and Santarelli, 2009, 542
2867	**A_M_50_av**	strong absorption	**CH2, CH3 stretching**	Spectrum A_av, Lombardi and Santarelli, 2009, 542
2931	**A_M_50_av**	strong absorption	**CH2, CH3 stretching**	Spectrum A_av, Lombardi and Santarelli, 2009, 542
2932	**A_av**	strong absorption	**CH2, CH3 stretching**	Lombardi and Santarelli, 2009, 542
2954	**A_av**	strong absorption	**CH2, CH3 stretching**	Lombardi and Santarelli, 2009, 542
2956	**A_M_50_av**	strong absorption	**CH2, CH3 stretching**	Spectrum A_av, Lombardi and Santarelli, 2009, 542
3190	**A_av**	(blank)	**(blank)**	(blank)
3205	**A_av**	(blank)	**(blank)**	(blank)
3267	**A_av**	(blank)	**(blank)**	(blank)
3276	**A_av**	(blank)	**(blank)**	(blank)
3473	**A_av**	(blank)	**(blank)**	(blank)
	A_M_50_av	weak absorption	**asphalt**	Spectrum A_av
3664	**A_av**	(blank)	**(blank)**	(blank)

Figure 35: continued.

Peak x (position)	Spectrum ID	Type of band	Chemical Band Assignement	Reference
713	**A_M_25_av**	sharp absorption	**v4 carbonate ion**	Spectrum Ca_av, spectrum M_av, Ylmen and Jaglid, 2013, p. 119
723	**A_av**	triplet	**(blank)**	Lombardi and Santarelli, 2009, 542
742	**A_av**	triplet	**(blank)**	Lombardi and Santarelli, 2009, 542
793	**A_M_25_av**	weak absorption	**quartz**	Spectrum Q_av, spectrum M_av
814	**A_av**	triplet	**(blank)**	Lombardi and Santarelli, 2009, 542
	A_M_25_av	triplet	**asphalt**	Spectrum A_av, Lombardi and Santarelli, 2009, 542
848	**A_M_25_av**	sharp absorption	**v2 carbonate ion**	Spectrum Ca_av, spectrum M_av, Ylmen and Jaglid, 2013, p. 119
868	**A_av**	triplet	**(blank)**	Lombardi and Santarelli, 2009, 542
873	**A_M_25_av**	sharp absorption	**v2 carbonate ion**	Spectrum Ca_av, spectrum M_av, Ylmen and Jaglid, 2013, p. 119
934	**A_M_25_av**	weak absorption	**asphalt**	Spectrum A_av
937	**A_av**	(blank)	**(blank)**	(blank)
952	**A_M_25_av**	weak absorption	**(blank)**	(blank)
975	**A_M_25_av**	weak absorption	**asphalt**	Spectrum A_av
976	**A_av**	(blank)	**(blank)**	(blank)
1017	**A_M_25_av**	weak absorption	**(blank)**	(blank)
1029	**A_M_25_av**	weak absorption	**quartz**	Spectrum A_av, Lombardi and Santarelli, 2009, 542
1032	**A_av**	sharp absorption	**quartz**	Lombardi and Santarelli, 2009, 542
1064	**A_av**	(blank)	**(blank)**	(blank)
1081	**A_M_25_av**	weak absorption	**v1 carbonate ion**	Spectrum Ca_av, Ylmen and Jaglid, 2013, p. 119
1160	**A_M_25_av**	sharp absorption	**quartz**	Spectrum Q_av, spectrum M_av, spectrum A_av
1169	**A_av**	weak absorption	**(blank)**	(blank)
1314	**A_av**	weak absorption	**CH2, CH3**	Lombardi and Santarelli, 2009, 542
1377	**A_av**	strong absorption	**CH2, CH3**	Lombardi and Santarelli, 2009, 542
1385	**A_M_25_av**	strong absorption	**CH2, CH3 stretching**	Spectrum A_av, Lombardi and Santarelli, 2009, 542
1401	**A_M_25_av**	strong absorption	**calcium carbonate**	Spectrum Ca_av, spectrum M_av
1453	**A_M_25_av**	shoulder	**v3 antisymmetric stretching CO3-2**	Spectrum Ca_av, Ylmen and Jaglid, 2013, p. 119
1461	**A_av**	strong absorption	**(blank)**	(blank)
	A_M_25_av	strong absorption	**asphalt**	Spectrum A_av

Figure 36: Filtered CPAD entries of asphalt (A_av) and 25% asphalt/mortar mixture (A_M_25_av).

1600	**A_M_25_av**	strong absorption	**C6H6 (benzene rings)**	Spectrum A_av, Lombardi and Santarelli, 2009, 542
1603	**A_av**	strong absorption	**C6H6 (benzene rings)**	Lombardi and Santarelli, 2009, 542
1642	**A_M_25_av**	shoulder	**asphalt**	Spectrum A_av
1643	**A_av**	(blank)	**(blank)**	(blank)
1649	**A_av**	(blank)	**(blank)**	(blank)
1794	**A_M_25_av**	combination band	**v1+v4**	Spectrum Ca_av, spectrum M_av, Ricci et al, 2006, p. 1222
1843	**A_av**	weak absorption	**quartz**	Spectrum Q_av, spectrum M_av, spectrum A_av
	A_M_25_av	weak absorption	**quartz**	Spectrum Q_av, spectrum M_av, spectrum A_av
1867	**A_av**	weak absorption	**quartz**	Spectrum Q_av, spectrum M_av, spectrum A_av
	A_M_25_av	weak absorption	**quartz**	Spectrum Q_av, spectrum M_av, spectrum A_av
1888	**A_av**	weak absorption	**quartz**	spectrum A_av, spectrum Q_av
2039	**A_av**	(blank)	**(blank)**	(blank)
2136	**A_M_25_av**	sharp and weak absorption	**calcium carbonate and quartz**	Spectrum Q_av, spectrum M_av, spectrum Ca_av
2239	**A_M_25_av**	weak absorption	**quartz**	Spectrum Q_av, spectrum M_av
2513	**A_M_25_av**	combination band	**v1+v3**	Spectrum M_av, spectrum Ca_av, Ricci et al, 2006, p. 1222
2598	**A_M_25_av**	weak absorption	**quartz**	Spectrum Q_av, spectrum M_av
2727	**A_av**	(blank)	**(blank)**	(blank)
2728	**A_M_25_av**	weak absorption	**asphalt**	Spectrum A_av
2858	**A_av**	strong absorption	**CH2, CH3 stretching**	Lombardi and Santarelli, 2009, 542
2866	**A_av**	strong absorption	**CH2, CH3 stretching**	Lombardi and Santarelli, 2009, 542
2868	**A_M_25_av**	strong absorption	**CH2, CH3 stretching**	Spectrum A_av, Lombardi and Santarelli, 2009, 542
2929	**A_M_25_av**	strong absorption	**CH2, CH3 stretching**	Spectrum A_av, Lombardi and Santarelli, 2009, 542
2932	**A_av**	strong absorption	**CH2, CH3 stretching**	Lombardi and Santarelli, 2009, 542
2953	**A_M_25_av**	strong absorption	**CH2, CH3 stretching**	Spectrum A_av, Lombardi and Santarelli, 2009, 542
2954	**A_av**	strong absorption	**CH2, CH3 stretching**	Lombardi and Santarelli, 2009, 542
3190	**A_av**	(blank)	**(blank)**	(blank)
3205	**A_av**	(blank)	**(blank)**	(blank)
3267	**A_av**	(blank)	**(blank)**	(blank)
3276	**A_av**	(blank)	**(blank)**	(blank)
3472	**A_M_25_av**	weak absorption	**asphalt**	Spectrum A_av
3473	**A_av**	(blank)	**(blank)**	(blank)
3643	**A_M_25_av**	sharp and weak absorption	**Ca(OH)2**	Spectrum Ca_av, spectrum M_av, Ylmen and Jaglid, 2013, p. 119
3664	**A_av**	(blank)	**(blank)**	(blank)

Figure 36: continued.

Peak x (position)	Spectrum ID	Type of band	Chemical Band Assignement	Reference
714	A_M_5_av	sharp absorption	v4 carbonate ion	Spectrum Ca_av, spectrum M_av, Ylmen and Jaglid, 2013, p. 119
723	A_av	triplet	(blank)	Lombardi and Santarelli, 2009, 542
742	A_av	triplet	(blank)	Lombardi and Santarelli, 2009, 542
793	A_M_5_av	weak absorption	quartz	Spectrum Q_av, spectrum M_av
814	A_av	triplet	(blank)	Lombardi and Santarelli, 2009, 542
	A_M_5_av	triplet	asphalt	Spectrum A_av, Lombardi and Santarelli, 2009, 542
848	A_M_5_av	sharp and weak absorption	v2 carbonate ion	Spectrum Ca_av, spectrum M_av, Ylmen and Jaglid, 2013, p. 119
868	A_av	triplet	(blank)	Lombardi and Santarelli, 2009, 542
876	A_M_5_av	strong absorption	v2 carbonate ion	Spectrum Ca_av, spectrum M_av, Ylmen and Jaglid, 2013, p. 119
937	A_av	(blank)	(blank)	(blank)
974	A_M_5_av	weak absorption	asphalt	Spectrum A_av
976	A_av	(blank)	(blank)	(blank)
1010	A_M_5_av	weak absorption	calcium carbonate	spectrum Ca_av
1032	A_av	sharp absorption	quartz	Lombardi and Santarelli, 2009, 542
1064	A_av	(blank)	(blank)	(blank)
1082	A_M_5_av	weak absorption	v1 carbonate ion	Spectrum Ca_av, Ylmen and Jaglid, 2013, p. 119
1159	A_M_5_av	sharp absorption	quartz	Spectrum Q_av, spectrum M_av
1169	A_av	weak absorption	(blank)	(blank)
1314	A_av	weak absorption	CH2, CH3	Lombardi and Santarelli, 2009, 542
1377	A_av	strong absorption	CH2, CH3	Lombardi and Santarelli, 2009, 542
1386	A_M_5_av	strong absorption	CH2, CH3 stretching	Spectrum A_av, Lombardi and Santarelli, 2009, 542
1401	A_M_5_av	weak absorption	calcium carbonate	Spectrum Ca_av, spectrum M_av
1453	A_M_5_av	shoulder	v3 antisymmetric stretching CO3-2	Spectrum Ca_av, Ylmen and Jaglid, 2013, p. 119
1461	A_av	strong absorption	(blank)	(blank)
1462	A_M_5_av	strong absorption	asphalt	Spectrum A_av
1599	A_M_5_av	strong absorption	C6H6 (benzene rings)	Spectrum A_av, Lombardi and Santarelli, 2009, 542
1603	A_av	strong absorption	C6H6 (benzene rings)	Lombardi and Santarelli, 2009, 542
1643	A_av	(blank)	(blank)	(blank)
1649	A_av	(blank)	(blank)	(blank)
1652	A_M_5_av	shoulder	asphalt	Spectrum A_av
1794	A_M_5_av	combination band	v1+v4	Spectrum Ca_av, spectrum M_av, Ricci et al, 2006, p. 1222
1843	A_av	weak absorption	quartz	Spectrum Q_av, spectrum M_av, spectrum A_av
1844	A_M_5_av	weak absorption	quartz	Spectrum Q_av, spectrum M_av, spectrum A_av

Figure 37: Filtered CPAD entries of asphalt (A_av) and 5% asphalt mortar mixture (A_M_5_av).

1867	**A_av**	weak absorption	**quartz**	Spectrum Q_av, spectrum M_av, spectrum A_av
	A_M_5_av	weak absorption	**quartz**	Spectrum Q_av, spectrum M_av, spectrum A_av
1888	**A_av**	weak absorption	**quartz**	spectrum A_av, spectrum Q_av
2039	**A_av**	(blank)	**(blank)**	(blank)
2135	**A_M_5_av**	weak absorption	**calcium carbonate and quartz**	Spectrum Q_av, spectrum M_av, spectrum Ca_av
2236	**A_M_5_av**	weak absorption	**quartz**	Spectrum Q_av, spectrum M_av
2512	**A_M_5_av**	combination band	**v1+v3**	Spectrum M_av, spectrum Ca_av, Ricci et al, 2006, p. 1222
2589	**A_M_5_av**	shoulder	**quartz**	spectrum Q_av
2727	**A_av**	(blank)	**(blank)**	(blank)
	A_M_5_av	weak absorption	**asphalt**	Spectrum A_av
2858	**A_av**	strong absorption	**CH2, CH3 stretching**	Lombardi and Santarelli, 2009, 542
2866	**A_av**	strong absorption	**CH2, CH3 stretching**	Lombardi and Santarelli, 2009, 542
2870	**A_M_5_av**	strong absorption	**CH2, CH3 stretching**	Spectrum A_av, Lombardi and Santarelli, 2009, 542
2928	**A_M_5_av**	strong absorption	**CH2, CH3 stretching**	Spectrum A_av, Lombardi and Santarelli, 2009, 542
2932	**A_av**	strong absorption	**CH2, CH3 stretching**	Lombardi and Santarelli, 2009, 542
2954	**A_av**	strong absorption	**CH2, CH3 stretching**	Lombardi and Santarelli, 2009, 542
	A_M_5_av	strong absorption	**CH2, CH3 stretching**	Spectrum A_av, Lombardi and Santarelli, 2009, 542
3190	**A_av**	(blank)	**(blank)**	(blank)
3205	**A_av**	(blank)	**(blank)**	(blank)
3267	**A_av**	(blank)	**(blank)**	(blank)
3276	**A_av**	(blank)	**(blank)**	(blank)
3451	**A_M_5_av**	weak absorption	**(blank)**	(blank)
3467	**A_M_5_av**	weak absorption	**asphalt**	Spectrum A_av
3473	**A_av**	(blank)	**(blank)**	(blank)
3572	**A_M_5_av**	weak absorption	**(blank)**	(blank)
3642	**A_M_5_av**	sharp and weak absorption	**Ca(OH)2**	Spectrum Ca_av, spectrum M_av, Ylmen and Jaglid, 2013, p. 119
3664	**A_av**	(blank)	**(blank)**	(blank)

Figure 37: continued.

Chapter 8: CPAD applicability in identification of reflectance micro-FTIR spectra.

8.1.1 Experimental set I

Blue	**Peaks of unknown spectrum**
Yellow	**Peaks of best matching standard spectrum**
Green	**Peaks of second-best matching standard spectrum**

Table 2: Colour-coding of peaks for the comparative assessment of the unknown spectrum (blue) with the best matching spectrum of standard (yellow) and the second-best matching (green).

UN_I_2

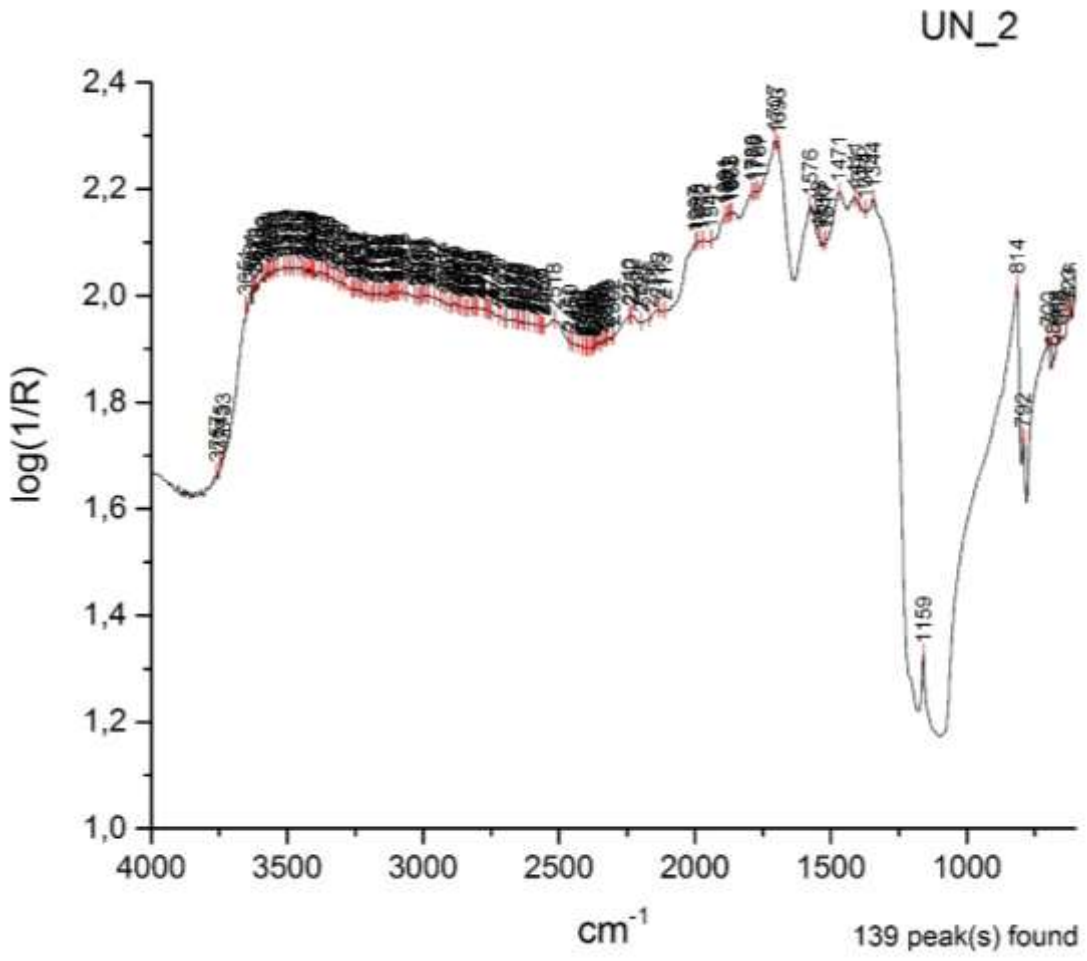

Figure 38: UN_I_2 correctly identified as 50% Bone glue additive in mortar (BG_M_50).

Peak x (position)	Spectrum ID	Type of band	Chemical Band Assignement	Reference
735	BG_M_25_av	weak absorption	(blank)	(blank)
738	BG_M_75_av	weak absorption	bone glue	Spectrum BG_av
761	BG_M_75_av	weak absorption	bone glue	Spectrum BG_av
	BG_M_25_av	weak absorption	(blank)	(blank)
770	BG_M_75_av	weak absorption	bone glue	Spectrum BG_av
790	BG_M_75_av	weak absorption	bone glue	Spectrum BG_av
1205	BG_M_25_av	weak bands	bone glue	Spectrum BG_av
1268	BG_M_75_av	stair-step type intensities	bone glue	Spectrum BG_av
1286	BG_M_25_av	stair-step type intensities	bone glue	Spectrum BG_av
1287	BG_M_75_av	stair-step type intensities	bone glue	Spectrum BG_av
1292	BG_M_50_av	stair-step type intensities	bone glue	Spectrum BG_av
1313	BG_M_50_av	stair-step type intensities	bone glue	Spectrum BG_av
1341	BG_M_75_av	stair-step type intensities	bone glue	Spectrum BG_av
1344	UN_2	(blank)	(blank)	(blank)
1347	BG_M_50_av	stair-step type intensities	bone glue	Spectrum BG_av
1411	UN_2	(blank)	(blank)	(blank)
1415	BG_M_75_av	stair-step type intensities	bone glue	Spectrum BG_av
1418	BG_M_50_av	stair-step type intensities	bone glue	(blank)
1461	BG_M_25_av	stair-step type intensities	Amide III	Spectrum BG_av, Rosi et al, 2009, p. 2099
1469	BG_M_25_av	stair-step type intensities	Amide III	Spectrum BG_av, Rosi et al, 2009, p. 2099
1471	BG_M_75_av	stair-step type intensities	Amide III	Spectrum BG_av, Rosi et al, 2009, p. 2099
	BG_M_50_av	stair-step type intensities	Amide III	Spectrum BG_av, Rosi et al, 2009, p. 2099
	UN_2	(blank)	(blank)	(blank)
1572	BG_M_75_av	strong absorption	C-N-H bending amide II, N-H bands	Spectrum BG_av, Rosi et al, 2009, p. 2099, Miliani et al, 2012, p. 304
1574	BG_M_50_av	strong absorption	C-N-H bending amide II, N-H bands	Spectrum BG_av, Rosi et al, 2009, p. 2099, Miliani et al, 2012, p. 304
1576	UN_2	(blank)	(blank)	(blank)
1693	BG_M_50_av	strong absorption	N-H bands	Spectrum BG_av, Rosi et al, 2009, p. 2104, Miliani et al, 2012, p. 304
	UN_2	(blank)	(blank)	(blank)
1694	BG_M_25_av	strong absorption	N-H bands	Spectrum BG_av, Rosi et al, 2009, p. 2104, Miliani et al, 2012, p. 304
1697	BG_M_75_av	strong absorption	N-H bands	Spectrum BG_av, Rosi et al, 2009, p. 2104, Miliani et al, 2012, p. 304
1702	BG_M_50_av	(blank)	bone glue	Spectrum BG_av
1707	UN_2	(blank)	(blank)	(blank)
2802	BG_M_75_av	weak absorption	C-H stretching	Rosi et al, 2009, p. 2099
2881	BG_M_75_av	weak absorption	C-H stretching	Spectrum BG_av, Miliani et al, 2012, p. 304; Rosi et al, 2009, p. 2104
2889	BG_M_75_av	weak absorption	C-H stretching	Spectrum BG_av, Miliani et al, 2012, p. 304; Rosi et al, 2009, p. 2104
2897	BG_M_25_av	weak bands	C-H stretching	Spectrum BG_av, Miliani et al, 2012, p. 304; Rosi et al, 2009, p. 2104
2905	BG_M_25_av	weak absorption	bone glue	Spectrum BG
2918	BG_M_5_av	weak bands	C-H stretching	Spectrum BG_av, Miliani et al, 2012, p. 304; Rosi et al, 2009, p. 2104
2927	BG_M_5_av	weak bands	bone glue	Spectrum BG_av
2935	BG_M_5_av	weak bands	bone glue	Spectrum BG_av
2940	BG_M_25_av	weak absorption	(blank)	(blank)
2949	BG_M_25_av	weak absorption	(blank)	(blank)
2985	BG_M_75_av	weak absorption	bone glue	Spectrum BG_av
2990	BG_M_50_av	weak absorption	bone glue	Spectrum BG_av
3099	BG_M_50_av	weak absorption	amide I	Spectrum BG_av, Rosi et al, 2009, p. 2099
3103	BG_M_75_av	weak absorption	amide I	Spectrum BG_av, Rosi et al, 2009, p. 2099

Figure 39: Filtered CPAD of peaks of interest for UN_I_2 spectrum and possible matches.

The overall spectral pattern suggests protein stair-step type intensities and presence of mortar (fig.38). The diagnostic peaks of bone glue in UN_I_2 spectrum (blue) match the 50% bone glue additive (yellow) best rather than the next possible match of 75% bone glue additive (green) (fig.39).

UN_I_4

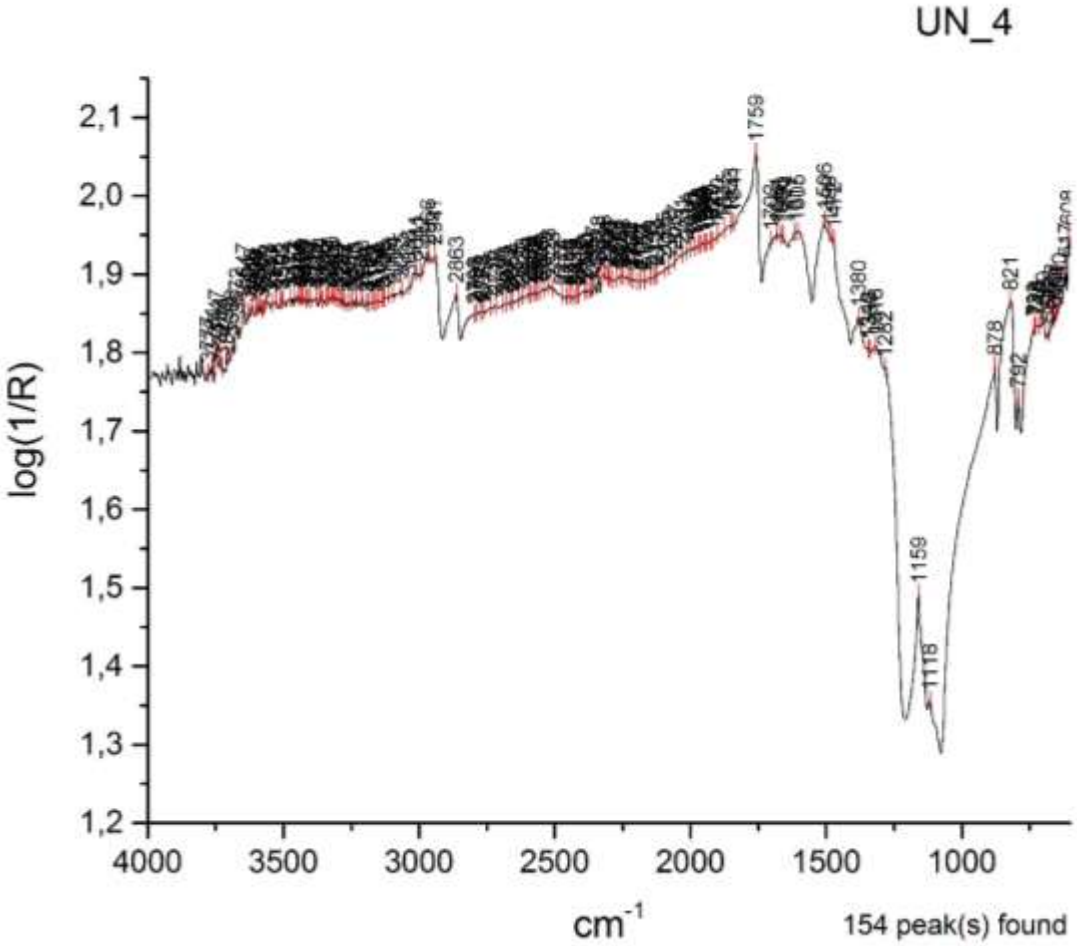

Figure 40: UN_I_4 correctly identified as 25% olive oil additive in mortar (O_M_25).

The overall spectral pattern suggests presence of lipids in mortar (fig.40). The diagnostic peaks of olive oil in UN_I_4 spectrum (blue) match the 25% olive oil additive (yellow) best rather than the next possible match of 50% olive oil additive (green) (fig.41).

Peak x (position)	Spectrum ID	Type of band	Chemical Band Assignement	Reference
667	O_M_25_av	sharp and weak absorption	olive oil	Spectrum O_av
668	O_M_50_av	sharp and weak absorption	olive oil	Spectrum O_av
	O_M_75_av	sharp and weak absorption	olive oil	Spectrum O_av
706	O_M_75_av	sharp and weak absorption	olive oil	Spectrum O_av
727	O_M_25_av	sharp and weak absorption	olive oil	Spectrum O_av
729	O_M_75_av	sharp and weak absorption	olive oil	Spectrum O_av
733	O_M_50_av	sharp and weak absorption	olive oil	Spectrum O_av
813	O_M_75_av	sharp and weak absorption	olive oil	Spectrum O_av
819	O_M_50_av	sharp absorption	olive oil	Spectrum O_av
821	O_M_25_av	sharp absorption	olive oil	Spectrum O_av
1119	O_M_25_av	sharp and weak absorption	C-O stretching	Spectrum O_av, Buti et al, 2013, p. 2705
1122	O_M_50_av	sharp and weak absorption	C-O stretching	Spectrum O_av, Buti et al, 2013, p. 2705
1184	O_M_50_av	sharp and weak absorption	C-O stretching	Spectrum O_av, Buti et al, 2013, p. 2705
1268	O_M_50_av	strong absorption	C-O stretching	Spectrum O_av, Buti et al, 2013, p. 2705
1271	O_M_75_av	strong absorption	C-O stretching	Spectrum O_av, Buti et al, 2013, p. 2705
1278	O_M_50_av	strong absorption	C-O stretching	Spectrum O_av, Buti et al, 2013, p. 2705
1281	O_M_75_av	strong absorption	olive oil	Spectrum O_av
1282	O_M_25_av	weak absorption	C-O stretching	Spectrum O_av, Buti et al, 2013, p. 2705
	UN_4	(blank)	(blank)	(blank)
1318	O_M_25_av	weak absorption	C-O stretching	Spectrum O_av, Buti et al, 2013, p. 2705
	UN_4	(blank)	(blank)	(blank)
1354	O_M_75_av	sharp and weak absorption	olive oil	Spectrum O_av
1364	O_M_75_av	sharp and weak absorption	olive oil	Spectrum O_av
1380	O_M_50_av	sharp and weak absorption	C-O bending	Spectrum O_av, Buti et al, 2013, p. 2705
	UN_4	(blank)	(blank)	(blank)
1381	O_M_25_av	sharp absorption	C-O bending	Spectrum O_av, Buti et al, 2013, p. 2705
	O_M_75_av	sharp and weak absorption	C-H bending	Spectrum O_av, Buti et al, 2013, p. 2705
1384	O_M_5_av	sharp absorption	C-O bending	Spectrum O_av
1420	O_M_75_av	weak absorption	olive oil	Spectrum O_av
1442	O_M_5_av	weak absorption	olive oil	Spectrum O_av, Buti et al, 2013, p. 2706
	O_M_75_av	weak absorption	olive oil	Spectrum O_av
1471	O_M_75_av	sharp absorption	C-H bending	Spectrum O_av, Ricci et al, 2006, p. 1223
1506	UN_4	(blank)	(blank)	(blank)
1507	O_M_25_av	strong absorption	C-O bending	Spectrum O_av, Ricci et al, 2006, p. 1223
1518	O_M_50_av	strong absorption	C-O bending	Spectrum O_av, Ricci et al, 2006, p. 1223
1530	O_M_5_av	strong absorption	C-O bending	Spectrum O_av, Ricci et al, 2006, p. 1223
1560	O_M_75_av	weak absorption	olive oil	Spectrum O_av
1605	UN_4	(blank)	(blank)	(blank)
1657	O_M_75_av	weak absorption	olive oil	Spectrum O_av
1660	O_M_25_av	weak absorption	quartz or olive oil	Spectrum Q_av, spectum M_av, spectrum O_av
	UN_4	(blank)	(blank)	(blank)
1669	O_M_25_av	weak absorption	olive oil	Spectrun O_av
1674	O_M_5_av	weak absorption	olive oil	Spectrun O_av
1678	O_M_25_av	weak absorption	olive oil	Spectrun O_av

Figure 41: Filtered CPAD of peaks of interest for UN_I_4 spectrum and possible matches.

1680	**O_M_5_av**	weak absorption	**olive oil**	Spectrun O_av
1683	**O_M_75_av**	weak absorption	**olive oil**	Spectrum O_av, Mazzeo et al, 2008, p. 69
1695	**O_M_5_av**	weak absorption	**olive oil**	Spectrun O_av
1703	**O_M_25_av**	weak absorption	**olive oil**	Spectrun O_av
1705	**O_M_75_av**	weak absorption	**free fatty acids**	Spectrum O_av, Ploeger et al, 2010, p. 37
1755	**O_M_5_av**	1st order derivative	**C=O stretching band**	Spectrum O_av, Ploeger et al, 2010, p, 37
1758	**O_M_25_av**	1st order derivative	**C=O stretching band**	Spectrum O_av, Ploeger et al, 2010, p, 37
	O_M_50_av	1st order derivative	**C=O stretching band**	Spectrum O_av, Ploeger et al, 2010, p, 37
1759	**O_M_75_av**	1st order derivative	**C=O stretching band**	Spectrum O_av
	UN_4	(blank)	**(blank)**	(blank)
2855	**O_M_5_av**	strong absorption	**CH2 stretching**	Spectrum O_av, Ploeger et al, 2010, p. 37
2863	**O_M_25_av**	strong absorption	**CH2 stretching**	Spectrum O_av, Ploeger et al, 2010, p. 37
	O_M_50_av	strong absorption	**CH2 stretching**	Spectrum O_av, Ploeger et al, 2010, p. 37
	UN_4	(blank)	**(blank)**	(blank)
2864	**O_M_75_av**	strong absorption	**CH2 stretching**	Spectrum O_av, Ploeger et al, 2010, p. 37
2929	**O_M_5_av**	strong absorption	**CH2 stretching**	Spectrum O_av, Ploeger et al, 2010, p. 37
2941	**O_M_25_av**	strong absorption	**CH2 stretching**	Spectrum O_av, Ploeger et al, 2010, p. 37
	O_M_50_av	strong absorption	**CH2 stretching**	Spectrum O_av, Ploeger et al, 2010, p. 37
	O_M_75_av	strong absorption	**CH2 stretching**	Spectrum O_av, Ploeger et al, 2010, p. 37
	UN_4	(blank)	**(blank)**	(blank)
2954	**O_M_5_av**	strong absorption	**v(CH) stretching**	Spectrum O_av, Miliani et al, 2007, p. 853
2964	**O_M_75_av**	strong absorption	**v(CH) stretching**	Spectrum O_av, Miliani et al, 2007, p. 853
2966	**O_M_25_av**	strong absorption	**v(CH) stretching**	Spectrum O_av, Miliani et al, 2007, p. 853
	O_M_50_av	strong absorption	**v(CH) stretching**	Spectrum O_av, Miliani et al, 2007, p. 853
	UN_4	(blank)	**(blank)**	(blank)
2992	**UN_4**	(blank)	**(blank)**	(blank)
3005	**O_M_5_av**	weak absorption	**v(CH) stretching**	Spectrum O_av, Miliani et al, 2007, p. 853
3009	**O_M_25_av**	weak absorption	**v(CH) stretching**	Spectrum O_av, Miliani et al, 2007, p. 853
3011	**UN_4**	(blank)	**(blank)**	(blank)
3012	**O_M_50_av**	weak absorption	**v(CH) stretching**	Spectrum O_av, Miliani et al, 2007, p. 853
3019	**O_M_75_av**	weak absorption	**v(CH) stretching**	Spectrum O_av, Miliani et al, 2007, p. 853
3062	**O_M_5_av**	weak absorption	**olive oil**	Spectrum O_av

Figure 41: continued.

UN_I_7

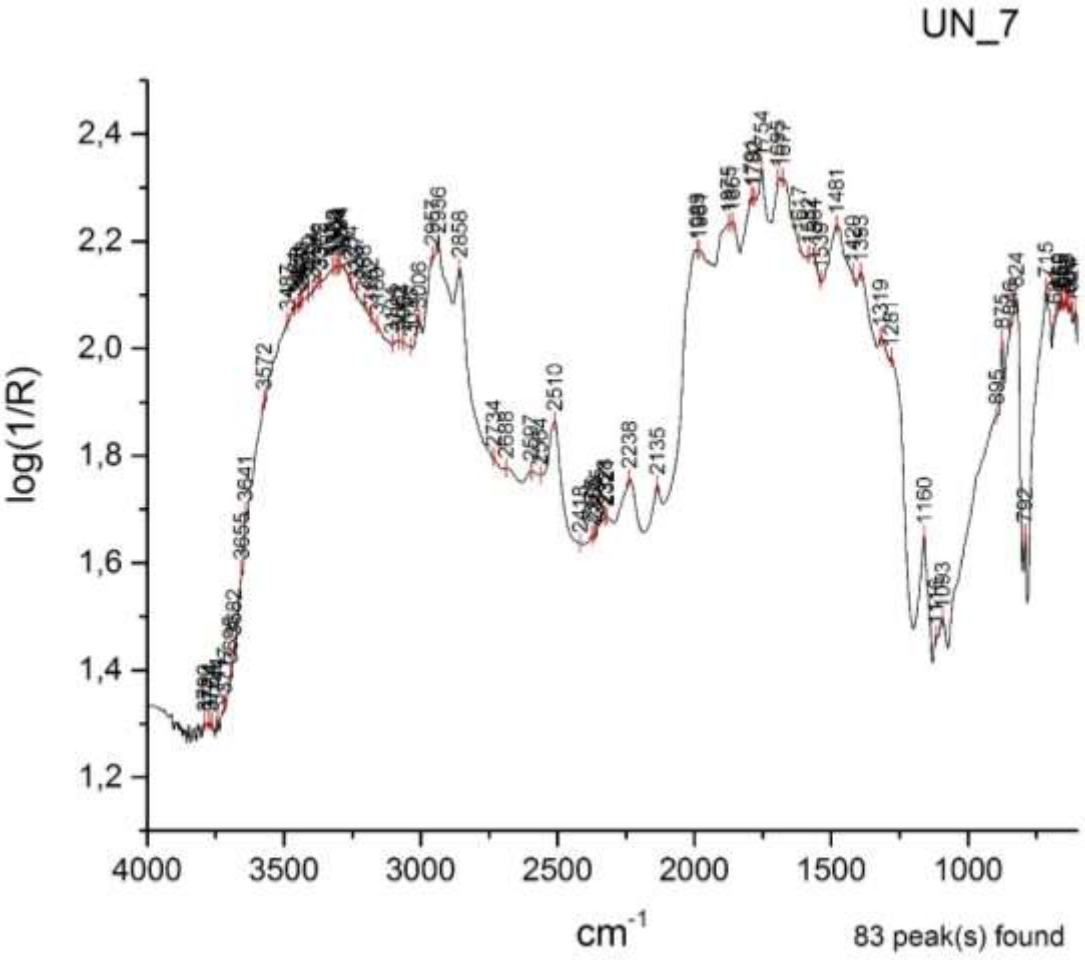

Figure 42: UN_I_7 correctly identified as 25% egg yolk additive in mortar (EY_M_25).

The overall spectral pattern suggests presence of lipids in mortar, whereas the shape and intensity of the peaks at 2957-3006 cm^{-1} the presence of egg yolk. The correct identification of concentration was based in the occurrence of 1481 and 1319 cm^{-1} peaks, common to the unknown and the 25% egg yolk mortar additive spectra (fig.42-43).

Peak x (position)	Spectrum ID	Type of band	Chemical Band Assignement	Reference
669	EY_M_75_av	weak absorption	egg yolk	spectrum EY_av
720	EY_M_75_av	sharp and weak absorption	in-plane rotation of linear long C chains δ(CH2)n	Spectrum EY_av, Iwanicka et al, 2017, p. 18
730	EY_M_75_av	sharp and weak absorption	in-plane rotation of linear long C chains δ(CH2)n	Iwanicka et al, 2017, p. 19
741	EY_M_75_av	sharp and weak absorption	in-plane rotation of linear long C chains δ(CH2)n	Spectrum EY_av, Iwanicka et al, 2017, p. 18
769	EY_M_75_av	weak absorption	egg yolk	spectrum EY_av
785	EY_M_75_av	weak absorption	egg yolk	spectrum EY_av
1198	EY_M_5_av	weak absorption	egg yolk	spectrum EY_av
1263	EY_M_75_av	strong absorption	egg yolk	spectrum EY_av
1271	EY_M_75_av	strong absorption	egg yolk	spectrum EY_av
1279	EY_M_25_av	strong absorption	egg yolk	spectrum EY_av
1281	EY_M_50_av	strong absorption	egg yolk	spectrum EY_av
	UN_7	(blank)	(blank)	(blank)
1301	EY_M_50_av	strong absorption	CH2, CH3	Lombardi and Santarelli, 2009, p. 542
1310	EY_M_50_av	strong absorption	CH2, CH3	Lombardi and Santarelli, 2009, p. 542
1315	EY_M_25_av	strong absorption	CH2, CH3	Lombardi and Santarelli, 2009, p. 542
1319	UN_7	(blank)	(blank)	(blank)
1381	EY_M_50_av	strong absorption	C-H bending	Spectrum EY_av, Buti et al, 2013, p. 2705
1382	EY_M_75_av	strong absorption	C-H bending	Spectrum EY_av, Buti et al, 2013, p. 2705
1390	EY_M_25_av	strong absorption	C-H bending	Spectrum EY_av, Buti et al, 2013, p. 2705
1399	EY_M_25_av	strong absorption	C-H bending	Spectrum EY_av, Buti et al, 2013, p. 2705
1420	EY_M_50_av	weak absorption	egg yolk	spectrum EY_av
1424	EY_M_75_av	strong absorption	egg yolk	spectrum EY_av
1448	EY_M_50_av	weak absorption	egg yolk	spectrum EY_av
1470	EY_M_75_av	strong absorption	C-O bending	Spectrum EY_av, Ricci et al, 2006, p. 1224
	EY_M_50_av	strong absorption	C-O bending	Spectrum EY_av, Ricci et al, 2006, p. 1224
1476	EY_M_25_av	strong absorption	C-O bending	Spectrum EY_av, Ricci et al, 2006, p. 1224
1481	UN_7	(blank)	(blank)	(blank)
1500	EY_M_75_av	weak absorption	C=O	Spectrum EY_av, Rosi et al, 2009, p. 2099
1508	EY_M_50_av	weak absorption	C=O	Spectrum EY_av, Rosi et al, 2009, p. 2095
1518	EY_M_50_av	weak absorption	C=O	Spectrum EY_av, Rosi et al, 2009, p. 2096
1520	EY_M_25_av	weak absorption	C=O	Spectrum EY_av, Rosi et al, 2009, p. 2097
1522	EY_M_75_av	weak absorption	C=O	Spectrum EY_av, Rosi et al, 2009, p. 2099
1529	EY_M_50_av	weak absorption	C=O	Spectrum EY_av, Rosi et al, 2009, p. 2097
1536	EY_M_25_av	weak absorption	C=O	Spectrum EY_av, Rosi et al, 2009, p. 2098
1538	EY_M_50_av	weak absorption	C=O	Spectrum EY_av, Rosi et al, 2009, p. 2098
1539	EY_M_5_av	weak absorption	C=O	Spectrum EY_av, Rosi et al, 2009, p. 2098

Figure 43: Filtered CPAD of peaks of interest for UN_I_7 spectrum and possible matches.

1560	**EY_M_75_av**	weak absorption	**C=O**	Spectrum EY_av, Rosi et al, 2009, p. 2099
	EY_M_50_av	weak absorption	**C=O**	Spectrum EY_av, Rosi et al, 2009, p. 2099
1561	**UN_7**	(blank)	**(blank)**	(blank)
1569	**EY_M_25_av**	strong absorption	**C=O**	Spectrum EY_av, Rosi et al, 2009, p. 2098
1667	**EY_M_75_av**	weak absorption	**C=O**	Spectrum EY_av, Rosi et al, 2009, p. 2099
1675	**EY_M_5_av**	strong absorption	**C=O**	Spectrum EY_av, Rosi et al, 2009, p. 2099
1677	**EY_M_25_av**	strong absorption	**C=O**	Spectrum EY_av, Rosi et al, 2009, p. 2099
1679	**EY_M_75_av**	weak absorption	**C=O**	Spectrum EY_av, Rosi et al, 2009, p. 2099
1682	**EY_M_50_av**	strong absorption	**C=O**	Spectrum EY_av, Rosi et al, 2009, p. 2099
1687	**EY_M_25_av**	strong absorption	**C=O**	Spectrum EY_av, Rosi et al, 2009, p. 2099
1690	**EY_M_50_av**	strong absorption	**C=O**	Spectrum EY_av, Rosi et al, 2009, p. 2099
1695	**UN_7**	(blank)	**(blank)**	(blank)
1732	**EY_M_50_av**	weak absorption	**C=O stretching band**	Spectrum EY_av, Ploeger et al, 2010, p, 37
1744	**EY_M_5_av**	1st order derivative	**C=O stretching band**	Spectrum EY_av, Ploeger et al, 2010, p, 37
1753	**EY_M_25_av**	1st order derivative	**C=O stretching band**	Spectrum EY_av, Ploeger et al, 2010, p, 37
1754	**UN_7**	(blank)	**(blank)**	(blank)
1755	**EY_M_50_av**	1st order derivative	**C=O stretching band**	Spectrum EY_av, Ploeger et al, 2010, p, 37
1757	**EY_M_75_av**	1st order derivative	**C=O stretching band**	Spectrum EY_av, Ploeger et al, 2010, p, 37
2033	**EY_M_75_av**	weak absorption	**(blank)**	(blank)
2189	**EY_M_50_av**	weak absorption	**egg yolk**	spectrum EY_av
2682	**EY_M_5_av**	weak absorption	**(blank)**	(blank)
2691	**EY_M_5_av**	weak absorption	**(blank)**	(blank)
2855	**EY_M_5_av**	strong absorption	**C-H stretching bands, esters**	Spectrum EY_av, Rosi et al, 2009, p. 2099
2857	**EY_M_25_av**	strong absorption	**C-H stretching bands, esters**	Spectrum EY_av, Rosi et al, 2009, p. 2099
2858	**EY_M_50_av**	strong absorption	**C-H stretching bands, esters**	Spectrum EY_av, Rosi et al, 2009, p. 2099
	UN_7	(blank)	**(blank)**	(blank)
2864	**EY_M_75_av**	strong absorption	**C-H stretching bands, esters**	Spectrum EY_av, Rosi et al, 2009, p. 2099
2908	**EY_M_50_av**	strong absorption	**C-H stretching bands, esters**	Spectrum EY_av, Rosi et al, 2009, p. 2099
2925	**EY_M_5_av**	strong absorption	**CH stretching**	Spectrum EY_av, Daher et al, 2017, p.8

Figure 43: continued.

2935	**EY_M_25_av**	strong absorption	**CH stretching**	Spectrum EY_av, Daher et al, 2017, p.8
2936	**EY_M_50_av**	strong absorption	**CH stretching**	Spectrum EY_av, Daher et al, 2017, p.8
	UN_7	(blank)	**(blank)**	(blank)
2942	**EY_M_75_av**	strong absorption	**C-H stretching bands, esters**	Spectrum EY_av, Rosi et al, 2009, p. 2099
2957	**EY_M_5_av**	strong absorption	**C-H stretching bands, esters**	Spectrum EY_av, Rosi et al, 2009, p. 2099
	UN_7	(blank)	**(blank)**	(blank)
2959	**EY_M_50_av**	strong absorption	**C-H stretching bands, esters**	Spectrum EY_av, Rosi et al, 2009, p. 2099
	EY_M_25_av	strong absorption	**C-H stretching bands, esters**	Spectrum EY_av, Rosi et al, 2009, p. 2099
2965	**EY_M_75_av**	strong absorption	**C-H stretching bands, esters**	Spectrum EY_av, Rosi et al, 2009, p. 2099
3004	**EY_M_50_av**	weak absorption	**CH stretching**	Miliani et al, 2012, p. 302
3006	**UN_7**	(blank)	**(blank)**	(blank)
3007	**EY_M_25_av**	weak absorption	**CH stretching**	Miliani et al, 2012, p. 302
3011	**EY_M_75_av**	weak absorption	**CH stretching**	Miliani et al, 2012, p. 302
3077	**EY_M_5_av**	weak absorption	**2δNH**	Rosi et al, 2010, p. 621

Figure 43: continued.

UN_I_8

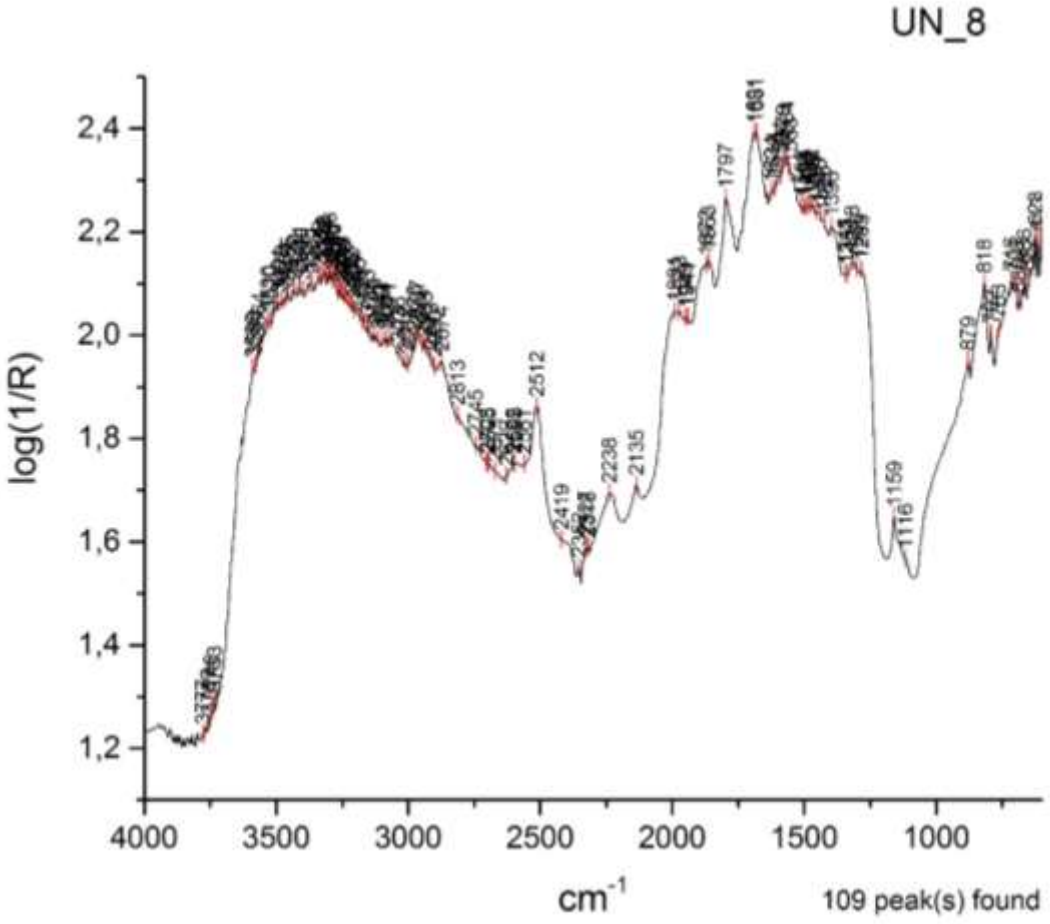

Figure 44: UN_I_8 correctly identified as 50% egg white additive in mortar (EW_M_50).

The overall pattern of the unknown spectrum indicates amides in mortar (fig.44). The comparison of the unknown spectrum with all the egg white/mortar mixtures shows that 50% egg white/mortar mixture shares the higher number of closely related organic peaks (fig.45).

Peak x (position)	Spectrum ID	Type of band	Chemical Band Assignement	Reference
875	EW_M_75_av	weak absorption	egg white, CaCO3 v2 carbonate ion	Spectrum EW_av, spectrum Ca_av, spectrum M_av, Ylmen and Jaglid, 2013, p. 119
1082	EW_M_50_av	weak absorption	egg white	spectrum EW_av
1085	EW_M_25_av	weak absorption	egg white	spectrum EW_av
1086	EW_M_5_av	weak absorption	egg white	spectrum EW_av
1116	EW_M_50_av	weak absorption	C-O stretching	Buti et al, 2013, p. 2705
1283	EW_M_50_av	weak absorption	egg white	spectrum EW_av
1285	EW_M_75_av	weak absorption	egg white	spectrum EW_av
1313	EW_M_50_av	weak absorption	egg white	spectrum EW_av
1314	EW_M_75_av	weak absorption	egg white	spectrum EW_av
1318	UN_8	(blank)	(blank)	(blank)
1412	EW_M_75_av	weak absorption	egg white	spectrum EW_av
1446	EW_M_50_av	weak absorption	egg white	spectrum EW_av
1453	EW_M_75_av	weak absorption	egg white	spectrum EW_av
1461	EW_M_75_av	weak absorption	egg white	spectrum EW_av
1476	EW_M_25_av	weak absorption	egg white	spectrum EW_av
1480	EW_M_50_av	weak absorption	egg white	spectrum EW_av
1498	EW_M_25_av	weak absorption	C=O	Rosi et al, 2002, p. 2099
1571	EW_M_25_av	strong absorption	C-N-H bending amide II, N-H bands	Spectrum EW_av, Rosi et al, 2009, p. 2104
1575	EW_M_75_av	strong absorption	C-N-H bending amide II, N-H bands	Spectrum EW_av, Rosi et al, 2009, p. 2104
1576	EW_M_50_av	strong absorption	C-N-H bending amide II, N-H bands	Spectrum EW_av, Rosi et al, 2009, p. 2104
1577	EW_M_25_av	strong absorption	C-N-H bending amide II, N-H bands	Spectrum EW_av, Rosi et al, 2009, p. 2104
1578	UN_8	(blank)	(blank)	(blank)
1579	EW_M_5_av	strong absorption	C-N-H bending amide II, N-H bands	Spectrum EW_av, Rosi et al, 2009, p. 2104
1601	EW_M_5_av	weak absorption	N-H bands	Miliani et al, 2012, p. 304; Rosi et al, 2009, p. 2104
1621	EW_M_25_av	weak absorption	N-H bands	Miliani et al, 2012, p. 304; Rosi et al, 2009, p. 2104
1629	EW_M_25_av	weak absorption	N-H bands	Miliani et al, 2012, p. 304; Rosi et al, 2009, p. 2104
1630	EW_M_5_av	weak absorption	N-H bands	Miliani et al, 2012, p. 304; Rosi et al, 2009, p. 2104
1641	EW_M_25_av	weak absorption	N-H bands	Miliani et al, 2012, p. 304; Rosi et al, 2009, p. 2104
1681	UN_8	(blank)	(blank)	(blank)
1685	EW_M_50_av	strong absorption	N-H bands	Spectrum EW_av, Ploeger et al, 2010, p.37, Miliani et al, 2012, p. 305
1691	UN_8	(blank)	(blank)	(blank)
1692	EW_M_75_av	strong absorption	N-H bands	Spectrum EW_av, Ploeger et al, 2010, p.37, Miliani et al, 2012, p. 305

Figure 45: Filtered CPAD of peaks of interest for UN_I_8 spectrum and possible matches.

2544	**EW_M_75_av**	weak absorption	**egg white**	spectrum EW_av
2564	**EW_M_50_av**	weak absorption	**egg white**	spectrum EW_av
2571	**EW_M_25_av**	weak absorption	**egg white**	spectrum EW_av
2585	**EW_M_25_av**	weak absorption	**egg white**	spectrum EW_av
2589	**EW_M_50_av**	weak absorption	**egg white**	spectrum EW_av
2595	**EW_M_50_av**	weak absorption	**egg white**	spectrum EW_av
2603	**EW_M_75_av**	weak absorption	**egg white**	spectrum EW_av
2616	**EW_M_75_av**	weak absorption	**egg white**	spectrum EW_av
2690	**EW_M_25_av**	weak absorption	**egg white**	spectrum EW_av
2694	**EW_M_50_av**	weak absorption	**egg white**	spectrum EW_av
2703	**EW_M_5_av**	weak absorption	**egg white**	spectrum EW_av
2874	**UN_8**	(blank)	**(blank)**	(blank)
2900	**UN_8**	(blank)	**(blank)**	(blank)
2913	**UN_8**	(blank)	**(blank)**	(blank)
2933	**UN_8**	(blank)	**(blank)**	(blank)
2934	**EW_M_25_av**	weak absorption	**CH stretching**	Spectrum EW_av, Daher et al, 2017, p. 8
	EW_M_50_av	weak absorption	**CH stretching**	Spectrum EW_av, Daher et al, 2017, p. 8
2936	**EW_M_5_av**	weak absorption	**CH stretching**	Spectrum EW_av, Daher et al, 2017, p. 8
2940	**EW_M_75_av**	weak absorption	**CH stretching**	Spectrum EW_av, Daher et al, 2017, p. 8
2943	**EW_M_50_av**	weak absorption	**CH3 stretching**	Spectrum EW_av, Iwanicka et al, 2017, p. 18
2944	**UN_8**	(blank)	**(blank)**	(blank)
2948	**EW_M_75_av**	weak absorption	**CH3 stretching**	Spectrum EW_av, Iwanicka et al, 2017, p. 18
2967	**UN_8**	(blank)	**(blank)**	(blank)
2975	**UN_8**	(blank)	**(blank)**	(blank)
3001	**UN_8**	(blank)	**(blank)**	(blank)
3012	**UN_8**	(blank)	**(blank)**	(blank)
3066	**EW_M_5_av**	1st overtone	**amide I**	Spectrum EW_av, Rosi et al, 2009, p. 2099
3083	**EW_M_25_av**	1st overtone	**amide I**	Spectrum EW_av, Rosi et al, 2009, p. 2099
3084	**EW_M_50_av**	1st overtone	**amide I**	Spectrum EW_av, Rosi et al, 2009, p. 2099
3085	**EW_M_5_av**	1st overtone	**amide I**	Spectrum EW_av, Rosi et al, 2009, p. 2099
3086	**EW_M_75_av**	1st overtone	**amide I**	Spectrum EW_av, Rosi et al, 2009, p. 2099
3094	**EW_M_50_av**	1st overtone	**amide I**	Spectrum EW_av, Rosi et al, 2009, p. 2099
3095	**EW_M_25_av**	1st overtone	**amide I**	Spectrum EW_av, Rosi et al, 2009, p. 2099
3304	**EW_M_25_av**	weak absorption	**N-H stretching**	Rosi et al, 2002, p. 2099
3314	**EW_M_5_av**	weak absorption	**N-H stretching**	Rosi et al, 2002, p. 2099

Figure 45: continued.

UN_I_10

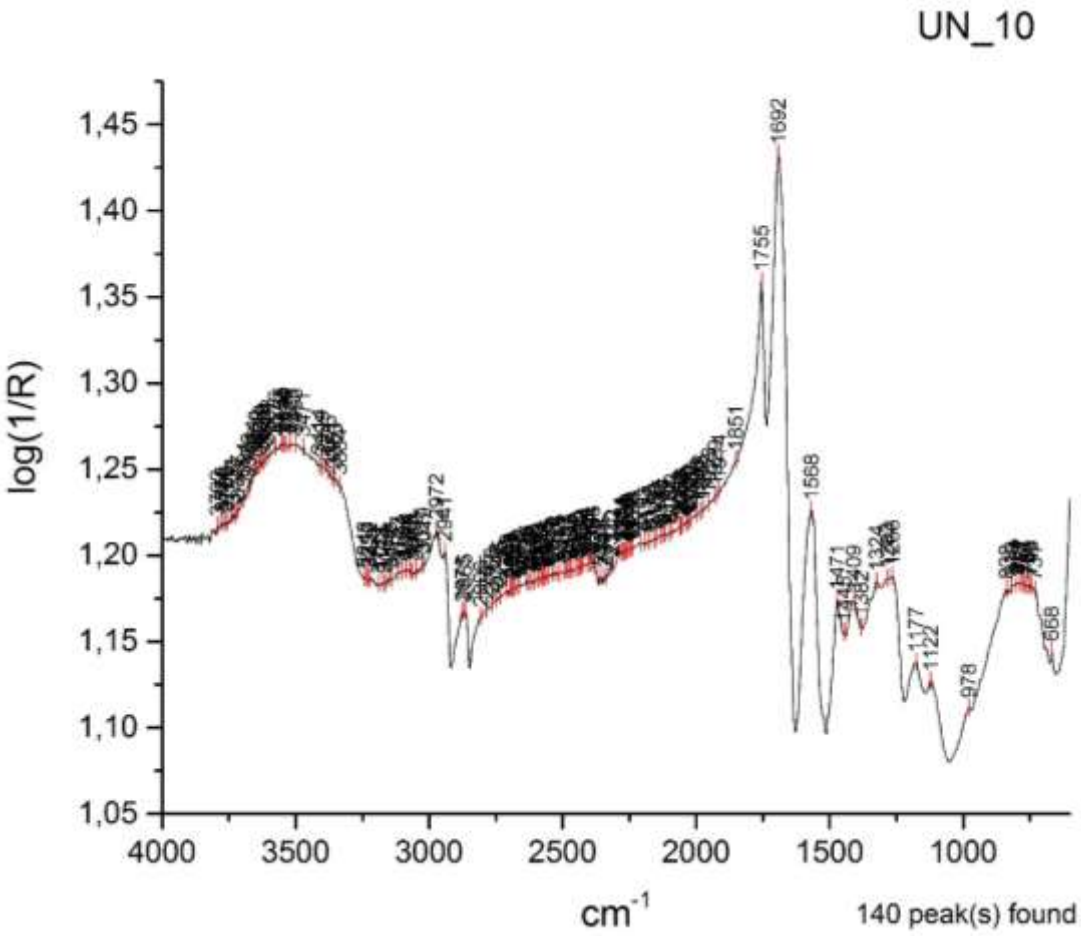

Figure 46: UN_I_10 correctly identified as egg (E).

The shape and intensity of the peaks and the presence of second-derivative distortions indicate the co-existence of lipids and amides and the absence of mortar (fig.46). Most peaks of interest on the unknown spectrum (blue) match those of egg standard (yellow) instead those of egg yolk (EY_av) (fig.47).

Peak x (position)	Spectrum ID	Type of band	Chemical Band Assignement	Reference
667	EY_av	sharp and weak absorption	(blank)	(blank)
668	E_av	sharp and weak absorption	(blank)	spectrum EY_av, spectrum EW_av
710	EY_av	weak absorption	(blank)	(blank)
734	E_av	weak absorption	(blank)	(blank)
744	EY_av	weak absorption	(blank)	(blank)
745	E_av	weak absorption	(blank)	spectrum EY_av
765	E_av	weak absorption	(blank)	spectrum EY_av
770	EY_av	(blank)	(blank)	(blank)
781	EY_av	(blank)	(blank)	(blank)
789	EY_av	(blank)	(blank)	(blank)
794	E_av	weak absorption	(blank)	spectrum EY_av
802	E_av	weak absorption	(blank)	spectrum EY_av
808	EY_av	(blank)	(blank)	(blank)
819	EY_av	(blank)	(blank)	(blank)
835	E_av	weak absorption	(blank)	(blank)
973	E_av	weak absorption	PO4-3anion stretching	Ricci et al, 2006, p. 1223, spectrum EY_av
974	EY_av	sharp and weak absorption	PO4-3anion stretching	Ricci et al, 2006, p. 1223
978	UN_10	(blank)	(blank)	(blank)
1070	EY_av	reststrahlen	PO4-3anion stretching	Ricci et al, 2006, p. 1223
1122	UN_10	(blank)	(blank)	(blank)
1123	E_av	weak absorption	PO4-3anion stretching	Ricci et al, 2006, p. 1223, spectrum EY_av
1124	EY_av	sharp and weak absorption	PO4-3anion stretching	Ricci et al, 2006, p. 1223
1177	E_av	weak absorption	v(C-O) stretching	Ricci et al, 2006, p. 1224, spectrum EW_av
	UN_10	(blank)	(blank)	(blank)
1198	EY_av	weak absorption	(blank)	(blank)
1266	UN_10	(blank)	(blank)	(blank)
1268	E_av	strong absorption	C-O	Ploeger et al, 2010, p. 37, spectrum EY_av
1270	EY_av	strong absorption	(blank)	(blank)
1283	EY_av	sharp absorption	(blank)	(blank)
	UN_10	(blank)	(blank)	(blank)
1324	E_av	(blank)	(blank)	spectrum EW_av
	UN_10	(blank)	(blank)	(blank)
1382	UN_10	(blank)	(blank)	(blank)
1385	EY_av	sharp absorption	C-H bending	Buti et al, 2013, p. 2705
1409	UN_10	(blank)	(blank)	(blank)
1411	E_av	(blank)	(blank)	spectrum EW_av
1420	EY_av	weak absorption	(blank)	(blank)
1445	E_av	weak absorption	Amide III	Buti et al, 2013, p. 2705, spectrum EW_av
	EY_av	weak absorption	(blank)	(blank)
	UN_10	(blank)	(blank)	(blank)
1471	UN_10	(blank)	(blank)	(blank)
1472	E_av	sharp absorption	C-O bending	Ricci et al, 2006, p. 1223, spectrum EW_av and EY_av
	EY_av	sharp absorption	C-O bending	Ricci et al, 2006, p. 1223

Figure 47: Filtered CPAD of peaks of interest for UN_I_10 spectrum and possible matches.

1507	**EY_av**	weak absorption	**C=O**	Rosi et al, 2009, p. 2099
1519	**EY_av**	weak absorption	**C=O**	Rosi et al, 2009, p. 2099
1559	**EY_av**	strong absorption	**C=O**	Rosi et al, 2009, p. 2099
1568	**E_av**	strong absorption	**N-H bands, amide I, II**	Miliani et al, 2012, p. 304, spectrum EW_av
	UN_10	(blank)	**(blank)**	(blank)
1667	**EY_av**	strong absorption	**C=O**	(blank)
1692	**UN_10**	(blank)	**(blank)**	(blank)
1693	**E_av**	strong absorption	**N-H bands, amide I, II**	Miliani et al, 2012, p. 304, spectrum EW_av
1755	**E_av**	strong absorption	**C=O stretching band, esters**	Mazzeo et al, 2008, p. 69, spectrum EY_av
	UN_10	(blank)	**(blank)**	(blank)
1758	**EY_av**	stretching band	**esters**	Mazzeo et al, 2008, p. 69
2864	**E_av**	strong absorption	**C-H stretching**	Rosi et al, 2009, p. 2099, spectrum EY_av
	EY_av	strong absorption	**C-H stretching**	Rosi et al, 2009, p. 2099
2865	**UN_10**	(blank)	**(blank)**	(blank)
2875	**UN_10**	(blank)	**(blank)**	(blank)
2876	**E_av**	strong absorption	**C-H stretching**	Rosi et al, 2009, p. 2099, spectrum EY_av
2941	**UN_10**	(blank)	**(blank)**	(blank)
2942	**E_av**	strong absorption	**C-H stretching bands, esters**	Spectrum EY_av, Rosi et al, 2009, p. 2099
	EY_av	sharp absorption	**C-H stretching**	Rosi et al, 2009, p. 2099
2967	**EY_av**	sharp absorption	**C-H stretching**	Rosi et al, 2009, p. 2099
2972	**UN_10**	(blank)	**(blank)**	(blank)
2973	**E_av**	strong absorption	**C-H stretching bands, esters**	Spectrum EY_av, Rosi et al, 2009, p. 2099
3015	**EY_av**	weak absorption	**CH stretching**	Miliani et al, 2012, p. 302
3019	**UN_10**	(blank)	**(blank)**	(blank)
3045	**E_av**	weak absorption	**2δNH**	Rosi et al, 2010, p. 621
3075	**E_av**	weak absorption	**2δNH**	Rosi et al, 2010, p. 621
3089	**E_av**	weak absorption	**2δNH**	Rosi et al, 2010, p. 621
3102	**E_av**	weak absorption	**2δNH**	Rosi et al, 2010, p. 621
3224	**E_av**	(blank)	**(blank)**	(blank)
3240	**E_av**	(blank)	**(blank)**	(blank)

Figure 47: continued.

8.1.2 Experimental set II

UN_II_1

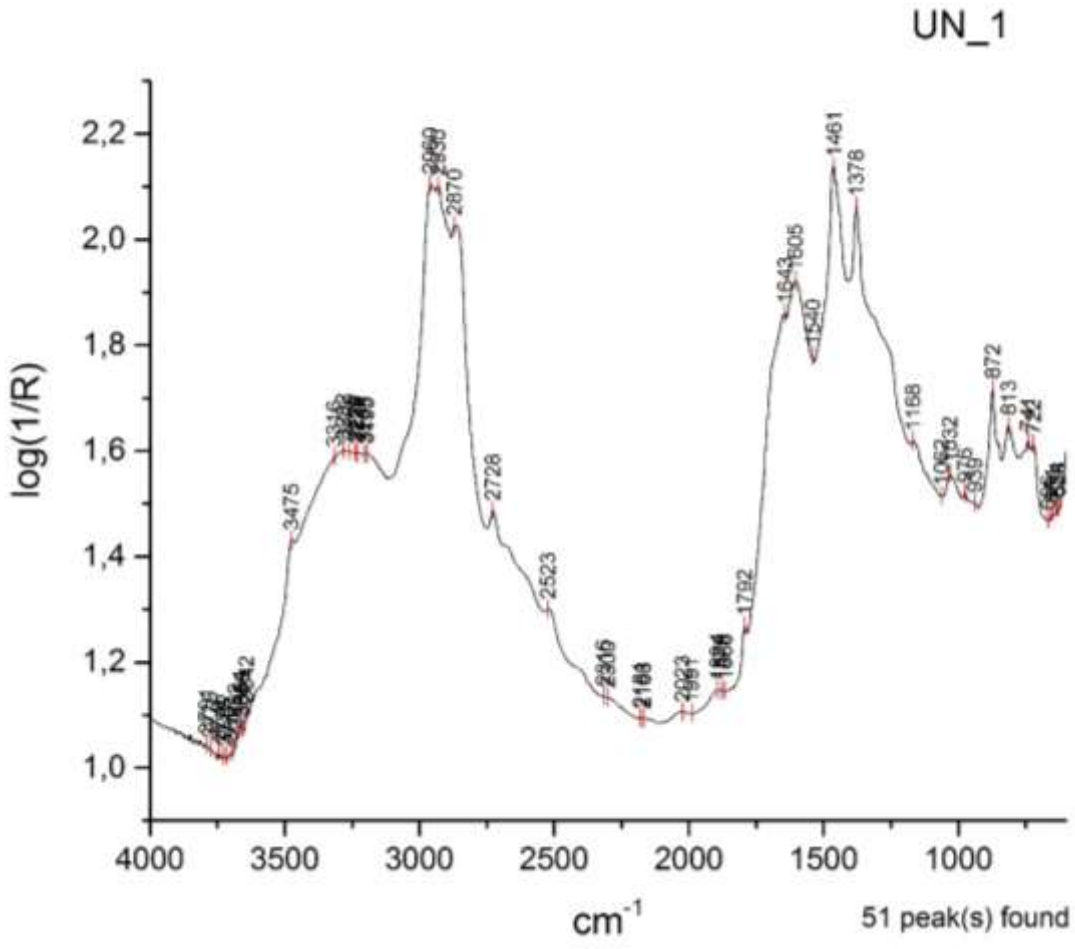

Figure 48: UN_II_1 identified as 75% asphalt additive in mortar (A_M_75) instead of the correct 50% asphalt in mortar (A_M_50).

Peak x (position)	Spectrum ID	Type of band	Chemical Band Assignement	Reference
722	A_M_50_av	triplet	asphalt	Spectrum A_av, Lombardi and Santarelli, 2009, 542
	UN_1	(blank)	(blank)	(blank)
724	A_M_75_av	triplet	asphalt	Spectrum A_av, Lombardi and Santarelli, 2009, 542
740	A_M_50_av	triplet	asphalt	Spectrum A_av, Lombardi and Santarelli, 2009, 542
741	UN_1	(blank)	(blank)	(blank)
742	A_M_75_av	triplet	asphalt	Spectrum A_av, Lombardi and Santarelli, 2009, 542
759	A_M_75_av	(blank)	(blank)	(blank)
793	A_M_50_av	weak absorption	quartz	Spectrum Q_av, spectrum M_av
813	UN_1	(blank)	(blank)	(blank)
814	A_M_75_av	triplet	asphalt	Spectrum A_av, Lombardi and Santarelli, 2009, 542
815	A_M_50_av	sharp absorption	Si-O antisymmetric stretching	Spectrum Q_av, spectrum M_av, Miliani et al, 2013, p. 303
849	A_M_50_av	weak absorption	v2 carbonate ion	Spectrum Ca_av, spectrum M_av, Ylmen and Jaglid, 2013, p. 119
872	A_M_75_av	triplet	asphalt	Spectrum A_av, Lombardi and Santarelli, 2009, 542
	A_M_50_av	triplet	asphalt	Spectrum A_av, Lombardi and Santarelli, 2009, 542
	UN_1	(blank)	(blank)	(blank)
934	A_M_50_av	weak absorption	asphalt	Spectrum A_av
937	A_M_75_av	(blank)	asphalt	Spectrum A_av
953	A_M_50_av	weak absorption	(blank)	(blank)
976	A_M_75_av	(blank)	asphalt	Spectrum A_av
	A_M_50_av	weak absorption	asphalt	Spectrum A_av
1016	A_M_50_av	(blank)	(blank)	(blank)
1030	A_M_50_av	(blank)	quartz	Spectrum A_av, Lombardi and Santarelli, 2009, 542
1033	A_M_75_av	sharp absorption	quartz	Spectrum A_av, Lombardi and Santarelli, 2009, 542
1160	A_M_50_av	sharp absorption	quartz	Spectrum A_av, spectrum Q_av, spectrum M_av
1169	A_M_75_av	weak absorption	asphalt	Spectrum A_av
1378	A_M_75_av	strong absorption	CH2, CH3	Spectrum A_av, Lombardi and Santarelli, 2009, 542
	A_M_50_av	strong absorption	CH2, CH3	Spectrum A_av, Lombardi and Santarelli, 2009, 542
	UN_1	(blank)	(blank)	(blank)
1461	A_M_75_av	strong absorption	asphalt	Spectrum A_av
	A_M_50_av	strong absorption	asphalt	Spectrum A_av
	UN_1	(blank)	(blank)	(blank)
1603	A_M_75_av	strong absorption	C6H6 (benzene rings)	Spectrum A_av, Lombardi and Santarelli, 2009, 542
	A_M_50_av	strong absorption	C6H6 (benzene rings)	Spectrum A_av, Lombardi and Santarelli, 2009, 542
1605	UN_1	(blank)	(blank)	(blank)
1643	A_M_75_av	weak absorption	(blank)	Spectrum A_av
	A_M_50_av	shoulder	(blank)	Spectrum A_av
	UN_1	(blank)	(blank)	(blank)

Figure 49: Filtered CPAD of peaks of interest for UN_II_1 spectrum and possible matches.

1792	**A_M_50_av**	combination band	**v1+v4**	Spectrum Ca_av, spectrum M_av, Ricci et al, 2006, p. 1222
1843	**A_M_75_av**	weak absorption	**quartz**	Spectrum Q_av, spectrum M_av, spectrum A_av
	A_M_50_av	weak absorption	**quartz**	Spectrum Q_av, spectrum M_av, spectrum A_av
1866	**A_M_75_av**	weak absorption	**quartz**	Spectrum Q_av, spectrum M_av, spectrum A_av
1867	**A_M_50_av**	weak absorption	**quartz**	Spectrum Q_av, spectrum M_av, spectrum A_av
1888	**A_M_75_av**	weak absorption	**quartz**	spectrum A_av, spectrum Q_av
	A_M_50_av	weak absorption	**quartz**	Spectrum Q_av, spectrum A_av
2016	**A_M_50_av**	weak absorption	**asphalt**	Spectrum A_av
2023	**A_M_50_av**	weak absorption	**asphalt**	Spectrum A_av
2032	**A_M_75_av**	weak absorption	**(blank)**	Spectrum A_av
2138	**A_M_50_av**	weak absorption	**(blank)**	Spectrum Q_av, spectrum M_av, spectrum Ca_av
2519	**A_M_50_av**	combination band	**v1+v3**	Spectrum M_av, spectrum Ca_av, Ricci et al, 2006, p. 1222
2727	**A_M_75_av**	weak absorption	**(blank)**	Spectrum A_av
	A_M_50_av	sharp and weak absorption	**asphalt**	Spectrum A_av
2728	**UN_1**	(blank)	**(blank)**	(blank)
2856	**A_M_50_av**	strong absorption	**CH2, CH3 stretching**	Spectrum A_av, Lombardi and Santarelli, 2009, 542
2858	**A_M_75_av**	strong absorption	**CH2, CH3 stretching**	Spectrum A_av, Lombardi and Santarelli, 2009, 542
2867	**A_M_75_av**	strong absorption	**CH2, CH3 stretching**	Spectrum A_av, Lombardi and Santarelli, 2009, 542
	A_M_50_av	strong absorption	**CH2, CH3 stretching**	Spectrum A_av, Lombardi and Santarelli, 2009, 542
2870	**UN_1**	(blank)	**(blank)**	(blank)
2930	**UN_1**	(blank)	**(blank)**	(blank)
2931	**A_M_75_av**	strong absorption	**CH2, CH3 stretching**	Spectrum A_av, Lombardi and Santarelli, 2009, 542
	A_M_50_av	strong absorption	**CH2, CH3 stretching**	Spectrum A_av, Lombardi and Santarelli, 2009, 542
2954	**A_M_75_av**	strong absorption	**CH2, CH3 stretching**	Spectrum A_av, Lombardi and Santarelli, 2009, 542
2956	**A_M_50_av**	strong absorption	**CH2, CH3 stretching**	Spectrum A_av, Lombardi and Santarelli, 2009, 542
2960	**UN_1**	(blank)	**(blank)**	(blank)
2961	**A_M_75_av**	strong absorption	**CH2, CH3 stretching**	Spectrum A_av, Lombardi and Santarelli, 2009, 542
3200	**A_M_75_av**	weak absorption	**asphalt**	Spectrum A_av
3215	**A_M_75_av**	weak absorption	**asphalt**	Spectrum A_av
3267	**A_M_75_av**	weak absorption	**asphalt**	Spectrum A_av
3288	**A_M_75_av**	weak absorption	**asphalt**	Spectrum A_av
3473	**A_M_75_av**	weak absorption	**asphalt**	Spectrum A_av
	A_M_50_av	weak absorption	**asphalt**	Spectrum A_av
3664	**A_M_75_av**	weak absorption	**asphalt**	Spectrum A_av

Figure 49: continued.

UN_II_3

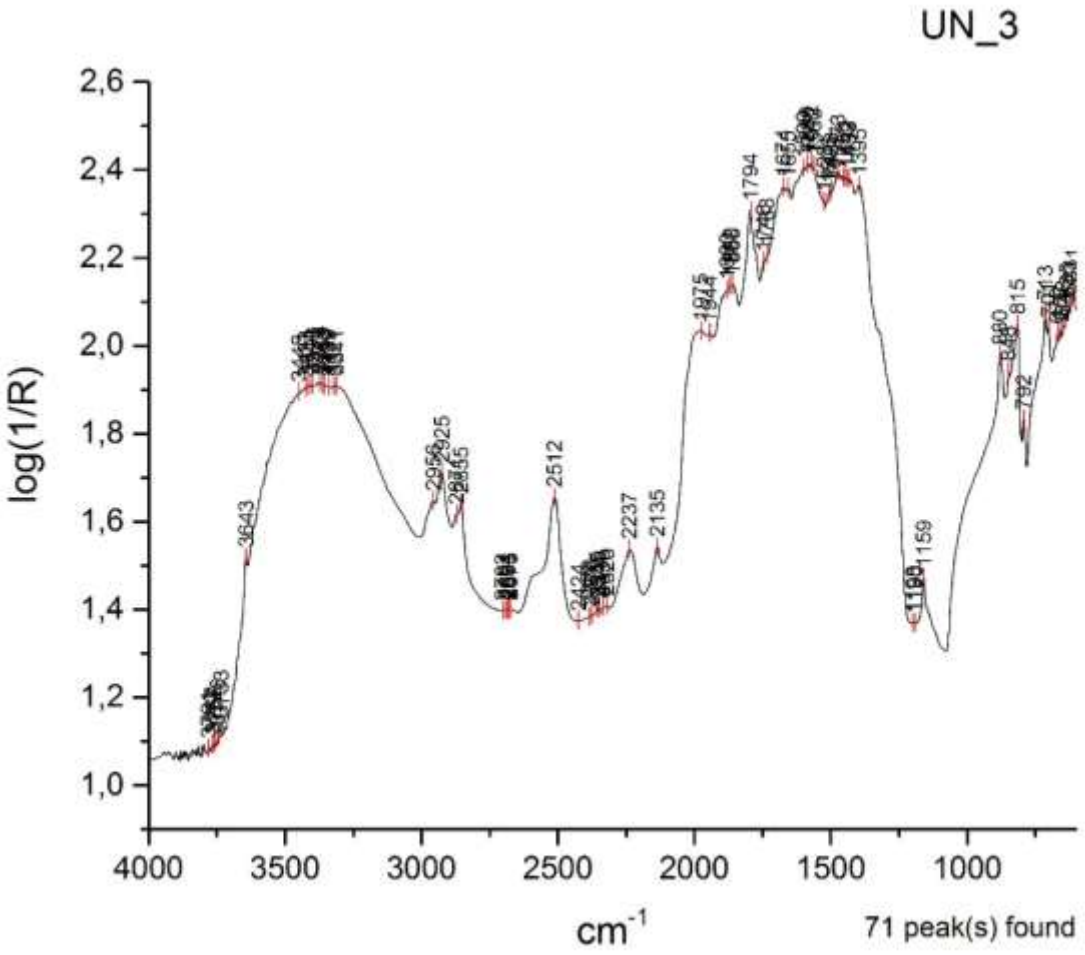

Figure 50: UN_II_3 correctly identified as 5% egg additive in mortar (E_M_5).

Peak x (position)	Spectrum ID	Type of band	Chemical Band Assignement	Reference
619	EY_M_5_av	weak absorption	CaCO3	Spectrum M_av, spectrum Ca_av
636	EY_M_5_av	weak absorption	CaCO3	Spectrum M_av, spectrum Ca_av
666	E_M_5_av	weak absorption	whole egg	Spectrum E_av
702	EY_M_5_av	strong absorption	quartz	Spectrum M_av, spectrum Q_av
713	EY_M_5_av	strong absorption	v4 carbonate ion	Spectrum M_av, spectrum Ca_av, Ylmen and Jaglid, 2013, p. 119
714	E_M_5_av	weak absorption	v4 carbonate ion	Spectrun M_av, Spectrum Ca_av, Ylmen and Jaglid, 2013, p. 119
791	EY_M_5_av	sharp absorption	quartz	Spectrum M_av, spectrum Q_av
792	E_M_5_av	sharp absorption	quartz	Spectrun M_av, Spectrum Q_av
815	E_M_5_av	strong absorption	quartz	Spectrun M_av, Spectrum Q_av
	EY_M_5_av	strong absorption	quartz	Spectrum M_av, spectrum Q_av
848	E_M_5_av	weak absorption	v2 carbonate ion	Spectrun M_av, Spectrum Ca_av, Ylmen and Jaglid, 2013, p. 119
	EY_M_5_av	sharp absorption	v2 carbonate ion	Spectrum M_av, spectrum Ca_av, Ylmen and Jaglid, 2013, p. 119
877	EY_M_5_av	strong absorption	v2 carbonate ion	Spectrum M_av, spectrum Ca_av, Ylmen and Jaglid, 2013, p. 119
880	E_M_5_av	weak absorption	v2 carbonate ion	Spectrun M_av, Spectrum Ca_av, Ylmen and Jaglid, 2013, p. 119
1081	E_M_5_av	weak absorption	v1 carbonate ion	Spectrum Ca_av, Ylmen and Jaglid, 2013, p. 119
1159	E_M_5_av	strong absorption	quartz	Spectrun M_av, Spectrum Q_av
	EY_M_5_av	sharp absorption	quartz	Spectrum M_av, spectrum Q_av
1198	EY_M_5_av	weak absorption	egg yolk	spectrum EY_av
1394	E_M_5_av	strong absorption	CaCO3	Spectrun M_av, Spectrum Ca_av
1399	EY_M_5_av	strong absorption	CaCO3	Spectrum M_av, spectrum Ca_av
1436	EY_M_5_av	strong absorption	v3 antisymmetric stretching CO3-2	Spectrum Ca_av, Ylmen and Jaglid, 2013, p. 119
1438	E_M_5_av	weak absorption	whole egg	Spectrum E_av
1451	EY_M_5_av	strong absorption	v3 antisymmetric stretching CO3-2	Spectrum Ca_av, Ylmen and Jaglid, 2013, p. 119
1460	E_M_5_av	weak absorption	v3 antisymmetric stretching CO3-2	Spectrum M_av, spectrum Ca_av, Ylmen and Jaglid, 2013, p. 119
1466	EY_M_5_av	strong absorption	v3 antisymmetric stretching CO3-2	Spectrum Ca_av, Ylmen and Jaglid, 2013, p. 119
1472	E_M_5_av	strong absorption	C-O bending	Spectrum E_av, Ricci et al, 2006, p. 1223
1473	UN_3	(blank)	(blank)	(blank)
1539	EY_M_5_av	weak absorption	C=O	Spectrum EY_av, Rosi et al, 2009, p. 2098
1573	E_M_5_av	weak absorption	v3 antisymmetric stretching CO3-2	Spectrum M_av, spectrum Ca_av, Ylmen and Jaglid, 2013, p. 119
1581	E_M_5_av	weak absorption	v3 antisymmetric stretching CO3-2	Spectrum M_av, spectrum Ca_av, Ylmen and Jaglid, 2013, p. 119
1584	EY_M_5_av	strong absorption	v3 antisymmetric stretching CO3-2	Spectrum Ca_av, Ylmen and Jaglid, 2013, p. 119
1586	UN_3	(blank)	(blank)	(blank)
1599	E_M_5_av	weak absorption	quartz	Spectrun M_av, Spectrum Q_av
1612	EY_M_5_av	weak absorption	quartz	spectrum Q_av
1655	UN_3	(blank)	(blank)	(blank)
1658	EY_M_5_av	weak absorption	quartz	Spectrum M_av, spectrum Q_av
1659	E_M_5_av	strong absorption	quartz	Spectrun M_av, Spectrum Q_av

Figure 51: Filtered CPAD of peaks of interest for UN_II_3 spectrum and possible matches.

1674	**UN_3**	(blank)	**(blank)**	(blank)
1675	**EY_M_5_av**	strong absorption	**C=O**	Spectrum EY_av, Rosi et al, 2009, p. 2099
1676	**E_M_5_av**	strong absorption	**quartz**	Spectrun M_av, Spectrum Q_av
1744	**EY_M_5_av**	1st order derivative	**C=O stretching band**	Spectrum EY_av, Ploeger et al, 2010, p, 37
1794	**E_M_5_av**	combination band	**v1+v4**	Spectrum M_av, spectrum Ca_av, Ricci et al, 2006, p. 1222
	EY_M_5_av	combination band	**v1+v4**	Spectrum M_av, spectrum Ca_av, Ricci et al, 2006, p. 1222
1858	**E_M_5_av**	weak absorption	**quartz**	Spectrun M_av, Spectrum Q_av
1860	**EY_M_5_av**	weak absorption	**quartz**	Spectrum M_av, spectrum Q_av
1867	**EY_M_5_av**	weak absorption	**quartz**	Spectrum M_av, spectrum Q_av
1942	**EY_M_5_av**	weak absorption	**quartz**	Spectrum M_av, spectrum Q_av
1943	**E_M_5_av**	weak absorption	**quartz**	Spectrun M_av, Spectrum Q_av
1971	**EY_M_5_av**	weak absorption	**quartz**	Spectrum M_av, spectrum Q_av
1974	**E_M_5_av**	weak absorption	**quartz**	Spectrun M_av, Spectrum Q_av
1990	**EY_M_5_av**	weak absorption	**quartz**	Spectrum M_av, spectrum Q_av
2135	**E_M_5_av**	sharp absorption	**CaCO3 and quartz**	Spectrun M_av, Spectrum Q_av, spectrum Ca_av
	EY_M_5_av	weak absorption	**calcium carbonate and quartz**	Spectrum Ca_av, spectrum M_av, spectrum Q_av
2237	**E_M_5_av**	sharp absorption	**quartz**	Spectrun M_av, Spectrum Q_av
	EY_M_5_av	weak absorption	**quartz**	spectrum Q_av
2512	**E_M_5_av**	combination band	**v1+v3**	Spectrum M_av, spectrum Ca_av, Ricci et al, 2006, p. 1222
	EY_M_5_av	combination band	**v1+v3**	Spectrum M_av, spectrum Ca_av, Ricci et al, 2006, p. 1222
2673	**E_M_5_av**	weak absorption	**CaCO3**	Spectrum M_av, spectrum Ca_av
2682	**E_M_5_av**	weak absorption	**CaCO3**	Spectrum M_av, spectrum Ca_av
	EY_M_5_av	weak absorption	**(blank)**	(blank)
2691	**EY_M_5_av**	weak absorption	**(blank)**	(blank)
2855	**E_M_5_av**	strong absorption	**CH stretching**	Spectrum E_av, Daher et al, 2017, p.8
	EY_M_5_av	strong absorption	**C-H stretching bands, esters**	Spectrum EY_av, Rosi et al, 2009, p. 2099
	UN_3	(blank)	**(blank)**	(blank)
2871	**E_M_5_av**	strong absorption	**CH stretching**	Spectrum E_av, Daher et al, 2017, p.8
	UN_3	(blank)	**(blank)**	(blank)
2925	**EY_M_5_av**	strong absorption	**CH stretching**	Spectrum EY_av, Daher et al, 2017, p.8
	UN_3	(blank)	**(blank)**	(blank)
2926	**E_M_5_av**	weak absorption	**CH2 stretching**	Spectrum E_av, Ploeger et al, 2010, p. 37
2956	**UN_3**	(blank)	**(blank)**	(blank)
2957	**E_M_5_av**	weak absorption	**CH2 stretching**	Spectrum E_av, Ploeger et al, 2010, p. 37
	EY_M_5_av	strong absorption	**C-H stretching bands, esters**	Spectrum EY_av, Rosi et al, 2009, p. 2099
3077	**EY_M_5_av**	weak absorption	**2δNH**	Rosi et al, 2010, p. 621
3642	**E_M_5_av**	doublet	**OH stretching of H2O**	Spectrum M_av, spectrum Ca_av, Rosi et al, 2009, p. 2100
3643	**EY_M_5_av**	doublet	**OH stretching**	Spectrum M_av, spectrum Ca_av, Rosi et al, 2009, p. 2100

Figure 51: continued.

UN_II_4

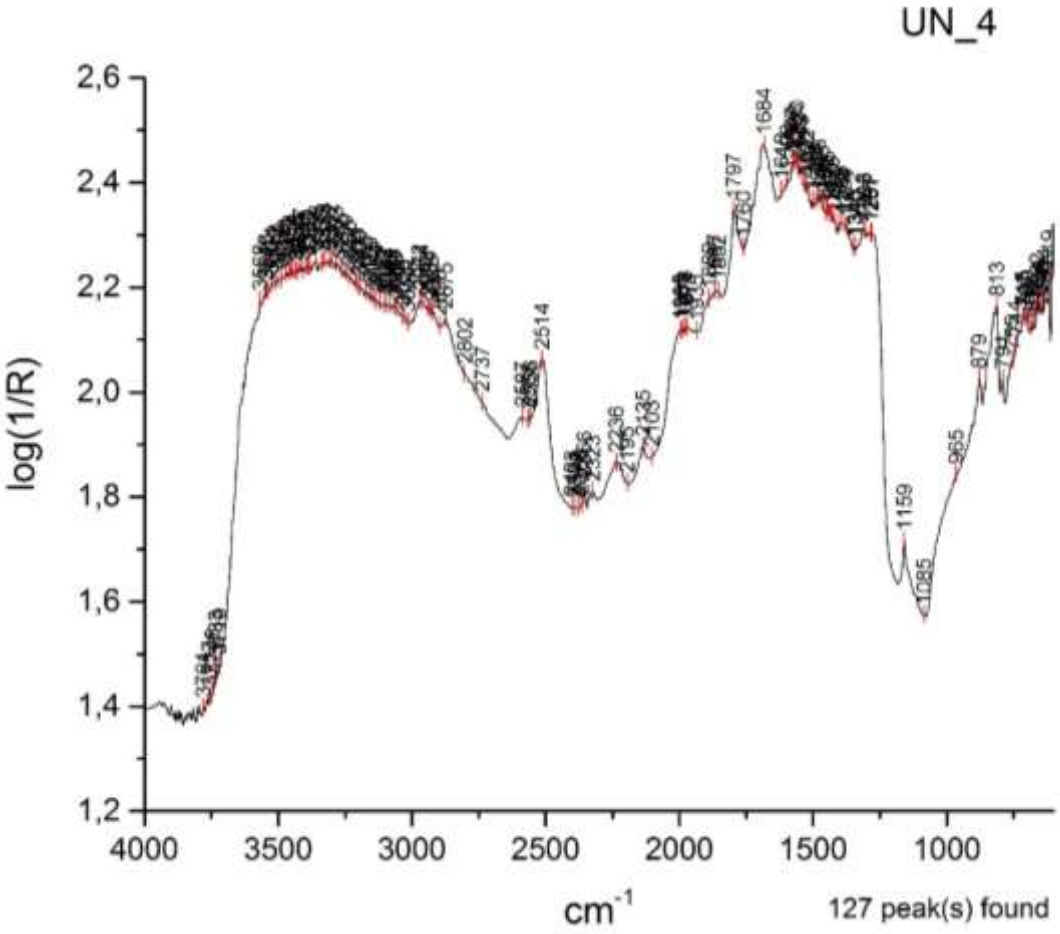

Figure 52: UN_II_4 correctly identified as 50% egg white additive in mortar (EW_M_50).

Peak x (position)	Spectrum ID	Type of band	Chemical Band Assignement	Reference
1082	EW_M_50_av	weak absorption	egg white	spectrum EW_av
1085	EW_M_25_av	weak absorption	egg white	spectrum EW_av
1086	EW_M_5_av	weak absorption	egg white	spectrum EW_av
1116	EW_M_50_av	weak absorption	C-O stretching	Buti et al, 2013, p. 2705
1281	UN_4	(blank)	(blank)	(blank)
1283	EW_M_50_av	weak absorption	egg white	spectrum EW_av
1287	UN_4	(blank)	(blank)	(blank)
1305	UN_4	(blank)	(blank)	(blank)
1313	EW_M_50_av	weak absorption	egg white	spectrum EW_av
	UN_4	(blank)	(blank)	(blank)
1340	UN_4	(blank)	(blank)	(blank)
1348	UN_4	(blank)	(blank)	(blank)
1374	UN_4	(blank)	(blank)	(blank)
1384	UN_4	(blank)	(blank)	(blank)
1398	UN_4	(blank)	(blank)	(blank)
1415	UN_4	(blank)	(blank)	(blank)
1429	UN_4	(blank)	(blank)	(blank)
1437	UN_4	(blank)	(blank)	(blank)
1446	EW_M_50_av	weak absorption	egg white	spectrum EW_av
	UN_4	(blank)	(blank)	(blank)
1453	UN_4	(blank)	(blank)	(blank)
1466	UN_4	(blank)	(blank)	(blank)
1476	EW_M_25_av	weak absorption	egg white	spectrum EW_av
1478	UN_4	(blank)	(blank)	(blank)
1480	EW_M_50_av	weak absorption	egg white	spectrum EW_av
1488	UN_4	(blank)	(blank)	(blank)
1498	EW_M_25_av	weak absorption	C=O	Rosi et al, 2002, p. 2099
1503	UN_4	(blank)	(blank)	(blank)
1522	UN_4	(blank)	(blank)	(blank)
1531	UN_4	(blank)	(blank)	(blank)
1543	UN_4	(blank)	(blank)	(blank)
1552	UN_4	(blank)	(blank)	(blank)
1560	UN_4	(blank)	(blank)	(blank)
1568	UN_4	(blank)	(blank)	(blank)
1571	EW_M_25_av	strong absorption	C-N-H bending amide II, N-H bands	Spectrum EW_av, Rosi et al, 2009, p. 2104
1576	EW_M_50_av	strong absorption	C-N-H bending amide II, N-H bands	Spectrum EW_av, Rosi et al, 2009, p. 2104
1577	EW_M_25_av	strong absorption	C-N-H bending amide II, N-H bands	Spectrum EW_av, Rosi et al, 2009, p. 2104
	UN_4	(blank)	(blank)	(blank)
1579	EW_M_5_av	strong absorption	C-N-H bending amide II, N-H bands	Spectrum EW_av, Rosi et al, 2009, p. 2104

Figure 53: Filtered CPAD of peaks of interest for UN_II_4 spectrum and possible matches.

1598	**UN_4**	(blank)	**(blank)**	(blank)
1601	**EW_M_5_av**	weak absorption	**N-H bands**	Miliani et al, 2012, p. 304; Rosi et al, 2009, p. 2104
1618	**UN_4**	(blank)	**(blank)**	(blank)
1621	**EW_M_25_av**	weak absorption	**N-H bands**	Miliani et al, 2012, p. 304; Rosi et al, 2009, p. 2104
1629	**EW_M_25_av**	weak absorption	**N-H bands**	Miliani et al, 2012, p. 304; Rosi et al, 2009, p. 2104
1630	**EW_M_5_av**	weak absorption	**N-H bands**	Miliani et al, 2012, p. 304; Rosi et al, 2009, p. 2104
1641	**EW_M_25_av**	weak absorption	**N-H bands**	Miliani et al, 2012, p. 304; Rosi et al, 2009, p. 2104
1684	**UN_4**	(blank)	**(blank)**	(blank)
1685	**EW_M_50_av**	strong absorption	**N-H bands**	Spectrum EW_av, Ploeger et al, 2010, p.37, Miliani et al, 2012, p. 305
2564	**EW_M_50_av**	weak absorption	**egg white**	spectrum EW_av
2571	**EW_M_25_av**	weak absorption	**egg white**	spectrum EW_av
2585	**EW_M_25_av**	weak absorption	**egg white**	spectrum EW_av
2589	**EW_M_50_av**	weak absorption	**egg white**	spectrum EW_av
2595	**EW_M_50_av**	weak absorption	**egg white**	spectrum EW_av
2690	**EW_M_25_av**	weak absorption	**egg white**	spectrum EW_av
2694	**EW_M_50_av**	weak absorption	**egg white**	spectrum EW_av
2703	**EW_M_5_av**	weak absorption	**egg white**	spectrum EW_av
2898	**UN_4**	(blank)	**(blank)**	(blank)
2926	**UN_4**	(blank)	**(blank)**	(blank)
2934	**EW_M_25_av**	weak absorption	**CH stretching**	Spectrum EW_av, Daher et al, 2017, p. 8
	EW_M_50_av	weak absorption	**CH stretching**	Spectrum EW_av, Daher et al, 2017, p. 8
	UN_4	(blank)	**(blank)**	(blank)
2936	**EW_M_5_av**	weak absorption	**CH stretching**	Spectrum EW_av, Daher et al, 2017, p. 8
2943	**EW_M_50_av**	weak absorption	**CH3 stretching**	Spectrum EW_av, Iwanicka et al, 2017, p. 18
	UN_4	(blank)	**(blank)**	(blank)
2964	**UN_4**	(blank)	**(blank)**	(blank)
2972	**UN_4**	(blank)	**(blank)**	(blank)
3014	**UN_4**	(blank)	**(blank)**	(blank)
3066	**EW_M_5_av**	1st overtone	**amide I**	Spectrum EW_av, Rosi et al, 2009, p. 2099
3083	**EW_M_25_av**	1st overtone	**amide I**	Spectrum EW_av, Rosi et al, 2009, p. 2099
3084	**EW_M_50_av**	1st overtone	**amide I**	Spectrum EW_av, Rosi et al, 2009, p. 2099
3085	**EW_M_5_av**	1st overtone	**amide I**	Spectrum EW_av, Rosi et al, 2009, p. 2099
3094	**EW_M_50_av**	1st overtone	**amide I**	Spectrum EW_av, Rosi et al, 2009, p. 2099
3095	**EW_M_25_av**	1st overtone	**amide I**	Spectrum EW_av, Rosi et al, 2009, p. 2099
3304	**EW_M_25_av**	weak absorption	**N-H stretching**	Rosi et al, 2002, p. 2099
3314	**EW_M_5_av**	weak absorption	**N-H stretching**	Rosi et al, 2002, p. 2099

Figure 53: continued.

UN_II_5

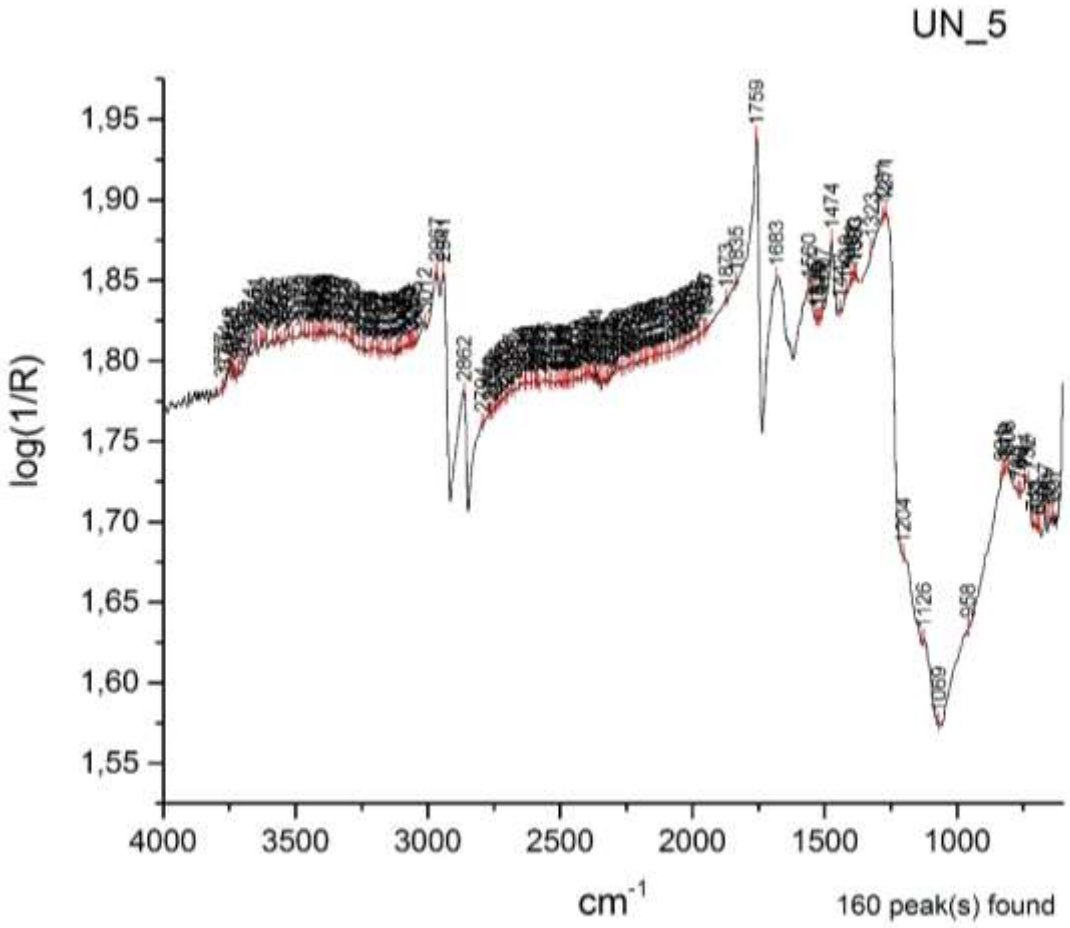

Figure 54: UN_II_5 correctly identified as egg yolk (EY).

Peak x (position)	Spectrum ID	Type of band	Chemical Band Assignement	Reference
667	EY_av	sharp and weak absorption	(blank)	(blank)
668	E_av	sharp and weak absorption	(blank)	spectrum EY_av, spectrum EW_av
710	EY_av	weak absorption	(blank)	(blank)
734	E_av	weak absorption	(blank)	(blank)
744	EY_av	weak absorption	(blank)	(blank)
745	E_av	weak absorption	(blank)	spectrum EY_av
765	E_av	weak absorption	(blank)	spectrum EY_av
770	EY_av	(blank)	(blank)	(blank)
781	EY_av	(blank)	(blank)	(blank)
789	EY_av	(blank)	(blank)	(blank)
794	E_av	weak absorption	(blank)	spectrum EY_av
802	E_av	weak absorption	(blank)	spectrum EY_av
808	EY_av	(blank)	(blank)	(blank)
819	EY_av	(blank)	(blank)	(blank)
835	E_av	weak absorption	(blank)	(blank)
973	E_av	weak absorption	PO4-3anion stretching	Ricci et al, 2006, p. 1223, spectrum EY_av
974	EY_av	sharp and weak absorption	PO4-3anion stretching	Ricci et al, 2006, p. 1223
1070	EY_av	reststrahlen	PO4-3anion stretching	Ricci et al, 2006, p. 1223
1123	E_av	weak absorption	PO4-3anion stretching	Ricci et al, 2006, p. 1223, spectrum EY_av
1124	EY_av	sharp and weak absorption	PO4-3anion stretching	Ricci et al, 2006, p. 1223
1177	E_av	weak absorption	v(C-O) stretching	Ricci et al, 2006, p. 1224, spectrum EW_av
1198	EY_av	weak absorption	(blank)	(blank)
1268	E_av	strong absorption	C-O	Ploeger et al, 2010, p. 37, spectrum EY_av
1270	EY_av	strong absorption	(blank)	(blank)
1271	UN_5	(blank)	(blank)	(blank)
1281	UN_5	(blank)	(blank)	(blank)
1283	EY_av	sharp absorption	(blank)	(blank)
1323	UN_5	(blank)	(blank)	(blank)
1324	E_av	(blank)	(blank)	spectrum EW_av
1383	UN_5	(blank)	(blank)	(blank)
1385	EY_av	sharp absorption	C-H bending	Buti et al, 2013, p. 2705
1390	UN_5	(blank)	(blank)	(blank)
1401	UN_5	(blank)	(blank)	(blank)
1411	E_av	(blank)	(blank)	spectrum EW_av
1419	UN_5	(blank)	(blank)	(blank)
1420	EY_av	weak absorption	(blank)	(blank)
1443	UN_5	(blank)	(blank)	(blank)
1445	E_av	weak absorption	Amide III	Buti et al, 2013, p. 2705, spectrum EW_av
	EY_av	weak absorption	(blank)	(blank)

Figure 55: Filtered CPAD of peaks of interest for UN_II_5 spectrum and possible matches.

1472	**E_av**	sharp absorption	**C-O bending**	Ricci et al, 2006, p. 1223, spectrum EW_av and EY_av
	EY_av	sharp absorption	**C-O bending**	Ricci et al, 2006, p. 1223
1474	**UN_5**	(blank)	**(blank)**	(blank)
1507	**EY_av**	weak absorption	**C=O**	Rosi et al, 2009, p. 2099
	UN_5	(blank)	**(blank)**	(blank)
1519	**EY_av**	weak absorption	**C=O**	Rosi et al, 2009, p. 2099
	UN_5	(blank)	**(blank)**	(blank)
1526	**UN_5**	(blank)	**(blank)**	(blank)
1535	**UN_5**	(blank)	**(blank)**	(blank)
1559	**EY_av**	strong absorption	**C=O**	Rosi et al, 2009, p. 2099
1560	**UN_5**	(blank)	**(blank)**	(blank)
1568	**E_av**	strong absorption	**N-H bands, amide I, II**	Miliani et al, 2012, p. 304, spectrum EW_av
1667	**EY_av**	strong absorption	**C=O**	(blank)
1683	**UN_5**	(blank)	**(blank)**	(blank)
1693	**E_av**	strong absorption	**N-H bands, amide I, II**	Miliani et al, 2012, p. 304, spectrum EW_av
1755	**E_av**	strong absorption	**C=O stretching band, esters**	Mazzeo et al, 2008, p. 69, spectrum EY_av
1758	**EY_av**	stretching band	**esters**	Mazzeo et al, 2008, p. 69
1759	**UN_5**	(blank)	**(blank)**	(blank)
2862	**UN_5**	(blank)	**(blank)**	(blank)
2864	**E_av**	strong absorption	**C-H stretching**	Rosi et al, 2009, p. 2099, spectrum EY_av
	EY_av	strong absorption	**C-H stretching**	Rosi et al, 2009, p. 2099
2876	**E_av**	strong absorption	**C-H stretching**	Rosi et al, 2009, p. 2099, spectrum EY_av
2941	**UN_5**	(blank)	**(blank)**	(blank)
2942	**E_av**	strong absorption	**C-H stretching bands, esters**	Spectrum EY_av, Rosi et al, 2009, p. 2099
	EY_av	sharp absorption	**C-H stretching**	Rosi et al, 2009, p. 2099
2967	**EY_av**	sharp absorption	**C-H stretching**	Rosi et al, 2009, p. 2099
	UN_5	(blank)	**(blank)**	(blank)
2973	**E_av**	strong absorption	**C-H stretching bands, esters**	Spectrum EY_av, Rosi et al, 2009, p. 2099
3012	**UN_5**	(blank)	**(blank)**	(blank)
3015	**EY_av**	weak absorption	**CH stretching**	Miliani et al, 2012, p. 302
3045	**E_av**	weak absorption	**2δNH**	Rosi et al, 2010, p. 621
3075	**E_av**	weak absorption	**2δNH**	Rosi et al, 2010, p. 621
3089	**E_av**	weak absorption	**2δNH**	Rosi et al, 2010, p. 621
3102	**E_av**	weak absorption	**2δNH**	Rosi et al, 2010, p. 621
3224	**E_av**	(blank)	**(blank)**	(blank)
3240	**E_av**	(blank)	**(blank)**	(blank)

Figure 55: continued.

UN_II_6

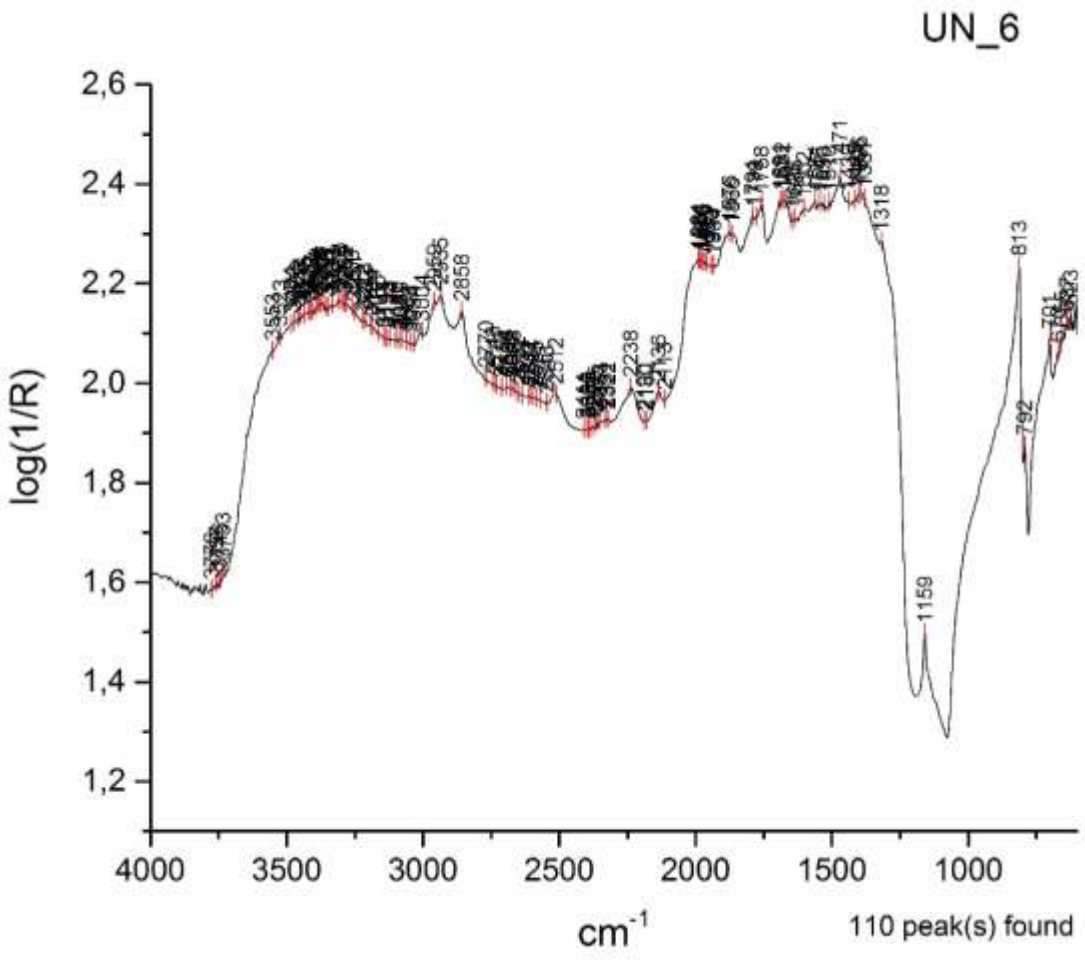

Figure 56: UN_II_6 identified as 25% egg yolk additive in mortar (EY_M_25) instead of the correct 50% egg yolk in mortar (EY_M_50).

Peak x (position)	Spectrum ID	Type of band	Chemical Band Assignement	Reference
1279	EY_M_25_av	strong absorption	egg yolk	spectrum EY_av
1281	EY_M_50_av	strong absorption	egg yolk	spectrum EY_av
1301	EY_M_50_av	strong absorption	CH2, CH3	Lombardi and Santarelli, 2009, p. 542
1310	EY_M_50_av	strong absorption	CH2, CH3	Lombardi and Santarelli, 2009, p. 542
1315	EY_M_25_av	strong absorption	CH2, CH3	Lombardi and Santarelli, 2009, p. 542
1381	EY_M_50_av	strong absorption	C-H bending	Spectrum EY_av, Buti et al, 2013, p. 2705
1390	EY_M_25_av	strong absorption	C-H bending	Spectrum EY_av, Buti et al, 2013, p. 2705
1399	EY_M_25_av	strong absorption	C-H bending	Spectrum EY_av, Buti et al, 2013, p. 2705
1420	EY_M_50_av	weak absorption	egg yolk	spectrum EY_av
1448	EY_M_50_av	weak absorption	egg yolk	spectrum EY_av
1470	EY_M_50_av	strong absorption	C-O bending	Spectrum EY_av, Ricci et al, 2006, p. 1224
1471	UN_6	(blank)	(blank)	(blank)
1476	EY_M_25_av	strong absorption	C-O bending	Spectrum EY_av, Ricci et al, 2006, p. 1224
1508	EY_M_50_av	weak absorption	C=O	Spectrum EY_av, Rosi et al, 2009, p. 2095
1518	EY_M_50_av	weak absorption	C=O	Spectrum EY_av, Rosi et al, 2009, p. 2096
1520	EY_M_25_av	weak absorption	C=O	Spectrum EY_av, Rosi et al, 2009, p. 2097
1529	EY_M_50_av	weak absorption	C=O	Spectrum EY_av, Rosi et al, 2009, p. 2097
1530	UN_6	(blank)	(blank)	(blank)
1536	EY_M_25_av	weak absorption	C=O	Spectrum EY_av, Rosi et al, 2009, p. 2098
1538	EY_M_50_av	weak absorption	C=O	Spectrum EY_av, Rosi et al, 2009, p. 2098
1545	UN_6	(blank)	(blank)	(blank)
1560	EY_M_50_av	weak absorption	C=O	Spectrum EY_av, Rosi et al, 2009, p. 2099
1561	UN_6	(blank)	(blank)	(blank)
1569	EY_M_25_av	strong absorption	C=O	Spectrum EY_av, Rosi et al, 2009, p. 2098
1635	UN_6	(blank)	(blank)	(blank)
1646	UN_6	(blank)	(blank)	(blank)
1671	UN_6	(blank)	(blank)	(blank)
1677	EY_M_25_av	strong absorption	C=O	Spectrum EY_av, Rosi et al, 2009, p. 2099
1682	EY_M_50_av	strong absorption	C=O	Spectrum EY_av, Rosi et al, 2009, p. 2099
	UN_6	(blank)	(blank)	(blank)
1687	EY_M_25_av	strong absorption	C=O	Spectrum EY_av, Rosi et al, 2009, p. 2099
1690	EY_M_50_av	strong absorption	C=O	Spectrum EY_av, Rosi et al, 2009, p. 2099
1691	UN_6	(blank)	(blank)	(blank)
1732	EY_M_50_av	weak absorption	C=O stretching band	Spectrum EY_av, Ploeger et al, 2010, p, 37
1753	EY_M_25_av	1st order derivative	C=O stretching band	Spectrum EY_av, Ploeger et al, 2010, p, 37
1755	EY_M_50_av	1st order derivative	C=O stretching band	Spectrum EY_av, Ploeger et al, 2010, p, 37
1758	UN_6	(blank)	(blank)	(blank)
2189	EY_M_50_av	weak absorption	egg yolk	spectrum EY_av
2857	EY_M_25_av	strong absorption	C-H stretching bands, esters	Spectrum EY_av, Rosi et al, 2009, p. 2099
2858	EY_M_50_av	strong absorption	C-H stretching bands, esters	Spectrum EY_av, Rosi et al, 2009, p. 2099
	UN_6	(blank)	(blank)	(blank)
2908	EY_M_50_av	strong absorption	C-H stretching bands, esters	Spectrum EY_av, Rosi et al, 2009, p. 2099
2935	EY_M_25_av	strong absorption	CH stretching	Spectrum EY_av, Daher et al, 2017, p.8
	UN_6	(blank)	(blank)	(blank)
2936	EY_M_50_av	strong absorption	CH stretching	Spectrum EY_av, Daher et al, 2017, p.8
2959	EY_M_50_av	strong absorption	C-H stretching bands, esters	Spectrum EY_av, Rosi et al, 2009, p. 2099
	EY_M_25_av	strong absorption	C-H stretching bands, esters	Spectrum EY_av, Rosi et al, 2009, p. 2099
	UN_6	(blank)	(blank)	(blank)
3004	EY_M_50_av	weak absorption	CH stretching	Miliani et al, 2012, p. 302
	UN_6	(blank)	(blank)	(blank)
3007	EY_M_25_av	weak absorption	CH stretching	Miliani et al, 2012, p. 302

Figure 57: Filtered CPAD of peaks of interest for UN_II_6 spectrum and possible matches.

UN_II_7

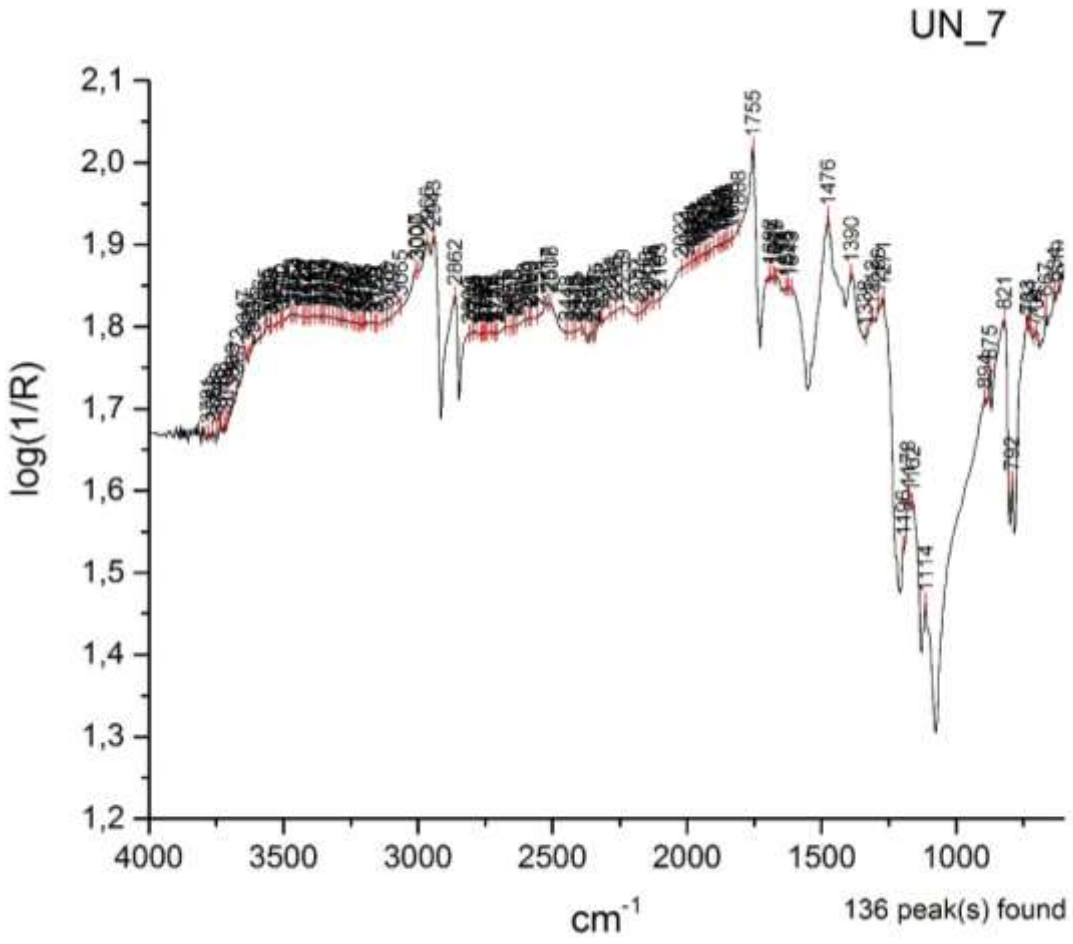

Figure 58: UN_II_7 correctly identified as 25% lard additive in mortar (L_M_25).

Peak x (position)	Spectrum ID	Type of band	Chemical Band Assignement	Reference
608	O_M_25_av	weak absorption	CaCO3	Spectrum Ca_av, spectrum M_av
641	O_M_25_av	weak absorption	CaCO3	spectrum Ca_av
667	O_M_25_av	sharp and weak absorption	olive oil	Spectrum O_av
701	L_M_25_av	weak absorption	lard	Spectrum L_av, spectrum M_av, Spectrum Q_av
	O_M_25_av	weak absorption	quartz	Spectrum Q_av, spectrum M_av
715	O_M_25_av	weak absorption	v4 carbonate ion	Spectrum Ca_av, spectrum M_av, Ylmen and Jaglid, 2013, p. 119
727	O_M_25_av	sharp and weak absorption	olive oil	Spectrum O_av
732	L_M_25_av	sharp and weak absorption	lard	Spectrum L_av
792	L_M_25_av	sharp and weak absorption	quartz	Spectrum Q_av, spectrum M_av
	O_M_25_av	sharp and weak absorption	quartz	Spectrum Q_av, spectrum M_av
821	L_M_25_av	strong absorption	Si-O antisymmetric stretching	Spectrum Q_av, spectrum M_av, Miliani et al, 2013, p. 303
	O_M_25_av	sharp absorption	olive oil	Spectrum O_av
876	L_M_25_av	weak absorption	v2 carbonate ion	Spectrum Ca_av and spectrum M_av, Ylmen and Jaglid, 2013, p. 119
878	O_M_25_av	sharp absorption	v2 carbonate ion	Spectrum Ca_av, Ylmen and Jaglid, 2013, p. 119
889	L_M_25_av	weak absorption	v2 carbonate ion	Spectrum Ca_av and spectrum M_av, Ylmen and Jaglid, 2013, p. 119
894	UN_7	(blank)	(blank)	(blank)
1098	O_M_25_av	sharp and weak absorption	v1 carbonate ion	Spectrum Ca_av, spectrum M_av, Ylmen and Jaglid, 2013, p. 119
1115	L_M_25_av	sharp and weak absorption	lard	Spectrum L_av
1119	O_M_25_av	sharp and weak absorption	C-O stretching	Spectrum O_av, Buti et al, 2013, p. 2705
1160	O_M_25_av	sharp absorption	quartz	Spectrum Q_av, spectrum M_av
1161	L_M_25_av	sharp and weak absorption	quartz	spectrum Q_av
1180	L_M_25_av	sharp absorption	v(C-O) stretching	Spectrum L_av, Ricci et al, 2006, p. 1224
1197	L_M_25_av	sharp absorption	v(C-O) stretching	Spectrum L_av, Ricci et al, 2006, p. 1224
1271	L_M_25_av	strong absorption	C-O	Spectrum L_av, Ploeger et al, 2010, p. 37
	UN_7	(blank)	(blank)	(blank)
1282	O_M_25_av	weak absorption	C-O stretching	Spectrum O_av, Buti et al, 2013, p. 2705
1288	L_M_25_av	strong absorption	C-O	Spectrum L_av, Ploeger et al, 2010, p. 37
	UN_7	(blank)	(blank)	(blank)
1311	L_M_25_av	weak absorption	lard	Spectrum L_av
1312	UN_7	(blank)	(blank)	(blank)
1318	O_M_25_av	weak absorption	C-O stretching	Spectrum O_av, Buti et al, 2013, p. 2705
1338	UN_7	(blank)	(blank)	(blank)
1381	O_M_25_av	sharp absorption	C-O bending	Spectrum O_av, Buti et al, 2013, p. 2705
1390	L_M_25_av	sharp absorption	C-H bending	Spectrum L_av, Buti et al, 2013, p. 2705
	UN_7	(blank)	(blank)	(blank)
1424	L_M_25_av	weak absorption	lard	Spectrum L_av
1475	L_M_25_av	sharp absorption	C-O bending	Spectrum L_av, Ricci et al, 2006, p. 1224
1476	UN_7	(blank)	(blank)	(blank)
1507	O_M_25_av	strong absorption	C-O bending	Spectrum O_av, Ricci et al, 2006, p. 1223

Figure 59: Filtered CPAD of peaks of interest for UN_II_7 spectrum and possible matches.

1600	O_M_25_av	weak absorption	**v3 antisymmetric stretching CO3-2**	Spectrum Ca_av, spectrum M_av, Ylmen and Jaglid, 2013, p. 119
1606	O_M_25_av	weak absorption	**quartz**	Spectrum Ca_av, spectrum M_av
1613	UN_7	(blank)	**(blank)**	(blank)
1616	O_M_25_av	weak absorption	**quartz**	Spectrum Ca_av, spectrum M_av
1626	UN_7	(blank)	**(blank)**	(blank)
1628	L_M_25_av	strong absorption	**(blank)**	Spectrum L_av, spectrum M_av, Spectrum Q_av
1635	UN_7	(blank)	**(blank)**	(blank)
1660	O_M_25_av	weak absorption	**quartz or olive oil**	Spectrum Q_av, spectum M_av, spectrum O_av
1669	L_M_25_av	strong absorption	**(blank)**	Spectrum L_av, spectrum M_av, Spectrum Q_av
	O_M_25_av	weak absorption	**olive oil**	Spectrun O_av
	UN_7	(blank)	**(blank)**	(blank)
1677	UN_7	(blank)	**(blank)**	(blank)
1678	O_M_25_av	weak absorption	**olive oil**	Spectrun O_av
1683	L_M_25_av	strong absorption	**(blank)**	Spectrum L_av, spectrum M_av, Spectrum Q_av
1692	L_M_25_av	strong absorption	**(blank)**	Spectrum L_av, spectrum M_av, Spectrum Q_av
	UN_7	(blank)	**(blank)**	(blank)
1703	O_M_25_av	weak absorption	**olive oil**	Spectrun O_av
1755	L_M_25_av	1st order derivative	**C=O stretching band**	Spectrum L_av, Mazzeo et al, 2008, p. 69
	UN_7	(blank)	**(blank)**	(blank)
1758	O_M_25_av	1st order derivative	**C=O stretching band**	Spectrum O_av, Ploeger et al, 2010, p, 37
2511	L_M_25_av	combination band	**v1+v3**	Spectrum Ca_av and spectrum M_av, Ricci et al, 2006, p. 1222
2518	L_M_25_av	combination band	**v1+v3**	Spectrum Ca_av and spectrum M_av, Ricci et al, 2006, p. 1222
2527	O_M_25_av	weak absorption	**v1+v2 CO3-2**	Miliani et al, 2012, p. 302
2862	L_M_25_av	strong absorption	**CH2 stretching**	Spectrum L_av, Ploeger et al, 2010, p. 37
	UN_7	(blank)	**(blank)**	(blank)
2863	O_M_25_av	strong absorption	**CH2 stretching**	Spectrum O_av, Ploeger et al, 2010, p. 37
2939	L_M_25_av	strong absorption	**CH2 stretching**	Spectrum L_av, Ploeger et al, 2010, p. 37
2941	O_M_25_av	strong absorption	**CH2 stretching**	Spectrum O_av, Ploeger et al, 2010, p. 37
2943	UN_7	(blank)	**(blank)**	(blank)
2966	L_M_25_av	strong absorption	**CH2 stretching**	Spectrum L_av, Ploeger et al, 2010, p. 37
	O_M_25_av	strong absorption	**v(CH) stretching**	Spectrum O_av, Miliani et al, 2007, p. 853
	UN_7	(blank)	**(blank)**	(blank)
3000	UN_7	(blank)	**(blank)**	(blank)
3005	L_M_25_av	weak absorption	**lard**	Spectrum L_av
3007	UN_7	(blank)	**(blank)**	(blank)
3009	O_M_25_av	weak absorption	**v(CH) stretching**	Spectrum O_av, Miliani et al, 2007, p. 853
3647	O_M_25_av	doublet	**OH stretching**	Spectrum M_av, spectrum Ca_av, Rosi et al, 2009, p. 2100

Figure 59: continued.

UN_II_8

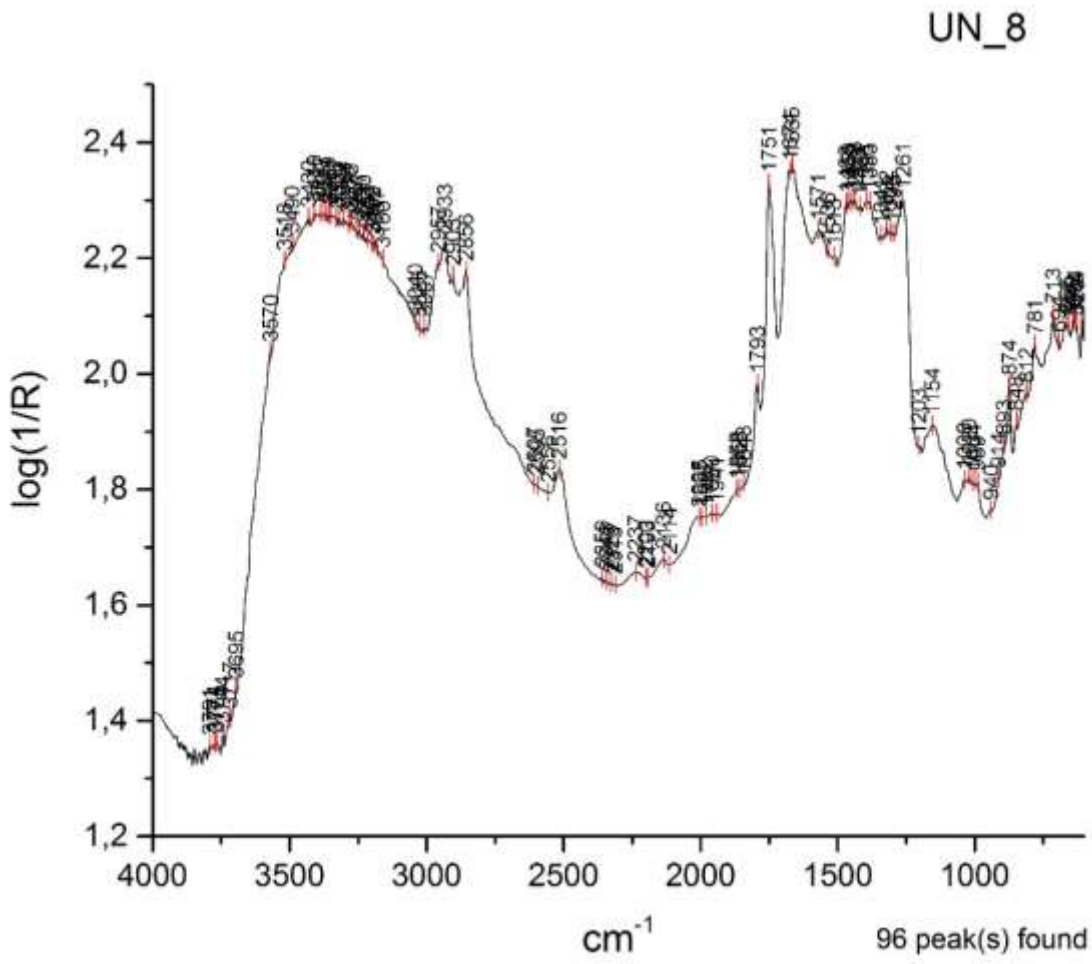

Figure 60: UN_II_8 correctly identified as 75% milk additive in mortar (Mi_M_75).

Peak x (position)	Spectrum ID	Type of band	Chemical Band Assignement	Reference
671	Mi_M_75_av	weak absorption	milk	Spectrum Mi_av
781	UN_8	(blank)	(blank)	(blank)
914	UN_8	(blank)	(blank)	(blank)
940	UN_8	(blank)	(blank)	(blank)
989	Mi_M_75_av	sharp absorption	sugar region	Spectrum Mi_av, Synytsya and Novak, 2014, p. 6
	UN_8	(blank)	(blank)	(blank)
1004	UN_8	(blank)	(blank)	(blank)
1020	UN_8	(blank)	(blank)	(blank)
1038	UN_8	(blank)	(blank)	(blank)
1203	Mi_M_75_av	weak absorption	sugar region	Spectrum Mi_av, Synytsya and Novak, 2014, p. 6
1261	UN_8	(blank)	(blank)	(blank)
1263	Mi_M_75_av	strong absorption	milk	Spectrum Mi_av
1281	EY_M_50_av	strong absorption	egg yolk	spectrum EY_av
1295	UN_8	(blank)	(blank)	(blank)
1301	EY_M_50_av	strong absorption	CH2, CH3	Lombardi and Santarelli, 2009, p. 542
1308	UN_8	(blank)	(blank)	(blank)
1310	EY_M_50_av	strong absorption	CH2, CH3	Lombardi and Santarelli, 2009, p. 542
1322	Mi_M_75_av	weak absorption	milk	Spectrum Mi_av
	UN_8	(blank)	(blank)	(blank)
1341	UN_8	(blank)	(blank)	(blank)
1381	EY_M_50_av	strong absorption	C-H bending	Spectrum EY_av, Buti et al, 2013, p. 2705
1383	Mi_M_75_av	strong absorption	C-H bending	Spectrum Mi_av, Buti et al, 2013, p. 2705
	UN_8	(blank)	(blank)	(blank)
1396	UN_8	(blank)	(blank)	(blank)
1420	EY_M_50_av	weak absorption	egg yolk	spectrum EY_av
	UN_8	(blank)	(blank)	(blank)
1424	Mi_M_75_av	strong absorption	CaCO3 or milk	Spectrum M_av, spectrum Ca_av, spectrum Mi_av
1438	UN_8	(blank)	(blank)	(blank)
1448	EY_M_50_av	weak absorption	egg yolk	spectrum EY_av
1449	UN_8	(blank)	(blank)	(blank)
1458	UN_8	(blank)	(blank)	(blank)
1468	UN_8	(blank)	(blank)	(blank)
1470	EY_M_50_av	strong absorption	C-O bending	Spectrum EY_av, Ricci et al, 2006, p. 1224
1508	EY_M_50_av	weak absorption	C=O	Spectrum EY_av, Rosi et al, 2009, p. 2095
1509	Mi_M_75_av	strong absorption	Carbonyl absorption	Rosi et al, 2002, p. 2099
1513	UN_8	(blank)	(blank)	(blank)
1518	EY_M_50_av	weak absorption	C=O	Spectrum EY_av, Rosi et al, 2009, p. 2096

Figure 61: Filtered CPAD of peaks of interest for UN_II_8 spectrum and possible matches.

1524	**Mi_M_75_av**	strong absorption	**milk**	Spectrum Mi_av
1529	**EY_M_50_av**	weak absorption	**C=O**	Spectrum EY_av, Rosi et al, 2009, p. 2097
1536	**UN_8**	(blank)	**(blank)**	(blank)
1538	**EY_M_50_av**	weak absorption	**C=O**	Spectrum EY_av, Rosi et al, 2009, p. 2098
1539	**Mi_M_75_av**	strong absorption	**N-H bands**	Spectrum Mi_av, Miliani et al, 2012, p. 304
1560	**EY_M_50_av**	weak absorption	**C=O**	Spectrum EY_av, Rosi et al, 2009, p. 2099
1571	**Mi_M_75_av**	strong absorption	**N-H bands**	Spectrum Mi_av, Miliani et al, 2012, p. 304
	UN_8	(blank)	**(blank)**	(blank)
1665	**Mi_M_75_av**	strong absorption	**N-H bands**	Spectrum Mi_av, Miliani et al, 2012, p. 304
	UN_8	(blank)	**(blank)**	(blank)
1673	**Mi_M_75_av**	strong absorption	**N-H bands**	Spectrum Mi_av, Miliani et al, 2012, p. 304
1674	**UN_8**	(blank)	**(blank)**	(blank)
1682	**EY_M_50_av**	strong absorption	**C=O**	Spectrum EY_av, Rosi et al, 2009, p. 2099
1690	**EY_M_50_av**	strong absorption	**C=O**	Spectrum EY_av, Rosi et al, 2009, p. 2099
1732	**EY_M_50_av**	weak absorption	**C=O stretching band**	Spectrum EY_av, Ploeger et al, 2010, p, 37
1750	**Mi_M_75_av**	1st order derivative	**C=O stretching band**	Spectrum Mi_av, Ploeger et al, 2010, p, 37
1751	**UN_8**	(blank)	**(blank)**	(blank)
1755	**EY_M_50_av**	1st order derivative	**C=O stretching band**	Spectrum EY_av, Ploeger et al, 2010, p, 37
2189	**EY_M_50_av**	weak absorption	**egg yolk**	spectrum EY_av
2856	**UN_8**	(blank)	**(blank)**	(blank)
2857	**Mi_M_75_av**	sharp absorption	**C=O stretching band**	Spectrum Mi_av, Rosi et al, 2009, p. 2099
2858	**EY_M_50_av**	strong absorption	**C-H stretching bands, esters**	Spectrum EY_av, Rosi et al, 2009, p. 2099
2903	**UN_8**	(blank)	**(blank)**	(blank)
2905	**Mi_M_75_av**	weak absorption	**CH stretching**	Miliani et al, 2012, p. 302
2908	**EY_M_50_av**	strong absorption	**C-H stretching bands, esters**	Spectrum EY_av, Rosi et al, 2009, p. 2099
2933	**Mi_M_75_av**	strong absorption	**CH stretching**	Spectrum Mi_av, Daher et al, 2017, p.8
	UN_8	(blank)	**(blank)**	(blank)
2936	**EY_M_50_av**	strong absorption	**CH stretching**	Spectrum EY_av, Daher et al, 2017, p.8
2957	**UN_8**	(blank)	**(blank)**	(blank)
2958	**Mi_M_75_av**	sharp absorption	**CH2 stretching**	Ploeger et al, 2010, p. 37
2959	**EY_M_50_av**	strong absorption	**C-H stretching bands, esters**	Spectrum EY_av, Rosi et al, 2009, p. 2099
3004	**EY_M_50_av**	weak absorption	**CH stretching**	Miliani et al, 2012, p. 302
3007	**Mi_M_75_av**	weak absorption	**CH stretching**	Miliani et al, 2012, p. 302

Figure 61: continued.

UN_II_9

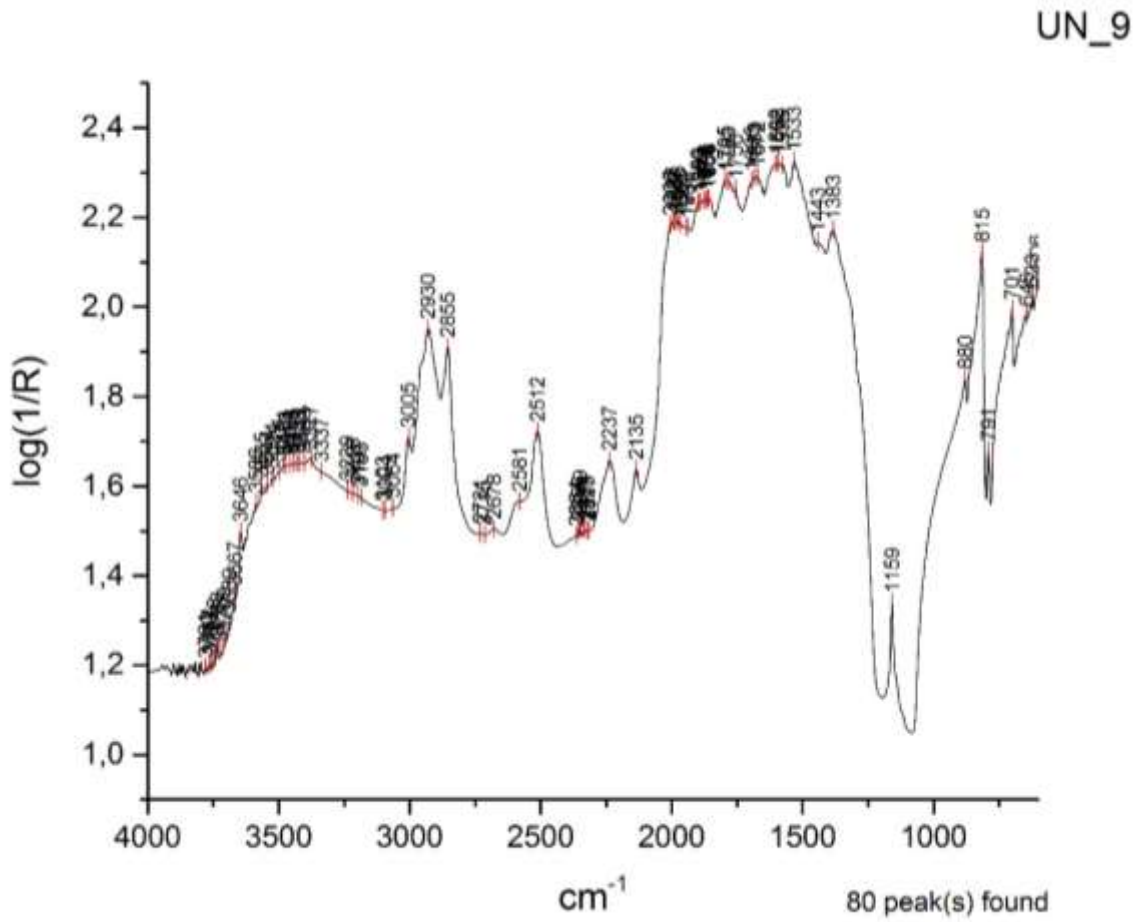

Figure 62: UN_II_9 correctly identified as 5% olive oil additive in mortar (O_M_5).

Peak x (position)	Spectrum ID	Type of band	Chemical Band Assignement	Reference
667	L_M_5_av	weak absorption	(blank)	Spectrum L_av
682	L_M_5_av	weak absorption	(blank)	Spectrum L_av
1383	UN_9	(blank)	(blank)	(blank)
1384	L_M_5_av	sharp absorption	lard	Spectrum L_av
	O_M_5_av	sharp absorption	C-O bending	Spectrum O_av
1433	L_M_5_av	weak absorption	lard	Spectrum L_av
1442	O_M_5_av	weak absorption	olive oil	Spectrum O_av, Buti et al, 2013, p. 2706
1443	UN_9	(blank)	(blank)	(blank)
1446	L_M_5_av	weak absorption	lard	Spectrum L_av
1473	L_M_5_av	weak absorption	C-O bending	Spectrum L_av, Ricci et al, 2006, p. 1224
1530	O_M_5_av	strong absorption	C-O bending	Spectrum O_av, Ricci et al, 2006, p. 1223
1533	UN_9	(blank)	(blank)	(blank)
1576	UN_9	(blank)	(blank)	(blank)
1593	UN_9	(blank)	(blank)	(blank)
1602	UN_9	(blank)	(blank)	(blank)
1672	UN_9	(blank)	(blank)	(blank)
1674	O_M_5_av	weak absorption	olive oil	Spectrun O_av
1680	O_M_5_av	weak absorption	olive oil	Spectrun O_av
1683	UN_9	(blank)	(blank)	(blank)
1695	O_M_5_av	weak absorption	olive oil	Spectrun O_av
	UN_9	(blank)	(blank)	(blank)
1747	L_M_5_av	1st order derivative	C=O stretching band	Spectrum L_av, Mazzeo et al, 2008, p. 69
1755	O_M_5_av	1st order derivative	C=O stretching band	Spectrum O_av, Ploeger et al, 2010, p, 37
1756	UN_9	(blank)	(blank)	(blank)
2854	L_M_5_av	strong absorption	CH2 stretching	Spectrum L_av, Ploeger et al, 2010, p. 37
2855	O_M_5_av	strong absorption	CH2 stretching	Spectrum O_av, Ploeger et al, 2010, p. 37
	UN_9	(blank)	(blank)	(blank)
2926	L_M_5_av	strong absorption	CH2 stretching	Spectrum L_av, Ploeger et al, 2010, p. 37
2929	O_M_5_av	strong absorption	CH2 stretching	Spectrum O_av, Ploeger et al, 2010, p. 37
2930	UN_9	(blank)	(blank)	(blank)
2954	O_M_5_av	strong absorption	v(CH) stretching	Spectrum O_av, Miliani et al, 2007, p. 853
3005	L_M_5_av	weak absorption	lard	Spectrum L_av
	O_M_5_av	weak absorption	v(CH) stretching	Spectrum O_av, Miliani et al, 2007, p. 853
	UN_9	(blank)	(blank)	(blank)
3062	O_M_5_av	weak absorption	olive oil	Spectrum O_av

Figure 63: Filtered CPAD of peaks of interest for UN_II_9 spectrum and possible matches.

8.1.3 Experimental set III

UN_III_1

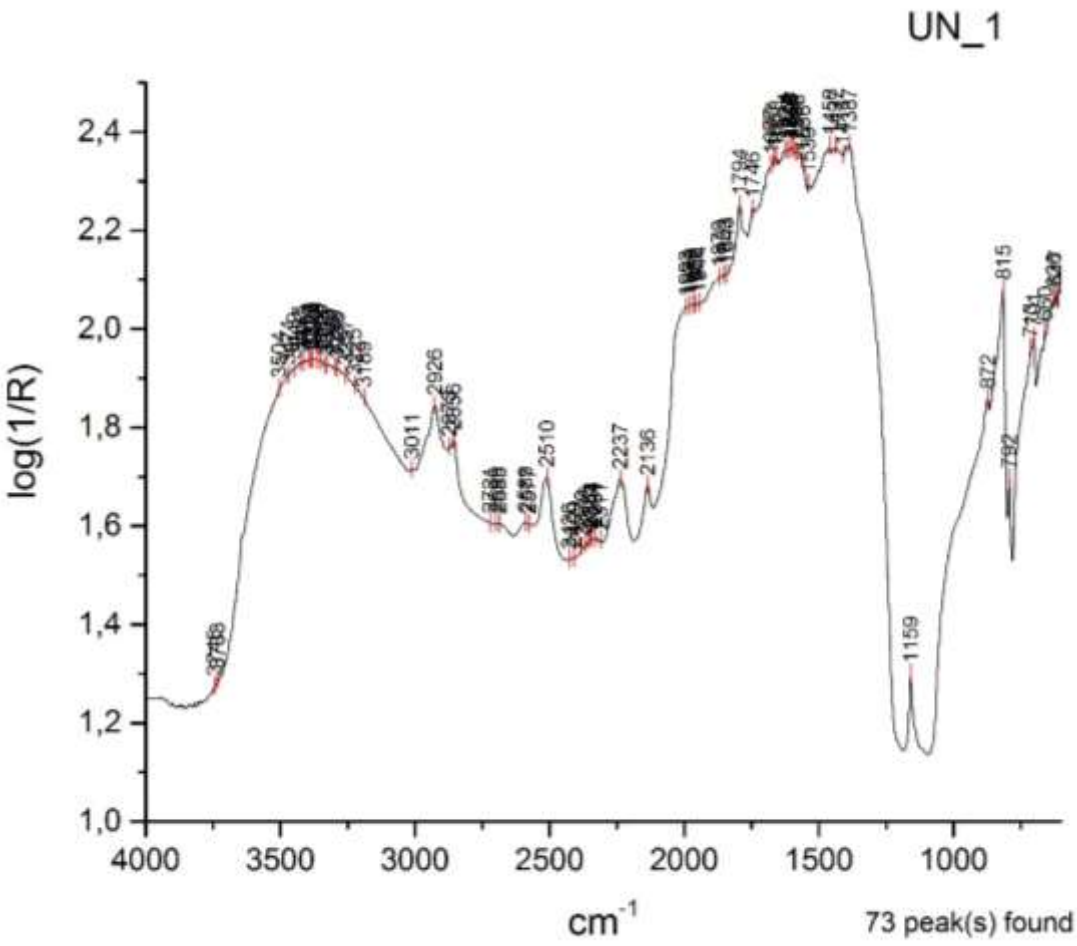

Figure 64: UN_III_1 correctly identified as 75% rice additive in mortar (R_M_75).

Peak x (position)	Spectrum ID	Type of band	Chemical Band Assignement	Reference
621	R_M_25_av	weak absorption	rice	Spectrum R_av
622	R_M_75_av	weak absorption	rice	Spectrum R_av
627	R_M_50_av	weak absorption	rice	Spectrum R_av
646	R_M_50_av	weak absorption	rice	Spectrum R_av
648	R_M_25_av	weak absorption	rice	Spectrum R_av
659	R_M_25_av	weak absorption	rice	Spectrum R_av
685	R_M_50_av	weak absorption	rice	Spectrum R_av
688	R_M_25_av	weak absorption	rice	Spectrum R_av
924	R_M_50_av	overlapping	sugar region	Spectrum R_av, Synytsya and Novak, 2014, p. 6
1001	R_M_50_av	strong absorption	rice	Spectrum R_av
1019	R_M_25_av	strong absorption	rice	Spectrum R_av
1387	UN_1	(blank)	(blank)	(blank)
1411	UN_1	(blank)	(blank)	(blank)
1437	UN_1	(blank)	(blank)	(blank)
1458	UN_1	(blank)	(blank)	(blank)
1474	R_M_75_av	strong absorption	C-H bending	Spectrum R_av, Buti et al, 2013, p. 2705
1475	R_M_25_av	weak absorption	C-H bending	Spectrum R_av, Buti et al, 2013, p. 2705
1518	R_M_25_av	weak absorption	rice	Spectrum R_av
1528	R_M_75_av	weak absorption	rice	Spectrum R_av
1535	R_M_25_av	weak absorption	rice	Spectrum R_av
1539	R_M_75_av	weak absorption	rice	Spectrum R_av
	UN_1	(blank)	(blank)	(blank)
1558	UN_1	(blank)	(blank)	(blank)
1578	UN_1	(blank)	(blank)	(blank)
1587	UN_1	(blank)	(blank)	(blank)
1597	R_M_75_av	strong absorption	rice	Spectrum R_av
	UN_1	(blank)	(blank)	(blank)
1605	UN_1	(blank)	(blank)	(blank)
1612	UN_1	(blank)	(blank)	(blank)
1624	UN_1	(blank)	(blank)	(blank)
1658	UN_1	(blank)	(blank)	(blank)
1667	UN_1	(blank)	(blank)	(blank)
1677	UN_1	(blank)	(blank)	(blank)
1746	R_M_75_av	sharp absorption	rice	Spectrum R_av
	R_M_50_av	sharp absorption	rice	Spectrum R_av
	UN_1	(blank)	(blank)	(blank)
2577	UN_1	(blank)	(blank)	(blank)
2589	UN_1	(blank)	(blank)	(blank)
2685	UN_1	(blank)	(blank)	(blank)
2688	R_M_25_av	weak absorption	(blank)	(blank)
2697	R_M_25_av	weak absorption	(blank)	(blank)
2699	UN_1	(blank)	(blank)	(blank)
2709	R_M_25_av	weak absorption	rice	Spectrum R_av
2721	UN_1	(blank)	(blank)	(blank)
2855	R_M_75_av	strong absorption	CH stretching	Spectrum E_av, Daher et al, 2017, p.8
2856	UN_1	(blank)	(blank)	(blank)
2857	R_M_50_av	strong absorption	CH stretching	Spectrum E_av, Daher et al, 2017, p.8
	R_M_25_av	strong absorption	CH stretching	Spectrum E_av, Daher et al, 2017, p.8
2926	R_M_75_av	strong absorption	CH stretching	Spectrum E_av, Daher et al, 2017, p.8
	R_M_25_av	strong absorption	CH stretching	Spectrum E_av, Daher et al, 2017, p.8
	UN_1	(blank)	(blank)	(blank)
2927	R_M_50_av	strong absorption	CH stretching	Spectrum E_av, Daher et al, 2017, p.8
3008	R_M_50_av	weak absorption	CH stretching	Miliani et al, 2012, p. 302
3009	R_M_25_av	weak absorption	CH stretching	Miliani et al, 2012, p. 302
3010	R_M_75_av	weak absorption	CH stretching	Miliani et al, 2012, p. 302
3011	UN_1	(blank)	(blank)	(blank)

Figure 65: Filtered CPAD of peaks of interest for UN_III_1 spectrum and possible matches.

UN_III_2

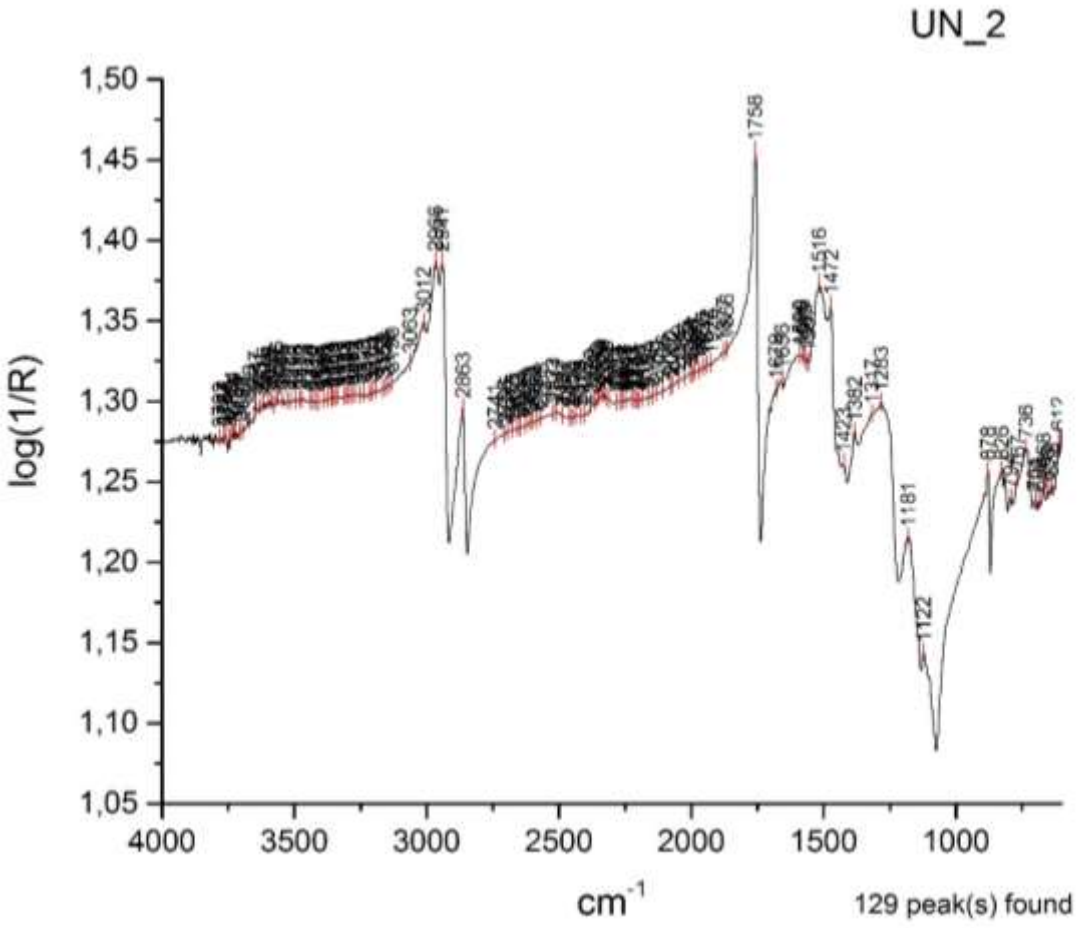

Figure 66: UN_III_2 correctly identified as 50% olive oil additive in mortar (O_M_50).

Peak x (position)	Spectrum ID	Type of band	Chemical Band Assignement	Reference
1281	O_M_75_av	strong absorption	olive oil	Spectrum O_av
1283	UN_2	(blank)	(blank)	(blank)
1289	L_M_75_av	strong absorption	C-O	Spectrum L_av, Ploeger et al, 2010, p. 37
1317	UN_2	(blank)	(blank)	(blank)
1354	O_M_75_av	sharp and weak absorption	olive oil	Spectrum O_av
1364	O_M_75_av	sharp and weak absorption	olive oil	Spectrum O_av
1380	O_M_50_av	sharp and weak absorption	C-O bending	Spectrum O_av, Buti et al, 2013, p. 2705
1381	L_M_75_av	sharp and weak absorption	C-H bending	Spectrum L_av, Buti et al, 2013, p. 2705
	O_M_75_av	sharp and weak absorption	C-H bending	Spectrum O_av, Buti et al, 2013, p. 2705
1382	UN_2	(blank)	(blank)	(blank)
1389	L_M_75_av	sharp and weak absorption	C-H bending	Spectrum L_av, Buti et al, 2013, p. 2705
1420	O_M_75_av	weak absorption	olive oil	Spectrum O_av
1421	L_M_75_av	weak absorption	(blank)	Spectrum L_av
1423	UN_2	(blank)	(blank)	(blank)
1442	O_M_75_av	weak absorption	olive oil	Spectrum O_av
1446	L_M_75_av	weak absorption	(blank)	Spectrum L_av
1471	O_M_75_av	sharp absorption	C-H bending	Spectrum O_av, Ricci et al, 2006, p. 1223
1472	UN_2	(blank)	(blank)	(blank)
1474	L_M_75_av	strong absorption	C-O bending	Spectrum L_av, Ricci et al, 2006, p. 1224
1516	UN_2	(blank)	(blank)	(blank)
1518	O_M_50_av	strong absorption	C-O bending	Spectrum O_av, Ricci et al, 2006, p. 1223
1560	O_M_75_av	weak absorption	olive oil	Spectrum O_av
1657	O_M_75_av	weak absorption	olive oil	Spectrum O_av
1662	L_M_75_av	weak absorption	(blank)	Spectrum L_av, spectrum M_av, Spectrum Q_av
1669	L_M_75_av	weak absorption	(blank)	Spectrum L_av, spectrum M_av, Spectrum Q_av
1679	L_M_75_av	weak absorption	(blank)	Spectrum L_av, spectrum M_av, Spectrum Q_av
	UN_2	(blank)	(blank)	(blank)
1683	O_M_75_av	weak absorption	olive oil	Spectrum O_av, Mazzeo et al, 2008, p. 69
1705	O_M_75_av	weak absorption	free fatty acids	Spectrum O_av, Ploeger et al, 2010, p. 37
1756	L_M_75_av	1st order derivative	C=O stretching band	Spectrum L_av, Mazzeo et al, 2008, p. 69
1758	O_M_50_av	1st order derivative	C=O stretching band	Spectrum O_av, Ploeger et al, 2010, p, 37
	UN_2	(blank)	(blank)	(blank)
1759	O_M_75_av	1st order derivative	C=O stretching band	Spectrum O_av
2862	L_M_75_av	strong absorption	CH2 stretching	Spectrum L_av, Ploeger et al, 2010, p. 37
2863	O_M_50_av	strong absorption	CH2 stretching	Spectrum O_av, Ploeger et al, 2010, p. 37
	UN_2	(blank)	(blank)	(blank)
2864	O_M_75_av	strong absorption	CH2 stretching	Spectrum O_av, Ploeger et al, 2010, p. 37
2940	L_M_75_av	sharp absorption	CH2 stretching	Spectrum L_av, Ploeger et al, 2010, p. 37
2941	O_M_50_av	strong absorption	CH2 stretching	Spectrum O_av, Ploeger et al, 2010, p. 37
	O_M_75_av	strong absorption	CH2 stretching	Spectrum O_av, Ploeger et al, 2010, p. 37
	UN_2	(blank)	(blank)	(blank)
2964	O_M_75_av	strong absorption	v(CH) stretching	Spectrum O_av, Miliani et al, 2007, p. 853
2966	O_M_50_av	strong absorption	v(CH) stretching	Spectrum O_av, Miliani et al, 2007, p. 853
	UN_2	(blank)	(blank)	(blank)
2968	L_M_75_av	sharp absorption	CH2 stretching	Spectrum L_av, Ploeger et al, 2010, p. 37
3003	L_M_75_av	weak absorption	CH stretching	Spectrum L_av, Miliani et al, 2012, p. 302
3012	O_M_50_av	weak absorption	v(CH) stretching	Spectrum O_av, Miliani et al, 2007, p. 853
	UN_2	(blank)	(blank)	(blank)
3018	L_M_75_av	weak absorption	CH stretching	Spectrum L_av, Miliani et al, 2012, p. 302
3019	O_M_75_av	weak absorption	v(CH) stretching	Spectrum O_av, Miliani et al, 2007, p. 853
3452	L_M_75_av	weak absorption	lard	Spectrum L_av
3461	L_M_75_av	weak absorption	lard	Spectrum L_av
3480	L_M_75_av	weak absorption	lard	Spectrum L_av

Figure 67: Filtered CPAD of peaks of interest for UN_III_2 spectrum and possible matches.

UN_III_3

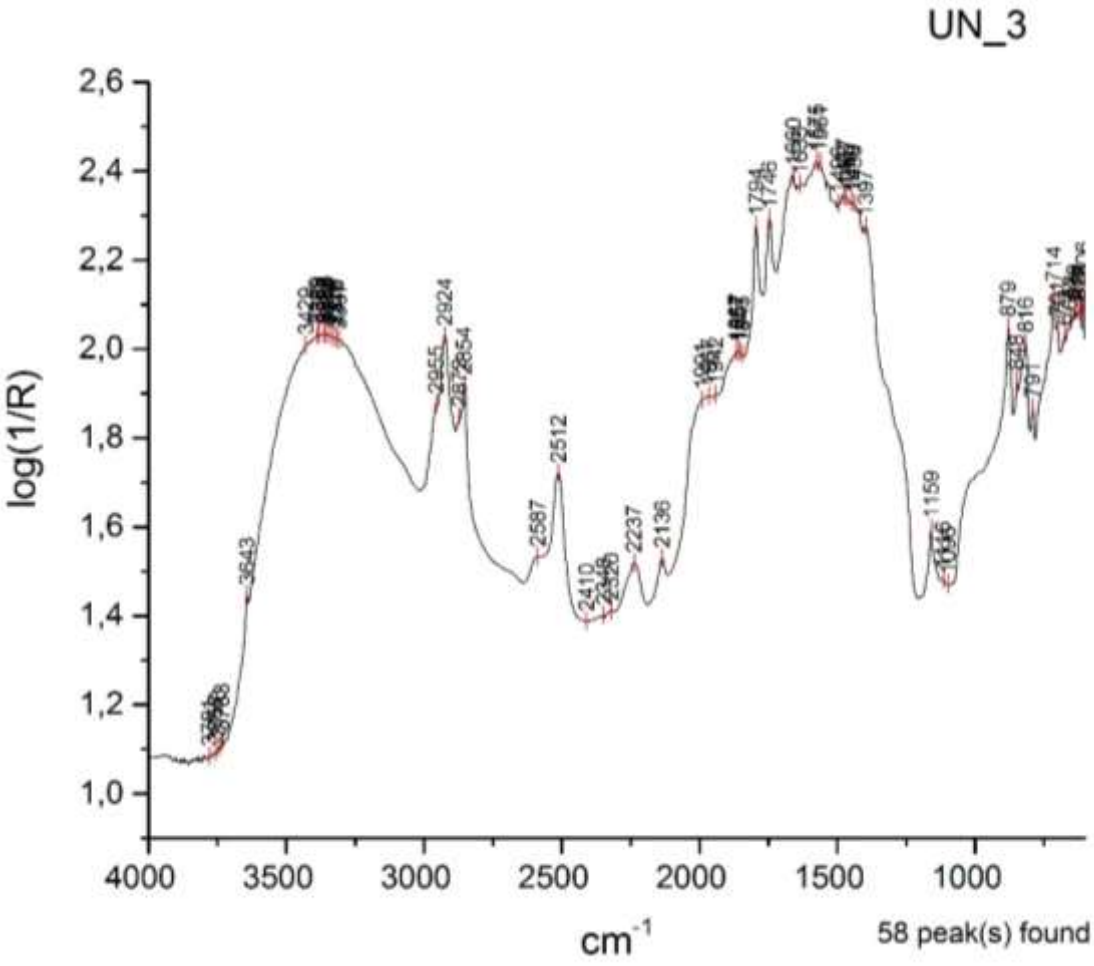

Figure 68: UN_III_3 correctly identified as 25% milk additive in mortar (Mi_M_25).

Peak x (position)	Spectrum ID	Type of band	Chemical Band Assignement	Reference
627	R_M_50_av	weak absorption	rice	Spectrum R_av
646	R_M_50_av	weak absorption	rice	Spectrum R_av
685	R_M_50_av	weak absorption	rice	Spectrum R_av
924	R_M_50_av	overlapping	sugar region	Spectrum R_av, Synytsya and Novak, 2014, p. 6
988	Mi_M_25_av	sharp absorption	sugar region	Spectrum Mi_av, Synytsya and Novak, 2014, p. 6
1001	R_M_50_av	strong absorption	rice	Spectrum R_av
1096	UN_3	(blank)	(blank)	(blank)
1116	UN_3	(blank)	(blank)	(blank)
1397	UN_3	(blank)	(blank)	(blank)
1476	Mi_M_25_av	strong absorption	Amide III	Spectrum Mi_av, Rosi et al, 2009, p. 2099
1477	UN_3	(blank)	(blank)	(blank)
1497	Mi_M_25_av	strong absorption	Carbonyl absorption	Rosi et al, 2002, p. 2099
1538	Mi_M_25_av	strong absorption	N-H bands	Spectrum Mi_av, Miliani et al, 2012, p. 304
1575	UN_3	(blank)	(blank)	(blank)
1624	Mi_M_25_av	strong absorption	N-H bands	Spectrum Mi_av, Miliani et al, 2012, p. 304
1660	UN_3	(blank)	(blank)	(blank)
1661	Mi_M_25_av	strong absorption	N-H bands	Spectrum Mi_av, Miliani et al, 2012, p. 304
1746	R_M_50_av	sharp absorption	rice	Spectrum R_av
	Mi_M_25_av	1st order derivative	C=O stretching band	Spectrum Mi_av, Ploeger et al, 2010, p, 37
	UN_3	(blank)	(blank)	(blank)
2854	Mi_M_25_av	sharp absorption	C=O stretching band	Spectrum Mi_av, Rosi et al, 2009, p. 2099
	UN_3	(blank)	(blank)	(blank)
2857	R_M_50_av	strong absorption	CH stretching	Spectrum E_av, Daher et al, 2017, p.8
2924	Mi_M_25_av	strong absorption	CH stretching	Spectrum Mi_av, Daher et al, 2017, p.8
	UN_3	(blank)	(blank)	(blank)
2927	R_M_50_av	strong absorption	CH stretching	Spectrum E_av, Daher et al, 2017, p.8
2954	Mi_M_25_av	sharp absorption	CH2 stretching	Ploeger et al, 2010, p. 37
2955	UN_3	(blank)	(blank)	(blank)
3008	R_M_50_av	weak absorption	CH stretching	Miliani et al, 2012, p. 302

Figure 69: Filtered CPAD of peaks of interest for UN_III_3 spectrum and possible matches.

UN_III_4

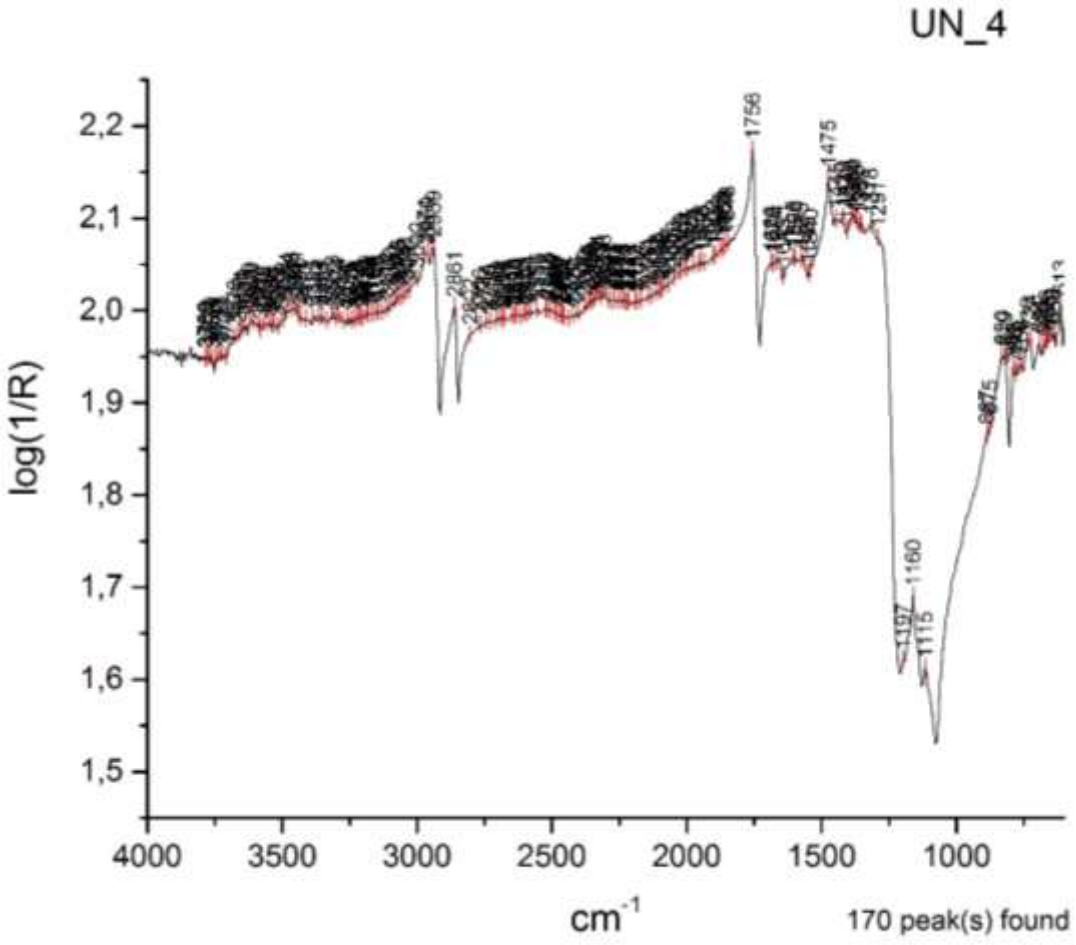

Figure 70: UN_III_4 correctly identified as 75% lard additive in mortar (L_M_75).

Peak x (position)	Spectrum ID	Type of band	Chemical Band Assignement	Reference
700	L_M_75_av	weak absorption	lard	Spectrum Q_av, spectrum M_av, spectrum L_av
701	L_M_25_av	weak absorption	lard	Spectrum L_av, spectrum M_av, Spectrum Q_av
725	L_M_75_av	sharp absorption	lard	Spectrum L_av
732	L_M_25_av	sharp and weak absorption	lard	Spectrum L_av
1115	L_M_75_av	sharp absorption	lard	Spectrum L_av
	L_M_25_av	sharp and weak absorption	lard	Spectrum L_av
1180	L_M_25_av	sharp absorption	v(C-O) stretching	Spectrum L_av, Ricci et al, 2006, p. 1224
1197	L_M_75_av	weak absorption	v(C-O) stretching	Spectrum L_av, Ricci et al, 2006, p. 1224
	L_M_25_av	sharp absorption	v(C-O) stretching	Spectrum L_av, Ricci et al, 2006, p. 1224
1271	L_M_25_av	strong absorption	C-O	Spectrum L_av, Ploeger et al, 2010, p. 37
1279	L_M_75_av	strong absorption	C-O	Spectrum L_av, Ploeger et al, 2010, p. 37
1288	L_M_25_av	strong absorption	C-O	Spectrum L_av, Ploeger et al, 2010, p. 37
1289	L_M_75_av	strong absorption	C-O	Spectrum L_av, Ploeger et al, 2010, p. 37
1311	L_M_25_av	weak absorption	lard	Spectrum L_av
1318	UN_4	(blank)	(blank)	(blank)
1369	UN_4	(blank)	(blank)	(blank)
1380	UN_4	(blank)	(blank)	(blank)
1381	L_M_75_av	sharp and weak absorption	C-H bending	Spectrum L_av, Buti et al, 2013, p. 2705
1389	L_M_75_av	sharp and weak absorption	C-H bending	Spectrum L_av, Buti et al, 2013, p. 2705
	UN_4	(blank)	(blank)	(blank)
1390	L_M_25_av	sharp absorption	C-H bending	Spectrum L_av, Buti et al, 2013, p. 2705
1420	UN_4	(blank)	(blank)	(blank)
1421	L_M_75_av	weak absorption	(blank)	Spectrum L_av
1424	L_M_25_av	weak absorption	lard	Spectrum L_av
1445	UN_4	(blank)	(blank)	(blank)
1446	L_M_75_av	weak absorption	(blank)	Spectrum L_av
1474	L_M_75_av	strong absorption	C-O bending	Spectrum L_av, Ricci et al, 2006, p. 1224
1475	L_M_25_av	sharp absorption	C-O bending	Spectrum L_av, Ricci et al, 2006, p. 1224
1575	UN_4	(blank)	(blank)	(blank)
1598	UN_4	(blank)	(blank)	(blank)
1605	UN_4	(blank)	(blank)	(blank)
1628	L_M_25_av	strong absorption	(blank)	Spectrum L_av, spectrum M_av, Spectrum Q_av
1662	L_M_75_av	weak absorption	(blank)	Spectrum L_av, spectrum M_av, Spectrum Q_av
1664	UN_4	(blank)	(blank)	(blank)
1669	L_M_75_av	weak absorption	(blank)	Spectrum L_av, spectrum M_av, Spectrum Q_av
	L_M_25_av	strong absorption	(blank)	Spectrum L_av, spectrum M_av, Spectrum Q_av
1678	UN_4	(blank)	(blank)	(blank)
1679	L_M_75_av	weak absorption	(blank)	Spectrum L_av, spectrum M_av, Spectrum Q_av
1683	L_M_25_av	strong absorption	(blank)	Spectrum L_av, spectrum M_av, Spectrum Q_av
1686	UN_4	(blank)	(blank)	(blank)
1692	L_M_25_av	strong absorption	(blank)	Spectrum L_av, spectrum M_av, Spectrum Q_av
1755	L_M_25_av	1st order derivative	C=O stretching band	Spectrum L_av, Mazzeo et al, 2008, p. 69
1756	L_M_75_av	1st order derivative	C=O stretching band	Spectrum L_av, Mazzeo et al, 2008, p. 69
	UN_4	(blank)	(blank)	(blank)
2861	UN_4	(blank)	(blank)	(blank)
2862	L_M_75_av	strong absorption	CH2 stretching	Spectrum L_av, Ploeger et al, 2010, p. 37
	L_M_25_av	strong absorption	CH2 stretching	Spectrum L_av, Ploeger et al, 2010, p. 37
2939	L_M_25_av	strong absorption	CH2 stretching	Spectrum L_av, Ploeger et al, 2010, p. 37
	UN_4	(blank)	(blank)	(blank)
2940	L_M_75_av	sharp absorption	CH2 stretching	Spectrum L_av, Ploeger et al, 2010, p. 37
2960	UN_4	(blank)	(blank)	(blank)
2966	L_M_25_av	strong absorption	CH2 stretching	Spectrum L_av, Ploeger et al, 2010, p. 37
2968	L_M_75_av	sharp absorption	CH2 stretching	Spectrum L_av, Ploeger et al, 2010, p. 37
2971	UN_4	(blank)	(blank)	(blank)
3003	L_M_75_av	weak absorption	CH stretching	Spectrum L_av, Miliani et al, 2012, p. 302
3005	L_M_25_av	weak absorption	lard	Spectrum L_av
3018	L_M_75_av	weak absorption	CH stretching	Spectrum L_av, Miliani et al, 2012, p. 302
3452	L_M_75_av	weak absorption	lard	Spectrum L_av
3461	L_M_75_av	weak absorption	lard	Spectrum L_av
3480	L_M_75_av	weak absorption	lard	Spectrum L_av

Figure 71: Filtered CPAD of peaks of interest for UN_III_4 spectrum and possible matches.

UN_III_5

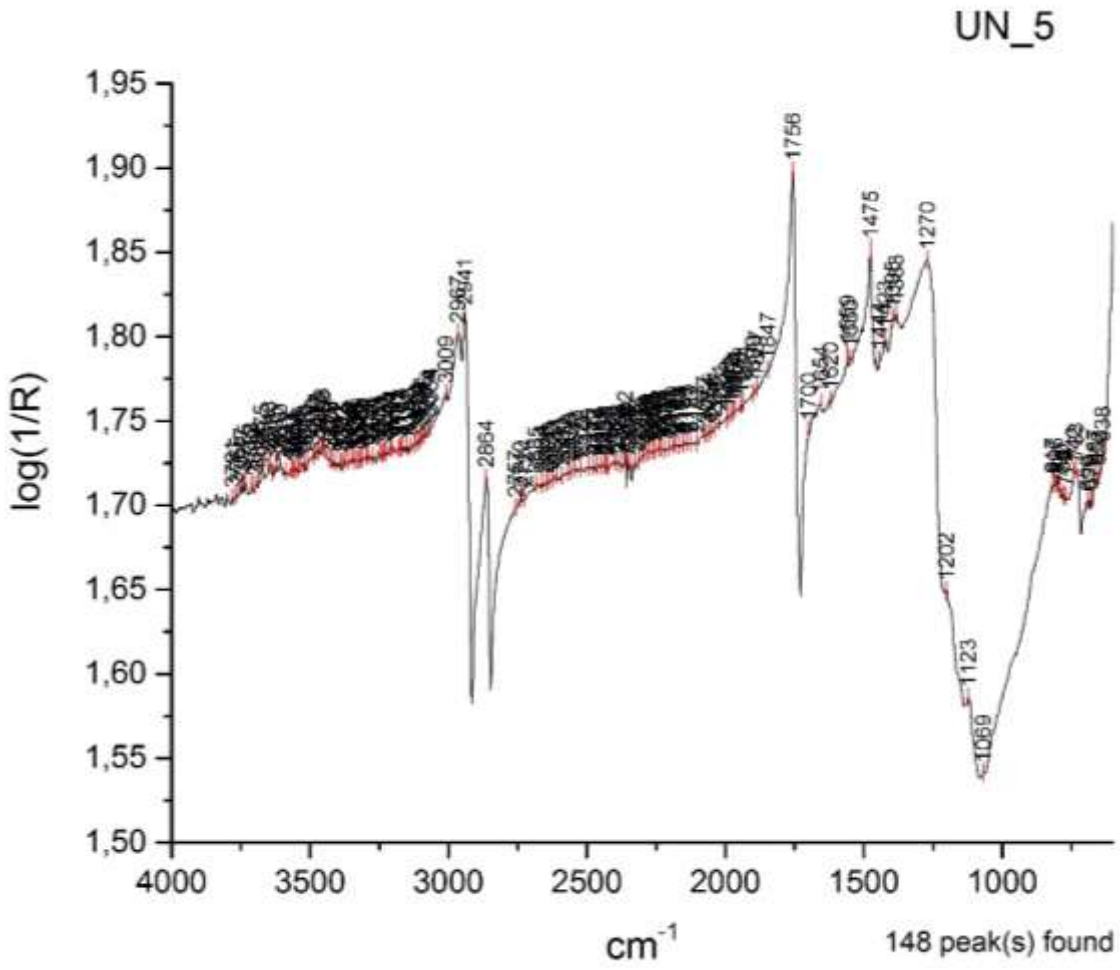

Figure 72: UN_III_5 correctly identified as lard (L_av).

Peak x (position)	Spectrum ID	Type of band	Chemical Band Assignement	Reference
1267	O_av	weak absorption	C-O stretching	Buti et al, 2013, p. 2705
1270	EY_av	strong absorption	(blank)	(blank)
	UN_5	(blank)	(blank)	(blank)
1275	L_av	strong absorption	C-O	Ploeger et al, 2010, p. 37
1282	O_av	weak absorption	(blank)	(blank)
1283	EY_av	sharp absorption	(blank)	(blank)
1303	O_av	weak absorption	(blank)	(blank)
1360	O_av	weak absorption	(blank)	(blank)
1370	L_av	weak absorption	C-H bending	Buti et al, 2013, p. 2705
1382	O_av	sharp and weak absorption	C-H bending	Buti et al, 2013, p. 2705
1384	L_av	sharp and weak absorption	(blank)	(blank)
1385	EY_av	sharp absorption	C-H bending	Buti et al, 2013, p. 2705
1395	UN_5	(blank)	(blank)	(blank)
1403	O_av	(blank)	(blank)	(blank)
1420	EY_av	weak absorption	(blank)	(blank)
1421	O_av	(blank)	(blank)	(blank)
1422	L_av	weak absorption	(blank)	(blank)
1437	O_av	(blank)	(blank)	(blank)
1445	EY_av	weak absorption	(blank)	(blank)
1446	L_av	weak absorption	(blank)	(blank)
	O_av	(blank)	(blank)	(blank)
1471	O_av	sharp absorption	C-O bending	Ricci et al, 2006, p. 1223
1472	EY_av	sharp absorption	C-O bending	Ricci et al, 2006, p. 1223
1475	L_av	strong absorption	C-O bending	Ricci et al, 2006, p. 1223
	UN_5	(blank)	(blank)	(blank)
1507	EY_av	weak absorption	C=O	Rosi et al, 2009, p. 2099
1519	EY_av	weak absorption	C=O	Rosi et al, 2009, p. 2099
1550	UN_5	(blank)	(blank)	(blank)
1559	EY_av	strong absorption	C=O	Rosi et al, 2009, p. 2099
	O_av	weak absorption	(blank)	(blank)
	UN_5	(blank)	(blank)	(blank)
1620	UN_5	(blank)	(blank)	(blank)
1653	O_av	weak absorption	(blank)	(blank)
1654	UN_5	(blank)	(blank)	(blank)
1660	O_av	weak absorption	(blank)	(blank)
1666	L_av	weak absorption	(blank)	(blank)
1667	EY_av	strong absorption	C=O	(blank)
1676	O_av	weak absorption	(blank)	(blank)
1678	L_av	weak absorption	(blank)	(blank)
1696	O_av	weak absorption	Free fatty acids	Mazzeo et al, 2008, p. 69
1700	UN_5	(blank)	(blank)	(blank)
1756	L_av	1st order derivative	C=O stretching band	Mazzeo et al, 2008, p. 69
	UN_5	(blank)	(blank)	(blank)
1758	EY_av	stretching band	esters	Mazzeo et al, 2008, p. 69
	O_av	1st order derivative	C=O stretching	Ploeger et al, 2010, p. 37, Miliani et al, 2012, p. 304
2284	O_av	weak absorption	(blank)	(blank)
2863	L_av	strong absorption	CH2 stretching	Ploeger et al, 2010, p. 37
	O_av	sharp absorption	CH2 stretching	Ploeger et al, 2010, p. 37
2864	EY_av	strong absorption	C-H stretching	Rosi et al, 2009, p. 2099
	UN_5	(blank)	(blank)	(blank)
2941	L_av	sharp absorption	CH2 stretching	Ploeger et al, 2010, p. 37
	O_av	sharp absorption	CH2 stretching	Ploeger et al, 2010, p. 37
	UN_5	(blank)	(blank)	(blank)
2942	EY_av	sharp absorption	C-H stretching	Rosi et al, 2009, p. 2099
2965	L_av	sharp absorption	CH2 stretching	Ploeger et al, 2010, p. 37
	O_av	sharp absorption	v(CH) stretching	Miliani et al, 2007, p. 853
2967	EY_av	sharp absorption	C-H stretching	Rosi et al, 2009, p. 2099
	UN_5	(blank)	(blank)	(blank)
3009	UN_5	(blank)	(blank)	(blank)
3010	L_av	sharp absorption	CH2 stretching	Ploeger et al, 2010, p. 37

Figure 73: Filtered CPAD of peaks of interest for UN_III_5 spectrum and possible matches.

UN_III_6

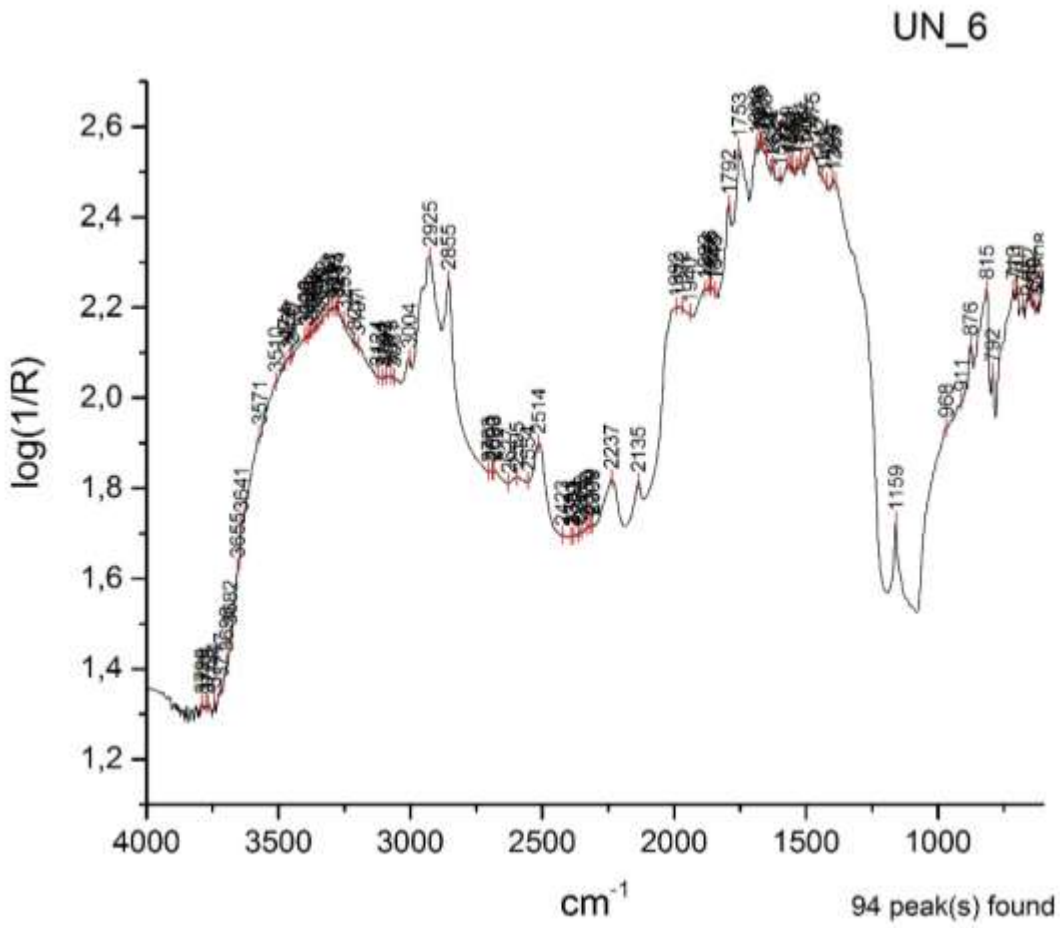

Figure 74: UN_III_6 correctly identified as 25% egg yolk additive in mortar (EY_M_25).

Peak x (position)	Spectrum ID	Type of band	Chemical Band Assignement	Reference
911	UN_6	(blank)	(blank)	(blank)
968	UN_6	(blank)	(blank)	(blank)
1279	EY_M_25_av	strong absorption	egg yolk	spectrum EY_av
1281	EY_M_50_av	strong absorption	egg yolk	spectrum EY_av
1301	EY_M_50_av	strong absorption	CH2, CH3	Lombardi and Santarelli, 2009, p. 542
1310	EY_M_50_av	strong absorption	CH2, CH3	Lombardi and Santarelli, 2009, p. 542
1315	EY_M_25_av	strong absorption	CH2, CH3	Lombardi and Santarelli, 2009, p. 542
1381	EY_M_50_av	strong absorption	C-H bending	Spectrum EY_av, Buti et al, 2013, p. 2705
1389	UN_6	(blank)	(blank)	(blank)
1390	EY_M_25_av	strong absorption	C-H bending	Spectrum EY_av, Buti et al, 2013, p. 2705
1399	EY_M_25_av	strong absorption	C-H bending	Spectrum EY_av, Buti et al, 2013, p. 2705
	UN_6	(blank)	(blank)	(blank)
1420	EY_M_50_av	weak absorption	egg yolk	spectrum EY_av
1423	UN_6	(blank)	(blank)	(blank)
1442	UN_6	(blank)	(blank)	(blank)
1448	EY_M_50_av	weak absorption	egg yolk	spectrum EY_av
1470	EY_M_50_av	strong absorption	C-O bending	Spectrum EY_av, Ricci et al, 2006, p. 1224
1475	UN_6	(blank)	(blank)	(blank)
1476	EY_M_25_av	strong absorption	C-O bending	Spectrum EY_av, Ricci et al, 2006, p. 1224
1495	UN_6	(blank)	(blank)	(blank)
1505	UN_6	(blank)	(blank)	(blank)
1508	EY_M_50_av	weak absorption	C=O	Spectrum EY_av, Rosi et al, 2009, p. 2095
1518	EY_M_50_av	weak absorption	C=O	Spectrum EY_av, Rosi et al, 2009, p. 2096
1520	EY_M_25_av	weak absorption	C=O	Spectrum EY_av, Rosi et al, 2009, p. 2097
1521	UN_6	(blank)	(blank)	(blank)
1529	EY_M_50_av	weak absorption	C=O	Spectrum EY_av, Rosi et al, 2009, p. 2097
1536	EY_M_25_av	weak absorption	C=O	Spectrum EY_av, Rosi et al, 2009, p. 2098
	UN_6	(blank)	(blank)	(blank)
1538	EY_M_50_av	weak absorption	C=O	Spectrum EY_av, Rosi et al, 2009, p. 2098
1552	UN_6	(blank)	(blank)	(blank)
1560	EY_M_50_av	weak absorption	C=O	Spectrum EY_av, Rosi et al, 2009, p. 2099
1561	UN_6	(blank)	(blank)	(blank)
1569	EY_M_25_av	strong absorption	C=O	Spectrum EY_av, Rosi et al, 2009, p. 2098
	UN_6	(blank)	(blank)	(blank)
1599	UN_6	(blank)	(blank)	(blank)
1624	UN_6	(blank)	(blank)	(blank)
1634	UN_6	(blank)	(blank)	(blank)
1653	UN_6	(blank)	(blank)	(blank)
1669	UN_6	(blank)	(blank)	(blank)
1676	UN_6	(blank)	(blank)	(blank)
1677	EY_M_25_av	strong absorption	C=O	Spectrum EY_av, Rosi et al, 2009, p. 2099
1682	EY_M_50_av	strong absorption	C=O	Spectrum EY_av, Rosi et al, 2009, p. 2099
1687	EY_M_25_av	strong absorption	C=O	Spectrum EY_av, Rosi et al, 2009, p. 2099
1688	UN_6	(blank)	(blank)	(blank)
1690	EY_M_50_av	strong absorption	C=O	Spectrum EY_av, Rosi et al, 2009, p. 2099
1732	EY_M_50_av	weak absorption	C=O stretching band	Spectrum EY_av, Ploeger et al, 2010, p, 37
1753	EY_M_25_av	1st order derivative	C=O stretching band	Spectrum EY_av, Ploeger et al, 2010, p, 37
	UN_6	(blank)	(blank)	(blank)
1755	EY_M_50_av	1st order derivative	C=O stretching band	Spectrum EY_av, Ploeger et al, 2010, p, 37
2189	EY_M_50_av	weak absorption	egg yolk	spectrum EY_av
2855	UN_6	(blank)	(blank)	(blank)
2857	EY_M_25_av	strong absorption	C-H stretching bands, esters	Spectrum EY_av, Rosi et al, 2009, p. 2099
2858	EY_M_50_av	strong absorption	C-H stretching bands, esters	Spectrum EY_av, Rosi et al, 2009, p. 2099
2908	EY_M_50_av	strong absorption	C-H stretching bands, esters	Spectrum EY_av, Rosi et al, 2009, p. 2099
2925	UN_6	(blank)	(blank)	(blank)
2935	EY_M_25_av	strong absorption	CH stretching	Spectrum EY_av, Daher et al, 2017, p.8
2936	EY_M_50_av	strong absorption	CH stretching	Spectrum EY_av, Daher et al, 2017, p.8
2959	EY_M_50_av	strong absorption	C-H stretching bands, esters	Spectrum EY_av, Rosi et al, 2009, p. 2099
	EY_M_25_av	strong absorption	C-H stretching bands, esters	Spectrum EY_av, Rosi et al, 2009, p. 2099
3004	EY_M_50_av	weak absorption	CH stretching	Miliani et al, 2012, p. 302
	UN_6	(blank)	(blank)	(blank)
3007	EY_M_25_av	weak absorption	CH stretching	Miliani et al, 2012, p. 302

Figure 75: Filtered CPAD of peaks of interest for UN_III_6 spectrum and possible matches.

UN_III_7

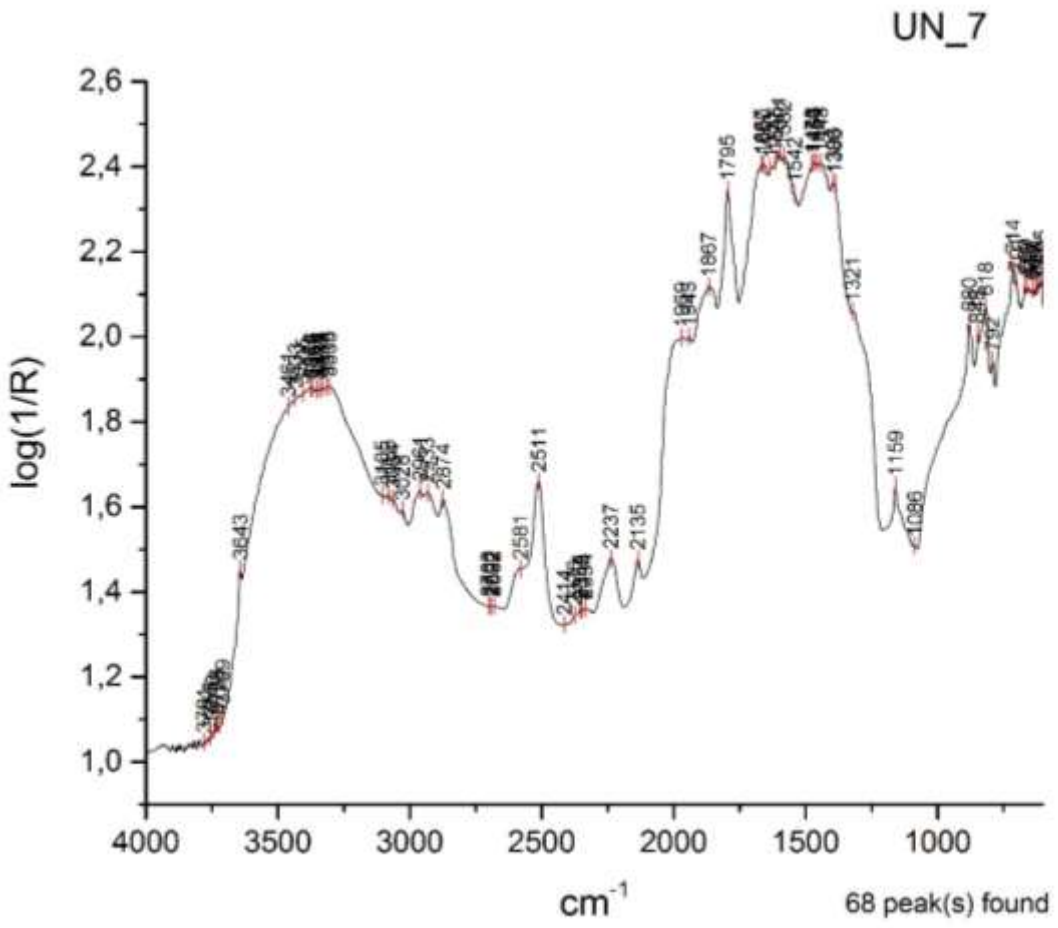

Figure 76: UN_III_7 correctly identified as 5% egg white additive in mortar (EW_M_5).

Peak x (position)	Spectrum ID	Type of band	Chemical Band Assignement	Reference
1321	UN_7	(blank)	(blank)	(blank)
1388	UN_7	(blank)	(blank)	(blank)
1395	EW_M_5_av	weak absorption	CaCO3	Spectrum Ca_av, spectrum M_av
1396	UN_7	(blank)	(blank)	(blank)
1400	EW_M_25_av	weak absorption	CaCO3	Spectrum Ca_av, spectrum M_av
1438	EW_M_25_av	weak absorption	v3 antisymmetric stretching CO3-2	Spectrum M_av, Ylmen and Jaglid, 2013, p. 119
1443	EW_M_5_av	weak absorption	v3 antisymmetric stretching CO3-2	Spectrum M_av, Ylmen and Jaglid, 2013, p. 119
	UN_7	(blank)	(blank)	(blank)
1446	EW_M_25_av	weak absorption	v3 antisymmetric stretching CO3-2	Spectrum Ca_av, Ylmen and Jaglid, 2013, p. 119
1452	EW_M_5_av	weak absorption	v3 antisymmetric stretching CO3-2	Spectrum M_av, Ylmen and Jaglid, 2013, p. 119
1459	UN_7	(blank)	(blank)	(blank)
1467	EW_M_5_av	weak absorption	v3 antisymmetric stretching CO3-2	Spectrum M_av, Ylmen and Jaglid, 2013, p. 119
	EW_M_25_av	weak absorption	v3 antisymmetric stretching CO3-2	Spectrum Ca_av, Ylmen and Jaglid, 2013, p. 119
	UN_7	(blank)	(blank)	(blank)
1475	UN_7	(blank)	(blank)	(blank)
1476	EW_M_25_av	weak absorption	egg white	spectrum EW_av
1498	EW_M_25_av	weak absorption	C=O	Rosi et al, 2002, p. 2099
1542	UN_7	(blank)	(blank)	(blank)
1561	EW_M_5_av	weak absorption	quartz	spectrum Q_av
	EW_M_25_av	weak absorption	quartz	spectrum Q_av
1571	EW_M_25_av	strong absorption	C-N-H bending amide II, N-H bands	Spectrum EW_av, Rosi et al, 2009, p. 2104
1577	EW_M_25_av	strong absorption	C-N-H bending amide II, N-H bands	Spectrum EW_av, Rosi et al, 2009, p. 2104
1579	EW_M_5_av	strong absorption	C-N-H bending amide II, N-H bands	Spectrum EW_av, Rosi et al, 2009, p. 2104
1582	UN_7	(blank)	(blank)	(blank)
1601	EW_M_5_av	weak absorption	N-H bands	Miliani et al, 2012, p. 304; Rosi et al, 2009, p. 2104
	UN_7	(blank)	(blank)	(blank)
1615	UN_7	(blank)	(blank)	(blank)
1621	EW_M_25_av	weak absorption	N-H bands	Miliani et al, 2012, p. 304; Rosi et al, 2009, p. 2104
1629	EW_M_25_av	weak absorption	N-H bands	Miliani et al, 2012, p. 304; Rosi et al, 2009, p. 2104
1630	EW_M_5_av	weak absorption	N-H bands	Miliani et al, 2012, p. 304; Rosi et al, 2009, p. 2104
1633	UN_7	(blank)	(blank)	(blank)
1641	EW_M_25_av	weak absorption	N-H bands	Miliani et al, 2012, p. 304; Rosi et al, 2009, p. 2104
1660	EW_M_5_av	strong absorption	quartz	Spectrum M_av
	UN_7	(blank)	(blank)	(blank)
1665	EW_M_25_av	strong absorption	quartz	Spectrum M_av
1667	UN_7	(blank)	(blank)	(blank)
1794	EW_M_25_av	combination band	v1+v4	Spectrum Ca_av, spectrum M_av, Ricci et al, 2006, p. 1222
1795	EW_M_5_av	combination band	v1+v4	Spectrum Ca_av, spectrum M_av, Ricci et al, 2006, p. 1222

Figure 77: Filtered CPAD of peaks of interest for UN_III_7 spectrum and possible matches.

1851	**EW_M_25_av**	weak absorption	**quartz**	spectrum Q_av
1859	**EW_M_5_av**	weak absorption	**quartz**	spectrum Q_av
1867	**EW_M_5_av**	weak absorption	**quartz**	spectrum Q_av
1941	**EW_M_5_av**	weak absorption	**quartz**	spectrum Q_av
1965	**EW_M_25_av**	weak absorption	**quartz**	spectrum Q_av
1967	**EW_M_5_av**	weak absorption	**quartz**	spectrum Q_av
2135	**EW_M_5_av**	weak absorption	**calcium carbonate and quartz**	Spectrum Ca_av, spectrum M_av, spectrum Q_av
	EW_M_25_av	weak absorption	**calcium carbonate and quartz**	Spectrum Ca_av, spectrum M_av, spectrum Q_av
2238	**EW_M_5_av**	weak absorption	**quartz**	spectrum Q_av
	EW_M_25_av	weak absorption	**quartz**	spectrum Q_av
2512	**EW_M_5_av**	combination band	**v1+v3**	Spectrum Ca_av, spectrum M_av, Ricci et al, 2006, p. 1222
	EW_M_25_av	combination band	**v1+v3**	Spectrum Ca_av, spectrum M_av, Ricci et al, 2006, p. 1222
2571	**EW_M_25_av**	weak absorption	**egg white**	spectrum EW_av
2585	**EW_M_25_av**	weak absorption	**egg white**	spectrum EW_av
2690	**EW_M_25_av**	weak absorption	**egg white**	spectrum EW_av
2703	**EW_M_5_av**	weak absorption	**egg white**	spectrum EW_av
2874	**EW_M_5_av**	sharp and weak absorption	**CaCO3**	Spectrum Ca_av, spectrum M_av
	EW_M_25_av	sharp and weak absorption	**CaCO3**	Spectrum Ca_av, spectrum M_av
2933	**UN_7**	(blank)	**(blank)**	(blank)
2934	**EW_M_25_av**	weak absorption	**CH stretching**	Spectrum EW_av, Daher et al, 2017, p. 8
2936	**EW_M_5_av**	weak absorption	**CH stretching**	Spectrum EW_av, Daher et al, 2017, p. 8
2961	**UN_7**	(blank)	**(blank)**	(blank)
2963	**EW_M_5_av**	sharp and weak absorption	**CaCO3**	Spectrum Ca_av, spectrum M_av
2964	**EW_M_25_av**	sharp and weak absorption	**CaCO3**	Spectrum Ca_av, spectrum M_av
3028	**UN_7**	(blank)	**(blank)**	(blank)
3030	**EW_M_5_av**	weak absorption	**CaCO3**	spectrum Ca_av
3066	**EW_M_5_av**	1st overtone	**amide I**	Spectrum EW_av, Rosi et al, 2009, p. 2099
3083	**EW_M_25_av**	1st overtone	**amide I**	Spectrum EW_av, Rosi et al, 2009, p. 2099
3085	**EW_M_5_av**	1st overtone	**amide I**	Spectrum EW_av, Rosi et al, 2009, p. 2099
3095	**EW_M_25_av**	1st overtone	**amide I**	Spectrum EW_av, Rosi et al, 2009, p. 2099
3304	**EW_M_25_av**	weak absorption	**N-H stretching**	Rosi et al, 2002, p. 2099
3314	**EW_M_5_av**	weak absorption	**N-H stretching**	Rosi et al, 2002, p. 2099
3642	**EW_M_25_av**	doublet	**OH stretching of H2O**	Spectrum M_av, spectrum Ca_av, Rosi et al, 2009, p. 2100
3643	**EW_M_5_av**	doublet	**OH stretching of H2O**	Spectrum M_av, spectrum Ca_av, Rosi et al, 2009, p. 2100

Figure 77: continued.

UN_III_8

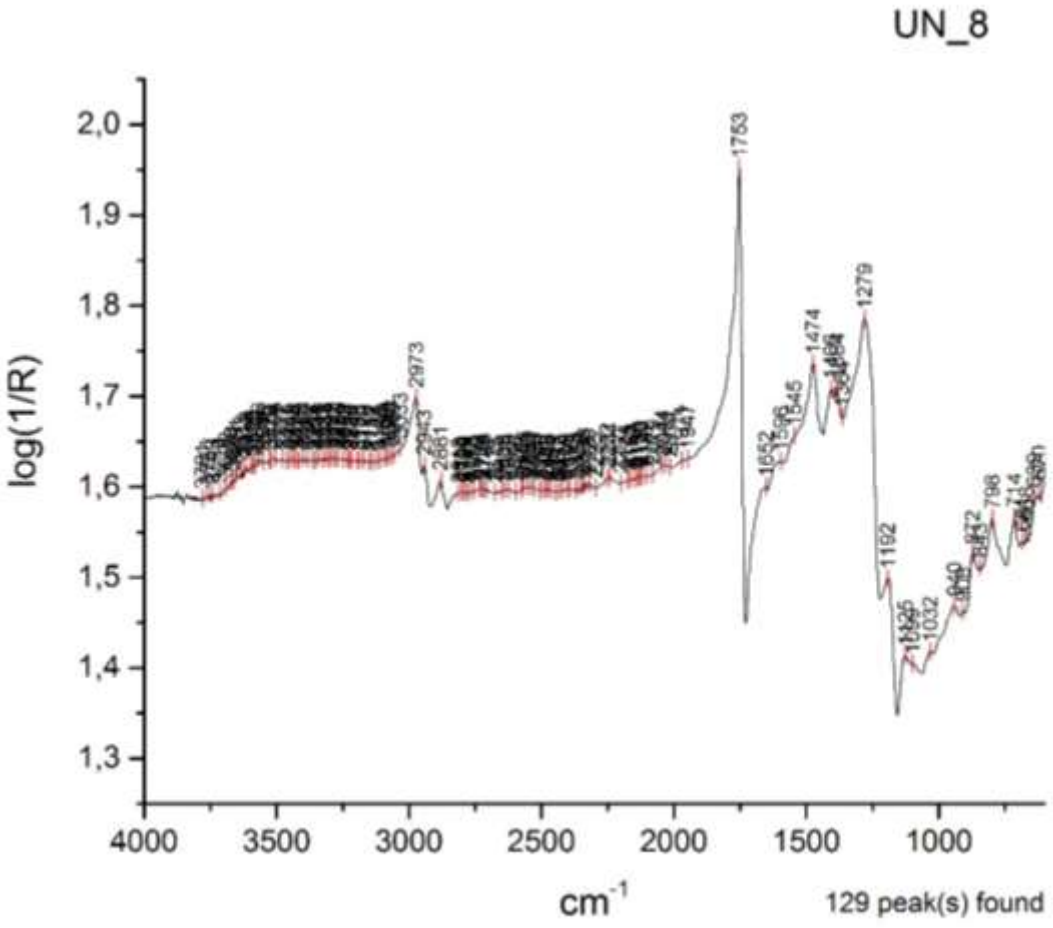

Figure 78: UN_III_8 correctly identified as 25% egg additive in mortar (E_M_25).

Peak x (position)	Spectrum ID	Type of band	Chemical Band Assignement	Reference
668	E_av	sharp and weak absorption	(blank)	spectrum EY_av, spectrum EW_av
715	E_M_25_av	doublet	in-plane rotation of linear long C chains δ(CH2)n	Spectrun E_av, Iwanicka et al, 2017, p. 18
729	E_M_25_av	doublet	in-plane rotation of linear long C chains δ(CH2)n	Spectrun E_av, Iwanicka et al, 2017, p. 18
734	E_av	weak absorption	(blank)	(blank)
745	E_av	weak absorption	(blank)	spectrum EY_av
765	E_av	weak absorption	(blank)	spectrum EY_av
775	E_M_25_av	weak absorption	whole egg	Spectrun E_av
786	E_M_25_av	weak absorption	whole egg	Spectrun E_av
794	E_av	weak absorption	(blank)	spectrum EY_av
802	E_av	weak absorption	(blank)	spectrum EY_av
805	E_M_25_av	weak absorption	whole egg	Spectrun E_av
835	E_av	weak absorption	(blank)	(blank)
844	E_M_25_av	weak absorption	whole egg	Spectrun E_av
908	UN_8	(blank)	(blank)	(blank)
909	E_M_25_av	weak absorption	v2 carbonate ion	Ylmen and Jaglid, 2013, p. 119
940	UN_8	(blank)	(blank)	(blank)
950	E_M_25_av	weak absorption	PO4-3 anion stretching	Spectrum E_av, Ricci et al. 2006, p. 1223
973	E_av	weak absorption	PO4-3anion stretching	Ricci et al, 2006, p. 1223, spectrum EY_av
1029	E_M_25_av	weak absorption	vSiO	Buti et al, 2013, p. 2705
1032	UN_8	(blank)	(blank)	(blank)
1099	E_M_25_av	weak absorption	v1 carbonate ion	Spectrum Ca_av, Ylmen and Jaglid, 2013, p. 119
	UN_8	(blank)	(blank)	(blank)
1123	E_av	weak absorption	PO4-3anion stretching	Ricci et al, 2006, p. 1223, spectrum EY_av
1125	E_M_25_av	sharp absorption	PO4-3 anion stretching	Spectrum E_av, Ricci et al. 2006, p. 1223
	UN_8	(blank)	(blank)	(blank)
1177	E_av	weak absorption	v(C-O) stretching	Ricci et al, 2006, p. 1224, spectrum EW_av
1192	E_M_25_av	sharp absorption	v(C-O) stretching	Spectrum E_av, Ricci et al. 2006, p. 1224
1268	E_av	strong absorption	C-O	Ploeger et al, 2010, p. 37, spectrum EY_av
1279	UN_8	(blank)	(blank)	(blank)
1280	E_M_25_av	strong absorption	C-O	Spectrum E_av, Ploeger et al, 2010, p. 17
1324	E_av	(blank)	(blank)	spectrum EW_av
1364	UN_8	(blank)	(blank)	(blank)
1384	E_M_25_av	strong absorption	CaCO3	Spectrun M_av, Spectrum Ca_av
	UN_8	(blank)	(blank)	(blank)
1405	E_M_25_av	strong absorption	CaCO3	Spectrun M_av, Spectrum Ca_av
1406	UN_8	(blank)	(blank)	(blank)
1411	E_av	(blank)	(blank)	spectrum EW_av
1445	E_av	weak absorption	Amide III	Buti et al, 2013, p. 2705, spectrum EW_av
1472	E_av	sharp absorption	C-O bending	Ricci et al, 2006, p. 1223, spectrum EW_av and EY_av
1473	E_M_25_av	strong absorption	C-O bending	Spectrum E_av, Ricci et al, 2006, p. 1223
1474	UN_8	(blank)	(blank)	(blank)

Figure 79: Filtered CPAD of peaks of interest for UN_III_8 spectrum and possible matches.

1545	**UN_8**	(blank)	**(blank)**	(blank)
1551	**E_M_25_av**	weak absorption	**quartz**	spectrum Q_av
1568	**E_av**	strong absorption	**N-H bands, amide I, II**	Miliani et al, 2012, p. 304, spectrum EW_av
1585	**E_M_25_av**	weak absorption	**v3 antisymmetric stretching CO3-2**	Spectrum M_av, spectrum Ca_av, Ylmen and Jaglid, 2013, p. 119
1596	**UN_8**	(blank)	**(blank)**	(blank)
1651	**E_M_25_av**	weak absorption	**quartz**	Spectrum Q_av, spectrum M_av
1652	**UN_8**	(blank)	**(blank)**	(blank)
1693	**E_av**	strong absorption	**N-H bands, amide I, II**	Miliani et al, 2012, p. 304, spectrum EW_av
1753	**E_M_25_av**	strong absorption	**C-H stretching bands, esters**	Spectrum E_av, Mazzeo et al, 2008, p. 69
	UN_8	(blank)	**(blank)**	(blank)
1755	**E_av**	strong absorption	**C=O stretching band, esters**	Mazzeo et al, 2008, p. 69, spectrum EY_av
1907	**E_M_25_av**	weak absorption	**(blank)**	(blank)
2030	**E_M_25_av**	weak absorption	**(blank)**	(blank)
2242	**E_M_25_av**	sharp absorption	**quartz**	Spectrun M_av, Spectrum Q_av
2864	**E_av**	strong absorption	**C-H stretching**	Rosi et al, 2009, p. 2099, spectrum EY_av
2876	**E_av**	strong absorption	**C-H stretching**	Rosi et al, 2009, p. 2099, spectrum EY_av
2880	**E_M_25_av**	strong absorption	**CH stretching**	Spectrum E_av, Daher et al, 2017, p.8
2881	**UN_8**	(blank)	**(blank)**	(blank)
2942	**E_av**	strong absorption	**C-H stretching bands, esters**	Spectrum EY_av, Rosi et al, 2009, p. 2099
2943	**E_M_25_av**	strong absorption	**CH stretching**	Spectrum E_av, Daher et al, 2017, p.8
	UN_8	(blank)	**(blank)**	(blank)
2973	**E_av**	strong absorption	**C-H stretching bands, esters**	Spectrum EY_av, Rosi et al, 2009, p. 2099
	UN_8	(blank)	**(blank)**	(blank)
2974	**E_M_25_av**	weak absorption	**CH2 stretching**	Spectrum E_av, Ploeger et al, 2010, p. 37
3045	**E_av**	weak absorption	**2δNH**	Rosi et al, 2010, p. 621
3075	**E_av**	weak absorption	**2δNH**	Rosi et al, 2010, p. 621
3089	**E_av**	weak absorption	**2δNH**	Rosi et al, 2010, p. 621
3102	**E_av**	weak absorption	**2δNH**	Rosi et al, 2010, p. 621
3224	**E_av**	(blank)	**(blank)**	(blank)
3240	**E_av**	(blank)	**(blank)**	(blank)

Figure 79: continued.

UN_III_9

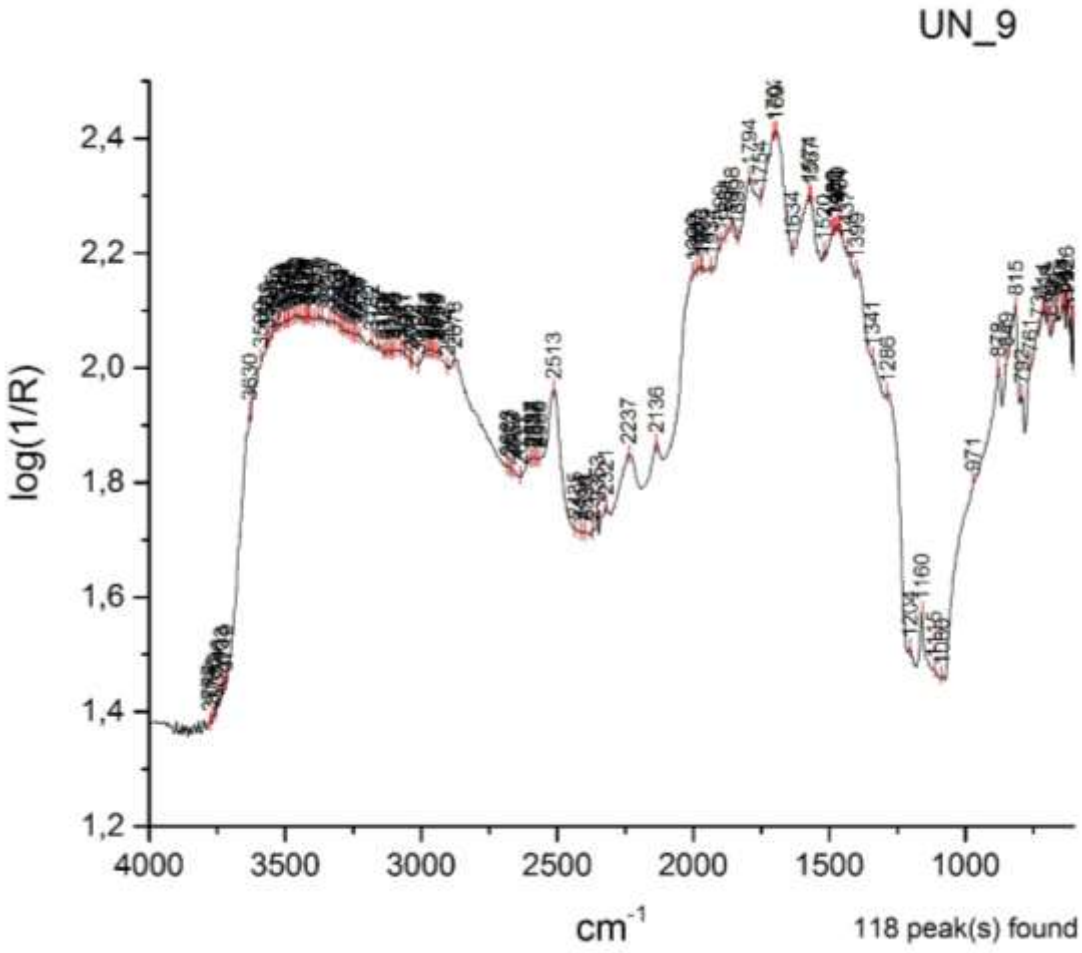

Figure 80: UN_III_9 correctly identified as 25% bone glue additive in mortar (BG_M_25).

Peak x (position)	Spectrum ID	Type of band	Chemical Band Assignement	Reference
1205	BG_M_25_av	weak bands	bone glue	Spectrum BG_av
1286	BG_M_25_av	stair-step type intensities	bone glue	Spectrum BG_av
	UN_9	(blank)	(blank)	(blank)
1341	BG_M_25_av	weak absorption	quartz	spectrum Q_av
	UN_9	(blank)	(blank)	(blank)
1399	BG_M_25_av	weak absorption	CaCO3	Spectrum Ca_av, spectrum M_av
	UN_9	(blank)	(blank)	(blank)
1400	EW_M_25_av	weak absorption	CaCO3	Spectrum Ca_av, spectrum M_av
1431	BG_M_25_av	weak absorption	CaCO3 and quartz	Spectrum M_av
1437	BG_M_25_av	weak absorption	CaCO3 and quartz	Spectrum M_av
	UN_9	(blank)	(blank)	(blank)
1438	EW_M_25_av	weak absorption	v3 antisymmetric stretching CO3-2	Spectrum M_av, Ylmen and Jaglid, 2013, p. 119
1446	EW_M_25_av	weak absorption	v3 antisymmetric stretching CO3-2	Spectrum Ca_av, Ylmen and Jaglid, 2013, p. 119
1461	BG_M_25_av	stair-step type intensities	Amide III	Spectrum BG_av, Rosi et al, 2009, p. 2099
	UN_9	(blank)	(blank)	(blank)
1467	EW_M_25_av	weak absorption	v3 antisymmetric stretching CO3-2	Spectrum Ca_av, Ylmen and Jaglid, 2013, p. 119
1469	BG_M_25_av	stair-step type intensities	Amide III	Spectrum BG_av, Rosi et al, 2009, p. 2099
1470	UN_9	(blank)	(blank)	(blank)
1476	EW_M_25_av	weak absorption	egg white	spectrum EW_av
1480	UN_9	(blank)	(blank)	(blank)
1486	UN_9	(blank)	(blank)	(blank)
1498	EW_M_25_av	weak absorption	C=O	Rosi et al, 2002, p. 2099
1520	UN_9	(blank)	(blank)	(blank)
1561	EW_M_25_av	weak absorption	quartz	spectrum Q_av
1567	UN_9	(blank)	(blank)	(blank)
1571	EW_M_25_av	strong absorption	C-N-H bending amide II, N-H bands	Spectrum EW_av, Rosi et al, 2009, p. 2104
1574	UN_9	(blank)	(blank)	(blank)
1575	BG_M_25_av	strong absorption	v3 antisymmetric stretching CO3-2 or amide III	Spectrum BG_av, spectrum M_av, Ylmen and Jaglid, 2013, 119; Miliani et al, 2012, p. 304
1577	EW_M_25_av	strong absorption	C-N-H bending amide II, N-H bands	Spectrum EW_av, Rosi et al, 2009, p. 2104
1597	BG_M_25_av	strong absorption	quartz	Spectrum Q_av, spectrum M_av
1621	EW_M_25_av	weak absorption	N-H bands	Miliani et al, 2012, p. 304; Rosi et al, 2009, p. 2104
1629	EW_M_25_av	weak absorption	N-H bands	Miliani et al, 2012, p. 304; Rosi et al, 2009, p. 2104
1634	UN_9	(blank)	(blank)	(blank)
1641	EW_M_25_av	weak absorption	N-H bands	Miliani et al, 2012, p. 304; Rosi et al, 2009, p. 2104
1665	EW_M_25_av	strong absorption	quartz	Spectrum M_av
1694	BG_M_25_av	strong absorption	N-H bands	Spectrum BG_av, Rosi et al, 2009, p. 2104, Miliani et al, 2012, p. 304
	UN_9	(blank)	(blank)	(blank)
1703	UN_9	(blank)	(blank)	(blank)
1793	BG_M_25_av	strong absorption	v1+v4	Spectrum Ca_av, spectrum M_av, Ricci et al, 2006, p. 1222
1794	EW_M_25_av	combination band	v1+v4	Spectrum Ca_av, spectrum M_av, Ricci et al, 2006, p. 1222

Figure 81: Filtered CPAD of peaks of interest for UN_III_9 spectrum and possible matches.

1851	**EW_M_25_av**	weak absorption	**quartz**	spectrum Q_av
1867	**BG_M_25_av**	weak absorption	**quartz**	Spectrum Q_av, spectrum M_av
1944	**BG_M_25_av**	weak absorption	**quartz**	Spectrum Q_av, spectrum M_av
1965	**EW_M_25_av**	weak absorption	**quartz**	spectrum Q_av
1973	**BG_M_25_av**	weak absorption	**quartz**	Spectrum Q_av, spectrum M_av
1988	**BG_M_25_av**	weak absorption	**quartz**	Spectrum Q_av, spectrum M_av
2135	**EW_M_25_av**	weak absorption	**calcium carbonate and quartz**	Spectrum Ca_av, spectrum M_av, spectrum Q_av
2136	**BG_M_25_av**	weak absorption	**CaCO3 and quartz**	Spectrum Q_av, spectrum M_av, spectrum Ca_av
2236	**BG_M_25_av**	weak absorption	**quartz**	Spectrum Q_av, spectrum M_av
2238	**EW_M_25_av**	weak absorption	**quartz**	spectrum Q_av
2512	**EW_M_25_av**	combination band	**v1+v3**	Spectrum Ca_av, spectrum M_av, Ricci et al, 2006, p. 1222
2513	**BG_M_25_av**	combination band	**v1+v3 carbonate ion**	Spectrum Ca_av, spectrum M_av, Ricci et al, 2006, p. 1222
2571	**EW_M_25_av**	weak absorption	**egg white**	spectrum EW_av
2585	**EW_M_25_av**	weak absorption	**egg white**	spectrum EW_av
2690	**EW_M_25_av**	weak absorption	**egg white**	spectrum EW_av
2874	**EW_M_25_av**	sharp and weak absorption	**CaCO3**	Spectrum Ca_av, spectrum M_av
2875	**BG_M_25_av**	strong absorption	**CaCO3**	Spectrum Ca_av, spectrum M_av
2897	**BG_M_25_av**	weak bands	**C-H stretching**	Spectrum BG_av, Miliani et al, 2012, p. 304; Rosi et al, 2009, p. 2104
2904	**UN_9**	(blank)	**(blank)**	(blank)
2905	**BG_M_25_av**	weak absorption	**bone glue**	Spectrum BG
2934	**EW_M_25_av**	weak absorption	**CH stretching**	Spectrum EW_av, Daher et al, 2017, p. 8
2939	**UN_9**	(blank)	**(blank)**	(blank)
2940	**BG_M_25_av**	weak absorption	**(blank)**	(blank)
2949	**BG_M_25_av**	weak absorption	**(blank)**	(blank)
	UN_9	(blank)	**(blank)**	(blank)
2959	**UN_9**	(blank)	**(blank)**	(blank)
2964	**EW_M_25_av**	sharp and weak absorption	**CaCO3**	Spectrum Ca_av, spectrum M_av
2979	**BG_M_25_av**	strong absorption	**CaCO3**	Spectrum Ca_av, spectrum M_av
3083	**EW_M_25_av**	1st overtone	**amide I**	Spectrum EW_av, Rosi et al, 2009, p. 2099
3095	**EW_M_25_av**	1st overtone	**amide I**	Spectrum EW_av, Rosi et al, 2009, p. 2099
3304	**EW_M_25_av**	weak absorption	**N-H stretching**	Rosi et al, 2002, p. 2099
3642	**EW_M_25_av**	doublet	**OH stretching of H2O**	Spectrum M_av, spectrum Ca_av, Rosi et al, 2009, p. 2100

Figure 81: continued.

UN_III_10

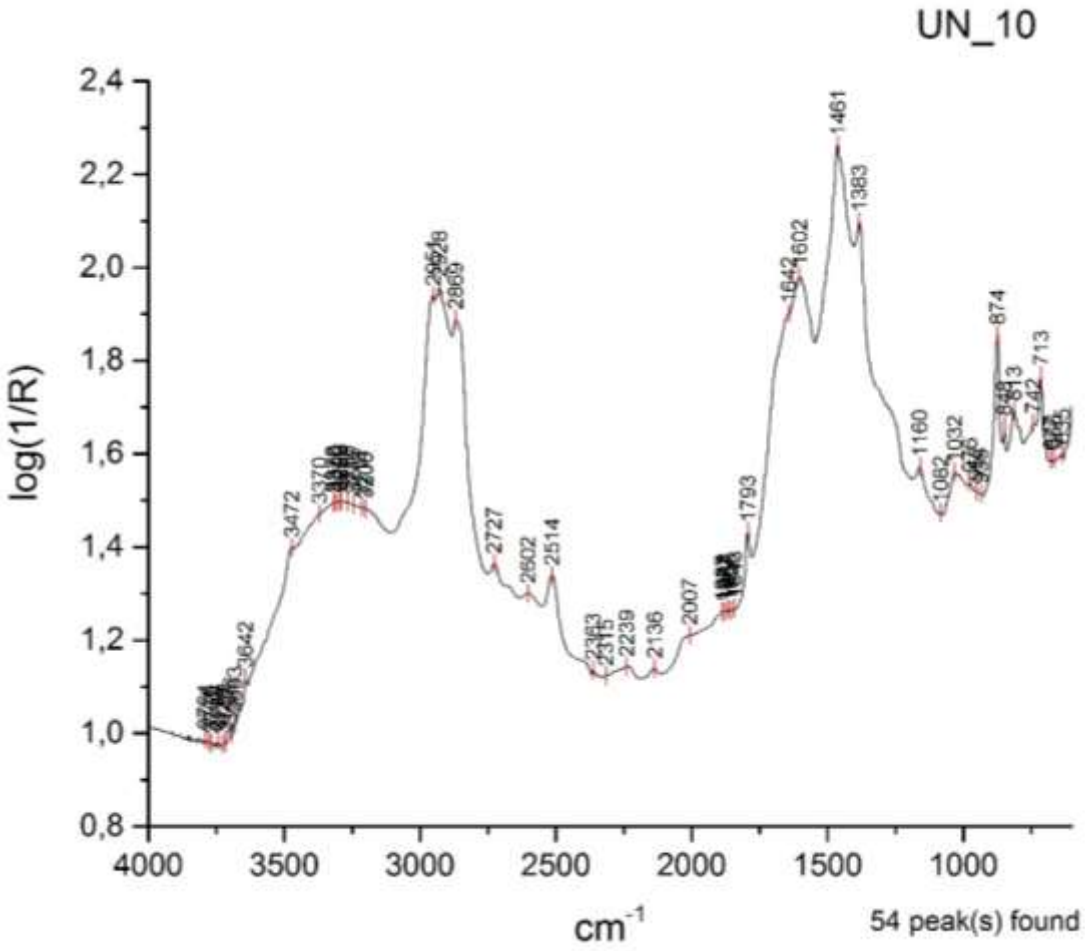

Figure 82: UN_III_10 correctly identified as 25% asphalt additive in mortar (A_M_25).

Peak x (position)	Spectrum ID	Type of band	Chemical Band Assignement	Reference
1383	UN_10	(blank)	(blank)	(blank)
1385	A_M_25_av	strong absorption	CH2, CH3 stretching	Spectrum A_av, Lombardi and Santarelli, 2009, 542
1386	A_M_5_av	strong absorption	CH2, CH3 stretching	Spectrum A_av, Lombardi and Santarelli, 2009, 542
1401	A_M_25_av	strong absorption	calcium carbonate	Spectrum Ca_av, spectrum M_av
	A_M_5_av	weak absorption	calcium carbonate	Spectrum Ca_av, spectrum M_av
1453	A_M_25_av	shoulder	v3 antisymmetric stretching CO3-2	Spectrum Ca_av, Ylmen and Jaglid, 2013, p. 119
	A_M_5_av	shoulder	v3 antisymmetric stretching CO3-2	Spectrum Ca_av, Ylmen and Jaglid, 2013, p. 119
1461	A_M_50_av	strong absorption	asphalt	Spectrum A_av
	A_M_25_av	strong absorption	asphalt	Spectrum A_av
	UN_10	(blank)	(blank)	(blank)
1462	A_M_5_av	strong absorption	asphalt	Spectrum A_av
1599	A_M_5_av	strong absorption	C6H6 (benzene rings)	Spectrum A_av, Lombardi and Santarelli, 2009, 542
1600	A_M_25_av	strong absorption	C6H6 (benzene rings)	Spectrum A_av, Lombardi and Santarelli, 2009, 542
1602	UN_10	(blank)	(blank)	(blank)
1603	A_M_50_av	strong absorption	C6H6 (benzene rings)	Spectrum A_av, Lombardi and Santarelli, 2009, 542
1642	A_M_25_av	shoulder	asphalt	Spectrum A_av
	UN_10	(blank)	(blank)	(blank)
1643	A_M_50_av	shoulder	(blank)	Spectrum A_av
1652	A_M_5_av	shoulder	asphalt	Spectrum A_av
1792	A_M_50_av	combination band	v1+v4	Spectrum Ca_av, spectrum M_av, Ricci et al, 2006, p. 1222
1794	A_M_25_av	combination band	v1+v4	Spectrum Ca_av, spectrum M_av, Ricci et al, 2006, p. 1222
	A_M_5_av	combination band	v1+v4	Spectrum Ca_av, spectrum M_av, Ricci et al, 2006, p. 1222
1843	A_M_50_av	weak absorption	quartz	Spectrum Q_av, spectrum M_av, spectrum A_av
	A_M_25_av	weak absorption	quartz	Spectrum Q_av, spectrum M_av, spectrum A_av
1844	A_M_5_av	weak absorption	quartz	Spectrum Q_av, spectrum M_av, spectrum A_av
1867	A_M_50_av	weak absorption	quartz	Spectrum Q_av, spectrum M_av, spectrum A_av
	A_M_25_av	weak absorption	quartz	Spectrum Q_av, spectrum M_av, spectrum A_av
	A_M_5_av	weak absorption	quartz	Spectrum Q_av, spectrum M_av, spectrum A_av
1888	A_M_50_av	weak absorption	quartz	Spectrum Q_av, spectrum A_av

Figure 83: Filtered CPAD of peaks of interest for UN_III_10 spectrum and possible matches.

2016	**A_M_50_av**	weak absorption	**asphalt**	Spectrum A_av
2023	**A_M_50_av**	weak absorption	**asphalt**	Spectrum A_av
2135	**A_M_5_av**	weak absorption	**calcium carbonate and quartz**	Spectrum Q_av, spectrum M_av, spectrum Ca_av
2136	**A_M_25_av**	sharp and weak absorption	**calcium carbonate and quartz**	Spectrum Q_av, spectrum M_av, spectrum Ca_av
2138	**A_M_50_av**	weak absorption	**(blank)**	Spectrum Q_av, spectrum M_av, spectrum Ca_av
2236	**A_M_5_av**	weak absorption	**quartz**	Spectrum Q_av, spectrum M_av
2239	**A_M_25_av**	weak absorption	**quartz**	Spectrum Q_av, spectrum M_av
2512	**A_M_5_av**	combination band	**v1+v3**	Spectrum M_av, spectrum Ca_av, Ricci et al, 2006, p. 1222
2513	**A_M_25_av**	combination band	**v1+v3**	Spectrum M_av, spectrum Ca_av, Ricci et al, 2006, p. 1222
2519	**A_M_50_av**	combination band	**v1+v3**	Spectrum M_av, spectrum Ca_av, Ricci et al, 2006, p. 1222
2589	**A_M_5_av**	shoulder	**quartz**	spectrum Q_av
2598	**A_M_25_av**	weak absorption	**quartz**	Spectrum Q_av, spectrum M_av
2727	**A_M_50_av**	sharp and weak absorption	**asphalt**	Spectrum A_av
	A_M_5_av	weak absorption	**asphalt**	Spectrum A_av
	UN_10	(blank)	**(blank)**	(blank)
2728	**A_M_25_av**	weak absorption	**asphalt**	Spectrum A_av
2856	**A_M_50_av**	strong absorption	**CH2, CH3 stretching**	Spectrum A_av, Lombardi and Santarelli, 2009, 542
2867	**A_M_50_av**	strong absorption	**CH2, CH3 stretching**	Spectrum A_av, Lombardi and Santarelli, 2009, 542
2868	**A_M_25_av**	strong absorption	**CH2, CH3 stretching**	Spectrum A_av, Lombardi and Santarelli, 2009, 542
2869	**UN_10**	(blank)	**(blank)**	(blank)
2870	**A_M_5_av**	strong absorption	**CH2, CH3 stretching**	Spectrum A_av, Lombardi and Santarelli, 2009, 542
2928	**A_M_5_av**	strong absorption	**CH2, CH3 stretching**	Spectrum A_av, Lombardi and Santarelli, 2009, 542
	UN_10	(blank)	**(blank)**	(blank)
2929	**A_M_25_av**	strong absorption	**CH2, CH3 stretching**	Spectrum A_av, Lombardi and Santarelli, 2009, 542
2931	**A_M_50_av**	strong absorption	**CH2, CH3 stretching**	Spectrum A_av, Lombardi and Santarelli, 2009, 542
2951	**UN_10**	(blank)	**(blank)**	(blank)
2953	**A_M_25_av**	strong absorption	**CH2, CH3 stretching**	Spectrum A_av, Lombardi and Santarelli, 2009, 542
2954	**A_M_5_av**	strong absorption	**CH2, CH3 stretching**	Spectrum A_av, Lombardi and Santarelli, 2009, 542
2956	**A_M_50_av**	strong absorption	**CH2, CH3 stretching**	Spectrum A_av, Lombardi and Santarelli, 2009, 542
3451	**A_M_5_av**	weak absorption	**(blank)**	(blank)
3467	**A_M_5_av**	weak absorption	**asphalt**	Spectrum A_av
3472	**A_M_25_av**	weak absorption	**asphalt**	Spectrum A_av
3473	**A_M_50_av**	weak absorption	**asphalt**	Spectrum A_av
3572	**A_M_5_av**	weak absorption	**(blank)**	(blank)
3642	**A_M_5_av**	sharp and weak absorption	**Ca(OH)2**	Spectrum Ca_av, spectrum M_av, Ylmen and Jaglid, 2013, p. 119
3643	**A_M_25_av**	sharp and weak absorption	**Ca(OH)2**	Spectrum Ca_av, spectrum M_av, Ylmen and Jaglid, 2013, p. 119

Figure 83: continued.

8.1.4 Experimental set IV

UN_IV_1

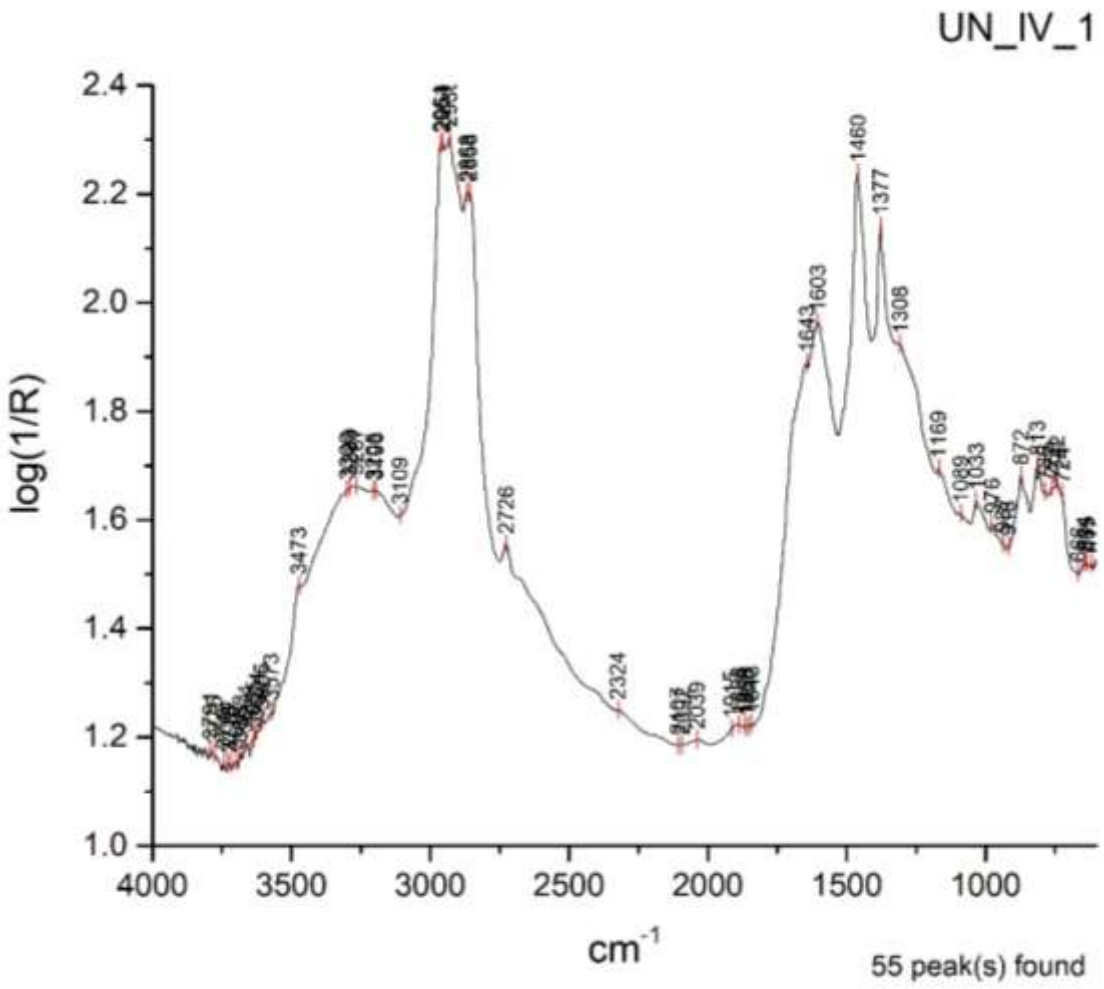

Figure 84: UN_IV_1 falsely identified as asphalt (A_av) instead of the correct 75% asphalt additive in mortar (A_M_75).

Peak x (position)	Spectrum ID	Type of band	Chemical Band Assignement	Reference
617	UN_IV_1	(blank)	(blank)	(blank)
635	UN_IV_1	(blank)	(blank)	(blank)
644	UN_IV_1	(blank)	(blank)	(blank)
666	UN_IV_1	(blank)	(blank)	(blank)
723	A_av	triplet	(blank)	Lombardi and Santarelli, 2009, 542
724	A_M_75_av	triplet	asphalt	Spectrum A_av, Lombardi and Santarelli, 2009, 542
	UN_IV_1	(blank)	(blank)	(blank)
742	A_av	triplet	(blank)	Lombardi and Santarelli, 2009, 542
	A_M_75_av	triplet	asphalt	Spectrum A_av, Lombardi and Santarelli, 2009, 542
	UN_IV_1	(blank)	(blank)	(blank)
759	A_M_75_av	(blank)	(blank)	(blank)
	UN_IV_1	(blank)	(blank)	(blank)
786	UN_IV_1	(blank)	(blank)	(blank)
813	UN_IV_1	(blank)	(blank)	(blank)
814	A_av	triplet	(blank)	Lombardi and Santarelli, 2009, 542
	A_M_75_av	triplet	asphalt	Spectrum A_av, Lombardi and Santarelli, 2009, 542
868	A_av	triplet	(blank)	Lombardi and Santarelli, 2009, 542
872	A_M_75_av	triplet	asphalt	Spectrum A_av, Lombardi and Santarelli, 2009, 542
	UN_IV_1	(blank)	(blank)	(blank)
918	UN_IV_1	(blank)	(blank)	(blank)
937	A_av	(blank)	(blank)	(blank)
	A_M_75_av	(blank)	asphalt	Spectrum A_av
	UN_IV_1	(blank)	(blank)	(blank)
976	A_av	(blank)	(blank)	(blank)
	A_M_75_av	(blank)	asphalt	Spectrum A_av
	UN_IV_1	(blank)	(blank)	(blank)
1032	A_av	sharp absorption	quartz	Lombardi and Santarelli, 2009, 542
1033	A_M_75_av	sharp absorption	quartz	Spectrum A_av, Lombardi and Santarelli, 2009, 542
	UN_IV_1	(blank)	(blank)	(blank)
1064	A_av	(blank)	(blank)	(blank)
1089	UN_IV_1	(blank)	(blank)	(blank)
1169	A_av	weak absorption	(blank)	(blank)
	A_M_75_av	weak absorption	asphalt	Spectrum A_av
	UN_IV_1	(blank)	(blank)	(blank)
1308	UN_IV_1	(blank)	(blank)	(blank)
1314	A_av	weak absorption	CH2, CH3	Lombardi and Santarelli, 2009, 542
1377	A_av	strong absorption	CH2, CH3	Lombardi and Santarelli, 2009, 542
	UN_IV_1	(blank)	(blank)	(blank)
1378	A_M_75_av	strong absorption	CH2, CH3	Spectrum A_av, Lombardi and Santarelli, 2009, 542
1460	UN_IV_1	(blank)	(blank)	(blank)
1461	A_av	strong absorption	(blank)	(blank)
	A_M_75_av	strong absorption	asphalt	Spectrum A_av
1603	A_av	strong absorption	C6H6 (benzene rings)	Lombardi and Santarelli, 2009, 542
	A_M_75_av	strong absorption	C6H6 (benzene rings)	Spectrum A_av, Lombardi and Santarelli, 2009, 542
	UN_IV_1	(blank)	(blank)	(blank)
1643	A_av	(blank)	(blank)	(blank)
	A_M_75_av	weak absorption	(blank)	Spectrum A_av
	UN_IV_1	(blank)	(blank)	(blank)
1649	A_av	(blank)	(blank)	(blank)

Figure 85: Filtered CPAD of peaks of interest for UN_IV_1 spectrum and possible matches.

1843	**A_av**	weak absorption	**quartz**	Spectrum Q_av, spectrum M_av, spectrum A_av
	A_M_75_av	weak absorption	**quartz**	Spectrum Q_av, spectrum M_av, spectrum A_av
	UN_IV_1	(blank)	**(blank)**	(blank)
1856	**UN_IV_1**	(blank)	**(blank)**	(blank)
1866	**A_M_75_av**	weak absorption	**quartz**	Spectrum Q_av, spectrum M_av, spectrum A_av
	UN_IV_1	(blank)	**(blank)**	(blank)
1867	**A_av**	weak absorption	**quartz**	Spectrum Q_av, spectrum M_av, spectrum A_av
1888	**A_av**	weak absorption	**quartz**	spectrum A_av, spectrum Q_av
	A_M_75_av	weak absorption	**quartz**	spectrum A_av, spectrum Q_av
	UN_IV_1	(blank)	**(blank)**	(blank)
1915	**UN_IV_1**	(blank)	**(blank)**	(blank)
2032	**A_M_75_av**	weak absorption	**(blank)**	Spectrum A_av
2039	**A_av**	(blank)	**(blank)**	(blank)
	UN_IV_1	(blank)	**(blank)**	(blank)
2092	**UN_IV_1**	(blank)	**(blank)**	(blank)
2107	**UN_IV_1**	(blank)	**(blank)**	(blank)
2726	**UN_IV_1**	(blank)	**(blank)**	(blank)
2727	**A_av**	(blank)	**(blank)**	(blank)
	A_M_75_av	weak absorption	**(blank)**	Spectrum A_av
2858	**A_av**	strong absorption	**CH2, CH3 stretching**	Lombardi and Santarelli, 2009, 542
	A_M_75_av	strong absorption	**CH2, CH3 stretching**	Spectrum A_av, Lombardi and Santarelli, 2009, 542
	UN_IV_1	(blank)	**(blank)**	(blank)
2866	**A_av**	strong absorption	**CH2, CH3 stretching**	Lombardi and Santarelli, 2009, 542
2867	**A_M_75_av**	strong absorption	**CH2, CH3 stretching**	Spectrum A_av, Lombardi and Santarelli, 2009, 542
2868	**UN_IV_1**	(blank)	**(blank)**	(blank)
2930	**UN_IV_1**	(blank)	**(blank)**	(blank)
2931	**A_M_75_av**	strong absorption	**CH2, CH3 stretching**	Spectrum A_av, Lombardi and Santarelli, 2009, 542
2932	**A_av**	strong absorption	**CH2, CH3 stretching**	Lombardi and Santarelli, 2009, 542
2954	**A_av**	strong absorption	**CH2, CH3 stretching**	Lombardi and Santarelli, 2009, 542
	A_M_75_av	strong absorption	**CH2, CH3 stretching**	Spectrum A_av, Lombardi and Santarelli, 2009, 542
	UN_IV_1	(blank)	**(blank)**	(blank)
2961	**A_M_75_av**	strong absorption	**CH2, CH3 stretching**	Spectrum A_av, Lombardi and Santarelli, 2009, 542
	UN_IV_1	(blank)	**(blank)**	(blank)

Figure 85: continued.

UN_IV_2

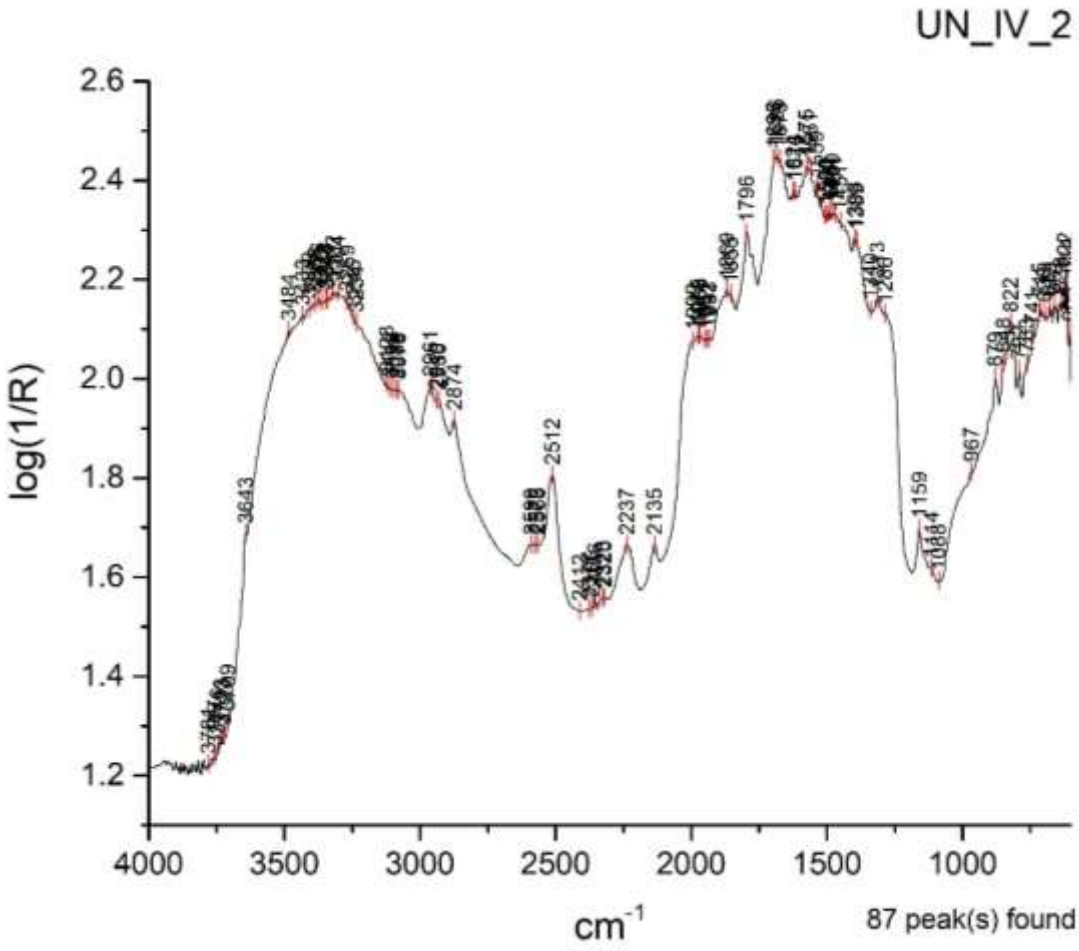

Figure 86: UN_IV_2 correctly identified as 50% egg white additive in mortar (EW_M_50).

Peak x (position)	Spectrum ID	Type of band	Chemical Band Assignement	Reference
967	UN_IV_2	(blank)	(blank)	(blank)
1082	EW_M_50_av	weak absorption	egg white	spectrum EW_av
1085	EW_M_25_av	weak absorption	egg white	spectrum EW_av
1116	EW_M_50_av	weak absorption	C-O stretching	Buti et al, 2013, p. 2705
1283	EW_M_50_av	weak absorption	egg white	spectrum EW_av
1286	UN_IV_2	(blank)	(blank)	(blank)
1313	EW_M_50_av	weak absorption	egg white	spectrum EW_av
	UN_IV_2	(blank)	(blank)	(blank)
1340	UN_IV_2	(blank)	(blank)	(blank)
1389	UN_IV_2	(blank)	(blank)	(blank)
1398	UN_IV_2	(blank)	(blank)	(blank)
1446	EW_M_50_av	weak absorption	egg white	spectrum EW_av
1451	UN_IV_2	(blank)	(blank)	(blank)
1471	UN_IV_2	(blank)	(blank)	(blank)
1476	EW_M_25_av	weak absorption	egg white	spectrum EW_av
1480	EW_M_50_av	weak absorption	egg white	spectrum EW_av
	UN_IV_2	(blank)	(blank)	(blank)
1491	UN_IV_2	(blank)	(blank)	(blank)
1498	EW_M_25_av	weak absorption	C=O	Rosi et al, 2002, p. 2099
1500	UN_IV_2	(blank)	(blank)	(blank)
1506	UN_IV_2	(blank)	(blank)	(blank)
1539	UN_IV_2	(blank)	(blank)	(blank)
1561	UN_IV_2	(blank)	(blank)	(blank)
1571	EW_M_25_av	strong absorption	C-N-H bending amide II, N-H bands	Spectrum EW_av, Rosi et al, 2009, p. 2104
1575	UN_IV_2	(blank)	(blank)	(blank)
1576	EW_M_50_av	strong absorption	C-N-H bending amide II, N-H bands	Spectrum EW_av, Rosi et al, 2009, p. 2104
1577	EW_M_25_av	strong absorption	C-N-H bending amide II, N-H bands	Spectrum EW_av, Rosi et al, 2009, p. 2104

Figure 87: Filtered CPAD of peaks of interest for UN_IV_2 spectrum and possible matches.

1616	**UN_IV_2**	(blank)	**(blank)**	(blank)
1621	**EW_M_25_av**	weak absorption	**N-H bands**	Miliani et al, 2012, p. 304; Rosi et al, 2009, p. 2104
1624	**UN_IV_2**	(blank)	**(blank)**	(blank)
1629	**EW_M_25_av**	weak absorption	**N-H bands**	Miliani et al, 2012, p. 304; Rosi et al, 2009, p. 2104
1641	**EW_M_25_av**	weak absorption	**N-H bands**	Miliani et al, 2012, p. 304; Rosi et al, 2009, p. 2104
1673	**UN_IV_2**	(blank)	**(blank)**	(blank)
1685	**EW_M_50_av**	strong absorption	**N-H bands**	Spectrum EW_av, Ploeger et al, 2010, p.37, Miliani et al, 2012, p. 305
1686	**UN_IV_2**	(blank)	**(blank)**	(blank)
1695	**UN_IV_2**	(blank)	**(blank)**	(blank)
2564	**EW_M_50_av**	weak absorption	**egg white**	spectrum EW_av
2571	**EW_M_25_av**	weak absorption	**egg white**	spectrum EW_av
2585	**EW_M_25_av**	weak absorption	**egg white**	spectrum EW_av
2589	**EW_M_50_av**	weak absorption	**egg white**	spectrum EW_av
2595	**EW_M_50_av**	weak absorption	**egg white**	spectrum EW_av
2690	**EW_M_25_av**	weak absorption	**egg white**	spectrum EW_av
2694	**EW_M_50_av**	weak absorption	**egg white**	spectrum EW_av
2930	**UN_IV_2**	(blank)	**(blank)**	(blank)
2934	**EW_M_25_av**	weak absorption	**CH stretching**	Spectrum EW_av, Daher et al, 2017, p. 8
	EW_M_50_av	weak absorption	**CH stretching**	Spectrum EW_av, Daher et al, 2017, p. 8
2940	**UN_IV_2**	(blank)	**(blank)**	(blank)
2943	**EW_M_50_av**	weak absorption	**CH3 stretching**	Spectrum EW_av, Iwanicka et al, 2017, p. 18
2961	**UN_IV_2**	(blank)	**(blank)**	(blank)
3078	**UN_IV_2**	(blank)	**(blank)**	(blank)
3083	**EW_M_25_av**	1st overtone	**amide I**	Spectrum EW_av, Rosi et al, 2009, p. 2099
3084	**EW_M_50_av**	1st overtone	**amide I**	Spectrum EW_av, Rosi et al, 2009, p. 2099
3086	**UN_IV_2**	(blank)	**(blank)**	(blank)
3094	**EW_M_50_av**	1st overtone	**amide I**	Spectrum EW_av, Rosi et al, 2009, p. 2099
3095	**EW_M_25_av**	1st overtone	**amide I**	Spectrum EW_av, Rosi et al, 2009, p. 2099
3099	**UN_IV_2**	(blank)	**(blank)**	(blank)
3112	**UN_IV_2**	(blank)	**(blank)**	(blank)
3123	**UN_IV_2**	(blank)	**(blank)**	(blank)
3304	**EW_M_25_av**	weak absorption	**N-H stretching**	Rosi et al, 2002, p. 2099

Figure 87: continued.

UN_IV_3

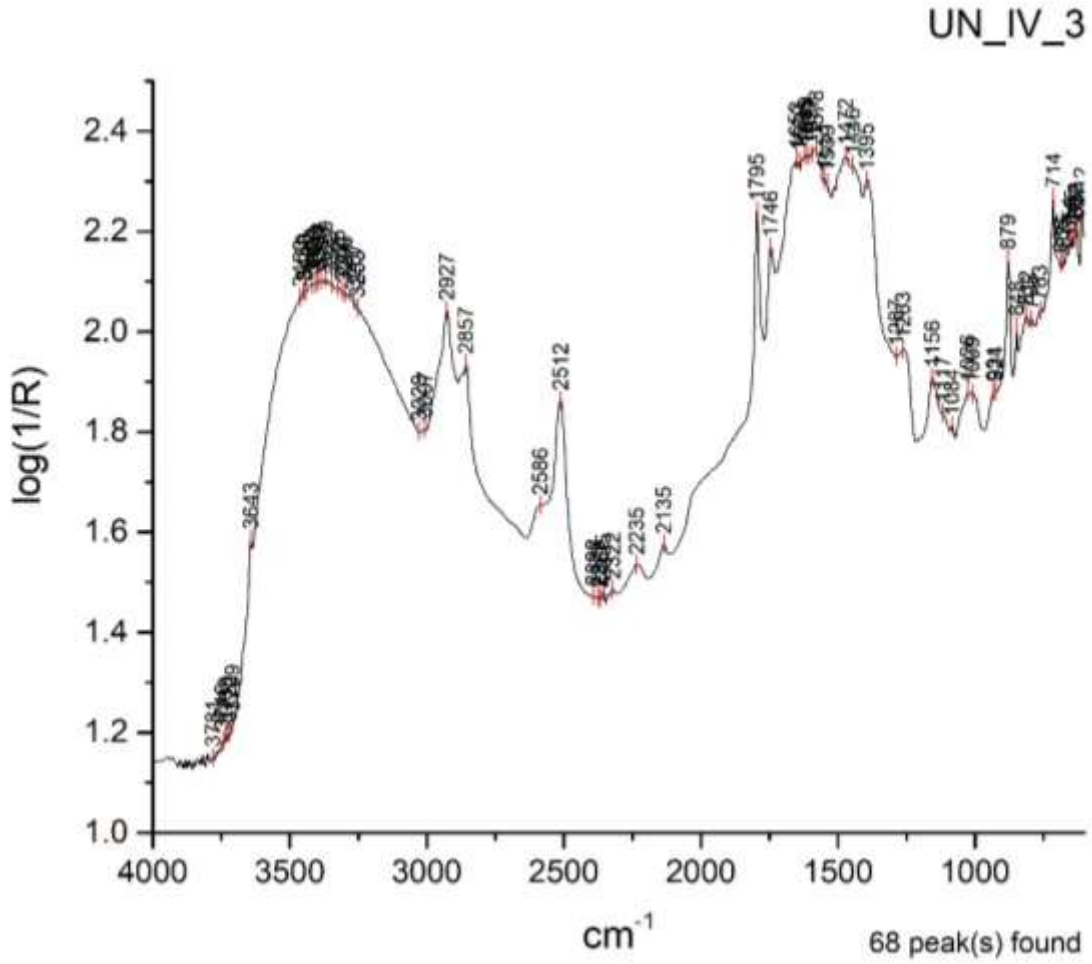

Figure 88: UN_IV_3 correctly identified as 50% rice additive in mortar (R_M_50).

Peak x (position)	Spectrum ID	Type of band	Chemical Band Assignement	Reference
612	UN_IV_3	(blank)	(blank)	(blank)
621	R_M_25_av	weak absorption	rice	Spectrum R_av
627	R_M_50_av	weak absorption	rice	Spectrum R_av
	UN_IV_3	(blank)	(blank)	(blank)
633	UN_IV_3	(blank)	(blank)	(blank)
645	UN_IV_3	(blank)	(blank)	(blank)
646	R_M_50_av	weak absorption	rice	Spectrum R_av
648	R_M_25_av	weak absorption	rice	Spectrum R_av
654	UN_IV_3	(blank)	(blank)	(blank)
659	R_M_25_av	weak absorption	rice	Spectrum R_av
675	UN_IV_3	(blank)	(blank)	(blank)
685	R_M_50_av	weak absorption	rice	Spectrum R_av
	UN_IV_3	(blank)	(blank)	(blank)
688	R_M_25_av	weak absorption	rice	Spectrum R_av
714	R_M_50_av	sharp absorption	v4 carbonate ion	Spectrum M_av, spectrum Ca_av, Ylmen and Jaglid, 2013, p. 119
	R_M_25_av	sharp absorption	v4 carbonate ion	Spectrum M_av, spectrum Ca_av, Ylmen and Jaglid, 2013, p. 119
	UN_IV_3	(blank)	(blank)	(blank)
763	UN_IV_3	(blank)	(blank)	(blank)
792	R_M_50_av	sharp absorption	quartz	Spectrum M_av, spectrum Q_av
793	R_M_25_av	sharp absorption	quartz	Spectrum M_av, spectrum Q_av
795	UN_IV_3	(blank)	(blank)	(blank)
812	UN_IV_3	(blank)	(blank)	(blank)
814	R_M_50_av	sharp absorption	quartz	Spectrum M_av, spectrum Q_av
816	R_M_25_av	sharp absorption	quartz	Spectrum M_av, spectrum Q_av
848	R_M_50_av	sharp and weak absorption	v2 carbonate ion	Spectrum M_av, spectrum Ca_av, Ylmen and Jaglid, 2013, p. 119
	R_M_25_av	sharp and weak absorption	v2 carbonate ion	Spectrum M_av, spectrum Ca_av, Ylmen and Jaglid, 2013, p. 119
	UN_IV_3	(blank)	(blank)	(blank)
879	UN_IV_3	(blank)	(blank)	(blank)
880	R_M_50_av	sharp absorption	v2 carbonate ion	Spectrum M_av, spectrum Ca_av, Ylmen and Jaglid, 2013, p. 119
	R_M_25_av	sharp absorption	v2 carbonate ion	Spectrum M_av, spectrum Ca_av, Ylmen and Jaglid, 2013, p. 119
924	R_M_50_av	overlapping	sugar region	Spectrum R_av, Synytsya and Novak, 2014, p. 6
	UN_IV_3	(blank)	(blank)	(blank)
931	UN_IV_3	(blank)	(blank)	(blank)
999	R_M_25_av	weak absorption	CaCO3	spectrum Ca_av
1001	R_M_50_av	strong absorption	rice	Spectrum R_av
1009	UN_IV_3	(blank)	(blank)	(blank)
1019	R_M_25_av	strong absorption	rice	Spectrum R_av
1026	UN_IV_3	(blank)	(blank)	(blank)
1080	R_M_25_av	sharp and weak absorption	v1 carbonate ion	Spectrum M_av, spectrum Ca_av, Ylmen and Jaglid, 2013, p. 119
1083	R_M_50_av	sharp and weak absorption	v1 carbonate ion	Spectrum M_av, spectrum Ca_av, Ylmen and Jaglid, 2013, p. 119
1084	UN_IV_3	(blank)	(blank)	(blank)
1117	UN_IV_3	(blank)	(blank)	(blank)
1156	UN_IV_3	(blank)	(blank)	(blank)
1158	R_M_50_av	sharp absorption	quartz	Spectrum M_av, spectrum Q_av
1159	R_M_25_av	sharp absorption	quartz	Spectrum M_av, spectrum Q_av

Figure 89: Filtered CPAD of peaks of interest for UN_IV_3 spectrum and possible matches.

1263	UN_IV_3	(blank)	(blank)	(blank)
1287	UN_IV_3	(blank)	(blank)	(blank)
1395	UN_IV_3	(blank)	(blank)	(blank)
1396	R_M_50_av	strong absorption	CaCO3	Spectrum M_av, spectrum Ca_av
1397	R_M_25_av	strong absorption	CaCO3	Spectrum M_av, spectrum Ca_av
1439	R_M_50_av	strong absorption	v3 antisymmetric stretching CO3-2	Spectrum M_av, spectrum Ca_av, Ylmen and Jaglid, 2013, p. 119
	R_M_25_av	strong absorption	v3 antisymmetric stretching CO3-2	Spectrum M_av, spectrum Ca_av, Ylmen and Jaglid, 2013, p. 119
1446	UN_IV_3	(blank)	(blank)	(blank)
1448	R_M_25_av	strong absorption	v3 antisymmetric stretching CO3-2	Spectrum M_av, spectrum Ca_av, Ylmen and Jaglid, 2013, p. 119
1449	R_M_50_av	strong absorption	v3 antisymmetric stretching CO3-2	Spectrum Ca_av, Ylmen and Jaglid, 2013, p. 119
1467	R_M_50_av	strong absorption	v3 antisymmetric stretching CO3-2	Spectrum Ca_av, Ylmen and Jaglid, 2013, p. 119
	R_M_25_av	strong absorption	v3 antisymmetric stretching CO3-2	Spectrum M_av, spectrum Ca_av, Ylmen and Jaglid, 2013, p. 119
1472	UN_IV_3	(blank)	(blank)	(blank)
1475	R_M_25_av	weak absorption	C-H bending	Spectrum R_av, Buti et al, 2013, p. 2705
1518	R_M_25_av	weak absorption	rice	Spectrum R_av
1535	R_M_25_av	weak absorption	rice	Spectrum R_av
1539	UN_IV_3	(blank)	(blank)	(blank)
1551	UN_IV_3	(blank)	(blank)	(blank)
1578	UN_IV_3	(blank)	(blank)	(blank)
1582	R_M_50_av	strong absorption	v3 antisymmetric stretching CO3-2	Spectrum Ca_av, Ylmen and Jaglid, 2013, p. 119
	R_M_25_av	strong absorption	v3 antisymmetric stretching CO3-2	Spectrum Ca_av, Ylmen and Jaglid, 2013, p. 119
1597	UN_IV_3	(blank)	(blank)	(blank)
1611	UN_IV_3	(blank)	(blank)	(blank)
1612	R_M_50_av	strong absorption	quartz	Spectrum M_av, spectrum Q_av
1619	UN_IV_3	(blank)	(blank)	(blank)
1620	R_M_50_av	strong absorption	quartz	Spectrum M_av, spectrum Q_av
1639	UN_IV_3	(blank)	(blank)	(blank)
1652	R_M_50_av	strong absorption	quartz	Spectrum M_av, spectrum Q_av
	R_M_25_av	strong absorption	quartz	Spectrum M_av, spectrum Q_av
	UN_IV_3	(blank)	(blank)	(blank)
1746	R_M_50_av	sharp absorption	rice	Spectrum R_av
	UN_IV_3	(blank)	(blank)	(blank)
1794	R_M_50_av	combination band	v1+v4	Spectrum M_av, spectrum Ca_av, Ricci et al, 2006, p. 1222
	R_M_25_av	combination band	v1+v4	Spectrum M_av, spectrum Ca_av, Ricci et al, 2006, p. 1222
1795	UN_IV_3	(blank)	(blank)	(blank)
1843	R_M_50_av	weak absorption	quartz	Spectrum M_av, spectrum Q_av
1844	R_M_25_av	weak absorption	quartz	Spectrum M_av, spectrum Q_av
1867	R_M_50_av	weak absorption	quartz	Spectrum M_av, spectrum Q_av
	R_M_25_av	weak absorption	quartz	Spectrum M_av, spectrum Q_av
1941	R_M_50_av	weak absorption	quartz	Spectrum M_av, spectrum Q_av
	R_M_25_av	weak absorption	quartz	Spectrum M_av, spectrum Q_av
1961	R_M_25_av	weak absorption	quartz	Spectrum M_av, spectrum Q_av

Figure 89: continued.

2135	**R_M_50_av**	weak absorption	**calcium carbonate and quartz**	Spectrum Ca_av, spectrum M_av, spectrum Q_av
	R_M_25_av	weak absorption	**calcium carbonate and quartz**	Spectrum Ca_av, spectrum M_av, spectrum Q_av
	UN_IV_3	(blank)	**(blank)**	(blank)
2235	**UN_IV_3**	(blank)	**(blank)**	(blank)
2237	**R_M_50_av**	weak absorption	**quartz**	spectrum Q_av
2238	**R_M_25_av**	weak absorption	**quartz**	spectrum Q_av
2512	**R_M_50_av**	combination band	**v1+v3**	Spectrum M_av, spectrum Ca_av, Ricci et al, 2006, p. 1222
	R_M_25_av	combination band	**v1+v3**	Spectrum M_av, spectrum Ca_av, Ricci et al, 2006, p. 1222
	UN_IV_3	(blank)	**(blank)**	(blank)
2586	**R_M_50_av**	weak absorption	**CaCO3**	(blank)
	UN_IV_3	(blank)	**(blank)**	(blank)
2688	**R_M_25_av**	weak absorption	**(blank)**	(blank)
2697	**R_M_25_av**	weak absorption	**(blank)**	(blank)
2709	**R_M_25_av**	weak absorption	**rice**	Spectrum R_av
2857	**R_M_50_av**	strong absorption	**CH stretching**	Spectrum E_av, Daher et al, 2017, p.8
	R_M_25_av	strong absorption	**CH stretching**	Spectrum E_av, Daher et al, 2017, p.8
	UN_IV_3	(blank)	**(blank)**	(blank)
2872	**R_M_50_av**	sharp and weak absorption	**CaCO3**	Spectrum Ca_av, spectrum M_av
2873	**R_M_25_av**	sharp and weak absorption	**CaCO3**	Spectrum Ca_av, spectrum M_av
2926	**R_M_25_av**	strong absorption	**CH stretching**	Spectrum E_av, Daher et al, 2017, p.8
2927	**R_M_50_av**	strong absorption	**CH stretching**	Spectrum E_av, Daher et al, 2017, p.8
	UN_IV_3	(blank)	**(blank)**	(blank)
3007	**UN_IV_3**	(blank)	**(blank)**	(blank)
3008	**R_M_50_av**	weak absorption	**CH stretching**	Miliani et al, 2012, p. 302
3009	**R_M_25_av**	weak absorption	**CH stretching**	Miliani et al, 2012, p. 302
3029	**UN_IV_3**	(blank)	**(blank)**	(blank)
3565	**R_M_25_av**	weak absorption	**quartz**	Spectrum M_av, spectrum Q_av
3643	**R_M_50_av**	doublet	**OH stretching**	Spectrum M_av, spectrum Ca_av, Rosi et al, 2009, p. 2100
	R_M_25_av	doublet	**OH stretching**	Spectrum M_av, spectrum Ca_av, Rosi et al, 2009, p. 2100

Figure 89: continued.

UN_IV_4

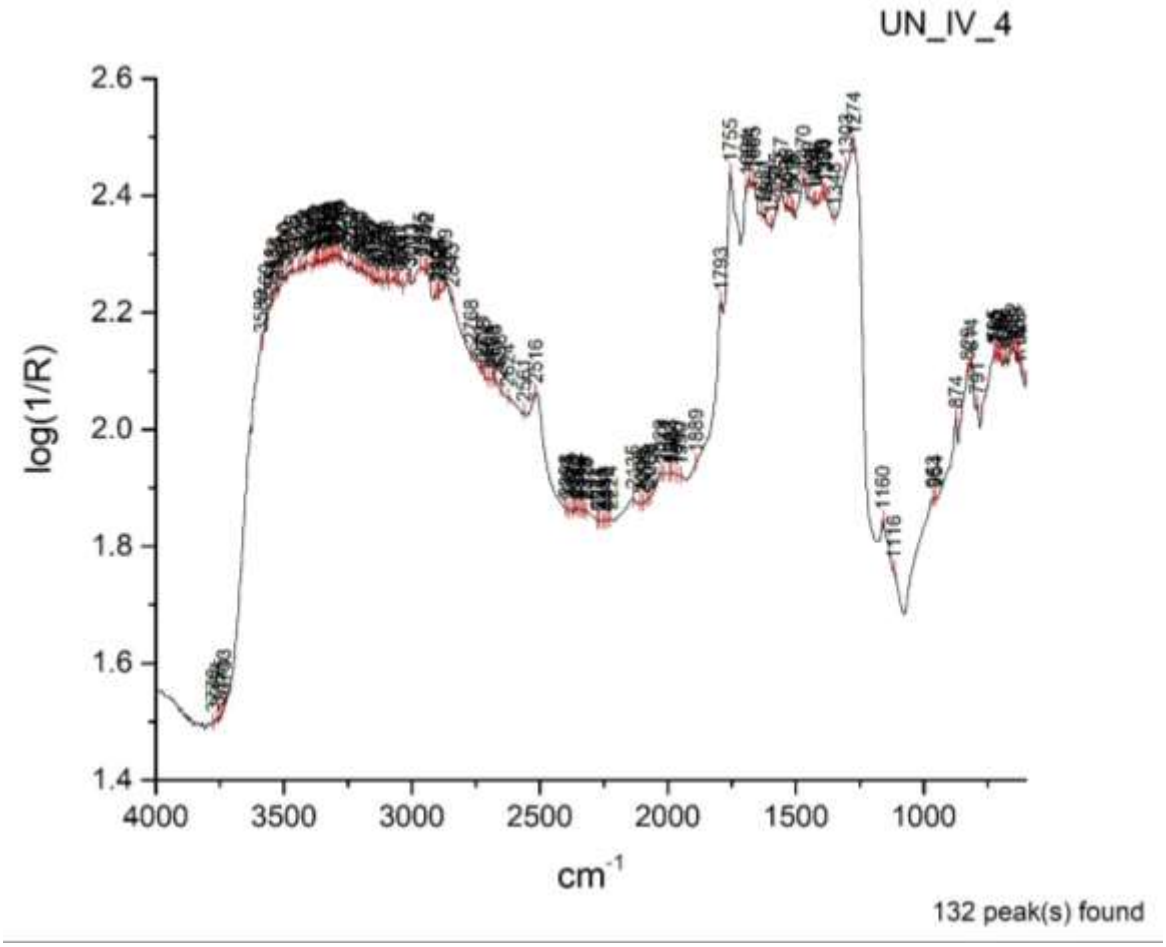

Figure 90: UN_IV_4 correctly identified as 50% egg yolk additive in mortar (EY_M_50).

Peak x (position)	Spectrum ID	Type of band	Chemical Band Assignement	Reference
660	E_M_50_av	weak absorption	(blank)	Spectrum E_av, Spectrum EW_av, spectrum EY_av
668	E_M_75_av	weak absorption	(blank)	Spectrum E_av, Spectrum EW_av, spectrum EY_av
743	E_M_50_av	weak absorption	whole egg	Spectrum E_av
954	UN_IV_4	(blank)	(blank)	(blank)
963	UN_IV_4	(blank)	(blank)	(blank)
970	E_M_50_av	weak absorption	PO4-3 anion stretching	Spectrum E_av, Ricci et al. 2006, p. 1223
1265	E_M_50_av	strong absorption	C-O	Spectrum E_av, Ploeger et al, 2010, p. 17
1274	E_M_75_av	strong absorption	C-O	Spectrum E_av, Spectrum Ca_av, Ploeger et al, 2010, p. 17
	UN_IV_4	(blank)	(blank)	(blank)
1281	EY_M_50_av	strong absorption	egg yolk	spectrum EY_av
1282	E_M_75_av	strong absorption	C-O	Spectrum E_av, Spectrum Ca_av, Ploeger et al, 2010, p. 17
1301	EY_M_50_av	strong absorption	CH2, CH3	Lombardi and Santarelli, 2009, p. 542
1303	E_M_50_av	weak absorption	whole egg	Spectrum E_av
	UN_IV_4	(blank)	(blank)	(blank)
1310	EY_M_50_av	strong absorption	CH2, CH3	Lombardi and Santarelli, 2009, p. 542
1313	E_M_50_av	weak absorption	whole egg	Spectrum E_av
1315	E_M_75_av	weak absorption	whole egg	Spectrum E_av
1348	UN_IV_4	(blank)	(blank)	(blank)
1381	EY_M_50_av	strong absorption	C-H bending	Spectrum EY_av, Buti et al, 2013, p. 2705
1384	UN_IV_4	(blank)	(blank)	(blank)
1390	UN_IV_4	(blank)	(blank)	(blank)
1396	UN_IV_4	(blank)	(blank)	(blank)
1420	EY_M_50_av	weak absorption	egg yolk	spectrum EY_av
1421	UN_IV_4	(blank)	(blank)	(blank)
1431	UN_IV_4	(blank)	(blank)	(blank)
1433	E_M_50_av	strong absorption	C-O bending	Spectrum E_av, Spectrum Ca_av, Ricci et al, 2006, p. 1223
1448	EY_M_50_av	weak absorption	egg yolk	spectrum EY_av
1449	UN_IV_4	(blank)	(blank)	(blank)
1468	E_M_50_av	strong absorption	C-O bending	Spectrum E_av, Spectrum Ca_av, Ricci et al, 2006, p. 1223
	E_M_75_av	strong absorption	C-O bending	Spectrum E_av, Spectrum Ca_av, Ricci et al, 2006, p. 1223
1470	EY_M_50_av	strong absorption	C-O bending	Spectrum EY_av, Ricci et al, 2006, p. 1224
	UN_IV_4	(blank)	(blank)	(blank)
1508	EY_M_50_av	weak absorption	C=O	Spectrum EY_av, Rosi et al, 2009, p. 2095
	UN_IV_4	(blank)	(blank)	(blank)
1518	EY_M_50_av	weak absorption	C=O	Spectrum EY_av, Rosi et al, 2009, p. 2096
	UN_IV_4	(blank)	(blank)	(blank)
1529	EY_M_50_av	weak absorption	C=O	Spectrum EY_av, Rosi et al, 2009, p. 2097
1535	UN_IV_4	(blank)	(blank)	(blank)
1538	EY_M_50_av	weak absorption	C=O	Spectrum EY_av, Rosi et al, 2009, p. 2098
1555	E_M_75_av	strong absorption	N-H bands, amide I, II	Spectrum E_av, Miliani et al, 2012, p. 304
1557	UN_IV_4	(blank)	(blank)	(blank)
1560	EY_M_50_av	weak absorption	C=O	Spectrum EY_av, Rosi et al, 2009, p. 2099
1561	E_M_50_av	strong absorption	N-H bands, amide I, II	Spectrum E_av, Miliani et al, 2012, p. 304
1575	UN_IV_4	(blank)	(blank)	(blank)
1596	UN_IV_4	(blank)	(blank)	(blank)
1617	UN_IV_4	(blank)	(blank)	(blank)
1631	UN_IV_4	(blank)	(blank)	(blank)
1665	UN_IV_4	(blank)	(blank)	(blank)

Figure 91: Filtered CPAD of peaks of interest for UN_IV_4 spectrum and possible matches.

1680	E_M_50_av	strong absorption	N-H bands, amide I, II	Spectrum E_av, Miliani et al, 2012, p. 304
1681	UN_IV_4	(blank)	(blank)	(blank)
1682	EY_M_50_av	strong absorption	C=O	Spectrum EY_av, Rosi et al, 2009, p. 2099
1686	E_M_50_av	strong absorption	N-H bands, amide I, II	Spectrum E_av, Miliani et al, 2012, p. 304
	E_M_75_av	strong absorption	N-H bands, amide I, II	Spectrum E_av, Miliani et al, 2012, p. 304
1690	EY_M_50_av	strong absorption	C=O	Spectrum EY_av, Rosi et al, 2009, p. 2099
1691	UN_IV_4	(blank)	(blank)	(blank)
1732	EY_M_50_av	weak absorption	C=O stretching band	Spectrum EY_av, Ploeger et al, 2010, p, 37
1747	E_M_50_av	strong absorption	C-H stretching bands, esters	Spectrum E_av, Mazzeo et al, 2008, p. 69
1751	E_M_75_av	strong absorption	C-H stretching bands, esters	Spectrum E_av, Mazzeo et al, 2008, p. 69
1755	EY_M_50_av	1st order derivative	C=O stretching band	Spectrum EY_av, Ploeger et al, 2010, p, 37
	UN_IV_4	(blank)	(blank)	(blank)
2189	EY_M_50_av	weak absorption	egg yolk	spectrum EY_av
2768	UN_IV_4	(blank)	(blank)	(blank)
2843	UN_IV_4	(blank)	(blank)	(blank)
2856	E_M_50_av	strong absorption	CH stretching	Spectrum E_av, Daher et al, 2017, p.8
2857	E_M_75_av	strong absorption	CH stretching	Spectrum E_av, Daher et al, 2017, p.8
2858	EY_M_50_av	strong absorption	C-H stretching bands, esters	Spectrum EY_av, Rosi et al, 2009, p. 2099
2869	UN_IV_4	(blank)	(blank)	(blank)
2891	UN_IV_4	(blank)	(blank)	(blank)
2898	UN_IV_4	(blank)	(blank)	(blank)
2906	UN_IV_4	(blank)	(blank)	(blank)
2908	EY_M_50_av	strong absorption	C-H stretching bands, esters	Spectrum EY_av, Rosi et al, 2009, p. 2099
2930	E_M_50_av	strong absorption	CH stretching	Spectrum E_av, Daher et al, 2017, p.8
2936	EY_M_50_av	strong absorption	CH stretching	Spectrum EY_av, Daher et al, 2017, p.8
2937	E_M_75_av	strong absorption	CH stretching	Spectrum E_av, Daher et al, 2017, p.8
2942	UN_IV_4	(blank)	(blank)	(blank)
2950	UN_IV_4	(blank)	(blank)	(blank)
2959	E_M_50_av	weak absorption	CH2 stretching	Spectrum E_av, Ploeger et al, 2010, p. 37
	E_M_75_av	weak absorption	CH2 stretching	Spectrum E_av, Ploeger et al, 2010, p. 37
	EY_M_50_av	strong absorption	C-H stretching bands, esters	Spectrum EY_av, Rosi et al, 2009, p. 2099
2965	UN_IV_4	(blank)	(blank)	(blank)
3003	UN_IV_4	(blank)	(blank)	(blank)
3004	EY_M_50_av	weak absorption	CH stretching	Miliani et al, 2012, p. 302
3005	E_M_50_av	weak absorption	(blank)	(blank)
3006	E_M_75_av	weak absorption	(blank)	(blank)
3011	UN_IV_4	(blank)	(blank)	(blank)
3034	UN_IV_4	(blank)	(blank)	(blank)
3051	UN_IV_4	(blank)	(blank)	(blank)
3061	UN_IV_4	(blank)	(blank)	(blank)
3071	E_M_50_av	weak absorption	2δNH	Spectrum E_av, Rosi et al, 2010, p. 621
	UN_IV_4	(blank)	(blank)	(blank)
3080	E_M_75_av	weak absorption	2δNH	Spectrum E_av, Rosi et al, 2010, p. 621
3084	E_M_50_av	weak absorption	2δNH	Spectrum E_av, Rosi et al, 2010, p. 621
3089	UN_IV_4	(blank)	(blank)	(blank)
3098	E_M_75_av	weak absorption	2δNH	Spectrum E_av, Rosi et al, 2010, p. 621
	UN_IV_4	(blank)	(blank)	(blank)
3106	E_M_50_av	weak absorption	2δNH	Spectrum E_av, Rosi et al, 2010, p. 621
3108	E_M_75_av	weak absorption	2δNH	Spectrum E_av, Rosi et al, 2010, p. 621

Figure 91: continued.

UN_IV_5

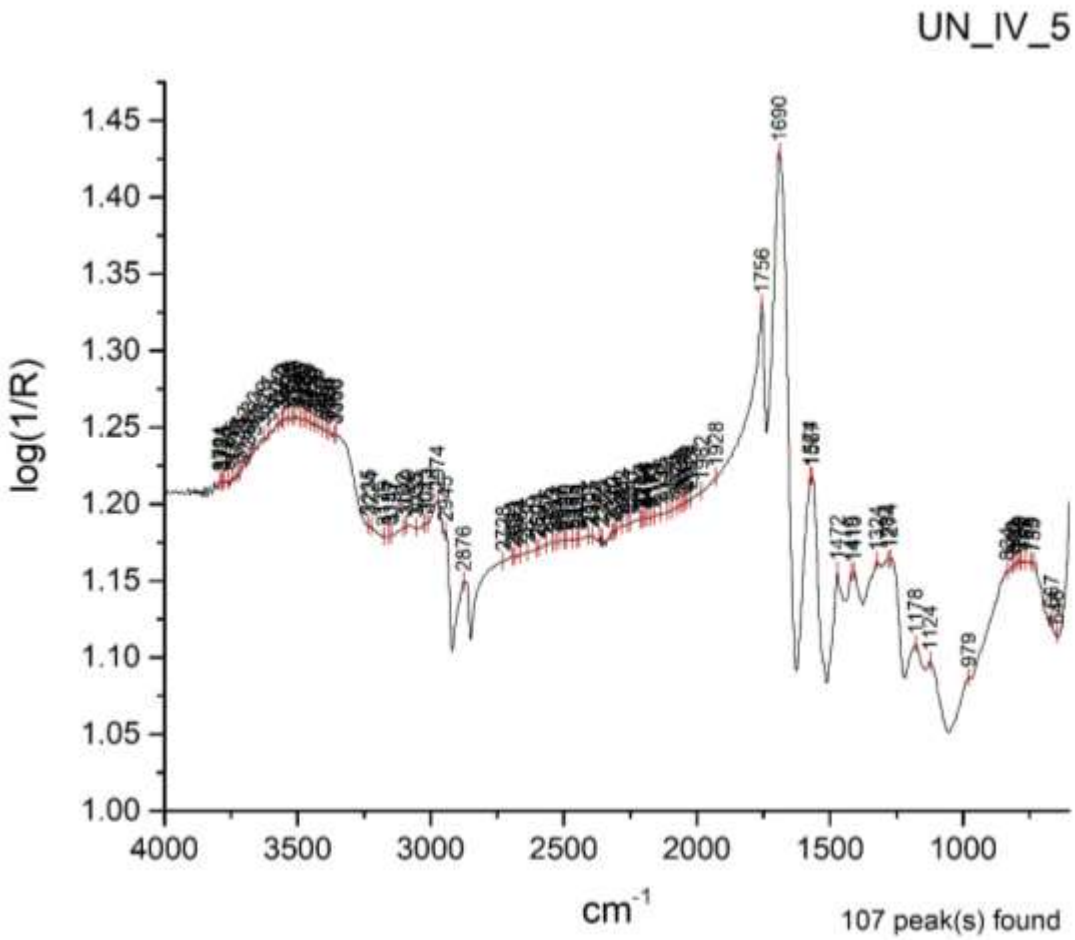

Figure 92: UN_IV_5 correctly identified as egg standard (E_av).

Peak x (position)	Spectrum ID	Type of band	Chemical Band Assignement	Reference
648	UN_IV_5	(blank)	(blank)	(blank)
667	EY_av	sharp and weak absorption	(blank)	(blank)
	Mi_av	weak absorption	(blank)	(blank)
	UN_IV_5	(blank)	(blank)	(blank)
668	E_av	sharp and weak absorption	(blank)	spectrum EY_av, spectrum EW_av
710	EY_av	weak absorption	(blank)	(blank)
729	Mi_av	weak absorption	(blank)	(blank)
734	E_av	weak absorption	(blank)	(blank)
735	UN_IV_5	(blank)	(blank)	(blank)
744	EY_av	weak absorption	(blank)	(blank)
745	E_av	weak absorption	(blank)	spectrum EY_av
	UN_IV_5	(blank)	(blank)	(blank)
765	E_av	weak absorption	(blank)	spectrum EY_av
	UN_IV_5	(blank)	(blank)	(blank)
770	EY_av	(blank)	(blank)	(blank)
781	EY_av	(blank)	(blank)	(blank)
782	UN_IV_5	(blank)	(blank)	(blank)
789	EY_av	(blank)	(blank)	(blank)
	UN_IV_5	(blank)	(blank)	(blank)
794	E_av	weak absorption	(blank)	spectrum EY_av
802	E_av	weak absorption	(blank)	spectrum EY_av
	Mi_av	strong absorption	(blank)	(blank)
	UN_IV_5	(blank)	(blank)	(blank)
808	EY_av	(blank)	(blank)	(blank)
813	UN_IV_5	(blank)	(blank)	(blank)
819	EY_av	(blank)	(blank)	(blank)
834	UN_IV_5	(blank)	(blank)	(blank)
835	E_av	weak absorption	(blank)	(blank)
907	Mi_av	strong absorption	PO4-3anion stretching	Ricci et al, 2006, p. 1223
973	E_av	weak absorption	PO4-3anion stretching	Ricci et al, 2006, p. 1223, spectrum EY_av
974	EY_av	sharp and weak absorption	PO4-3anion stretching	Ricci et al, 2006, p. 1223
979	UN_IV_5	(blank)	(blank)	(blank)
982	Mi_av	sharp absorption	sugar region	Synytsya and Novak, 2014, p.6
1054	Mi_av	sharp absorption	sugar region	Synytsya and Novak, 2014, p.6
1070	EY_av	reststrahlen	PO4-3anion stretching	Ricci et al, 2006, p. 1223
1123	E_av	weak absorption	PO4-3anion stretching	Ricci et al, 2006, p. 1223, spectrum EY_av
1124	EY_av	sharp and weak absorption	PO4-3anion stretching	Ricci et al, 2006, p. 1223
	UN_IV_5	(blank)	(blank)	(blank)
1125	Mi_av	sharp and weak absorption	sugar region	Synytsya and Novak, 2014, p.6
1177	E_av	weak absorption	v(C-O) stretching	Ricci et al, 2006, p. 1224, spectrum EW_av
1178	UN_IV_5	(blank)	(blank)	(blank)
1182	Mi_av	strong absorption	sugar region	Synytsya and Novak, 2014, p.6
1198	EY_av	weak absorption	(blank)	(blank)
1268	E_av	strong absorption	C-O	Ploeger et al, 2010, p. 37, spectrum EY_av
1270	EY_av	strong absorption	(blank)	(blank)
	Mi_av	strong absorption	(blank)	(blank)
1274	UN_IV_5	(blank)	(blank)	(blank)

Figure 93: Filtered CPAD of peaks of interest for UN_IV_5 spectrum and possible matches.

1283	**EY_av**	sharp absorption	**(blank)**	(blank)
1284	**UN_IV_5**	(blank)	**(blank)**	(blank)
1323	**Mi_av**	weak absorption	**(blank)**	(blank)
1324	**E_av**	(blank)	**(blank)**	spectrum EW_av
	UN_IV_5	(blank)	**(blank)**	(blank)
1385	**EY_av**	sharp absorption	**C-H bending**	Buti et al, 2013, p. 2705
	Mi_av	weak absorption	**C-H bending**	Buti et al, 2013, p. 2705
1403	**Mi_av**	weak absorption	**(blank)**	(blank)
1410	**UN_IV_5**	(blank)	**(blank)**	(blank)
1411	**E_av**	(blank)	**(blank)**	spectrum EW_av
1419	**UN_IV_5**	(blank)	**(blank)**	(blank)
1420	**EY_av**	weak absorption	**(blank)**	(blank)
1422	**Mi_av**	weak absorption	**(blank)**	(blank)
1445	**E_av**	weak absorption	**Amide III**	Buti et al, 2013, p. 2705, spectrum EW_av
	EY_av	weak absorption	**(blank)**	(blank)
1472	**E_av**	sharp absorption	**C-O bending**	Ricci et al, 2006, p. 1223, spectrum EW_av and EY_av
	EY_av	sharp absorption	**C-O bending**	Ricci et al, 2006, p. 1223
	UN_IV_5	(blank)	**(blank)**	(blank)
1473	**Mi_av**	sharp absorption	**Amide III**	Rosi et al, 2009, p. 2099
1507	**EY_av**	weak absorption	**C=O**	Rosi et al, 2009, p. 2099
1519	**EY_av**	weak absorption	**C=O**	Rosi et al, 2009, p. 2099
1522	**Mi_av**	weak absorption	**(blank)**	(blank)
1559	**EY_av**	strong absorption	**C=O**	Rosi et al, 2009, p. 2099
1567	**UN_IV_5**	(blank)	**(blank)**	(blank)
1568	**E_av**	strong absorption	**N-H bands, amide I, II**	Miliani et al, 2012, p. 304, spectrum EW_av
1572	**Mi_av**	strong absorption	**N-H bands**	Miliani et al, 2012, p.304, Rosi et al, 2009, p. 2104
1574	**UN_IV_5**	(blank)	**(blank)**	(blank)
1667	**EY_av**	strong absorption	**C=O**	(blank)
1690	**Mi_av**	strong absorption	**N-H bands**	Rosi et al, 2009, p. 2104
	UN_IV_5	(blank)	**(blank)**	(blank)
1693	**E_av**	strong absorption	**N-H bands, amide I, II**	Miliani et al, 2012, p. 304, spectrum EW_av
1755	**E_av**	strong absorption	**C=O stretching band, esters**	Mazzeo et al, 2008, p. 69, spectrum EY_av
	Mi_av	strong absorption	**C=O stretching band, esters**	Ricci et al, 2006, p. 1223
1756	**UN_IV_5**	(blank)	**(blank)**	(blank)
1758	**EY_av**	stretching band	**esters**	Mazzeo et al, 2008, p. 69
1841	**Mi_av**	weak absorption	**(blank)**	(blank)
1854	**Mi_av**	weak absorption	**C-O**	Ploeger et al, 2010, p. 37
1972	**Mi_av**	weak absorption	**(blank)**	(blank)
2083	**Mi_av**	weak absorption	**(blank)**	(blank)
2197	**Mi_av**	weak absorption	**(blank)**	(blank)
2431	**Mi_av**	weak absorption	**(blank)**	(blank)
2530	**Mi_av**	weak absorption	**(blank)**	(blank)

Figure 93: continued.

2546	**Mi_av**	weak absorption	**(blank)**	(blank)
2640	**Mi_av**	(blank)	**(blank)**	(blank)
2647	**Mi_av**	(blank)	**(blank)**	(blank)
2655	**Mi_av**	(blank)	**(blank)**	(blank)
2664	**Mi_av**	(blank)	**(blank)**	(blank)
2860	**Mi_av**	sharp absorption	**C=O stretching band**	Rosi et al, 2009, p. 2099
2864	**E_av**	strong absorption	**C-H stretching**	Rosi et al, 2009, p. 2099, spectrum EY_av
	EY_av	strong absorption	**C-H stretching**	Rosi et al, 2009, p. 2099
2876	**E_av**	strong absorption	**C-H stretching**	Rosi et al, 2009, p. 2099, spectrum EY_av
	UN_IV_5	(blank)	**(blank)**	(blank)
2938	**Mi_av**	strong absorption	**CH stretching**	Daher et al, 2017, p.8
2942	**E_av**	strong absorption	**C-H stretching bands, esters**	Spectrum EY_av, Rosi et al, 2009, p. 2099
	EY_av	sharp absorption	**C-H stretching**	Rosi et al, 2009, p. 2099
2945	**UN_IV_5**	(blank)	**(blank)**	(blank)
2967	**EY_av**	sharp absorption	**C-H stretching**	Rosi et al, 2009, p. 2099
	Mi_av	sharp absorption	**CH2 stretching**	Ploeger et al, 2010, p. 37
2973	**E_av**	strong absorption	**C-H stretching bands, esters**	Spectrum EY_av, Rosi et al, 2009, p. 2099
2974	**UN_IV_5**	(blank)	**(blank)**	(blank)
3013	**UN_IV_5**	(blank)	**(blank)**	(blank)
3015	**EY_av**	weak absorption	**CH stretching**	Miliani et al, 2012, p. 302
3025	**UN_IV_5**	(blank)	**(blank)**	(blank)
3045	**E_av**	weak absorption	**2δNH**	Rosi et al, 2010, p. 621
3055	**UN_IV_5**	(blank)	**(blank)**	(blank)
3075	**E_av**	weak absorption	**2δNH**	Rosi et al, 2010, p. 621
3089	**E_av**	weak absorption	**2δNH**	Rosi et al, 2010, p. 621
	UN_IV_5	(blank)	**(blank)**	(blank)
3102	**E_av**	weak absorption	**2δNH**	Rosi et al, 2010, p. 621
	UN_IV_5	(blank)	**(blank)**	(blank)
3147	**UN_IV_5**	(blank)	**(blank)**	(blank)
3157	**UN_IV_5**	(blank)	**(blank)**	(blank)
3176	**UN_IV_5**	(blank)	**(blank)**	(blank)
3224	**E_av**	(blank)	**(blank)**	(blank)
	UN_IV_5	(blank)	**(blank)**	(blank)
3235	**UN_IV_5**	(blank)	**(blank)**	(blank)
3240	**E_av**	(blank)	**(blank)**	(blank)

Figure 93: continued.

UN_IV_7

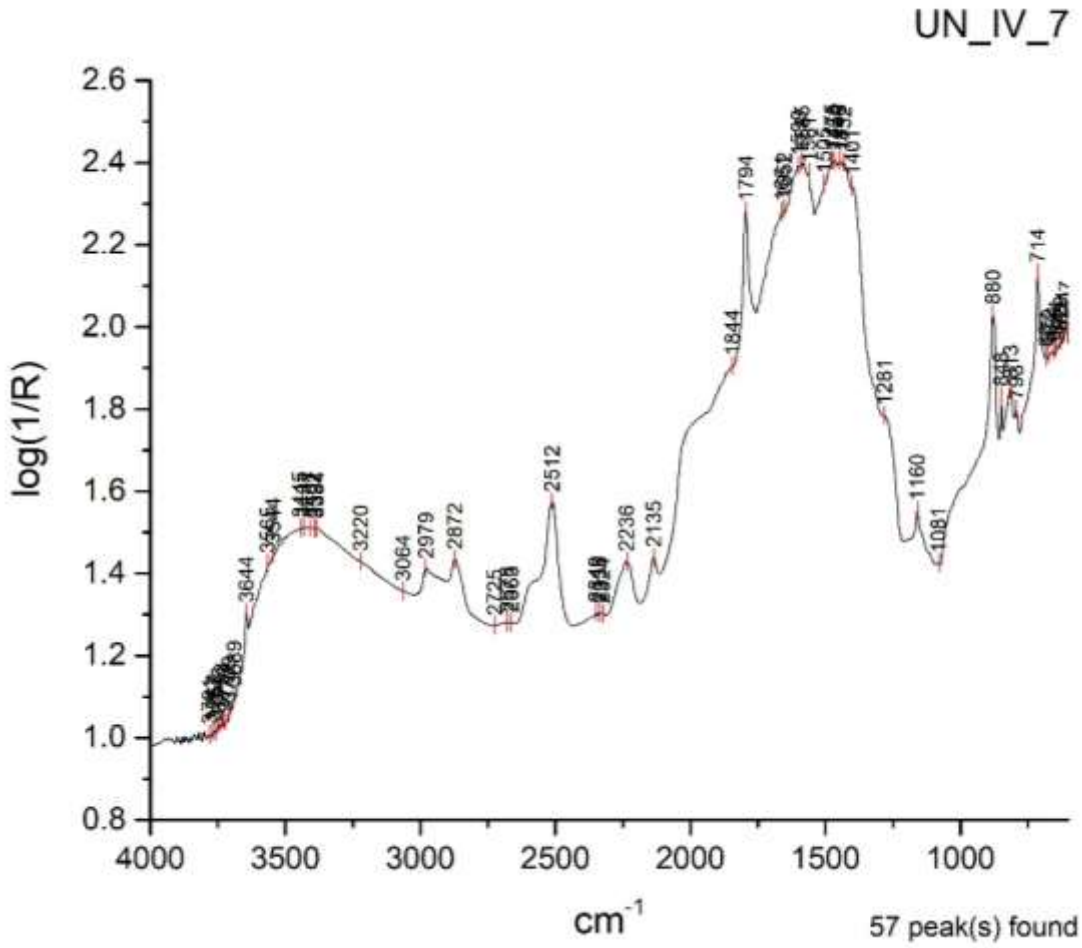

Figure 94: UN_IV_7 falsely identified as 5% egg white additive in mortar (EW_M_5) instead of the correct mortar standard (M_av).

Peak x (position)	Spectrum ID	Type of band	Chemical Band Assignement	Reference
607	EW_M_5_av	weak absorption	CaCO3	spectrum Ca_av
	UN_IV_7	(blank)	(blank)	(blank)
621	UN_IV_7	(blank)	(blank)	(blank)
629	UN_IV_7	(blank)	(blank)	(blank)
644	UN_IV_7	(blank)	(blank)	(blank)
654	UN_IV_7	(blank)	(blank)	(blank)
672	UN_IV_7	(blank)	(blank)	(blank)
682	UN_IV_7	(blank)	(blank)	(blank)
701	EW_M_5_av	weak absorption	quartz	spectrum Q_av
702	M_av	sharp and strong absorption	quartz	spectrum Q_av
713	M_av	sharp and strong absorption	v4 carbonate ion	Ylmen and Jaglid, 2013, p. 119, spectrum Ca_av
714	EW_M_5_av	sharp absorption	v4 carbonate ion	Spectrum Ca_av, spectrum M_av, Ylmen and Jaglid, 2013, p. 119
	UN_IV_7	(blank)	(blank)	(blank)
791	M_av	sharp absorption	quartz	spectrum Q_av
792	EW_M_5_av	sharp and weak absorption	quartz	Spectrum Q_av, spectrum M_av
793	UN_IV_7	(blank)	(blank)	(blank)
813	UN_IV_7	(blank)	(blank)	(blank)
815	M_av	sharp and strong absorption	quartz	spectrum Q_av
816	EW_M_5_av	sharp absorption	quartz	Spectrum Q_av, spectrum M_av
848	M_av	weak absorption	v2 carbonate ion	Ylmen and Jaglid, 2013, p. 119, spectrum Ca_av
	EW_M_5_av	weak absorption	v2 carbonate ion	Spectrum Ca_av, spectrum M_av, Ylmen and Jaglid, 2013, p. 119
	UN_IV_7	(blank)	(blank)	(blank)
873	M_av	sharp absorption	v2 carbonate ion	Ylmen and Jaglid, 2013, p. 119, spectrum Ca_av
880	UN_IV_7	(blank)	(blank)	(blank)
881	EW_M_5_av	sharp absorption	v2 carbonate ion	Spectrum Ca_av, spectrum M_av, Ylmen and Jaglid, 2013, p. 119
1081	UN_IV_7	(blank)	(blank)	(blank)
1086	EW_M_5_av	weak absorption	egg white	spectrum EW_av
1159	M_av	sharp absorption	quartz	spectrum Q_av
	EW_M_5_av	sharp absorption	quartz	Spectrum Q_av, spectrum M_av
1160	UN_IV_7	(blank)	(blank)	(blank)
1281	UN_IV_7	(blank)	(blank)	(blank)
1395	EW_M_5_av	weak absorption	CaCO3	Spectrum Ca_av, spectrum M_av
1401	M_av	strong absorption	calcium carbonate	spectrum Ca_av
	UN_IV_7	(blank)	(blank)	(blank)
1420	M_av	strong absorption	v3 antisymmetric stretching CO3-2	Ylmen and Jaglid, 2013, p. 119, spectrum Ca_av
1431	M_av	strong absorption	v3 antisymmetric stretching CO3-2	Ylmen and Jaglid, 2013, p. 119, spectrum Ca_av
1432	UN_IV_7	(blank)	(blank)	(blank)
1443	EW_M_5_av	weak absorption	v3 antisymmetric stretching CO3-2	Spectrum M_av, Ylmen and Jaglid, 2013, p. 119
1448	UN_IV_7	(blank)	(blank)	(blank)
1452	EW_M_5_av	weak absorption	v3 antisymmetric stretching CO3-2	Spectrum M_av, Ylmen and Jaglid, 2013, p. 119
1466	UN_IV_7	(blank)	(blank)	(blank)
1467	EW_M_5_av	weak absorption	v3 antisymmetric stretching CO3-2	Spectrum M_av, Ylmen and Jaglid, 2013, p. 119
1475	UN_IV_7	(blank)	(blank)	(blank)
1505	UN_IV_7	(blank)	(blank)	(blank)
1561	EW_M_5_av	weak absorption	quartz	spectrum Q_av
	UN_IV_7	(blank)	(blank)	(blank)

Figure 95: Filtered CPAD of peaks of interest for UN_IV_7 spectrum and possible matches.

1578	**M_av**	strong absorption	**v3 antisymmetric stretching CO3-2**	Ylmen and Jaglid, 2013, p. 119, spectrum Ca_av
1579	**EW_M_5_av**	strong absorption	**C-N-H bending amide II, N-H bands**	Spectrum EW_av, Rosi et al, 2009, p. 2104
1585	**UN_IV_7**	(blank)	**(blank)**	(blank)
1596	**M_av**	strong absorption	**quartz**	spectrum Q_av
1599	**UN_IV_7**	(blank)	**(blank)**	(blank)
1601	**EW_M_5_av**	weak absorption	**N-H bands**	Miliani et al, 2012, p. 304; Rosi et al, 2009, p. 2104
1630	**EW_M_5_av**	weak absorption	**N-H bands**	Miliani et al, 2012, p. 304; Rosi et al, 2009, p. 2104
1652	**M_av**	weak absorption	**quartz**	spectrum Q_av
	UN_IV_7	(blank)	**(blank)**	(blank)
1660	**EW_M_5_av**	strong absorption	**quartz**	Spectrum M_av
1661	**M_av**	weak absorption	**quartz**	spectrum Q_av
	UN_IV_7	(blank)	**(blank)**	(blank)
1683	**M_av**	weak absorption	**quartz**	spectrum Q_av
1794	**M_av**	combination band	**v1+v4**	Ricci et al, 2006, p. 1222, spectrum Ca_av
	UN_IV_7	(blank)	**(blank)**	(blank)
1795	**EW_M_5_av**	combination band	**v1+v4**	Spectrum Ca_av, spectrum M_av, Ricci et al, 2006, p. 1222
1844	**M_av**	weak absorption	**quartz**	spectrum Q_av
	UN_IV_7	(blank)	**(blank)**	(blank)
1859	**EW_M_5_av**	weak absorption	**quartz**	spectrum Q_av
1867	**EW_M_5_av**	weak absorption	**quartz**	spectrum Q_av
1868	**M_av**	weak absorption	**quartz**	spectrum Q_av
1941	**EW_M_5_av**	weak absorption	**quartz**	spectrum Q_av
1942	**M_av**	weak absorption	**quartz**	spectrum Q_av
1967	**M_av**	weak absorption	**quartz**	spectrum Q_av
	EW_M_5_av	weak absorption	**quartz**	spectrum Q_av
1991	**M_av**	weak absorption	**v+δ Si-O**	Miliani et al, 2012, p. 303, spectrum Q_av
2135	**M_av**	sharp absorption	**calcium carbonate and quartz**	spectrum Q_av and spectrum Ca_av
	EW_M_5_av	weak absorption	**calcium carbonate and quartz**	Spectrum Ca_av, spectrum M_av, spectrum Q_av
	UN_IV_7	(blank)	**(blank)**	(blank)
2236	**UN_IV_7**	(blank)	**(blank)**	(blank)
2238	**M_av**	sharp absorption	**quartz**	spectrum Q_av
	EW_M_5_av	weak absorption	**quartz**	spectrum Q_av
2512	**M_av**	combination band	**v1+v3**	Ricci et al, 2006, p. 1222, spectrum Ca_av
	EW_M_5_av	combination band	**v1+v3**	Spectrum Ca_av, spectrum M_av, Ricci et al, 2006, p. 1222
	UN_IV_7	(blank)	**(blank)**	(blank)
2663	**M_av**	weak absorption	**(blank)**	spectrum Ca_av
	UN_IV_7	(blank)	**(blank)**	(blank)
2676	**M_av**	weak absorption	**(blank)**	spectrum Ca_av
2678	**UN_IV_7**	(blank)	**(blank)**	(blank)
2703	**EW_M_5_av**	weak absorption	**egg white**	spectrum EW_av
2725	**UN_IV_7**	(blank)	**(blank)**	(blank)

Figure 95: continued.

2872	**M_av**	(blank)	**calcium carbonate**	spectrum Ca_av
	UN_IV_7	(blank)	**(blank)**	(blank)
2874	**EW_M_5_av**	sharp and weak absorption	**CaCO3**	Spectrum Ca_av, spectrum M_av
2936	**EW_M_5_av**	weak absorption	**CH stretching**	Spectrum EW_av, Daher et al, 2017, p. 8
2963	**EW_M_5_av**	sharp and weak absorption	**CaCO3**	Spectrum Ca_av, spectrum M_av
2979	**M_av**	(blank)	**calcium carbonate**	spectrum Ca_av
	UN_IV_7	(blank)	**(blank)**	(blank)
3030	**EW_M_5_av**	weak absorption	**CaCO3**	spectrum Ca_av
3064	**UN_IV_7**	(blank)	**(blank)**	(blank)
3066	**EW_M_5_av**	1st overtone	**amide I**	Spectrum EW_av, Rosi et al, 2009, p. 2099
3085	**EW_M_5_av**	1st overtone	**amide I**	Spectrum EW_av, Rosi et al, 2009, p. 2099
3314	**EW_M_5_av**	weak absorption	**N-H stretching**	Rosi et al, 2002, p. 2099
3384	**M_av**	weak absorption	**(blank)**	spectrum Q_av
3643	**EW_M_5_av**	doublet	**OH stretching of H2O**	Spectrum M_av, spectrum Ca_av, Rosi et al, 2009, p. 2100
3644	**M_av**	doublet	**OH stretching**	Rosi et al, 2009, p. 2100, spectrum Ca_av

Figure 95: continued.

UN_IV_8

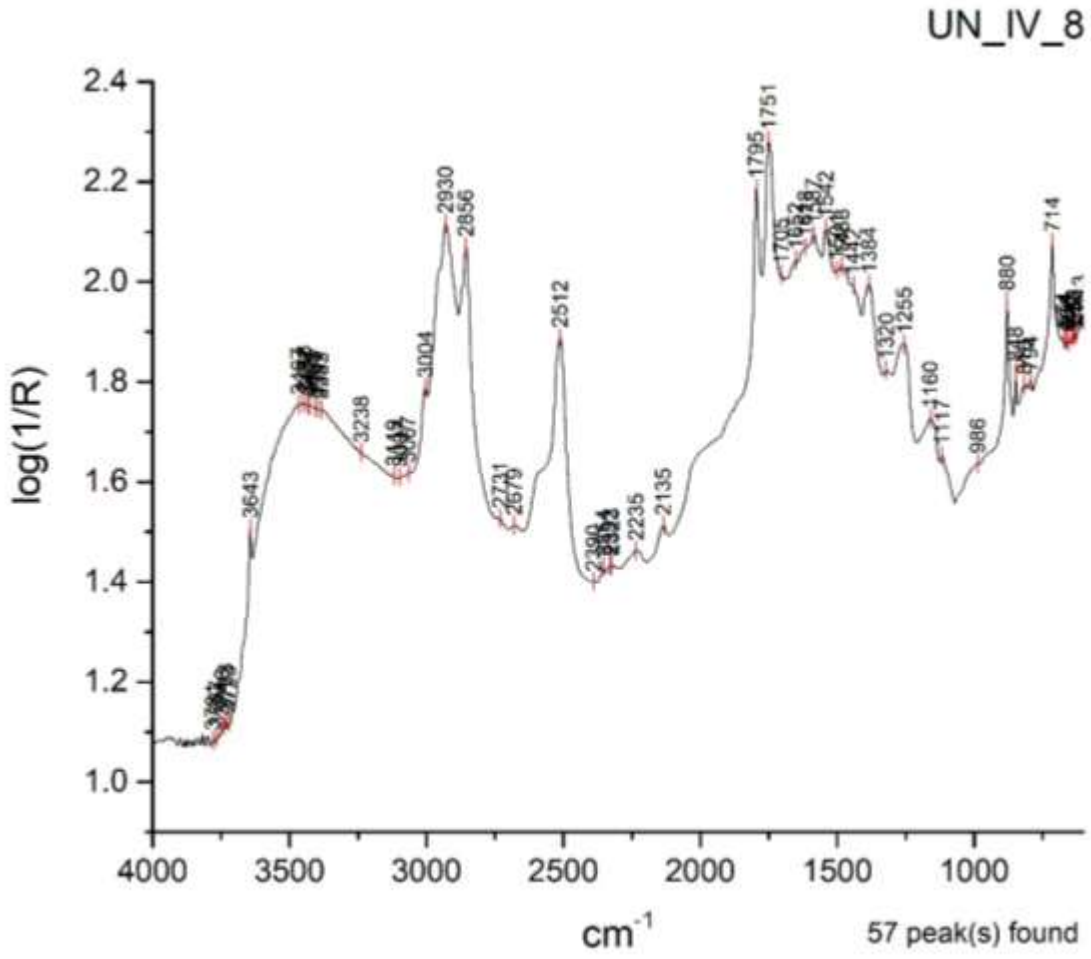

Figure 96: UN_IV_8 correctly identified as 5% lard additive in mortar (L_M_5).

Peak x (position)	Spectrum ID	Type of band	Chemical Band Assignement	Reference
667	L_M_5_av	weak absorption	(blank)	Spectrum L_av
682	L_M_5_av	weak absorption	(blank)	Spectrum L_av
986	UN_IV_8	(blank)	(blank)	(blank)
1255	UN_IV_8	(blank)	(blank)	(blank)
1320	UN_IV_8	(blank)	(blank)	(blank)
1384	L_M_5_av	sharp absorption	lard	Spectrum L_av
	O_M_5_av	sharp absorption	C-O bending	Spectrum O_av
	UN_IV_8	(blank)	(blank)	(blank)
1433	L_M_5_av	weak absorption	lard	Spectrum L_av
1442	O_M_5_av	weak absorption	olive oil	Spectrum O_av, Buti et al, 2013, p. 2706
	UN_IV_8	(blank)	(blank)	(blank)
1446	L_M_5_av	weak absorption	lard	Spectrum L_av
1473	L_M_5_av	weak absorption	C-O bending	Spectrum L_av, Ricci et al, 2006, p. 1224
1483	UN_IV_8	(blank)	(blank)	(blank)
1501	UN_IV_8	(blank)	(blank)	(blank)
1530	O_M_5_av	strong absorption	C-O bending	Spectrum O_av, Ricci et al, 2006, p. 1223
1542	UN_IV_8	(blank)	(blank)	(blank)
1587	UN_IV_8	(blank)	(blank)	(blank)
1618	UN_IV_8	(blank)	(blank)	(blank)
1652	UN_IV_8	(blank)	(blank)	(blank)
1674	O_M_5_av	weak absorption	olive oil	Spectrun O_av
1680	O_M_5_av	weak absorption	olive oil	Spectrun O_av
1695	O_M_5_av	weak absorption	olive oil	Spectrun O_av
1705	UN_IV_8	(blank)	(blank)	(blank)
1747	L_M_5_av	1st order derivative	C=O stretching band	Spectrum L_av, Mazzeo et al, 2008, p. 69
1751	UN_IV_8	(blank)	(blank)	(blank)
1755	O_M_5_av	1st order derivative	C=O stretching band	Spectrum O_av, Ploeger et al, 2010, p, 37
2679	UN_IV_8	(blank)	(blank)	(blank)
2731	UN_IV_8	(blank)	(blank)	(blank)
2854	L_M_5_av	strong absorption	CH2 stretching	Spectrum L_av, Ploeger et al, 2010, p. 37
2855	O_M_5_av	strong absorption	CH2 stretching	Spectrum O_av, Ploeger et al, 2010, p. 37
2856	UN_IV_8	(blank)	(blank)	(blank)
2926	L_M_5_av	strong absorption	CH2 stretching	Spectrum L_av, Ploeger et al, 2010, p. 37
2929	O_M_5_av	strong absorption	CH2 stretching	Spectrum O_av, Ploeger et al, 2010, p. 37
2930	UN_IV_8	(blank)	(blank)	(blank)
2954	O_M_5_av	strong absorption	v(CH) stretching	Spectrum O_av, Miliani et al, 2007, p. 853
3004	UN_IV_8	(blank)	(blank)	(blank)
3005	L_M_5_av	weak absorption	lard	Spectrum L_av
	O_M_5_av	weak absorption	v(CH) stretching	Spectrum O_av, Miliani et al, 2007, p. 853
3062	O_M_5_av	weak absorption	olive oil	Spectrum O_av
3067	UN_IV_8	(blank)	(blank)	(blank)
3097	UN_IV_8	(blank)	(blank)	(blank)
3119	UN_IV_8	(blank)	(blank)	(blank)

Figure 97: Filtered CPAD of peaks of interest for UN_IV_8 spectrum and possible matches.

UN_IV_9

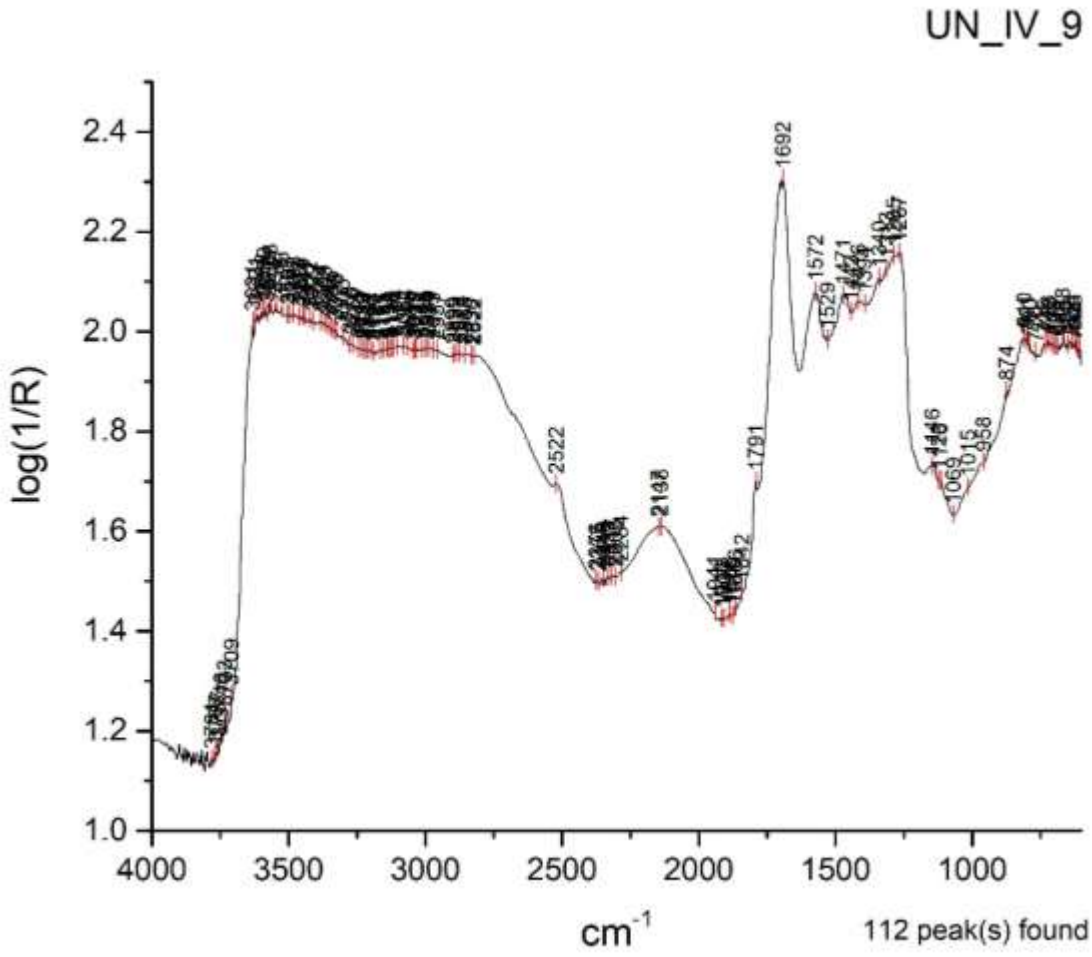

Figure 98: UN_IV_9 correctly identified as 75% bone glue additive in mortar (BG_M_75).

Peak x (position)	Spectrum ID	Type of band	Chemical Band Assignement	Reference
606	EW_M_75_av	weak absorption	CaCO3	spectrum Ca_av
	UN_IV_9	(blank)	(blank)	(blank)
614	UN_IV_9	(blank)	(blank)	(blank)
618	EW_M_75_av	weak absorption	CaCO3	spectrum Ca_av
623	UN_IV_9	(blank)	(blank)	(blank)
638	UN_IV_9	(blank)	(blank)	(blank)
652	UN_IV_9	(blank)	(blank)	(blank)
659	EW_M_75_av	weak absorption	CaCO3	spectrum Ca_av
668	BG_M_75_av	sharp and weak absorption	CaCO3	spectrum Ca_av
	UN_IV_9	(blank)	(blank)	(blank)
685	UN_IV_9	(blank)	(blank)	(blank)
696	UN_IV_9	(blank)	(blank)	(blank)
699	EW_M_75_av	weak absorption	quartz	spectrum Q_av
703	UN_IV_9	(blank)	(blank)	(blank)
713	UN_IV_9	(blank)	(blank)	(blank)
715	EW_M_75_av	weak absorption	v4 carbonate ion	Spectrum Ca_av, spectrum M_av, Ylmen and Jaglid, 2013, p. 119
723	UN_IV_9	(blank)	(blank)	(blank)
735	UN_IV_9	(blank)	(blank)	(blank)
738	BG_M_75_av	weak absorption	bone glue	Spectrum BG_av
761	BG_M_75_av	weak absorption	bone glue	Spectrum BG_av
770	BG_M_75_av	weak absorption	bone glue	Spectrum BG_av
	UN_IV_9	(blank)	(blank)	(blank)
790	BG_M_75_av	weak absorption	bone glue	Spectrum BG_av
	UN_IV_9	(blank)	(blank)	(blank)
791	EW_M_75_av	sharp and weak absorption	quartz	Spectrum Q_av, spectrum M_av
801	UN_IV_9	(blank)	(blank)	(blank)
810	UN_IV_9	(blank)	(blank)	(blank)
817	BG_M_75_av	sharp absorption	Si-O antisymmetric stretching	Spectrum Q_av, spectrum M_av, Miliani et al, 2012, p. 303
	EW_M_75_av	sharp absorption	quartz	Spectrum Q_av, spectrum M_av
874	UN_IV_9	(blank)	(blank)	(blank)
875	BG_M_75_av	weak absorption	v2 carbonate ion	Spectrum Ca_av, spectrum M_av, Ylmen and Jaglid, 2013, p. 119
	EW_M_75_av	weak absorption	egg white, CaCO3 v2 carbonate ion	Spectrum EW_av, spectrum Ca_av, spectrum M_av, Ylmen and Jaglid, 2013, p. 119
958	UN_IV_9	(blank)	(blank)	(blank)
1015	UN_IV_9	(blank)	(blank)	(blank)
1069	UN_IV_9	(blank)	(blank)	(blank)
1116	BG_M_75_av	weak absorption	CaCO3	spectrum Ca_av
	UN_IV_9	(blank)	(blank)	(blank)
1123	UN_IV_9	(blank)	(blank)	(blank)
1146	BG_M_75_av	weak absorption	CaCO3 and quartz	Spectrum Ca_av, spectrum Q_av, spectrum M_av
	UN_IV_9	(blank)	(blank)	(blank)
1153	BG_M_75_av	weak absorption	CaCO3 and quartz	Spectrum Ca_av, spectrum Q_av, spectrum M_av
1159	EW_M_75_av	sharp absorption	quartz	Spectrum Q_av, spectrum M_av
1267	UN_IV_9	(blank)	(blank)	(blank)
1268	BG_M_75_av	stair-step type intensities	bone glue	Spectrum BG_av
1285	EW_M_75_av	weak absorption	egg white	spectrum EW_av
	UN_IV_9	(blank)	(blank)	(blank)
1287	BG_M_75_av	stair-step type intensities	bone glue	Spectrum BG_av
1313	UN_IV_9	(blank)	(blank)	(blank)
1314	EW_M_75_av	weak absorption	egg white	spectrum EW_av

Figure 99: Filtered CPAD of peaks of interest for UN_IV_9 spectrum and possible matches.

1340	UN_IV_9	(blank)	(blank)	(blank)
1341	BG_M_75_av	stair-step type intensities	bone glue	Spectrum BG_av
1394	UN_IV_9	(blank)	(blank)	(blank)
1412	EW_M_75_av	weak absorption	egg white	spectrum EW_av
1415	BG_M_75_av	stair-step type intensities	bone glue	Spectrum BG_av
1416	UN_IV_9	(blank)	(blank)	(blank)
1424	EW_M_75_av	weak absorption	v3 antisymmetric stretching CO3-2	Spectrum M_av, Ylmen and Jaglid, 2013, p. 119
1432	EW_M_75_av	weak absorption	v3 antisymmetric stretching CO3-2	Spectrum M_av, Ylmen and Jaglid, 2013, p. 119
1443	UN_IV_9	(blank)	(blank)	(blank)
1453	EW_M_75_av	weak absorption	egg white	spectrum EW_av
1461	EW_M_75_av	weak absorption	egg white	spectrum EW_av
1471	BG_M_75_av	stair-step type intensities	Amide III	Spectrum BG_av, Rosi et al, 2009, p. 2099
	UN_IV_9	(blank)	(blank)	(blank)
1529	UN_IV_9	(blank)	(blank)	(blank)
1561	EW_M_75_av	weak absorption	quartz	spectrum Q_av
1572	BG_M_75_av	strong absorption	C-N-H bending amide II, N-H bands	Spectrum BG_av, Rosi et al, 2009, p. 2099, Miliani et al, 2012, p. 304
	UN_IV_9	(blank)	(blank)	(blank)
1575	EW_M_75_av	strong absorption	C-N-H bending amide II, N-H bands	Spectrum EW_av, Rosi et al, 2009, p. 2104
1692	EW_M_75_av	strong absorption	N-H bands	Spectrum EW_av, Ploeger et al, 2010, p.37, Miliani et al, 2012, p. 305
	UN_IV_9	(blank)	(blank)	(blank)
1697	BG_M_75_av	strong absorption	N-H bands	Spectrum BG_av, Rosi et al, 2009, p. 2104, Miliani et al, 2012, p. 304
1790	BG_M_75_av	weak absorption	v1+v4 carbonate ion	Spectrum Ca_av, spectrum M_av, Ricci et al, 2006, p. 1222
1791	UN_IV_9	(blank)	(blank)	(blank)
1794	EW_M_75_av	combination band	v1+v4	Spectrum Ca_av, spectrum M_av, Ricci et al, 2006, p. 1222
1842	UN_IV_9	(blank)	(blank)	(blank)
1860	EW_M_75_av	weak absorption	quartz	spectrum Q_av
1866	UN_IV_9	(blank)	(blank)	(blank)
1867	EW_M_75_av	weak absorption	quartz	spectrum Q_av
1876	UN_IV_9	(blank)	(blank)	(blank)
1888	UN_IV_9	(blank)	(blank)	(blank)
1907	UN_IV_9	(blank)	(blank)	(blank)
1916	UN_IV_9	(blank)	(blank)	(blank)
1930	EW_M_75_av	weak absorption	quartz	spectrum Q_av
1941	UN_IV_9	(blank)	(blank)	(blank)
1947	EW_M_75_av	weak absorption	quartz	spectrum Q_av
1968	EW_M_75_av	weak absorption	quartz	spectrum Q_av
1976	EW_M_75_av	weak absorption	quartz	spectrum Q_av
1992	EW_M_75_av	weak absorption	quartz	spectrum Q_av

Figure 99: continued.

2131	**BG_M_75_av**	weak absorption	**CaCO3 and quartz**	Spectrum Q_av, spectrum M_av, spectrum Ca_av
2135	**EW_M_75_av**	weak absorption	**calcium carbonate and quartz**	Spectrum Ca_av, spectrum M_av, spectrum Q_av
2138	**UN_IV_9**	(blank)	**(blank)**	(blank)
2147	**UN_IV_9**	(blank)	**(blank)**	(blank)
2235	**EW_M_75_av**	weak absorption	**quartz**	spectrum Q_av
2238	**BG_M_75_av**	weak absorption	**quartz**	Spectrum Q_av, spectrum M_av
2515	**EW_M_75_av**	combination band	**v1+v3**	Spectrum Ca_av, spectrum M_av, Ricci et al, 2006, p. 1222
2522	**UN_IV_9**	(blank)	**(blank)**	(blank)
2523	**BG_M_75_av**	combination band	**v1+v3 carbonate ion**	Spectrum Ca_av, spectrum M_av, Ricci et al, 2006, p. 1222
2544	**EW_M_75_av**	weak absorption	**egg white**	spectrum EW_av
2603	**EW_M_75_av**	weak absorption	**egg white**	spectrum EW_av
2616	**EW_M_75_av**	weak absorption	**egg white**	spectrum EW_av
2660	**BG_M_75_av**	weak absorption	**CaCO3**	Spectrum Ca_av, spectrum M_av
2677	**BG_M_75_av**	weak absorption	**CaCO3**	Spectrum Ca_av, spectrum M_av
2802	**BG_M_75_av**	weak absorption	**C-H stretching**	Rosi et al, 2009, p. 2099
2873	**EW_M_75_av**	sharp and weak absorption	**CaCO3**	Spectrum Ca_av, spectrum M_av
2881	**BG_M_75_av**	weak absorption	**C-H stretching**	Spectrum BG_av, Miliani et al, 2012, p. 304; Rosi et al, 2009, p. 2104
2889	**BG_M_75_av**	weak absorption	**C-H stretching**	Spectrum BG_av, Miliani et al, 2012, p. 304; Rosi et al, 2009, p. 2104
2940	**EW_M_75_av**	weak absorption	**CH stretching**	Spectrum EW_av, Daher et al, 2017, p. 8
2948	**EW_M_75_av**	weak absorption	**CH3 stretching**	Spectrum EW_av, Iwanicka et al, 2017, p. 18
2965	**EW_M_75_av**	sharp and weak absorption	**CaCO3**	Spectrum Ca_av, spectrum M_av
2985	**BG_M_75_av**	weak absorption	**bone glue**	Spectrum BG_av
3086	**EW_M_75_av**	1st overtone	**amide I**	Spectrum EW_av, Rosi et al, 2009, p. 2099
3103	**BG_M_75_av**	weak absorption	**amide I**	Spectrum BG_av, Rosi et al, 2009, p. 2099

Figure 99: continued.

UN_IV_10

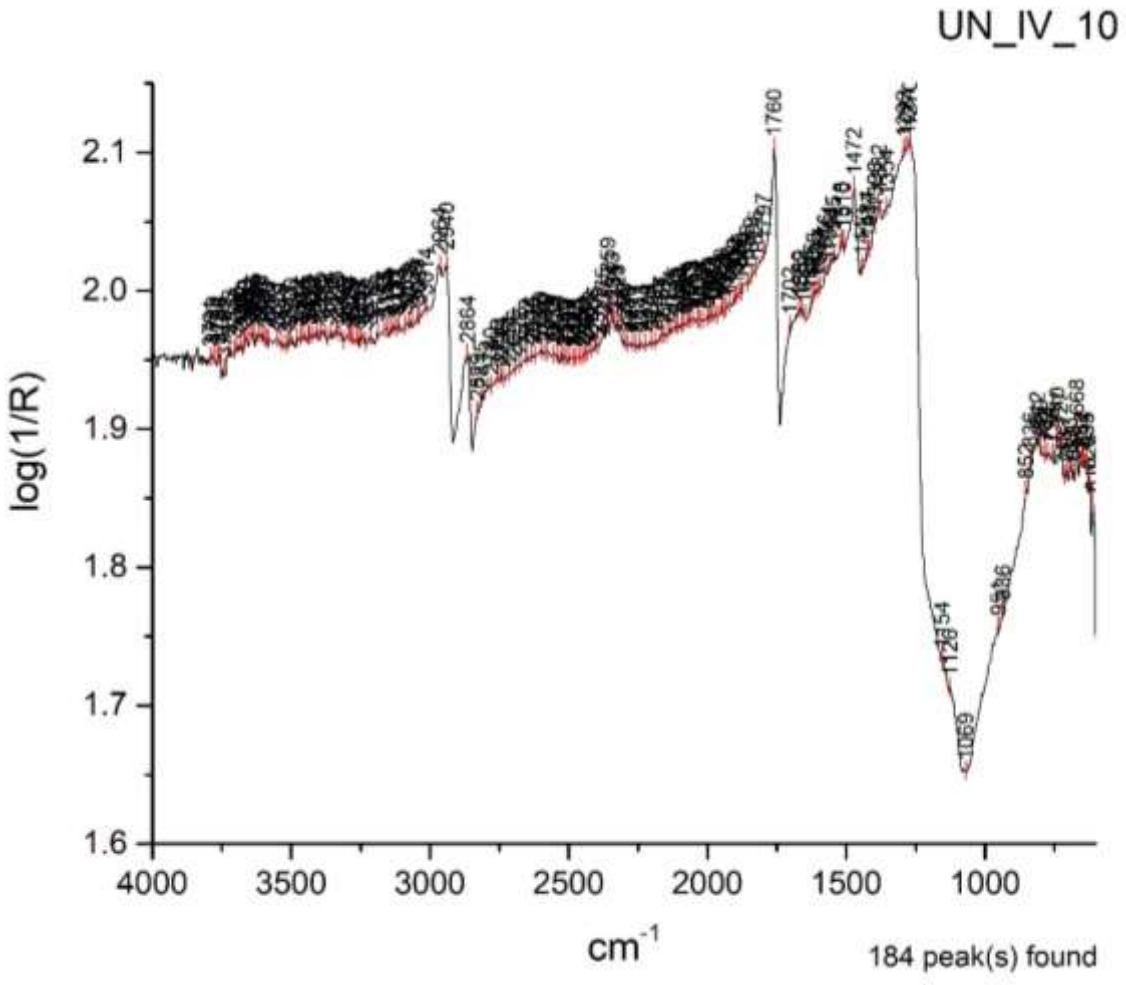

Figure 100: UN_IV_10 correctly identified as 75% olive oil additive in mortar (O_M_75).

Peak x (position)	Spectrum ID	Type of band	Chemical Band Assignement	Reference
610	UN_IV_10	(blank)	(blank)	(blank)
623	UN_IV_10	(blank)	(blank)	(blank)
633	UN_IV_10	(blank)	(blank)	(blank)
644	UN_IV_10	(blank)	(blank)	(blank)
652	UN_IV_10	(blank)	(blank)	(blank)
668	O_M_75_av	sharp and weak absorption	olive oil	Spectrum O_av
	UN_IV_10	(blank)	(blank)	(blank)
680	UN_IV_10	(blank)	(blank)	(blank)
693	UN_IV_10	(blank)	(blank)	(blank)
700	L_M_75_av	weak absorption	lard	Spectrum Q_av, spectrum M_av, spectrum L_av
705	UN_IV_10	(blank)	(blank)	(blank)
706	O_M_75_av	sharp and weak absorption	olive oil	Spectrum O_av
713	UN_IV_10	(blank)	(blank)	(blank)
725	L_M_75_av	sharp absorption	lard	Spectrum L_av
727	UN_IV_10	(blank)	(blank)	(blank)
729	O_M_75_av	sharp and weak absorption	olive oil	Spectrum O_av
740	UN_IV_10	(blank)	(blank)	(blank)
758	UN_IV_10	(blank)	(blank)	(blank)
774	UN_IV_10	(blank)	(blank)	(blank)
782	UN_IV_10	(blank)	(blank)	(blank)
791	L_M_75_av	sharp absorption	quartz	Spectrum Q_av, spectrum M_av
799	UN_IV_10	(blank)	(blank)	(blank)
812	UN_IV_10	(blank)	(blank)	(blank)
813	O_M_75_av	sharp and weak absorption	olive oil	Spectrum O_av
818	L_M_75_av	sharp absorption	Si-O antisymmetric stretching	Spectrum Q_av, spectrum M_av, Miliani et al, 2013, p. 303
836	UN_IV_10	(blank)	(blank)	(blank)
852	UN_IV_10	(blank)	(blank)	(blank)
936	UN_IV_10	(blank)	(blank)	(blank)
951	UN_IV_10	(blank)	(blank)	(blank)
1069	UN_IV_10	(blank)	(blank)	(blank)
1115	L_M_75_av	sharp absorption	lard	Spectrum L_av
1126	UN_IV_10	(blank)	(blank)	(blank)
1154	UN_IV_10	(blank)	(blank)	(blank)
1160	L_M_75_av	sharp absorption	quartz	Spectrum Q_av, spectrum M_av
1197	L_M_75_av	weak absorption	v(C-O) stretching	Spectrum L_av, Ricci et al, 2006, p. 1224
1270	UN_IV_10	(blank)	(blank)	(blank)
1271	O_M_75_av	strong absorption	C-O stretching	Spectrum O_av, Buti et al, 2013, p. 2705
1279	L_M_75_av	strong absorption	C-O	Spectrum L_av, Ploeger et al, 2010, p. 37
1281	O_M_75_av	strong absorption	olive oil	Spectrum O_av
	UN_IV_10	(blank)	(blank)	(blank)
1289	L_M_75_av	strong absorption	C-O	Spectrum L_av, Ploeger et al, 2010, p. 37
1292	UN_IV_10	(blank)	(blank)	(blank)
1349	L_M_75_av	sharp and weak absorption	quartz	spectrum Q_av
1354	O_M_75_av	sharp and weak absorption	olive oil	Spectrum O_av
	UN_IV_10	(blank)	(blank)	(blank)
1364	O_M_75_av	sharp and weak absorption	olive oil	Spectrum O_av
1381	L_M_75_av	sharp and weak absorption	C-H bending	Spectrum L_av, Buti et al, 2013, p. 2705
	O_M_75_av	sharp and weak absorption	C-H bending	Spectrum O_av, Buti et al, 2013, p. 2705
1382	UN_IV_10	(blank)	(blank)	(blank)
1389	L_M_75_av	sharp and weak absorption	C-H bending	Spectrum L_av, Buti et al, 2013, p. 2705

Figure 101: Filtered CPAD of peaks of interest for UN_IV_10 spectrum and possible matches.

1396	**UN_IV_10**	(blank)	**(blank)**	(blank)
1417	**UN_IV_10**	(blank)	**(blank)**	(blank)
1420	**O_M_75_av**	weak absorption	**olive oil**	Spectrum O_av
1421	**L_M_75_av**	weak absorption	**(blank)**	Spectrum L_av
1424	**UN_IV_10**	(blank)	**(blank)**	(blank)
1442	**O_M_75_av**	weak absorption	**olive oil**	Spectrum O_av
1443	**UN_IV_10**	(blank)	**(blank)**	(blank)
1446	**L_M_75_av**	weak absorption	**(blank)**	Spectrum L_av
1471	**O_M_75_av**	sharp absorption	**C-H bending**	Spectrum O_av, Ricci et al, 2006, p. 1223
1472	**UN_IV_10**	(blank)	**(blank)**	(blank)
1474	**L_M_75_av**	strong absorption	**C-O bending**	Spectrum L_av, Ricci et al, 2006, p. 1224
1510	**UN_IV_10**	(blank)	**(blank)**	(blank)
1518	**UN_IV_10**	(blank)	**(blank)**	(blank)
1545	**UN_IV_10**	(blank)	**(blank)**	(blank)
1560	**O_M_75_av**	weak absorption	**olive oil**	Spectrum O_av
1561	**UN_IV_10**	(blank)	**(blank)**	(blank)
1576	**UN_IV_10**	(blank)	**(blank)**	(blank)
1579	**L_M_75_av**	weak absorption	**quartz**	Spectrum Q_av, spectrum M_av
1594	**UN_IV_10**	(blank)	**(blank)**	(blank)
1595	**O_M_75_av**	weak absorption	**quartz**	Spectrum M_av, spectrum Q_av
1604	**UN_IV_10**	(blank)	**(blank)**	(blank)
1606	**L_M_75_av**	weak absorption	**quartz**	Spectrum Q_av, spectrum M_av
1615	**UN_IV_10**	(blank)	**(blank)**	(blank)
1626	**UN_IV_10**	(blank)	**(blank)**	(blank)
1649	**UN_IV_10**	(blank)	**(blank)**	(blank)
1657	**O_M_75_av**	weak absorption	**olive oil**	Spectrum O_av
1662	**L_M_75_av**	weak absorption	**(blank)**	Spectrum L_av, spectrum M_av, Spectrum Q_av
	UN_IV_10	(blank)	**(blank)**	(blank)
1669	**L_M_75_av**	weak absorption	**(blank)**	Spectrum L_av, spectrum M_av, Spectrum Q_av
	UN_IV_10	(blank)	**(blank)**	(blank)
1679	**L_M_75_av**	weak absorption	**(blank)**	Spectrum L_av, spectrum M_av, Spectrum Q_av
1683	**O_M_75_av**	weak absorption	**olive oil**	Spectrum O_av, Mazzeo et al, 2008, p. 69
1702	**UN_IV_10**	(blank)	**(blank)**	(blank)
1705	**O_M_75_av**	weak absorption	**free fatty acids**	Spectrum O_av, Ploeger et al, 2010, p. 37
1756	**L_M_75_av**	1st order derivative	**C=O stretching band**	Spectrum L_av, Mazzeo et al, 2008, p. 69
1759	**O_M_75_av**	1st order derivative	**C=O stretching band**	Spectrum O_av
1760	**UN_IV_10**	(blank)	**(blank)**	(blank)
1797	**UN_IV_10**	(blank)	**(blank)**	(blank)
2135	**O_M_75_av**	weak absorption	**calcium carbonate and quartz**	Spectrum Ca_av, spectrum M_av, spectrum Q_av
2584	**O_M_75_av**	weak absorption	**quartz**	spectrum Q_av
2601	**O_M_75_av**	weak absorption	**quartz**	spectrum Q_av
2862	**L_M_75_av**	strong absorption	**CH2 stretching**	Spectrum L_av, Ploeger et al, 2010, p. 37
2864	**O_M_75_av**	strong absorption	**CH2 stretching**	Spectrum O_av, Ploeger et al, 2010, p. 37
	UN_IV_10	(blank)	**(blank)**	(blank)
2940	**L_M_75_av**	sharp absorption	**CH2 stretching**	Spectrum L_av, Ploeger et al, 2010, p. 37
	UN_IV_10	(blank)	**(blank)**	(blank)
2941	**O_M_75_av**	strong absorption	**CH2 stretching**	Spectrum O_av, Ploeger et al, 2010, p. 37
2964	**O_M_75_av**	strong absorption	**v(CH) stretching**	Spectrum O_av, Miliani et al, 2007, p. 853
	UN_IV_10	(blank)	**(blank)**	(blank)
2968	**L_M_75_av**	sharp absorption	**CH2 stretching**	Spectrum L_av, Ploeger et al, 2010, p. 37
3003	**L_M_75_av**	weak absorption	**CH stretching**	Spectrum L_av, Miliani et al, 2012, p. 302
3014	**UN_IV_10**	(blank)	**(blank)**	(blank)
3018	**L_M_75_av**	weak absorption	**CH stretching**	Spectrum L_av, Miliani et al, 2012, p. 302
3019	**O_M_75_av**	weak absorption	**v(CH) stretching**	Spectrum O_av, Miliani et al, 2007, p. 853
3452	**L_M_75_av**	weak absorption	**lard**	Spectrum L_av
3461	**L_M_75_av**	weak absorption	**lard**	Spectrum L_av
3480	**L_M_75_av**	weak absorption	**lard**	Spectrum L_av

Figure 101: continued.

Appendix II

Chapter 10: Principal Component Analysis

Section 10.1: Design of PCA Methodology

10.2 Results: PCA on Regions of Interest (ROIs)

ROI_1_correlation

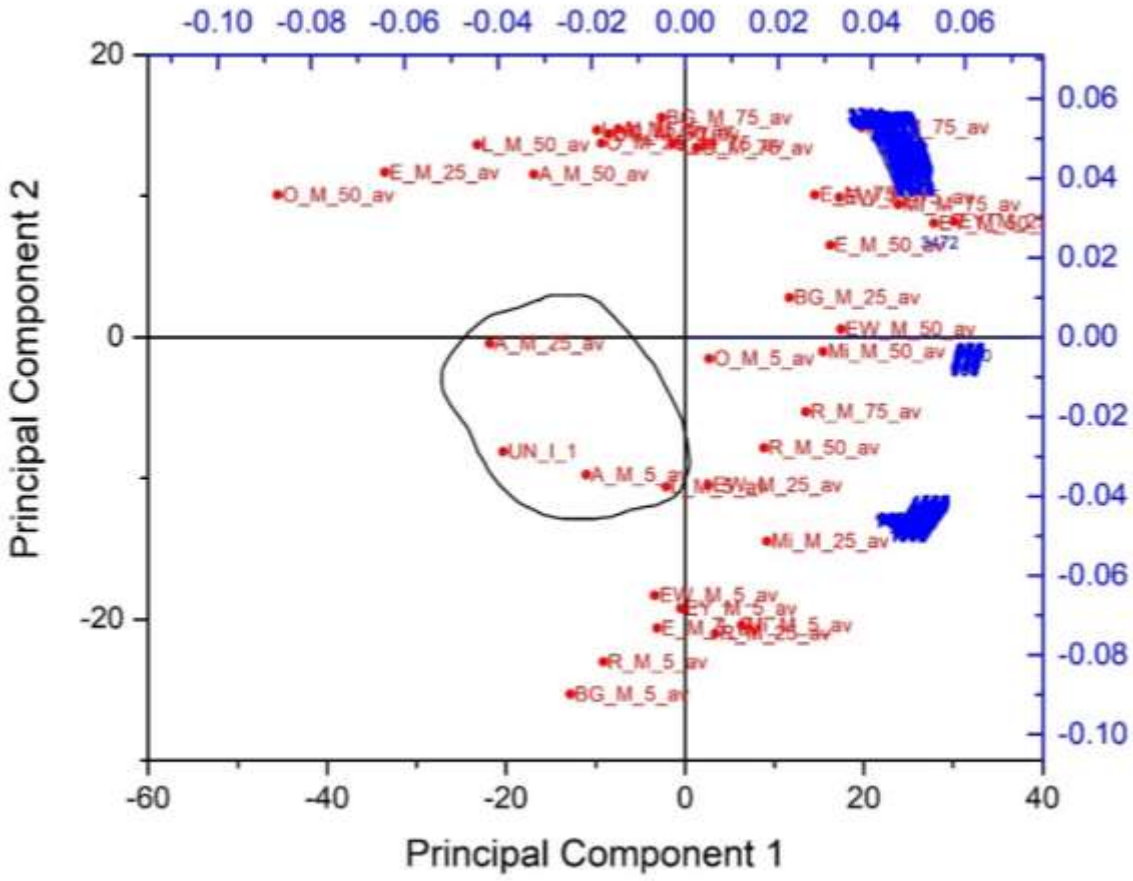

Figure 1: UN_I_1 classified correctly with asphalt/mortar mixtures. PC1 explains the 56.61% of the total variance and PC2 the 36.50%.

ROI_8_correlation

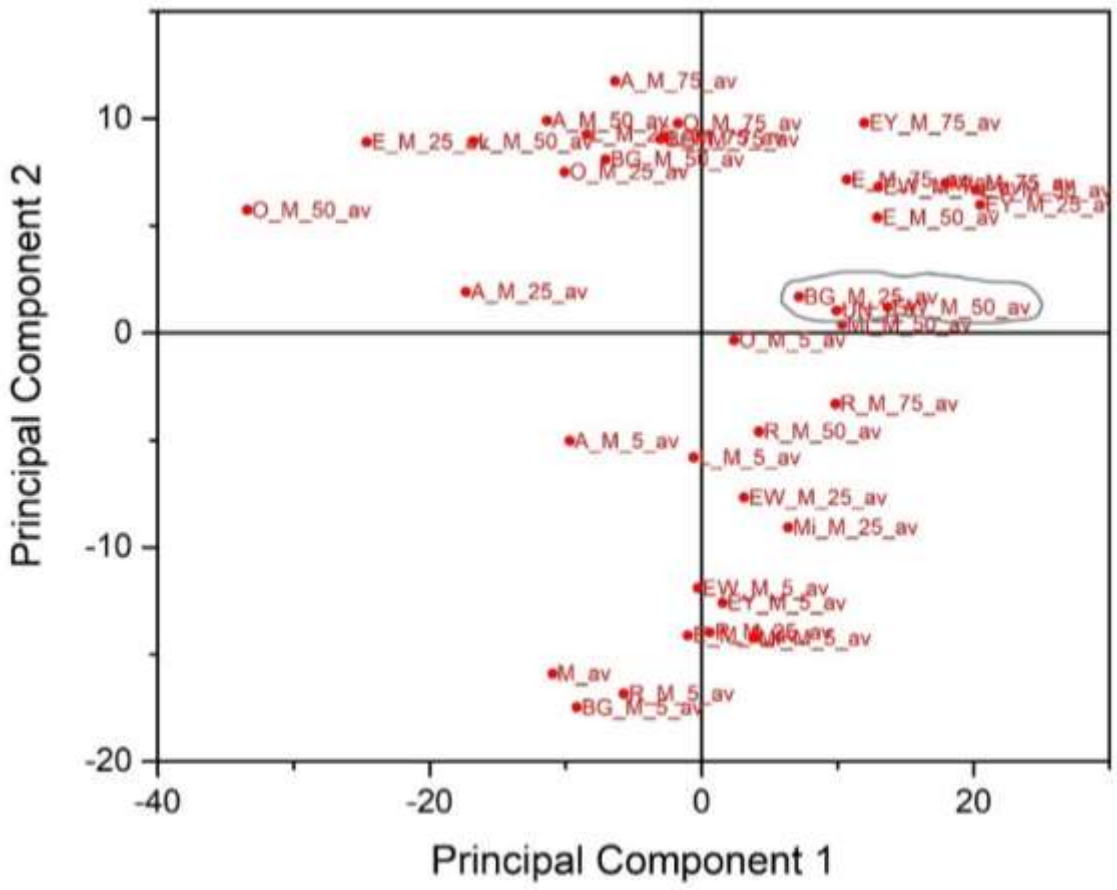

Figure 2: UN_I_8 classified among protein standards and the true identity (EW_M_50). PC1 explained variance is 59.32%, PC2 is 35.33% and PC3 is 3.36%

10.3 Results: PCA on Diagnostic peaks

D_1_covariance

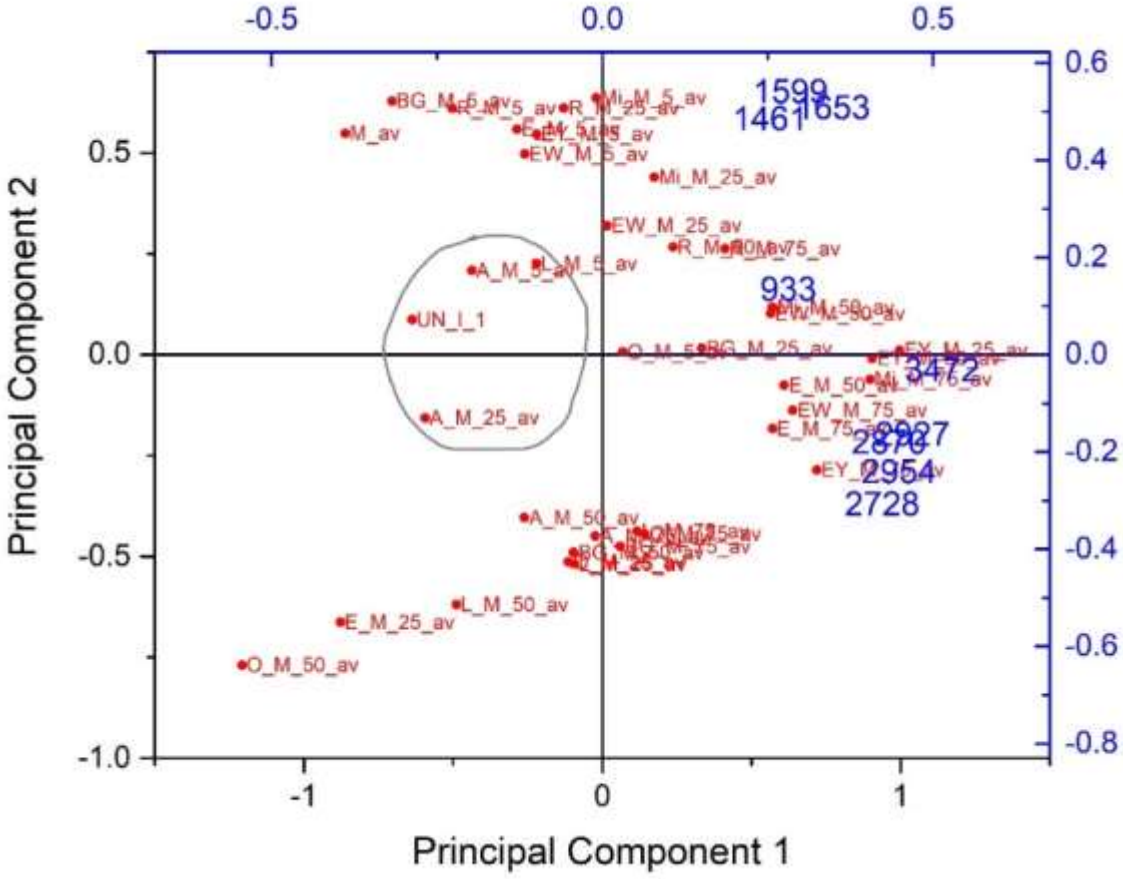

Figure 3: PC1vsPC2 for UN_I_1. PC1 explains the 55.54%, PC2 the 34.71% and PC3 the 8.23% of the total variance. True identity is A_M_25.

D_2_covariance

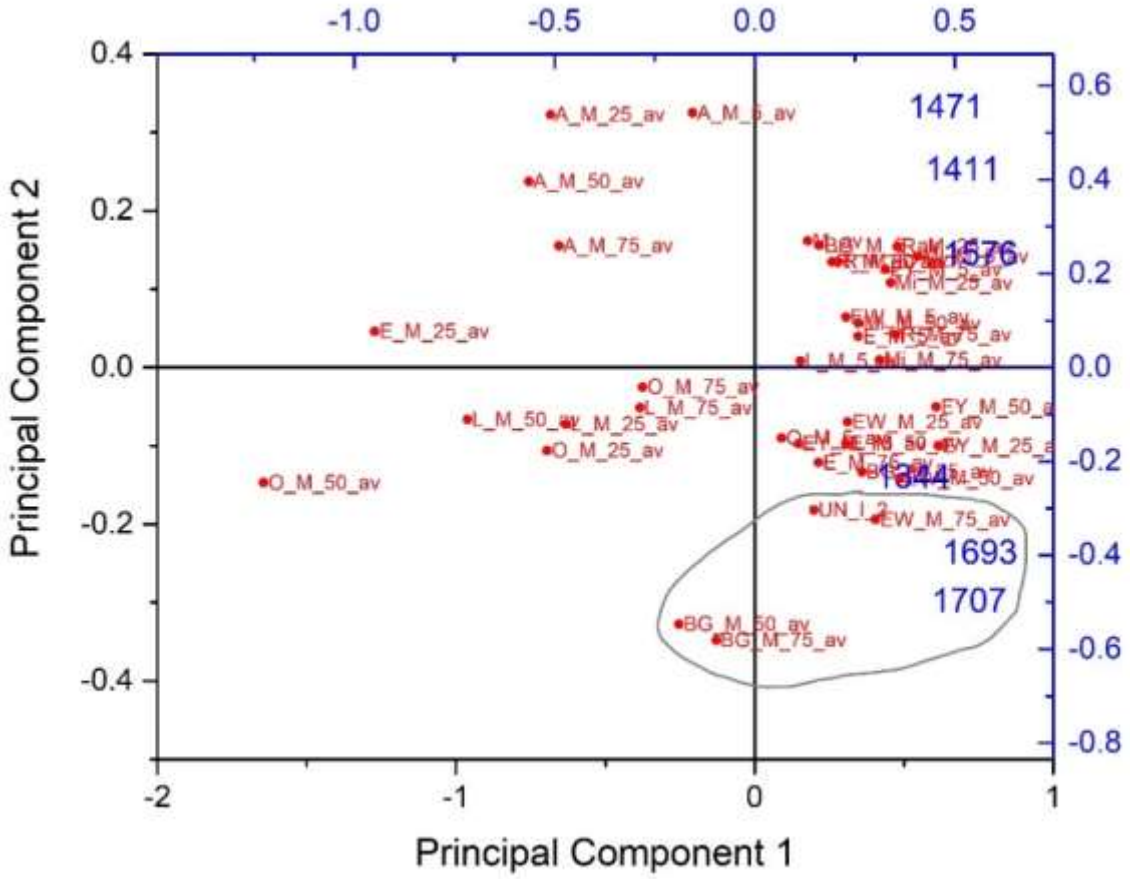

Figure 4: PC1vsPC2 for UN_I_2. PC1 explains the 89.61%, PC2 the 7.03% and PC3 the 2.70% of the total variance. True identity is BG_M_50.

D_3_ covariance

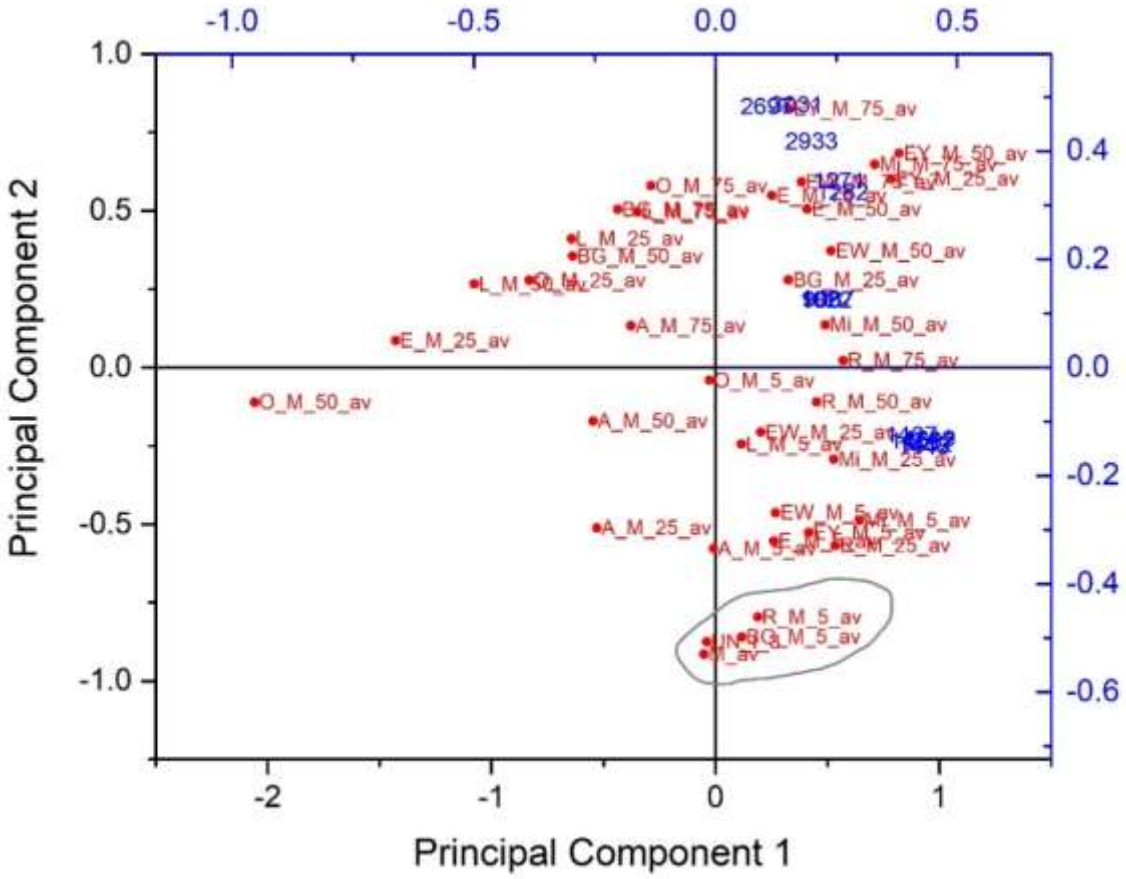

Figure 5: PC1vsPC2 for UN_I_3. PC1 is 57.21%, PC2 is 36.66% and PC3 is 3.15%. True identity is R_M_5.

D_3_correlation

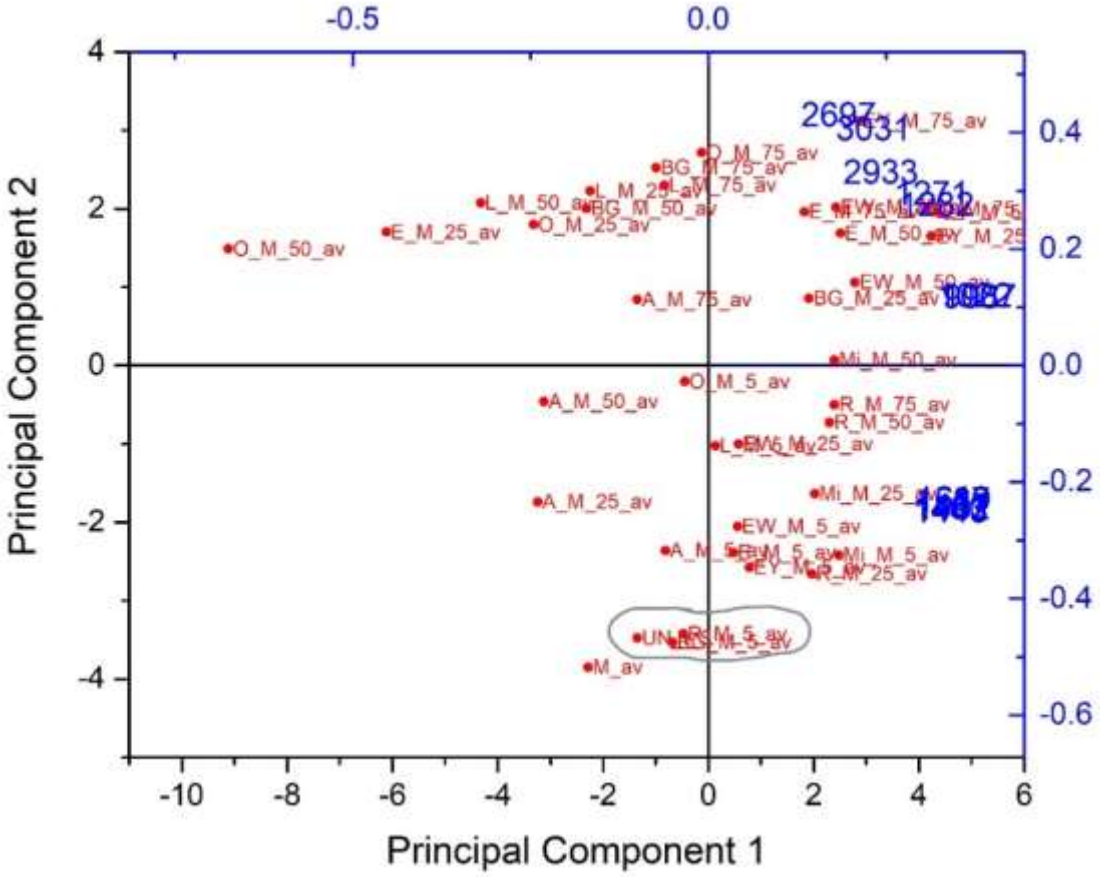

Figure 6: Correlation PC1vsPC2 for UN_I_3. PC1 is 60.70%, PC2 is 32.65% and PC3 is 2.87% of the total variance.

D_4_covariance

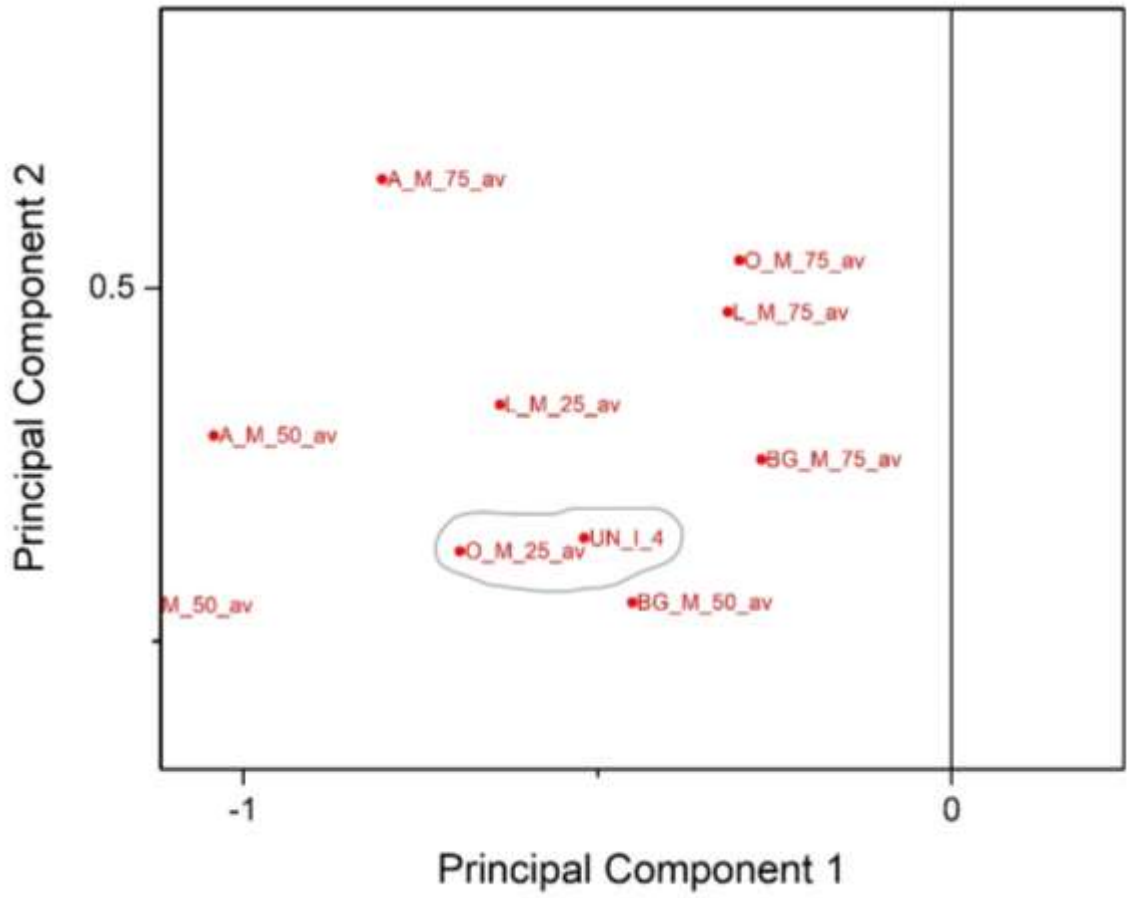

Figure 7: Enlarged PC1vsPC2 for UN_I_4. Successful classification to true identity (O_M_25).

D_5_covariance

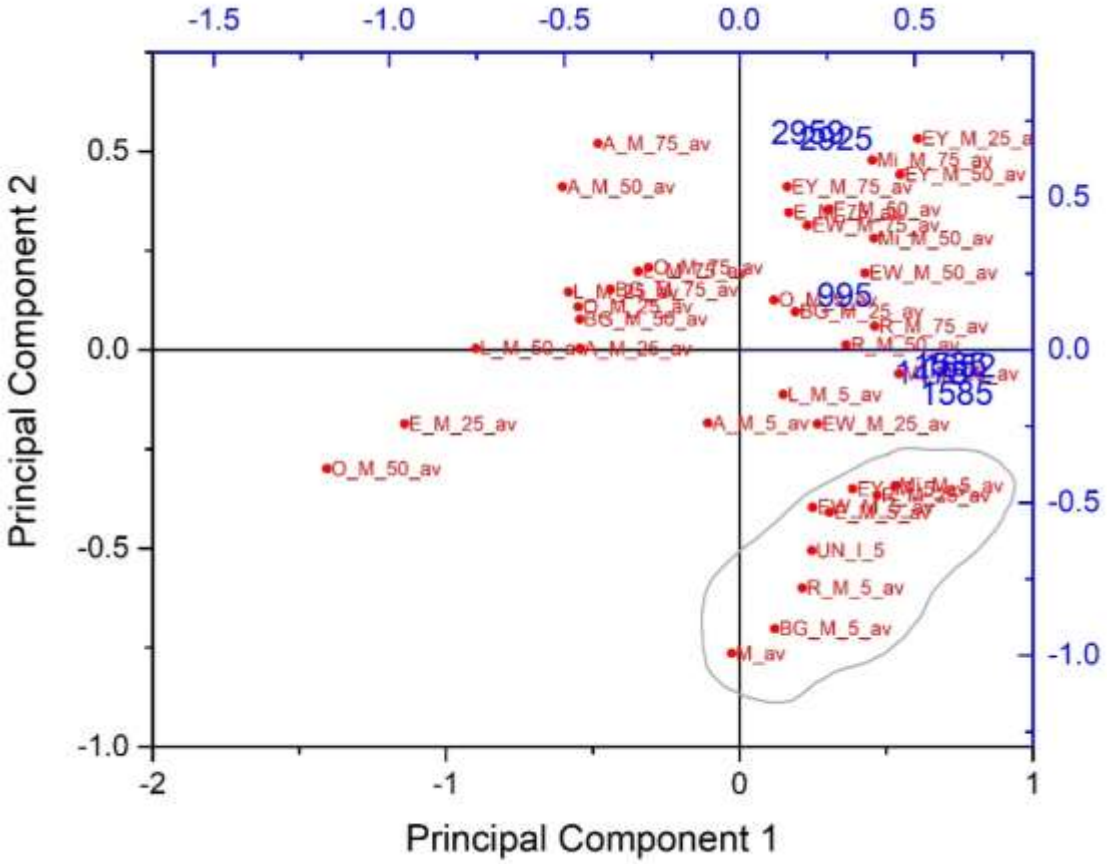

Figure 8: PC1vsPC2 for UN_I_5. True identity is Mi_M_5.

D_6_covariance

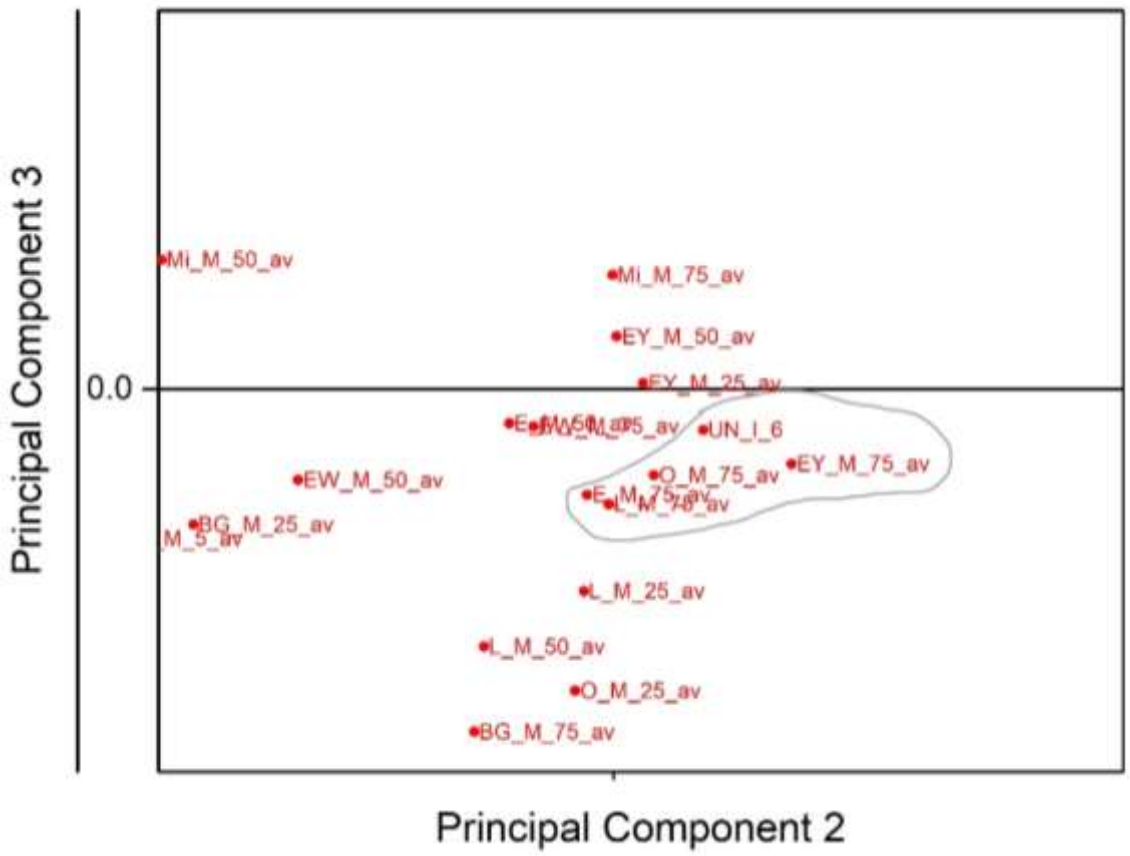

Figure 9: Enlarged PC1vsPC2 for UN_I_6. True identity is L_M_75.

D_7_covariance

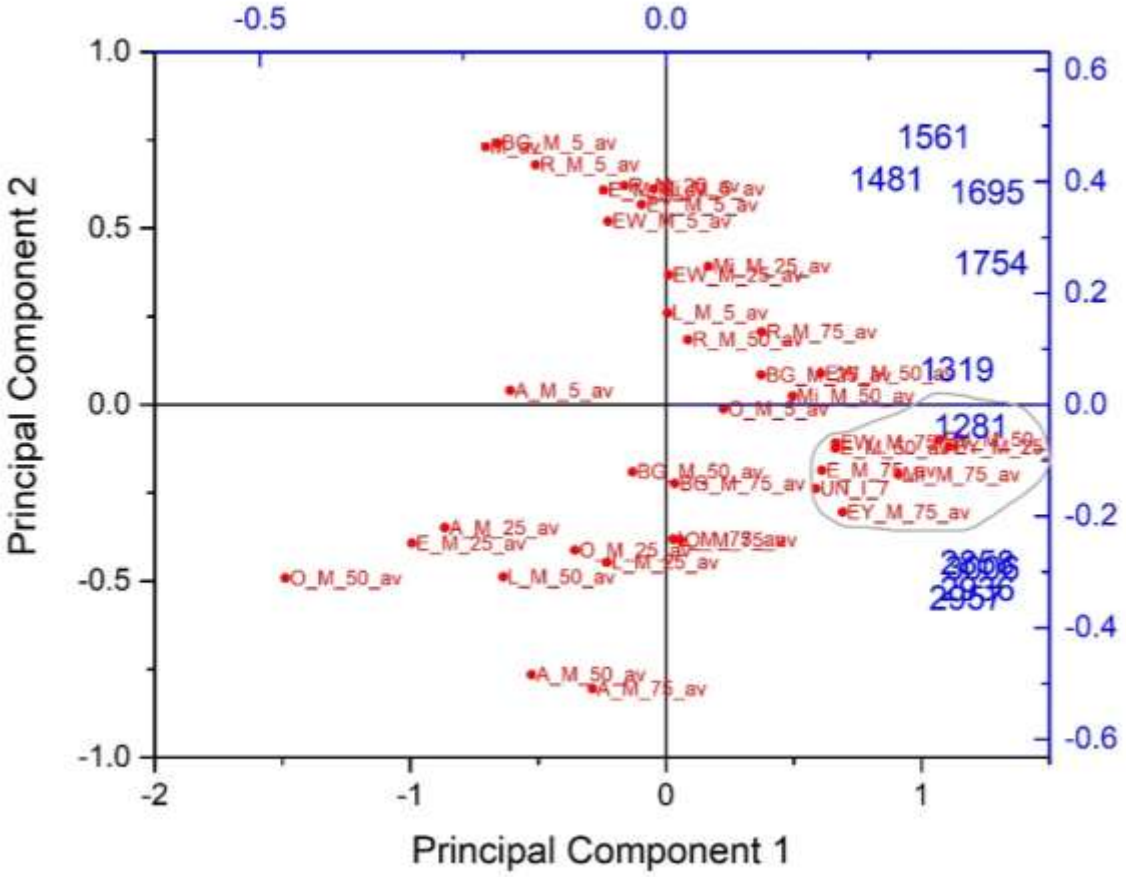

Figure 10: PC1vsPC2 for UN_I_7. True identity is EY_M_25.

D_8_covariance

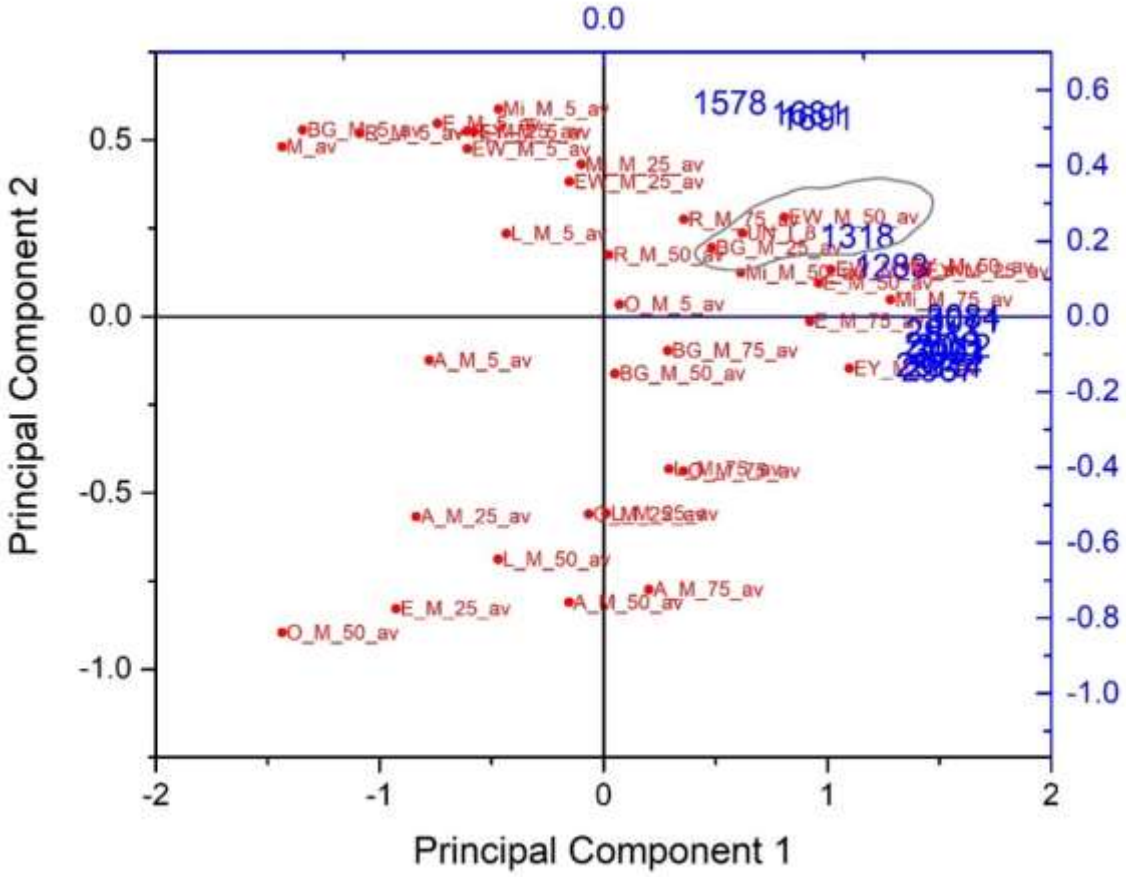

Figure 11: PC1vsPC2 for UN_I_8. PC1 is 70.75%, PC2 is 23.09% and PC3 is 4.59%. True identity is EW_M_50.

D_9_covariance

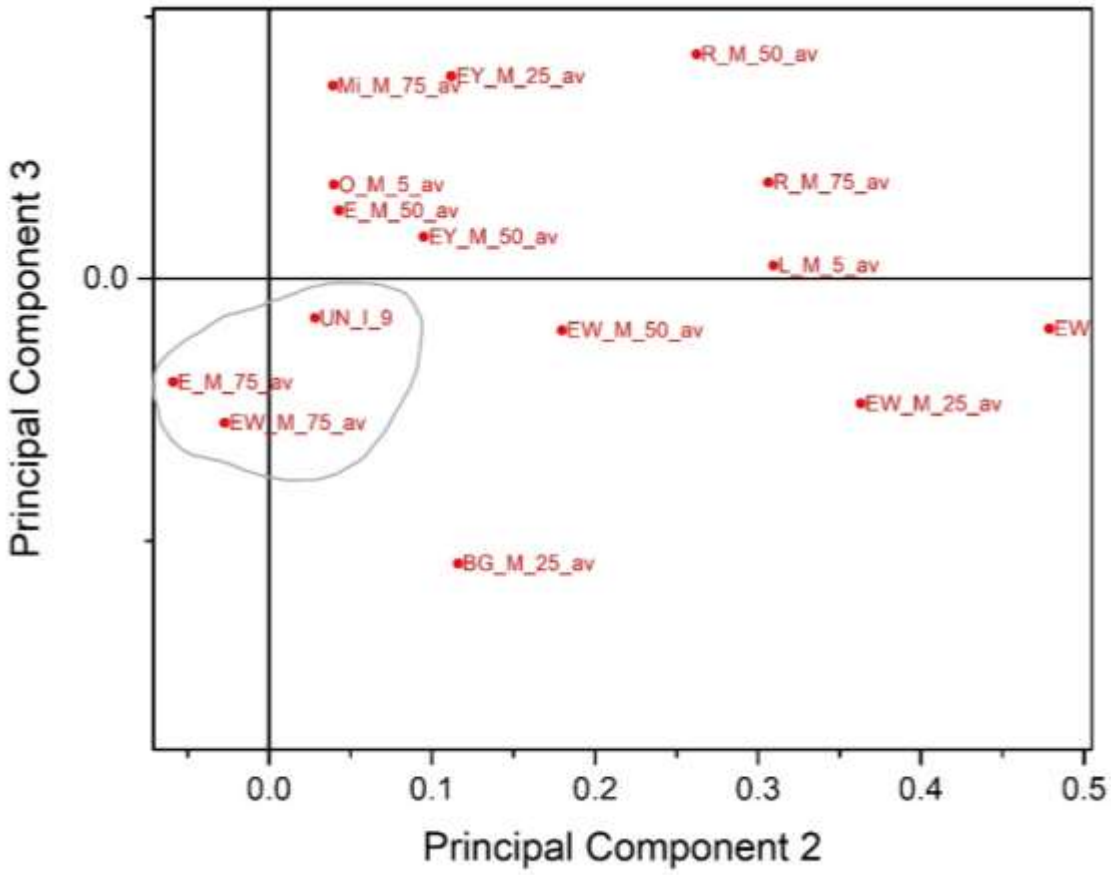

Figure 12: Enlarged PC1vsPC2 for UN_I_9. True identity is E_M_75.

D_10_covariance

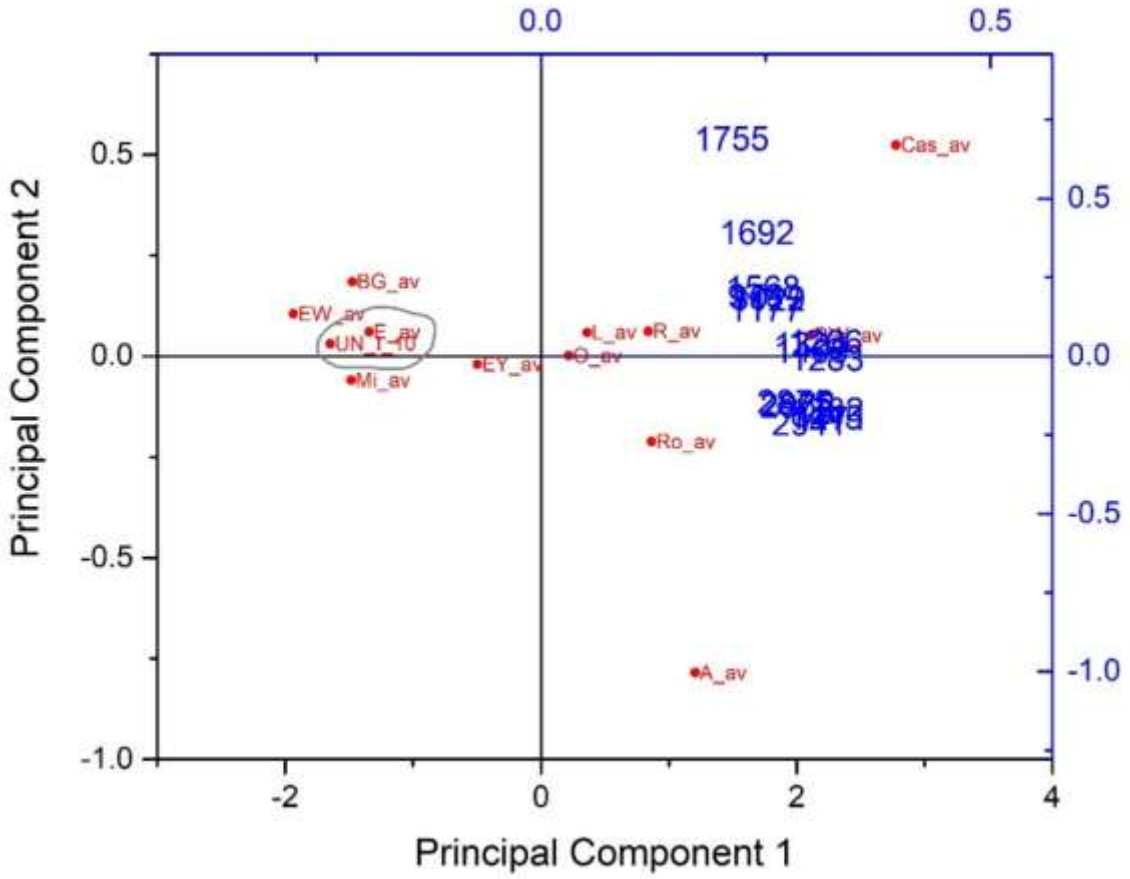

Figure 13: PC1vsPC2 for UN_I_10. PC1 is 93.20%, PC2 is 3.31% and PC3 is 2.13%. True identity is E_av.

Section 10.5: Evaluation of PCA Methodology

10.5.1 Results of PCA on Reflectance micro-FTIR spectra from Experimental Set IV

UN_IV_3_correlation

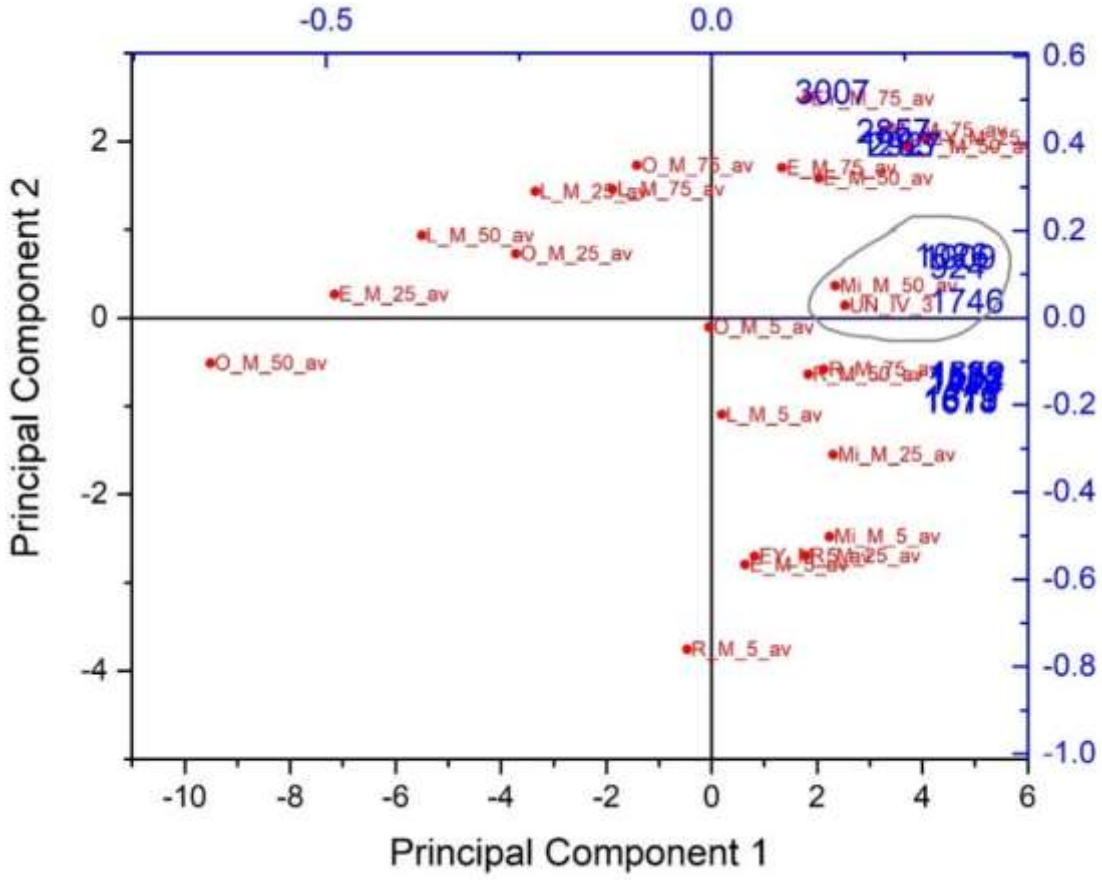

Figure 14: Correlation PC1vsPC2 for UN_IV_3. PC1 is 74.79%, PC2 is 20.84% and PC3 is 2.43%.

UN_IV_8 (before CPAD) _ covariance

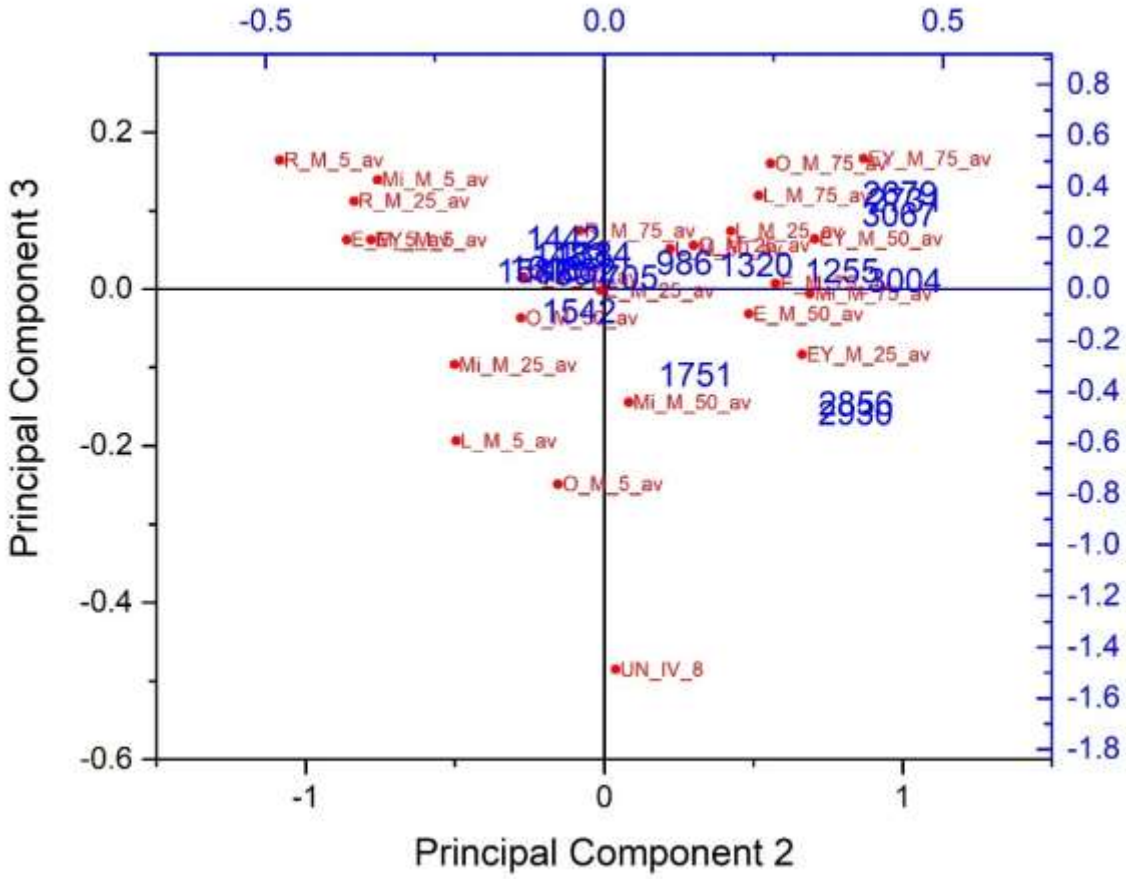

Figure 15: PC2vsPC3 for UN_IV_8.

UN_IV_10_covariance

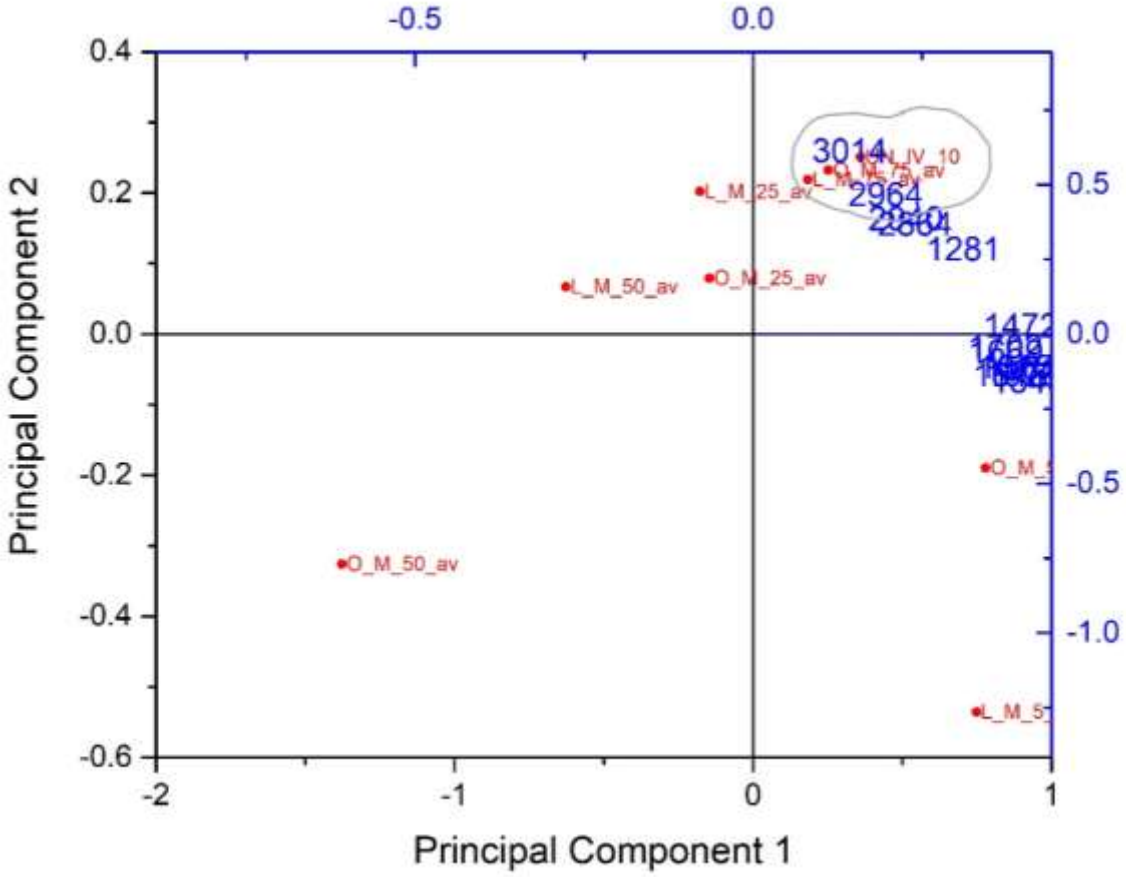

Figure 16: PC1vsPC2 for UN_IV_10.

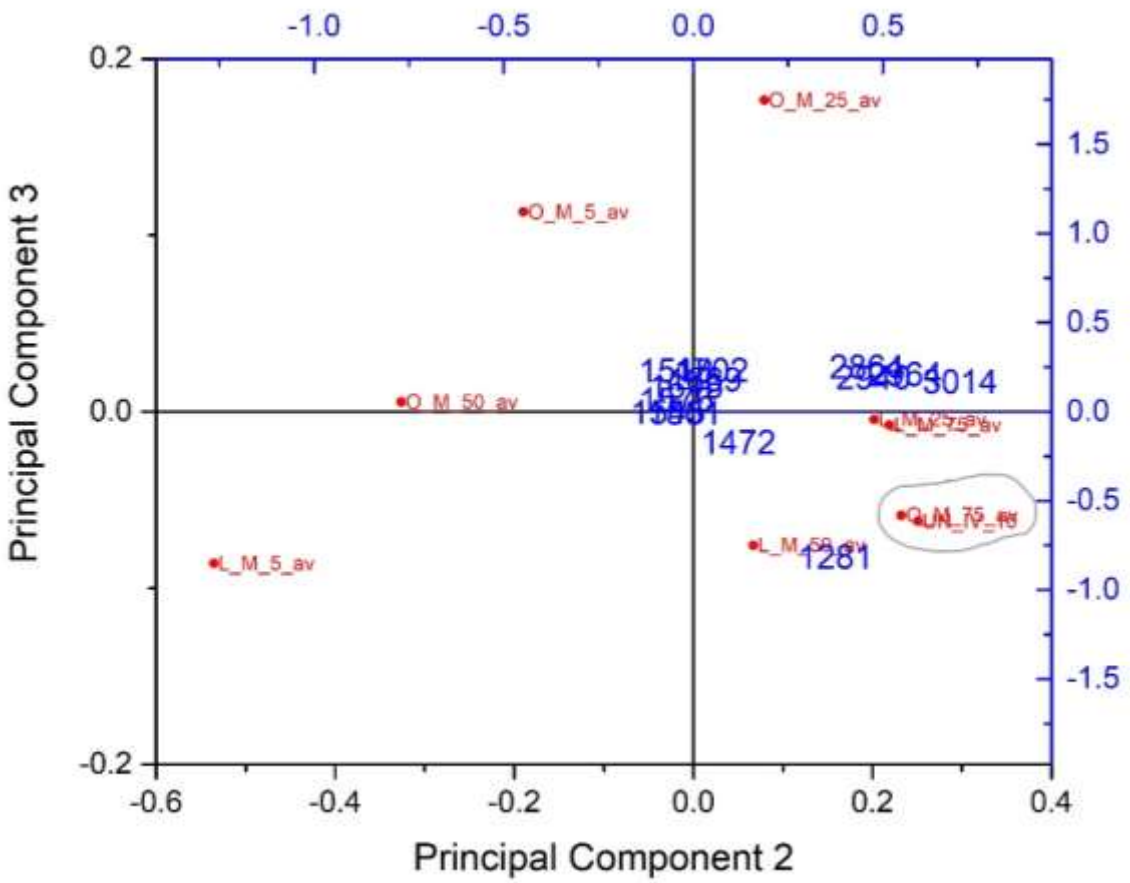

Figure 17: PC2vsPC3 for UN_IV_10.

Appendix III

11.1.1 Polyrrhenia Sampling Locations

Figure 1: The floor of the open cistern after its excavation.

Figure 2: The dark brown-black substance on the surface of the floor of the open cistern.

Figure 3: The stone, related to the wall of the cistern, plastered with mortar.

Figure 4: Detail from the surface of the stone, where the brown-black substance is observed on the mortar.

Figure 5: The low wall between the rock-cut aqueduct and the open cistern.

Figure 6: The surface of the low wall that separates the aqueduct from the open cistern. Dark brown-black substance is observed on the surface.

11.1.2 Phalasarna Sampling Locations

Figure 7: The sampled area on the S wall of the cistern.

Figure 8: The plaster on the interior surface of basin 1.

Figure 9: Surviving mortar from the cistern in the area of Three Hierarchs Church.

11.1.3 Aptera Sampling Locations

Figure 10: Sampling location on the plastered wall of the bathtub.

Figure 11: Sampling from the floor of the 1st aisle (Three-aisled cistern).

Figure 12: Connection of floor to the wall, 2nd aisle (Three-aisled cistern).

Figure 13: The wall surface, 2nd aisle (Three-aisled cistern).

Figure 14: The wall surface, 3nd aisle (Three-aisled cistern).

Figure 15: The wall on the NW section of the gamma-shaped cistern.

Figure 16: The floor and its connection to the wall at the NW section of the gamma-shaped cistern.

11.3 Results

Sample S1 – Cistern Floor - Polyrrhenia

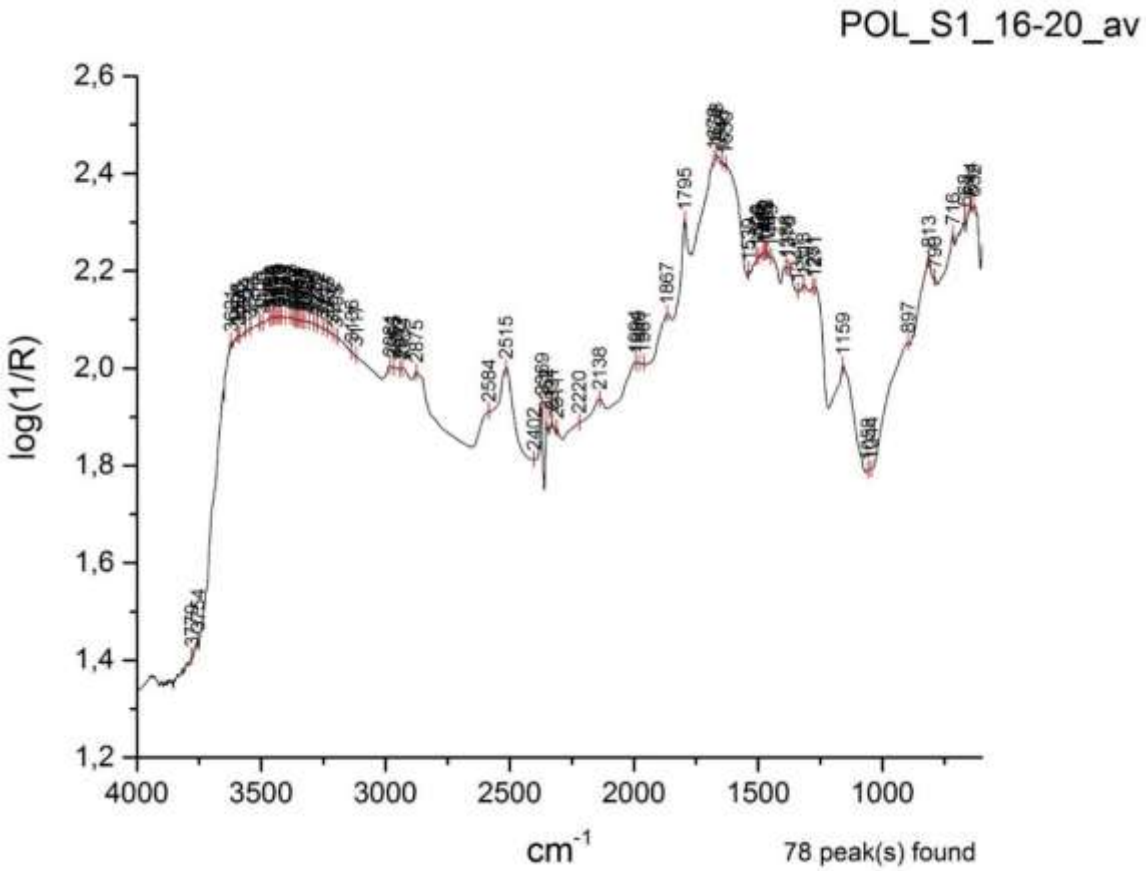

Figure 17: S1 surface layer spectrum (cross-section positioning under the FTIR microscope).

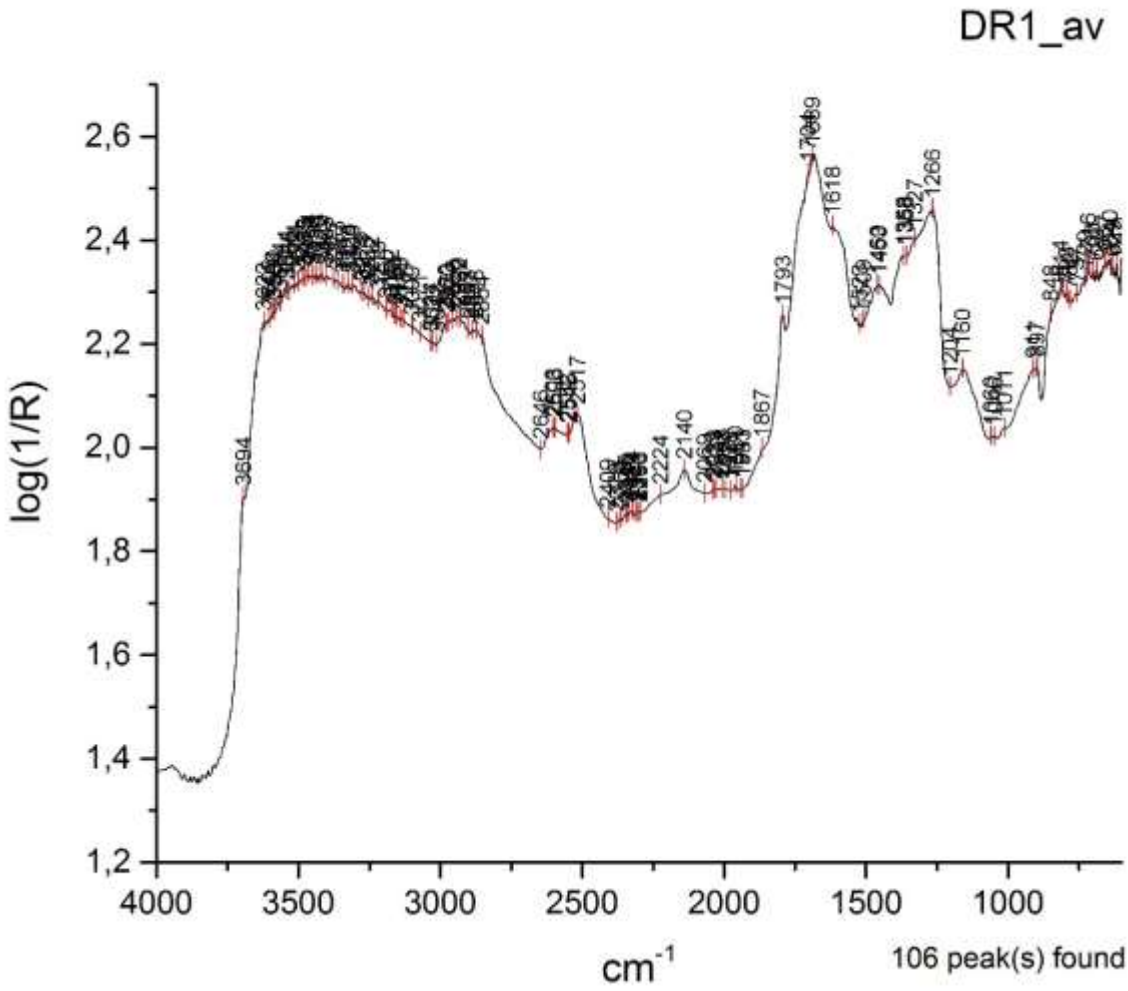

Figure 18: The spectrum of pigeon droppings.

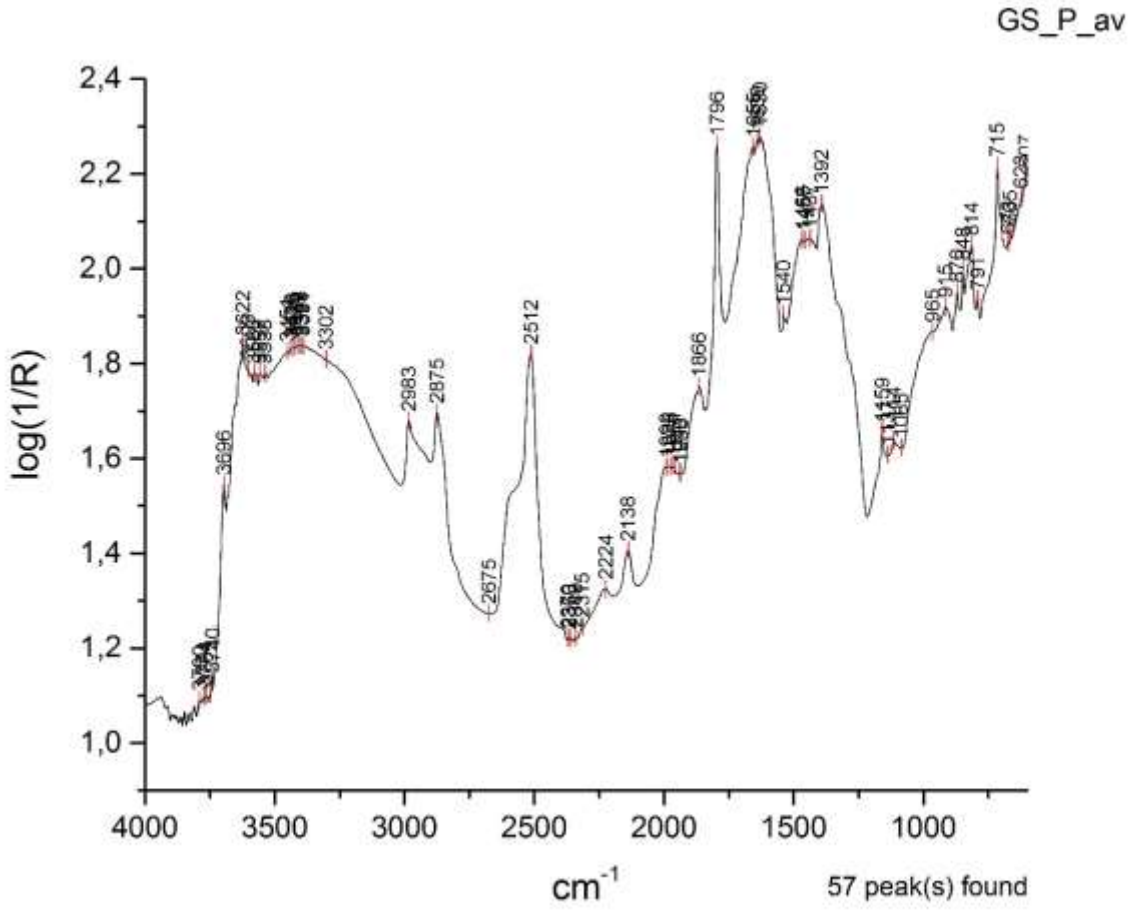

Figure 19: The spectrum of grey soil standard.

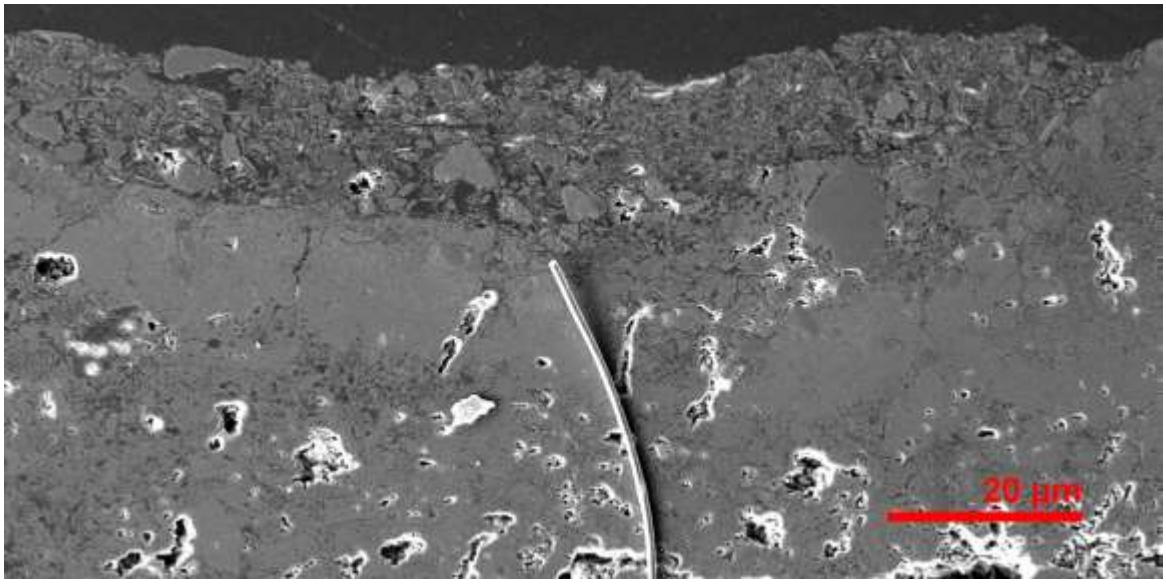

Figure 20: SE image of the polished cross-section of S1.

Sample S2 – Cistern Floor – Polyrrhenia

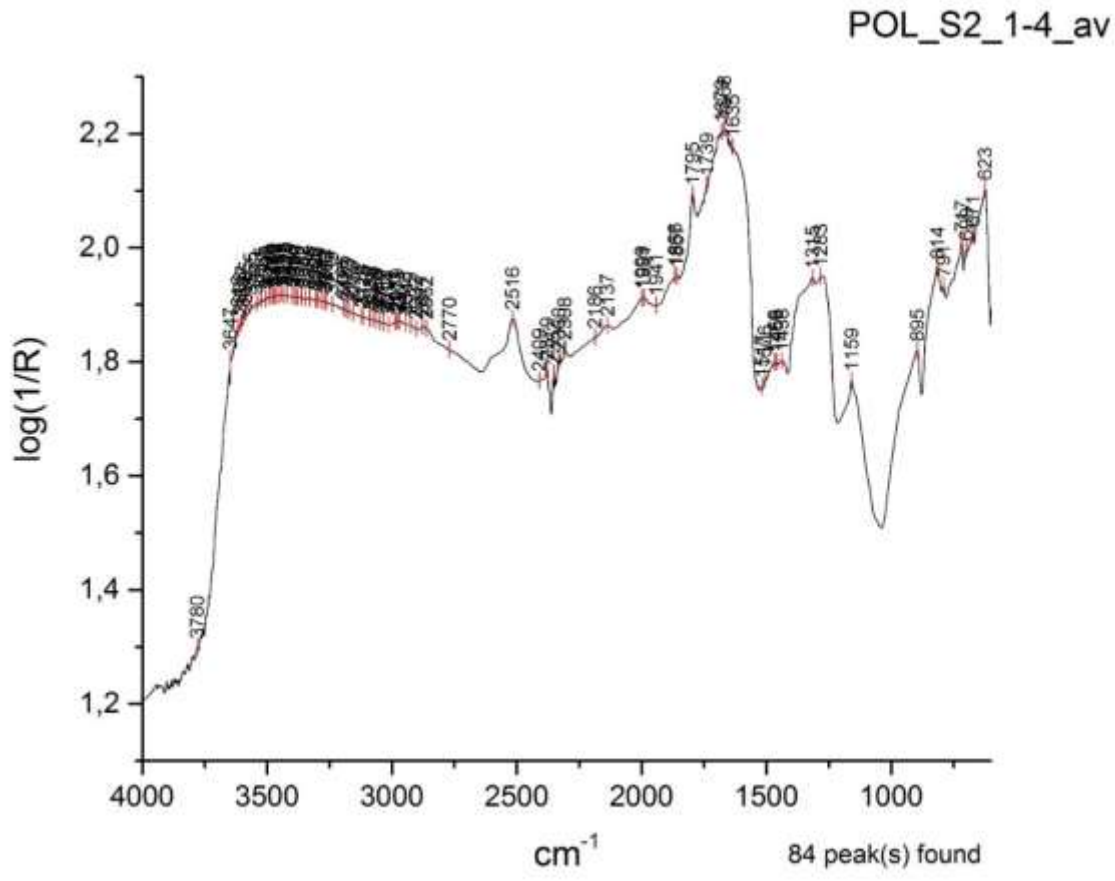

Figure 21: S2 surface layer spectrum.

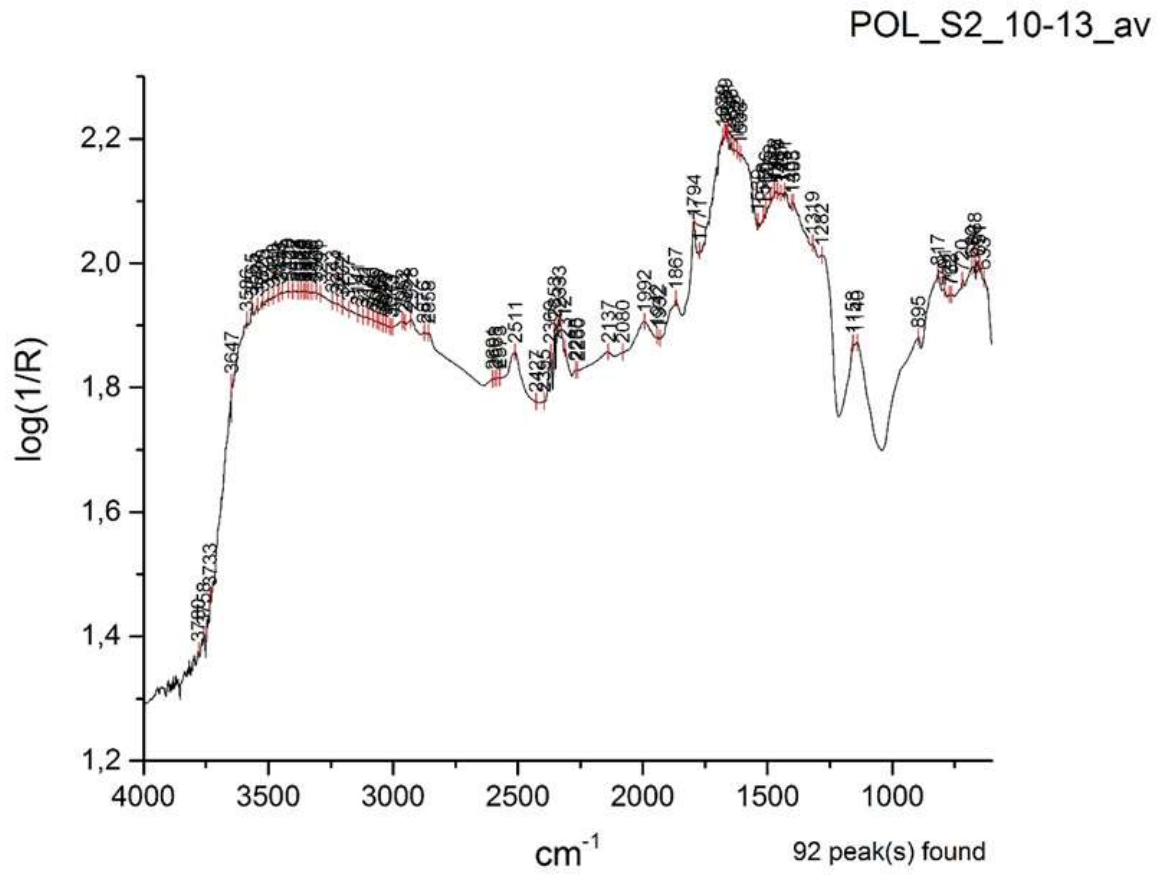

Figure 22: The inverted (I) surface spectrum of S2.

Sample S3 – Cistern Floor – Polyrrhenia

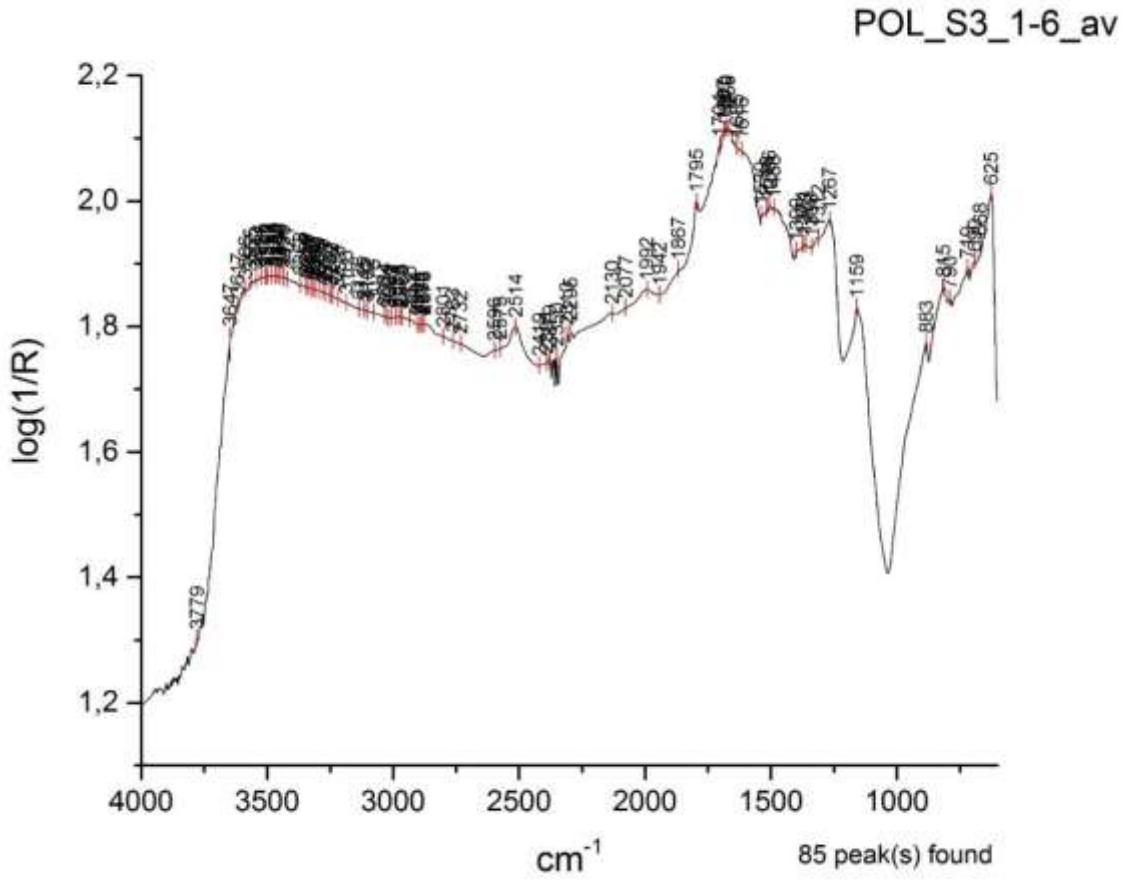

Figure 23: The S3 surface spectrum.

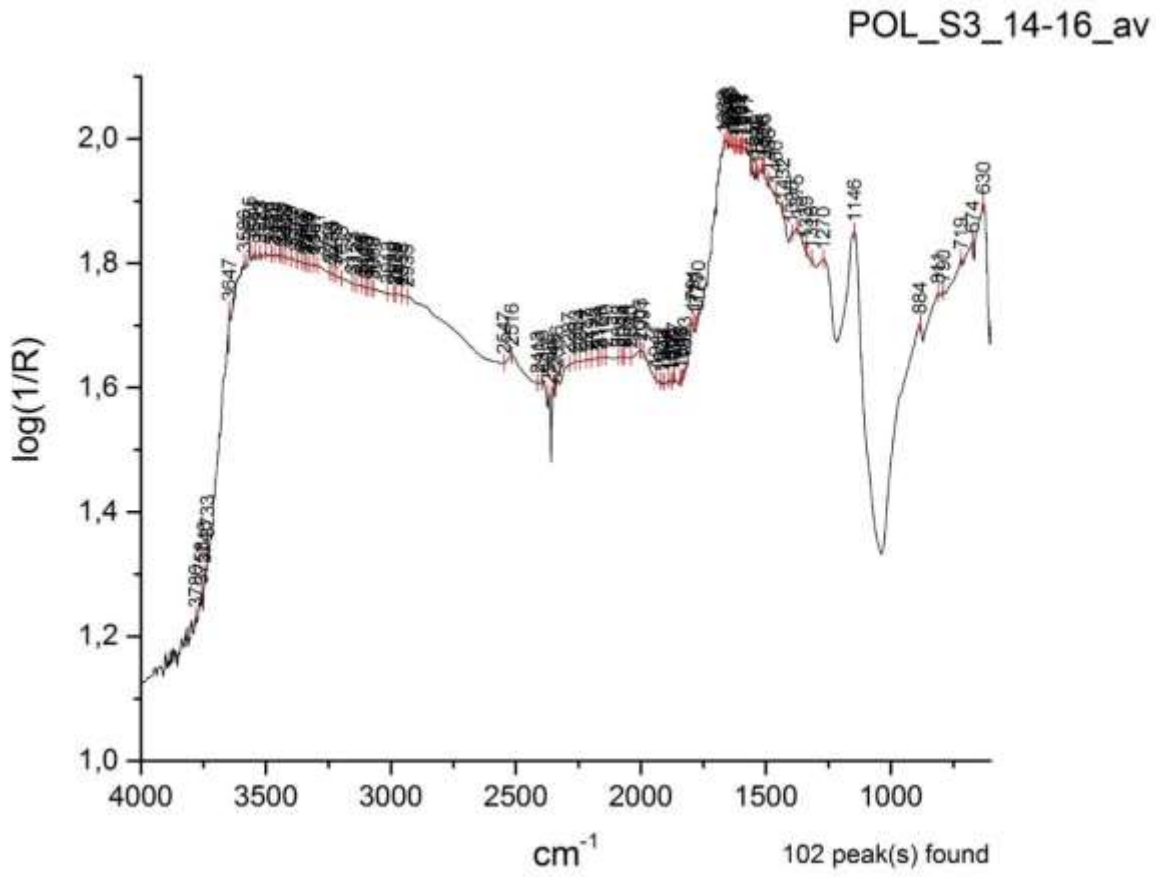

Figure 24: The S3 inverted surface spectrum.

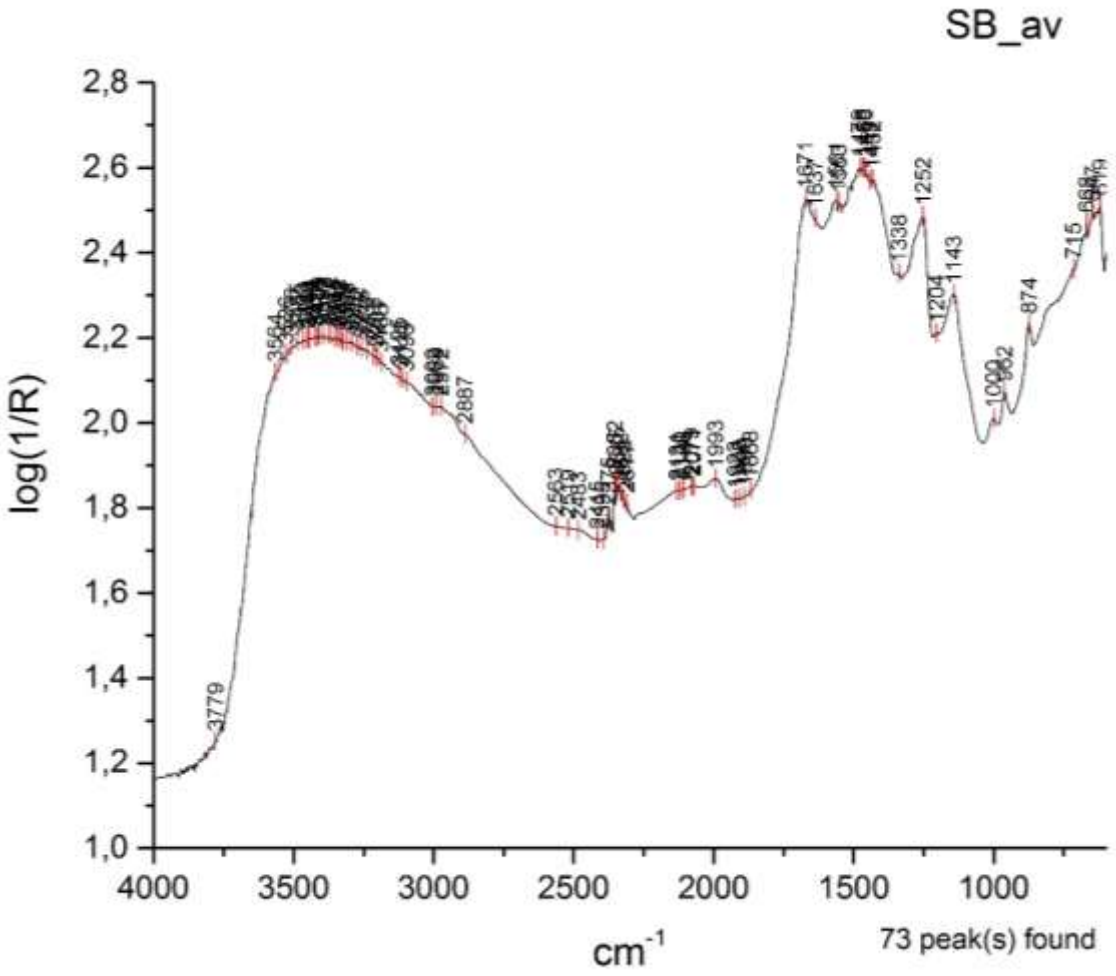

Figure 25: The spectrum of sheep bone standard.

Sample S4 – Mortar on Stone – Polyrrhenia

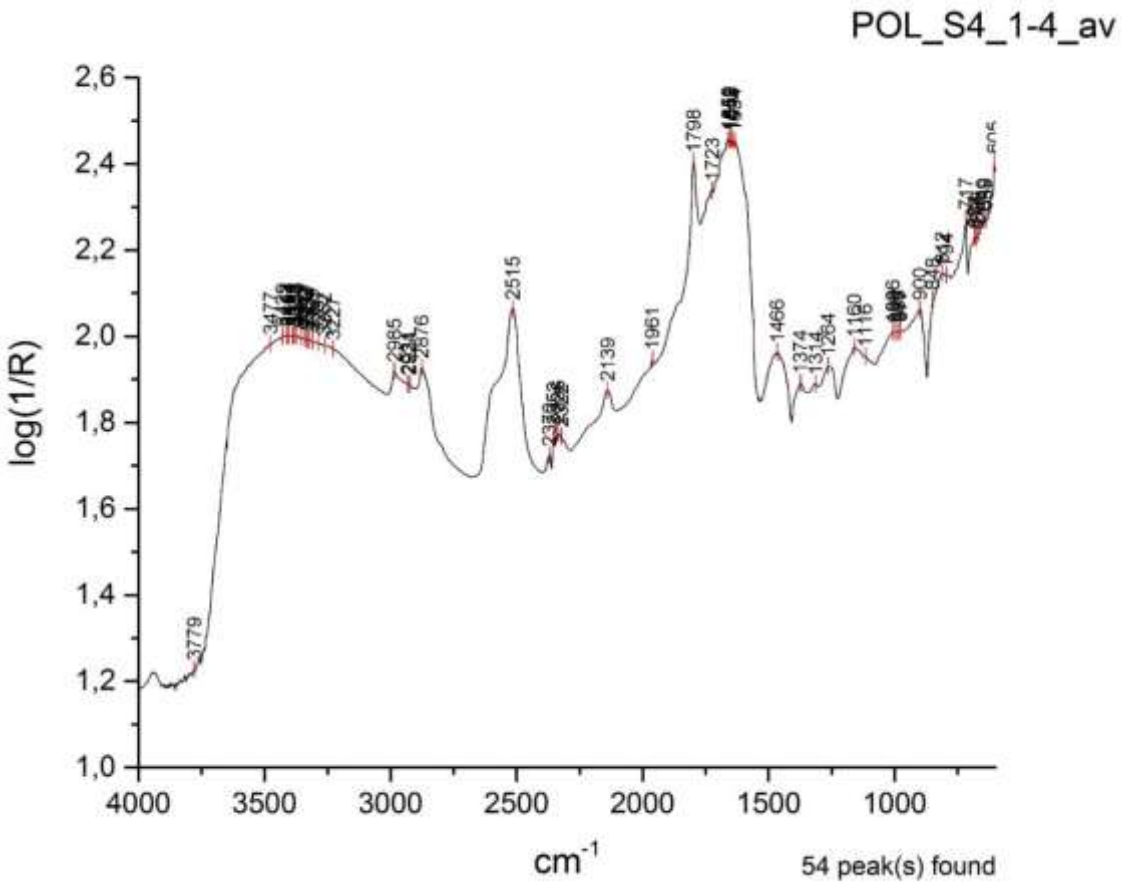

Figure 26: S4 surface spectrum.

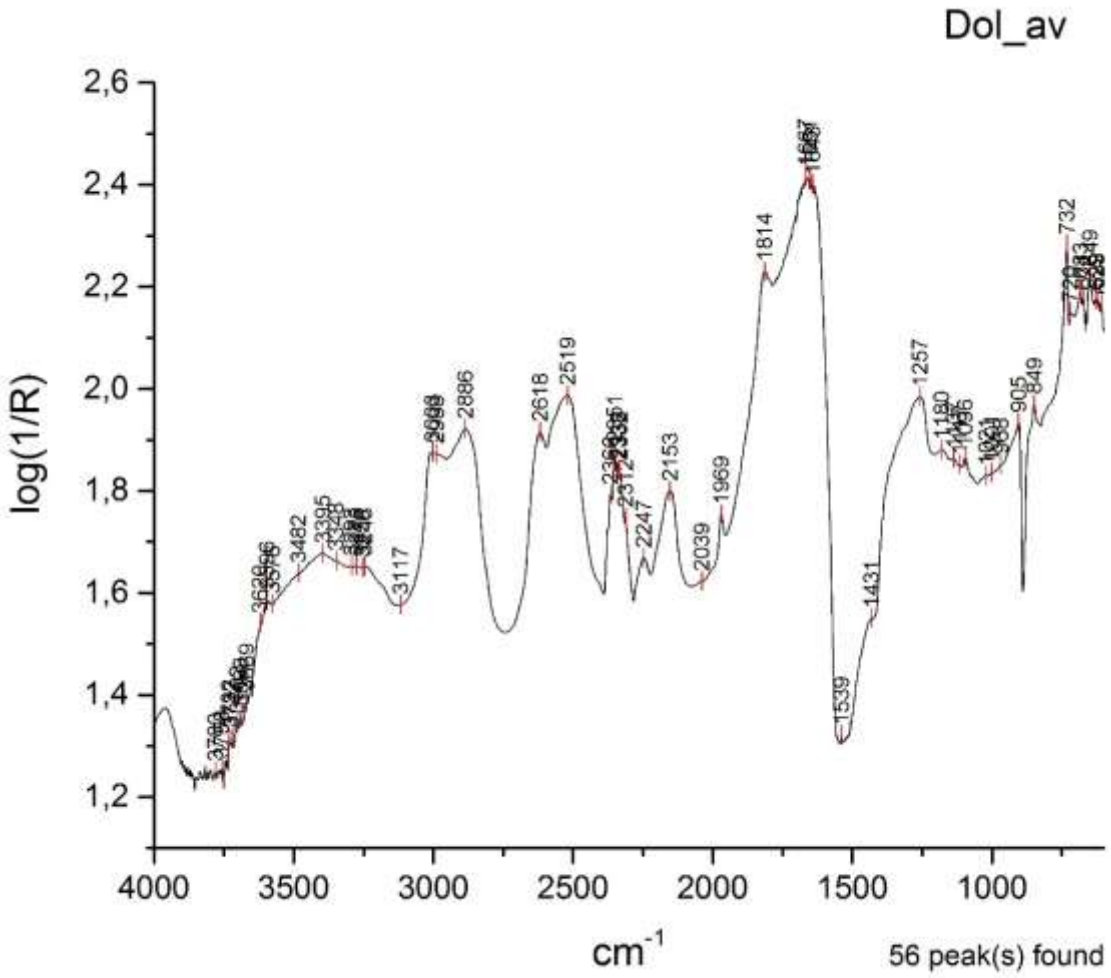

Figure 27: The spectrum of dolomite standard.

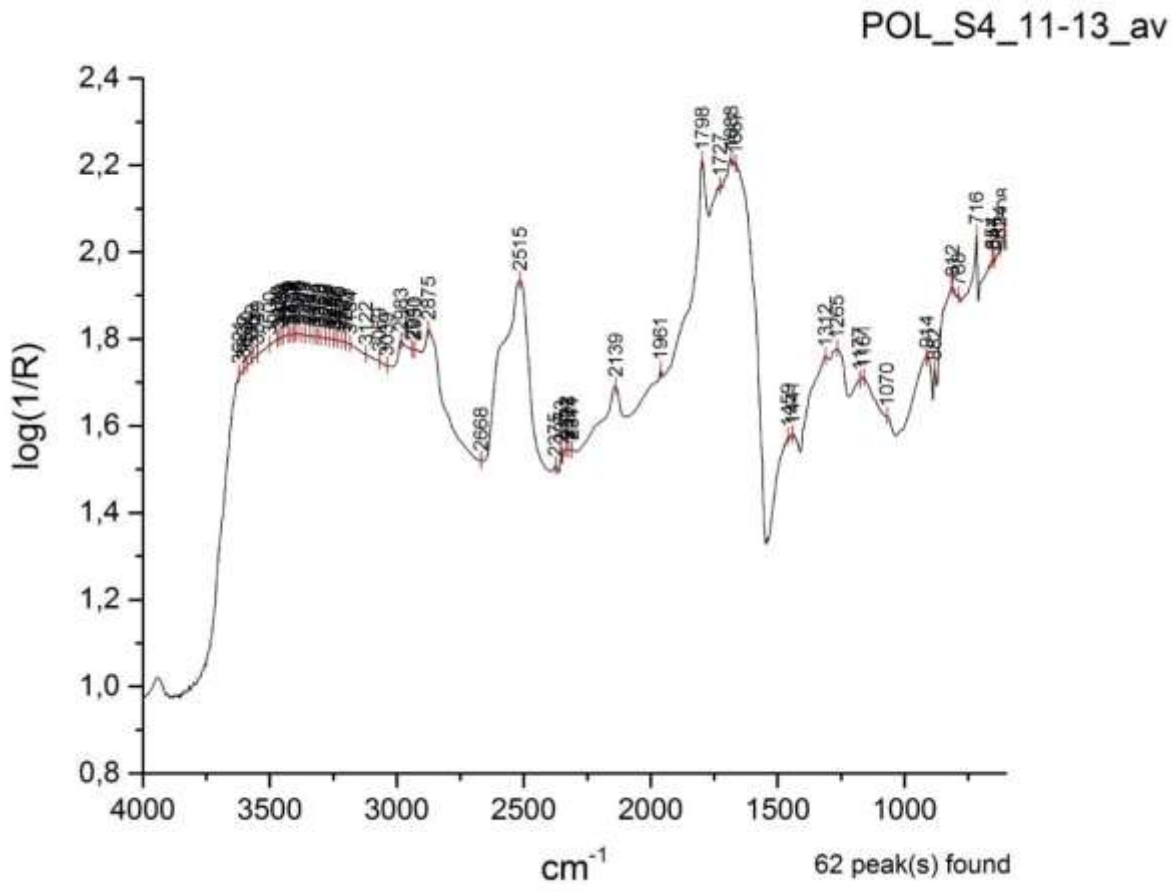

Figure 28: S4 flat surface spectrum (F).

Sample S5 – Mortar on Stone - Polyrrhenia

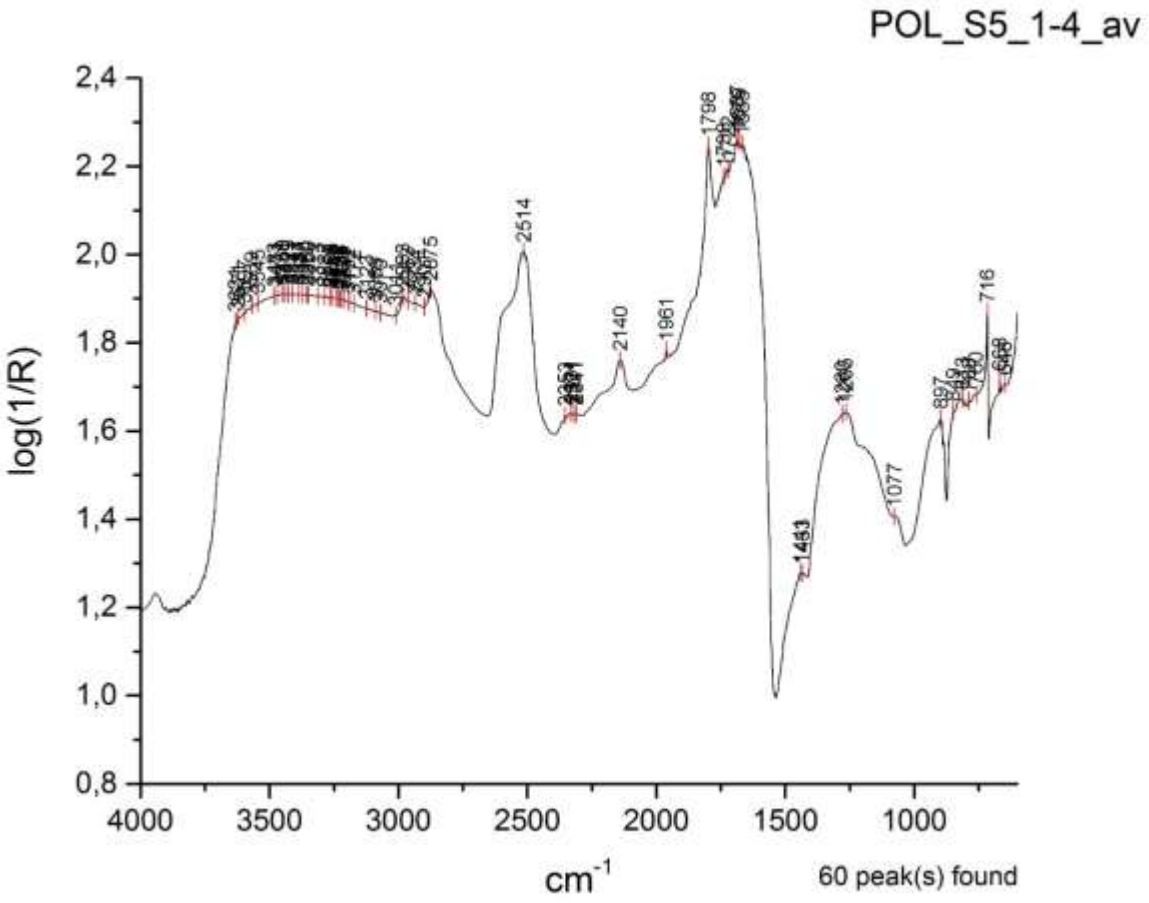

Figure 29: S5 flat surface spectrum.

Sample S6– Mortar on Stone - Polyrrhenia

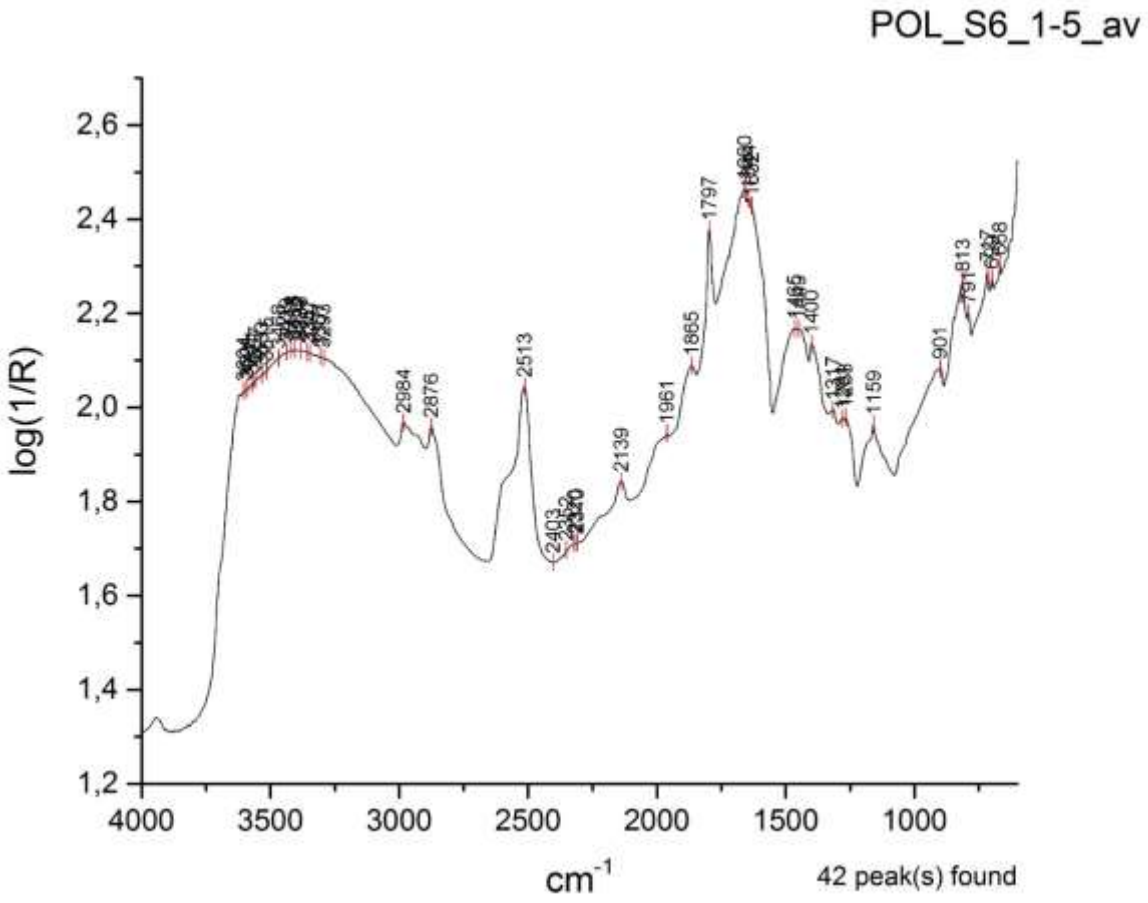

Figure 30: S6 surface spectrum.

Sample S14 – Low Wall between cistern and aqueduct

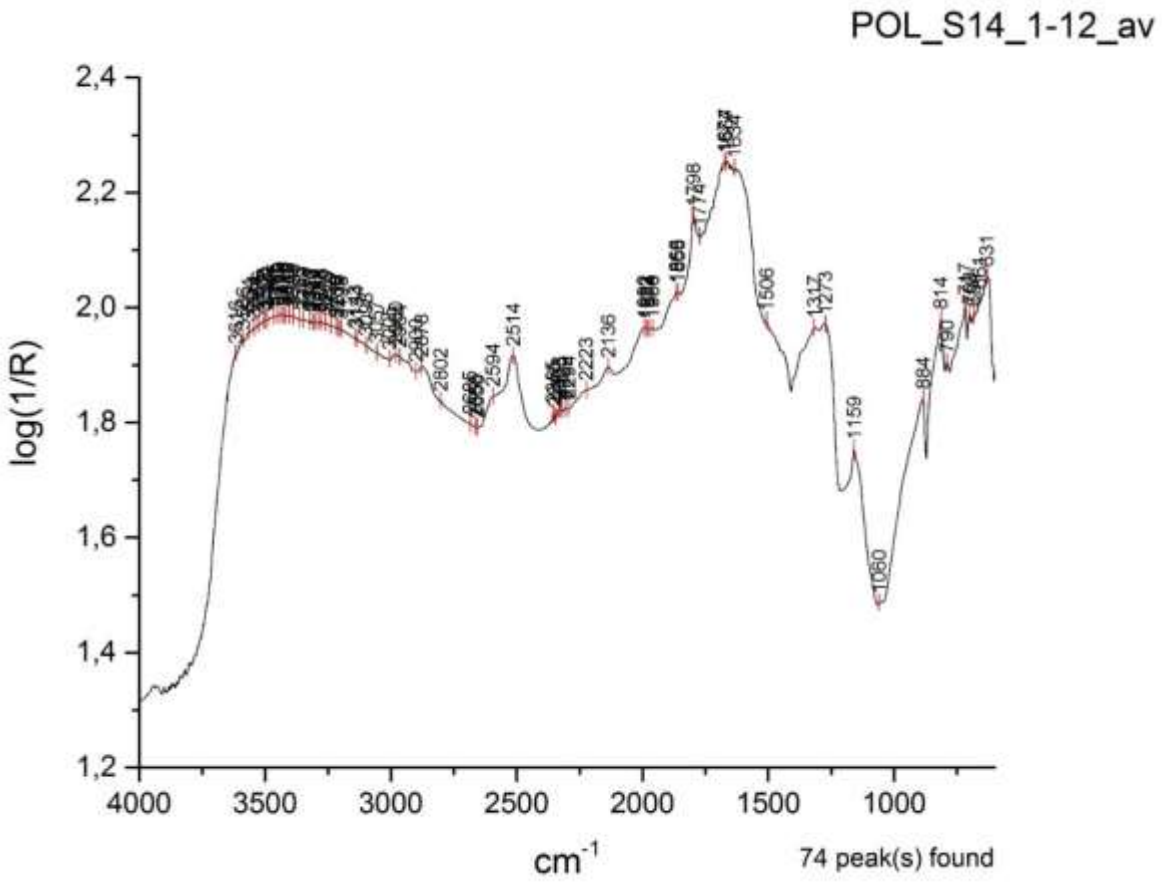

Figure 31: The S14 surface spectrum.

Sample S15a - Low Wall between cistern and aqueduct

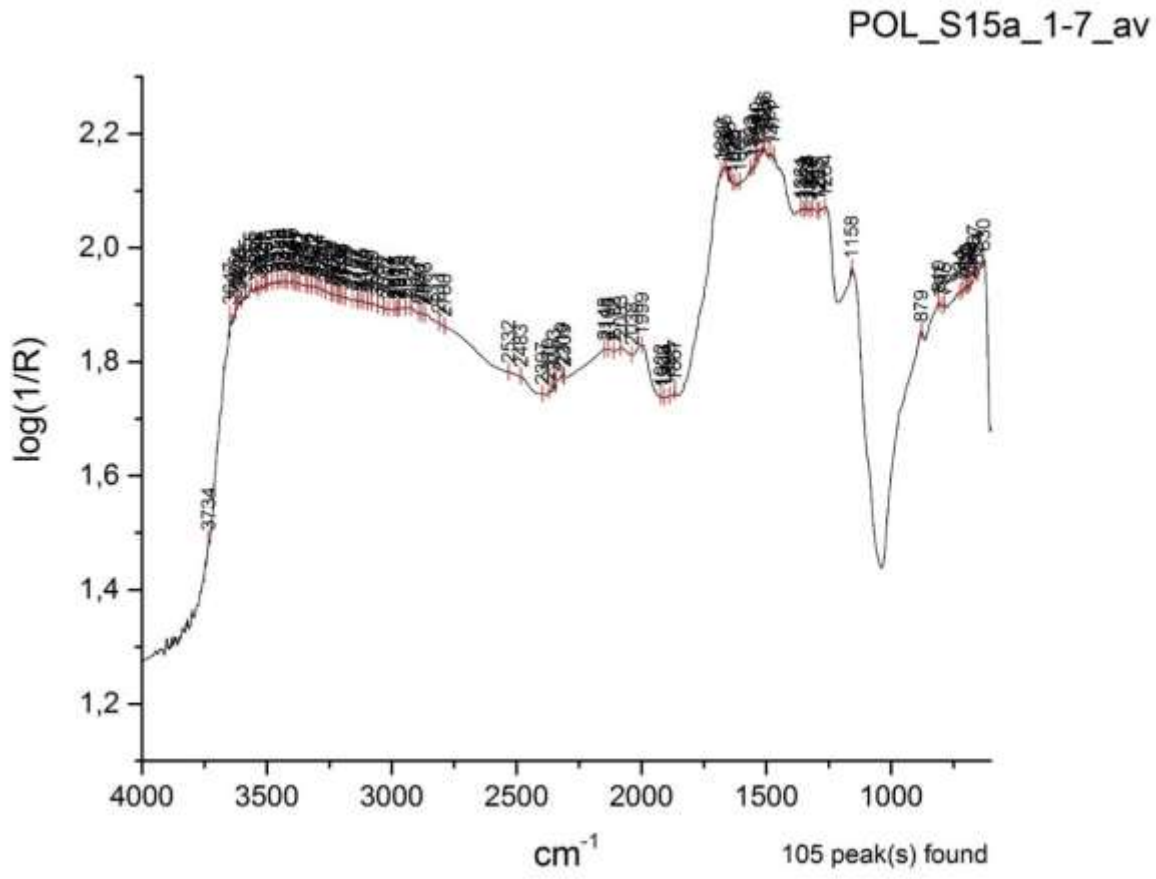

Figure 32: S15a inverted surface spectrum.

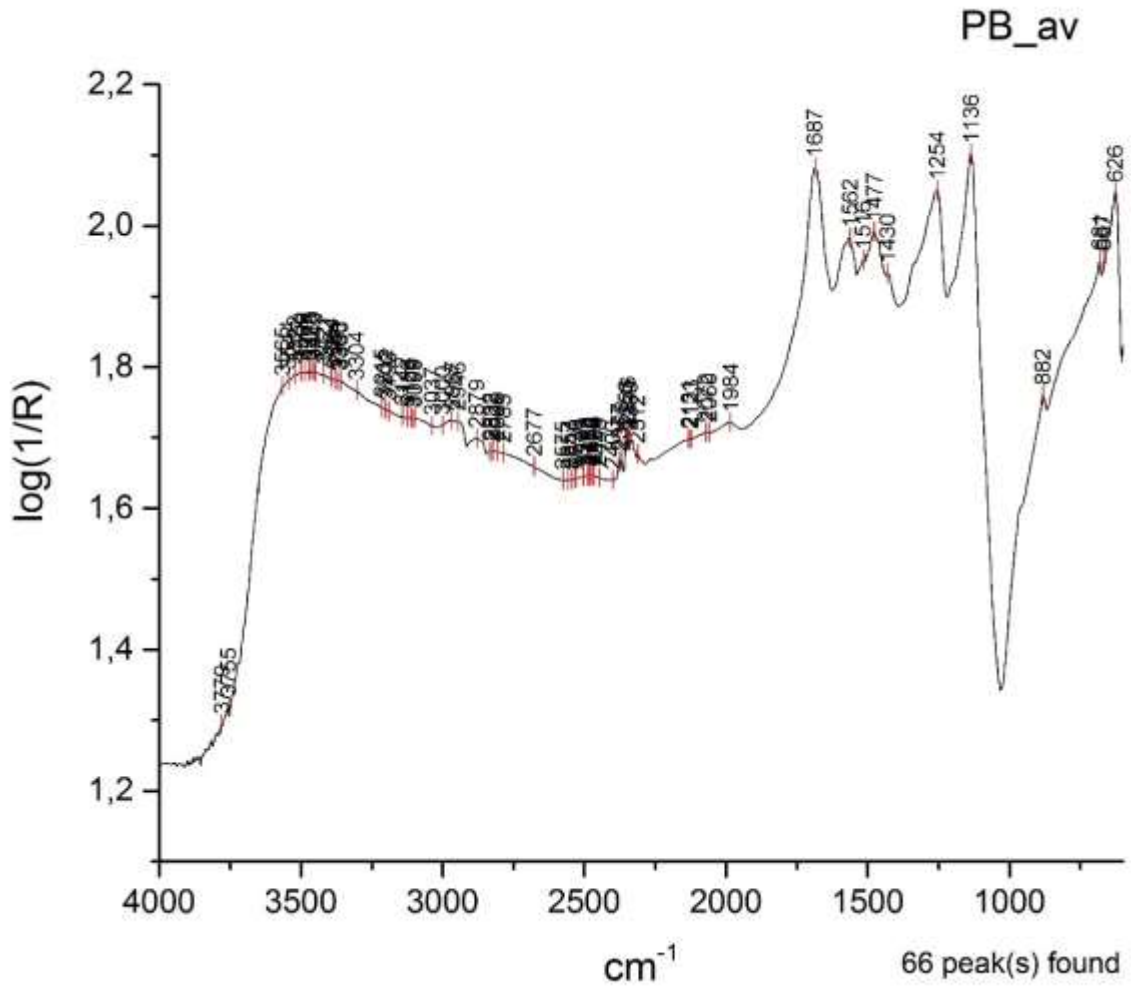

Figure 33: The spectrum of pig bone standard.

Sample S15b - Low Wall between cistern and aqueduct

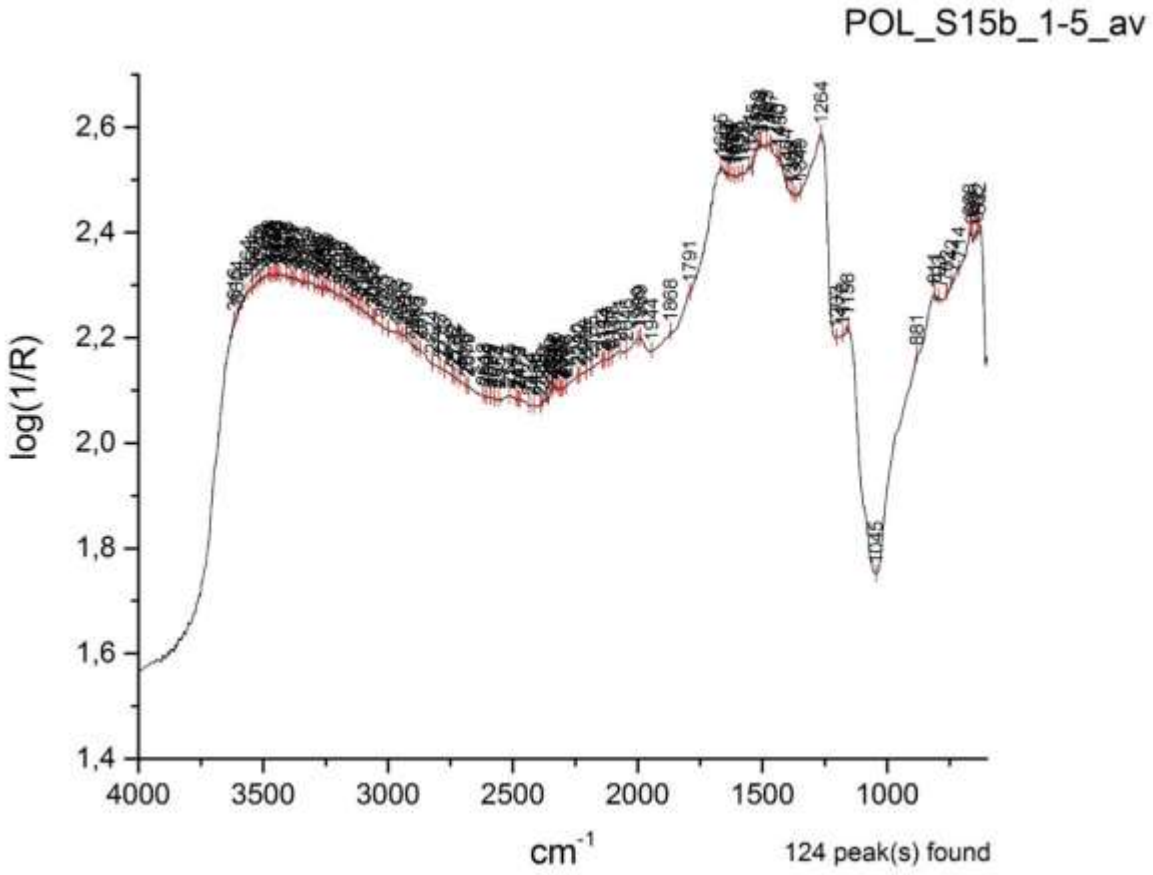

Figure 34: S15b surface spectrum.

Sample S7 – Cistern Wall (South) – Phalasarna

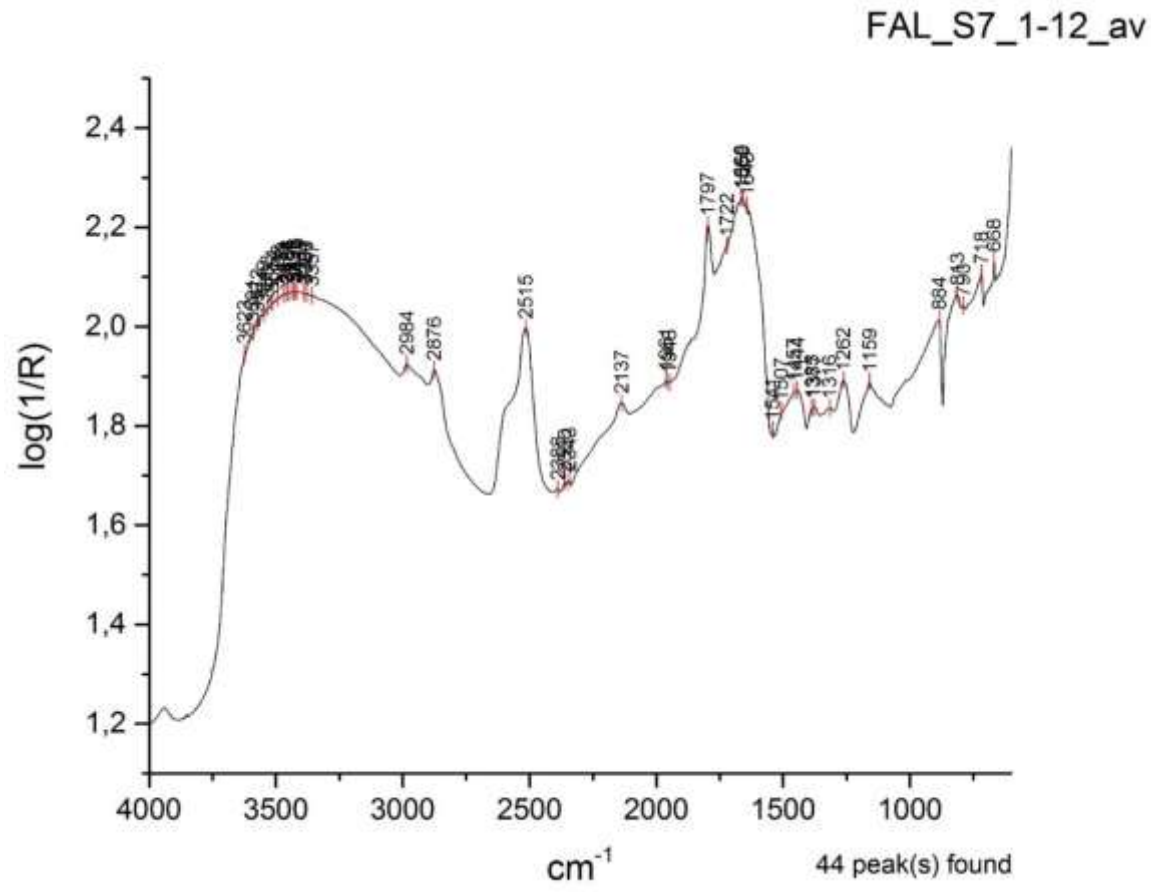

Figure 35: The surface spectrum of S7.

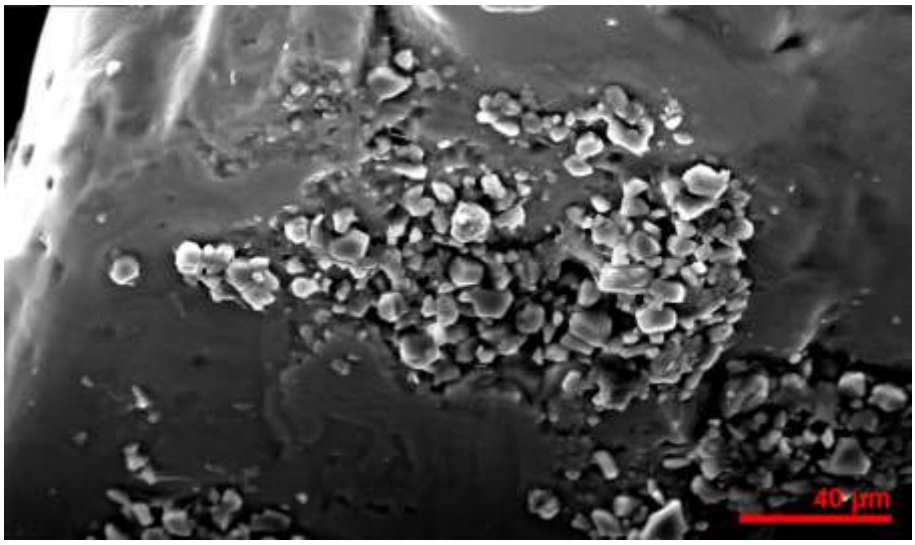

Figure 36: Cubic crystals of sea salt standard.

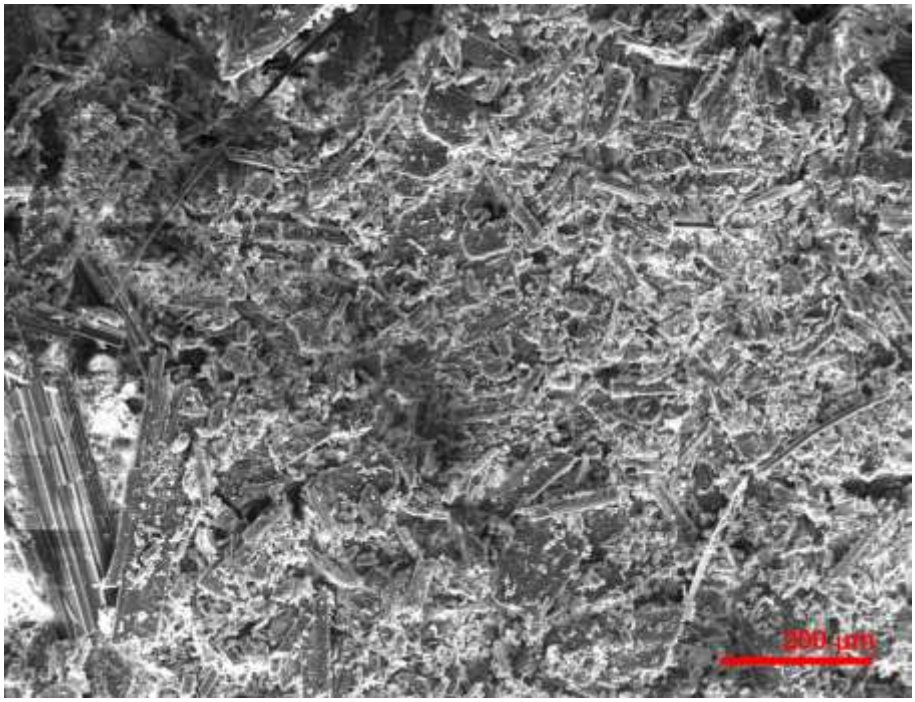

Figure 37: Spike crystals of mineral gypsum.

Sample S9 – Bathtub 1 - Phalasarna

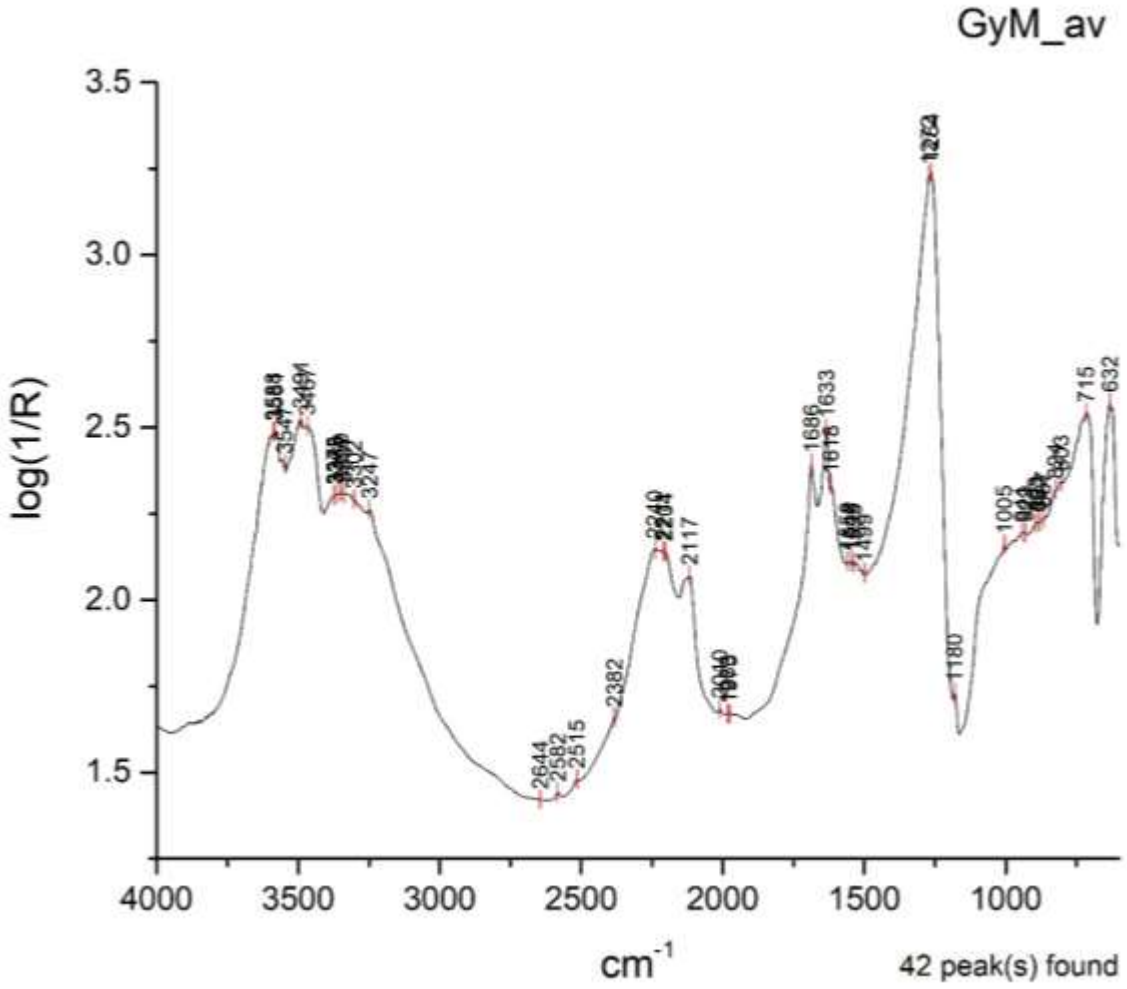

Figure 38: The spectrum of gypsum mineral standard.

Sample S12 – Cistern – Area of Three Hierarchs Church

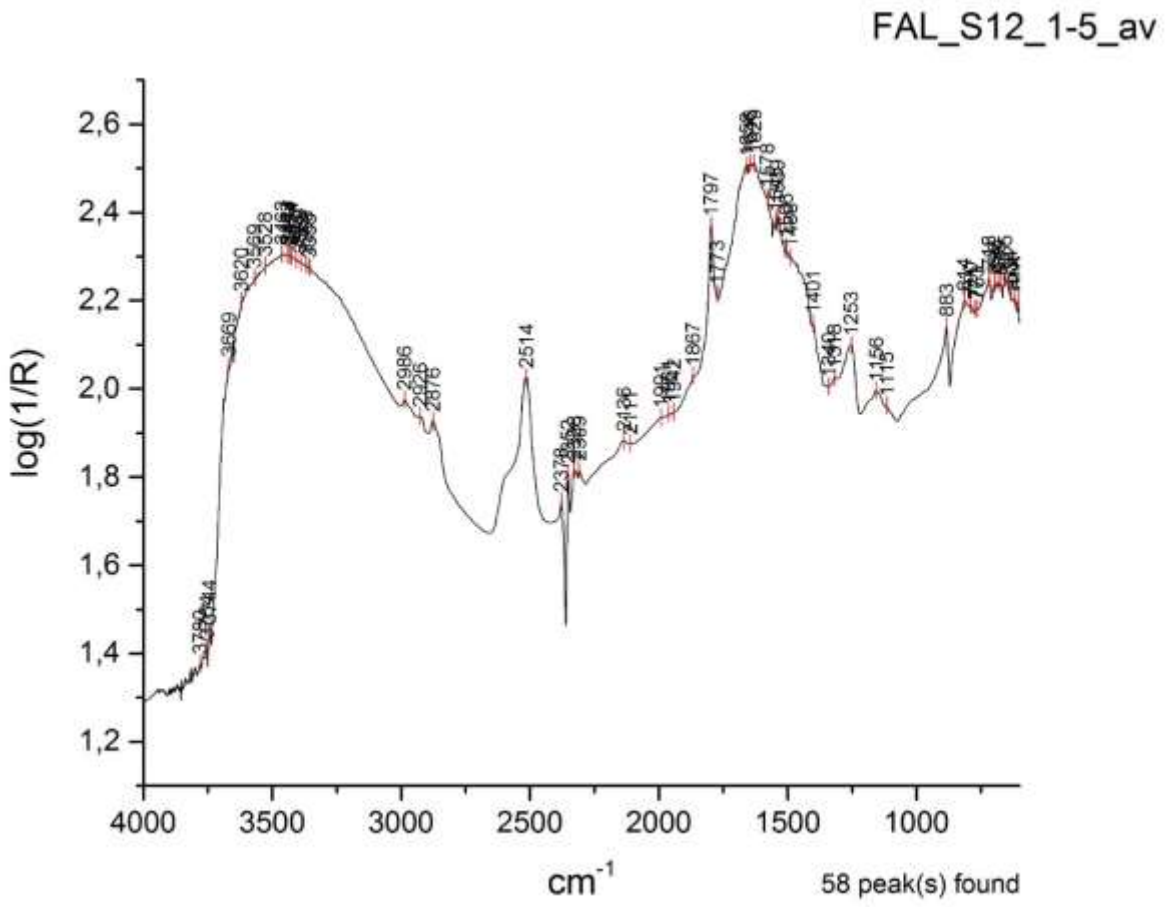

Figure 39: The S12 surface spectrum.

Sample S17 – Bottle Shaped Cistern - Aptera

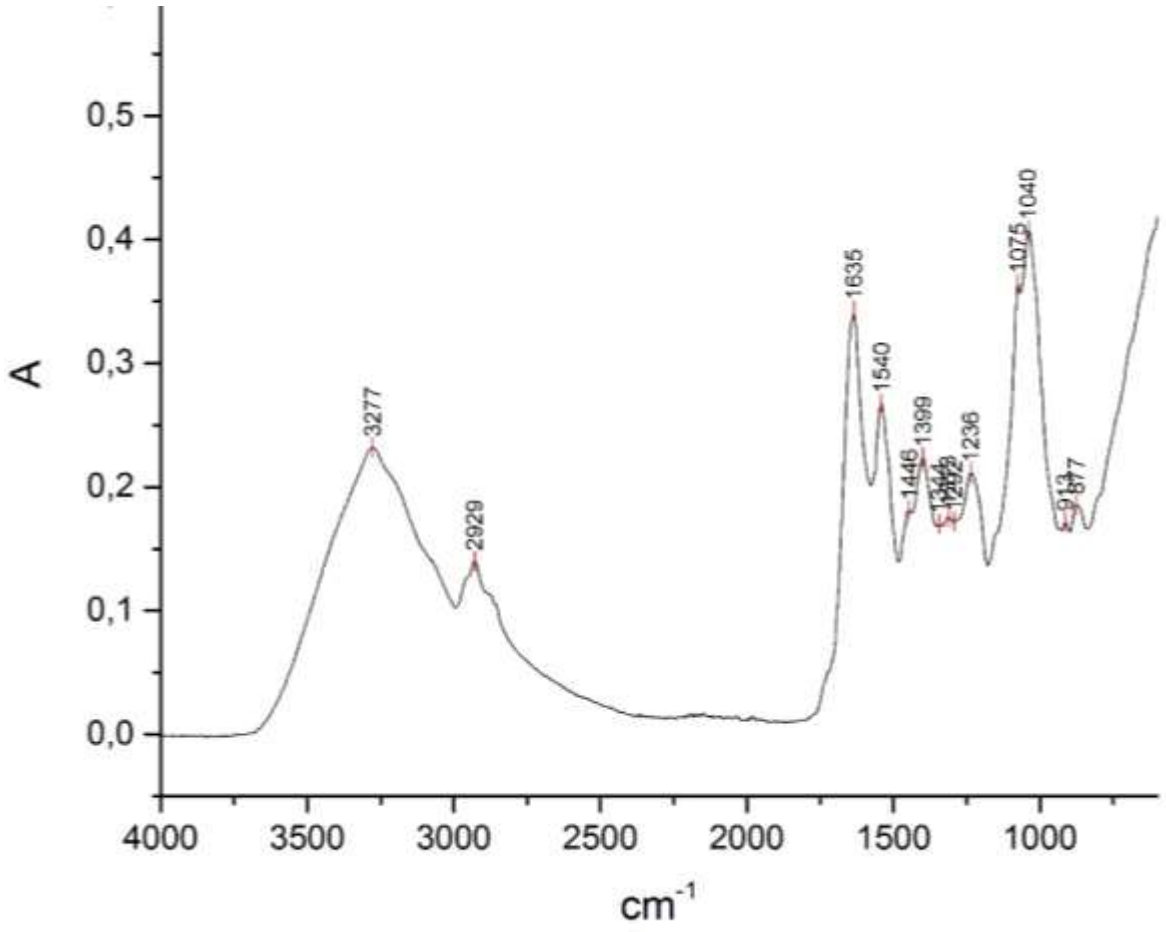

Figure 40: ATR-FTIR spectrum of white mold on bone glue standard.

Sample S19 – Three-aisled cistern - Aptera

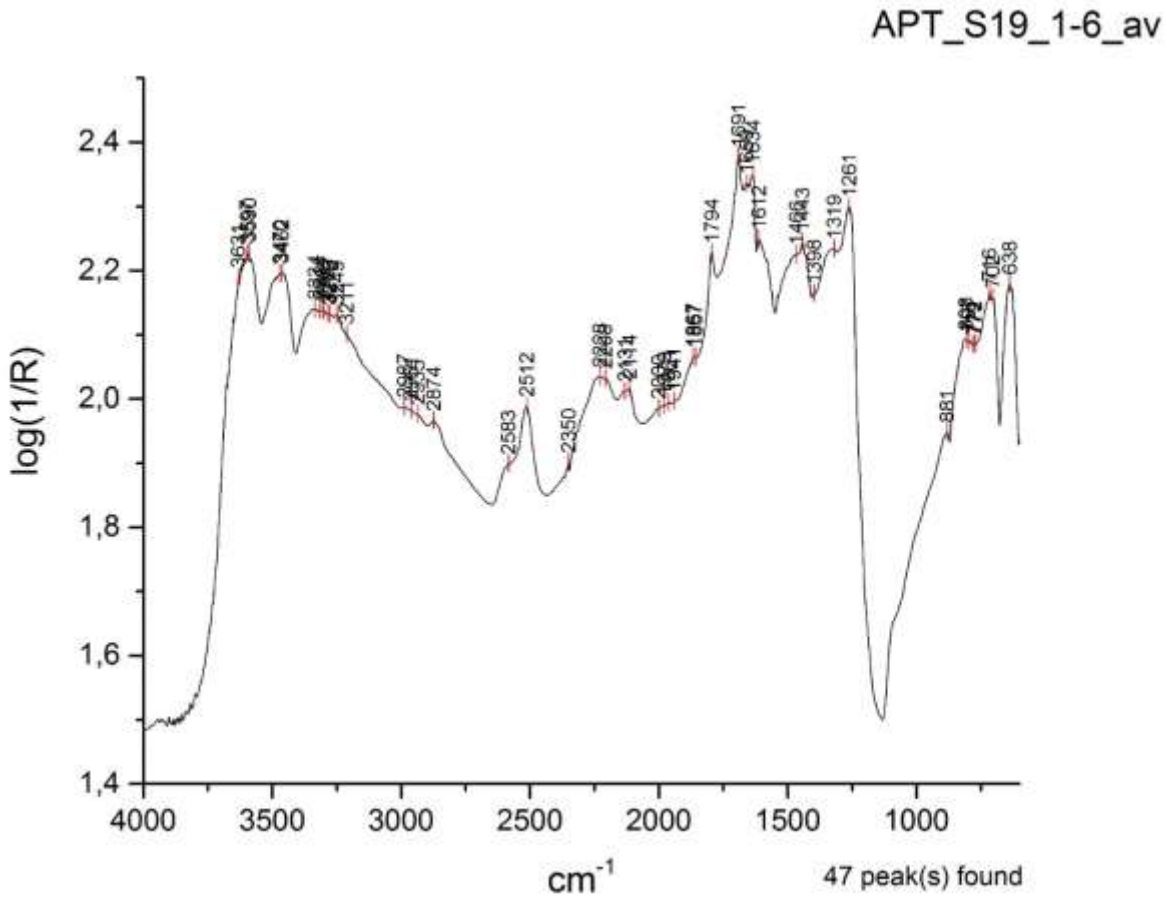

Figure 41: The S19 surface spectrum.

Sample/ Origin / Sampling Location	FTIR - Flat Surface (F)	FTIR - Surface (S)	FTIR - Below Surface (B)	FTIR - Inverted Surface (I)	FTIR - Mortar (M)	OM - Surface	OM - Inverted	OM - Cross-Section	SEM - Surface	SEM - Cross-Section	Outcome
POL_S1 Cistern floor (2nd AD - Roman). Buried in rural soil.	Similar to (S).	Protein at 1044, 1058 (phosphates), 1271-1388, 1472-1539, 1630-1678, 2931-2965 - Egg white/mortar (main), bone glue/mortar resemblance.	Reduced organic compared to surface.	N/A	Mostly lime mortar with ceramic and sand inclusions.	Soil and resinous brown substance underneath soil.	N/A	Thin soil and brown resinous layer over mortar.	Soil similar to GS_av standard, loose fibres on surface, dense and resinous original surface resembles BG_M_25.	Loose upper surface over dense mortar.	Presence of protein on the surface and outest layer. Similarities with Egg White standards. Protein reduces gradualy going inwards. Supported by OM and SEM.
POL_S2 Cistern floor (2nd AD - Roman). Buried in rural soil - surface cleaned with spring water.	High organic presence, 1400 mortar peak absent.	As S1. Egg white spectrum similar shape in 1285 region (egg related protein-lipid indication), weak peak at 2770 appears on both BG_M_50 and E_M_25 spectra.	High inorganic but retains protein in 1265-1535.	1282-1679, 1771, 2858, 2928-3029 show protein. 1771 like EW_M_75 indicating C=O ester of egg.	High inorganic but retains protein in 1265-1535.	Brown resinous substance.	Thick resinous substance different from mortar.	Resinous surface layer over mortar of ceramic inclusions and calcite.	Similarities to BG_M_25 standard, low soil, dense resinous surface, absence of biological activity.	Honeycomb (collagen type) features on S and B layers, dense calcite.	Detected protein (main) and lipid. Similarities with egg related protein (Egg White) on the surface/outest layer. Protein reduces gradualy going inwards. Supported by OM and SEM.
POL_S3 Cistern floor (2nd AD - Roman). Buried in rural soil - same area with S2.	1159 phosphates not quartz. Egg protein due to phosphorous presence. Similarities with Bone glue and BG/mortar standards.	Identical to S2 - 1704 amide, phosphates due to shape at 1159, 2077 and 2801 related to lipids or proteins, BG/mortar standards.	Organic presence still evident mainly at 1339-1395, 1660-1679 and 2936.	VIP: 1146 phosphate, stair-step type intensities 1270-1668, protein peak at 1577. Protein close to egg, 1376 C-H bending lipid. Resembles sheep bone spectrum. 1770-1779 is also seen in EW_M_75.	Mostly lime mortar with ceramic inclusions and sand.	Grey thick soil over homogenous, brown resinous substance that covers the entire surface of mortar.	N/A	As OM surface.	Substance like brush-stroke, cracked in places, smooth wavy morphology that does not resemble either mortar or soil, no biological activity. Similar to egg/mortar standard.	No biological activity, upper layer is darker (not soil but weathered surface layer).	Detected protein (main) and lipid. Similarities with egg related protein (Egg White) on the surface/outest layer. Protein reduces gradualy going inwards. Supported by OM and SEM.

Table 2: Reflectance micro-FTIR, OM and SEM results for each ancient mortar sample.

Sample/ Origin / Sampling Location	FTIR - Flat Surface (F)	FTIR - Surface (S)	FTIR - Below Surface (B)	FTIR - Inverted Surface (I)	FTIR - Mortar (M)	OM - Surface	OM - Inverted	OM - Cross-Section	SEM - Surface	SEM - Cross-Section	Outcome
POL_S4 Mortar on stone related to the cistern wall (2nd AD - Roman). Exposed to rural environment.	High inorganic - low organic. Peaks 914, 1070, 1161-1177 (phosphates) in combinations with strange-shaped peaks at 1265-1459, 1667-1683-1727 and 2930-2941 should indicate some organic.Egg or egg white amide similarities.	Low protein-lipid at 1466-1264, 1634, 1652, 1723 and 2924. Dolomite at 900, 848, 812, 794 and 1006-977. Egg yolk, bone glue/mortar peaks at 1634, 1652 respectively.	Retains some organic and phosphate at the 2924 and 1659-1506 and 969-1007 respectively. 1264-1477 highly affected by mortar components.	N/A	Mostly lime mortar with ceramic inclusions and sand.	Grey layer over white mortar with ceramic inclusions and quartz.	N/A	Thick, light brown to grey outest layer. The color is lighter than that observed at S3.	No biological activity. Loose particles, some cubic, over homogenous, dense surface layer.	Outest layer differs from that of calcite. Not compact layer. Aggregates similar to those in the mortar layer.	Similarities with S1-S3 samples show that surface layer and presence of egg protein-lipid derives from the composition of the sample but reduced due to exposure. Dolomite on surface. Organic reduces towards mortar.
POL_S5 Mortar on stone related to the cistern wall (2nd AD - Roman). Exposed to rural environment - surface cleaned with spring water.	Similar to S4. Organic peaks at 1687-1738, 2901-3011. Pronounced shape of dolomite. Phosphates at 1077, 897 and protein- esters at 1679-1738.	N/A	Reduced organic presence but visible.	N/A	Reduced organic presence but visible.	Thin coherent grey layer.	N/A	As surface OM and similar to S4.	Surface resembles mortar standard. No biological activity.	Coarse thin surface layer.	Dolomite and presence of protein-ester and phosphates. Organic retained in all layers but reduced moving inwards.
POL_S6 Mortar on stone related to the cistern wall (2nd AD - Roman). Exposed to rural environment - same area with S5.	Water cleaning does not affect composition (comparison with cleaned S5). Dolomite and phosphoproteins (less phospholipids) at 1643-1755 and 2912-3026.	Less dolomite than in F spectrum. Egg white similarities, presence of protein-lipids.	Reduced organic presence but visible.	N/A	Reduced organic presence but visible.	Thin coherent grey layer - black spots on the upper mortar.	N/A	S1-S6 all samples show similar mortar.	Compact layer of both amorphous material and particles. Amorphous covers particles. No biological activity.	The upper layer is either deposition or degraded layer.	Dolomite on surface. Presence of protein-ester and phosphates. Organic retained in all layers but reduced moving inwards.

Table 2: continued.

Sample/ Origin / Sampling Location	FTIR - Flat Surface (F)	FTIR - Surface (S)	FTIR - Below Surface (B)	FTIR - Inverted Surface (I)	FTIR - Mortar (M)	OM - Surface	OM - Inverted	OM - Cross-Section	SEM - Surface	SEM - Cross-Section	Outcome
POL_S14 Low wall between cistern and aqueduct (2nd AD - Roman). Inner Part towards aqueduct - Horizontal surface - buried beneath masonry - surface cleaned with spring water.	N/A	Egg and egg yolk related amide-lipid content close to S2 and S3. Phosphates or sulfates linked to egg. Lack of strong absorption at 1064 show no fungal activity and relates all the organic peaks to egg.	Organic presence close to that of surface.	N/A	Reduced organic presence but visible.	Dark grey layer similar to S4-S6 samples.	N/A	Thin layer. Black spots grow or move inwards through fissures. Large aggregate quartz particles in mortar.	No organic indication, no biological activity, wavy pattern shows accumulation of deposits.	2 surface layers: one thin and dense, one thinner and less dense on the outest surface. Round particles should be the black spots.	Egg related coating, decreased but present in mortar layer. Probably better preserved due to burial. Close to cistern floor spectra.
POL_S15a Low wall between cistern and aqueduct (2nd AD - Roman). Outer Part towards cistern - Horizontal surface - buried beneath masonry - surface cleaned with spring water.	Similar to inverted spectrum, pig bone resemblance, protein peaks, phosphates.	N/A	Retains protein although reduced but no resemblance to bone.	Similar to sheep bone 1999-2148, 2010 (bone black diagnostic), 2483, 1338. Egg white, bone glue and mortar mixtures similar peaks at 1264-1295. Amides are present in 1471-1680 (bone glue mortar mixtures). No lipids. CaCO3 almost absent.	Retains protein but no resemblance to bone, more calcite present.	Subsequent accumulated layers, probably deposits of calcite (slit). Dark grey to black surface.	Very dense black layer. Some areas similar to S1, S2 and S3.	Dense and thin surface.	Smooth surface preserved locally. Exposed mortar (the right hole) coarser than upper layer. Redeposition of calcite like in OM. Cracked crust incorporates or covers round particles. No biological activity.	Upper surface layer detached from the mortar. S14 and S15a thin layer of surface coating(?) below upper layer of accumulation or by product of the original layer.	Protein based material on the surface, highly similar to bone standards spectra, no indication of biological activity. Reduces going towards mortar. Supported by OM and SEM.

Table 2: continued.

Sample/ Origin / Sampling Location	FTIR - Flat Surface (F)	FTIR - Surface (S)	FTIR - Below Surface (B)	FTIR - Inverted Surface (I)	FTIR - Mortar (M)	OM - Surface	OM - Inverted	OM - Cross-Section	SEM - Surface	SEM - Cross-Section	Outcome
POL_S15b Low wall between cistern and aqueduct (2nd AD - Roman). Outer Part towards cistern - Horizontal surface - buried beneath masonry - surface cleaned with spring water - different texture from S15a.	Some presence of mortar, protein related to bone (due to peak shape) although 1257-1390 is absent.	Similar to S15a, weak mortar peaks, phosphates-amides, similar to pig bone (and BG and EW films and mortar mixtures).	Retains protein although reduced but no resemblance to bone.	Very high resemblance to pig bone standard and high content of protein. Mortar peaks are almost absent.	Retains protein but no resemblance to bone, more calcite present.	Calcite accumulation or differential decay of surface layer.	N/A	Large silica aggregates, black spots also within mortar layer and even in the ceramic pores.	No biological activity. Similar to mortar standard. Some evidence of differential decay of thin surface layer under accumulated layers.	Dense and coherent, mainly calcite surface, some similarities of particles to pig bone standard.	Protein based material on the surface, highly similar to bone spectra, no indication of biological activity. Reduces going towards mortar.No calcite sediments from water on the surface. Supported by OM and SEM.
FAL_S7 Cistern wall (4th BC - Hellenistic). From the S wall - exposed to marine environment since the 80s excavation.	Dolomite reststrahlen in 909-819 and 1961 peak. Protein-phosphorous at 1085-1160. Lipid resembling egg peaks (not the shape so much) due to 1755-66 peaks C=O of esters, and amides at 1659-1738. 1268-1372 and 2929 also organic (egg protein).	Almost identical to POL_S4. 1262-1722, 1507-1541 protein-lipid content, similar to egg white and yolk. 1961 is dolomite. As protein concentration decreases 1690 and 1570 merge into one broad peak at 1640-1670. High water content.	Organic presence similar to that of surface.	N/A	Low organic, strong amide peak at 1263.	Dark almost black surface layer covered by thick whitish crust. Surface layer dense but cracked.	N/A	As in surface OM. Black layer fades out as it moves inwards.	Surface covered by cubic sea salt and spike crystals of gypsum. Smooth brush stroke-like area pushed upwards due to salts. The surface looks homogenous. It resembles standards of mortar mixture with organic. No biological activity.	Similar to the surfaces of the POL samples. Salts visible also in the mortar. Distinct surface layer.	Dolomite and presence of protein-ester and phosphates. Similarities with egg white and yolk standards. Organic retained in all layers but reduced moving inwards. Supported by OM and SEM.

Table 2: continued.

Sample/ Origin / Sampling Location	FTIR - Flat Surface (F)	FTIR - Surface (S)	FTIR - Below Surface (B)	FTIR - Inverted Surface (I)	FTIR - Mortar (M)	OM - Surface	OM - Inverted	OM - Cross-Section	SEM - Surface	SEM - Cross-Section	Outcome
FAL_S13 Cistern wall (4th BC - Hellenistic). Loose piece from the N wall - exposed to marine environment since the 80s excavation.	N/A	N/A	The reststrahlen 1256 is lipid C-O. Possible coexistence of amides and some lipid. 1320 some lipid content and 1400-1652 mainly protein. Low organic mortar mixtures of milk and egg show similarities.	N/A	N/A	Lime-quartz-crushed ceramics mortar.	N/A	N/A	Mortar, sea salt crystal growth and aluminosilicates from the aggregates.	N/A	Mainly mortar with low indication of protein and lipid. Simlar to egg related protein (mortar below surface).
FAL_S8 Bathtub 1 (4th - 3rd BC - Hellenistic). Seat - exposed to marine environment.	1390-1540, 1444-1659 and 2937 similar to EW_M_5. Dolomite indication.	N/A	N/A	N/A	Very thin sample. Mainly mortar peaks, 1507 and 1633-1643 organic retention.	Thick whitish crust covers almost the entire surface. This crust resembles that seen in S7. A dark layer underneath is visible.	N/A	Very thin sample. White, thick crust, fine calcite layer, quartz mixed with lime in the lowest layer.	Sea salt and spike crystals of gypsum.	Sea salt and spike crystals of gypsum over fine calcite layer.	Organic presence similar to egg related protein, thin layer overall.
FAL_S8_10 Bathtub 1 (4th - 3rd BC - Hellenistic). Black area on the surface.	Dolomite, region between 1755-1444 high ester and protein content. Same stands for 2943-2925.	N/A	N/A	N/A	N/A	N/A	N/A	N/A	N/A	N/A	Presence of lipid-protein and dolomite.

Table 2: continued.

Sample/ Origin / Sampling Location	FTIR - Flat Surface (F)	FTIR - Surface (S)	FTIR - Below Surface (B)	FTIR - Inverted Surface (I)	FTIR - Mortar (M)	OM - Surface	OM - Inverted	OM - Cross-Section	SEM - Surface	SEM - Cross-Section	Outcome
FAL_S9 Bathtub 1 (4th - 3rd BC - Hellenistic). Bottom - exposed to marine environment.	Gypsum mineral, low calcite, protein in 1310-1540, 2991 and the strong peak at 1600. No biological activity. 1600 amide of egg. Bone glue and eggs and their mortar mixtures similarities.	N/A	N/A	N/A	Low organic, strong amide peak at 1632, CH stretching.	Dark layer underneath whitish crust due to high quartz content. Very thin sample.	N/A	Fine calcite upper layer is lost, exposing quartz. Whitish cruct covers entire surface. Dark substance in-between.	Gypsum and salt crystals, no biological activity, mainly mortar texture underneath.	Spikes growth on the white crust. Some indication of organic or bone texture (similarities with standards) on the surface.	Organic presence similar to egg related protein, thin layer overall. Protein in all layers.
FAL_S9_6 Bathtub 1 (4th - 3rd BC - Hellenistic). Black area on the surface.	Dolomite. Phosphate-lipid content. 788-1800, 2712, 2802-2931 show mainly C-H stretching that is also found in asphalt.	N/A	N/A	N/A	N/A	N/A	N/A	N/A	N/A	N/A	Mainly lipid and dolomite aggregate.
FAL_S10 Bathtub 3 (4th - 3rd BC - Hellenistic). Side wall - exposed to marine environment.	Gypsum, mortar and protein at 2939 and 2992, 1770, in between 1692-1640, 1606 (egg), 1540-1280.	N/A	N/A	N/A	Protein is indicated at 1275, 1643, 1659, and 2881-2988. Mainly calcite, some sulphates.	Whitish crust accumulation over quartz particles.	N/A	Fine layer of calcite followed by a mortar of calcite and quartz, is preserved below a thin whitish crust.	Salt and gypsum crystals, no biological activity.	Spikes of gypsum growth.	Protein coating, egg similarities, decreased but present in mortar layer.

Table 2: continued.

Sample/ Origin / Sampling Location	FTIR - Flat Surface (F)	FTIR - Surface (S)	FTIR - Below Surface (B)	FTIR - Inverted Surface (I)	FTIR - Mortar (M)	OM - Surface	OM - Inverted	OM - Cross-Section	SEM - Surface	SEM - Cross-Section	Outcome
FAL_S11 Bathtub 3 (4^{th} - 3^{rd} BC - Hellenistic). Front wall - exposed to marine environment.	Gypsum and dolomite. Lipid and protein (low). As in S10.	N/A	N/A	N/A	Mainly calcite and very low amide content in 1315, 1540, 1633, 1643 and 1657.	Dark layer underneath whitish crust due to high quartz content. Very thin sample, similar to S9.	N/A	Uniform layer covers or is mixed with the upper calcite surface.	Layer (not mortar) is visible and cracked, uniform under depositions. Original layer is ruptured due to prsessure from salts underneath. Raptures indicate elasticity, similar to BG_M standards. Gypsum and low salt.	Fibre or hair in the layer below the surface. Some particles of biocalcite in pores.	Protein-lipid under gypsum and dolomite aggregate. Supported by OM and SEM.
FAL_S12 Cistern - 3 Hierarchs Church area - (2^{nd} - 4^{th} AD). Exposed to marine environment.	Protein predominant-lipid content (EW_M_75). More organic than in S spectrum. Low gypsum.	Protein-lipid content (EW_M_75).	Protein-lipid content (EW_M_75). Almost identical to surface.	N/A	Almost entirely calcite and small indications of protein in 1320, 1488, 1561 and 1662.	Fine and polished pinkish surface.	N/A	Fine calcite mortar and fine aggregate with ceramic inclusions.	Low deposition, parallel lines indicate polishing.	Hopper-like crystals most likely chlorides, colloidal mass of amorphous material (maybe phosphates).	Protein-lipid (egg white) on the surface layer under gypsum, reduces in mortar layer.

Table 2: continued.

Sample/ Origin / Sampling Location	FTIR - Flat Surface (F)	FTIR - Surface (S)	FTIR - Below Surface (B)	FTIR - Inverted Surface (I)	FTIR - Mortar (M)	OM - Surface	OM - Inverted	OM - Cross-Section	SEM - Surface	SEM - Cross-Section	Outcome
APT_S16 Bottle-shaped cistern (Roman Villa - 1st - 3rd AD). North inner side surface of the opening - 0.5m depth - exposure to high humidity.	High inorganic and water content. Protein-lipid less than in the S spectrum indicating better preservation of organic in the cross-section surface.	High inorganic and water content. Protein-lipid content, C-O stretching at 1265 and CH3 / CH2 at 1313 similar to egg parts and bone glue/mortar standards, mould on bone glue and droppings standards.	Protein-lipid content - lower than that of the surface.	N/A	Reduced organic presence but visible.	Mortar, not polished surface. Biological activity in three life stages: green, white and black.	N/A	High surface biological activity. High ceramic content mortar.	Biological activity filamentous and other.	Decayed upper surface.	Mortar mixture with organic instead of coating, or biological activity proteins-lipids, or degraded protein-lipid due to bio-activity. NOT Representative sample - exact location unknown.Supported by OM and SEM.
APT_S17 Bottle-shaped cistern (Roman Villa - 1st - 3rd AD). Loose piece from the bottom - exposure to high humidity.	Less organic peaks than in S spectrum. Egg white amide peaks similarities. Milk and mould shape of 2928 peak.	Mortar peaks and high water content. Similarities to droppings below 1200. 1200 sugars - cellulose material or droppings. 2921 shape of mould on BG. Mostly amides. Milk similarities.	Protein and calcite higher than the mortar - lower than surface.	N/A	Low protein, evidence at 1771. Shape of peaks show clay (ceramic mortar).	Mortar, not polished surface. Biological activity in three life stages: green, white and black.	N/A	High surface biological activity. Mortar of high ceramic content.	Biomineralization from bacteria calcite consumption. Different forms of biologival activity.	High biological activity.	Milk similarity is firstly introduced mostly explaining sugars. Mould is evident from the shape of 2929 but not from the rest of the organic peaks. Supported by OM and SEM.

Table 2: continued.

Sample/ Origin / Sampling Location	FTIR - Flat Surface (F)	FTIR - Surface (S)	FTIR - Below Surface (B)	FTIR - Inverted Surface (I)	FTIR - Mortar (M)	OM - Surface	OM - Inverted	OM - Cross-Section	SEM - Surface	SEM - Cross-Section	Outcome
APT_S18 Bathtub (Roman Baths - 1st AD). From the wall - exposed to rural environment.	Very low mortar. Lard, egg yolk and milk lipid-protein similarities. Lipids prevail. Egg yolk mainly due to peaks (shape matches DR1).	Low mortar, high water. Lard, egg yolk and milk lipid-protein similarities. Lipids prevail. 1261 C-O related to lipids. The same stands for 1317 and 1375-1386. 1450-1517, 1631-1666 show proteins. Shapes do not match.	Highest calcite content from all layers, similar organic to surface.	N/A	Similar organic to surface and below spectra, with calcite content closer to B spectrum.	Built-up of deposits, white-pinkish patina. Light brown layer is over a fine white calcite layer. Black spots locally.	N/A	Light brown layer over a fine white calcite layer.	Polished original layer, built-up of deposits. Decayed original layer shows polygonal crystals with amorphous colloidal phase. Algal cells growth from within the calcite - consuming the calcite or any organic. Similarities with E_M_25 standard.	Biomineralization due to presence of lichens (most likely).	Milk indication due to sugars and high lipid content. Lipid-protein content may also show egg yolk supported by most peaks in 1261-1660. Biological cannot be ruled out due to shape similarities with pigeon droppings. Either contamination of all layers or organic mixture (not coating). Physical evidence of organic/mortar consumed by microorganisms.
APT_S19 3-aisled cistern (Roman - 1st AD). 1st aisle - wall opposite the entrance - Biological growth on the wall - high humidity content - Pigeon nests.	Less gypsum than in S spectrum. Protein content as in bone glue and egg white mixtures, low esteric content.	Gypsum and calcite. No silica. Protein content at 1398, 1443-1466, 1659, 1691. Esters at 2935-2961 and 1319. Similar to milk, bone glue and egg white mortar mixtures.	Gypsum and protein low, similar to flat surface spectrum.	N/A	Mainly calcite, protein low.	Thick white crust and loose white particles. Brown surface underneath.	N/A	Mortar of high crushed ceramic content. White crust visible. Surface layer decayed/incorporated to white crust.	Thick layer of calcite crystals. Organic material as in POL samples, but also bacterial presence in limited scale (worm-like particles).	As on surface SEM.	Gypsum and protein mainly seen in the cross-section surface under the white calcite crust. Protein is visible in all layers but reduced inwards.

Table 2: continued.

Sample/ Origin / Sampling Location	FTIR - Flat Surface (F)	FTIR - Surface (S)	FTIR - Below Surface (B)	FTIR - Inverted Surface (I)	FTIR - Mortar (M)	OM - Surface	OM - Inverted	OM - Cross-Section	SEM - Surface	SEM - Cross-Section	Outcome
APT_S20 3-aisled cistern (Roman - 1st AD). 1st aisle - floor - highly contaminated by pigeon droppings and other deposits from frequent flooding (rain water).	Weak mortar peaks. Protein prevails, some esters, similar to droppings spectra.	Weak mortar peaks. Protein prevails, some esters, similarities with egg parts, bone glue, milk (low) and droppings spectra.	Lower organic content, more calcite.	N/A	Lowest organic content, more calcite.	Different deposits: black and thin, loose white particles, ceramic exposed, dark green surface locally, resinous substance locally.	N/A	Mortar of high crushed ceramic content and low amorphous calcite.	Flaking resinous substance, biological activity, original surface shows polishing.	Lower density surface over mortar, built-up of deposits.	Pigeon droppings derived protein most likely. Protein prevails but esteric bonds present. Surface protein, not a mixture with mortar. High biological activity. Supported by OM and SEM.
APT_S21 3-aisled cistern (Roman - 1st AD). 2nd aisle - connection of floor to wall towards the entrance.	Gypsum and less calcite. Maybe mould at 2927. Stair-step type intensities of egg and bone glue although similarities are found in droppings too.	Gypsum and calcite. Protein and ester content similar to egg mortar mixtures and droppings.	No gypsum. High protein content.	S14 similarities. Mostly dolomite. Absence of peaks in 1300-1500 region. 1606-1661 amide. Indication of ester at 2904.	Does not contain gypsum. High protein content.	Greenish biological, white loose crystals and reddish-brown resinous substance that covers the entire surface.	Resinous substance also seen in POL samples.	N/A	Limited biological activity -fibre substance on surface. Also amorphous substance.	Uniform layer of lime with low quartz aggregate and ceramics.	Gypsum on surface and protein-ester similar to egg mortar mixtures and droppings. Biological activity not certain - maybe early gypsum formation. Protein is retained in all layers.
APT_S22 3-aisled cistern (Roman - 1st AD). 2nd aisle - wall opposite the entrance.	More organic than in S spectrum. Similar shape of 1153-1164 with EY_M_75. Protein of egg and bone glue 1461-1471, 1634-1666-1681 (could this indicate early gypsum - loose white particles).	High calcite, 801-808 esters from egg yolk,egg and milk. 1261-1341 similar to POL_S14(S). 1619-1659, 1507 amides of egg mortar mixtures. 1201 possibly sugars.	Similar to F spectrum. Low 1262 but organic is present.	N/A	Organic portion is retained but reduced.	Pink to light cream, with loose white particles. Some black-green spots.	N/A	Visible cream-coloured layer. Mortar mainly of calcite and quartz with small and scarse ceramics. Differs from S19 ceramic inclusions mortar.	Mortar surface, no biological activity or organic, loose particles built-up of cubic crystals.	Pumice with some fibres in its pores.	High calcite, no biological activity, similarities with egg related organic, mainly on surface, reduces gradually towards mortar.

Table 2: continued.

Sample/ Origin / Sampling Location	FTIR - Flat Surface (F)	FTIR - Surface (S)	FTIR - Below Surface (B)	FTIR - Inverted Surface (I)	FTIR - Mortar (M)	OM - Surface	OM - Inverted	OM - Cross-Section	SEM - Surface	SEM - Cross-Section	Outcome
APT_S23 3-aisled cistern (Roman - 1st AD). 3rd aisle - low part of the side wall - water staining - biological activity.	2931-2991 protein. Rest of spectrum identical to surface. Similarities with egg white but also bone glue. Less gypsum than S spectrum.	Mortar absent, Gypsum prevails. Protein high and lipid present. 1339-1578 bone glue and egg white mortars as well as milk and egg similarities.	High gypsum, low calcite. Organic presence.	N/A	No gypsum, low calcite and quartz. Protein 1771 and lipids.	Similar to 2nd aisle S21. White loose particles over darkened resinous surface over whitish mortar.	Distinct black layer.	Weathered surface, ceramic-calcite-quartz mortar.	Fibres, hyphae network, growth of worm-like and spike crystals show gypsum.	Spikes of gypsum growth.	High gypsum and low calcite. Protein on surface, (some lipid), similar to egg white mortars, but high biological activity.
APT_S24 Gamma-shaped cistern (Roman - 1st AD). NW section - right wall (towards the south section) - exposed to external, dry, rural and marine environment.	Content similar to egg yolk ester - protein. 1264 indicates sulphate. Inorganic almost absent.	High organic, protein-lipid content similar to egg mixtures. 1263 could be sulphate.	Similar to surface, organic content and 1739 ester peak.	N/A	N/A	Cream surface covered by dark patina and black spots.	N/A	Black layer is visible over the mortar.	Black spots grow from within surface layer. Calcite biomineralization from amorphous surface substance. Spheres of protein-lipid. Mycogenic minerals.	Fine layer, maybe clay inclusions.	Sulphate present although not gypsum. Organic content similar to egg protein-lipid. Bio-activity. Supported by OM and SEM.
APT_S25 Gamma-shaped cistern (Roman - 1st AD). NW section - left wall towards the south - exposed to external, rural and marine environment.	1992-2136 similar to DR2 and bone (calcite probably). Similar spectrum to surface.	Mortar and organic. Protein and lipid, close to egg yolk, similar to S24.	Organic presence, close to surface spectrum but affected from increased inorganic.	N/A	Organic presence, peak intensity changes due to increased mortar presence.	Weathered surface, white crust locally, exposed ceramic inclusions.	N/A	Weathered upper layer, mainly calcite.	Flat smooth surface exists underneath the white crust, no biological activity.	N/A	Egg protein-lipid similarities, no biological activity. Surface layer organic reduces inwards.

Table 2: continued.

Sample/ Origin / Sampling Location	FTIR - Flat Surface (F)	FTIR - Surface (S)	FTIR - Below Surface (B)	FTIR - Inverted Surface (I)	FTIR - Mortar (M)	OM - Surface	OM - Inverted	OM - Cross-Section	SEM - Surface	SEM - Cross-Section	Outcome
APT_S26 Gamma-shaped cistern (Roman - 1st AD). NW section - connection of the right wall to the floor - exposed to external, rural and marine environment.	VIP for biological activity. Similar to S21 (F), S17 (S) and S17(F) and mould on bone glue at 2928. Very low calcite. Lipid-protein content.	Phosphates, sulphates, protein and lipid close to egg yolk. Resemblanse to DR1. Similar 1263 with the S22 (S) and S14 (S).	Similar to surface, organic content but higher inorganic.	N/A	Mainly calcite, protein low at 1631-1659, 1314 lipid.	Thick black crust deposited over smooth lime plaster with ceramic inclusions. Similar to S24.	N/A	Mainly lime, ceramic inclusions and quartz at lower layers.	Similar biological growth as S24 and honeycomb polygonal as on S18. Smooth mortar layer. Lichens most likely.	Weathered surface from biological activity that moves inwards pushing upper layer to detach.	Organic mainly on the surface, biological activity on the flat surface. Protein-lipid content close to egg parts. Flat surface similar to DR with indications of mould. Supported by OM and SEM.
APT_S27 Gamma-shaped cistern (Roman - 1st AD). NW section -floor - exposed to rural and marine environment - occasional rain water accumulation.	High organic with some mortar. Sulphates and phospates. Free fatty acids at 1706 or yolk amides. Egg white similarities (DR2 too but not physical presense).	Very high organic, similar 1263 to egg yolk. C-H in 1369-1389. Egg yolk and egg white amides 1472-1578, 1668-1684. DR2 similarities.	Similar to F spectrum, inorganic increases but organic is retained.	N/A	Mainly calcite, protein low at 1660, 1472 and 1318 (lipid).	Similar to S26. Salt crystals, dark deposits, black thick crust (on other piece).	N/A	Surface seems flat and fine.	Microorganisms are present. Smooth resinous layer partially preserved.	Biological activity moves inwards, leaving fibres in mortar.	Organic mainly on the surface, biological activity. Protein-lipid content close to egg products and DR. Supported by OM and SEM.
APT_S28 Gamma-shaped cistern (Roman - 1st AD). S. section - from wall - exposed to rural and marine environment.	Calcium C-O possibly in 1254 related to organic materials such as bones, bone glue and milk. 1317-1338 matching to eggs. Egg yolk and white similarities in 1634-1660.	Lipid-protein similar to egg yolk. 1741lipid present. 1256 is organic.	Preserves organic, minor intensity differences.	N/A	Preserves organic, minor intensity differences.	Biological activity and white crust on weathered mortar.	N/A	Decayed surface layer.	No biological activity on the surface, flake particles from ceramics.	Honeycomb growth within the mortar layer in depth, similar to S18 and S26.	Egg yolk lipid-protein similarities. Biological activity seems to affect calcite rather than the organic.

Table 2: continued.